VOLUME 80
PART B

ISSN 0037-1106
NUMBER 6

BULLETIN OF THE SEISMOLOGICAL SOCIETY OF AMERICA

DECEMBER 1990

Special Symposia Issue

REGIONAL SEISMIC ARRAYS AND NUCLEAR TEST BAN VERIFICATION

Frode Ringdal—Guest Editor

(Contents continues on back cover)

SEISMOLOGICAL SOCIETY OF AMERICA

ITS OBJECT

I. To promote research in seismology, the scientific investigation of earthquakes and related phenomena.

II. To promote public safety by all practical means.

III. To enlist the interest of engineers, architects, contractors, insurers, and property owners in the obligation to protect the community against disasters due to earthquakes and earthquake fires by showing that it is reasonably practicable and economical to build for security.

IV. To inform the public by appropriate publications, lectures, and other means to an understanding of the fact that earthquakes are dangerous chiefly because we do not take adequate precautions against their effects, whereas it is possible to insure ourselves against damage by proper studies of their geographic distribution, historical sequence, activities, and effects on buildings.

BULLETIN OF THE SEISMOLOGICAL SOCIETY OF AMERICA

The subscription rate for institutions and other non-members is $110 per annual volume. Orders for subscriptions should be sent to the Secretary with remittance in U. S. dollars. Society members receive the *Bulletin* as a perquisite of membership. Individuals may apply for membership using the form printed near the back of this *Bulletin*.

The *Bulletin of the Seismological Society of America* was first issued in 1911 and was a quarterly publication through 1962. It is now issued six times a year. Most back numbers of the *Bulletin* are still available in hard copy with the price for single copies as follows:

Volume 29, number 1	$10.00 per copy
Volumes 1 to 51 (1911 to 1961)	6.00 per number
Volumes 52 to 57 (1962 to 1967)	8.00 per number
Volumes 58 to 69 (1968 to 1979)	10.00 per number
Volumes 70 to 74 (1980 to 1984)	15.00 per number
Volumes 75 to — (1985 to ——)	18.00 per number

All back numbers are available on microfilm and microfiche. On fiche, Volumes 1 to 77 (1911 to 1987) are available for $575 ($475 for SSA members). On 35-mm film, the complete set is sold for $750. Individual fiche are $2 by annual volume only; individual reels of film are $40. Contact SSA Headquarters for details.

COMMUNICATIONS

Changes of address notices, subscriptions, renewals, and communications regarding back numbers, missed numbers, and membership should be addressed to SSA, Suite 201, Plaza Professional Building, El Cerrito, California 94530.

MANUSCRIPTS

Manuscripts offered for publication should be submitted to the Editor (see back cover for current address). Manuscripts should be submitted *in triplicate*, and the text should be double-spaced on one side of the paper. *Upon acceptance*, all text (including the abstract, references, figure legends, footnotes, and tabular matter) should be double-spaced on one side of the paper (copies are acceptable). Publication-quality figures should not be sent until requested, and when sent, the authors' names, figure number, and *an indication of orientation* (up arrow or top label) should be placed on the back of each publication-quality figure. The format of the paper should follow the pattern of recent numbers; in-house or research-contract reports are usually not acceptable. Figure captions and table headings should be typed separately and placed at the end of the manuscript, together with all tabular material. *Preparation of Disks.* Authors are encouraged to submit electronic diskettes of their manuscripts along with the typed REVISED manuscript. Diskettes produced on IBM or IBM-compatible computers are preferred, but those produced on Apple or Wang computers can also be converted. The following word processing programs are preferred: XyWrite III Plus, Word Perfect, Multimate, Display Write, Wordstar, CPT, Wang, MacWrite, Microsoft Word (Apple/Macintosh or IBM), Xerox, Volkswriter. Identify the diskette by providing journal name, manuscript number, senior author's name, manuscript title, name of computer file, type of hardware, operating system and version number, and software program and version number used. Only manuscripts with the equivalent of less than 20 printed *Bulletin* pages will normally be considered for publication. A referee's opinion is sought on each paper. Announcements of new results may be submitted as a *Short Note*. Discussions of published papers are welcome. Reprints, if desired by authors, must be ordered at the time corrected page proofs are returned to the printer.

Information for Contributors is reproduced in detail in the August (No. 4) issue of each annual *Bulletin* volume.

COPYRIGHT

Effective 01 January 1978, under Public Law 94-553, written transfer of copyright by authors to the Society is required to allow dissemination of material through abstracting journals, translations, etc. The previous implicit assignment by submission of the article is no longer sufficient. The assignment statement will accompany the acknowledgment form for signature. Authors retain the right to use the article in future works of their own.

◆ ◆ ◆

Published bimonthly in February, April, June, August, October, and December by
The Seismological Society of America
Suite 201, Plaza Professional Building, El Cerrito, California 94530
Second-class postage paid at El Cerrito, California 94530 and at additional mailing offices.
ISSN 0037-1106
Communications regarding publications apart from submission of manuscript
should be addressed to the Secretary, Suite 201, Plaza Professional Building, El Cerrito,
California 94530.

REPORT DOCUMENTATION PAGE

Form Approved
OMB No. 0704-0188

1. AGENCY USE ONLY (Leave blank)	2. REPORT DATE	3. REPORT TYPE AND DATES COVERED
	February 1991	Reprint

4. TITLE AND SUBTITLE
Regional Seismic Arrays and Nuclear Test Ban Verification

5. FUNDING NUMBERS
F49620-89-C-0038
Program Element: 62714E
PR 9A10 TA DA WU BH

6. ~~AUTHOR(S)~~ Editors:
David M. Boore, C. B. Crouse, John E. Vidale,
Steven G. Wesnousky, Frode Ringdal

7. PERFORMING ORGANIZATION NAME(S) AND ADDRESS(ES)
Royal Norwegian Council for Science & Industrial Research
NTNF/NORSAR
P. O. Box 51
N-2007 Kjeller, Norway

8. PERFORMING ORGANIZATION REPORT NUMBER

9. SPONSORING/MONITORING AGENCY NAME(S) AND ADDRESS(ES)
Phillips Laboratory
Hanscom AFB, MA 01731-5000

Contract Manager, James F. Lewkowicz/LWH

10. SPONSORING/MONITORING AGENCY REPORT NUMBER
PL-TR-91-2047

11. SUPPLEMENTARY NOTES
Bulletin of the Seismological Society of America
Volume 80, Part B, Number 6 - 1990

12a. DISTRIBUTION/AVAILABILITY STATEMENT
Approved for public release; distribution unlimited

12b. DISTRIBUTION CODE

13. ABSTRACT *(Maximum 200 words)*

This special issue of the Bulletin of the Seismological Society of America contains a collection of papers presented at an international symposium held in Oslo, Norway, on 14-17 February 1990. The purpose of the symposium was to assess recent scientific and technical advances in seismic monitoring of underground nuclear explosions, with emphasis on results obtained using advanced arrays specially designated to detect, locate, and characterize weak seismic events at local and regional distances.

14. SUBJECT TERMS
digital data recording systems; three-component stations; advanced arrays; NORESS; ARCESS

15. NUMBER OF PAGES
551

16. PRICE CODE

17. SECURITY CLASSIFICATION OF REPORT	18. SECURITY CLASSIFICATION OF THIS PAGE	19. SECURITY CLASSIFICATION OF ABSTRACT	20. LIMITATION OF ABSTRACT
UNCLASSIFIED	UNCLASSIFIED	UNCLASSIFIED	SAR

Bulletin of the
Seismological Society of America

Vol. 80 December 1990 No. 6

INTRODUCTION TO THE SPECIAL ISSUE ON REGIONAL SEISMIC ARRAYS AND NUCLEAR TEST BAN VERIFICATION

BY FRODE RINGDAL

This special issue of the Bulletin of the Seismological Society of America contains a collection of papers presented at an international symposium held in Oslo, Norway, on 14–17 February 1990. The purpose of the symposium was to assess recent scientific and technical advances in seismic monitoring of underground nuclear explosions, with emphasis on results obtained using advanced arrays specially designed to detect, locate, and characterize weak seismic events at local and regional distances.

Seismological methods provide today the primary means for detecting and identifying underground nuclear explosions and for estimating their yields. The importance of seismology in this very specialized field has long been recognized, and for more than three decades research programs have been conducted by a number of countries with the aim of improving the capabilities in this regard.

The results of this research have been significant and have had ramifications far beyond the field of seismic monitoring. It has led to improved understanding of a wide range of problems within general seismology, such as the nature of seismic sources, seismic wave propagation and attenuation, regional and global seismicity as well as the structure of the Earth.

An integral part of, and indeed a prerequisite for, these scientific advances has been the development of high-quality seismic instrumentation, digital data recording systems, and advanced data processing facilities. It is sufficient here to mention the impact of the World Wide Standardized Seismograph Network in the early 1960s, the large array experiment initiated in the mid-1960s, the digital Seismic Research Observatories in the 1970s, and additional advanced digital seismic stations in the past decade.

The recent development of sophisticated regional seismic arrays represents another milestone. After several years of design work including experimentation with trial configurations, the first such array, NORESS, was installed in southern Norway in 1984. Comprising 25 seismometer sites deployed in concentric rings over an area of only 3 km diameter, this array was especially designed to record and process signals of higher frequency that propagate in the local and regional distance range. In addition to significantly lowering the detection threshold for events at such distances, the array allows determination of the direction and distance from which seismic waves reach the station, as well as giving important information on the phase type. A high degree of automation in data processing is essential in view of the large amounts of data generated by such an array, and this was achieved at NORESS using a number of specially developed analysis algorithms.

Following the NORESS deployment, a second regional array (ARCESS) was established in northern Norway in 1987, and a third array of similar type (GERESS) is now coming into regular operation in Germany. A fourth, somewhat smaller

array, FINESA in southern Finland, has been operating experimentally for some time, and together these arrays form a network that will provide valuable data for research purposes within the field of regional monitoring.

Overviews of these four arrays, initial results from data analysis, and descriptions of the advanced data processing algorithms employed both in single- and multi-array analysis are given in several papers in the first part of this special issue. Other papers deal with evaluating the performance of such arrays and demonstrate their high potential, not only at regional distances but also in the teleseismic range. Many of the papers focus attention upon the direction estimation capabilities of small arrays and make comparisons to corresponding capabilities of high-quality three-component stations. It is important in this context to note that future monitoring networks are likely to be composed of a combination of this latter type of stations and advanced arrays.

While most of the contributions focus upon signal processing techniques for detection and location of weak seismic events, additional topics are also addressed. Seismic source identification is discussed in several papers, but it is recognized that the problem of discriminating between underground explosions and other seismic sources at low magnitudes will require much additional research. Promising results are reported on using the *Lg* phase to obtain stable estimates of the source size of underground explosions.

Several of the contributions are devoted to studies of general problems in seismology and geophysics. Among the topics discussed are seismic noise at high frequencies, frequency-dependent attenuation of seismic phases, wave-scattering phenomena, and the structure of the crust and upper mantle in parts of northern Eurasia. Again, much of this research emphasizes the value of regional arrays in addressing these problems.

In conclusion, it is fair to say that the papers in this special issue demonstrate that advanced regional arrays and the associated development and implementation of increasingly powerful data processing techniques represent a major advance in the field of seismic monitoring. Still, the process of exploiting the full potential of networks of regional arrays is only at its beginning. To fully exploit this potential represents both challenges and opportunities in the years ahead.

ACKNOWLEDGMENTS

Funding for the publication of this special issue has been provided by the Advanced Research Projects Agency of the Department of Defense, through the Air Force Geophysics Laboratory under NORSAR's Contract No. F49620-89-C-0038.

Bulletin of the Seismological Society of America, Vol. 80, No. 6, pp. 1777–1800, December 1990

APPLICATION OF REGIONAL ARRAYS IN SEISMIC VERIFICATION RESEARCH

BY SVEIN MYKKELTVEIT, FRODE RINGDAL, TORMOD KVÆRNA, AND RALPH W. ALEWINE

ABSTRACT

This paper gives an account of the work related to the development of the NORESS concept of a regional array. The array design considerations and objectives are reviewed, and a description is given of the NORESS and ARCESS array facilities in Norway with their field installations, data transmission lines, and data-receiving center functions.

The automatic signal detection processing of NORESS data applies multiple narrow-band frequency filters in parallel and forms array beams from selected subgeometries. The detection algorithm is based on computing the STA/LTA ratio for each beam individually, and a detection is declared whenever this ratio exceeds a given threshold. It is explained how the beam deployment and the individual threshold values can be tuned to ensure that the interesting phase arrivals are not missed, but at the same time how to avoid coda detections.

For each detected signal, frequency-wavenumber analysis is invoked to determine arrival azimuth and apparent velocity. Currently, a broadband estimator is used, and it is demonstrated that the use of this algorithm increases the stability of the azimuth and apparent velocity estimates, relative to narrow-band methods. Local and regional events are automatically located on the basis of identification and association of *P*- and *S*-wave arrivals. The uncertainty in the arrival azimuth is the limiting factor in accurately determining single-array event locations, and it is shown that this uncertainty is as large as 10° to 15° for *Pn* phases from certain regions.

In order to further investigate the potential of the NORESS concept, work was initiated toward installing a network of regional arrays in northern Europe. This involved the development of the ARCESS array in northern Norway and the installation of the FINESA array in Finland in cooperation with the University of Helsinki. Data from these three arrays have been used jointly in a location estimation scheme. It is shown that, for events in the Fennoscandian region of magnitude typically around 2.5 and for which at least one phase is detected by each array, location estimates can be obtained automatically that deviate from published network locations by only 16 km on the average.

In the future, it is anticipated that additional arrays and single stations in northern Europe will contribute real-time data to NORSAR for analysis jointly with existing arrays. The first additional data to become available will be from the GERESS array, which will be established in the Federal Republic of Germany in 1990. Future perspectives also include the use of expert system technology in the data analysis, and the IMS system already in operation represents the initial attempt in this regard. A summary is given of problem areas where further work is needed in order to fully exploit the regional array concept.

INTRODUCTION

The suggestion to use seismic arrays in order to detect, locate, and identify low-magnitude events for the purpose of verifying compliance with nuclear testing treaties dates back to the Geneva Conference of experts in 1958. In the 1960s and 1970s, seismic arrays were established in several countries around the world, and

the arrays were generally designed for optimum detection capabilities for events at teleseismic distances. The most ambitious undertaking in this regard was the development of the LASA arrays in the United States (525 short-period seismometers over an aperture of 200 km) and the NORSAR array in Norway (132 short-period seismometers, array aperture 100 km). Over the years, operation of teleseismic arrays has testified to their excellent performance in detecting weak arrivals, as well as their ability to estimate the direction and apparent velocity of incoming signals. A detailed review of these developments is given by Ringdal and Husebye (1982).

The trilateral negotiations of 1977 to 1980 on a Comprehensive Test Ban Treaty prompted a shift of interest from observations made at teleseismic distances to wave propagation in the regional regime (up to 2,000 to 3,000 km). It is in this context that experiments were initiated in Norway in 1979 toward the development of a "prototype" regional array, suitable for monitoring of low-level seismic activity within regional distance range. It was anticipated that this work would be aided and facilitated by the experience and knowledge gained from 10 yr of operation of the NORSAR array, but it was also realized that new experimental data had to be obtained to adequately design an array with the desirable performance for regional seismic phases.

The purpose of this paper is both to offer an overview of the work conducted since 1979 relating to the development of the NORESS and ARCESS arrays, and at the same time to give an assessment of the capabilities of these arrays. The regional array program with its associated research activities from its inception in 1979 has grown to become significant in both size and diversity. A complete review of these developments in beyond the scope of this paper. We will instead focus upon those aspects of these developments that, in our judgment, are the most important ones in the seismic monitoring context. This is done by first reviewing the considerations that went into the NORESS design efforts before details are given on the array installations and the NORESS and ARCESS field sites. The various steps in the automatic data processing are described, and the individual performance of each of the arrays in detecting and locating events at regional distances is assessed. Thereupon, we consider the capabilities of a network of NORESS-type arrays. In making our assessments, we summarize important findings available in the literature and supplement these with hitherto unpublished results from our own recent research. Finally, the results obtained during these past 10 yr are discussed, and some perspectives for the future are given.

NORESS Design Considerations

The desirable characteristics of a prospective prototype regional array were formulated at the outset of the experiments initiated in 1979: the array should be designed for optimum detection of regional seismic signals, and it should provide sufficient resolution to reliably estimate the apparent velocity and azimuth of all such signals. Furthermore, it was clear that the desirable performance of the array with respect to signal detection and characterization would need to be obtained over the wide range of frequencies typical of regional wave propagation. These requirements can be formulated in a more technical language, as follows:

- The array should provide close to optimum gain by beamforming for the phases and frequencies characteristic of regional wave propagation.

- The array geometry should be symmetric in order to offer equal capabilities for signals from all directions, and the response pattern should have a narrow main lobe and small side lobes.

It was clear at the outset that data from the NORSAR teleseismic array could not be used to infer an optimum array configuration for a regional array, as regional signals recorded at NORSAR with its minimum sensor separation of the order of 2.5 km are spatially aliased and furthermore do not correlate well even across the 10 km aperture subarrays. The main emphasis in the initial experiments was, therefore, placed on deriving signal and noise correlation curves for various frequency bands for intersensor separations in the distance interval of 0 to 2 km. Such curves can be used to express the beamforming gain G via the formula:

$$G^2 = \sum_{i,j=1}^{N} C_{ij} \Big/ \sum_{i,j=1}^{N} \rho_{ij} \tag{1}$$

where C_{ij} is the signal correlation between sensors i and j, ρ_{ij} is the corresponding noise correlation, and N is the number of sensors. The provisional configuration deployed in 1979 comprised only six instruments unevenly spaced within an aperture of 2 km. Still, signal and noise correlation curves were obtained that possesed most of the characteristic features and thus qualitatively resembled the curves derived later on from configurations comprising many more sensors. Examples of such curves, derived from the eventual 25-sensor NORESS geometry, are shown in Figure 1.

Analytical representations of the very early versions of the signal and noise correlation curves were used by Mykkeltveit *et al.* (1983) in equation (1) to find geometries that maximized the array gain G. It was demonstrated in that paper that optimized geometries could be obtained that were associated with theoretical gains well in excess of the standard $\sqrt{N}$ gain by utilizing negative minima in the observed noise correlation curves (see Fig. 1). Such optimum geometries, however, tended to

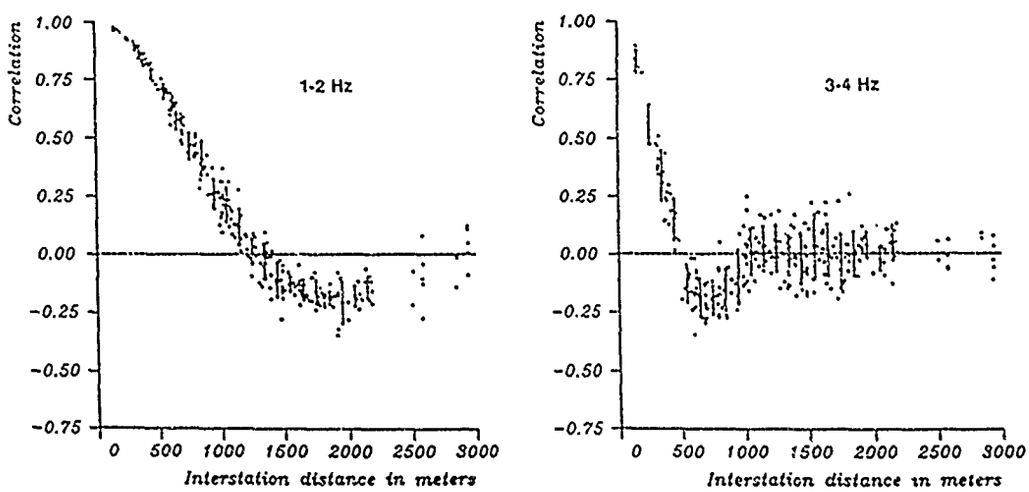

FIG. 1. NORESS noise correlations versus interstation separation for the two frequency bands of 1 to 2 Hz and 3 to 4 Hz. The noise segment used is 30 sec long and taken at 05:15 GMT on day 323 of 1985. Mean values and standard deviations with 100 m distance intervals are plotted on top of the population, except for short and long distances, where the number of correlation values is low.

be rather "peaked" in their frequency response, i.e., a very high gain at one particular frequency was generally accompanied by low gains at other frequencies. The optimized geometries were characterized by one particular intersensor spacing being represented as many times as possible in the geometry. This distance reflected the separation for which the noise correlation curve attained its minimum for a given frequency interval. For optimization explicitly taking several frequency bands into consideration (e.g., by giving equal weight, in the gain expression, to each of five different frequency bands), again one single intermediate frequency dominated the geometry. At this stage, it was realized that it would be difficult to arrive at configurations with a sufficiently broad frequency response following this strategy. Instead, the approach of estimating the gain via equation (1) was pursued in combination with design ideas set forth by Followill and Harris (1983). They proposed a geometry based on concentric rings spaced at log-periodic intervals in radius R, according to the relation:

$$R = R_{\min} \cdot \alpha^n, \qquad n = 0, 1, 2, 3. \tag{2}$$

The geometry of the NORESS array deployed in 1984 is a realization of (2), with $R_{\min} = 150$ m and $\alpha = 2.15$. Additional details on how the partly conflicting demands made on array performance were balanced by the adoption of this configuration can be found in Mykkeltveit (1985).

The NORESS array configuration is shown in Figure 2. There is a center element denoted A0, 3 elements in the innermost ring (A-ring, nominal radius 150 m), 5 elements in the B-ring (radius of 323 m), 7 elements in the C-ring (radius

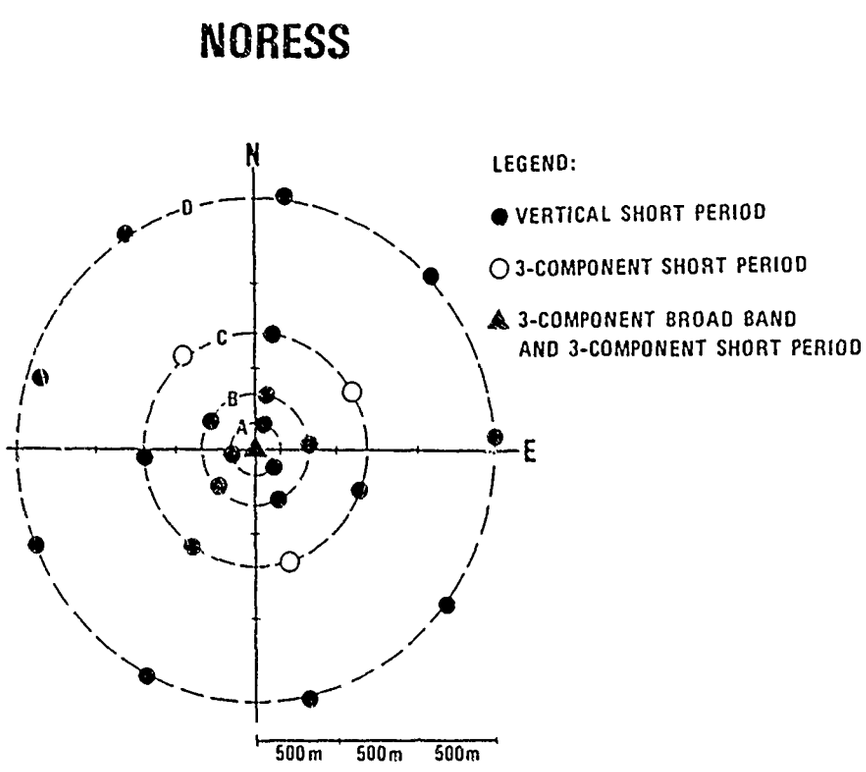

FIG. 2. The geometry of the NORESS array. The instrument at the center is denoted A0. The other sensors are arranged in four concentric rings: the A-ring, B-ring, C-ring and D-ring. The type of instrumentation at each of the sensor sites is given in the legend.

of 693 m), and 9 elements in the D-ring (radius of 1,491 m, giving an array aperture of approximately 3 km). The short-period stations at A0, C2, C4, and C7 are equipped with three-component instruments. It is readily seen from Figure 2 that there is a substantial range of intersensor separations present in the NORESS geometry, and that it offers a possibility of using widely different subgeometries for different signal frequencies.

Description of NORESS and ARCESS

The NORESS array was installed in southeastern Norway in the fall of 1984 (see Fig. 13 for location; array center coordinates are 60.735°N, 11.541°E) as a joint undertaking between NORSAR, the Defense Advanced Research Projects Agency, and Sandia National Laboratories. The array site is in a wooded area with relatively low population density. There is no human activity within the array except occasional forest work by the landowner. Competent bedrock with *P*-wave velocities of the order of 5.5 to 6.0 km/sec is found either at the surface or underneath a layer of soil of thickness up to a few meters. The rock is of Precambian age and is composed of gneisses and gabbro. A seismic reflection profile running north-south slightly east of the array center showed strong indications of a dipping reflector intersecting the surface in the southeastern part of the array (Mykkeltveit, 1987). Tomographic mapping of the velocity structure of the upper few kilometers beneath NORESS has been attempted by Ruud and Husebye (1990).

All NORESS short-period instruments are placed in shallow vaults on concrete pads anchored to the bedrock. The seismometer housing is a fiberglass construction sealed to the concrete pad to prevent water leakage. The three component broadband seismometer at the array center is deployed in a 60 m deep borehole. All data from the vaults and borehole are transmitted to the hub building at the array center via trenched fiber optic cables, which are used since they are immune to electrical disturbances from, e.g., nearby power lines and lightning. Each seismometer site is powered via buried cables from the hub building.

The NORESS short-period instruments are of type GS-13, and the broadband borehole seismometer is a KS-36000 instrument. The conversion of data from analog to digital form takes place in the vaults and in the borehole. A 16-bit A/D converter is used, with 2 of the 16 bits used for gain ranging in steps of 1, 8, 32, and 128. Short-period data are digitized at a rate of 40 Hz, whereas data from the broadband instrument are sampled both at 1 Hz for a long-period band at at 10 Hz for an intermediate-period band. The system transfer functions for the various passbands are shown in Figure 3. The high-frequency station that was integrated in NORESS in 1985 uses the analog output from the three-component short-period instrument at site A0 and digitizes this data at a rate of 125 Hz, using a 24-bit A/D converter. A detailed description of this system is given by Ringdal *et al.* (1990).

The ARCESS array installed in northern Norway in the fall of 1987 (array center coordinates are 69.534°N, 25.511°E; see location in Fig. 13) represented the first step toward a network of NORESS-type arrays. ARCESS is located at a distance of 1,174 km from NORESS in an area of low population density and little or no industrial activity. The array sensors are deployed on gabbro, which is mostly exposed since the soil cover is nonexistent or very thin (up to 0.5 m). The short-period seismometers are located in drums placed on the surface and covered with turf and moss, and the broadband instrument is in a 50 m deep borehole. Otherwise, the ARCESS field installation closely resembles that of NORESS: the geometries

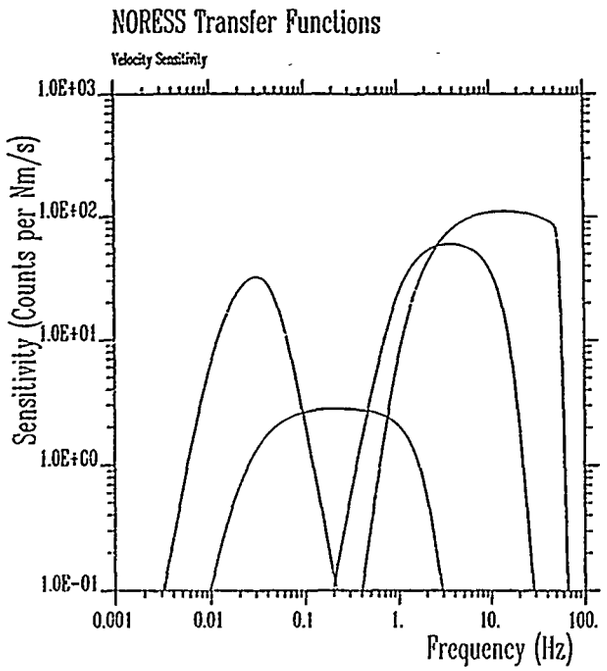

FIG. 3. NORESS transfer functions (velocity sensitivity) for (from left to right) the long-period, intermediate-period, short-period, and high-frequency band.

are nearly the same (deviations of the order of a few tens of meters in relative sensor positions exist due to adjustment to local terrain), and the seismic systems with sensors and other electronic components are identical.

All data from the field installations of NORESS and ARCESS are collected by the hub processors at the central sites and transmitted in real time to the NORSAR data processing center at Kjeller. NORESS data are transmitted over a 64 Kbits/sec land line, whereas a domestic satellite link with the same capacity is used to transmit ARCESS data. At Kjeller, the data are acquired on cyclic disk buffers that hold 72 hr of data for each array, processed, and permanently archived on magnetic tapes (on 8 mm video cassettes from February 1990). In this way, data from the last 3 days can be directly accessed from disk, whereas any data can be retrieved from the archive. NORESS and ARCESS data contain a substantial amount of environmental information (temperatures, humidities, wind speed, and direction), as well as state-of-health and instrument calibration data, which are being analyzed automatically at Kjeller to assist in detecting system malfunction. The total amount of data generated by each array per day and stored in the archives is approximately 400 Mbytes.

AUTOMATIC DATA PROCESSING

With the amount of data received continuously from arrays like NORESS, it is of paramount importance that reliable schemes for fully automatic event detection and location in near real time be developed and implemented. The development of such algorithms and procedures for NORESS went in parallel with the array design work in the early 1980s. The RONAPP (Regional ON-line Array Processing Package) code, described in Mykkeltveit and Bungum (1984) was the result of these efforts. In short, RONAPP detects phase arrivals using an STA/LTA detector applied to a number of beams, estimates arrival azimuth and apparent velocity for

the signals detected, and associates *P* and *S* arrivals for event location. Figure 4 serves as an illustration of this procedure. It shows NORESS data for a presumed nuclear explosion in the White Sea region of the USSR on 18 July 1985, at a distance of 1,550 km from NORESS. RONAPP detected *Pn*, *Sn*, and *Lg* arrivals from this event, as indicated in the figure. The information on arrival azimuth and apparent velocity derived by computing frequency-wavenumber spectra for short data segments around the arrival times is used together with standard travel time tables to identify the phases and locate the event.

The RONAPP processing package has evolved through several generations into the version currently in use. The main underlying ideas, however, remain the same as those described in detail in Mykkeltveit and Bungum (1984). In the following description of the current version of the package we, therefore, focus on those aspects that have undergone changes since 1984 in light of experience gained.

Signal Detection

The NORESS and ARCESS detection processing is similar to that of most other arrays: to enhance weak signals, a number of filtered beams (steered toward various hypothetical epicentral locations) are computed in real time and subjected to a

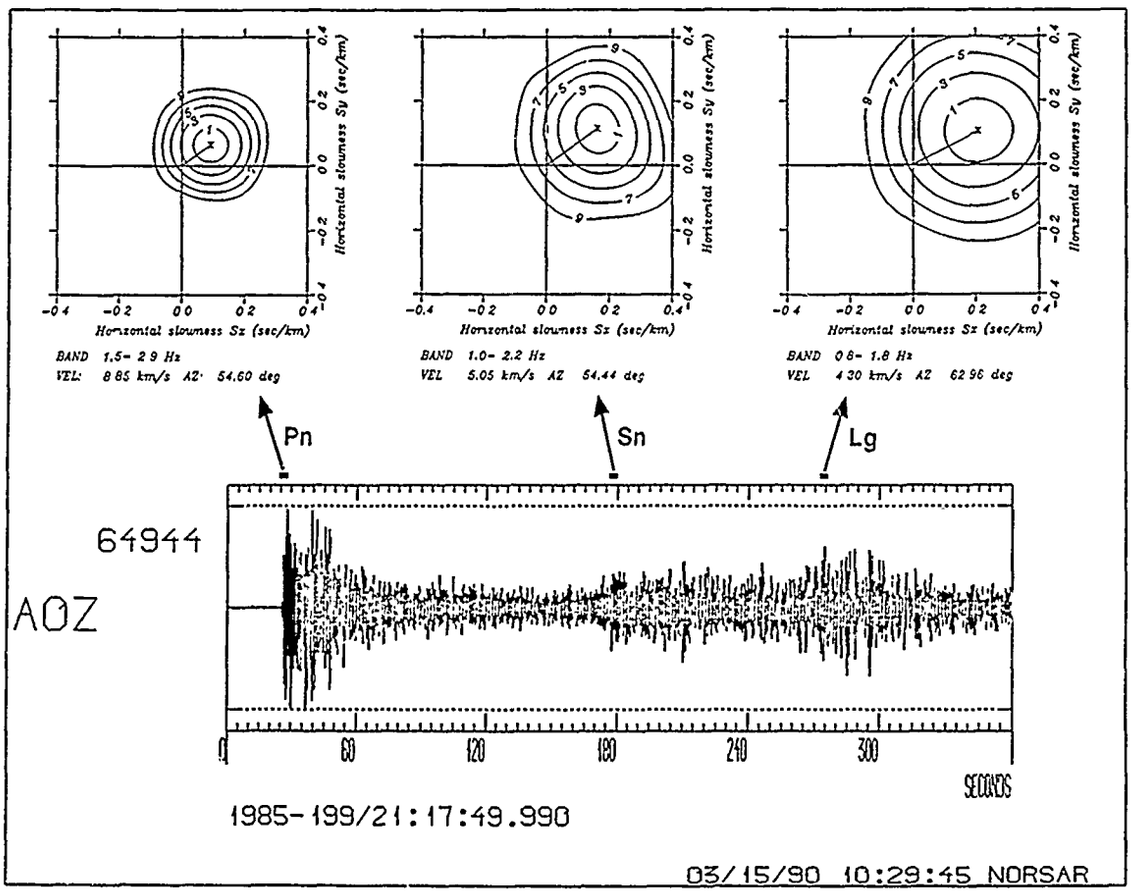

FIG. 4. The figure shows data from the vertical short-period sensor at NORESS site A0 for an explosion in the White Sea region of the USSR on 18 July 1985. (ISC solution: origin time of 21.14.57.7; epicenter at 65.96°N, 40.86°E; depth of 0 km; $m_b = 5.1$). Also shown are broadband frequency-wavenumber spectra computed for the short data windows (indicated on top of the trace) centered around the onsets of the *Pn*, *Sn*, and *Lg* arrivals.

conventional STA/LTA detector. Whenever the STA/LTA ratio exceeds a preset threshold, a detection is declared. When the threshold is exceeded for several beams within a 4-sec-long window, only one detection is declared, and it is attributed to the beam with the highest STA/LTA ratio.

The real challenge in the design of the detector is the selection of a proper beam deployment with associated detection thresholds. Figure 5 serves to illustrate some of the considerations involved. It shows NORESS data from a small event in western Norway, at an epicentral distance of approximately 350 km. The regional phases *Pn*, *Pg*, *Sn*, and *Lg* are clearly seen after enhancement by filtering the data in widely different frequency bands and also by displaying different components of the three-axis station at site A0. It is found for this particular event and many other events as well that the *Pn* and *Pg* phases are best observed on vertical channels, but in different frequency bands (here: 10 to 16 Hz for *Pn* and 3.5 to 5.5 Hz for *Pg*). The *Lg* phase stands out clearly in the 1 to 2 Hz band, also on vertical channels. The onset of the *Sn* phase, however, is very often found to have an impulsive character on the horizontal channels and in a relatively high filter band (here: 5 to 8 Hz). These examples show that a beam deployment designed for detection of regional phases must include several beams filtered within different narrow frequency bands for each steering direction. It is also important to utilize the horizontal components of the three-component stations for detection of phases like *Sn*.

The NORESS beam deployment in use since 13 April 1989 is given in Table 1. It is composed of 76 beams, of which 66 are conventional, coherent ones.

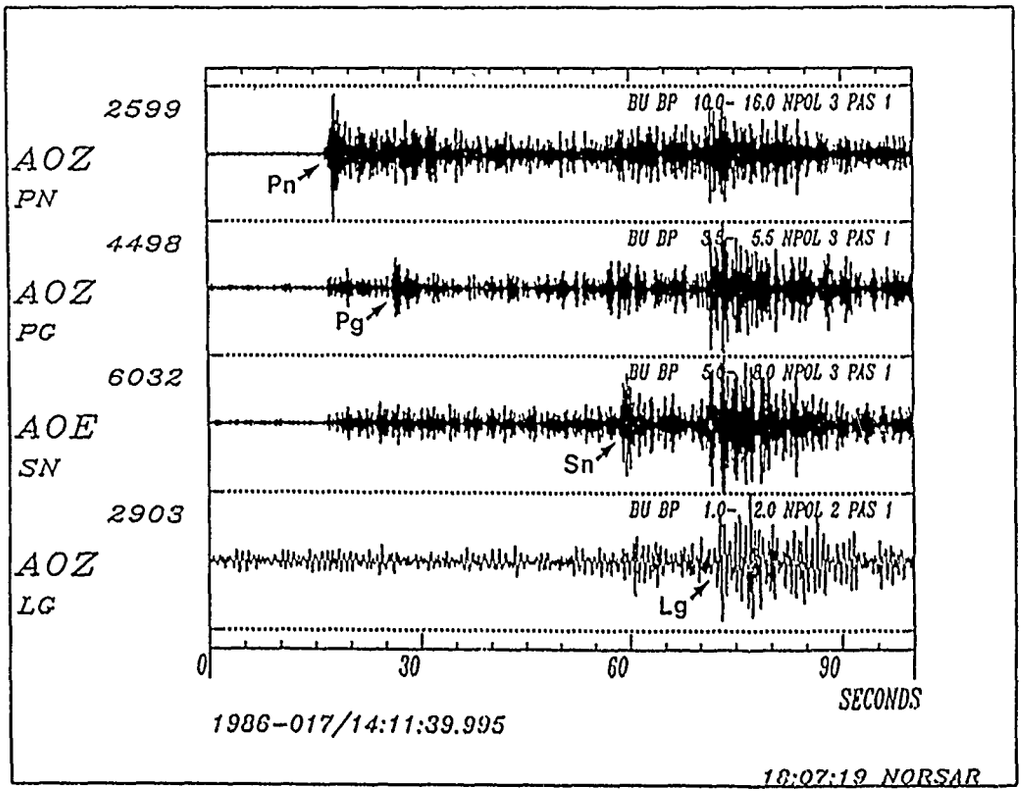

FIG. 5. NORESS data for a small event in western Norway at epicentral distance 350 km. The various regional phases are enhanced by frequency filtering in different passbands, as explained in the text. A0Z denotes the vertical component of the short-period sensor at the array center, whereas A0E is the horizontal east-west component at the same site.

TABLE 1

NORESS BEAM DEPLOYMENT

Beam	Velocity	Azimuth	Filter Band	Threshold	Configuration
N011	99999.9	0.0	0.5- 1.5	4.0	D
N021	99999.9	0.0	1.0- 3.0	4.0	CD
N031	99999.9	0.0	1.5- 3.5	4.0	CD
N032-037	11.0	*	1.5- 3.5	4.0	CD
N038	15.8	80.0	1.5- 3.5	3.5	CD
N039	10.0	30.0	1.5- 3.5	3.5	CD
N041	99999.9	0.0	2.0- 4.0	4.0	CD
N042-047	10 2	*	2.0- 4.0	4.0	CD
N048	15.8	80.0	2.0- 4.0	3.5	CD
N049	10.0	30.0	2.0- 4.0	3.5	CD
N051	99999.9	0.0	2.5- 4.5	4.0	BCD
N052-057	8.9	*	2.5- 4.5	4.0	BCD
N058	15.8	80.0	2.5- 4.5	3.5	BCD
N059	10.0	30.0	2.5- 4.5	3.5	BCD
N061	99999.9	0.0	3.0- 5.0	4.0	BCD
N062-067	10.5	*	3.0- 5.0	4.0	BCD
N068	15.8	80.0	3.0- 5.0	3.5	BCD
N069	10.0	30.0	3.0- 5.0	3.5	BCD
N071	99999.9	0.0	3.5- 5.5	4.0	BC
N072-077	11.1	*	3.5- 5.5	4.0	BC
N081	99999.9	0.0	4.0- 8.0	4.0	BC
N082-087	9.5	*	4.0- 8.0	4.0	BC
N091	99999.9	0.0	5.0-10.0	4.5	BC
N092-097	10.5	*	5.0-10.0	4.5	BC
N101	99999.9	0.0	8.0-16.0	4.5	AB
N102-107	9.9	*	8.0-16.0	4.5	AB
NH01	99999.9	0.0	2.0- 4.0	2.4	ne
NH02	99999.9	0.0	3.5- 5.5	2.4	ne
NH03	99999.9	0.0	5.0-10.0	2.4	ne
NH04	99999.9	0.0	8.0-16.0	2.5	ne
NV01	99999.9	0.0	0.5- 1.5	2.5	D
NV02	99999.9	0.0	1.0- 2.0	2.5	C
NV03	99999.9	0.0	1.5- 2.5	2.5	C
NV04	99999.9	0.0	2.0- 3.0	2.5	C
NV05	99999.9	0.0	2.0- 4.0	2.4	C
NV06	99999.9	0.0	3.5- 5.5	2.4	C

The table gives name of beam, steering velocity (in km/sec), steering azimuth (in °), filter band (in Hz), STA/LTA threshold, and subconfiguration (in terms of which rings are included; the sensor at the central site A0 participates in *all* beams). The NH01-04 beams are incoherent and use the eight horizontal channels (ne in the table, for north-south and east-west) of the stations at A0, C2, C4, and C7. The NV01-06 beams are also incoherent, and use vertical sensors as indicated. The remaining beams are conventional, coherent ones, using vertical channels only. The six coherent beams NH032-N037 are identical except for the steering azimuths, which have values of 30°, 90°, 150°, 210°, 270°, and 330°, respectively. The same pattern repeats for other coherent beams further down the table and is indicated by an asterisk in the azimuth column. Four special coherent beams are steered toward each of the test sites at Semipalatinsk and Novaya Zemlya (at azimuths of 80° and 30°, respectively).

These 66 beams are aimed at detection of P phases at all frequencies, and are designed and deployed in accordance with the criterion that the gain loss due to mis-steering should be less than 3 dB for any signal from any direction, arriving at NORESS with an apparent velocity above 6.0 km/sec. The subconfiguration defined for each of these beams is the one that has been found to provide the best SNR gain for the frequency band in question (see Kværna, 1989). Incoherent beams are

particularly suited for detection of secondary phases, which are often of an emergent nature. Ten such beams are included in the NORESS beam set, and are specifically aimed at detecting *Sn* (beams NH01–04) and *Lg* (beams NV01–06) arrivals. Details on incoherent beamforming are given in Ringdal *et al.* (1975).

The determination of detection thresholds needs special attention, and one important aspect is the balancing of thresholds between the coherent and incoherent beams. The thresholds given in Table 1 were determined on the basis of operational experience as well as theoretical considerations on false alarm rates. Details of how this was done are given in Kværna *et al.* (1987).

The beam set used at NORESS during 1 January 1985 to 13 April 1989 comprised 20 beams (see Ringdal, 1990), of which three were incoherent, and with individual thresholds very similar to the ones of the new beam set. The "old" beam deployment resulted in approximately 50,000 detections/yr, and the new and more extensive beam set has caused an increase in the number of detections, mainly due to an improved beam coverage for high frequencies. The ARCESS beam set is, since 1989, identical to that of NORESS, except for the steering parameters of the special beams directed toward Novaya Zemlya and Semipalatinsk. The number of detections on ARCESS exceeds that of NORESS (see Bratt *et al.*, 1990).

Estimation of Signal Attributes

Following the detection of a signal, best estimates of the arrival time, signal frequency, and amplitude are obtained as outlined in Mykkeltveit and Bungum (1984). A frequency-wavenumber (*f-k*) spectrum is then computed for a 3-sec-long time window, starting 0.5 sec before the detection time. Initially, the narrow-band *f-k* method described in Capon (1969) was used, but in 1989 a wide-band method described by Kværna and Doornbos (1986) was adopted. This analysis gives estimates of the arrival azimuth and apparent velocity of the detected signal. The signal is classified as *P* or *S*, corresponding to the apparent velocity being above or below 6.0 km/sec, respectively. In addition, various attributes characterizing the particle motions are extracted from the three-component stations, in accordance with a scheme devised by Jurkevics (1988). These attributes can be useful to distinguish *Pn* phases from *Pg* and *Sn* phases from *Lg*, although consistent separation is difficult to achieve.

Phase Association and Event Location

Simple rules and procedures are used to associate regional phases and determine event locations, based on the signal attributes estimated during the postdetection processing. These rules and procedures are given explicitly in Mykkeltveit and Bungum (1984). Modifications since then have essentially amounted to the following:

- Polarization information from the three-component stations is used in an attempt to determine whether a *P* arrival is *Pn* or *Pg*, and whether an *S* arrival is *Sn* or *Lg*.
- All regional signals with a phase assignment are used in the event location (previously only *Pn* and *Lg* were used). Events are located using the TTAZLOC algorithm by Bratt and Bache (1988).
- Phases are associated if their arrival azimuths deviate by less than 30° (previously 20°), and arrivals with apparent velocities exceeding 12 km/sec are not considered regional and are not used in event location.

Experience from more than 5 yr of continuous operation of NORESS (and more than 2 yr with ARCESS) has shown that the procedure described in this chapter is successful in completely automatically detecting and locating with a reasonable accuracy a substantial number (typically 10 to 20 per day, depending on day-of-week) of small regional events. In particular, we want to emphasize that it has proved to be possible to design the detector, with its beam definitions, associated thresholds, etc., in such a way that detections are declared in the routine processing for almost all regional phases that can be caught by the human eye (including those that can only be seen on the beams), without causing a high number of irrelevant detections, e.g., in the codas following the phase onsets. Too many detections will generally cause degradation of the performance of the phase association and event location steps. Figure 6 serves to illustrate this point. It shows the final output from the automatic processing of NORESS data from a mining explosion in Estonia, at an epicentral distance of 795 km. The *Pn*, *Sn*, and *Lg* phases have been detected and identified as such and subsequently used in the event location step. The *Pn* arrival was detected on the N073 beam with an STA/LTA ratio of 5.3. This beam is shown as trace no. 2 from the bottom of the plot. It has a steering azimuth of 90°, which is close to the azimuth of 96.5° estimated by the $f - k$ analysis for this phase. The *Sn* phase was detected on beam NH02 (this beam is not shown), and the *Lg* phase was detected on beam NV04, which is displayed in the form of a coherent beam as the bottom trace in Figure 6. Two additional detections in the *Lg* coda (indicated by small arrows above the upper trace) show *Lg*-type phase velocities and cause no difficulties in the automatic phase association and event location steps.

In addition to the regional arrivals, many teleseismic signals are detected by NORESS and ARCESS. In fact, the beam deployment in Table 1 was designed also with the teleseismic detection performance in mind, and several studies (e.g., Ringdal, 1990) have testified to the excellent capabilities of NORESS and ARCESS in this regard. Fluctuations in the seismic noise field also give rise to many detections at both NORESS and ARCESS, and these are usually characterized by very low (Rayleigh-type) apparent velocities. Kværna (1990) has demonstrated that one class of such detections at NORESS can be correlated with the waterflow in a nearby major river.

Capabilities of NORESS and ARCESS

In this section, we will review and assess the individual capabilities of NORESS and ARCESS to detect and characterize regional signals, as well as their ability to locate regional events.

Signal Detection Capabilities

Numerous investigations have testified to the excellent capabilities of NORESS and ARCESS to suppress the noise and thus obtain considerable beamforming gain. NORESS noise suppression spectra taken hourly during a 1-week period in July 1986 are shown in Figure 7. A noise suppression spectrum is estimated as the ratio of the beam power spectrum to the average power spectrum, taken over all contributing sensors. For the specific subconfiguration (A0, C- and D-ring sensors) used in Figure 7, the noise suppression is particularly effective in the 1.3 to 2.7 Hz band, where the suppression exceeds the $\sqrt{N}$ level expected for uncorrelated noise by up to 6 dB. The trend of the noise suppression curves in this frequency interval is the frequency-domain manifestation of the negative correlations observed in the curves

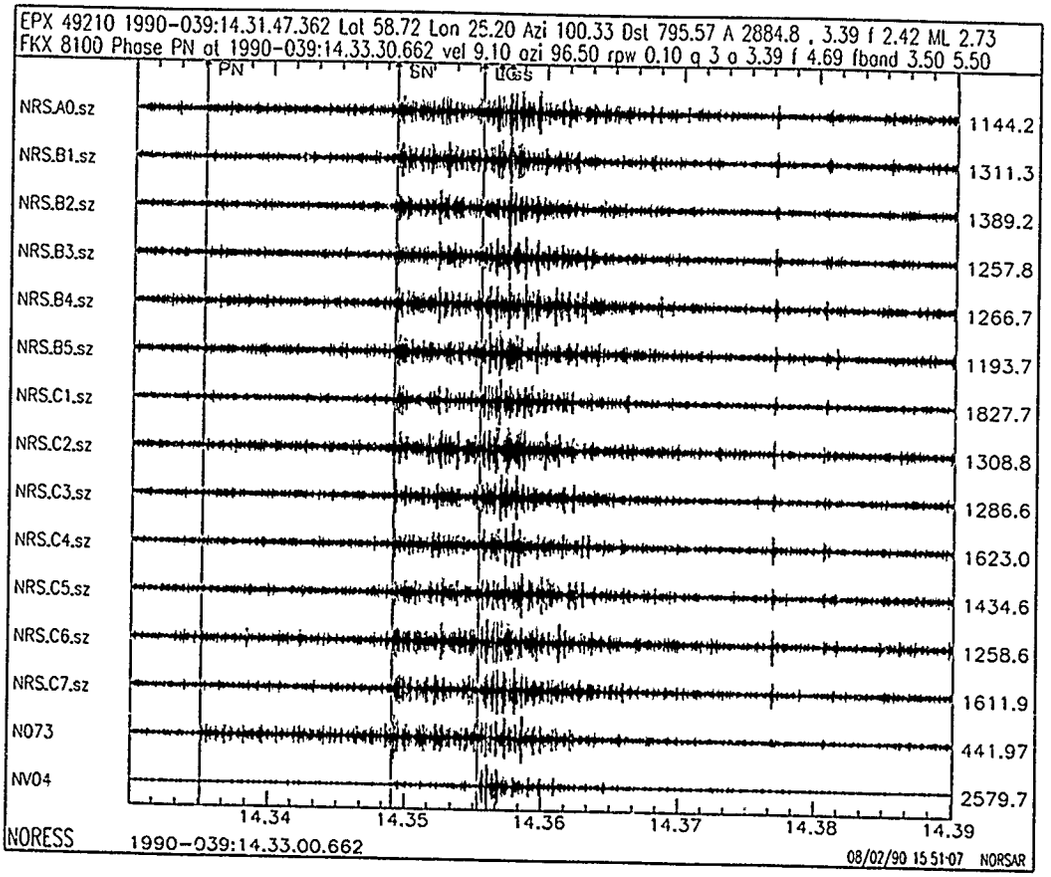

FIG. 6. NORESS event processor plot for a mining explosion in Estonia. The plot shows data for the vertical channels of A0 and all instruments in the B- and C-rings. The two bottom traces are the beams on which the *Pn* (beam N073) and *Lg* phase (beam NV04) were detected. Note that the incoherent beam is plotted here as a coherent beam, but with the steering delays, filters, and configuration as defined for the incoherent beam. Vertical bars across the panel indicate detected phases that are used in the TTAZLOC scheme (Bratt and Bache, 1988) to locate the event. Bulletin information is given in the upper line on top of the traces. The second line contains information pertinent to the *Pn* phase.

in Figure 1. Additional details on the NORESS noise suppression capabilities are found in Mykkeltveit *et al.* (1990), where it is also demonstrated that these capabilities are stable over time, and furthermore show no strong dependency on the actual noise level. Noise level variations at NORESS have been extensively studied by Fyen (1990).

Taking also signal correlations into account, Kværna (1989) has conducted a study to determine the achievable *P* phase SNR gains at NORESS for various frequencies. He concludes that, by carefully choosing the proper subgeometry at different frequencies, gains exceeding 10 dB can be consistently achieved over almost the entire band 0.5 to 10 Hz, with the highest average gains of 12 to 14 dB being obtained in the 1 to 4 Hz band.

The capability of NORESS and ARCESS to detect regional signals can be inferred from comparison with network bulletins for the region under study. Adopting the regional bulletin published by the University of Helsinki as a reference, we have associated *P* phases detected at ARCESS during January to March 1988 with events reported in this bulletin from the region of southern Finland and the surrounding areas of the western USSR, with epicentral distances relative to ARCESS in the range of 800 to 1200 km. Figure 8 gives a histogram of the number of reference

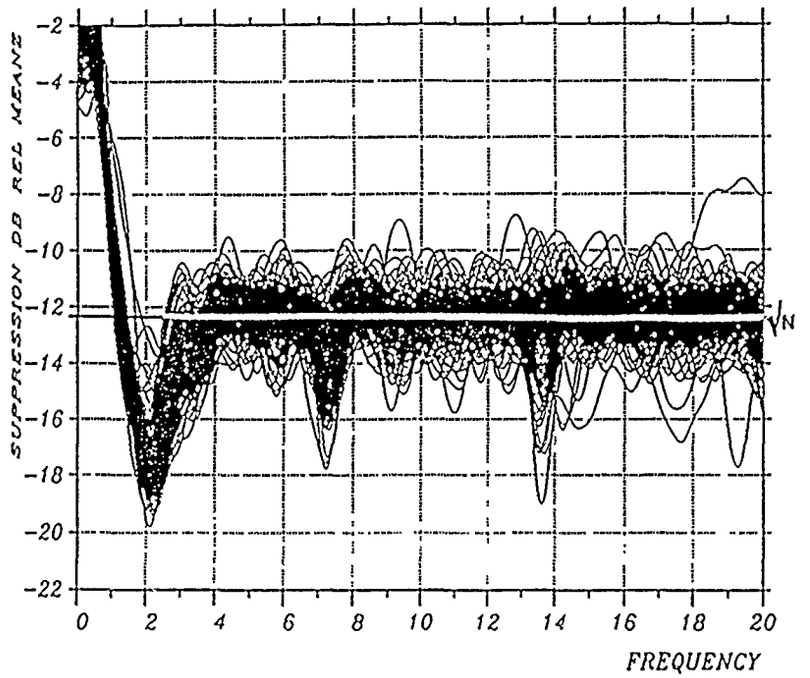

FIG. 7. The figure shows 168 NORESS noise suppression spectra taken hourly during a 1-week period in July 1986. The subgeometry used comprises the A0, C-, and D-ring sensors. The horizontal line indicates the $\sqrt{N}$ ($N = 17$ in this case) suppression level.

events at each magnitude with the events detected by ARCESS marked specially. The figure further contains a detection probability curve with associated confidence limits, estimated by the maximum likelihood method of Ringdal (1975). We note that the 90 per cent *P*-wave detection capability in the region studied is close to $M_L = 2.5$. This can be compared to the NORESS threshold of $M_L = 2.7$ found by Ringdal (1986) for detection of *P* waves for events in the same region. If the criterion is relaxed to detection of *either* a *P or* an *S* arrival, the 90 percent detection threshold is approximately 0.2 magnitude units lower.

The Novaya Zemlya Test Site is located at regional distance relative to both ARCESS and NORESS, and it is therefore of special interest to take a closer look at signals from this site. Figure 9 shows data for an m_b 5.9 (NEIC) explosion on 4 December 1988, for both ARCESS and NORESS. For both arrays, raw (upper trace) and filtered data (lower trace) in the 5 to 10 Hz band are shown for the sensor at C1. The *P* wave was detected at ARCESS with an STA/LTA of 9136 (filter band of 3 to 5 Hz for the detecting beam), and at NORESS with an STA/LTA of 796 (filter band of 2.5 to 4.5 for the detecting beam). While the ARCESS detection capability is definitely better than that of NORESS for Novaya Zemlya, the difference is not as large as indicated by the STA/LTA values. Thus, the reason for the low value for NORESS is partly that the first *P* arrival has a low amplitude relative to the main phase that arrives about 4 sec later. The maximum *P* amplitude is, in fact, similar for NORESS and ARCESS, even though the distance to NORESS is twice as large as the distance to ARCESS (20° and 10°, respectively). A comparison of the amplitudes of the data filtered in the 5 to 10 Hz band shows that the higher frequencies attenuate rapidly with distance. The secondary phase seen at ARCESS in *Sn*; the *Lg* phase is absent, most likely due to structural inhomogeneities and lateral variation of sediment thicknesses in the Barents Sea

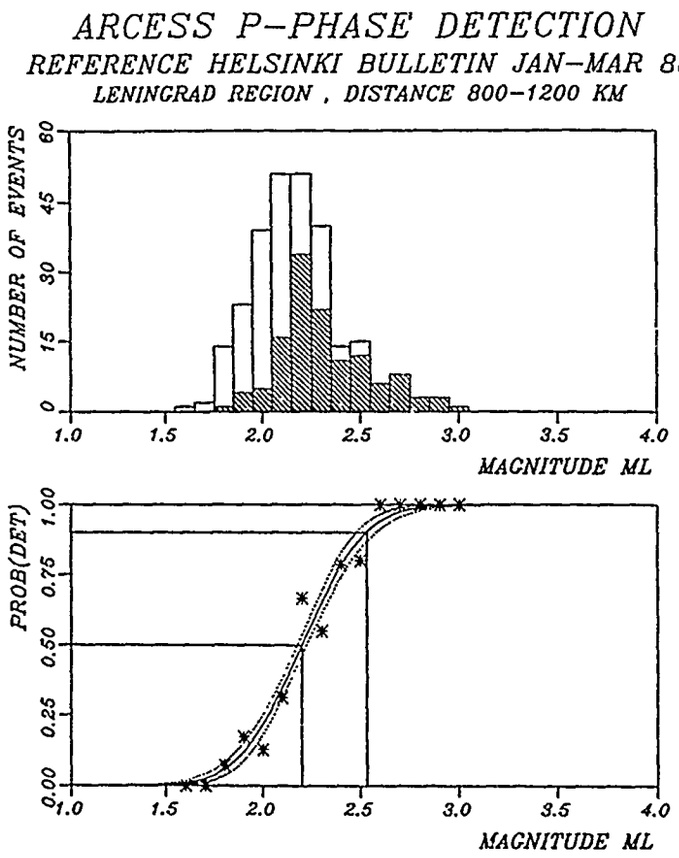

FIG. 8. *P*-phase detection statistics for ARCESS for regional events in the distance range from 800 to 1,200 km, using the *Helsinki Bulletin* as a reference. The upper part of the figure shows the distribution of events by magnitude with detected events corresponding to the hatched columns. The bottom part of the figure shows the estimated detection probability curve as a function of magnitude, with the observed detection percentages marked as asterisks. The stippled curves mark the 90 per cent confidence limits.

(Baumgardt, 1990). At NORESS, no secondary phases are readily visible in Figure 9, but at closer examination a weak *Sn* phase is seen in a low-frequency passband.

Comprehensive studies on spectral characteristics of regional phases in Fennoscandia have been carried out by several workers (see, e.g., Suteau-Henson and Bache, 1988; Ringdal *et al.*, 1990).

Signal Estimation Capabilities

As mentioned in the previous chapter, a broadband *f-k* estimator (Kværna and Doornbos, 1986) has replaced the narrow band *f-k* analysis technique in the signal estimation stage of the on-line data processing of NORESS and ARCESS data. Before this was done, the performance of the two techniques was compared on several different data sets. One such set was a suite of 10 chemical explosions at a dam construction site (Blåsjø) in southern Norway at a distance of 301 km from NORESS. The two analysis techniques were applied to the *Pn*, *Sn*, and *Lg* phases from the events, and the results in terms of estimated arrival azimuth and apparent velocity are shown in Figure 10. It is readily seen that the broadband method offers more stable results than the narrow-band technique for all phases. The separation between the *Sn* and *Lg* phases in quite clear for this data set. It is difficult, however, in general to separate *Sn* and *Lg* based on apparent velocities alone.

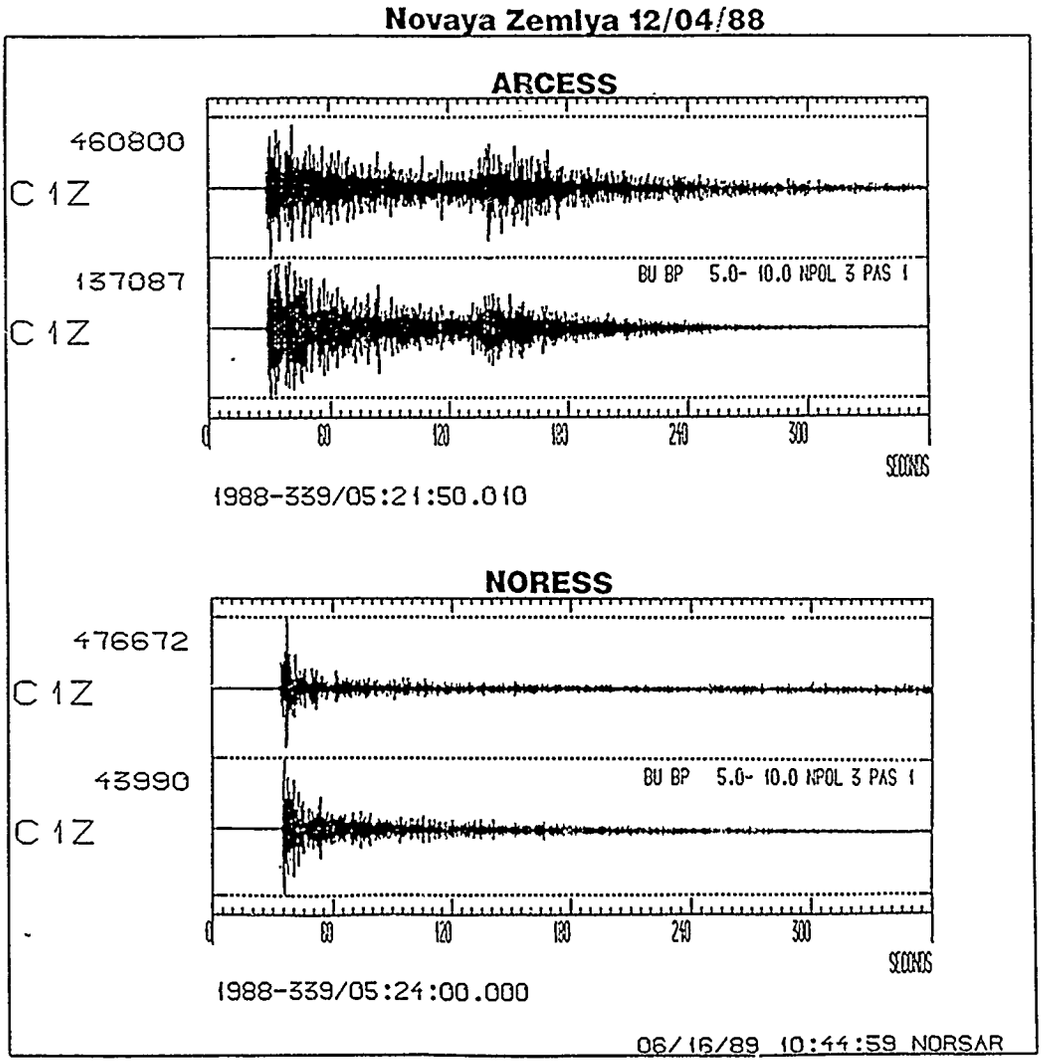

FIG. 9. NORESS and ARCESS data for the sensor at C1 for a nuclear test at Novaya Zemlya on 4 December 1988. Data are shown both unfiltered (upper trace) and filtered in the band 5 to 10 Hz (lower trace) for both arrays.

Our experience with this broadband estimator is in general very good, and it appears to be the best tool currently available for estimation of arrival azimuth and apparent velocity from NORESS and ARCESS data. Occasionally though, it is observed for events with known epicenters that the estimates deviate substantially from the true values, and deviations as large as 10° to 15° are observed for certain source regions even at high signal-to-noise ratios. These arrivals are coming in off azimuth due to structural inhomogeneities along the propagation path, and the estimates just reflect true propagation characteristics.

The three-component stations at NORESS and ARCESS can also be used to infer slownesses. These are, however, less accurate than those obtained by the f-k analysis using the vertical sensors of the array, particularly at low values of SNR (see Harris, 1990; Henson, 1990). In addition, three-component estimates are susceptible to surface topography (Ødegaard *et al.*, 1990). However, polarization information derived from three-component stations can aid in the classification of the phases (Jepsen and Kennett, 1990).

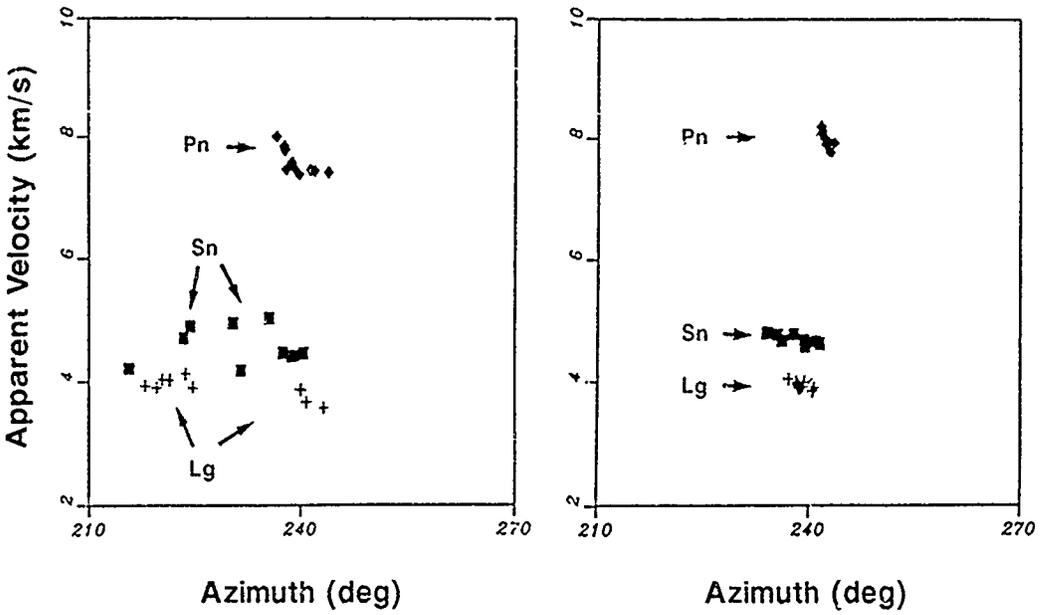

FIG. 10. The figure shows the results of the narrow-band (*left*) and broadband (*right*) *f-k* estimator applied to the *Pn*, *Sn*, and *Lg* phases observed at NORESS from a suite of 10 chemical explosions at a dam construction site in southern Norway. The processing frequencies for the narrow-band method were 7 Hz for *Pn* and 4 Hz for *Sn* and *Lg*. For the broadband method, estimates are given for the frequency intervals of 5.25 to 8.75 Hz for *Pn* and 3 to 5 Hz for *Sn* and *Lg*.

Event Location Capabilities

In order to accurately locate regional events using one-array data, both the epicentral distance and event azimuth must be reliably determined. The epicentral distance is determined on the basis of the travel-time difference between the various regional phases. Our operational experience indicates that the key issue in this regard is the proper assignment of phase types (*Sn*, *Lg*, and *Rg*) for the *S* waves detected. When only one *S* wave has been detected, it may be very difficult to decide whether it is an *Sn* or *Lg* arrival. An illustration of this is provided in Figure 11, which shows the relative strength of *Sn* and *Lg* for six events recorded on a short period sensor of the NORSAR array (the NORSAR array is co-located with NORESS). Figure 11 shows that *Lg* is strongly attenuated for certain propagation paths (as also observed in Figure 9 for the Novaya Zemlya to ARCESS and NORESS paths), and that *Sn* likewise is sometimes not seen at all (event 1). It is well known that these differences are related to structural inhomogeneities along the propagation paths.

A misidentification of *Sn* as *Lg* (or vice-versa) will easily cause an error in the epicentral distance estimate of several hundred kilometers. However, when phase types are correctly assigned, the epicentral distance can usually be determined to within a few tens of kilometers. As a rule of thumb, an error of 1 sec in the travel-time difference between an *S* and a *P* phase results in an error of 6 km in the epicentral distance. The accuracy in the travel-time difference largely depends on how well the arrival time of the *S* phase can be determined, and emergent arrivals represent a problem in this regard. When the phase onsets can be as reliably determined as shown in the example in Figure 6, however, the travel-time tables used become the limiting factor for accurate determination of epicentral distance.

Figure 12 shows azimuth residuals for *Pn* phases detected at NORESS during

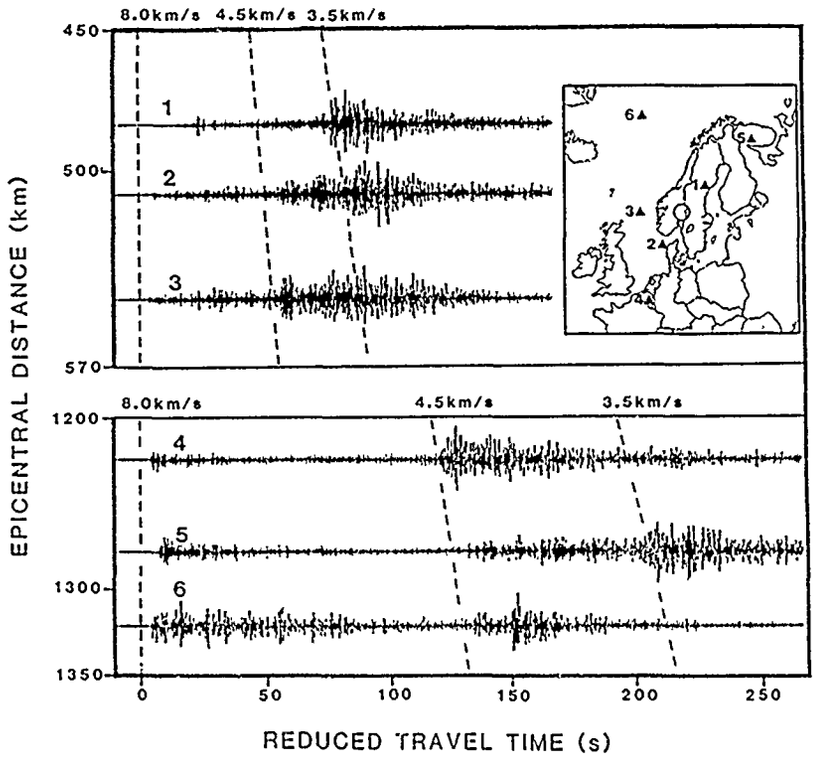

FIG. 11. Illustration of variation of relative importance of the phases *Sn* and *Lg* for six events with locations as indicated in the map. The standard group velocities of 4.5 and 3.5 km/sec, commonly assigned to *Sn* and *Lg*, respectively, are marked by dashed lines. The upper three traces cover the distance interval of 480 to 550 km, while the lower three traces correspond to epicentral distances in the range from 1,225 to 1,320 km. The location of the NORSAR array is denoted by a ring on the map, and the traces are from NORSAR seismometer 02B01. The data are bandpass-filtered 1 to 5 Hz. The reduction velocity is 8.0 km/sec.

1985 to 1988. The data were derived as follows: the NORESS detection lists were searched for *Pn* phases that could be associated with regional events reported in the Helsinki bulletin for this 4-yr period. The NORESS detection lists provide information on the arrival azimuth estimated for these *Pn* phases. The azimuth residuals (estimated azimuth minus "true" azimuth) were computed and averaged on a grid of 1° × 2° blocks (north–south and east–west, respectively). These average values are then represented as shown in the figure. For some of the blocks in the Estonian-Leningrad region of the USSR, averaging is done over several hundred azimuth residuals. Figure 12 shows that the azimuth residuals are moderate (less than 2.5° in absolute value) for large geographical areas, but there are also areas with complicated behavior, like the Estonian-Leningrad region. We note that the arrival azimuths derived during 1985 to 1988 were computed using the narrow-band *f-k* method, and that the broadband method currently being used is likely to cause a reduction in the absolute values of the residuals. In any case, the event locations will inevitably reflect such arrival azimuth uncertainties, and some kind of regional calibration will be needed (e.g., by taking information such as presented in Figure 12 into account and correcting the arrival azimuths accordingly).

NETWORK OF NORESS-TYPE ARRAYS

We have seen in the previous chapter that single-array event locations may deviate from true locations by typically several tens of kilometers and even more, if

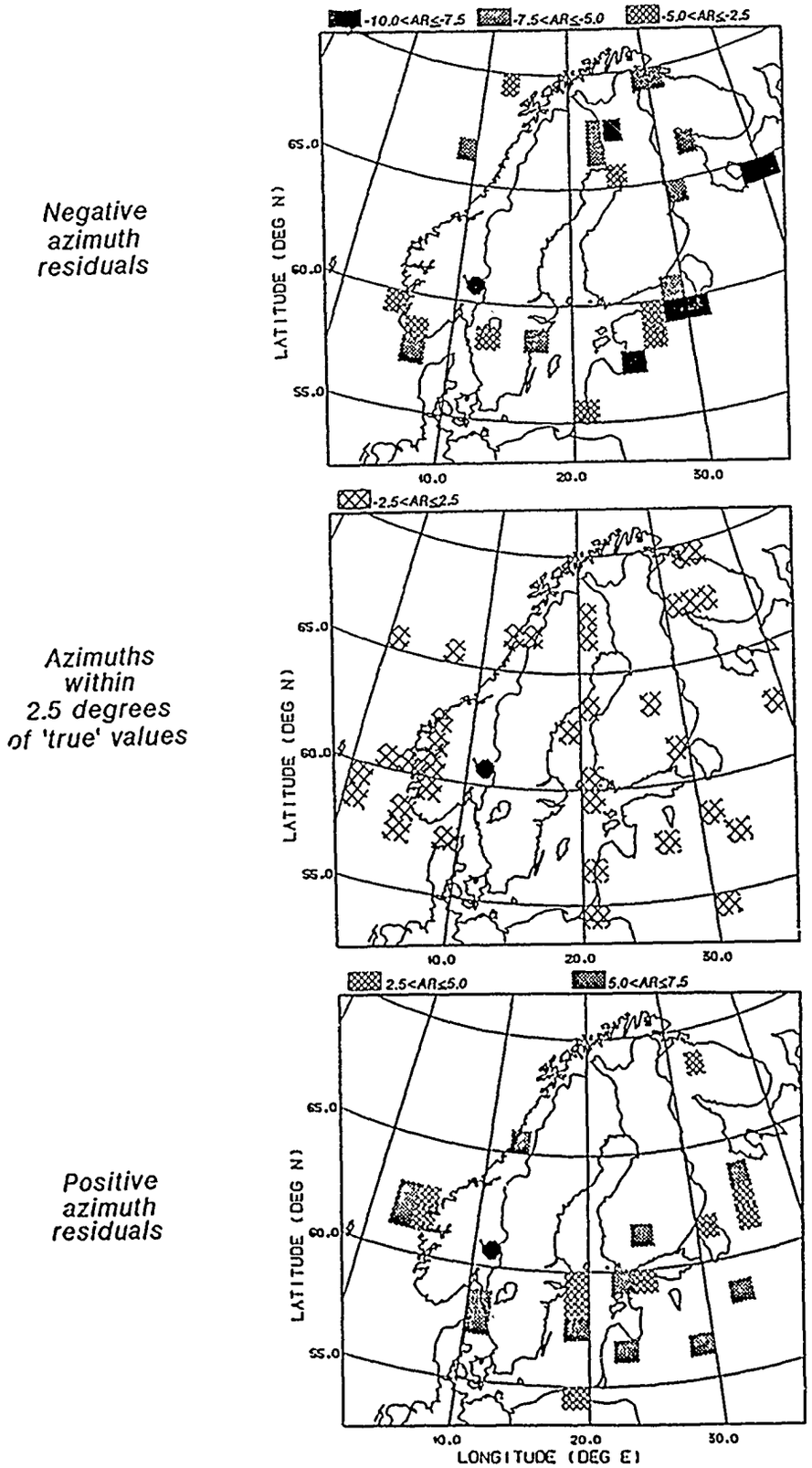

FIG. 12. Azimuth residuals [AR = estimated azimith minus "true" azimuth (in °)] for *Pn* phases detected at NORESS during 1985 to 1988, for events reported in the *Helsinki Bulletin*. See text for further explanation.

phases are incorrectly assigned. The next step to improve the event location capability would be to install a network of NORESS-type arrays. This effort started with the installation of the ARCESS array in 1987, and continued with the deployment of the somewhat smaller FINESA array in Finland (Uski, 1990) in cooperation with the University of Helsinki, and the GERESS array in the Federal Republic of Germany (Harjes, 1990). Data from FINESA are since 1 January 1990 available in real time at the NORSAR data processing center at Kjeller and are being processed in the same way as data from ARCESS and NORESS. (The first version of the FINESA array was installed in 1985, but before 1 January 1990 data were recorded in trigger mode and on tapes at the array site only.) Data from GERESS will be available from the summer of 1990 and will also be transmitted to Kjeller for on-line processing.

We report here on the findings of an investigation where data recorded at FINESA during experimental operation in March 1988 were used together with NORESS and ARCESS data in assessing the capabilities of this three-array network in locating events in the Fennoscandian region. A set of 10 events, for which there was at least one detected phase for each array, was selected for an event location experiment. The events are listed in Table 2 and shown in Figure 13. The event magnitudes range from less than 2.0 to 3.2. The epicentral locations for the 10 events are taken from the Helsinki bulletin.

The continuous processing of data recorded at each of the three regional arrays provides (among others) estimates of arrival times, arrival azimuths, and indication of phase type, as explained in the previous chapters. These parameters together with the associated uncertainties were used as input to the TTAZLOC program developed by Bratt and Bache (1988). TTAZLOC incorporates the arrival time and azimuth data into a generalized-inverse location estimation scheme, and can be applied to both single-array and multiple-array data. Table 2 gives the results of the location experiment. On the average, the joint three-array locations deviate from the network locations published in the Helsinki bulletin by 16 km. Two-array

TABLE 2

TTAZLOC LOCATION EXPERIMENT RESULTS

Event No.	Network		Magnitude (M_L)	No. of Phases Used	Three-Array "Error" (km)	Average 2-Array "Error" (km)	Average 1-Array "Error" (km)
	Latitude	Longitude					
1	67.1	20.6	<2	5	19	31	36
2	59.5	26.5	2.5	8	9	8	39
3	60.93	29.19	2.4	6	34	34	34
4	59.5	25.0	2.3	8	8	23	95
5	63.2	27.8	2.5	6	32	31	41
6	58.33	10.93	2.7	7	16	24	44
7	69.6	29.9	2.9	8	4	13	45
8	59.3	27.2	2.3	5	15	36	108
9	59.72	5.62	3.2	6	9	51	179
10	69.2	34.7	2.6	5	15	12	57
Average over 10 events					16	26	68

Results from TTAZLOC location experiments using data from NORESS, ARCESS, and FINESA. Epicentral locations are given as reported in the *Helsinki Bulletin* for a set of ten regional events that occurred between 12-18 March 1988. The table gives the deviation from these reference locations, as inferred from the TTAZLOC experiment described in the text.

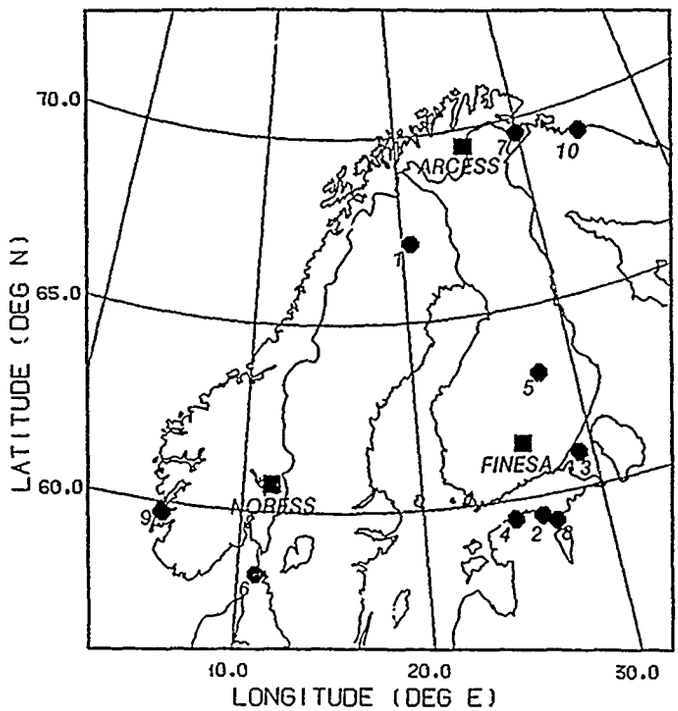

FIG. 13. The map shows the location of the three regional arrays NORESS and ARCESS in Norway and FINESA in Finland, as well as the location of the 10 events used in the TTAZLOC location estimation experiment.

and one-array locations were computed for all combinations of events and array subnetworks, also using the TTAZLOC algorithm. The resulting average deviations from the network solutions are 26 and 68 km, respectively. Bratt and Bache (1988) and Bratt *et al.* (1990) have also considered event mislocations using one-array and two-array data, and their results agree well with those reported here.

We see that the result for two-array locations represents a significant improvement over one-array locations, and that there is a further improvement when invoking data from three arrays. We consider the results reported here as quite promising, when considering the following:

- The arrival times used were those determined automatically by the on-line processing. It is conceivable that human intervention for adjustment of arrival times and/or refinement of the automatic procedure would improve the location estimates.
- Only standard travel-time tables for the phases *Pn*, *Sn*, and *Lg* were used. The introduction of regionalized travel-time tables is likely to result in improvements.
- Master event location schemes of various kinds hold considerable promise and are expected to further enhance the capabilities of accurately locating regional events.

DISCUSSION AND PERSPECTIVES FOR THE FUTURE

This paper has summarized the main results from 10 yr of research at NORSAR on regional arrays and their capabilities in detecting and characterizing seismic phases from events at regional distance. Assessments have also been given of the

accuracy in determination of event locations from one-, two-, and three-array data. In summary, we have found that P waves from events in the magnitude range 2.5 to 2.7 at distances around 1,000 km are detected with a probability of 90 per cent, that the detector can be tuned so as to ensure detection also of emergent S-wave arrivals, that the important signal attributes of regional phases (like arrival azimuth, apparent velocity, state of polarization, etc.) can be adequately characterized using a broadband f-k estimator on the vertical sensors of the array in combination with techniques for analysis of three-component data, that the regional phases can be associated with a set of simple rules, and finally, that regional events can be located with an accuracy of the order of 15 km when data from a network of three arrays are used. It is noteworthy that these results are all obtained from fully automatic data processing, i.e., without human intervention of any kind.

Throughout this paper, we have dealt with the issue of formulating rules that can be used in the automatic data processing. Such rules are generally suitable for the application of artificial intelligence technologies in the form of so-called expert systems. While several such systems have been designed and experimentally applied to processing of regional array data (e.g., Mason *et al.*, 1988; Hiebert-Dodd, 1989), the most ambitious development so far is the Intelligent Monitoring System (IMS), described by Bache *et al.* (1990). The aim of the IMS is to automate as much as possible the seismic data interpretation process, thus taking advantage of results such as those reported in this paper. It is currently being developed into a complete system for integrated, automatic processing of data from a network of regional arrays and single stations. The first version of the IMS has been operated at the Center for Seismic Studies in Arlington, Virginia, and at NORSAR since the fall of 1989. Initial results for the performance of IMS on data from NORESS and ARCESS are given by Bratt *et al.* (1990).

The deployment of advanced regional arrays, and the associated development and implementation of automated and increasingly powerful data processing techniques, represents one of the major advances in the field of seismic monitoring in recent years. Arrays of the NORESS/ARCESS design have demonstrated capability to lower the detection threshold by more than 0.5 magnitude units over a wide range of signal frequencies relative to traditional seismic stations. Furthermore, such regional arrays provide reliable phase identification and azimuth estimates that are particularly useful in locating weak events that are detected by only a few stations. In a seismic monitoring context, these are precisely those events that will need to be given the most emphasis.

Still, the process of exploiting the full potential of regional arrays is only at its beginning. Much research remains to be done in developing methods for integrated processing of data from a regional network composed of arrays and three-component stations, and to assess its capabilities in a seismic monitoring context.

An essential aspect will be the further development of advanced processing technology to handle the data acquisition and quality control, data base organization, automatic interpretation, and interactive computer graphics that will be required in an actual monitoring situation. From a seismological point of view, research topics to be addressed will include:

Signal processing: An important task will be to improve current methods for automatic detection, phase identification, and onset time determination, with particular emphasis on *Sn* and *Lg* phases. Methods should be developed to exploit the potential for array processing of three-component recordings offered by

NORESS-type arrays and to improve polarization analysis techniques at low SNR. There is a need to address the problem of how to automatically resolve multiple events, i.e., two or more events with detected phases that are intermixed in time (e.g., multiple mining explosions).

Regional cclibration: An important aspect is the development of region-specific corrections for travel-time and azimuth anomalies. Furthermore, as attenuation characteristics of various seismic phase types (*Pn*, *Pg*, *Sn*, *Lg*, and *Rg*) are highly path-dependent, it will be essential to accumulate regional-specific knowledge in this regard. This will also contribute to the establishment of consistent regional magnitudes scales, which should be developed and calibrated for compatibility with teleseismic magnitude.

Master event techniques: The most powerful method currently available to obtain very precise epicenter and depth estimates is joint hypocentral determination using well-recorded master events. This concept should be systematically extended to more general script-based pattern matching techniques, using the full array capabilities and incorporating both time domain and frequency domain features. This would be particularly useful to monitor specific mining locations and test sites, and should be accompanied by optimized beam and filter settings for such areas of special interest. The method for continuous threshold monitoring (Ringdal and Kværna, 1989) should be further developed and applied in such a context.

Source identification: Although efforts to develop regional discriminants so far have met with little success, this essential research should be pursued, aiming at obtaining systematic rules, developed on a region-specific basis. An important task will be to identify mining shots, and the very promising approach of characterizing spectral attributes of ripple-fired explosions should be given particular attention. The use of regional surface waves (e.g., *Rg*) in source identification is also an important area of further research.

The key to further progress in this field would appear to be development and application of regional-specific knowledge, both for the purpose of detection, location, depth estimation, and source characterization. Much of the necessary knowledge can only be obtained through experimental operation over an extended period of time. The regional array network now being developed will in a unique way contribute to the establishment of such a knowledge base. The associated data management and processing facilities will ensure the availability of the data and the dissemination of the accumulated knowledge, and will thus aid in future efforts directed toward these research goals.

ACKNOWLEDGMENTS

Over the years, numerous individuals both in Norway and elsewhere, have contributed actively to the research reported in this paper. In particular, the entire NORSAR staff is thanked for their efforts and enthusiasm, and we are especially indebted to Hilmar Bungum, Jan Fyen, Paul W. Larsen, and Rune Paulsen for their valuable contributions to the regional array research program. This research was supported by the Advanced Reserach Projects Agency of the Department of Defense and was monitored by the Air Force Office of Scientific Research under Contract F49620-89-C-0038.

REFERENCES

Bache, T. C., S. R. Bratt, J. Wang, R. M. Fung, C. Kobryn, and J. Given (1990). The Intelligent Monitoring System, *Bull. Seism. Soc. Am.* **80**, Part B, 1833–1851.

Baumgardt, D. R. (1990). Investigation of teleseismic *Lg* blockage and scattering using regional arrays, *Bull. Seism. Soc. Am.* **80**, Part B, 2261–2281.

Bratt, S. R. and T. C. Bache (1988). Locating events with a sparse network of regional arrays, *Bull. Seism. Soc. Am.*, **78**, 780–798.

Bratt, S. R., H. J. Swanger, R. J. Stead, F. Ryall, and T. C. Bache (1990). Initial results from the Intelligent Monitoring Systems, *Bull. Seism. Soc. Am.* **80**, Part B, 1852–1873.

Capon, J. (1969). High-resolution frequency-wavenumber spectrum analysis, *Proc. IEEE* **57**, 1408–1418.

Followill, F. and D. B. Harris (1983). Comments on small aperture array designs. Informal Report, Lawrence Livermore National Laboratory, Livermore, California.

Fyen, J. (1990). Diurnal and seasonal variations in the microseismic noise level observed at the NORESS array, *Phys. Earth Planet. Interiors* **63**, 252–268.

Harjes, H.-P. (1990). Design and siting of a new regional array in Central Europe, *Bull. Seism. Soc. Am.* **80**, Part B, 1801–1817.

Harris, D. B. (1990). A comparison of the direction estimation performance of high-frequency seismic arrays and three-component stations, *Bull. Seism. Soc. Am.* **80**, Part B, 1951–1968.

Hiebert-Dodd, K. L. (1989). Assisting experts in their data analysis tasks—an AI approach, *Mathematics and Computers in Simulation* **31**, 475–484.

Jepsen, D. C. and B. L. N. Kennett (1990). Three component array analysis of regional seismograms, *Bull. Seism. Soc. Am.* **80**, Part B, 2032–2052.

Jurkevics, A. (1988). Polarization analysis of three-component array data, *Bull. Seism. Soc. Am.* **78**, 1725–1743.

Kværna, T. (1989). On exploitation of small-aperture NORESS type arrays for enhanced *P*-wave detectability, *Bull. Seism. Soc. Am.* **79**, 888–900.

Kværna, T. (1990). Sources of short-term fluctuations in the seismic noise level at NORESS, *Phys. Earth Planet. Interiors* **63**, 269–276.

Kværna, T. and D. J. Doornbos (1986). An integrated approach to slowness analysis with arrays and three-component stations, *Semiannual Tech. Summary, 1 October 1985–31 March 1986*, NORSAR Sci. Rept. No. 2-85/86, Kjeller, Norway.

Kværna, T., S. Kibsgaard, and F. Ringdal (1987). False alarm studies and threshold determination for regional event detection. *Semiannual Tech. Summary, 1 April–30 September 1987*, NORSAR Sci. Rept. No. 1-87/88, Kjeller, Norway.

Mason, C. L., R. R. Johnson, R. M. Searfus, D. Lager, and T. Canales (1988). A seismic event analyzer for nuclear test ban treaty verification. Technical Report UCRL-98069, Lawrence Livermore National Laboratory, Livermore, California.

Mykkeltveit, S. (1985). A new regional array in Norway: design work and results from analysis of data from a provisional installation, in *The VELA Program. A Twenty-Five Year Review of Basic Research*, A. U. Kerr, Editor, Defense Advanced Research Projects Agency.

Mykkeltveit, S. (1987). Local geology of the regional array sites in Norway. *Semiannual Tech. Summary, 1 April–30 September 1987*, NORSAR Sci. Rept. No. 1-87/88, Kjeller, Norway.

Mykkeltveit, S., K. Åstebøl, D. J. Doornbos, and E. S. Husebye (1983). Seismic array configuration optimization, *Bull. Seism. Soc. Am.* **73**, 173–186.

Mykkeltveit, S. and H. Bungum (1984). Processing of regional events using data from small-aperture arrays, *Bull. Seism. Soc. Am.* **74**, 2313–2333.

Mykkeltveit, S., J. Fyen, F. Ringdal, and T. Kværna (1990). Spatial characteristics of the NORESS noise field and implications for array detection processing. *Phys. Earth Planet. Interiors* **63**, 277–283.

Ødegaard, E., D. J. Doornbos, and T. Kværna (1990). Surface topographic effects at arrays and three-component stations, *Bull. Seism. Soc. Am.* **80**, Part B, 2214–2226.

Ringdal, F. (1975). On the estimation of seismic detection thresholds, *Bull. Seism. Soc. Am.* **65**, 1631–1642.

Ringdal, F. (1986). Regional event detection using the NORESS array, *Semiannual Tech. Summary, 1 October 1985–31 March 1986*, NORSAR Sci. Rept. No. 2-85/86, Kjeller, Norway.

Ringdal, F. (1990). Teleseismic event detection using the NORESS array, with special reference to low-yield Semipalatinsk explosions. *Bull. Seism. Soc. Am.* **80**, Part B, 2127–2142.

Ringdal, F., E. S. Husebye, and A. Dahle (1975). *P*-wave envelope representation in event detection using array data, in *Exploitation of Seismograph Networks*, K. G. Beauchamp, Editor, Nordhoff-Leiden, The Netherlands, 353–372.

Ringdal, F. and E. S. Husebye (1982). Application of arrays in the detection, location and identification of seismic events, *Bull. Seism. Soc. Am.* **72**, S201–S224.

Ringdal, F. and T. Kværna (1989). A multi-channel processing approach to real-time network detection, phase association, and threshold monitoring, *Bull. Seism. Soc. Am.* **79**, 1927–1940.

Ringdal, F., S. Mykkeltveit, J. Fyen, and T. Kværna (1990). Spectral analysis of seismic signals and noise recorded at the NORESS high-frequency element, *Phys. Earth Planet. Interiors* **63**, 243–251.

Ruud, B. O. and F. S. Huebye (1990). Exploring the upper crystalline crust: a joint interpretation of 3D imaging and reflection profiling at the NORESS array, *Tectonophysics* (in press).

Suteau-Henson, A. (1990). Estimating azimuth and slowness from three-component and array stations, *Bull. Seism. Soc. Am.* **80**, Part B, 1987–1998.

Suteau-Henson, A. and T. C. Bache (1988). Spectral characteristics of regional phases recorded at NORESS, *Bull. Seism. Soc. Am.* **78**, 708–725.

Uski, M. (1990). Event detection and location performance of the FINESA array in Finland, *Bull. Seism. Soc. Am.* **80**, Part B, 1818–1832.

NTNF/NORSAR
P.O. Box 51
N-2007 Kjeller, Norway
(S.M., F.R., T.K.)

DARPA/NMRO
1400 Wilson Boulevard
Arlington, Virginia 22209
(R.W.A)

Manuscript received 30 April 1990

Bulletin of the Seismological Society of America, Vol. 80, No. 6, pp. 1801–1817, December 1990

DESIGN AND SITING OF A NEW REGIONAL ARRAY IN CENTRAL EUROPE

By Hans-Peter Harjes

Abstract

In recent years, increased interest has emerged in the evaluation of high-frequency seismic signals from events at regional distances. Small-sized and many-element arrays, like NORESS in Scandinavia, have proven capable of taking advantage of the very efficient propagation of high-frequency seismic phases.

After an extensive field survey, the Bavarian Forest (BF) area at the south-eastern border of the Federal Republic of Germany with Austria and Czechoslovakia was chosen as a target region to install a NORESS-type array. The BF area—as part of the Bohemian Massif—represents the largest outcropping crystalline complex in Central Europe.

Detailed noise measurements show average values for the power spectrum slightly lower than 1 nm^2/Hz at 1 Hz and a fairly smooth decay proportional to f^{-4} per decade up to 40 Hz, leading to a value of 10^{-4} nm^2/Hz at 10 Hz and 10^{-5} nm^2/Hz at 20 Hz. Diurnal variations due to industrial noise sources, such as saw mills, are primarily found in the 4 Hz to 10 Hz band. Compared to Scandinavia, the noise level in Central Europe is comparable or even lower for frequencies about 1 Hz, but it is about a decade higher at 10 Hz and above.

The spatial correlation properties of noise and signals were investigated using data from a temporary 9-element array with a diameter of 3 km. In the 1 to 2 Hz band, the noise coherence values drop to 0.25 at interstation distances of 800 m and in the 2 to 4 Hz band at 400 m, respectively. There is no clear evidence for a negative noise correlation distance at these frequencies. Signal coherence in the same frequency bands proved to be excellent (>0.9) for all regional phases over the 3 km aperture of the test array.

The final configuration of the new regional array in the BF area—named GERESS—has been selected as a slightly enlarged NORESS-type ring geometry with an innermost radius of 200 m and with a large radius of about 2,000 m.

Introduction

Since the establishment of the Graefenberg (GRF) array in 1980, array research in Germany has focused on teleseismic data, due to the broadband instrument response with a high-cut filter at 5 Hz and average interstation distance of more than 10 km. In recent years, increased interest has emerged in the evaluation of high-frequency signals from events at regional distances. Small-sized and many-element arrays like NORESS have proven capable of taking advantage of the very efficient propagation of high-frequency seismic phases. Together with a similar recently installed array in Northern Norway (ARCESS), the proposed array in Southern Germany (tentatively named GERESS = GERman Experimental Seismic System) would comprise an array network with nodes at roughly 1,000 km intervals. Such a configuration is particularly suited for automated location procedures applying antenna theory, and it is relevant in view of a possible deployment of "in-country" seismic systems for surveillance of a possible future nuclear test ban treaty.

In Central Europe, a siting survey has to carefully investigate noise sources due to the dense population, high traffic, and various industries. Apart from the local noise conditions, a sufficient number of seismic signals from different azimuths should be recorded and evaluated to assess the propagation of high-frequency

signals, especially across tectonic boundaries like the Tornquist–Teisseyre suture between the Russian Platform and Western Europe or the influence of the Alps on signals originating from the Mediterranean earthquake region.

After describing the site survey, a typical noise power spectrum, taken from data recorded in Southern Germany, will be compared with spectral noise conditions in Scandinavia. A low-noise profile is only one condition for a reasonable array site. Equally important is the transfer function of the receiver crust that influences the signal characteristics and the signal-to-noise ratio. Unlike the fairly homogeneous Scandinavian shield, the geologic conditions in Central Europe are rather complex, reaching from thick alluvial sediments in the North German Basin which is separated by the Variscan mountain front from the Alpine foreland to the Alps itself. Besides the Black Forest at the Eastern Rhinegraben, the Bavarian Forest area at the border to Czechoslovakia and Austria represents the largest outcropping crystalline block in Germany. This region is particularly suited for an array installation of the proposed kind, as has been demonstrated by the excellent detection capabilities of conventional seismic stations in Austria and Czechoslovakia.

In the section on "Array Design," signal and noise correlation measurements in the Bavarian Forest area will be described that are used as important constraints for the array design. For this purpose, a nine-element array was operated temporarily around the site where the lowest noise values were found previously. From these measurements, the final geometry of the GERESS array was determined and its array response is compared with the existing Scandinavian arrays. A preview on the installation schedule of the new array will be given in the "Discussion and Preview" section, including information on the type of instruments and the data acquisition units used.

Site Survey

Field work was carried out initially in October 1987 and then continuously from April to July 1988. Some additional data were collected later in 1988 to assess the long-term variability of noise conditions and to calibrate the results with data from well-defined events (e.g., JVE explosions in Nevada and Kasakhstan).

Unlike NORESS, which is built within a subarray of the large teleseismic NORSAR array, it was not possible to collocate the new high-frequency array with an existing GRF subarray because the latter teleseismic broadband array is placed on a sedimentary column that strongly attenuates high frequencies. As shown in Figure 1, the new array site is situated about 150 km east of the GRF array location.

The noise measurements are concentrated on the outer Bavarian Forest just east of a major fault line named the "Pfahl," which separates the Bohemian Massif from the western Molasse—a quaternary and tertiary sedimentary basin in the Alpine foreland. The advantage of the Bavarian Forest area is its geological setting (crystalline outcropping rocks) and the low population density. The landscape is mostly mountainous, up to 1,200 m elevation. Nearly all recording sites were situated in extensive forest areas to minimize cultural noise, and instruments were installed on granite of gneiss rocks to record high frequencies, especially from events at regional distances. Due to the installation on the surface, the seismometers were quite sensitive to wind noise but for technical and financial reasons, no other arrangement was feasible. Detection capabilities derived from noise estimates of these data should represent conservative values.

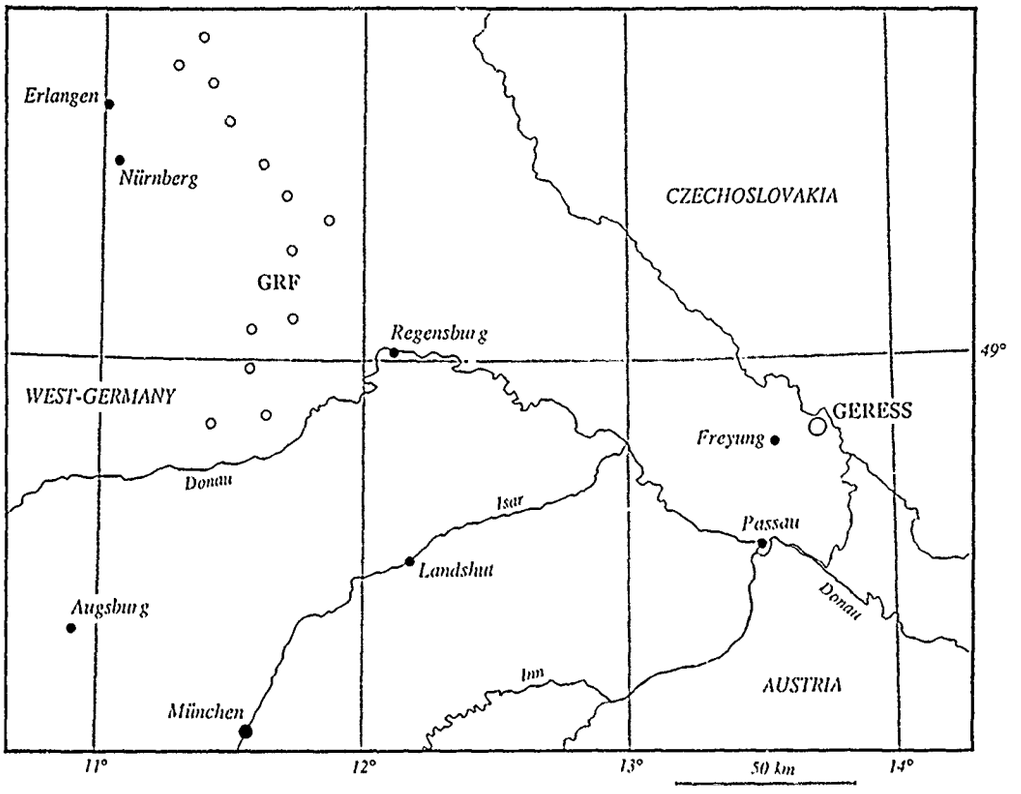

FIG. 1. Geographical location of the existing teleseismic GRF broadband array and the planned regional GERESS array.

For survey purposes, three portacorders with direct recording were used. In case of favorable places, one of three digital data acquisition systems was installed for a time period of several weeks. The digital systems were PCM recording instruments of Lennartz 5800-type with the following specifications:

ADC = 66 dB resolution, Gain ranging 126 dB dynamic range
Sampling frequency = 250 Hz Low-pass filter = 44 Hz, 6-pole Bessel.

Each PCM system was equipped with three vertical short-period seismometers (1 Hz Geotech S-13), which were installed at distances between 100 and 300 m to avoid false alarms by coincidence triggering.

Very soon, the site survey concentrated on an area which is closest to the CSFR border. Very few roads, low population density, and extensive woodland offered adequate preconditions for seismic installations. The first station was established in April 1988. It was placed on weathered granite. Later, two other stations were established on gneiss. During the US/USSR Joint Verification Experiment in 1988, an additional station was installed on granite at a place where adequate housing and power facilities were available to operate as a hub for a temporary small array subsequently. All four sites were located within a radius of 5 km. Portacorder records showed a generally low noise background and small day-to-night variation. The only obvious disadvantage appeared to be some sawmills that generated monochromatic seismic noise during working hours.

For comparison, some noise samples were taken at the GRF array (station B5), which confirmed earlier measurements showing relatively high cultural noise levels. Finally, during a short trip to Norway in October 1988, some recordings were made at NORESS to get a direct comparison of noise values using the same data acquisition system and, more important, the same processing procedure as for the area under investigation in Germany.

The processing of field data included several steps. At the beginning, the PCM field tapes had to be converted to a standard 9-track IBM-compatible format. Having recorded the field data in event mode, the pre-event window can be used for noise evaluation. There are many well-established methods to estimate the power spectral density of stationary time series (e.g., Welch, 1967; Oppenheim and Schafer, 1975). In this report, the following procedure was applied: all together 20 sec of the pre-event window were divided into 19 blocks of 2 sec length each with an overlap of one sec. Each data block was padded with zeros to get a FFT-transformation length of 2^{10}, keeping in mind that the original sampling frequency of the field data was 250 Hz. The 19 raw Fourier spectra were averaged to lower the variance without affecting stationary noise peaks. The final step includes an average of 12 noise spectra from each station and a plot of the mean values and their standard deviation.

The noise spectra were calculated separately for day and night. They covered the whole time period during which the corresponding station was operating. By that procedure, working hours, weekends, and different weather conditions are included in the noise estimate.

Figure 2 shows a typical noise spectrum for the Bavarian Forest area. The solid line represents the average and the dotted lines one standard deviation calculated as explained in the preceding text. The estimate includes data from summer and from winter when the ground was covered with snow. In the individual spectra, no significant difference could be observed. The spectrum shows a continuous slope with a small variance, and the 2 Hz peak, commonly observed at stations in Central Europe, can only be recognized at night. The day spectrum is dominated by a noise maximum at 4 to 5 Hz, which is assumed to originate from a sawmill at a distance of a few kilometers. Apart from this peak, the noise spectrum shows a smooth decay proportional to f^{-4} from 1 to 30 Hz and a small standard deviation. Taking into account that the recording time covered nearly a period of 4 months, this area seemed to be promising for an array installation.

To confirm this suggestion, three other sites were explored in the vicinity. Indeed, their spectra looked very similar and confirmed the favorable opinion about the area. To put our noise results from the Bavarian Forest into proper perspective, additional data were collected at the GRF array and at NORESS. GRF can be regarded as a typical Western European site, whereas NORESS is well known for its excellent noise conditions on the Scandinavian shield.

The daytime GRF spectrum (Fig. 3) shows much larger noise values than in any of the Bavarian Forest spectra. The influence of industry and traffic is especially pronounced as seen in the large variation. The nighttime spectrum at GRF looks similar to the Bavarian Forest spectra between 1 and 8 Hz. For higher frequencies, the different geological setting (sediments) causes still higher noise values for GRF. From this direct comparison, we can conclude that the Bavarian Forest area exceeds most other places in the Federal Republic of Germany—and certainly GRF—as a potential site for the establishment of a high-frequency array.

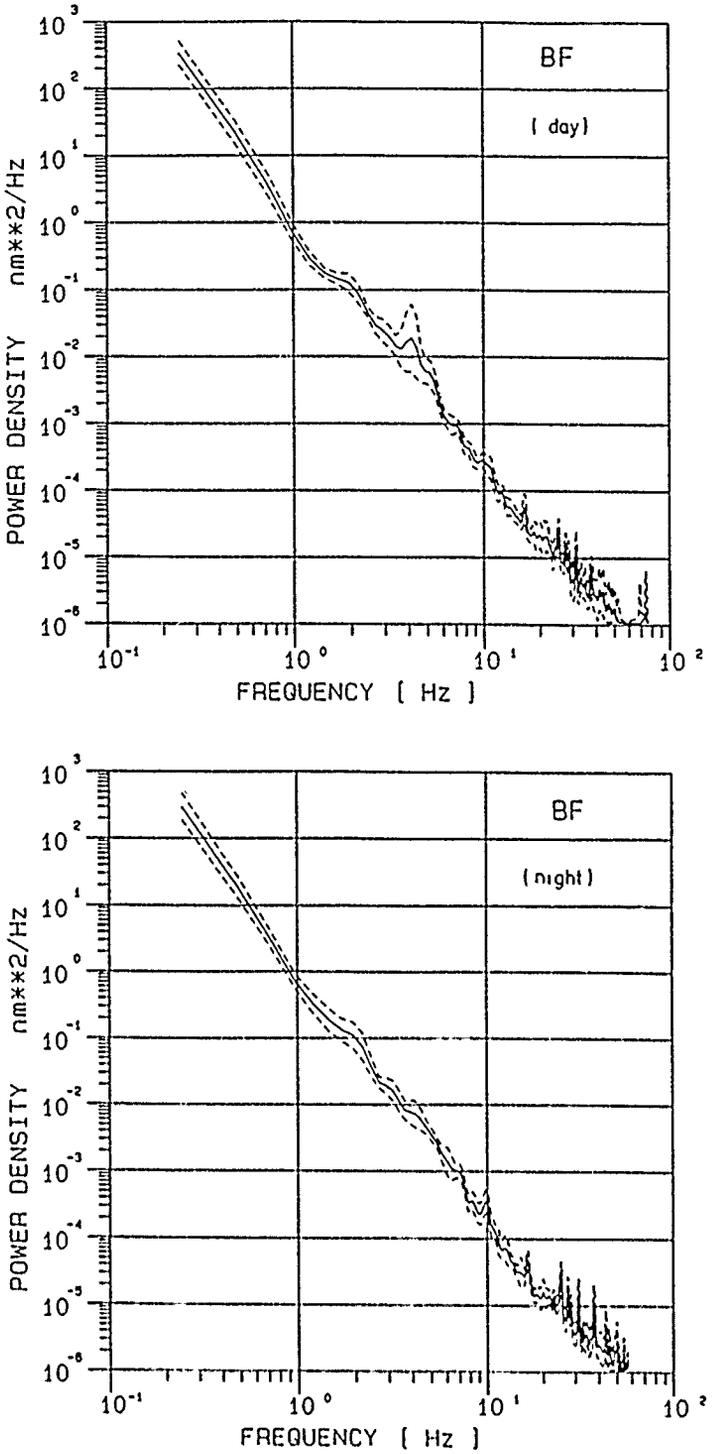

FIG. 2. Displacement power spectra of noise in the Bavarian Forest (BF) area for day and night. Solid line represents an average of 12 different data samples; dotted lines denote ±1 S.D.

More interesting is the comparison of the proposed Bavarian area with NORESS. The spectra shown in Figure 4 were calculated from a 24-hr noise sample analyzed with the same procedure as described previously. There are remarkable differences in the noise spectra. For low frequencies around 1 Hz, NORESS clearly suffers

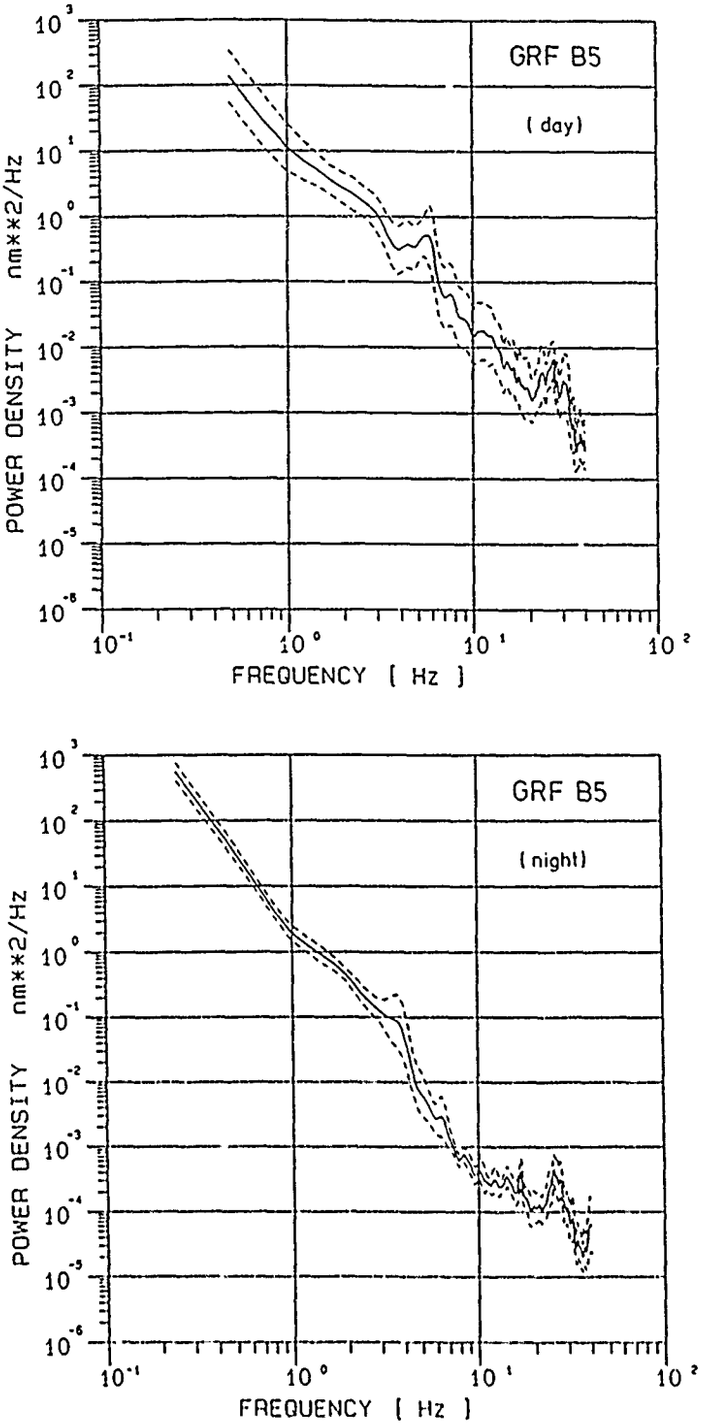

FIG. 3. Displacement power spectra of noise at the GRF array (site B5). For explanation, see Figure 2.

from the influence of the Norwegian coast, which results in an order of magnitude higher peak spectral displacement (PSD) values compared to the Bavarian Forest area (10 nm^2/Hz to less than 1 nm^2/Hz). Apparently, these microseisms lead to a steep slope of the spectrum, proportional to f^{-5} up to frequencies of 2 to 5 Hz. For

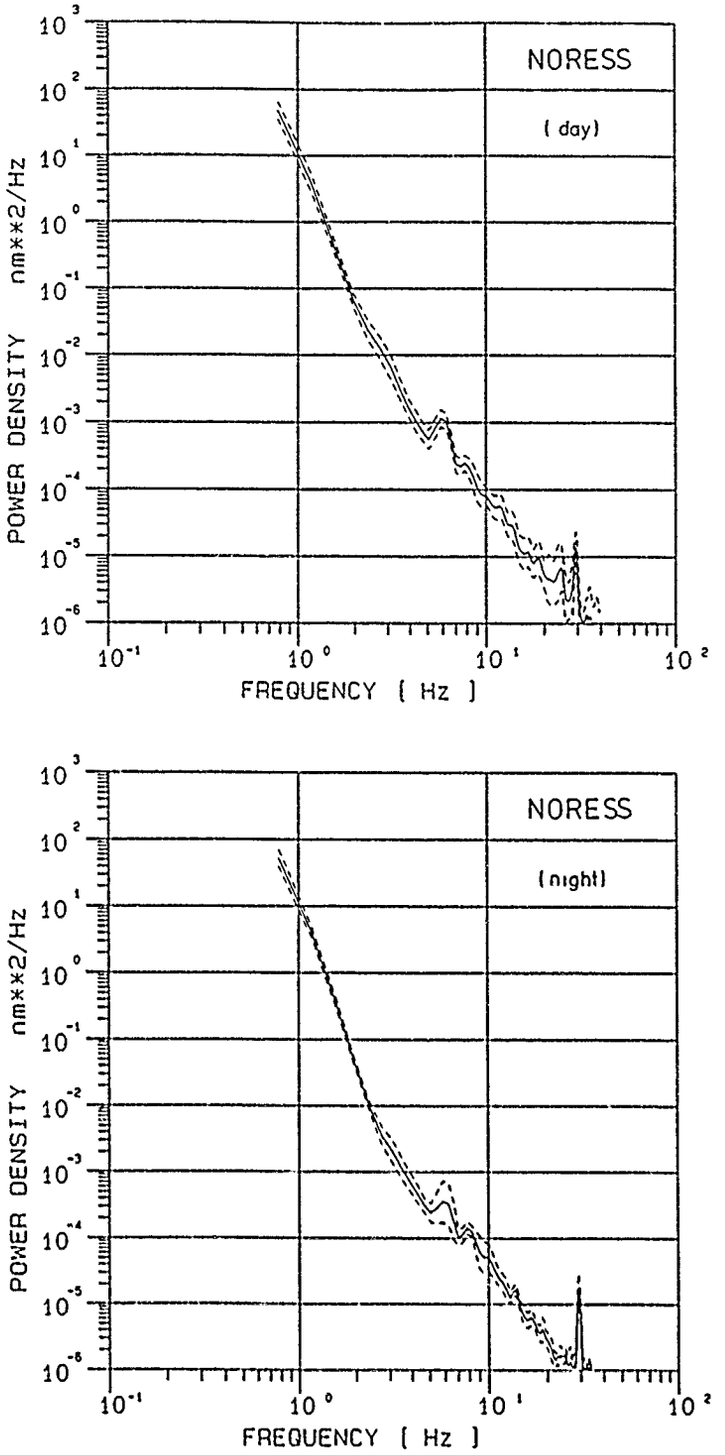

FIG. 4. Displacement power spectra of noise at NORESS (site C4). For explanation, see Figure 2.

higher frequencies, this slope is flattened and becomes comparable to the f^{-4} fall-off at the Bavarian Forest area. The absolute noise values at 10 and 20 Hz are certainly lower at NORESS, but also some influence of industrial noise between 5 and 8 Hz can be identified in the spectrum. According to personal information from

the NORSAR staff, there is also a sawmill operating at a distance of roughly 10 km from the NORESS array.

In summarizing the comparison between NORESS and the Bavarian Forest area, we found higher noise values at NORESS for frequencies below 2 Hz, and higher noise values at the Bavarian Forest site for frequencies between 2 and 20 Hz. The consequence of this difference in terms of detection capabilities can only be evaluated by comparing events recorded at the two arrays.

The GERESS array is planned as part of a multi-array network that will include the NORESS and ARCESS arrays in Scandinavia. Consequently, the design philosophy followed those existing arrays, and it is well documented in several publications (e.g., Followill and Harris, 1983; Mykkeltveit, 1985).

The geometry of these regional arrays is based on concentric rings spaced at log-periodic intervals in radius, R, following the relation

$$R = R_{\min}\alpha^n, \quad n = 0, 1, 2, 3 \tag{1}$$

with 3, 5, 7, and 9 elements in each ring, plus one in the center. With an odd number of elements in each ring, the corresponding co-array samples the local wave field in the least redundant way. In this sense, such a configuration comprises subsets of sensors with very different intersensor separations, implying that both high-frequency and low-frequency regional phases can be well enhanced by appropriate subsets of the array (Kværna, 1989).

An essential aspect of the array design is the supposition that intersensor spacings should correspond to maximum correlation for the signal and minimum correlation for the noise. Seismic signal and noise characteristics are influenced not only by the geologic formations of the array site, but also by the type and strength of sources and their locations with respect to the array. Consequently, determination of the actual values of the parameters in (1) for a specific site is to be based on observed signal and noise correlations.

Our correlation curves are derived from measurements made with a nine-sensor test array operating from December 1988 to April 1989 in the Bavarian Forest area where we found the lowest noise conditions earlier. The configuration of the test array and its corresponding co-array are shown in Figure 5. Interstation distances range from 200 to 3,000 m. Short-period instruments (Geotech S-13) were placed in small vaults at 2 to 4 m depth. At this depth, the overburden of soil was penetrated in general, but the underlying crystalline bedrock was still heavily weathered. The main advantage of the vault installation was to avoid wind noise induced by the surrounding forest.

New digital data acquisition systems (Geotech PDAS-100) were used for recording, which sampled at 100 Hz with a resolution of 16 bits. Data synchronization was controlled by an external radio signal (DCF-77). The test array operated in detector mode with a conventional STA/LTA detector, and recording length was generally 3 min, with a pre-event window of 30 sec.

Figure 6 shows an average noise power spectrum of the test array. The trend and absolute values coincide quite well with the results of the previous site survey (Fig. 2), confirming that the selected area is suited for an array installation. Noise correlations were calculated from the pre-event window of 35 different

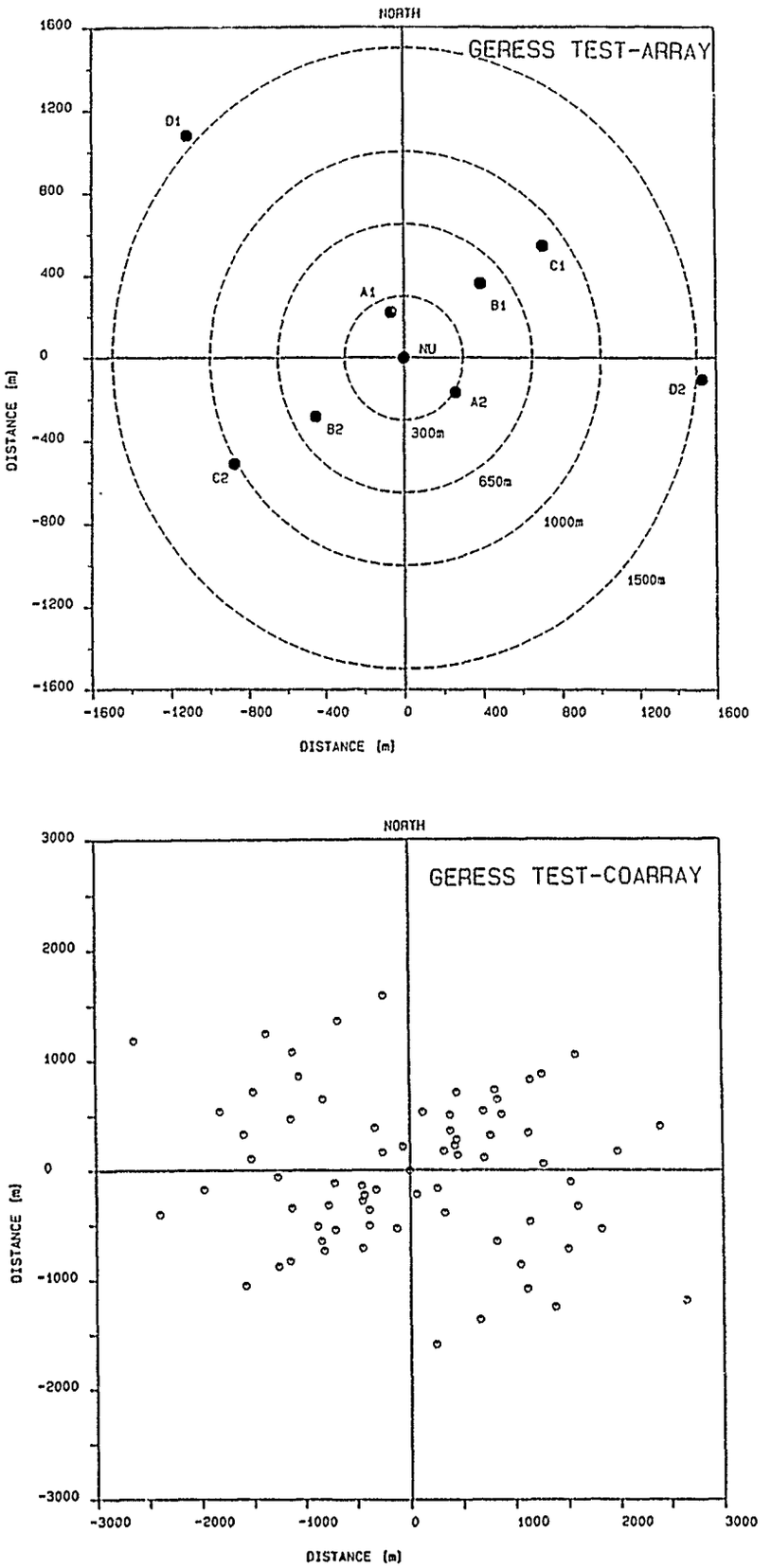

FIG. 5. Nine-element test array in the Bavarian Forest area. Co-ordinates of central vault: 48.845N, 13.700E. The co-array on the bottom shows all interstation distances in vector space.

events covering the whole recording period. The raw data were bandpass-filtered between 1 to 2 Hz and from 2 to 4 Hz, respectively, with a two-pole, both-directional (zero-phase) Butterworth filter.

The correlations are expressed by

$$c = \frac{\sum_{i=1}^{N} (x(i) - \bar{x})(y(i) - \bar{y})}{[\sum_{i=1}^{N} (x(i) - \bar{x})^2]^{1/2}[\sum_{i=1}^{N} (y(i) - \bar{y})^2]^{1/2}}. \quad (2)$$

$x(i)$ and $y(i)$ are sample values for sensor x and y, N is the number of samples, and $\bar{x}$ and $\bar{y}$ are the mean values of the N samples. The window length was taken as 10 sec (1,000 samples). The correlations were calculated for all 36 different combinations of seismometer pairs [i.e., all the co-array points (Fig. 5)].

Our results are summarized in Figure 7. In the lower half, the individual correlation values are shown within the 1 to 2 Hz passband, together with a smoothed average. The large scatter in the data may reflect as well the short window length as synchronization problems which occurred during data acquisition. On the other hand, the solid line representing an average trend indicates a quite reasonable behavior, especially when we add the upper half of the figure that presents the corresponding data in the 2 to 4 Hz passband. Defining the correlation length as that station separation for which the noise coherence drops below 0.25, we get a correlation length of about 800 m for the 1 to 2 Hz passband and 400 m for the 2 to 4 Hz passband. In a wide sense, this result is consistent with values found for NORESS. The main difference from noise correlation studies in Scandinavia is the absence of a significant minimum. The noise correlation curves for the Bavarian Forest area show a smooth decay without a pronounced negative correlation distance. If this preliminary result is confirmed by a comprehensive analysis of the

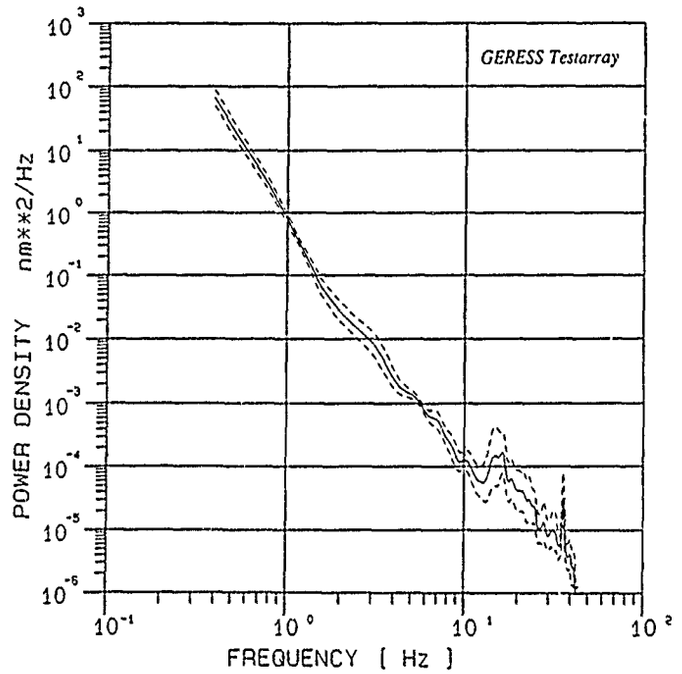

FIG. 6. Average displacement power spectra of noise for all elements of the test array in the Bavarian Forest area. Dotted lines denote ±1 S.D.

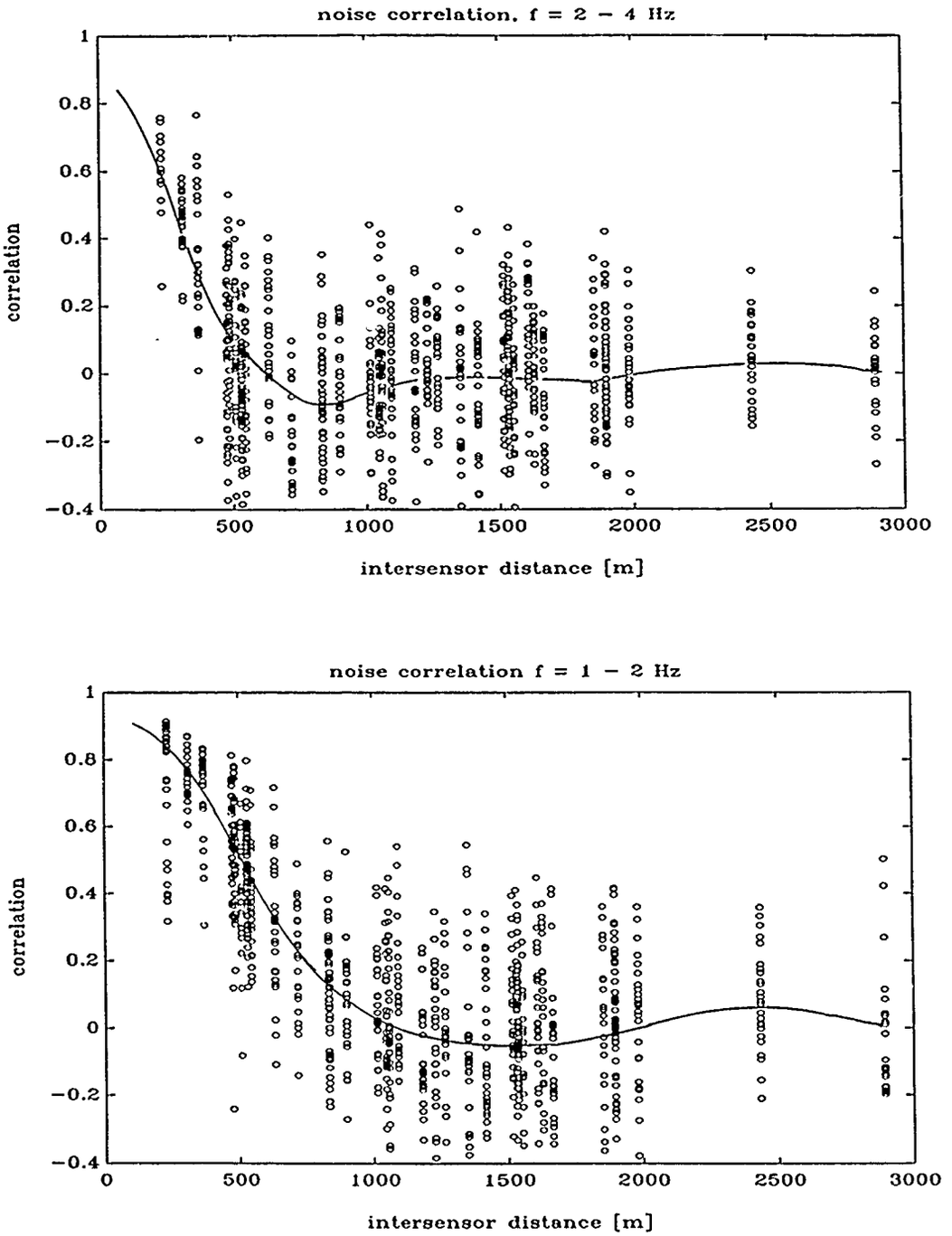

FIG. 7. Noise correlation values within the test array (bottom: prefilter 1 to 2 Hz; top: 2 to 4 Hz passband). Solid lines represent smoothed average curves.

future array data, there could be various explanations: the isotropic noise model (Backus *et al.*, 1964) might not be applicable in an azimuthally heterogeneous geologic region like Central Europe or, alternatively, the minimum in noise correlation for Scandinavian stations originates from directional propagating noise that could be higher mode microseisms. The higher level at low frequencies that was earlier mentioned in comparing Figures 2 and 4 supports the latter hypothesis. However, in the final design of the NORESS array, not much use has been made

of the noise minimum because in the range of interesting frequencies the corresponding interstation distance varies, and optimum geometries would be vastly different (Mykkeltveit, 1985).

As a consequence of the noise correlation curves, the minimum station distances for the planned GERESS array could be slightly increased in comparison to NORESS, taking into account that the detection window with the best signal-to-noise ratio is generally shifted to lower frequencies for stations in Central Europe. Whether this can lead to a larger overall aperture depends on signal correlation. Figure 8 shows a regional earthquake recorded by the test array in the Bavarian Forest area. It is a mining-induced event originating at Lubin in the Polish copper mines at a distance of 360 km from the test array. Besides the first arriving *Pn*- phase, we recognize *Pg* and *Lg* wavetrains as dominant signals, a typical picture for events from northern or northwestern azimuths.

In Figure 9, the signal spectra are plotted together with the background noise. Although all three phases stay above the noise level up to frequencies of 30 Hz, the best signal-to-noise ratio is obviously in the 1 to 5 Hz band. Certainly, this figure changes with azimuth, and at the Bavarian Forest site, there are particular wave paths along the Alps where we see much higher signal frequencies, and *Pn* and *Sn*

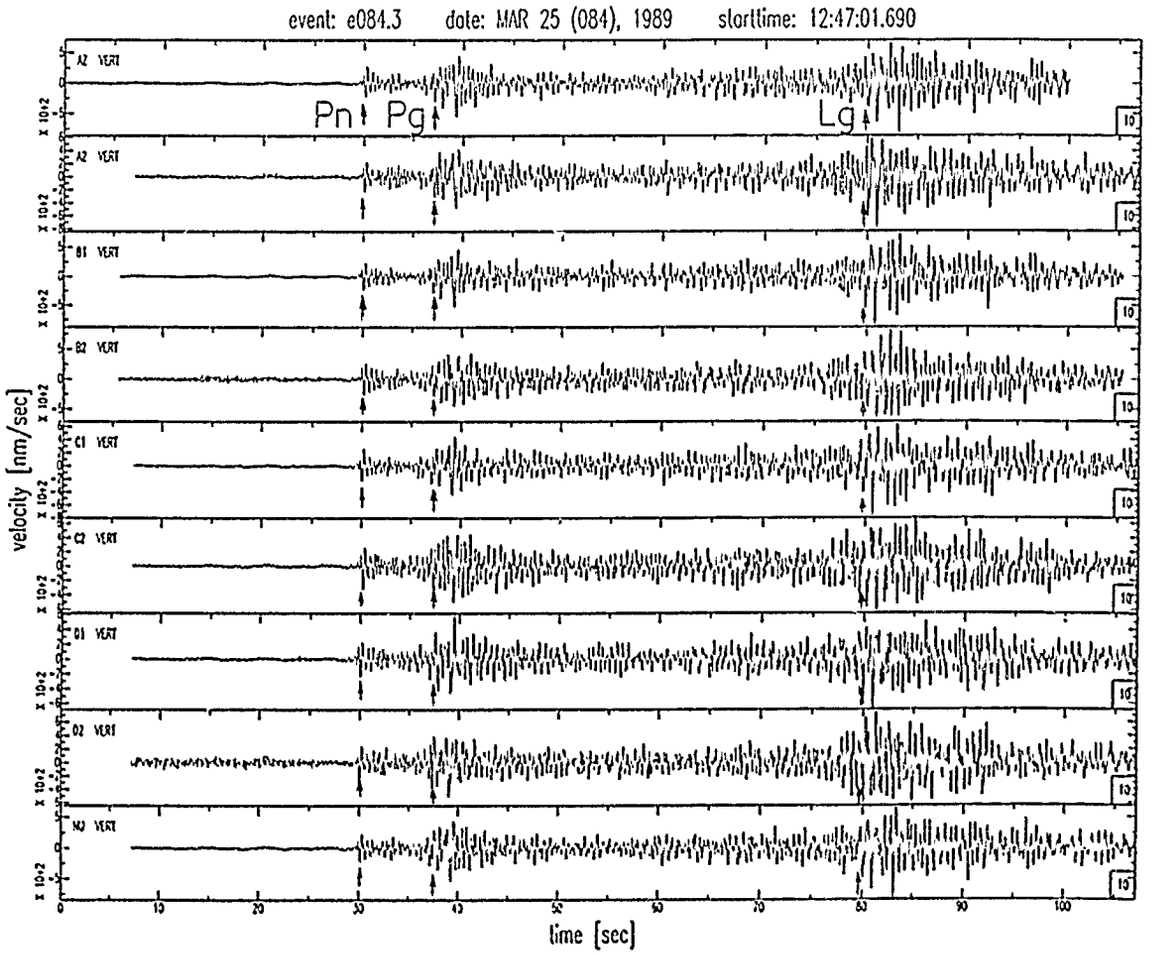

FIG. 8. Test array data (9 traces) of an m_L = 3.8 (KBA) earthquake near Lubin (Poland). Epicentral distance is 360 km. Prominent regional phases are marked as *Pn*, *Pg*, and *Lg*.

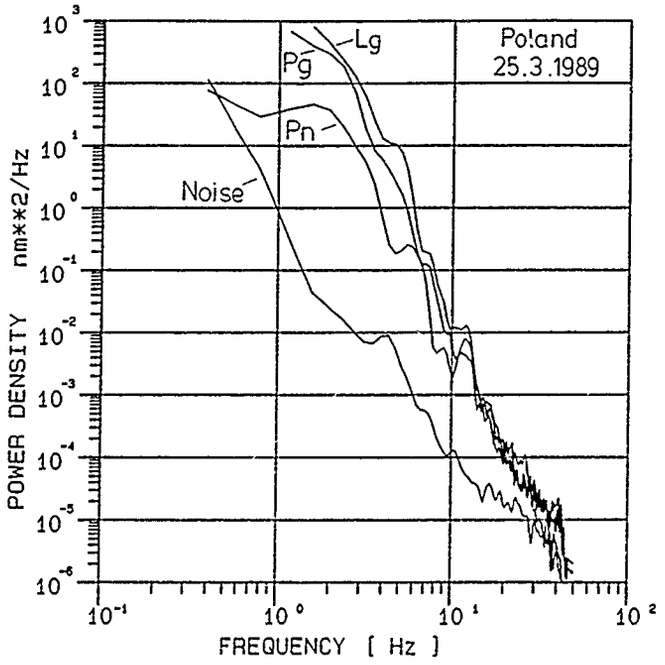

FIG. 9. Signal and noise power spectra for Lubin event for site A1 from Figure 8.

become the dominant phases. But, in general, frequencies below 10 Hz are most important for the evaluation of regional waves within 1,000 km distance.

Signal correlations were calculated with the same procedure used to establish the noise correlation curves. Time shifts were performed with an optimum line-up of peaks and troughs at the different sensors, and 1 or 2 sec windows of each phase were analyzed. In Figure 10, the signal correlation curves are shown for the *Pn*, *Pg*, and *Lg* phases using the same 1 to 2 Hz and 2 to 4 Hz passbands for noise correlation. Additionally, the noise correlation is marked in Figure 10 by stars, which represent the ±1 S.D. range. As can be seen from the figure, all signal correlation values stay above 0.9 for all interstation distances out to 3,000 m, with the exception of the *Lg* phase in the 2 to 4 Hz passband. Similar signal correlation curves were obtained analyzing a number of regional events from different azimuths.

From these measurements, it was decided to maintain the general geometry of the NORESS array but to enlarge it for the planned GERESS array by a factor of $\frac{4}{3}$, which results in a radius of 200 m for the innermost ring and about 2,000 m for the outermost ring. In conclusion, the parameters in equation (1) for the concentric array layout were specified as $R_{\min} = 200$ m and $\alpha = 2.15$.

The final siting of the 25 array elements had to take some local geologic and topographic peculiarities into account. In addition, some restrictions, imposed by the forest authorities, had to be considered. Nevertheless, the final configuration, displayed in Figure 11, is still sufficiently close to the concentric ring concept. Consequently, the GERESS array will represent a uniform element in the multi-array network, including ARCESS and NORESS.

On the right side of Figure 11, the array response of the planned GERESS array is plotted. Due to the larger aperture, the main lobe is smaller than the NORESS main lobe, but on the other hand, minor side lobes can be seen in the reject region in the wavenumber domain. For a fixed number of sensors, this reflects the well-

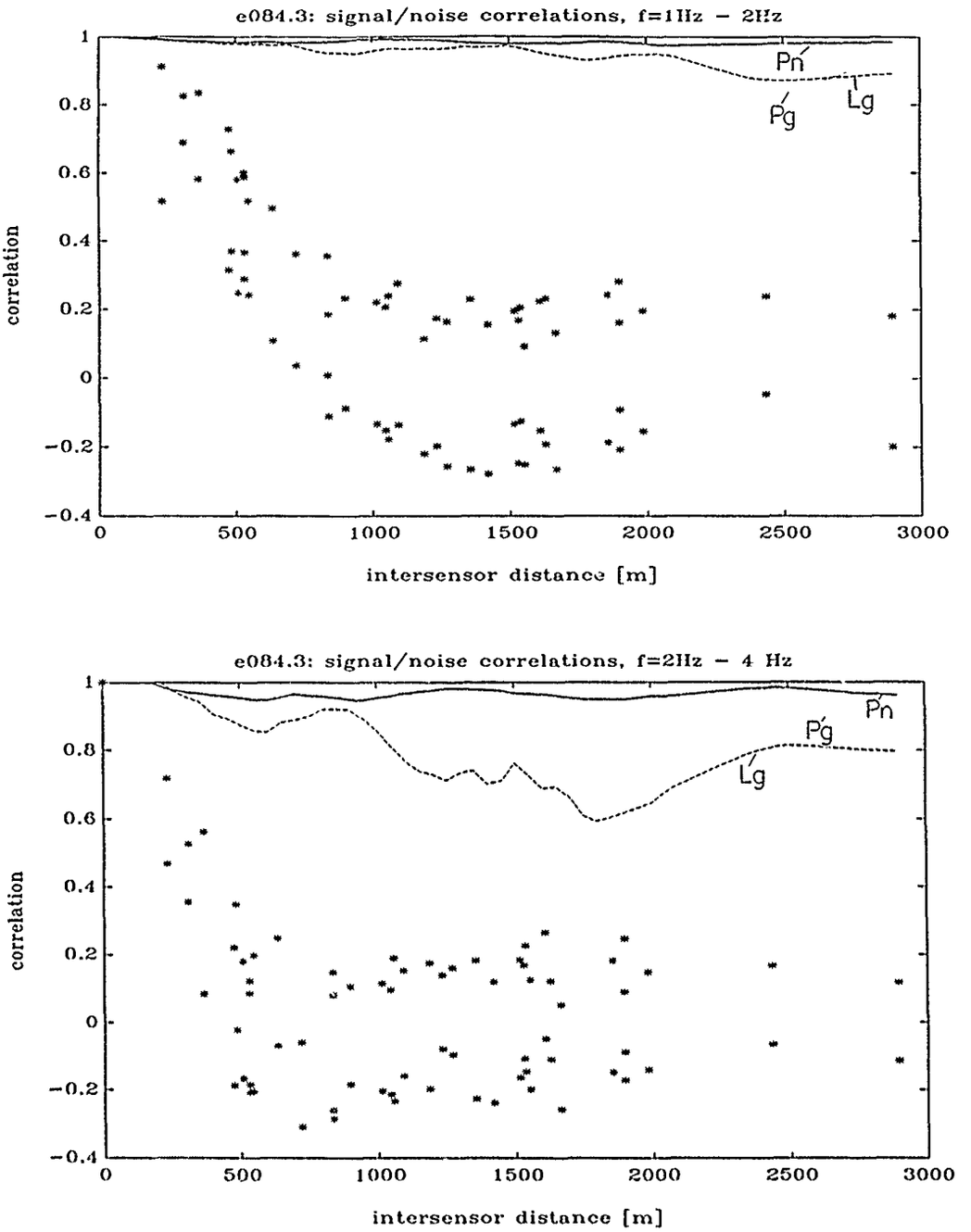

FIG. 10. Signal coherence curves (*top*: 1 to 2 Hz passband; *bottom*: 2 to 4 Hz passband) for the test array calculated from data of the Lubin event shown in Figure 8. The stars represent ±1 S.D. of the preceding noise window.

known trade-off between resolution and aliasing properties. A conclusion on whether the superior resolution of the GERESS array will lead to improved location and phase identification capabilities has to be deferred until the new array becomes operational.

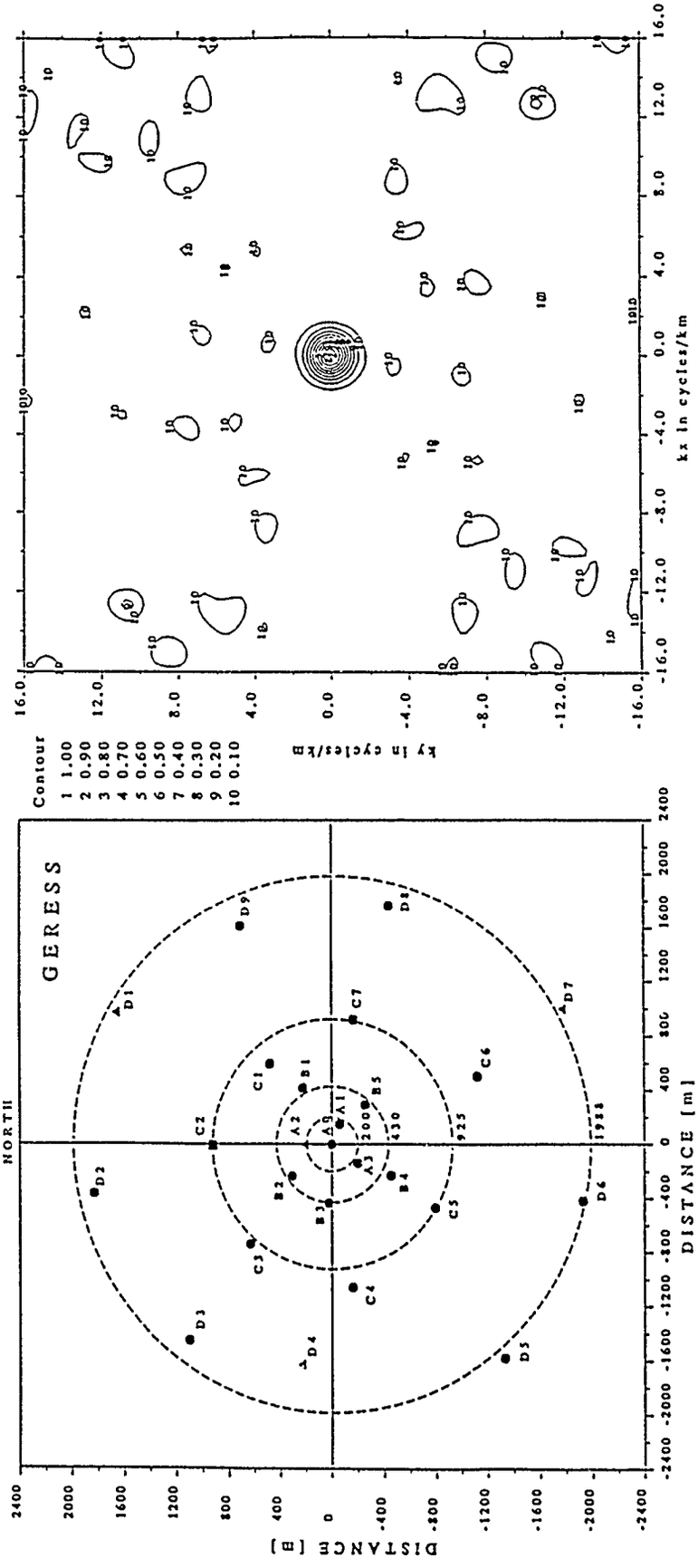

FIG. 11. Final configuration of the GERESS array, including 25 vertical seismometer sites. On the right, the corresponding array response in wavenumber domain is displayed.

Discussion and Preview

Since several conflicting demands can be put on array performance, it is difficult to make general comparisons of array design. For the regional array concept developed at NORSAR, the underlying objectives are determined in the context of a monitoring system for a future low-yield or compressive nuclear test ban treaty. A special aspect of such a system is the identification of weak seismic events using high-frequency data (Archambeau *et al.*, 1986). As a prototype array, NORESS has demonstrated promising capabilities. It is, however, difficult to generalize NORESS results because this array is located within an old shield region with high Q values. Additionally, the natural seismicity within regional distances is relatively weak. The GERESS array, on the other hand, will be situated in a rather complex geologic and geotectonic environment, where high Q and low Q wave paths drastically change with azimuth. The array site is surrounded by various artificial seismic sources like quarries and mines but more important, the Alpine earthquake belt and the Mediterranean earthquake zone lie within about 1,000 km distance. Consequently, the number and nature of regional seismic events recorded at GERESS should be more manifold than at any recording site in Scandinavia. For optimum performance of a seismic surveillance system, detection, location, and identification of events at low signal-to-noise ratios is important. It will be interesting to observe whether automatic procedures developed for these tasks at NORSAR can be adapted to the seismic situation in Central Europe. In any case, the use of arrays as components of a global seismic network can be evaluated more realistically the more the arrays and their recordings represent typical conditions of a global monitoring system.

During the summer of 1990, the GERESS array should become fully operational. After the final configuration was defined, excavation of vaults and trenching of cables started in October 1989. In addition to the 25 vertical instruments displayed in Figure 11, four sites will include horizontal components. All of these are short-period (1 Hz) Geotech GS-13 type instruments sampled at 40 Hz. The array will be supplemented by one three-component set of GS-13's sampled at 120 Hz, and these instruments will be collocated with a three-component set of broadband seismometers (BB-13) sampled at 10 Hz. As all sites are equipped with data acquisition units using 24-bit A/D converters, the data will provide sufficient resolution and dynamic range to evaluate small-size and large-size earthquakes simultaneously. For interesting events, data from the three-component high-frequency and broadband instruments can be pieced together to study the seismic wave field in a very broadband sense.

The GERESS array will be installed and operated as a joint project of the Geophysical Laboratory of Southern Methodist University Dallas and the Geophysical Institute of Ruhr-University Bochum. Data will be available at NORSAR and Bochum.

Acknowledgments

This project is supported by the Defense Advanced Research Projects Agency and is monitored by AFGL under Contract F-49620-88-C-45. The personal encouragement from R. Alewine is acknowledged. The author is deeply indebted to the technical staff and students of the Institute of Geophysics at Ruhr-University Bochum for their engaged cooperation during field work. N. Gestermann and D. Wand assisted in programming and providing the figures.

References

Archambeau, C. A., J. F. Evernden, and E. Cranswick (1986). An evaluation of seismic decoupling and underground nuclear test monitoring using high frequency seismic data, *Rev. Geophys.* **24**, 143–215.

Backus, M., J. Burg, D. Baldwin, and E. Bryan (1964). Wide-band extraction of mantle *P* waves from ambient noise, *Geophysics* **29**, 672–692.

Followill, F. and D. Harris (1983). Comments on small aperture array designs, Internal Report, Lawrence Livermore National Laboratory, Livermore, California.

Kværna, T. (1989). On exploitation of small-aperture NORESS type arrays for enhanced *P*-wave detectability, *Bull. Seism. Soc. Am.* **79**, 888–900.

Mykkeltveit, S., K. Astebol, D. J. Doornbos, and E. S. Husebye (1983). Seismic array configuration optimization, *Bull. Seism. Soc. Am.*.**73**, 173–186.

Mykkeltveit, S. (1985). A new regional array in Norway: design work and results from analysis of data from a provisional installation, in *The VELA Program: A Twenty-Five Year Review of Basic Research*, A. U. Kerr, Editor, Defense Advanced Research Projects Agency.

Oppenheim, A. V. and R. W. Schafer (1975). *Digital Signal Processing*, Prentice-Hall, Inc., Englewood Cliffs, New Jersey.

Welch, P. D. (1967). The use of Fast Fourier Transform for the estimation of power spectra: a method based on time averaging over short, modified periodograms, *IEEE Trans. Audio Electroacoust. AU*-15, 70–73.

INSTITUTE OF GEOPHYSICS
RUHR-UNIVERSITY
BOCHUM, FEDERAL REPUBLIC OF GERMANY

Manuscript received 2 March 1990

Bulletin of the Seismological Society of America, Vol. 80, No. 6, pp. 1818–1832, December 1990

EVENT DETECTION AND LOCATION PERFORMANCE OF THE FINESA ARRAY IN FINLAND

By Marja Uski

Abstract

The experimental seismic array FINESA in Finland is designed to monitor weak seismic events at regional and teleseismic distances. The array geometry currently comprises 15 short-period vertical seismometers in three concentric rings (A-, B-, and C-rings), with a diameter of the outer ring of about 2 km. In late 1989, the data acquisition system of the array was completely modernized. Signals are now transferred continuously via high-speed telephone lines to the processing centers at the Institute of Seismology in Helsinki and NORSAR in Norway, therefore allowing automatic real-time processing of the recorded data.

In this paper, the detection performance of the array in the current configuration has been evaluated. The results are encouraging: during a 2-week test period, FINESA detected at least one *P* and one *S* phase for 84 per cent of the events reported in the regional bulletin of the University of Helsinki, and 99 per cent of the events in the weekly teleseismic bulletins. Many additional events at both distance ranges were also found.

The estimated phase velocities obtained by the broadband frequency-wavenumber analysis confidently identify the phase type (teleseismic *P*/regional *P*/regional *S*). However, the resolution of the analysis is not sufficient to separate *Pg* from *Pn* and *Lg* from *Sn*. The estimated backazimuths are reliable for phase association, the standard deviation of the estimates being 7° for regional *P* phases, 6° for regional *S* phases, and 23° for teleseismic *P* phases.

Finally, preliminary results from FINESA's on-line event location capability showed that the average error in the location estimates is 21 per cent of the true epicentral distance. The greatest error sources are uncertainty in the estimated azimuths and occasional misidentification of secondary phases (*Lg*, *Sn* and *Rg*). The error could be reduced by constructing a regional correction term for the azimuth estimates and "tuning" the phase identification algorithms for FINESA. The characteristics of the *Rg*-phase need to be especially considered.

Introduction

The Finnish Experimental Seismic Array (FINESA) is a small-aperture array installed in November 1985 at Sysmä, about 100 km northeast of Helsinki. The establishment, as well as the array operation, is performed as a cooperative project between the Institute of Seismology of the University of Helsinki and NTNF/NORSAR in Norway. NORSAR operates two similar arrays: NORESS near Oslo and ARCESS in Finnmark, northern Norway. The locations of these three regional arrays and seismic stations of the standard network in Finland are shown in Figure 1. A detailed description of the FINESA instrumentation and system operation has been published by Korhonen *et al.* (1987).

The main objective of the FINESA experiment is to provide high-quality data for research projects aiming at improved detection, location, and identification of weak seismic events at regional and teleseismic distances. FINESA data will also be utilized in bulletin work to supplement the data recorded by the standard network in Finland, and together with NORESS and ARCESS recordings to assess and further develop the combined capability of small-aperture arrays in monitoring seismic activity.

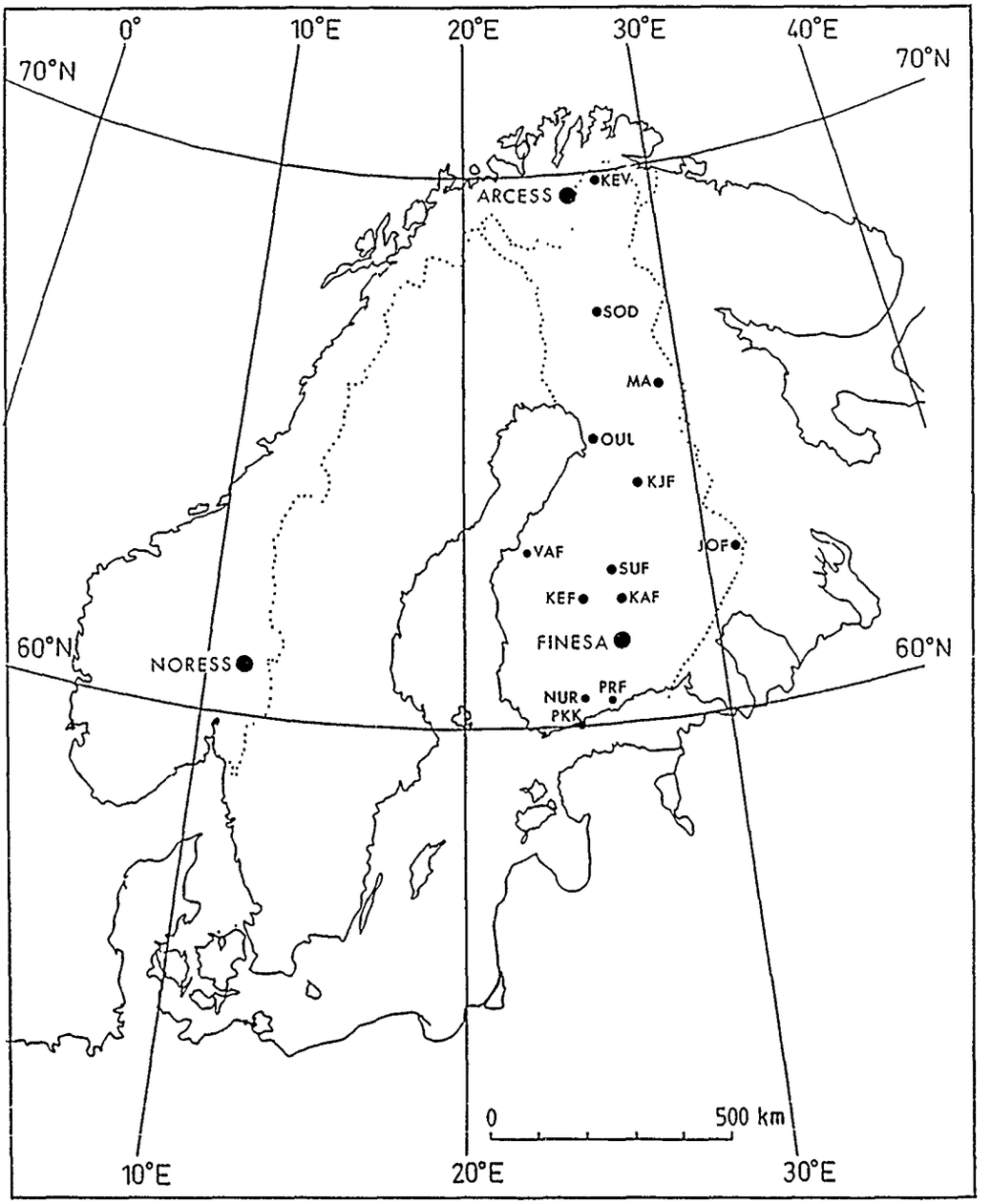

FIG. 1. Locations of the three regional arrays—FINESA, ARCESS, and NORESS—and the stations of the Finnish Seismograph Network.

The geometry of the array (Fig. 2) comprises, since January 1988, 15 short-period vertical seismometers in three concentric rings (A-, B-, and C-rings) with a diameter of the outer ring of about 2 km. Initially, the FINESA data were only recorded in the field. In late 1989, the data recording system at the array site was modernized, and high-speed telephone lines to the Data Processing Centres in Helsinki and at NORSAR were installed. The recorded signals are now transferred continuously to both processing centers, hence allowing automatic real-time processing of the FINESA data. Technical details of the array modernization are given in Paulsen *et al.* (1989).

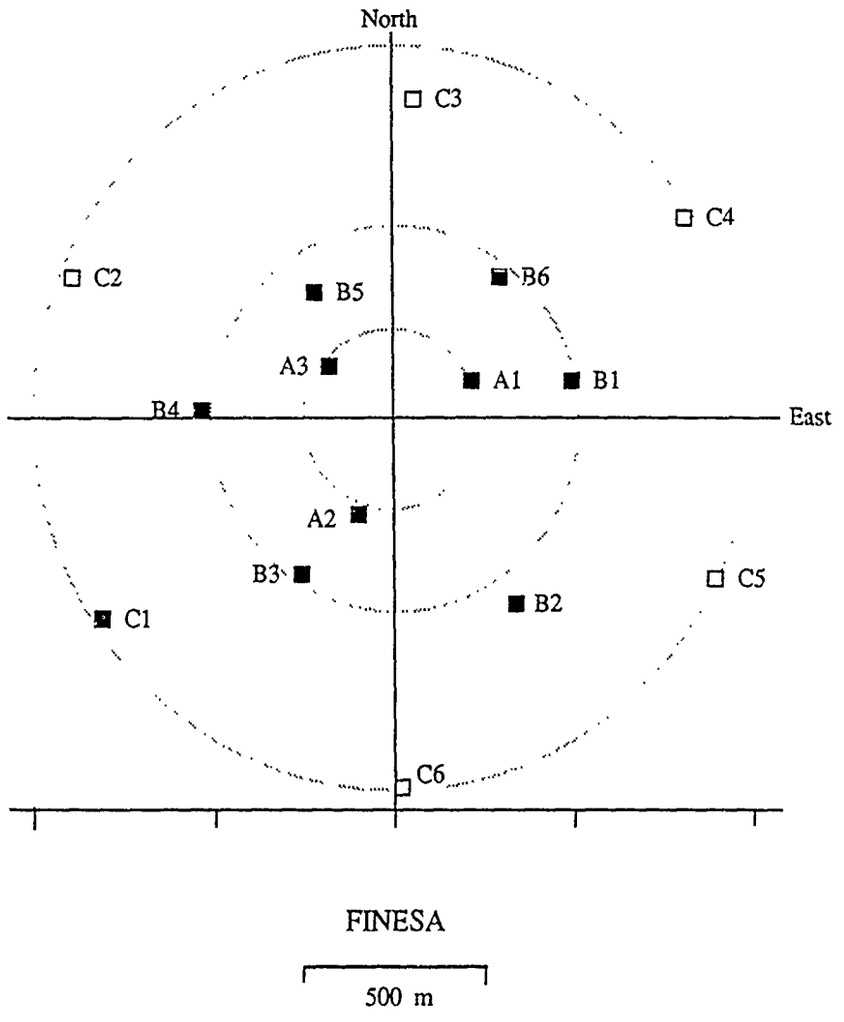

FIG. 2. The present geometry of the FINESA array. Open squares denote array elements added in January 1988. The central recording unit is at site A1.

In this paper, the detection performance of FINESA at regional and teleseismic distances is assessed. The data for the study were obtained during the 2-week test period from 8 to 21 March 1988, while FINESA was in a continuous recording mode. Resolution of the array in estimating backazimuth and phase velocity of the detected signals is also studied. Finally, preliminary results of FINESA's regional event location capability, based on the automatic event bulletins from the first days (30 November to 9 December 1989) of on-line array processing in Helsinki are presented.

THE DETECTION PERFORMANCE OF FINESA

In this section, FINESA's detection capability both at regional and at teleseismic distances is evaluated. The data for the study were obtained during the 2-week period from 8 to 21 March 1988, while FINESA was recording data continuously on magnetic tape at the array site. The data analysis was carried out using the RONAPP array processing package developed at NORSAR (Mykkeltveit and

Bungum, 1984; Fyen, 1989). Briefly, the recordings were subjected to:

- beam-forming using a set of 72 beams (66 coherent and 6 incoherent) created by summing signals from different subsets of the array configuration
- digital narrow-band filtering of the coherent beams using second- or third-order recursive Butterworth filters (for incoherent beams, the signals were filtered individually before stacking)
- STA/LTA detector algorithm applied for each beam
- broadband frequency-wavenumber (f-k) analysis (Kværna and Doornbos, 1986) of the detections giving estimates for the backazimuth and phase velocity
- identification of the detected phases using the results from the f-k analysis.

The filter bands and the best subgeometry for beamforming within each frequency band were selected on the basis of the recommendations by Kværna *et al.* (1987) and Kværna (1989).

In this off-line processing, we encountered technical problems in reading some of the magnetic tapes, and consequently not all the data could be analyzed. Altogether, a total of 195 hr of recordings were processed and used as a data base for this study.

Regional Events

To investigate FINESA's detection performance on a regional scale, we used as a reference the bulletin "Seismic Events in Northern Europe" (*Helsinki Bulletin*), published by the Institute of Seismology of the University of Helsinki. Table 1 lists the events that occurred during time intervals with available FINESA data. These reference events comprise two earthquakes, with magnitudes of 2.7 and 3.2, whereas the remaining events are presumed regional explosions of low magnitude. The coda duration (M_c), magnitudes (Wahlström and Ahjos, 1982), and the known charges for some mining explosions are given in the table. Unfortunately, the magnitude scale is not applicable if the coda length is less than 20 sec (i.e., for most of our events). Those magnitudes are expressed by the symbol <2, indicating that the size of the event is clearly less than $M_c = 2$, but more accurate measure cannot be given. The dash denotes that the coda could not be measured (e.g., due to two overlapping events). For each of the events in Table 1, we calculated the expected arrival times of the *Pn*, *Lg*, and *Sn* phases at FINESA. This information was then associated with the actual FINESA detections by requiring a reasonable match between predicted and actual arrival times as well as expected and estimated phase velocities. For the associated detections, the estimated azimuth and phase velocity of the first arriving *P* and *S* phases are included in Table 1.

Figure 3 illustrates FINESA's detection capability as a function of M_c magnitude and epicentral distance. It is worth noting that, for events of $M_c \geq 2$, the detection performance is excellent throughout the whole distance interval. However, at about 300 km, the primary phases in the $M_c < 2$ group start to drop out. From Figure 3, it is also clear that no detection threshold as a function of M_c magnitude can be given before more data are available from the greatest regional distances and/or the coda magnitude scale is extended to events with coda length less than 20 sec.

Table 2 summarizes the detection statistics versus M_c magnitude, showing that for 91 (84 per cent) of the 108 reference events, both the primary and secondary phases were detected. In addition, for 96 per cent of all events, at least one phase was detected.

At distances less than 500 km, most of the phases that were not detected at FINESA are associated with small explosions from the Lahnaslampi and Elijärvi

TABLE 1

REGIONAL EVENT DETECTION RESULTS FOR FINESA

Day	Origin Time	Latitude (°)	Longitude (°)	M_c	Size (tons)	f-k analysis				Distance (km)	Azimuth (°)
						V_p (km/sec)	P-az. (°)	Vs (km/sec)	S-az. (°)		
08	06:01:42.9	61.184N	27.145E	<2		***	***	3.1	125.7	64.0	116.9
08	07:50:57.6	62.767N	29.068E	<2		9.0	48.3	4.0	49.7	214.9	45.3
08	12:03:14.0	53.200N	27 800E	2.0	4.46	—	—	4.6	26.8	215.0	23.8
08	13:03:50.0	62.228N	23.276E	2.0		6.4	307.7	4.7	305.8	171.5	301.9
08	13:29:02.0	64.200N	28.000E	—	0.45	***	***	***	***	322.3	16.8
08	14:25:10.9	62.124N	26.404E	<2		6.6	4.4	3.6	8.1	77.2	12.5
08	15:02:39.1	60.327N	24.758E	1.9		7.3	218.9	3.5	228.0	143.3	210.6
09	12:05:43.0	64.200N	28.000E	<2	1.85	***	***	5.0	4.6	322.3	16.8
10	08:47:04.0	59.300N	27.200E	<2		6.9	170.6	3.6	168.3	246.8	165.0
10	09:22:08.0	59.300N	27.600E	<2		6.9	162.0	3.9	164.8	253.2	160.0
10	09:57:40.0	59.200N	27.600E	<2		7.1	160.2	4.0	159.0	263.8	160.8
10	10:41:14.0	59.300N	27.600E	<2		6.9	158.3	4.8	278.8	263.8	160.8
10	11:07:37.0	59.200N	27.600E	2.1		7.1	158.1	4.0	169.5	263.8	160.8
10	11:14:23.0	59.300N	27.600E	<2		6.7	160.7	4.1	169.4	253.2	160.0
10	11:25:34.0	59.500N	25.000E	2.2		7.2	185.9	4.1	182.2	224.6	195.8
10	11:49:54.0	59.300N	27.600E	<2		7.2	154.7	4.3	167.5	253.2	160.0
10	12:05:20.0	59.500N	26.500E	2.2		7.2	170.0	4.0	171.2	217.9	173.7
10	12:07:05.2	61.218N	28.929E	—		7.1	106.2	4.4	103.4	154.7	98.0
10	12:10:50.0	59.300N	28.100E	2.1		7.0	153.8	5.2	155.7	263.6	154.1
10	16:03:30.0	64.264N	23.978E	<2		7.3	350.5	4.0	348.9	331.5	342.1
10	16:20:55.6	62.017N	24.375E	<2		6.7	304.6	3.7	304.8	110.8	306.1
10	18:16:15.0	65.800N	24.700E	<2	5.0	***	***	3.8	353.5	490.3	352.6
10	18:29:30.0	67.100N	20.600E	2.2		8.1	347.9	4.9	346.9	684.0	339.6
10	20:27:28.6	63.638N	26.178E	<2		6.9	5.4	4.7	357.6	245.0	1.2
11	08:18:59.1	62.870N	25.852E	1.8		6.7	3.4	3.8	1.5	159.3	355.8
11	09:23:17.0	67.600N	34.000E	—		***	***	4.2	18.4	783.2	25.5
11	09:24:26.0	67.600N	34.000E	—		***	***	4.4	21.2	783.2	25.5
11	09:25:40.0	67.600N	34.000E	2.7		8.4	24.1	4.5	18.2	783.2	25.5
11	09:48:06.0	61.400N	34.300E	2.3		9.5	65.0	4.6	78.9	438.6	87.0
11	10:21:09.4	62.239N	25.909E	<2		6.8	340.1	3.0	356.4	89.1	354.3
11	10:21:35.0	59.300N	27.600E	2.2		6.8	160.4	3.9	159.9	253.2	160.0
11	10:56:54.0	59.500N	25.000E	2.1		7.2	185.9	4.0	182.4	224.6	195.8
11	11:27:25.0	59.300N	27.600E	<2		6.8	157.9	3.9	167.9	253.2	160.0
11	11:46:58.0	69.400N	30.800E	2.3		10.0	27.4	3.6	19.0	913.1	11.8
11	12:00:27.0	59.300N	27.600E	—		6.7	161.3	—	—	253.2	160.0
11	12:03:37.0	63.200N	27.800E	2.3	33.7	7.1	24.9	4.3	27.9	215.0	23.8
11	12:17:09.0	59.500N	25 000E	2.1		7.3	183.4	4.0	189.2	224.6	195.8
11	12:33:24.0	60.800N	29.300E	2.3		7.2	114.6	3.6	117.2	187.8	111.1
11	12:57:59.0	59.300N	27.600E	<2		6.7	162.3	3.8	172.5	253.2	160.0
11	13:33:05.0	59.300N	28.100E	<2		6.8	158.7	4.6	165.3	263.6	154.1
12	09:12:28.0	59.400N	28.400E	2.1		6.9	150.6	4.4	153.8	261.2	149.7
12	09:59:59.0	64.700N	30.700E	2.9		9.0	34.3	4.3	38.8	431.3	30.7
12	10:43:17.0	59.500N	25.000E	2.2		7.3	186.6	4.4	193.8	224.6	195.8
12	10:48:21.6	61.770N	36.123E	2.4		8.1	99.7	4.9	68.6	533.6	81.7
12	11:03:58.0	68.100N	33.200E	2.1		8.4	29.0	3.8	17.3	814.5	21.4
12	11:11:12.0	68.100N	33.200E	2.9		8.7	29.2	5.1	16.8	814.5	21.4
12	12:25:01.0	59.300N	27.200E	2.3		7.0	166.2	3.9	166.6	246.8	165.0
12	12:40:45.0	67.600N	30.500E	—		***	***	4.7	20.6	717.9	15.2
12	12:41:07.0	67.600N	30.500E	2.4		8.0	24.4	4.4	13.5	717.9	15.2
12	14:15:38.0	67.100N	20.600E	<2		***	***	4.7	351.2	683.5	339.0
13	06:49:10.0	67.700N	33.700E	2.4		8.7	28.3	4.3	36.2	786.0	24.2
14	09:01:41.0	59.300N	27.600E	<2		6.9	160.5	4.1	162.7	253.2	160.0
14	09:13:21.4	62.749N	22.571E	<2		7.3	317.3	4.4	314.7	234.0	304.0
14	09:29:16.0	59.300N	27.200E	2.1		7.1	165.3	3.6	160.7	246.8	165.0
14	10:32:41.0	59.300N	27.600E	<2		6.8	161.0	4.1	167.4	253.2	160.0
14	10:35:25.0	59.300N	27.600E	<2		6.9	159.3	3.9	165.5	253.2	160.0
14	10:45:02.0	59.300N	27.600E	2.1		4.1	160.4	3.9	164.3	253.2	160.0
14	12:41:49.0	59.600N	30.000E	2.1		7.2	139.8	5.0	127.9	297.6	131.9
14	13:10:52.0	59.500N	25.000E	2.6		7.8	187.8	4.5	187.7	224.6	195.8
14	14:07:27.0	59.300N	28.100E	<2		6.7	158.9	4.6	163.7	263.6	154.1

Association of FINESA's regional event detections for 8 to 21 March 1988 with the events in the Helsinki bulletin. The distance and azimuth from FINESA are derived from the epicenter information. The phases not detected at FINESA are denoted by asterisks. Dashes indicate that estimation of the arrival azimuth and velocity failed, since a calibration pulse was overlapping the detected phase.

TABLE 1—*Continued*

Day	Origin Time	Latitude (°)	Longitude (°)	M_c	Size (tons)	*f-k* analysis				Distance (km)	Azimuth (°)
						V_p (km/sec)	*P*-az. (°)	*Vs* (km/sec)	*S*-az. (°)		
15	08:59:57.0	67.600N	34.000E	<2		***	***	4.9	33.4	783.2	25.5
15	09:06:42.0	67.600N	34.000E	2.4		***	***	4.7	22.8	783.2	25.5
15	10:31:30.5	59.235N	27.371E	2.5		6.8	159.5	4.0	164.4	256.8	163.3
15	11:26:30.0	61.600N	21.700E	<2		8.2	278.8	4.5	276.5	233.7	276.2
15	11:34:36.0	59.500N	26.500E	2.5		7.1	176.3	3.8	171.8	217.9	173.7
15	11:41:57.5	60.492N	25.908E	1.8		6.9	173.1	3.7	177.7	106.8	185.0
15	12:10:38.0	59.200N	27.600E	<2		6.8	162.5	4.0	169.6	263.8	160.8
15	12:11:37.0	59.200N	27.600E	<2		***	***	3.9	162.3	263.8	160.8
15	12:19:15.0	59.300N	27.200E	2.2		6.9	168.7	3.9	165.9	246.8	165.0
15	12:33:35.6	62.519N	21.679E	<2		7.8	304.6	4.2	305.7	259.9	299.4
15	12:40:39.0	59.400N	28.500E	1.9		7.1	151.9	4.8	156.6	263.9	148.6
15	13:16:45.0	59.300N	24.400E	2.3		7.5	201.6	4.4	193.9	256.3	201.9
15	13:22:14.0	61.900N	30.600E	2.0		7.1	75.9	3.7	78.3	244.7	76.0
15	13:51:30.7	58.945N	25.784E	<2		6.7	185.7	4.4	182.7	278.4	183.5
15	14:09:35.0	59.500N	25.000E	<2		7.3	186.4	4.5	190.7	224.6	195.8
15	14:20:59.5	60.927N	29.189E	2.4		7.4	111.8	4.6	103.7	176.9	107.5
15	14:36:30.6	63.061N	22.173E	<2		7.3	318.6	4.2	320.1	271.4	313.3
15	14:39:35.0	59.500N	25.000E	2.3		7.3	186.0	3.8	193.4	224.6	195.8
15	17:57:51.0	65.800N	24.700E	<2	2.5	***	***	4.0	355.6	490.3	352.6
16	08:37:13.0	59.200N	27.600E	<2		6.7	158.1	4.1	158.8	263.8	160.8
16	09:44:50.0	69.600N	29.900E	2.4		9.8	28.3	5.0	2.6	925.9	9.3
16	10:25:03.0	59.300N	27.600E	<2		6.9	159.4	3.9	164.2	253.2	160.0
16	10:45:40.9	60.901N	26.834E	<2		6.4	151.3	3.8	160.5	72.9	146.0
16	11:26:47.0	59.200N	27.600E	<2		6.7	160.3	4.1	163.3	263.8	160.8
16	11:45:36.0	63.200N	27.800E	2.5	50.9	6.4	22.8	3.5	21.1	215.0	23.8
16	11:49:51.0	59.500N	25.000E	<2		7.2	185.9	4.6	190.0	224.6	195.8
16	23:04:26.1	67.842N	19.966E	<2		***	***	***	***	769.7	340.5
17	09:07:13.2	58.334N	10.927E	2.7		9.8	249.3	5.1	262.0	913.8	254.4
17	10:21:17.0	69.600N	29.900E	2.9		9.5	15.8	4.9	19.7	925.9	9.3
17	10:27:20.0	59.200N	27.600E	2.3		6.8	162.9	3.9	159.2	263.8	160.8
17	10:46:21.0	59.200N	27.600E	<2		7.0	156.5	4.8	158.2	263.8	160.8
17	11:18:48.0	59.300N	27.200E	2.3		7.2	166.4	3.8	161.7	246.8	165.0
17	12:02:23.0	64.200N	28.000E	<2		***	***	***	***	322.3	16.8
17	12:02:36.0	59.400N	28.500E	2.1	0.75	6.5	155.8	4.0	154.6	263.9	148.6
17	18:05:44.0	65.800N	24.700E	<2	2.0	***	***	***	***	490.3	352.6
17	18:58:07.1	59.715N	5.624E	3.2		11.9	261.1	4.6	270.1	1133.0	269.3
18	05:16:20.0	69.200N	34.700E	2.6		8.2	25.7	4.2	30.3	951.4	21.0
19	10:04:08.0	61.100N	30.200E	<2		6.9	111.2	4.3	97.2	224.3	98.0
19	10:05:02.0	59.300N	27.200E	—		6.4	167.0	3.9	168.8	246.8	165.0
19	12:15:34.0	68.100N	33.200E	—		8.3	28.6	—	—	814.5	21.4
19	12:15:39.0	68.100N	33.200E	—		9.2	30.6	4.5	17.5	814.5	21.4
19	12:39:09.0	68.100N	33.200E	<2		8.8	30.2	4.5	18.4	814.5	21.4
19	13:03:39.0	67.600N	30.500E	—		8.1	27.9	3.7	20.9	717.9	15.2
19	13:03:54.0	67.600N	30.500E	—		8.1	27.9	4.7	19.7	717.9	15.2
19	13:07:00.0	61.900N	30.600E	2.6		7.5	87.6	4.5	72.4	244.7	76.0
19	13:42:33.0	67.600N	30.500E	<2		***	***	4.3	16.1	717.9	15.2
20	04:45:17.0	67.700N	33.700E	2.5		8.1	27.0	4.7	33.2	786.0	24.2
21	12:03:49.0	59.300N	28.100E	<2		6.6	154.7	4.0	159.1	263.6	154.1

quarries, at 322 and 490 km from FINESA, respectively. The reason for the poor detectability is that these quarry blasts were quite small, a couple of tons at the maximum. High-frequency *Pg* phases from small and very local (distance of less than 100 km) events may also remain undetected. This was, however, expected since the signal correlation between the array elements is not very good at the highest frequencies, and also because the beams are deployed especially to detect the *Pn* phase. Nevertheless, since most of those events are small chemical explosions (road work, etc.), it would not be reasonable to make efforts to further increase the detectability for this event category.

At distances greater than 500 km, the undetected *P* phases are associated with

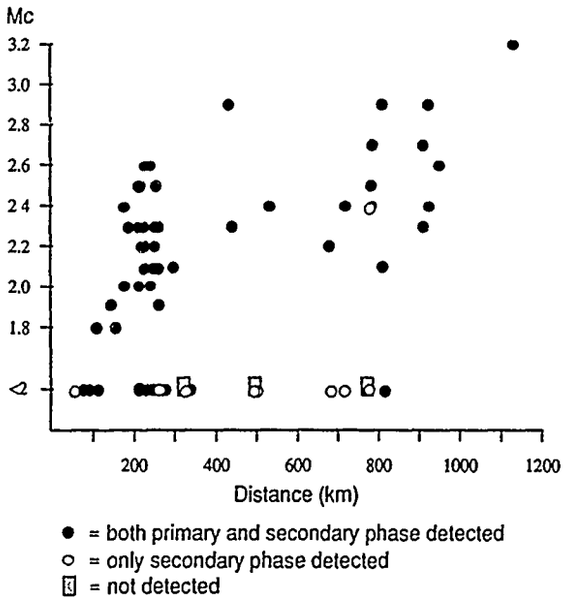

FIG. 3. FINESA's regional event detections plotted against the epicentral distance and coda duration magnitude.

TABLE 2

DETECTION STATISTICS FOR THE REGIONAL EVENTS

M_c	–	<2	1.8-2.1	2.2-2.5	2.6-2.9	3.0-3.4	Total
P only	1	0	0	0	0	0	1
S only	3	8	0	1	0	0	12
P+*S*	6	35	17	24	8	1	91
Not detected	1	3	0	0	0	0	4
Total	11	46	17	25	8	1	108

FINESA's regional phase detections versus the M_c magnitude in the Helsinki bulletin. The dash indicates that the coda duration was not measured because of intermixed events. The symbol <2 denotes an event size clearly less than $M_c = 2$.

seismic events from mining areas in the Kola Peninsula and northern Sweden. The charge sizes of these mine blasts are not known, but all except one belong to the $M_c < 2$ group. The results of Kværna (1989) indicate that enhanced. SNR gain for FINESA at frequencies typical of these regional *P* waves could be obtained by expanding the array geometry to include a NORESS-type D-ring (aperture of 3 km).

In addition to the events in our database, FINESA detected a great number of regional events too weak to be included in the *Helsinki Bulletin*. Requiring both *P* and *S* phases to be detected, it was possible to extract 87 such additional events. Inclusion of these events in the regional bulletin would increase the number of events by 81 per cent.

Teleseismic Events

In the present array configuration, FINESA's aperture clearly is not optimum for sampling teleseismic arrivals. However, Korhonen *et al.* (1987) showed that even the initial and smaller ten-element FINESA array detected teleseismic events quite

well. In this section, we assess FINESA's teleseismic detection capability in its current configuration. As a reference, we use the weekly teleseismic bulletins of the University of Helsinki (derived from the Finnish standard network) and the Preliminary Determination of Epicenters (PDE) bulletin, issued by the U.S. Geological Survey.

During the time when FINESA data were available, the Helsinki weekly bulletins reported 73 *P*-phase readings (*P*, *PKP*, and *PP*), of which 57 were verified by the PDE bulletin. Only one of these 73 phases was not detected by FINESA, a very weak signal with the first detected arrival being *PP*. In addition to the 72 phase readings found in the Helsinki weekly bulletins, FINESA's detection lists comprised 95 arrivals, which according to the signal attributes, could be classified as teleseismic *P* phases. Seventeen, of these 95 arrivals can be associated with events reported in the PDE bulletin. Thus, inclusion of the FINESA data in the Helsinki weekly bulletin would increase the number of teleseismic events verified also by the PDE bulletin by about 30 per cent.

Estimation of Phase Velocity and Backazimuth

In the on-line array processing, the performance of the automatic phase identification, phase association, and epicentral determination of regional events rely on the accuracy of estimated phase velocity and backazimuth obtained by the *f-k* analysis. Our objective here is to examine FINESA's capability to estimate these signal attributes and also to propose means to improve the resolution of the array.

Estimates of Phase Velocity

In Figure 4, the estimated phase velocities for the regional *P* and *S* detections in Table 1 are plotted against the "true" backazimuths (A_t), which were derived from the event epicenters in the Helsinki bulletin. The figure shows that a phase velocity of 6 km/sec, used to separate primary and secondary phases at NORESS, also works well for FINESA data. The velocity is in error only in one case where the *S* phase

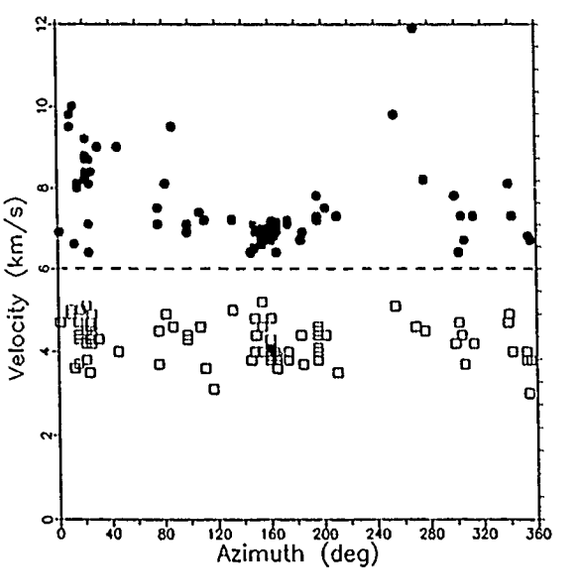

FIG. 4. Estimated phase velocity versus true azimuth for regional *P* phases-filled circles and *S* phases-open squares.

of an earlier event interferes with the *P* onset. On the other hand, it is not possible to distinguish *Pg* from *Pn*, nor *Lg* from *Sn* by using phase velocity only, a result also found for NORESS.

The teleseismic data indicate that estimates of the phase velocities, although they may not be very precise, in many cases are sufficient to identify the phases as teleseismic *P* waves. Thus, an estimated phase velocity greater than 14 km/sec will almost always correspond to a teleseismic *P* or *PKP*. Separation between regional and teleseismic phases becomes more problematic in the interval 12 to 14 km/sec. Here, additional information on the signal (e.g., frequency, presence of secondary detection from the same azimuthal direction, etc.) will be required.

Estimates of Backazimuth

Figure 5 (a and b) shows the residuals ($A_{f\text{-}k} - A_t$) for estimated *P* and *S* azimuths, respectively, plotted against the "true" backazimuth (A_t). The standard deviation of the residuals is 7° for *P* and 6° for *S*. One clearly erroneous estimate of the *S* azimuth was left from the calculation.

The azimuth residuals in Figure 5 shows systematic patterns, reflecting the effect of local geological structure on the azimuth estimates. In the future, as observations with better azimuthal coverage become available, this bias could be reduced by introducing regionally dependent azimuth correction terms.

For teleseismic events, we calculated a standard deviation of 23° for the azimuth residuals. Four clearly erroneous estimates were not included in these calculations. The *f-k* azimuths for core phases were particularly imprecise, but we feel, however, that in this phase of the FINESA experiment this is not a serious shortcoming. For teleseismic events, the *f-k* velocity and azimuth will be considered as preliminary estimates only, and they will not be applied in the bulletin work. Further improvement of the array's resolution at teleseismic frequency range would require extension of the aperture (i.e., more elements should be installed).

Initial Results from the On-Line Processing of the FINESA Data

In this section, we present preliminary results of FINESA's on-line and automatic event association and location capability at regional distances. It must be noted that the data were obtained during the first days of on-line operation (30 November to 9 December 1989), and it must be expected that the processing parameters and algorithms can be further improved as experience is gained. A more thorough evaluation of the location performance will be carried out as soon as a more extensive database is available.

Automatic Event Association Procedure

In the RONAPP event-forming procedure, automatic phase identification and association of the arrivals are based on the results from *f-k* analysis, as well as knowledge on the characteristics of the regional wave propagation represented in the rules and constraints of the algorithm (Fyen, 1989). In order to examine the performance of the event association algorithm, we compared the FINESA bulletins from the period 30 November to 9 December 1989 with the *Helsinki Bulletin* from the same time period. The FINESA bulletins comprised 184 automatically associated and located regional events, for which about 20 to 30 per cent were artificial due to noise detections and/or wrongly associated seismic phases, whereas the *Helsinki Bulletin* reported 79 events. Of those "Helsinki events," for which FINESA

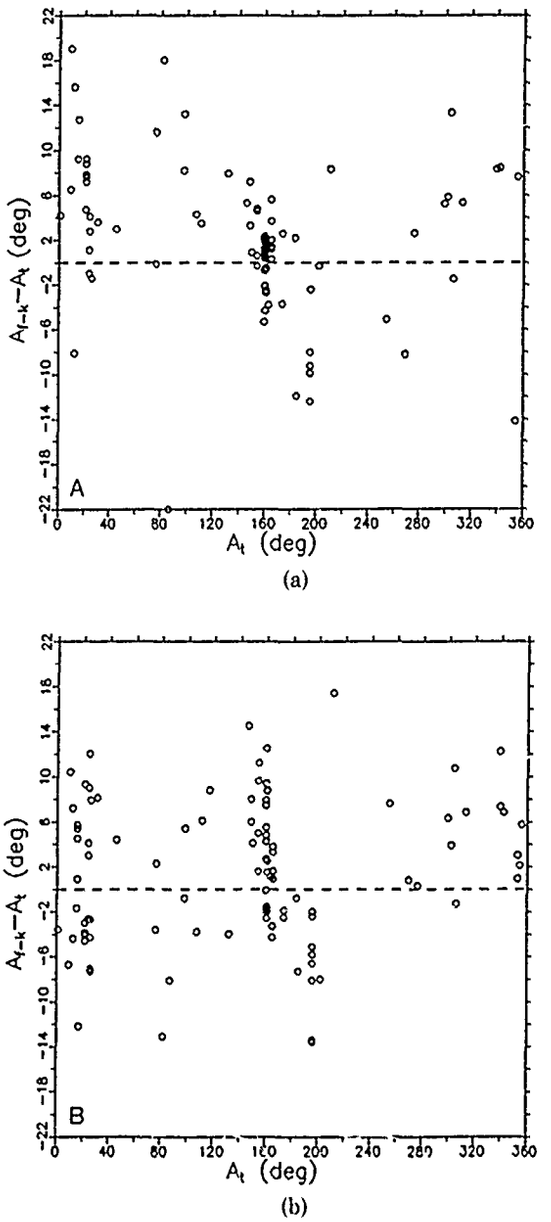

FIG. 5. The azimuth residuals ($A_{f-k} - A_t$) for (a) regional P phases and (b) S phases plotted versus the "true" azimuth (A_t) derived from the event epicenter in the Helsinki bulletin.

detected both a primary and a secondary phase, only three were unassociated: one P was misinterpreted as teleseismic (velocity 16.4 km/sec), one P was identified as an S phase (velocity 6 km/sec), and one P was misinterpreted as noise due to low SNR. However, these events could all be correctly associated through modifications of the event identification algorithm and by slightly changing the phase velocity separation values of 6 and 14 km/sec.

Six of the bulletin events were missed as a result of intermixed phases from several events, and this represents a problem that will require further study. At present, analyst review will be required in such cases.

Event Location Experiment

In order to estimate FINESA's location capability, we selected from the automatic bulletins 13 regional quarry blasts for which independent and accurate locations were available. The events were located using the program TTAZLOC (Bratt and Bache, 1988), which is incorporated in the FINESA processing system. The epicenter determination is based on the azimuth of the maximum secondary detection plus the travel-time difference between the phase onset identified as *Lg* or *Rg* and the *Pn*. The travel-time tables were derived from a simple velocity model for Fennoscandia (Bungum *et al.*, 1980), which was adopted from the NORESS analysis.

Table 3 lists the location solution from the on-line processing and the true epicenter information (latitude, longitude, and azimuth). The location

TABLE 3

RESULTS FROM THE AUTOMATIC EVENT LOCATION EXPERIMENT

Event No.	Origin time	Latitude (°N) / True Latitude	Longitude (°E) / True Longitude	Azimuth (°) / True Azimuth	D (km)	Location Error	
						km	%
1	30.11 12.03.23	60.67	28.84	118.9	122	54	44
		61.03	28.18	111.1			
2	01.12 04.51.16	63.62	25.33	351.4	273	29	11
		63.85	25.05	349.3			
3	01.12 10.00.58	64.82	29.34	22.1	431	63	15
		64.68	30.63	30.7			
4	01.12 13.20.34	62.79	28.87	42.8	226	20	9
		62.82	29.25	45.7			
5	02.12 02.40.41	63.52	25.92	358.1	247	17	7
		63.66	26.05	359.7			
6	04.12 12.03.08	60.62	28.84	120.3	122	58	48
		61.03	28.18	111.1			
7	04.12 12.46.33	62.92	23.97	327.2	218	26	12
		63.15	24.02	331.5			
8	04.12 18.31.30	65.42	23.20	343.4	683	214	31
		67.12	21.00	340.2			
9	05.12 19.16.33	63.66	25.57	354.2	273	33	12
		63.85	25.05	349.3			
10	05.12 19.34.54	65.61	23.68	346.7	683	207	30
		67.12	21.00	340.2			
11	06.12 10.01.11	64.30	31.78	39.8	431	70	16
		64.68	30.63	30.7			
12	07.12 12.04.02	60.78	28.45	119.2	122	31	25
		61.03	28.18	111.1			
13	07.12 12.16.29	63.03	27.11	16.3	205	33	16
		63.12	27.74	24.0			
				Averages:		66	21

Latitude, longitude, and arrival azimuth obtained from on-line processing are underlined. The true epicenter information is given below these values. D = distance from FINESA.

error is given both in kilometers and in per cent of the true epicentral distance. Within the distance range of 200 to 500 km, the relative location accuracy is about 12 per cent, which corresponds well to what we could expect from uncertainties in the estimated azimuths and automatically picked onset times. However, the location estimates of events at the two mines at 122 and 683 km from FINESA are much less accurate. The errors are caused by phase misidentifications, following from the assumption that the maximum secondary detection will be either *Lg* (group velocity 3.5 km/sec) or *Rg* (group velocity 2.95 km/sec). At the greatest regional distances, and especially when passing through geological border zones, the *Lg* amplitudes are reduced, and the dominant secondary phase may be found in the *Sn*-wave group. The Bothnian Bay, across which the seismic waves from events 8 and 10 from northern Sweden (see Figure 6) are propagating, seems to form such a structural barrier for *Lg*. For those events, the *Sn/Lg* misidentification results in a distance underestimation of 200 km.

Another problematic feature in terms of automatic location estimation is the presence of a strong *Rg* phase, even at distances up to 430 km (as shown in Figure 7) and possibly at even greater distances. Since NORESS seldom observes *Rg* beyond 100 km, the RONAPP procedure has insufficient rules for identifying this phase, and *Rg* at FINESA is often misinterpreted as *Lg* (events 1, 6, 11, and 12).

To summarize, the initial automatic location accuracy of FINESA is comparable to what has been obtained for other single arrays. The event location procedure can be improved by correct identification of the secondary phases. In FINESA's

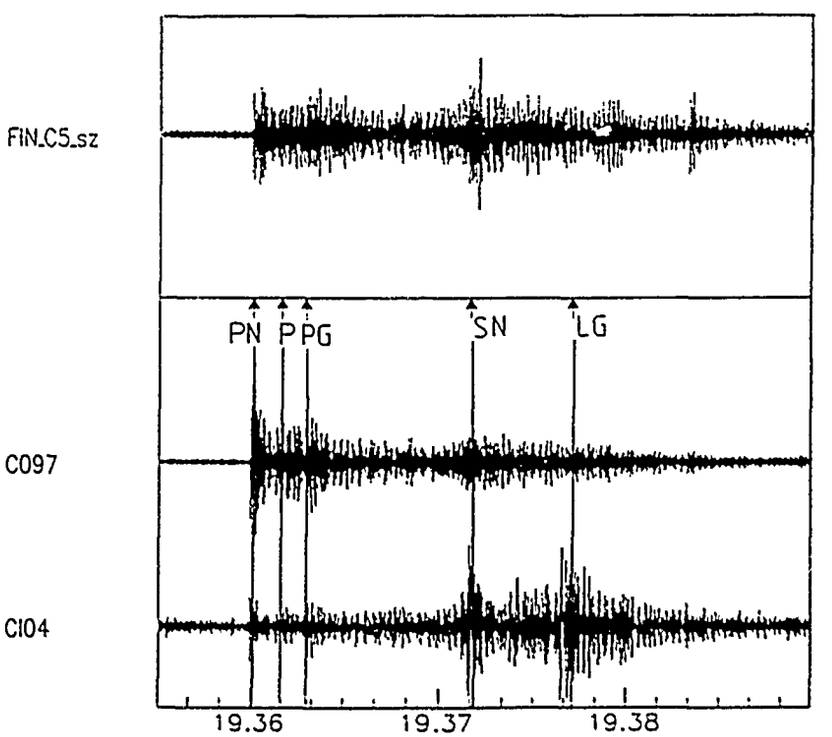

FIG. 6. One single trace from the instrument at site C5 plus the "best" *P* beam (C097) and *S* beam (CI04) for event 10 in Table 3. Arrows show the onset time for each phase detection. The *Pn* phase was automatically identified, but *Sn* was misinterpreted as *Lg*. In the plot, the identification of *Pg*, *Sn*, and *Lg* is made by an analyst.

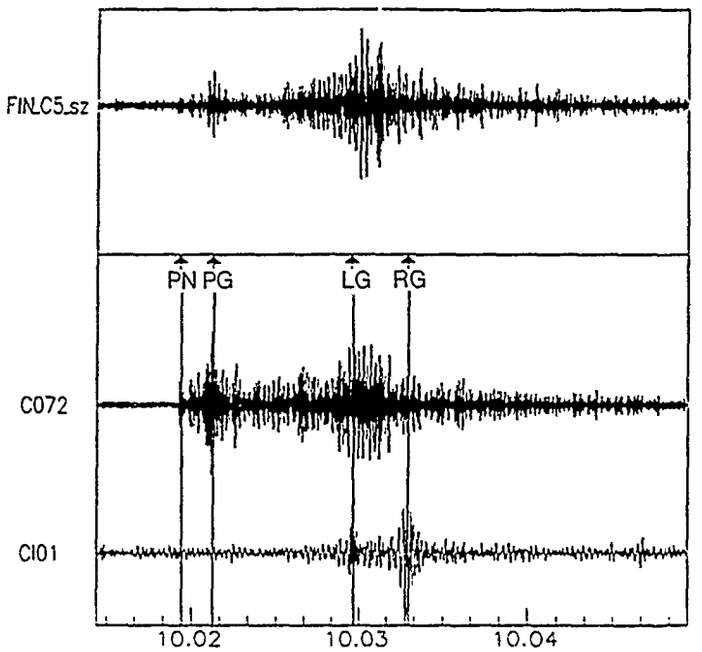

FIG. 7. One single trace (site C5) plus the "best" *P* beam (C072) and *S* beam (CI01) for event 3 in Table 3. Arrows show the onset time for each phase detection. The *Pn* and *Rg* phases were automatically identified. For *Pg* and *Lg*, the identification is made by an analyst.

detection lists, even the estimated velocity and frequency may be sufficient to distinguish *Rg* from *Lg*. Knowledge on the geological structures that block *Lg* and *Rg* should be utilized in the processing. As also seen in Table 3, for events from the same sites, the error in the azimuth estimation is systematic. When this information is applied in the procedure, the location estimates will become more accurate. Additional fine-tuning of the results could be achieved by constructing regionally dependent velocity models and by relocation using manually adjusted onset times.

CONCLUSIONS

Detection Statistics

We have shown that with the current configuration, FINESA detected both primary and secondary phases for 84 per cent of the regional events reported in the *Helsinki Bulletin*, and for 96 per cent of the events, at least one phase was detected. Inclusion of regional events recorded and located by FINESA alone would increase the number of events in the *Helsinki Bulletin* by 81 per cent.

At teleseismic distances, 99 per cent of the phase readings reported in the weekly bulletins of Helsinki were detected. Many additional teleseismic signals were detected by FINESA, and inclusion of these in the weekly teleseismic bulletin of the University of Helsinki would increase the number of teleseismic events verified by the PDE bulletin by about 30 per cent.

Estimates of Phase Velocity and Backazimuth

The estimated phase velocities confidently identify the phases in question: the phase velocity of 6 km/sec works well as a separation line between regional primary

and secondary arrivals. Similarly, 14 km/sec separates between teleseismic and regional *P* phases. Additional constraints (frequency, presence of secondary detection from the same direction, etc.) near the separation values will further improve the identification. Phase velocity alone does not separate *Pn* from *Pg* nor *Sn* from *Lg*.

For regional *P* phases, the standard deviation of the *f-k* azimuths is 7°, for *S* phases 6°, and for teleseismic phases 23°. Systematic trends in the *f-k* azimuths from the same location indicate that regionally dependent azimuth correction terms could be derived and used in the data analysis.

Automatic Event Association and Location Procedure

Under normal conditions, the event association procedure works well. The algorithm fails to interpret situations where two or more events within the azimuth association window of 30° are intermixed. It may, however, be possible to recognize and resolve some of these cases on the basis of the travel-time differences between regional seismic phases.

FINESA's initial event location accuracy is 21 per cent of the true epicentral distance. The greatest errors are caused by uncertainty in the estimated azimuths and insufficient rules to discriminate *Rg* and *Sn* from *Lg*. Mapping of the characteristics of *Rg*- and *Lg*-wave propagation and regional azimuth corrections will improve the location capability.

ACKNOWLEDGMENTS

This study was supported by the cooperative research project agreed between the Institute of Seismology of the University of Helsinki, Finland, and NTNF/NORSAR in Norway. Data processing for the detection study was carried out in Norway. I am very grateful to the NORSAR staff for the help and technical advice during the work. I also thank Dr. Svein Mykkeltveit and Professor Heikki Korhonen for comments on the manuscript.

REFERENCES

Bratt, S. R. and T. C. Bache, (1988). Locating events with a sparse network of regional arrays, *Bull. Seism. Soc. Am.* **78**, 780–798.

Bungum, H., S. E. Pirhonen, and E. S. Husebye (1980). Crustal thicknesses in Fennoscandia *Geophys. J. R. Astr. Soc.* **63**, 759–774.

Fyen, J. (1989). Event processor program package, in *Semiannual Technical Summary, 1 October 1988–31 March 1989, NORSAR Sci. Rept. No. 2-88/89*, Kjeller, Norway.

Korhonen, H., S. Pirhonen, F. Ringdal, S. Mykkeltveit, T. Kværna, P. W. Larsen, and R. Paulsen (1987). The FINESA array and preliminary results of data analysis, Institute of Seismology, University of Helsinki, Report S-16, 70 pp.

Kværna, T. and D. J. Doornbos (1986). An integrated approach to slowness analysis with arrays and three-component array data in *Semiannual Technical Summary, 1 October 1985–31 March 1986, NORSAR Sci. Rept. No. 2-85/86*, Kjeller, Norway.

Kværna, T., S. Kibsgaard, S. Mykkeltveit and F. Ringdal, (1987). Towards an optimum beam deployment for NORESS; experiments with a North Sea/Western Norway data base, in *Semiannual Technical Summary, 1 April–30 September 1987, NORSAR Sci Rept. No. 1-87/88*, Kjeller, Norway.

Kværna, T. (1989). On exploitation of small-aperture NORESS type arrays for enhanced *P*-wave detectability, *Bull. Seism. Soc. Am.* **79**, 888–900.

Mykkeltveit, S., K. Åsteból, D. J. Doornbos, and E. S. Husebye, (1983). Seismic array configuration optimization, *Bull. Seism. Soc. Am.* **73**, 173–186.

Paulsen, R., J. Fyen, P. W. Larsen, and S. Mykkeltveit, (1990). A new data acquisitions system for FINESA in *Semiannual Technical Summary, 1 April 1989–31 September 1989, NORSAR Sci. Rept. No. 1-89/90*, Kjeller, Norway.

Wahlström, R. and T. Ahjos (1982). Determination of local magnitude and calibration of magnitude scales for earthquakes in the Baltic shield, *Seism. Inst., Upps., Report I-82*, 39 pp.

INSTITUTE OF SEISMOLOGY
UNIVERSITY OF HELSINKI
ET. HESPERIANKATU 4
SF-00100 HELSINKI, FINLAND

Manuscript received 7 March 1990

Bulletin of the Seismological Society of America, Vol. 80, No. 6, pp. 1833–1851, December 1990

THE INTELLIGENT MONITORING SYSTEM

BY THOMAS C. BACHE, STEVEN R. BRATT, JAMES WANG, ROBERT M. FUNG, CRIS KOBRYN, AND JEFFREY W. GIVEN

ABSTRACT

The Intelligent Monitoring System (IMS) is a computer system for processing data from seismic arrays and simpler stations to detect, locate, and identify seismic events. The first operational version processes data from two high-frequency arrays (NORESS and ARCESS) in Norway. The IMS computers and functions are distributed between the NORSAR Data Analysis Center (NDAC) near Oslo and the Center for Seismic Studies (Center) in Arlington, Virginia. The IMS modules at NDAC automatically retrieve data from a disk buffer, detect signals, compute signal attributes (amplitude, slowness, azimuth, polarization, etc.), and store them in a commercial relational database management system (DBMS). IMS makes scheduled (e.g., hourly) transfers of the data to a separate DBMS at the Center. Arrival of new data automatically initiates a "knowledge-based system (KBS)" that interprets these data to locate and identify (earthquake, mine blast, etc.) seismic events. This KBS uses general and area-specific seismological knowledge represented in rules and procedures. For each event, unprocessed data segments (e.g., 7 min for regional events) are retrieved from NDAC for subsequent display and analyst review. The interactive analysis modules include integrated waveform and map display/manipulation tools for efficient analyst validation or correction of the solutions produced by the automated system. Another KBS compares the analyst and automatic solutions to mark overruled elements of the knowledge base. Performance analysis statistics guide subsequent changes to the knowledge base so it improves with experience.

The IMS is implemented on networked Sun workstations, with a 56 kbps satellite link bridging the NDAC and Center computer networks. The software architecture is modular and distributed, with processes communicating by messages and sharing data via the DBMS. The IMS processing requirements are easily met with major processes (i.e., signal processing, KBS, and DBMS) on separate Sun 4/2xx workstations. This architecture facilitates expansion in functionality and number of stations.

The first version was operated continuously for 8 weeks in late-1989. The Center functions were then transferred to NDAC for subsequent operation. Later versions will be distributed among NDAC, Scripps/IGPP (San Diego), and the Center to process data from many stations and arrays. The IMS design is ambitious in its integration of many new computer technologies, but the operational performance of the first version demonstrates its validity. Thus, IMS provides a new generation of automated seismic event monitoring capability.

INTRODUCTION

For decades, the need for improved capabilities to detect, locate, and identify underground nuclear explosions has been a major motivation for development of new technology in seismology. Seismic arrays were originally developed for this problem, and much work has been done over the years to improve their effectiveness (Ringdal and Husebye, 1982). During the 1970s, advancing technology and political developments shifted attention toward regional networks and the detection and identification of small events (magnitude < 3). This led to the design and deployment of the NORESS array in southern Norway (Mykkeltveit *et al.*, 1983), which

provides a significant advance in capabilities to detect and characterize the signals from regional events (e.g., Ringdal, 1985, 1986; Sereno *et al.*, 1988; Sereno and Bratt, 1989; Kværna, 1989). The success of NORESS motivated the deployment of a second array (ARCESS) in northern Norway (Mykkeltveit *et al.*, 1987). The locations and geometry of these essentially identical 25 element arrays are shown in Figure 1. For a more detailed review of the work leading to the deployment of these arrays and an assessment of their capabilities, see Mykkeltveit *et al.* (1990).

Each of these regional arrays produces a data volume (~2.6 Kb/sec) that is twice that of NORSAR, which is the largest teleseismic array in operation. Under normal conditions, the two arrays together detect an average of about 400 regional and 70 teleseismic signals/day (Bratt *et al.*, 1990), even though they are located in seismically quiet Scandinavia. There are days when there are more than 1,500 detections (most are from local sources), and it is important to prepare for the possibility that new arrays will be installed in much more active areas. Thus, substantial automation of the data analysis is important if we are to be able to take advantage of the full monitoring potential of these arrays. A major step was taken with the RONAPP program (Mykkeltveit and Bungum, 1984) that automatically detects and locates seismic events using NORESS data, and the work described in this paper builds on this experience.

The Intelligent Monitoring System (IMS) was developed as a new approach to the automation of seismic data analysis. It is a substantial departure from previous systems in its integration of artificial intelligence (knowledge-based systems) and

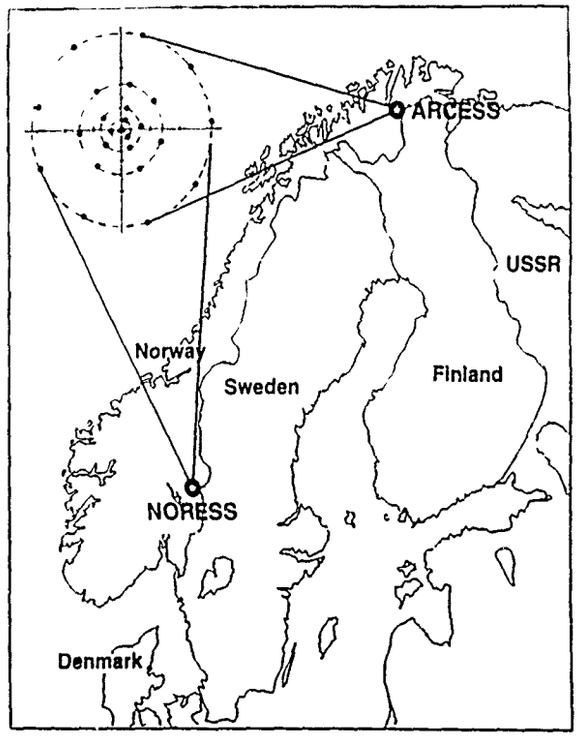

FIG. 1. The locations and array geometry are shown for the NORESS and ARCESS arrays. The two are essentially identical, each having 24 elements in four concentric rings (called A, B, C, and D) plus a center element (hub). The diameter of the outer (D) ring is 3 km. There are three-component seismometers at the hub and three of the seven sites in the C-ring. (Figure courtesy of Frode Ringdal, NORSAR.)

database management systems (DBMS) technology in an automated and interactive data analysis system. These computer science technologies provide a new capability for addressing several important issues in treaty monitoring seismology. First, to approach the performance of human analysts, the automated processing must represent complex area-specific knowledge. Second, the system must have facilities for rapid acquisition and addition of new knowledge (especially important when new stations are installed). Finally, there are some important unsolved problems (e.g., confident identification of small regional events), for which convenient access to a high-quality database of representative events is critical for future progress.

The purpose of this paper is to describe the first operational version of the IMS that produces a bulletin (detection and event lists) for the two-array network (NORESS and ARCESS). A much more complete and detailed description of the system is given by Bache *et al.* (1990), and an analysis of its operational performance is given by Bratt *et al.* (1990). The IMS system is being extended to larger networks, including both arrays and simpler stations, but the concepts and many aspects of the design will remain quite similar to those described here.

Architecture

The basic functions of the IMS are shown in Figure 2. The data are acquired and analyzed (Signal Processing) to detect signals and extract features that characterize them. From these features the knowledge-based system (KBS) locates and identifies events. As indicated, further signal processing is often required during Event Identification. There is an additional requirement to estimate the yield of underground nuclear explosions, but this is outside the IMS described in this paper.

The Interactive Analyst Review provides the capability to validate the solutions produced by the automated system, correcting them and making new solutions as

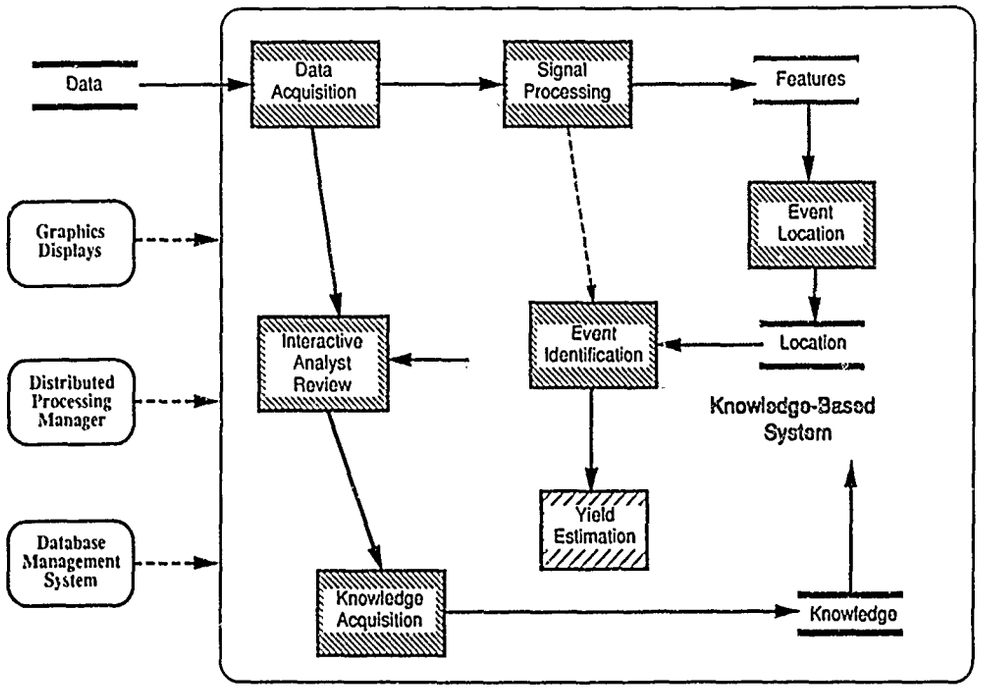

FIG. 2. The major functions performed by IMS are shown with solid arrows indicating the dominant direction of dataflow. Key software facilities that integrate the overall system are indicated at the left with dashed arrows to the box enclosing the functions.

necessary. As indicated in the figure, access to the original data is required for these tasks. The results of the analyst review are used in the acquisition of new knowledge to improve the automated processing. Figure 2 also shows three classes of software that provide key support facilities. These include the graphics displays that provide the man-machine interface, the facilities which manage the flow of data and control information among the various processes (Distributed Processing Manager), and the DBMS.

The software architecture of IMS is shown in Figure 3. The hardware architecture has been upgraded, but the configuration used for the initial operation in October–November 1989 illustrates the minimum requirements. During this period, the system included two Sun 4/2xx workstations at the NORSAR Data Analysis Center (NDAC) in Norway and five Sun workstations (two 4/2xx, 4/110, 3/160, 3/110) at the Center for Seismic Studies (Center) in Arlington, Virginia. These were on UNIX local-area networks (LANs) at each site, and the two LANs were connected with a Proteon gateway implemented on Proteon 4200-10 computers at the two sites. This gateway routes inter-LAN packets over the satellite link, creating a wide-area network (WAN).

Raw data from the arrays are digitized and recorded automatically in the field and telemetered to NDAC where the seismic data from each array are separated from the maintenance (state-of-health) data. The data are checked for validity and

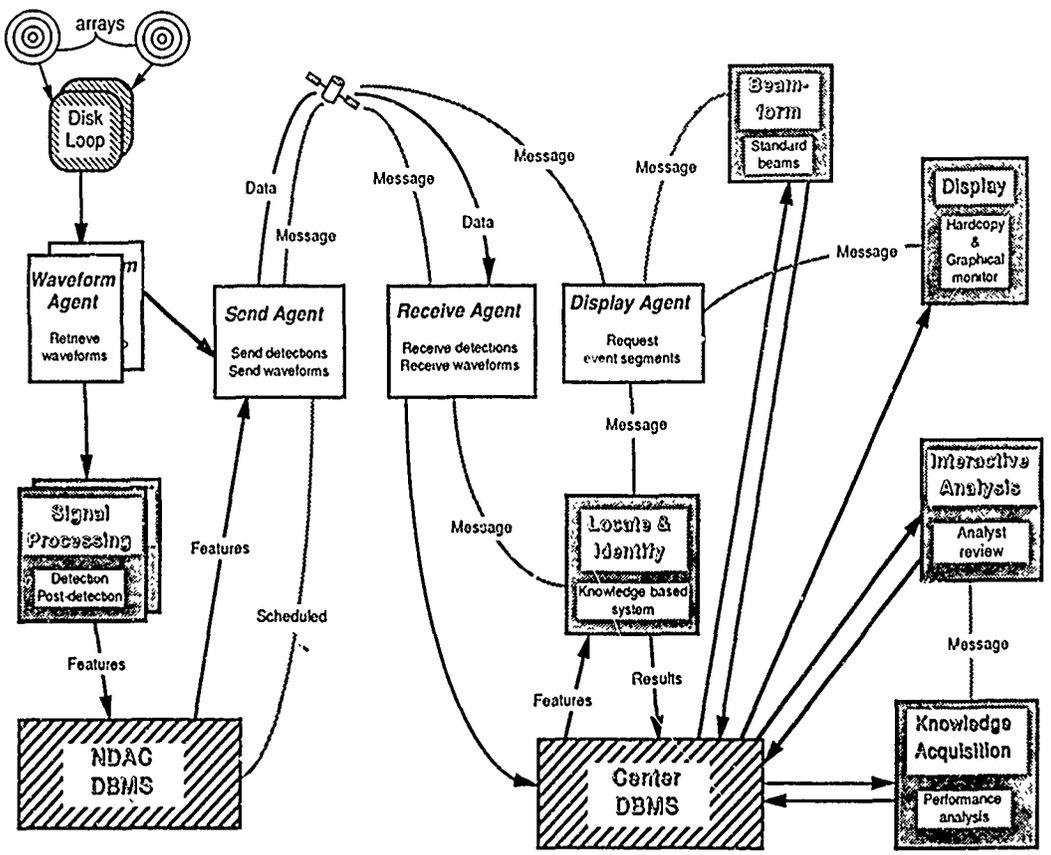

FIG. 3. The architecture of IMS is shown by the major groups of processes in the NDAC (left) and Center LANs, which are bridged by a wide-area network connection over a satellite link. The dark arrows indicate the flow of the most important data, and the light arrows show the key messages exchanged during the automated processing. The function of the Agent processes is to control the data flow. The arrays and Disk Loops are external to IMS.

stored on a first-in, first-out disk buffer called a Disk Loop (see Paulsen, 1986, 1988, for details on the data acquisition). The Disk Loops provide the external interface to IMS that begins with the Waveform Agent, which retrieves waveforms from the Disk Loop for each array, converts them to IMS database format, and feeds them to the Signal Processing process for that array. This process detects signals and computes the characterizing features using algorithms described in a later section. These features include attributes stored in the relational DBMS and UNIX files (e.g., spectra) managed by pointers in the DBMS.

On a regular schedule (usually once per hour), the Send Agent retrieves the features from the NDAC DBMS and transfers them to the Receive Agent at the Center. The latter inserts the features into a DBMS and sends a message telling the Locate & Identify process that new data are available for processing. This KBS is described in a later section. When the Locate & Identify process completes its interpretation of the data, it puts the results in the Center DBMS and sends a message to the Display Agent (DA). The DA retrieves the location from the DBMS and uses travel-time tables to select the waveform segments to be requested from the Disk Loops at NDAC and transmitted across the link to the Center. The Send and Receive Agents handle the transmission of the waveforms, and the latter sends a message to the DA when the waveforms for a particular event arrive. At this time, the DA initiates the Beamform process to compute a set of standard beams for summary output and later analyst review. When the beamforming is finished, the DA is informed, and it initiates the production of a hardcopy display (see Fig. 8 and related discussion).

The processes described so far are fully automatic, requiring no human interaction. The delay between signal arrival at an array and insertion of an event solution in the DBMS is somewhat arbitrary since there are several buffers introduced for operational convenience. It could be made as short as a few minutes after the *Lg* arrival. In the 1989 implementation, the minimum time segment for signal processing was 30 min, and detections and features were transferred to the Center each hour. Thus, the time lag before a location appeared in the Center DBMS varied between 30 min or so and several hours, depending on the arrival time of the last detected signal and the number of detections in the segment (the processing time is roughly proportional to the number of detections). Also shown in Figure 3 are the Interactive Analysis and Knowledge Acquisition functions that are done after the automated processing is completed. These will be described in a later section.

This distributed processing architecture locates the data-intensive signal processing near the source of the data at NDAC. Only waveforms including events thought to be interesting are transmitted across the link, and the volume of data retrieved depends on the criteria used. In the 1989 operation, the criteria were quite simple: 7 min segments of all channels at each array beginning 30 sec before the *Pn* arrival time for every regional event. The KBS formed about 50 regional events/day, and these simple criteria required retrieval of less than 20 per cent of the data (many event segments overlap, so the average length of the segments retrieved is less than 7 min). It is straightforward to reduce this by adding more complex criteria (e.g., shorter segments for local events) if the volume of data retrieved becomes an issue.

Figure 3 presents an abstract view of the IMS architecture that hides much of the complexity. The automatic processing involves 23 UNIX processes plus the two DBMS processes. The interactive analysis tools include 12 processes, and there are 8 others for process management and system administration. The software written specifically for IMS includes more than 200,000 lines of Fortran, C, Bourne shell,

and Lisp code (about 35 per cent are in-code comments that are essential for maintaining the software). IMS also includes commercial DBMS software (Oracle and Ingres), the X Window System (used for all graphics), and a commercial natural-language interface to the DBMS (from Natural Language, Inc.).

The individual processes within IMS communicate control information via interprocess communication (IPC) messages. All data are managed by the DBMS. Thus, process A transfers data to process B by inserting it in the DBMS and sending an IPC message to process B informing it that new data are available. This design allows substantially independent development of separate functional elements of the system with coordination achieved by shared database and IPC message dictionaries. It also facilitates the distribution of processes across a network of workstations, providing an architecture that is easily scaled up for future expansion. However, one of the major challenges of the development was implementation of this complex design in a robust and fault-tolerant operational system. At this stage of its development, UNIX does not provide the facilities needed for fault-tolerant management of IPC message traffic, and software to provide these facilities was written for IMS. It is designed to rout all IPC messages through a central Dispatcher process that ensures that they reach their destination and takes appropriate action if they do not. The Dispatcher is complemented by a Manager process that provides facilities for system administration and monitoring.

Database Management

All parametric data generated by IMS are managed by a commercial relational DBMS, and the processes retrieve and store data via SQL (a database query language) embedded in the source code. The database structure is an extension of the "Center for Seismic Studies Database Structure Version 2.8" (Brennan, 1987), with attributes and relations added to manage new data objects introduced during the IMS development (mainly to manage data generated by the KBS). The database also includes data that do not fit conveniently in the tabular structure of a DBMS, and these are managed by the UNIX file system with pointers maintained in DBMS relations (Berger *et al.*, 1984). Data in this category include the time series, Fourier spectra, and f-k power spectra.

As shown in Figure 3, IMS includes independent DBMS at NDAC (using Oracle) and the Center (using Ingres). Two different DBMS products are used for administrative reasons, and either will meet all IMS requirements. Data are transferred between the two with UUCP (a UNIX-to-UNIX file transfer utility) with independent counters providing unique indices. The waveform and spectrum files are transferred in an analogous way, with independent pointer relations maintained in the two DBMS.

An abstract view of the organization of the IMS DBMS is shown in Figure 4. The major relations (tables with rows called tuples that contain a fixed number of parameters called attributes) are detection, detloc, loc that describe events, and the audit relation that stores a history of the decision process. Each detected signal is represented by a tuple in the detection relation, and each event is represented by one or more tuples in loc. The detloc relation links events to detected signals associated with them. The many-to-one linkages from detloc indicate that many detections are associated with one event solution and that a single detection may be associated with several (hypothesized) event solutions. This method of linking detections with events is a powerful concept introduced in the original Center DBMS (Berger *et al.*, 1984) where it appears in the arrival, assoc, origin triad. As

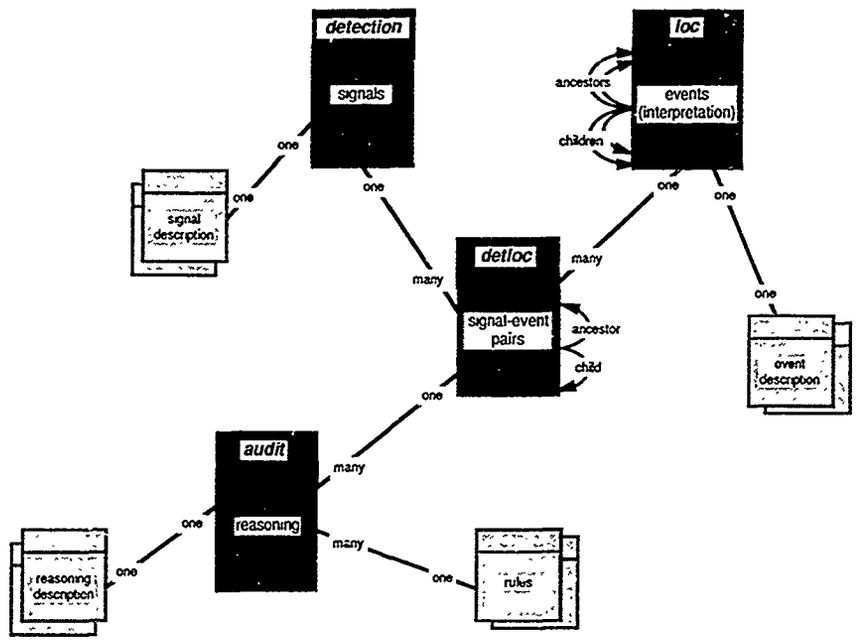

FIG. 4. The organization of relations (tables) in the IMS relational DBMS is sketched with the most important linkages among these relations.

shown in the figure, many relations can be added (with one-to-one linkages) as the need arises to describe the signals and events.

New features introduced in the IMS DBMS include the audit relations and the hierarchical linkage within the detloc and loc relations (represented by "ancestors" and "children"). In detloc, this is used to link several interpretations of a particular detection (e.g., the automated processing identifies it as *Sn*, but the analyst changes it to *Lg*). In loc this is used to link an evolving series of hypotheses for the solution for a particular event by the Locate & Identify processes. These processes write a sequence of audit tuples to maintain a record of the reasoning for each association between a detected signal and an event solution. Each audit tuple is linked to a tuple in a relation describing the knowledge base and to tuples in another relation describing how that knowledge was applied in this particular case (see the section on "Audit Trail and Explanation"). Also maintained in the DBMS are relations that provide process and state information for control and fault recovery.

The IMS database includes 25 dynamic relations and 14 quasi-static relations (beam recipes, instrument locations, etc.). There are 371 attributes in the dynamic relations, including 68 occurrences of 24 keys that link the relations. During the first 8 weeks of operation, some of these relations grew to more than 10^5 tuples, and they are continuing to grow at this rate. The rapid retrieval of data from this large and complex database is a major achievement of IMS best expressed in the smooth performance of the interactive analyst review station.

SIGNAL PROCESSING

The functions performed by Signal Processing are shown in Figure 5. Many of the algorithms (and FORTRAN subroutines implementing them) were adapted directly from the RONAPP code (Mykkeltveit and Bungum, 1984). The "Detection" algorithms are essentially identical to those in RONAPP. They begin with quality control to identify and repair or mask (exclude from subsequent processing) bad

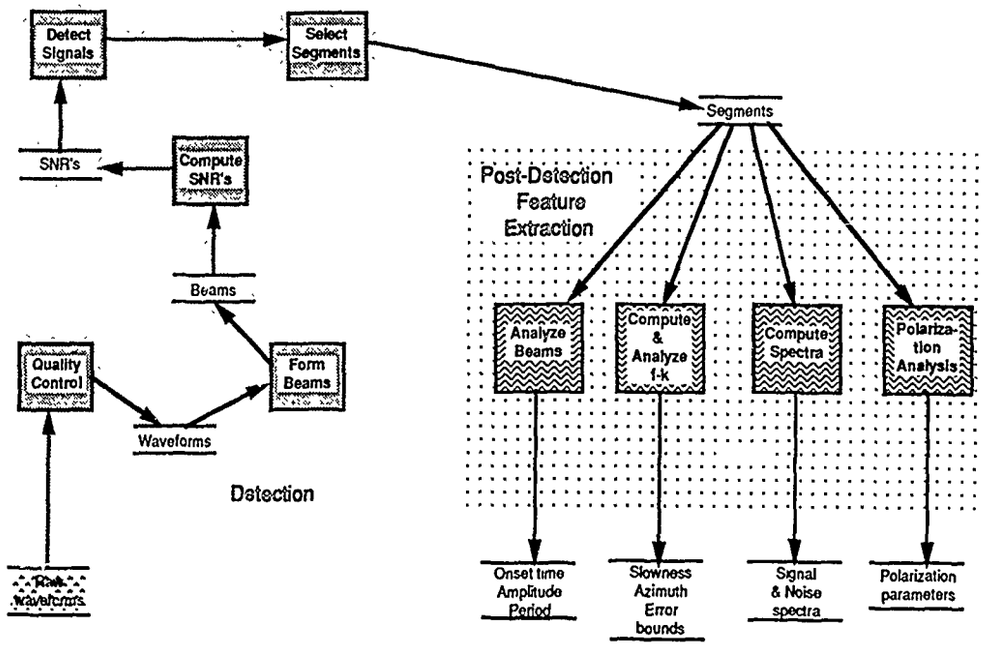

FIG. 5. The IMS signal processing is described in a dataflow diagram. The processing is divided into "Detection" and "Post-Detection Feature Extraction." In the former, seismic signals are detected and time segments containing signals are selected for subsequent analysis by the latter to compute the features shown along the bottom.

data. A fixed set of coherent and incoherent filtered beams are then formed on the vertical and horizontal channels. In the 1989 operation of IMS, 74 beams were computed, including 70 vertical beams selected according to the recommendations of Kværna (1989). These include 5 incoherent beams (formed by summation of selected channels after filtering and rectifying) that are filtered to detect the lower frequency *Lg* phase, 9 infinite velocity (unsteered) beams in different filter bands, and 8 beams selected to detect *P* waves from the major Soviet test sites at Novaya Zemlya and Semipalatinsk. The other 48 vertical beams are steered by simple delay-and-sum operations to 6 evenly spaced azimuths (30°, 90°, etc.) in 8 filter bands from 1.5–3.5 to 8–16 Hz. There are also 4 horizontal incoherent beams formed by summation of all (up to 8) horizontal channels after filtering and rectifying. The channels included in the beams are selected to optimize signal/noise (Kværna, 1989). For example, the lower frequency-steered beams are done with 17 seismometers (A0, C and D rings), and the highest frequency beams are done with 9 seismometers (A0, A and B rings). The RONAPP short-term average/long-term average (STA/LTA) detector is applied to each of the computed beams and a detection is declared whenever the SNR (= STA/LTA) exceeds a specified threshold. Simple rules are used to select the preferred "detecting" beam when several beams go into a detection state simultaneously.

As indicated in Figure 5, the "Detection" processing selects segments for four distinct post-detection processes. In Analyze Beams, the RONAPP algorithms are used to refine the detection onset time and estimate the amplitude and dominant frequency of the detected signal. The standard deviation in the onset time (used in subsequent location calculations) is computed here and varies from 4 sec when the SNR is at the threshold to 1 sec when SNR $\geqq$ 5 times the threshold (Bratt and Bache, 1988).

The *f-k* computation is done with the wide-band algorithm of Kværna and Doornbos (1986) using a 3 sec segment starting 1.1 sec before the onset time at the center element of the array. The frequency band for the calculation is one octave centered over the dominant frequency. The resolution is 0.02 sec/km in slowness between 0.0 and 0.4 sec/km. Estimates for the azimuth and slowness of the detected signal are obtained by interpolation around the peak power. The error in these estimates depends on the wavenumber resolution in this frequency band and the quality of the particular solution [see Bratt and Bache (1988) and Bache *et al.* (1990) for details on the error estimates]. Also computed are array-averaged spectra for each detection and a preceding noise segment using the method of Bache *et al.* (1985). The signal spectrum is computed for a 5 sec window starting 0.3 sec before the onset time, and the noise segment begins 12 sec before onset time.

The polarization analysis is done using the method of Jurkevics (1988) modified for automated application. This analysis is done in the time domain in thirteen 2 sec overlapping windows spaced 0.5 sec apart in an 8 sec data segment starting 4 sec before the onset time. Various features are computed from the eigenvalues of the polarization ellipsoid. These include the rectilinearity and apparent incidence angle in the time window of maximum rectilinearity, and the horizontal/vertical amplitude ratio and incidence angle of the smallest eigenvalue in the time window with the maximum three-component amplitude.

Automatic Signal Association and Event Location

As indicated in Figure 3, the Location & Identify KBS retrieves the most recent detections and their characteristics (features) from the DBMS on receipt of a message from the Receive Agent. The KBS associates detections with events and locates those events. This process requires the representation and evaluation of multiple hypotheses, and this is done with an "active multiple worlds" architecture. The association and location hypotheses are represented by "worlds," which are built up from the feature input through rule-based and procedural inference. This KBS is programmed in Lisp using Flavors for object-oriented programming and the Meta-level Representation System [(MRS), see Russell, 1985] for rule-based knowledge representation and inferencing.

As indicated in Figure 6, the reasoning process is divided into stages with independent rules at each stage. The detections from each array are first analyzed separately (Single-Array Processing), and the results are then fused to obtain the final solution in Network Processing. The reasoning process and knowledge applied at each stage is described in this section. The focus is almost entirely on event location, with only brief comments made about the complex subject of event identification.

Initial Phase Identification

Phase classification based on horizontal phase velocity (vel) from *f-k* provides a major simplification of the interpretation task. Phases with peak *f-k* power less than 2 dB above background are marked *N* (noise) in the detection list, so all phases considered to be seismic signals have reasonably accurate vel estimates. Following Mykkeltveit and Bungum (1984), we separate *P* and *S* phases at vel = 6 km/sec. In our experience, there are almost no exceptions to this rule. Separating teleseismic *P* and regional *P* is not as easy, but signals with vel > 14 km/sec are almost always from teleseismic events, and signals with vel $\leq$ 2.8 km/sec are almost always noise or late *S* coda detections (not useful for location) that can safely be treated as noise.

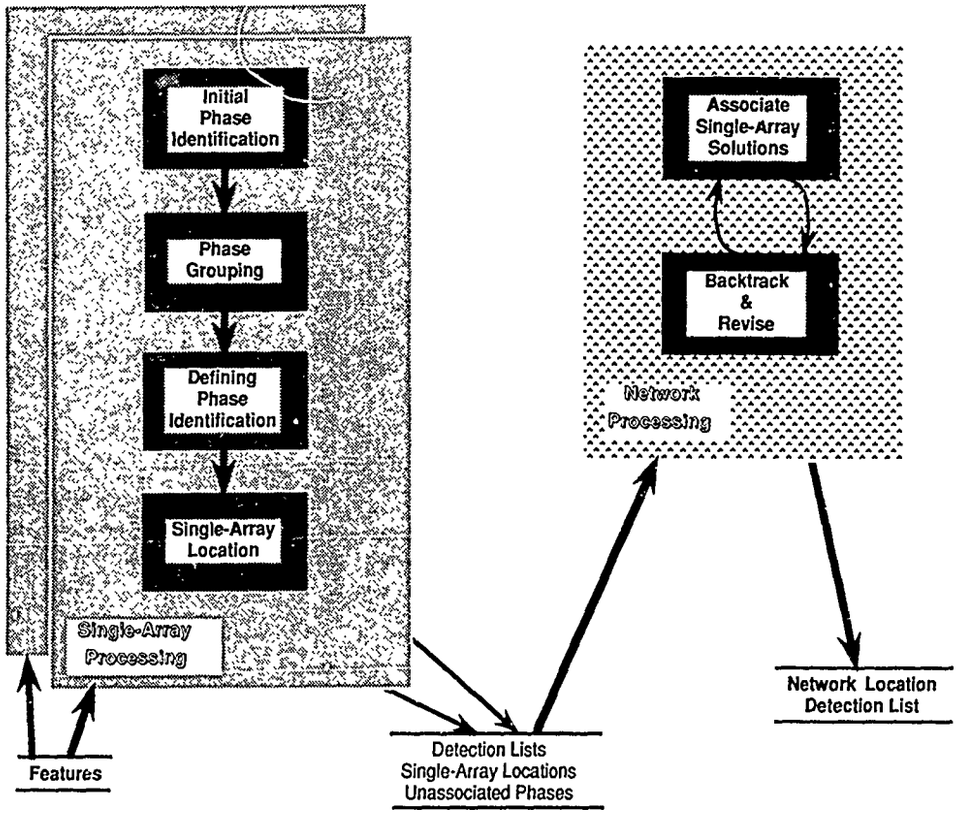

FIG. 6. The reasoning process employed by the IMS data interpretation expert system is sketched. The figure shows the major steps in the reasoning process applied to the data from each array. The results of the single-array processing are combined in Network Processing that is described in more detail in Figure 7.

Thus, phases with $14 \geqq \text{vel} > 6$ are identified as regional P, phases with $6 \geqq \text{vel} > 2.8$ are identified as regional S, and the other phases are marked in the detection list as T (teleseism) or N (noise) and removed from consideration as regional phases. Some of the remaining P will actually be teleseisms, and some of the remaining S will actually be noise. Many of these could be removed from the regional event interpretation by applying more knowledge (e.g., frequency content), but winnowing out these phases at this stage provides few advantages to offset the added complexity, at least in this first implementation.

Phase Grouping

The next stage is to form groups of P and S phases that could be generated by the same event. The detections are first separated into "initial groups." A detection is added to an initial group if it occurs within 6 min of the last detection in that group and if its azimuth overlaps (within signal-specific error bounds on the f-k estimate) with the azimuth of any detection in the group. Otherwise, a new group is formed. Each initial group is then analyzed to determine if the detections are from one or more events. An obvious indication of a second event is the presence of a P following an S. More complex rules comparing the patterns of P and S phases with the travel times for regional phases are also used to infer that the initial group includes detections from more than one event.

When there are two or more events, each P and S phase is assigned to an "event group." This can be very difficult since it is not always possible, even for a skilled human analyst, to unravel mixed signals correctly using data from only one array. Thus, the objective is to find the combinations of P and S phases that are most likely to be correct, recognizing that detections from another station might be needed to resolve ambiguity. This is done at a later stage (Network Processing). A significant simplification to the grouping problem is made by collecting closely spaced phases of the same type (P or S) into bins. Individual phases in the bins retain their individual identity, but it is sometimes convenient to treat a bin as a single phase (e.g., a phase and following coda detections). Various rules are applied to form these bins and associate P bins with S bins to form events. These rules consider the pattern of phases, their relative amplitudes and their azimuths. The result is assignment of phases to event groups that contain at least one P and one S phase. Some phases are ungrouped at this stage, but these may be associated with events during the subsequent Network Processing.

Defining Phase Identification

In this stage at least two "defining phases" (*Pn*, *Pg*, *Sn*, *Lg*, and *Rg*) are identified to provide the information necessary to locate the event with data from one array. The specific rules implemented in the 1989 version of IMS are given by Bache *et al.* (1990). They consider the apparent range from the array (based on the arrival time separation between the first P and largest S in the event group), the polarization, the pattern of P and S phases, relative amplitudes of phases, and the apparent location relative to major structural features (e.g., *Lg* does not propagate on oceanic paths).

Location

All seismic locations computed in IMS are done with an automated location program called LocSAT (from Bratt and Bache, 1988). This program uses back-azimuth and arrival-time estimates together with their error estimates (that depend on the signal/noise) in a least-squares-inverse location algorithm. The output includes the location solution (latitude, longitude, and origin time) and the 90 per cent confidence error ellipsoid. The depth is constrained to zero for all location solutions done during automated processing. The LocSAT algorithm allows the use of both *a priori* (the error estimates on the individual data) and *a posteriori* (the solution residuals) information about the data uncertainties. In the 1989 operation, the controlling parameters were chosen to make the confidence ellipsoids much more dependent on the input data error estimates than on the solution residuals.

The *Pn* and *Sn* travel-time curves are computed from the P-wave model provided by Mykkeltveit (personal communication) given in Table 1. The S-wave velocities in the crust are obtained by assuming a Poisson's ratio is 0.25, and the mantle S velocities were estimated from observations of 102 events recorded at NORESS and ARCESS. Constant group velocities of 6.20, 3.55, and 3.00 km/sec were assumed for *Pg*, *Lg*, and *Rg*, respectively. This model is most appropriate for paths from NORESS to the east. Paths to the west and to ARCESS are known to be different, but no attempt was made to account for these differences in the first operational version of IMS.

Network Processing

The results of Single-Array Processing are combined in Network Processing to obtain the final interpretation. The general concept is to start with solutions from one array, seek corroboration from observations at the other array, and resolve inconsistencies by backtracking to change earlier decisions. The objective is a consistent explanation of as many phases as possible. This reasoning process is sketched in Figure 7. In Event Grouping, single-array locations from each array are grouped if there is any possibility that they include defining phases (*Pn*, *Pg*, *Sn*, and *Lg*) from the same event. The rules group single-array locations if their origin times are within 6 min, and if the location from one array has at least one defining phase consistent (within large error bounds) with an event providing at least one defining phase for the location at the other array.

The ellipses from grouped single-array locations are compared to determine if their 90 per cent confidence ellipsoids (location and origin time) overlap. If they do, the single-array locations are assumed to be correct (i.e., the associated phases are assumed to be identified correctly), and the Network Location is computed. If they do not, rules are used to backtrack and revise earlier decisions to seek overlapping ellipses. First, the location nearest its locating array (array A) is assumed to be correct, and the defining phases from the array B location are revised using rules defining appropriate revisions. Each revision gives a new array B location, and this is tested to see if the new confidence ellipsoid overlaps with that from array A. If so, these single-array locations are assumed to be correct, and the Network Location is computed. If these revision options are exhausted without success, the original array B solution is fixed, and the same revision process is followed for the array A

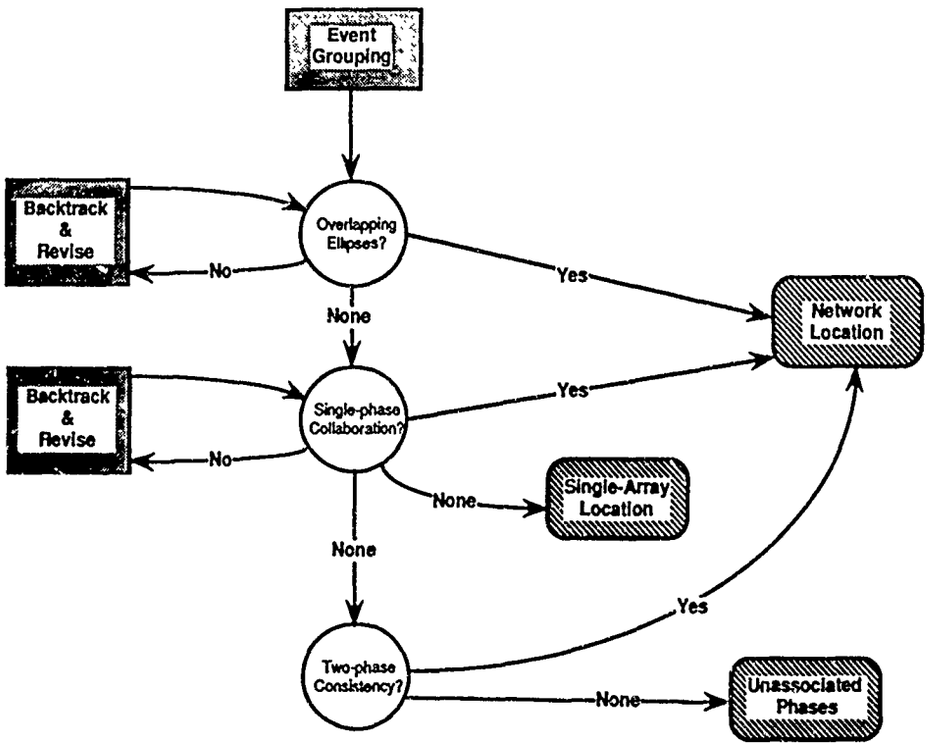

FIG. 7. The reasoning used for network processing is sketched. The output of this processing is indicated in the three boxes at the right side of the figure.

solution. If overlapping confidence ellipsoids are found during this process, it becomes the Network Location. As implemented in 1989, the backtracking is limited to revision of one defining phase from one array and associated changes needed to maintain consistency (e.g., if *Sn* is changed to *Lg* and *Lg* was already defined, this *Lg* is changed to undefining *S*). There are no rules that allow changing undefining *P* or *S* into a defining phase or that allow revision of defining phases at both arrays.

When the search for overlapping ellipsoids is completed, individual phases are sought to corroborate the remaining single-array locations. Each of these single-array locations is considered in order of origin time. The 90 per cent confidence ellipsoid is used to compute the minimum and maximum arrival times for each defining phase at the other station. If a phase at the other array has its arrival time within this time window, is of the correct type (e.g., *P* for *Pn* and *Pg*), and is not already a defining phase for another event, it is taken to be a corroborating phase. If several phases satisfy these criteria, the one with arrival time closest to the center of the time window is chosen. There are no limitations on the number (up to four) of corroborating phases found during this procedure, but usually there is only one. Occasionally, both *Pn* and *Pg* are found, and rarely both *Sn* and *Lg* are found. We do not expect to find both *P*-type and *S*-type defining phases at this stage, since phases that meet the conditions for corroboration would almost certainly have been associated during single-array processing. If no corroborating phases are found for the original single-array location, it is revised using the same rules applied during backtracking with overlapping ellipsoids. If all revision options are exhausted without finding a corroborating phase, the original single-array location is assumed to be correct and becomes the final solution.

In the last part of Network Processing, all phases not associated with an event during the previous steps are analyzed to form events from one defining phase at each array. Any two phases that are consistent with the same regional event (considering the error bounds on onset time and azimuth) are used to define a possible event. When there are several mutually exclusive possibilities for pairing phases (a common occurrence), rules are applied to select the solution most likely to be correct. Most of the events formed this way are later rejected by the analyst. The rules were designed to form nearly all possible events, recognizing that this will result in many false events, since an event hypothesis provides the basis for retrieving waveform data for analyst review. This bias toward false events reduces the possibility that an interesting event will be missed.

Magnitude

A magnitude is computed for each location after analyst review to validate that location is completed. This is computed from the peak amplitude of a filtered (2 to 4 Hz) incoherent beam (no steering) of 13 vertical channels (A0, B and C rings) in the time window defined by group velocities between 3.0 and 3.6 km/sec. A distance correction from Båth *et al.* (1976) is added to convert to magnitude. This magnitude is computed for each station that has any defining phase (i.e., it need not have an identified *Lg*), and the network magnitude is the mean of the solution magnitudes.

Event Identification

Since the focus in this paper is on automatic and interactive event location, we make only some brief comments on event identification. The Locate and Identify process includes a rule-based fusion of information that includes the location itself,

comparison of the pattern of detections with those from previous events of known type (Baumgardt, 1987), evidence of ripple-firing (Baumgardt and Ziegler, 1988), and *Pn/Lg* spectral ratios. Location is sufficient to identify many events, ripple-fired events are clearly industrial explosions, and some earthquakes are identified with high confidence with spectral ratios. However, many of the small events located by IMS are very difficult to identify. In fact, testing new concepts for identification is inhibited by uncertainty about the true source-type of many interesting events. Thus, the identification of small regional events remains a difficult and unsolved problem, and much work is needed to develop the knowledge required for reliable identification.

Audit Trail and Explanation

One of the major features that distinguishes the IMS KBS system from most other applications of this artificial intelligence technology is the integration with a relational DBMS for maintaining an audit record of the decision process. This audit record is central to the IMS knowledge acquisition concept (described in a later section), but it is also used for explanation of the reasoning (explanation is often cited as a distinguishing attribute of KBS). In more typical KBS applications, explanation is provided while all relevant data are resident in memory. However, in IMS interesting events happen at unpredictable and inconvenient times, and the practical options are to cache the explanation information within the relatively rigid framework of the DBMS, or to rerun the KBS on the original input data. The emphasis in IMS has been on the DBMS approach that offers persistent storage and the ability to sort and synthesize explanation information accumulated over a long period of time.

The audit record is designed to allow a reconstruction of the decision process, and no attempt is made to record every decision. Rules, groups of rules, and procedures used to make important decisions are represented by knowledge sources (KS) that are segmented into seven distinct KS classes. These KS classes follow closely the reasoning steps shown in Figure 6. They include signal processing, initial phase identification, initial detection grouping, phase grouping, defining phase identification, event grouping, and network location.

In the 1989 implementation, there were 40 KS, including 22 in the "defining phase identification" KS class. Some KS classes (signal processing, initial detection grouping, and event grouping) contain only one KS. The information they provide about the decision process can be inferred, but they are written for convenience in accumulating statistics for knowledge acquisition, as explained later. The audit record is stored in DBMS relations linked to the detloc relation (Fig. 4). For each detloc tuple, there are seven audit tuples (one for each KS class) that are linked to descriptions of the KS used to make the decisions. Explanation is provided in the analyst-review station by the capability to retrieve human-readable versions of these KS for each detection displayed.

Analyst Review

The analyst-review station (ARS) provides interactive display and editing tools to review, explain, and correct the solutions produced by the Locate & Identify process. It is integrated with separate processes that provide capabilities to display and manipulate digital maps and satellite imagery. Figure 8 shows a typical screen display after the analyst has selected a particular event for review and correction. In this example, the KBS has made a minor error in the interpretation of the

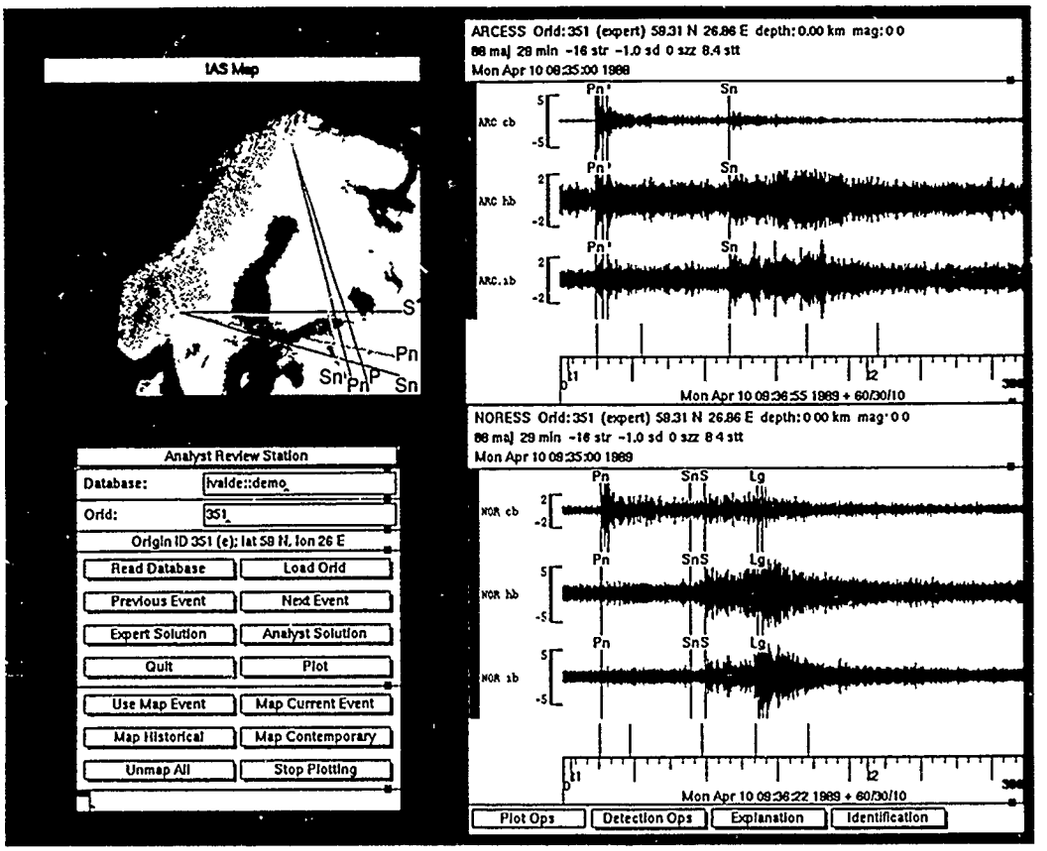

FIG. 8. A typical Analyst Review Station display is shown for an event solution (denoted by a unique Orid) obtained by the Locate & Identify expert system. The buttons on the control panel at the lower left are used to initiate operations, and the buttons on the waveform displays bring up menus with various operations. The waveform displays show standard beams for each array with the phase identifier at the onset time for all detections in the time segment. The vertical line with the phase identifier indicates that the phase is associated with the current Orid (in this case all phases are associated with Orid 351). The expected arrival times for *Pn*, *Pg*, *Sn*, *Lg*, and *Rg* (at ARCESS) are computed for the location solution and are shown as vertical lines above the time axis. The event solution has been sent to the map (with the "Map Current Event" button), and each phase is plotted with a line at the estimated azimuth. Also shown are the location and its confidence ellipse.

NORESS data (the second *S* is a better choice for *Sn*). Using ARS tools, the analyst can fix this error, expand the data to refine the onset timing, add, delete, associate, and disassociate phases, etc. Revised locations can be computed at any stage and plotted on the map at this or more detailed scales. The hardcopy plot of the KBS solution produced by the Display module (Fig. 3) as part of the automatic processing includes waveform and map displays that are nearly identical to those shown in Figure 8, plus lists of the most important information about the solution.

When the analysis is complete, the analyst can choose to validate or invalidate the KBS solution as a whole or write his corrected solution to the DBMS. The results of these analyst decisions are maintained in the DBMS with links between the KBS solution and revised solutions made by the analyst (for details, see Bache *et al.*, 1990). This linkage allows the analyst and KBS solutions to be compared in detail by the Knowledge Acquisition processes.

KNOWLEDGE ACQUISITION

The IMS knowledge acquisition concept is sketched in Figure 9. The Performance Validation process is a rule-based KBS that compares the automated processing

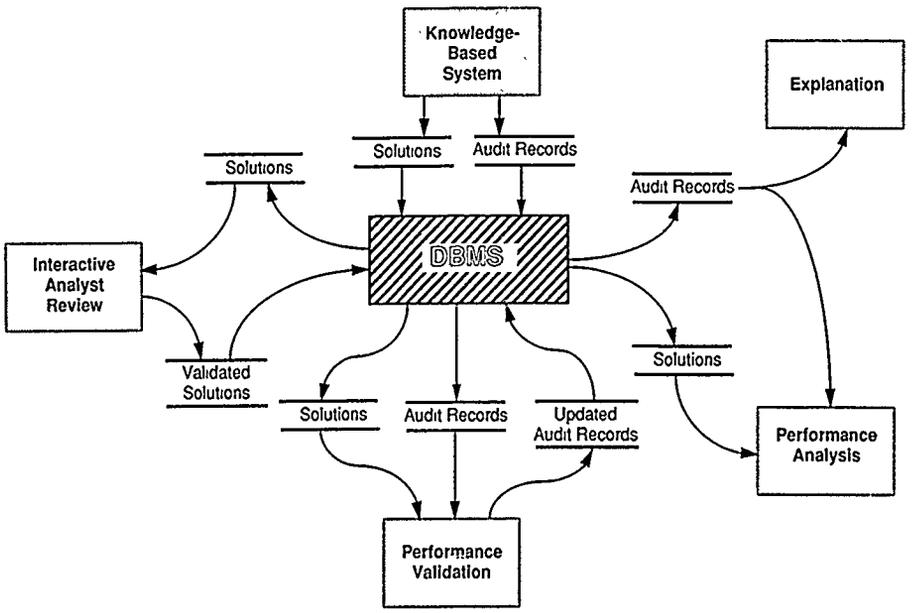

FIG. 9. The IMS concept for knowledge acquisition.

KBS and analyst solutions to determine which elements of the knowledge base (KS) have implicitly been invalidated by analyst corrections. The rules select the KS class where the error was made, and the audit tuple for this KS is marked invalid. The audit tuples earlier in the sequence are marked valid, and later tuples are marked to be ignored when statistics are computed (since earlier errors may be the cause of apparent errors in later decisions). The results of many analyst changes (retiming, renaming) are written to the DBMS with a one-to-one link between the KBS and analyst interpretation of a particular detection, and for these changes, the rules to select the responsible KS are relatively straightforward. More complex rules compare patterns in the groups of detections associated with the KBS and analyst event solutions to select the KS that has been invalidated by the changes made by the analyst.

The Performance Validation process also computes a variety of information that is maintained in summary relations in the DBMS. The attributes computed include array-event distances, number of associated phases of each type, etc. Other summary relations maintain statistics on the difference between KBS and analyst solutions (distance between the two, difference in number of defining phases, number of phases retimed, etc.).

Figure 9 indicates that the audit records provide the basis for Explanation (described earlier) and Performance Analysis. The latter includes organization and analysis of information about the performance of the KBS to develop new knowledge (rules). For example, a seismologist might find each KS that has been invalidated more than x per cent of the time it was used. All events that use one of these KS could then be plotted on the map to review the spatial distribution of events for which this KS was valid and invalid. Selected examples could then be retrieved for more detailed review. The objective is to focus attention on deficient elements of the knowledge base and to facilitate a systematic review of relevant examples to understand the deficiencies. Automated augmentation of the knowledge base is not attempted in IMS. Also, note that accumulation of adequate experience to develop

new rules takes time, so changes in the knowledge base are expected to be infrequent. New rules are validated by regression testing using previously processed events. The audit records help select an appropriate data set for regression testing, since they include a record of each use of a particular element of the knowledge base.

Conclusions

This first operational version of IMS provides a new generation of automated seismic data analysis capability. Even with the initial knowledge base, which was developed before the accumulation of much experience with these array data, the performance is quite good (see Bratt *et al.*, 1990). Much more important is that IMS provides a framework for rapid and convenient growth, both in performance and in the volume of data processed.

Most of the seismic data analysis concepts and algorithms included in IMS are well-known to seismologists. Where this system represents a major departure from previous work is in its integration of near state-of-the-art signal processing, KBS, DBMS, distributed processing, and computer graphics technologies in a robust operational system. The thorough integration of a commercial relational DBMS to manage all data is especially noteworthy in view of the size and complexity of the database and the stringent requirements for rapid data retrieval. Thus, one major conclusion is that DBMS technology offers the potential for large gains in R&D productivity across a wide range of problems requiring manipulation of large amounts of data.

The distributed processing architecture of IMS provides a cost-effective and scalable system by distributing the processing load across a network of relatively inexpensive workstations. Expansion in functionality and/or volume of data processed is done in a straightforward way by adding or modifying processes or processors. Another important advantage of this architecture is that it facilitates parallel software development since the individual processes are nearly independent. One of the major achievements of the IMS project is the successful implementation of this ambitious distributing processing architecture in a reliable operational system (full-time operation requires only one system administrator and one analyst). Since the software developed to manage the distributed processing is nearly independent of the details of IMS, it can be used for other distributed applications.

From the seismological perspective, the major advance of IMS is the integration of KBS technology into a complete system for detecting, locating, and identifying seismic events and acquiring new knowledge to improve the performance of the system. The initial period of operation identified a number of areas where better capabilities are needed (Bratt *et al.*, 1990). Some of them are in the signal processing; for example, there is a need for a better measure of onset time, improved detection of *Lg*, improved use of polarization information, and consistent measures of signal amplitude. In signal association and location, the KBS sometimes has difficulty with multiple event sequences, and there are many examples where improved use of station and region-specific knowledge is needed and would improve the location.

Identification of small regional events remains a difficult and unsolved problem, and this first operational version does not include the knowledge for a major breakthrough in this area. However, IMS does provide the framework for automated and interactive testing and evaluation of event identification procedures, which is expected to encourage rapid progress in the future.

In early 1990, the portion of IMS operated at the Center during 1989 was moved to NDAC for continued operation. The architecture differs only in that data are

moved between two DBMS at the same facility rather than across a satellite link. The system is currently being expanded to process data from two new NORESS-type arrays (in Finland and Germany) and several three-component stations elsewhere in Eurasia. The architecture of the first operational version of the expanded system will be like that shown in Figure 3, with processing again distributed among multiple sites.

ACKNOWLEDGMENTS

The authors were the leaders of a team effort involving many seismologists and computer scientists at SAIC and several subcontractors. The KBS for automatic location of regional seismic events was developed by Advanced Decision Systems (ADS), with important contributions from Greg Stachnick, Richard Chestek, and Sam Owre. Much of the software for event identification was developed by a subcontractor team including Ensco, Springfield, Virginia, and ISX, Thousand Oaks, California (Doug Baumgardt, Project Manager). While this portion of the system is not described in this paper, it is appropriate to acknowledge their significant contribution to the overall success of the project.

SAIC was prime contractor and system integrator. One of the authors (T.C.B.) was IMS project manager, and the other authors were task leaders for major elements of the system. The success of their efforts owes much to the innovation and leadership of senior SAIC staff, including Bill Farrell (database management and hardware design), Henry Swanger (interactive analysis and knowledge acquisition KBS), Anne Suteau-Henson (signal processing), and Jean Anderson (database management). Key software developers included Ethan Brown (signal processing and KBS integration), Laurie Clow (interactive map displays), Jerry Jackson (distributed processing management), Rick Johnson (interactive map displays), Brian Smithey (interactive analysis), Ed Tharp (user interface and KBS integration), Pete Ware (distributed processing management and interactive analysis), and Tom Yonkman (knowledge acquisition KBS). Jon Jump did much of the hardware integration, and Rick Strobridge led the installation of the communication links. Installation and integration of the IMS hardware at NDAC was done by NORSAR staff led by Rune Paulsen, and installation and integration at the Center for Seismic Studies was done by Bill Whyte and David Comay of Teledyne Geotech. A key to the success of the entire project was the early work done by NORSAR to automate the processing of NORESS array data, and their RONAPP program is properly viewed as the first version of IMS. Advice and assistance over the course of the project by Frode Ringdal, Svein Mykkeltveit, Tormod Kværna, and Rune Paulsen of NORSAR is gratefully acknowledged as an outstanding example of international cooperation. The work was supported by the Defense Advanced Research Projects Agency under Contract MDA-903-87-C-0037.

REFERENCES

Bache, T. C., P. D. Marshall, and L. B. Bache (1985). *Q* for teleseismic *P* wave from central Asia, *J. Geophys. Res.* **90**, 3575–3587.

Bache, T. C. and SAIC Staff (1990). Intelligent array system: System introduction and functional description, *SAIC Technical Report*, San Diego, California.

Båth, M., O. Kulhánek, T. Van Eck, and R. Wahlström (1976). Engineering analysis of ground motion in Sweden: Fourier and response spectra, attenuation, Seismological Institute, Uppsala University.

Baumgardt, D. R. (1987). Case-based reasoning applied to regional seismic event characterization, in *DARPA/AFGL Seismic Research Symposium*, Harbor House, Nantucket, Massachusetts, June 15–18, 173–178.

Baumgardt, D. R. and K. A. Ziegler (1988). Spectral evidence for source multiplicity in explosions: Application to regional discrimination of earthquakes and explosions, *Bull. Seism. Soc. Am.* **78**, 1773–1795.

Berger, J., R. G. North, R. C. Goff, and M. A. Tiberio (1984). A seismological data base management system, *Bull. Seism. Soc. Am.* **74**, 1849–1862.

Bratt, S. R. and T. C. Bache (1988). Locating events with a sparse network of regional arrays, *Bull. Seism. Soc. Am.* **78**, 780–798.

Bratt, S. R., H. J. Swanger, R. J. Stead, and F. Ryall (1990). Initial results from the intelligent monitoring system, *Bull. Seism. Soc. Am.* **80**, Part B, 1852–1873.

Brennan, M. A. (1987). Center for Seismic Studies Database Structure Version 2.8, Center for Seismic Studies Technical Report C87-04, Arlington, Virginia.

Jurkevics, A. (1988). Polarization analysis of three-component data, *Bull. Seism. Soc. Am.* **78**, 1725–1743.

Kværna, T. (1989). On exploitation of small-aperture NORESS type arrays for enhanced *P*-wave detectability, *Bull. Seism. Soc. Am.* **79**, 888–900.

Kværna, T. and D. J. Doornbos (1986). An integrated approach to slowness analysis with arrays and three-component stations, in *Semiannual Technical Summary, 1 October 1985–31 March 1986, NORSAR Sci. Rept. 1-86/87,* Kjeller, Norway.

Mykkeltveit, S., K. Åstebol, D. J. Doornbos, and E. S. Husebye (1983). Seismic array configuration optimization, *Bull. Seism. Soc. Am.* **73**, 173–186.

Mykkeltveit, S. and H. Bungum (1984). Processing of regional seismic events using data from small aperture arrays, *Bull. Seism. Soc. Am.* **74**, 2313–2333.

Mykkeltveit, S., F. Ringdal, J. Fyen, and T. Kværna (1987). Initial results from analysis of data recorded at the new regional array in Finnmark, Norway, in *NORSAR Sci. Rept. 1-87/88,* NTNF/NORSAR, Kjeller, Norway.

Mykkeltveit, S., F. Ringdal, T. Kværna, and R. W. Alewine (1990). Application of regional arrays in seismic verification research, *Bull. Seism. Soc. Am.* **80**, Part B, 1777–1800.

Paulsen, R. (1986). NORESS online system, in *NORSAR Tech. Rept. 1-86,* NTNF/NORSAR, Kjeller, Norway.

Paulsen, R. (1988). State-of-health system for NORESS/ARCESS, in *NORSAR Tech. Rept. 1-88,* NTNF/NORSAR, Kjeller, Norway.

Ringdal, F. (1985). Initial results from NORESS detection processing, in *NORSAR Sci. Rept. 1-85/86,* NTNF/NORSAR, Kjeller, Norway.

Ringdal, F. (1986). Regional event detection using the NORESS array, in *NORSAR Sci. Rept. 2-85/86,* NTNF/NORSAR, Kjeller, Norway.

Ringdal, F. and E. S. Husebye (1982). Application of arrays in the detection, location, and identification of seismic events, *Bull. Seism. Soc. Am.* **72**, S201–S224.

Russell, S. (1985). The compleat guide to MRS, in *Stanford Knowledge Systems Laboratory Report KSL-85-12,* Palo Alto, California.

Sereno, T. J., S. R. Bratt, and T. C. Bache (1988). Simultaneous inversion of regional wave spectra for attenuation and seismic moment in Scandinavia, *J. Geophys. Res.* **93**, 2019–2035.

Sereno, T. J. and S. R. Bratt (1989). Seismic detection capability at NORESS and implications for the detection threshold of a hypothetical network in the Soviet Union, *J. Geophys. Res.* **94**, 10,397–10,414.

SCIENCE APPLICATIONS INTERNATIONAL CORPORATION
10260 CAMPUS POINT DRIVE
SAN DIEGO, CALIFORNIA 92121
(T.C.B., J.W., C.K., J.W.G.)

ADVANCED DECISION SYSTEMS
1500 PLYMOUTH STREET
MOUNTAIN VIEW, CALIFORNIA 94043
(R.M.F.)

CENTER FOR SEISMIC STUDIES AND SCIENCE APPLICATIONS
INTERNATIONAL CORPORATION
1300 N. 17th STREET
SUITE 1450
ARLINGTON, VIRGINIA 22209
(S.R.B.)

Manuscript received 20 March 1990

Bulletin of the Seismological Society of America, Vol. 80, No. 6, pp. 1852–1873, December 1990

INITIAL RESULTS FROM THE INTELLIGENT MONITORING SYSTEM

BY STEVEN R. BRATT, HENRY J. SWANGER, RICHARD J. STEAD, FLORIANA RYALL, AND THOMAS C. BACHE

ABSTRACT

The Intelligent Monitoring System (IMS) integrates advanced technologies in a knowledge-based distributed system that automates most of the seismic data interpretation process. Results from IMS during its first 8 weeks of operation (1 October through 25 November 1989) are analyzed to evaluate its performance. During this test period, the IMS processed essentially all data recorded by the NORESS and ARCESS high-frequency arrays in Norway. The emphasis was on detection and location of regional events within 2,000 km of these arrays. All events were reviewed and corrected if necessary by a skilled analyst. The final *IMS Bulletin* for the period includes 1,580 regional events (~28 events/day). Approximately 55 per cent were smaller than M_{Lg} 1, with the largest just over M_{Lg} 3.

Comparison of IMS locations in southern Finland and northwestern USSR (800 to 900 km from both arrays) with event locations from the University of Helsinki's local network bulletin are used to assess the detection and location capabilities of the system. Two or more phases (minimum needed to locate) were detected for 96 per cent of the events with magnitude greater than 2.5. The median separation between the IMS and Helsinki locations for all common events was 23.5 km. A consistent bias in arrival-time and azimuth residuals was observed for events in small geographic areas, indicating that refined travel-time models and path corrections could further improve location accuracy.

The knowledge base in this first version of IMS was based on analysis of NORESS data, and many of the errors in interpretation corrected by the analysts can be attributed to differences encountered when this knowledge is used to interpret ARCESS data. Nevertheless, nearly 60 per cent of the events appearing in the final bulletin are automatic solutions approved without change or moved (by analyst corrections) less that 25 km from the automatic locations. The IMS had the most difficulty interpreting the overlapping signals generated by closely spaced explosions commonly detonated at mines in the Kola Peninsula and northern Sweden. Using the knowledge acquisition facilities included in the system, the deficiencies responsible for these and other errors are isolated, leading to development of new knowledge to be incorporated in the next version of the IMS knowledge base.

INTRODUCTION

The Intelligent Monitoring System (IMS) was designed for efficient and accurate processing of the large volumes of high-frequency data provided by new and proposed single-site and array stations in Eurasia (e.g., Mykkeltveit *et al.*, 1983; Korhonen *et al.*, 1987; Berger *et al.*, 1988). The IMS exploits advanced technology, including knowledge-based systems (KBS) for automatic detection and location, interactive waveform and map manipulation tools for analyst review of the solutions, and data management by an integrated relational database management system (DBMS). The input data are continuous waveforms, and the output is an on-line database, including identified phase detections, located seismic events, waveform segments, and a history of the decision process. A detailed description of the design of the IMS is provided by Bache *et al.* (1990).

The current performance and future promise of this new approach to automated analysis of seismic data is evaluated here by reviewing the results of IMS processing during an initial 8-week test period from 1 October through 25 November 1989. During this test period, the system processed regional data from the NORESS and ARCESS high-frequency arrays in Norway and was distributed between the NORSAR Data Analysis Center (NDAC) near Oslo, Norway and the Center for Seismic Studies (Center) in Arlington, Virginia. The specific objectives of this test were to:

- Assess the operational reliability and efficiency of the system.
- Collect an on-line database of parameters and waveforms from regional events in northern Europe, organized to facilitate the acquisition of new knowledge.
- Determine the regional monitoring capability of the overall system, including the instrumentation and analysis software.
- Explore the advantages of KBS technology for seismic data analysis, especially its capability to incorporate new knowledge acquired with experience.

Operational Experience

The IMS is an operational system with near-real-time performance requirements, and we assess its operational reliability and efficiency in this section. A complete description of the IMS architecture is presented by Bache *et al.* (1990), including Figure 1, which is reproduced here to provide a context for the discussion.

Instrumentation

The input data are from the NORESS and ARCESS arrays in Norway (Mykkeltveit *et al.*, 1983). These high-frequency arrays sample data at 40 Hz on 21 vertical and 4 three-component GS-13 seismometers distributed in four concentric circles with a maximum aperture of 3 km (Fig. 2). The full-period data (about 240 Mbytes/array/day) are telemetered continuously to NDAC. These arrays provided data to the IMS for 98 per cent (NORESS) and 97 per cent (ARCESS) of the 8-week test period.

Signal Processing

There is a separate computer (Sun 4/2xx), magnetic disk buffer (Disk Loop), and Signal Processing process at NDAC for each array in the system (Fig. 1). Raw waveform data telemetered from the field are placed on these Disk Loops where they remain for about 60 hr. Each Signal Processing process retrieves raw data from the Disk Loop, computes 74 beams, detects signals, measures signal features, and stores the results in the local DBMS. The most important features (see Bache *et al.*, 1990, for details) include onset time, amplitude, horizontal phase velocity, and azimuth from frequency-wavenumber (f-k) analysis, and measures of the polarization ellipsoid. On a Sun 4/2xx workstation, this processing requires an average of about 50 per cent of real time. During periods of anomalously high detection rates (discussed later), Signal Processing may fall behind real time, but it recovers quickly as the detection rate recedes toward normal. The IMS computers at NDAC in Norway are linked to the IMS computers at the Center in Virginia by a wide-area network bridge on a 56 kbit/sec satellite link. During the test period, the IMS made hourly transfers of all features from a DBMS at NDAC to a parallel DBMS at the Center. The average daily volume of features transferred was about 16 Mbytes for about 625 phase detections. The typical lag time between event origin

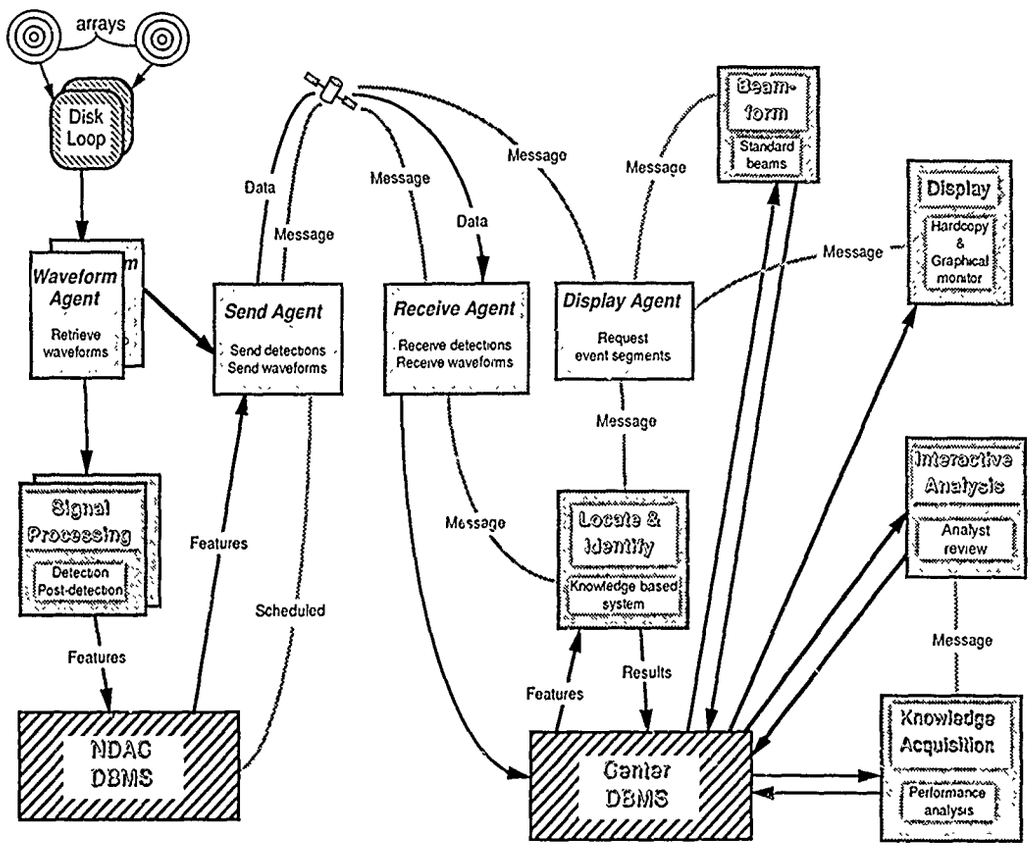

FIG. 1. Overview of the architecture and data flow for the IMS. Major processes are denoted by dark boxes, while "Agent" processes, which control data flow throughout the system, are shown as light boxes. Dark arrows indicate the flow of the most important data, and the light arrows show the key messages exchanged to schedule process operations. Processes in the NDAC (left) and Center (right) local area networks are bridged by a wide-area network connection over a satellite link. See Bache *et al.* (1990) for a detailed discussion of the IMS architecture.

time and the appearance of related features in the Center DBMS was between 1 and 2 hr. About 99 per cent of all waveform data received at NDAC were successfully processed and the features transferred to the Center.

KBS Location

Arrival of new data in the Center DBMS initiates the KBS (Locate & Identify, Fig. 1) that interprets the features. The signal detections are associated with events and identified as "defining" regional phases (e.g., phases used to locate: *Pn, Pg, Sn, Lg,* and *Rg*), or marked as unidentified regional phases, teleseisms, or noise detections. Using the onset time and *f-k* azimuth data for defining phases, surface locations are computed for regional events using the method of Bratt and Bache (1988). Magnitudes (M_{Lg}) are computed from *Lg* amplitudes measured on an incoherent beam filtered between 2 and 4 Hz and corrected with an amplitude-distance function modeled after Båth *et al.* (1976). The knowledge base used for this interpretation includes both general and area-specific rules and procedures. It is designed to form nearly all possible event solutions, since waveform data are retrieved for subsequent analyst review only for events located by the KBS. A history of the rules and data used to derive each solution is maintained in an "audit trail" output by the KBS. This is important for future improvement of the system,

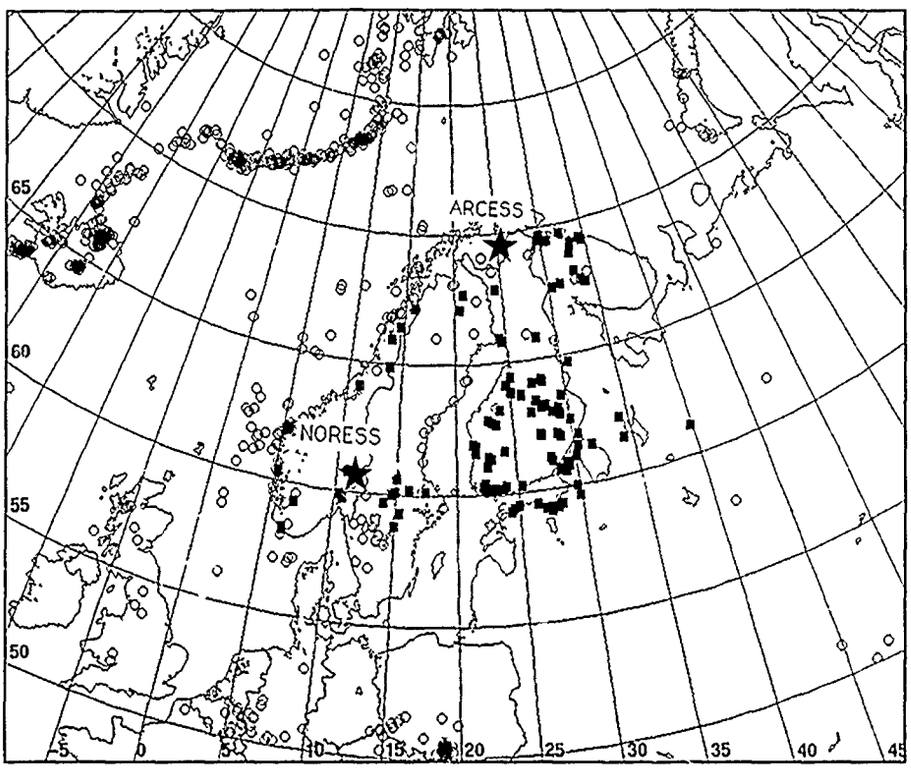

FIG. 2. Map of northern Europe showing the area monitored by the IMS. NORESS and ARCESS are marked by stars. Also shown are presumed earthquakes recorded between 1970 and 1979 (Bungum *et al.*, 1991; open circles), and the location of known mines and quarries (solid squares).

as will be explained later. On a Sun 4/2xx workstation, KBS processing requires about 25 per cent of real time to form an average of 44 events each day. The KBS location results are normally output to the DBMS within 1 to 4 hr of event origin time. This lag time is controlled by the duration selected for several buffers, and it could be reduced to minutes after the arrival of the last detected phase.

Waveform Retrieval and Hardcopy

The KBS initiates a request to retrieve the waveforms from the NDAC disk loop for each located event. During the test period, the system requested 420 sec segments of all channels from each array, with each segment starting 30 sec before the predicted time of the first *P* arrival. With these simple criteria, an average of 100 Mbytes of waveform data were retrieved daily for events formed by the KBS. Note that this is only about 20 per cent of the data recorded by the two arrays. Upon arrival at the Center, these data are beamformed (Beamform, Fig. 1) to accentuate regional phases from the direction of the hypothesized event, and a hardcopy display of the solution is made (Display).

Interactive Analyst Review

The Interactive Analysis processes include integrated waveform and map display and manipulation tools for efficient review of the solutions produced automatically by the KBS. Each KBS solution is validated as correct; corrected by the analyst if necessary, or rejected if the analyst cannot verify its existence. Thorough review of one day's data from two arrays generally requires 4 to 6 hr. The final *IMS Bulletin*, containing an average of 28 analyst-approved events per day, is completed within a

day of the event. All KBS and analyst-corrected solutions are permanently archived in the DBMS. The raw and beamformed waveform segments and the Fourier and *f-k* spectra are also archived for events larger than m_{Lg} 2 (~6 events/day). This archive grew at a rate of about 20 Mbytes/day during the test period.

Staffing

By the end of the test period, IMS operation required a system administrator to maintain the automated processes (Signal Processing, KBS Location, and Waveform Retrieval), and a seismic analyst to review the results (Interactive Analysis), with occasional hardware and software support from others. All IMS staff were located at the Center, with operation and maintenance of the NDAC processes performed remotely over the network bridge.

Final System Results

The principal products of the IMS are extensive parametric descriptions of detections and events and the appropriate waveform segments. These results are maintained in an on-line DBMS at the Center and are published in regular bulletins (e.g., IMS Staff, 1989). All results in this paper were compiled by queries to the on-line DBMS. They are viewed as samples of the information on seismicity patterns, crustal structure, and wave propagation that can be retrieved easily from the DBMS. In this section, we summarize detection and event statistics compiled from final (analyst-reviewed) IMS bulletins for the test period.

Setting

Fennoscandia and neighboring areas are situated on a relatively stable and aseismic shield region (e.g., Flinn and Engdahl, 1974; Jordan, 1981; Young and Pooley, 1985; Okal and Talandier, 1989), though felt earthquakes are not uncommon (e.g., Slunga and Ahjos, 1986). Large numbers of natural and cultural seismic events are recorded each year by several networks in the region (Bungum *et al.*, 1986). The largest known earthquake in northwestern Europe was a M_S 5.8 event near the central Norwegian coast (66.5 °N, 14.5°E) in 1819, but the vast majority of recorded events are smaller than magnitude 3 (Bungum and Selnes, 1988).

Figure 2 shows the location of presumed earthquakes (Bungum *et al.*, 1990) in northern Europe and adjacent waters recorded between 1970 and 1979. Although most are located along the Mid-Atlantic Ridge, a significant number of intraplate earthquakes have been identified, especially along coastal regions of Norway and Sweden. Also shown in Figure 2 are the locations of known mines and quarries in Fennoscandia. The major products of these include oil shale, granite, marble, pegmatite, phosphorite, apatite, iron, nickel, and copper (B. Leith, personal communication). Many of these open-pit mines can be seen on satellite images from the SPOT Image Corporation (Fox, 1989) and are quite large. Some of the oil-shale mines in Estonia are as large as 20 km across. Most of the seismicity detected by the IMS appears to be due to explosions in mapped (Fig. 2) and unmapped mines and quarries.

Detection Statistics

During the 8-week test period, 36,470 phases were detected at the two arrays and reported in the final *IMS Bulletin* (after analysis and correction of the KBS solutions). About 68 percent of these were detected at ARCESS. The KBS assigns initial phase identifications to each detection based on the horizontal phase

velocity (vel) measured from the *f-k* power spectra (Bache *et al.*, 1990). A detection is initially classified as noise (N) if $0.0 < \text{vel} \leqq 2.8$ km/sec, as a regional S if $2.8 < \text{vel} \leqq 6.0$ km/sec, as a regional P if $6.0 < \text{vel} \leqq 14.0$ km/sec, and as a teleseism (T) if 14.0 km/sec < vel. By these criteria, 28 per cent of the detections during the test period were noise, 45 per cent regional S, 16 per cent regional P, and 11 per cent teleseisms.

At NORESS, the largest number of detections are from the direction (90°) of the southern Sweden and northern Estonia mines and quarries. The number of NORESS noise detections peaks in the same direction. Many of these are likely to be from a sawmill located 15 km east of NORESS, which is known to contribute to noise levels at the array (Fyen, 1986). The dominant azimuths for regional signals at ARCESS are around 90°, 190°, and 230°—the azimuths to the Kola Peninsula, Estonia, and northern Sweden mines. The largest number of teleseismic detections at both arrays are from the direction of the Kurile–Kamchatka trench.

A severe test of the operational capacity of IMS was provided by several periods of very high rates of noise detections. These appear to be related to temperature changes near the arrays. Plotted in Figure 3 are the temperature and number of detections per hour at ARCESS for the 56 days of the test period. Note that, when the temperature drops rapidly and is below 0°C, the detection rate often rises as high as 50 or more detections/hr, which is well above the background level of 10 to 15 detections/hr. Almost all of the surplus detections have very low phase velocities (<2.8 to 3.0 km/sec), thus suggesting a near-local source. Given the coincidence in time of the low-velocity detections with falling, freezing temperatures, and the coincidence in azimuth of these detections (100°, 135°, 255°, and 325°) with the direction of lakes within 20 km of ARCESS, we propose ice tectonics as a possible source. (In further support of this hypothesis, the number of detections/month was lower by 30 to 40 per cent throughout continuing operation in January to June 1990, when rapid temperature drops were less frequent.)

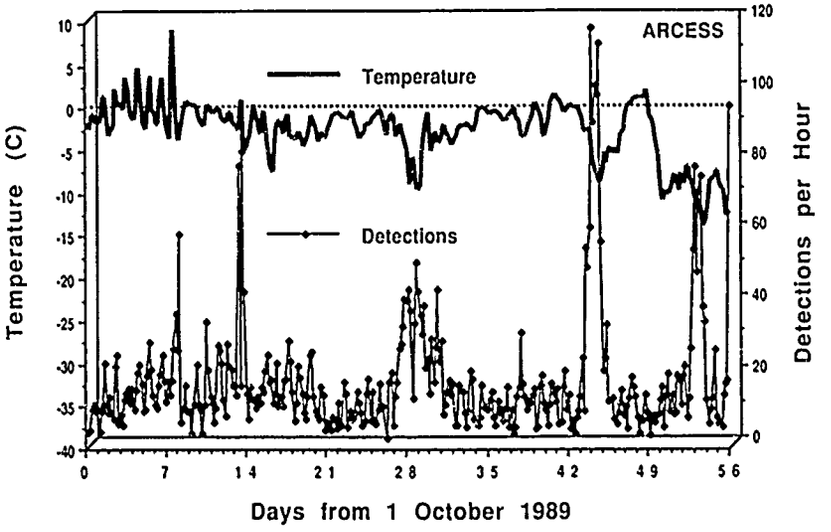

FIG. 3. The temperature at the center array element and the number of detections per hour are shown versus time at ARCESS. The detections in each of four categories, distinguished by their horizontal phase velocity, are also shown. The values plotted are averages over 4-hr intervals. Note the correspondence of increasing noise and regional S detection rates and sharply decreasing temperatures below freezing (0°C).

Table 1 summarizes the numbers of detections grouped by the final, analyst-reviewed phase identifications. About 30 per cent of phases likely to be from local and regional seismic sources (3.0 km/sec < vel ≦ 14.0 km/sec) are either defining and associated with events, or are *Px* and *Sx* detections (regional *P* and *S* with unknown paths) in the coda of defining phases. The *N* detections and the majority of the low phase (<3.0 km/sec) velocity *Sx* are detections triggered by seismic noise. About 11 per cent of all detections are teleseismic in origin.

Event Statistics

The plane-layer velocity model of Table 2 was used to compute IMS locations. The 1,580 event locations in the final bulletin for the test period are shown in Figure 4. Some of the events are probably earthquakes (e.g., those in the Norwegian and North Seas). Others are located in coastal or inland regions with known historical earthquakes (Fig. 2). Sixty-three per cent of all events are located within 50 km of one of the known mines in Figure 2, and the mining regions with the most activity during the test period are summarized in Table 3. There are also clusters of events in areas with no mapped mines (e.g., 62°N, 9°E; 69°N, 22°E).

The seismicity as a function of the hour of the day is plotted in Figure 5. Seismicity peaks around the middle of the work day and work week in this region. The rate of seismicity is 2.4 events/hr during normal working hours (800 to 1600 GMT) versus 0.7 events/hr at night and on weekends. The obvious anomaly is the local maximum between 2200 and 2400 GMT. A total of 212 events occurred during these hours, almost all of them near two mines in northern Sweden (Table 3).

During the test period, 35 per cent of all events were detected by NORESS only, 50 per cent by ARCESS only, and 15 per cent were large enough to be detected at both arrays. Figure 6 shows the seismicity as a function of magnitude for a 17-day period when magnitudes were consistently computed for all events (magnitudes

TABLE 1

PHASE DETECTION STATISTICS (OCTOBER 1–NOVEMBER 25, 1989)

Associated and Defining		Coda Detections		Unassociated Detections	
Phase	No.	Phase	No.	Phase	No.
Pn	1,466	*Px*	578	*Px*	3,167
Pg	444	*Sx*	621	*Sx* (3 < vel ≦ 6)	8,201
Sn	373			*Sx* (2.8 < vel ≦ 3)	5,751
Lg	1,647			*N*	10,258
Rg	2			*T*	3,962

TABLE 2

IMS VELOCITY STRUCTURE FOR NORTHWESTERN EUROPE

Layer	Thicknes (km)	V_P (km/sec)	V_S (km/sec)
1	16.0	6.20	3.58
2	24.0	6.70	3.87
3	15.0	8.10	4.60
4		8.23	4.68

Group velocities used for *Pg*, *Lg*, and *Rg* were 6.20 km/sec, 3.55 km/sec, and 3.00 km/sec, respectively.

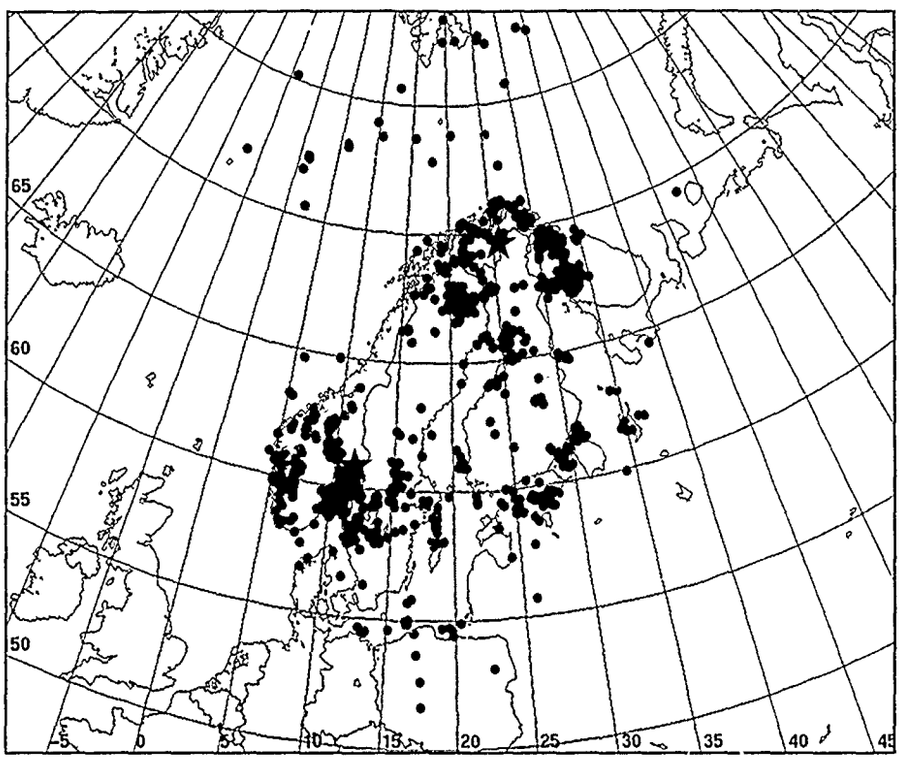

FIG. 4. Locations of all 1,580 final IMS solutions (solid circles) reported by the system from 1 October through 25 November 1989.

TABLE 3

MOST SEISMICALLY ACTIVE MINING REGIONS
(1 OCTOBER TO 25 NOVEMBER 1989)

Area Name	Latitude Range (°N)	Longitude Range (°E)	No. of Events within 50 km of a Mine	% of Final IMS Events
SW Norway	57–63	4–6	34	2
S Norway	58–60	8–12	118	7
S Sweden	58–61	14–16	154	10
N Sweden	67–68	20–22	225	14
N Estonia	58–60	24–28	47	3
W Kola Peninsula	67–70	30–35	320	20

were computed only for the larger events during the rest of the test period). About 55 per cent of these events are smaller than M_{Lg} 1, with the largest near M_{Lg} 3. The events with M_{Lg} between 0 and 1 are detected by one array and occur within 300 to 400 km of that array. Events between M_{Lg} 1 and 2 are distributed over a larger region, but only 15 per cent are detected at both arrays. About 85 per cent of the events between M_{Lg} 2 and 3 are detected by both arrays, even though some of these are as much as 2,000 km from one of the detecting arrays.

DETECTION AND LOCATION CAPABILITY

An estimate of the detection and location capability of the IMS requires a comparison with accurate independent estimates of the source parameters of typical

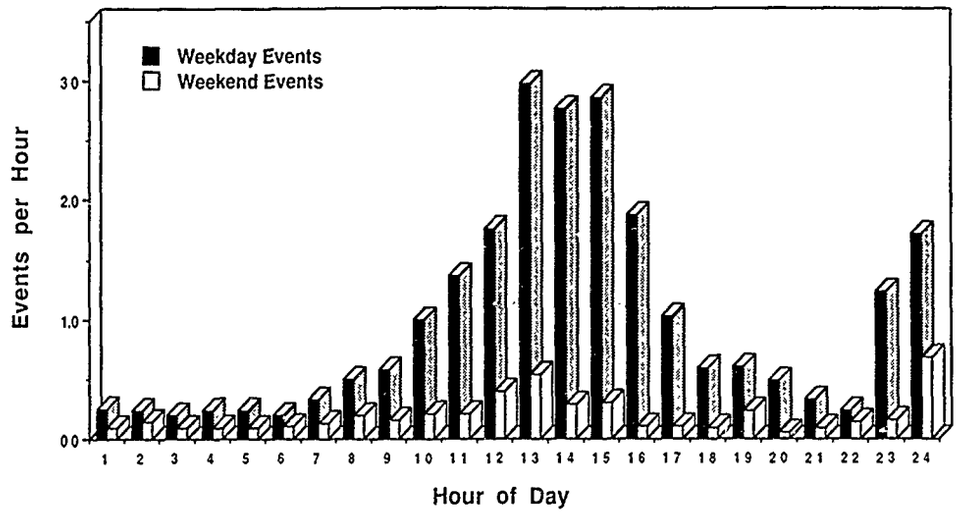

FIG. 5. IMS events per hour are plotted versus hour of day during week-days and weekends. Times are given relative to Greenwich Mean Time (GMT) and the local time in this area is between GMT to GMT + 2 hr.

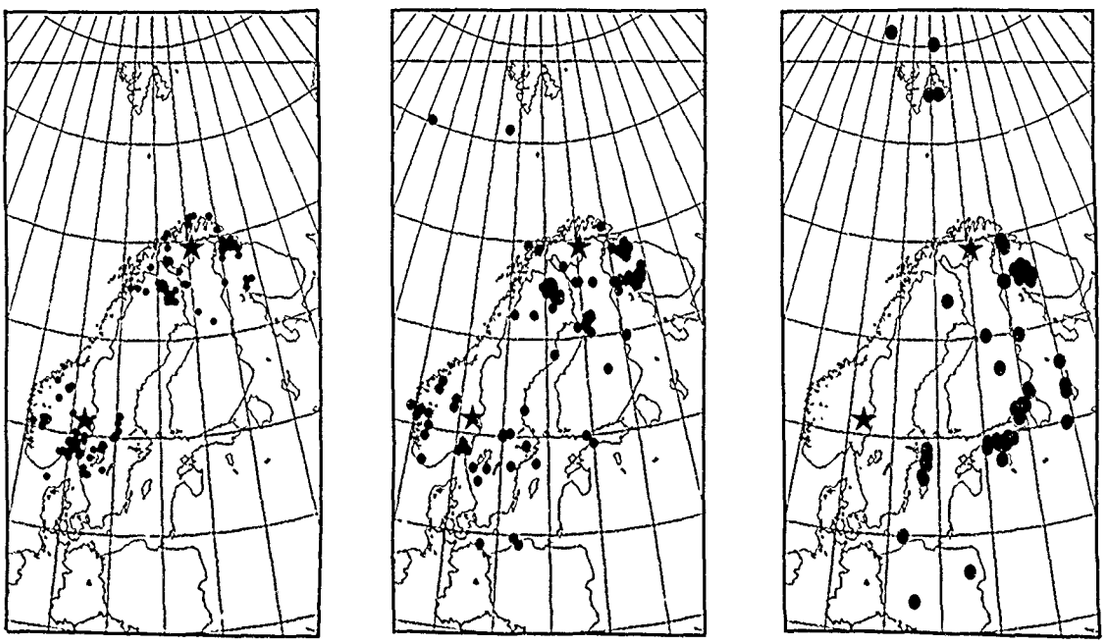

(a) $0 < M_{Lg} \leq 1$ (b) $1 < M_{Lg} \leq 2$ (c) $2 < M_{Lg} \leq 3$

FIG. 6. Location of events reported between 9 through 25 November 1989 with magnitudes between (a) M_{Lg} 0 and 1, (b) M_{Lg} 1 and 2, and (c) M_{Lg} 2 and 3.

events. For this purpose, we use the University of Helsinki monthly bulletins for the Finnish seismic network (Ahjos *et al.*, 1989). In particular, we focus on events from the test period located in a "comparison region" between 59° and 66°N, and 23° and 31°E (Fig. 7), where the Finnish network solutions should be better than those from the more distant arrays. There are 12 Finnish network stations within or near the borders of this comparison region that provide 90 per cent of the detections listed in the *Helsinki Bulletin* for the events in this region. All of these events are within 200 km of the nearest station, and most have two or three stations

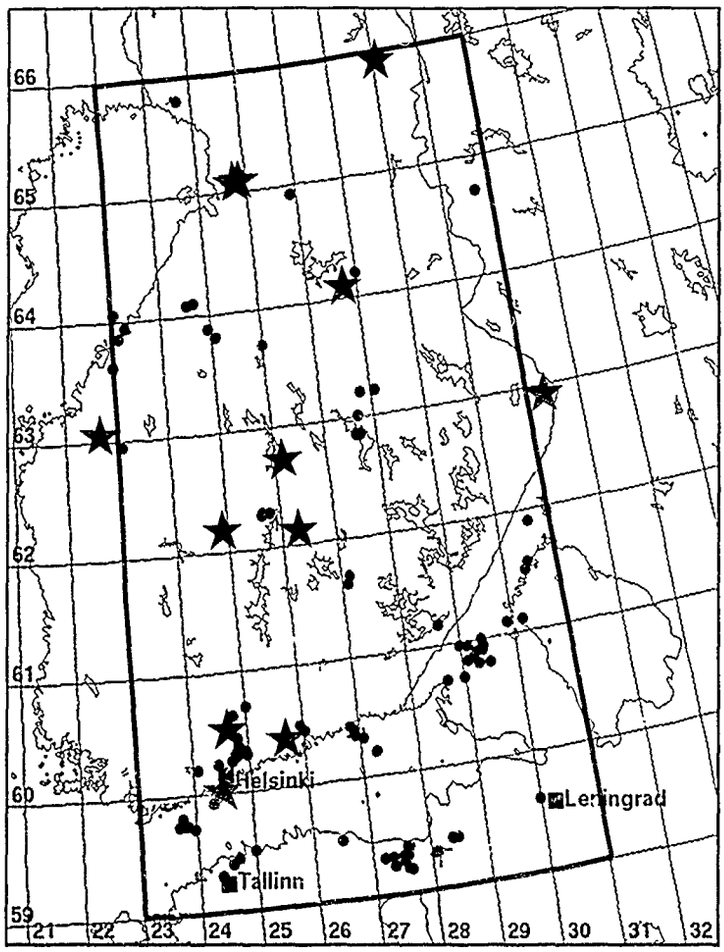

FIG. 7. IMS detection and location capability were assessed for the area shown, which is between 59° and 66°N, and 23° and 31°E. The 435 *Helsinki Bulletin* events used in the study (closed circles) and Finnish network stations that contributed to the bulletin (stars) are shown.

that close. By contrast, NORESS and ARCESS are 800 to 900 km from most of the events in the comparison region.

The *Helsinki Bulletin* lists 435 events in the comparison region for the test period. Of these, 331 (76%) have "manual locations," indicating that they were associated with a known mine based on visual inspection of relative arrival times and the appearance of the waveforms (an example of pattern recognition by skilled analysts that is difficult to reproduce on digital computers). For these events, the bulletin lists the known mine location with an origin time computed from one or more phase arrival times. Manual locations are reported to 0.1° in latitude and longitude, and analysis of satellite imagery (Fox, 1989) indicates that they are accurate within this precision. Other *Helsinki Bulletin* solutions are computed via standard least-squares inversion of the phase onset times and are reported to 0.001°. The true accuracy of these locations is unknown, but since most of the events are inside the detecting network, the location accuracy is probably similar to that for the manual locations (0.1°).

Detection Capability

To analyze the detection capability of the IMS, we predict the expected arrival times, azimuths, and phase velocities of *Pn, Sn,* and *Lg* for each Helsinki event,

then search the IMS database for detections that fall within a "correlation window" for all three attributes. *Pg* is rarely observed at the arrays from southern Finland events and is excluded from this comparison. The correlation window for time is ±10 sec of the time predicted from a Helsinki event using the IMS velocity model (Table 2). When more than one detection falls within the *Pn* or *Sn* correlation window, the earliest detection is selected. For *Lg*, the detection closest to the predicted time is selected. The window for azimuth is ±30° of the predicted azimuth. The correlation windows for phase velocity are 7 to 14 km/sec for *Pn*, 4 to 6 km/sec for *Sn*, and 2.8 to 5 km/sec for *Lg*.

The *Helsinki Bulletin* includes coda magnitudes (M_c) for 96 of the 435 events listed in the region. These are presumably the larger events (only $M_c \geqq 2.0$ are listed), and IMS detected at least one phase from 79 per cent of these, but from only 38 per cent of the others. To estimate the IMS detection capability, we compute the percentage of the 96 Helsinki events detected by the IMS as a function of M_c. This percentage converts directly to a "probability of detection" if the 96 events with M_c are a representative sample. Figure 8 shows this "probability" for detecting one, two, three, and four or more phases from events in the comparison region. Two or more phases (the minimum number required to locate using arrival times and azimuths) are detected for 96 per cent of the events with $M_c > 2.5$. For 83 per cent of these events, three or more phases were detected, thus providing more accurate locations. Overall, three or more phases were detected for 58 per cent of these events with $M_c > 2.0$.

Table 4 summarizes the IMS detection statistics for all 435 events listed in the *Helsinki Bulletin* for the comparison region. Approximately 47 per cent were detected by the IMS network. Each array detected about the same per centage of all events (34 per cent at NORESS, 36 per cent at ARCESS) and of events not detected by the other array (11 per cent at NORESS, 13 per cent at ARCESS). Since the two arrays are approximately the same distance from the comparison

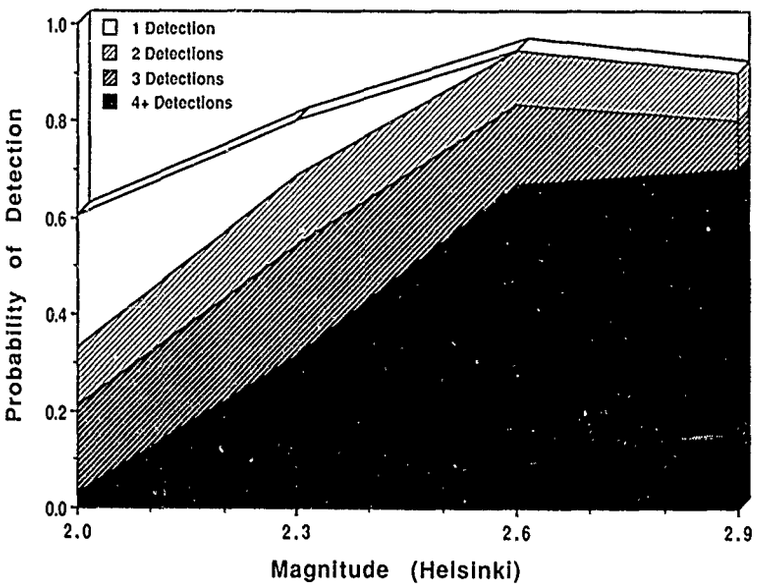

FIG. 8. Probability of detecting one, two, three, and four or more detections by the two arrays for events in the area outlined in Figure 9. These statistics are based on comparison of the *IMS* and *Helsinki Bulletins*. The median location of events used in the study were 890 and 820 km from NORESS and ARCESS, respectively.

TABLE 4
IMS DETECTION STATISTICS FOR 435 HELSINKI EVENTS

Detecting Grouping	No. of Events Detected	% of Events Detected
Detected by 1 or 2 arrays	204	47
Detected by NOR	146	34
Detected by ARC	156	36
Detected at both arrays	98	23
Pn at NOR	102	23
Pn at ARC	134	31
Sn at NOR	45	10
Sn at ARC	63	14
Lg at NOR	98	23
Lg at ARC	68	16
Only *Pn* at NOR	9	2
Only *Pn* at ARC	24	6
Only *Lg* at NOR	25	6
Only *Lg* at ARC	7	2

region, this similarity indicates similar capability. However, there are some interesting differences. A higher per centage of NORESS events include *Lg* (23 per cent versus 16 per cent at ARCESS), while a higher per centage of ARCESS events include *Pn* (31 per cent versus 23 per cent at NORESS). This difference in detectability of *Pn* and *Lg* is also seen in those events (probably small) that have only one detected phase. This phase is *Lg* more often at NORESS and *Pn* more often at ARCESS.

Location Capability

To assess the location capability, we correlate IMS final locations with *Helsinki Bulletin* locations in the comparison region. Two locations are said to be for the same event if they are separated by less than 2° latitude, 4° longitude (~220 km), and 60 sec in origin time. If two or more event pairs satisfy these criteria, the pair with the smallest origin time separation is selected. There are 114 events with locations in both bulletins according to these criteria, including 54 with both M_{Lg} (*IMS Bulletin*) and M_c (*Helsinki Bulletin*). The mean magnitude difference ($M_{Lg} - M_c$) was -0.03 ± 0.26, indicating no significant bias between the two magnitudes in this region.

Figure 9 is a histogram of the separation between the IMS and Helsinki event locations. Out to about 100 km, this histogram is consistent with the skewed normal distribution expected for a random distribution of (positive) location differences about a mean. The median location separation for the entire population is 23.5 km. The 10 events with separation greater than 100 km were analyzed in detail. Eight were detected by only one array (one at NORESS and seven at ARCESS). Four of the ARCESS solutions were mislocated by the IMS analyst due to the misidentification of *Sn* as *Lg*. In each case, *Sn* had low signal-to-noise and *Lg* was not detected; thus, correct phase identification is very difficult without knowledge of the Helsinki solutions. The other four single-array solutions were mislocated due to poor azimuth estimates from low signal-to-noise detections.

Fourteen events in the *IMS Bulletin* that have no correlated Helsinki location were also examined in detail. Nine appear to be correct, but were either mislocated or not reported in the *Helsinki Bulletin*. One was a very small event with an

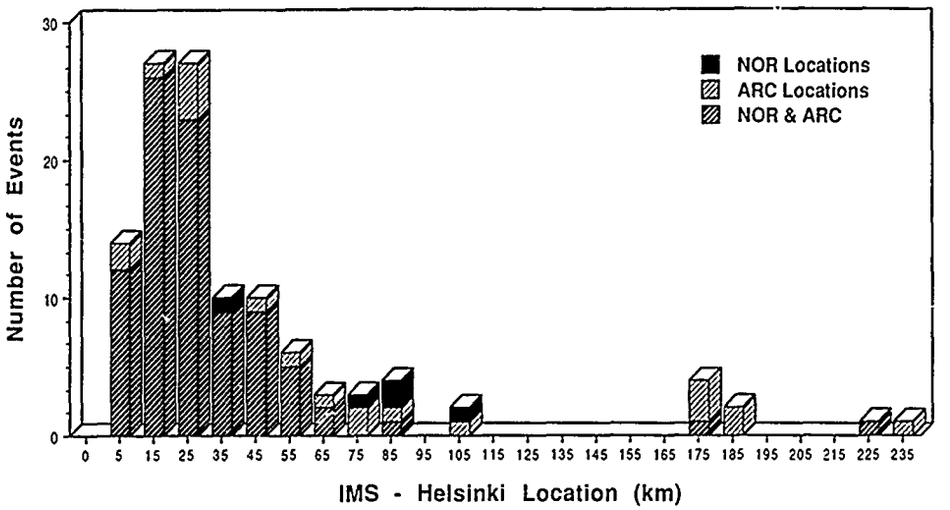

FIG. 9. Number of events binned by the distance separation between IMS and *Helsinki Bulletin* locations from the area outlined in Figure 9. The median separation is 23.5 km.

uncertain IMS single-array location, one was a misidentified teleseism, and three were single-array locations with poorly associated, mixed signals from multiple events. These multiple events were a major problem for the analyst, as will be discussed later.

Residual Analysis

Systematic bias and random scatter to structural heterogeneity and different analysis procedures are likely causes for small location differences (0 to 20 km). We estimate the bias and scatter from the difference between the IMS observations and the values predicted from the *Helsinki Bulletin* locations with the IMS velocity model (Table 2). The mean residual (Δt for arrival time and $\Delta\alpha$ for azimuth) is partly a measure of the bias relative to the IMS velocity model. Bias in the velocity model used for the *Helsinki Bulletin* also contributes to the residuals (especially for arrival time), but this contribution should be relatively small since most events are within the observing network. The standard deviation in the residual (σ_t for arrival time and σ_α for azimuth) indicates the scatter about the mean, which provides an estimate of the accuracy possible when bias is removed.

Table 5 lists the residual statistics for IMS detections that correlate with Helsinki events in the comparison region. Although little bias is evident in the Δt for most station/phase combinations, the IMS velocity model is apparently too slow ($-\Delta t$) for *Lg* propagation to ARCESS. No significant bias is evident from the $\Delta\alpha$ for any phase. However, the σ_α for *Pn* and *Sn* at ARCESS is substantially smaller (~4° to 5°) than for other station/phase combinations (~8° to 11°). For small subregions, the residuals are often quite large and typically more consistent (small σ) relative to those measured over the entire comparison region, as shown by the statistics for 14 events in an Elijaervi, Finland, mine (Table 5). This indicates the potential value of subregion-specific path corrections to improve location accuracy. These are being developed now and will be applied in future versions of IMS.

KBS PERFORMANCE

A unique and important part of the IMS is the integration of KBS technology into a seismic processing and analysis system. Bache *et al.* (1990) describe the

TABLE 5

MEAN AND STANDARD DEVIATION OF TIME AND AZIMUTH RESIDUALS RELATIVE TO *HELSINKI BULLETIN*

Array	Phase	No.	Δt (sec)	$\Delta\alpha$ (°)
Comparison Region (59°–66°N, 23°–31°E)				
NOR	*Pn*	102	0.5 ± 2.5	−1.9 ± 11.1
	Sn	45	1.0 ± 2.4	−0.6 ± 9.8
	Lg	98	0.2 ± 2.9	3.9 ± 7.1
ARC	*Pn*	134	−0.3 ± 1.9	−1.8 ± 5.4
	Sn	63	0.3 ± 2.9	1.3 ± 4.1
	Lg	68	−2.4 ± 3.0	−3.9 ± 11.0
Elijaervi Mine Region (65°–66°N, 23°–25°E)				
ARC	*Pn*	13	−0.1 ± 1.7	−6.9 ± 1.1
	Sn	13	1.9 ± 3.8	1.6 ± 4.0
	Lg	14	−3.5 ± 3.8	−6.7 ± 4.8

architecture of the KBS and the "knowledge" (rules and procedures) included in the initial operational version. A principal motivation for using KBS technology is to facilitate the addition of new knowledge to improve the performance of the system as experience accumulates, and Bache *et al.* also describe the IMS "knowledge acquisition" concept. It includes careful analyst review of all solutions produced by the automated processing to provide a standard for evaluating the KBS performance. Each automated KBS solution is cached in the DBMS together with audit records describing the key decisions. The results of subsequent analyst review are then written to the DBMS with links to the corresponding KBS solutions, and the knowledge acquisition software compares the two to analyze the performance of the KBS.

In this section, we describe the performance of the first operational version of IMS from the "knowledge acquisition" perspective. Since this initial knowledge base was developed by studying NORESS data, an unsurprising conclusion is that many mistakes are caused by features of the ARCESS data that differ from those seen at NORESS. Thus, added knowledge that accounts for these and other region-specific characteristics of seismic signals and local seismicity will significantly improve the performance of the KBS.

Comparison of KBS and Analyst Solutions

During the 8-week test period, the KBS generated 2,450 event solutions, and each was validated, corrected, or rejected by the analyst to obtain the 1,580 events in the IMS final bulletin (and discussed in previous sections). The analyst decisions about the KBS solutions are summarized in Table 6. The "added" events are those created by the analyst and appear in the DBMS as event solutions with no direct antecedents among the KBS solutions. About half the added events are later events in multiple event sequences, and the other half are events near the detection threshold formed by adding detections missed by the automatic detector. Relatively few KBS solutions (7 per cent) are accepted without modification (validated), while 39 per cent are rejected because the analyst cannot verify their validity. The latter is expected since the initial knowledge base was designed to form nearly all plausible event solutions to minimize the possibility of missing an event entirely. (Waveforms are retrieved from NDAC for analyst review only for "events" found by the KBS.) About 65 per cent of these rejected events are formed from only one defining phase at each array.

It is often difficult to know whether these solutions are real events or solutions formed by a coincidental association of unrelated phases, so they are seldom accepted by the analyst without some corroborating evidence (e.g., a previously undetected phase). Thus, the analyst rejected 628 of the 691 such solutions formed by KBS during the test period.

About 83 per cent of the events in the final bulletin are KBS events that have been corrected in some way by the analyst. Careful analysis of these corrections provides new knowledge to improve the KBS. The effect of the analyst changes is indicated by comparing the KBS and analyst locations (Fig. 10). An obvious conclusion is that the analyst corrections have much more effect for the ARCESS-only solutions. Table 7 summarizes the analyst corrections for those events moved more than 50 km (i.e., the events with the most significant analyst corrections). The corrections were divided into the indicated categories by a successive screening in the order indicated. That is, events that are part of multiple event sequences were counted first and removed from further consideration. Then, events that began as KBS solutions formed from one phase at each array were counted and removed. The footnoted categories are for cases where the analyst adds or corrects a phase that is essential for reliable location. Included is any phase that is the only arrival of its phase type in the final solution. This phase is absolutely necessary for single-array locations and very important for two-array locations. Therefore, changes in these categories usually move the location significantly. This screening into simple categories accounts for nearly all events moved more than 50 km by the analyst

TABLE 6

SUMMARY OF ANALYST REVIEW OF KBS SOLUTIONS

Action	No.	% of KBS Solutions	% of Final Solutions
Validated	168	7	11
Corrected by Analyst	1,315	54	83
Rejected or Unverified	967	39	—
Added Events	97	—	6

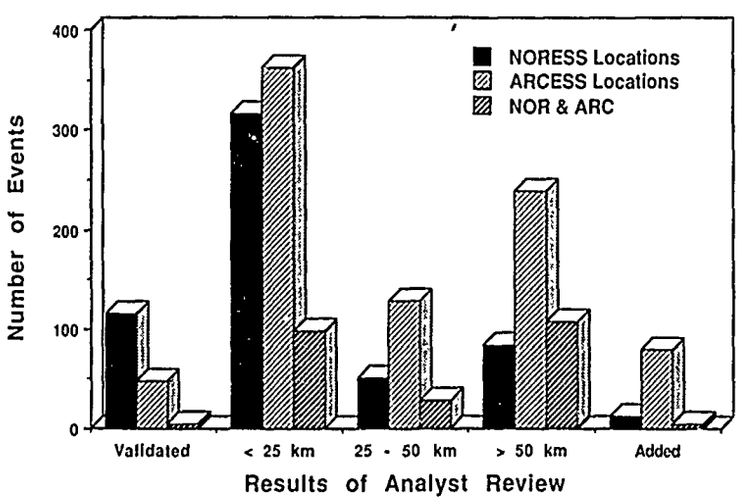

FIG. 10. The separation between the KBS and analyst locations is shown for the 1,315 events formed by the KBS, then corrected by the analyst. The events are grouped into those including defining phases from only ARCESS, from only NORESS, and from both arrays.

TABLE 7

SUMMARY OF ANALYST CORRECTIONS FOR EVENTS MOVED MORE THAN 50 KM

Analyst Correction	ARCESS Only	NORESS Only	Both Arrays	Total
Correct Multiple Event Sequence	75	17	27	119
Detection				
Added to two-array, two-phase event solution	17	3	32	52
Add the only defining S^*	14	8	0	22
Add the only defining P^*	8	7	5	20
Add two or more phases	0	1	8	9
Phase Grouping				
Associate the only defining S^*	18	6	1	25
Associate the only defining P^*	8	7	8	23
Phase Identification				
Correct the only defining S^*	50	18	3	71
Correct the only defining P^*	28	10	10	48
Correct two or more phases	8	0	4	12
Network Processing				
Repair split event	0	0	4	4
Other	12	8	5	25
Total corrected	238	85	107	430

* This defining phase is the only defining phase of the indicated type.

corrections; only a small number fall through to the "other" category. Most of the categories are grouped under the headings Detection, Phase Grouping, Phase Identification, and Network Processing. These are major stages in the KBS reasoning process (Bache *et al.*, 1990), and each has knowledge that is nearly independent of that at other stages. This makes it much easier to develop and implement new knowledge to reduce the need for analyst corrections in each category.

The largest numbers in Table 7 are for analyst corrections for events that are part of multiple event sequences, and 27 per cent of the ARCESS-only events in Table 7 are in this category. The seismicity recorded at ARCESS is dominated by mining explosions from northern Sweden and the Kola Peninsula, and multiple explosions separated by minutes are common at several of these mines. Overall, 292 (18 per cent) of the events in the final *IMS Bulletin* for the test period were noted to be part of multiple event sequences, with 190 (65 per cent) being ARCESS-only solutions. These include the 119 (41 per cent) in Table 7 and another 19 per cent that were added by the analyst. The other 40 per cent were moved less than 50 km by the analyst corrections, but most of them are the first event in the sequence. This KBS problem with multiple events is not surprising since they often have complex phase-arrival sequences that are very difficult for even a skilled analyst to interpret. The problem is partly due to failure to detect key phases and partly due to incorrect grouping of the phases with events. An example is shown in Figure 11 with the initial phase type assigned by the KBS (using results of *f-k* analysis) noted for each automatic detection. The *f-k* analysis also indicates that all of these phases come from nearly the same azimuth. While the four *S* arrivals are clearly visible on the incoherent vertical beam (bottom trace), two of the corresponding *P* waves are obscured by other phases and were not detected. It will be very difficult to give the

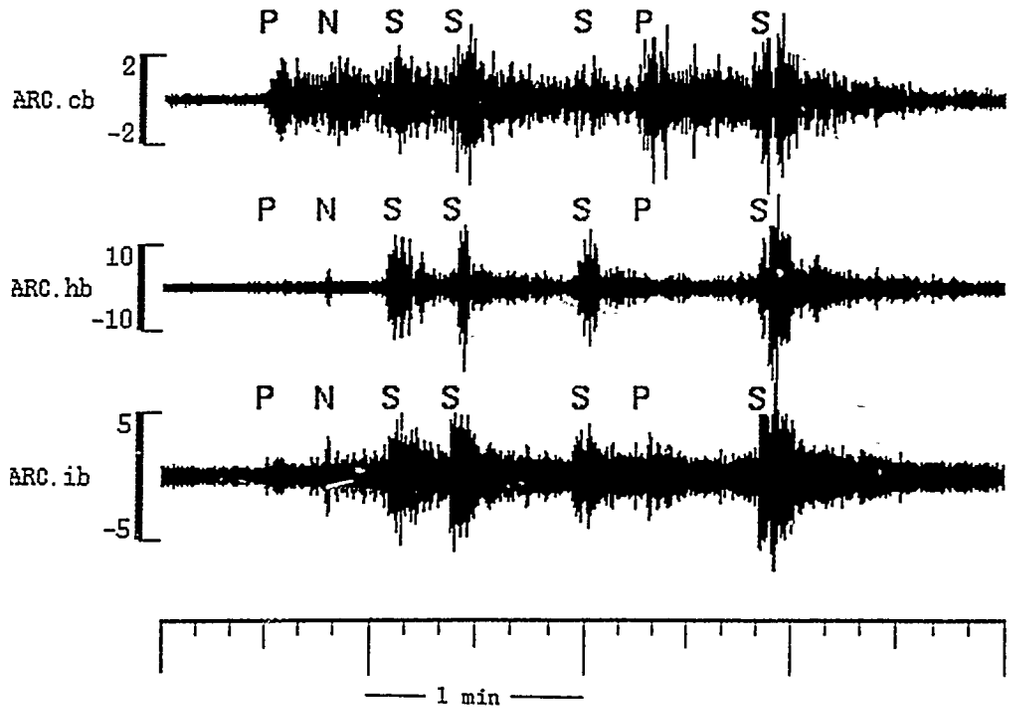

FIG. 11. Three beamed ARCESS seismograms are shown for a multiple event sequence generated by a mine in northern Sweden. The seismograms include a coherent high-frequency (4 to 8 Hz) vertical beam (cb), an incoherent low-frequency (1 to 4 Hz) vertical beam (ib), and an incoherent 1 to 4 Hz beam of the horizontal channels (hb). The automatic detections are identified by phase type based on phase velocity, and *N* denotes a low-phase velocity arrival treated as a noise detection. Amplitudes are in nanometers.

KBS enough knowledge to sort out complex arrival sequences like this, particularly with data from only one array.

Events detected only at ARCESS are not interpreted as reliably by the KBS as those detected only at NORESS. For example, there are rules to distinguish *Sn* and *Lg* that are based on differences in the polarization properties of these phases observed at NORESS, but the *Sn* and *Lg* polarization differences are less significant at ARCESS. In fact, the analyst corrections for 45 of the 50 ARCESS-only events in the "Correct Only Defining *S*" category can be attributed to the failure of one rule that identifies the first *S* arrival as *Sn* if it has *Sn*-like polarization attributes and appears to be 250 to 500 km from the array. There are also 92 ARCESS-only events, where this rule gave the correct answer so it appears to work about 67 per cent of the time. At NORESS, the rule was 76 per cent correct (26 of 34), but none of the 8 events where it was incorrect were moved as much as 50 km by the analyst correction. More complex rules considering phase velocity and frequency content are being derived to increase the reliability at ARCESS, and these extensions to the knowledge base are discussed later.

About 25 per cent of the events in Table 7 were detected at both arrays. These 107 two-array solutions represent about 45 per cent of the validated and analyst-corrected two-array solutions in the final bulletin. Thus, the percentage of two-array solutions that have moved more than 50 km due to analyst corrections is large compared to that for the NORESS-only (15 per cent) and ARCESS-only (31 per cent) solutions. However, this is misleading since the two-array solutions are generally at much larger ranges (the mean range to the closest array is

624 km compared to a mean range of 271 km for single-array locations). Note that there are only four events in the "Repair Split Events" category that includes those cases where independent single-array NORESS and ARCESS solutions were combined by the analyst to form a two-array solution. This shows that the KBS rules for forming network solutions are performing rather well.

There are 885 solutions that were moved less than 50 km by the analyst corrections. For nearly half of them, the only analyst corrections were to retime one or more defining phases. In fact, nearly 70 per cent of all defining phases were retimed during the test period. This turned out to be due in part to a fault in the data acquisition software, which was later repaired. Current experience is that the analyst retimes about 35 per cent of the defining phases, with half of these retimed phases being *Lg*. This highlights the need for improved automatic onset-time estimation procedures, particularly for *Lg*.

Knowledge Acquisition

The objective is to add to the knowledge base to make its performance closer to that of the analyst. The major deficiencies in the KBS knowledge base identified in our analysis fall into five areas: (1) signal processing, particularly in phase detection and onset-time estimation; (2) phase grouping, particularly for multiple event sequences; (3) station-dependent phase identification; (4) formation of a large number of unverifiable event solutions; and (5) gaps in the knowledge base that cause events to be missed under some peculiar circumstances. In this section, we describe the improvements underway in each of these areas and point out issues that require further investigation.

The IMS signal detection scheme was adapted directly from the NORSAR RONAPP program (Mykkeltveit and Bungum, 1984) and is entirely independent of the KBS processing to form events. Thus, an undetected phase cannot be considered in the interpretation until the analyst adds it. Missing detections do not appear to be a major problem, but there are a significant number of events where better signal detection would help the KBS. One approach is to add knowledge to the detection process. That is, use the current context (e.g., a *P* phase was detected so *Lg* is expected) to reconfigure the detector. This is certainly possible within the IMS architecture (Fig. 1), but would add to the complexity to the system. Thus, implementation of this approach is deferred while we develop a better understanding of the true limitations of the current approach. (All signal detection is done the same way to all data at the beginning of the processing.) A simple way to increase the number of detections is to lower the signal-to-noise threshold for detection on selected beams. Overall, the thresholds cannot be too high because a majority of the detections are never associated with events (Table 1). Careful analysis of the data is needed, particularly for ARCESS, to tune the detection thresholds on particular beams to improve detection capability without significantly increasing the number of unassociated detections.

The onset-time algorithm in the IMS was also adapted from RONAPP. The need for frequent analyst corrections to the onset time is an inconvenience rather than indication of a serious interpretation problem, but some improvement would be welcome. More work is needed in this area, particularly for emergent phases like *Lg*.

Errors in the phase grouping are most common in single-array solutions involving mixed signals from several events at the same azimuth. As noted earlier, these are very difficult to sort out, even for a skilled analyst. In most cases, the mixed signals

are from events in the same mine. Thus, the objectives for the KBS are to obtain a good solution for the first event in the sequence and give a stronger weight to the presumption that subsequent detections are probably phases from other events in the vicinity of the first.

Regional seismicity and the character of regional phases vary substantially from one area to another, and it is in the acquisition and addition of this area-specific knowledge that the KBS approach has its greatest promise. This is seen even in this two-array implementation. That is, the knowledge base was based on NORESS experience, and the two arrays were treated the same except for recognition that oceanic paths (suppressing *Lg*) are at different locations with respect to the arrays. However, the ARCESS data turned out to be more complex in several aspects, and relatively simple rules that worked at NORESS were not so successful when used to interpret ARCESS data. The best example is that polarization characteristics were found to be effective for discriminating *Sn* from *Lg* and *Pn* from *Pg* at NORESS, but are much less so at ARCESS. This motivated development of a more general approach to phase identification takes into account the arbitrary number of phase attributes, such as relative amplitude, dominant frequency, phase velocity, polarization, etc. The approach uses an extension of Bayesian inference methods to estimate the likelihood that a phase has a particular identity (e.g., *Lg*) in a given circumstance by combining estimates of conditional probabilities derived from observations ($P(a \mid b, c)$ = the probability of a given conditions b and c). The desired probabilities can be written:

$$P(\text{phase} \mid \text{attribute}, \text{context}) = \frac{P(\text{attribute} \mid \text{phase}, \text{context})\, P(\text{phase} \mid \text{context})}{P(\text{attribute} \mid \text{context})} \quad (1)$$

where the right-hand side contains those quantities that can be estimated from the data. The context is a parameterization of the identified arrival patterns and other contextual features (station and source region) determined such that each phase can be assigned to one context. The arrival patterns include such features as the number of arrivals of a phase type, the relative amplitudes, the time separation, and the position of an arrival in the sequence (e.g., first or not first).

This Bayesian approach has wide application for accumulating knowledge in a form that is easily represented within the KBS architecture. It has been applied to develop new rules for identifying the defining phases. While the details are not appropriate here, the major trends are interesting. Phase velocity and polarization are equally effective (75 per cent correct for isolated events) for distinguishing *Sn* and *Lg* at NORESS (the initial rules did not consider phase velocity), but combining the two increases the reliability to nearly 90 per cent. At ARCESS, polarization is not as useful, and rules based on a combination of phase velocity and dominant frequency are more effective. In some cases, the pattern of arrivals (context) is itself enough to identify phases. For example, when the first *P*, first *S*, and a later *S* fit the travel times for *Pn*, *Sn*, and *Lg*, the *P* is *Pn* and the *S* is *Sn* more than 90 per cent of the time.

Another KBS deficiency is the formation of many unverifiable event solutions. This is not a serious problem (for reasons outlined earlier), but the number can be reduced substantially by introducing knowledge to check the consistency of questionable solutions (primarily those formed from one phase at each array) with

expected behavior for events in the vicinity. Most of these consistency checks can be based on *a priori* knowledge (e.g., *Pg* only observed at small distance, etc.). The Bayesian approach outlined earlier could be extended to this situation to represent more subtle features of the data, but this must be done very carefully because the presence of false events is only a minor inconvenience easily endured to increase the probability of forming nearly all interesting events. Finally, a few gaps in the knowledge base were repaired by adding new rules to account for previously un anticipated circumstances.

This analysis led to the development of many new rules. These were tested for consistency by recomputing solutions for old data. The ability to identify events that use particular elements of the knowledge base helps assure the relevance of the testing. The updated knowledge base was installed in the operational system in mid-April 1990. Preliminary analysis of results from this version indicate significant improvement in several areas, most notably a decrease in the number of "Repeated or Unverified" KBS solutions from 39 per cent (Table 6) to 27 per cent of the total, and an increase in the number of "Validated" KBS solutions from 7 per cent (Table 6) to 21 per cent. Based on our tests on old data, we are confident of improved performance in other areas (e.g., interpretation of multiple event sequences), but this is difficult to quantify due to effects of variations in the seismicity and analyst procedures. Rules developed from the Bayesian approach were not incorporated in the April version of the KBS, but they will be included in the next version to provide another substantial improvement in performance.

Conclusions

The potential capability of a seismic monitoring network is defined by the signal-to-noise threshold of the stations that comprise it. But, it is the final bulletin produced from the network's data that define its actual performance. In the past, obtaining results close to the potential capability of a network has required detailed and careful interpretation of all or nearly all data by skilled human analysts. This labor-intensive approach has many obvious disadvantages when consistent, reliable, and steadily improving (with experience) capabilities are needed, and it borders on the impractical for the large volume of complex data for small events collected by a network of NORESS-type arrays. Thus, the primary goal of the IMS is to provide an automated real-time data interpretation system that requires little human labor, but obtains consistent results that represent the full monitoring potential of the network. The results of the 8-week test period summarized in this paper show that the IMS is well on the way toward that goal.

The ambitious objectives for the IMS led to a complex system architecture integrating many advanced technologies, and one of our major achievements is the reliability and fault tolerance of IMS in continuous operation. Operation requires the full-time attention of only two staff, including an analyst who reviews all solutions produced by the automated processing. The final *IMS Bulletin* listing the events detected and located during the test period includes a daily average of 650 phase detections and 28 analyst-reviewed regional events. As an indication of the capability, this appears to include 96 per cent of all events larger than M 2.5 at a distance of 800 to 900 km from both arrays, and the median accuracy of their locations appears to be less than 25 km in this distance range.

Our objective is not (at least at this stage) complete automation of the analysis. Rather, the objective is for the automated processing to produce reasonable solutions

for all events of possible interest and present them to an analyst along with the tools to correct these solutions efficiently and accurately. The integration of KBS and relational database management technologies into the IMS was designed to serve that objective. During the initial operational period, we gained the experience to improve the automated analysis of ARCESS data, and some examples of the use of information archived in the IMS DBMS to acquire new knowledge for this purpose were described in earlier sections. These examples represent only a small fraction of the relevant information available in the DBMS, and results continue to accumulate as the system is operated.

The KBS and analyst-review functions of the IMS were moved to the NORSAR facility in early 1990, and the routine operation continues at that site. As described in the previous section, analysis of results from the test period were used to improve the knowledge base, and significant improvements have been seen in operation since April 1990. Work is continuing on relatively immature elements of the system, including the incorporation of methods to refine the locations by using knowledge from previous events in the same area and implementation of automated event identification procedures. Also, future versions of the IMS will interpret the data from a larger network of arrays and single-site stations in Eurasia. The facilities for acquiring knowledge about station-specific features of the data and adding them to the knowledge base will play an important role in adapting the IMS to obtain results close to the potential capability of this expanded seismic monitoring network.

ACKNOWLEDGMENTS

We are grateful for the research advice and technical support provided by the NORSAR staff, particularly Frode Ringdal, and the staff at the Center for Seismic Studies, particularly Carl Romney. We also thank an anonymous reviewer for a number of constructive suggestions. The IMS project was supported by DARPA Contract MDA-972-88-C-0024 monitored by the Air Force Geophysics Laboratory.

REFERENCES

Ahjos, A., P. Heikkinen, E. Pelkonen, M. Franssila, L. Mustila, and M. Raime (1989). Seismic events in northern Europe, October 1989, Report R-22, Institute of Seismology, University of Helsinki, Finland.

Bache, T. C., S. R. Bratt, J. Wang, R. M. Fung, C. Kobryn, and J. W. Given (1990). The intelligent monitoring system, *Bull. Seism. Soc. Am.* **80**, 1833–1851.

Båth, M., O. Kulhánek, T. Van Eck, and R. Wahlström (1976). Engineering analysis of ground motion in Sweden, Seismological Institute Report, Uppsala, Sweden, pp. 17–19, 44.

Berger, J., H. K. Eissler, F. L. Vernon, I. L. Nersesov, M. B. Gokhberg, O. A. Stolyrov, and N. T. Tarasov (1988). Studies of high-frequency seismic noise in eastern Kazakhstan, *Bull. Seism. Soc. Am.* **78**, 1744–1758.

Bratt, S. R. and T. C. Bache (1988). Locating events with a sparse network of regional arrays, *Bull. Seism. Soc. Am.* **78**, 780–798.

Bungum, H., J. Havshov, B. K. Hokland, and R. Newmark (1986). Contemporary seismicity of northwest Europe, *An. Geophysicae* **48**, 567–576.

Bungum, H. and R. B. Selnes (Editors) (1988). ELOCS: Earthquake loading on the Norwegian Continental Shelf, Summary Report, Norwegian Geotechnical Institute (Oslo), NTNF/NORSAR (Kjeller), and Principia Mechanica Ltd. (London).

Bungum, H., A. Alsaker, L. B. Kvamme, and R. A. Hansen (1990). Seismicity and seismotectonics of Norway and nearby continental shelf areas, *J. Geophys. Res.* (submitted for publication).

Flinn, E. A. and E. R. Engdahl (1974). Seismic and geographic regionalization, *Bull. Seism. Soc. Am.* **74**, 771–993.

Fox, W. (1989). Satellite imagery of areas in northwest Europe, Science Applications International Corporation Technical Report, Center for Seismic Studies, Arlington, VA.

Fyen, J. (1986). NORESS noise spectral studies—noise level characteristics, NORSAR Scientific Report 2-85/86, Kjeller, Norway.

IMS Staff (1989). Bulletin of the Intelligent Monitoring System, October 1, 1989–October 7, 1989, Center for Seismic Studies Technical Report, Arlington, VA, 70 pp.

Jordan, T. H (1981). Global tectonic regionalization for seismological data analysis, *Bull. Seism. Soc. Am.* **71**, 1131–1141.

Korhonen, H., S. Pirhonen, F. Ringdal, S. Mykkeltveit, T. Kvaerna, P. W. Larsen, and R. Paulsen (1987). The FINESA array and preliminary results of data analysis, Report S-16, Institute of Seismology, University of Helsinki, Finland.

Mykkeltveit, S., K. Åstebol, D. J. Doornbos, and E. S. Husebuye (1983). Seismic array configuration optimization, *Bull. Seism. Soc. Am.* **73**, 173–186.

Mykkeltveit, S. and H. Bungum (1984). Processing of regional seismic events using data from small-aperture arrays, *Bull. Seism. Soc. Am.* **74**, 2313–2333.

Okal, E. A. and J. Talandier (1989). M_m: a variable-period mantle magnitude, *J. Geophys. Res.* **94**, 4169–4193.

Slunga, R. and T. Ahjos (1986). Fault mechanisms of Finnish earthquakes, crustal stresses and faults, *Geophysica* **22**, 1–13.

Young, J. B. and C. I. Pooley (1985). Classifiers of Seismic and Geographic Regionalisation, Atomic Weapons Research Establishment Report 6/85, United Kingdom, 53 pp.

CENTER FOR SEISMIC STUDIES
SCIENCE APPLICATIONS INTERNATIONAL CORPORATION
1300 N. 17TH STREET
SUITE 1450
ARLINGTON, VA 22209
(S. R. B., R. J. S., F. R.)

SCIENCE APPLICATIONS INTERNATIONAL CORPORATION
10260 CAMPUS POINT DRIVE
SAN DIEGO, CA 92121
(H. J. S., T. C. B.)

Manuscript received 17 April 1990

Bulletin of the Seismological Society of America, Vol. 80, No. 6, pp. 1874–1892, December 1990

REGIONAL SEISMIC WAVEFORM DISCRIMINANTS AND CASE-BASED EVENT IDENTIFICATION USING REGIONAL ARRAYS

BY DOUGLAS R. BAUMGARDT AND GREGORY B. YOUNG

ABSTRACT

In this study, we have investigated regional-phase spectra, spectral ratios, and amplitude ratios as discriminants for case-based, regional seismic-event identification using western Norway explosions and earthquakes recorded at the NORESS array. All events were in a comparable local magnitude range (2 to 3) and distance range (300 to 500 km) from the NORESS array. Thus, the propagation paths from the earthquakes and explosions were similar but not identical. Many of the events, previously not identified as blasts, had time-independent spectral modulations indicative of ripple-firing. These include a number of offshore events, which appear to be underwater explosions. The modulations for the offshore events may have been caused by bubble pulse interference effects and/or underwater reverberations. Amplitude ratios of *Pn/Sn* and *Pn/Lg*, measured off of incoherent beams, were examined on a region-by-region basis for a group of confirmed blasts, events strongly suspected to be earthquakes, and other events that had time-independent spectral modulations. The blast and earthquake groups were well separated by both ratios, with the blasts producing more *P*-wave energy relative to *S*-wave energy than the earthquakes. However, the *Lg* spectral ratio provided no separation. This result agrees with others in shield regions that amplitude ratios between compressional and shear waves discriminate better than low-frequency to high-frequency spectral ratios for individual phases. The converse holds for events in orogenic regions, such as the Basin and Range tectonic region of the Western United States, for reasons that are not well understood but may relate to differences in crustal attenuation. This fact argues in favor of using a case-based approach to event identification, where events are identified by comparing them to previous events or cases that occur in the same or similar tectonic environments. In the absence of a well-understood, unifying theory for regional-event identification, characterizing events on the basis of geophysical and signal similarities to previous cases may be the only way of providing meaningful event identifications.

INTRODUCTION

Effective seismic event identification of nuclear explosions and earthquakes has long been a major goal in test ban treaty monitoring, as evidenced by the many studies reviewed by Pomeroy *et al.* (1982) that were done up to the early 1980s. Many subsequent studies have been undertaken motivated to a large extent by the increased availability of regional seismic data, including regional array data. In spite of all the research in this area, no consistently reliable and universally applicable regional waveform discriminant has yet been discovered.

Part of the problem has been a lack of a unifying theory of regional seismic event identification that completely explains how seismic source phenomenology affects recorded seismic signals. For example, simple source physics of earthquakes and explosions would suggest that earthquakes, being dislocation sources, should generate more shear-wave energy relative to compressional-wave energy than explosions, and many of the studies reviewed by Pomeroy *et al.* (1982) that tested *S*-to-*P* ratio discriminants showed some separation between earthquakes and explosions.

However, studies of the *P/Lg* ratios discriminant by Nuttli (1981), Bennett and Murphy (1986), and Taylor *et al.* (1989) have found significant overlap in the earthquake and explosion populations for events in Eurasia and in the Western United States. However, more recent studies by Pulli and Dysart (1987), for events in Scandinavia, and Bennett *et al.* (1989), for events in the Eurasian craton, have shown *P/Lg* type ratios to be effective for separating earthquakes and explosions. Evidently, differences in propagation paths may have caused the poor performance of this discriminant in some of the studies, but the exact nature of the tradeoff between source and propagation path effects on the *P/Lg* ratio discriminant is not well understood.

Mixed results have also been reported for spectral discriminants. Murphy and Bennett (1982) and Bennett and Murphy (1986) found that NTS explosions and Western United States earthquakes separated on *Lg* spectral ratios, with earthquake *Lg* waves having more high-frequency content than explosions. Similar results were obtained by Taylor *et al.* (1988) for *Lg* and other phases for events in the same region. However, Pulli and Dysart (1987) and Bennett *et al.* (1989) reported that the discriminant is less effective in separating earthquakes and explosions in Scandinavia and in the eastern European shield, respectively. Again, as pointed out by Bennett *et al.* (1989), propagation path differences for the explosion and earthquake populations may have an effect on the performance of this discriminant.

Another problem associated with small-event identification is distinguishing economic blasting from nuclear explosions and earthquakes. Baumgardt and Ziegler (1988) and Hedlin *et al.* (1989) have shown that economic blasting can be identified by observing persistent spectral modulations produced by ripple fire. However, this discriminant could be spoofed since nuclear explosions can also be ripple-fired although it might be difficult. For example, Baumgardt and Ziegler (1988) found that NORSAR recordings of presumed peaceful nuclear explosions in Eurasia had the same persistent modulations observed in ripple-fired mine blasts, indicating that the nuclear explosions were ripple-fired. Moreover, Bennett *et al.* (1989) argued that spectral modulations are unobservable for known mine blasts in the United States, perhaps because the ripple-fire delay times were too short to be observed in the limited bandwidth of the data. The observation of spectral modulations may identify many, perhaps most, economic explosions, depending on number and delay times of the ripple-fired explosions and the bandwidth of the recording instrumentation. However, there are conceivable scenarios where the discriminant may fail.

Taken together, these studies have shown that regional discriminants cannot be applied in the same way everywhere, that they are highly dependent on the nature of the regional phase propagation-path effects, and that there is a strong regional variability in the effectiveness of discriminants. Because of this, a "case-based" approach may have to be applied, where the waveform characteristics of an event are compared with those of previously observed, known events and identified on the basis of the comparison, assuming that the propagation paths are common. Ideally, the unknown event and the known reference events must be in the same region so that propagation-path differences do not bias the discrimination results. However, it has been difficult in previous discrimination research to find populations of earthquakes and explosions that are collocated, and there is no guarantee that in practice collocated reference events of known identity will be available to compare with unknown events. Thus, in an operational event identification scenario, the seismic analyst will be forced to work with what is available and try to account

for any propagation effects that might bias event identification using previously observed cases.

In this paper, we will explore some of the problems associated with using the case-based approach to event identification. Baumgardt (1990) has discussed the application of an artificial intelligence technique, known as "case-based reasoning," for systematically identifying seismic events on the basis of comparison with cases. In this paper, we will focus primarily on the seismological and signal processing aspects of the problem. Our emphasis will be on the analysis of regional-array data from the NORESS array and the discrimination of earthquakes and mine explosions located in western Norway. We will discuss the question of whether propagation-path effects bias waveform discriminants and what considerations need to be made when attempting to identify actual case events.

Data and Processing Methods

NORESS Database

For this study, NORESS data for a group of earthquakes and economic explosions located in western Norway were analyzed. Figure 1 shows the locations of the

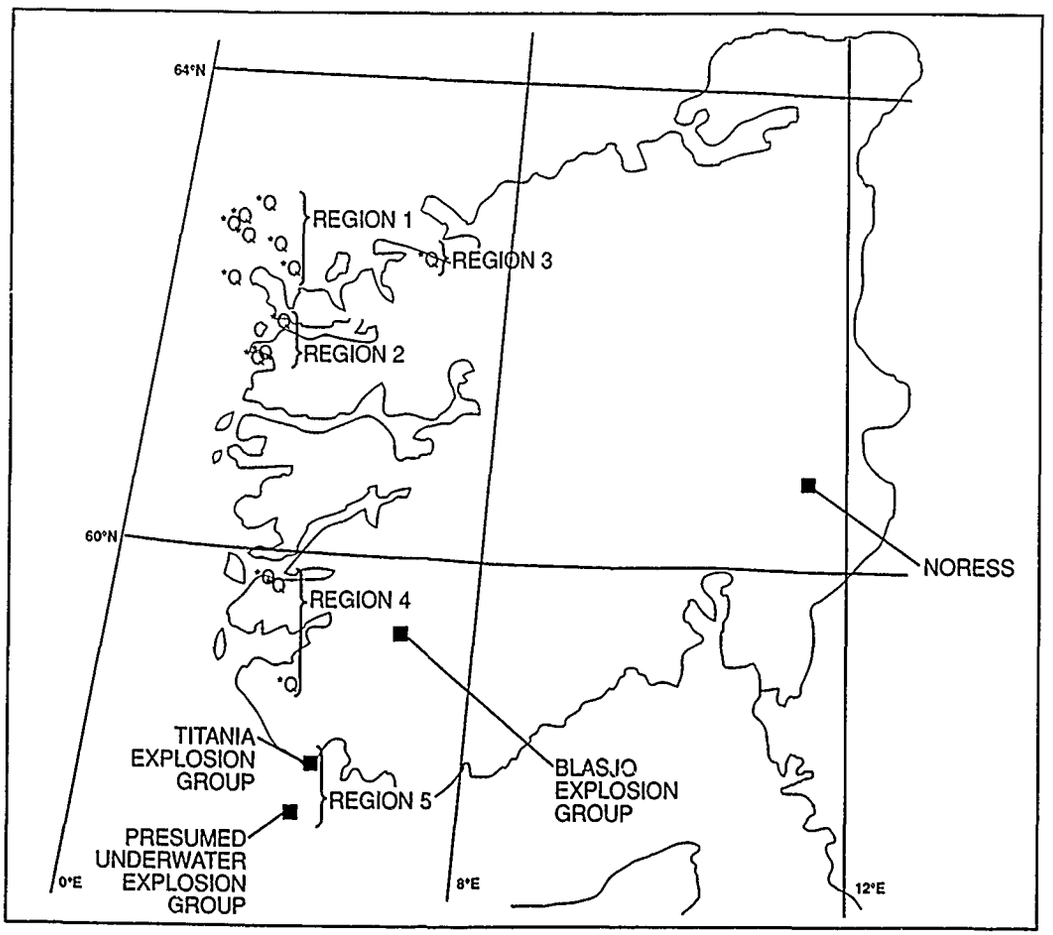

FIG. 1. Map showing the locations of the presumed earthquakes, labeled as Q, and the locations of the Blasjo and Titania blast sites. The brackets refer to the regionalization of the events discussed in the text. All event locations, except for the event in Region 3 (Q12), were determined by the regional seismic network of the Unversity of Bergen. The location of Q12 comes from NORESS.

presumed earthquakes, labeled as Q, and the blasting sites, Blasjo (BLA), a dam excavation site, and the Titania (TITA) mine. The source parameters of the earthquakes and blasts are shown in Tables 1 and 2, respectively. All the events in Table 1 were reported in the *Bergen Regional Bulletin*, except Q12, which was presumably below the detection threshold of the Bergen network. The location of Q12 in Table 1 was determined by NORESS. The basis for the presumption of earthquakes for these events is simply that they were not reported as explosions in the *Bergen Bulletin* or otherwise known to be blasts at active mines. All the events in Table 2 were reported in the *Bergen Bulletins* and confirmed to be blasts at the Titania mine and the Blasjo dam excavation site.

In order to examine the effect of event location on seismic waveform features, the events in Table 1 and in Figure 1 have been divided into five regions. Region 1 events occurred offshore near the Mäloy–Ulstein region. Event Q1 has the highest local magnitude, 4.2, reported in the *Bergen Bulletin* and was also reported in the *Preliminary Determination of Epicenters Bulletin* as having a body-wave magnitude of 5.0. This event was one of the largest events to occur in Norway in the past 30 years and was felt over most of southern and central Norway (Hansen *et al.*, 1989). The events that occurred shortly afterwards (Q2 to Q6) were aftershocks of Q1, whose spectral scaling properties were studied by Chael and Cromer (1988).

TABLE 1

EPICENTERS OF PRESUMED WESTERN NORWAY EARTHQUAKES AND OTHER UNKNOWN EVENTS

Event	Date (m/d/y)	Origin Time (UTC)	Latitude (°N)	Longitude (°E)	M_L	Distance (km)
			Region 1			
Q1	02/05/86	17:53:16.2	62.74	4.63	4.2	429
Q2	02/05/86	18:50:03.4	62.27	4.69	2.8	403
Q3	02/05/86	20:23:29.8	62.41	6.06	2.7	303
Q4	02/05/86	20:31:37.0	62.79	4.59	2.2	433
Q5	02/05/86	23:35:41.1	62.74	4.50	2.6	434
Q6	02/06/86	06:19:52.4	62.90	4.86	2.3	427
Q7	02/13/86	13:39:00.3	62.40	5.28	2.5	381
Q8	02/13/86	19:03:48.2	62.61	5.07	2.6	401
			Region 2			
Q9(?)	02/05/86	15:57:02.4	62.05	5.37	2.0	361
Q10(?)	02/16/86	18:19:41.3	61.69	4.90	2.0	373
Q11(?)	02/14/86	16:51:05.1	61.68	4.97	1.8	369
			Region 3			
Q12(?)	02/05/86	15:22:44.0	62.5	6.82	1.6	325
			Region 4			
Q13(?)	12/07/85	14:39:09.0	58.90	5.98	2.0	373
Q14	11/27/85	04:53:32.8	59.73	5.71	2.9	342
Q15	02/15/86	18:31:46.4	59.86	5.73	2.1	336
			Region 5			
UND1	11/20/85	22:10:44.2	57.61	5.67	2.3	483
UND2	11/20/85	22:24:38.1	57.66	5.72	2.2	478
UND3	11/20/85	22:57:10.8	57.63	6.27	2.2	459
UND4	11/20/85	23:10:47.5	57.66	5.35	2.3	493
UND5	11/20/85	23:17:28.9	57.69	5.45	2.3	486
UND6	11/20/85	23:23:10.0	57.64	5.62	2.2	483

TABLE 2

EPICENTERS FOR CONFIRMED ECONOMIC EXPLOSIONS

Event	Date (m/d/y)	Origin Time (UTC)	Size (tons)	M_L
Blasjo Explosions	59.31°N, 6.95°E	Distance = 301 km		
EX1	08/05/85	17:42:58.7	62.9	2.6
EX2	08/06/85	17:50:07.9	30.8	2.4
EX3	10/17/85	10:00:00.4	32.7	2.4
Titania Mine Explosions	58.342°N, 6.425°E	Distance = 394 km		
EX4	11/08/85	14:18:54.6	132.5	2.4
EX5	02/14/86	14:13:24.9	95.7	2.7
EX6	02/14/86	17:54:10.6	16.2	2.3
EX7	01/07/86	14:14:28.9	43.5	2.2
EX8	01/17/86	14:11:0.15	43.9	2.7
EX9	01/07/88	14:24:43.5	77.4	2.2
EX10	02/10/88	14:17:46.5	103.2	2.5
EX11	03/17/88	14:13:10.3	95.1	2.4
EX12	03/28/88	13:17:27.0	74.2	2.4

Region 2 events (Q9, Q10, and Q11) all occurred onshore in the Mäloy region. The question marks indicate that we suspect they may actually be explosions rather than earthquakes, for reasons that will be discussed later. Region 3 has one event located to the northeast of the events in Region 2. This small event was detected at NORESS but not by the Bergen network, and the source parameters in Table 1 were determined by NORESS. We also believe this event is a blast rather than an earthquake.

Region 4 contains two events (Q14 and Q15) that occurred in the vicinity of Bergen and a third event (Q13) that occurred further south in the Stavanger region. The Q14 event, with the largest magnitude of 2.9, may have been felt locally (F. Ringdal and S. Mykkeltveit, personal communication). These are the closest events to the TITA and BLA sites and were not reported as blasts, although, as shall be discussed later, we suspect that the Stavanger event, Q13, may actually be a blast.

Finally, we have included a group of events in Region 5, near the TITA blast site, that we have indexed in Table 1 as UND1 through UND6. Suteau-Henson and Bache (1988) studied these events and compared *Lg* spectral ratios of these events with those of events at TITA. They suggested that these events were earthquakes because they occurred offshore. However, later we shall show data that suggests that these events may have actually been underwater explosions, which is why we refer to them by the UND# index.

Incoherent Beam Analysis

Incoherent beams on bandpass-prefiltered waveforms were used to measure regional-phase amplitudes. Incoherent beamforming consists of computing log-rms amplitudes in adjacent, 1 sec time windows on each channel of the array, starting about 1 min before the *Pn*-wave onset time and extending through the seismogram into the *Lg* coda. The log-rms amplitudes for each time window are then averaged across all the array elements. When plotted versus time, incoherent beams give an envelope description of the seismic trace viewed in log-amplitude, or magnitude, space.

Figures 2 and 3 show filtered waveforms from the NRA0 element of NORESS and incoherent beams, computed using all vertical, short-period NORESS elements, plotted on the same time axes, for an earthquake and explosion. The horizontal dashed lines on the incoherent beams are the average rms noise levels over a 1 min time interval ahead of the *Pn* onset. The 8 to 16 Hz incoherent beam and average noise level have been shifted up for visibility relative to the 2 to 4 Hz beam. The presumed onsets of the regional phases, *Pn*, *Pg*, *Sn*, and *Lg*, are indicated on both the waveform and incoherent beam plots. Comparison of the waveform plots with the incoherent beams indicates that some phases, notably *Sn*, are easier to see on the incoherent beam plots. A comparison of Figures 2 and 3 reveals that the *Pn* wave is not visible in the low-frequency (2 to 4 Hz) filter band for the earthquake in Figure 2, whereas it is apparent in both the 2 to 4 Hz and 8 to 16 Hz bands for the explosion in Figure 3. This observation was first pointed out by Baumgardt and Ziegler (1988) and has important implications for discriminating these events, which will be discussed in the next section.

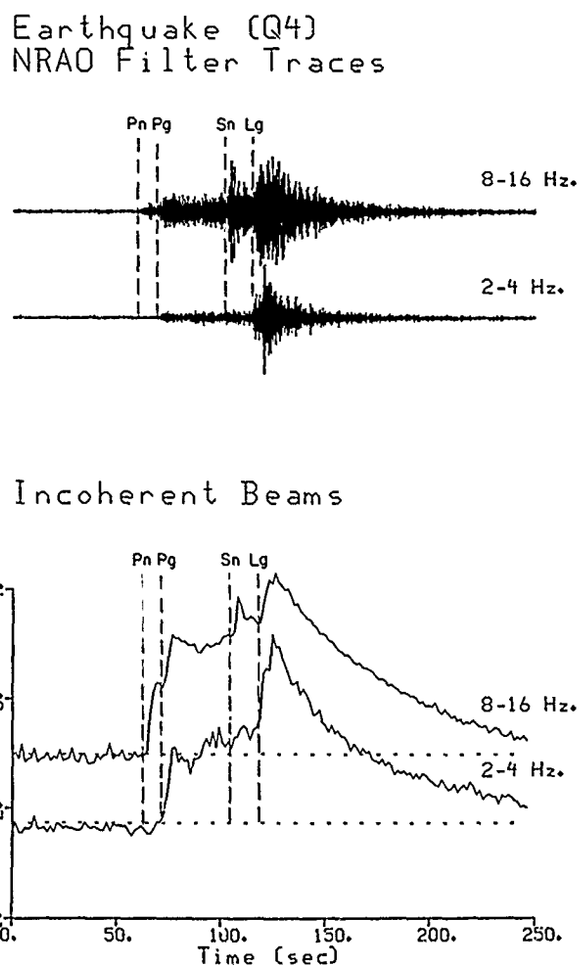

FIG. 2. (*Top*) Waveforms recorded at the NRAO array element of NORESS for the Q4 earthquakes after bandpass-filtering in the 2 to 4 and 8 to 16 Hz bands. (*Bottom*) Incoherent beams, using 1 sec averaging windows, computed from all 25 NORESS vertical component traces after prefiltering the traces in the 2 to 4 and 8 to 16 Hz bands.

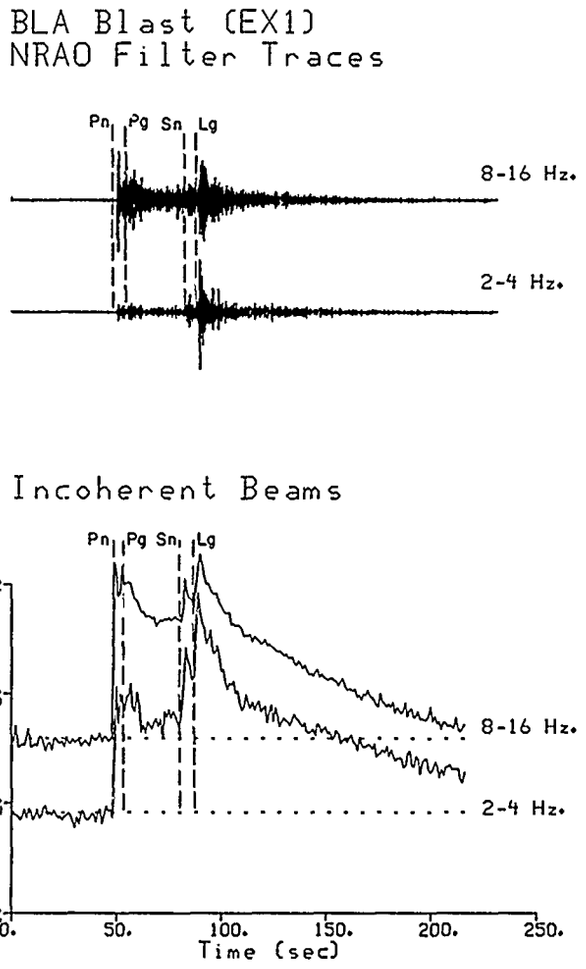

FIG. 3. Same as Figure 2 for BLA blast EX1.

Spectral Analysis

Our spectral analysis method is the same array stacking procedure described by that of Baumgardt and Ziegler (1988). In brief, the Fourier power spectrum is computed on each channel on the windowed phases and on the noise background to *Pn*. The power spectra on each channel are then corrected for noise and instrument, and averaged across the array. The window lengths for each phase varied depending on the duration of each phase, but in general were between 7 and 14 sec for *Pn*, *Pg*, and *Sn*, and 25.6 sec for *Lg* and noise.

DISCRIMINATION ANALYSIS RESULTS

Regional Phase Spectra

Figures 4, 5, and 6 show selected array-averaged spectra for the regional phases, *Pn*, *Pg*, *Sn*, and *Lg*, for events in the five regions. In each case, the spectra for the *Pg*, *Sn*, and *Lg* phases were shifted upward by 0.5 log units relative to the *Pn* and noise spectra for purposes of visibility. The spectra of the *Pn* background noise are plotted as dashed lines.

Figure 4a shows the spectra for one of the Region 1 events compared with spectra for an explosion in Figure 4b. All the spectra in Region 1 resembled that in

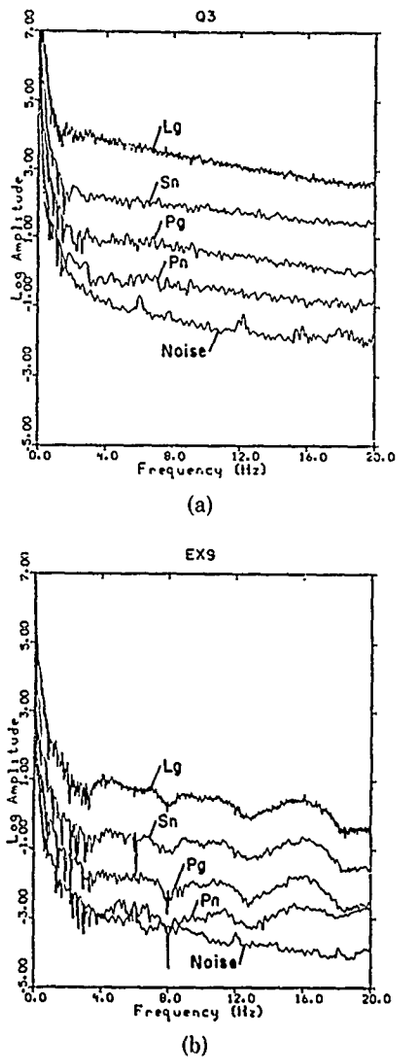

FIG. 4. (a) Regional phase spectra for a region event (Q3) in Region 1, strongly suspected to be an earthquake. The *Pg*, *Sn*, and *Lg* spectra have been shifted up by 0.5 log-amplitude units relative to the noise and *Pn* spectrum. (b) Regional phase spectra for a confirmed explosion (EX9) located at the Titania mine, which exhibits time-independent spectral modulations indicative of ripple-firing.

Figure 4a in that the regional phase spectra in general were very simple and, at frequencies above 2 Hz, above the frequencies where the low-frequency effects of the instrument removal are apparent, the spectra falloff linearly with frequency into the noise. In contrast, the explosion spectra in Figure 4b exhibit strong modulations or scalloping, which Baumgardt and Ziegler (1988) attributed to multiple explosions or "ripple fire." The key feature, which is diagnostic of ripple fire, is that the same modulation is apparent in all spectra, hence, the modulations are time-independent. Hedlin *et al.* (1989) have shown that the time-independent modulations are apparent in coda waves as well as in regional-phase spectra. Most of the events that we have studied at TITA and BLA showed obvious spectral modulations. The exception was the 17 January 1985 event (EX10), which showed no evidence of modulations. Thus, modulations may or may not be present in blasts, and when present, may vary in intensity and periodicity, depending on how the ripple-fire pattern is designed and the bandwidth of the recording seismometers.

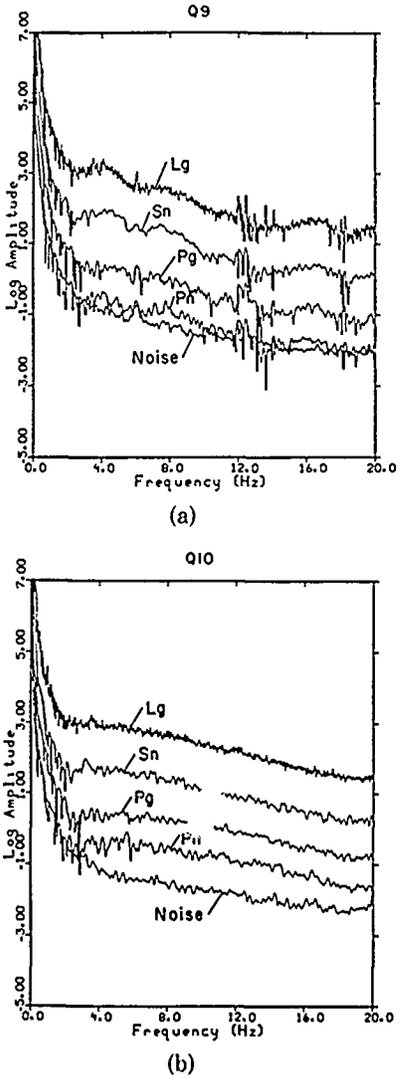

FIG. 5. (a) Regional phase spectra for a regional event (Q9) in Region 2. Originally presumed to be an earthquake, this event has time-independent spectral modulations indicative of ripple fire. (b) Regional phase spectra for a regional event (Q10) in Region 2, which has an indication of a single half-cycle of a modulation pattern for a ripple fire with delay time less than 0.05 sec.

Figure 5a shows the spectra of one of the three events in Region 2 (Q9). This event shows a strong modulation pattern apparent in all spectra that could only have been produced by a multiple event. Event Q12 in Region 3 had a very similar set of spectra, whose modulations closely resemble those observed for known blasts. Figure 5b shows a second event in Region 2 (Q10) that has a broad hump from about 3 Hz to near 20 Hz. This may be a very subtle modulation produced by multiple events delayed by times near or less than 0.05 sec, which would produce nulls near or beyond the Nyquist frequency of 20 Hz. Event Q11 had regional phase spectra similar to those of Q11.

Figure 6a shows the spectra of the Stavanger event Q13. These spectra have a strong null between 10 and 11 Hz, which appears to be caused by a spectral modulation. Figure 6b shows one of the spectra of the offshore events near TITA (UND5). This event and all the UND events had very strong spectral modulations.

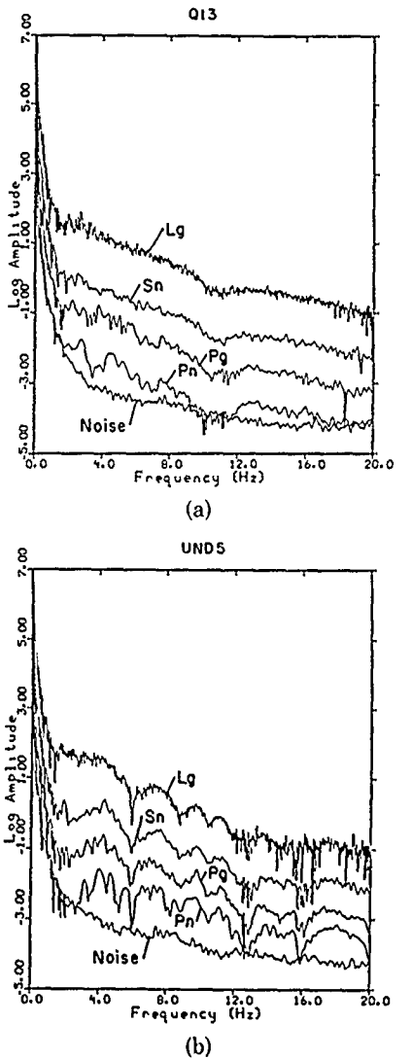

FIG. 6. (a) Regional phase spectra for the southernmost event in Region 4 (Q13). Originally presumed to be an earthquake, the event exhibits time-independent spectral modulations indicative of ripple fire. (b) Regional phase spectra for an event in Region 5 (UND5), which appears to be an underwater explosion. The time-independent modulations may be due to bubble-pulse interference and/or underwater reverberations.

Interestingly, the periodicity of the modulations for all the events in this group were nearly the same.

The key question that must be addressed when considering whether time-independent spectral modulations imply ripple-fired blasts is whether or not earthquakes can produce time-independent modulations as well. In principle, there is nothing that precludes earthquakes from consisting of multiple ruptures, which is commonly observed for large earthquakes. Blandford (1975), for example, has modeled complex earthquakes as consisting of the superposition of many "subearthquakes" in order to explain a number of teleseismic discriminants. It is unknown whether such a model might also apply to small earthquakes and whether such complex earthquakes can produce the kinds of coherent time-independent modulations that have been observed for ripple-fired explosions. Thus, the presence of

time-independent spectral modulations alone does not prove that events Q9 to Q13 are ripple-fired blasts.

It is more likely that UND1 through UND6 are in fact underwater blasts. First, the origin times of the events, although uncertainly determined by the Bergen network, are very evenly spaced in time by about 14 min. Second, the time-independent modulations in all the spectra indicate that the multiple events were delayed by nearly the same time, which is about 0.3 sec. It is unlikely that either of these two phenomena would be observed in earthquakes. Baumgardt and Ziegler (1989) have suggested that the spectral modulations in these events, if they are underwater explosions, may have been caused by interference of bubble pulses in the water or reverberations in the acoustic wave guide produced by the water column. The consistency of the time-independent modulations indicates that each of the underwater blasts were probably detonated at about the same depth in the water.

Comparison of Incoherent Beam Amplitude Ratios

As has been discussed previously, the relative excitation of compressional and shear wave energy, represented in terms of *P*-to-*S* ratios, has been considered as a possible discriminant between explosions and earthquakes. In theory, earthquakes should generate more shear energy relative to compressional energy than explosions. However, propagation effects must also be considered when comparing these ratios for populations of earthquakes and explosions. In this section, we examine regional-phase amplitude ratios for NORESS recordings of blasts and earthquakes on a region-by-region basis in order to consider possible regional variations in these features.

Frequency-dependent amplitude ratios between the phase pairs, *Pn* and *Pg*, *Pn* and *Sn*, *Pn* and *Lg*, *Pg* and *Sn*, and *Pg* and *Lg*, were determined from the incoherent beams. First, incoherent beams were computed for the vertical component traces after prefiltering the seismograms using a set of six-pole, Butterworth recursive filters. The prefilter bandpasses were 2.0 to 4.0, 2.5 to 4.5, 3.0 to 5.0, 4.0 to 6.0, 5.0 to 7.0, 6.0 to 8.0, 8.0 to 10.0, and 8.0 to 16.0 Hz. The beam traces were then plotted and the times of the *Pn*, *Pg*, *Sn*, and *Lg* peaks were noted (as shown in Figs. 2 and 3). We have found all these phases to be most distinct on the incoherent beam in the 8 to 16 Hz filter band. Therefore, we picked the peak amplitudes in this filter band and used the same times to measure the amplitudes in the other filter bands.

For these events, we have two choices for regional *P*, *Pn*, and *Pg*, and regional *S*, *Sn*, and *Lg*, for computing amplitude ratios. Baumgardt (1990) considered the frequency dependence of all possible ratios, *Pn/Pg*, *Pn/Sn*, *Pn/Lg*, *Pg/Sn*, and *Pg/Lg*, and found that the greatest difference between the blast and earthquake groups was apparent in the *Pn/Sn* and *Pn/Lg* ratios at high frequency (8 to 16 Hz). Figures 7 and 8 show the *Pn/Sn* and *Pn/Lg* ratios, respectively, on incoherent beams for the 8 to 16 Hz prefilter plotted separately for each of the five regions and for the two blast sites. Note that the BLA blast site is near Region 4 and the TITA blast site is close to Region 5.

Different symbols are also used to indicate the different kinds of sources. The triangles indicate the events that we are reasonably sure are earthquakes and did not exhibit time-independent spectral modulations. The diamonds indicate events that were originally thought to be earthquakes, but whose spectra appear to have time-independent spectral modulation that resemble those produced by ripple-fired

explosions. The circles represent all the confirmed blasts, most of which had time-independent spectral modulations.

Both Figures 7 and 8 show that the events in Region 1 and two events in Region 4, all of which we strongly suspect are earthquakes, have very low values of *Pn/Sn* and *Pn/Lg* ratios. It is interesting to note that the variance of the ratios in Region 1 is very low, in spite of the fact that the Bergen locations of these events are distributed out over a 30 to 50 km area. Also, the amplitude ratios for the two Region 4 presumed earthquakes, about 300 km south of the Region 1 events, are the same as the Region 1 earthquakes. Thus, for the events that are most likely earthquakes, the amplitude ratios are consistent and do not seem to depend on differences in propagation path from the two regions to NORESS.

The confirmed mine blasts have much higher ratios than the earthquakes. Also, the variance in these estimates for the same mine are much larger than those of the earthquake group, even though the blasts at each site supposedly occurred at the same location. The BLA blasts also appear to have greater excitation of *Pn* relative to *Sn* and *Lg* than the TITA events. However, the confirmed blasts appear to be clearly separated from the earthquake group, with the blasts having greater compressional wave energy relative to shear-wave energy than the earthquakes.

It is also apparent in Figures 7 and 8 that the events in Regions 2 to 4, which we suspected as being explosions based on their having time-independent modulations in the spectra, have higher *Pn/Sn* and *Pn/Lg* ratios than do the earthquakes, although they are not quite as high as the average of all the blast ratios. However, they do overlap the bottom part of the TITA population, as might be expected since the distances of the events in these regions are close to those of the TITA blasts.

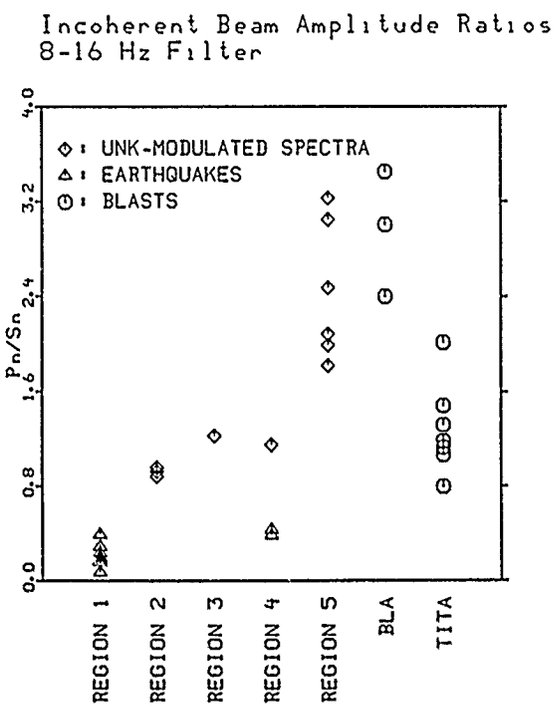

FIG. 7. Plot of the values of the *Pn/Sn* ratio in the 8 to 16 Hz frequency band for each of the five regions and for the two confirmed economic blast regions, BLA and TITA. The values or *Pn* and *Sn* amplitudes were measured from incoherent beams of prefiltered waveforms.

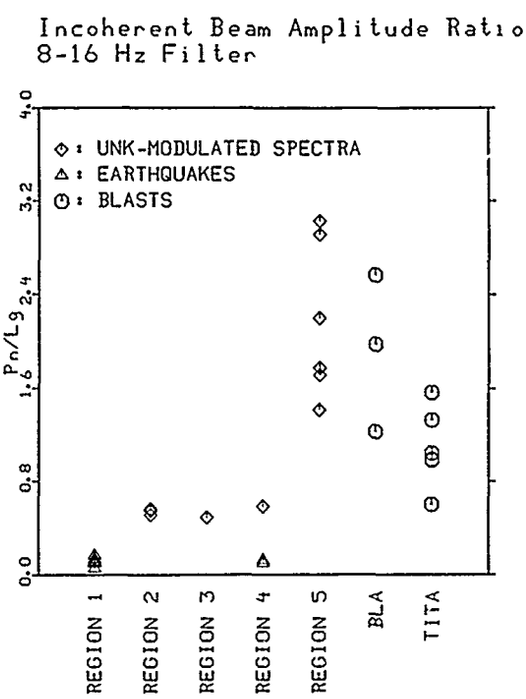

FIG. 8. Same as Figure 7 for the *Pn/Lg* amplitude ratios.

The suspected underwater explosions in Region 5 have higher ratios than the earthquakes, and they are about the same as those of the BLA events. Also, the variance in the amplitude ratios for the Region 5 group is much smaller than those of either the TITA or BLA groups. The higher excitation of *Pn* relative to *Sn* and *Lg* compared with the other events is consistent with the UND events being blasts in the water, since these events should have generated no intrinsic shear-wave energy. Thus, the *Sn* and *Lg* energy comes entirely from mode conversions at the water-bottom interface with the solid earth and by scattering in the earth.

In order to determine how the amplitude ratios depend on the absolute levels of *Pn*, *Sn*, and *Lg*, Figure 9 shows scatter plots of the logs of the ratios versus the logs of the absolute rms amplitudes. For both the *Pn/Sn* and *Pn/Lg* ratios, we find that the variations in the ratios seem to be slightly more correlated with the *Pn* amplitudes than with the *Sn* or *Lg* amplitudes, particularly within the blast and modulated-spectra group. Notice also that all the events, save one, which is the large foreshock (Q1), have nearly the same *Sn* and *Lg* amplitudes and that the earthquake population cleanly separates from the explosion and modulated spectra group on the basis of the *Pn/Sn* and *Pn/Lg* ratios. This was expected since the events were selected for a limited local magnitude range, based on the Bergen coda-duration magnitude measure. Thus, we conclude that most of the variation in the ratios comes from variations in the *Pn* excitation, not the *Lg* excitation.

Our results are consistent with those of other studies that the *Pn* wave is stronger, relative to the other phases, for explosions than for earthquakes and that the discriminatory capability of *Pn* to *Sn* and *Lg* ratios increases with frequency (e.g., Blandford, 1981; Bennett *et al.*, 1989). However, it should be noted that, for the western Norway events, this result is due to the *Pn* amplitude being much increased relative to the *Lg* amplitude.

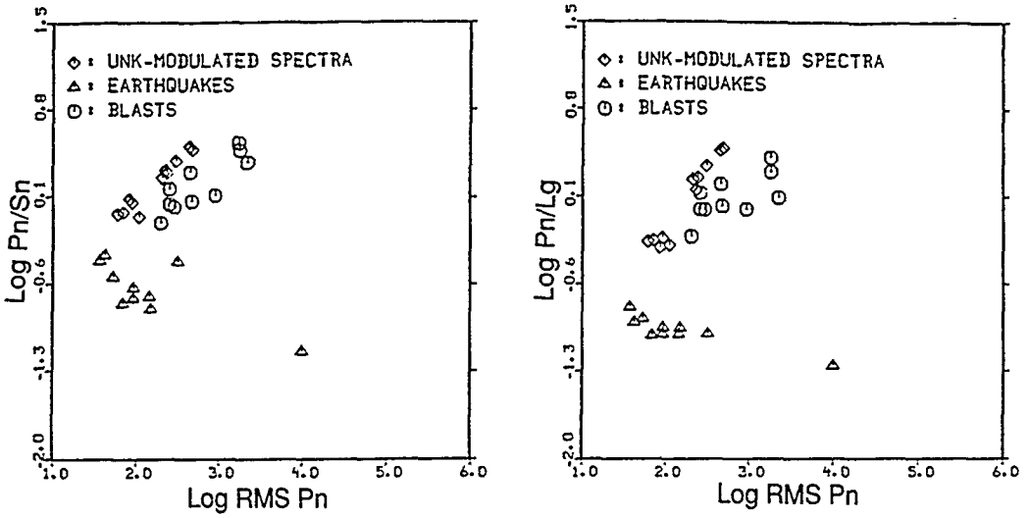

(a)

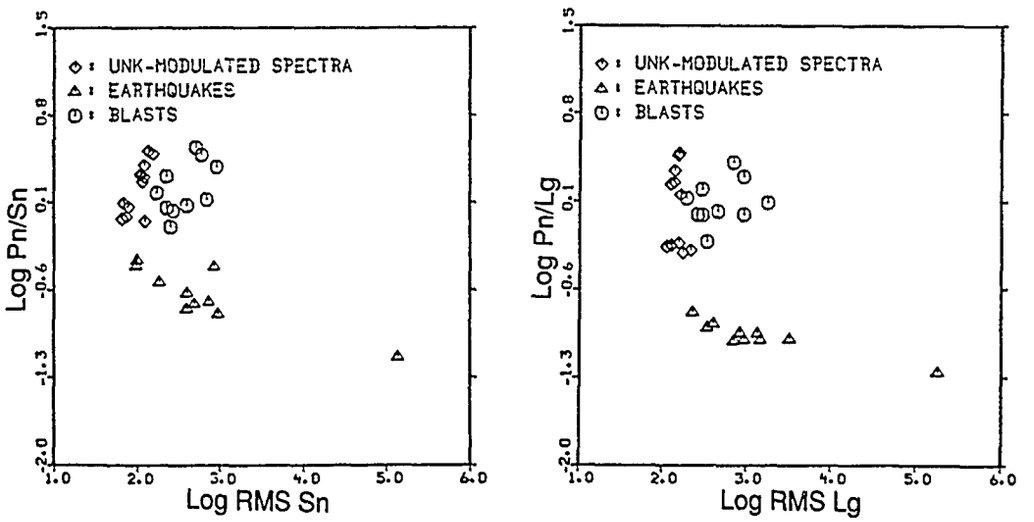

(b)

FIG. 9. (a) Scatter plot of the log of the *Pn/Sn* ratios (*left*) and the *Pn/Lg* ratios (*right*) versus the log of the *Pn* amplitudes. (b) Scatter plot of the log of the *Pn/Sn* ratios (*left*) and the *Pn/Lg* ratios (*right*) versus the log of the *Lg* amplitudes.

It is surprising that the amplitude ratios for the confirmed blasts in the same blasting site have greater variance in the amplitude ratios than the suspected earthquakes in Regions 1 and 4 which are distributed over a much larger area. The blast variations may be related to differences in the shooting practice from event to event, such as in the number and delay times of the ripple-fired shots. As has been shown in earlier studies (Baumgardt and Ziegler, 1988) and this study, the complexity of the spectral modulations varies significantly from shot to shot, although these variations should be the same for all phases. Sometimes, the nulls introduced by the modulations are very deep and fall below the noise level, particularly for the *Pn* phases which, for some events, have lower signal-to-noise ratios in the 8 to 16 Hz band than do the *Sn* and *Lg* waves. Notice, for example, that the EX9 spectrum in Figure 4b has a very deep null at about 8 Hz in the *Pn* spectrum, which is the

first spectrum above the noise spectrum at the bottom. This null is less deep in the case of the *Lg* spectrum at the top. Perhaps the *Pn* amplitudes are more affected by variations in the number and spacing of the deep nulls that result in more noise contamination than the *Sn* and *Lg* amplitudes, causing the observed variation in amplitude ratios. No such variation is seen for the presumed underwater explosions in Region 5 because they have more similar spectral modulations than the confirmed blasts on land, and the signal-to-noise ratios of *Pn* are high enough that the nulls do not drop into the noise.

Another possibility is that differences in the time and space distribution of the shots in the ripple-fire pattern may actually produce varying amounts of shear-wave energy compared with compressional-wave energy. However, examination of the points on the scatter plots in Figure 9 for the confirmed blasts shows that there is more correlation between the amplitude ratios with the *Pn* amplitudes than with the *Sn* or *Lg* amplitudes. This is not consistent with the amplitude-ratio variations being caused by the variations in the amount of *Sn* and *Lg* wave energy produced by the different blasts.

In summary, we find that regional *Pn/Sn* and *Pn/Lg* ratios discriminate well between known blasts, suspected blasts, and known earthquakes in western Norway, and that this discriminant does not seem to be significantly related to regional propagation effects. We observe very consistent ratio values for our earthquake population, and the variations observed in the blast population seem to be caused by ripple-fire effects. We also find that the observed differences in the ratios correlate more with variations in the *Pn* amplitudes than with the *Sn* and *Lg* amplitudes, and that our populations of blasts and earthquakes in the 2.0 to 2.5 local magnitude range generate very similar amounts of shear-wave energy. However, our sample size is too small to determine if this is a result of selection. In trying to get events of comparable magnitude, determined by coda (probably *Lg* coda) duration magnitudes, we may have purposely selected events of comparable *Lg* excitation. If we had selected events on the basis of some *Pn* magnitude, we may have found more correlation of the amplitude ratios with the *Sn* and *Lg* amplitudes rather than with the *Pn* amplitude.

Comparison of Lg Spectral Ratios

We now consider regional variations in the ratio of low- to high-frequency energy in the *Lg* spectrum, a feature that has been found to effectively separate nuclear explosions and earthquakes in the Western United States (Murphy and Bennett, 1982; Bennett and Murphy, 1986; Taylor *et al.*, 1988). As mentioned previously, the *Lg* spectra have all been corrected for instrument and *Pn* background noise. For each of the *Lg* spectra, the ratios of the rms levels in the 2 to 6 Hz to the 6 to 10 Hz bands were computed as follows:

$$R = \log_{10} \frac{A_{\text{rms}} \quad (2\text{–}6 \text{ Hz})}{A_{\text{rms}} \quad (6\text{–}10 \text{ Hz})}.$$

Figure 10 shows the *Lg* spectral ratio values by region. Previous discrimination studies in the Western United States found that earthquakes had lower spectral ratios than explosions, indicating that earthquakes have more high-frequency content than explosions. However, our populations of earthquakes and blasts populations almost completely overlap each other in their spectral ratios. The presumed underwater explosions in Region 5 have somewhat lower spectral ratios

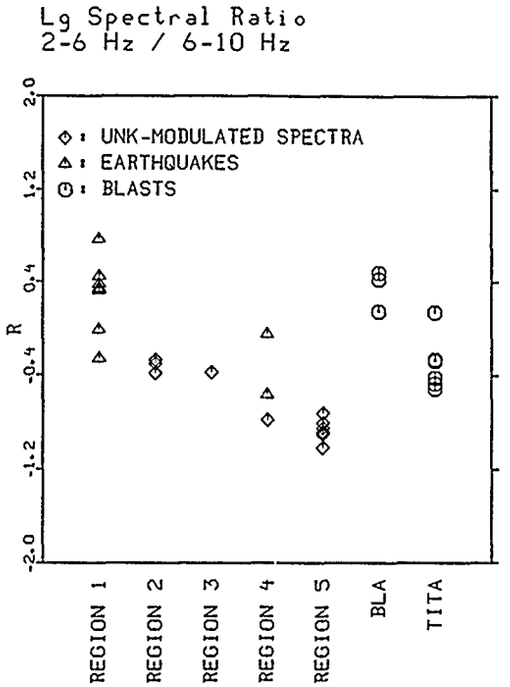

FIG. 10. Plot of the values of *Lg* spectral ratio, *R*, for the same events as Figures 7 and 8.

than the nearby TITA blasts. This result agrees with the results of Suteau-Henson and Bache (1988), who suggested that the Region 5 events were earthquakes. However, these events clearly have lower spectral ratios than the suspected earthquakes in Region 1. Since the TITA blasts are in Region 5, this difference must be an indication of source differences, with the offshore underwater blasts having more high-frequency content than the onshore TITA blasts. Thus, these results show that spectral ratio does not discriminate between blasts and earthquakes but may serve as a means of distinguishing underwater blasts from blasts on land.

As in the case of the amplitude ratios, there seems to be no significant regional dependence of the *Lg* spectral ratio. The earthquakes in Region 4 have similar spectral ratios to those in Region 1. Moreover, ripple-fire effects do not seem to greatly affect spectral-ratio measurements, since the variance of the spectral ratios for the TITA and BLA blasts is comparable to that of the earthquake group.

DISCUSSION

The consideration of case-based methods has been motivated by the failure of previous seismic-discrimination research to develop a set of consistent regional seismic discriminants and a model that explains how intrinsic seismic-source differences affects seismic-waveform features. Lacking such a model, we would identify seismic events by simply comparing them with historic events of known identity and not worry about the explanation of why the waveform features of explosions and earthquakes differ.

However, this study has pointed out some of the problems that would be encountered in an operational setting in trying to use case-based methods to identify seismic events to monitor a low-yield, nuclear test ban treaty using the regional arrays. Ideally, a seismic-discrimination experiment requires there to be large

populations of known earthquakes, economic blasts, and low-yield nuclear explosions in the same region so that useful waveform features sensitive to source differences, not propagation-path differences, can be identified as discriminants. However, in reality, for any given region, this situation will almost never be realized. At low magnitudes, there will be many events detected by the arrays, both natural and man-made, that will usually not occur in the same region. Moreover, in any future test ban treaty scenario, there will almost certainly be no small nuclear explosion tests available for comparison.

Our study has shown how case-based methods may be useful, in spite of all the difficulties. The approach would involve first establishing a baseline of "normal" seismic activity in a region, characterized by the location of historic events and the nature of the waveform features for the events. As much as possible, demographic information would be exploited (e.g., locations of events relative to high-population centers, mines, and previous test sites, felt reports, and time of occurrence of events) although not relied on exclusively. It should be possible to have a population of confirmed explosions and other events that are most likely earthquakes, although it will be hard to positively identify earthquakes in areas of low natural seismicity. We have found in our study that many of the discriminants appear to work in identifying obvious event types and that the propagation effects in western Norway seem to be essentially homogeneous throughout the region. Earthquakes can be identified on the basis of low *P*-to-*S* ratios and lack of spectral modulations. Mine and offshore explosions usually have time-independent spectral modulations and high *P*-to-*S* ratios. Obvious event types can be quickly identified based on these features.

An important question about discrimination raised by this study is why the spectral ratio discriminant fails to work as well for separating earthquakes and economic explosions in western Norway as it did in separating small nuclear explosions and earthquakes in the Western United States (Murphy and Bennett, 1986; Bennett and Murphy, 1986)? Yet, the *P*-to-*S* ratio seems to work better in western Norway than it did in the Western United States. Bennett *et al.* (1989) also found that *P*-to-*S* ratios worked better in separating earthquakes and explosions in the Soviet Union than *Lg* spectral ratio, although their earthquakes and explosions were not located in the same regions. In our study, propagation-paths effects do not seem to have a strong effect on the *Lg* spectral ratios. Moreover, large variations in spectral ratios were observed for mine explosions in the same location, presumably caused by the ripple-fire effects. However, we also found that even for the closely clustered earthquakes in Region 1, whose *P*-to-*S* ratios were very similar, the *Lg* spectral ratios exhibited high variance.

Lilwall (1988) has offered an explanation of the spectral ratio discriminant in terms of the effects of evanescent waves or S^* on *Lg*-wave generation. Such waves would be more strongly generated by shallow explosions near the surface than deeper earthquakes, and thus, the S^* waves would build up the low-frequency levels in the *Lg* waves from explosions relative to earthquakes. Such effects do not seem to present in our blast group. In fact, the underwater explosions in Region 5 seem to have slightly lower values of *R* than other events (including mine explosions), indicating that the higher frequencies in *Lg* are enhanced for these events.

Taylor *et al.* (1988) suggest that the presence of a low-Q region in the upper crust of the Western United States might explain why explosions, which are shallow and occur in the low Q region, have less high frequencies than earthquakes, which might occur below the highly attenuative region. Perhaps no such low-Q region exists in

western Norway, thus explaining why the *Lg* spectra of both earthquakes and explosions are similar. Also, if the Region 5 events are underwater explosions, the water medium may be less attenuative than the solid continental crust, thus resulting in these events having more high-frequency *Lg* waves than the other events on land in western Norway.

The performance of the *P*-to-*S* ratio may be more a result of intrinsic source differences (i.e., explosions have less shear energy compared to compressional energy at high frequency than earthquakes). Our *P*-to-*S* ratio data seems to correlate more with the *P*-wave levels than with the *S*-wave levels. This suggests that explosions and earthquakes generate the same amount of shear-wave energy but that explosions produce more compressional-wave energy than earthquakes. However, this may be more a result of event sampling based on the Bergen local magnitude, as was discussed previously. Differences in depth of focus may also be partly responsible. The mine explosions apparently occurred at the surface (S. Mykkeltveit, personal comm.), whereas the earthquakes were deeper. Perhaps near-surface effects, such as *PS* conversions and S^* generation, may build up the shear-wave energy for the earthquakes.

Conclusions

This study has shown how seismic events can be identified, relative to case events, by means of a systematic assessment of the similarities and differences between waveform characteristics, always keeping in mind the possible effects of propagation-path differences. We have found that array-averaged spectra and incoherent beams, computed using regional-array data, provide robust estimates of waveform features important for seismic discrimination. We have shown that the explosions and earthquakes in a small region of western Norway, recorded at the NORESS array, can be well separated on the basis of high-frequency amplitude-ratio discriminants, but that the *Lg* spectral-ratio discriminants do not separate as well. This seems to agree in general with other regional discrimination studies in Scandinavia and Eurasia.

This study has also demonstrated that the ripple-fire discriminant based on the observation of time-independent modulations, proposed by Baumgardt and Ziegler (1988) and Hedlin *et al.* (1989), may prove to be highly useful in identifying many unknown regional events that are produced by unreported economic blasting. Apparently, at the low-magnitude monitoring level required for a low-yield or comprehensive test ban treaty, many such events will be detected by the regional arrays.

Because discriminants seem to be inconsistent in their performance and that we are not sure how to correct discriminants for propagation-path effects, we have advocated the use of a case-based approach to regional seismic discrimination. In this approach, events should be characterized in a step-by-step fashion, testing individual discriminants and always trying to relate the signal characteristics of unidentified events to events of known identity in the same or similar regions. Because of the current lack of a unifying theory for regional seismic-event identification, the case-based approach may be the only way to reliably characterize and identify seismic events.

Acknowledgments

Jeanne Carney wrote most of the programs and displays used in this study. The comments of an anonymous reviewer on an earlier version of this paper motivated a number of improvements. This

research was funded by the Defense Advanced Research Projects Agency under Contract DAA-H01-89-C-0778, monitored by U.S. Army Missile Command, and by Contract F19628-90-C-0049, monitored by the Air Force Geophysics Laboratory.

REFERENCES

Baumgardt, D. R. (1980). Knowledge-based seismic event identification using seismic event case knowledge and explanations, Technical Report, SAS-TR-90-36, ENSCO, Inc., Springfield, Virginia.

Baumgardt, D. R. and K. A. Ziegler (1988). Spectral evidence of source multiplicity in explosions: application to regional discrimination of earthquakes and explosions, *Bull. Seism. Soc. Am.* **78**, 1773–1795.

Bennett, T. J. and J. R. Murphy (1986). Analysis of seismic discrimination capabilities using regional data from western United States events, *Bull. Seism. Soc. Am.* **76**, 1069–1086.

Bennett, T. J., B. W. Barker, K. L. McLaughlin, and J. R. Murphy (1989). Regional discrimination of quarry blasts, earthquakes and underground nuclear explosions, Final Report, GL-TR-89-0114, S-Cubed, La Jolla, California.

Blandford, R. R. (1975). A source theory for complex earthquakes, *Bull. Seism. Soc. Am.* **65**, 1385–1405.

Blandford, R. R. (1981). Seismic discrimination problems at regional distances, in *Identification of Seismic Sources—Earthquake or Underground Explosion*, E. S. Husebye and S. Mykkeltveit, Editors, Reidel, Boston, 695–740.

Chael, E. P. and R. P. Cromer (1988). High-frequency spectral scaling of a mainshock/aftershock sequence near the Norwegian coast, *Bull. Seism. Soc. Am.* **78**, 561–570.

Hansen, R. A., H. Bungum, and A. Alsaker (1989). Three recent larger earthquakes offshore Norway, *Terra Motae* **1**, 284–295.

Hedlin, M. A., J. Bernard Minster, and J. A. Orcutt (1989). The time-frequency characteristics of quarry blasts and calibration explosions recorded in Kazakhstan, USSR, *Geophys. J. Interiors* **99**, 109–121.

Lilwall, R. C. (1988). Regional m_b:M_S, *Lg*/*Pg* amplitude ratios and *Lg* spectral ratios as criteria for distinguishing between earthquakes and explosions: a theoretical study, *Geophys. J.* **93**, 137–147.

Murphy, J. R. and T. J. Bennett (1982). A discrimination analysis of short-period regional seismic data recorded at Tonto Forest Observatory, *Bull. Seism. Soc. Am.* **72**, 1351–1366.

Nuttli, O. W. (1981). On the attenuation of *Lg* waves in western and central Asia and their use as a discriminant between earthquakes and explosions, *Bull. Seism. Soc. Am.* **71**, 249–261.

Pomeroy, P. W., W. J. Best, and T. V. McEvilly (1982). Test ban treaty verification with regional data—a review, *Bull. Seism. Soc. Am.* **72**, S89–S129.

Pulli, J. J. and P. S. Dysart (1987). Spectral study of regional earthquakes and chemical explosions recorded at the NORESS array, Technical Report, C87-03, Center for Seismic Studies, Arlington, Virginia.

Suteau-Henson, A. and T. C. Bache (1988). Spectral characteristics of regional phases recorded at NORESS, *Bull. Seism. Soc. Am.* **78**, 708–725.

Taylor, S. R., N. W. Sherman, and M. D. Denny (1988). Spectral discrimination between NTS explosions and western United States earthquakes at regional distances, *Bull. Seism. Soc. Am.* **78**, 1563–1579.

Taylor, S. R., M. D. Denny, E. S. Vergino, and R. E. Glaser (1989). Regional discrimination between NTS explosions and western United States earthquakes, *Bull. Seism. Soc. Am.* **79**, 1142–1176.

ENSCO, INC.
5400 PORT ROYAL ROAD
SPRINGFIELD, VIRGINIA 22151

Manuscript received 12 March 1990

Bulletin of the Seismological Society of America, Vol. 80, No. 6, pp. 1893–1909, December 1990

PROGRAMMING AS A GEOPHYSICAL INVERSE PROBLEM

BY KENNETH R. ANDERSON

ABSTRACT

The detections and events produced by autonomous seismic data analysis systems, such as those of the NORESS and ARCESS seismic arrays, and seismic networks around the world, are a fundamental source of seismic data that underlies a wide variety of seismic research. While shortcomings in the performance of such systems may become obvious over time, remedying them can be difficult and problems with an autonomous system may persist indefinitely. This paper describes how the performance of autonomous systems can be improved over time using optimization and machine learning techniques. For example:

1. **Optimization techniques such as Genetic Algorithms can optimize the rule thresholds of existing systems.**
2. **Supervised learning techniques such as neural networks, ID3, and CART can synthesize algorithms out of the data itself given only the levels of human supervision used in routine seismic processing. Experiments using autonomic detections from the NORESS and ARCESS array demonstrate how components of an autonomous system can be developed automatically with minimal human guidance.**

INTRODUCTION

Since the 1960s, there has been steady interest in developing array seismology techniques for use in nuclear test monitoring. In recent years, emphasis has shifted away from the analysis of teleseismic signals using large aperture seismic arrays, such as LASA and NORSAR (Ringdal and Husebye, 1982), toward the analysis of regional signals using smaller high-frequency seismic arrays, such as NORESS and recently ARCESS (Mykkeltveit *et al.*, 1990).

Also during this time, there has been a steady increase in the sophistication of the computer hardware and software used to process this data. For example, processing at NORESS has gone from RONAPP (Regional On-Line Array Processing Package) written in FORTRAN for a single processor (Mykkeltveit and Bungum, 1984) to the IAS (Intelligent Array System) written in C, FORTRAN, LISP, and other languages for a distributed computing environment (Bache *et al.*, 1990). The scope of processing has also increased from one seismic array, to several (Bratt and Bache, 1988).

Such automatic algorithms are important because they provide data that is the basis of seismological knowledge. While shortcomings of such algorithms become obvious over time, remedying them can be difficult, and problems with automatic algorithms may persist indefinitely.

There are several reasons for this. First, improving the existing algorithm is often subtle. Trying to add an additional "good idea" into the algorithm can require complicated software that may not produce much improvement. For example, identifying several types of glitches and nonseismic noise that easily produce false detections in a power law detector, can be surprisingly difficult (Anderson, 1982).

Second, while using artificial intelligence programming techniques, such as an expert system, and symbolic waveform description (Anderson and Gaby, 1982; Anderson *et al.*, 1982; Bache *et al.*, 1990) may help; they require expert knowledge and handcrafted rules. While seismologists can provide general, high-level rules,

getting down to the level of raw data can be difficult because it requires getting tests and thresholds right.

Third, once a new algorithm is proposed, its performance must be carefully evaluated before it can be fielded. The entire process of improving an algorithm, evaluating its performance, and fielding it can take some time.

Last, although improvements to automatic processing algorithms are encouraged, they do impact the history of important seismic parameters. For example, reducing the detection threshold of a seismic array will affect b value estimates and make event bulletins from different years difficult to compare.

Seismic array processing algorithms are divided into several steps, such as beam forming, detection, feature extraction, arrival association, and location. Each step requires many decisions to be made, and each decision uses several predicates (functions that return truth values) that generally involve a threshold comparison. In a system as complicated as RONAPP or IAS, there are likely to be several hundred rules and thresholds that must be determined. It is a formidable task to properly balance the performance of each stage to work well with the next.

This paper shows how optimization and machine learning techniques can be used to estimate these parameters and learn rules. The performance of autonomous systems developed using these techniques can also improve over time automatically as new data become available, or as the configuration of the system is changed. The advantage of these techniques is that they do not require explicit programming. The appropriate programming is developed algorithmically from training examples of appropriate input–output behavior. The disadvantage of these techniques is that they require plenty of data and computer time for training.

One advantage that seismology has is that it has an almost limitless supply of data to work with. Since analysts routinely review the results of automatic processing, providing training data for supervised learning is almost free. Also, in principle, learning and performance evaluation could be done incrementally as the data are collected.

To demonstrate the potential of these techniques we will show how three stages of the IAS can be determined algorithmically. These stages are:

1. Initial phase identification
2. Detection grouping
3. Phase identification

These stages are used to go from a stream of raw detections to an estimated epicenter. An algorithm for the first two stages is estimated from a dataset of detections and their corresponding event bulletin. Starting from a template for the algorithm containing several unknown threshold values, the optimum values of the thresholds are determined that maximize the algorithm's performance. In the third stage, a set of rules are deduced using an ID3-like tree classifier (Quinlan, 1983).

Stages of Seismic Array Data Processing

The data processing performed by seismic arrays are organized into several stages. We will consider the steps performed by the IAS (Bache *et al.*, 1990) because it is currently the most sophisticated algorithm, although much of the single-array processing is similar to that of RONAPP.

1. Data input: Acquire the raw data and make it available for further processing.
2. Beamforming and detection: The incoming array data are filtered and beamed, and a STA/LTA power detector is used to detect signals on each beam.

3. Postdetection processing:
   (a) Beam analysis: Refine the arrival time, and estimate its error.
   (b) Frequency-wavenumber analysis: Determine the velocity and azimuth of the detection, and estimate the error in azimuth and velocity. Also estimate the *F-K* quality.
   (c) Spectral computation: Estimate the spectrum for both the signal and the noise.
   (d) Polarization analysis: Compute the polarization ellipse from three-component sensors.
4. Single-array processing:
   (a) Initial phase identification: Velocity is used to assign each detection to one of four classes: Noise (N), regional *S* (S), regional *P* (P), or teleseismic (T).
   (b) Detection grouping: Group the *P* and *S* detections that appear to be generated by the same event.
   (c) Phase identification: Identify *P* detections as *Pn* or *Pg*, and *S* detections as *Sn* or *Lg* based on polarization measurements and *S-P* time.
   (d) Location: Locate the event.
5. Network processing: Fuse information from several arrays to form improved locations. Several heuristics are used to identify corroborating information from each array. For example, the detections from an event should group in time and the location confidence ellipses should overlap.
6. Magnitude calculation: Compute the event magnitude based on the final location and its associated arrivals.
7. Script matching: The detections that make up the event are matched against known scripts that represent detailed knowledge about certain classes of events, such as quarry blasts.

Optimization of an Existing Algorithm

This section shows how parameters used in stages 4a and 4b of the IAS system can be determined as a somewhat different kind of geophysical inverse problem. (The software examples below are written in a generic pseudo-programming language that should be easily understood by most people familiar with a programming language. The software used in this project was written in Common LISP.)

The rules used by IAS for initial phase identification can be written in terms of an arrival's velocity as:

```
function initial-phase-identification (velocity)
  begin
    if (velocity ≤ 2.8) N              # Noise.
    else if (velocity < 6.0) S         # Regional S.
      else if (velocity < 14.0) P      # Regional P.
      else T                           # Teleseismic.
  end
```

The velocity thresholds used in the rules have been shown to be reasonably good. However, when the NORESS array was originally installed, the velocity of 6.0 km/sec used to distinguish between *P* and *S* arrivals was determined by a relatively small number of data points (<50). The original data by Mykkeltveit and Bungum (1984; Fig. 6) shows a gap of 6 km/sec that does not contain any arrivals.

One gets a more accurate picture by looking at more data. Figure 1 shows histograms of velocity for 4,428 arrivals from ARCESS and 3,716 arrivals from NORESS over the period from 6 January 1988 to 16 February 1988. While the ARCESS data show a broad minimum centered near 6.0 km/sec, the NORESS data have a more narrow minimum well below 6.0 km/sec. It may be that some arrivals classified as S by the previously mentioned rules should have been classified as P.

Rather than accept these threshold values for phase identification, they can be determined along with the parameters of the detection grouping algorithm. Such an algorithm follows easily from general seismic knowledge and might be described in words as follows: a group of related arrivals, must start with a regional P arrival,

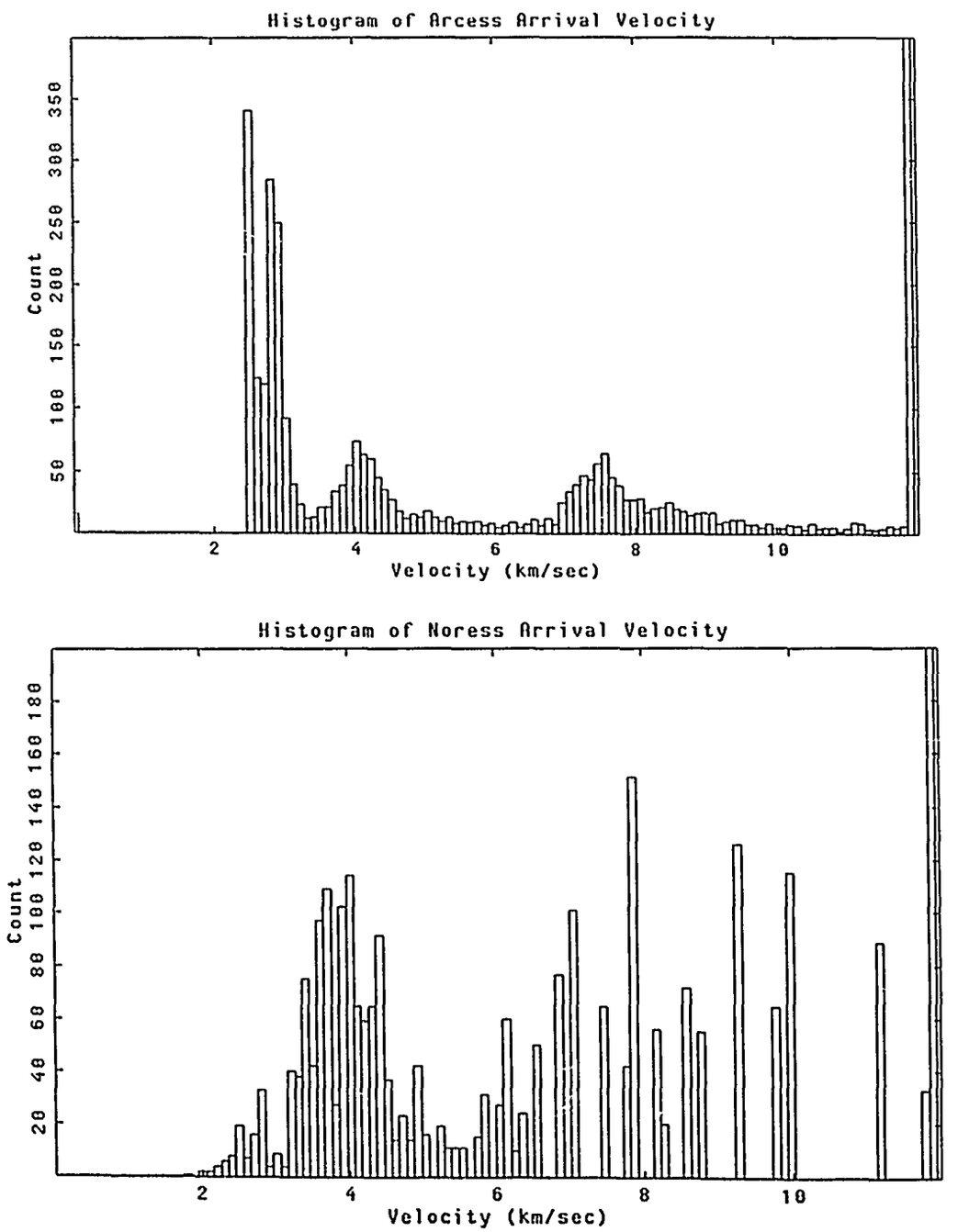

FIG. 1. Histograms of detection velocity (km/sec) for ARCESS and NORESS arrivals.

cannot exceed some overall duration, and may consist of any number of regional P arrivals followed by any number of regional S arrivals. Also, all arrivals must be azimuthally consistent.

For concreteness, this could be written in the pseudo-programming language as:

```
function events (arrival, x)
  begin
  # Search for events.
  while more-arrivals?(arrival)
    begin
    new-event( )
    # Find a regional P.
    first = find regional-p?(arrival)
    collect(first)
  # Followed by P arrivals
    while duration-ok?(arrival, first)
      if (azimuth-ok?(first, arrival) and
        regional-p?(arrival))
        collect(arrival)
    # Followed by S arrivals
    while duration-ok?(arrival, first)
    if (azimuth-ok?(first, arrival) and
      regional-s?(arrival))
      collect(arrival)
    end
  end
```

The arguments to `events` are `arrival`, an arrival to start searching at, in a time sorted sequence of arrivals, and `x`, a vector of parameters that will be determined below. The algorithm is written using the following forms to simplify its specification:

`find condition(`*arrival*`)` finds the next arrival matching *condition*, and binds it to the variable `arrival`.
`more-arrivals?(`*arrival*`)` is true while there are more arrivals.
`new-event( )` starts collecting arrivals for a new event.
`while` *condition action* moves over the arrivals while *condition* is true, performing *action*.
`collect(`*arrival*`)` collects *arrival* into the list of arrivals for the event being constructed.

This algorithm is similar to that used by RONAPP and IAS. However, to run it, one must specify the definition of the predicates `regional-p?`, `regional-s?`, `azimuth-ok?`, and `duration-ok?` Following the IAS, it is reasonable to assume predicates of the form:

```
function regional-p? (arrival)
  begin
    MIN-P-VELOCITY
    ≤ velocity(arrival)
    ≤ MAX-P-VELOCITY
  end
```

```
function regional-s? (arrival)
  begin
    MIN-S-VELOCITY
    ≤ velocity(arrival)
    ≤ MAX-S-VELOCITY
  end

function azimuth-ok? (arrival-1, arrival-2)
  begin
    abs(azimuth-(azimuth(arrival-1), azimuth(arrival-2)))
    < MAX-AZIMUTH-DIFFERENCE
  end

function duration-ok? (arrival-1, arrival-2)
  begin
    arrival-time(arrival-1) −
    arrival-time(arrival-2)
    < MAX-DURATION
  end
```

The values of the variables in capitals must be determined. This can be done as an optimization problem that determines the set of thresholds that identifies the largest number of true events. This can be posed as the following optimization problem:

find x that minimizes

$$E = \sum_{e \in \text{events(arrivals},x)} \text{cost}(e)$$

where x is the vector of unknown thresholds, and events(arrivals, x) is the set of events produced by the *events* algorithm for a given training set, *arrivals*, and parameter vector, x. Here, cost(e) is -1 if event e is a valid event, or 1 otherwise. Thus, false events (false positives) and missed events (false negatives) are weighted equally.

Since partial derivatives, dE/dx, are not available, the methods used traditionally in geophysical inverse problems, such as Gauss–Newton or Levenberg–Marquardt (Aki and Richards, 1980), cannot be used. Instead, one must rely on methods that only require function evaluations. The performance of three such methods were compared:

RANDOM	Random search,
AMOEBA	The simplex method, and
GA	Genetic algorithms.

The following subsections describe each of these techniques briefly. This is followed by a comparison of the methods.

Random Search

This is a shotgun approach where a random number of trial solutions, x_i, $i = 1, N$ are chosen in a volume of the parameter space. The best x_i is then chosen to become the center of another random search over a reduced volume of the parameter space. This process is then repeated until the search volume becomes small.

The advantage of this method is that it is extremely simple. One disadvantage of this method is that many function evaluations are performed. As the search volume shrinks, these evaluations tend to become progressively more redundant. Another disadvantage is that it is a "greedy" algorithm that always moves in the direction of improvement. Thus it can become stuck in at a local minimum. For this experiment, 100 random solutions were generated (over 10 solutions per dimension), and the search space was shrunk by 0.75 at each iteration.

Simplex Method

The simplex method of Nelder and Mead (1965) (Schnabel, 1962; Parkinson and Hutchison, 1972; Nash, 1979; Press *et al.*, 1986) should not be confused with the simplex method used in linear programming. Here, a simplex of $N + 1$ points, in an N dimensional parameter space, is chosen. Then, at each iteration, a set of rules are applied that tend to move the simplex to surround a local minimum. The size and shape of the simplex changes accordingly as it slithers toward a minimum. The algorithm is called *Amoeba* by Press *et al.* (1986) because of this behavior.

The advantage of this approach is that, although it does not use derivatives, the simplex contains some information about the shape of the function to be minimized. This shape information is used to move toward the minimum. The disadvantages of the method are that, in high-dimensional vector spaces, many function evaluations are required. Also, if the objective function contains flat regions, the simplex becomes stuck, unable to improve its solution.

Genetic Algorithms

Genetic algorithms approach optimization as an analog to natural evolution in population genetics (Holland, 1975; Goldberg, 1989). The basic features of a genetic algorithm are:

1. Represent a solution to the problem to be solved as a chromosome. For example, traditionally a bit vector has been used as chromosomes.
2. An initial population of chromosome is generated.
3. An evaluation function plays the role of the environment, ranking solutions by their "fitness."
4. Survival of the fittest: The population of chromosomes is evolved using random genetic operations, such as mutation and cross-over. Mutation is a random change to a feature (gene) of a chromosome that occurs at some mutation rate. Cross-over is the exchange of genetic material between two chromosomes (parents) to produce new children. Fitter parents are more likely to be involved in cross-over. If the bit vector representation of a chromosome is used, then mutation is randomly flipping a bit, while cross-over exchanges bits between parents to produce one or two offspring. Offspring are added to the population, replacing less fit population members.

These steps are then iterated to allow the population to evolve. Holland shows that, even in large and complicated search spaces, genetic algorithms tend to converge to nearly globally optimal solutions.

The threshold optimization problem can be posed as the following genetic algorithm:

1. A chromosome is simply the vector, x, of unknown thresholds for the `events` algorithm.

2. A population size of 40 was used. The initial population was generated randomly.
3. The following genetic operators were used:
   - Cross-over: The components of the vector of each parent are randomly switched to produce two new children. Only children different from the parents are used.
   - Creep: A component of the chromosome vector is adjusted up or down by a small random amount. The probability of a component being changed is 0.3.
   - Mutation: A component of the chromosome vector is randomly altered to a new value, in the range of possible values. The probability of mutating a single component is 0.2.

   After an operator was applied, the offspring was added immediately into the population.
4. The relative rates at which these operators were applied to the population were adjusted during the run (Davis, 1989). This allows the algorithm to use different strategies at different times in the search. For example, early in the search, cross-over is an important operator because it can produce good offspring from parents from different parts of the search space. Later on, creep becomes important because it tends to move a solution toward a local optimum.
5. The fitness of a vector, x, is an exponential function of the rank, $n(x)$, of x in terms of the objective function:

$$K^{n(x)}$$

where $K < 1$ is the exponential decay constant. This constant is reduced during the run. Early in the run, K is near 1 so that a large fraction of the population can exchange genetic material. Later in the run, K is reduced so that only the most fit members of the population are involved.

Comparison of Optimization Methods

Each optimization method was run several times on a 40-day detection list from NORESS consisting of 3,716 detections from 494 events. The following data show the best solution found by each method, the number of true and extra events found, and the range of function evaluations required to solve this problem.

OPTIMIZATION METHOD	RANDOM	AMOEBA	GA
MIN-P-VELOCITY	5.47	5.44	6.02
MAX-P-VELOCITY	14.71	14.75	13.72
MIN-S-VELOCITY	1.47	1.53	2.04
MAX-S-VELOCITY	5.47	5.44	5.94
MAX-DURATION	299.91	279.50	255.50
MAX-AZIMUTH-DIFFERENCE	52.91	49.62	67.03
TRUE EVENTS FOUND	471	472	469
EXTRA EVENTS FOUND	68	67	45
MISSED EVENTS	23	22	25
FUNCTION EVALUATIONS	400–500	30–50	40–100

Each method easily finds reasonably good solutions. Both the RANDOM and AMOEBA methods choose MIN-P-VELOCITY and MAX-S-VELOCITY values that

are below the 6.0 km/sec used by RONAPP and IAS. In fact, when the values of the thresholds were set to the values suggested from reading Mykkeltveit and Bungum (1984),

$$x = [6.0, 14.0, 2.0, 6.0, 360.0, 20]$$

the performance was a few per cent worse than any of these methods.

The extra events were often plausible except that either they did not begin with what RONAPP called a *P* wave, or were rejected by an analyst because of noise problems that could not be distinguished from the detections alone. Comparing the number of function evaluations required to reach a minimum, we see that, as one might expect, RANDOM takes significantly longer than the other two methods. The AMOEBA method does best for this problem, while the performance of GA is slightly worse. These results are reasonable for a simple problem like this that is of low dimensionality and has a minimum with a broad basin of attraction.

In some sense, the GA behaves a bit like a combination of both methods. In the AMOEBA, the simplex is analogous to the population in GA; both contain knowledge about the objective function. The rules that change the shape of the simplex are similar to the cross-over rule of the GA except that the former tend to be more local. The GA is like RANDOM in that random search plays an important part in its behavior, except that the GA make better use of its population than RANDOM does. It has been our experience that the GA algorithm is effective on a wide range of difficult problems.

Learning Phase Identification Rules

Once the detections are grouped into possible events, the next step performed by the IAS, 4c, is to determine the phase identification of each detection, that is to identify it as either *Pn*, *Pg*, *Sn*, *Lg*, or *Rg*.

The IAS algorithm bases its decisions on rules that involve the following features:

1. The arrival time separation between the first *P* and the largest *S* in the detection group.
2. The number of *P* and *S* waves in a group.
3. The *S* and *P* wave polarizations.
4. The signal-to-noise ratio (SNR) of each detection.

In the following experiment, a similar set of rules is developed using a tree classifier similar to ID3 (Quinlan, 1983; Pao, 1989). A description of the algorithm is presented below. For each detection, the following attributes were used (polarization information was not available):

- CENTER-FREQUENCY: Center frequency of the arrival in Hz.
- PERIOD: Period of the arrival in sec (=1/center-frequency).
- DELTA-AZIMUTH: Azimuthal error.
- SLOWNESS: Slowness km/sec.
- DELTA-SLOWNESS: Slowness error.
- SNR: Signal-to-noise ratio.
- STA: Short-term average signal power of the detector.

- F-STATISTIC: F-statistic.
- DELTA-TIME: Arrival time error.
- BANDWIDTH: Detection bandwidth.
- FK-QUALITY: An integer quantifying the quality of the frequency wavenumber (f-k) spectrum.
- LTA: The long-term average signal power of the detector.
- SLOW-PREVIOUS: Slowness of previous arrival in event.
- DT-PREVIOUS: Arrival time difference between this arrival and the previous one in the event, or 0.0 if this is the first arrival.
- SLOW-NEXT: Slowness of the next arrival in the event.
- DT-NEXT: Arrival time difference between this arrival and the next one in the event, or 0.0 if this is the last arrival.
- S-P-GROUP TIME: The time between the first regional P arrival and the first regional S arrival.

It is not expected that all of these features are relevant to phase identification, but it is useful to give them to the learning algorithm in case they prove to be of benefit.

Two experiments were performed. In the first, a set of training detections from NORESS was used to determine a classification tree. This led to a deep tree that over-fits the data. The tree was then applied to test data from the same time period from ARCESS, and branches of the tree that did not improve the performance of the classifier were pruned. This results in a compact tree that is useful for both networks. In the second experiment, the roles of NORESS and ARCESS are reversed. Thus, the two arrays cooperate in training each other. The resulting rules are:

```
NORESS Pn Rule:
IF (    SLOWNESS        <  0.1668 AND
        S-P-GROUP-TIME  <  4.356
    OR  SLOWNESS        <  0.1668 AND
        S-P-GROUP-TIME  < 24.855  AND
        S-P-GROUP-TIME  ≥ 22.0    AND
        DELTA-AZIMUTH   <  4.7867
    OR  SLOWNESS        <  0.1668 AND
        S-P-GROUP-TIME  < 24.855  AND
        S-P-GROUP-TIME  ≥ 22.0    AND
        DELTA-AZIMUTH   ≥  6.6624
    OR  SLOWNESS        <  0.1257 AND
        S-P-GROUP-TIME  ≥ 24.855  AND
    OR  SLOWNESS        <  0.1668 AND
        SLOWNESS        ≥  0.1257 AND
        S-P-GROUP-TIME  ≥ 24.855  AND
        F-STATISTIC     < 15.885  AND
        DT-PREVIOUS     <  6.923
```

```
     OR SLOWNESS        <  0.1668 AND
        SLOWNESS        ≥  0.1257 AND
        S-P-GROUP-TIME  ≥ 24.855  AND
        F-STATISTIC     ≥  15.885 AND
        DT-NEXT         < 28.383

     OR SLOWNESS        <  0.1668 AND
        SLOWNESS        ≥  0.1257 AND
        S-P-GROUP-TIME  ≥ 24.855  AND
        F-STATISTIC     ≥ 15.885  AND
        DT-NEXT         ≥ 28.393  AND
        DT-PREVIOUS     <  6.374
   ) PN

NORESS Pg Rule:

IF (    SLOWNESS        <  0.1668 AND
        S-P-GROUP-TIME  ≥  4.356  AND
        S-P-GROUP-TIME  < 22.0

     OR SLOWNESS        <  0.1668 AND
        S-P-GROUP-TIME  ≥ 22.0    AND
        S-P-GROUP-TIME  < 24.855  AND
        DELTA-AZIMUTH   ≥  4.7867 AND
        DELTA-AZIMUTH   <  6.6624

     OR SLOWNESS        ≥  0.1257 AND
        SLOWNESS        <  0.1668 AND
        S-P-GROUP-TIME  ≥ 24.855  AND
        F-STATISTIC     < 15.885  AND
        DT-PREVIOUS     ≥  6.923

     OR SLOWNESS        ≥  0.1257 AND
        SLOWNESS        <  0.1668 AND
        S-P-GROUP-TIME  ≥ 24.855  AND
        F-STATISTIC     ≥ 15.885  AND
        DT-NEXT         ≥ 28.393  AND
        DT-PREVIOUS     ≥  6.374
   ) PG

NORESS Sn Rule:

IF (    SLOWNESS ≥  0.1668 AND
        SLOWNESS <  0.2504 AND
        DT-NEXT  ≥  7.009
   ) SN

NORESS Lg Rule:

IF (    SLOWNESS ≥  0.1668 AND
        DT-NEXT  <  7.009

     OR SLOWNESS ≥  0.2504 AND
        DT-NEXT  ≥  7.009
   ) LG
```

ARCESS Pn Rule:

```
IF (   SLOWNESS        <  0.1667 AND
       S-P-GROUP-TIME  < 24.232  AND
       SLOW-NEXT       <  0.1031 AND
       DT-NEXT         < 16.377
    OR SLOWNESS        <  0.1349 AND
       SLOW-NEXT       ≥  0.1031 AND
       S-P-GROUP-TIME  < 24.232  AND
       DT-NEXT         ≥ 22.8
    OR SLOWNESS        <  0.1667 AND
       S-P-GROUP-TIME  ≥ 24.232  AND
       DT-PREVIOUS     <  4.293
   ) PN
```

ARCESS Pg Rule:

```
IF (   SLOWNESS        <  0.1667 AND
       S-P-GROUP-TIME  < 24.232  AND
       SLOW-NEXT       <  0.1031 AND
       DT-NEXT         ≥ 16.377
    OR SLOWNESS        <  0.1349 AND
       S-P-GROUP-TIME  < 24.232  AND
       SLOW-NEXT       ≥  0.1031 AND
       DT-NEXT         < 22.8
    OR SLOWNESS        ≥  0.1349 AND
       SLOWNESS        <  0.1667 AND
       S-P-GROUP-TIME  < 24.232  AND
       SLOW-NEXT       ≥  0.1031
    OR SLOWNESS        <  0.1667 AND
       S-P-GROUP-TIME  ≥ 24.232  AND
       DT-PREVIOUS     ≥  4.293
   ) PG
```

ARCESS Sn Rule:

```
IF (   SLOWNESS     ≥  0.1667 AND
       DT-NEXT      ≥  5.125  AND
       DT-PREVIOUS  ≥ 31.632
   ) SN
```

ARCESS Lg Rule:

```
IF (   SLOWNESS  ≥  0.1667 AND
       DT-NEXT   <  5.125
    OR SLOWNESS     ≥  0.1667 AND
       DT-NEXT      ≥  5.125  AND
       DT-PREVIOUS  < 31.632
   ) LG
```

Figure 2 shows the travel times of *Pg*, *Sn*, and *Lg* arrivals relative to the first *P* arrival, *Pg*, or *Pn* (S. R. Bratt, personal comm., 1990). From this and the fact that from velocity alone one can only deduce that the arrival is one of the two *P* or *S* arrivals, one would expect that velocity (or slowness), and arrival time differences will be important in the rules.

Of course, the rules are determined from data the arrays actually see. NORESS' view of the relative travel times are shown in Figure 3. It is this view that is reflected in the rules produced. For example, the *Pn* and *Pg* rules are complex because they are difficult to distinguish at distances less than about 300 km. *Pn* and *Pg* are relatively easy to separate beyond 300 km, and *Pg* is not observed beyond 700 km. The rules reflect these distance relationships using `dt-next`, `dt-previous`, and `s-p-group-time`.

After a decision tree is grown from detections from one array, the tree is pruned using data from the other array. The pruned tree is then run again on the original data. The following data summarize the performance of each rule set on detections from each array:

Training set:	NORESS	ARCESS
# Detections:	1602	1362
ARCESS % Error:	7.8	4.8
NORESS % Error:	5.5	6.1

The ARCESS rule set has slightly better performance, and simpler rules. The corresponding decision tree is shown in Figure 4. The learning algorithm clearly had trouble distinguishing between *Pn* and *Pg* arrivals from NORESS. It thus

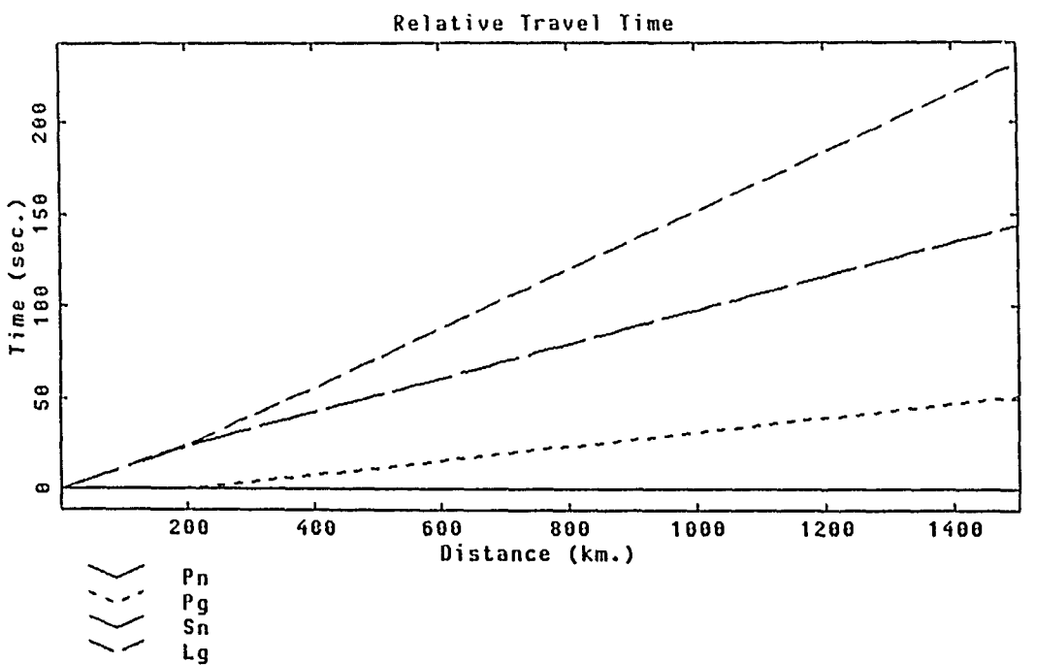

FIG. 2. Relative travel times versus distance for *Pn*, *Pg*, *Sn*, and *Lg*.

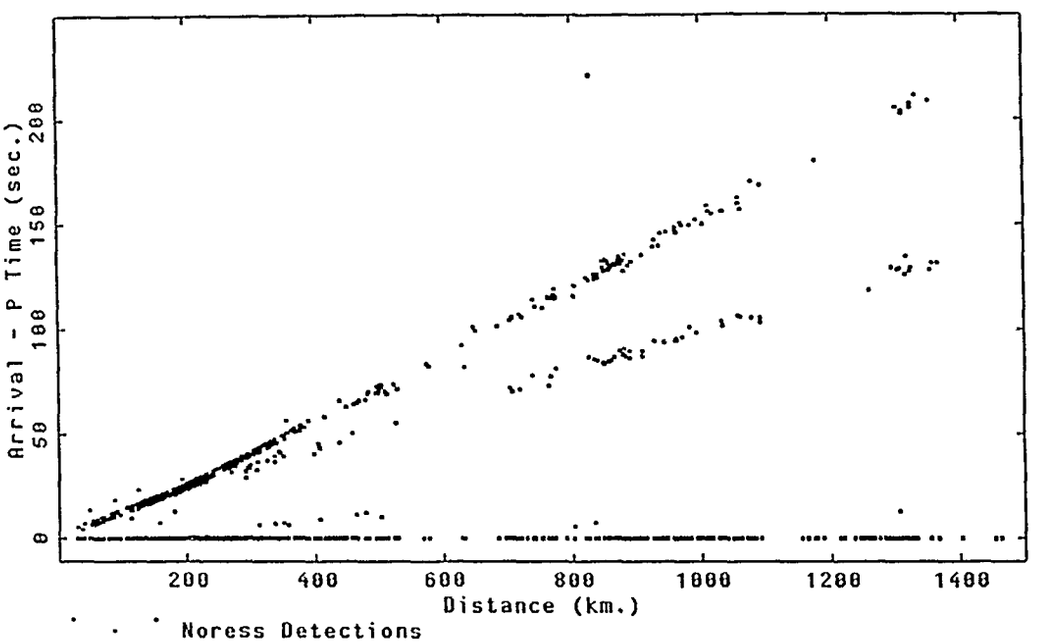

FIG. 3. Relative travel times versus distance for NORESS detections used to produce phase identification rules.

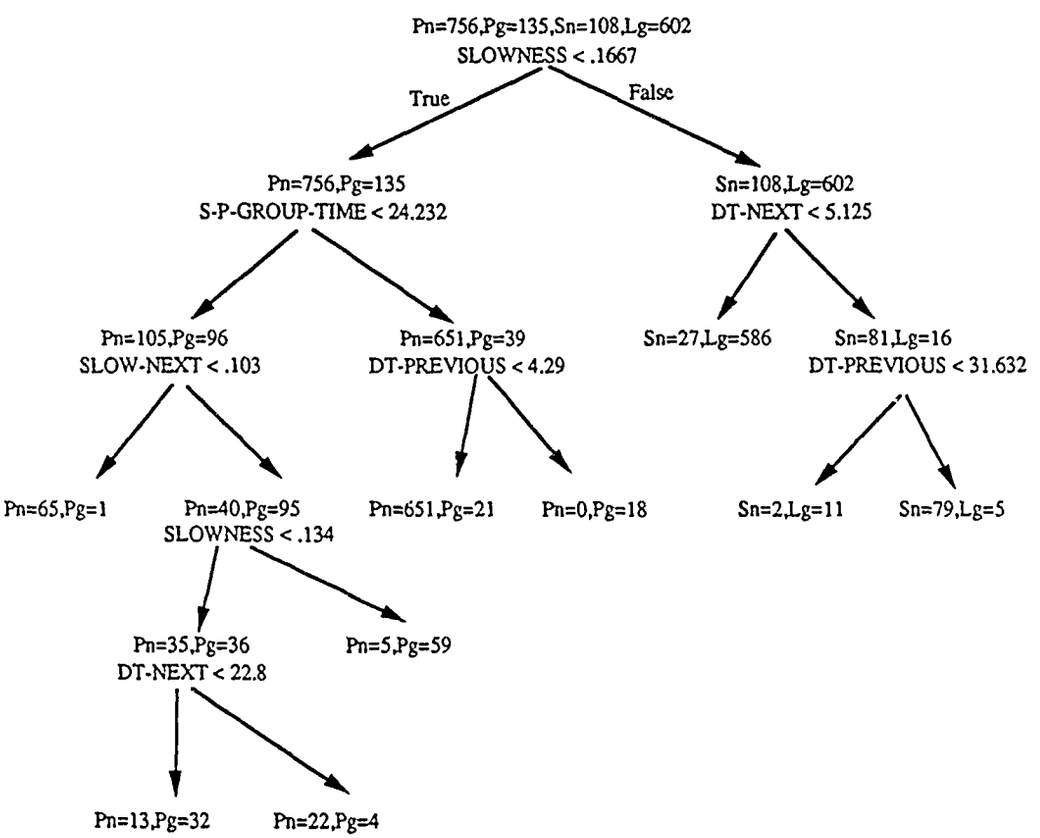

FIG. 4. Decision tree grown from ARCESS data after pruning by NORESS data.

produced unnecessarily complex rules. By comparing the NORESS and ARCESS rules for *Pn* and *Pg*, we see that the terms involving `delta-azimuth` and `F-statistic` are irrelevant. Quinlan (1989) shows how to identify such terms. Both sets of rules contain simple rules for *Sn* and *Lg*.

The ID3 Learning Algorithm

ID3 is an algorithm for inductively synthesizing a binary decision tree for classification given a set of labeled training examples in the form of feature vectors (Quinlan, 1983; Pao, 1989). As in the game of "twenty questions," the object is to find as few questions as possible that will correctly classify the data. ID3 determines the binary question that provides the most information about the identity of the data. Each question divides the dataset, S, into two groups, S_t and S_f, depending on whether the answer to the question is true or false for a particular datum. ID3 is then applied recursively to each group until the data cannot be classified further.

At each stage, ID3 chooses to ask the question that maximizes the information (reduces the uncertainty) about the class membership of the data. The entropy, or uncertainty, before the question is asked is:

$$H(S) = \sum_i - P_i \log_2(P_i)$$

where P_i is the fraction of the elements in S belonging to class C_i. After the binary question Q is applied, the data are divided into two groups, S_t and S_f, and the remaining entropy is:

$$H(S, Q) = P(S_t)H(S_t) + P(S_f)H(S_f),$$

where $P(S_t)$ is the fraction of the elements of S for which the question, Q, is *true*, similarly for $P(S_f)$.

The information gained by asking Q is then

$$I(Q) = H(S) - H(S, Q)$$

and the best question to ask is the one that maximizes $I(Q)$. When the training data has binary-valued features, one simply chooses the feature, F, for which $H(S, F)$ is maximum. When the values of the features of the data are continuous, as they are here, one must determine a feature, F, and a threshold, T, for which $H(S, F > T)$ is maximized. For a given feature, the best threshold can be found by a linear search.

ID3 has the problem that it over-fits the data. CART (Breiman *et al.*, 1984; Crawford, 1989) tries to solve this problem by trimming tree limbs that don't improve some heuristic measure of the goodness of the tree.

Discussion

The two previously described experiments indicate how the development of seismic signal processing software can be automated. There are clearly several benefits to developing seismic software this way (below we will refer to a generic learning system as "the learner"):

1. Conjuring software out of data is easier than programming.
2. Learning and performance estimation go hand in hand. Thus, not only is the

algorithm learned automatically, but we also have a reasonable estimate of what its performance on new data will be like.

3. Potentially, a seismic analyst could provide the learner with immediate feedback. For example, each time an analyst changes an arrival time, or a phase identification, this could be used as a new training example. Thus, the system could adaptively improve its performance in nearly real time.
4. Specialized knowledge can be added to the system incrementally, as in the Script Matching step of the IAS. For example, the rule learning system has been taught to recognize quarry blasts simply by being shown examples of what quarry blasts look like. Regional variations in wave propagation characteristics could also be learned this way.
5. The learner could act like a seismologist's apprentice. For example, if a seismologist is interested in a certain type of data, he gives the learning system several examples. The learner produces a set of rules and then uses the rules to search a database for more data of interest to the seismologist. The seismologist then accepts or rejects each example, which leads to a refined set of rules.

Genetic Algorithm optimization and tree classifiers are only two machine learning techniques. Other methods, such as neural networks (see Lippmann 1987, for a survey), are likely to be useful in various aspects of seismic processing, particularly in large dimensional parameter spaces with correlated dimensions, as one is likely to encounter when dealing more directly with waveform data than was done here.

Potentially, any component of a seismic system is a candidate for machine learning. The parameter optimization approach can clearly be used to improve the performance of existing software. Such optimization problems should not be significantly harder to solve than the geophysical inverse problems solved routinely today. The components that have been notoriously hard to program might be good candidates for machine learning. For example, arrival time estimation has been difficult to automate, at least for regional and teleseismic signals. A neural network approach might be applicable here.

The data must contain enough information so that the learner can learn as needed. For example, discriminating between nuclear explosions and earthquakes is a difficult problem, at least in part, because of the limited data available. Luckily, for routine seismic processing, there is more than enough data available. The experiments here indicate that several months of data are sufficient for learning postdetection rules. Other processing stages will require different amounts of training data.

Seismologists have always used computers to extract information about the earth. Machine learning techniques allow them to treat programming of complex data analysis systems as another geophysical inverse problem.

ACKNOWLEDGMENTS

I would like to thank the following individuals who helped make this research happen. Michael Tiberio extracted the 1989 NORESS and ARCESS data from the Center for Seismic Studies databases. Richard Baumstark provided the 1988 NORESS and ARCESS data. Steve Bratt and Richard Stead of the Center for Seismic Studies answered questions about the Center's databases and IAS processing. Frode Ringdal provided information about NORESS. Albert Boulanger and Jeff Morrill provided valuable discussions about how machine learning could be applied to this domain, and offered direction and guidance. David Davis provided the object-oriented Genetic Algorithm Package, OOGA, and helped tweak its performance. David Montana provided his insights into optimizing the performance of a real autonomous data analysis system.

REFERENCES

Aki, K. and P. G. Richards (1980). *Quantitative Seismology Theory and Methods*, W. H. Freeman and Co., San Francisco, California.

Anderson, K. R. (1982). Syntactic analysis of seismic waveforms using augmented transition network grammars, *Geoexploration* **20**, 161–182.

Anderson, K. R. and J. E. Gaby (1982). Dynamic waveform matching, *Information Sciences* **31**, 231–242.

Anderson, K. R., S. T. Rosenberg, and D. Lanan (1982). Automatic association using expert system techniques, in *Seismic Discrimination, Semiannual Technical Summary*, Lincoln Lab., MIT, Cambridge, Massachusetts.

Bache, T. C., R. S. Bratt, J. Wang, R. M. Fung, C. Kobryn, and J. W. Given (1990). The Intelligent Monitoring System, *Bull. Seism. Soc. Am.* **80**, Part B, 1833–1851.

Blandford, R. R. (1982). Seismic event discrimination, *Bull. Seism. Soc. Am.* **72**, S69–S87.

Bratt, S. R. and T. C. Bache (1988). Locating events with a sparse network of regional arrays, *Bull. Seism. Soc. Am.* **78**, 780–798.

Breiman, L., J. H. Friedman, R. A. Olsen, and C. J. Stone (1984). *Classification and Regression Trees*, Wadsworth, Belmont, California.

Crawford, S. L. (1989). Extensions to the CART algorithm, *Int. J. Man-Machine Studies* **31**, 197–217.

Davis, D. (1989). Adaptive operator probabilities in genetic algorithms, in *Proc. 3rd Int'l Conf. on Genetic Algorithms*, Morgan Kaufmann, Pub., June 1989, 61–69.

Efron, B. (1983). Estimating the error rate of a prediction rule: improvements on cross-validation, *J. Am. Stat. Assoc.* **78**, 316–331.

Goldberg, D. E. (1989). *Genetic Algorithms in Search, Optimization and Machine Learning*, Addison-Wesley Publishing Co., Inc., Reading, Massachusetts.

Holland, J. (1975). *Adaptation in Natural and Artificial Systems*, University of Michigan Press, Ann Arbor, Michigan.

Lippman, R. (1987). An introduction to computing with neural nets, *IEEE SSP Magazine*, 4–22.

Mykkeltveit, S. and H. Bungum (1984). Processing of regional seismic events using data from small-aperture arrays, *Bull. Seism. Soc. Am.* **74**, 2313–2333.

Mykkeltveit, S., F. Ringdal, T. Kværna, and R. W. Alewine (1990). Application of regional arrays in seismic verification research, *Bull. Seism. Soc. Am.* **80**, Part B, 1777–1800.

Nash, J. C. (1979). *Compact Numerical Methods for Computers: Linear Algebra and Function Minimization*, John Wiley & Sons, New York, 141–152.

Nelder, J. A. and R. Mead (1965). A simplex method for function minimization, *Computer. J.* **7**, 308.

Pao, Y.-H. (1989). *Adaptive Pattern Recognition and Neural Networks*, Addison-Wesley Publishing Co., Inc., Reading, Massachusetts, 85–93.

Parkinson, J. M. and D. Hutchison (1972). An investigation into the efficiency of variants of the simplex method, in *Numerical Methods for Non-linear Optimization*, F. A. Lootsma, Editor, Academic Press, New York, 115–137.

Press, W. H., B. P. Flannery, S. A. Teukolsky, and W. T. Vetterling (1986). *Numerical Recipes of the Art of Scientific Computing*, Cambridge University Press, Cambridge, Massachusetts, 289–293.

Quinlan, J. R. (1983). Learning efficient classification procedures and their application to chess end games, in *Machine Learning: An Artificial Intelligence Approach*, R. S. Michalski, J. G. Carbonell, and T. M. Mitchell, Editors, Tioga Publishing Co., Palo Alto, California, 463–482.

Ringdal, F. and E. S. Husebye (1982). Application of arrays in the detection, location and identification of seismic events, *Bull. Seism. Soc. Am.* **72**, S201–S224.

Schnabel, B. K. (1962). An investigation into the effects of random error on a selection of current minimization methods, *M. S. Dissertation*, University of Leeds, Leeds, England.

BBN STC
10 MOULTON STREET
MAIL STOP 14/1B
CAMBRIDGE, MASSACHUSETTS 02238

Manuscript received 28 February 1990

Bulletin of the Seismological Society of America, Vol. 80, No. 6, pp. 1910–1933, December 1990

REGIONAL SEISMIC EVENT CLASSIFICATION AT THE NORESS ARRAY: SEISMOLOGICAL MEASUREMENTS AND THE USE OF TRAINED NEURAL NETWORKS

BY PAUL S. DYSART AND JAY J. PULLI

ABSTRACT

The results are presented from a two-part study of regional earthquakes and chemical explosions recorded by the NORESS seismic array. The first part of the study examines various signal parameters extracted from *Pn*, *Sn*, and *Lg* phases with regard to discrimination capability. These parameters include familiar spectral discriminants and other spectral measures that quantify high-frequency content, spectral complexity, and shear wave generation. Part two of the study focuses on an application of backpropagation learning to the problem of automatic event classification through the use of trained neural networks. Of the 95 events examined, 66 were selected for the classification study based on high signal-to-noise ratio and positive identification in local seismicity bulletins. Events are located in eastern Europe, southern and western Norway, Sweden, the western Soviet Union, and the Norwegian and Greenland Seas. Local magnitudes range from 1.4 to 4.7, and epicentral distances for most events are less than 1000 km.

Results from the discrimination analysis indicate that the wide-band spectral ratios *Pn/Sn* and *Pn/Lg* provide good discrimination capability between earthquakes and mining explosions, although there are anomalous events in both populations and a region of overlapping event types. Mining explosions can frequently be identified by their spectral complexity as measured by the cepstra of *Pn*, *Sn*, and *Lg*. This complexity is assumed to occur due to a combination of ripple-firing of the charges and reverberations within the shallow source region.

In part two of the study, an artificial neural network employing the backpropagation learning paradigm was trained with input vectors formed by the two spectral amplitude ratios and the mean cepstral variance. A length-2 output vector was binary coded to identify each input vector as an explosion or earthquake. Two hidden layers were used, consisting of 8 and 2 units, respectively. The network was trained first using input vectors from the entire data set. This resulted in 100 per cent correct classification when the events were processed with the trained network. This is compared to the optimum planar decision surface which resulted in 5 errors and 19 uncertain classifications. In a control experiment, the network was trained with half of the events and tested with the remaining half. This resulted in 5 errors and 2 uncertain classifications. This compares with 3 errors in training, 2 errors in testing, and a total of 19 uncertain events obtained by the optimal linear classifier. One apparent advantage of the neural network over the linear classifier is the network's ability to determine complex patterns in the data, thus reducing the number of uncertain events.

INTRODUCTION

The success of a Comprehensive or Low-Yield Test Ban Treaty, which includes the provision for seismic monitoring stations within the Soviet Union, will depend on the ability to distinguish low-yield or decoupled nuclear explosions from both chemical mining explosions and small shallow earthquakes at regional distances. The regional discrimination problem has been approached in a variety of ways by several researchers in the past with success limited many times to the particular

region of study. Presently, no single discriminant exists that works in all areas (see Pomeroy *et al.*, 1982 for a review of regional discriminants). For example, there are chemical explosions in Scandinavia and the western Soviet Union that generate seismic waves of higher frequency than earthquakes of similar magnitude. This is opposite to what has been observed in California by Aviles and Lee (1986). Similarly, Bennett and Murphy (1986) found that the spectra of nuclear explosions recorded from the Nevada Test Site appear to generate less high-frequency energy than earthquakes at about the same distance.

The goal of this project was to examine the signal characteristics of chemical explosions and earthquakes recorded by the NORESS array in order to develop a methodology for conducting seismic event discrimination in this region on an automated or semi-automated basis. The strategy that guided the study is based on a three-step approach to the problem. The first step was to select a database of regional events identified by local seismologists in Scandinavia as earthquakes or chemical explosions based on coincident location with known quarries and repeatable signal characteristics. The second step was to extract a large number of signal parameters in order to quantify any clearly visible differences between the explosions and the earthquakes. This second step is highly iterative, i.e., a process is applied to the data set and subsequent visual interpretation by the analyst is necessary to identify characteristic features of the signal. The third and final step was to distill the knowledge gained in the multi-dimensional analysis to a level manageable by an on-line event processor. Ideally, this processor would automate the classification procedure and provide a means of incorporating new information from future events.

The results indicate that wide-band *Pn/Sn* and *Pn/Lg* ratios provide some discrimination capability between earthquakes and explosions recorded in this region, although there are a number of outliers, and a significant overlap between the two populations. Mine blasts were most often identified by their spectral complexity as measured by the variance in the cepstrum of *Pn* and *Sn*. To automate the classification procedure using the best diagnostic information available, an artificial neural network structure and learning paradigm were chosen that satisfied most closely the on-line system requirements previously described. A two (hidden) layer backpropagation network using the Generalized Delta Rule and a sigmoid nonlinearity (Rumelhart and McClelland, 1986) was designed and trained to identify event type on the basis of the cepstral variance and the two amplitude ratios. The two-layer network was successfully trained to identify 100 per cent of the events in the training set. The same network, trained to identify half the events from the original training set, was able to classify 85 per cent of the remaining events correctly. Finally, to provide a comparison with the network's performance, the same experiment was performed with an optimum linear discriminant.

These results and the general behavior of trained neural networks can be interpreted in terms of the geometry of the decision regions formed by the network, the generalized inverse operator (Aki and Richards, 1980), and to some extent the connection strengths or weights (Gorman and Sejnowski, 1988). When simple network architectures are used in conjunction with raw data input (e.g., spectral amplitudes, autocovariance values), the network weights can indicate combinatorial aspects of the input data suggesting potentially useful parameterizations. As in the general linear inverse problem (Menke, 1984), the Generalized Delta Rule employs an iterative parameter update scheme that can be used to derive data and model resolution measures. In this study, the results are interpreted largely in terms of

the complexity of decision regions, although other interpretative methods are regarded as important areas for future investigation.

The Data Set and Data Reduction

The data set includes 95 events recorded by the 25-element NORESS array in southern Norway. Figure 1 shows an epicenter map of the 66 events chosen for complete analysis in this report. The spectra of the remaining events were also analyzed, although they were not included in the supervised learning experiment that must rely on confident event identifications and high signal-to-noise ratios. Events with local magnitudes of about 1.5 or greater were selected from the 2-yr period of 1985 to 1987. Selection of the events was made by examining the local network bulletins of the Bergen Seismological Observatory and the University of Helsinki Institute of Seismology. Additional events were selected from the U.S. Geological Survey's Preliminary Determination of Epicenters (PDE). A listing of all 95 events is found in Table 1. The locations listed in Table 1 were taken either from the local bulletins or from the PDE listing.

Chemical explosions were recorded from mines in Sweden, Norway, and the western Soviet Union. In several cases, a number of events were recorded from the same mine (e.g., the Titania mine TI in southern Norway, and mines in the western Soviet Union referred to as E7 and E8 by the Helsinki Institute of Seismology). Earthquakes were located in the Shetland Islands, the western coast of Norway, and several isolated events in the Norwegian Sea, Greenland Sea, and Eastern Europe. Events 10 to 16 and event 74 have been tentatively identified as underwater explosions off the southwest coast of Norway. Events 10 to 16 occurred in a seismically inactive region within a single 2-hr period.

For each event, time windows surrounding *Pn*, *Sn*, and *Lg* waves, and the noise, were chosen interactively on a Sun workstation. The onset time and length of the window were picked from seismograms filtered in two octave bands (3 to 6 and 6 to 12 Hz) on the basis of the visible duration of the phase. These two bands were

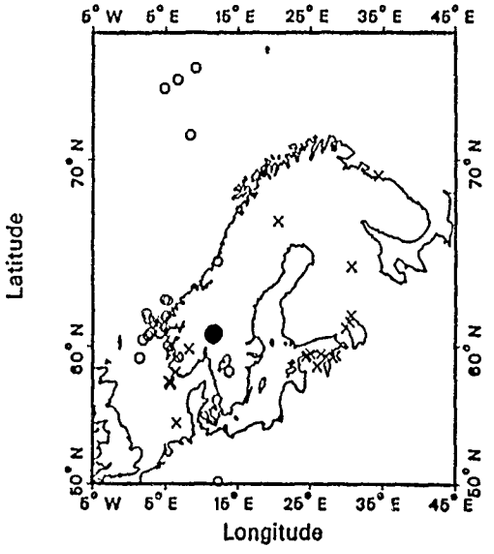

FIG. 1. Epicenter map of the events used in this study. The circle indicates the site of the NORESS array. O = earthquake; X = explosion.

TABLE 1

EVENTS USED IN THIS STUDY

No.	Yr/DoY	Time	Latitude (°)	Longitude (°)	Distance (°)	Azimuth (°)	m_b	Type*
1	85/106	12:46:45	39.79	20.56	21.70	348.00	—	E
2	85/213	11:17:35	45.82	26.65	17.35	142.46	4.7	E
3	85/298	12:03:47	59.30	28.10	8.38	92.62	2.3	X-E7
4	85/300	04:36:43	61.12	4.92	3.24	279.62	2.8	E
5	85/312	14:18:54	58.34	6.43	3.53	229.41	2.4	X-TI
6	85/313	14:42:46	57.80	7.20	3.68	218.91	2.1	?
7	85/313	18:20:48	62.00	7.70	2.23	306.08	2.0	?
8	85/317	16:32:10	58.30	6.40	3.57	229.13	1.8	X-TI
9	85/317	12:07:48	59.30	28.10	8.38	92.62	2.3	X-E7
10	85/324	22:10:44	57.61	5.67	4.34	226.41	2.3	u
11	85/324	22:24 38	57.66	5.72	4.28	226.58	2.2	u
12	85/324	22:57:10	57.64	5.62	4.33	226.94	2.3	u
13	85/324	23:10:47	57.66	5.35	4.42	228.51	2.3	u
14	85/324	23:17:28	57.69	5.49	4.34	228.06	2.3	u
15	85/324	23:23:10	57.50	5.62	4.44	225.73	2.2	u
16	85/324	23:28:23	57.58	5.49	4.42	227.09	2.2	u
17	85/325	14:18:13	59.80	8.20	1.90	241.88	1.4	X
18	85/325	14:48:07	54.80	6.50	6.52	206.51	2.8	X
19	85/325	09:16:30	58.37	12.36	2.41	169.70	—	?
20	85/327	13:06:18	59.50	25.00	6.81	94.59	2.1	X-E3
21	85/331	04:53:32	59.73	5.71	3.06	253.31	2.8	E
22	85/344	12:05:39	59.40	28.50	8.54	91.57	2.2	X-E8
23	85/357	02:35:08	60.38	1.90	4.75	269.87	2.3	E
24	85/358	12:37:57	59.80	22.50	5.51	95.02	1.9	?
25	85/359	13:19:01	58.70	26.00	7.55	99.30	2.6	X
26	85/361	12:16:08	59.40	28.50	8.54	91.57	2.4	X-E8
27	85/365	06:57:17	73.31	6.62	12.71	353.57	4.8	E
28	86/003	14:58:41	61.90	30.60	9.19	74.46	2.5	X-V7
29	86/007	14:14:28	58.34	6.43	3.53	229.41	2.2	X-TI
30	86/009	09:18:43	54.70	19.50	7.37	141.43	2.7	?
31	86/017	14:11:01	58.34	6.43	3.53	229.41	2.3	X-TI
32	86/019	04:59:22	65.00	12.13	4.27	3.35	3.0	E
33	86/020	23:38:28	50.19	12.37	10.56	177.10	4.9	E
34	86/021	08:55:40	55.30	13.60	5.55	167.78	2.5	?
35	86/031	12:10:15	59.30	28.10	8.38	92.62	3.2	X-E7
36	86/035	12:14:59	59.50	26.50	7.54	92.90	2.8	X-E9
37	86/035	12:58:59	59.40	24.60	6.64	95.91	2.5	X-E2
38	86/035	14:22:57	59.30	24.40	6.57	97.00	2.6	X-E1
39	86/036	17:53:16	62.81	4.86	3.77	306.15	4.7	E
40	86/037	16:29:55	67.10	20.60	7.49	28.05	2.7	X-R1
41	86/037	12:22:04	59.30	28.10	8.38	92.62	2.7	X-E7
42	86/038	11:00:01	64.70	30.70	9.58	57.40	3.1	X-V1
43	86/041	12:41:46	59.40	28.50	8.54	91.57	2.5	X-E8
44	86/045	14:13:19	58.34	6.43	3.53	229.41	2.4	X-TI
45	86/045	17:54:04	58.34	6.43	3.53	229.41	2.3	X-TI
46	86/045	12:10:21	59.40	28.50	8.54	91.57	2.7	X-E8
47	86/045	16:44:08	67.10	20.60	7.49	28.05	2.6	X-R1
48	86/049	10:46:16	59.30	27.20	7.94	93.57	2.6	X-E4
49	86/049	12:45:50	64.70	30.70	9.58	57.40	2.6	X-V1
50	86/057	02:11:44	62.76	5.29	3.58	307.05	2.5	E
51	86/062	07:26:06	43.70	31.40	20.76	136.13	4.4	E
52	86/064	14:16:31	66.30	21.70	7.15	34.70	—	?
53	86/064	12:13:19	59.50	26.50	7.54	92.90	2.6	X-E9
54	86/064	13:02:05	60.63	2.58	4.38	272.47	2.1	E
55	86/067	16:21:17	61.67	2.58	4.41	286.06	2.4	E

TABLE 1—*Continued*

No.	Yr/DoY	Time	Latitude (°)	Longitude (°)	Distance (°)	Azimuth (°)	m_b	Type*
56	86/069	12:02:09	59.30	28.10	8.38	92.62	2.6	X-E7
57	86/069	04:20:04	62.81	4.91	3.75	306.32	2.5	E
58	86/070	12:02:28	59.30	28.10	8.38	92.62	2.6	X-E7
59	86/071	11:07:21	59.50	26.50	7.54	92.90	2.5	X-E9
60	86/071	12:01:38	59.40	28.50	8.54	91.57	2.5	X-E8
61	86/078	12:06:40	59.40	28.50	8.54	91.57	2.6	X-E8
62	86/089	03:22:37	61.66	4.53	3.50	288.29	2.2	E
63	86/091	09:56:53	56.42	12.10	4.33	175.89	3.6	E
64	86/094	22:42:30	71.08	8.35	10.42	354.27	4.6	E
65	86/097	00:34:37	61.84	4.88	3.38	291.88	2.3	E
66	86/108	00:44:13	59.22	1.42	5.28	257.72	2.4	E
67	86/154	14:30:04	61.46	4.08	3.67	284.54	2.8	E
68	86/155	09:06:31	61.50	30.40	9.11	77.00	3.3	X-V3
69	86/163	09:30:55	61.50	30.40	9.11	77.00	3.1	X-V3
70	86/166	15:01:07	61.67	3.85	3.82	287.44	3.0	E
71	86/168	12:12:07	59.40	28.50	8.54	91.57	2.6	X-E8
72	86/169	11:05:08	59.40	28.50	8.54	91.57	2.5	X-E8
73	86/170	03:55:08	59.31	6.54	2.88	242.39	2.4	X-BLA
74	86/171	22:07:53	61.47	3.92	3.75	284.53	2.0	u
75	86/177	04:06:21	61.88	5.10	3.29	293.05	2.4	E
76	86/178	03:49:46	59.28	6.76	2.80	240.66	2.5	E
77	86/185	11:13:27	59.30	28.10	8.38	92.62	2.6	X-E7
78	86/189	16:15:04	37.80	20.87	23.70	348.60	—	E
79	96/195	13:50:32	58.35	13.82	2.65	153.21	4.0	E
80	86/195	14:30:27	61.10	29.90	8.90	79.67	2.9	X-V8
81	86/195	15:02:19	69.30	34.40	12.76	38.43	2.9	X-K9
82	86/222	05:01:04	59.99	5.34	3.15	258.96	1.7	E
83	86/228	04:24:36	62.82	4.98	3.73	306.70	2.5	E
84	86/244	22:11:26	60.82	2.93	4.20	274.85	3.5	E
85	86/273	20:02:47	60.79	4.23	3.57	273.99	2.4	E
86	86/283	19:56:31	61.97	2.33	4.58	289.58	2.3	E
87	86/299	11:45:06	61.46	3.29	4.05	283.83	2.6	E
88	86/299	11:57:03	61.72	3.27	4.10	287.43	2.6	E
89	86/327	03:30:32	73.74	9.08	13.03	356.94	4.7	E
90	86/342	14:44:27	43.29	25.99	19.50	348.00	—	E
91	86/346	16:33:30	72.96	4.80	12.49	350.85	4.7	E
92	86/351	21:18:32	39.81	19.72	21.60	349.00	—	E
93	86/352	17:16:16	43.28	26.01	19.50	338.50	—	E
94	87/067	17:42:21	39.48	20.52	22.00	348.20	—	E
95	87/109	03:55:06	43.69	20.44	17.90	345.70	—	E

* E = earthquake; X-E7 = explosion from the E7 mine; ? = unknown source type; u = presumed underwater explosion.

observed to give the clearest separation of all three phases. The use of variable length windows minimizes contamination of the desired phase by subsequent phases, as sometimes occurs when constant phase velocity windows are used. A 30 per cent cosine taper was applied to each window, and the power spectrum for each phase was computed as the mean of all the recording elements, in the manner of a periodogram (Oppenheim and Schafer, 1975). This procedure reduces the spectral variance without the reduction of high-frequency amplitudes that occur during beamforming. All the spectra were smoothed with a 5-point equal weight operator.

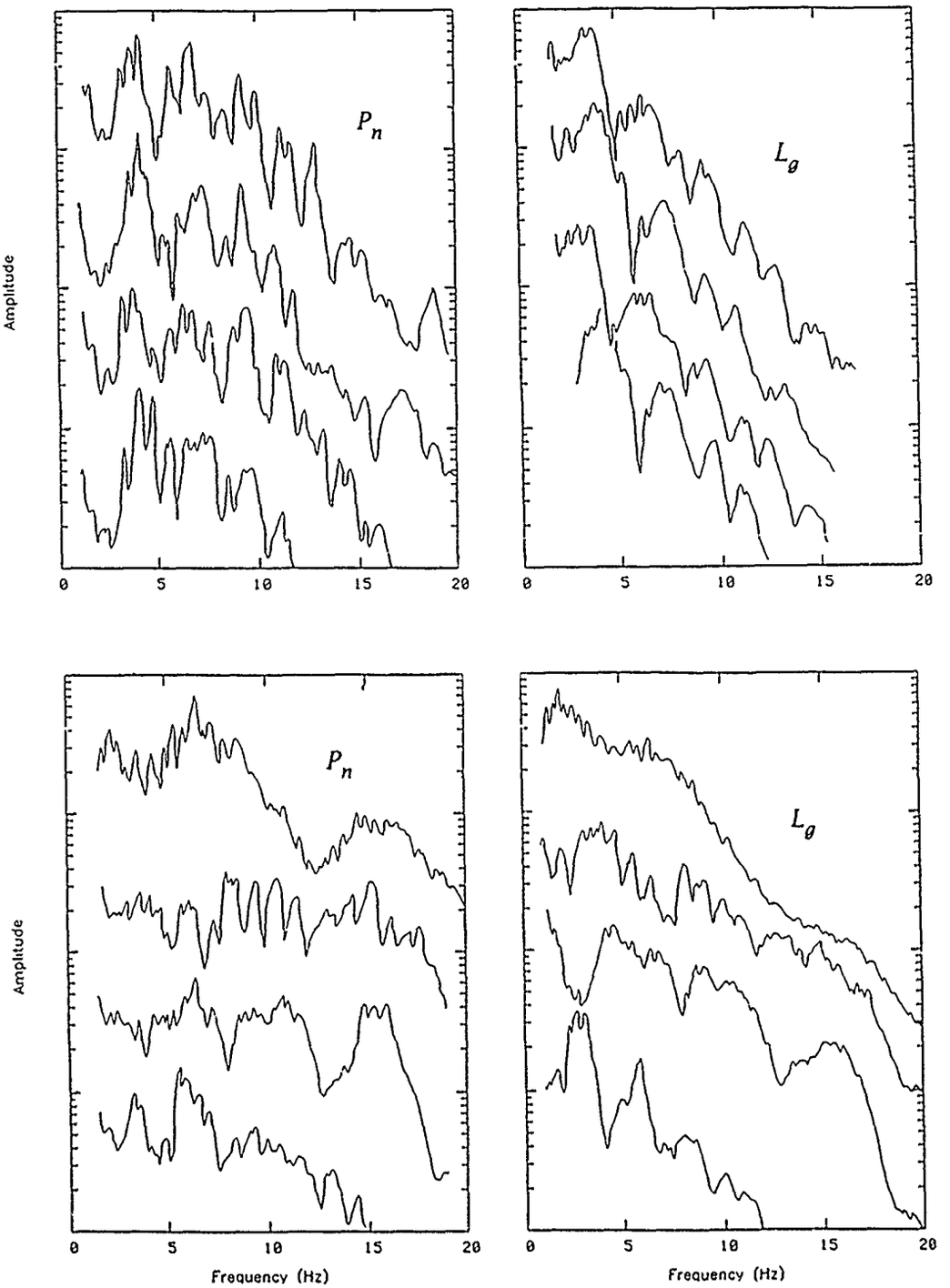

FIG. 2. (*Top*) Uncorrected *Pn* and *Lg* spectra for four presumed underwater explosions off the southern coast of Norway. Note the similarity in spectral shape for the four events. (*Bottom*) *Pn* and *Lg* spectra for four explosions at the Titania Mine in southern Norway. Note the large differences in spectral shape for these events. Since these events are from the same mine, the differences in the observed spectra are likely due to varying explosive source configurations.

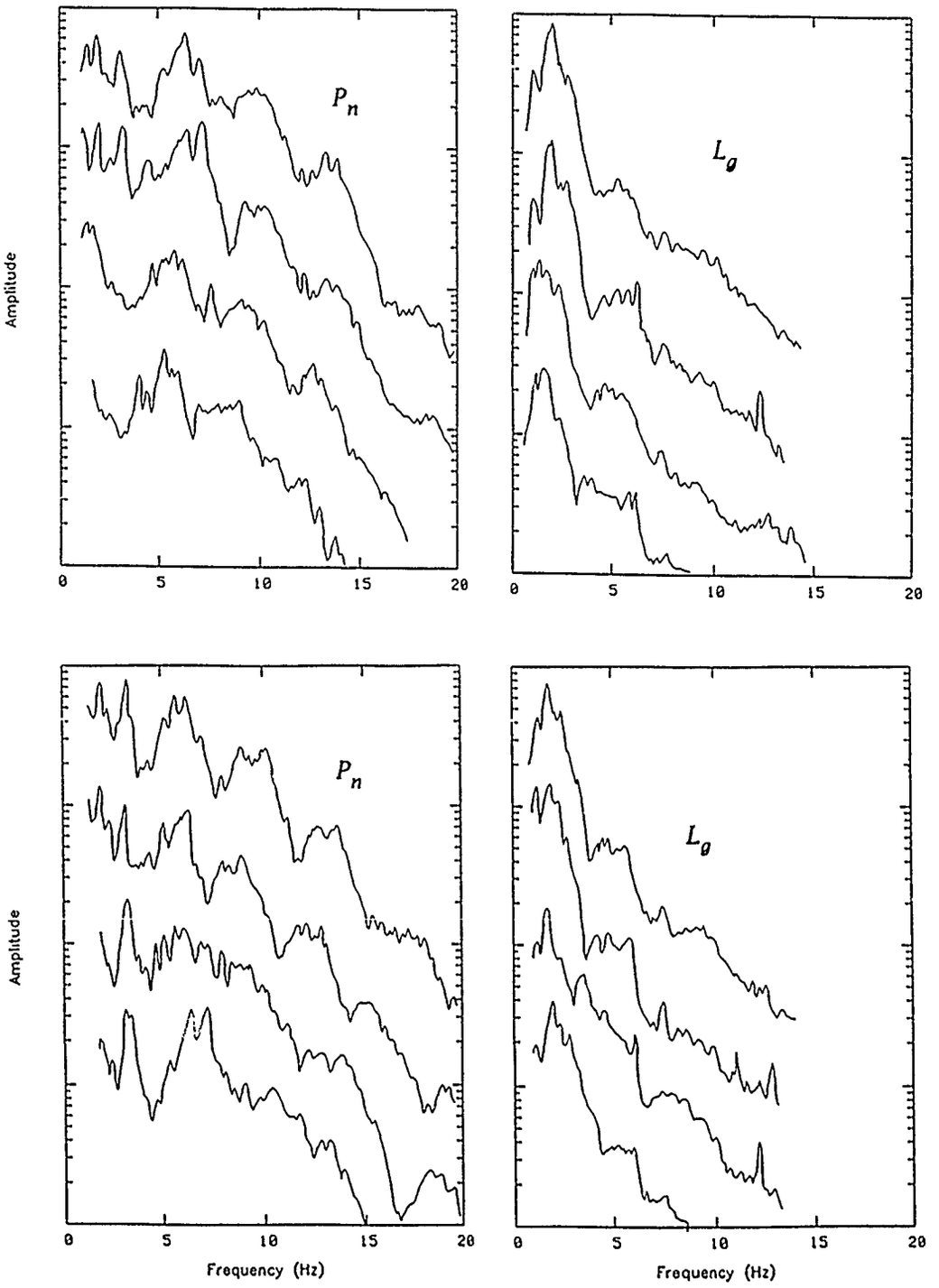

FIG. 3. Uncorrected *Pn* and *Lg* spectra for four explosions at mine E7 (*top*) and E8 (*bottom*). Both mines are southwest of Leningrad.

Characteristics of Regional Propagation

In a regional study of seismic events, it is important to identify areas of frequent shallow seismicity, such as mines and oceanic fault zones. The analysis of identified events grouped by region can often reveal waveform and spectral characteristics imposed by the uniqueness of the source and path, which are useful in identifying new events. During the course of this study spectral characteristics were examined for events grouped by both region and source type. There were five groups of events for which all three phases, and four or more events, were recorded from the same region. These groups contain repeated events identified as blasts from two mines in the western Soviet Union (E7 and E8), a molybdenum mine in southern Norway (Titania), earthquakes to the northwest of the array, and a sequence of presumed underwater explosions off the southwestern coast of Norway.

Spectral Characteristics

The variation in spectral character among repeated events from the five groups provides an important insight into wave propagation in this region. For example, the small group of events tentatively identified as underwater explosions are nearly identical for both *Pn* and *Lg* waves; however, blasts recorded from the Titania mine at approximately the same distance and azimuth (the mine is located on the coast) show notable differences in their spectra (Fig. 2). Explosions from the E7 and E8 mines are only 30 km apart, but show discernible variations in the pattern of spectral scalloping from the different mines, and among repeated events from the same mine (Fig. 3). In contrast, the spectra of earthquakes to the northwest of NORESS span a much greater distance range but are very similar (Fig. 4). The earthquakes appear to be simple sources that vary primarily in size (moment) and

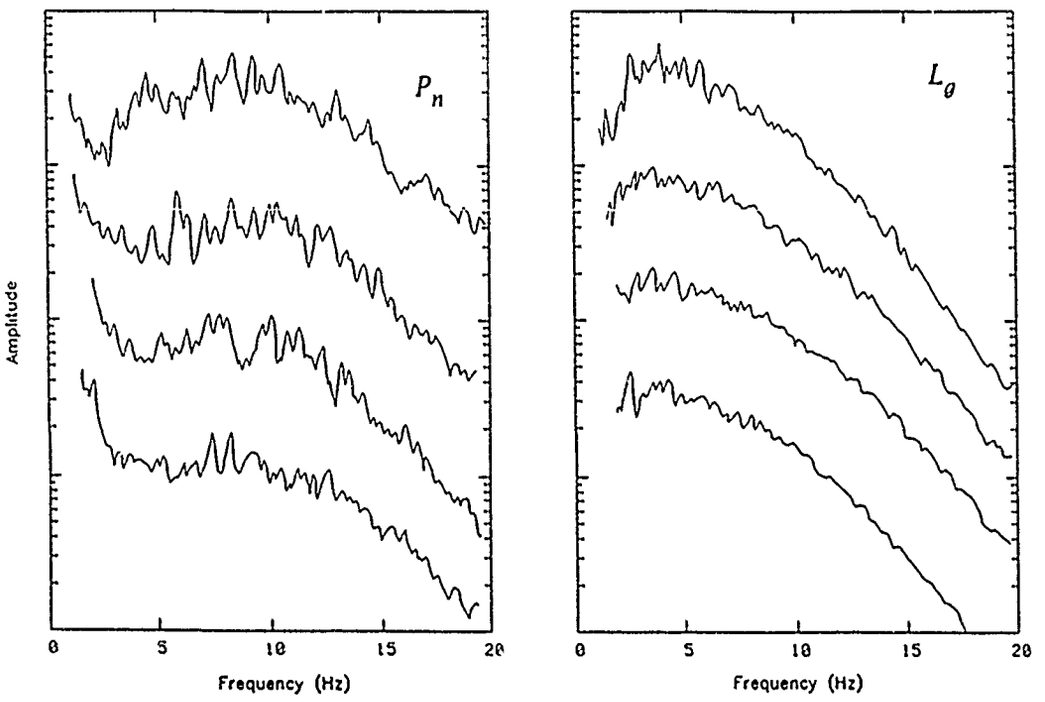

FIG. 4. Uncorrected *Pn* and *Lg* spectra from four earthquakes off the west coast of Norway. Note the simplicity and similarity of the spectra for these four events, even though they are not located in the same source area.

source duration (corner frequency). This implies that the spectra of mine explosions exhibit real-source differences, most probably due to the differences in the spatial configuration and timing of the charges (Greenhalgh, 1980). This is an important observation, especially in the case where an attempt is made to discriminate between earthquakes and explosions recorded from these two source regions.

One of the most important observations from the spectral analysis is the relative simplicity of earthquake spectra versus the complexity of mine blast spectra. To illustrate this, two events are chosen that are close to one another to ensure that path effects will be nearly the same. The contrast is illustrated in Figure 5, where *Pn*, *Sn* and *Lg* spectra of a chemical explosion at the BLA Mine north of the Titania mine in southern Norway (event 73) and a nearby earthquake (event 82) are compared. Note that the earthquake spectrum is relatively simple and varies smoothly across the entire band. The spectrum of the BLA explosion is more complex in appearance and exhibits spectral nulls near 5 and 10 Hz.

Spectral characteristics that appear to be strongly path-related are the peak frequency and the high-frequency content. Peak frequencies of *Pn*, *Sn*, and *Lg* were picked as the maximum amplitude from the smoothed spectra in a frequency band with a SNR > 4. This constraint was relaxed for spectra with a total bandwidth of less than 5 Hz. Figure 6a is a plot of peak frequency versus distance for all events that show a decrease in peak frequency with distance.

The third moment of frequency (Weichert, 1971) was computed to obtain a measure of the relative high-frequency content of the signal. The plot of TMF (Fig. 6b) versus distance also illustrates the attenuation of high frequencies at greater distances. Neither TMF nor the peak frequency showed a similar relationship to magnitude, suggesting that distance is dominant in the attenuation of

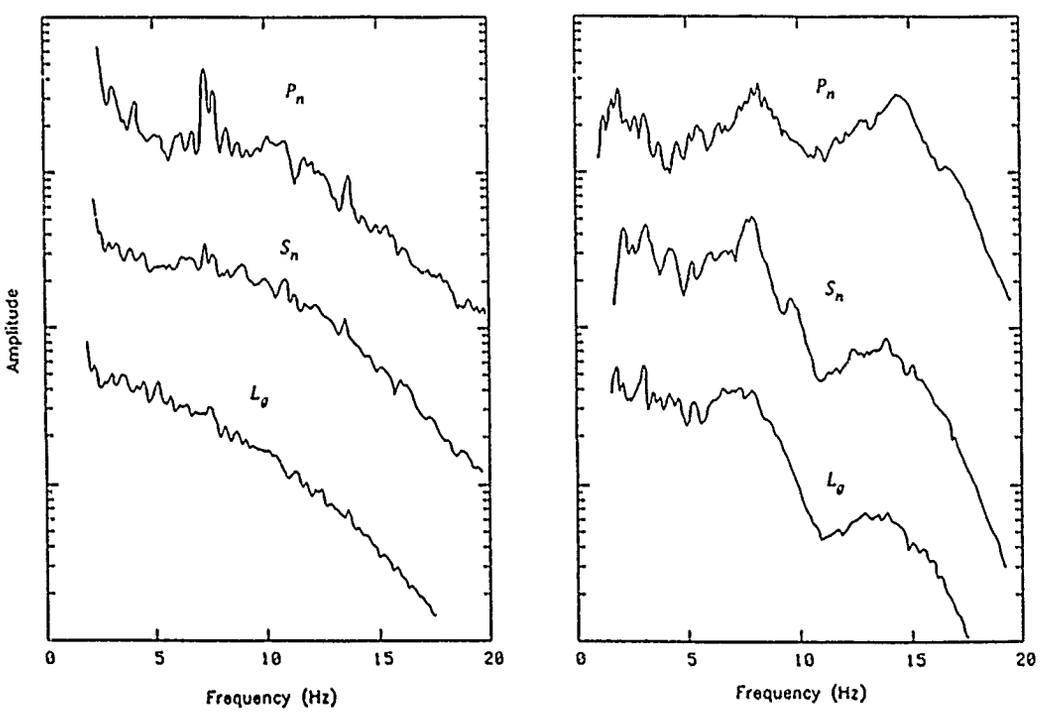

FIG. 5. A comparison of typical *Pn*, *Sn*, and *Lg* spectra (uncorrected) from an earthquake (*left*) and a nearby explosion (*right*). The earthquake occurred off the southwest coast of Norway, and the explosion was at the BLA mine.

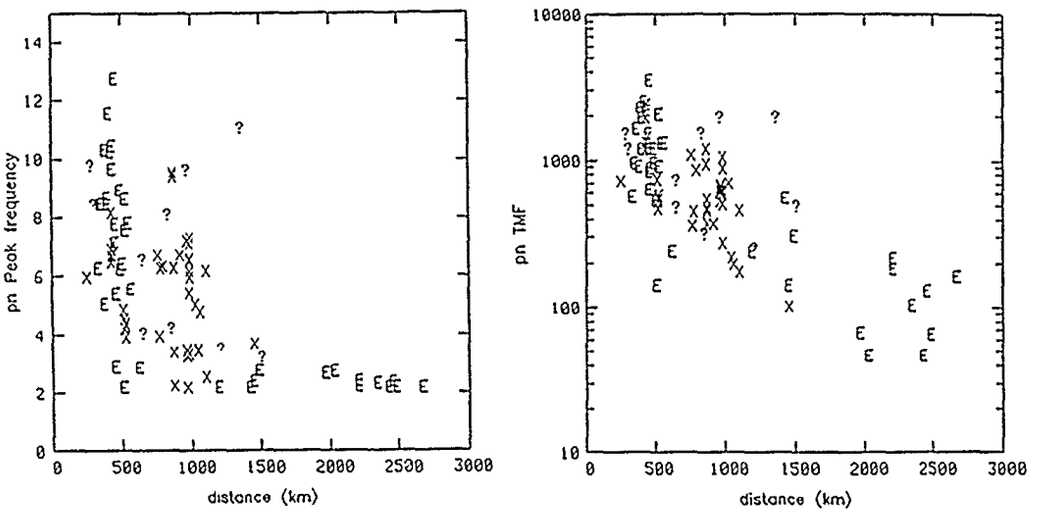

(a) (b)

FIG. 6. Peak frequency (a) and TMF (b) of *Pn* waves versus distance for the entire data set. E = earthquakes; X = explosions; ? = unidentified events.

high-frequency energy. However, the TMF for the Titania mine blasts and nearby earthquakes shows that high frequencies are propagated from both sources. It is clear that a discriminant based simply on the high-frequency enrichment of explosions relative to earthquakes would likely fail.

SOURCE DISCRIMINATION

As shown in the previous section, discrimination between earthquakes and explosion sources based on their relative high-frequency content would fail due to path effects over greater distances, if indeed such source differences existed. Baumgardt and Ziegler (1988) caution that the enrichment of high frequencies sometimes seen in the spectra of mine blasts may be the result of ripple-firing and may not represent any intrinsic difference in source type. Correction for path effects based on single-array Q estimates was not encouraged by the results of an attenuation study of these events (Dysart and Pulli, 1987), since the simple Q model and source representation were generally inadequate to fit all the data, especially the complex explosion spectra. However, differences in the spectra of co-located events suggested that path effects were not so severe as to completely obscure all characteristics of the source that might aid in discriminating between the two source types.

Amplitude Ratios

Since source theory predicts the generation of more shear energy from earthquake sources compared to explosions, the spectral ratios *Pn/Sn* and *Pn/Lg* were among the spectral parameters extracted from all the events. Figures 7 and 8 show *Pn/Sn* and *Pn/Lg* amplitude ratios. In Figure 7, the amplitude ratios *Pn/Sn* and *Pn/Lg* are plotted for different frequency bands. Figure 8a shows the ratio of peak amplitudes above the SNR cutoff of 4. These plots show where in the spectra of explosions and earthquakes there is information that separates the two populations. The explosion amplitude ratios are similar to the earthquake ratios at low frequencies even above the noise peak at about 1 Hz, but appear to migrate to higher values at higher frequencies. The reason for this is unknown, but an analysis of additional

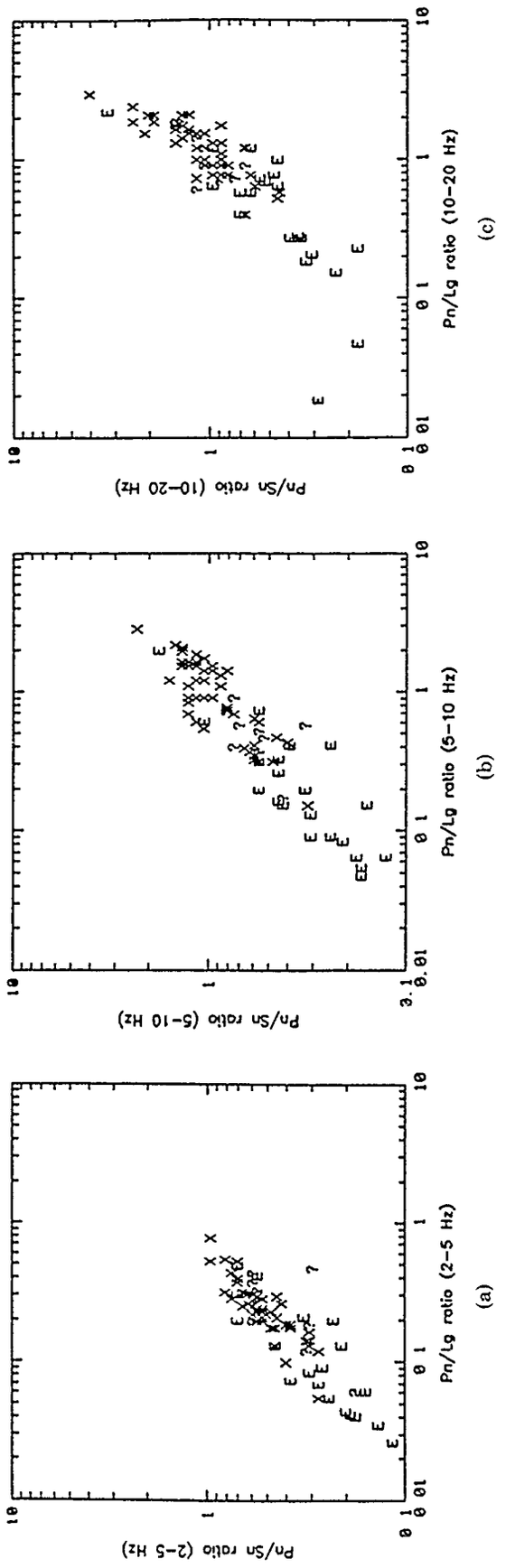

FIG. 7. *Pn/Sn* versus *Pn/Lg* amplitude ratios formed in three frequency bands.

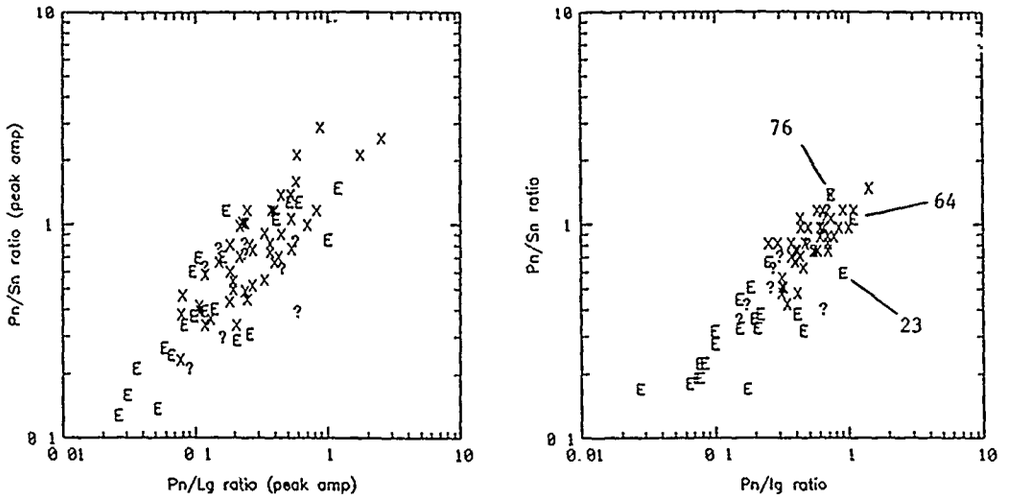

FIG. 8. *Pn/Sn* versus *Pn/Lg* amplitude ratios formed from peak amplitudes in the signal band (a) compared with the same amplitude ratios formed in optimum signal band (b). Outliers indicated by event number are discussed individually in the text.

events in multiple frequency bands may reveal a similar trend that could act as a useful discriminant.

The spectral ratios shown in Figure 8b were formed by averaging spectral amplitudes over the optimum signal band (SNR > 4). A distinct improvement is seen immediately when these results are compared to ratios of peak spectral amplitudes or ratios formed in selected frequency bands. These ratios provide fairly good separation between the two source types, although there remain many events for which this discriminant would yield ambiguous results. The outliers indicated in Figure 8b will be discussed in detail in a later section.

Spectral Complexity

Figures 2 and 3 illustrated the spectral complexity seen in nearly all the explosion spectra. The spectral complexity of explosion spectra in this data set could occur for a number of reasons. For instance, chemical explosions detonated during mining activities are often composed of multiple shots such as in the practice of ripple-firing. Baumgardt and Ziegler (1988) provide a detailed analysis of many of the explosions in this data set. In the case of single shots, multiples due to shallow structure or topography in the source medium could account for a pattern of spectral interference. Similar phenomena have been observed for sources in other areas (e.g., Anderson, 1987) and for recording sites in areas of rugged topography (Bard and Tucker, 1985). The complexity seen in the spectra of underwater explosions is commonly attributed to the bubble pulse and reverberations within the water column. These effects are nearly always seen in marine seismic data.

Several measures of spectral complexity were considered in this study. A simple measure was the actual length of the spectrum defined as the sum of the amplitude differences between successive frequency points. The problem with this measure is that it arbitrarily reflects any spectral complexity whether it be due to harmonic

interference or simply the spectral variance. Another measure of spectral complexity was the variance of an N-point moving average. This method was unsatisfactory since it is highly dependent on window length and falloff rate of the spectrum. A third method was to compute the least-squares error (LSE) from the regression analysis in the attenuation study. Since most explosion spectra were not well fit by the simple source model, the LSE did not accurately reflect the complexity of many events. The measure that worked most effectively in quantifying the complexity seen in mine blast spectra was the cepstral variance. This method not only enhances the presence of harmonic interference patterns in the spectra, but is also consistent with physical interpretations of the source.

Cepstral Variance

As the most effective measure of spectral complexity found, the cepstrum of each phase was computed for all events. Cepstral analyses of seismic data have been used in the past to identify depth phases (Kemerait and Sutton, 1982) and mine blasts (Baumgardt and Ziegler, 1988), and to retrieve source functions from teleseismic recordings (Clayton and Wiggins, 1976). These studies include theoretical background discussions and references that are not repeated here.

Several preprocessing steps were necessary before the variance of the cepstrum was obtained. A zero-phase deconvolution of the pre-*Pn* noise was made by subtracting the log-amplitude of the noise before inverse transformation. In addition, the trend and the mean were removed from the deconvolved log-spectra to reduce the differential effects of attenuation and high-frequency falloff. Tribolet (1979) provides a comprehensive text on homomorphic signal processing, and methods for precluding cepstral artifacts commonly discussed in other studies (e.g., Stoffa *et al.*, 1974; Bennett *et al.*, 1989). To quantify the cepstral complexity, the variance of the cepstra was computed for all phases and all events in the quefrency range of 0.1 to 0.5 sec. This range in delay times was chosen to include all frequencies in the available signal band of the spectra. The shortest delay time corresponds to destructive interference at a frequency of ½ Nyquist, and the longest delay at a frequency of 1 Hz, just above the microseismic noise seen in most of the events.

Figure 9 shows deconvolved cepstra of *Pn*, *Sn*, and *Lg* for four of the explosion sources. Figure 9b is a case where the cepstra suggests a specific delay time at about 150 msec, a typical delay time in a ripple-fire sequence (Baumgardt and Ziegler, 1988). The cepstra of the offshore explosions indicate a clear delay time of about 300 msec (not shown). Reverberations within the water layer are typically seen at longer periods, but this delay time is within the range produced by a bubble pulse from a 1 ton explosion at a depth of about 800 m. This value is within the water column in the vicinity of these explosions according to local bathymetry data, and the size and depth of the charge are consistent with typical transmission loss experiments.

In most cases, a clear delay time is not seen in the cepstrum, but the cepstrum can be used as a reliable measure of spectral complexity even when specific delay times are not indicated. The cepstra of earthquakes from different source areas are shown in Figure 10. The difference in the degree of complexity between the earthquake and explosion source types is illustrated by the appearance of cepstral peaks in the explosion cepstra, and the absence of such peaks in the earthquake

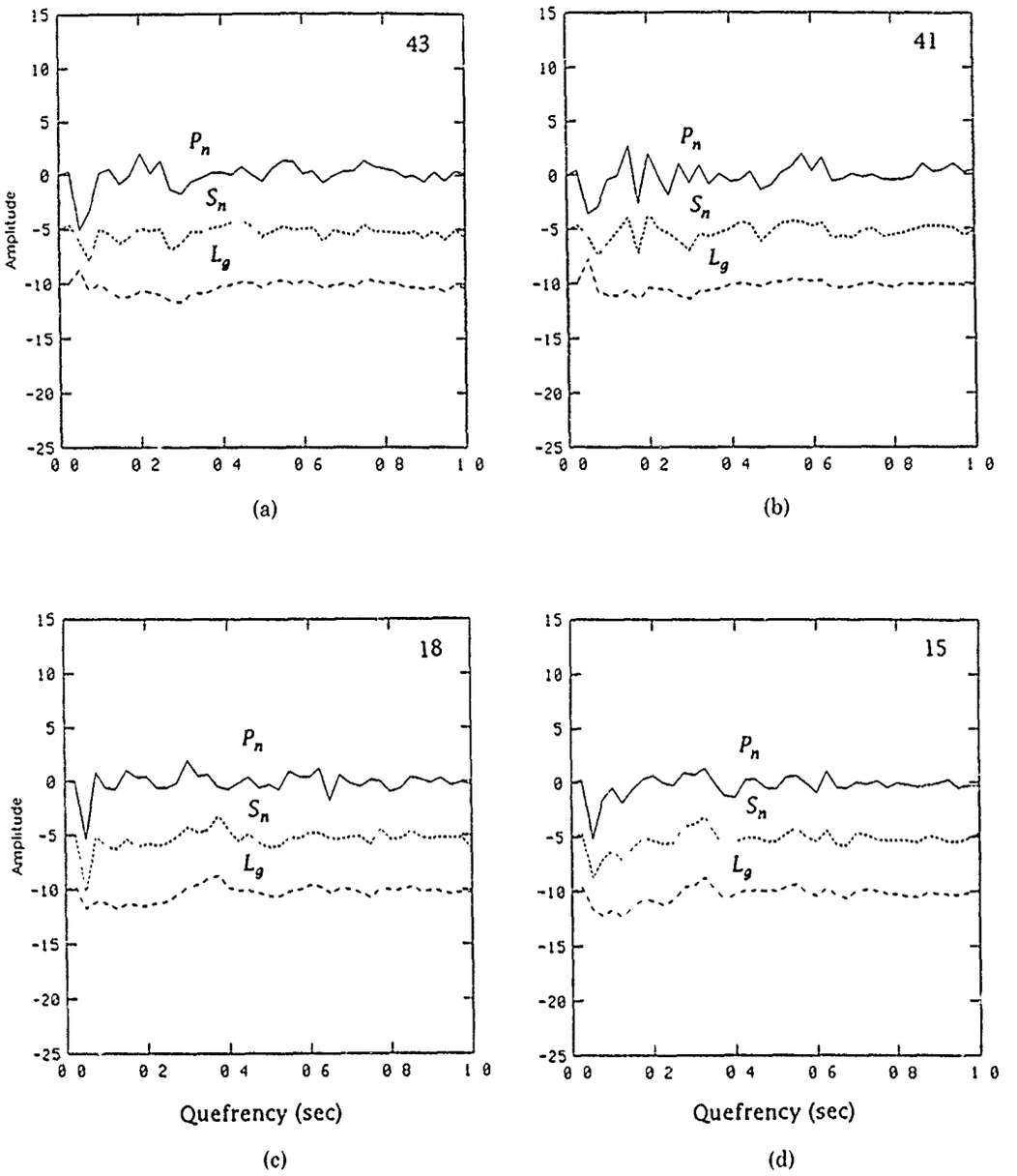

FIG. 9. Deconvolved cepstra of *Pn* (solid lines), *Sn* (dotted lines), and *Lg* (dashed lines) waves for four explosions. The cepstral peaks are indicative of the complexity of the source.

cepstra. The *Pn* spectra of earthquakes shown in Figure 4 are somewhat complex, but they do not exhibit a harmonic interference pattern seen in the explosion spectra, and as a result, peaks do not appear in the cepstra.

Figure 11 shows the mean *Pn*, *Sn* cepstral variance plotted against the *Pn/Sn* and *Pn/Lg* amplitude ratios. The separation between the two populations is fairly good, with several clear exceptions. It is interesting to note that the cepstral variance points to only one of the outliers (event 23) targeted by the spectral amplitude ratios (Fig. 8b). To this extent, the cepstral variance parameter provides an indicator of event type that is independent of the amplitude ratios.

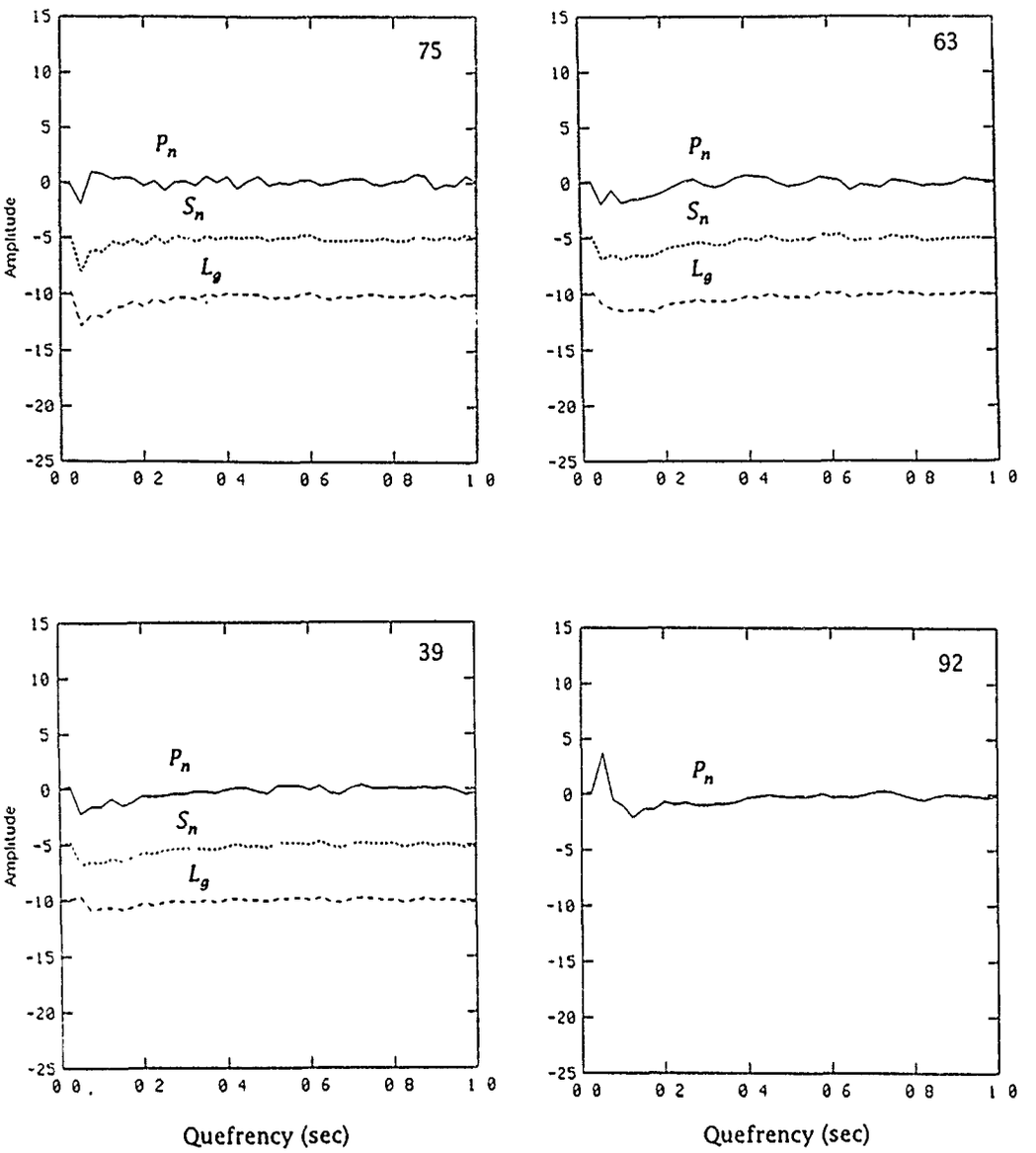

FIG. 10. Deconvolved cepstra of *Pn* (solid lines), *Sn* (dotted lines), and *Lg* (dashed lines) waves for four earthquakes. Note the relative simplicity of the earthquake cepstra when compared with the cepstra of the explosions shown in Figure 9.

Discussion of Outliers

In Figures 8b and 11, five events were identified as examples where the cepstral variance, the *Pn/Sn* and *Pn/Lg* ratios, or both failed as discriminants between earthquakes and explosions. It is worthwhile examining each of these examples individually to see what reasons caused them to fail.

In Figure 12 (a and b), the *Pn*, *Sn*, and *Lg* cepstra are plotted for events 32 and 8. Event 32 is an earthquake recorded in northern Sweden, and event 8 is a chemical explosion from the Titania mine in southern Norway. Both events were identified correctly by their spectral amplitude ratios, but they were misidentified on the basis of mean cepstral variance. The cepstra of event 32 in Figure 12a exhibit

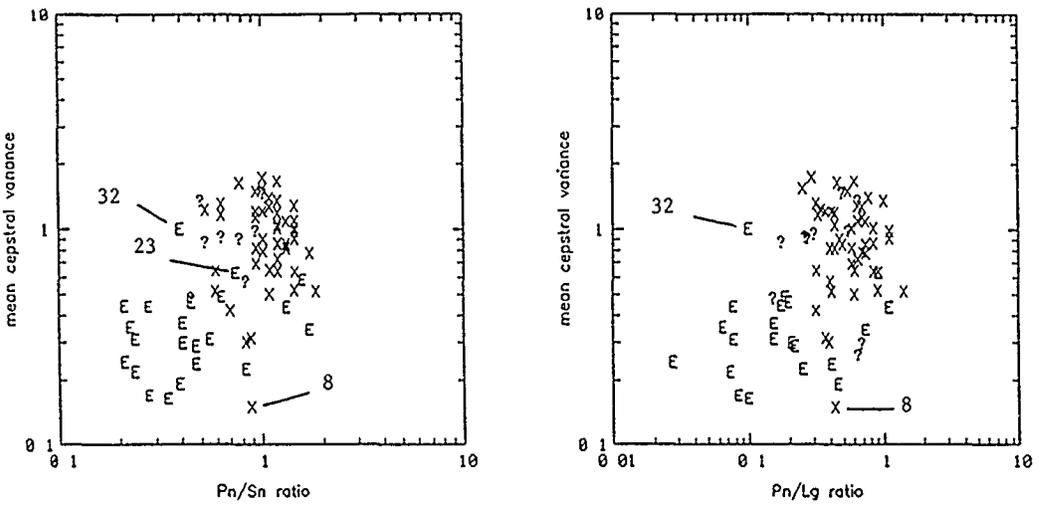

FIG. 11. Mean of the *Pn*, *Sn*, and *Lg* cepstral variance for each event plotted as a function of *Pn/Sn* (*left*) and *Pn/Lg* amplitude ratios (*right*). Although the separation between populations is good, a number of outliers exist, and these are discussed individually in the text.

a number of anomalously low cepstral amplitudes in the low quefrency range. These amplitudes are an artifact of the cepstrum near the lower limit of resolution, which resulted in a high variance. In this case, the variance was not a reliable measure of complexity. However, by visual inspection, the smooth cepstra of event 32 are seen to be very similar to the cepstra of other earthquakes such as those in Figure 10. The cepstra of the mine explosion shown in Figure 12b are cases where the cepstra are only marginally adequate to identify source type. It is the cepstrum of *Lg* alone that suggests that this is an explosion when it is compared with the *Lg* cepstra of other earthquakes shown in Figure 10. Nearly all the earthquake *Lg* cepstra are flat.

In Figure 12 (c and d), the *Sn* spectra are plotted for two earthquakes (events 76 and 64) that were misidentified on the basis of their spectral amplitude ratios. The SNR and the *Pn/Sn* ratio are plotted in these two figures as functions of frequency. The SNR curve shows that these two events are well recorded in a band from about 1 to 20 Hz. The cepstra of both these events reflected the simple character of their spectra, and they were identified as earthquakes on that basis. The spectral shape of these two events is similar to other earthquakes in this region, but the spectral ratio curve for event 76 in Figure 12c indicates that the *Pn/Sn* ratio is anomalously high when compared with earthquakes from the same source region. This is especially true in the high-frequency band from 10 to 20 Hz. Likewise, the curve for event 64 in Figure 12d shows a high *Pn/Sn* ratio, with an unexplained increase between 5 and 10 Hz. The reason for these observations is unknown, although one possible reason for the high amplitude ratio is the effect of the radiation pattern. The presence of an *Sn* node could account for an anomalously high-amplitude ratio.

The final example in Figure 12 shows the *Pn*, *Sn*, and *Lg* cepstra (Fig. 12e), and the *Sn* spectrum (Fig. 12f) for the only event (event 23) for which both discriminants clearly failed. In this case, failure was clearly due to the fact that the S/N ratio was low for all phases. As a result, the amplitude ratios were close to one, and the cepstra reflect the complexity of the noise.

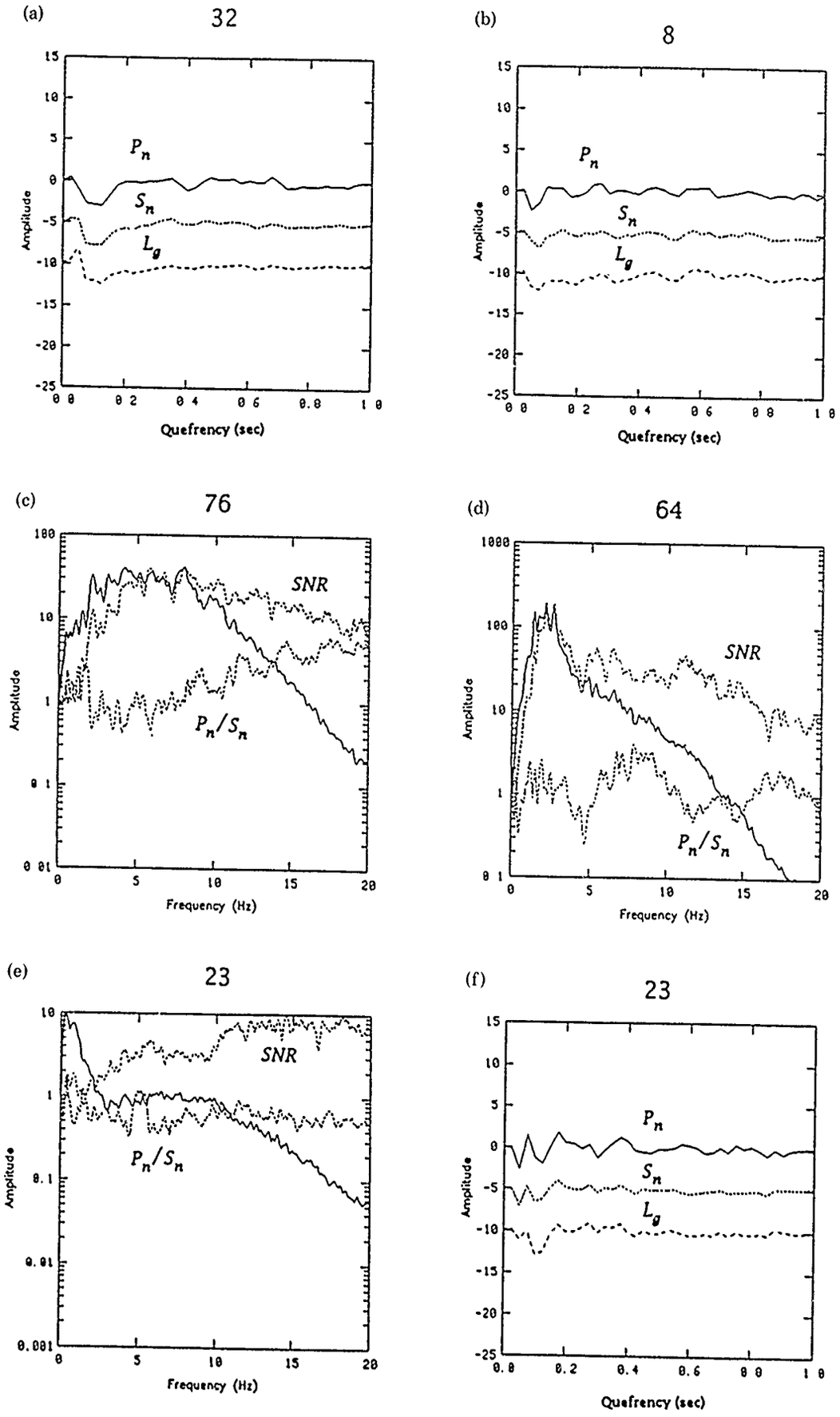

FIG. 12. Cepstra (a, b, f) and spectra [solid lines in (c, d, e)] of outliers shown in Figures 8 and 11. Dotted lines in (c, d, e) are SNR and *Pn/Sn* amplitude ratios.

Classification Using Trained Neural Networks

Several authors have sought to classify seismic event types using multi-dimensional discrimination techniques (e.g., Tjostheim, 1975). Dowla *et al.* (1990) have recently applied a simple feed-forward network to the problem of discriminating regional earthquakes and NTS explosions using spectral amplitudes corrected for distance and attenuation. In their study, an analysis of network weights suggested that the trained network formed appropriate amplitude ratios from the input spectral amplitudes. An automated classification of explosions and earthquakes in any data set is made difficult not only by outliers and overlap, but also by the inability to include diagnostic information that is not easily quantified. Neural networks have fundamental advantages over conventional least-squares classifiers in their ability to form complex decision regions based on mixed multi-dimensional and qualitative input and desired output by minimizing simple measures of classification error. Consequently, linear methods are not as versatile since they are either incapable of forming nonplanar decision surfaces between populations with significant overlap, or they cannot easily incorporate nonparametric or pathologic information gained from the analysis of events in a particular region. In addition, artificial neural networks are capable of forming disconnected decision regions and thereby operate as discriminators and clusterers simultaneously (Lippmann, 1987). Although there always exists the natural trade-off between model resolution and variance, the computational and modeling advantages of neural networks render them an attractive alternative to other classification schemes.

Neural Network Design

Four decisions must necessarily be made in the design of a supervised network training application: the input and output structures, hidden layer structure, the unit activation function, and the network training paradigm (see Lippmann, 1987, for a discussion of network dynamics, training paradigms, and terminology). The input structure in this case consisted of a single layer with 3 units containing the spectral ratios *Pn/Sn* and *Pn/Lg*, and the mean cepstral variance of *Pn* and *Sn*. The output was composed of a single layer with 2 units. The first unit was coded for an explosive source, and the second unit was coded for an earthquake source. Two hidden layers were used. The first hidden layer consisted of 8 units (so-called "fan-out"), and the second hidden layer consisted of 2 units ("fan-in"). The response of the network at each node is computed by the sigmoid activation function that acts as a nonlinear threshold element, acting on a weighted and biased input value. This configuration results in 56 connections (weights and biases) between the input and the output. These connections strengths and the sigmoid transfer function represent a large number of free parameters and a rich functional basis with which the neural network can fit the observed data.

No strict rules appear to exist for deciding on the number of hidden layers or the number of units in each hidden layer. Lippmann (1987) discusses empirical rules for choosing hidden layer structures based on the number of input and output units, and desired constraints on the geometry of decision regions. Makhoul *et al.* (1989) present a more quantitative approach to choosing the number of hidden units for a single layer network with hard limited threshold elements based on a desired cell resolution of the input space. The hidden layer structure was chosen in this case in an attempt to avoid disconnected decision regions while preserving the maximum flexibility in the curvature of decision boundaries. Trials using reduced network structures did not appear to provide the resolution necessary to correctly classify

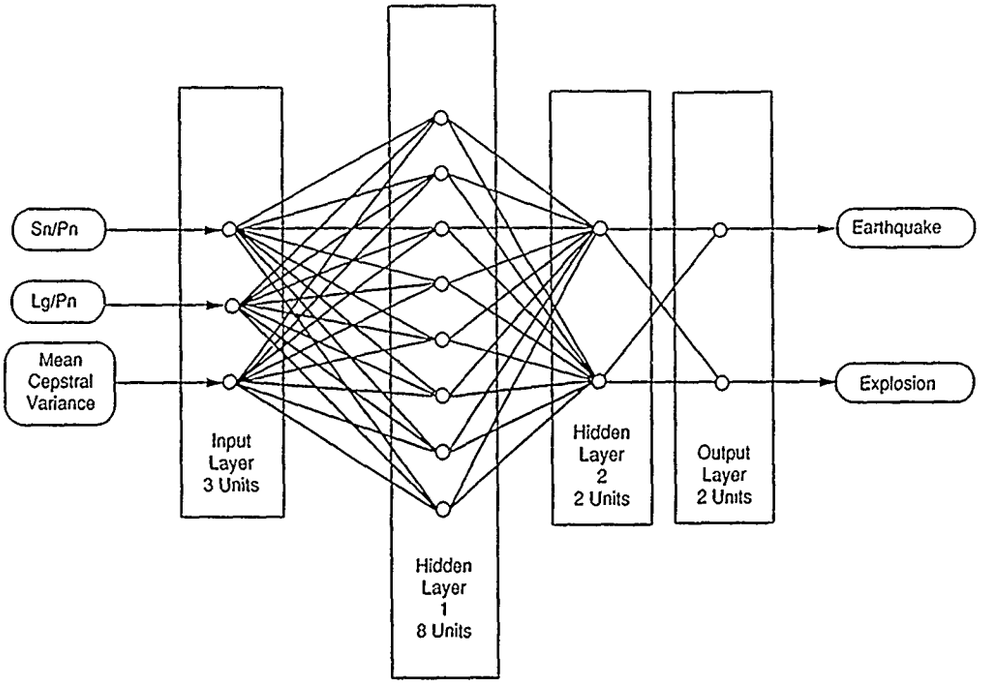

FIG. 13. Configuration of the neural network.

every event. The type of training chosen for the network was backpropagation, a supervised learning technique based on the Generalized Delta Rule (Rumelhart and McClelland, 1986). The Generalized Data Rule, a variant of gradient decent minimization, automatically determines the nonlinear model function as it minimizes a simple rms prediction error. Analogous to the general linear inverse problem, data and model resolution matrices can be extracted after training and used to determine the number of unique weights and the resolvability of the data (K. Anderson, personal communication). A schematic diagram of the neural network configuration is shown in Figure 13.

During training, the weights that connect the input and output units, and the transfer biases were set at large random values [−2, 2]. The learning rate also was set initially at a high value to force quick convergence and later reset to a low rate to obtain a refined solution. Conventionally, these parameters are initialized to small values, but larger values can sometimes significantly decrease learning time. This has been referred to as learning by oscillation. Following this training strategy, the momentum was set moderately low at the start and then reset to a high value near the end of training. About 2,000 input presentation cycles were required to train the network with the full data set, with about 75 per cent of these cycles taking place during the slow convergence phase.

Network Training Experiments

Two individual experiments were performed with the neural network. In the first experiment, the network was trained with the entire training set of 66 events. In the second experiment, the network was trained using a random selection of half the events from each population, and then used to process the remaining half. In a

more comprehensive simulation of the network's performance on new events, many random selections would be tested. Dowla *et al.* (1989) adopt a performance evaluation scheme where each event acts in turn as a new event to be processed by a network trained on the remaining events.

Figure 14 shows the resultant network activations within cross-sections of the input space, i.e., the output of the trained network given a grid of all possible input vectors. As the figure indicates, the network has formed two contiguous decision regions based on the input data, and a small region of uncertainty indicated by the asterisks. For this particular network design, an activation of +0.5 indicates an explosion while an activation of −0.5 indicates an earthquake. We define the region of uncertainty as the activations between ±0.25. The choice of the uncertainty range is somewhat arbitrary, being set to 5 times the maximum rms prediction error used as the convergence criterion during training.

Figure 15a shows the result of processing the input data with the trained neural network. The figure shows the resultant output activations for each processed event. It is clear that the network has perfectly classified the input data set with no errors and no uncertain classifications. This points to an important consideration in the use of trained neural networks for classification. One must be certain that the training set consists of correctly identified events, otherwise false information may be incorporated by the trained neural network.

Figure 15 (b and c) shows the results of training the network with half of the data set and testing the remaining half. As before, the neural network has perfectly modeled the input events with no errors and no uncertainties (Fig. 15b). When the remaining half of the data set is processed (Fig. 15c), 5 errors and 2 uncertain classifications are encountered. It is interesting to note that, when the neural network fails, it fails with certainty, having made no assumptions about an underlying error distribution. Regions of uncertainty are associated with areas where no data were given, and points on the decision surface whose topology is determined by the number and arrangement of network connections. Clearly, the larger the number of training events, the better the neural network will be able to classify new events. In an operating seismic array or network, one would add more and more events to the training set as they were confidently identified.

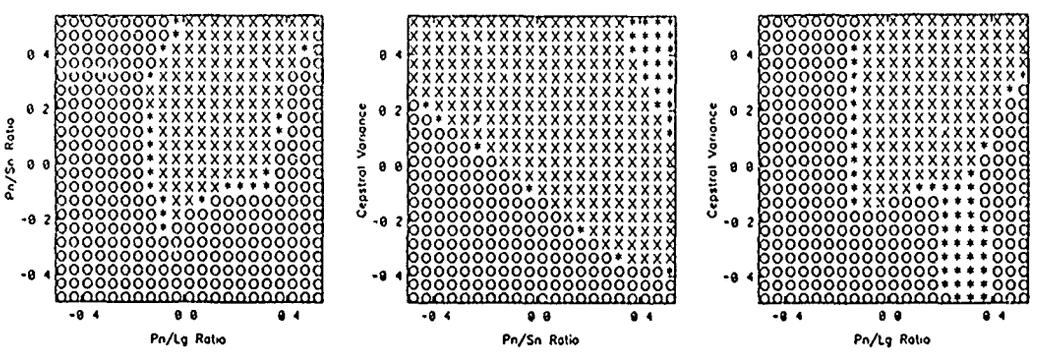

FIG. 14. Cross-sections of network activations in normalized input space. An open circle indicates an earthquake classification with an output value less than or equal to −0.25, while an X indicates an explosion with an output value greater than or equal to +0.25. Asterisks indicate the region of uncertainty (output value from −0.25 to +0.25). (a) *Pn/Sn* versus *Pn/Lg*; (b) cepstral variance versus *Pn/Sn*; (c) cepstral variance versus *Pn/Lg*.

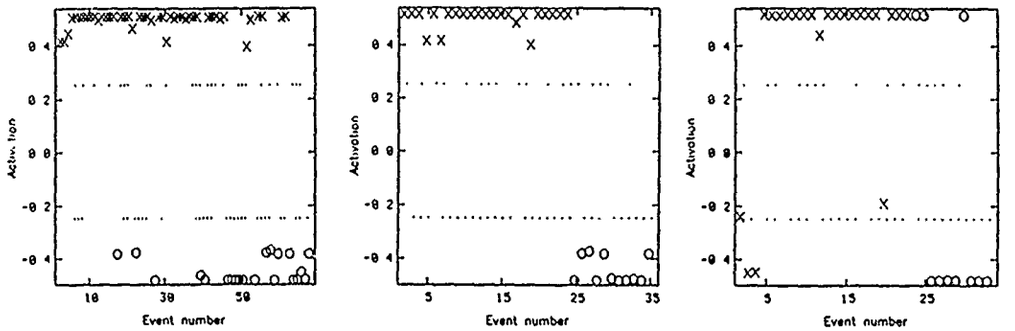

FIG. 15. (a) Result of processing the training set with the neural network. Note that there are no erroneous or uncertain classifications produced by the network. (b) Result of training the neural network with half of the data set. Note that there are no errors or uncertain classifications. (c) Processing of the remaining half of the data set. There are 5 erroneous classifications and 2 uncertain classifications.

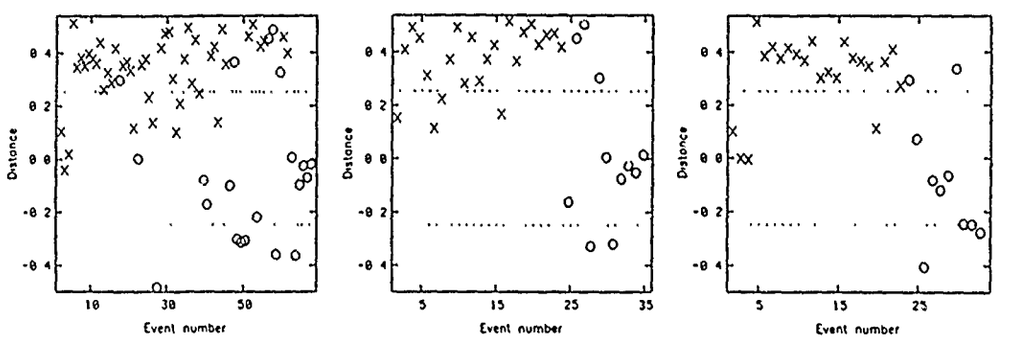

FIG. 16. (a) Optimum linear discriminant for the entire data set. Note that there are 5 misclassified events and 19 uncertain classifications. (b) Optimum linear discriminant calculated for half of the data set. There are 3 misclassified events and 10 uncertain classifications. (c) Processing of the remaining half of the data set. There are 2 misclassified events and 9 uncertain classifications.

Comparison with Optimum Linear Discriminant

To demonstrate whether or not the neural network provides any better classification of these events than commonly used linear discriminants, optimum discriminant planes were computed for the same two input training sets used in the previous section. The linear discriminant used for comparison in this case, minimizes both the number of misclassified events and the rms distance from the planar decision surface, the later providing an error statistic in the final analysis (Enslein *et al.*, 1977).

Figure 16a shows the results when the optimum decision plane is obtained from the entire data set. Plotted here are the normal distances from the decision plane to each processed event, scaled to the sigmoid activation range [−0.5, 0.5]. The dashed lines indicate the same area of uncertainty used in the neural network processing. The figure shows that 5 events were misclassified. This compares with 0 errors for the neural network experiment. In addition, there are also 19 events classified as uncertain. In the neural network experiment, there were no uncertain classifications.

To repeat the second experiment, the optimum linear discriminant is computed from half the data set and used to process the remaining half. In this case, the optimum linear discriminant produced 3 errors and 10 uncertain classifications shown in Figure 16b. The processing of the remaining half of the data set shown in Figure 16c produced an additional 2 errors and 9 uncertainties, resulting again in a total of 5 errors and 19 uncertain classifications.

SUMMARY

In this report, spectral characteristics were examined for a group of 95 regional events recorded by the NORESS array in southern Norway. Early in the analysis, it was observed that earthquakes and chemical explosions positively identified by local networks and recorded at similar distances contain similar high-frequency energy. For events at greater distances, the high-frequency amplitudes appear to attenuate strongly with distance. The third moment of frequency (TMF) and peak frequencies both demonstrate a distance-dependent decay of high-frequency amplitudes with little dependence on the magnitude. Due to this path-imposed similarity in high-frequency content, discriminants based on the predicted high-frequency content of explosions versus earthquakes would be ineffective.

Results from the measurement of amplitude ratios and spectral complexity indicate that effective discrimination of earthquakes and chemical explosions in this region is possible using a small set of spectral parameters. For events with clear *Pn*, *Sn*, and *Lg* arrivals, most wide-band estimates of the *Pn/Sn* and *Pn/Lg* ratios are consistent with the prediction of greater shear wave energy from earthquake sources. Observations of chemical explosions at several known mining sites in Norway, Sweden, and the western Soviet Union indicate that a complex pattern of spectral interference, presumably due to near-source effects or multiple firing, is a repeatable spectral characteristic of mine blasts recorded in this region. This complexity is seemingly absent from the earthquake spectra. Event discrimination on the basis of these parameters is generally successful, with exceptions that are dependent on the SNR, and to some extent on the choice of constraints and ranges that were selected for the computation of spectra ratios and cepstral variances. In addition, there are anomalous events that remain unexplained, and events in an overlap region that are difficult to classify by conventional least-squares techniques.

As an alternative means of automating the classification of events recorded in this region, an artificial neural network was designed and tested using a subset of the events that were positively identified by local seismic networks. A two-layer backpropagation network was trained to identify 100 per cent of the events on the basis of the mean cepstral variance and the *Pn/Sn* and *Pn/Lg* amplitude ratios. The same network, trained to identify half the events from the original training set, was able to correctly classify 85 per cent of the remaining events. The superior performance of neural networks over linear discrimination techniques is most simply interpreted in terms of the respective decision regions formed each process and assumptions made by each regarding the measure of prediction error.

Artificial neural networks that are capable of coding qualitative and quantitative input and output, and quickly incorporating the knowledge gained from the analysis of new events, appear a promising way of using both empirical and theoretical knowledge in a single automated classification system. Although the supervised learning technique employed in this study worked well, many potentially useful variations of the network design, input, and interpretation are left uninvestigated.

This was due in part to limitations in the number and variety of events in the data set, and the scope of the project. However, the performance of this network encourages application to other data sets, and the investigation of other networks and learning paradigms.

ACKNOWLEDGMENTS

The authors would like to thank Richard Baumstark, Andy Jurkevics, Robert Blandford, and Carl Romney for useful discussions during the course of this study. This research was supported by the Defense Advanced Research Projects Agency under Contract MDA-903-84-C-0020, and by internal research funds at Radix Systems, Inc., and Science Applications International Corporation.

REFERENCES

Aki, K. and P. G. Richards (1980). *Quantitative Seismology,* W. H. Freeman and Co., San Francisco, California.

Anderson, D. (1987). Deconvolution of mine-blast ground motion (abstract), *Trans. Am. Geophys. Union* **68**, 355.

Aviles, C. A. and W. H. K. Lee (1986). Variations in signal characteristics of small quarry blasts and shallow earthquakes (abstract), *Trans. Am. Geophys. Union* **67**, 1093.

Bard, P. and B. E. Tucker (1985). Underground and ridge site effects: a comparison of observation and theory, *Bull. Seism. Soc. Am.* **75**, 905–922.

Baumgardt, D. R. and K. A. Ziegler (1988). Spectral evidence for source multiplicity in explosions: application to regional discrimination of earthquakes and explosions, *Bull. Seism. Soc. Am.* **78**, 1773–1795.

Bennett, T. J. and J. R. Murphy (1986). Analysis of seismic discrimination capabilities using regional data from western United States events, *Bull. Seism. Soc. Am.* **76**, 1069–1086.

Bennett, T. J., B. W. Barker, K. L. McLaughlin, and J. R. Murphy (1989). Regional discrimination of quarry blasts, earthquakes and underground nuclear explosions, S-Cubed Final Report SSS-TR-89-10395.

Clayton, R. W. and R. Wiggins (1976). Source shape estimation and deconvolution of teleseismic bodywaves, *Geophys. J. R. Astr. Soc.* **47**, 151–177.

Dowla, F., S. Taylor, and R. Anderson (1990). Seismic discrimination with artificial neural networks: preliminary results with regional spectral data, *Bull. Seism. Soc. Am.* **80**, 1346–1373.

Dysart, P. S. and J. J. Pulli (1987). Spectral study of regional earthquakes and chemical explosions recorded at the NORESS array, SAIC Technical Report C87-03, Center for Seismic Studies, Arlington, Virginia.

Enslein, K., A. Ralston, and H. S. Wilf (Editors) (1977). *Statistical Methods for Digital Computers*, vol. 3, Wiley, New York, 96–120.

Gorman, R. P. and T. J. Sejnowski (1988). Analysis of hidden units in a layered network trained to classify sonar targets, *Neural Networks* **1**, no. 1.

Greenhalgh, S. A. (1980). Effects of delay shooting on the nature of *P*-wave seismograms, *Bull. Seism. Soc. Am.* **70**, 2037–2050.

Kemerait, R. C. and A. F. Sutton (1982). A multidimensional approach to seismic depth determination, *Geoexploration* **20**, 113–130.

Lippmann, R. P. (1987). An introduction to computing with neural nets, *IEEE ASSP Magazine,* April, 4–22.

Makhoul, J., A. El-Jaroudi, and R. Schwartz (1989). Formation of disconnected decision regions with a single hidden layer, *IEEE Proceedings of the International Joint Conference on Neural Networks,* Washington, D.C., June, 1989.

Menke, W. *Geophysical Data Analysis: Discrete Inverse Theory,* Academic Press, Inc., Florida, 260 pp.

Oppenheim, A. V. and R. W. Schafer (1975). *Digital Signal Processing*, Prentice-Hall, Inc., Englewood, New Jersey.

Pomeroy, P. W., J. W. Best, and T. V. McEvilly (1982). Test ban treaty verification with regional data—a review, *Bull. Seism. Soc. Am.* **72**, S89–S129.

Pulli, J. J. and P. S. Dysart (1990). An experiment in the use of trained neural networks for regional seismic event classification, *Geophys. Res. Lett.* **17**, 977–980.

Rumelhart, D. E. and J. L. McClelland (Editors) (1986). *Learning Internal Representations by Error Propagation*, vol. 1, Parallel Distributed Processing, MIT Press.

Stoffa, P. L., P. Buhl, and G. M. Bryan (1974). The application of homomorphic deconvolution to shallow-water marine seismology—Part 1: Models, *Geophysics* **39**, 410–416.

Tjostheim, D. (1981). Multidimensional discrimination techniques—theory and application, in Identification of Seismic Sources—Earthquake or Underground Explosion, *Proceedings of the NATO Advanced Study Institute held at Voksenasen, Oslo, Norway, September 8–18, 1980,* E. S. Husebye and S. Mykkeltveit, Editors, D. Reidel Publishing Company, Boston, Massachusetts.

Tribolet, J. M. (1979). *Seismic Application of Homomorphic Signal Processing*, Prentice Hall, Inc., Englewood, New Jersey.

Weichert, D. H. (1971). Short period spectral discriminant for earthquake and explosion differentiation. *Z. Geophys.* **37**, 147–152.

SCIENCE APPLICATIONS INTERNATIONAL
CORPORATION
1710 GOODRIDGE DRIVE
MCLEAN, VIRGINIA 22102
(P.S.D.)

RADIX SYSTEMS, INC.
2 TAFT COURT
SUITE 203
ROCKVILLE, MARYLAND 20850
(J.J.P.)

Manuscript received 16 February 1990

Bulletin of the Seismological Society of America, Vol. 80, No. 6, pp. 1934–1950, December 1990

STATISTICALLY OPTIMAL EVENT DETECTION USING SMALL ARRAY DATA

BY A. F. KUSHNIR, V. M. LAPSHIN, V. I. PINSKY, AND J. FYEN

ABSTRACT

A generalization of Capon's maximum-likelihood technique for detection and estimation of seismic signals is introduced. By using a multi-dimensional autoregressive approximation of seismic array noise, we have developed a technique to use Capon's multi-channel filter for on-line processing. Such autoregressive adaptation to the curent noise matrix power spectrum is shown to yield good suppression of mutually correlated array noise processes. As an example, this technique is applied to detection of a small Semipalatinsk underground explosion recorded at the ARCESS array.

INTRODUCTION

Nuclear explosion monitoring using seismic data is faced with the problem that signals of small explosions are masked by noise, and thus have to be extracted using features of both the noise and the signal. Small arrays appear to be especially suited for that purpose. This is due to the strong correlation of noise between different closely located receivers that give us an opportunity to obtain significant noise suppression. To realize this opportunity, special software needs to be developed.

We have to solve two main problems: (1) detecting event signals and (2) classifying detected signals as originating from either an explosion or an earthquake. The second task is very complex. To aid in the classification process, it is desirable to have an undistorted representation of the signal waveform as well as estimates of signal parameters, such as onset times of different phases, power, spectral features, and so on. While the detection of a signal can be done in a relatively narrow frequency band (for example using a high-frequency band only), the classification must, in principle, be based on wide-band methods. This is so because bandpass filtering distorts not only the noise, but also the signal; thus, possibly eliminating useful classification features.

In this paper we will focus on discussing the application of optimal multi-channel filtering to three problems: signal detection, signal waveform estimation, and onset time estimation of seismic phases. Each of these problems has been the subject of extensive research in the past, and some of these earlier publications are given in the list of references. Early papers by Burg (1964) and Backus *et al.* (1964) demonstrated the value of optimal Wiener filtering for detection with small-aperture arrays. Several attractive implementations of constrained beamforming of the type proposed by Capon (197υ) have demonstrated significant gains (Kobayashi, 1970; Frost, 1972; Shen, 1979). More recently, Der *et al.* (1988) described a frequency-domain multi-channel filtering scheme that uses measured characteristics of both the signal and the noise to optimize detection. This latter work was specifically directed at the NORESS.

Special features of the approach described in this paper include the following: for synthesis of the data processing algorithms, we implement strict statistically optimal methods under rather weak and commonly valid assumptions about signal and noise features; for practical realizations of the algorithms, we use the adaptive approach

that ensures that the algorithms are optimal when the statistical features of the ambient noise vary; for estimation of the multi-dimensional noise power spectral density, we use autoregressive modeling of the observations, which is computationally efficient and thus gives the possibility to detect signals in an on-line mode; and data processing is performed in the time domain and is designed to be applied to broadband data.

Bayesian Optimal Statistical Treatment of Signal Detection

The problems mentioned in the introduction can be formulated in terms of mathematical statistics, and optimal decision rules for these mathematical problems have to be found. The first task is to detect the signal. The time series received by the array has the following structure:

$$X_t = S_t + \xi_t, \quad t \in \cdots -1, 0, 1, \cdots \tag{1}$$

where S_t is signal, ξ_t is noise, and X_t is a vector of different receiver outputs. We assume that ξ_t is a Gaussian multi-dimensional time series with known power matrix spectral density $F(\lambda)$ and that S_t has the coherence structure:

$$S_t = G_t \times u_t \tag{2}$$

where u_t is a scalar seismic source signal that is assumed to be a realization of a Gaussian random time series with unknown power spectral density $g(\lambda)$, and G_t is a vector impulse transfer function of the medium on the paths from the seismic source to the receivers. For frequency-independent media, this vector is defined by the time delays τ_l only.

The outputs X_t are observed through a moving window. Using data in the window, we must make a decision: does it contain a signal or not? This problem can be solved in terms of statistical hypothesis testing theory. It is necessary to test hypothesis H_0 (that observations in the moving window are pure noise) versus hypothesis H_1 (that they comprise signal plus noise). We consider hypothesis H_0 to be simple, but hypothesis H_1 to be complex. Thus, when using the adaptive approach, the statistical characteristics of the noise can be measured before the signal arrival in a stage of adaptation. On the other hand, statistical features of seismic signals are almost completely unknown and cannot be measured in short moving time windows.

The problem is now to choose a decision function that would provide the smallest average error probability for all possible signals. This problem can be solved using a Bayesian approach and finite dimensional parameterization of the signal (Kushnir and Lapshin, 1984 (see Appendix). The decision has the form of an algorithm as shown in Figure 1. It consists of a multi-channel filter followed by autocorrelators, calculation of a quadratic form, and a trigger that compares the quadratic form value with a threshold. The transfer function of the multi-channel filter is a vector described as a product of the inverse matrix power spectrum $F^{-1}(\lambda)$ of the noise ξ_t and a vector $G(\lambda)$ that represents the frequency response of the medium (the discrete Fourier transform of the G_t). Here, $\lambda = \pi f / f_N$, where f_N is the Nyquist frequency. The algorithm shown has a form that can be easily realized as an on-line procedure. This is primarily due to the use of a multi-dimensional autoregressive modeling of the noise, ξ_t. This allows us to avoid direct inversion of spectral power

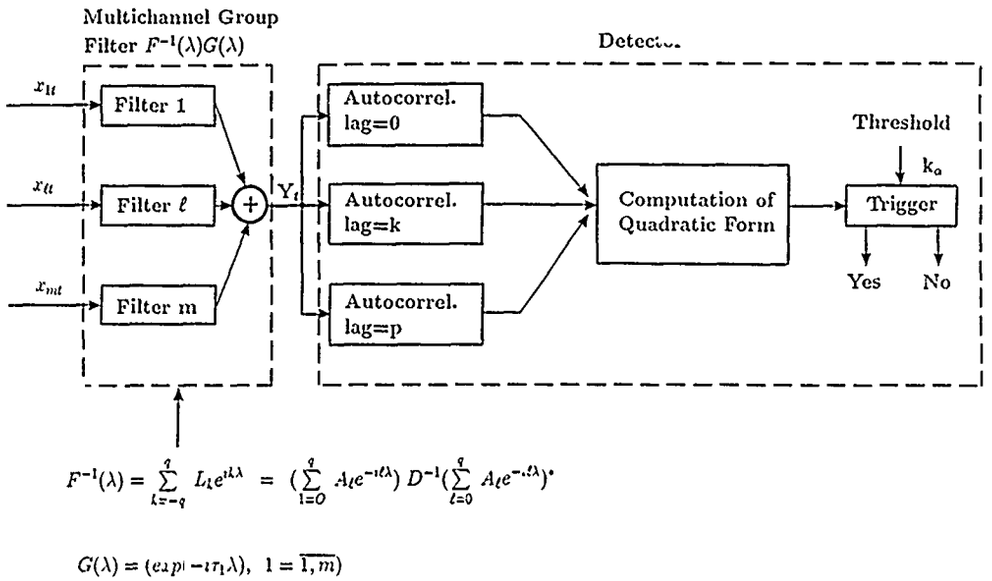

FIG. 1. Statistically optimal array detector flowchart.

matrices and is very convenient in an adaptive procedure (Haykin, 1979; Kushnir *et al.*, 1980).

Autoregressive modeling of the noise, ξ_t, is done by approximating the inverse power spectrum with a matrix polynomial:

$$F^{-1}(\lambda) \approx \sum_{k=-q}^{q} L_k e^{ik\lambda} \tag{3}$$

where $L_{-k} = L_k^T$, and q is the autoregressive model degree. In most practical cases, the vector $G(\lambda)$ has the same structure, and the product $F^{-1}(\lambda)G(\lambda)$ is the vector filter with finite impulse response.

The Bayesian statistical approach to detecting unknown random signals leads to a one-component detection procedure that differs from the well-known STA/LTA detector. This procedure coincides with STA/LTA under the assumption that the source signal is white noise. If, on the other hand, the seismic source signal has nonzero autocorrelations, it is statistically preferable to use a detector in the form shown in Figure 1. This can be explained more easily if we examine the statistically equivalent but simpler case of an optimal one-dimensional detector shown in Figure 2. Noise whitening filtering of the multi-channel filter output reduces the quadratic form calculation to a summation of the autocorrelation squares. If the observations are pure noise, $X_t = \xi_t$, then the mean values of all autocorrelations with nonzero lags are equal to zero. Otherwise, if $X_t = \xi_t + S_t$, then these values are nonzero because the signal $\tilde{S}_t$ at the output of the whitening filter is not white noise. This yields an additional raise of the detection statistic value compared to STA/LTA when the signal arrives.

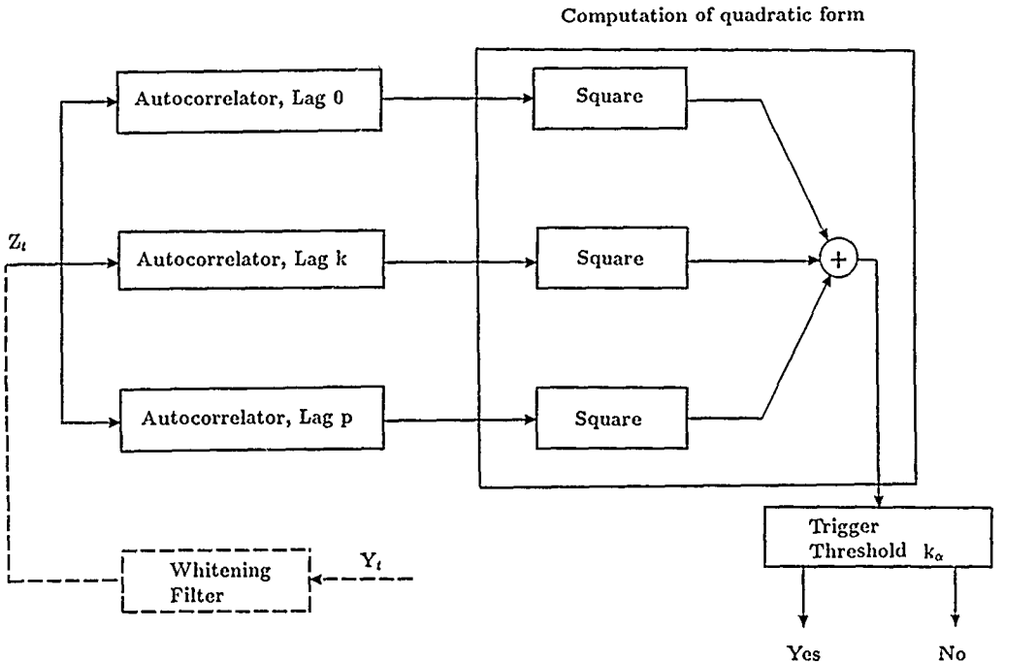

FIG. 2. One-component on-line detector flowchart.

SIGNAL WAVEFORM ESTIMATION

After signal detection, the second problem to be addressed is to estimate properly the signal waveform. The model of observation here has the following form:

$$X_t = G_t * u_t + \xi_t \tag{4}$$

where $*$ denotes convolution, u_t is a signal waveform to be estimated (the particle motion along the seismic ray), and G_t is as earlier defined. For solving the estimation problem, a conditional Wiener filter can be constructed. This filter minimizes the variance of the estimate $E\{(\hat{u}_t - u_t)^2\}$ under the condition that the mathematical expectation of the estimate coincides with the real signal: $E\{\hat{u}_t\} = u_t$.

The Wiener filter that we are looking for consists of the same multi-channel filter $F^{-1}(\lambda)G(\lambda)$ that is used for the detection followed by a restitution filter $[G^*(\lambda)F^{-1}(\lambda)G(\lambda)]^{-1}$, which makes it possible to obtain the signal undistorted. Capon was the first to propose this filter for seismic signal extraction from array data (Capon, 1970).

The complete adaptive statistically optimal procedure for signal detection and estimation is shown in Figure 3. We adapt to the noise matrix power spectrum by estimating its autoregressive parameters and computing vector coefficients of the multi-channel filter. Then, we perform multi-channel filtering and detect the signal in a moving window. The first two operations are made periodically according to the interval of noise stationarity. The third—multi-channel filtering and detection—can be devised as an on-line procedure. After the signal is detected, it must be filtered by the restitution filter, which refines its shape.

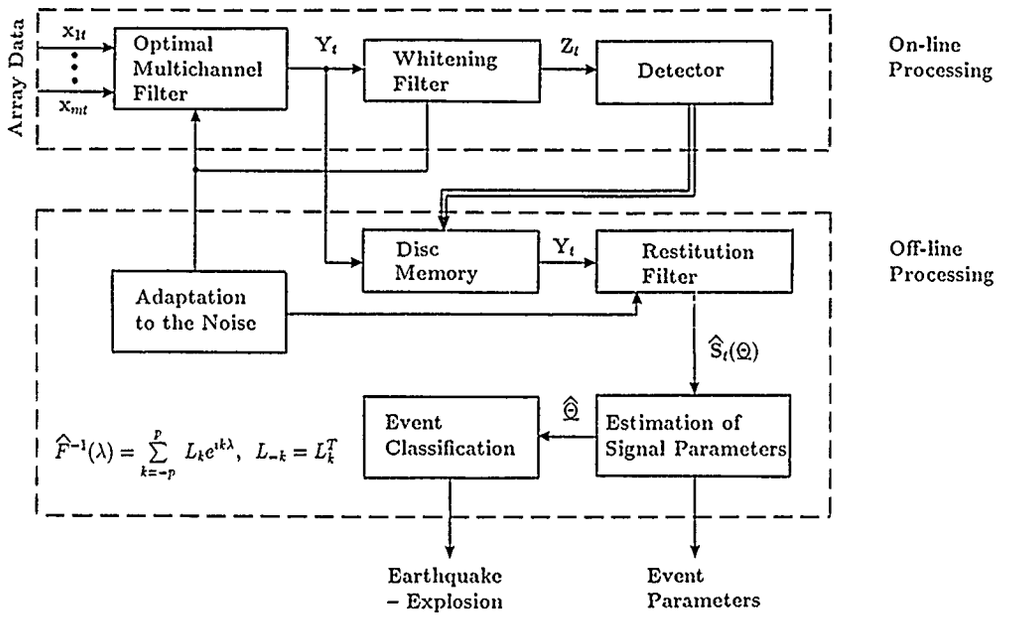

FIG. 3. Adaptive signal detection and waveform estimation flowchart.

ONSET TIME ESTIMATION OF SEISMIC PHASES

The precise estimation of onset time of different seismic phases, such as P and S, is necessary to obtain accurate seismic source location, especially depth determination. Therefore, this is important for event classification. We will show how onset time can be determined using the broadband signal waveform at the output of the restitution filter where the noise components have been substantially suppressed.

The algorithm is based on regarding signal onset time as the moment in time when the statistical features of the observed time series are abruptly changed. We will thus investigate the following model:

$$Z_t = \begin{cases} n_t & t_1 < t < \tau \text{ is Gaussian noise with power spectrum } f_0(\lambda) \\ n_t + s_t & \tau < t < t_2 \text{ signal plus noise is a Gaussian process} \\ & \text{with power spectrum } f_i(\lambda) \end{cases} \tag{5}$$

where (t_1, t_2) is the signal arrival interval known as a result of signal detection, and τ is the unknown onset time to be estimated. We describe here an estimator of τ based on autoregressive approximations of the unknown spectral densities, $f_0(\lambda)$ and $f_i(\lambda)$. It appears to be effective for seismic phase onset time determination (Pisarenko *et al.*, 1987). This is a maximum-likelihood algorithm that calculates the likelihood function $L(\tau)$ and uses the global maximum of this function to estimate onset time. A flowchart of this algorithm is shown in Figure 4. Calculations are made for all τ from t_1 to t_2. At each step, autoregressive models of observations in the intervals (t_1, τ) and (τ, t_2) are calculated by a Levinson-Durbin procedure. Then, the $L(\tau)$ value is evaluated in accordance with formula (Kushnir *et al.*, 1983).

$$L(\tau) = [\tau \ln \sigma_1(\tau) - (N - \tau)\ln \sigma_2(\tau)] \tag{6}$$

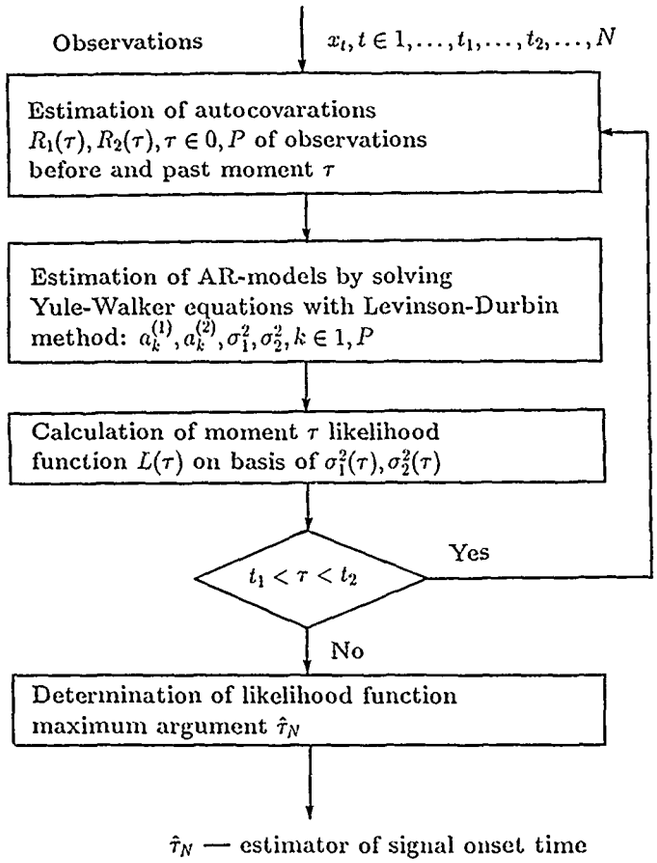

FIG. 4. Maximum-likelihood onset time estimation flowchart. AR = autoregressive.

where $\sigma_i^2(\tau)$, i = 1, 2, are the variances of the autoregressive model residuals. The maximum of $L(\tau)$ is found numerically.

For three-component seismogram processing, a three-dimensional version of the described algorithm can be developed. In this case, the onset time is estimated as the moment when the matrix power spectrum of the observations abruptly changes. It takes into account changes not only in the power and frequency contents, but also the polarization of the three-component observations at the moment when the signal arrives.

TESTING OF THE OPTIMAL PROCEDURE

The software designed was tested using simulated data with the aim of comparing its actual efficiency with the theoretical one. The calculations were made for the central subarray of the NORSAR array, which consists of six receivers. The strong coherence noise, ξ_t, was simulated as the sum of a plane wave and white random noise. The plane wave was generated by using NORSAR noise records and had apparent velocity of 10 km/sec, azimuth 30°, which differs from those for the signal (50 km/sec, 0°). For simulated noise power spectrum estimation, a six-dimensional tenth degree autoregressive model was used. The learning noise realization comprised 1,024 samples with a sampling rate of 10 Hz.

The results of these tests are shown in Figure 5. The depicted curves are the gains in power signal-to-noise ratio of undistorting optimal multi-channel filtering with frequency response $F^{-1}(\lambda)G(\lambda) \cdot [G^*(\lambda)F^{-1}(\lambda)G(\lambda)]^{-1}$ relative to a conventional beam versus the coherence coefficient of the noise. The latter is defined as the ratio between the power of the coherent noise component and the random one. We see that the mentioned gain may be very significant if the array noise is coherent enough. This happens in practice at small aperture arrays. We also note that the gains obtained in this simulated case are close to the theoretical predictions.

Highly promising results were obtained by the use of ARCESS data for signals from one of the smallest nuclear tests known to have been conducted at the Semipalatinsk test site (28 December 1988). In Figure 6, we display the records for four ARCESS channels filtered in the band 0.5 to 5 Hz. Note that the signal is obscured by the noise. For the conventional beam trace (Fig. 7), the signal is likewise not seen, but inspecting the output of the undistorting multi-channel filter we can see the signal clearly. The power signal-to-noise ratio gain relative to the beam is approximately a factor of 70 to 80, and it is 140 to 160 when compared with a single channel. The trace shown is calculated using six matrix autoregressive parameters

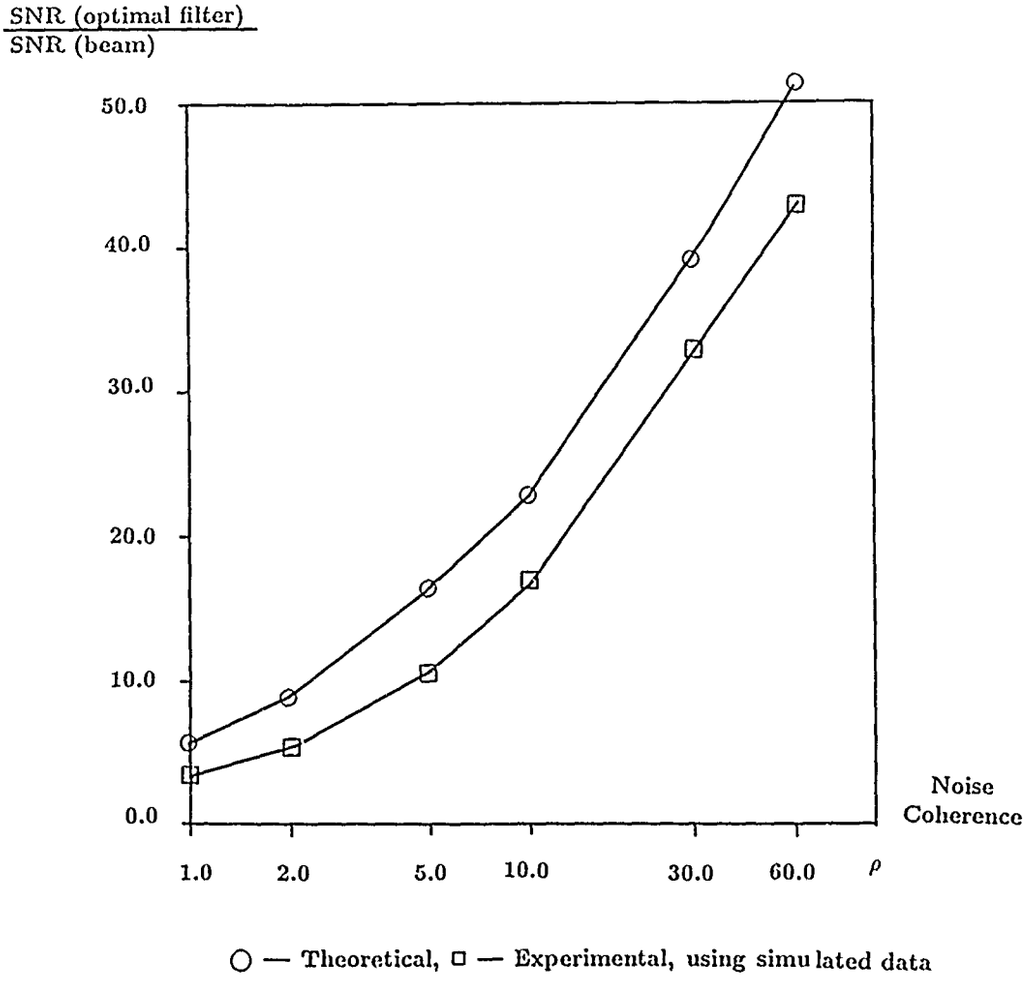

FIG. 5. Signal-to-noise ratio (SNR) gain of optimal multi-channel filtering as compared with the beam (broadband processing).

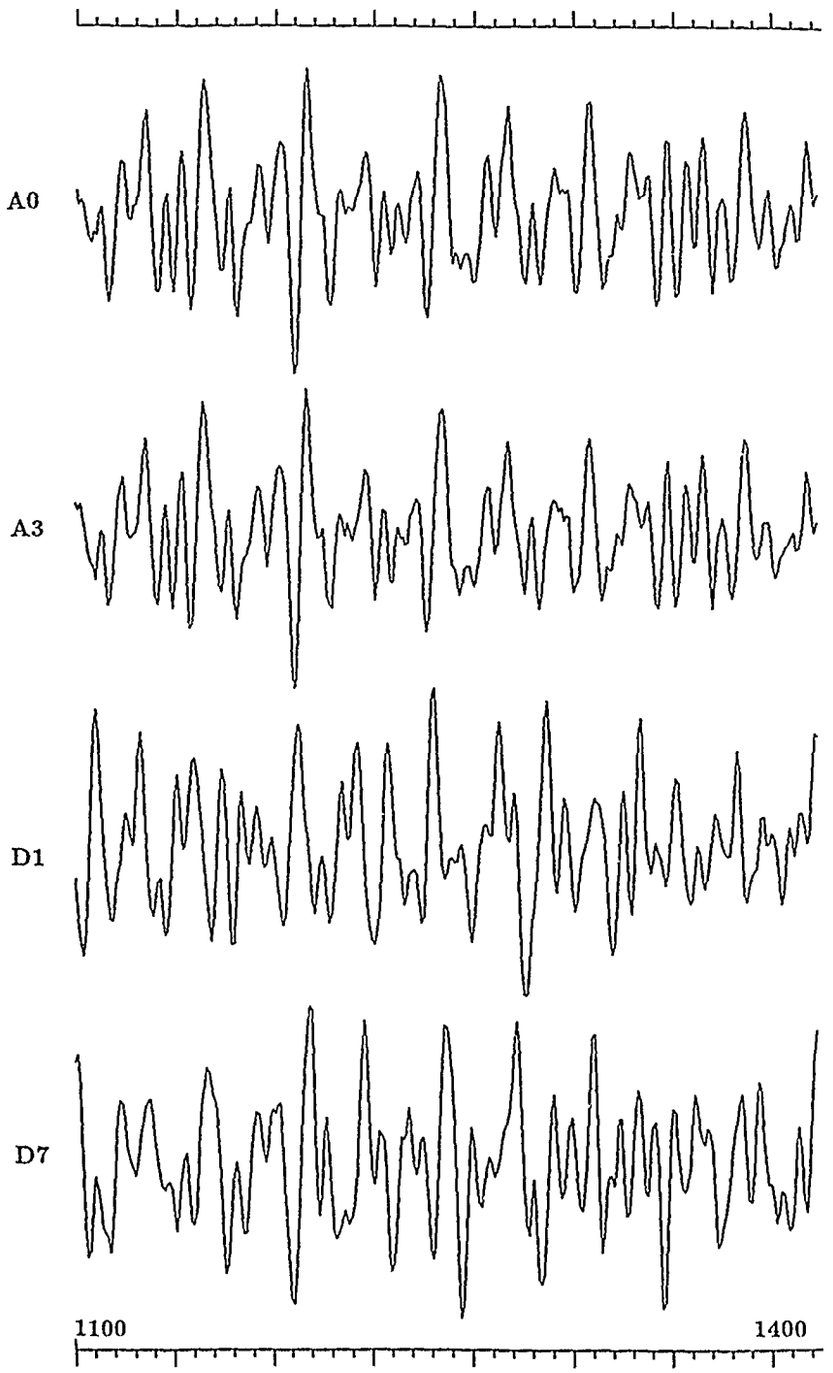

FIG. 6. ARCESS recording (data shown for four individual sensors) of a weak underground nuclear explosion signal obscured by noise. The data are filtered in the band 0.5 to 5 Hz. The sampling rate is 40 Hz, and the window length is 300 samples.

of noise. We also used other numbers of autoregressive parameters, and the results seemed to be stable. Such high suppression of noise is achieved mainly because of the high correlation of noise among the innermost ARCESS sensors (see Fig. 6, traces A0 and A3).

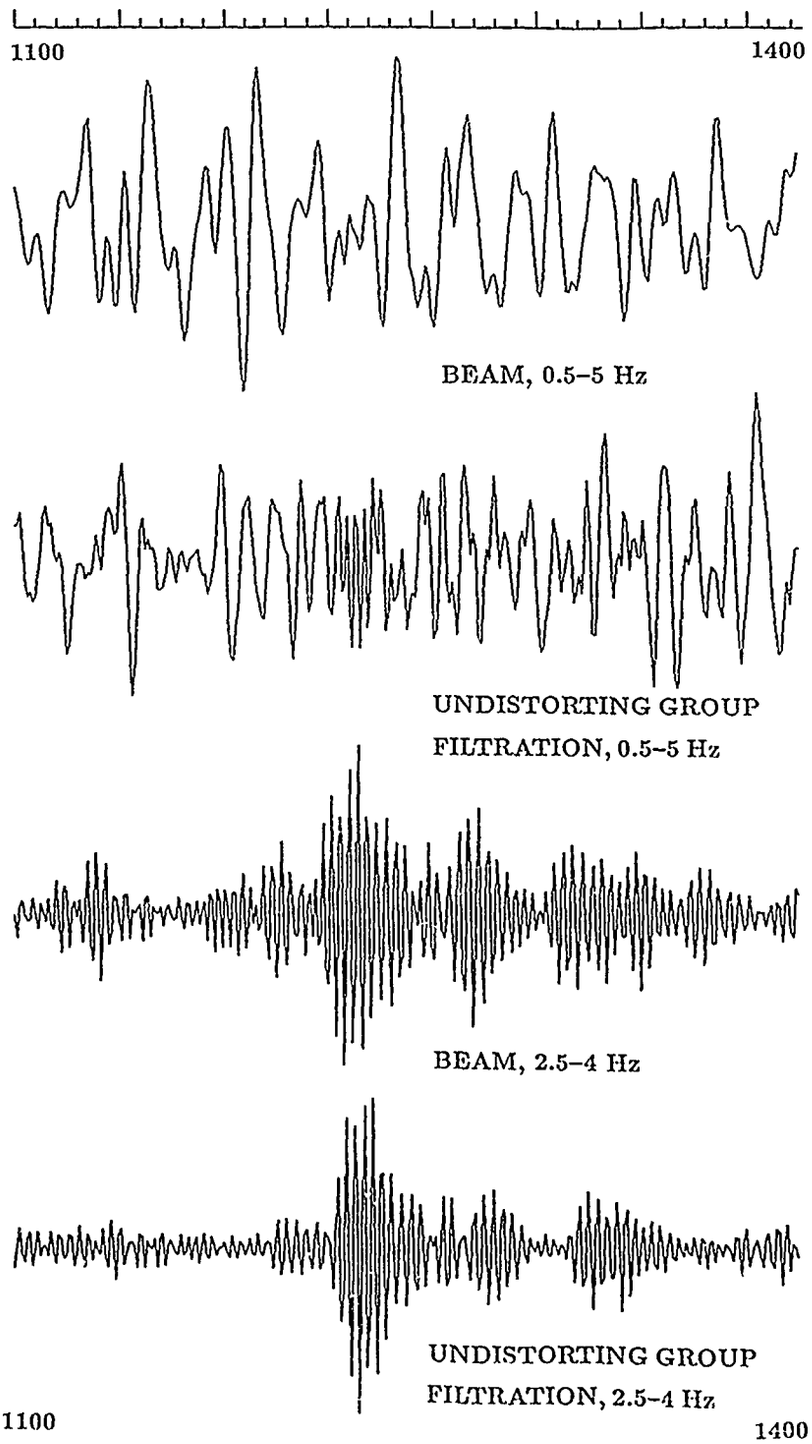

FIG. 7. Comparison of the conventional array beam and the output trace after undistorting multichannel filtering for a broad frequency band (*upper two traces*) and a narrow band (*lower traces*) for the ARCESS data shown in Figure 6.

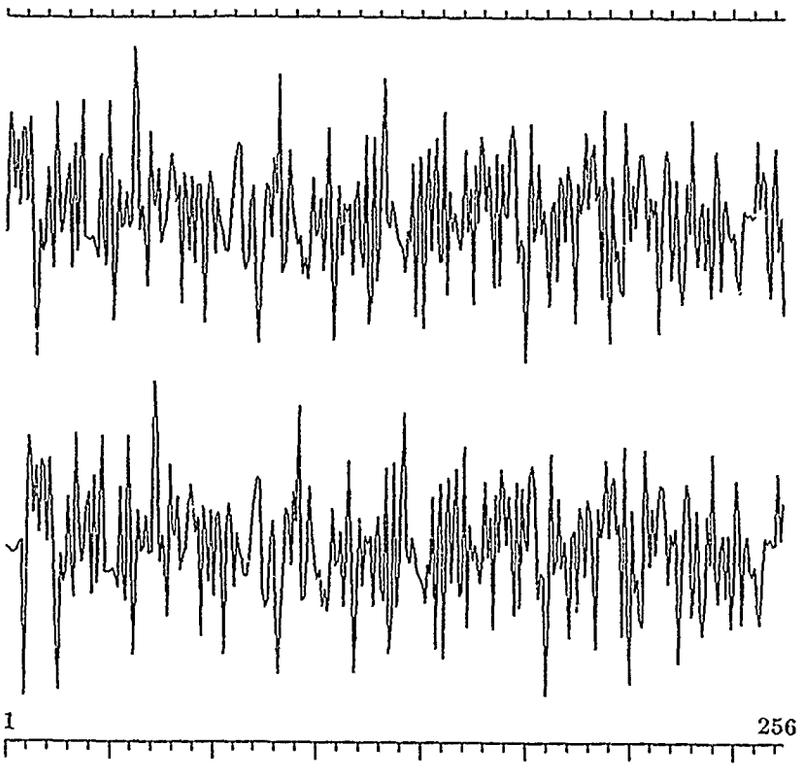

FIG. 8. Illustration of the undistorting property of the optimal multi-channel filter. The output from the restitution filter (*bottom*) is practically identical to the original trace (*top*), except for a small phase shift introduced by the filter.

Figure 8 shows that the multi-channel filter used does in fact retain the shape of the original waveform. The first trace is a wide frequency band waveform used for simulating the plane wave arriving at ARCESS. These simulated data were processed by the multi-channel filter used for the previously shown signal extraction. The resulting (second) trace practically coincides with the first. So, if the real signal is a plane wave, it will be undistorted by the multi-channel filter in the frequency band from 0.5 to 5 Hz.

The conventional method used for the detection of weak signals is the filtration of the array beam in a band of optimum signal-to-noise ratio (Kværna, 1989). The two traces at the bottom of Figure 7 show the signal filtered in the frequency band at 2.5 to 4 Hz after beamforming and after undistorting multi-channel filtering. The gain here is not as large as in the broadband case, but still exceeds a factor of 5 in power SNR. Figure 9 (at the top) shows the same signals, but in another time scale. The frequency band chosen seems to be the best for filtering the signal after beamforming. For comparison, we have plotted two traces at the bottom of Figure 9 presenting the same signals filtered in the frequency band 3 to 5 Hz.

For the detection of signals in our experiments, four different variants of the optimal detector previously described were used. All of these detectors are sensitive not only to the increase in trace power due to signal arrival, but also to changes of the trace spectrum (Kushnir *et al.*, 1983). The first is optimal in a statistical sense,

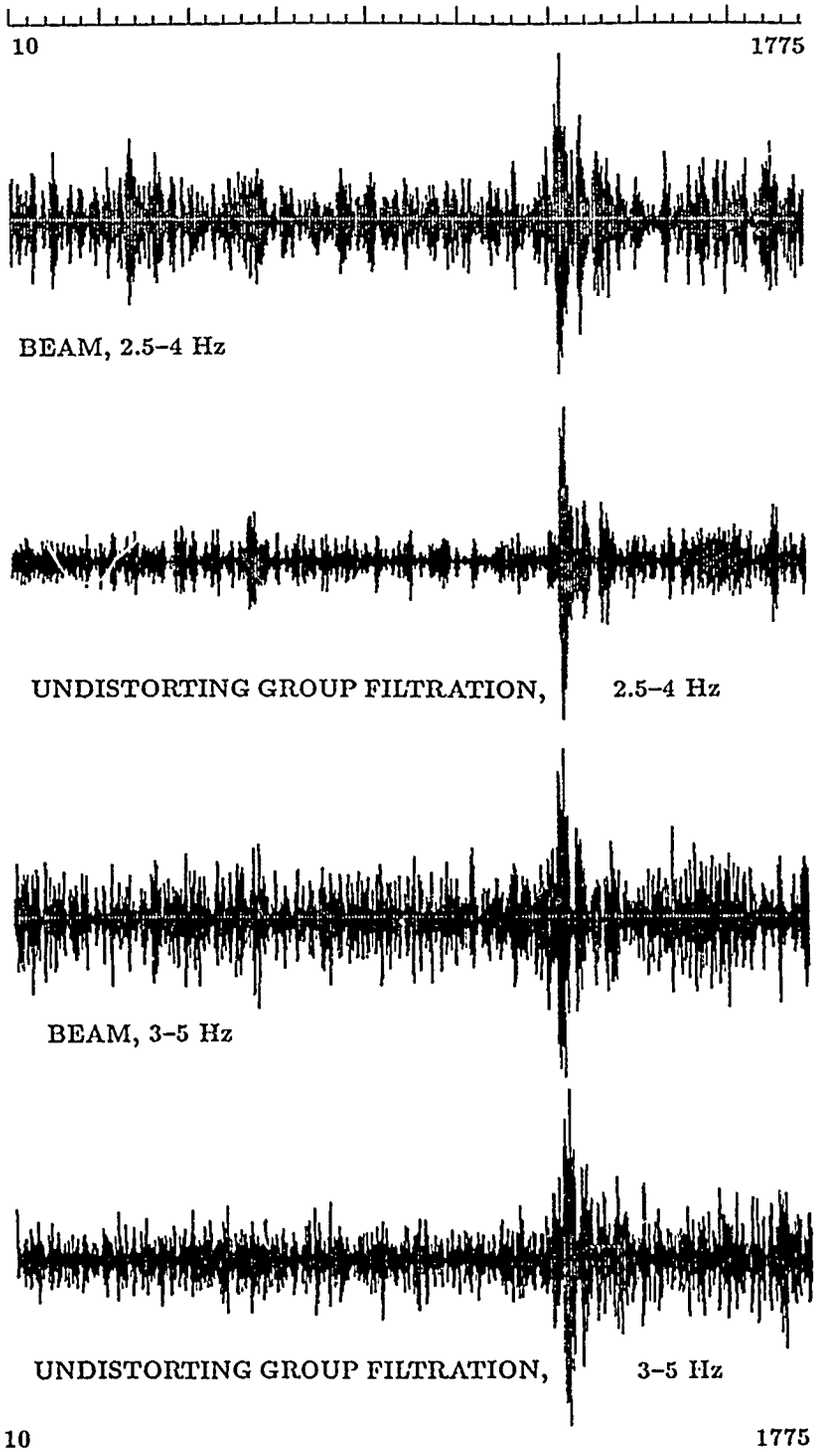

FIG. 9. Results of array data processing in different narrow frequency bands.

the second is a modification of STA/LTA using prewhitening of the noise, and the last two are components of the first. Figure 10 shows how the detectors work when applied to the beam and multi-channel filter outputs. The gain due to optimal multi-channel filtering is evident.

The final figure (Fig. 11) shows the results of the signal onset time estimation. Estimation is performed by an algorithm based on the maximum-likelihood method

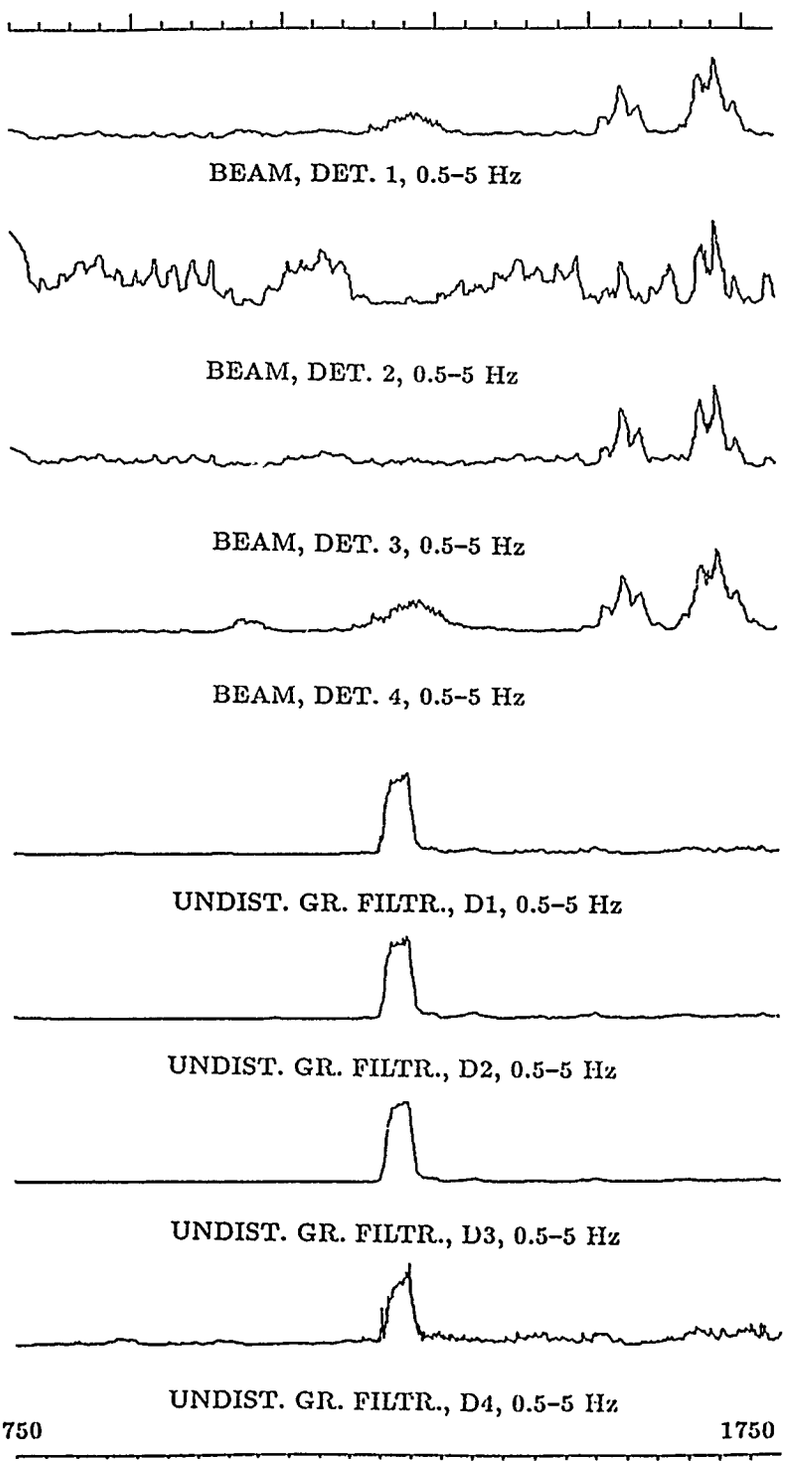

FIG. 10. Detection of a weak underground explosion signal after beamforming and undistorting optimal multi-channel filtering.

applied to the problem of estimating the moment in time when parameters of the autoregressive process are abruptly changed (Pisarenko *et al.*, 1987). One can see that the likelihood function maximum coincides exactly with the beginning of the signal.

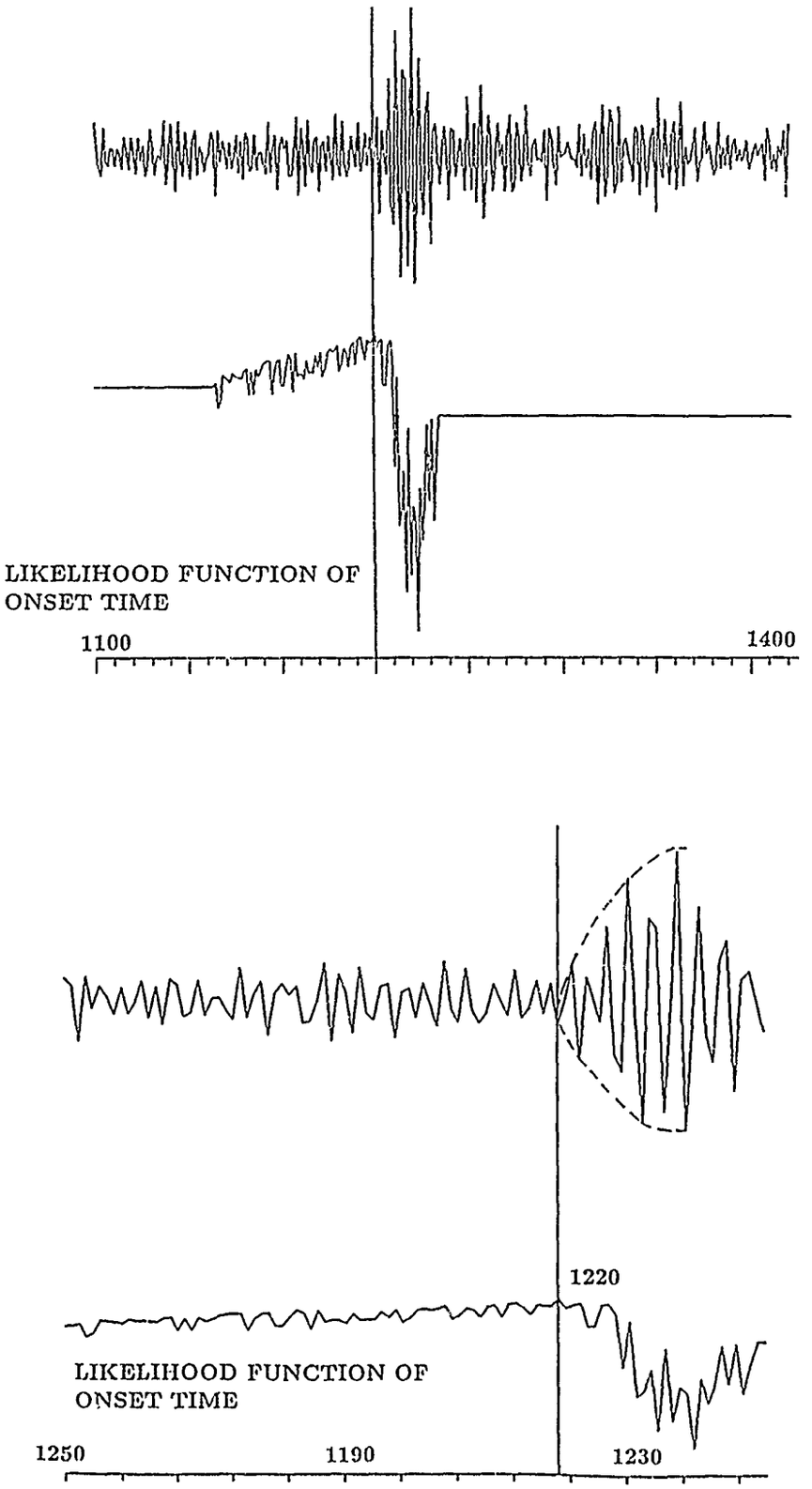

FIG. 11. Maximum-likelihood estimation of signal onset time. Results are shown for two different time scales for the same signal.

CONCLUSIONS

From our research, we have drawn the following conclusions:

1. Application of an adaptive optimal multi-channel filtering technique to data from small aperture arrays can provide large gains in signal-to-noise ratio; this is in comparison to conventional beamforming and is due to high mutual correlation of array noise. The technique is especially useful in broadband signal processing.
2. By using autoregressive estimation of the power noise spectrum for multi-channel filter adaptation, we greatly reduce time and memory needed for the adaptation procedure while providing high-quality noise suppression.
3. Optimal multi-channel filtering does not distort the signal. Thus, when seen in connection with (1) and (2), it is clear that optimum filtering has great advantages as a preprocessor to be applied prior to subsequent broadband operations, such as source classification.

ACKNOWLEDGMENT

The authors are grateful to the reviewer for valuable comments and suggestions concerning the contents and style of this paper.

REFERENCES

Backus, M., J. Burg, D. Baldwin, and E. Bryan (1964). Wide-band extraction of mantle *P* waves from ambient noise, *Geophysics* **29**, 672–692.

Burg, J. P. (1964). Three-dimensional filtering with an array of seismometers, *Geophysics* **29**, 693–713.

Capon, J. (1970). Application of signal detection and estimation theory to the large-array seismology, *Proc. IEEE* **58**, 170–181.

Dez, Z. A., R. H. Shumway, and A. C. Lees (1988). Frequency domain coherent processing of regional seismic signals at small arrays, *Bull. Seism. Soc. Am.* **78**, 326–338.

Frost, O. L. (1972). An algorithm for linearly constrained adaptive array processing, *Proc. IEEE* **60**, 926–935.

Haykin, S. (Editor) (1979). Nonlinear methods of spectral analysis, in *Applied Physics*, vol. 34, Springer-Verlag, 234 pp.

Kobayashi, H. (1970). Iterative synthesis methods for a seismic array processor, *IEEE Trans. Geosci. Electron.* **GE-8**, 169–178.

Kushnir, A. F. and V. M. Lapshin (1984). Optimal processing of the signals received by a group of spatially distributed sensors, in *Computational Seismology*, Allerton Press, Inc., vol. 17, 163–174.

Kushnir, A. F., I. V. Nikiforov, and I. V. Savin (1983). Statistical adaptive algorithms for automatic detection of seismic signals, in *Computational Seismology*, Allerton Press, Inc., vol. 15, 145–162.

Kushnir, A. F., V. F. Pisarenko, and T. A. Rukavishnikova (1980). Noise compensation in multidimensional geophysical observations. I. Theory and method of data processing, in *Computational Seismology*, Allerton Press, Inc., vol. 13, 146–151.

Kværna, T. (1989). On exploitation of small-aperture NORESS type arrays for enhanced *P*-wave detectability, *Bull. Seism. Soc. Am.* **79**, 888–900.

Pisarenko, V. F., A. F. Kushnir, and I. V. Savin (1987). Statistical adaptive algorithms for estimations of onset moments of seismic phases, *Phys. Earth Planet. Interiors* **47**, 4–10.

Shen, W. W. (1979). A constrained minimum power adaptive beamformer with time-varying adaptation rate, *Geophysics* **44**, 1088–1096.

INSTITUTE OF PHYSICS OF THE EARTH
MOSCOW, USSR
(A.F.K., V.M.L., V.I.P.)

NTNF/NORSAR
KJELLER, NORWAY
(J.F.)

Manuscript received 16 February 1990

APPENDIX

Let us assume that the noise $\xi_t = (\xi_{1t}, \cdots, \xi_{mt})^T$ at the m receivers of the array is a multi-dimensional Gaussian time series with zero mean and matrix power spectral density $F(\lambda)$, $\lambda \in [0, 2\pi]$ and that the signal $S_t = (s_{1t}, \cdots, s_{mt})^T$ is generated by a Gaussian scalar process $\mu u_t(\Theta)$ at the seismic event source. The power spectral density of $u_t(\Theta)$ is denoted $g_\Theta(\lambda)$, $\lambda \in [0, 2\pi]$, where Θ is an unknown vector parameter. The medium transfer functions are assumed to be known. Then, the observed process $x_t = (x_{1t}, \cdots, x_{mt})^T$ has the form $G_t * \mu u_t + \xi_t$. Here, $G_t = (G_{1t}, \cdots, G_{mt})^T$ is the vector impulse response function of the media along the paths from the seismic source to the receivers; $*$ denotes convolution. The process x_t is a multi-dimensional Gaussian time series, and it is easy to write down the likelihood function $w(X_N \mid \mu, \Theta)$ for the moving window observations $X_N = (x_1^T, \cdots, x_N^T)^T$. Then the signal detection can be treated as testing the hypothesis H_0 that $\mu = 0$ versus the hypothesis H_1 that $\mu \neq 0$. We consider the function $w(X_N \mid 0)$ to be known through adaptive estimation. If the unknown signal parameters have an *a priori* distribution, $P(\Theta)$, then the best (Bayesian) test for testing these hypotheses (providing the least average signal miss probability for a given false alarm probability) has the form:

$$q(X_N) = \begin{cases} 1 \text{ (signal is present)} & \text{if } \rho(X_N) > k_\alpha \\ 0 \text{ (signal is absent} & \text{if } \rho(X_N) < k_\alpha \end{cases} \tag{A-1}$$

where

$$\rho(X_N) = \int_\Theta \frac{w(X_N \mid \mu, \Theta)}{w(X_N \mid 0)}\, dP(\Theta). \tag{A-2}$$

Here, k_α is the detection threshold, determined on the basis of the given false alarm probability α.

It is practically impossible to devise an on-line algorithm on the basis of the statistic (A-1) when the distribution $P(\Theta)$ is arbitrary. But in the important case of weak signal detection, where the signal-to-noise ratio, μ^2/σ^2, is sufficiently small and the moving window size, N, is sufficiently large, the statistic $\rho(X_N)$ can be simplified. As it is shown in Kushnir and Lapshin (1984), in this case the likelihood ratio $w(X_N \mid \gamma/\sqrt{N}, \Theta)/w(X_N \mid 0)$ in (A-2) can be replaced by its exponential approximation and the statistic $\rho(X_N)$ in (A-2) is replaced by the more computationally convenient statistic:

$$r(X_N) = \int_\Theta \exp\left\{\gamma \Delta(X_N, \Theta) - \frac{\gamma^2}{2}\, \Gamma_N(\Theta)\right\} dP(\Theta). \tag{A-3}$$

The asymptotic error probability limits for the test (A-1) with the statistic (A-2) are the same as for the test (A-1) with the statistic (A-3) when $\mu^2 = \gamma/\sqrt{N}$, and $N \to \infty$.

The functions $\Delta(X_N, \Theta)$ and $\Gamma_N(\Theta)$ in (A-3) have the following forms (Kushnir

and Lapshin, 1984):

$$\Delta(X_N, \Theta) = \frac{1}{2\sqrt{N}} \sum_{j=1}^{N} g_j(\Theta) | W_j^* X_j |^2 - g_j(\Theta) V_j,$$

$$\Gamma_N(\Theta) = \frac{1}{4N} \sum_{j=1}^{N} [g_j(\Theta) V_j]^2,$$

where $\Delta(X_N, \Theta)$ is an asymptotically sufficient statistic of the observations X_N, and

$$W_j^* = G^*(\lambda_j) F^{-1}(\lambda_j), \qquad V_j = W_j^*(G(\lambda_j), \qquad g_j(\Theta) = g_\Theta(\lambda_j).$$

$\Gamma_N(\Theta)$ = the Fisher information quantity, divided by N
$G(\lambda)$ = the Fourier transform of G_t
$X_j = (1/\sqrt{N}) \sum_{t=1}^{N} x_t \exp(i\lambda_j t)$ is the discrete Fourier transform of the observations x_t
$\lambda_j = (2/N)\pi j$
$F(\lambda)$ = the matrix power spectral density of the noise ξ_t.

For calculation of the integral (A-3) in analytic form, we will assume that:

$$g_\Theta(\lambda) = \sum_{k=0}^{p} c_k \cos\, k\lambda, \qquad \Theta = (c_0, \cdots, c_p)^T, \tag{A-4}$$

where $c_k = E\{u_t u_{t+k}\}$ are the autocorrelations of the source signal.

We further assume that the *a priori* distribution $P(\Theta)$ in (A-3) is Gaussian:

$$dP(\Theta) = \{(2\pi)^p \det B\}^{-1/2} \exp\{-\tfrac{1}{2}(\Theta - b)^T B^{-1} (\Theta - b)\}. \tag{A-5}$$

Then, we have

$$\log\{r(X_N)\} = K + \tfrac{1}{2}[\Delta^T \Gamma^{-1} \Delta - (\Delta - a)^T A^{-1} (\Delta - a)] = K + r(X_N), \tag{A-6}$$

where K is a constant independent of X_N, $\Delta = (\Delta_0, \cdots, \Delta_p)^T$,

$$\Delta_k = \frac{1}{2\sqrt{N}} \sum_{j=1}^{N} (| W_j^* X_j |^2 - V_j) \cos(k\lambda_j)$$

$$a = \Gamma b$$

$$A = (\Gamma + \Gamma B \Gamma)$$

$$\Gamma = \left[\frac{1}{4N} \sum_{j=1}^{N} V_j^2 \cos(m\lambda_j) \cos(n\lambda_j);\ m, n \in [\overline{1, P}] \right].$$

Therefore, the asymptotically optimal Bayes test for array detection of seismic signals with unknown spectrum is:

$$q(X_N) = \begin{cases} 1 \text{ (signal is present)} & \text{if } \tau(X_N) > k_\alpha \\ 0 \text{ (signal is absent)} & \text{if } \tau(X_N) < k_\alpha, \end{cases} \tag{A-7}$$

where the threshold, k_α, is determined on the basis of the given false alarm error probability (Kushnir *et al.*, 1983).

Let us consider two important (diametrically opposite) cases, where:

1. The power spectrum parameters of the source signal are almost known:

$$\| B \| \ll \| \Gamma^{-1} \|.$$

2. The *a priori* information about these parameters is negligible:

$$\| B \| \gg \| \Gamma^{-1} \|.$$

In these cases, the statistic, $\tau(X_N)$, of the test (A-7) is simplified and looks like, respectively:

$$\begin{aligned} \tau_1(X_N) &= b^T \Delta \\ \tau_2(X_N) &= \Delta^T \Gamma^{-1} \Delta. \end{aligned} \tag{A-8}$$

Calculation of the test statistic, $\tau_2(X_N)$, can be realized in the time domain as shown in Figure 1.

Bulletin of the Seismological Society of America, Vol. 80, No. 6, pp. 1951–1968, December 1990

COMPARISON OF THE DIRECTION ESTIMATION PERFORMANCE OF HIGH-FREQUENCY SEISMIC ARRAYS AND THREE-COMPONENT STATIONS

By David B. Harris

Abstract

This paper presents a theoretical comparison of the backazimuth and velocity estimation performance of arrays and three-component stations in severe noise conditions. Theoretical estimates of performance for low signal-to-noise ratios (SNRs) are validated through simulation. The high SNR limits of array performance are determined through an empirical study of 23 events at a single source location. Theory and simulation indicate a gradual and uniform deterioration in three-component station performance as the SNR is decreased, beginning at relatively high SNR. At very low SNR, the signal is overwhelmed by the noise, and the performance reaches an asymptotic plateau determined by *a priori* physical limitations on the velocity of incident waves. By contrast, arrays exhibit a sharp transition between a high SNR performance floor determined, presumably, by scattering effects in the signal, and a low SNR plateau. The SNR threshold for the transition in array performance is low enough that a band of SNRs exist for which arrays have usefully small direction and velocity errors, but three-component stations do not.

Introduction

The relative performance of arrays and three-component stations for direction and velocity estimation is an important consideration in the design of internal seismic networks for monitoring compliance with nuclear test ban treaties. Reliable estimates of direction and velocity are important for solving location and interpretation problems, especially with automated systems. Direction (backazimuth) estimates can contribute to location estimates made with sparse networks (e.g., Bratt and Bache, 1988). They are essential for resolving location ambiguities when events are detected only at two stations, and for obtaining any location when an event is detected at only one station. Direction estimates are also used to associate phases. Velocity estimates are important for phase identification. Both arrays and three-component stations can estimate these parameters from waveform data. They do so using different physical characteristics of propagating waves: propagation delays across an aperture for arrays, polarization for three-component stations. Because direction and velocity are encoded differently in the observed waveforms, and because arrays gather so much more data, it is reasonable to expect a major difference in performance between arrays and three-component stations.

This expectation is partly borne out by observation (e.g., Suteau-Henson and Ryall, 1989). Performance at high signal-to-noise ratios (SNR) is roughly the same for three-component stations and arrays. It is common experience that refraction and scattering limit performance in the high-SNR regime (Goldstein and Archuleta, 1990). Over sufficiently small apertures, refracted or scattered waves are approximately planar; three-component stations and arrays produce similarly biased results. However, as the SNR decreases performance becomes noise-limited (Dowla and Harris, 1987; Suteau-Henson and Ryall, 1989). Provided the array aperture is larger than the spatial correlation length of the noise, arrays have a superior data gathering capability when compared to three-component stations. This fact, along with the

manner in which propagation parameters are encoded in the waveforms (i.e., as time delays), gives arrays a definite advantage over three-component stations.

This paper presents theoretical and simulation results on the relative performance of arrays and three-component stations when estimating the *vector* slowness (equivalent to direction and velocity) of a single plane wave in spatially uncorrelated ambient noise. The paper also includes the results of a small empirical study, to illustrate the limitations of the theoretical analysis. The theoretical analysis of the single-source slowness estimation problem supplements empirical studies (Bame *et al.*, 1989, Suteau-Henson and Ryall, 1989) by describing the expected performance of arrays and three-component stations under conditions of very low SNR. Theoretical studies have a role to play for examining low-SNR behavior, even with fairly simple assumptions about the signal. At low SNR, irregularities in the signal model due to scattering and refraction produce errors that are smaller than those due to noise.

Comparing the performance of arrays and three-component stations presents a problem of choosing representative slowness estimation algorithms. A specific choice may bias the comparison, if the chosen algorithm has less than optimal performance. The best estimator for each type of station, defined as the algorithm with minimum mean square error (MSE), may not be known. This problem may be solved by comparing the performance of a good estimator with theoretical (lower) bounds on the MSE of all estimators. Where the bounds and the realized MSE coincide, the bounds estimate error with precision, and the estimator is optimal. Otherwise, they bracket the best attainable performance. I use two different methods: the Cramér–Rao bound (Van Trees, 1968) and the Weiss–Weinstein bound (Weinstein and Weiss, 1988) to obtain lower bounds on performance. For the upper bound, I use the MSE of a maximum-likelihood array slowness estimator (Ziskind and Wax, 1988; Cadzow, 1988) and its three-component counterpart. This estimator is equivalent to conventional beamforming for a single wave in white Gaussian noise. The empirical study shows that it has good performance also for estimating the slowness parameters of two superimposed waves.

The theoretical analyses and simulations indicate a range of SNRs for which arrays have usefully small slowness errors, but three-component stations do not. Three-component stations experience a gradual, uniform deterioration in performance with declining SNR. The three-component MSE exceeds the error level caused by signal imperfections at a fairly high SNR (>10 power SNR, 4 Hz bandwidth). On the other hand, arrays postpone poor performance to a much lower SNR, but exhibit a pronounced threshold phenomenon. The deterioration of performance is gradual to a point, called the threshold SNR, then proceeds rapidly with any further decrease in SNR (Harris, 1987; Dowla and Harris, 1987).

Theoretical Background

To obtain a concrete comparison between arrays and three-component stations, it is necessary to study a specific scenario. To keep the analysis tractable, I choose the simplest scenario possible; compressional plane waves with perfect spatial coherence superimposed upon spatially uncorrelated noise. The signal and noise are modeled as samples of Gaussian random processes with flat spectra within a specified passband. The signals and ambient noise are uncorrelated with each other, but are individually temporally correlated because of limited bandwidth.

The results of the analysis are tied to this model. Because the model assumptions emphasize coherent signals and incoherent noise, the comparison may be biased somewhat in favor of arrays. Real signal coherence is imperfect, shrinking the effective aperture of arrays and reducing resolution. Similarly, real seismic noise is spatially correlated, which can limit beamforming gain and narrow the performance gap between arrays and single stations. There are, however, characteristics of the data tending to counteract a bias in favor of arrays. Model error makes estimates of three-component performance optimistic as well. For example, three-component slowness estimates appear to be more strongly affected by topographic irregularities than array estimates (Ødegaard *et al*, 1990). Spatially correlated noise may be polarized also, tending to increase the error in three-component slowness estimates. It is difficult to say if the net effect of these competing factors is to make an analysis of array performance more optimistic than that of three-component stations.

An analysis of the simple scenario is useful because it provides a baseline for comparison, from which discussions of the perturbing effects of model complications can proceed. The analysis requires an evaluation of the MSE's of the most commonly used array and three-component slowness estimation algorithms. These algorithms were derived for plane waves in spatially uncorrelated noise; it is interesting to know their performance under the conditions for which they were derived.

Signal Models

A compressional-phase waveform recorded by a three-component station can be represented in the frequency domain by (Jarpe and Dowla, 1989):

$$\mathbf{r}(\omega) = \mathbf{c}s(\omega) + \mathbf{n}(\omega). \tag{1}$$

Here, $s(\omega)$ represents the Fourier amplitude of the signal measured along the direction of propagation and evaluated at frequency $\omega = 2\pi f$. The signal is superimposed upon ambient noise represented by the vector $\mathbf{n}(\omega)$. The cosine direction vector $\mathbf{c}$ determines the type of polarization and the direction of propagation. For P waves, it points along the path of propagation, and is usually defined in terms of the angle of incidence ϕ and backazimuth ξ:

$$\mathbf{c}(\xi, \phi) = \begin{bmatrix} \cos \phi \\ -\sin \phi \cos \xi \\ -\sin \phi \sin \xi \end{bmatrix}.$$

I use a different parameterization in terms of the horizontal slowness vector $\theta = [\theta_N \theta_E]^T$ and the surface medium velocity v_m in order to facilitate comparison with arrays.

$$\mathbf{c}(\theta) = \begin{bmatrix} \sqrt{1 - (\theta_N^2 + \theta_E^2) v_m^2} \\ -\theta_N v_m \\ -\theta_E v_m \end{bmatrix} = \begin{bmatrix} \sqrt{1 - \theta^T v_m^2} \\ -\theta v_m \end{bmatrix}. \tag{2}$$

Here, the superscript T represents the transpose operation. This model is appropriate for *Pn*, *Pg*, and teleseismic *P* phases, neglecting scattering effects.

The array signal model is similar:

$$\mathbf{r}(\omega) = s(\omega)\,\underline{\underline{\sqrt{1 - \theta^T\theta v_m^2}}}\,\epsilon(\omega\theta) + \mathbf{n}(\omega) \tag{3}$$

where

$$\epsilon(\omega\theta) = \begin{bmatrix} e^{-i\omega\theta^T\mathbf{z}_1} \\ e^{-i\omega\theta^T\mathbf{z}_2} \\ \vdots \\ e^{-i\omega\theta^T\mathbf{z}_N} \end{bmatrix}.$$

The array station locations are denoted by the set of two-dimensional vectors $\{\mathbf{z}_i: i = 1, \cdots, N\}$. The array consists of N elements. The array response to a plane wave is characterized by the steering vector $\epsilon(\cdot)$, which encodes the propagation delays $\theta^T\mathbf{z}_i$ at the stations as a vector of complex phase factors. Arrays of vertical sensors are considered only; the doubly underlined factor represents the $\cos\phi$ projection of the incident wave upon the vertical axis.

Both three-component and array signal models fit into a common framework:

$$\mathbf{r}(\omega) = s(\omega)\mathbf{g}(\omega, \theta) + \mathbf{n}(\omega), \tag{4}$$

which simplifies analysis. The model is easily extended to multiple (d) simultaneously incident waves:

$$\mathbf{r}(\omega) = \mathbf{G}(\omega, \boldsymbol{\Theta})\mathbf{s}(\omega) + \mathbf{n}(\omega)$$

where

$$\mathbf{s}(\omega) = \begin{bmatrix} s_1(\omega) \\ s_2(\omega) \\ \vdots \\ s_d(\omega) \end{bmatrix}$$

and

$$\mathbf{G}(\omega, \boldsymbol{\Theta}) = [\mathbf{g}(\omega, \theta_1)\ \mathbf{g}(\omega, \theta_2)\ \cdots\ \mathbf{g}(\omega, \theta_d)].$$

The matrix $\boldsymbol{\Theta} = [\theta_1\ \cdots\ \theta_d]$ contains the slowness parameters for the d incident waves.

To introduce uncertainty into the model in a tractable manner, the signal and noise waveforms are assumed to be finite segments (T sec long) of zero-mean Gaussian random processes with bandwidths of B Hertz. Because the waveforms have finite duration, they are approximately representable in the frequency domain by a finite number (M) of discrete uncorrelated samples at frequencies ω_i, spaced at intervals of $2\pi/T$ (Papoulis, 1965). For convenience, these samples can be

collected into a vector:

$$\mathbf{X} = \begin{bmatrix} \mathbf{r}(\omega_1) \\ \mathbf{r}(\omega_2) \\ \vdots \\ \mathbf{r}(\omega_M) \end{bmatrix}.$$

The joint conditional probability density for the data given the parameter is:

$$P(\mathbf{X} \mid \Theta) = \prod_{i=1}^{M} \frac{1}{(2\pi)^N \mid \Lambda(\omega_i, \Theta) \mid} \exp\left(-\frac{1}{2}\, \mathbf{r}^H(\omega_i)\Lambda^{-1}(\omega_i, \Theta)\mathbf{r}(\omega_i)\right) \tag{5}$$

and is completely specified by the data covariance matrices:

$$\Lambda(\omega_i, \Theta) = \mathrm{E}\{\mathbf{r}(\omega_i)\mathbf{r}^H(\omega_i)\}.$$

The symbol $|\cdot|$ denotes the determinant, and the superscript H indicates the conjugate transpose operation.

The model can be simplified by considering a single plane wave ($d = 1$) and by invoking the assumption of spatially uncorrelated noise. The covariance matrices simplify

$$\Lambda(\omega_i, \theta) = \sigma_S^2(\omega_i)\mathbf{g}(\omega_i, \theta)\mathbf{g}^H(\omega_i, \theta) + \sigma_N^2(\omega_i)\mathbf{I} \tag{6}$$

where $\mathbf{I}$ is the identity matrix, σ_S^2 is the signal power, and σ_N^2 is the noise power. The ratio of signal and noise power spectra

$$\gamma(\omega_i) = \frac{\sigma_S^2(\omega_i)}{\sigma_N^2(\omega_i)}$$

is defined to be the power SNR. Hereafter, all references to the SNR refer to this quantity.

One final modeling assumption is made: it is reasonable to make *a priori* assumptions about the distribution of the slowness vectors of the incident waves. For a general monitoring situation, the incident waves are equally likely to be coming from any direction (i.e., they are uniformly distributed in backazimuth). By confining this discussion to compressional waves, it is possible also to place an upper bound on propagation slowness. In a regional monitoring context, the major compressional phases generally propagate with horizontal phase velocities no lower than 5 km/sec. Combining these observations, it is reasonable to assume a uniform probability density for the vector slowness θ over the disk $\| \theta \| \leqq \theta_{\max}$:

$$\begin{aligned} p(\theta) &= \frac{1}{\pi\theta_{\max}^2}; & \theta^T\theta &\leqq \theta_{\max}^2 \\ &= 0; & \theta^T\theta &> \theta_{\max}^2 \end{aligned}$$

where the maximum slowness $\theta_{\max} = \frac{1}{5}$. Completing the model, the joint density for

the data and the slowness parameters is:

$$P(\mathbf{X}, \theta) = P(\mathbf{X} \mid \theta)p(\theta).$$

The probabilistic signal model $P(\mathbf{X}, \theta)$ completely specifies the scenario for comparing the performances of arrays and three-component stations. It is the type of model commonly used within the sonar and radar community to ascertain the performance (MSE) of array systems. In spite of the fact that it provides a complete description of the data (however simplified), its existence does not guarantee that one can evaluate the performance of an array or three-component system directly. The best algorithms (estimators) for estimating slowness may be unknown. However, it is possible to calculate a lower bound on the MSE of *all* estimators. The performance of the best estimator can be bracketed between this lower bound and any convenient upper bound. One suitable upper bound is the MSE of any good realizable estimator, measured through Monte Carlo simulation.

Bounding MSE

The notion of the existence of lower bounds on the MSE of all estimators of a particular parameter for a given signal model is one of the more remarkable ideas to come out of statistical estimation theory. It implies that performance is limited by the characteristics of the data itself and that no amount of clever signal processing can improve performance beyond this limit. This notion is consistent with the idea that the data contain a finite amount of information, since, with a finite duration and bandwidth, signals are approximately representable with just $2TB$ parameters.

Because the notion of statistical bounds may be somewhat unfamiliar, the main aspects of the theory are pointed out, taking the simple case of a single parameter θ. The theory assumes a probabilistic model for the data of the form $P(\mathbf{X}, \theta)$. An estimator $\hat{\theta}(\mathbf{X})$ is any rule that assigns a value for the parameter, given the data $\mathbf{X}$. Statistical bounds estimate a floor for the expected MSE

$$\mathrm{E}\{(\hat{\theta}(\mathbf{X}) - \theta)^2\}.$$

Following Weiss and Weinstein (1988), if a function $\psi(\mathbf{X}, \theta)$ can be found that satisfies the orthogonality condition

$$\int d\theta\, \psi(\mathbf{X}, \theta)P(\mathbf{X}, \theta) = 0,$$

the Schwartz inequality can be invoked to show that:

$$\mathrm{E}\{(\hat{\theta}(\mathbf{X}) - \theta)^2\} \geqq \frac{(\mathrm{E}\{\theta\psi(\mathbf{X}, \theta)\})^2}{\mathrm{E}\{\psi^2(\mathbf{X}, \theta)\}}. \tag{7}$$

A family of bounds with different properties can be obtained by choosing different functions, ψ. The bound that is simplest to evaluate is the Cramér–Rao bound (Van Trees, 1968), obtained with:

$$\psi(\mathbf{X}, \theta) = \frac{\partial \ln P(\mathbf{X}, \theta)}{\partial \theta}.$$

The bound that results is:

$$\mathrm{E}\{(\hat{\theta}(\mathbf{X}) - \theta)^2\} \geqq \frac{1}{\mathrm{E}\left\{\left(\frac{\partial \ln P(\mathbf{X}, \theta)}{\partial \theta}\right)^2\right\}}. \tag{8}$$

The main attraction of this bound is that it can often be evaluated in close form, providing a compact formula for estimating performance. It has important asymptotic properties. The MSE of the maximum-likelihood estimator for θ is approximately equal to the bound for sufficiently large SNR and sufficiently long time records. This means that the bound is an accurate predictor of performance and that the maximum-likelihood estimator is the best possible estimator under these conditions.

However, the Cramér–Rao bound generally underestimates attainable MSE under conditions of low SNR and for short data analysis windows. The Cramér–Rao bound resembles perturbation analysis in that it can be shown to rely upon a linearization of the signal model with respect to the slowness parameters. When errors become large, as they do under marginal SNR conditions, a linearized model does not capture the important features of the error statistics, resulting in an inaccurate bound. In particular, the Cramér–Rao bound does not predict the sort of threshold phenomenon that arrays exhibit, wherein the MSE increases rapidly below a threshold SNR, following a more gradual increase in MSE with declining SNR.

The need for a more accurate bound providing some prediction of threshold effects led Weiss and Weinstein (1988) to propose the function

$$\psi(\mathbf{X}, \theta) = \left[\frac{\mathrm{P}(\mathbf{X}, \theta + h)}{\mathrm{P}(\mathbf{X}, \theta)}\right]^{1/2} - \left[\frac{\mathrm{P}(\mathbf{X}, \theta - h)}{\mathrm{P}(\mathbf{X}, \theta)}\right]^{1/2}$$

where h is a parameter offset. The bound that results is more complicated:

$$\mathrm{E}\{(\hat{\theta}(\mathbf{X}) - \theta)^2\} \geqq \frac{h^2 f^2(h)}{2(1 - f(2h))} \tag{9}$$

where

$$f(h) = \int d\mathbf{X} \int d\theta \; \mathrm{P}^{1/2}(\mathbf{X}, \theta)\mathrm{P}^{1/2}(\mathbf{X}, \theta + h).$$

The offset parameter is selected to maximize the bound, usually by scanning h over a range of possible values. The indicated integrals often must be computed numerically, particularly for a wideband signal model.

The Weiss–Weinstein bound is more accurate than the Cramer–Rao bound under low SNR conditions because it compares global features of the probability model, rather than the local derivative at the true parameter value. It measures the overlap of the probability density of the data evaluated at one parameter value θ with the probability density evaluated at a different value $\theta + h$. Intuitively, if the densities do not significantly overlap, there is little chance that an ambiguity will occur between θ and $\theta + h$, and little chance of an error. Consequently, $f(h)$ is small, the bound is small, and MSE is small. If, on the other hand, the probability density

does not change significantly with large changes in the parameter, ambiguity is high, and the bound (and MSE) are large. The Weiss–Weinstein bound makes it possible to compare density ambiguity for large variations in the parameter, which accounts for its ability to predict MSE under large error conditions.

Returning to the problem at hand, the vector slowness estimation problem requires simultaneous estimation of more than one parameter (the north and east components of slowness). Multi-parameter forms for both the Cramér–Rao (Van Trees, 1968) and Weiss–Weinstein (Weinstein and Weiss, 1988) bounds exist. I use these to bound the MSE $\mathrm{E}\{(\hat{\theta}_N - \theta_N)^2 + (\hat{\theta}_E - \theta_E)^2\}$ of the estimated slowness vector.

The Cramér–Rao bound can be evaluated analytically for three-component stations in the case of a single incident plane wave. As seen in the next section, it appears to be a good predictor of three-component performance. Consequently, it is not necessary to use more complicated bounding methods to obtain a good picture of three-component performance. Assuming the signal window is T sec long, and that the signal and noise spectra are flat inside a frequency band of width B Hz and zero outside that band, the bound on the MSE averaged over both slowness parameters is:

$$\mathrm{E}\{(\hat{\theta}_N - \theta_N)^2 + (\hat{\theta}_E - \theta_E)^2\} \geqq \frac{1}{TB}\frac{1}{J}\frac{\gamma + 1}{\gamma^2} \tag{10}$$

where

$$J = \frac{1}{2}\upsilon_m{}^2 + \frac{1}{2}\frac{1}{\theta_{\max}^2}\ln\left(\frac{1}{1 - \upsilon_m{}^2\theta_{\max}^2}\right).$$

The behavior of the bound is consistent with expectations for performance. The rms error declines as $(\mathrm{SNR})^{-1}$. It is also inversely proportional to the time-bandwidth product (TB) of the data, which is, roughly, a measure of the number of independent samples (degrees of freedom) in the signal waveforms. Note that the bound estimates an average error for the ensemble of plane waves incident from all directions and for all slownesses below $\theta_{\max}$. Consequently, it shows no dependence on backazimuth or upon angle of incidence. It is inversely proportional to the surface medium velocity υ_m for large $\theta_{\max}$, which is reasonable. The lower the surface velocity, the more incoming waves are refracted into near-vertical propagation. Slowness estimates are then less reliable, because rays from all directions and velocities are packed tightly together, and noise perturbations will result in large errors. As $\theta_{\max}$ tends to zero, the *a priori* search region in slowness space becomes very restricted. The MSE is small, in this case, because *a priori* knowledge eliminates the possibility of any large errors.

The bound is derived for samples of Gaussian random processes that have roughly constant amplitude across the analysis window and flat bandwidth. The amplitude of seismic waveforms varies in time and frequency. To use the bound, I suggest estimating the effective duration and bandwidth of signals using a moment estimate (Franks, 1981):

$$\Delta = \left[12\,\frac{\int (x - x_0)^2 S^2(x)\,dx}{\int S^2(x)\,dx}\right]^{1/2} \tag{11}$$

where

$$x_0 = \frac{\int xS^2(x)\,dx}{\int S^2(x)\,dx}.$$

With S representing the signal, Δ estimates the duration T. When S represents the signal's spectrum, Δ estimates the spectral bandwidth B.

The Cramér–Rao bound is not useful for predicting array performance using the simplified model of equation (3). With the assumption of perfect spatial signal coherence, it estimates slowness MSE that is much smaller than values obtained empirically. For arrays, slowness errors are dominated in the high SNR region by signal imperfections attributable to scattering. It is only in the very low SNR region that errors become dominated by ambient noise. The Cramér–Rao bound is not useful at low SNR, again because it cannot predict the nonlinear behavior of a threshold phenomenon.

The Weiss–Weinstein bound offers the possibility of modeling large error performance at low SNR. It is one of the few methods that will work under these conditions, justifying its extra complexity. Closed-form evaluation is not possible, even with the simple signal model. Results in the following section on array performance were obtained through numerical integration, neglecting the doubly underlined term in equation (3) representing the wave field projection onto the vertical axis. This provision has the effect of making the bound slightly optimistic, since the signals are assumed to be slightly larger on the vertical axis than they actually are.

Maximum-Likelihood Estimator

To obtain an upper bound on the performance of the best three-component and array slowness estimators, the performance of a specific estimator is measured through Monte Carlo simulation. The method used is the joint maximum-likelihood estimator for both the signals and slowness parameters (Wax, 1985; Ziskind and Wax, 1988). This leads to the so-called subspace fitting methods, in which the signal model $\mathbf{G}(\omega, \boldsymbol{\Theta})\mathbf{s}(\omega)$ is fit to the observed data $\mathbf{r}(\omega)$. The best fit is obtained by minimizing the mean-square residual function:

$$E = \sum_i \| \mathbf{r}(\omega_i) - \mathbf{G}(\omega_i, \boldsymbol{\Theta})\mathbf{s}(\omega_i) \|^2. \tag{12}$$

The solution is the maximum-likelihood estimator under the assumption that the noise spectrum is flat in the frequency band where the fitting is taking place.

The mean square residual, E, is separable in the signals $\mathbf{s}(\omega)$ and the propagation parameter set Θ (Golub and Pereyra, 1973). This fact simplifies the model-fitting problem, since it allows us to fix $\boldsymbol{\Theta}$, and solve for $\mathbf{s}(\omega)$. The solution is:

$$\hat{\mathbf{s}}(\omega) = [\mathbf{G}^H(\omega, \boldsymbol{\Theta})\mathbf{G}(\omega, \boldsymbol{\Theta})]^{-1}\mathbf{G}^H(\omega, \boldsymbol{\Theta})\mathbf{r}(\omega). \tag{13}$$

This particular estimator for the signals has been shown to be superior to beamforming (see, e.g., Blandford *et al.*, 1976). To estimate the slowness parameters, substitute this expression for $\mathbf{s}(\omega)$ into (12). The resulting equation for the error

function is independent of the signal:

$$E = \sum_i \| \Pi(\omega_i, \Theta)\mathbf{r}(\omega_i) \|^2 \tag{14}$$

where

$$\Pi(\omega, \Theta) = \mathbf{I} - \mathbf{G}(\omega, \Theta)[\mathbf{G}^H(\omega, \Theta)\mathbf{G}(\omega, \Theta)]^{-1}\mathbf{G}^H(\omega, \Theta).$$

A nonlinear optimization routine minimizes (14) for the best-fitting set of slowness parameters $\hat{\Theta}$. Because the slowness parameters are restricted to the disk $\| \theta \| \leqq \theta_{\max}$ (the compressional wave assumption), the optimization is restricted to this region. The optimal slowness parameters are substituted into (13) to obtain estimates of the signals.

Results

Simulation and Theory

A comparison of arrays with three-component stations requires a specific choice of array geometry. I used the 13-element array shown in Figure 1, which was deployed in southeastern Kansas for a period of about 8 months in 1986 and 1987 (Harben *et al.*, 1987). The array aperture is about 2.2 km, and the minimum element separation is 400 m. Data were simulated for a single plane-wave incident upon the array and a three-component station at a variety of SNRs. The received signal was modeled as indicated in equation (1) for a three-component station, and as indicated in equation (3) for the array.

The purpose of the theoretical estimates of error and of the simulations is to estimate performance at low SNR, for which it is difficult to obtain adequate empirical data samples. Theoretical estimates using a plane-wave model are likely to be more accurate at low SNR than at high SNR, since the low-SNR MSE is likely to be dominated by noise effects rather than by model error. To keep the simulation consistent with the theoretical development, incident waves were simulated with perfect spatial coherence, and ambient noise was simulated to be spatially uncorrelated. Signal and noise were generated as samples of Gaussian random processes.

The signal duration and bandwidth were chosen to lie in a range representative of many *P* arrivals at moderate regional distances. Bame *et al.* (1989) report that

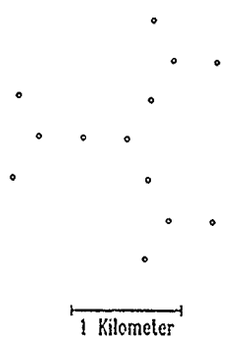

FIG. 1. Map showing the geometry of the small-aperture array used in this study. The array consisted of 13 elements spread over a 2.2 km aperture.

best results with the NORESS are obtained in the 4 to 8 Hz band. Consequently, I generated signals flat in this band with small time duration (6.4 sec). The surface medium (P) velocity was chosen to be 4.0 km/sec. The simulations were conducted using some 2,000 waveforms for each of 20 different values of SNR. The true slowness vectors were distributed uniformly in azimuth and velocity, with a minimum horizontal phase velocity of 5.0 km/sec.

The results of the theoretical analyses and simulations are summarized in Figure 2 and demonstrate markedly different behavior for arrays and three-component stations. The figure shows the Cramér–Rao bound of equation (10) for three-component stations as a function of SNR as the upper solid curve. The Weiss–Weinstein bound for the Kansas array is displayed as the lower solid curve. The simulation MSE values at discrete SNRs are shown as symbols: triangles for the three-component station and circles for the array. The theory and simulation results are consistent, which validates their correctness.

Three-component station performance declines gradually with decreasing SNR, displaying a smooth transition to a low-SNR asymptotic plateau determined by the *a priori* limits on slowness. On the other hand, array performance exhibits a fairly sharp transition at a threshold SNR around 0.2 to 0.4 from a regime of fairly low error to the asymptotic value. Between this sharp threshold and an SNR of about 1.0, the array provides useful slowness information, but the three-component station does not.

The Cramér–Rao bound on three-component station performance indicates that no other choice of estimator will close the gap between three-component station and array performance. The maximum-likelihood estimator achieves the optimal MSE down to an SNR of one. The array maximum-likelihood estimator is also optimum for high SNR, as expected. On the other hand, at low SNR, the Weiss–Weinstein bounds on array performance indicates that the array estimator might

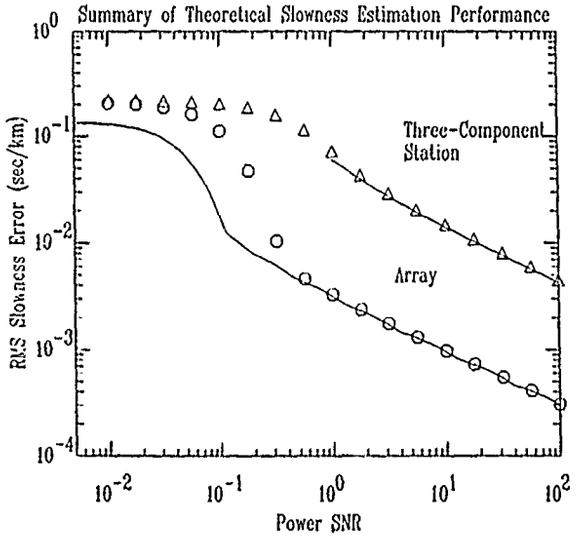

FIG. 2. Summary of theoretical and simulation estimates of rms slowness error for the Kansas array and a three-component station, assuming a frequency band of 4 to 8 Hz and a signal duration of 6.4 sec. The top solid line is the Cramér–Rao bound on three-component MSE, and the triangles are the three-component simulation MSEs. The bottom line is the Weiss–Weinstein bound on the array MSE. The open circles are the array simulation MSEs. The Cramér–Rao bound ensures that the performance gap between three-component stations and arrays will not be closed by new three-component estimators.

be improved, potentially widening the gap between array and three-component station performance.

The contrast between the abrupt transition of array performance and gradual decline of three-component station performance is graphically evident in Figure 3, where slowness estimates are rendered as scatter diagrams. In this simulation, slowness vectors were estimated for 2,000 sample waveforms nominally propagating from the same direction. The estimates disperse due to the effects of additive noise. Array slowness estimates are characterized by a single cluster down to a low SNR (0.1), whereupon a significant number of outliers appear. This effect may not be commonly observed, since at a power SNR of 0.1, the signal is not visible on any single channel. Most events used in empirical studies are at least visible. Operating an array in this region entails an element of risk: good slowness estimates are obtained most of the time, but occasional large outliers occur.

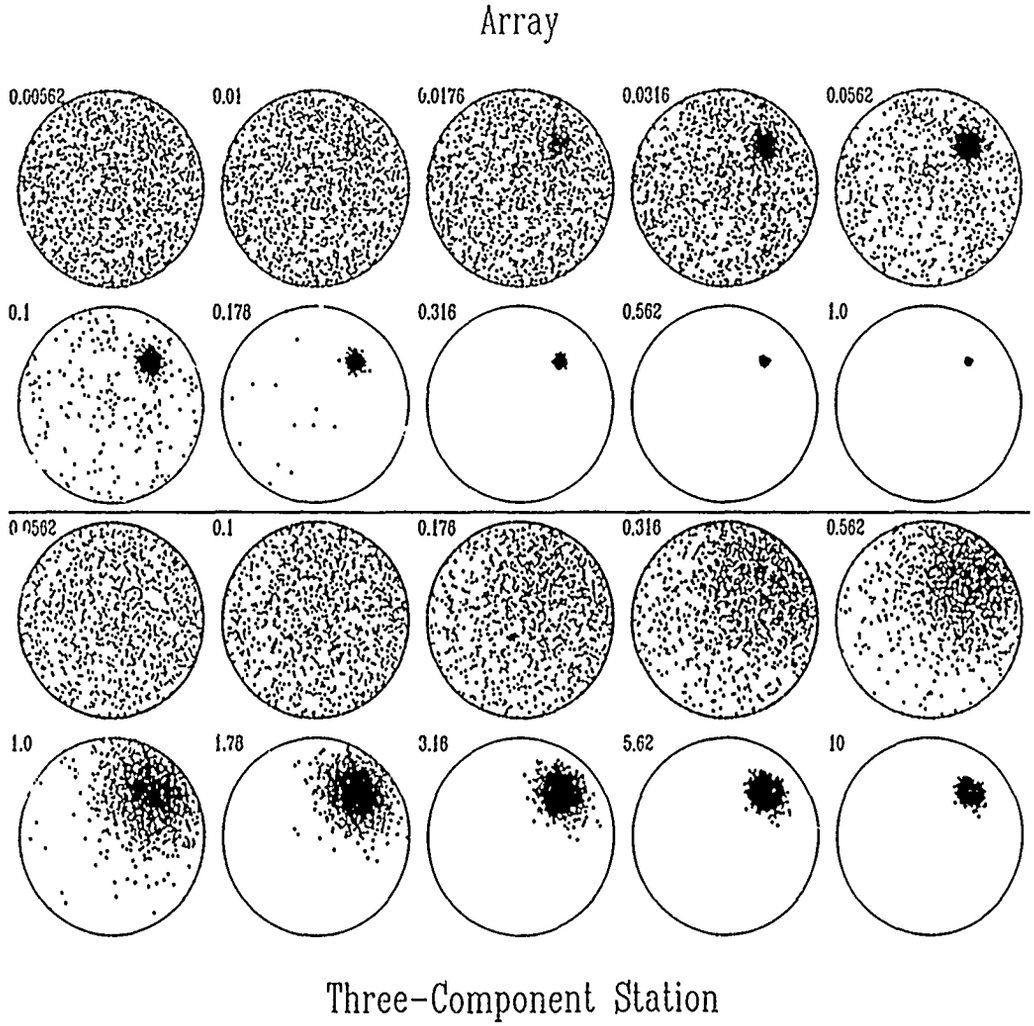

FIG. 3. Scatter diagrams showing the distribution of 2,000 slowness estimates for waves with a nominal fixed slowness (backazimuth 45°, velocity 8.2 km/sec) for the array and a three-component station. Each circle represents the slowness plane out to a radius of 0.2 sec/km. The (power) SNRs for the array plots (*above*) are a factor of 10 lower than the SNRs for the three-component station (*below*). SNRs are indicated at the upper left of each diagram. Three-component stations exhibit a gradual decay of performance with decreasing SNR; the array shows an abrupt transition at SNR = 0.1.

Empirical Results

To determine the limitations of the theoretical analysis and to obtain realistic estimates of high-SNR array performance, an empirical study was conducted with 23 events located at one mine and recorded at the Kansas array. A sample waveform for the P phase is shown in Figure 4. Note that the power SNR exceeds 100 for most frequencies in this example waveform. The SNR was generally in excess of 30 for the 23 events used in the study. The mine was located 150 km from the array, which is near the crossover distance for *Pn* and *Pg*. These phases are superimposed in the 6 sec P window shown in the figure. Because the waves are superimposed, it is necessary to perform a joint estimation ($d = 2$) of the slowness parameters of both phases. Failure to perform a joint estimation results in excessively large estimates of MSE.

The results of slowness estimation using the maximum-likelihood algorithm with $d = 1$ and $d = 2$ are shown as scatter diagrams in Figure 5. Two cases are shown: a

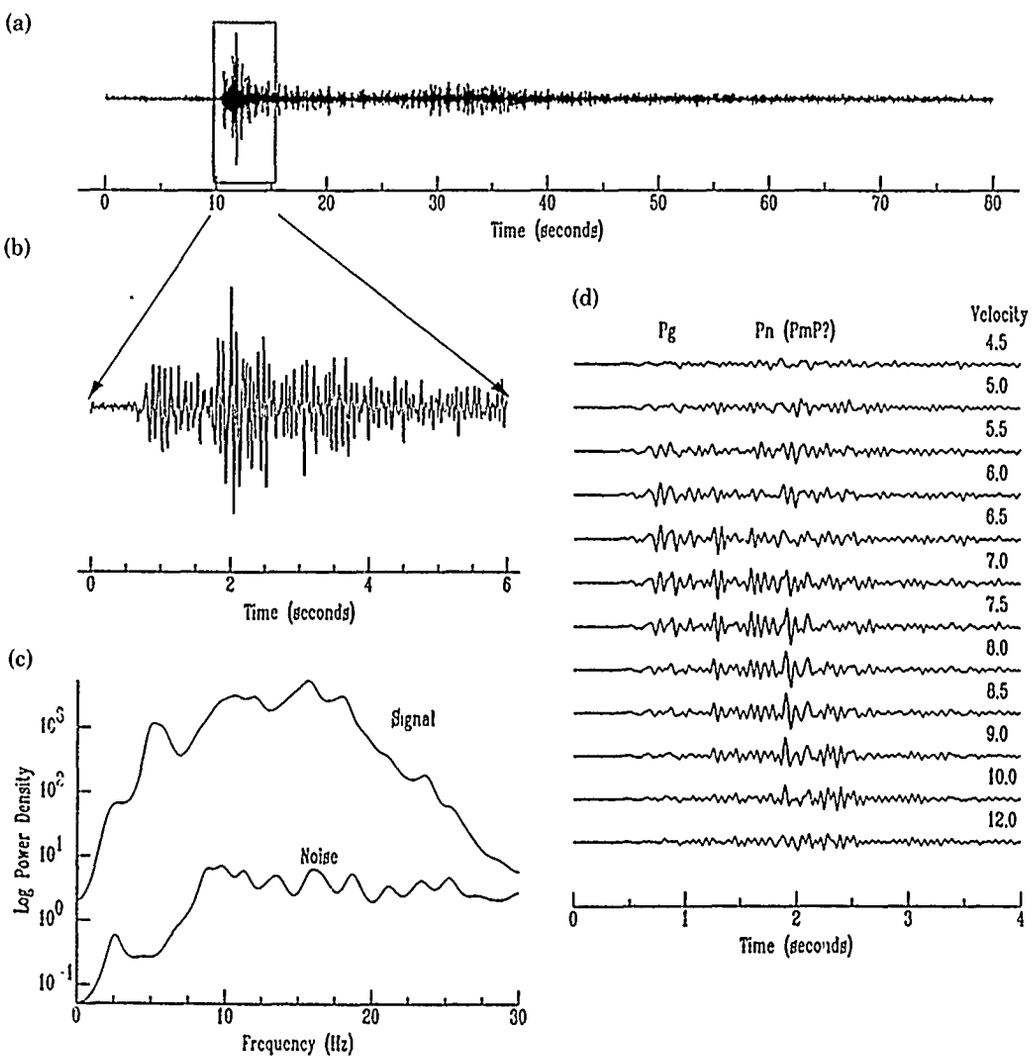

FIG. 4. (a) Typical event used in the empirical study. (b) Six second P analysis window. (c) Representative signal and noise spectra. (d) Spread of beams scanned over velocity. The traces are labeled on the right with their respective velocities. Both *Pn* and *Pg* are present in the analysis window. The source region was 150 km from the array, near the *Pn*/*Pg* crossover.

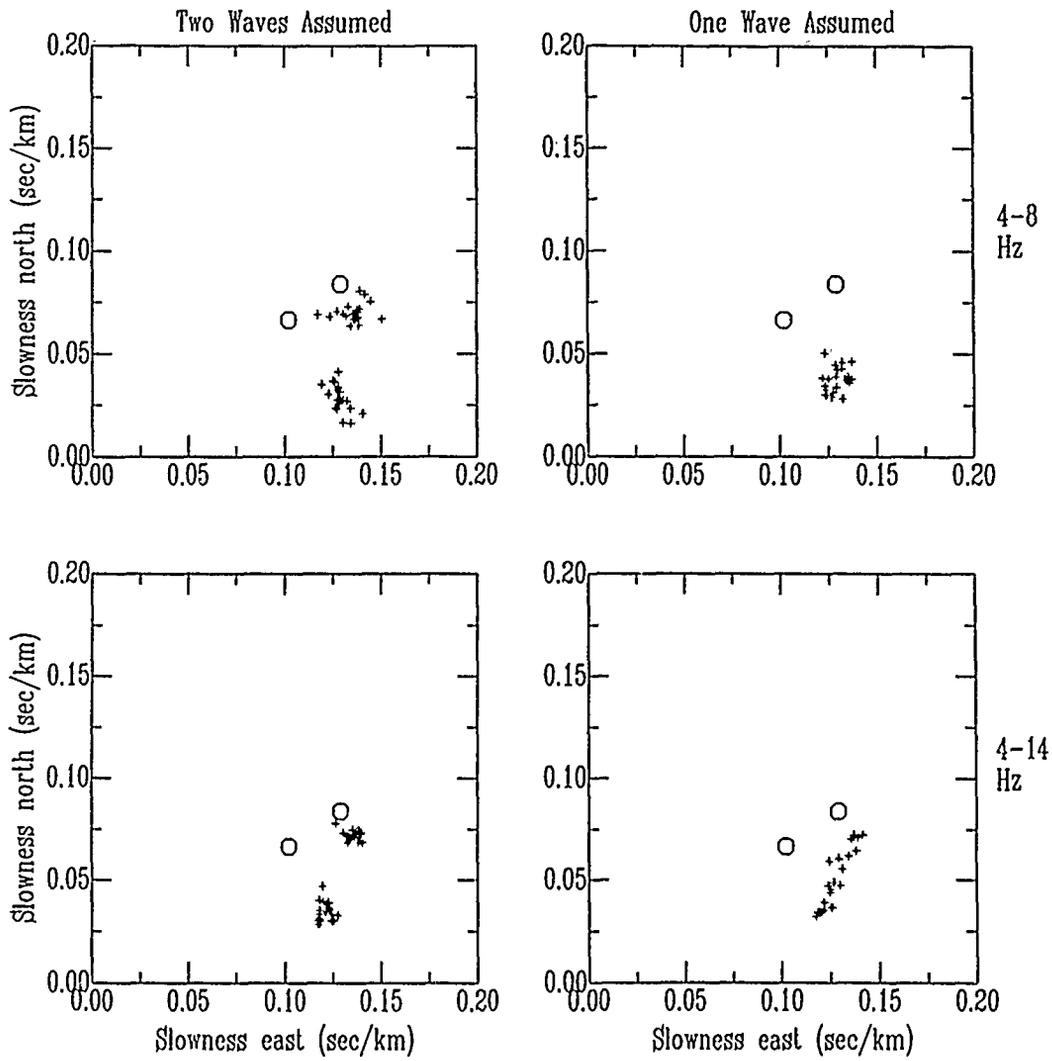

FIG. 5. Scatter plots showing the slowness estimates for *P* windows from 23 events. Each plot represents the northeast quadrant of slowness space. Two frequency bands were used: 4 to 8 and 4 to 14 Hz. The measured signal duration was 3.6 sec, and the measured bandwidth was 3.0 Hz in the first band. Using the maximum-likelihood estimator assuming two waves were present, *Pn* and *Pg* are well resolved. The open circles represent the theoretical slownesses for the two phases, and indicate substantial refraction for both phases in the clockwise direction. In the 4 to 14 Hz band, the measured signal duration was 3.9 sec, and the measured bandwidth was 8.4 Hz. Resolution in this band is approximately 1.6 times better. The slowness estimates, assuming a single wave present, are shown on the right. In the 4 to 14 Hz band, estimated rms error triples with the single arrival assumption.

low-frequency case with the data filtered to a moderate bandwidth (4 to 8 Hz), and a relatively wideband, high-frequency case (4 to 14 Hz). When two waves ($d = 2$) are assumed, the estimator produces two distinct clusters of slowness vectors corresponding to *Pn* and *Pg*. The "true" locations of the slowness vectors determined by the direction to the mine (backazimuth: 57°), and assumed *Pn* and *Pg* velocities (8.2 and 6.5 km/sec, respectively) are indicated on the plots. Lateral refraction is severe in this environment, with both *Pn* and *Pg* slowness estimates being rotated clockwise from their theoretical locations. *Pn* is affected more strongly than *Pg*, showing a bias of approximately 20°.

The bias caused by horizontal refraction from the slowness estimates prior to calculating the MSE was subtracted. This correction seems permissible in the

context of calibrated array operations. The rms error is 0.0078 sec/km in the 4 to 8 Hz band and 0.0049 sec/km in the 4 to 14 Hz band. These errors are small compared to empirical calculations of MSE made from uncorrected estimates. Jarpe and Dowla (1989) report a standard deviation for backazimuth error of 6° for a three-component station within the NORESS. From simple geometrical considerations, the standard deviation of slowness estimates and backazimuth estimates are related approximately by

$$\sigma_\theta = \sigma_\xi \frac{\pi}{180v},$$

where v is the horizontal phase velocity, ξ represents backazimuth, and θ represents slowness. For a horizontal phase velocity of 7.0 km/sec and an average backazimuth error of 6°, the equivalent slowness standard deviation is 0.014 sec/km (2 to 3 times larger than the results obtained here). This result may reflect regional differences, the unavailability of calibrations, or the use of a three-component station instead of an array.

Estimates of backazimuth MSE are commonly made assuming that the P phase window contains a single phase. If the several phases are present, this assumption can lead to an overestimate of the error. This situation is illustrated in Figure 5 for the scatter plots labeled "one wave assumed." In the 4 to 8 Hz band, the single cluster of estimates has a corrected rms error of 0.0078 sec/km, which is the same as the error when two waves were assumed. However, in the 4 to 14 Hz band, an elongated cluster (stretched between the two clusters of the $d = 2$ case) has a corrected rms error of 0.0162 sec/km. This value is three times the error obtained when two waves are assumed in the signal model.

The empirical results modify the theoretical picture of performance by placing a floor on the MSE at large SNR. The theoretical picture suggests three distinct regions of performance behavior as a function of SNR: a high SNR region where the error behaves as $(\mathrm{SNR})^{-1}$, a transition region where it undergoes a rapid increase to an asymptotic plateau, and the low SNR plateau where the signal has been completely overwhelmed by noise. The empirical MSE is much larger than the theoretical estimate of performance in the high SNR region. Figure 6 displays theoretical bounds and the empirical error levels obtained for the $d = 2$ analysis covering the two frequency bands (4 to 8 and 4 to 14 Hz). Recognizing that the signals are not flat in the time or in the frequency domain, the actual durations and bandwidths of the signals were measured in these two bands from the sample waveforms of Figure 4, using the method of moments (equation 11).

The Weiss–Weinstein bounds were computed for the measured durations, bandwidths, and center frequencies, and are displayed in Figure 6. The increase in bandwidth and center frequency significantly lowers the error at high SNR and moves the threshold lower by a factor of two in power SNR. The empirical rms errors are plotted as levels, and indicate that array performance will saturate at levels approximately equal to the threshold error. Consequently, the theoretical picture of a high SNR region with MSE inversely proportional to SNR is replaced with a region of saturation beginning close to the threshold SNR.

Discussion

It is no surprise that arrays perform better than three-component stations under low SNR conditions. However, the difference in their failure mechanisms is

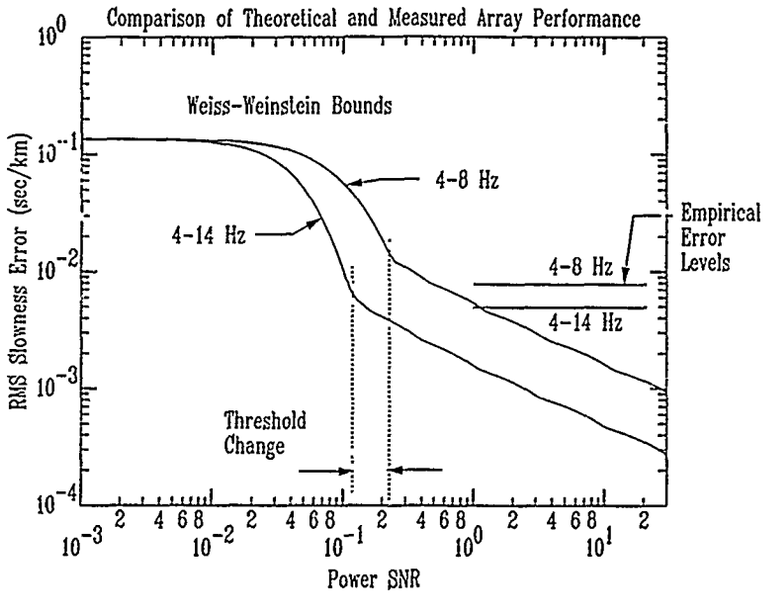

FIG. 6. Empirical measurements indicate that array performance saturates at high SNR and that performance improves with increasing bandwidth. Theoretical results indicate that increased bandwidth should lower the SNR threshold below which array performance deteriorates rapidly.

less well known and noteworthy. The phenomenon of the array performance "cliff" occurs because of the way slowness parameters are embedded in the signal. Generally, a threshold phenomenon is expected when the parameters being estimated appear in the signal in a *nonlinear* fashion (Wozencraft and Jacobs, 1965). Slowness parameters appear in the propagation delays of an array signal, which is a highly nonlinear model (i.e., changing the parameters does not just scale the signal). At high SNR, slowness estimates are "locked" by the relative propagation delays between stations. Seismic signals are characteristically medium-bandwidth signals and are often oscillatory with some dominant period. Estimates of propagation time delay between pairs of stations in an array tend to jump by integer multiples of the dominant period. At high and even medium SNR, such "cycle-skipping" errors are rare. Consequently, the errors in estimating slowness remain small. At the point where noise completely overwhelms the signals, the "lock" is broken and the slowness error rises quickly, accounting for the threshold phenomenon.

By contrast, the slowness parameters appear almost linearly in the three-component signal model (cf. equation 2). Since the signal amplitudes depend almost linearly on the slowness parameters, additive ambient noise directly affects parameter estimates. Hence, performance declines in nearly direct proportion to decreases in the SNR.

Optimality of Estimators

Comparison of the measured performance of the maximum-likelihood estimator to the Cramer–Rao bound indicates that the bound is tight for three-component stations. This implies that the maximum-likelihood estimator is optimal for a single plane wave in spatially uncorrelated noise. This estimator is equivalent to the conventional method described by Jarpe and Dowla (1989). They found little difference between this estimator and many others (Christoffersson *et al.*, 1988;

Jurkevics, 1988; Magotra *et al.*, 1989; Mantalbetti and Kanasewich, 1970; Rūūd *et al.*, 1988). The optimality, or near optimality, of all of these methods is a result of the simplicity of the three-component signal model. The results shown here indicate that there is little scope for improving existing three-component direction estimation methods, except for methods derived from more complicated models. More complicated models might take into account scattering, interference by other signals, or spatially correlated noise.

The Weiss–Weinstein results for arrays suggest that there is some scope for improvement in slowness estimators, even within the simple signal model. This result confirms another evaluation of the bound for narrowband signals (Nohara and Haykin, 1988). One possibility for improvement, raised by Weiss and Stein (1987), is that better threshold region performance can be obtained with an incoherent beamforming method using cross-correlations of the signal envelopes instead of the signals themselves.

Conclusions

For the specific array geometry considered in this paper, the array appears to have usable performance in a power SNR range (0.2 to 1.0) where three-component stations provide no usable estimates of incident wave slowness. The slowness errors of three-component stations appear to be dominated by noise below a power SNR of 10 (amplitude SNR of 3.2) in a 4 Hz frequency band. This result is consistent with the results of Suteau-Henson and Ryall (1989), who found that noise affected bearing estimates for three component stations below an SNR threshold of about 2. Above the array threshold SNR, the performance of the Kansas array appears to be dominated by variations in the signal, presumably induced by scattering (cf. Goldstein and Archuleta, 1990). With calibration, the high SNR rms slowness error may be as low as 0.005 sec/km (4 to 14 Hz). For regional P phases, that value is equivalent to a 95 per cent backazimuth confidence interval of ±4°.

The empirical study demonstrated that the maximum-likelihood estimation algorithm has the capability of resolving waves separated by less than 0.05 sec/km in slowness. The resolution of the Kansas array probably approaches 10° for regional P phases when this algorithm operates in the 4 to 14 Hz band. Since three-component stations theoretically have no ability to resolve superimposed waves of like polarization, arrays have the additional advantage of being able to detect arrivals in the presence of strong interference.

Acknowledgments

This research was work performed under the auspices of the U.S. Department of Energy by the Lawrence Livermore National Laboratory under Contract No. W-7405-ENG-48. I would like to thank the Office of Arms Control, DOE, for supporting this research and NORSAR for providing support to present this work at the Symposium on Regional Seismic Arrays and Nuclear Test Ban Verification in Oslo, Norway. I would like to thank an anonymus reviewer, Peter Goldstein, and Steve Jarpe for their careful reviews of the manuscript and many helpful suggestions. I would also like to thank Jim Berryman, Eric Chael, John Claassen, and Fred Followill for their helpful comments.

References

Bame, D., M. Walck, K. Hiebert-Dodd, and G. Elbring (1989). Azimuth estimation capabilities of the NORESS regional seismic array, 1989 AGU Fall Meeting, San Francisco (abstract in *EOS* **70**, 1223).

Blandford, R., T. Cohen, and J. Woods (1976). An iterative approximation to the mixed-signal processor, *Geophys. J. R. Astr. Soc.* **45**, 677–687.

Bratt, S. and T. Bache (1988). Locating events with a sparse network of regional arrays, *Bull. Seism. Soc. Am.* **78**, 780–798.

Cadzow, J. (1988). A high resolution direction-of-arrival algorithm for narrow-band coherent and incoherent sources, *IEEE Trans. Acoustics, Speech, and Signal Proc.* **36**, no. 7, 965–979.

Christoffersson, A., E. Husebye, and S. Ingate (1988). Wavefield decomposition using *ML*-probabilities in modelling single-site 3-component records. *Geophys. J.* **93**, 197–213.

Dowla, F. and D. Harris (1987). Direction estimation of vector-planewave fields, *IEEE Intl. Conf. Acoustics, Speech, and Signal Proc.* **4**, 2225–2228.

Franks, L. (1981). *Signal Theory*, Dowden & Culver, Stroudsburg, Pennsylvania, 136.

Goldstein, P. and R. Archuleta (1990). Deterministic frequency-wavenumber methods and direct measurements of rupture propagation during earthquakes using a dense array—theory and methods, *J. Geophys. Res.* (in press).

Golub, G. and V. Pereyra (1973). The differentiation of psuedo-inverses and non-linear least squares problems whose variables separate, *SIAM J. Numer. Anal.* **10**, 413–432.

Harben, P., A. Smith, and D. Harris (1987). Siting and deployment of the Kansas seismic array, UCID-21048, Lawrence Livermore National Laboratory, Livermore, California.

Harris, D. (1987). Planar array bearing estimation performance bounds, *Proc. 21st Asilomar Conf. on Signals, Systems and Computers*, November 2–4, Pacific Grove, California.

Jarpe, S. and F. Dowla (1989). Performance of high-frequency three-component stations for azimuth estimation from regional seismic phases, UCRL-101181, Lawrence Livermore National Laboratory, Livermore, California.

Jurkevics, A. (1988). Polarization analysis of three-component array data, *Bull. Seism. Soc. Am.* **78**, 1725–1743.

Magotra, N., N. Ahmed, and E. Chael (1989). Single-station seismic event detection and location, *IEEE Trans. Geosci. Remote Sensing* **27**, 15–23.

Montalbetti, J. and E. Kanasewich (1970). Enhancement of teleseismic body phases with a polarization filter, *Geophysical J. R. Astr. Soc.* **21**, 413–416.

Nohara, T. and S. Haykin (1988). Application of the Weiss–Weinstein bound to a two-dimensional antenna array, *IEEE Trans. Acoustics, Speech and Signal Proc.* **36**, 1533–1534.

Ødegaard, E., D. Doornbos, and T. Kværna (1990). Surface topographic effects on arrays and three-component stations, *Bull. Seism. Soc. Am.* **80**, 2214–2226.

Papoulis, A. (1965). *Probability, Random Variables, and Stochastic Processes*, McGraw-Hill, New York, 456.

Rūūd, B., E. Husebye, S. Ingate, and A. Christoffersson (1988). Event location at any distance using seismic data from a single three-component station, *Bull. Seism. Soc. Am.* **78**, 308–325.

Suteau-Henson, A. and A. Ryall (1989). Azimuth and slowness estimation from three-component and array stations at NORESS, 1989 AGU Fall Meeting, San Francisco, California (abstract in *EOS* **70**, 1223).

Van Trees, H. (1968). *Detection, Estimation and Modulation Theory*, vol. 1, John Wiley and Sons, New York.

Wax, M. (1985). Detection and estimation of superimposed signals, *Ph.D. Dissertation*, Stanford University, Stanford, California.

Weinstein, E. and A. Weiss (1988). A general class of lower bounds in parameter estimation, *IEEE Trans. Information Theory* **34**, 338–343.

Weiss, A. and Z. Stein (1987). Optimal below threshold delay estimation for radio signals, *IEEE Trans Aerospace Elec. Systems* **23**, 726–730.

Wozencraft, J. and I. Jacobs (1965). *Principles of Communcation Engineering*, John Wiley and Sons, New York.

Ziskind, I. and M. Wax (1988). Maximum likelihood localization of multiple sources by alternating projection, *IEEE Trans. Acoustics, Speech and Signal Proc.* **36**, 1553–1560.

TREATY VERIFICATION PROGRAM
LAWRENCE LIVERMORE NATIONAL LABORATORY
LIVERMORE, CALIFORNIA 94550

Manuscript received 18 February 1990

Bulletin of the Seismological Society of America, Vol. 80, No. 6, pp. 1969–1986, December 1990

TELESEISMIC *P* CODA ANALYZED BY THREE-COMPONENT AND ARRAY TECHNIQUES: DETERMINISTIC LOCATION OF TOPOGRAPHIC *P*-TO-*Rg* SCATTERING NEAR THE NORESS ARRAY

BY S. C. BANNISTER, E. S. HUSEBYE,* AND B. O. RUUD

ABSTRACT

P-wave coda of 75 sec duration from eight teleseismic events recorded by the NORESS array, Norway, were examined using both array and three-component analysis techniques. The array data have been analyzed using the semblance technique that allows us to determine accurately the time of arrival, apparent velocity, and azimuth of the scattered waves. Coda coherency was found to vary considerably, probably reflecting extended source duration for some events. Slow beam amplitude decay rates support significant coda generation within the source region although source-end scattering could not be separated from the source pulse *per se*. At the receiver end of the path, we resolved locally scattered wavelets even within highly coherent teleseismic *P* coda by subtracting the teleseismic array beam from the records. The majority of receiver-end scattering contributions appear to be *P*-to-*Rg* conversions occurring in both forward and backward directions from two nearby areas with pronounced topographic relief, namely Bronkeberget (distance ~ 10 km, azimuth ~ 80°) and Skreikampen (distance ~ 30 km, azimuth ~ 225°). The scattering is multiple in the sense that both primary and secondary phases from the source region contribute to the scattered *Rg* waves. *P*-to-*S* scattering constitutes a significant part of the receiver-end scattering observed later in the *P* coda, although it is more diffuse than *Rg* and forward scattering is more dominant. *P*-to-*P* scattering is weak and mostly confined to the immediate vicinity of the array. The analysis of individual three-component records shows high sensitivity to interference from locally scattered waves. This interference is probably responsible for a marked decrease in apparent velocity observed for some events 3 to 4 sec after *P* onset.

INTRODUCTION

The classical earth model involving spherically symmetric layers is valid only as a first approximation besides being useful in the computation of synthetic seismograms. Although dominant and deterministic seismogram features like *P*, *S*, and surface waves can be accounted for using such models, their codas cannot be. Coda waves arriving after deterministic phases are broadly attributed to seismic wave scattering phenomena associated with lateral heterogeneities located within the crust and mantle, while precursors to *PKIKP* and related phases reflect heterogeneities near the core-mantle boundary. Velocity and density heterogeneities, in addition to generating coda waves, can cause changes in waveform, phase (or travel time), and amplitude fluctuations as well as attenuation of the direct (deterministic) phase arrivals. Overall, the wave scattering reflects the dominant wavelength of the seismic signal relative to the scale length of the heterogeneities, which may vary from the grain size of rocks to the lowest mode of global spherical harmonics; an instructive overview is given by Wu and Aki (1988).

Seismic wave scattering in a heterogeneous earth has motivated numerous theoretical studies. Most of these studies are aimed at obtaining approximate solutions to the wave equation for a medium characterized by a few parameters such as scale

* E. S. Husebye is on leave of absence from NTNF/NORSAR, P.O. Box 51, N-2007 Kjeller, Norway.

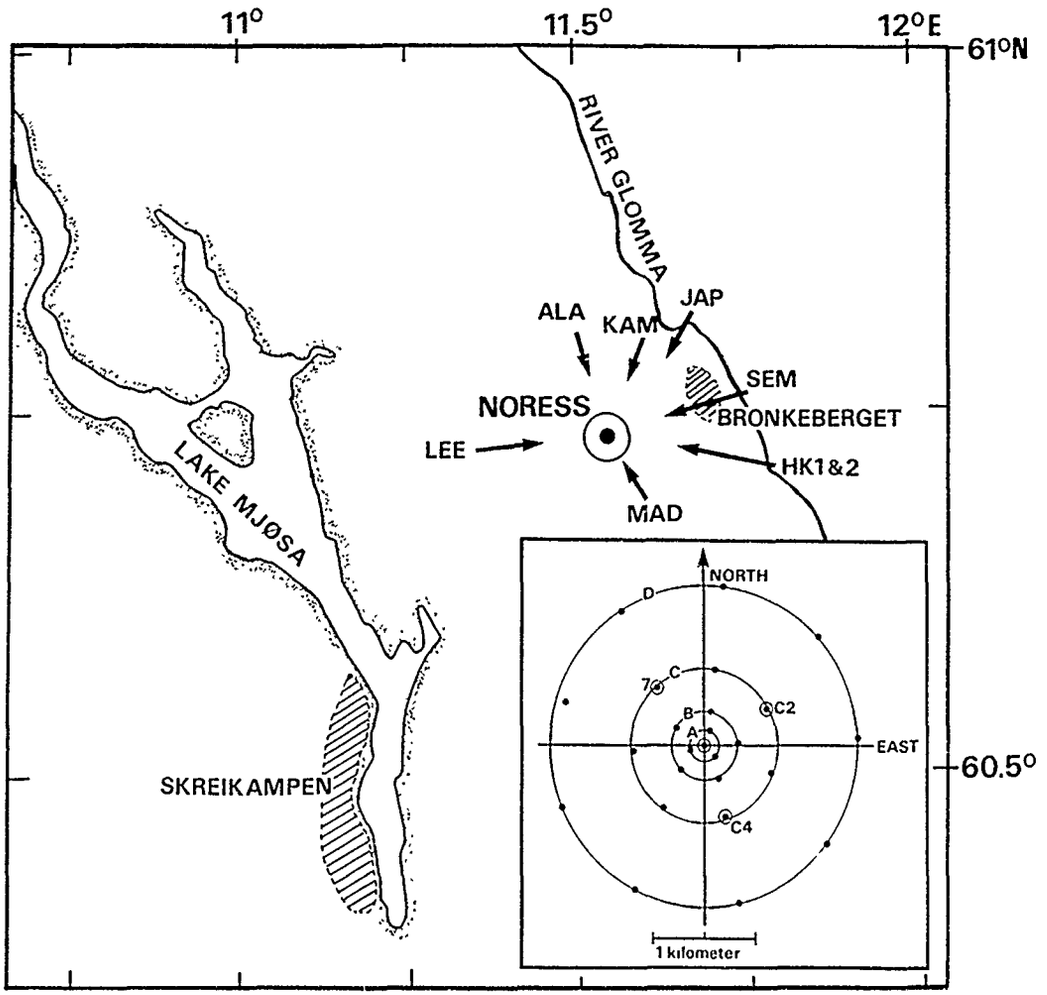

FIG. 1. The general NORESS array area with scattering locations hatched. The arrows give the direction of approach of arrivals from the events analyzed (Table 1). The array configuration is given in the lower right insert where encircled stations indicate three-component sites.

length and perturbation index (rms variation of velocity and density). Other studies concentrate on calculating the seismic response of wedge structures, Moho and topographic undulations, and geological structures of irregular geometry. In such studies, it is not always clear which propagation effects (e.g., mode conversion, diffraction, and medium-related anisotropy) are included. Some of these problems can be reduced by using finite-element methods (Herraiz and Espinosa, 1987; Frankel, 1989).

Observational studies of wave scattering effects are problematic due to weak signal correlation, even when small arrays are used. This seems to be one reason why observational scattering parameters are often tied to coda envelopes and decay rates while wave types and associated propagation paths constituting the coda waves are often not specified. An exception is the amplitude and phase fluctuations of initial *P*-wave arrivals, as demonstrated by Aki (1973) and Berteussen *et al.* (1975) using the random media theory of Chernov (1960). These studies led to the tomographic mapping approach or ACH method of Aki *et al.* (1977).

In this study we focus on attributes of teleseismic *P*-coda waves as recorded by the small aperture NORESS array in southern Norway (Fig. 1; Ingate *et al.*, 1985).

Our aims are to first decompose the coda waves into specific phase arrivals and associated slowness vectors and second, to provide an insight into the scattering processes that are most important in generating the coda waves of teleseismic *P* signals.

P Coda Generation: Source or Receiver Contributions?

An important parameter in scattering theory is the dimensionless quantity ka where k is the wavenumber and a the correlation distance in random media theory or scale length of the structural heterogeneities. For teleseismic *P* coda with frequencies in the range of 1 to 3 Hz and structural heterogeneities of the order of 0.1 to 10 km, the factor ka may vary from 0.1 to approximately 30. The latter size of heterogeneity has been confirmed from *P* phase and amplitude studies in the area of the NORESS site (Aki *et al.*, 1978; Haddon and Husebye, 1978; Flatté and Wu, 1988) while the smaller scale length of about 1 km or less has been observed in many scattering studies around the world from coda analysis of high-frequency local events. Small angle or forward scattering would be important for $ka \gg 1$ in which case sections of the coda should realistically be associated with scatterers in the source-azimuthal plane. When $ka \sim 1$, however, wide-angle scattering contributions are expected to be relatively strong. Conversions between different wave types are most efficient when structural anomalies involve both velocity and density. The crust and the surface topography are, on this basis, likely to play an important role in the generation of scattered waves. Second-order or multiple scattered waves are generally considered to be of little importance since the earth appears to be weakly heterogeneous (i.e., density and velocity rms fluctuations seldom exceed 5 per cent). The relative excitation of the coda may vary with wavelength or equivalent signal frequencies given that the length distribution of scatterers is peaked around 10 km (Flatté and Wu, 1988).

Scattering can conceptionally be thought of as occurring in three principal areas for teleseismic waves, namely in the source region of the earthquake, along the wave path in the mantle (say below 400 km) and finally, near the receiver. We discuss each of these areas below.

Source Area Scattering. The size and focal depth of an earthquake is obviously of some importance, at least in regards to the time duration of scattering within the source region. Scattering contributions may arise from multiple *P* reflections within layers of the crust and lithosphere as well as possible *S*- or *Rg*-wave conversions to *P*. Intuitively, the coda contribution of near-source scattering is expected to be relatively coherent when observed at teleseismic distances because of the small variation in take-off angle. To study source-end scattering, it would be necessary to use data from several stations (Lynnes and Lay, 1989).

Transmission Path Scattering. For relatively short distances of 20° to 30°, layered structures within the lithosphere and asthenosphere may act as a wave guide, thus contributing significantly to the *P* coda as demonstrated by Kennett (1987) and Korn (1988). Somewhat similar effects have been noted by King *et al.* (1977) in the analysis of *PP* precursors, where distinct differences between observed slownesses were attributed to $P_{400}PP$ at the source end and $PP_{400}P$ at the receiver end of the propagation path; see also Nikolaev and Troitskiy (1981).

Receiver-End Scattering. In general, there is some differentiation here between two effects—that resulting from large scale heterogeneities, including continental and oceanic transition structural regimes, such as off the west coast of Norway, and second, small-scale scatterers in the crust and lithosphere, including

rough topography. In the latter case *P*-to-*Rg* conversion should result if the topography undulations are at least of the order of half the Rayleigh wavelength, approximately 1 to 2 km (Frankel, 1989). The west Norway mountain area about 100 to 300 km away from the NORESS seismic array is thus a candidate for such scattering.

Data and Analysis Techniques

Given that several mechanisms may contribute to coda wave generation, we attempt to isolate individual scattering sources through careful event selection. Chosen events (listed in Table 1) give good azimuth coverage, thus illuminating potential scatterers from a multitude of directions. We used three-component recordings from the 4 three-component stations within the NORESS array (Fig. 1), as well as vertical component data from the A0, C-, and D-rings of the whole array (i.e., A0, C-, and D-rings). Essential signal parameters extracted—those necessary for deducing wave type and propagation paths—are polarization (particle motion) and slowness vectors in specific time windows.

Analysis Techniques

Optimum use of the various filtering options is important in array wave field recording and coda analysis. Bandpass filtering in the range of 0.5 to 3.0 Hz is used to suppress part of the ambient noise. Source-end scattering contributions and the signal pulse itself are taken to be represented by the array beam trace resulting from aiming the array toward the epicenter. The residual trace (i.e., the difference between single sensor records and the beam trace) enhances receiver-end scattering contributions. Beamforming on the basis of residual traces then gives a relatively powerful tool for pinpointing scattered wavelets. Simple rotation of the NS and EW components into radial and transverse components relative to the epicenter and/or scattering sources can be used to isolate specific wave types in the records.

Data analysis included *f-k* and semblance analysis (Husebye and Ruud, 1989). Both of these give good separation of body and surface waves even for a small aperture array like NORESS. We also experimented with semblance velocity analysis of the radial and transverse components of the 4 three-component stations (Fig. 1), but the results were not instructive due to the odd configuration of this

TABLE 1

Hypocenter Parameter Events

Event	Date	Origin Time	Latitude	Longitude	Distance	Azimuth	Depth	m_b/Ms
KAM	11 Jan. 88	21:07:29.7	54.78N	161.66E	62.1	19.0	43	5.8/4.9
JAP	12 Dec. 87	04:51:50.5	29.69N	140.02E	80.3	43.6	164	6.3/—
SEM	14 Sept. 88	04:00.00.0	49.87N	78.82E	37.9	75.2	0	6.0/4.5
HK1	29 July 85	07:54:44.5	36.21N	70.90E	44.2	95.7	102	6.5/—
HK2	7 May 86	23:25:25.9	36.37N	70.71E	44.0	95.8	223	5.6/—
MAD	14 May 85	13:25:01.2	10.72S	41.26E	75.2	149.8	37	5.8/5.6
LEE	16 Mar. 85	14:54:43.7	16.98N	62.46W	67.4	264.6	20	6.1/6.4
ALA	6 Mar. 88	22:35:38.1	56.95N	143.03W	60.6	344.4	10	6.8/7.6

Hypocenter parameters of the events analyzed (from ISC and PDE catalogs); distances and azimuths (in °) are calculated relative to the NORESS array. Event regions are: KAM, Kamchatka; JAP, Japan (south of Honshu); SEM, Semipalatinsk (East Kazakh); HK1 and HK2, Hindu Kush; MAD, NW of Madagascar; LEE, Leeward Island; and ALA, Alaska.

mini-array. At least one additional three-component station is needed in the C-ring to facilitate such analysis.

Three-component analysis techniques available include that of Vidale (1986), Plešinger *et al.* (1986), Park *et al.* (1987), Jurkevics (1988), Christoffersson *et al.* (1988), and Roberts and Christoffersson (1990). We have used the latter in our coda analysis. This technique works in the complex demodulate domain, a complex time domain, efficiently decomposing three-component signals to obtain instantaneous estimates of the real and quadrature parts (amplitude and phase) of the energy within selected frequency bands. Various attributes of the seismic coda can be easily obtained from the array and three-component records. Below, we outline the attributes used in this study.

Azimuth. The azimuth is estimated from the observed cross-spectral densities between the horizontal and vertical components. Although this estimate is instantaneous, some averaging within a window around 1 cycle long is usually done to improve stability. In the analysis of array data, the slowness vector (apparent velocity and azimuth) is tied to the maximum beam power (f-k) or the maximum coherence (semblance).

Incidence Angle and Apparent Velocity. The incidence angle is determined from the cross-spectral density between the vertical and radial components. This angle can be converted to a velocity estimate given assumptions about the local P-wave velocity and Poissons ratio or using known epicenter locations for calibration. For an array, the apparent velocity is estimated directly from move-out times; the resolution is poor when the apparent wavelength of the signal greatly exceeds the array aperture (i.e., the teleseismic window for the NORESS array).

Phase Difference Between Components. We can examine the instantaneous phase difference between the rotated radial and vertical component, or equally between other pairs of components, using the phase information retained in the three-component analysis. A phase difference of 180° between the two components corresponds to pure P-wave particle motion, 0° difference represents pure SV-wave particle motion, while a phase difference of ±90° represents elliptical particle motion, as expected for example for Rayleigh waves but also for SV waves with postcritical incident angles.

Array Semblance and Three-Component Signal Polarity. Our confidence in the signal attributes derived above depends on the associated semblance and polarity estimates. Semblance values (A0 plus C- and D-ring) for random data seldom exceed 0.2 for the frequency range and time window lengths used. If corresponding values are observed in the coda sections, they are considered marginal or not significant unless the associated estimates of the slowness vector remain stationary over a few cycles. For three-component analysis, we can use various measures of the extent of polarization of the signal, including for example the chi-square model fit measure of Christoffersson *et al.* (1988), for which the significance is marginal for values below 0.5. To avoid lengthy explanations, we use a common denominator for both semblance and polarity measured: signal coherency.

Practical Considerations. The major difficulty faced in coda analysis is that of dealing with interference resulting from multiple wavelets arriving, at least partly, simultaneously. In such case, the recorded signal involves rapid variations in the polarization, with fluctuations in both calculated azimuth and angle of incidence. The previously mentioned signal attributes are calculated using a sliding window approach. Window lengths are around 1 to 2 cycles (1 to 2 sec), while the updating frequency is $\frac{1}{3}$ or $\frac{1}{4}$ of this length. Overall, we concentrate on separating signals

where the polarization, phase, semblance, and slowness are such that clearly definable phases exist, examining their consistency over time and their spatial correlation across the NORESS array.

Results

Together, eight events were analyzed, and the results will be presented with a subdivision into source- and receiver-end contributions. Appropriate results from individual events are addressed in some detail. Hypocenter information is listed in Table 1, while trace displays are in Figure 2. In general, events to the south and west (MAD, LEE, and ALA) (Fig. 2b) have a relatively low-frequency content as well as a relatively long *P*-signal duration. The acronyms MAD, LEE, ALA, etc., are, respectively, for Madagascar, Leeward Island, and Alaska. They are detailed in Table 1 and illustrated in Figure 1. A long duration is also observed for the HK1 event (Fig. 2a), a Hindu Kush earthquake with a focal depth of 100 km, which appears to be a double or triple event. A quantitative measure of *P*-signal duration (including source-end scattering) is given in terms of coherency (ratio of teleseismic beam power to average single channel power) in Table 2 and is further illustrated in Figure 3. Here, the upper curves show rms amplitudes averaged over individual sensors as a function of time while the lower curves give rms amplitudes for the teleseismic beam traces. Note that, for the deep events, JAP and HK2 as well as the SEM explosion the energy is concentrated in a strong source pulse of only 3 to 5 sec duration (Fig. 2a), while for other events there is a total duration of more than 60 sec in terms of coherent *P*-teleseismic arrivals (Fig. 3).

Source-End Scattering

Scattered waves are not easily separable from complex source pulses given that, on travel-time considerations, source-end scattered waves within the early *P* coda will have teleseismic *P* slownesses. Three-component techniques, however, were found useful in source-end scattering analysis, the results of which are displayed in Figure 2 and will be discussed in some detail for the Kamchatka (KAM) event (Fig. 2a). The records for site A0 have been bandpass-filtered and rotated with the radial component aligned along the source backazimuth. Processing parameters are explained in the figure caption. An important note is that the azimuth coherency and velocity plots in Figure 2 (parts ii and iv) assume *P*-wave presence while there is no such assumption on wave type in the calculation of the phase difference between vertical and radial components. Note also that, for wavelets with arrival azimuths greatly different from "true" azimuth, the observed phase differences are not directly interpretable in terms of *P*-, *S*-, and *Rg*-wave types. Signal coherency, and hence confidence in the azimuth estimates, is good for the first 7 sec of the signal (5 to 12 s) as seen in the upper left-hand corner of the figure. A small discontinuity at 8 to 9 sec has a counterpart in the *R-Z* phase diagram, also corresponding with a pronounced drop in apparent velocity. Between 12 to 13.5 sec signal coherency is low (below 0.5), while the phase difference drops toward 90°, implying elliptical particle wave motion. From 13.5 to 15 sec, the signal coherency is again high and the associated *R-Z* phase difference is that of a typical *P* wave. This contrasts with the values between 17 and 20 sec, where coherency is good and the phase difference (Fig. 2, part iii) implies *P*-wave motion. In the remaining parts of the displayed record signal, coherency is primarily low, and particle motion is predominantly elliptical, with the phase difference fluctuating between

90° and 270°. The corresponding velocity estimates are calculated at a lower coherency level (above 0.2), subject to the condition that the standard deviation of the estimate is less than 1.6 of the actual velocity value. The reliability of the obtained velocity estimate is probably poor, the low coherency representing strong interference from non-*P* wavelets. Summarizing the three-component results for the KAM event, strongly coherent *P*-wave motion is observed in the first part of the record with the estimated azimuth and apparent velocity close to that expected for the event location. After about 3 sec, we have a sharp drop in velocity although the azimuth does not change significantly.

The three-component results from the other seven events (also shown in Fig. 2) are not much different from those for KAM. The common characteristics are as follows: *R-Z* phase results imply that interference starts 3 to 4 sec after *P* onset and is often so prominent that velocity and azimuth estimation fails. In addition, phase values fluctuate between 90° and 270°, indicating a dominance of elliptical (probably Rayleigh) wave motion. Later arriving *P* waves are seldom recognized, although the HK1, MAD, LEE, and ALA events have extended *P*-signal duration. Another feature is that the estimate of the apparent velocity sometimes drops significantly after just 3 to 5 sec (e.g., KAM, LEE, and ALA). This is rather puzzling since the time lag between direct *P* and "secondary" *P* wavelets is small; the velocity drop is difficult to explain unless we invoke multipathing confined to the azimuth plane. We have calculated apparent velocities using the A0, C-, and D-ring of the array—the observed velocity decreases are very moderate. However, the three-component results have a counterpart in the displayed traces in that the ratio of amplitudes of the radial and vertical components (*R/Z*) increases after the first *P* phase. The vertical components are relatively coherent across the array (as seen in Table 2), while the three-component records are far more sensitive to interference. This point is further illustrated in Figure 3.

Receiver-End Scattering

Source-end contributions appear from the aforementioned discussion and Figure 3 to be rather energetic. We have removed such contributions by forming the beam trace and subtracting this from the single *z* traces, then conducting semblance analysis on the residual traces. The coda was screened in two segments of 40 sec (Fig. 2 shows the traces in the first segment) using velocities appropriate for *P* (6 to 8 km/sec), *Sn* (4.5 km/sec), and *Rg* (3.0 km/sec) waves. In the first time segment shown in Figure 4, the coda is clearly dominated by *Rg* contributions. The truly striking feature is that the *P*-to-*Rg* scattered phases are observed from principally two azimuth directions of 80° and 225° (thin lines in the figure), irrespective of event azimuth. Examples of estimated *Rg* waveforms are shown in Figure 5. For each of the two events shown, the upper trace is the teleseismic beam while the two lower traces are beams formed from the residual traces using azimuths of 80° and 225° and a velocity of 3.0 km/sec. Although the peak amplitudes of the scattered phases are only about one-tenth of that of the teleseismic beam traces, the *Rg* waves are clearly observable in time segments matching those of the semblance analysis results in Figure 4. From the time lags of the estimated *Rg* wavelets, we have located the corresponding scattering source areas at Bronkeberget (distance ~ 10 km, azimuth ~ 80°) and Skreikampen (distance ~ 30 km, azimuth ~ 225°). Both of these areas have prominent topographic relief and are marked in

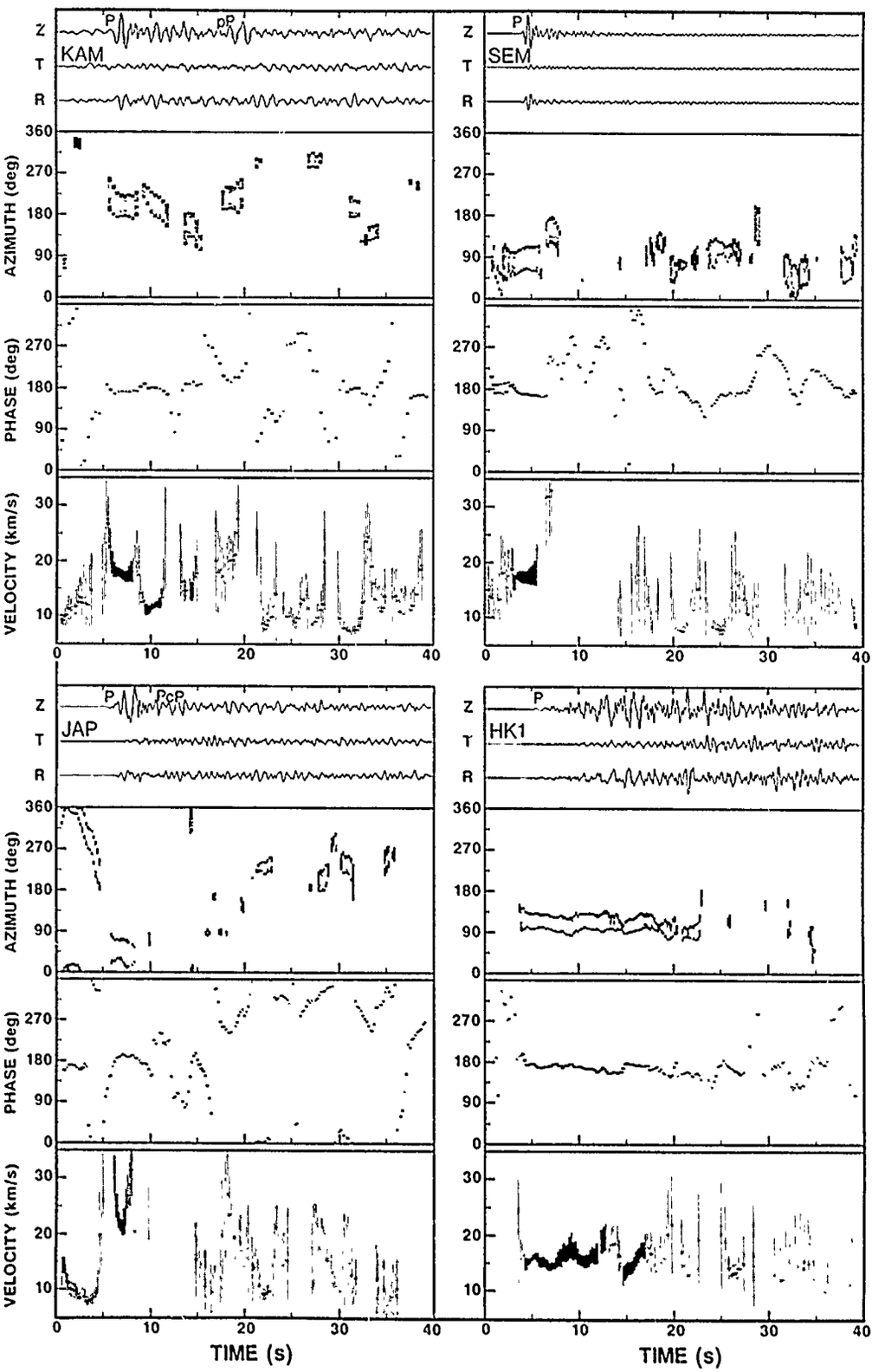

(a)

FIG. 2. (a) Results from three component analysis of the first four events in Table 1. Each event is shown in a compartment box of four sections: (i) The three-component seismic traces, rotated into a vertical-radial-tangential (Z, R, T), coordinate system. (ii) ML probabilities exceeding 0.50 for P-wave polarization. For all events, the sliding window was 1.6 sec long, incremented in 0.2 sec in time and 4° in azimuth. The KAM and ALA events have been shifted 180° in azimuth. (iii) The phase difference

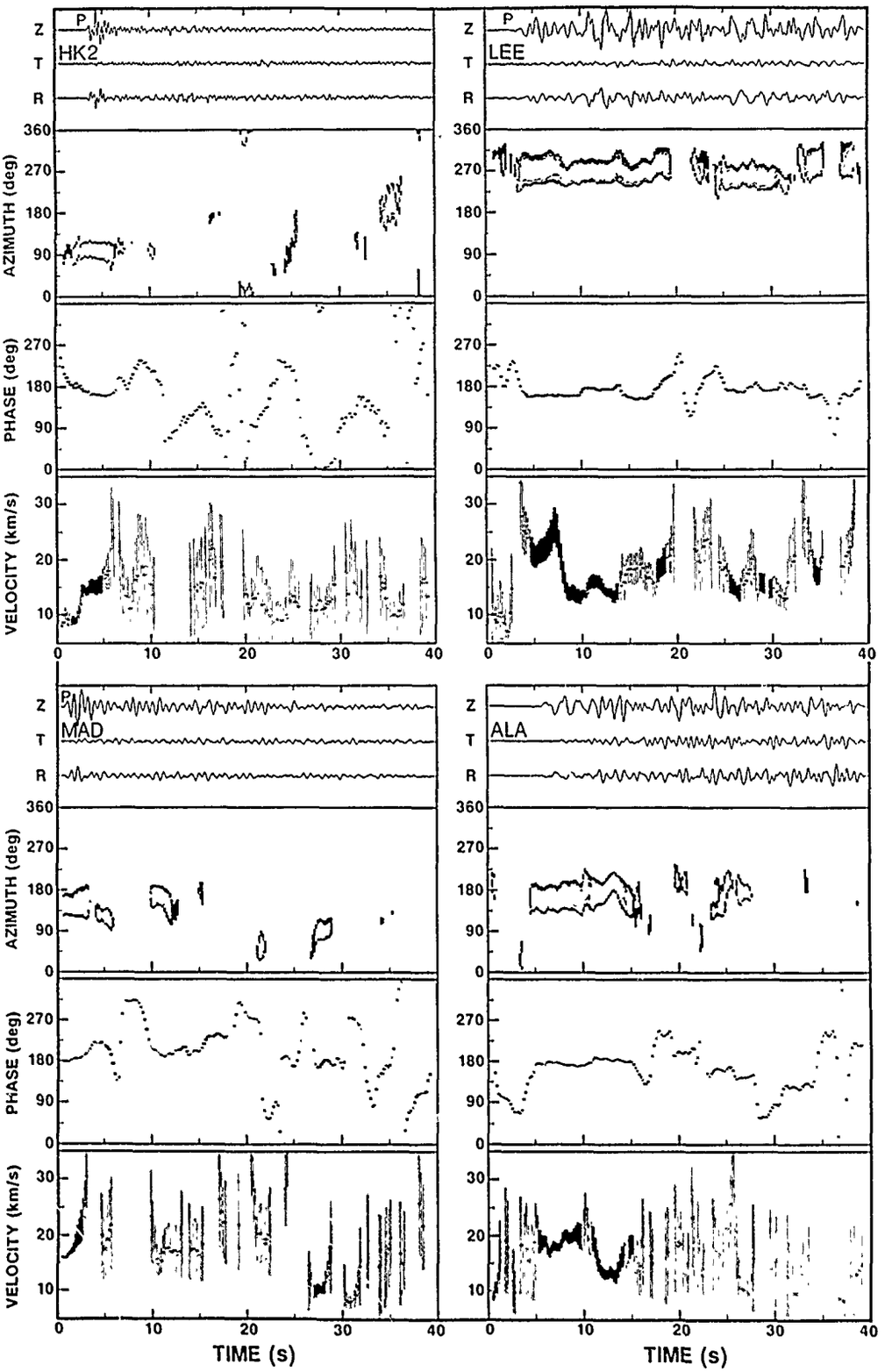

(b)

between the radial (R) and vertical (Z) components. The particle motion is pure P, elliptical or pure SV for phase differences of 180° ± 90°, and 0°, respectively. The phase difference estimate is unreliable in cases where the arriving wavelets are not approximately (±30°) in the radial plane. (iv) Apparent three-component velocities, including error bars as calculated from estimates of angle of incidence. (b) Results from three-component analysis of the last four events in Table 1.

TABLE 2

PERCENTAGES OF COHERENT POWER ON THE TELESEISMIC BEAM FOR DIFFERENT TIME INTERVALS

Event	Time after *P* Onset (sec)			
	0–5	5–10	10–35	35–75
KAM	94	63	44	44
JAP	94	67	34	21
SEM	96	63	45	42
HK1	92	90	63	43
HK2	92	52	26	28
MAD	97	84	75	26
LEE	98	95	90	71
ALA	93	94	61	45

Coherent power is calculated as the energy on the beam divided by the average energy of the single-channel sensors for the same time interval. Data used are from the A0, C-, and D-ring instruments and were filtered in the 1 to 3 Hz passband. The beam steering directions were those giving the highest coherency in the first 3 sec of the signal.

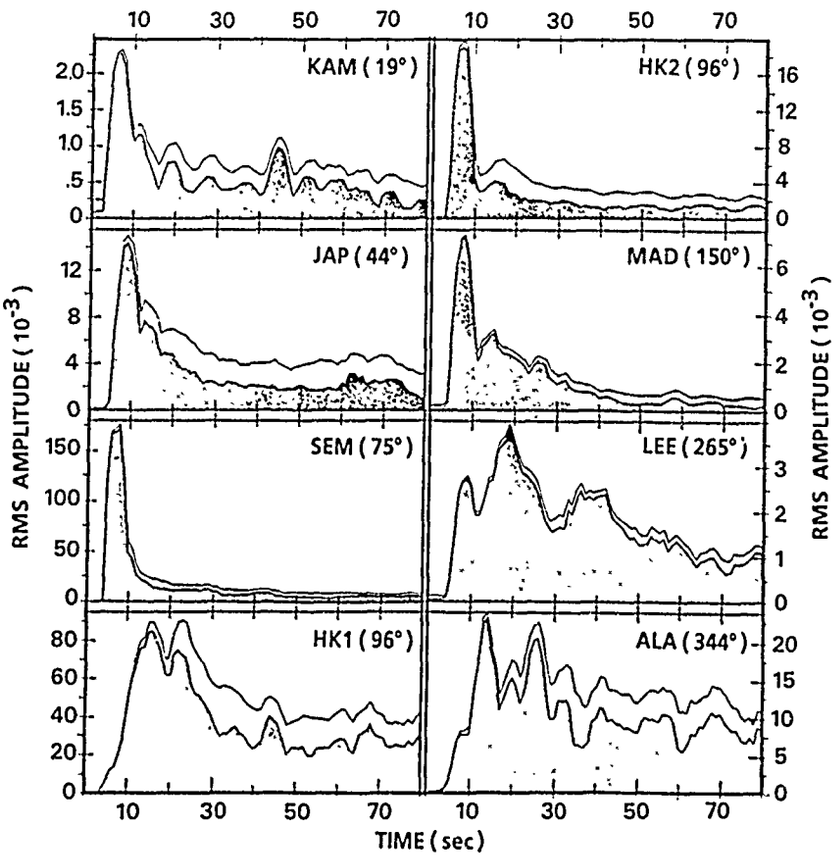

FIG. 3. rms amplitudes (counts) for average single-channel and beam traces for the events analyzed (Table 1). The traces from the A0, C-, and D-ring sensors were bandpass-filtered 1 to 3 Hz prior to rms calculations in a 4 sec window. The upper traces are the average single-channel amplitudes while the beam amplitudes are shown with shading.

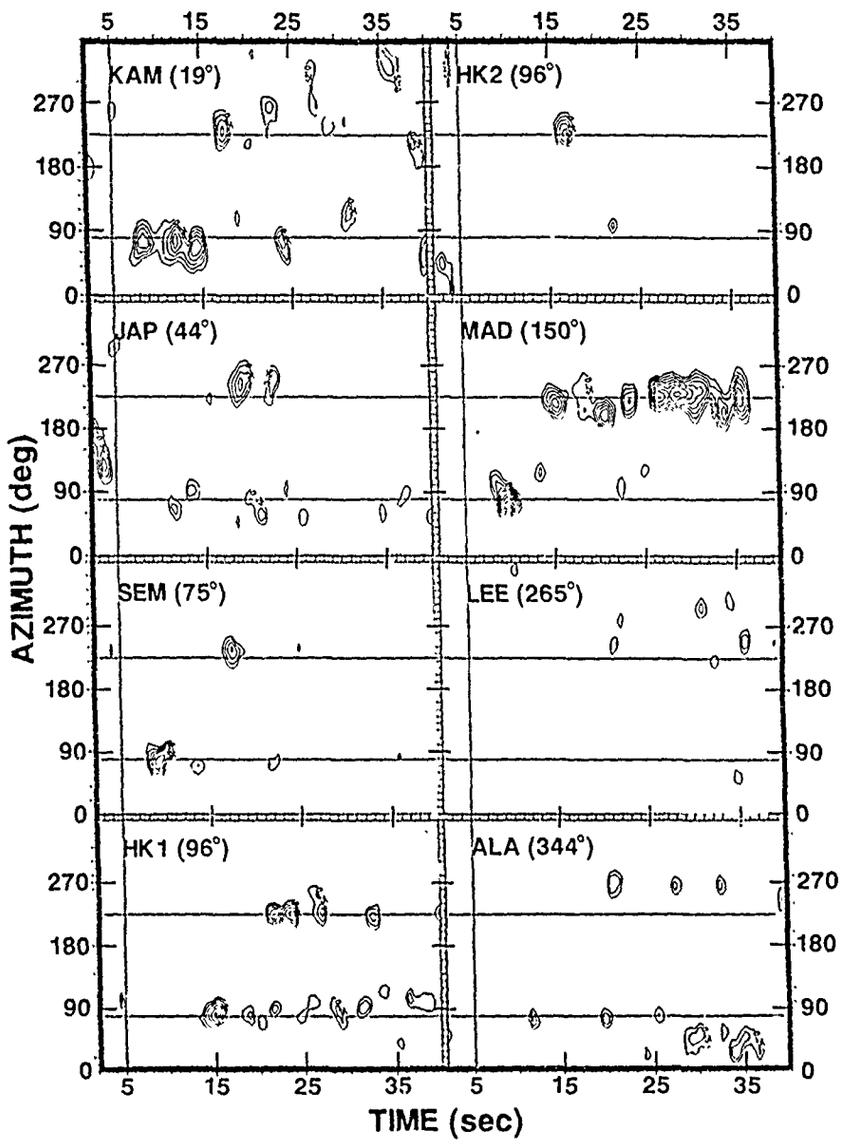

FIG. 4. Outcome of residual trace semblance analysis aimed at identifying *Rg* wavelets in the coda. Semblance is shown as a function of time and azimuth for a fixed-phase velocity of 3.0 km/sec. The calculation of residual traces are explained in the text. All traces were filtered in the 1 to 3 Hz passband, and semblance calculations are for a 1.5 sec window. The semblance contouring levels start at 0.25 and increase in steps of 0.05. The thin horizontal lines mark azimuths of 80° and 225°, while the thin vertical lines indicate *P*-onset time.

Figure 1. Furthermore, the scattering appears to be multiple in the sense that *Rg* wavelets repeatedly arrive from the two azimuths. This is perhaps most clearly illustrated by the ALA event, where the time lags between scattered waves from 80° and 225° azimuth form a distinct pattern. *Rg* attenuation is seemingly very strong as waves from larger distances and other azimuths are hardly observed, surprising in view of the mountainous area to the north and west of the array (60 km or more distant).

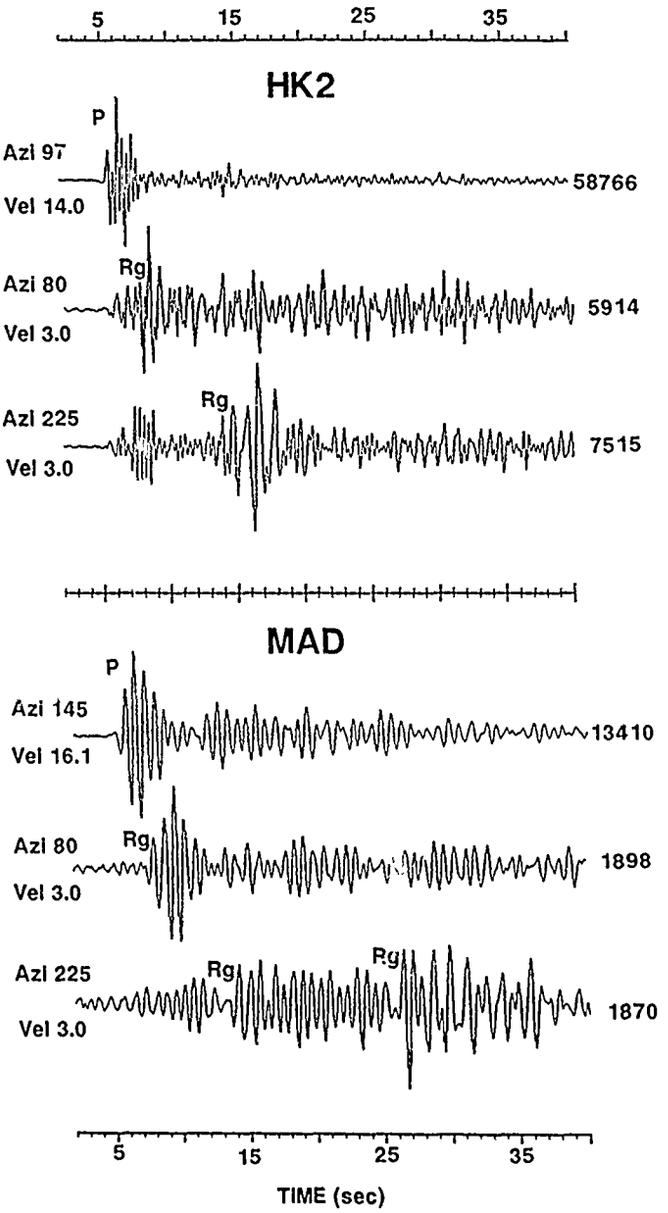

FIG. 5. Examples of waveforms estimated through beamforming. For each event, the "best" teleseismic beam is shown first followed by *Rg* waveforms estimated by residual trace beamforming aimed at the two scattering areas. All traces were filtered in the 1 to 3 Hz passband.

Semblance analysis was also performed for a velocity of 4.5 km/sec. The results (not shown) have many similarities to those shown in Figure 4 in that the two semblance patterns overlap considerably. Although this could mean that the "true" velocities are around, say, 3.6 to 3.8 km/sec (e.g., *Sg* phases), we consider that *Rg* wavelets dominate given the phase difference results and higher semblances observed. An exception here is the high semblances found for ALA at about 50° azimuth (30 to 35 sec), which are much stronger in the 4.5 km/sec semblance results. A search for crustal *P* phases (6 to 8 km/sec velocity range) turned out to be mainly negative. We found a few indications of *Pg* phases at 4 to 6 sec

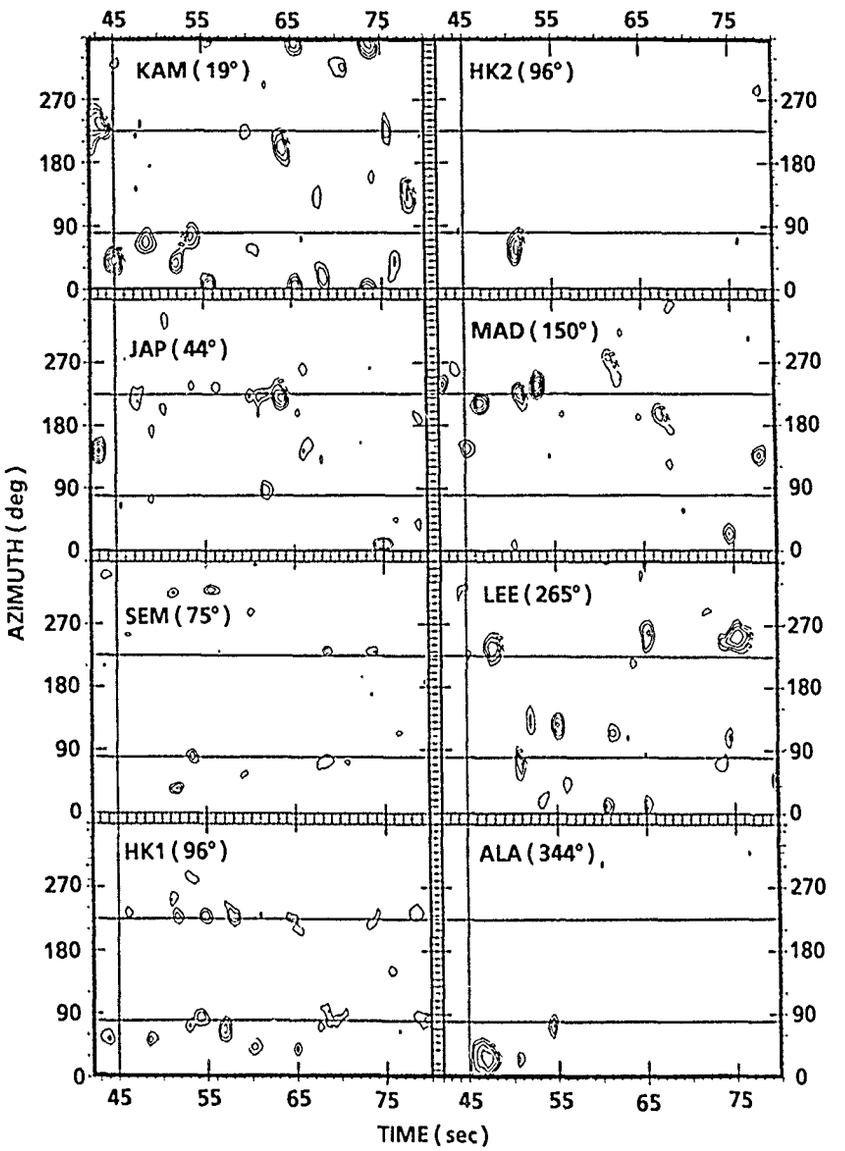

FIG. 6. Coda semblance analysis aimed at identifying *Rg* wavelets (velocity 3.0 km/sec) in the 40 sec time segment following that shown in Figure 4. The thin horizontal lines mark azimuths of 80° and 225°, while the thin vertical lines indicate 40 sec after *P*-onset time. See caption for Figure 4.

after *P* onset time but negligible contributions later in the coda. This implies that *P*-to-*P* scattering in the general area of the array site is weak.

Results from semblance analysis in the second time segment (35 to 75 sec after *P* onset) are shown in Figures 6 and 7 for velocities of 3.0 and 4.5 km/sec. *Rg* contributions are again observed and are mainly from azimuths of 80° and 225°. The preference for these two azimuths (in Fig. 6) again indicates that the scattering is multiple, noting (from Fig. 3) that source-end contributions are still present at times far into the coda. From Figure 7, we see that *S*-wave scattering dominates in this time segment. This may mean that *S*-wave attenuation is less pronounced than that of *Rg* given that, over time, more distant scattering source areas may become activated. Again, there is still some preference for azimuths of

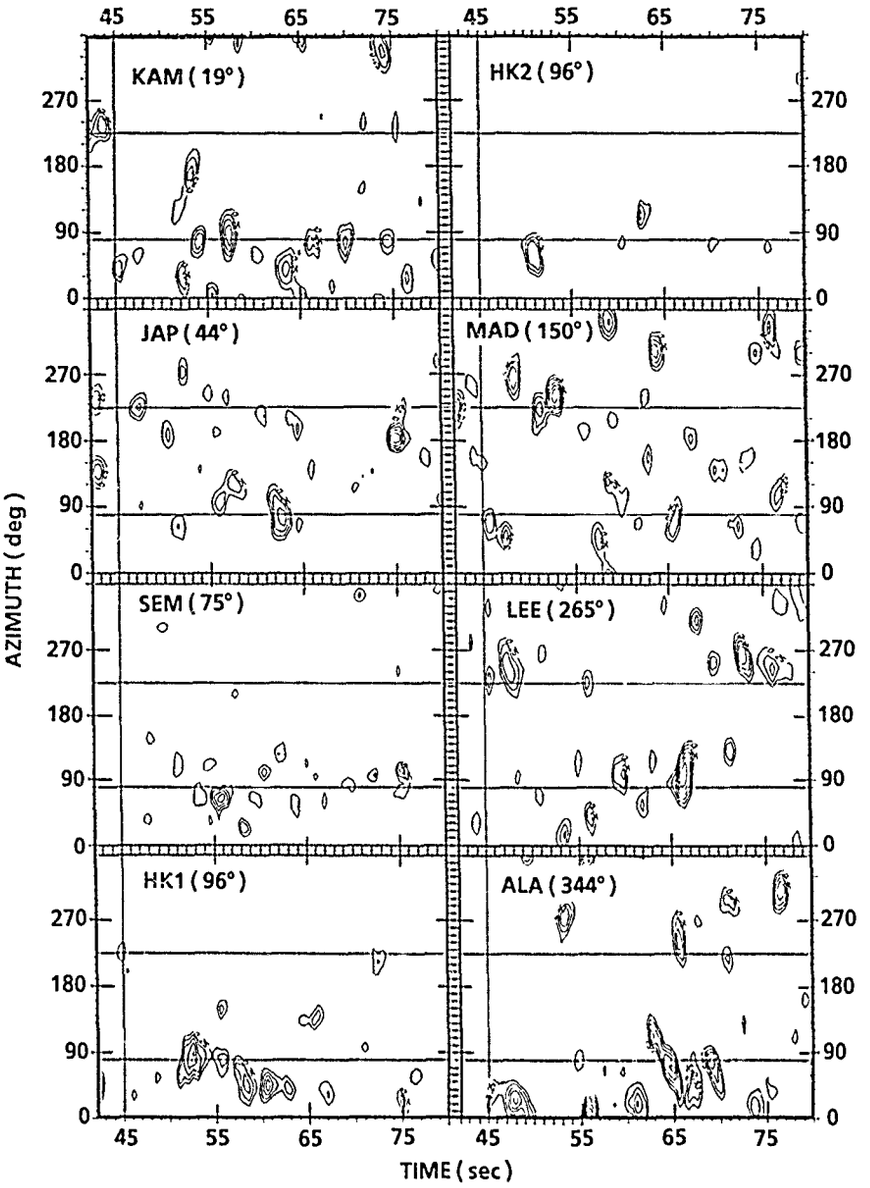

FIG. 7. Coda semblance analysis aimed at identifying *Sn* wavelets for the same time segment as in Figure 6. The fixed-phase velocity here is 4.5 km/sec (see caption for Fig. 6). In cases where semblance contours coincide with those in Figure 6, the true phase velocity is probably of an intermediate *Sg* type (i.e., approximately 3.6 km/sec).

80° and 225°, although forward scattering appears to be significant for the two northern events KAM and ALA, as well as for SEM and HK to the east. *P*-to-*P* scattering at the receiver end, with crustal velocities in the range 6 to 8 km/sec, remains weak.

DISCUSSION

Teleseismic *P* coda has also been examined in other studies. Key (1967), for example, identified discrete arrivals in the *P* coda at the Eskdalemuir array in Scotland that suggested *P* to Rayleigh wave scattering stemming from the local

topography. Recently, Langston (1989) observed a strong phase on the transverse component just 3 sec after the *P* arrival in three-component analysis of teleseismic recordings at Pasadena, California. This was interpreted as *P*-to-*S* conversion at a dipping interface of strong *S*-velocity contrast at a depth of 20 km. Of most interest for our study are investigations by Dainty and Harris (1989), Gupta *et al.* (1990), and Dainty (1990) using *f-k* analysis of NORESS teleseismic codas. Dainty and Harris found evidence of low-velocity scattering contributions that were mostly attributed to *Lg* and surface waves without details of azimuth or time dependencies. Gupta *et al.* reported low-velocity secondary arrivals from the east and south-west in the early *P* coda. We prefer using the semblance technique instead of high-resolution *f-k* methods in the array data analysis because semblance works well even for short windows (1 to 2 cycles) and thus the individual slowness estimates can be directly related to arrivals seen in the records. We also find that the three-component records are useful for pinpointing where wave interference takes place, although the information potential of the horizontal components has yet to be fully utilized in coda studies.

Mechanism for NORESS P-Coda Generation

Although teleseismic scattering is generally considered quite a complex problem, the NORESS coda observations presented in the previous section can be explained simply. First, we consider source-end contributions to be of long duration (i.e., more than 1 min) even for the deep events JAP, HK2, as well as the SEM explosion. A number of *P* waves are generated at the source end, the dominant of which stem from the source itself while other secondary phases are likely related to reverberations, reflections, mode conversions, etc., in the source region (Lynnes and Lay, 1989). The common characteristic of these phases in our teleseismic records is their high apparent velocity. At the receiver end, *P*-to-*Rg* conversion related to topographic relief appears to be most efficient. Naturally the scattering areas cannot be too far away from the array because of strong *Rg* attenuation. In NORESS data, short-period Rayleigh waves are seldom observed for events beyond 100 km. The results, however, suggest that the first 30 sec of the coda is dominated by *Rg* wavelets originating from the Bronkeberget and Skreikampen areas. The scattering illumination of NORESS appears to be somewhat dependent on event azimuth and is quite weak for events such as LEE and ALA. Although scattered arrivals of most events were predominantly from 80° and 225° azimuth, the efficiency of particular scattering sources is obviously related to the geometry involved. The scattering is multiple in the sense that *P* waves following the initial *P* phase, presumably generated by scattering within the source region themselves generated *Rg* phases. As the *P*-wave energy decreases with time, we note a corresponding weakening in the generation of *Rg*.

Phases with *Sg* and *Sn* velocities become more predominant further into the coda at approximately 30 to 70 sec. Although the area of potential scattering sources increases greatly with time, the number of significant wavelets remains modest. Arrivals are mainly from the west to northeast (i.e., the most mountainous part of southern Norway), although they are also observed from source azimuths. These *S* waves are most probably generated by *P*-to-*S* scattering so their late arrival simply reflects larger travel distances.

We have found very little evidence of *P*-to-*P* scattering (6 to 8 km/sec velocity) in our analysis. We take this to imply that structural heterogeneities in the

crust/lithosphere are not prominent enough to act as efficient scattering sources. Even the nearby Oslo Rift, with an elevated Moho of 3 to 5 km (Kinck *et al.*, 1991), does not seem to generate significant *P*-to-*P* scattering. Weak lithospheric *P* scattering at depths around 100 km as reported by Troitskiy *et al.* (1981) for NORSAR (100 km aperture) is not easily separated from source-end scattering using NORESS (only 3 km aperture). It remains puzzling why *P*-to-*Rg* and *P*-to-*S* conversions are far more efficient than *P*-to-*P* conversions. Such problems will be explored in future three-dimensional wave field synthesis.

The aforementioned results and the suggested mechanism for coda generation apply strictly only to NORESS recordings from events at teleseismic ranges. It was rather surprising to find that about 30 to 50 per cent of the coda (Table 2) is associated with wavelets with teleseismic apparent velocities (i.e., the coherent coda) while 10 to 30 per cent appear to be scattered by rough topography in the two areas near the array. The remaining part of the coda is considered to represent diffuse scattering at the receiver end. Other scattering mechanisms may be more relevant for local and regional distances, since we would then be dealing with horizontally propagating waves with shorter wavelengths. An interesting observation by Toksöz *et al.* (1990) is that *Rg* propagation seems to be far more efficient, up to 300 km, in the vicinity of arrays in northern Norway (ARCESS) and Finland (FINESA).

Conclusions

We have examined teleseismic *P* coda waves as recorded by the NORESS array in southeast Norway in the time interval of 0 to 75 sec after *P* onset. The essential elements in the data analysis are as follows:

- In three-component analysis, the phase difference attribute (Z/R) has proved efficient in indicating where interference takes place.
- Semblance analysis and beamforming proved very valuable in estimating the slowness vector from non-*P* phases such as *Rg*, *Sg*, and *Sn*.
- Ideally, three-component NORESS recordings would be more useful for coda studies given additional three-component stations.

The main results obtained are:

- Early *P* coda at NORESS shows prominent *P*-to-*Rg* scattering from local hills with pronounced topographic relief, namely Bronkeberget (distance ~ 10 km, azimuth ~ 80°) and Skreikampen (distance ~ 30 km, azimuth ~ 225°). *Rg* scattering is both forward and backward.
- *P*-to-*S* scattering is also quite efficient, and continues further into the coda than *Rg*, but scattering locations are more obscure.
- *P*-to-*P* scattering takes place in the immediate vicinity of the array (within 4 to 5 sec from onset), particularly to the east, but is generally weakly developed.
- Source-end scattering in the early *P* coda could not be separated from extended source pulse duration with the data at hand.
- Scattering is multiple in the sense that later *P* phases as well as the first *P* phase from the source region result in *Rg* scattering, again mainly from the two mentioned locations. Also, this probably applies to *P*-to-*S* scattering.

Acknowledgments

We appreciate many stimulating discussions with A. Dainty and P. Troitskiy. A postdoctoral fellowship for S.C.B. from NTNF (Norwegian Technical Research Council) is gratefully acknowledged. This

research is supported by the Defence Advanced Research Projects Agency under AFOSR Grant AFOSR-89-0259 monitored by the Air Force Geophysical Laboratory.

REFERENCES

Aki, K. (1973) Scattering of *P*-waves under the Montana LASA, *J. Geophys. Res.* **78**, 1334–1346.

Aki, K., A. Christoffersson, and E. S. Husebye (1977). Three-dimensional seismic structure of the lithosphere, *J. Geophys. Res.* **82**, 277–296.

Berteussen, K.-A., A. Christoffersson, E. S. Husebye, and A. Dahle (1975). Wave scattering theory in analysis of *P*-wave anomalies at NORSAR and LASA, *Geophys. J. R. Astr. Soc.* **42**, 403–417.

Chernov, L. A. (1960). *Wave Propagation in Random Medium*, McGraw-Hill, New York.

Christoffersson, A., E. S. Husebye, and S. F. Ingate (1988). Wavefield decomposition using *ML* probabilities in modeling single site 3-component records, *Geophys. J. Int.* **93**, 197–213.

Dainty, A. M. (1990). Studies of coda using array and three-component processing, *PAGEOPH* **132**, 221–244.

Dainty, A. M. and D. B. Harris (1989). Phase velocity estimation of diffusely scattered waves, *Bull. Seism. Soc. Am.* **79**, 1231–1250.

Flatté, S. M. and R. S. Wu (1988). Small scale structure in the lithosphere and asthenosphere deduced from arrival time and amplitude fluctuations at NORSAR, *J. Geophys. Res.* **93**, 6601–6614.

Frankel, A. (1989). A review of numerical experiments on seismic wave scattering, *PAGEOPH* **131**, 639–685.

Gupta, I. N., C. S. Lynnes, and R. A. Wagner (1990). Broadband *f-k* analysis of array data to identify sources of local scattering, *Geophys. Rcs. Letters* **17**, 183–186.

Haddon, R. A. W. and E. S. Husebye (1978). Joint interpretation of *P*-wave travel time and amplitude anomalies in terms of lithospheric heterogeneities, *Geophys. J. R. Astr. Soc.* **56**, 263–288.

Herraiz, M. and A. F. Espinosa (1987). Coda waves: a review. *Pageoph* **125**, 499–577.

Husebye, E. S. and B. O. Ruud (1989). Array seismology—Past, present and future developments, in *Observatory Seismology*, J. J. Litehiser, Editor, Berkeley University Press, Berkeley, California.

Ingate, S. F., E. S. Husebye, and A. Christoffersson (1985). Regional arrays and optimum processing schemes, *Bull. Seism. Soc. Am.* **75**, 1155–1177.

Jurkevics, A. (1988). Polarization analysis of three-component array data, *Bull. Seism. Soc. Am.* **78**, 1725–1743.

Kennett, B. L. N. (1987). Observational and theoretical constraints on crustal and upper mantle heterogeneity, *Phys. Earth Planet. Interiors* **47**, 319–332.

Key, F. A. (1967). Signal-generated noise recorded at the Eskdalemuir seismometer array station, *Bull. Seism. Soc. Am.* **57**, 27–37.

Kinck, J. J., E. S. Husebye, and C.-E. Lund (1991). The S. Scandinavia Crust—Structural complexities from seismic reflection and refraction profiles, *Tectonophysics* (in press).

King, D. W., R. A. W. Haddon, and E. S. Husebye (1977). Precursors to *PP*, *Phys. Earth Planetary Interiors* **10**, 103–127.

Korn, M. (1988). *P*-wave coda analysis of short-period array data and the scattering and absorptive properties of the lithosphere, *Geophys. J.* **93**, 437–449.

Langston, C. A. (1989). Scattering of teleseismic body waves under Pasadena, California, *J. Geophys. Res.* **94**, 1935–1951.

Lynnes, C. S. and T. Lay (1989). Inversion of *P* coda for isotropic scatterers at the Yucca Flat test site, *Bull. Seism. Soc. Am.* **79**, 790–804.

Nikolaev, A. V. and P. A. Troitskiy (1987). Lithospheric studies based on array analysis of *P*-coda and microseisms, *Tectonophysics* **140**, 103–113.

Park, J., F. L. Vernon, and C. R. Lindberg (1987). Frequency dependent polarization analysis of high frequency seismograms, *J. Geophys. Res.* **92**, 12664–12674.

Plešinger, A., M. Hellweg, and D. Seidl (1986). Interactive high-resolution polarization analysis of broad-band seismograms, *J. Geophys.* **59**, 129–139.

Roberts, R. G. and A. Christoffersson (1990). Decomposition of complex single-station 3-component seismograms, *Geophys. J. Int.* (in press).

Toksöz, M. N., A. M. Dainty, and E. E. Charrette (1990). Coherency of ground motion at regional distances and scattering, *Phys. Earth Planet. Interiors* (in press).

Troitskiy, P., E. S. Husebye, and A. Nikolaev (1981). Lithospheric studies based on holographic principles, *Nature* **294**, 618–623.

Vidale, J. E. (1986). Complex polarization analysis of particle motion, *Bull. Seism. Soc. Am.* **76**, 1393–1405.

Wu, R.-S. and K. Aki (1988). Introduction. Seismic wave scattering in three-dimensionally heterogeneous earth, *PAGEOPH* **128**, 1–6.

DEPARTMENT OF GEOLOGY
OSLO UNIVERSITY
P.O. BOX 1047
BLINDERN, N-0316 OSLO 3, NORWAY
(S.C.B., E.S.H., B.O.R.)

Manuscript received 16 February 1990

Bulletin of the Seismological Society of America, Vol. 80 No. 6, pp. 1987–1998, December 1990

ESTIMATING AZIMUTH AND SLOWNESS FROM THREE-COMPONENT AND ARRAY STATIONS

BY ANNE SUTEAU-HENSON

ABSTRACT

The capabilities of three-component (3-C) and array stations for estimating azimuth and slowness are compared for short-period *P*-type phases recorded at the NORESS array. For vertical array data, azimuth and slowness estimates are obtained from broadband frequency-wavenumber (*f-k*) analysis. For 3-C data, polarization analysis is performed. The data processing is automated, using arrival time and dominant frequency information from the *NORESS Bulletin*. Independent determinations of azimuth and/or slowness, obtained from locations in the NEIS or regional network bulletins, are used as reference estimates. Over 100 events are analyzed, both teleseismic and regional. They were selected from a variety of distances and azimuths, and cover a wide range of signal-to-noise ratios (SNR).

The capability of 3-C stations for azimuth and slowness estimation critically depends on SNR. For SNR below a threshold of ~2, the scatter in the estimates is very large for both parameters, and the slowness of teleseismic events tends to be overestimated. Also, the results are site-dependent within the NORESS array. The array measurements obtained with the broadband *f-k* method are not significantly affected by noise at the levels of SNR considered. For events with sufficient SNR, both methods compare well, and only a slightly better performance is observed with the *f-k* method.

INTRODUCTION

The capabilities of three-component (3-C) and array stations for estimating azimuth and slowness are compared. In a theoretical investigation by Harris (1982), upper bounds on the uncertainty of the direction estimates of a plane incident *P* wave in the presence of noise were derived for various sensor configurations. Arrays were found to perform better than 3-C stations. Experiments by Kværna and Doornbos (1986) indicated that measurements of the slowness vector at the individual 3-C NORESS stations are site-dependent and have a larger standard deviation than measurements using the array of vertical sensors.

In this empirical study, azimuth and slowness estimates from broadband frequency-wavenumber (*f-k*) analysis using Kværna's algorithm (Kværna and Ringdal, 1986) and polarization analysis, using the technique developed by Jurkevics (Jurkevics, 1988) are compared for *P*-type phases recorded at the NORESS array in the short-period band. One hundred forty-five events were analyzed: 74 teleseismic and 71 regional events. They were selected from a variety of distances and azimuths, and cover a wide range of signal-to-noise ratios (SNR). Independent determinations of azimuth and/or slowness were obtained from locations in the *NEIS Bulletin* for teleseismic events, and in regional network and PDE bulletins for regional events.

The *f-k* method is found to be more robust over a wide range of SNR. However, for sufficient SNR, the two methods are comparable. These results confirm those from theoretical studies. Also, the results from 3-C processing are in good agreement with those from other studies using NORESS and RSTN short-period data and NORESS high-frequency data (US/GSE/49, 1987; Jurkevics, 1988; Walck and Chael, 1989).

NORESS high-frequency data (US/GSE/49, 1987; Jurkevics, 1988; Walck and Chael, 1989).

Review of Theoretical Investigation

Harris (1982) compared the performance of small arrays and three-component stations in estimating the wave field direction. His study is a theoretical investigation into the uncertainty of direction estimates in the presence of noise. A lower bound on this uncertainty is obtained using the Cramer–Rao bound.

For simplicity, Harris assumed additive, spatially uncorrelated noise, and a simple signal model, free of refraction and scattering effects. This study is limited to the case of a plane incident P wave, for which there is a simple model of particle motion that can be used to derive the slowness vector using 3-C stations. The particle motion measured at the free surface is linearly polarized and oriented along the azimuth. The apparent incidence angle, inc_a, is easily derived from the true incidence angle, inc, for given compressional and shear velocities. For most regional and teleseismic P waves, the incidence angle is between 0° and 60°, in which case inc_a is very close to inc.

The main conclusions of Harris' investigation were:

- The bounds for arrays are smaller than the bounds for 3-C stations. Therefore, arrays perform better in estimating direction parameters.
- Since arrays provide better estimates of incidence angles than 3-C stations, they perform better in identifying P waves.
- The difference in performance between arrays and 3-C stations significantly increases as the SNR decreases.

Methods

In this study, the capabilities of arrays and 3-C single stations in estimating direction parameters are compared for two sizeable data sets of events (regional and teleseismic) detected by the NORESS array, and recorded at both the vertical and 3-C elements of the array. Azimuth and slowness estimates are obtained using f-k analysis for the array of vertical sensors, and polarization ("3-C") analysis for a 3-C single station. While a measurement of slowness can be directly obtained from f-k analysis, it has to be derived from a measurement of incidence angle when 3-C processing is used.

We applied the broadband f-k analysis technique developed by Kværna (Kværna and Ringdal, 1986; Kværna, 1987). It provides better estimates than the monochromatic f-k method. The processing procedure is the same as that used in the "Intelligent Monitoring System" (IMS) (Bache *et al.*, 1990). For each phase, the arrival time—used to select the analysis window—and the center frequency were the arrival time and dominant frequency, respectively, from the *NORESS Bulletin*.

The polarization method used to analyze the 3-C data is based on that developed by Jurkevics (1988). It is a principal-component estimator based on an eigensystem decomposition of the wave field. Although it is a time-domain technique, a frequency decomposition is also performed through bandpass filtering. For each seismic phase, the assumption is made that the particle motion in a given frequency band is purely polarized over the duration of the selected time window. The polarization ellipsoid is computed using an eigensystem decomposition. Then, "polarization attributes" can be estimated, in particular, P-wave azimuth and incidence angle.

In practice, a set of frequency bands covering the range of interest is selected. For each band, the data are bandpass-filtered, and a measure of SNR is estimated.

It is based on the "3-C amplitude," which is the sum of the amplitudes on all three axes of the polarization ellipsoid. The "3-C SNR" used in this study is the ratio of maximum signal 3-C amplitude to average noise 3-C amplitude. The frequency band to measure the attributes is then selected. We have experimented with two methods of frequency band selection, hereafter referred to as "broadband" and "narrow-band," respectively. With the broadband method, a subset of frequency bands, for which the SNR is above a given threshold, is selected (if no band is above the threshold, that with the largest SNR is chosen instead). For overlapping time windows in a segment around the arrival, the covariance matrices are computed in each of the selected bands and averaged over the bands. The resulting wide-band covariance matrix is used to measure polarization attributes. With the narrow-band method, only the band with the largest SNR is selected. The most stable estimates are obtained using wide frequency bands.

Some criteria must be used to select the time window in which to extract polarization attributes for each type of seismic phase. The time of largest rectilinearity is selected for *P*-type phases. As for the *f-k* analysis, the processing procedure used in this study is the same as that in the IMS, and the arrival times used to select the data segment for analysis were obtained from the *NORESS Bulletin.*

Two data sets are used to compare the capabilities of the array of vertical elements with 3-C single stations at NORESS for azimuth and slowness estimation. The first includes teleseismic *P* arrivals, and the second consists of regional *P*-type phases. First *P* arrivals detected at NORESS were analyzed for events carefully selected from bulletins. Although slowness was also measured for the regional events, the results are not discussed here, since slowness estimates are not used to locate such events. For each set, azimuth and slowness differences are obtained by comparing the estimates from both *f-k* and 3-C processing to reference estimates derived from the bulletin locations. The effect of noise is studied, using an estimate of the SNR measured for the 3-C single station in the frequency band used for signal analysis (i.e., ratio of maximum signal 3-C amplitude to average pre-event noise 3-C amplitude). For this study, the broadband method of frequency selection is used for 3-C processing, although the effect of applying the narrow-band method instead is also investigated. Clearly, the 3-C SNR estimate is smaller than the SNR for the array beam. However, we use it for both methods to ensure consistency and because it helps evaluate the robustness of the 3-C method in the presence of noise.

Results from Teleseismic *P*-Wave Analysis

Seventy-four teleseismic events were selected, covering a wide range of epicentral distance (from ~20° to 90°), azimuth, and SNR. Independent locations were obtained from the *NEIS Bulletin* and are plotted in Figure 1. Polarization analysis was performed at station NRA0. The set of frequency bands used is 0.5 to 1, 1 to 2, 2 to 4, and 4 to 8 Hz, and a moving window of 3.5 sec length was used to select the best time for measurement within a 14 sec data segment centered on the detection time. For this data set, the SNR advantage of the array over the single 3-C station is approximately a factor of 7.

Comparison of f-k and 3-C Results

The means, standard deviations, and medians of the azimuth differences (observed azimuth minus azimuth to NEIS location) obtained for each method are given in Table 1 (after removing one outlier for the *f-k* method). The 3-C method has a significantly larger standard deviation, which is similar to those obtained

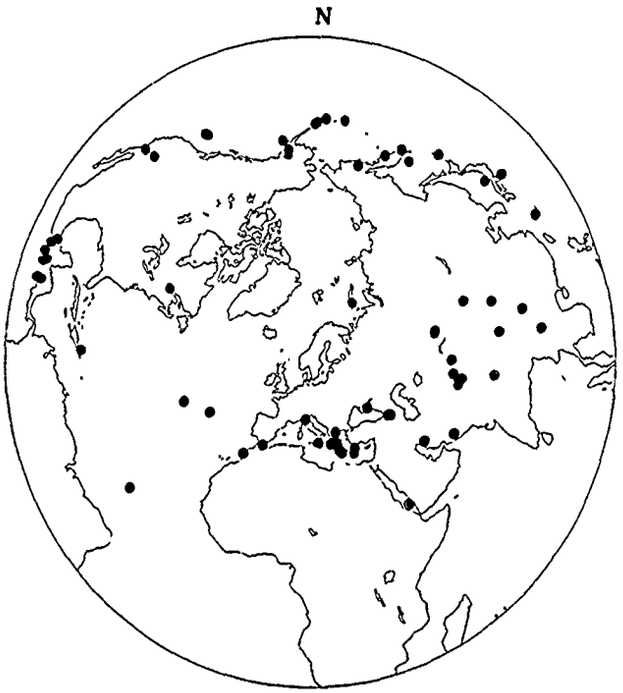

FIG. 1. Polar map centered at NORESS (60.735°N, 11.541°E) showing the locations of the 74 teleseismic events used in this study. They cover a range of epicentral distances from 16° to 84°.

TABLE 1
AZIMUTH DIFFERENCES OF TELESEISMIC *P* PHASES

	Mean (°)	S.D. (°)	Median (°)
f-k	−1	11	−1
f-k (SNR > 2)	−2	12	0
3-C	5	39	5
3-C (SNR > 2)	3	13	4

for teleseismic *P* waves recorded at RSTN stations, using a similar technique (US/GSE/49, 1987). Next, we study the effect of low SNR events on the standard deviations of the distributions. In Figure 2, the azimuth differences are plotted as a function of 3-C SNR for each method. Low SNR phases, below a threshold of ~2 (indicated by the dashed vertical lines), do not show more scatter for the *f-k* estimates, but are characterized by a large and abrupt increase in scatter for the 3-C estimates. For the 40 phases with 3-C SNR above 2, the difference between the standard deviations of the two methods is not significant (Table 1).

A similar comparison was performed for the slowness differences (observed minus reference slowness). The 3-C slowness was obtained by converting the measured incidence angle, using a surface *P*-wave velocity of 6.0 km/sec. The reference slowness was derived from J-B tables as a function of epicentral distance. A comparison of the measurements for the two methods is given in Table 2. A skewness is observed in the distribution of the 3-C differences, with a large number of positive anomalies. In Figure 3, the slowness differences are plotted as a function of 3-C SNR for each method. It shows that the anomalously large 3-C slownesses are mostly for low SNR events (below a threshold of ~2, as indicated by the dashed

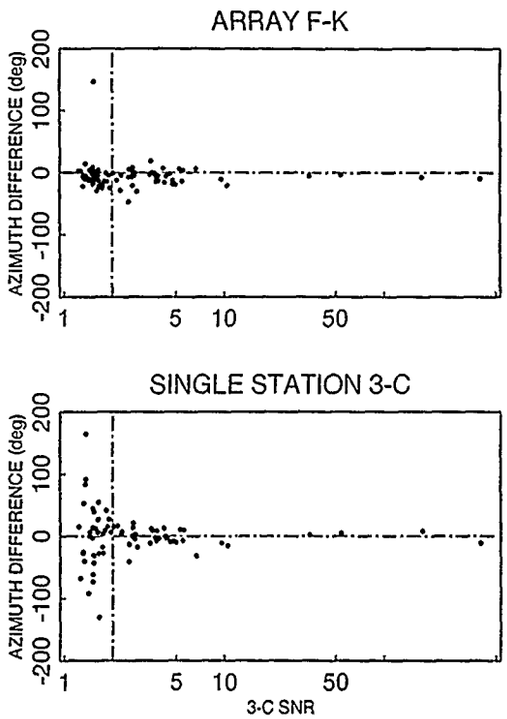

FIG. 2. Azimuth differences versus 3-C SNR for a data set of 74 teleseismic *P* arrivals (the dashed vertical lines indicate an SNR of 2). At the 3-C single station, the scatter in the estimates is large for SNR less than 2.

TABLE 2

SLOWNESS DIFFERENCES OF TELESEISMIC *P* PHASES

	Mean (sec/km)	S.D. (sec/km)	Median (sec/km)
F-K	−0.001	0.012	−0.003
F-K (SNR > 2)	−0.003	0.010	−0.003
3-C	0.017	0.032	0.006
3-C (SNR > 2)	0.004	0.014	0.002

vertical line). This is probably due to the increase in incidence angle produced by the increase in noise level on the horizontal channels, which have small signal amplitudes for the large apparent velocities of teleseismic *P* arrivals. When only phases with SNR above 2 are included in the statistical analysis, the difference between the standard deviations for the two methods, as well as the skewness of the 3-C distribution toward positive anomalies, almost disappear (Table 2).

Our 3-C slowness estimates can be refined by deriving them from estimates of "true" instead of "apparent" incidence angle, using standard formulas (Bullen, 1959). Assuming a *P*-wave velocity of 5.8 km/sec and a Poisson's ratio of 0.25, we obtained new estimates of 3-C slowness differences. Their distributions do not differ significantly from those previously obtained. The main change is a reduction of the mean of the slowness difference for the entire population (from 0.017 to 0.013 sec/km). This is probably due to the fact that, for incidence angles between 0° and 60° (which is the range observed for most teleseismic *P* arrivals), the "true" incidence angle is slightly smaller than the "apparent" one. However, the bias toward positive slowness anomalies remains, and our conclusions still hold.

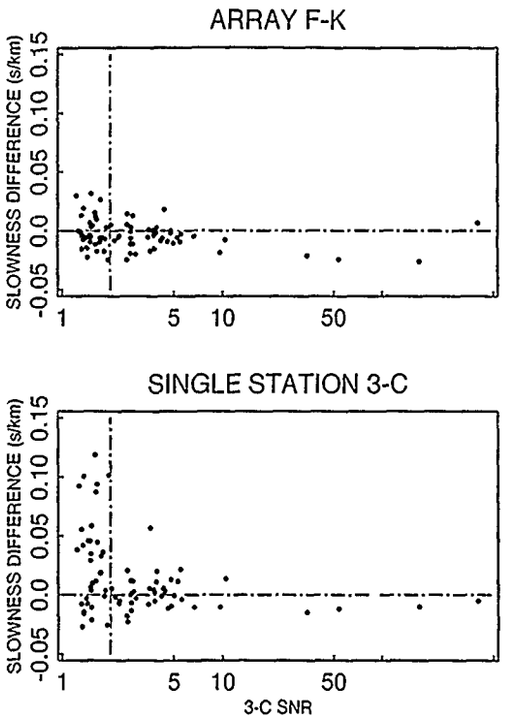

FIG. 3. Slowness differences versus 3-C SNR for a data set of 74 teleseismic *P* arrivals (the dashed vertical lines indicate an SNR of 2). At the 3-C single station, large scatter and bias in the estimates are observed for SNR less than 2.

The observed variation of the 3-C solutions with SNR does not crucially depend on the particular measure of SNR used. For example, if the "array beam SNR" (i.e., STA/LTA measured on the beam that provided the "best" detection in automated processing) is used instead of the 3-C SNR, the 3-C solutions still become stable above a certain SNR threshold (~15). Also, the decrease in variance of the 3-C estimates for the subset with 3-C SNR > 2 could be partly due to a less uniform distribution in the direction from NORESS. However, for our data set, the uniformity of the azimuthal (and distance) coverage is not significantly decreased when arrivals from this subset only are included.

Effect of Frequency Band Selection on 3-C Results

The polarization method is sensitive to parameter settings, such as the length and position of the time window and the frequency band selected for attribute measurement (see, e.g., Jurkevics, 1988). Here, we investigate the effect of the selection of frequency band on the azimuth and slowness differences when using polarization analysis for direction parameter estimation. The 74 teleseismic events were reprocessed through single station 3-C processing, using narrow frequency bands for extracting polarization attributes. The difference between this and the previous processing is that the band with the highest SNR is selected. A new narrow-band 3-C SNR is defined as the 3-C SNR for data prefiltered in this selected band, as opposed to our previous estimate, which was a wide-band average for bands with SNR above 2. The distribution of the new azimuth and slowness differences as a function of this narrow-band SNR shows the same abrupt threshold for SNR of ~2. For our data set, the population of events with SNR larger than 2 is the same, regardless of which estimate of 3-C SNR is used to define it. Therefore, we

can compare the statistical results using broadband and narrow-band polarization for the entire population and the population of arrivals with SNR above 2. For events with SNR above 2, the standard deviation of the azimuth differences is increased from 13° to 15°, and that of the slowness differences is increased from 0.014 to 0.017 sec/km, when the narrow-band method is used. This indicates that the broadband estimates are slightly better.

Dependence of 3-C Results on Polarization Attributes

We showed the effect of SNR on azimuth and slowness differences obtained from 3-C processing. We now investigate their dependence on various polarization attributes that are measured as part of the automated processing (see Jurkevics, 1988, for a description of those attributes). This will help us assess how they can help predict the errors on the azimuth and slowness estimates.

Two "polarization attributes" are significantly correlated with the azimuth and slowness differences. Figure 4 (*top*) shows the azimuth difference (hereafter referred to as δaz) as a function of rectilinearity. There is high correlation between rectilinearity and SNR. All phases with SNR above 2 have rectilinearity above 0.7, and most phases with rectilinearity above 0.87 have SNR above 2 and small azimuth (and slowness) differences. This suggests that low SNR is a major contributing factor to decrease in rectilinearity, which in turn causes an increase in the scatter of the estimates. Figure 4 (*bottom*) shows δaz as a function of the ratio of horizontal to vertical amplitude (H/V). The azimuth (and slowness) differences are highly correlated with H/V and SNR. Phases with H/V less than 0.3 have small azimuth differences, and most have SNR above 2.

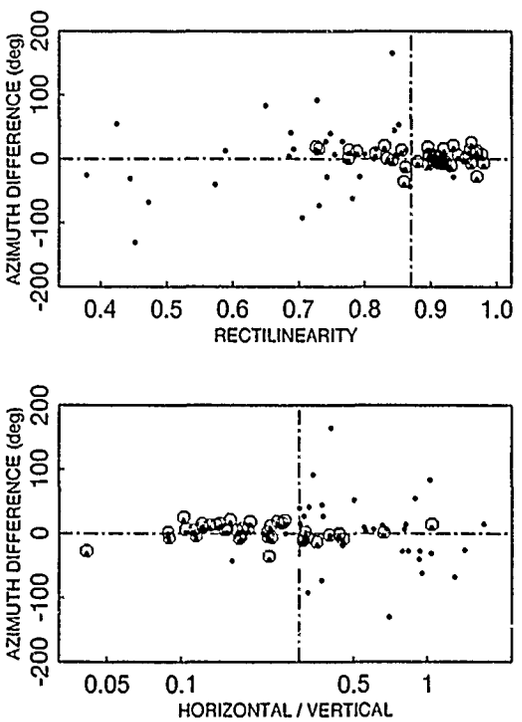

FIG. 4. Azimuth differences versus rectilinearity (*top*) and versus ratio of horizontal to vertical amplitude (*bottom*) for a data set of 74 teleseismic *P* arrivals at NORESS 3-C single station NRA0. Data points for which 3-C SNR is greater than 2 are circled. The scatter in the estimates is large for rectilinearity smaller than about 0.87 and H/V greater than 0.3 (dashed vertical lines).

In conclusion, for this data set of teleseismic *P* arrivals, the azimuth and slowness differences are not only well correlated with 3-C SNR, but also with rectilinearity and ratio of horizontal to vertical amplitude. This is because a loss in rectilinearity (due to complex near-receiver effects), and low SNR on the horizontal components (due to small incidence angle combined with high noise level) contribute to increasing the scatter in the estimates. Therefore, along with 3-C SNR, those polarization attributes can help predict the magnitude of the error on the azimuth and slowness measurements from 3-C processing.

Results from Regional *P*-Wave Analysis

A similar comparison was performed for a set of 68 regional *P*-type phases detected at NORESS. It was extracted from a larger research data set compiled at the Center for Seismic Studies (Jurkevics, 1988). They cover a large range of distances (from local to far-regional), azimuths, and SNR. For all events, independent azimuth estimates were obtained from network locations published in the bulletins of Helsinki and Bergen Universities, or from the *PDE Bulletin*. Polarization analysis was performed at station NRA0, except for 20 events, for which NRC4 was used instead because NRA0 data were missing. The set of frequency bands was 1 to 2, 2 to 4, 4 to 8, and 8 to 16 Hz. A 2 sec moving window was used to select the optimal measurement time within an 8 sec data segment centered on the detection time.

Comparison of f-k and 3-C Results

Azimuth differences were obtained with each method for all 68 regional events. Only a few phases have SNR below 2. The 60 phases with SNR above 2 were further analyzed (one outlier with anomalously large 3-C azimuth difference was excluded). The *f-k* method provides somewhat better estimates: a standard deviation of 11° is observed as opposed to 14° for the 3-C method.

Comparison of 3-C and Beam SNR

The relevant SNR for the array method is the "beam SNR," which is the ratio of STA to LTA for the best detecting beam. For the single station method, we use the "3-C SNR," or the ratio of maximum signal 3-C amplitude to average pre-event noise 3-C amplitude in the frequency band used for measuring the azimuth. We compared these two measures of SNR. There is a good correlation between the two. For this data set of 68 regional *P* arrivals, the ratio of array beam SNR to 3-C SNR varies from 2 to 8 on average. A ratio of 3 to 5 is expected from theoretical considerations on noise reduction through beamforming. Therefore, our results show somewhat more scatter than expected from such predictions. This may be partly due to the differences in channels, frequency bands, and particular techniques used to obtain these two SNR measures.

Effect of Frequency Band Selection on 3-C Results

As for the teleseismic data set, we studied the effect of frequency band selection on the results from polarization analysis. For the data set of 48 regional *P* arrivals at NRA0, four different methods were used to select the frequency band for azimuth estimation: broadband from 1 to 16 Hz (all four bands, 1 to 2, 2 to 4, 4 to 8, 8 to 16 Hz, included); broadband from 1 to 8 Hz (only first three bands included); narrow-band from 1 to 16 Hz; and narrow-band from 1 to 8 Hz.

The azimuth differences were estimated for each method and are plotted in Figure 5 as a function of 3-C SNR for the narrow-band method. The main effect of

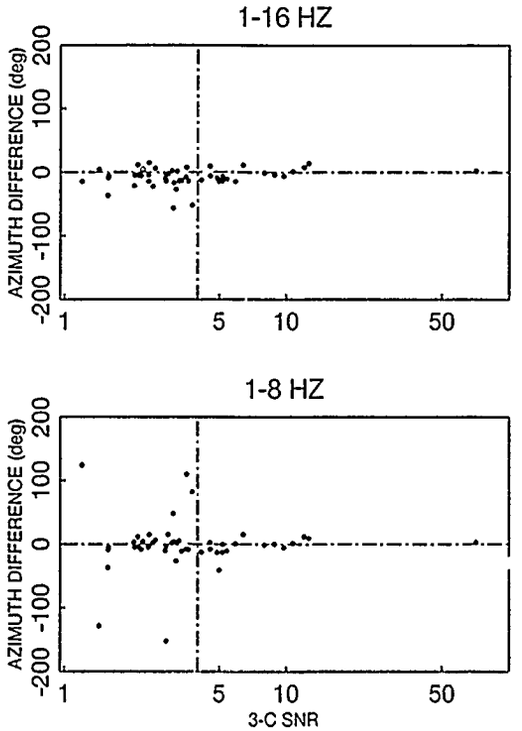

FIG. 5. Azimuth differences versus 3-C SNR for a data set of 48 regional *P* arrivals at NRA0. 3-C processing was performed using two different methods of frequency band selection: narrow-band, including the 8 to 16 Hz band (*top*), and narrow-band, excluding that band (*bottom*) (see text for further description of the methods). In each case, the 3-C SNR is the estimate obtained using the broadband, 1 to 16 Hz method. For SNR less than 4 (dashed vertical lines), excluding the high-frequency band produces outliers.

excluding the high-frequency band (8 to 16 Hz) is to increase the number of outliers. Therefore, for our data set of regional *P* arrivals at NRA0, automated azimuth estimation from polarization is more stable when all bands from 1 to 16 Hz are included in the analysis. We compared the standard deviations for the four methods when outliers are excluded. For the narrow-band estimates, they are slightly lower (by about 1.5°). This may reflect the fact that broadband estimates can be contaminated by the inclusion of frequency bands with relatively low SNR (close to 2). This suggests using SNR to weight the contribution of individual bands as a possible improvement to the broadband method.

Comparison of 3-C Results at Various Stations

Previous studies have indicated that azimuth estimates from single-station 3-C processing and/or their variances are site-dependent (Kværna and Doornbos, 1986; US/GSE/49, 1987). In order to assess this effect for our data set of regional events, we performed the same analysis at all four NORESS 3-C stations and compared the results. For most of the events analyzed, not all four stations were recording. Since we processed all available 3-C data, each station has a different event population. Arrivals covering the entire range of SNR were analyzed, but most (~90 per cent) have SNR larger than 2.

In spite of different event populations, NRA0, NRC2, and NRC4 have similar distributions of azimuth differences, with standard deviations of 15° to 16° (excluding outliers). This compares well with our previous result of a standard deviation of 14° for a population of 48 NRA0 and 20 NRC4 regional *P* arrivals with SNR > 2.

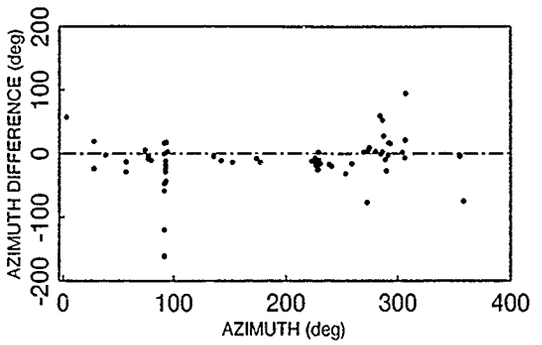

FIG. 6. Azimuth differences versus reference azimuth for a data set of 70 regional *P* arrivals at NORESS 3-C single station NRC7. Note the large scatter and bias in the estimates for two azimuth ranges, around 100° and 300°.

The similarity of the distributions for NRA0 and NRC4 justifies our use of a mixed population from both stations.

Although NRC4 and NRC7 have almost identical event populations, their distributions are very different. NRC7 has a standard deviation of 25°, much larger than that of NRC4 (and the other two stations), and more outliers. This illustrates the site-dependence of the single-station 3-C method for azimuth estimation. Since the paths to NRC4 and NRC7 are very close, the differences must be due to near-receiver structure. Similar results were obtained in RSTN stations (US/GSE/49, 1987): RSSD showed much more scatter than RSNY and RSON, and this was attributed to differences in local geology near the receivers.

To investigate a possible correlation between the large scatter at NRC7 and specific azimuth ranges, the azimuth differences are plotted as a function of theoretical azimuth in Figure 6. Two azimuth ranges show systematic biases, large scatter, and outliers. For 17 events in the 90° to 100° range, the bias is negative, with a median of −18°. For 14 events in the 280° to 310° range, the bias is positive, with a median of 14°. No such biases and scatter are observed at NRC4 and NRC2, but a similar bias is apparent at NRA0, although less pronounced. These results suggest that better estimates could be obtained at NRC7 by applying azimuth-dependent corrections for those two azimuth ranges. Further investigations are required to determine what causes these anomalies at NRC7.

A study of the outliers observed at three of the stations shows they are due to various causes. Although some might be remedied through improvements in the automated processing procedure, very low SNR appears to be an intrinsic limitation. Other outliers may be due to signal complexities at NRC7 for some directions to NORESS.

CONCLUSIONS

The capability of 3-C stations for azimuth and slowness estimation critically depends on SNR. For 3-C SNR below a threshold of ~2, the scatter in the estimates is very large for both parameters, and the slowness tends to be overestimated. The array measurements obtained with the broadband *f-k* method are not significantly affected by noise in the range of SNR considered. For events with sufficient SNR, both methods compare well, with only a slightly better performance by the *f-k* method (more pronounced for regional arrivals). The results from this study agree

with those from a theoretical investigation by Harris (1982). Also, the effects of SNR on the uncertainty of direction estimates from 3-C processing are similar to those reported in other studies (US/GSE/49, 1987; Jurkevics, 1988; Walck and Chael, 1989).

For regional arrivals, the ratio of beam (or array) SNR to 3-C SNR varies from 2 to 8 on average, which is a somewhat larger variation than expected from theoretical considerations (3 to 5). This ratio is larger for teleseismic *P* phases, on average, with a mean of 7.

The performance of the 3-C method for teleseismic arrivals is slightly improved when using broadband instead of narrow-band estimates for SNR > 2. The opposite is true for regional arrivals, possibly due to noise contamination in frequency bands with SNR close to 2, when using the broadband method. The inclusion of a high-frequency band (8 to 16 Hz) in the 3-C analysis of regional *P* arrivals reduces the number of outliers, therefore increasing the stability of the method.

As shown by a detailed analysis of the results from 3-C processing of teleseimic *P* arrivals, the azimuth and slowness differences are not only correlated with 3-C SNR, but also with other "polarization attributes," especially rectilinearity and ratio of horizontal to vertical amplitude. Therefore, these are good candidates for predicting estimated errors of azimuth and slowness measurements from 3-C processing.

A comparison of 3-C processing of regional arrivals at the four NORESS 3-C stations showed the results are site-dependent. In particular, the distribution of azimuth differences at NRC7 differs significantly from those at the other stations (larger standard deviation and more outliers). These anomalies seem mostly confined to two azimuth ranges, with biases in their estimates, suggesting that azimuth-dependent corrections could improve the performance at this station.

ACKNOWLEDGMENTS

I would like to thank A. Ryall for his encouragement and many helpful discussions. F. Ryall and J. Coyne provided valuable assistance in selecting and assembling the data sets for this study. Useful comments by S. Bratt and an anonymous reviewer are also appreciated. This research was supported by the Defense Advanced Research Projects Agency under Contract MDA-903-87-C-0037.

REFERENCES

Bache, T. C., S. R. Bratt, J. Wang, R. M. Fung, C. Kobryn, and J. W. Given (1990). The Intelligent Monitoring System, *Bull. Seism. Soc. Am.* **80**, Part B, 1833–1851.

Bullen, K. E. (1959). *An Introduction to the Theory of Seismology*, Cambridge University Press, London, England, 126–128.

Harris, D. B. (1982). Uncertainty in direction estimation: a comparison of small arrays and three-component stations, in *Technical Report UCID-19589-82*, Lawrence Livermore National Laboratory, Livermore, California, 31 pp.

Jurkevics, A. (1988). Polarization analysis of three-component array data, *Bull. Seism. Soc. Am.* **78**, 1725–1743.

Kværna, T. and F. Ringdal (1986). Stability of various F-K estimation techniques, in *NORSAR Semiannual Technical Summary, 1-86/87*, Kjeller, Norway, 29–40.

Kværna, T. (1987). Wide-band slowness estimation using a small aperature seismic array, in *NORSAR Semiannual Technical Summary, 2-86/87*, Kjeller, Norway, 38–45.

Kværna, T. and D. J. Doornbos (1986). An integrated approach to slowness analysis with arrays and three-component stations, in *NORSAR Semiannual Technical Summary, 2-85/86*, Kjeller, Norway, 60–69.

US/GSE/49 (1987). A recommendation for inclusion of azimuth as a reportable parameter for three-component stations, in *United States Delegation to the Conference on Disarmament*, Geneva, Switzerland, 37 pp.

Walck, M. C. and E. P. Chael (1989). Optimal back-azimuth estimation for three-component recordings of regional events (abstract), *EOS* **70**, 1197.

CENTER FOR SEISMIC STUDIES
1300 N. 17TH STREET
SUITE 1450
ARLINGTON, VIRGINIA 22209

Manuscript received 1 February 1990

Bulletin of the Seismological Society of America, Vol. 80, No. 6, pp. 1999–2015, December 1990

AZIMUTH ESTIMATION CAPABILITIES OF THE NORESS REGIONAL SEISMIC ARRAY

BY DORTHE A. BAME, MARIANNE C. WALCK, AND KATHIE L. HIEBERT-DODD

ABSTRACT

We have investigated the regional P_n backazimuth estimation capabilities of the NORESS seismic array as a function of element spacing, frequency band, and time window to determine which parameters are optimal for reducing azimuth errors. We used a broadband frequency-wavenumber estimator to calculate backazimuths from the P_n arrival for each of 274 regional events recorded at NORESS for 126 parameter combinations. The large data base provides a wide range of signal-to-noise ratio (SNR) (0 to 70 dB), distance (up to 10.5°), and azimuth characteristics, and includes identified earthquakes and explosions as well as "unknown" sources. Most of the errors in backazimuth are less than 20° when appropriate parameters are used, and mean backazimuth errors are close to zero. The best results are obtained using a 13-element array configuration that has a 1.4 km aperture and a maximum station spacing of about 600 m. With the 13-element configuration and the data filtered to include frequencies between 3 and 10 Hz, the mean errors for the 274 event data set are less than 1.4°, and standard deviations are as small as ±11.1°. The entire array also produces good results for 3 to 10 Hz, and a 9-element configuration (two inner rings) performs well at high frequencies. The five-element B-ring (600 m aperture) appears to be important in obtaining good backazimuth estimates for regional P_n waves. Of the frequency bands considered in this study, the 3 to 6 Hz, 4 to 8 Hz, and 5 to 10 Hz bands yield the most reliable backazimuth estimates, even better than an "optimal" band that calculates the azimuth in the fixed frequency band that has the largest average SNR. The time-window length has little effect on the backazimuth estimates. Other factors investigated include SNR, source region, and phase type. We found that event backazimuth accuracy degrades if the SNR of a beamed P_n signal is less than 5 dB in the frequency band of interest. Conversely, the backazimuth estimation statistics improve if only events with 5 dB of SNR are included in the event set. These data sets yield near-zero mean errors and smaller standard deviations than the entire data set. For specific source regions, standard deviations are as low as 2° for some parameter combinations, but there can also be large biases in the backazimuth estimates. Events farther than 500 km from NORESS tend to have larger azimuth errors than the closer events, but combinations of small aperture configurations and middle (3 to 10 Hz) frequency bands work well for events over the entire distance range of 40 to 1200 km. The P_n arrival and RONAPP azimuths calculated from the L_g phase have similar accuracy statistics for a 220 event common data base, implying that the two phases work equally well for regional event backazimuth estimation. In fact, averaging of the L_g and P_n estimates provides the most accurate backazimuths relative to PDE reference information.

INTRODUCTION

One issue involved in seismic verification of a nuclear test ban treaty is the ability of a sparse network of seismic stations to locate accurately small regional seismic events. Recent studies have considered regional locations using either multiple arrays (Bratt and Bache, 1988; Mykkeltveit *et al.*, 1988) or a sparse network of

three-component stations (Ballard *et al.*, 1989; Thurber *et al.*, 1989). For very small events or a very sparse network, events may have to be located using data from only one or two reporting stations. Such locations require the use of both multiple-phase picks from each station and backazimuth estimates. Seismic arrays should provide reliable backazimuth estimates because of their noise suppression and spatial sampling characteristics. It is important, however, to determine just how accurate the array-estimated backazimuths are to be able to predict the location accuracy of sparse networks that include arrays as components. It also would be useful to know how to optimize regional backazimuth estimates in terms of controllable parameters, such as the frequency band and choice of array elements used in the calculation.

Kværna and Ringdal (1986) have documented excellent backazimuth accuracy at NORESS for a limited, high signal-to-noise ratio (SNR) data set; they did note significant variations in backazimuth accuracy for different frequency-wavenumber estimators. Mykkeltveit *et al.* (1985) also obtained good backazimuth accuracy for 18 USSR mine blasts recorded at NORESS, but noted that the calculated azimuths vary strongly with frequency. These and other investigations (Mykkeltveit and Bungum, 1984; Mykkeltveit, 1985) have shown that the accuracy of array backazimuth estimates depends on the method used, the frequency band, the phase type (P_n, S_n, or L_g), and the configuration (element spacing) of the array. Other factors that could influence backazimuth estimates include the time-window length over which the calculation is done, and the SNR of the signal in the analysis frequency band. Regional factors, such as path effects at certain azimuths, can also bias results. Previous studies have laid the groundwork for making the best possible backazimuth estimates from regional arrays but a more comprehensive investigation using a large data set is necessary to quantify the effects of the different parameters on regional backazimuth estimates.

We have used an automated analysis approach to study quantitatively backazimuth accuracy as a function of array configuration, frequency band, and time-window length for 274 events with known locations recorded at NORESS. We have also investigated backazimuth accuracy as a function of SNR and region for our data set. The large data base is important, since it allows us to make statistical comparisons between sets of backazimuth errors computed with varying parameters. The results show that NORESS backazimuth estimates are extremely accurate and unbiased in a statistical sense for appropriate combinations of parameters; mean errors are near zero and standard deviations are as low as 11°. Significant degradation is observed for some variations in configuration, frequency band, and SNR, however, implying that care in selecting processing parameters is essential for obtaining good backazimuth estimates from automated array processing algorithms.

Data Base

Our data base contains 274 events with known locations from three sources: the *Preliminary Determination of Epicenters* (*PDE*) *Bulletin* from the National Earthquake Information Service, and the seismic bulletins from the University of Bergen and the University of Helsinki. Almost all of the located events that occurred within 6° of NORESS between November 1985 and December 1987, regardless of magnitude, are in the data base, plus events between 6° and 10.5° with magnitudes over 3.0 during the same time period (Fig. 1). The duration magnitudes of the events less than 6° away range from 1.5 to 3.8. There are 70 known explosions and 53 known earthquakes in the data base, and the rest are categorized as unknown

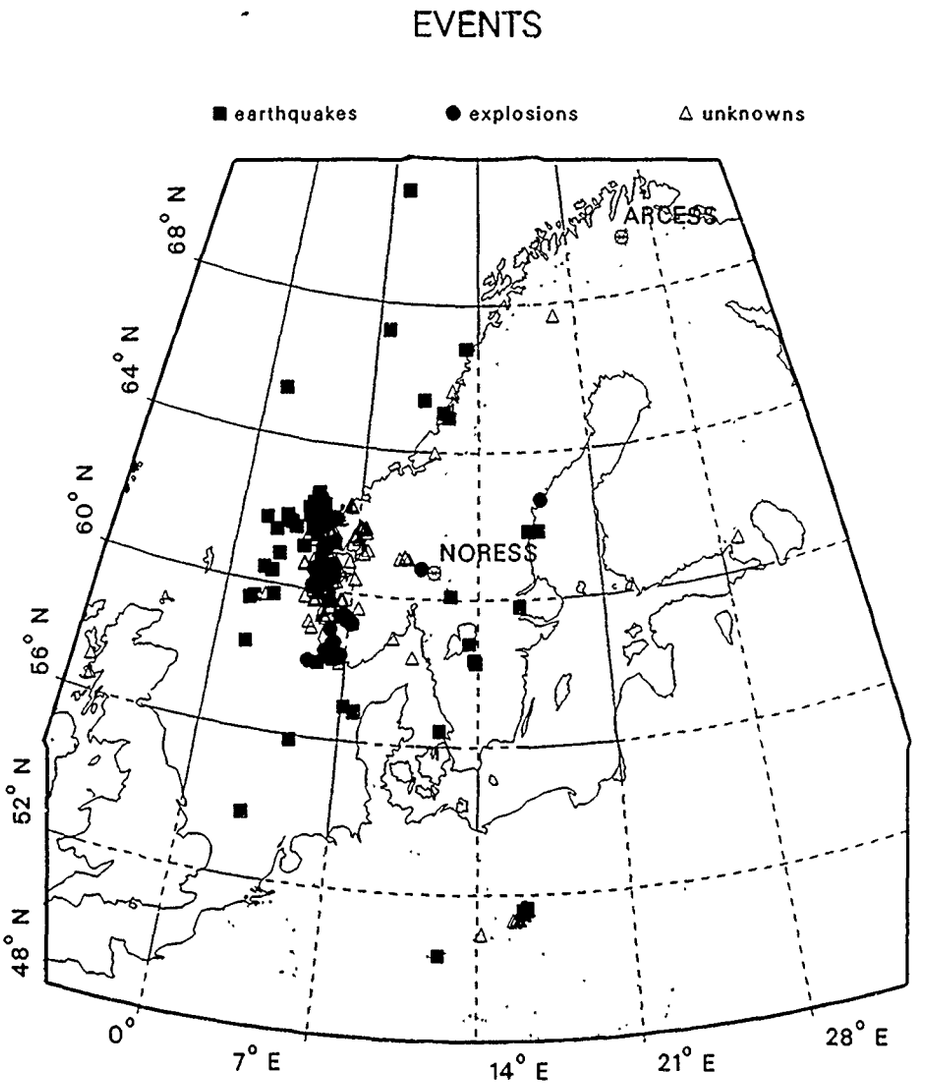

FIG. 1. Map showing NORESS array and the PDE locations for the 274 events in the data base. The location of the ARCESS array is also shown.

source type. The peak SNR of array beams for the events in our data base concentrate in the 10 to 30 dB range.

Ninety-one per cent of the events in the data base come from the *PDE Bulletin*. Events from this bulletin have different estimated location accuracies, depending on the source of the data. The geometric mean of the semi-major and semi-minor axes of the horizontal 90 per cent confidence ellipse is less than or equal to 16 km for 73 per cent of the PDE-located events. The events from the *Helsinki Bulletin* have smaller reported errors than the *PDE Bulletin* events, and although error estimates for events from the *Bergen Bulletin* were not available, they represent only a small portion of the data set. Based on a 16 km error, the error in azimuth from the known reference locations is about 3° at a distance of 350 km for our data base.

Most of the events (73 per cent) are concentrated along the western coast of Norway between the azimuths of 210° and 300°, and at distances between 240 and 440 km where there are known mines. Many of the identified earthquakes are

located in the Norwegian Sea. There are very few events to the east of NORESS in the data base. Although many events east of NORESS are recorded by the array, we analyzed only events with independent locations, and there are very few events east of NORESS listed in the *PDE Bulletin* and our limited set of bulletins from the University of Helsinki. Some earthquakes occur in Sweden, but there is only one known explosion east of the array in the data base. Other interesting events include four in the British Isles, and numerous earthquakes induced by mining in the Lubin copper basis of southeast Poland (Gibowicz, 1987).

Analysis Technique

We used an automated approach to process and analyze our large NORESS data base of regional events. The data processing included windowing and saving 33 channels of short-period around the P_n arrival for each event. Since we had reference locations for all the events, we were able to predict arrival times at NORESS and then use a conventional P-picker algorithm based on the square of the signal (e.g., Allen, 1982) to obtain a more precise P arrival time. The P window starts 5 sec before the picked arrival time and continues for 30 sec. The windowed data are stored on disk for subsequent calculations. All the data were examined by an analyst to ensure proper phase identification and reliable timing, and any elements with spikes or data drop-outs were labeled as bad and eliminated from the data base for that event. We also calculated the SNR for the array beam using the 17-element configuration (A0, C- and D-rings in Fig. 2, Table 1) and the known location. We define SNR as the ratio of the power in a 10 sec signal window (that includes signal and noise) to that in a 5 sec noise window, with the result given in decibels. SNR values are calculated at 33 frequencies over the 0 to 20 Hz range.

We used a broadband azimuth estimator that follows the method by Nawab *et al.* (1985) to calculate the backazimuth from the P_n arrival. The method calculates a two-dimensional zero-delay wavenumber spectrum. The source azimuth is estimated from a grid of 120 azimuth and 64 wavenumber points by radially integrating the

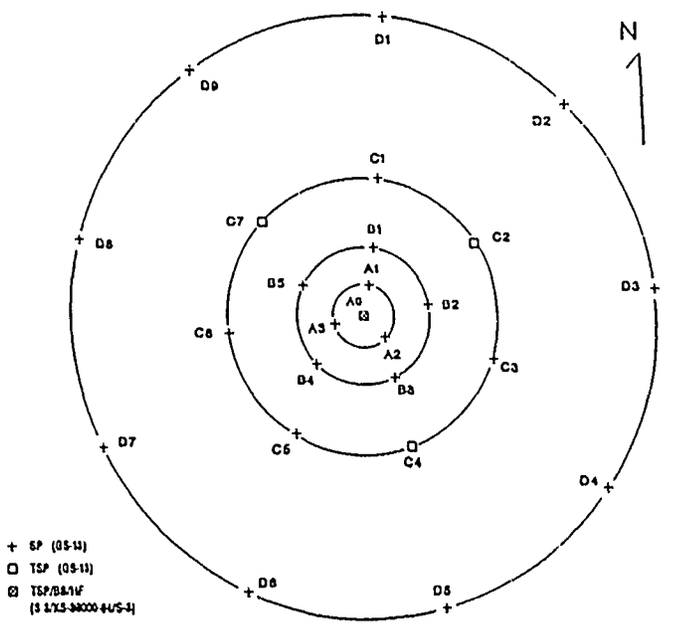

FIG. 2. Array geometry for the NORESS array. The array aperture is 3 km. The A-ring has a radius of 150 m; the B-ring, 300 m; the C-ring, 700 m; and the D-ring, 1500 m.

TABLE 1

ANALYSIS PARAMETERS USED IN THIS STUDY

Array Configurations	Elements
25	A0, A-, B-, C-, D-rings
10	A0, D-ring
17	A0, C-, D-rings
8	A0, C-ring
13	A0, B-, C-rings
9	A0, A-, B-rings
Frequency Bands (Hz)	
Unfiltered	
2–4	
3–6	
4–8	
5–10	
8–16	
Optimal	
Time Windows (sec)	
2	
3	
5	

Array configurations are listed in order of decreasing interelement spacing after the entire 25-element array. The "optimal" frequency band is the fixed band (2 to 4, 3 to 6, 4 to 8, 5 to 10, or 8 to 16 Hz) that has the largest average SNR.

spectrum for each azimuth and then fitting a parabola to the region around the peak of the power versus azimuth function.

Besides determining backazimuth accuracy statistics for regional P_n phases, we are also interested in how different array configurations, frequency bands, and time windows over which the estimate is made can affect the calculated azimuth. Table 1 lists the different parameters that are used in the analysis. The configurations, listed in order of decreasing aperture and decreasing element separation, include the entire array (all 25 elements) and five subsets of the 4-ring structure (Fig. 2). An entire ring is always used to ensure a uniform response regardless of the event azimuth. Our six fixed frequency bands consist of the unfiltered data, and five different octave-wide bands over the bandwidth of the system, effectively 0.1 to 16.0 Hz. A flexible "optimal" frequency band where the backazimuth was estimated using the fixed frequency band (2 to 4, 3 to 6, 4 to 8, 5 to 10, or 8 to 16 Hz) that had the largest average SNR was also investigated. We compare the fixed bands to the "optimal" band because other workers (e.g., Suteau-Henson, 1990) use an optimal-type approach to determine frequency band for backazimuth calculations. We used time windows of 2, 3, and 5 sec; backazimuths were calculated for all 42 configuration-frequency band combinations over each of the three time windows. An azimuth error was calculated for each case by subtracting the reference azimuth of the event from the broadband frequency-wavenumber backazimuth estimate.

After processing the data to obtain azimuth errors, we examined the backazimuth accuracy results by calculating the mean error and sample standard deviation for different data groups. The mean error tells us how much bias we have in the

backazimuth estimate, while the standard deviation provides a measure of the precision. Azimuth error dependence on several independent variables was also studied. This analysis was made tractable through the use of an object-oriented expert system to organize the data base and access the analysis results.

Expert System

The analysis for this study required more than 30,000 runs of the FORTRAN broadband azimuth estimator code. Processing and analysis of such a large set of events was made feasible by using an object-oriented expert system (Hiebert-Dodd, 1989). This system does not automatically process seismic signals, but is an assistant to the analyst, saving the analyst's time by managing data and automating procedures. It is implemented on an artificial intelligence (AI) computer (Symbolics 3610) connected to a conventional numerical computer. The system itself is written in Lisp and interfaces with existing analysis code via Ethernet hardware and operating system specific software.

The expert system saves time in two important ways. First, it organizes and manages the many pieces of pertinent information needed for analysis. This includes the data and all relevant information, the numerical analysis codes and the input and output file names, variables and error flags associated with them, and the results. Second, the expert system saves time by automating routine tasks. For each of the 274 events in the data base, the analyst entered reference information for an event, such as the location, magnitude, and event type, into the data base. The expert system would then invoke the FORTRAN data processing code, which determines information such as the P and S arrival times and the SNR, and enter those results into the data base. In the actual analysis of the data, the scientist defines a parametric study by specifying the code to be used and the values for the variables of the study, e.g., the events, array configurations, frequency bands, and time windows. The expert system would methodically work through all combinations of the variable values, invoke the proper code, collect the results (expressed in the proper units), and store them into the data base. Based on the directions given by the analyst, the expert system would gather the appropriate data and automatically run a set of standard statistical tests and plotting routines to examine and summarize the results.

Results

The calculated backazimuth errors for the 274 event data set are typically small, but the variation in mean error and standard deviation between different parameter combinations is striking (Figure 3, Table 2). Most of the frequency band-configuration combinations yield average backazimuth errors of less than 5°, indicating generally unbiased backazimuth estimates for NORESS regional events. Typical sample standard deviations for those cases are 11° to 30°. Certain parameter

FIG. 3. Three-dimensional representation of the analysis results for the 274 event data set, 5 sec time window. (a) Absolute value of the mean azimuth error for the 42 combinations of configuration and frequency band. Errors have been cut off at 10° for ease of display. Results for the 25-element configuration (entire array) and unfiltered data have been offset from the results for the filtered data with array subconfigurations. Note that the smallest errors generally occur for data filtered between 3 and 10 Hz, and for configurations that contain the B-ring. (b) Standard deviations for the cases where the mean error $< \pm 2°$. Some cases with small mean errors have relatively large deviations. The 13-element configuration combined with the 5 to 10 Hz frequency bands results in small mean errors with the smallest standard deviations.

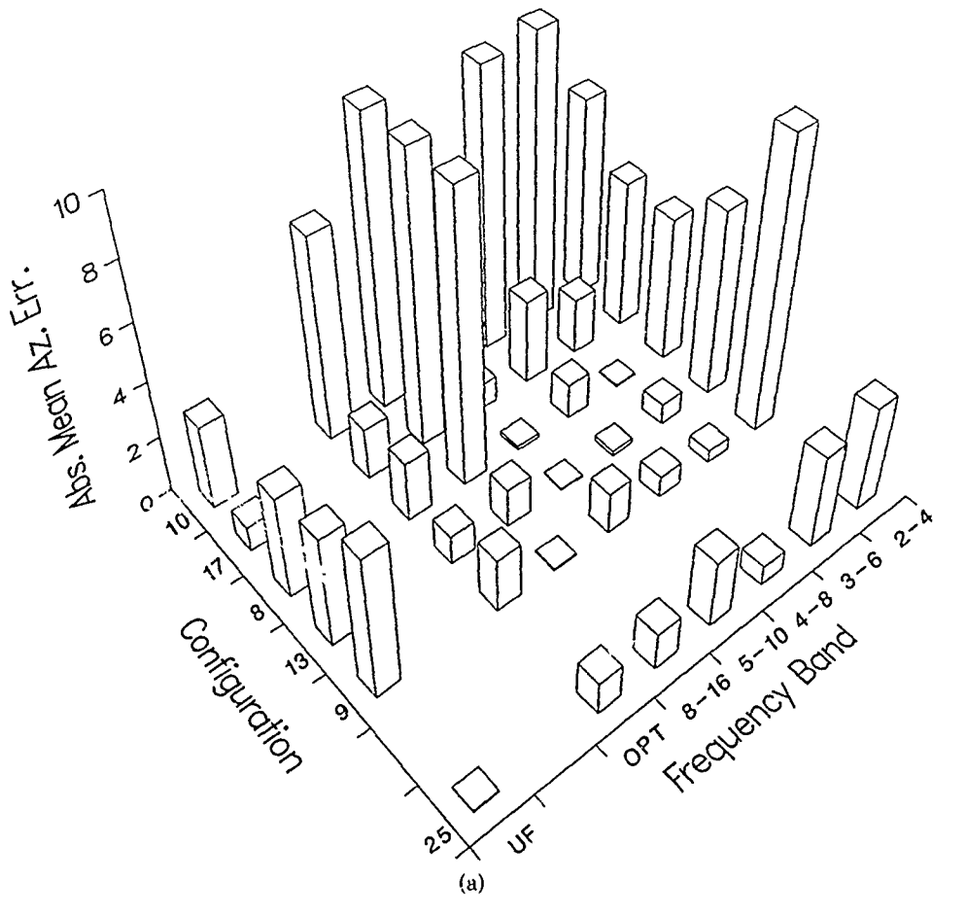
Abs. Mean Az. Err.
10
8
6
4
2
0
Configuration
10
17
8
13
9
25
Frequency Band
OPT
8-16
5-10
4-8
3-6
2-4
UF

(a)

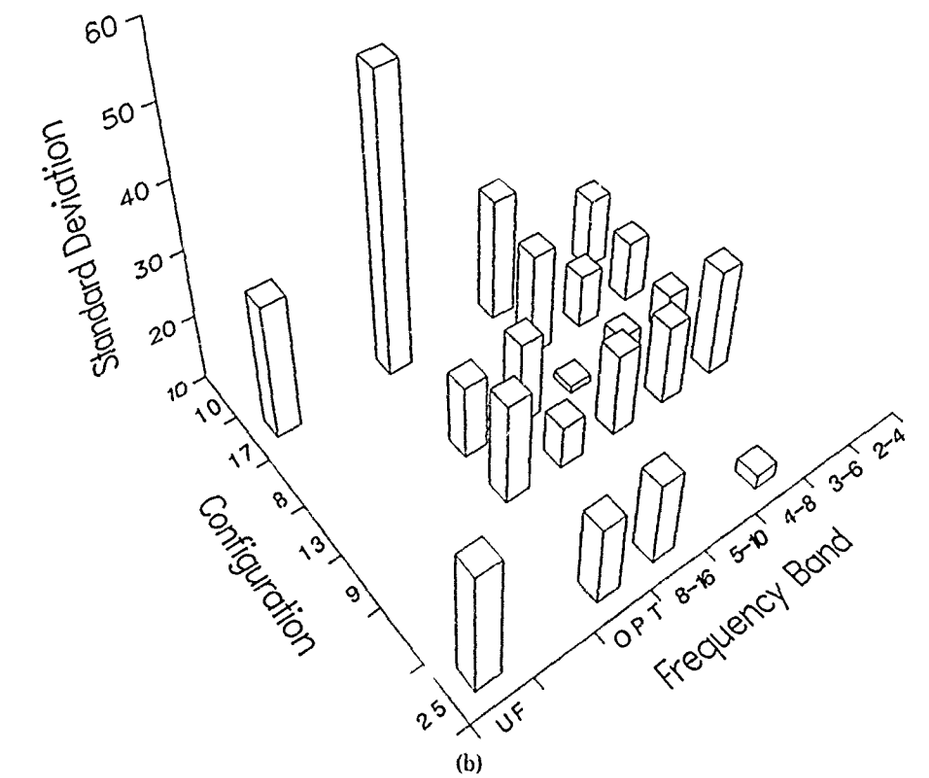
Standard Deviation
60
50
40
30
20
10
Configuration
10
17
8
13
9
25
Frequency Band
OPT
8-16
5-10
4-8
3-6
2-4
UF

(b)

TABLE 2

MEAN ERRORS AND STANDARD DEVIATIONS FOR THE ENTIRE DATA SET

Configuration	Frequency						
	UF	Optimal	8-16	5-10	4-8	3-6	2-4
25 elements	0.06	−1.15	−1.30	−2.36	−0.69	−3.29	−3.72
	28.03	21.63	22.26	15.32	12.12	17.87	34.36
9 elements	−5.03	1.89	0.07	1.45	0.75	0.43	−11.29
	32.51	25.23	16.40	22.55	22.15	26.29	52.89
13 elements	−3.91	1.02	1.36	−0.05	−0.18	−0.73	−6.53
	31.08	21.09	22.74	11.06	14.26	16.47	41.96
8 elements	−3.63	2.10	−12.97	−0.14	1.24	0.06	−5.08
	30.60	47.47	94.83	25.75	18.21	19.42	32.86
17 elements	−0.88	1.84	−19.85	−0.90	−3.01	−1.96	−5.19
	30.23	53.94	93.23	28.76	20.53	20.95	39.82
10 elements	−2.98	−7.15	−21.66	−5.46	−9.74	−10.09	−7.00
	43.27	57.30	91.38	63.66	46.36	36.95	52.02

Mean azimuth errors and standard deviations (both in degrees) for the 274 event data set and 5 sec time window. The mean azimuth error is the top number, and the standard deviation is the bottom number. The table is set up in a similar fashion as Figure 3. Small mean errors occur for a variety of configuration-frequency band combinations, particularly those including the B-ring (9, 13, and 25 elements) and mid-range frequencies. The smallest standard deviation occurs with the 13-element configuration and 5 to 10 Hz frequency band.

combinations, as discussed below, produce unbiased estimates and small data variances.

The results for the entire data set appear in Figure 3a, which shows the mean azimuth error for 42 different combinations of array configurations and frequency bands, calculated with a 5 sec time window. For simpler displays, the absolute value of the mean error has been plotted and is cut off at a maximum of 10°. The array configurations are along the left axis and have been ordered with the larger apertures at the back (see Table 1). The frequency bands are ordered with the lower frequencies to the right. We have separated the unfiltered data and the 25-element configuration from the remainder of the results because they represent the baseline performance for the array. The precision of the mean azimuth errors are shown in Figure 3b, which displays the standard deviations for the configuration-frequency band combinations with mean errors less than 2°. Table 2 contains the analysis results displayed in Figure 3.

The most striking feature of Figure 3a is the regular variation in mean error with configuration and frequency band. Small mean errors occur for the small aperture array configurations, 13- and 9-elements; the full array aperture (3 km) does not appear to be essential for reliable backazimuth estimation. The configuration with the lowest mean errors over the entire suite of frequency bands is the 13-element subset. The average backazimuth errors all have absolute values less than 1.4° except for the unfiltered and 2 to 4 Hz bands (Table 2). The mean error and standard deviation for the six configurations filtered in the 5 to 10 Hz band are shown in Figure 4. The mean errors for all but the 10-element configuration are low, but the precision of the estimates vary. The performance of the 10-element configuration with any frequency band is the worst of the six array subsets tested. Its larger aperture and interelement spacing, along with the shallow incidence angles and high-frequency energy of regional events, result in poor correlation between the

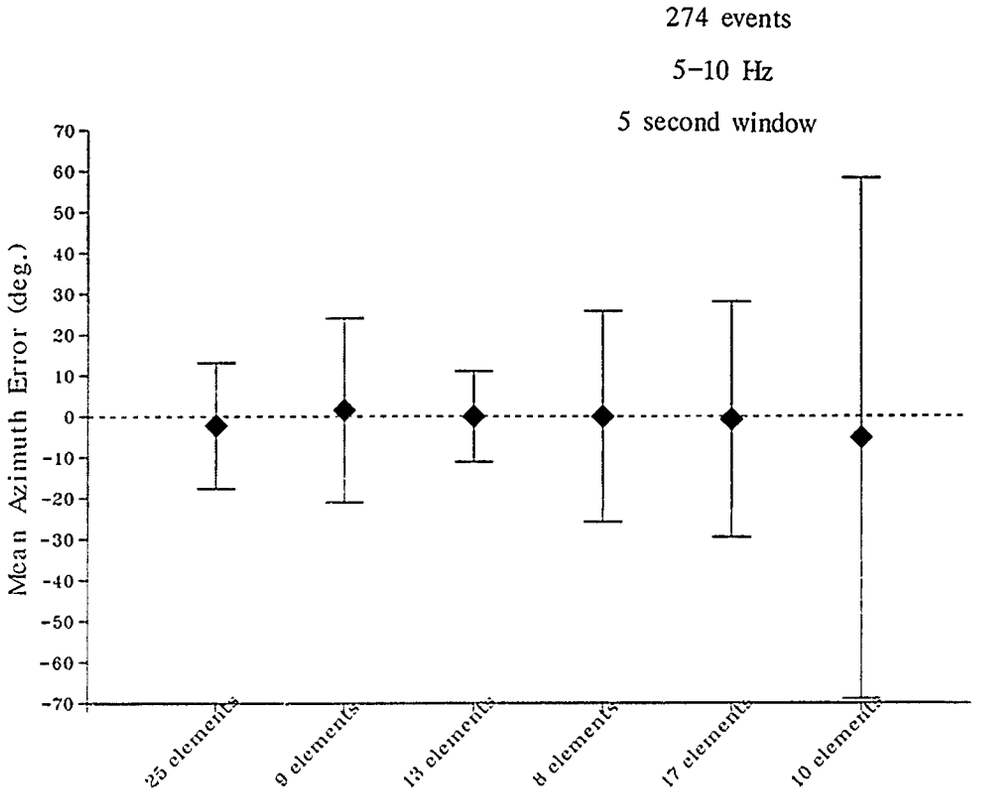

FIG. 4. Variation in the mean azimuth error and standard deviation with configuration for the 5 to 10 Hz frequency band, 5 sec time window, and 274 event data set. The 13-element configuration produces the best results, while the 10-element configuration has the largest mean error and standard deviation.

10-array elements. When elements from the C-ring are added (17-element configuration), the results improve (Figs. 3 and 4). The importance of the 600-m B-ring in estimating the azimuth is demonstrated by comparison between the 8-element (B-ring excluded) and 13-element (B-ring included) configurations. In almost all frequency bands, mean errors and standard deviations are reduced when the B-ring is added (Figs. 3 and 4). The surprisingly small mean errors calculated for unfiltered data using the 17-element and 25-element configurations are somewhat deceptive because the standard deviations are large (Fig. 3b).

As can be observed from Figure 3, filtering the data generally improves the azimuth error statistics. In Figure 5, the mean errors and standard deviations are plotted for the different frequency bands using the 13-element configuration. The largest mean errors and standard deviations occur for the unfiltered data and 2 to 4 Hz band. The 3 to 6, 4 to 8, and 5–10 Hz frequency bands all have very small mean azimuth errors that are not statistically different. Overall, the best frequency bands are 4 to 8 and 5 to 10 Hz (Fig. 3). Array performance for NORESS should be optimal near these frequencies (Ingate *et al.*, 1985). The 8 to 16 Hz band also yields good results, but only when combined with the 13-, 9-, and 25-element configurations (Fig. 3). The large errors that result from the combination of the 8 to 16 Hz band and larger aperture configurations (10, 17, and 8 elements), indicates that small interelement spacing is essential for use of frequencies at the high end of NORESS' frequency range. Use of the "optimal" frequency band does not improve the results as one might expect. For every array configuration, at least one frequency band works better than the "optimal" band. We believe that the reason the "optimal"

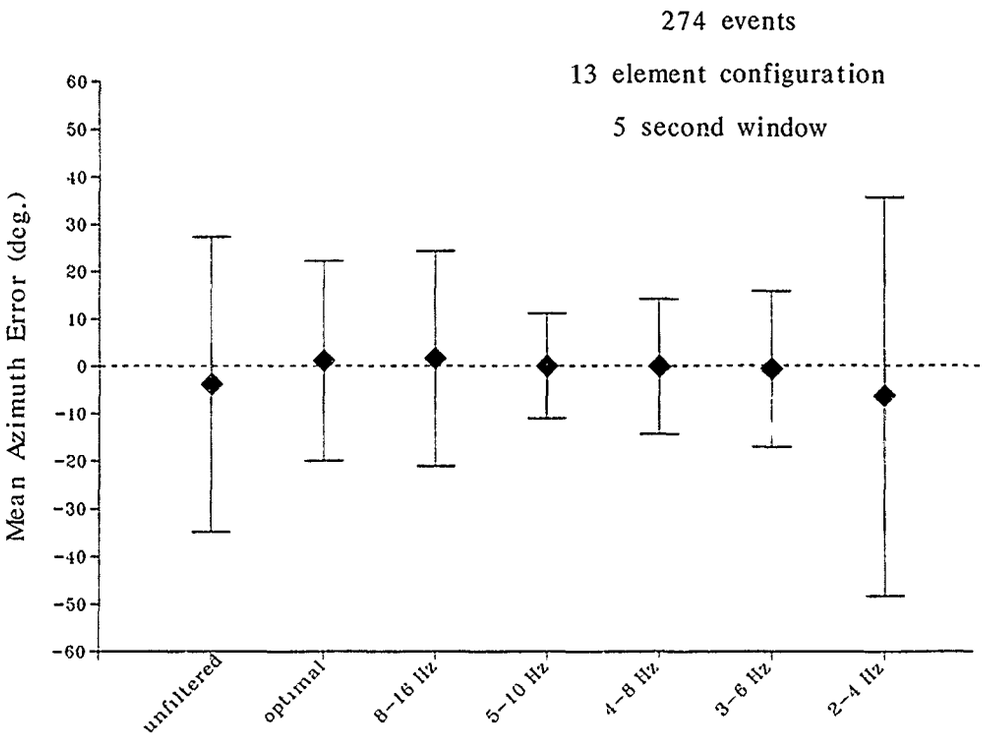

FIG. 5. Variation in the mean azimuth error and standard deviation with frequency band for the 13-element configuration, 5 sec time window, and 274 event data set. The unfiltered data, 2 to 4 Hz band, and "optimal" frequency band produce relatively poor results, but the other frequency ranges have mean errors near zero and small standard deviations.

band does so poorly with the larger aperture configurations (10, 17, and 8 elements) is that many of the events have "optimal" SNR in the 8 to 15 Hz band. The largest mean errors occur for the 2 to 4 Hz frequency band, which is also surprising because many events in the data base have high SNR in the 2 to 4 Hz frequency range. The correlation between elements in this frequency band should be reasonably good because the frequencies are low, so the problem may be a lack of resolution due to the combination of small aperture and low frequencies.

We also investigated the effect of varying the time-window lengths used in the broadband estimator. When the mean errors and standard deviations calculated with 2, 3, or 5 sec time windows are compared for specific configuration-frequency band combinations, the results are not statistically different. From examination of our data, we feel that the 3 and 5 sec windows generally perform better, possibly because the longer windows include more signal for weak SNR events. In general, however, the time-window length has only a weak effect on the backazimuth estimates.

All of the results discussed previously were obtained using the entire data base, regardless of SNR. To investigate the effect of SNR on backazimuth estimates, we selected an array configuration and frequency band that produces good results, (13 elements, 4 to 8 Hz, 5 sec), and plotted the backazimuth error of all events against the SNR averaged over the 4 to 8 Hz band (Fig. 6). Most of the events (96 per cent) have errors that are less than 20° and many of these events have low SNR. There is a clear tendency for the large azimuth errors to occur for low SNR events as suggested on theoretical grounds by Harris (1982); 6 of the 10 events with errors larger than 20° have SNR less than 5 dB. Of the other four outliers, three

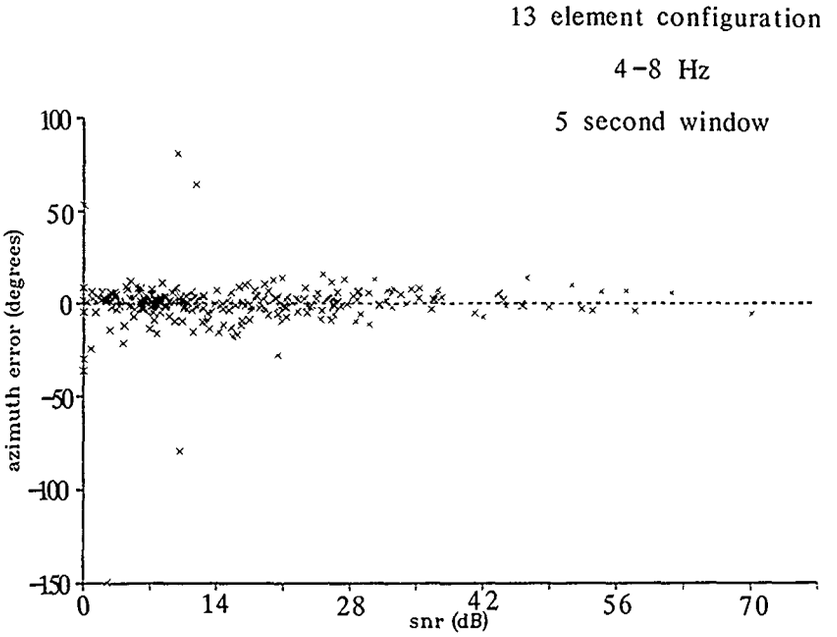

FIG. 6. Comparison of SNR to the azimuth error for azimuths calculated with the 13-element configuration, 4 to 8 Hz band, and 5 sec time window. SNR is averaged over the 4 to 8 Hz band. The majority of large errors occur for very low SNR.

occur at distances greater than 940 km from NORESS, and the fourth is an explosion at a known mine approximately 400 km away.

Because most of the large errors seem to occur for low SNR events, one reasonable approach to azimuth optimization would be to impose an SNR cutoff below which the backazimuth accuracy rapidly degrades, but which excludes the fewest possible events with good azimuth estimates. An alternative method would be to weight the data by SNR. We chose to look at the effects of SNR by imposing a 5 dB cutoff; Table 3 lists the mean and standard deviations for the 42 configuration-frequency band combinations for these cases. The sample size is listed for each frequency band because different events fit the cutoff criteria in the different bands. Ninety-three per cent of the events in the data base have SNR over 5 dB in at least one frequency band ("optimal" band). The smallest data set was the 8 to 16 Hz band, where only 59 per cent of the events met the cutoff criterion. After application of the 5 dB SNR cutoff, the mean errors are generally similar in magnitude to those displayed in Table 2. There is a tendency for the mean errors to move closer to zero, but this is not always the case; an example is the "optimal" band results. Almost all the standard deviations in Table 3 have decreased from the corresponding entries in Table 2, implying that removing the low SNR events tightens up the backazimuth error distributions. The best parameter combination overall when imposing a 5 dB SNR cutoff appears to be the 13-element configuration, 4 to 8 Hz frequency band, which has a mean error of 0.3° and a standard deviation of only 10.63°. The standard deviation has decreased from 14.26°, calculated for the same parameters and the entire data set. Several other parameter combinations (25 elements, 3 to 6 or 4 to 8 or 5 to 10 Hz; 13 elements, 3 to 6 or 5 to 10 Hz; 8 elements, 3 to 6 Hz) have statistics that are very similar (Table 3).

Other authors (Harris, 1986; Kværna and Ringdal, 1986; Gibowicz, 1987) have looked at event backazimuths from specific regions and found biases that can be

TABLE 3

MEAN ERRORS AND STANDARD DEVIATIONS FOR DATA SETS WITH AN SNR CUTOFF

Configuration	Frequency						
	UF	Optimal	8-16	5-10	4-8	3-6	2-4
25 elements	0.46	0.98	0.69	−2.39	−0.71	−1.42	0.05
	23.53	15.04	19.67	12.65	12.22	12.28	24.82
9 elements	−2.52	1.99	−0.61	1.78	0.58	2.67	−3.79
	19.57	24.84	17.89	16.13	15.24	20.32	43.35
13 elements	−2.95	1.80	0.89	−0.16	0.33	0.67	−2.56
	24.52	13.48	16.61	11.14	10.63	10.73	29.27
8 elements	−2.63	4.44	−5.50	0.20	0.51	0.19	−2.47
	23.81	41.72	80.60	14.14	13.14	12.03	23.11
17 elements	0.18	5.47	0.83	−0.98	−1.92	−0.95	−1.99
	24.16	51.07	88.53	19.51	15.98	14.27	30.24
10 elements	1.14	−6.69	−18.10	−7.53	−11.36	−7.32	−3.42
	40.53	55.74	94.50	59.01	38.73	32.12	41.38
Sample size	172	254	163	206	230	237	224

Mean azimuth errors and standard deviations for the data sets that include only events with SNR > 5 dB in each frequency band. Setup is as in Table 2. The number of events in each data set is listed for each frequency band. For this data set, the mean errors tend to be more positive and the standard deviations smaller than for the 274 event data set.

attributed to path effects. To investigate path effects in our data base, we chose two regions where the sample size was large enough to obtain meaningful statistics. These areas are the Blåsjø Mine in western Norway (24 events) and the Lubin copper basin in Poland (13 events). Pertinent information about these areas plus the mean error and standard deviation for the best parameter combination can be found in Table 4. Twenty-three of 42 parameter combinations have mean errors less than 4° and standard deviations less than 5° for the Blåsjø events. The largest errors occurred for data filtered in the 2 to 4 and 8 to 16 Hz bands, even though the SNRs in these bands are good. A small positive bias of 2° to 3° is seen for combinations of the 13- and 8-element configurations with the 4 to 8 and 5 to 10 Hz frequency bands. The Polish events are earthquakes induced by mining in the Lubin basin and have highly accurate locations (Gibowicz, 1987). Since the earthquakes are over 1,000 km from NORESS, the larger aperture configurations, 17 and 10 elements, have the best results. Surprisingly though, the middle frequencies (4 to 10 Hz) are important (Table 4). These events have a large negative bias, −10° to −15°, so the array is locating them farther north then they actually occur. However, the precision is good, with standard deviations under 5° for the large aperture, mid-frequency parameter combinations.

Distances vary from 40 to 1,200 km for events in the data base, but the majority are at distances between 300 and 500 km from NORESS. In general, as the distance increases, the azimuth estimates become less reliable. Not surprisingly, the 2 to 4 Hz band and 10-element configuration show improved performance for events at distances over 500 km, but the combination of small aperture configurations and middle (3 to 10 Hz) frequency bands provides good performance over the entire distance range.

TABLE 4

THE BLÅSJØ MINE AND THE LUBIN COPPER BASIN EVENTS

Region	Location	Average Distance (km)	Average Azimuth (°)	Mean Error (°)	Standard Deviation (°)	Best Parameters
Blåsjø	59.31N 6.95E	300	240	3.70	1.80	8 elements 5–10 Hz
Lubin, Poland	51–52N 15–17W	1,064	163	−14.73	2.33	17 elements 5–10 Hz

The mean error and standard deviation are those calculated using the best parameter combination and a 5 sec time window. Backazimuth estimates from the Blåsjø Mine have a small positive bias when using the 8-element configuration and the 5 to 10 Hz frequeny band. The backazimuth estimates for the Polish earthquakes have a large negative bias with the best parameter combination of 17 elements and 5 to 10 Hz.

While our backazimuth estimates are the P_n arrival, the real-time RONAPP system, which generates the NORESS event bulletin (Mykkeltveit and Bungum, 1984), calculates the backazimuth with the L_g phase. Mykkeltveit (1985) compared the backazimuths calculated from the P_n and L_g phases for 132 events west of NORESS and selected the L_g arrival to calculate backazimuths. Our larger, more distributed data base should be useful for further comparison of the relative backazimuth estimation accuracy of the two phases.

Of the 274 events in the data base, 18 were not listed in the *NORESS Bulletin* and thus do not have a RONAPP azimuth value. These events either have low SNR or $\Delta > 1{,}000$ km, and many of their P_n backazimuth errors are over 20°. Figure 7 shows histograms comparing the backazimuth error for the different phases using a 220 event common data base for which SNR is greater than 5 dB in the 4 to 8 Hz band. The backazimuths in Figure 7 were calculated using the 13-element configuration, 4 to 8 Hz frequency band, and a 5 sec time window. Only the events with errors between ±20° are plotted; all of the data sets in Figure 7 have some outliers that do not appear. Figure 7a compares the P_n backazimuths from this study to the reference (PDE) azimuths. The mean error is 0.3° and the standard deviation is ±9.1°. RONAPP L_g azimuths are compared to the PDE azimuths in Figure 7b. The mean error and standard deviation are similar to the P_n − PDE data set at −0.5° and ±8.7°. The P_n backazimuth errors appear to have a somewhat more tightly clustered distribution than the L_g azimuths (Fig. 7, a and b), but the P_n outliers tend to have larger errors than the L_g outliers, resulting in a slightly higher standard deviation for the P_n − PDE data set. The similar accuracy statistics for the two phases implies that P_n and L_g perform equally well for regional event backazimuth estimation. The histogram of the difference between the RONAPP and P_n backazimuths (Fig. 7c) shows a less peaked distribution, indicating that the L_g and P_n azimuths for individual events often differ considerably, and that averaging the two estimates together for each event might improve the backazimuth accuracy statistics. Figure 7d shows the distribution of the averaged RONAPP and P_n backazimuths relative to the PDE azimuth values. The standard deviation decreases to ±6.2°, slightly less than the expected improvement for two independent data sets (Bevington, 1969; p. 60). This result suggests that improved backazimuth estimates can be achieved using an average of the P_n and L_g phases.

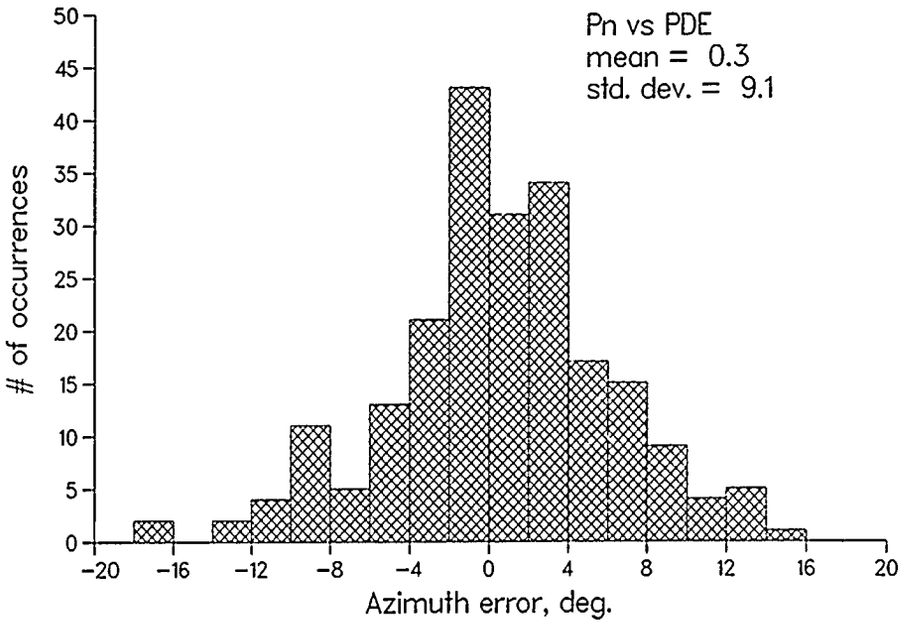

(a)

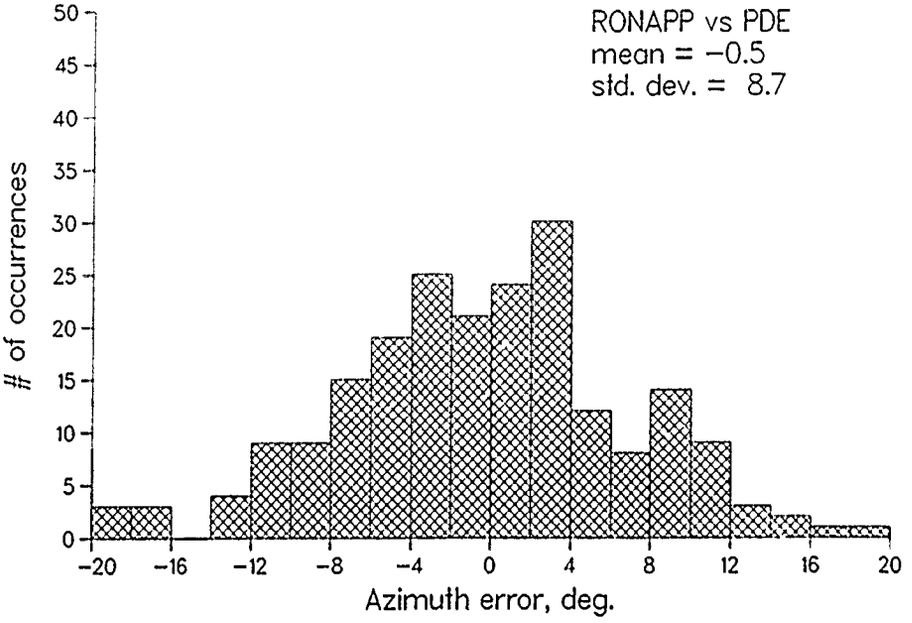

(b)

FIG. 7. Histograms of azimuth error between ±20° for a 220 event data set that includes all events with SNR > 5 dB between 4 to 8 Hz that have both P_n and RONAPP azimuth estimates. P_n calculation parameters are the 13-element configuration, 4 to 8 Hz frequency band, and 5 sec window. (a) P_n azimuths compared to PDE reference azimuths. 217 of 220 azimuths shown; the rest are outliers with errors > 20°. (b) RONAPP azimuths compared to PDE reference azimuths. 212 events have errors smaller than 20°. (c) Comparison of RONAPP and P_n azimuth estimates. 210 events appear. (d) The average of the P_n and RONAPP azimuths for each event compared to the PDE azimuths. 218 events are plotted. Note the smaller standard deviation for the averaged azimuths.

DISCUSSION AND CONCLUSIONS

Small-aperture arrays, such as NORESS, provide reliable backazimuth estimates that should be useful for locating regional events. For NORESS-type arrays, we have documented specific array configurations and frequency bands that can be

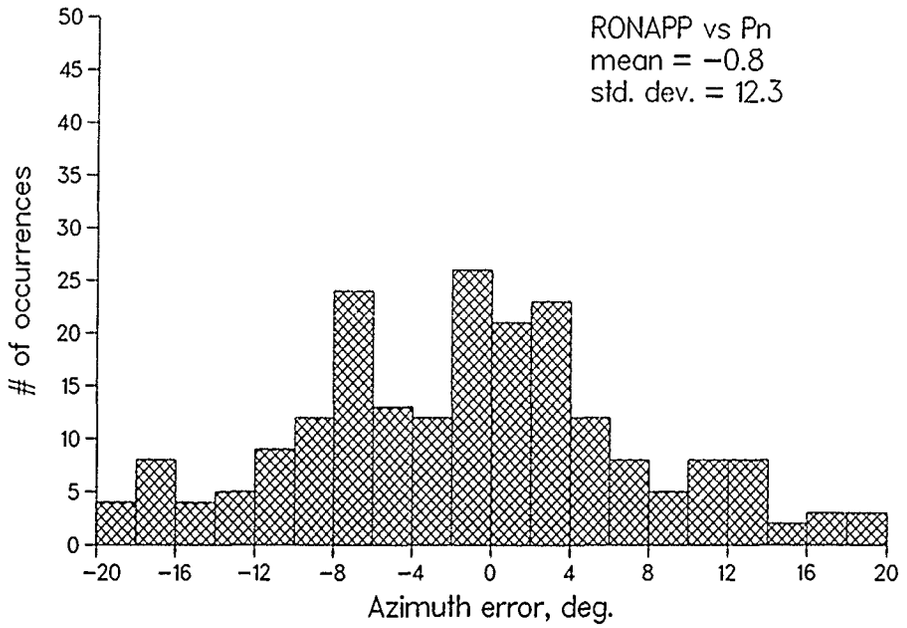

(c)

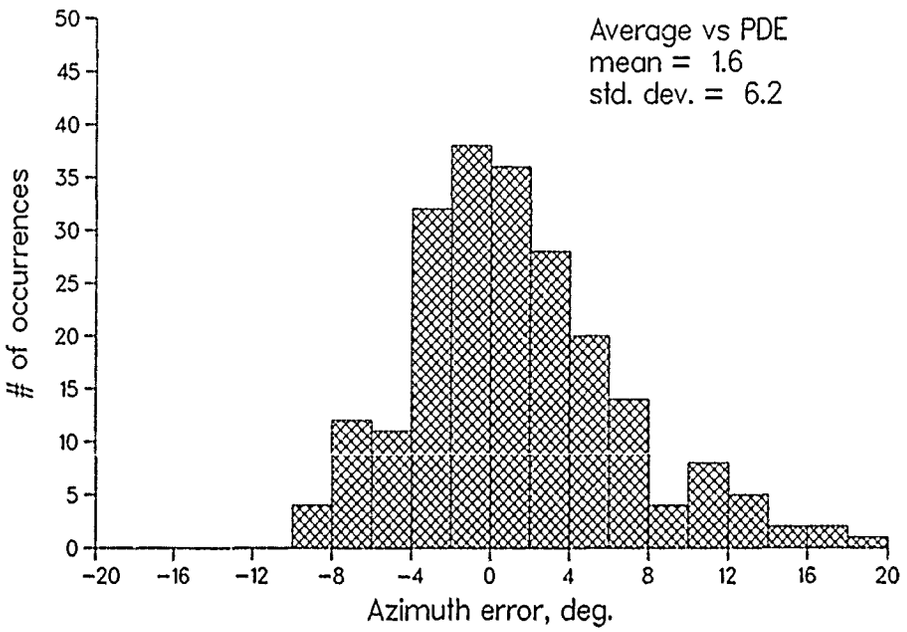

(d)

FIG. 7.—*Continued*

used to obtain accurate backazimuth estimates for events at distances less than 1,200 km. The 13-element configuration of NORESS produces the best results, regardless of SNR. For a data base of 274 events, mean backazimuth errors are less than 1.4° in five different frequency bands for this configuration, and the standard deviations average only ±17.1°. The entire array (25 elements) and the 9- and 8-element configurations also have small mean errors and standard deviations in the mid- to high-frequency ranges. With the addition of a 5 dB SNR cutoff, the

precision of the backazimuth estimates improve (Table 3). Using these same parameters, the average standard deviation is reduced to 12.5°, and the mean errors remain small.

Overall, it appears that the D-ring is superfluous when determining backazimuths of regional events. Inspection of Table 2 and 3 reveals that the 10 and 17-element arrays, which contain the D-ring, provide the poorest azimuth estimates of any of the configurations tested. Mean azimuth errors are very large for several frequency bands, especially for the 10-element configuration. The combination of larger station spacing and higher frequencies results in particularly poor azimuth estimates, with correspondingly large data scatter, as indicated by the standard deviations. The presence of the D-ring is not always a detriment, however, as can be seen from the 25-element configuration results. The addition of the inner rings results in reasonable azimuth statistics for all but the 2 to 4 Hz band. Any configuration containing the B-ring produces accurate azimuths, particularly when the data are filtered above 3 Hz. The 8 to 16 Hz frequency band yields good estimates for the small-aperture configurations, but not for subsets without the B-ring. The 8- and 17-element configurations do provide satisfactory results in the 3 to 6, 4 to 8, and 5 to 10 Hz bands.

The poor performance of the 2 to 4 Hz frequency band over all configurations is surprising because peak SNR is in this frequency range for a significant fraction of the events in the data base. These results suggest that eliminating regional P_n azimuths using a flexible "optimal" band may not be the best solution. In fact, the results are not as good when backazimuths are estimated using our "optimal" band where the data is filtered in the fixed band with the largest average SNR. The best results occur when the data is filtered in one of the middle frequency bands (3 to 6, 4 to 8, or 5 to 10 Hz), which are consistent with Ingate *et al.*'s (1985) statement that NORESS' 3-km aperture effectively defines an operational bandwidth of 3 to 8 Hz for P_n.

Other factors can also affect the azimuth estimation capabilities of the array. The length of the time window has a very small effect on azimuth estimation; both 3 and 5 sec time windows provide good, stable results. If the SNR of an event is not above a threshold value, the azimuth estimates will be less reliable, as shown in Figure 6. We found that azimuth estimates improve if event beams have SNR of at least 5 dB. Statistics for data sets containing only events above 5 dB of SNR have smaller standard deviations, indicating that fewer outliers are present in the calculated azimuth errors when only higher SNR events are included. Azimuths from specific regions can be very accurate, although there are correctable biases. Also, small aperture array configurations work surprisingly well for the available events at distances over 500 km.

Our P_n backazimuth estimates and the NORESS RONAPP (L_g) estimates have similar accuracy statistics relative to the PDE locations for our data base, and better azimuth statistics can be obtained if the two phases are averaged, since the two sets of azimuth errors are essentially uncorrelated. The decrease in standard deviation for the averaged data set (Fig. 7d) is very close to that predicted from standard error propagation techniques for two sets of independent measurements (Bevington, 1969).

We plan to continue this investigation using other azimuth estimation techniques, and also by examining data from the ARCESS array (Fig. 1) to determine if this northern Norway twin of NORESS has similar azimuth accuracy characteristics.

ACKNOWLEDGMENTS

We thank David Harris for providing us with the frequency-wavenumber computer program. Greg Elbring adapted the frequency-wavenumber code for use with the expert system and did the graphics programming. We also thank Eric Chasel, Greg Elbring, John Claassen, and an anonymous reviewer for their comments that improved the manuscript. This work was performed at Sandia National Laboratories and was supported by the U.S. Department of Energy under Contract DE-AC04-76DP00789.

REFERENCES

Allen, R. V. (1982). Automatic phase pickers: their present use and future prospects, *Bull. Seism. Soc. Am.* **72**, S225–S242.

Ballard, S., M. C. Walck, and E. P. Chael (1989). Location performance of a sparse regional network, *Geophys. Res. Letters* **16**, 1101–1104.

Bevington, P. R. (1969). *Data Reduction and Error Analysis for the Physical Sciences*, McGraw-Hill Inc., New York, 336 pp.

Bratt, S. R. and T. C. Bache (1988). Locating events with a sparse network of regional arrays, *Bull. Seism. Soc. Am.* **78**, 780–798.

Gibowicz, S. J. (1987). NORESS capability for detection and location of mining tremors in the Lubin area in Poland, *Semiannual Technical Summary, 1 Oct. 86–31 March 87, NORSAR Sci. Rept. No. 2 86/87*, Kjeller, Norway, 91–124.

Harris, D. B. (1982). Uncertainty in direction estimation: a comparison of small arrays and three-component stations, Lawrence Livermore National Laboratory Report, UCID-19589-82, 30 pp.

Harris, D. B. (1986). Toward a master event strategy for location with arrays, *Proceedings of the 1985 RSTN/NORESS Research Symposium, LLNL Conference Report 8604196, 170–186.*

Hiebert-Dodd, K. L. (1989). Assisting experts in their data analysis tasks—an AI approach, *Math. Comput. Simul.* **31**, 475–484.

Ingate, S. F., E. S. Husebye, and A. Christoffersson (1985). Regional arrays and optimum data processing schemes, *Bull. Seism. Soc. Am*, **75**, 1155–1177.

Kværna, T. and F. Ringdal (1986). Stability of various *f-k* estimation techniques, *Semiannual Technical Summary, 1 April–30 September 1986, NORSAR Sci. Rept. No. 1 86/87*, Kjeller, Norway, 29-40.

Mykkeltveit, S. (1985). Evaluation of NORESS real time processing performance: case study for 132 western Norway/North Sea events, *Semiannual Technical Summary, 1 April–30 September 1985, NORSAR Sci. Rept. No. 1 85/86*, Kjeller, Norway, 30-39.

Mykkeltveit, S. and H. Bungum (1984). Processing of regional seismic events using data from small-aperture arrays, *Bull. Seism. Soc. Am.* **74**, 2313–2333.

Mykkeltveit, S., D. Harris, and T. Kværna (1985). Preliminary evaluation of the event detection and location capability of the small-aperture NORESS array, *Semiannual Technical Summary, 1 October 1984–31 March 1985, NORSAR Sci. Rept. No. 2 84/85*, Kjeller, Norway, 30-43.

Mykkeltveit, S., J. Fyen, T. Kværna, and M. Uski (1988). Analysis of regional seismic events using the NORESS/ARCESS/FINESA arrays, *Semiannual Technical Summary, 1 April–30 September 1988, NORSAR Sci. Rept. No. 1 88/89*, Kjeller, Norway, 74-87.

Nawab, S. H., F. U. Dowla, and R. T. Lacoss (1985). Direction determination of wideband signals, *IEEE Trans. Acoust., Speech, Signal Processing* **ASSP-33**, 1114–1122.

Suteau-Henson, A. (1990). Estimating azimuth and slowness from three-component and array stations, *Bull. Seism. Soc. Am.* **80**, Part B, 0000–0000.

Thurber, C., H. Given, and J. Berger (1989). Regional seismic event location with a sparse network: application to Eastern Kazakhstan, USSR, *J. Geophys. Res.* **94**, 17767–17780.

VERIFICATION SYSTEMS AND TECHNOLOGY
DIVISION I, 9241
SANDIA NATIONAL LABORATORIES
ALBUQUERQUE, NM 87185-5800
(D.A.B.)

GEOPHYSICS DIVISION, 6231
SANDIA NATIONAL LABORATORIES
ALBUQUERQUE, NM 87185-5800
(M.C.W.)

SYSTEMS RESEARCH DIVISION V, 9115
Sandia National Laboratories
Albuquerque, NM 87185-5800
(K.L.H.-D.)

Manuscript received 5 April 1990

Bulletin of the Seismological Society of America, Vol. 80, No. 6, pp. 2016-2031, December 1990

ANALYSIS OF REGIONAL EVENTS RECORDED AT NORESS

By Kristin S. Vogfjord and Charles A. Langston

Abstract

Events recorded by NORESS are analyzed to determine the velocities and times of coherent crustal phases to be used in accurate locations and determination of crustal structure. The events straddle two azimuthal directions, and range in distance from 50 to 300 km, thus sampling two cross-sections of the crust and upper mantle: one in the Caledonides to the northwest of NORESS and the other to the south along the eastern rim of the Oslo Graben. *f-k* analysis is used to search for coherent phases in the data. All vertical channels are then stacked with the appropriate time delays calculated from the phase velocities and azimuths obtained for the coherent arrivals. Finally, a composite seismogram is made for each event by piecing together time sections from the stacks, where each time piece represents a coherent arrival. All detectable coherent phases are enhanced in the composite seismograms, and on closer inspection it is possible to improve some of the locations from the *NORESS Bulletin*. This causes a number of events to group together to the same location. Travel-time curves are constructed from plane-layered homogeneous models to match travel times and phase velocities in the composite seismograms.

Introduction

Studies of wave propagation from regional seismic events (here used for distances out to a few hundred kilometers) and seismic refraction lines have generally been hampered by low signal-to-noise ratio and by poor phase identification. With the use of high-frequency, small-aperture seismic arrays, such studies can be greatly improved. Array analysis not only enhances the s/n ratio to bring out more details in the seismograms, but also allows the association of phase velocities and back-azimuths with the arrivals. At regional distances, the prominent phases in seismograms are most often the *Pg* and *Lg* wave trains, which are made up of a sequence of multiply reflected postcritical *P* and *S* waves trapped in the crustal wave guide. The main reflectors are the free surface and the Moho, but internal discontinuities in the crust also act to increase the complexity of the wave trains. The number of multiples increases with source distance as the critical distance for each multiple reflection is reached (Bouchon, 1982). Relative arrival times and amplitudes of phases in the wave trains are sensitive to crustal structure and source depth. They are therefore ideally suited for studying crustal structure and source effects in regional events.

The present study uses regional events recorded by the NORESS array, which was designed to enhance the detection of such events (Mykkeltveit *et al.*, 1983), to study structure and its effects on wave propagation at regional distances. The array is located in the Baltic Shield, northeast of the Oslo Graben, which was formed by a continental rifting episode during the Permian. Volcanics and intrusions are prevalent in the Graben area, and results from previous seismic and gravity studies indicate undulations of several kilometers in the Moho under the Oslo Graben (Kanestrom and Haugland, 1971; Ramberg, 1976; Wessel and Husebye, 1987).

The events are listed in Table 1. They were chosen from the *NORESS Bulletin* based on location and local magnitude to allow sampling of the crust on two

TABLE 1

LIST OF EVENTS

Event	Origin Time (yr/day/hr:min sec)	M_L
A-1a	1988/244/12:09:52.60	1.7
A-1b	1988/316/15:38:27.90	2.1
A-2a	1988/133/17:45:55.90	2.0
A-2b	1988/147/11:56:46.80	2.1
A-2c	1988/159/13:06:14.40	2.1
A-2d	1988/267/05:46:40.40	2.0
A-3	1988/137/14:25:55.50	(3.3) 1.8*
A-4	1987/183/14:07:39.90	(3.8) 1.4*
A-5a	1987/294/16:25:38.90	2.8
A-5b	1988/205/13:53:40.70	2.3
A-5c	1988/257/13:34:51.30	2.6
A-5d	1988/286/10:30:28.50	2.2
A-6	1985/313/18:21:12.37	2.0
B-1	1988/099/11:33:06.70	1.9
B-2	1988/237/14:49:45.30	(3.3) 1.8*
B-3	1988/154/08:34:52.70	2.0
B-4	1988/075/17:03:51.20	2.4

* Recalculated magnitude according to Båth (1976).

different profiles extending from the array. Location of events, which range in magnitude from 1.7 to 3.8, is shown in Figure 1. The NW–SE crustal profile, delineated by the event distribution extends into the Caledonian mountain range, while the N–S profile runs along the eastern rim of the Oslo Graben. These profiles will be referred to as profiles A and B, respectively. The events are subject to *f-k* analysis to search for coherent arrivals, which are then used to infer crustal structure and to improve event locations where necessary. Each event is presented in the form of a single composite seismogram, made from time pieces of array beams representing detectable coherent arrivals. The composite seismogram enhances all the main phases observed at the array, whereas a single array beam does so for only one. In this form, the data is thus better suited for structure and source modeling. The composite seismograms are compared with travel-time curves calculated for two different crustal models obtained from previous refraction studies in the region (Sellevoll and Warrick, 1971; Kanestrom and Haugland, 1971).

DATA ANALYSIS

In order to find coherent phases in the data and to identify their phase velocities, *f-k* analysis is performed in sliding time windows on all 25 vertical components of the array. Window lengths and their locations in time are chosen after inspection of the record sections, so that the phases are centered and fully contained within the windows. The data are then multiplied by a Hanning smoothing function and Fourier transformed in time to find the spectral peaks within the window. Two-dimensional Fourier transform on the space dimensions is then calculated at the peak frequencies to obtain the power spectrum in the wavenumber plane. If a window contains a coherent arrival, then there will be a distinct maximum peak of power somewhere in the wavenumber plane. The location of the peak determines the phase velocity and the direction from which the wave is coming. Phase velocities and backazimuths obtained for the various frequency peaks within a window often

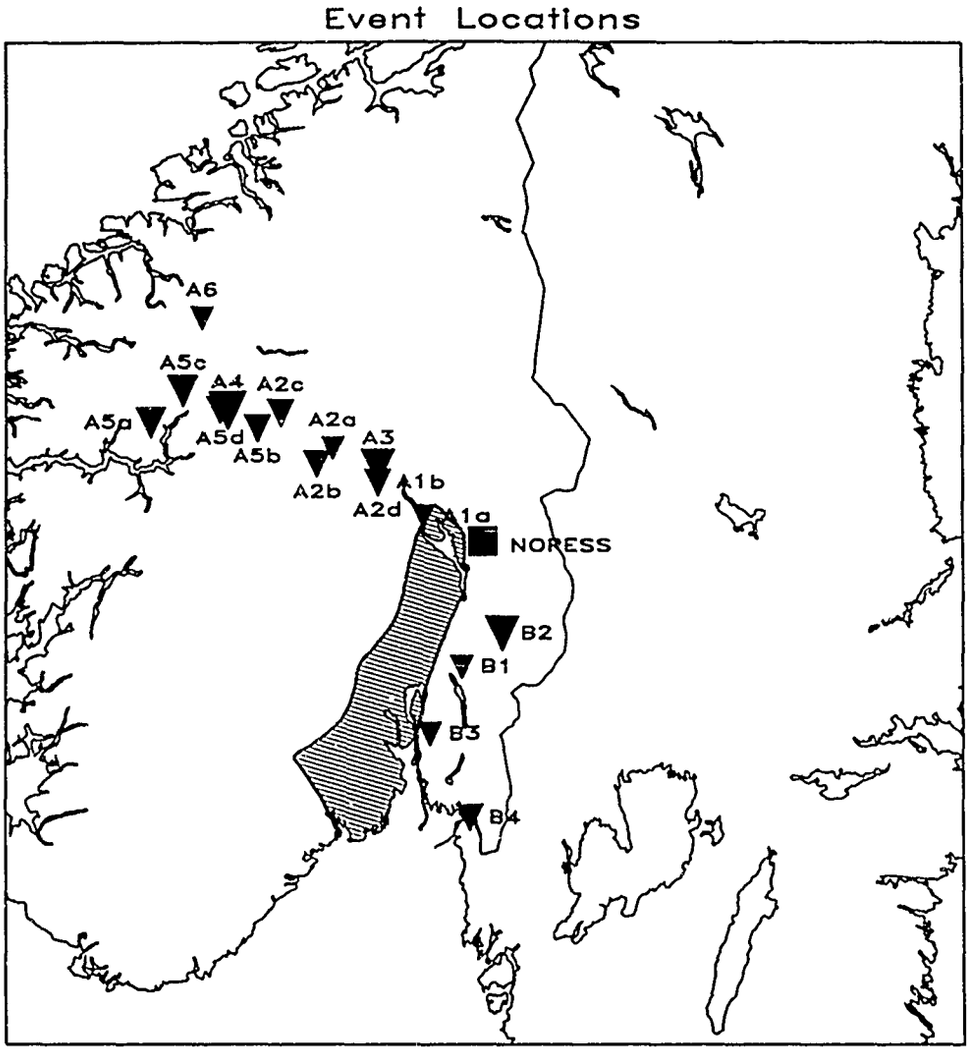

FIG. 1. Map showing event locations (solid triangles) and location of NORESS (solid square). Hatched area represents the Oslo Graben.

show some variation. This can be due to interference between phases with different travel paths, caused by layering or heterogeneities in the crust. Lack of resolution can also be the cause if phase velocities are high. In this situation, the phase velocity and backazimuth of the frequency with the greatest power is chosen to represent the arrival. When there is variation in backazimuth between the main P and S phases within one event, the backazimuth of the largest phase is chosen to represent the event.

With the backazimuth and phase velocities for all detectable phases of an event in hand, the vertical channels are stacked and corrected to zero altitude. This creates several beams for the event. Time sections from the different beams are then pieced together to form one composite seismogram as shown in Figure 2. The beams have an improved s/n ratio so that major crustal phases clearly stand out and some of the more obscure ones, such as Pn, become apparent. However, each beam only enhances arrivals over a small range of phase velocities. This is clearly seen on the bottom trace of Figure 2, which shows the $2 \times SmS$ beam; compared to

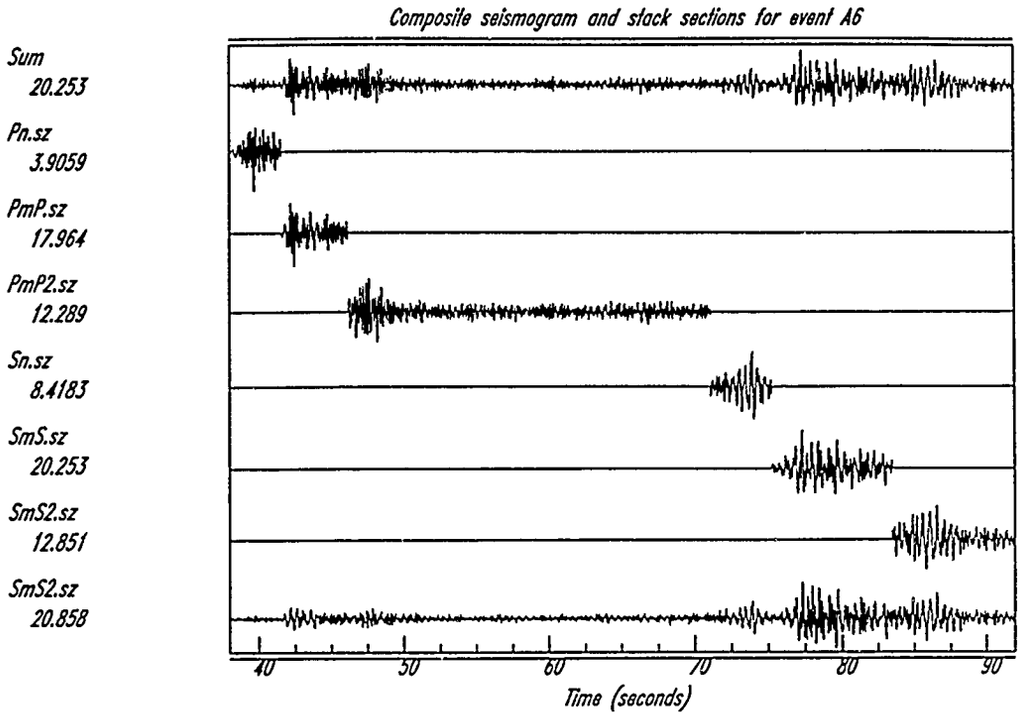

FIG. 2. Composite seismogram for event A-6 and time sections from the array beams used to make up the composite. Bottom trace shows the whole 2 × *SmS* beam.

the composite seismogram at the top, the *P* phases are very small. By piecing the beams together, the event is represented by a single composite seismogram with all detectable phases enhanced. In some of the more distant events with small magnitudes, the s/n ratio is only 2 to 5. In such cases, the *f-k* analysis is performed on the raw data, but the channels are high-pass filtered with a three-pole, zero-phase Butterworth filter before stacking to eliminate the low-frequency noise.

When the channels are stacked, coherent arrivals with the preferred backazimuth and incidence angle are enhanced, while incoherent amplitude and coherent amplitude arriving with a different backazimuth and incidence angle are diminished. If a substantial variation in backazimuth or phase velocity occurs within the major arrivals, the event will appear to have low coherency and the composite seismogram will thus be a poor representation of the event. For a quantitative estimate of coherency in the events, and in order to compare effects of different travel paths, envelopes of all vertical channels are time shifted, stacked, and time sections pieced together in the same manner as the seismograms. This composite envelope approximates the true total amplitude. The envelope of the composite seismogram, which approximates the true coherent amplitude is then subtracted to obtain the incoherent amplitude.

EVENT LOCATIONS

After stacking the events presented in Figure 1, it became apparent that several were mislocated, some by as much as 80 km. The composite seismograms for the events in question are presented in Figures 3, 4 and 5, where the arrows indicate time picks of coherent arrivals from the *NORESS Bulletin*. Some of the events were recorded during a period of unknown time drift of <2 sec, occurring in the on-line

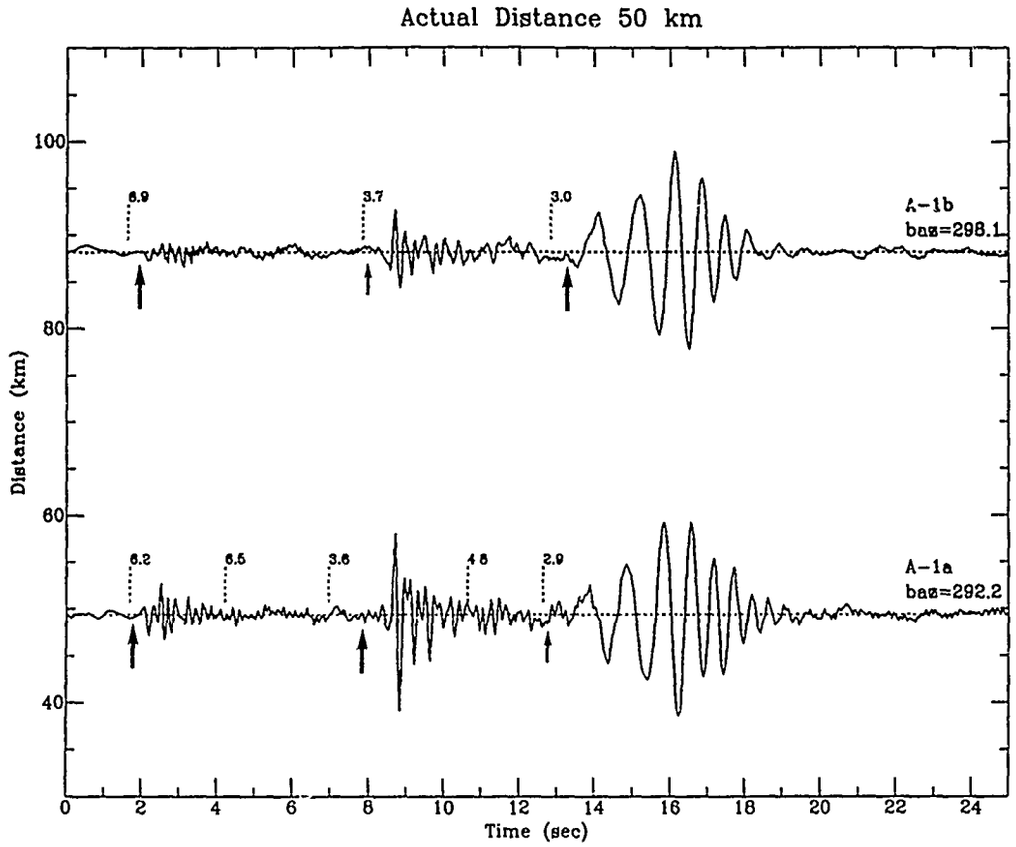

FIG. 3. Composite seismograms for events A-1a and A-1b plotted at the source distance determined by NORESS. The traces are normalized to their maximum amplitude. The stacking windows are indicated by dashed lines, and the stacking velocities are shown on the left margin of each window. Arrows indicate arrival times of phases as listed in the *NORESS Bulletin*. The thick arrows represent the phases picked by NORESS as *P* and *Lg*, and are used in the automatic location.

data. This time drift is indicated in the figures by the time bars. The two thicker arrows and arrow bars in each event indicate arrivals of the *P* and *Lg* waves used by NORESS to locate the event.

There are two main reasons for the mislocations. The first main reason involves the picking of the largest *S*-wave arrival on the record as the arrival of the *Lg* wave. The two events in Figure 3 have two main *S* arrivals: *Sg*, which is used here to represent an *S* wave that turns or reflects in the crust, with a phase velocity of 3.7 km/sec, and the longer period *Rg* surface wave, with a velocity of 3 km/sec. A schematic plot explaining the travel paths of the various phases is shown in Figure 6. By picking the larger amplitude *Rg* wave as the onset of *Lg* in event A-1b, the source distance is overestimated by 40 km. Figure 4 shows the same misinterpretation of the onset of *Lg* for four nearly identical events, with three major *S*-wave arrivals: *Sg*, the Moho reflected *SmS*, and *Rg*. Depending on which phase is picked as the *Lg* arrival, the events are misplaced from the actual distance of about 85 km, by as much as 80 km.

The second main reason for mislocation is demonstrated in Figure 5, which shows four events with the same relative times but located over a 70 km distance range. The two closer events, A-5b and A-5d, have local magnitudes of 2.3 and 2.2, whereas the other two, A-5c and A-5a have local magnitudes 2.6 and 2.8. *Lg* is picked at

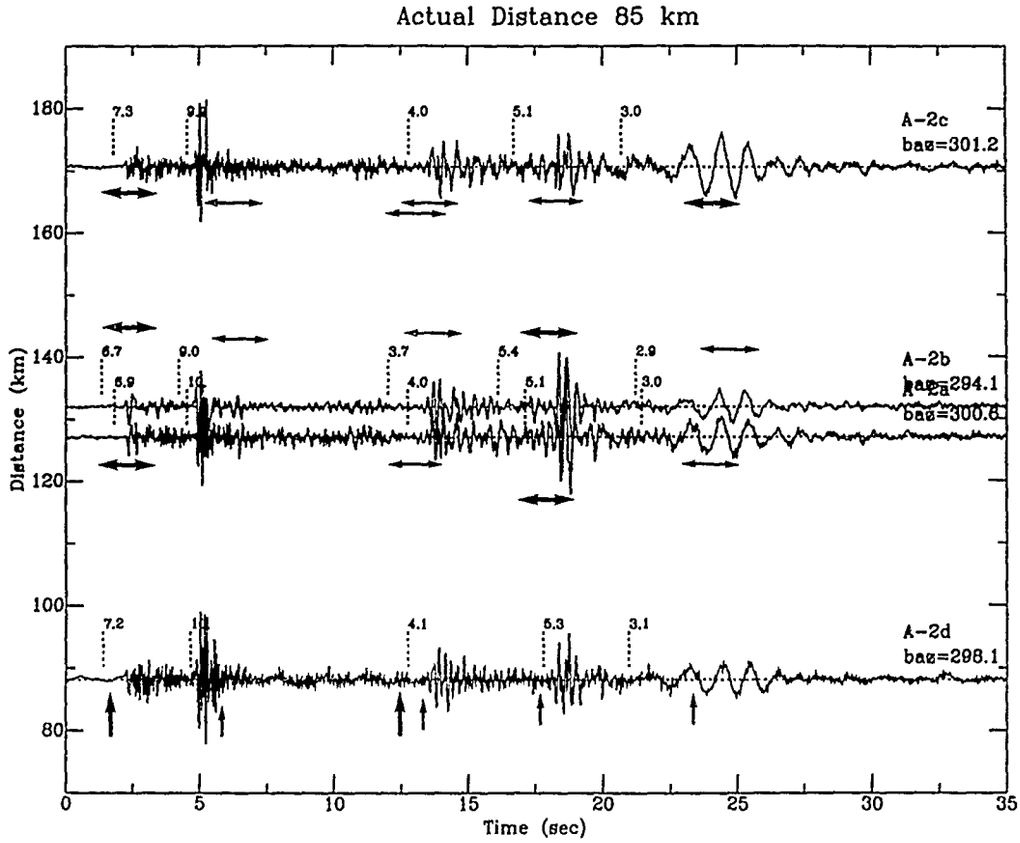

FIG. 4. Composite seismograms for events A-2a, A-2b, A-2c, and A-2d plotted at their source distance from NORESS. Same scheme as in Figure 3, except for arrival times in events A-2a, A-2b, and A-2c, which were recorded during a period of unknown time drift of <2 sec, occurring in the on-line data. The arrow bars indicate the uncertainty in the arrival times, and the thick bars represent NORESS automatic time picks.

about the same time in all events, at the arrival of *SmS*. *Pn* is picked as the first *P* arrival in the two larger events, but due to its smaller amplitude it is missed in events A-5d and A-5b. 2 × *PmP* is picked for event A-5b, and the time pick for A-5d is late in the *PmP* phase. Thus, when the first arriving *P* phases from small distant events are not detected, the distance is underestimated. The actual distance for the four events is about 240 km, depending on velocity model. The mislocated events show a variation in backazimuth, of up to 7°, indicating some errors in backazimuth also.

The events are replotted in Figure 7 in their relocated positions, calculated from the velocity model of Kanestrom and Haugland (1971) and the magnitudes of events A-3, A-4, and B-2 corrected according to Båth (1976). The velocity model is given in Table 2.

RECORD SECTIONS

Section A

Five events define profile A. They range in distance from about 50 to 300 km and the variation in backazimuth among the four closest ones is small (293° to 299°). The most distant one, however, is further out of line, at 313°. There are more than

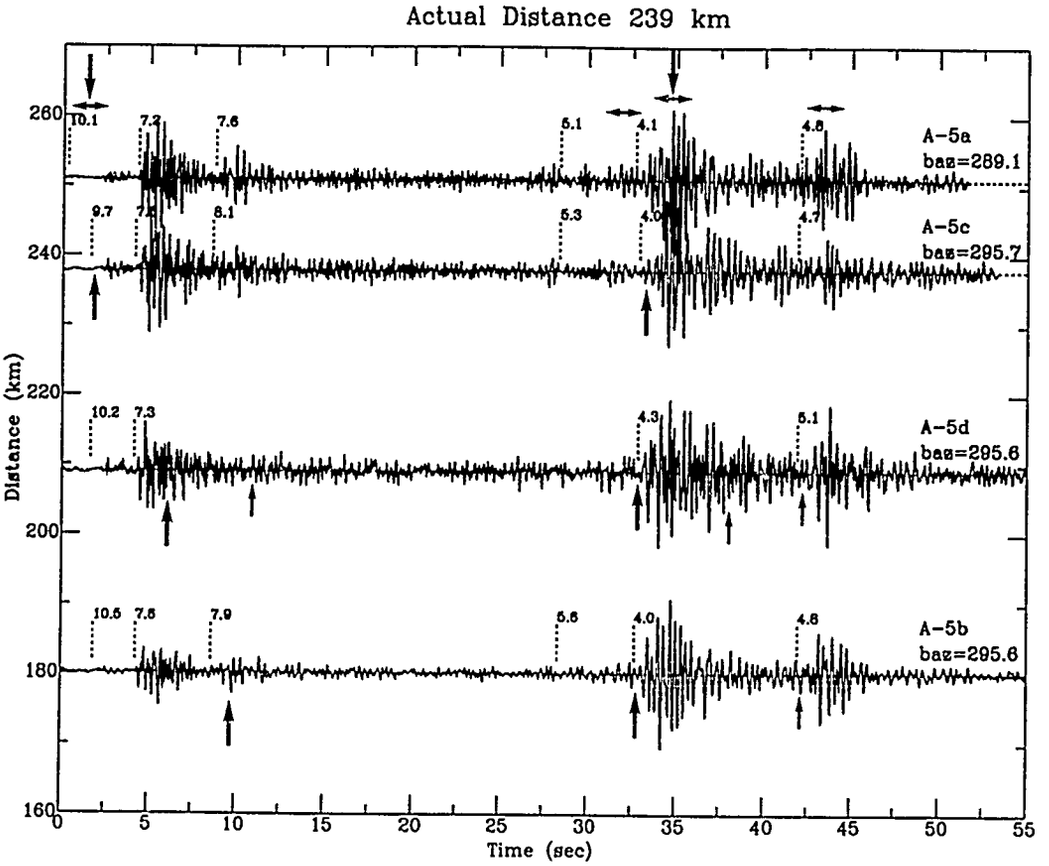

FIG. 5. Composite seismograms for events A-5a, A-5b, A-5c, and A-5d. Same scheme as Figures 3 and 4.

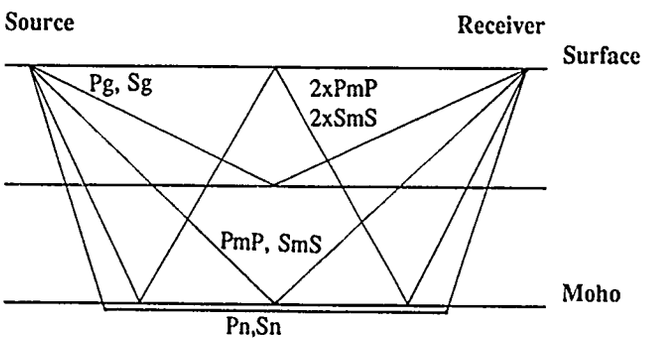

FIG. 6. A schematic explaining the notation and travel paths of the major crustal and upper mantle phases. *P* waves converted to *S* waves at the crustal and mantle interfaces will be denoted by *Pg*-*S* and *PmS*, respectively.

one event at locations A-1, A-2, and A-5, and as seen in Figures 3 to 5, there are variations in frequency content and relative amplitudes between events at the same location. Since our immediate goal is to match arrival times of major phases, the events with the clearest phases were the ones chosen for the record section. The record section is shown in Figures 8 and 9, with events A-4 and A-6 high-pass filtered for clearer phase identification.

Pg is the first arrival in the two closest events, with a phase velocity of about 6.2 km/sec, but *Pn* takes over before the source distance of the third event is reached. The closest event, A-1a at about 50 km distance, has well-defined *Pg*

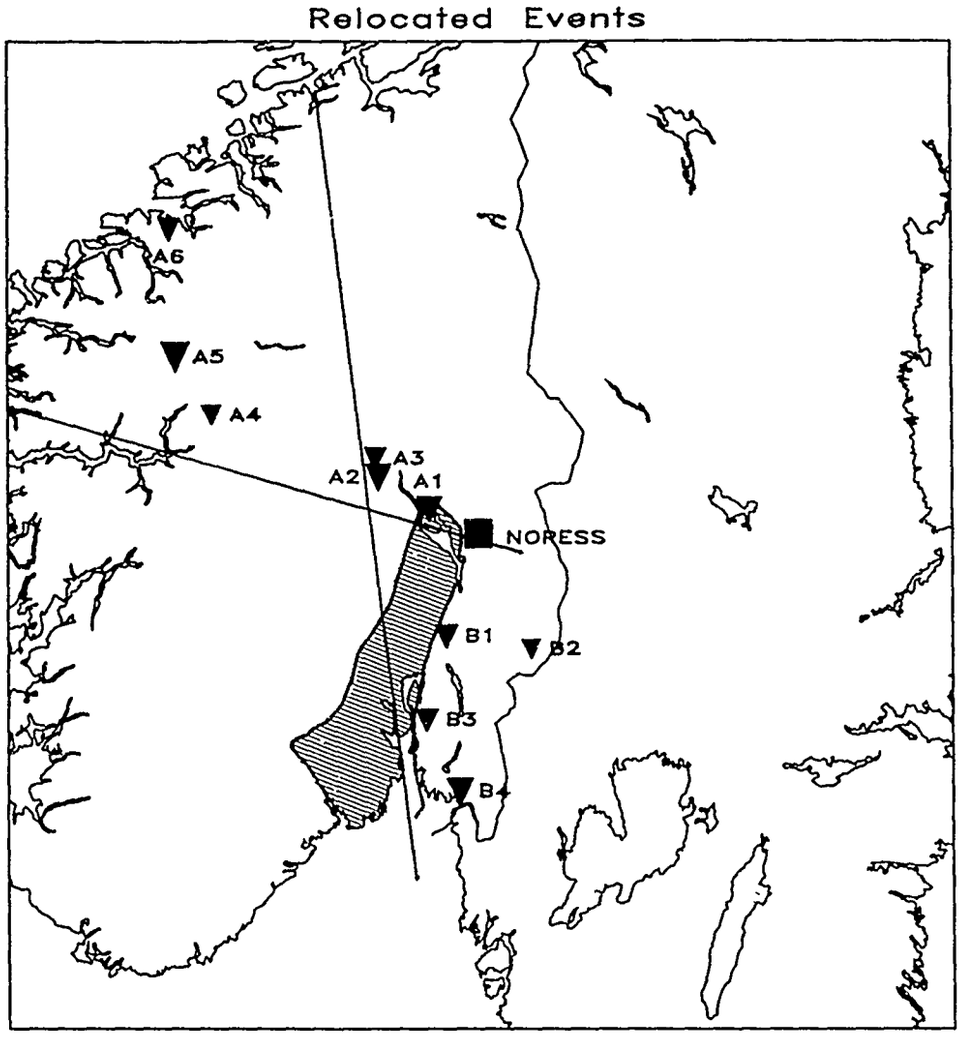

FIG. 7. Map showing relocated events (solid triangles) and location of NORESS (solid square). Hatched area represents the Oslo Graben. The NW-SE line represents the Flora-Asnes refraction line, and the N-S line represents the Profile 3-4 refraction line.

TABLE 2

VELOCITY MODELS

V_p (km/sec)	V_s (km/sec)	Density (g/cm)	Thickness (km)
Flora-Asnes Crustal Model (Sellevoll and Warrick, 1971)*			
5.20	3.00	2.60	1
6.00	3.46	2.80	14
6.51	3.76	3.00	22
8.05	4.65	3.30	Half-space
Profile 3-4 Crustal Model (Kanestrom and Haugland, 1971)*			
5.20	3.00	2.60	1†
6.20	3.58	2.88	16
6.55	3.78	2.93	10
7.20	4.16	3.13	10
8.20	4.73	3.35	Half-space

* *S*-wave velocities are calculated assuming a Poisson solid.

† Surface layer added to the model.

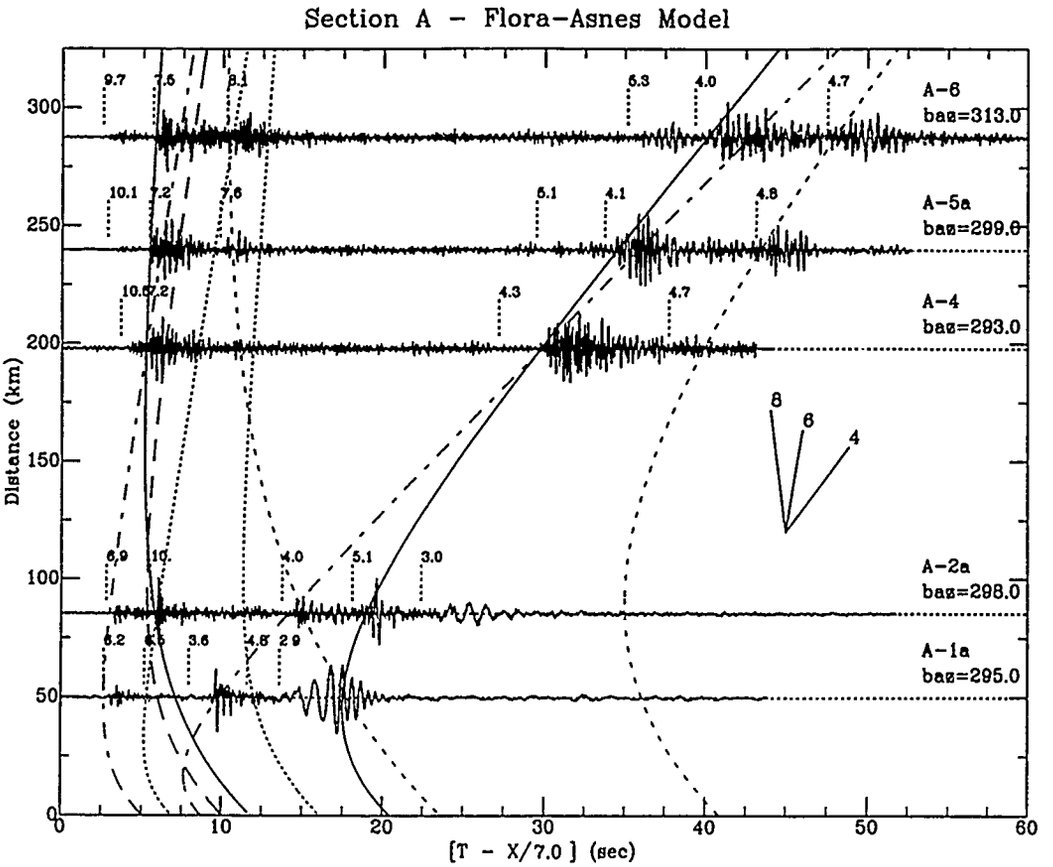

FIG. 8. Composite seismograms for the events from the Caledonian section plotted as a function of distance, reduced with a velocity of 7 km/sec, and normalized to maximum amplitude. Dashed lines above seismograms indicate where the slant-stack sections have been pieced together. Stacking velocity is shown on the left margin of each interval. Travel-time curves for the Flora-Asnes model are overlaid on the plot. They represent: ———, *PmP* and *SmS*; – – –, *Pg* and *Sg*; · · · · , *Pg*-*S* and *PmS*; – – – –, 2 × *PmP* and 2 × *SmS*; ———, 2 × *Pg*. Slopes representing velocities on the curves can be read from the velocity template to the right of center on the plot.

and *Sg* phases and a large *Rg* phase, but no mantle reflection is apparent. Event A-2a, on the other hand, is close to the critical distance for mantle reflection and therefore has large *PmP* and *SmS* arrivals following *Pg* and *Sg*. The *Rg* phase is also still prominent. *Pn* is the first arrival in the remaining events with a phase velocity of about 10 km/sec. A large *PmP* phase follows, with a phase velocity of about 7.2 km/sec, and 2 × *PmP* with a phase velocity of approximately 8 km/sec starts to build up from a distance of 200 km and farther. *Sn* is clearly seen in event A-6 and can be detected in A-5a and A-5c as well (see Fig. 5). Its phase velocity is about 5.2 km/sec. *SmS* has a phase velocity of approximately 4.1 km/sec from distances greater than 200 km. Furthermore, it is the largest phase in the *Lg* wave train at these distances. 2 × *SmS* with a phase velocity of about 4.7 km/sec is prominent in A-5 and A-6, and a small phase with the correct velocity for 2 × *SmS* is also detected about 2 sec too early in A-4.

Arrival times in the events are fitted to travel-time curves calculated for *P* and *S* phases propagating from a surface focus and reflecting off the interfaces of the two crustal models given in Table 2. They were obtained for the E–W trending Flora-Asnes profile by Sellevoll and Warrick (1971), and the N–S trending Profile 3–4 by

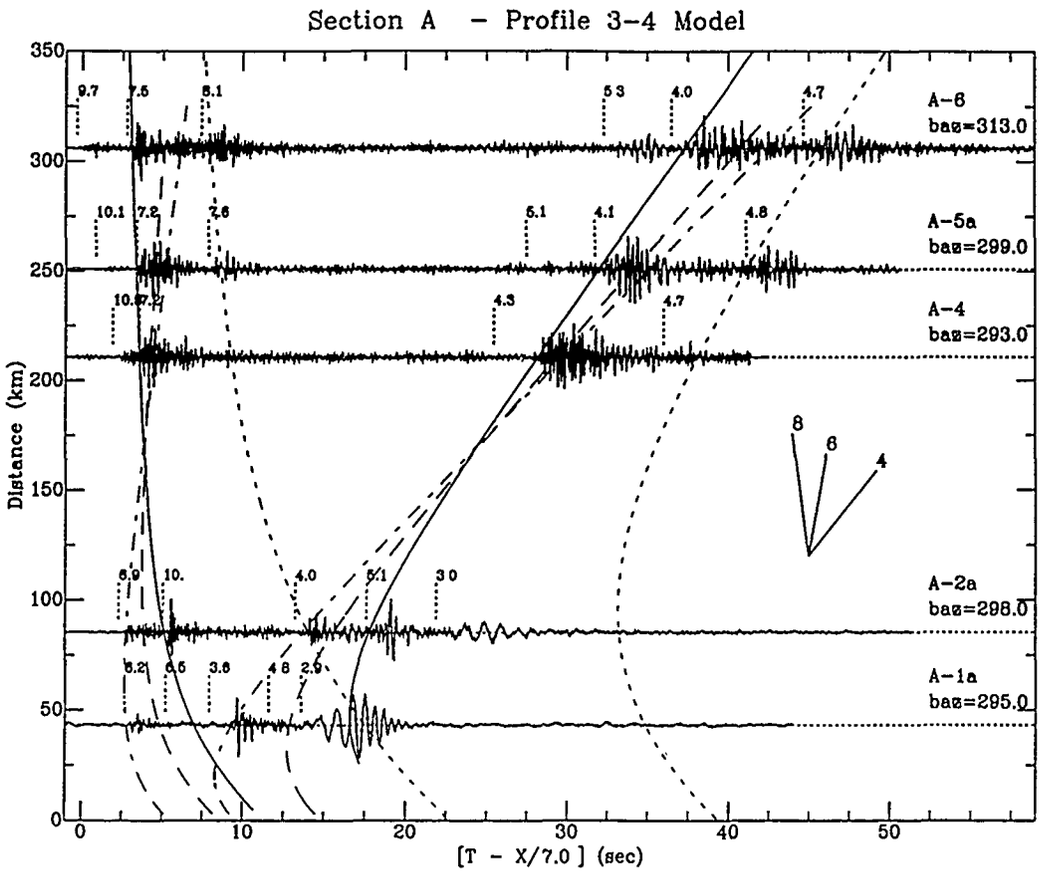

FIG. 9. Same record section as in Figure 8, but with the travel-time curves for the Profile 3–4 model overlaid. Reflections off the two interfaces in the crust are referred to as *Pg*1 and *Pg*2, respectively. Same for *S* waves. Travel-time curves represent: - - -, *Pg*1 and *Sg*1; ———, *Pg*2 and *Sg*2. Same notation for Moho reflections as in Figure 8.

Kanestrom and Haugland (1971). The locations of the profiles are shown in Figure 7. Source distances and origin times are adjusted until an acceptable match in travel time is obtained. Travel-time curves for the Flora-Asnes profile and for Profile 3–4 are plotted with the record section in Figures 8 and 9, respectively. Both models can match relative arrival times of *Pg*, *Sg*, and the Moho reflections, but slopes of the travel-time curves for Profile 3–4 better match the observed phase velocities of the seismograms; slopes on the *PmP* and *SmS* curves approach the limits 7.2 and 4.1 km/sec, respectively. Slopes on 2 × *PmP* and 2 × *SmS*, however, are somewhat lower than the observed phase velocities. Slopes on the Flora-Asnes travel-time curves are generally lower than the observed phase velocities. Despite the overall match, reflections from a second crustal interface, *Pg*2 and *Sg*2, predicted by the Profile 3–4 model are not observed, indicating gradual velocity increases within the lower crust. Travel-time curves of *P*-to-*S* converted phases are included in Figure 8 (dotted curves). Converted phases are predicted by both models in events A-1 and A-2, but are not observed in the composite seismograms. This may be indicative of velocity gradients, in which case no *P*-*S* conversions occur, and/or smaller velocity discontinuities decreasing the already small *P*-*S* conversions so they become hard to detect in the *P* coda.

Section B

Figure 1 shows four events defining profile B, but after relocation event B-2 moved out of the profile (see Fig. 7). It is still included in the record section for comparison. The record section is shown in Figure 10. Events B-3 and B-4 have been high-pass filtered and event B-2 shifted in distance for easier phase identification. The distance range of the events is 73 to 167 km, and even when B-2 is excluded, the variation in backazimuth is much greater than on profile A (186° to 202°). Considering this deviation from a true profile section and the proximity to the Graben, where crustal thickness is changing, some travel-time deviations are to be expected from those predicted by plane-layered models.

All events have a clear *Pg* first arrival, with a phase velocity of approximately 6.2 km/sec. *Sg*, however is more emergent. Its phase velocity is 3.7 km/sec. *PmP* is very faint in the two closest events (around 80 km), which are near the critical distance, but it becomes clearer with increasing distance. In event B-4, at 167 km distance, *PmP* has started to interfere with *Pg*. The crossover of their travel-time curves must, therefore, occur just after that distance. *SmS* is a large arrival in all events. In events B-1 and B-2, it arrives at about the same time as *Rg*, but the stacking enhanced *SmS* so *Rg* appears to arrive after it. Event B-4 has a faint high-frequency arrival, which can be identified with *Pn*. With a phase velocity around 8.2 km/sec, it arrives 0.6 sec before *PmP*. Due to its small amplitude, however, the beam is not included in the composite seismogram. No signs of *Sn* are detected.

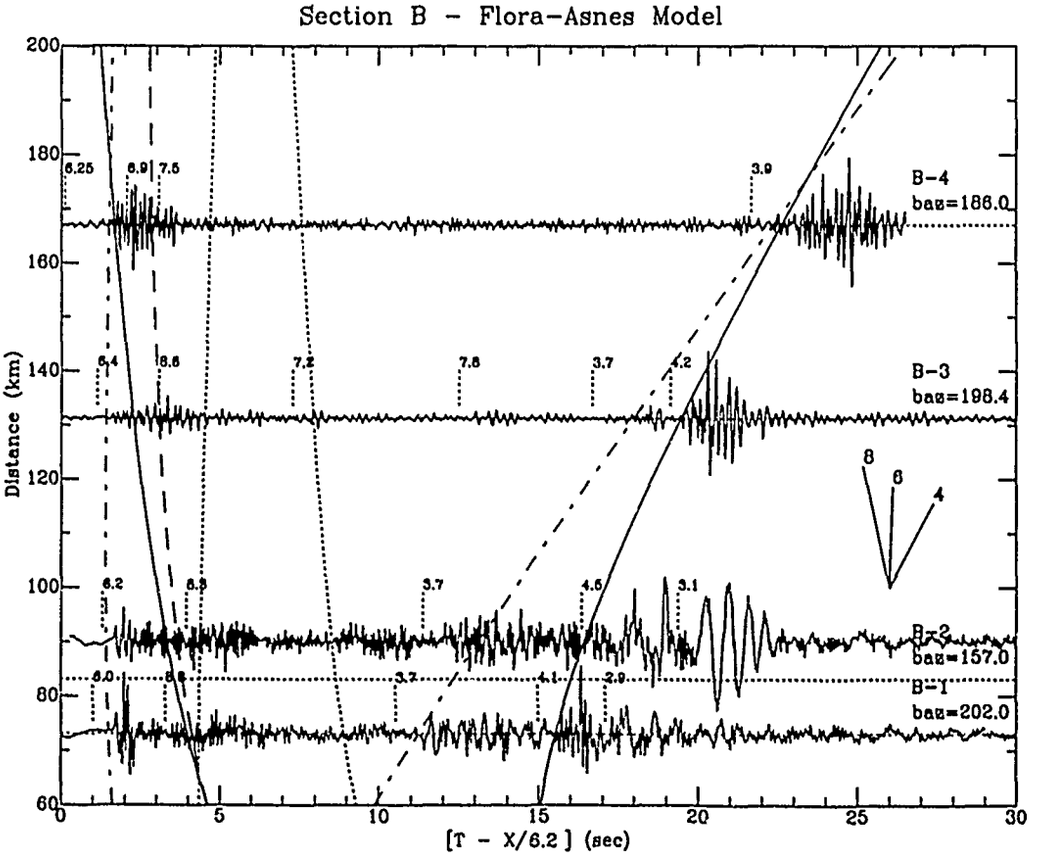

FIG. 10. Composite seismogram record section from the N–S profile, with the travel-time curves for the Flora Asnes profile overlaid. Same scheme as in Figure 8 except travel-time curves for the double Moho reflections, 2 × *PmP* and 2 × *SmS* are not shown.

Arrival times for this record section are also fitted to travel-time curves for the two crustal models. The best match for events B-1 and B-3, which are located just east of the Graben (see Fig. 7), is obtained with a modified version of the Flora-Asnes model: a crustal thickness of 33 km. B-2 and B-4, however, are better matched with the 37 km thick crust. Their locations are also farther away from the Graben. Travel-time curves for the modified Flora-Asnes model are plotted with the record section in Figure 10. The Profile 3–4 model is too fast and the *Pg-PMP* crossover occurs too early, at less than 170 km distance. Event B-3 has two small arrivals between the *P* and *S* wave trains, the first of which approximately coincides with *PmS*. However, *PmS* is not observed in B-1. B-2 has increased amplitude where *PmS* is expected, but a clear coherent arrival cannot be determined. The backazimuths of the arrivals in event B-3 are around 213°, which may instead suggest reflections from structures within the Graben. These amplitudes, however, are small and more events are needed to determine their cause.

The records from event B-2 are rich in high frequencies and show evidence of multipathing at frequencies above 10 Hz. In event B-1, scattering is also high at these frequencies. Records from the other two events have little energy above 10 Hz. The average amplitude spectra of the records for all four events are plotted in Figure 11. For B-2, it shows a relatively flat spectrum up to 13 Hz, but the others start to fall off around 8 Hz. Due to its magnitude, however, event B-1 still has considerable amplitude above 10 Hz. *P* waves from event B-2, with peak frequencies above 10 Hz, generally have more than one power maximum in the wavenumber plane, at backazimuths around 130°, 155°, and 170°, whereas lower frequency *P* and *S* waves have only one at backazimuths between 155° and 160°. This is demonstrated

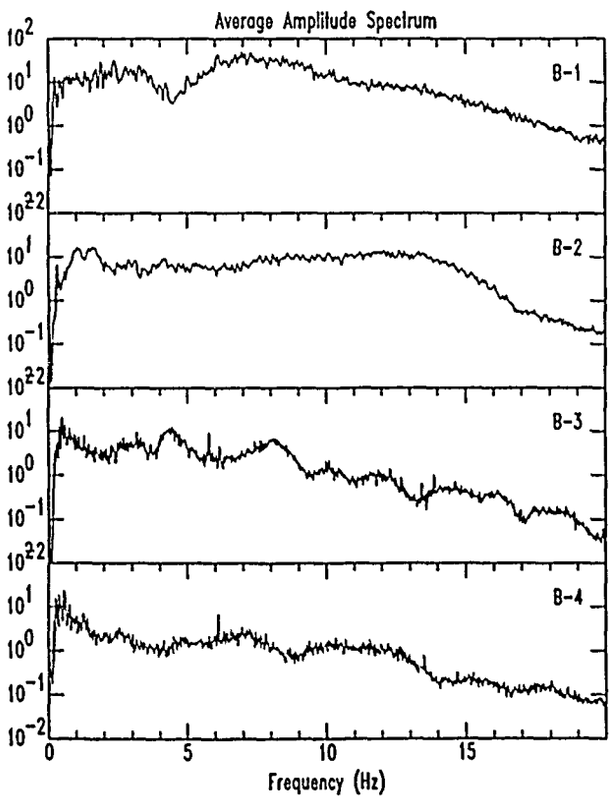

FIG. 11. Average amplitude spectra of the records from the four events in the N-S record section, each calculated for a 30 sec time window containing the whole waveform.

in Figure 12 (a and b) for the *Pg* phase. At the primary peak frequency (10.8 Hz), clear double maxima, with the same phase velocities and different backazimuths, are observed. At the secondary peak frequency (4.8 Hz), only one occurs. When relocating the event, a backazimuth of 157 was chosen. For a comparison with

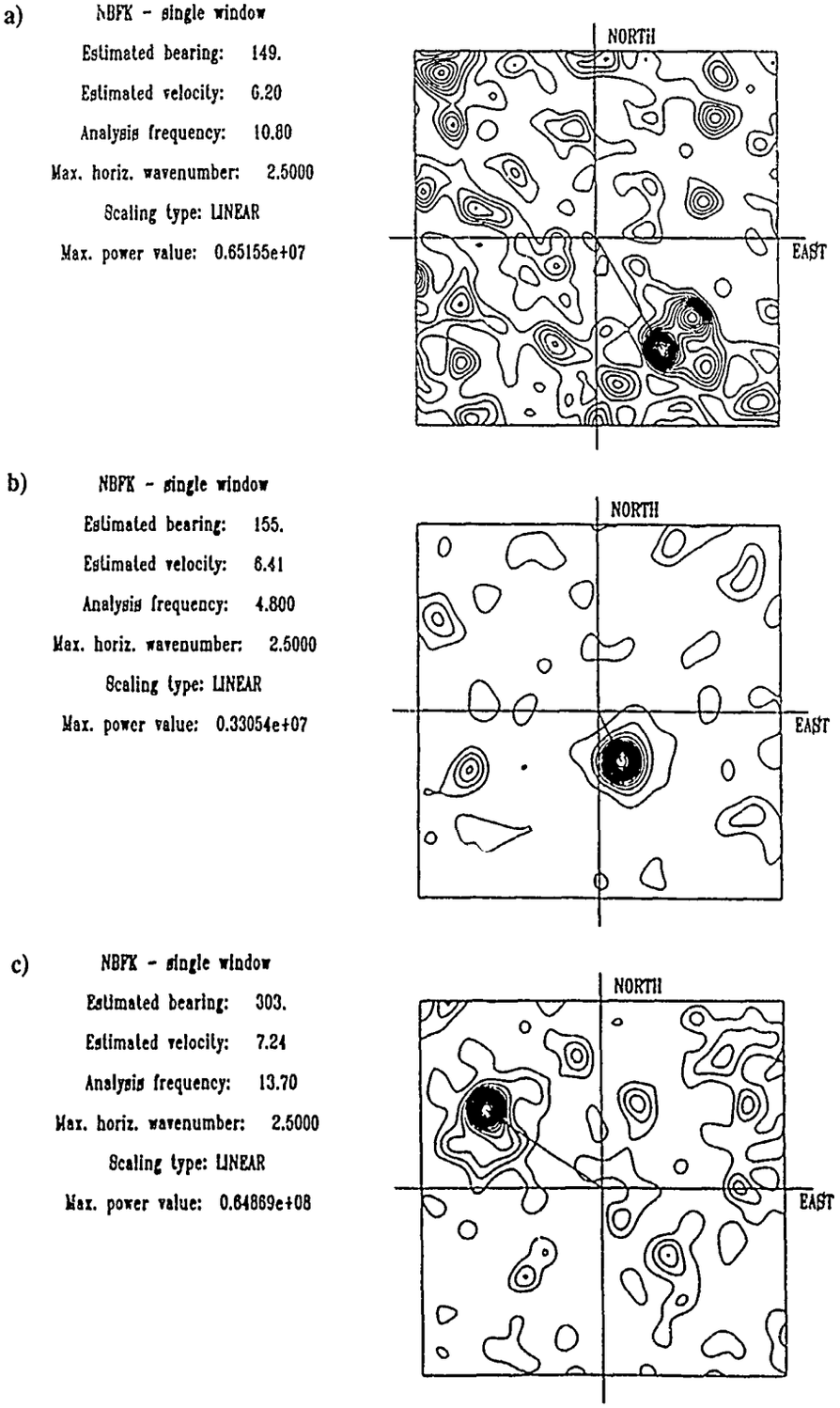

FIG. 12. Power spectra at peak frequencies in *Pg* for events B-2 and A-2d. (a) Event B-2, maximum peak frequency. (b) Event B-2, secondary peak frequency. (c) Event A-2d, peak frequency.

profile A, the power spectrum at the peak frequency (13.7 Hz) of *Pg* in event A-2d is plotted in Figure 12c. It shows much less scattering, and a single maximum.

Discussion and Conclusions

The relatively simple structure of the Baltic Shield is the dominant cause for the clear separation and sharpness of the observed crustal arrivals in the events of both record sections, and accounts for the successful modeling of the major arrivals in the events of profile A with homogeneous plane-layered models. Profile B, due to its closeness to the Oslo Graben, requires a varying crustal thickness, with thickness increasing away from the Graben. This is in agreement with previous studies, which have shown thinning of the crust, by several kilometers in the Graben area (Kanestrom and Haugland, 1971; Kanestrom, 1973; Cassell *et al.*, 1983). The high-phase velocities obtained for *Pn* also indicate a dip in the Moho near the array of approximately 10°, depending on velocity model. High *Pn* velocities under the NORSAR array have also been reported previously by Kanestrom and Haugland (1971) and Kanestrom (1973). Indeed, velocities in a NNW direction were found to be 10 km/sec. The structure east of the Oslo Graben is better approximated by the slower Flora-Asnes model, whereas the Profile 3–4 model works better with the Caldeonian cross-section A. This indicates higher velocities along profile A. *PmP*, around the 80 km distance, is much smaller on profile B, while *SmS* appears to have similar relative amplitudes on both profiles. This could be caused by radiation patterns from the sources, but since both B-1 and B-2 show the same effect, a structural cause is more likely. Furthermore, the lack of any clear *PmS* arrivals on both profiles is probably a structure rather than a source effect. The scattering observed in *P* waves at frequencies above 10 Hz in events B-1 and B-2, and the multipathing in B-2, are evidence of structural heterogeneities in the region east of the Graben.

Although plane-layered constant velocity models can account for the major body-wave arrivals in the seismograms, the dispersive *Rg* waves require velocity gradients near the surface, and for further modeling of relative amplitudes, gradients are also needed in the lower crust. This is in accordance with the refraction study of Mykkeltveit (1980) of a profile north of profile A.

To determine whether the composite seismograms represent good approximations of the true seismograms, an estimate of the coherency in the events is obtained; the coherent amplitude is estimated by the envelope of the composite seismogram and the total amplitude is estimated by the composite of stacked envelopes. The difference represents the amount of incoherent amplitude. Figure 13 shows plots of the estimated total amplitude (dashed curves) and the incoherent amplitude (solid curves) for four events: A-2c, A-3, A-5d, and B-2. Event A-5d is at 250 km distance and the other three are between 83 and 93 km. Event A-3 is located close to A-2 (see Fig. 7). It was not included in record section A, however, because the relative arrival times of major phases could not be matched with either model, assuming a surface focus. It is shown here for comparison with event A-2c. Between the major phase arrivals, the incoherent amplitude is generally about 70 per cent of the total amplitude, but at the arrivals of the large crustal phases, it drops down to between 20 and 50 per cent for the *P* phases, somewhat higher for the *S* phases. In event B-2, incoherency remains high throughout all the crustal reflections due to scattering in the high-frequency range, and to the stacking, which favored the 157° backazimuth. The only phase with high coherency is the low-frequency *Rg* wave at about 20 sec on the plot. Event A-2c also has high coherency during the arrival of

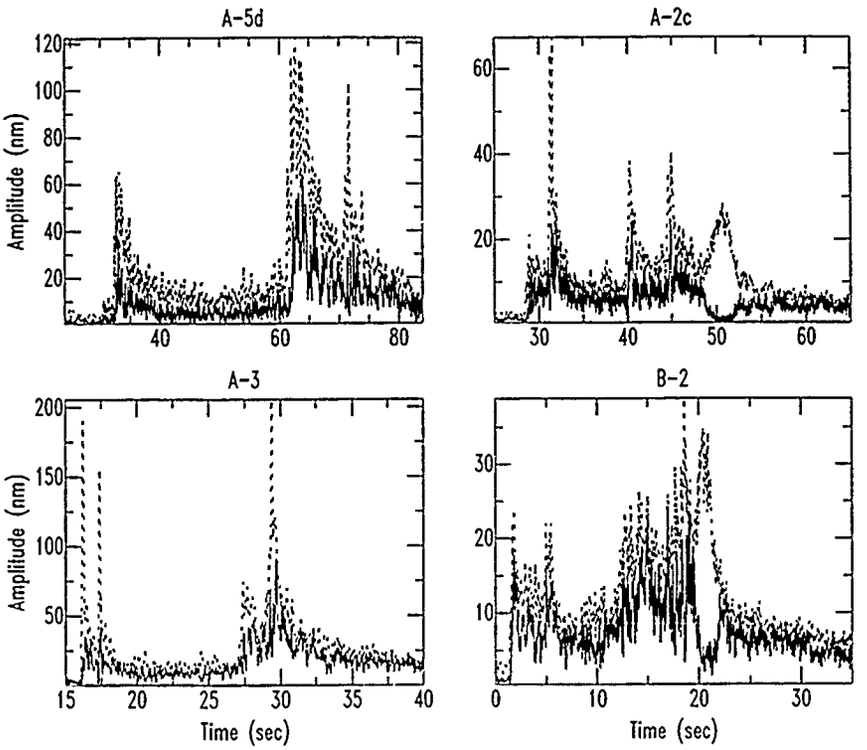

FIG. 13. Estimated total amplitude (dashed) and incoherent amplitude (solid) for events A-5d, A-3, A-2c, and B-2.

Rg, whereas event A-3, probably due to a greater source depth, has no *Rg* wave. Furthermore, coherency at the major body wave arrivals is higher in event A-3 than in A-2c, which may indicate less scattering with increasing source depth. Incoherency is somewhat higher in the most distant event, A-5d, indicating more scattering due to the longer travel path. Even though Figure 13 shows a decrease in coherency with increasing frequency and distance, it still shows high coherency during the major arrivals, and thus justifies approximating the true seismograms with a composite of array beams.

The events presented here clearly show that the *Pg* and *Lg* wave trains on regional seismograms (distances up to 300 km) have separate arrivals within them with distinctive phase velocities, which constrain their travel path, and at the same time the crustal structure. These phases can be valuable in modeling structure, as well as in event location and source depth determination. Describing these phases only in terms of *Pg* and *Lg* is, therefore, an oversimplification and leaves valuable information contained in them unused.

ACKNOWLEDGMENTS

We would like to thank the staff at the Center for Seismic Studies for their help with data acquisition and the reviewer for helpful comments which improved the paper substantially. All of the data analysis was performed using the XAP and SAC seismic analysis codes developed at the Lawrence Livermore Laboratory. This research was supported by the Defense Advanced Research Projects Agency through the Air Force Geophysics Laboratory under Contract F19628-89-K-0013.

REFERENCES

Båth, M. (1976). Engineering analysis of ground motion in Sweden, Seismological Institute Report, Uppsala, Sweden, pp. 17–19, 44.

Bouchon, M. (1982). The complete synthesis of seismic crustal phases at regional distances, *J. Geophys. Res.* **87**, 1735–1741.

Cassell, B. R., S. Mykkeltveit, R. Kanestrom, and E. S. Husebye (1983). A North Sea-southern Norway seismic crustal profile, *Geophys. J. R. Astr. Soc.* **72**, 733–753.

Kanestrom, R. and K. Haugland (1971). Profile section 3-4, in *Deep Seismic Sounding in Northern Europe*, A. Vogel, Editor, Swedish Natural Science Research Council, Stockholm, Sweden, 76–91.

Kanestrom, R. (1973). A crust mantle model for the NORSAR area, *Pure Appl. Geophys.* **105**, 729–740.

Mykkeltveit S. (1980). A seismic profile in southern Norway, *Pure Appl. Geophys.* **118**, 1310–1325.

Mykkeltveit, S., K. Åstebol, D. J. Doornbos, and E. S. Husebye (1983). Seismic array configuration optimization, *Bull. Seism. Soc. Am.* **73**, 173–186.

Ramberg, I. (1976). Gravity interpretation of the Oslo Graben and associated igneous rocks, *Norg. Geol. Unders.*, No. 325.

Sellevoll, M. A. and R. E. Warrick (1971). Refraction study of the crustal structure in southern Norway, *Bull. Seism. Soc. Am.* **61**, 457–471.

Wessel, P. and E. S. Husebye (1987). The Oslo Graben gravity high and taphrogenesis, *Tectonophysics* **142**, 15–26.

Department of Geosciences
The Pennsylvania State University
University Park, Pennsylvania 16802

Manuscript received 5 March 1990

Bulletin of the Seismological Society of America, Vol. 80, No. 6, pp. 2032–2052, December 1990

THREE-COMPONENT ANALYSIS OF REGIONAL SEISMOGRAMS

By D. C. Jepsen and B. L. N. Kennett

Abstract

Both phased array techniques for single-component sensors and vectorial analysis of three-component recordings can provide estimates of the azimuth and slowness of seismic phases. However, a combination of these approaches provides a more powerful tool to estimate the propagation characteristics of different seismic phases at regional distances.

Conventional approaches to the analysis of three-component seismic records endeavor to exploit the apparent angles of propagation in horizontal and vertical planes as well as the polarization of the waves. The basic assumption is that for a given time window there is a dominant wavetype (e.g., a *P* wave) traveling in a particular direction arriving at the seismic station. By testing a range of characteristics of the three-component records, a set of rules can be established for classifying much of the seismogram in terms of wavetype and direction. It is, however, difficult to recognize *SH* waves in the presence of other wavetypes. Problems also arise when more than one signal (in either wavetype or direction) arrive in the same window. The stability and robustness of the classification scheme is much improved when records from an array of three-component sensors are combined.

For a set of three-component instruments forming part of a larger array, it is possible to estimate the slowness and azimuth of arrivals from the main array and then extract the relative proportions of the current *P*-, *SV*-, and *SH*-wave contributions to the seismogram. This form of wavetype decomposition depends on a model of near-surface propagation. A convenient choice for hard-rock sites is to include just the effect of the free surface, which generates a frequency-independent operation on the three-component seismograms and which is not very sensitive to surface velocities. This approach generates good estimates of the character of the *S* wavefield, because the phase distortion of *SV* induced by the free surface can be removed. The method has been successfully applied to regional seismograms recorded at the medium aperture Warramunga array in northern Australia, and the two small arrays NORESS and ARCESS in Norway, which were designed for studies of regional phases.

The new wavefield decomposition scheme provides results in which the relative proportions of *P*, *SV*, and *SH* waves as a function of time can be compared without the distortion imposed by free surface amplification. Such information can provide a useful adjunct to existing measures of signal character used in source discrimination.

Introduction

Seismograms at regional ranges are built up from a complex mixture of seismic propagation phenomena involving multiple reflections and guided waves in the crust (e.g., the phases *Pg* and *Lg*) as well as waves returned from the uppermost mantle (*Pn* and *Sn*). In order to be able to both locate events and to assess the nature of the seismic source, it is necessary to be able to recognize and characterize different parts of the seismic wavefield.

With an array of seismic sensors, processing techniques are now well developed for generating estimates of the azimuth and horizontal slowness of a wavefront crossing the array (see, e.g., Ringdal and Husebye, 1982). Such procedures rely on combining the signals from the various sensors with the phase delays expected from

a single, coherent plane wave crossing the array. A similar set of assumptions may be used to estimate the azimuth and slowness of a seismic signal from three-component records by exploiting vectorial information on the seismic wavefield (Jurkevics, 1988; Christoffersson *et al.*, 1988). However, the accuracy of such estimates is generally lower than from an array, especially for *S* waves. For a set of three-component instruments forming part of a larger array of single-component sensors, improved characterization of the seismic wavefield can be achieved by combining both classes of information.

In this article, we show how the successive application of a number of different measures of the vectorial character of the seismic wavefield can be used to generate a set of rules for classifying the current wavetype on the seismogram as a function of time. The stability and robustness of this classification scheme is markedly improved when records from an array of three-component sensors are combined with time offsets determined by a cross-correlation scheme. Each of the characteristics used is based on the assumption that there is a dominant wavetype (e.g., *P* waves) traveling in a single direction arriving at a three-component station in a particular time window. Thus, when more than one significant signal in terms of direction or wavetype arrives in the same time window, the classification scheme fails. Because the classification scheme is based on the elimination of possibilities, it proves to be difficult to recognize *SH* waves in the presence of other wavetypes.

If the current slowness of azimuth of the incoming wave front are known, the relative contributions of different wavetypes (*P*, *SV*, *SH*) to the seismic wavefield can be estimated from three-component records. This process requires a physical model for the interaction of a seismic wave with near-surface structure. For a hard-rock site, a convenient choice is to include solely the effect of the free surface. Such a free-surface correction is frequently independent, and so can be readily applied to three-component seismograms without any loss of temporal resolution. The correction factors are a slowly varying function of the near surface velocities, and thus the decomposition of the wavefield by wavetypes is not very sensitive to detailed knowledge of surface geology.

This wavefield decomposition scheme overcomes many of the limitations of the wavefield classification scheme and is well suited to use with array data. The full array can be used to estimate the current slowness and azimuth and the wavefield decomposition for this direction of propagation can then be applied to the three component data. This approach to the characterization of seismograms has been successfully applied to seismograms at regional ranges recorded at the Warramunga array in northern Australia (Cleary *et al.*, 1968) and at the two Norwegian arrays NORESS and ARCESS, which are specifically designed for the analysis of regional phases (Mykkeltveit *et al.*, 1983). A major benefit of the new procedure is that phase distortions associated with *S*-wave interaction with the free surface are removed, and also there is no difficulty with handling comparable proportions of *SV* and *SH* motion.

The decomposition of the seismic wavefield by wavetype as a function of time not only has considerable benefits for the recognition of seismic phases, but also provides a domain in which the relative proportions of *P*, *SV*, and *SH* waves can be compared directly, because free-surface amplification effects have been removed. This information on the current proportions of different wavetypes summarizes much of the propagation processes between source and receiver and therefore can help to provide specific measures of wavefield character which can be beneficial in attempts to discriminate between different source types.

Wavetype Classification from Three-Component Records

The exploitation of three-component seismic records has hitherto been most successful when applied to low frequency data (<0.2 Hz), as in the work of Boore and Toksöz (1969). At higher frequencies, the influences of scattering, multipathing, phase shifts and mode conversions all limit our ability to determine important wavefield parameters such as wavetype, slowness, and azimuth.

The analysis of three-component data has been mostly based on two basic procedures. The first class of procedure is based on the development of polarization measures designed to enhance particular wavetypes (e.g., Shimshoni and Smith, 1964; Montalbetti and Kanasewich, 1970; Vidale, 1986) or to estimate the horizontal slowness and azimuth of a wavefront (Jurkevics, 1988). The second approach is to estimate the parameters of some *a priori* model of particle motion that is matched to the data in a time varying manner (e.g., Christofferson *et al.*, 1988; Nagano *et al.*, 1989).

The aim of the present work is to exploit the full three-component data set for an event in order to characterize the seismic wavefield as a function of time and frequency. A sequence of parameters describing the wavefield based on both polarization and particle motion characteristics are derived from the three-component information. These parameters are then used in a sequence of tests to establish a set of rules for classifying the current dominant wavetype on the seismogram.

The basic assumption will be that the seismic wavefield at the recording site at each instant comprises a single wavetype traveling in a fixed direction. If the proposition of other wavetypes is considerable or if there is more than one signal of the same wavetype arriving at the same time, then the classification scheme will not be able to assign a wavetype.

Models of the Wave Field

We will work with North, East, and Down components of the ground motion, which form a right-handed coordinate system. The seismic records are normally made at the free surface so that we have to take into account the amplification effects associated with seismic wave interaction with the surface. We will work with the assumption that the medium in the vicinity of the seismometers can be treated as horizontally stratified and isotropic, so that we can describe the wave field in terms of compressional (P) waves and shear waves polarized in vertical (SV) and horizontal (SH) planes. We may then ascribe specific models for the particle motion associated with plane waves for the different classes of seismic phases described by two parameters: θ = the azimuth of the normal to the wave front; ϕ = the apparent propagation angle with the vertical. Thus for plane P waves, the displacement $\mathbf{u}(\omega) = [u_N, u_E, u_D]^T$ at frequency ω would take the form

$$\mathbf{u}(\omega) = [\sin\phi\cos\theta, \sin\phi\sin\theta, \cos\phi]^T s(\omega) \tag{1}$$

for source spectrum $s(\omega)$. In an unbounded medium, ϕ would represent the true propagation direction in the vertical plane. However the presence of a free surface modifies the apparent direction of propagation as measured by the ratio of the vertical and horizontal components, and so

$$\tan\phi = F\tan i, \tag{2}$$

where i would be the actual angle to the vertical made by the normal to the plane wave front. The free surface correction factor F is given by

$$F = \frac{2 \cos i \cos j}{1 - 2\beta_0^2 \sin^2 i/\alpha_0^2} = \frac{2 \cos i \cos j}{1 - 2 \sin^2 j}, \tag{3}$$

where j is the true propagation angle for an SV wave for which

$$\sin j/\beta_0 = \sin i/\alpha_0$$

in terms of the surface P- and S-wave velocities α_0 and β_0. Equation (2) is an awkward transcendental equation which has to be solved before an accurate slowness estimate $p = \sin i/\alpha_0$ can be made.

For SV waves incident at the surface at less than the critical angle $j_c = \sin^{-1}(1/\alpha_0)$, the displacement vector can be written as

$$\mathbf{u}(\omega) = [\sin \phi \cos \theta, \sin \phi \sin \theta, \cos \phi]^T s(\omega). \tag{4}$$

Note that because the particle motion is transverse to the wave front, even in an unbounded medium the apparent propagation direction ϕ will be 90° off from the actual normal to the wavefront. When we allow for the effect of the free surface, the true direction of propagation j is to be found from

$$\tan \phi = F \cot j, \tag{5}$$

where F has the same form as in (3).

Once the angle of incidence j is greater than the critical angle j_c, there is a phase shift introduced into the SV wave on reflection from the surface and the surface displacement can be described by

$$\mathbf{u}(\omega) = [\mathrm{i} \sin \phi \cos \theta, \mathrm{i} \sin \phi \sin \theta, \cos \phi]^T s(\omega), \tag{6}$$

where $\phi = \tan^{-1} e$, and $|e|$ is the eccentricity of the elliptical motion. This description of the particle motion is also appropriate for higher and fundamental mode Rayleigh waves.

For SH waves, there is no motion in the vertical direction and the displacement takes the form

$$\mathbf{u}(\omega) = [\sin \theta, -\cos \theta, 0]^T s(\omega). \tag{7}$$

If the azimuth of such a plane SH wave were to be estimated from the ratio of the North and East components (which would be appropriate for P and SV waves), the estimate would be out by 90°.

Parameters of the Wave Field

The set of parameters which we extract from the three-component seismic records in order to characterize the seismic wave field are as follows.

1. *Directional Parameters*: *Apparent Azimuth and Apparent Angle of Incidence.* These two parameters are estimated by three signal directional finding (SDF)

techniques, which primarily average the directional vector over a specified time interval. The first two techniques estimate the direction of the signal by determining the direction cosines of the projection of the ground motion on the unit upper hemisphere.

(a) Triax: For motion $\mathbf{u}_i = [u_{i\mathrm{N}}, u_{i\mathrm{E}}, u_{i\mathrm{D}}]^{\mathrm{T}}$ the instantaneous direction cosines are defined by

$$l = u_{i\mathrm{N}}/r_i, \qquad m = u_{i\mathrm{E}}/r_i, \qquad n = u_{i\mathrm{D}}/r_i,$$

where the instantaneous power $r_i = (u_{i\mathrm{N}}^2 + u_{i\mathrm{E}}^2 + u_{i\mathrm{D}}^2)^{1/2}$. These quantities are then averaged over a time interval to give estimates for the direction cosines L, M, N and a measure of the stability of the directional estimate $s = (L^2 + M^2 + N^2)^{1/2}$, which would be unity for motion in a fixed direction (Greenhalgh *et al.*, 1990). The apparent azimuth can then be constructed from $\tan \theta = M/L$, and the apparent angle of incidence from $\cos \phi = N$.

(b) Ls: The effective direction cosines over a given time window are estimated by a least squares fit to the actual motion.

(c) Power: Estimates direction by using a cross-power matrix method, which effectively maximizes the energy in one of the three orthogonal directions. For instantaneous motion $\mathbf{u}_i$, the cross power matrix is

$$\mathbf{S} = \frac{1}{N} \sum_{i=1}^{N} u_{ij} u_{ik} \quad j, k = \mathrm{N}, \mathrm{E}, \mathrm{D}.$$

The eigenvectors $\mathbf{v}$ and eigenvalues λ of $\mathbf{S}$ can be found from

$$(\mathbf{S} - \lambda^2 \mathbf{l})\mathbf{v}_m = \mathbf{0}, \quad m = 1, 2, 3$$

and are ordered by size, $\mathbf{l}$ is the unit matrix. The normalized eigenvector $\mathbf{v}_1 = (v_{1\mathrm{N}}, v_{1\mathrm{E}}, v_{1\mathrm{D}})$ corresponding to the largest eigenvalue λ may then be used as an estimate of the dominant signal direction. The apparent azimuth and angle of incidence are to be found from

$$\tan \theta = v_{1\mathrm{E}}/v_{1\mathrm{N}}, \qquad \cos \phi = v_{1\mathrm{D}}.$$

The size of λ_1 can be used as a measure of the stability of this procedure since it will be unity for purely rectilinear motion. These directional parameters are calculated from the particle motion of the coda, hence they do not necessarily give the actual direction of propagation.

2. *Polarization parameters: Rectilinearity, Planarity, and Stability.* The measures of rectilinearity and planarity are based on the eigenvalues of the covariance matrix employed in the power technique, while the stability parameter gives an indication of the stability of the two directional parameters determined.

(a) Rectilinearity: rect $= 1 - (\lambda_2 + \lambda_3)/2\lambda_1$, where λ_1, λ_2, λ_3 are the eigenvalues (largest to smallest) of the cross-power matrix $\mathbf{S}$.

(b) Planarity: plan $= 1 - 2\lambda_3/(\lambda_1 + \lambda_2)$.

(c) Stability: mean of the stabilities of the triax and power methods.

3. *Phase Difference Polarization Parameters.* White (1964) defined two motion product detectors. *HV* (corresponding to zero phase) and *HiV* (90° phase shift):

$$P_N = u_N u_D \qquad P_E = u_E u_D \qquad (HV)$$

$$Q_N = H(u_N) u_D \qquad Q_E = H(u_E) u_D, \qquad (HiV)$$

where u_N, u_E, and u_D are the displacements in the N, E, and D directions respectively, and H is the Hilbert transform. A summary of the phase characteristics of purely polarized wave forms is listed in Table 1.

An estimate of the azimuth can be based on the ratio of the motion product detectors (P_N/P_E, Q_N/Q_E), and if the actual propagation path (azimuth) of the signals is known the wave types with similar phase properties can be distinguished by comparing these values. Any one of the motion products may be zero, either theoretically or due to the orientation of the particle motion with respect to the receiver, hence combined motion products P_{NE} and Q_{NE} are defined:

$$P_{NE} = \sqrt{P_N^2 + P_E^2} \quad \text{and} \quad Q_{NE} = \sqrt{Q_N^2 + Q_E^2}.$$

4. *ZRT Parameters and Products.* Displacements in the NED coordinate system can be transformed into radial (R) and transverse (T) components by the simple transformation:

$$\begin{pmatrix} Z \\ R \\ T \end{pmatrix} = \begin{pmatrix} 1 & 0 & 0 \\ 0 & \cos\theta & \sin\theta \\ 0 & -\sin\theta & \cos\theta \end{pmatrix} \begin{pmatrix} \mathrm{D} \\ \mathrm{N} \\ \mathrm{E} \end{pmatrix}, \tag{8}$$

where θ is the azimuth and *ZRT* forms a right-handed system. The component product *RZ* and the ratio of $|R|/|T|$ are employed in distinguishing between different wave types.

Where energy comes in within 10° of the expected source-receiver azimuth, component product operators can be used to separate out *P/SV* motion. For a linearly polarized wave *P* wave: *RZ* is negative; *SV* wave: *RZ* is positive; and Rayleigh wave: *RZ* oscillates about zero. For an *SH* wave, *RZ* vanishes as all motion is on the *T* component. Because of our choice of the NED coordinate system, the sign of *RZ* is opposite to that defined by Plesinger *et al.*, (1986). To resolve any

TABLE 1

PHASE DISCRIMINATION RESULTS

Wave Type	*HV*	*HiV*	Azimuth
P wave	$\|P\|_N, \|P\|_E > 0$	Q_N & $Q_E = 0$	$\vartheta = \tan^{-1} P_N/P_E$ (Points away from source)
$SV < j_c$	$\|P\|_N, \|P\|_E > 0$	Q_N & $Q_E = 0$	$\vartheta = \tan^{-1} P_N/P_E$ (Points to source)
$SV > j_c$	P_N & $P_E = 0$	$\|Q\|_N, \|Q\|_E > 0$	$\vartheta = \tan^{-1} Q_N/Q_E$ (Points to source)
Rayleigh	P_N & $P_E = 0$	$\|Q\|_N, \|Q\|_E > 0$	$\vartheta = \tan^{-1} Q_N/Q_E$ (Points away from source)
SH/Love	P_N & $P_E = 0$	Q_N & $Q_E = 0$	Indeterminate

ambiguity, we will not display RZ directly in the figures, but divide the waves into three fields: P, SV, and elliptical/SH based on their RZ values.

Wave Classification

Discrimination between wavetypes is based on the parameters we have just described. From a range of test with synthetic seismograms calculated with wavenumber integration techniques (see, e.g., Kennett, 1983), we have been able to produce a set of rules for classifying the behavior into three groups based on the character of the particle motion in three dimensions (Jepsen, 1989).

A. Waves with Essentially Rectilinear Motion. The criteria employed to determine rectilinear motion is: (a) the mean stability > 0.85 (Triax and Power) or (b) rectilinearity > 0.9. These waves can be classified into two groups: P/SV ($\phi < j_c$) and SH.

P/SV Waves: (1) $P_{NE} > 1.5Q_{NE}$ (in the figures $PQXY$ represents the ratio $P_{NE}:Q_{NE}$). (2) $PQ_{abs} > 0.25$, where PQ_{abs} = abs (P_{NE}, Q_{NE}). (3) $|R| > 1.5\,|T|$. Due to an 180° ambiguity in azimuth, P cannot be distinguished from SV unless the actual azimuth is known. In this case, the component product RZ is positive for P waves and negative for SV waves.

SH Waves: (1) P_{NE} and Q_{NE} are small compared to the amplitude, i.e., $PQ_{abs} < 0.15$. (2) $|T| > 1.5\,|R|$.

B. Waves with 2D Motion. The following criteria must hold: (1) planarity > 0.9; (2) $\lambda_2 > 0.1$ or $\lambda_2 > 0.05$ for SV/Rayleigh waves. These waves can be classified into two groups: *The superposition of two rectilinear waves*: In this case there is no phase shift between the horizontal and vertical components and this sort of motion can be constructed from a combination of P, SV, and SH waves. Conditions are: (a) $P_{NE} > 1.5\ Q_{NE}$; (b) $PQ_{abs} > 0.25$. *Purely elliptically polarized waves*: Here the horizontal motion is 90° out of phase with respect to the vertical motion. Rayleigh waves and SV ($j > j_c$) have this form. The criteria are: (a) $Q_{NE} > 1.5\ P_{NE}$; (b) $PQ_{abs} > 0.25$. Obviously the two types of motion can be separated, but it is difficult or impossible to determine what types of waves make up the motion. If one knows the source to receiver azimuth and employs it as the correct azimuth (a major assumption) the wavetypes that compose the above types of motion can be distinguished.

In the case of two rectilinear waves, three types of waves can be determined: (1) A combination of two P waves or the dominant wave is a P wave, in which case there will be hardly any motion in the T direction. The following criteria can define this motion: (a) $P_{NE} > 1.5\ Q_{NE}$ and $PQ_{abs} > 0.25$; (b) $|R| > 1.5\,|T|$; and (c) the component product $RZ > 0$. (2) A combination of two SV waves or the dominant wave is a SV wave, again there will be little motion in the T direction. This type of motion has the same criteria as above except that in this case the component operator $RZ < 0$. (3) A S wave, as long as the criteria above is not satisfied and the following conditons are met: $P_{NE} > 1.5\ Q_{NE}$ and $PQ_{abs} > 0.25$. Once the magnitude of the motion in the T direction surpasses a certain limit, there is enough SH motion to classify the wave as a S wave.

In the case of purely elliptical polarized waves, the two types of waves can be separated based on the comparison of the estimated azimuth versus the source-receiver (s-r) azimuth. If the estimated azimuth is essentially the same as the s-r azimuth the wavetype present is a Rayleigh wave, whereas if the azimuths are out by roughly 180° the wave can be classified as a SV wave. Neither of the wavetypes is determined if the azimuths do not correspond to the above cases.

The PQ_{abs} criteria limits the detection of weakly polarized waves, as the values established via synthetic calculations ensure that no false identifications arise. If the propagation characteristics of the signals are known these conditions can be relaxed.

C. 3D Motion. In this case, the wave field corresponding to such motion is too difficult to classify in terms of wave type. This is an important limitation of the technique.

Application to Array Records

This wave classification scheme has been successfully applied to regional records recorded at the two small arrays NORESS and ARCESS in Norway, which have been designed for the analysis of such events.

We will illustrate this scheme by application to a small regional event recorded at the ARCESS array in northern Norway at a range of 171 km and an azimuth from source to receiver of 266°. As a result, the records are nearly naturally polarized with dominantly *SH* motion on the *N* component and *P-SV* motion on the *E*, *Z* components (see Fig. 3). However, both *SV* and *SH* signals arrive together with amplitudes of a similar size, so that they both affect any measures of the polarization of the wavefield.

The set of wavefield measures are calculated from the three-component data in progressive 1 sec time windows in a number of frequency bands generated by the application of a fourth-order Butterworth filter. The choice of 1 sec intervals gives good results for a broad range of frequencies up to 12 Hz or more. Generally the behavior is very complex for unfiltered data and simplifies somewhat for lower frequency bands, as much locally scattered energy is excluded. The behavior of the various measures of the wavefield is most consistent for frequencies below 4 Hz, and this frequency dependence is commonly found for regional records at ARCESS and NORESS. The rule-based classification scheme can be applied as the seismograms are scanned so that the general wave group can be determined as a function of time and then component based estimators used to try to refine the estimate of the actual wavetype (see Fig. 3).

The set of filtered records for the vertical component from the four individual three-component recording sites are shown in Figure 1 for the frequency band 1 to 2 Hz, for which the most effective results have been obtained with the classification scheme. The C stations lie on a ring 1.4 km in radius about the central site A0. The behavior of this vertical component gives a good representation of the type of variation in seismograms seen across such a small array. Although the seismograms have similar behavior at each site, there are sufficient differences between the different records to have a significant influence on the behavior of the estimators of azimuth, angle of incidence, and other wave field parameters.

The variability in such wave field measures is illustrated in Figure 2, where we show the apparent azimuth and angle of incidence, for the 1 to 2 Hz frequency band, at the central site A0 and the site C2, compared with the comparable analysis on a composite record (indicated by the sum trace in Fig. 1). The behavior of the azimuth estimates is generally similar in all three cases, although the sum trace shows fewer extraneous excursions. However, the most notable difference is for the apparent angle of incidence; the behavior of sites A0 and C2 shows considerable differences as well as quite rapid changes in angle. The array sum trace shows a more consistent trend of the angle of incidence as a function of time with less total variation, while preserving the general character seen at the individual sites. The

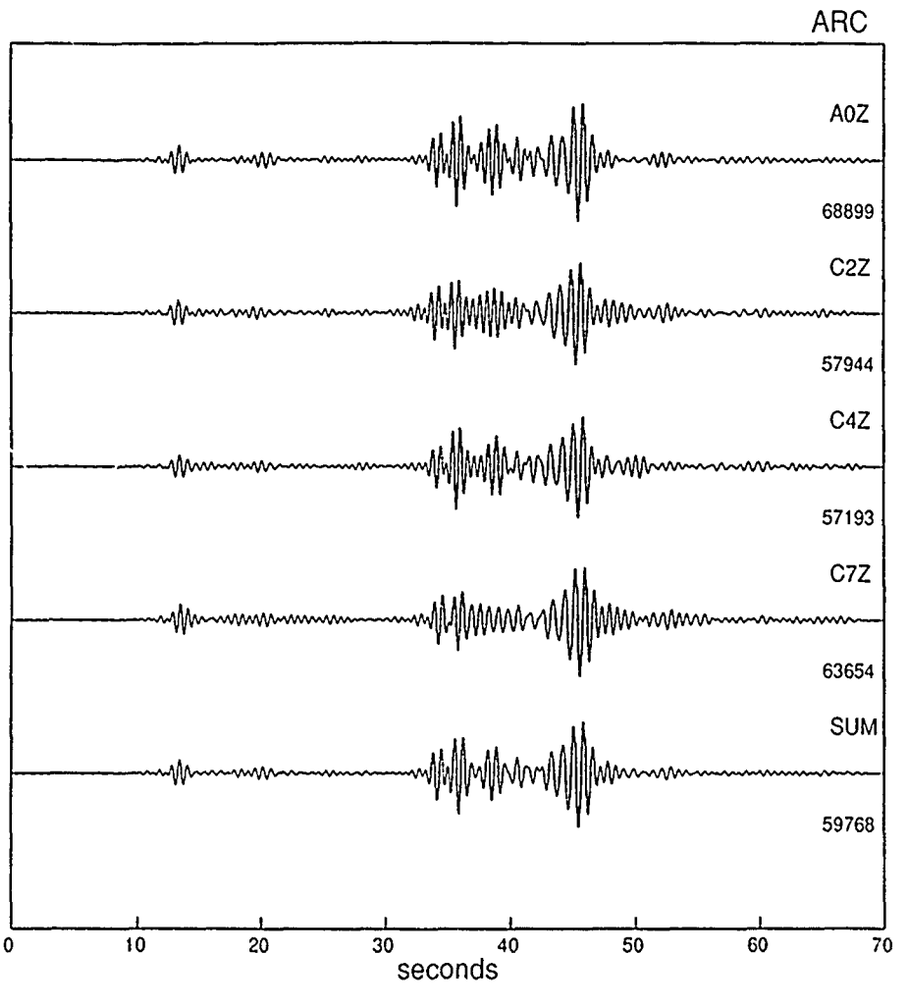

FIG. 1. A regional event (17 March 1988 10:21:17, 29.9°E 69.6°N) at the ARCESS array in northern Norway at a range 171 km and azimuth 266°. The vertical component traces recorded at the four three-component sites are displayed together with a composite trace produced by the method described in the text.

relatively unstable nature of the apparent angle of incidence is commonly observed, and this is the reason that it has been excluded from the criteria used in wave type classification.

We will subsequently consider just the summed three-component data from the array. This has been generated by the following procedure based on adaptive processing techniques originally developed for single component array data (King *et al.*, 1973):

1. Array beams for each component are calculated without time shifts.
2. For each station, subtract the appropriately aligned channel of each component from its respective beam and cross-correlate with the corresponding depleted beam. Find the time shift where the overall correlation of the three components is maximum, then add the realigned channels back into the beams.
3. Repeat step 2 eight times to ensure maximum correlation between the individual channels. A limit is placed in the maximum time shift allowed for the correlation based on the size of the array and the maximum expected slowness to keep the time shift aligned to the correct portion of the data.

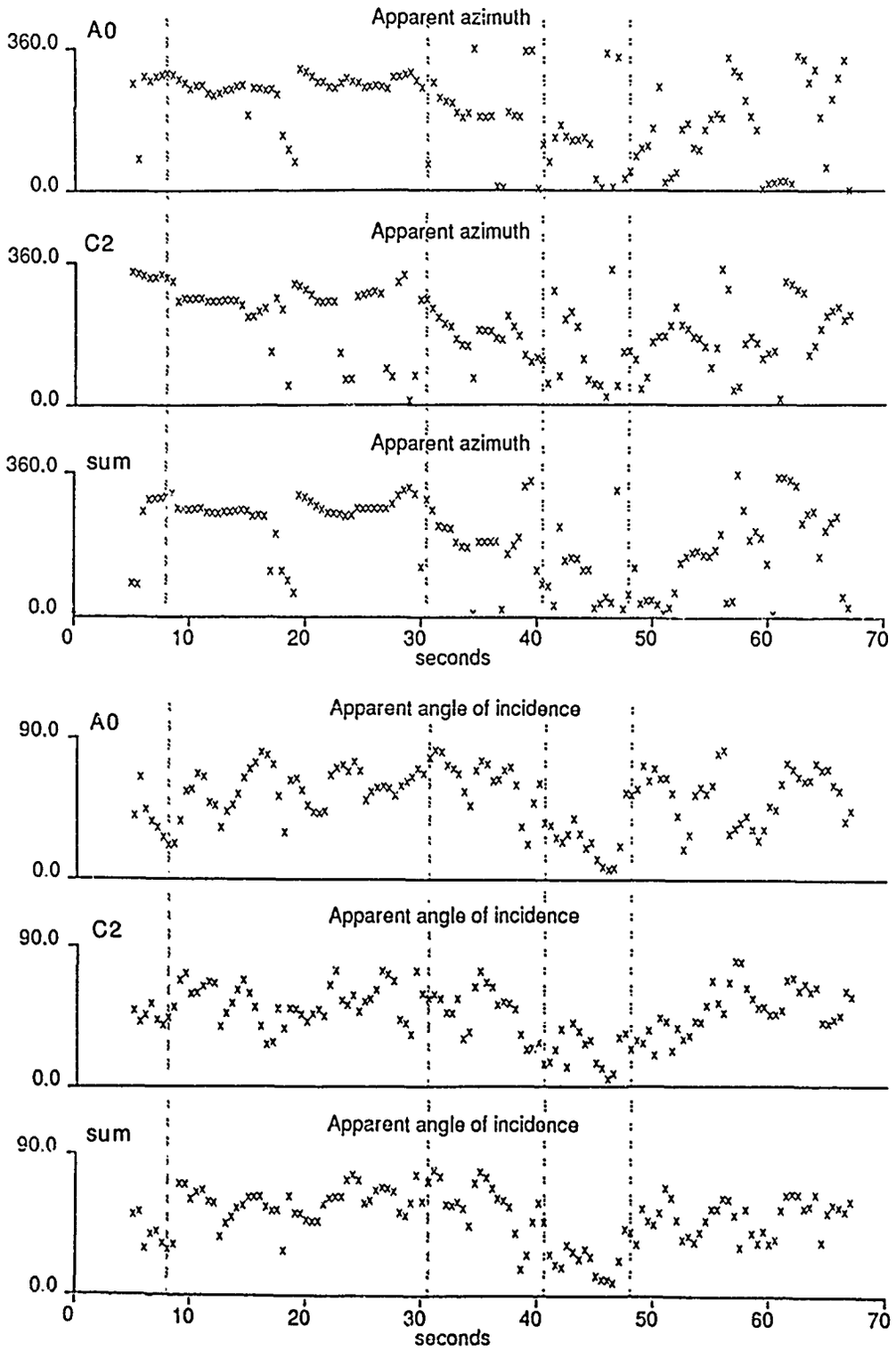

FIG. 2. Comparison of estimates of apparent azimuth and apparent angle of incidence at the individual sites A0 and C2 with the summed three-component data combining the records from the four individual sites.

For NORESS and ARCESS, the radius of the three-component array is 1.4 km and a reasonable maximum slowness is 0.3 sec/km, hence the greatest time shift allowed is 0.42 sec. The merit of this three-component summation procedure is that the influence of signal-generated noise is reduced, and as a result some of the partially

coherent arrivals can be recognized because of the greater stability of the sum trace. The disadvantage is that there is some inevitable loss in resolution associated with averaging over slightly different wave forms.

This array summation procedure is only really suitable for small aperture arrays. For larger arrays, the best three-component stacks are produced by slowness and azimuth alignment for each time window at stage 1, the procedure above can then be used to optimize the sum trace.

Analysis of the Three-Component Array Sum Record: ARCESS. The seismograms of the regional event at ARCESS are dominated by clear *P*, *S*(*Lg*), and *Rg* phases, and the distinct character of the different parts of the seismogram allow us to consider it in four sections marked by the dashed lines in Figure 3: (a) 8 to 30 sec: initial *P* phase and *P* coda; (b) 31 to 40 sec: *S* coda (*Lg*); (c) 41 to 47 sec: Rayleigh wave motion (*Rg*); and (d) 48 to 70 sec: later coda.

In Figure 3, we display the wave field measures introduced above, together with summary classification of the wave field behavior deduced from these measures, first by wave group and finally by apparent wave type. The parameter *PQXY* is the ratio of the combined motion product detectors P_{NE} Q_{NE}; if the values fall outside the range (0.67 to 1.5), they are plotted just outside the appropriate limit.

The apparent azimuth is fairly stable for the first three sections of the seismogram, but some fluctuations are seen. For the *P* waves, the estimated azimuth is close to the source-receiver azimuth (266°), while in other sections the azimuth stabilizes around different values that reflect the orientation of the particle motion (e.g., 90° shift for dominant *SH*). The late coda shows little consistency in apparent azimuth. The apparent angle of incidence shows considerable variability but clearly indicates low values (i.e., particle motion close to vertical) for the *Rg* phase. Despite the fluctuations in the apparent angle of incidence, we can see that the *P*, *S*, and Rayleigh sections have distinct polarization characteristics, whereas most of the late coda is randomly polarized.

High rectilinearity and stability values are generally associated with stable azimuth values, and where the azimuth fluctuates the values indicate that the waves are not rectilinear. For Rayleigh waves, the rectilinearity is lower but the corresponding planarity values are high. The motion product detector *PQXY* results indicate that in-phase vertical and horizontal motion is prominent in the *P* coda ($PQXY > 1.5$). For much of sections 2 and 3, on the other hand, the vertical motion is 90° out-of-phase with the horizontal ($PQXY < 0.67$), which is indicative of the presence of elliptical *P*/*SV* behavior.

The combination of the classification criteria based on these wavefield measures allows an estimate of the main wave groups. The first section corresponds to rectilinear *P*/*SV* waves, and elliptical *P*/*SV* is prominent in sections 2 and 3 of the seismogram. Despite the clear visual evidence for *SH* waves, they are identified only at their greatest amplitude, because of the contaminating influence of the *SV* waves.

In order to try to define the wavetypes, we now assume that we have a reliable estimate of the source-receiver azimuth from the onset of the *P* wave and use component based estimators assuming on-azimuth propagation. The values of the component product *RZ* are displayed directly, as well as the ratio of components in the horizontal plane ($|R|/|T|$) and between the vertical and net horizontal motions. For section 1, it would appear that most of the energy is *P* arriving close to the true azimuth. In section 2, the ratio $|R|/|T|$ is small, suggesting *SH* motion,

but other indicators suggest the simultaneous presence of another wavetype (SV/Rayleigh) so that positive identification is limited. The individual stations show a good deal of off-azimuth energy, some of which is distinct to the particular station and therefore likely to have a local cause, but some signals do correlate suggesting coherent scattering from features along the direct propagation path.

The classification scheme we have described performs well in separating much of the seismogram into major wave groups, so that it can have a useful role in phase recognition. The P waves and the Rg phase are clearly identified by the classification scheme but, although the S character of the second section of the seismogram can be recognized, classification is limited because of the presence of both SV and SH waves at the same time. Analysis of other events confirms that phase identification is readily achievable in the P coda but tends to deteriorate rapidly in the S-wave coda.

Wave Field Decomposition

We have seen in the previous section that the systematic application of wavefield measures derived from three-component records is severely limited by the assumption of a single dominant wavetype present on the seismogram at a particular time.

We can overcome this limitation by developing a new analysis scheme based more closely on physical models of the propagation process, which can allow multiple wavetypes to be present. Such models require knowledge of the current slowness vector (azimuth and horizontal slowness), which can be determined accurately using a full array.

Description of the Surface Wave Field. In the neighborhood of the three-component stations, we consider a locally horizontally stratified medium with an incident upcoming wavefield. The surface wavefield at frequency ω can then be expressed as a superposition of signals of different slowness and wavetype

$$\begin{pmatrix} Z(\omega) \\ N(\omega) \\ E(\omega) \end{pmatrix} = \int d\theta \int dp\ \mathbf{C}(p, \theta, \omega) \begin{pmatrix} P(p, \theta, \omega) \\ S(p, \theta, \omega) \\ H(p, \theta, \omega) \end{pmatrix}, \tag{9}$$

in terms of incoming P-, SV-, and SH-wave components.

In order to exploit array processing techniques, we make the simplifying assumptions that all the signal is associated with a single source wavelet and that the field at any instant can be represented with a single slowness vector. We can then express the surface displacement as

$$\begin{pmatrix} Z(\omega) \\ N(\omega) \\ E(\omega) \end{pmatrix} = \begin{pmatrix} 1 & 0 & 0 \\ 0 & \cos\theta & -\sin\theta \\ 0 & \sin\theta & \cos\theta \end{pmatrix} \begin{pmatrix} w_{ZP}(p,\omega) & w_{ZS}(p,\omega) & 0 \\ w_{RP}(p,\omega) & w_{RS}(p,\omega) & 0 \\ 0 & 0 & w_{TH}(p,\omega) \end{pmatrix} \begin{pmatrix} P(p,\omega) \\ S(p,\omega) \\ H(p,\omega) \end{pmatrix}, \tag{10}$$

where the first matrix transforms between ZRT and ZNE coordinate systems and the second matrix includes the physical model of the propagation process for horizontal slowness p.

We can summarize equation (10) as a relation between the surface displacement $\mathbf{u}$ and the incoming wave vector $\mathbf{v}$ as

$$\mathbf{u} = \mathbf{R}(\theta)\mathbf{M}(p, \omega)\mathbf{v}. \tag{11}$$

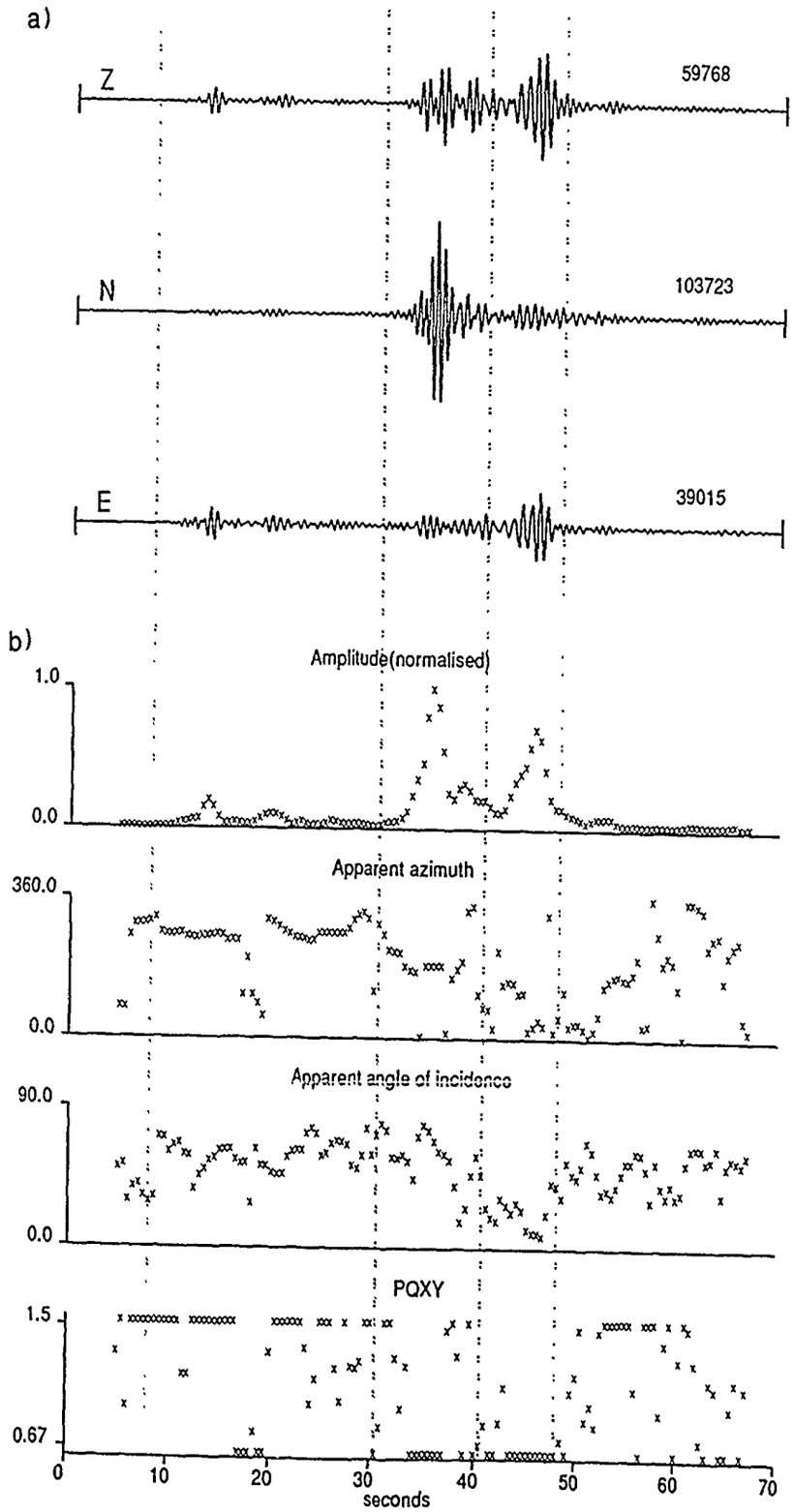

FIG. 3. Analysis of three-component wavefield measures for the summed data for the regional event at the ARCESS array. (a) The three components of the seismogram. (b) Estimates of wavefield parameters derived directly from the seismograms.

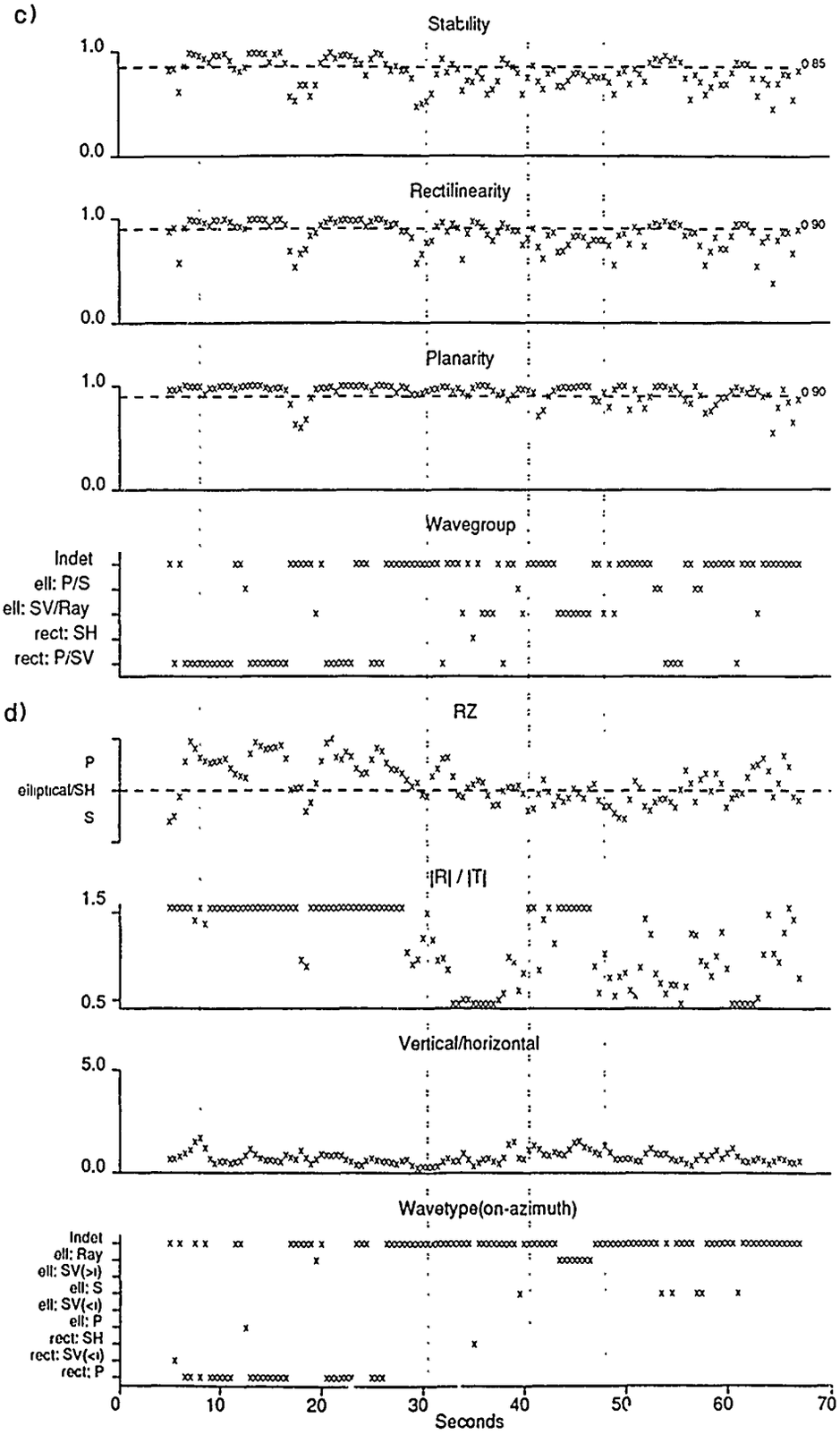

FIG. 3.—*Continued.*
(c) Wavefield measures derived from polarization analysis and classification of wave group. (d) Wavefield measures derived for on-azimuth propagation and classification of wavetype.

The wave vector $\mathbf{v}$ can then be recovered if the matrix $\mathbf{R}(\theta)\mathbf{M}(p, \omega)$ can be inverted, and then

$$\mathbf{v} = [\mathbf{M}(p, \omega)]^{-1}[\mathbf{R}(\theta)]^{-1}\mathbf{u}. \tag{12}$$

The observed displacement $\mathbf{u}$ is already known. The angular dependence $\mathbf{R}$ can be found once the azimuth is known and can readily be inverted. Hence recovery of $\mathbf{v}$ depends on the way in which the structural matrix $\mathbf{M}(p, \omega)$ is described.

Frequency-Independent Model: Free Surface Only. The simplest model that can describe data collected at the surface is one in which the interaction of P and S waves at the surface are included. The combination of incident and reflected waves leads to the matrix (Aki and Richards, 1980, Chapter 5)

$$\mathbf{M}(p) = \begin{pmatrix} -\alpha_0 q_{\alpha 0} C_1 & \beta_0 p C_2 & 0 \\ \alpha_0 p C_2 & \beta_0 q_{\beta 0} C_1 & 0 \\ 0 & 0 & 2 \end{pmatrix}, \tag{13}$$

where α_0, β_0 are the surface P and S wave speeds. The vertical slownesses

$$\begin{aligned} q_{\alpha 0} &= (\alpha_0^{-2} - p^2)^{1/2}, \\ q_{\beta 0} &= (\beta_0^{-2} - p^2)^{1/2}, \end{aligned} \tag{14}$$

where the radicals are chosen such that $\mathrm{Im}(\omega q) > 0$ for evanescent waves of a particular wavetype. The form of $\mathbf{M}(p)$ is very similar to that for an infinite medium except for the introduction of the slowness dependent quantities C_1 and C_2 representing the effect of free-surface amplification on the P-SV system:

$$C_1 = \frac{2\beta_0^{-2}(\beta_0^{-2} - 2p^2)}{(\beta_0^{-2} - 2p^2)^2 + 4p^2 q_{\alpha 0} q_{\beta 0}} \qquad C_2 = \frac{4\beta_0^{-2} q_{\alpha 0} q_{\beta 0}}{(\beta_0^{-2} - 2p^2)^2 + 4p^2 q_{\alpha 0} q_{\beta 0}}. \tag{15}$$

For slownesses greater than α_0^{-1}, for which P waves are no longer propagating, $q_{\alpha 0}$ is imaginary and C_1 and C_2 become complex. There is, therefore, a phase shift between the resulting displacement and the incoming wave. The behavior of the coefficients C_1 and C_2 is generally smooth with slowness, although there is relatively rapid change in the immediate neighborhood of $p = \alpha_0^{-1}$.

For SH waves, the incident and reflected waves add to give a surface amplification factor of 2.

Frequency-Dependent Models. Where detailed knowledge of the seismic velocity structure is available for the vicinity of a three-component seismometer site, the structural matrix $\mathbf{M}(p, \omega)$ representing upward transmission to the surface can be constructed to include the details of propagation in this zone (see, e.g., Kennett, 1983, chapter 6). Once structures such as sedimentary layers are included, the structural effects are frequency dependent, and so when we try to analyze three-component records there will be a loss of temporal resolution. However, this may be worthwhile to remove strong reverberations in the near-surface zone.

Recovery of the Wave Vector. The wave field model that is to be used for the calculation of the wave vector $\mathbf{v}$ must provide an adequate account of the interaction of waves near the recording station. We have therefore chosen the half-space model

in (13), which allows for the dominant free-surface effects. This term will appear as an element in all structural matrices, and so this level of correction will always be useful.

As this model is frequency independent, its application in the time and frequency domains could follow that used in the wave classification procedure. Thus the seismograms are segmented into 1-sec intervals, which are tapered at both ends to eliminate edge effects, and the data is then bandpassed into a set of frequency bands. The calculation of the amplitude vector is performed in the time domain and to allow for phase shifts is evaluated from:

$$\begin{pmatrix} P \\ S \\ H \end{pmatrix} = \text{real}[\mathbf{R}(\theta)\mathbf{M}(p)]^{-1}\begin{pmatrix} Z \\ N \\ E \end{pmatrix} + \text{imag}[\mathbf{R}(\theta)\mathbf{M}(p)]^{-1}\mathrm{H}\begin{pmatrix} Z \\ N \\ E \end{pmatrix}. \tag{16}$$

The Hilbert transform is calculated using the fast Fourier transform and so the data has to be padded with zeroes to avoid aliasing artefacts. In this way, we remove the phase distortions associated with the free-surface interaction.

The estimate of the wave amplitude vector depends on four parameters: the surface compressional and shear velocities (α_0, β_0), the horizontal slowness (p), and the azimuth (θ) of the signal. The sensitivity of the wave vector recovery procedure has been investigated by application to synthetic seismograms with known incident wave vector (Jepsen, 1989). These trials have demonstrated that the control parameters need to be quite well known in order for the estimation of the wave vector to give accurate results without cross-contamination between different wavetypes.

In order for the amplitude estimates for the different wavetypes to be within 10 per cent of the correct values, we require the following restrictions on the control parameters: (a) the errors in the surface wave speeds must not exceed 10 per cent; (b) the horizontal slowness value should be within 0.01 sec/km of the actual slowness (unless p is close to α_0^{-1}, when much higher accuracy is needed); and (c) the azimuth should be within 10° of the actual azimuth. This level of accuracy for the slowness vector can be achieved with medium aperture arrays, e.g., for coherent arrivals at the 25 km aperture Warramunga array in northern Australia, horizontal slowness can be determined to 0.002 sec/km and azimuths to 2°. At smaller aperture arrays (e.g., NORESS and ARCESS), the accuracy is lower but the solutions for dominant arrivals will normally be within 0.01 sec/km in slowness and 5° in azimuth. Bad solutions will be a result of interfering signals and signal-generated noise, and as a result their wave vector estimates will be misleading. Estimates of the slowness vector from three-component data alone will normally be inadequate.

Surface velocities in the vicinity of an array can be well determined, but the optimum estimate may vary with frequency in the presence of deep weathering or a sedimentary overburden. For hard-rock sites and a limited frequency band, constant values can be used.

In addition, we require the three seismometers for the orthogonal components to be well calibrated. We are applying a complex operator (16) to the triplet of seismograms at one site, which will result in the combination of all three traces in the resultant wave vector. Miscalibration will result in distorted estimates of the amplitudes of the different wave types.

The propagation model we have considered is based on the assumption of an isotropic medium. If local anisotropy is significant, the free surface correction we

apply would not be appropriate, and we would therefore distort the estimates of the amplitudes of the different wave types and, in particular, expect to see signs of coupling between the *SV* and *SH* components.

Wave Field Decomposition from Array Records. For a three-component sensor located within a larger array of single-component seismometers the processing sequence for the application of the wave field decomposition procedure requires estimation of the slowness and azimuth from the full array followed by the construction of the wave vector.

In order to allow comparison with the waveform classification scheme in the previous section, we have applied the wavefield decomposition scheme to date in the 1 to 2 Hz frequency band, which has been processed at 0.5 intervals. This choice of frequency window also has the merit of reducing the complications due to high-frequency scattered energy from heterogeneity in the vicinity of the arrays. For each 0.5 sec window, slowness and azimuth estimates were determined via beam forming the vertical component data set with a scan over all reasonable values (i.e., slownesses from 0.0 to 0.3 sec/km, azimuth 0 to 360°). After the wave field decomposition procedure, the three components (*P*, *SV*, *SH*) of the wave vector are displayed as seismic traces (see Figs. 4 and 5). However, due to the time segmenting and the variations in the slowness/azimuth solutions, the traces can be disjointed and zeroes also can occur for particular segments of the coda.

The wave vector extraction has been carried out for a fixed set of surface-wave velocities: $\alpha_0 = 5.8$ km/sec, and $\beta_0 = 3.46$ km/sec, which represent reasonable values for hard-rock sites such as the Warramunga array in Australia and NORESS and ARCESS in Norway. Constant values have been assumed rather than site-specific velocities in order to assess the performance of the wave form decomposition procedure under realistic conditions.

ARCESS Event. We consider the regional event that we have previously analyzed by the wave classification scheme and apply the waveform decomposition scheme to the three-component records from the central site of the ARCESS array (A0). The seismograms are displayed in the upper part of Figure 4; beneath them are the estimates of the *P*, *SV*, and *SH* contributions extracted from the three-component records. The azimuth and slowness estimates derived from the full array are displayed in the lower part of the diagram. Comparison with Figure 3 shows the much greater stability of the array estimates than those derived from even the summed three-component data. The onset of the *S* phase is also reflected in the shift to higher slowness values at 29 sec. There are clear indications of interfering signals with *S*-wave slowness within the *P* coda, which may well be associated with signal-generated noise. The separation of the different wave types generally has been very successful. There is slight cross-talk between the *P* and *S* components in the *P*-wave coda (10 to 28 sec) probably arising from slight errors in the surface velocity estimates, but the *P*-wave nature of the principal arrivals is clearly indicated. The previous classification scheme also allowed the identification of the *P* waves but ran into considerable problems for the *S*-wave arrivals (29 to 41 sec), which are now clearly separated into *SV*- and *SH*-wave parts. The relative proportions of *SV* and *SH* with the free surface amplifications effects removed is approximately 1:1. There is also a certain amount of *P*-wave motion indicated in this portion of the seismogram; this may arise from wave type conversion in the near-surface weathered zone which was not taken into consideration in our simple propagation model. Also, we know that the *Lg* segment of the seismogram is composed of the interference of a number of reflected *S* phases, so that we may be

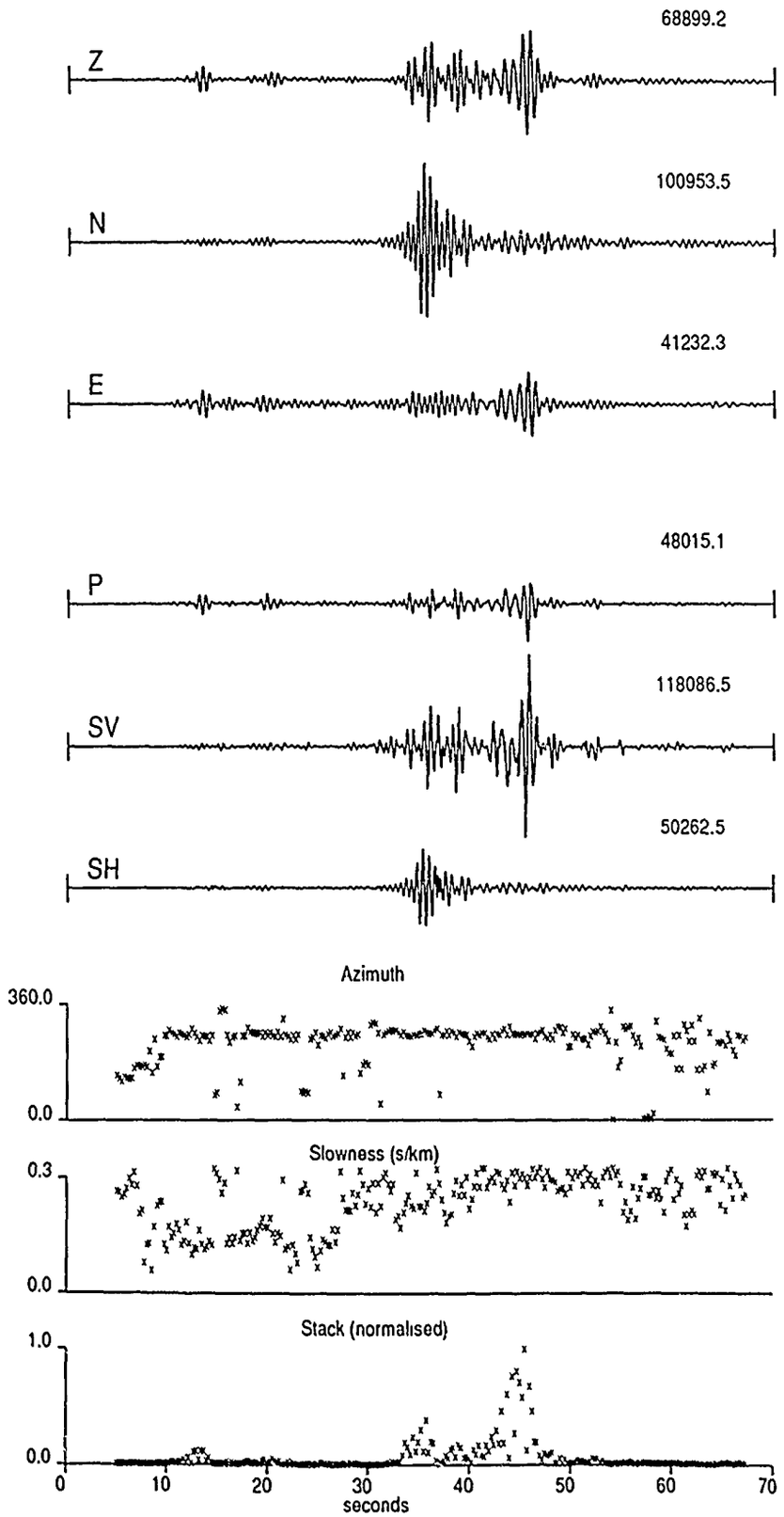

FIG. 4. Waveform decomposition scheme applied to the regional event at the ARCESS array: central site A0. The upper three traces show the original three-component seismograms and the lower traces the estimates of the *P*, *SV*, and *SH*-wave contributions extracted from the original data. The azimuth and slowness estimates are derived from using all the vertical component instruments in the ARCESS array.

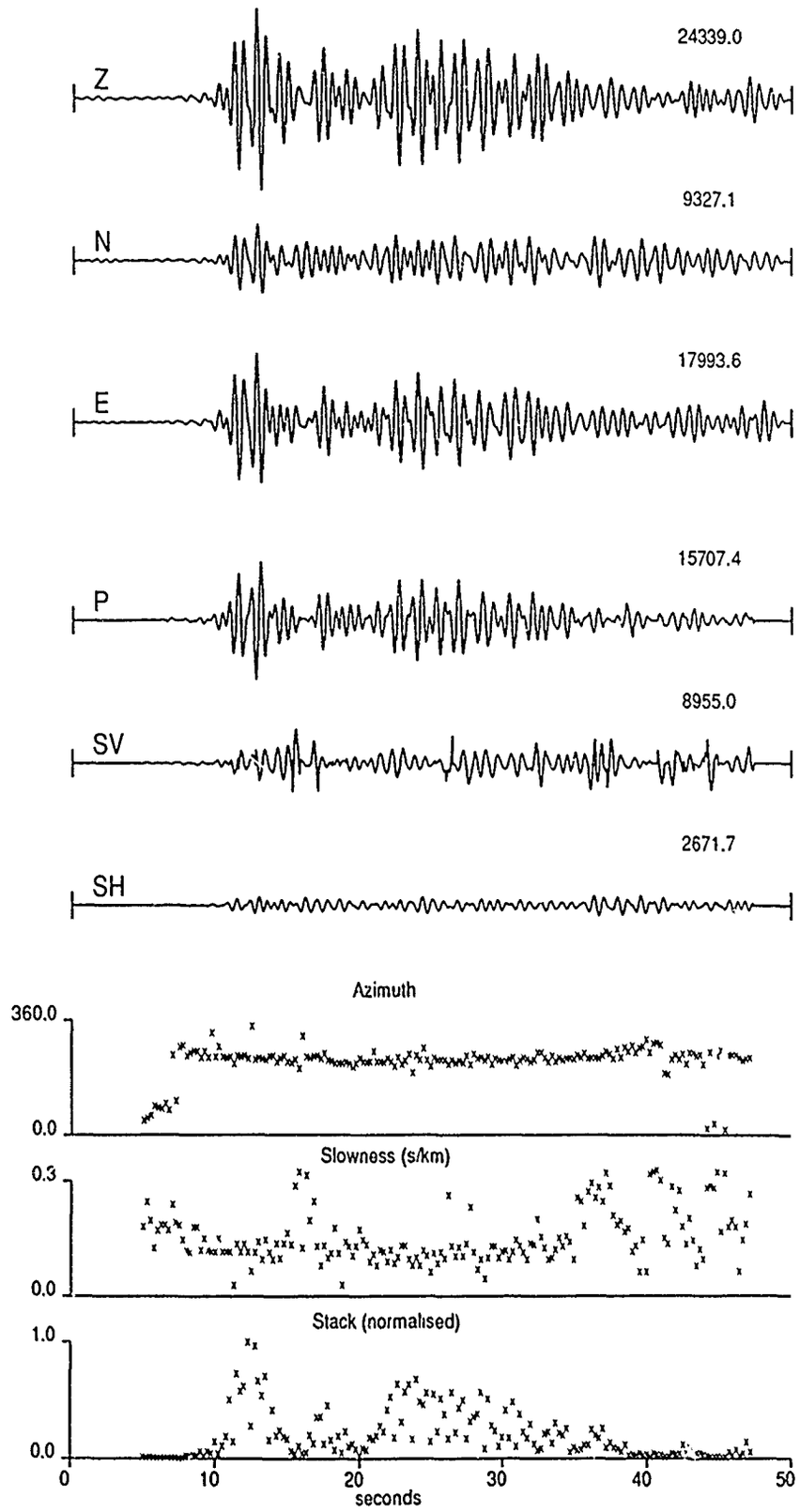

FIG. 5. Waveform decomposition scheme applied to an event in the White Sea (18 March 1987 21:14:58, 40.86°E 65.97°N) recorded at the NORESS array in southern Norway at an azimuth of 235° and range 1562 km. For the central site A0, the upper three traces show the original three-component seismograms and the lower traces the estimates of the P, SV, and SH-wave contributions extracted from the original data. The azimuth and slowness estimates are derived from using all the vertical component instruments in the NORESS array.

seeing the limitations of our assumption that we can employ a single slowness value in each time window.

The *Rg* phase between 41 and 49 sec was successfully identified by the wave classification scheme (Fig. 3) and in Figure 4 can be recognized via large amplitude linked *P* and *SV* arrivals, whose pulses are in phase with an amplitude ratio of approximately 1:3.

NORESS Event. As a further illustration of the wave form decomposition procedure, we consider a much more distant event from the White Sea recorded at the central site (A0) of the NORESS array at distance of 1562 km with an azimuth of 235°. We now examine the first 50 sec of the seismograms, which largely consists of *P*-wave arrivals. The seismograms for the event and the wavetype separation are shown in Figure 5, in the same format as was used for Figure 4.

The azimuth and slowness estimates from the array are relatively stable for the first 35 sec, although there is a clear excursion to *S*-wave slowness at about 16 sec. The later part of the record shows considerable slowness variability but also rather low amplitudes.

The relative amplitudes of the various wavetypes show, as would be expected, dominantly *P*-wave motion with an *SV* component that is smaller but still significant. The apparent *SH* component is quite small, indicating that propagation along the path from the receiver has remained largely in the vertical plane. The disjointed nature of the *SV*-wave trace arises from the fact that significantly different slownesses can be applied to contiguous time segments when the array estimate of the slowness is changing quickly. There is an indication of a *P-S* conversion at about 36 sec, with any associated azimuth anomaly. For times later than 38 sec, the derived amplitudes for the various wavetypes are not likely to be very reliable because of the instability of the slowness estimates.

Similar results have been found for the onsets of regional events at the Warramunga array in northern Australia, although the level of the *S* signal was a little higher. This may arise in part because the matching of the instrument response between the vertical and horizontal components is not as close as for the two more recent Norwegian arrays.

Discussion

For regional wave trains we have shown that it is possible to use three-component data alone to classify the wavefield into major wave groups that are sufficient to identify *P* waves and fundamental mode Rayleigh waves (*Rg*). Further classification by wavetype is frequently possible but is of limited effectiveness when more than one wavetype is present in the wavefield.

The wavefield decomposition scheme, on the other hand, is able to separate the different wavetypes and provide a useful description of the character of the seismic wavefield and its evolution in time. Even though we have used a simple correction for just the free-surface, the relative amplitudes of the different wavetypes allow a clear assessment of the character of seismic phases and avoid the ambiguities inherent in conventional three-component analyses. The frequency-independent correction for the effect of the free surface alone can be regarded as the first stage in a hierarchy of frequency-dependent corrections that incorporate greater detail into the propagation model to match the local geological characteristics in the vicinity of the array.

Since we are now able to compare the wave forms associated with the different wavetypes with surface phase and amplitude effects removed, we have a new domain in which to look at source character exploiting the vector wavefield.

Transformation of regional wave trains into the wave vector domain via wave form decomposition is therefore likely to be a useful adjunct to present techniques for discriminating between seismic sources of different types.

REFERENCES

Aki, K. and P. G. Richards, (1980). *Quantitative Seismology: Theory and Methods*, vols. 1 and 2, W. H. Freeman, San Francisco.

Boore, D. M. and M. N. Toksöz, (1969). Rayleigh wave particle motion and crustal structure, *Bull. Seism. Soc. Am.* **59**, 331–346.

Christoffersson, A., E. S. Husebye, and S. F. Ingate, (1988). Wave field decomposition using ML-probabilities in modelling single-site 3-component records, *Geophys. J.* **93**, 197–213.

Cleary, J. R., C. Wright, and K. J. Muirhead (1968). The effects of local structure upon measurements of the travel time gradient at the Warramunga seismic array, *Geophys. J. R. Astr. Soc.* **16**, 21–29.

Greenhalgh, S. A., I. M. Mason, E. Lucas, D. Pant, and R. T. Eames (1990). Controlled direction reception filtering of *P* and *S* waves in Tau-p space, *Geophys. J. Int.* **100**, 221–234.

Jepsen, D. C. (1989). Multi component seismic array analysis, *Ph.D. Thesis, Australian National University*

Jurkevics, A. (1988). Polarization analysis of three-component array data, *Bull. Seism. Soc. Am.* **78**, 1725–1743.

Kennett, B. L. N. (1983). *Seismic Wave Propagation in Stratified Media*, Cambridge University Press, London.

King, D. W., R. F. Mereu, and K. J. Muirhead (1973). The measurement of apparent velocity and azimuth using adaptive processing techniques on data from the Warramunga seismic array, *Geophys. J. R. Astr. Soc.* **35**, 137–167.

Montalbetti, J. F. and E. R. Kanasewich (1970). Enhancement of teleseismic body phases with a polarization filter, *Geophys. J. R. Astr. Soc.* **21**, 119–129.

Mykkeltveit, S., K. Astebøl, D. J. Doornbos, and E. S. Husebye (1983). Seismic array configuration optimization, *Bull. Seism. Soc. Am.* **73**, 173–186.

Mykkeltveit, S. and H. Bungum (1984). Processing of regional seismic events using data from small-aperture arrays, *Bull. Seism. Soc. Am.* **74**, 2313–2333.

Nagano, K., H. Niitsuma, and N. Chubachi (1989). Automatic algorithm for triaxial hodogram source location in downhole acoustic emission measurement, *Geophysics* **54**, 508–513.

Plešinger, A., M. Hellweg, and D. Seidl (1986). Interactive high-resolution polarization analysis of broad-band seismograms, *J. Geophys.* **59**, 129–139.

Ringdal, F. and E. S. Husebye (1982). Application of arrays in the detection, location, and identification of seismic events, *Bull. Seism. Soc. Am.* **72**, S201–S224.

Ruud, B. O., E. S. Husebye, S. F. Ingate, and A. Christoffersson (1988). Event location at any distance using seismic data from a single, three-component station, *Bull. Seism. Soc. Am.* **78**, 308–325.

Shimshoni, M. and S. W. Smith (1964). Seismic signal enhancement with three-component detectors, *Geophysics* **29**, 664–671.

Vidale, J. E. (1986). Complex polarization analysis of particle motion, *Bull. Seism. Soc. Am.* **76**, 1393–1405.

White, J. E. (1964). Motion product seismograms, *Geophysics* **29**, 288–298.

RESEARCH SCHOOL OF EARTH SCIENCES
AUSTRALIAN NATIONAL UNIVERSITY
GPO BOX 4
CANBERRA ACT 2601, AUSTRALIA

Manuscript received 20 December 1989

Bulletin of the Seismological Society of America, Vol. 80, No. 6, pp. 2053-2071, December 1990

AN ON-LINE ANALYSIS SYSTEM FOR THREE-COMPONENT SEISMIC DATA: METHOD AND PRELIMINARY RESULTS

By O. K. Kedrov and V. M. Ovtchinnikov

Abstract

This paper presents the basic method and algorithm of a system for automatic on-line analysis of seismic data at three-component stations and gives preliminary experimental results. Data processing consists of four steps: (1) preliminary detection and estimation of the signal arrival time by using the energy-based γ-detector; (2) refinement of signal parameters (arrival time, amplitude, period, and coda duration); (3) estimation of the azimuth and incident angle of the seismic ray by using polarization analysis; and (4) approximate estimation of event parameters (epicenter coordinate, origin time, and magnitude) from teleseismic *P* waves for a constrained focal depth.

The software package, which is called "SEISMOSTANSIA," has been tested in an on-line environment at an experimental seismic station in Eastern Kazakhstan. Testing results show that the system can handle an input flow of up to 100 signals in a 24-hr period. Comparison of the results of automatic detection with data of the station bulletin obtained by visual analysis of analog seismograms shows that: (1) with the present threshold setting, the automatic system detects practically all teleseismic signals seen by the analyst together with typically 10 to 15 signals per day not confirmed by visual analysis; (2) in 70 per cent of the cases, the residual between the arrival time obtained from the automatic and subjective procedures is 0.5 sec or less for SNR > 10 and 1 sec or less for SNR < 10; (3) in 70 per cent of the cases, the residual between the signal period obtained from the automatic and subjective procedures is 0.2 sec or less. Analysis of data indicates that an effective means of identifying false alarms with low SNR can be the level of polarization rectilinearity of *P* and *S* waves. By analyzing azimuth estimates for a suite of explosions at the Nevada Test Site, it is shown that a systematic bias forms the main contribution to the residual relative to true azimuth. In the general case, the azimuth residuals are due to the features of the medium both at the epicenter and at the station, and consequently depend on both azimuth and epicentral distance. An analysis of azimuth residuals points to a periodic dependence on azimuth. The value of the period is about 120°. Additional information (azimuth and angle of incidence) reported from three-component stations to data centers is shown to improve significantly the reliability of phase association in the processing of data from a global seismic network.

Introduction

The ongoing development of the global seismic station network, with increased emphasis on standardized equipment and digital data recording, creates a need to improve significantly the quality and operational efficiency in preparing seismic bulletins at national and international data centers. In turn, such a bulletin can be an important basis to improve the effectiveness of geophysical investigations comprising both fundamental and applied tasks; in particular, the verification of a nuclear test ban.

This paper presents a method and program package, called "SEISMOSTANSIA," for automatic detection and parameter extraction of seismic events recorded at a single three-component station. Preliminary experimental results are also given.

The need for such a program stems from the tasks of both seismograph networks for general geophysical purposes and of an international system for seismic verification of the nonconduct of nuclear tests (CCD/558, 1978; CD/43, 1979; CD/448, 1984; CD/720, 1987).

The basic principles of the proposed method were studied earlier in research done at the Institute of Earth Physics of the USSR Academy of Sciences (Kedrov and Bashilov, 1975; Kondorskaya and Kedrov, 1982). During the course of further investigations, the method and algorithm in question have been finalized and tested on real seismic signals. The programming of the algorithm was done with participation of Moscow State University personnel and is documented in Kedrov *et al.* (1939a, b).

There are a number of published studies (Mykkeltveit and Bungum, 1984; Plesinger *et al.*, 1986; Magotra *et al.*, 1987; Jurkevics, 1988; Ruud *et al.*, 1988) that examine the tasks of detection and initial processing of seismic signals at a single station or array.

What distinguishes the proposed algorithm is the complete automation of the entire processing of data in real time and a more thorough analysis of the signals from seismic events for the purpose of approximate calculation of their focal parameters. We expand the data set used by Kedrov *et al.* (1989a, b) and study the influence of azimuth and epicentral distance on phase association and the estimation of focal parameters.

Phase Association by a Global Network

In network processing, signals and focal event parameters obtained at individual stations are used for the subsequent data center processing to refine the coordinates of a seismic event. In this section we discuss the importance of obtaining azimuth and epicentral distance estimates at each station in the phase association process.

In the input data set, there will often appear interfering detections that cannot be associated with the event under consideration. If the number of such detections exceeds some threshold, the correct data interpretation in terms of focal parameters will become impossible. In a paper by Gesan (1974), a theorem has been proved that determines conditions under which such interfering measurements will not influence the calculation of focal parameters. The expression following from the theorem is

$$n > m + 2l \tag{1}$$

in which

n = the number of measurements in the data sample
m = the number of unknown parameters
l = the number of interfering measurements

Define $n_0 = n - l$ (i.e., the number of "informative measurements"). Then, expression (1) can be rewritten as

$$n_0 > m + l. \tag{2}$$

Expression (2) allows us to formulate the requirement on the unassociated signal flow from the station to the data center.

Let N be the number of stations in the network. Suppose that the unassociated signals occur at an equal rate per day for each station: $\lambda_i = \lambda$. Then, the total number of such signals received by the data center becomes:

$$N_1 = N\lambda\Delta t, \tag{3}$$

where Δt is the time interval under consideration. Using (2), we obtain for the λ value

$$\lambda < (n_0 - m)/(N\Delta t). \tag{4}$$

From (4), we see that λ has an upper limit for a fixed m, n, Δt, and N. In particular, for $n_0 = m$, we obtain $\lambda = 0$. This is the natural result that shows the number of informative measurements must be at least equal to the number of unknown parameters. In the case of equality, no interfering measurements must be present.

From (4), it follows that the greater the number of stations in the network, the stricter the requirement on the signal flow will be. To determine the value n_0 for which the influence of interfering detections will be negligible, we used the bulletin of the Experimental International Data Center in Washington, D.C. (Final Event Bulletin, 1985).

From the global network used in generating this bulletin, we find the following typical values of the parameters we have been considering: $N = 75$, $m = 4$, $\lambda = 3 - 4$ (per day), and $\Delta t = 30$ min. Based on these parameter values, we find $n_0 > 10$. This value agrees with the practical experience of robust estimation of event coordinates in the data centers and also with the results obtained from experiments using synthetic data (Ohlsson, 1982).

With additional information from network stations about the azimuth and angle of incidence, we can obtain an approximate initial estimate of the event coordinates and thereby decrease significantly the interval Δt (by a factor of 5 to 10), during which signals can possibly be associated with a given event. As a result, a reliable association of detections at a data center can be obtained for smaller values of n_0. Alternatively, for a fixed n_0, the requirement with regard to the rate of unassociated signals from the stations can be weakened. This forms one of the main motivations for extracting such additional information at three-component stations, as described in the following sections.

ALGORITHM

The choice of the algorithm has been governed by the requirements to achieve continuous on-line processing of seismic data for a single three-component seismic station and to adapt this process to the limited resources of the available computer equipment (SM-4 with 128 K memory). Analysis of one year's experimental data at a single three-component station in Kazakhstan has shown that the rate of detected signals can be satisfactorily described by Poisson's distribution:

$$\mathrm{P}(k) = \frac{\lambda t e^{-\lambda t}}{k!} \tag{5}$$

where $\mathrm{P}(k)$ is the probability that, during an interval of time, t, after a given signal, k new signals will be recorded, provided that the frequency of detection of signals

(λ) at the station per unit of time is known. Calculations of this kind show that, if 50 signals are recorded at the station per day, the probability that one new signal will be detected within 2 min following a given signal is $P(k = 1) = 0.06$.

Thus, it is clear that, in most cases, a recorded signal will be preceded by a noise section of more than 2 to 3 min length. This is important for the organization of on-line processing.

The general processing algorithm consists of two stages:

- *detection processing* of the signal and transfer to a special buffer (SB) of a segment containing 30 sec of noise and 60 sec of signal for the three short-period components
- *event processing* (i.e., processing all detected signals accumulated in the SB) is conducted during time intervals free of signal arrivals.

The search for a new signal usually begins 6 sec after the previous signal detection, but this time limit may be set differently if desired.

Figure 1 shows a block diagram of the algorithm for short-period, three-component data processing.

Detection Processing:

The first processing stage—detection processing—consists of:

- entry of the initial three-component data in short segments into the main memory of the computer
- frequency filtering of the data
- signal detection and approximate arrival time determination
- transfer of data segments for each detected signal (30 sec of noise and 60 sec of signal) for the three components (Z, N–S, E–W) into the special buffer.

Frequency filtering of the data is achieved using a Butterworth bandpass filter (0.7 and 2.7 Hz as 3 dB points and a slope of 30 dB/octave). This filter has been found suitable for teleseismic and regional signal detection.

The overall dynamic range of the SP recording system is divided into two subranges. The data processing algorithm provides for automatic switching from one range to the other, depending on the intensity of the recorded signal or the level of the signal-to-noise ratio.

For the purpose of continuous signal detection, functions of the type

$$\gamma = \sigma_s^2/\sigma_l^2 \tag{6}$$

are calculated for each individual component (Z, N–S, E–W). Here, σ_s^2 and σ_l^2 are the estimated variances of the seismic vibrations in short- (1 sec) and long- (20 sec) time windows.

A detection is declared when $\gamma > \gamma_0$ on any one of the three components during a given time interval, where γ_0 is a fixed threshold. At this initial processing stage, the signal arrival time is defined as the point in time when γ crosses the threshold. If a signal is detected on any one of the three components, the raw signal and noise data are transferred into the SB in a standard format for the three components.

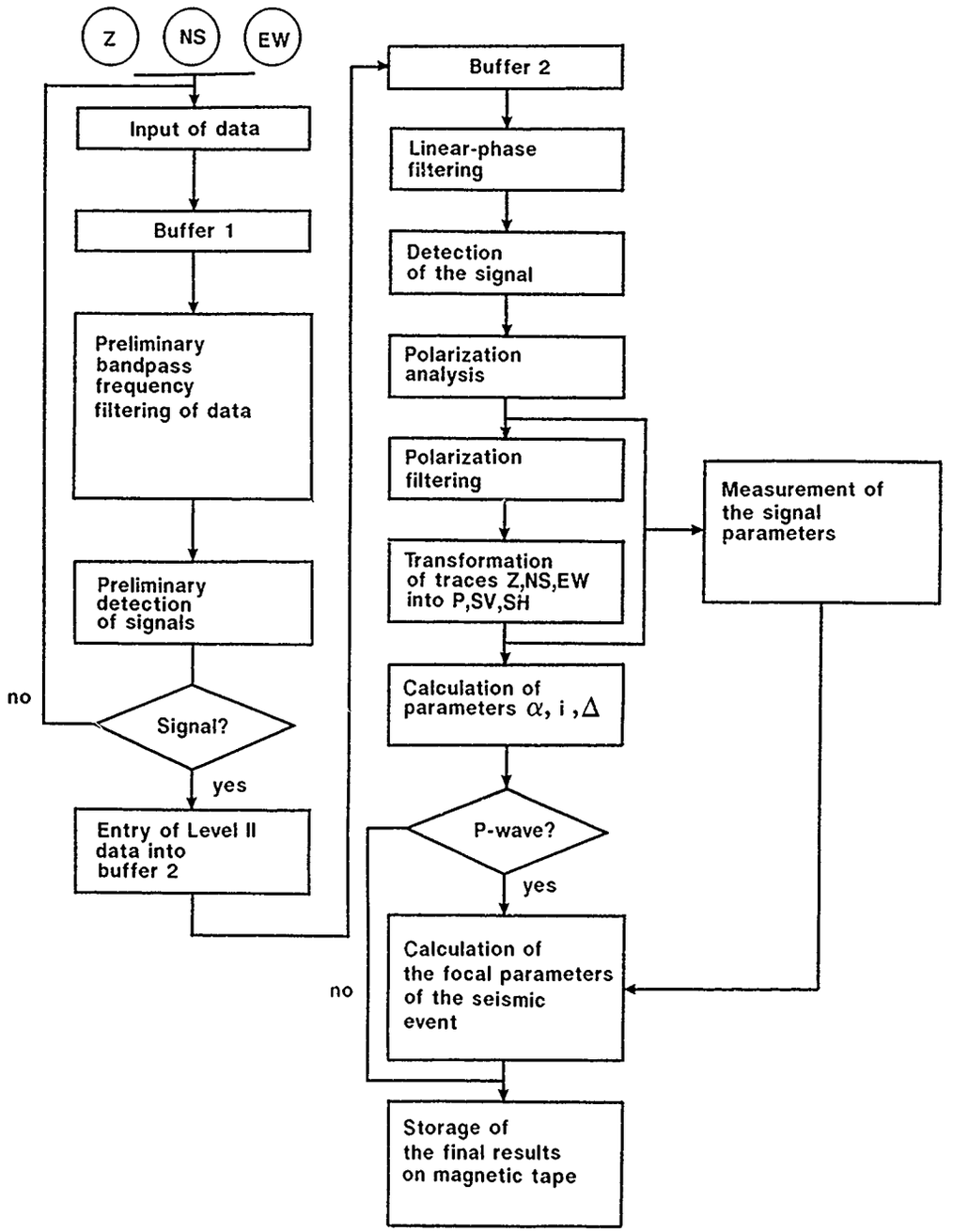

FIG. 1. Flowchart of the algorithm for the short-period, three-component data processing.

Event Processing:

The second processing stage—event processing—consists of:

- linear-phase filtering of the Z, N–S, and E–W components for the waveform segment contained in the special buffer
- iterated detection of the signal and more precise determination of its arrival time
- polarization analysis of the signal
- determination of the phase type of the signal

- polarization filtering of the signal
- calculation of the focal parameters of the seismic event
- measurement of the signal parameters
- printout of the results.

At this second stage of processing, a linear-phase bandpass frequency filter is applied to avoid introduction of phase distortions into the data before polarization analysis. This filter has the same bandpass and cutoff characteristics as the Butterworth filter used earlier. Experiments have established that linear-phase filtering is needed only for weak signals, whereas for strong signals no filtering is required.

In the existing version of the program, however, signal processing is consistently conducted both with and without filtering to determine more precisely under which conditions filtering is necessary. Detection of the signal is repeated with the same algorithm that was used in the first stage of processing; the only difference is that the onset time of the signal is determined more precisely. Thus, at this second stage, the arrival time of the signal is determined as the time of intersection of the regression line (calculated from the current γ_i values in the vicinity of the initially determined arrival time) and the zero line of the function γ.

Polarization analysis of the signal is used for the purpose of defining the type of wave and determining the azimuth to epicenter and angle of incidence of the seismic ray at the point where the recording is taking place. The method used is that developed by Flinn (1965) in which a covariance matrix is used to obtain a quantitative measurement of the linearity and direction of ground movement with respect to the recording point. The quadratic form (ellipsoid) given by this matrix is reduced to its principal axes. The longest axis of the ellipsoid shows the orientation in three-dimensional space of the complete vector of particle displacement and is determined by the angles α (azimuth) and i (apparent angle of ray incidence), while the relations of the intermediate and minor semi-axes to the major semi-axis (b/a and c/a) give the degree of elongation of the ellipsoid, i.e., the level of polarization rectilinearity in the wave.

The polarization analysis is performed close to the onset of the signal in an interval containing some of the first oscillations in the wave using covariance calculation in a window close to the typical period of a P wave. (In this study, a fixed window length of 1 sec has been used.) The values of angles α and i are determined at the time the maximum polarization rectilinearity is reached.

It has been found experimentally that P and S waves have a high level of polarization rectilinearity and, hence, this parameter can serve to distinguish signals from false alarms. In addition, the value of angle i serves to determine the wave type, denoted as either P, PKP, S, or X (X is used when the result is ambiguous). The most reliable phase identification is that of P and S waves in the teleseismic range ($20° \leq \Delta \leq 100°$). Less reliable is the separation of PKP waves from P waves, and the greatest difficulties are encountered in the identification of regional phases.

Provision is also made in the algorithm for polarization filtering of the vibrations of each detected signal. This procedure consists of converting the initial system of Z, N–S, and E–W coordinates into complete vectors of displacement (P, SV, and SH) using the angles α and i obtained in the polarization analysis of the signal.

If the detected signal is identified as a P or a PKP phase, the maximum trace calculated during this procedure is a longitudinal wave. In cases where the arrival is identified as an S phase, the maximum trace cannot be identified as an SV or

SH wave in the automatic on-line process without additional data concerning the azimuth to the epicenter.

As in Flinn (1965), the algorithm also provides for the amplitude weighting of *P*, *SV*, and *SH* traces by the operator $G = G_1 * G_2 (0 < G < 1)$ for the purpose of suppressing vibrations with low level polarization rectilinearity (using $G_1 = 1 - b/a$) and vibrations coming from directions other than the direction of the source (using $G_2 = d * e$, where d is direction toward the source and e is the direction of the longest axis of the ellipsoid at the current point in time). In the existing version, this procedure is not used in automatic on-line data processing because the nonlinear character of the calculations may distort the dynamic parameters of the signals (amplitude, period, etc.). The procedure may, however, prove useful in interactive analysis of weak signals.

If the detected signal is identified as a teleseismic *P* wave (we require here that $i < 40°$ and $b/a < 0.20$), source parameters (epicentral coordinates, origin time, and magnitude) are determined approximately. These parameters are calculated using the azimuth and angle of incidence values obtained for the *P* wave. Calibration functions for calculating epicentral distance and magnitude are then applied using a fixed focal depth (e.g., $H = 33$ km).

Regardless of the type of wave, the parameters of the signal are measured according to a standard scheme. The standard parameters so calculated and printed are:

- phase type
- signal arrival time (in hour, min, sec)
- indicators describing channel gain (low/high) and whether frequency filtering has been applied
- signal-to-noise ratio
- azimuth and angle of ray incidence (in degrees)
- ratios of the polarization ellipsoid's half-axes b/a and c/a
- parameters $t_{\max}$, $\tau_{0.5}$, and $\tau_{0.3}$ (sec), giving, respectively, the time from signal arrival to the maximum trace amplitude $A_{\max}$ and from $A_{\max}$ to $\frac{1}{2} * A_{\max}$ and $\frac{1}{3} * A_{\max}$
- epicentral distance (in degrees)
- epicentral coordinates (in degrees)
- magnitude (m_b)
- origin time—UTC (in hour, min, sec).

For each detected signal, we also measure the following standard set of parameters for the Z, N–S, and E–W components, and for the maximum trace rotated in the direction of the source:

- maximum amplitude of the noise (in nm) and corresponding period over an interval of 30 sec before signal arrival
- amplitude, period, and direction of motion of the first arrival
- maximum amplitude, period, and arrival time (in sec relative to first onset) in each of the following four windows: 0 to 6 sec, 6 to 12 sec, 12 to 18 sec, and 18 to 60 sec.

The signal-to-noise ratio is determined by the formula:

$$\mathrm{SNR} = A_{\max}/\sigma_n. \tag{7}$$

Here, A_{max} is the maximum zero-to-peak amplitude (absolute value) measured during the 0 to 18 sec signal interval on the Z-component (P waves) or on one of the horizontal components (S waves). The quantity σ_n is the root-mean-square value of the noise amplitudes during an interval of 30 sec prior to the signal arrival.

Analysis of Experimental Data

The algorithm was tested using data collected in 1986 and 1989 at an experimental station installed by the Institute of Earth Physics, USSR Academy of Sciences, in Eastern Kazakhstan near the town of Kokchetav. The altitude of the area around the station is about 300 m and the basement rock is granite. The station can be classified as "quiet" in terms of the level of short-period microseismic noise ($A < 5$ nm) because it is situated on the continental platform and is far from artificial noise sources.

Recordings were carried out by short-period, three-component instruments with a sensitivity of $1 * 10^5$ counts/micron and a dynamic range of 100 dB. The data sampling rate was 33 Hz. The instrument response is given in Table 1.

In earlier papers (Kedrov *et al.*, 1989a, b), some results of the analysis of effectiveness of the "SEISMOSTANSIA" software were given. In this paper, we include data obtained in 1989 in addition to the data from 1986 and expand upon these studies. The observed signal parameters as well as event parameters were used to determine differences between automatically measured parameters and those of the station bulletin obtained from visual analysis of the seismograms.

The experiments show that the entire process of automatic data analysis, including detection and subsequent analysis of signals, can be carried out on-line for detection rates of up to 100 signals per 24-hr period. The interval between the time a signal is detected and the completion of event processing is a few minutes and depends on the number of on-line detections at the time in question.

The experiments demonstrated an excellent performance for detection of first arrivals, except that some P phases from local events were missed, and there were also some problems in detecting P phases that occurred less than 20 sec after a previous detection with a comparable amplitude. Such cases add up to about 5 per cent of the total output flow of automatically detected signals. A substantial proportion (40 per cent) of detections were found to be due to signals of local origin. These were characterized by a specific record form and frequency content, low intensity, and a low level of polarization rectilinearity for the maximum phase of the vibrations.

TABLE 1

Seismometer Amplitude Response

Frequency (Hz)	Response (counts/μm)
0.3	4308
0.5	31560
0.67	77460
0.8	97260
1.0	101870
1.5	100930
2.0	101130
3.0	101900
5.0	98060
8.0	75480
10.0	48045

Figure 2 shows the distribution of the SNR for signals that could not be associated with an entry in the station bulletin. It is seen that 80 per cent of these unassociated signals have SNR < 5. Thus, as expected, the main difference between the automatic and visual analysis is seen for weak signals. It would not be correct to interpret all of these unassociated signals as false alarms, since some of them may well be real signals that were missed in the visual analysis. The number of such unassociated detections (10 to 15 per day) still serves to give an upper bound on the false alarm rate.

It was found experimentally that the first arrivals of both earthquakes and explosions generally have a relatively high level of polarization rectilinearity. Figure 3 shows the distribution of the parameter b/a for associated and unassociated

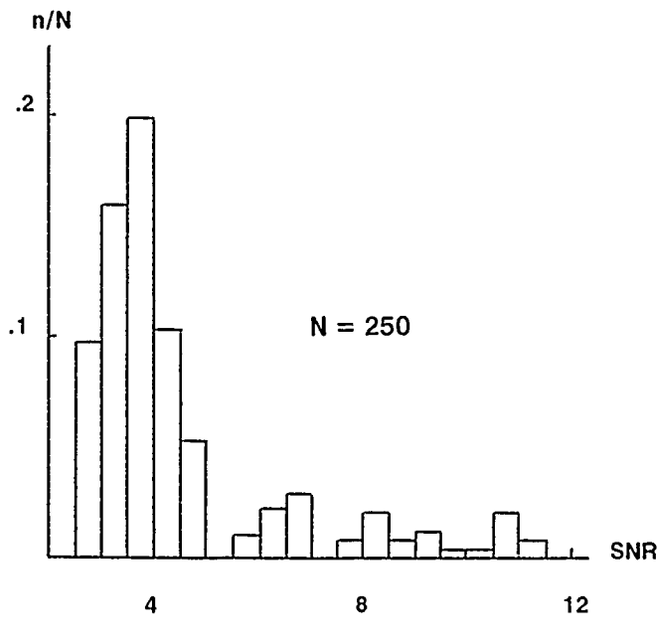

FIG. 2. Distribution of the signal-to-noise ratio for signals unassociated with data from the station bulletin.

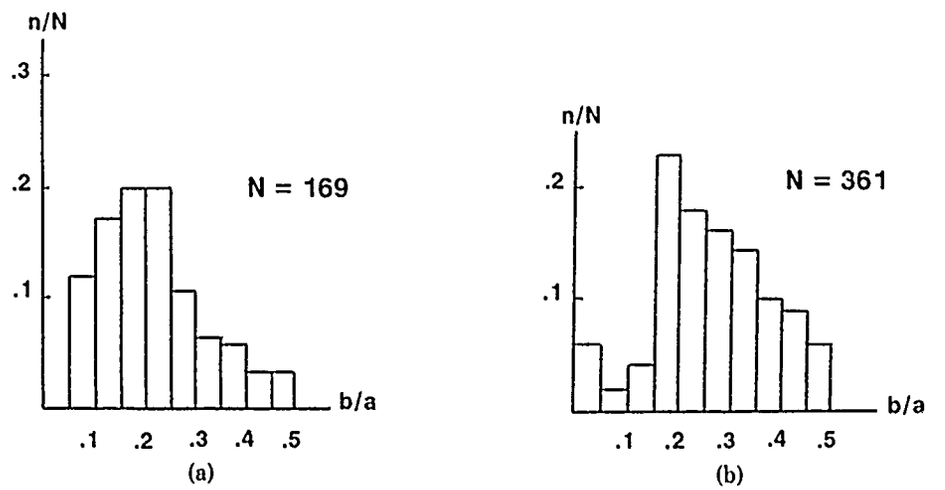

FIG. 3. Distribution of the parameter b/a for signals associated with data from the station bulletin (a) and unassociated signals (b).

signals. More than 50 per cent of the unassociated signals have $b/a > 0.25$. It will be noted that the parameter b/a is slightly dependent on SNR. The b/a versus the signal-to-noise level can be represented by the expression (Kedrov *et al.*, 1989a, b):

$$\log(b/a) = -0.3 \log(\text{SNR}) - 0.7. \tag{8}$$

More detailed information about the characteristics of detected signals can be obtained from Tables 2 to 4. Table 2 shows the distribution of maximum amplitude of signals associated and not associated with events reported in the *PDE Bulletin*. Table 3 shows the distribution of the duration of P waves ($\tau_{0.5}$), and Table 4 shows the distribution of the emergence time of P waves, t_{max} (i.e., the time from first onset to the maximum deflection).

TABLE 2

DISTRIBUTION OF MAXIMUM AMPLITUDES (A_{max}) OF P WAVES (%)

A_{max} (nm)	P Waves Associated with PDE ($b/a < 0.20$) ($N = 41$)	P Waves Unassociated with PDE ($N = 93$)	
		$b/a < 0.20$	$b/a \geq 0.20$
<5	10.3	37.5	73.4
5–10	31.0	40.0	16.6
10–15	13.8	7.5	10.0
15–20	10.4	5.0	—
>20	34.5	10.0	—

TABLE 3

DISTRIBUTION OF THE DURATION, $\tau_{0.5}$, OF P WAVES (%)

$\tau_{0.5}$ (sec)	P Waves Associated with PDE ($b/a < 0.20$) ($N = 41$)	P Waves Unassociated with PDE ($N = 93$)	
		$b/a < 0.20$	$b/a \geq 0.20$
0–10	15.2	16.2	3.9
10–20	15.2	13.5	5.9
20–30	15.2	16.2	5.9
30–40	15.2	13.5	5.9
40–50	18.2	8.1	13.7
50–60	12.1	24.3	37.2
>60	9.1	8.1	27.4

TABLE 4

DISTRIBUTION OF THE EMERGENCE TIME OF P WAVES, t_{max} (%)

t_{max} (sec)	P Waves Associated with PDE ($b/a < 0.20$) ($N = 41$)	P Waves Unassociated with PDE ($N = 93$)	
		$b/a < 0.20$	$b/a \geq 0.20$
0–5	73.4	74.4	42.5
5–10	13.4	4.7	6.4
10–15	3.3	7.0	8.5
15–20	3.3	—	4.3
20–25	—	4.6	2.1
25–30	3.3	7.0	4.3
30–60	3.3	2.3	31.9

As seen from the data in Tables 2 to 4, signals associated with PDE-reported events have a high level of polarization rectilinearity ($b/a < 0.2$), while unassociated signals can be divided into two subsets, with $b/a < 0.2$ and $b/a \geq 0.2$. The distribution of the parameters A_{max}, $\tau_{0.5}$, and t_{max} in the first subset is similar to those signals associated with PDE entries, whereas the distribution of parameters for the second subset is different.

In total, unassociated signals with $b/a \geq 0.2$ have the following characteristics:

$A_{max} < 10$ nm: 90 per cent of the cases
$0.2 \leq b/a < 0.5$: 100 per cent of the cases
$\tau_{0.5} > 30$ sec: 85 per cent of the cases
$t_{max} > 15$ sec: 60 per cent of the cases.

On the basis of these data, it can be inferred that unassociated signals with $b/a < 0.2$ are likely due to small seismic events that were not detected by the seismic network used in preparing the *PDE Bulletin*, whereas signals with $b/a \geq 0.2$ are mainly due to local events or caused by noise sources.

It thus appears that the proposed set of simple signal parameters (b/a, A_{max}, $\tau_{0.5}$, t_{max}) can be used for discriminating false alarms and local signals from regional and teleseismic ones. This requires, of course, that specific acceptance intervals for these parameters are determined.

The successive stages of processing of a P wave from an earthquake in the Kamchatka region are shown in Figure 4. From top to bottom, the figure shows:

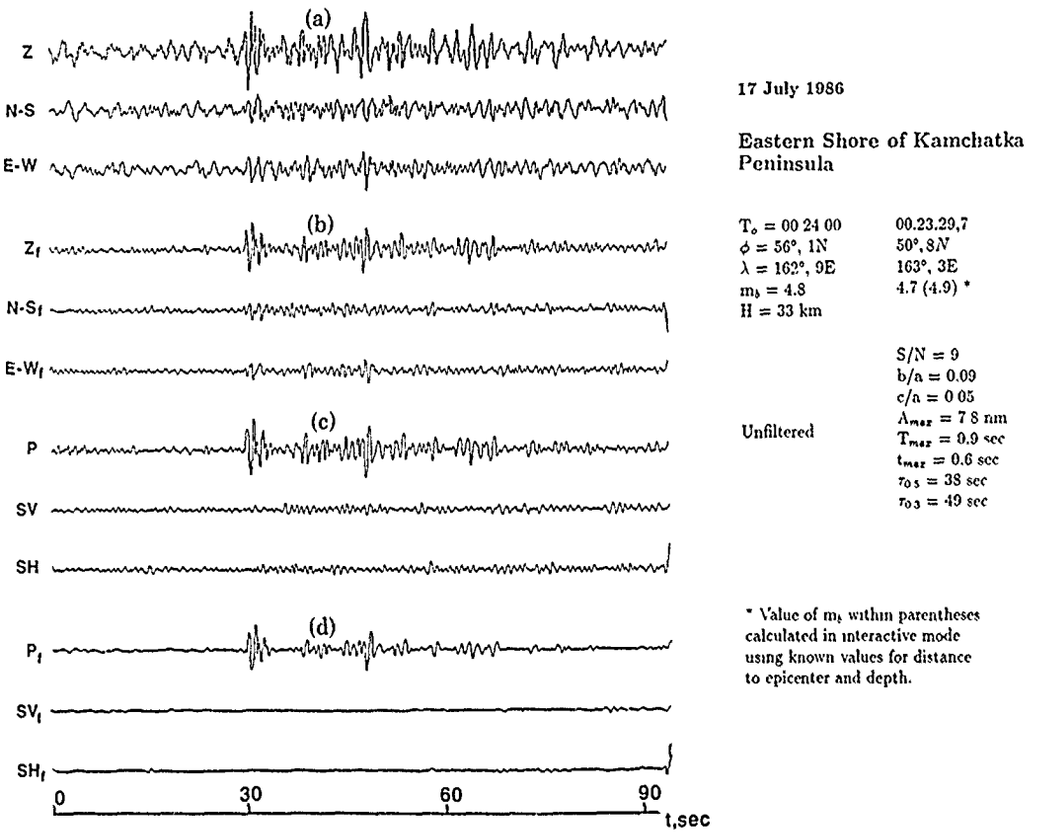

FIG. 4. Results of on-line processing of an earthquake in the Kamchatka region using the "SEISMOSTANSIA" software: (a) raw recordings of the P wave for the Z, N–S, and E–W components in the short-period channel; (b) P wave recordings after linear-phase frequency filtration; (c) recordings of the P, SV, and SH waves after rotation of the coordinate system in the direction of the source; (d) recordings of the P, SV, and SH waves after multiplication of the vibrations by weighting functions of linearity (G_1) and direction (G_2), as described in the text.

(a) the raw recording of the P wave for Z, N–S, and E–W components; (b) the recordings of the P wave for the three components after linear-phase frequency filtration; (c) the recordings of complete P, SV, and SH vectors after rotation of the coordinate system in the direction of the source; and (d) the P, SV, and SH records after multiplication of the amplitudes of the vibrations by the linearity operator (G_1) and the direction operator (G_2).

The right-hand side of Figure 4 shows focal parameter data for the earthquake in question taken from the *Bulletin of the International Seismological Centre* (ISC) and the results from calculation of a number of principal signal and focal parameters made on-line using "SEISMOSTANSIA."

Table 5 shows the complete list, in the final output format, of the information derived for the same signal by the automatic system. Examples of processing of P waves of earthquakes from other regions of the earth are shown in Figures 5 and 6.

The arrival time residual, $\delta t_i = t_{ai} - t_{bi}$ (here and in the following the index "a" refers to the automatic procedure and "b" to visual analysis), depends on the signal-to-noise ratios and the waveform shape of the signal. For pulse-form signals, the estimation of the arrival time is more precise than for emergent signals. Figure 7a shows the distribution of arrival time residuals for events with SNR > 10. In 70 per cent of the cases, the residual does not exceed ± 0.5 sec. Figure 7b shows corresponding results for events of SNR ≤ 10. In the latter case, the residuals are less than ± 1.0 sec in 70 per cent of the cases.

Figure 8 shows the distribution of the residuals of the signal period, $\delta T_i = T_{ai} - T_{bi}$, with indices as defined before. Most of the residuals (70 per cent) are within ± 0.2 sec. The large negative residuals correspond to the signals with waveform complicated by high-frequency noise, whereas, on the other hand, the large positive values are due to the influence of low-frequency noise on the signals.

The analysis of processed P wave records of Nevada Test Site explosions, with well-known focal parameters, has shown that the errors in determining azimuth and epicentral distance contain a systematic and a random component. Figure 9 shows the dependence of the polarization rectilinearity versus time for 12 NTS explosions. It is seen that, in the vicinity of the maximum of the signal, estimates of cosine directions n, m, l can be made with a low level of random error.

A similar analysis was done for signals recorded at the station during July 1986 and from February to May 1989. Detected signals were associated with earthquakes

TABLE 5

FORMAT OF THE PRINTOUT OF THE RESULTS OF THE PROCESSING OF AN EARTHQUAKE IN THE KAMCHATKA REGION

P (21)	S/N	9.0	τ_5 35.7	Distance	53.4
0:32:50.39	Azimuth	52.2	τ_3 48.5	Coordinates	50.8
July 17, 1986	Angle Inc.	26.3	t_{max} 0.6		163.3
	Axes	0.09		Magnitude	4.7
W/F		0.05		T	0:23:29.7

	Z			NS			EW			Max		
	A	T		A	T		A	T		A	T	
Noise	2.5	1.5		1.8	1.6		1.8	1.0				
Arrival	−7.8	1.0	0.0	−0.7	1.0	0.2	−1.0	0.9	0.2			
0–6	7.8	0.9	0.8	3.3	0.9	2.3	3.1	1.1	1.3	8.5	1.0	1.3
6–12	4.2	0.8	9.2	2.3	0.6	7.1	3.0	1.0	9.7	5.2	0.8	9.2
12–18	4.6	1.1	14.8	2.7	1.4	15.4	2.2	0.9	13.7	4.8	1.0	17.3
18–60	7.3	1.4	19.0	3.4	0.3	22.7	4.5	1.1	19.1	8.5	1.2	19.1

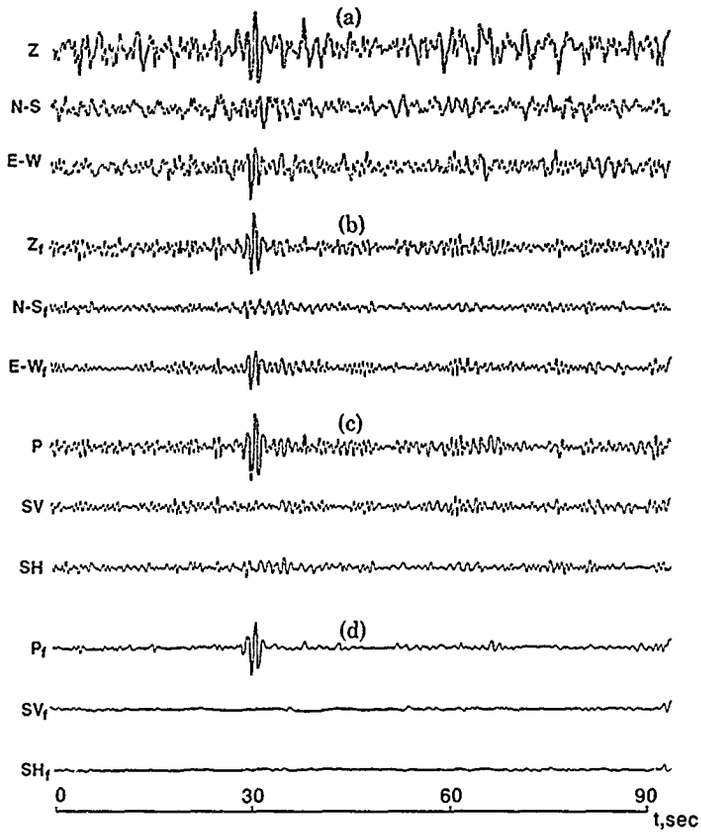

FIG. 5. Results of the processing of an earthquake from Poland (for explanation, see Fig. 4).

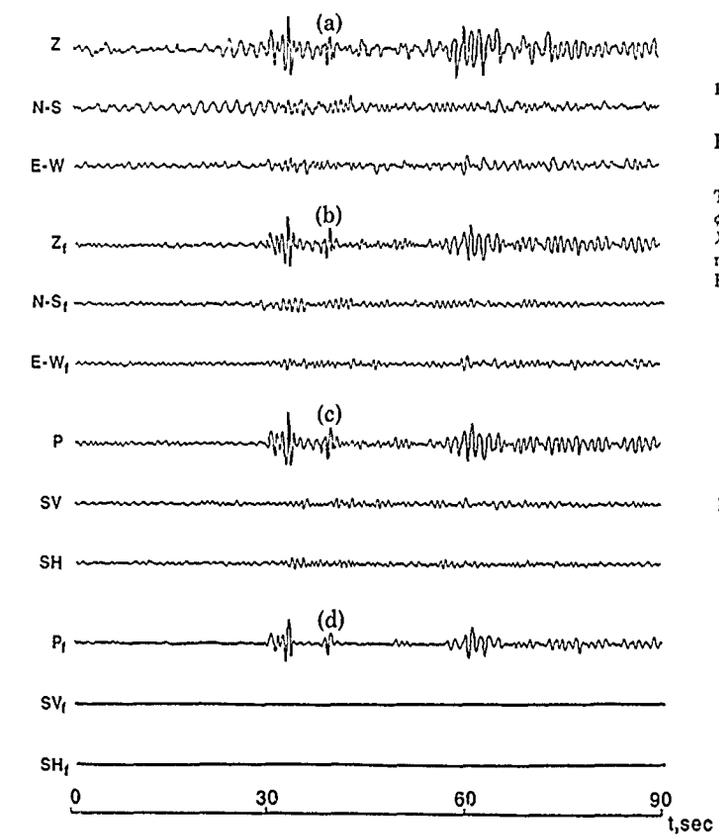

FIG. 6. Results of the processing of an earthquake from the Halmahera Sea region (for explanation, see Fig. 4).

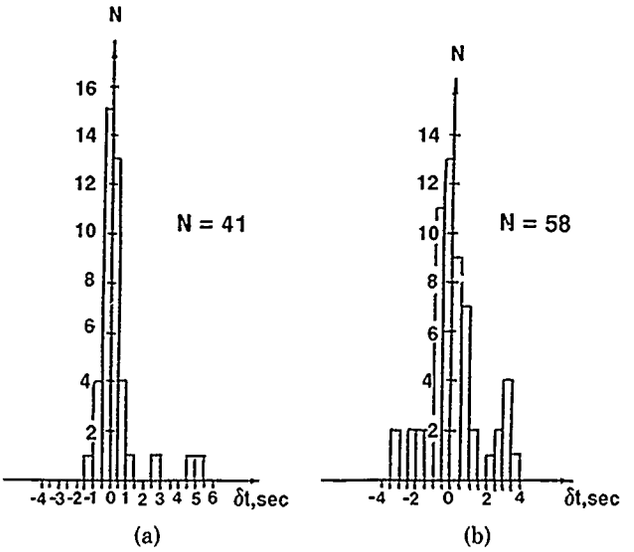

FIG. 7. Distribution of arrival-time residuals (differences between automatic and visual measurements) for (a) events of SNR > 10 and for (b) events of SNR ≦ 10.

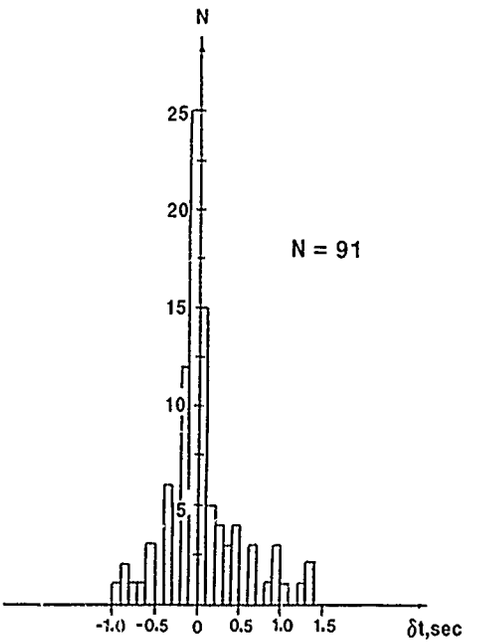

FIG. 8. Distribution of signal period residuals (differences between automatic and visual measurements).

reported by PDE or ISC, whenever the predicted arrival time fell within ±6 sec of the observed arrival time. Table 6 lists results for 25 of the total 118 associated events. Azimuth distribution (station to epicenter) for processed P waves is shown in Figure 10. The observations of azimuth were used to determine the correction, $\delta\alpha_i$, relative to data from the *PDE Bulletin* and the *Bulletin of the International Seismological Centre*:

$$\delta\alpha_i = \alpha_{ai} - \alpha_{bi} \tag{9}$$

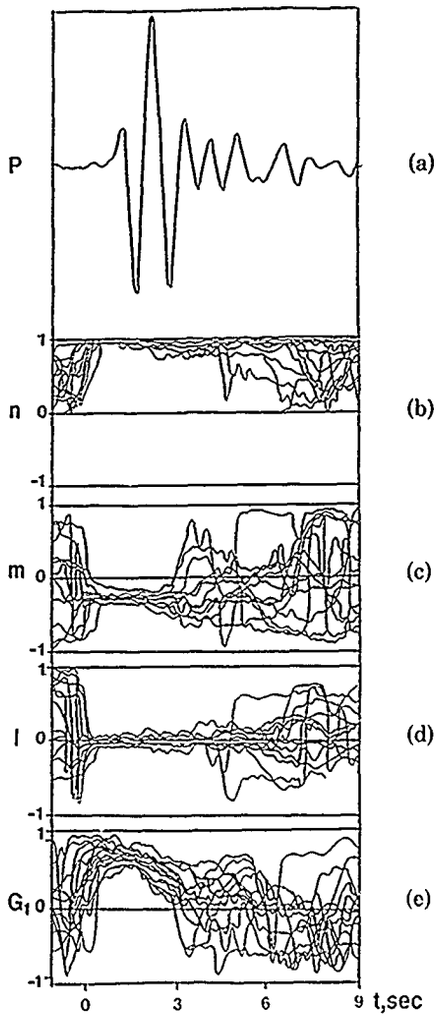

FIG. 9. Behavior of cosine directions (n, m, l) and the level of polarization rectilinearity (G_1) of the P-wave vector within 9 sec after the arrival time for 12 signals from the Nevada test site: (a) SPZ recording of a typical P signal (16.07.69, T_0 = 14h 55m 00s); (b) to (e) diagrams of the parameters n, m, l, and G_1.

where

α_{ai} = is the automatically estimated azimuth to the epicenter
α_{bi} = is the true azimuth to the epicenter reported by PDE or ISC.

The greatest number of observations were made in the direction of Molucca Islands. In order to investigate the effects of differences in source zones, the set $\delta\alpha_i$ was averaged over 30° azimuth intervals with moving 5° steps.

$$\overline{\delta\alpha_k} = \frac{1}{n_k} \sum_{i \in I_k} \delta\alpha_i \qquad I_k = \{i;\ 5k \leqq \alpha_i < 5k + 30\}, \quad k = 0, \ldots, 71. \tag{10}$$

Figure 11 shows the curve of mean values, $\overline{\delta\alpha_k}$, and standard deviations, $\sigma_{\delta\alpha}$, associated with the maximum and minimum values. Despite the scatter in the data, the difference in $\overline{\delta\alpha}$ for the maximum and minimum of this curve is clearly seen. In

TABLE 6

RESULTS OF DATA PROCESSING USING THE "SEISMOSTANSIA" SOFTWARE

Results of Three-Component Analysis of *P* Waves							Data from *ISC* and *PDE Bulletins*					
Date	Origin Time (h m s)	Coordinates		m_b	b/a	SNR	Origin Time (h m s)	Coordinates		H (km)	m_b	Azimuth Difference
		Latitude	Longitude					Latitude	Longitude			
1	2	3		4	5	6	7	8		9	10	11
06-07-86	20 39 19.5	30.4	78.7	—	0.06	22 2	20 39 59	34.5	80.0	33	4.6	6.2
07-07-86	19 34 39.0	50.2	34.3	4.0	0.17	5.4	19 33 02	51.6	16.2	10	4.5	−12.5
07-07-86	20 54 22.4	−10.4	99.9	4.7	0.08	6.8	20 54 15	1.8	126.4	—	4.8	29.6
10-07-86	01 28 42.1	−12.7	117.3	—	0.04	112.7	01 29 36	1.8	126.4	33	5.6	23.0
10-07-86	02 10 23.3	31.3	138.1	5.1	0.08	15.1	02 10 48	36.4	140.1	105	4.4	17.8
10-07-86	07 09 26.0	−17.9	118.0	5.0	0.10	12.4	07 10 44	1.8	126.5	33	5.0	16.5
10-07-86	16 11 15.8	6.2	143.2	4.5	0.13	9.8	16 13 28	28.5	140.3	106	5.0	13.3
10-07-86	19 43 10.8	−24.1	109.1	5.0	0.05	13.3	19 44 21	1.0	126.9	33	5.0	27.8
11-07-86	00 24 04.1	3.1	116.2	5.0	0.10	16.6	02 23 26	1.7	126.6	33	4.5	9.1
11-07-86	02 12 23.6	78.6	77.7	4.4	0.19	6.5	02 11 23	81.1	120.9	10	4.5	−9.7
11-07-86	07 19 03.9	−9.1	133.7	4.7	0.17	5.6	07 17 58	−26.2	132.8	10	5.6	−9.8
11-07-86	17 01 08.0	11.1	121.4	5.7	0.07	51.7	17 02 04	24.3	126.9	33	5.3	15.0
12-07-86	09 05 10.2	−20.6	123.4	5.2	0.12	8.2	09 06 57	1.8	127.4	123	5.0	14.9
12-07-86	16 04 25.0	−9.3	122.1	5.7	0.05	152.1	16 05 13	1.9	126.4	33	5.3	9.4
12-07-86	17 00 31.2	35.4	45.3	4.9	0.05	26.3	17 00 50	38.4	45.0	10	4.8	−5.0
14-07-86	12 01 45.7	−17.1	130.4	5.0	0.06	20.7	12 02 30	−2.1	138.9	33	5.0	14.9
14-07-86	20 12 52.9	−10.3	152.7	6.0	0.05	84.3	20 14 50	12 3	144.0	21	5.0	8.3
15-07-86	14 37 05.7	−27.2	132.1	5.5	0.09	14.7	14 39 34	2.0	126.5	33	4.9	11.0
15-07-86	15 10 04.5	7.4	−23.2	5.7	0.19	5.7	15 15 55	36.7	−23.4	150	4.0	15.0
16-07-86	02 18 28.5	−23.6	101.4	5.5	0.12	22.3	02 19 49	−8.3	105.8	33	4.6	10.4
16-07-86	22 03 08.1	30.4	73.7	6.1	0.02	350.1	22 03 11	30.9	77.9	33	5.6	0.0
17-07-86	00 11 27.0	37.3	39.2	4.6	0.10	17.3	00 12 01	38.4	45.4	33	4.5	7.0
17-07-86	00 23 38.8	51.6	162.5	4.8	0.09	9.0	00 24 00	56.1	162.9	33	4.8	4.6
17-07-86	10 56 58.3	3.4	95.5	4.7	0.12	6.3	10 54 31	−6.9	130.6	81	4.8	30.0
17-07-86	21 14 57.8	−20.1	108.2	5.3	0.04	20.5	21 15 13	−10.2	123.9	33	4.9	18.3

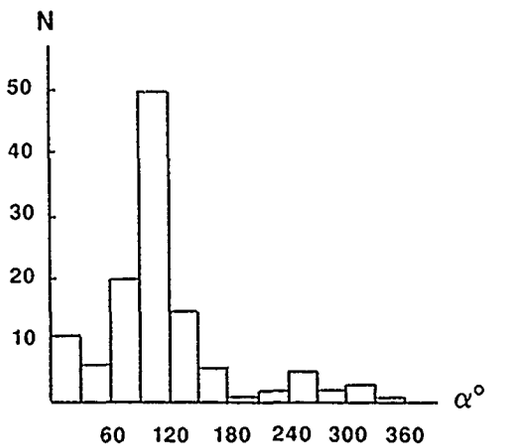

FIG. 10. Azimuthal distribution of the events in the data set.

accordance with a comparison criterion f (Pagurova, 1968), the compared values can be considered as different at a given significance level η, if

$$|f| = |f_1 - f_2|/(\sigma_1^2 + \sigma_2^2) \geqq f_\eta. \tag{11}$$

Comparison of $\overline{\delta\alpha}$ in the direction 40° and the direction 120° shows that there is difference at the significance level of $\eta = 0.9$ ($f_{0.9} = 1.7$, $|f| = 4$). Figure 11 also indicates the presence of a 120° periodicity in the variation of $\overline{\delta\alpha}$. Of course, additional observations will need to be made to confirm this pattern.

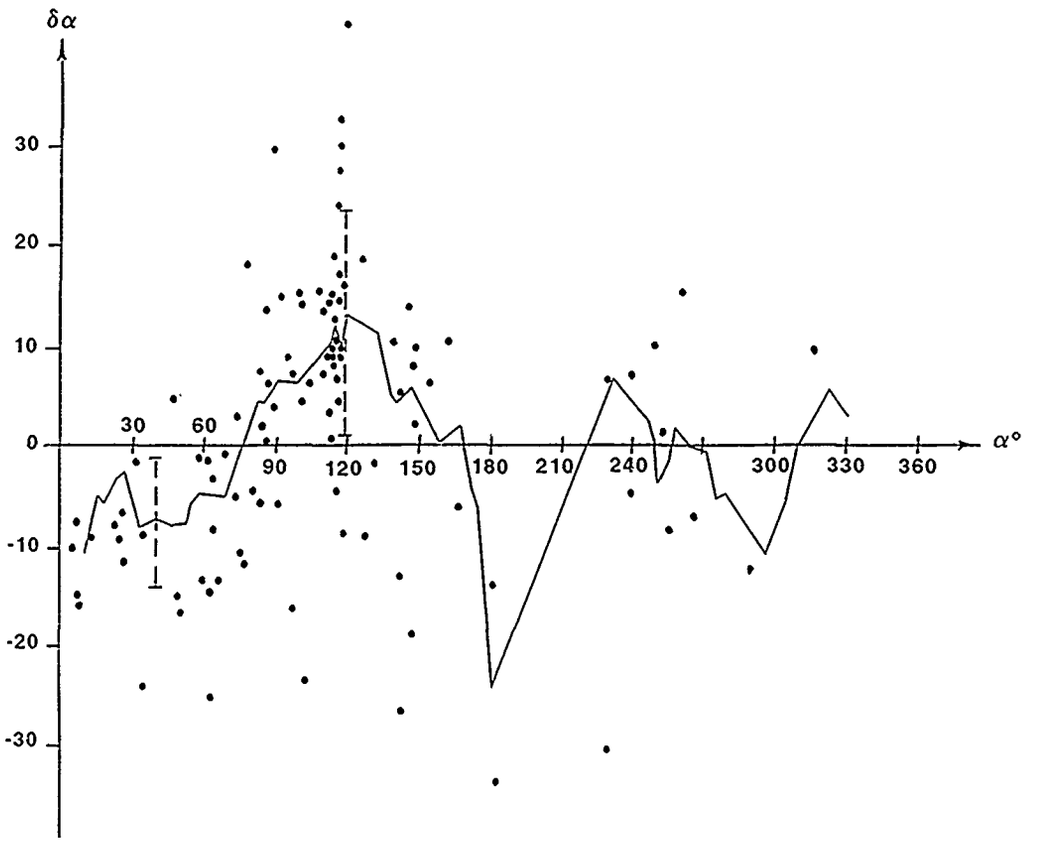

FIG. 11. The dependence of azimuth residuals versus azimuth: closed circles are observed residuals (calculated minus true azimuth); solid line is an average over sliding 30° windows, as described in the text; and the dashed vertical line represents ±1 S.D. of a single measurement.

It appears that systematic azimuth anomalies are due to crust-mantle inhomogeneities in the station region. Allowing for the dependence observed in Figure 11, the systematic overall error in the azimuth estimation can be reduced.

CONCLUSIONS

This paper has presented the algorithm and the principles underlying the SEISMOSTANSIA software, the purpose of which is the automatic on-line processing of seismic information at a single, three-component digital station.

The objectives of the data processing are detection of seismic signals, measurement of signal parameters (level 1 data), extraction of signal segments [including preceding seismic noise (level 2 data)], and approximate estimation of event parameters (azimuth, distance, epicenter coordinates, origin time, and magnitude).

Analysis of experimental data obtained during the trial running of "SEISMOSTANSIA" in 1986 and the routine running in 1989 at a station of the USSR Academy of Sciences in Eastern Kazakhstan has shown that:

1. The system works successfully in an on-line environment for a data flow of up to 100 signals per day.
2. The residuals of the arrival time obtained by automatic and visual means are, in 70 per cent of the cases, within ±0.5 sec for SNR > 10 and within ±1.0 sec for SNR < 10.

3. The residuals in estimates of signal period obtained by automatic and visual means are within ±0.2 sec in 70 per cent of the cases.
4. Analysis of seismic events with known focal parameters (explosions from NTS) and a set of earthquakes with well-determined focal parameters (Molucca Islands) has shown that the errors in determining the azimuth, the incident angle, and, consequently, the epicentral distance and epicenter coordinates, contain a systematic and a random component.
5. Azimuth residuals $\delta\alpha_i$ are due to the geological and tectonic features of the medium beneath the station and probably the source.
6. Average azimuth residuals $\overline{\delta\alpha_i}$ at the station appear to have a periodic dependence of azimuth (the period being about 120°), with typical maximum deviation 15°.
7. The systematic bias values $\overline{\delta\alpha}$ can be determined by statistical means for various regions and then taken into account when calculating focal parameters. This can, in the future, improve the estimation of event coordinates made from three-component analysis.
8. The level of polarization rectilinearity as well as other parameters describing the waveform ($A_{\max}$, $\tau_{0.5}$, $t_{\max}$) can serve as an effective means of discriminating between teleseismic, regional and local signals, and false alarms.
9. It is shown that azimuth and angle of incidence, when reported from stations to data centers, can improve the reliability of associating phases to form events. Such data will reduce the problems caused by unassociated detections, relative to what is possible when using phase arrival times only.

ACKNOWLEDGMENTS

The authors would like to thank V. V. Adushkin and V. A. An for their support in this work, F. Ringdal for contributive discussions of the manuscript and E. Golikova and S. Pankova for data processing support.

REFERENCES

CCD/558 (1978). First Report of the Ad hoc Group of Scientific Experts to the Conference on Disarmament, Geneva.

CD/43 (1979). Second Report of the Ad hoc Group of Scientific Experts to the Conference on Disarmament, Geneva.

CD/448 (1984). Third Report of the Ad hoc Group of Scientific Experts to the Conference on Disarmament, Geneva.

CD/720 (1987). Fourth Report of the Ad hoc Group of Scientific Experts to the Conference on Disarmament, Geneva.

Final Event Bulletin (1985). Group of scientific experts technical test, Washington Experimental International Data Center, Center for Seismic Studies, Arlington, Virginia.

Flinn, E. A. (1965). Signal analysis using rectilinearity and direction of particle motion, *Proc. IEEE* **12**, 2085–2087.

Gesan, A. V. (1974). Preliminary method to define the smallest model for reliable detemination of the orientation of a solid body using the L1 norm (in Russian), *Proc. from the 6th Symposium on the Problem of Overdetermination in Information Systems*, Leningrad.

Jurkevics, A. (1988). Polarization analysis of three-component array data, *Bull. Seism. Soc. Am.* **78**, 1725–1743.

Kedrov, O. K. and I. P. Bashilov (1975). Polarization method of separating body waves from a remote seismic source (in Russian), *Izv. AN SSSR*, Ser. Fizika Zemli, No. 8.

Kedrov, O. K., A. I. Nemytov, N. N. Kalinina, and O. P. Villemson (1989a). Algorithm and program for real-time detection and processing of seismic signals at a single three-component station, *GSE/USSR/44*, Conference on Disarmament, Geneva.

Kedrov, O. K., A. I. Nemytov, N. N. Kalinina, and O. P. Villemson (1989b). Algorithm and program for real-time detection and location of seismic events at a single three-component station (in Russian), *Dokl. AN SSSR* **307**, no. 1, 67–73.

Kondorskaya, N. V. and O. K. Kedrov (1982). Estimation of earthquake source parameters from observations by a standard network, *Phys. Earth Planet. Interiors* **30**, 94–104.

Magotra, N., N. Ahmed, and E. Chael (1987). Seismic event detection and source location using single-station (three-component) data, *Bull. Seism. Soc. Am.* **77**, 958–971.

Mykkeltveit, S. and H. Bungum (1984). Processing of regional seismic events using data from small-aperture arrays, *Bull. Seism. Soc. Am.* **74**, 2313–2333.

Ohlsson, H. (1982). Investigation of computer algorithm for automatic association of arrivals using synthetic data, FOA Report No. C-20447-T1, Stockholm.

Pagurova, V. I. (1968). A comparison criterion of mean values by two normal samples (in Russian), in *Communications on Computational Mathematics*, no. 5, Computer Center, Moscow.

Plesinger, A., M. Hellweg, and D. Seidl (1986). Interactive high-resolution polarization analysis of broad-band seismograms, *J. Geophys.* **59**, 129–139.

Ruud, B. O., E. S. Husebye, S. F. Ingate, and A. Christoffersson (1988). Event location at any distance using seismic data from a single three-component station, *Bull. Seism. Soc. Am.* **78**, 308–325.

INSTITUTE OF PHYSICS OF THE EARTH
MOSCOW, USSR

Manuscript received 16 February 1990

Bulletin of the Seismological Society of America, Vol. 80, No. 6, pp. 2072–2088, December 1990

VARIATIONS IN BROADBAND SEISMIC NOISE AT IRIS/IDA STATIONS IN THE USSR WITH IMPLICATIONS FOR EVENT DETECTION

By Holly K. Given

Abstract

Ambient noise conditions at four IRIS/IDA sites in the USSR are characterized from 0.01 to 100 Hz as part of a study to ascertain the utility of broadband three-component seismic stations in monitoring regional Eurasian seismicity. Estimates of the power spectral density of noise levels were computed for a 5-day period in two seasons (winter and summer), at two times of the day. Of these periods, lower noise conditions were found at night in the summer. In general, at 1 Hz and above, noise levels and their variations correlate predictably with the soundness of vault construction and the proximity of the station to civilization. Absolute noise levels at the IRIS/IDA/USSR sites range from a high of about −120 dB to a low of −155 dB relative to $(1\ m/s^2)^2/Hz$, between 1 and 5 Hz. A time-of-day variation in noise was observed at all sites, with noise levels during the work day ranging from 7 to 14 dB higher than night levels, depending on the site. This effect was observed only for frequencies above about 1 Hz. Observed seasonal variations (winter versus summer) are highly station dependent, although the seasonal effect is restricted to frequencies below 1 Hz and is in general centered on the microseism peak (0.1 to 0.2 Hz). Below 0.1 Hz, noise levels are influenced by the thermal and barometric isolation of the site. Low-frequency levels were not studied below 0.01 Hz. Minimum detectable magnitudes are estimated for the IRIS/IDA stations using the observed noise levels over 1 Hz. In general, a magnitude 3 event should be detectable at 1,000 km by all stations under night noise conditions if the dominant signal frequency is 1 Hz; the magnitude estimates increase with increasing frequency. These detectability estimates assume a conservative signal-to-noise ratio of 6.

High-frequency data recorded by independent equipment co-located with the IRIS/IDA system during a 2-week experiment allow estimation of noise levels at the sites up to 100 Hz. Borehole versus surface noise levels recorded during the high-frequency experiment showed significant noise reduction (20 dB) can be achieved by borehole deployment at sites with exposed surface vaults. With well-isolated surface vaults, borehole noise reduction is about a factor of 2. Absolute noise levels between 1 to 10 Hz observed at IRIS/IDA/USSR sites are systematically higher than average NORESS noise by about 7 dB to 25 dB, depending on the station.

Introduction

Ambient seismic ground noise levels observed by 4 three-component broadband digital IRIS/IDA stations in the USSR are studied to define the factors that influence ground noise levels in the interior of the Eurasian continent, for the general purpose of establishing network criteria for detecting small seismic sources. This study looks at how the average noise spectrum depends on site, time of day, season, and depth of the sensor. The frequency band discussed in this study is 0.01 to 100 Hz.

IRIS/IDA/USSR sites are shown in Figure 1 and Table 1. The continuously recorded IRIS/IDA broadband system uses Streckeisen STS1-VBB seismometers sampled at 20 samples/sec, providing noise observations from very low frequencies

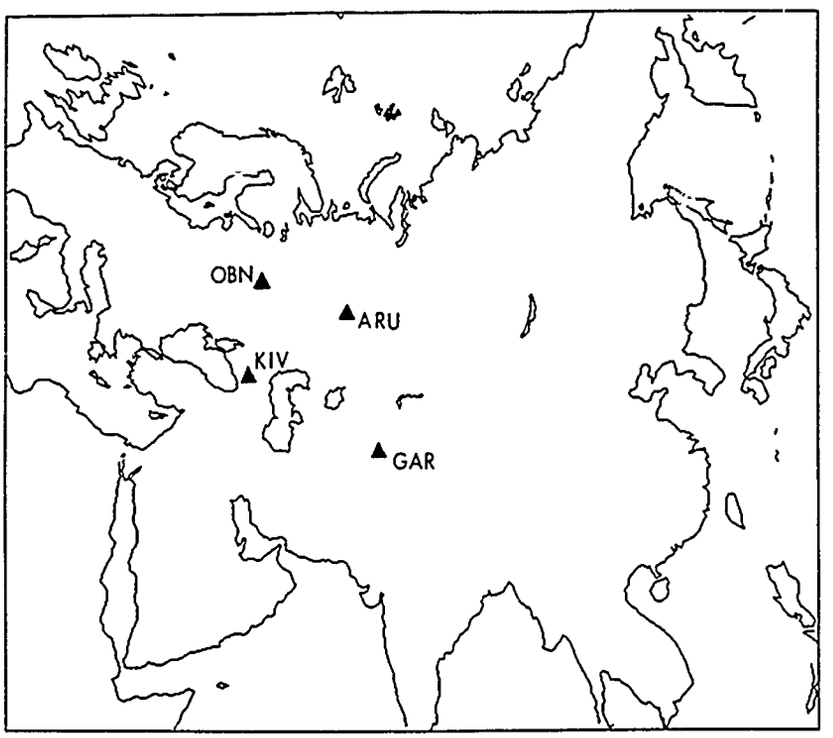

FIG. 1. Locations of IRIS/IDA/USSR stations discussed in this study.

TABLE 1
STATION LOCATIONS

STA	Station	North Latitude	East Longitude	Elevation (m)
ARU	Arti	56.40°	58.60°	250
CHS	Chusal	39.10°	70.77°	1600
GAR	Garm	39.00°	70.32°	1300
KIV	Kislovodsk	43.95°	42.68°	1206
OBN	Obninsk	55.10°	36.60°	160

up to 5 Hz. In addition, a high-frequency system similar to that described by Berger *et al.* (1988) operated for a 2-week experiment at the IRIS/IDA sites, providing data from 1 to 100 Hz. The high-frequency systems comprised both surface and borehole seismometers. In all cases except Garm (GAR), surface sensors from the broadband and high-frequency systems were co-located on the same pier.

Varying vault conditions are found at the IRIS/IDA/USSR sites. The most soundly constructed "vault" is at Obninsk, where an underground complex comprising two long tunnels and many instrument rooms was excavated 30 m below the surface in a large limestone inclusion. The tunnels are accessible from a vertical shaft at one end. The IRIS/IDA sensors occupy a separate room sealed by an air-tight door. The temperature is reported to be stable at a constant 7.5 ± 1°C. Although the sensors are very well isolated, the observatory is located at the edge of Obninsk, a technological center with a population of roughly 100,000, and hence cultural noise is substantial. The high-frequency borehole seismometer is deployed at a depth of 87 m.

At Garm, the IRIS/IDA sensors are located approximately 40 m into a horizontal tunnel blasted out of granitic rock in the side of a mountain. The high-frequency system was located about 100 km away at Chusal, where the surface sensors were located in a similar tunnel in rock. The borehole high-frequency sensor was deployed at 113 m depth near the surface sensors. Garm is located in a rugged mountainous area with only small agricultural villages; both tunnel sites are susceptible to traffic noise from a nearby major road.

Stations at Kislovodsk and Arti have lower quality vault conditions. The Kislovodsk site is at the top of a limestone ridge at an elevation of approximately 1,200 m in the foothills of the Caucasus Mountains. The site is shared with television, radio, and other telemetry equipment, including several large antennas. Winds on the ridge can be extremely high. The pier at Kislovodsk is located in the basement of the recording building. The pier was constructed before the building by excavating about 3 m to clean limestone and is presumably well isolated from the building; however, the height of the pier (4 m) may introduce considerable horizontal component noise due to tilt. The 60 m deep borehole for the high-frequency sensor at Kislovodsk is located about 20 m from the building. Aside from potential noise sources associated with the equipment on site, Kislovodsk is fairly isolated in terms of cultural noise.

The Arti station is located in a small agricultural town. Of the four present IRIS/IDA/USSR sites, Arti has the most exposed vault; it is partially buried and accessible by a staircase entered through a door at ground level. The high-frequency borehole sensor at Arti was deployed at a smaller depth (35 m) than at the other sites during the period discussed in this study. Human traffic and associated noise can be substantial at the site.

Broadband Noise

Spectral estimates of ambient noise power levels recorded on the broadband instruments were computed for two 5-day time segments, one in February or March (winter) and one in July or August (summer). The 5 days chosen were, in general, contiguous; the exact time period chosen depended on data availability. Each time series was windowed to exclude earthquakes or other anomalous signals, but is otherwise representative of the data in that time period (that is, the 5 days were not chosen to have particularly low noise levels). Spectra were computed at two times for each day, corresponding to 2 p.m. (day) and 2 a.m. (night) local time. Power spectral estimates were calculated by section averaging using eight sections of 500 sec length with a 50 per cent overlap, where a Hann taper was applied to each section. The 95 per cent confidence levels of individual spectral estimates are within −2.2 and +3.0 dB of the calculated value at each frequency; the standard deviation introduced by averaging over 5 days is given at reference frequencies for the vertical component spectra in Table 2. The IRIS/IDA broadband channels have a low-pass, antialiasing filter with a corner frequency of 5 Hz; this filter has not been removed from the ground noise spectra, which explains the apparent decrease in noise levels beginning at that frequency. For a closer look at noise levels above 5 Hz, data from the high-frequency experiment are discussed in a following section.

Noise from 1 to 5 Hz

Figure 2 shows broadband three-component average estimates of power spectral density from the local nighttime summer sample for each station. Noise levels are shown in units of acceleration, in decibels relative to $(1\ m/s^2)^2/Hz$. To convert from

TABLE 2

ONE STANDARD DEVIATION RANGE OF NOISE AVERAGES AT GIVEN FREQUENCIES

Station	Broadband Averages			
	0.01 Hz	0.1 Hz	1 Hz	10 Hz
ARU	−182.0*−−174.5	−158.4−−149.6	−157.4−−144.8	−154.7−−150.5
OBN	−174.7 −−169.8	−166.0−−157.1	−144.6−−140.7	−154.5−−151.7
KIV	−181.6 −−176.1	−163.1−−158.0	−150.2−−142.0	−155.4−−149.8
GAR	−182.3 −−175.5	−162.4−−154.4	−152.4−−147.7	−154.9−−149.4
Station	High-Frequency Averages			
	0.1 Hz	1 Hz	10 Hz	100 Hz
ARU	−140.2 −−138.3	−143.1−−141.4	−144.7−−140.3	−154.3−−149.0
OBN	−152.6 −−141.9	−145.6−−139.1	−140.0−−126.9	−169.0−−148.5
KIV	−154.5 −−148.5	−146.9−−138.3	−158.5−−138.8	−154.4−−146.3
CHS	−151.9 −−151.4	−155.5−−152.7	−152.1−−139.9	−178.1−−134.9

* dB relative to $(1\ m/s^2)^2/Hz$.

velocity to acceleration units, 20 log ω is added to the velocity power spectrum where $\omega = 2\pi f$. This study shows that summer and night represent low noise conditions at the IRIS/IDA sites, with both day and winter conditions tending to raise the noise levels in certain frequency bands. In general, station GAR shows the lowest noise levels above 1 Hz; noise levels on all components stay well below −140 dB. At ARU, noise levels are comparable to GAR at 1 Hz but increase with frequency toward the corner of the low-pass filter, and horizontal noise levels at higher frequencies are notably (about 10 dB) higher than vertical noise.

Whereas noise at GAR and ARU is well below −140 dB at 1 Hz and increases toward 5 Hz, KIV noise fairly constant at −140 dB at 1 Hz and above. Both KIV and ARU show spectral lines between 1 and 5 Hz, where the lines are stronger at KIV. The presence of the lines is variable, but the frequencies are fairly constant. One causative factor of the lines at KIV may be wind-induced resonance of the large telemetry antennas at the site. OBN is disappointing in its high-frequency noise performance considering the quality of the vault construction. The shape of the noise spectrum over 1 Hz at OBN has been observed to be very consistent over many months of operation, particularly the noise peaks at 2.3 Hz (vertical) and 4.3 Hz (horizontal). For reference, the array-averaged vertical noise estimate for NORESS reported by Suteau-Henson and Bache (1988) would plot at a fairly constant level of −155 dB between 1 and 10 Hz in acceleration power units.

Noise below 0.1 Hz

Vertical-component, low-frequency noise levels (below 0.1 Hz) do not vary significantly between stations. At 0.01 Hz, vertical-component noise levels observed in the USSR approach the lowest noise observed globally (Agnew and Berger, 1978). At OBN, where the vault depth is 30 m, low-frequency horizontal noise is almost as low as vertical noise. This is usually seen only for stations with sensors at depth, and results in part from the constant temperature in the tunnel and its isolation from barometric effects. Low-frequency horizontal noise levels at ARU and KIV are significantly higher than at OBN. At ARU, horizontal noise can be attributed to the exposed vault, while at KIV, the tall pier results in exaggerated large horizontal motion as the pier's base reacts to tilts induced by the daily temperature variation. Although the KIV instruments are located in the basement of the recording building, there is little isolation from wind or barometric changes on the

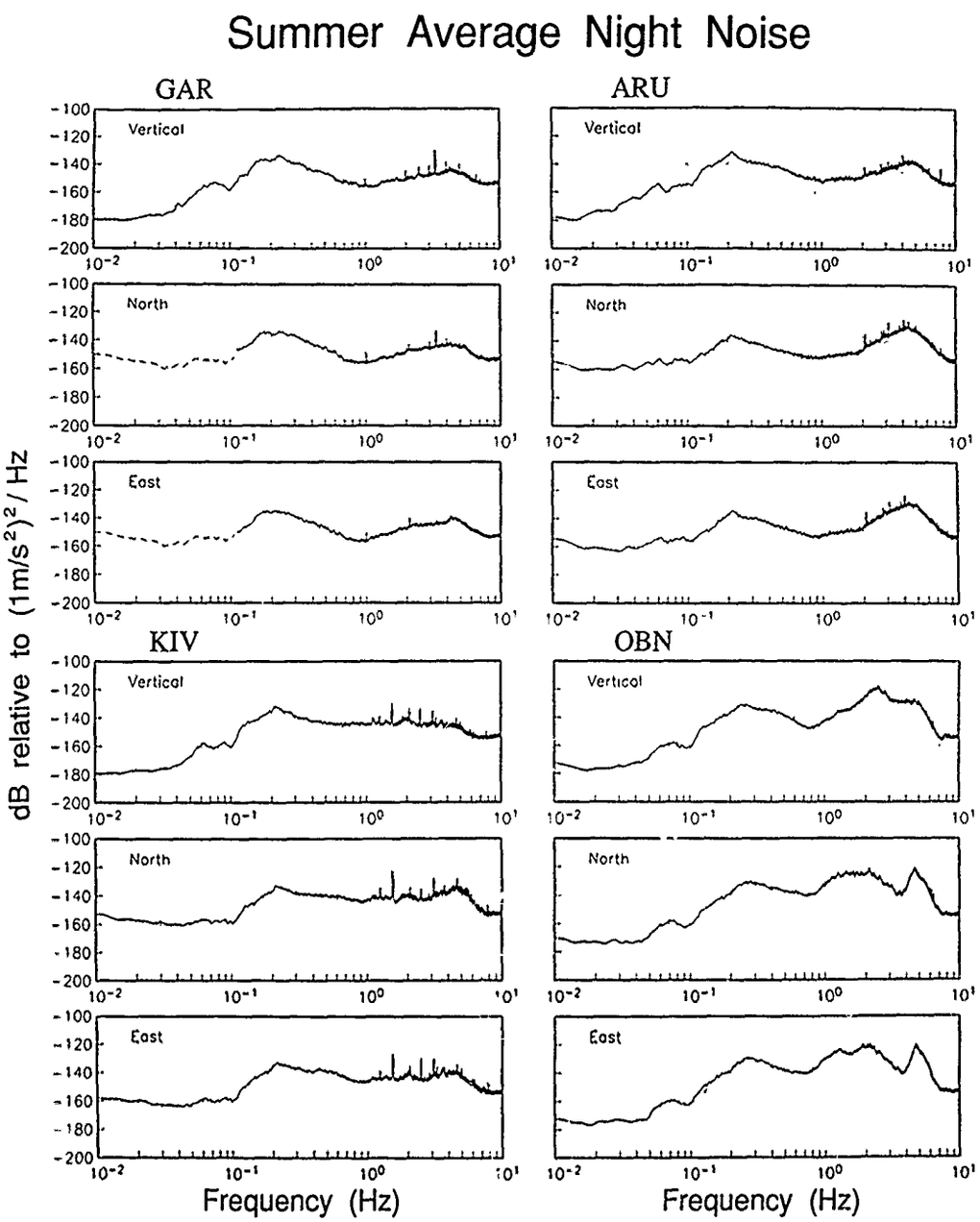

FIG. 2. Power spectral density of ambient ground noise recorded by three-component STS1-VBB sensors as a function of frequency between 0.01 to 10 Hz at IRIS/IDA/USSR sites. Each spectral estimate is an average of noise samples recorded at approximately 2 a.m. local time during a 5-day period in the summer. The dashed line for horizontal channels at GAR below 0.1 Hz show averaged noise levels during a 5-day period in the winter (see text). The apparent downturn in amplitude at 5 Hz is the effect of a low-pass, antialiasing filter that was not removed.

exposed ridge. At GAR, the centering mechanisms of the horizontal seismometers were damaged, prohibiting measurements of horizontal low-frequency noise during the same period as the other stations. Horizontal seismometers were replaced in December 1989. A 5-day nighttime average for horizontal noise from February 1990 is shown by the dashed line below 0.1 Hz at GAR in Figure 2. Average horizontal low-frequency noise at GAR is comparable to levels at ARU and KIV. At all sites, low-frequency horizontal noise varied much more than vertical noise. However, at

GAR and OBN only, it was noted that low-frequency horizontal levels occasionally matched low vertical levels, which can be attributed to the more favorable deployment conditions.

Time-of-Day Variations in Noise Levels

Figure 3 shows the difference in decibels of the 5-day average vertical noise levels observed during the day and at night in the summer at the four IRIS/IDA sites as a function of frequency. In all cases, time-of-day variations are not significant below 0.8 Hz. OBN shows insignificant time-of-day variation below 2 Hz. Above this, the structure in the time-of-day variation occurs because the underlying spectral shape of the night noise (Fig. 2) is masked by a constant raised noise level of about −120 dB between 2 to 4 Hz during the day. GAR shows low time-of-day variation, with the increase in noise power being about 7 dB during the day above 1.5 Hz. Correspondingly, GAR also has the lowest *absolute* daytime noise levels. KIV and ARU show dramatic increases in daytime noise levels. At ARU, the increase in day

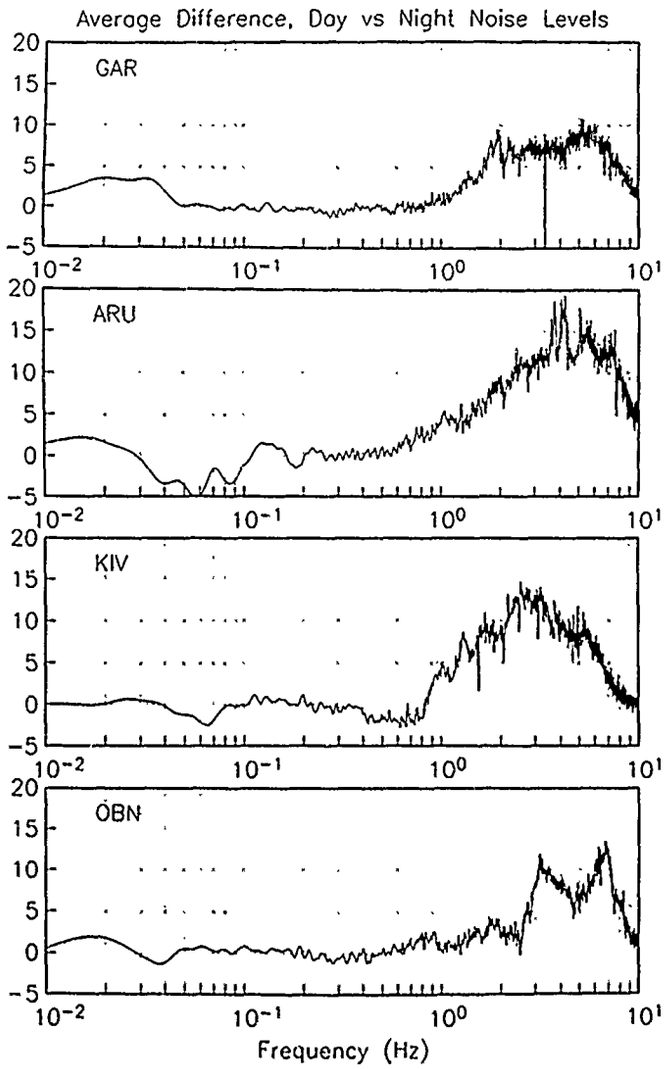

FIG. 3. Difference in decibels in averaged vertical summer noise spectra observed during the day (2 p.m. local time) and at night. Daytime noise increases are most significant at ARU and KIV, where the sensors are less isolated than at GAR and OBN.

noise relative to night noise begins at a lower frequency than elsewhere, 0.7 Hz. ARU noise levels reach −120 dB during the day, and multiple spectral lines between 3 to 6 Hz, which raise noise levels further, have been observed periodically. Absolute daytime noise levels at KIV reach a broad maximum of about −130 dB at 3 Hz, although noise can be higher at certain frequencies due to spectral lines. Reasons behind raised daytime noise levels at KIV are not obvious, since the site is fairly well isolated from the city. Lower time-of-day variations at OBN and GAR can be attributed directly to the isolating effects of the tunnel deployments.

Seasonal Variations in Noise Levels

Figure 4 shows the difference in decibels between vertical acceleration power levels observed at night in winter versus summer as a function of frequency. In most cases, seasonal variations are confined to the low end of the spectra and are largest near the microseism peak due to the increase in ocean storms during winter. GAR shows the lowest seasonal variation, about 7 dB at the microseism peak,

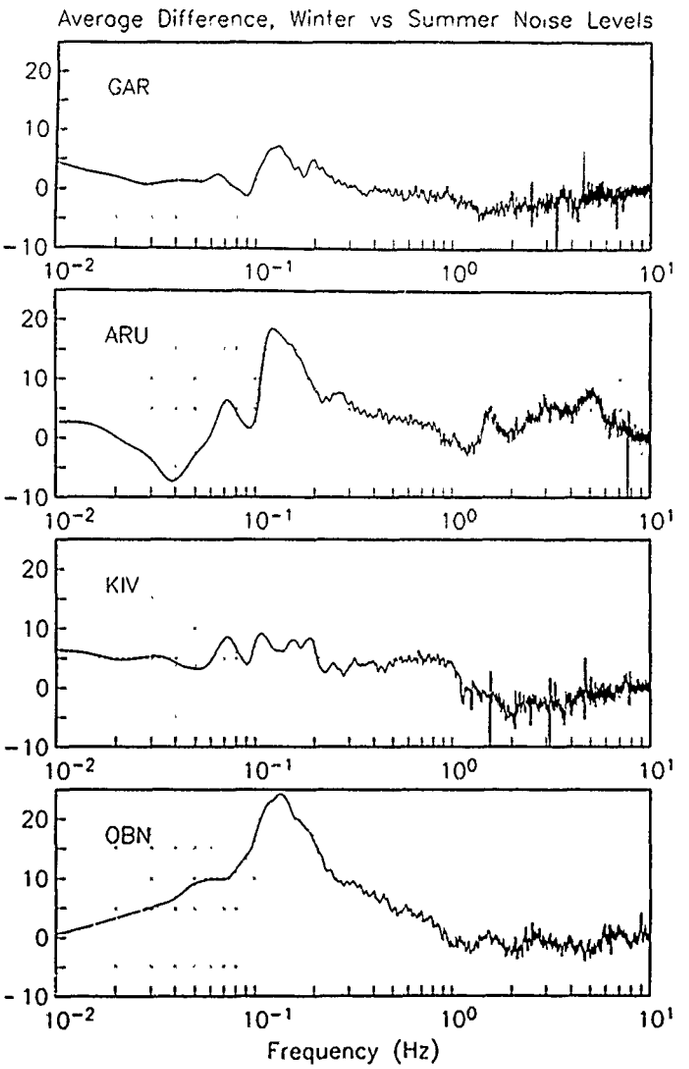

FIG. 4. Difference in decibels in averaged vertical night noise spectra observed in the winter and in summer. Large increases in noise in the microseism band are seen at ARU and OBN. GAR and KIV shows less of a seasonal variation, most likely due to their geographical locations.

presumably due to its location in the interior of the Eurasian continent. At KIV, winter noise increases over a broad frequency band, but is still only 7 dB higher than summer noise. KIV is located on the isthmus between the Black and Caspian Seas, which may control microseism noise more than the ocean storms. ARU and OBN show extreme seasonal variation, with an increase in 18 and 24 dB, respectively, in microseism noise levels. No significant seasonal change in noise is observed above 1 Hz with the exception of ARU, where winter noise power levels were about a factor of 2 over summer levels. This implies that the summer noise level at ARU shown in Figure 2 may be unrepresentatively low.

High-Frequency Noise

Because the high-frequency systems (250 samples/sec) operated only briefly at the IRIS/IDA sites, time-of-day or seasonal variations cannot be studied as systematically. Care was taken to average as many spectral estimates of noise as possible; the number of estimates available for each station is found in Table 3. Time-of-day variations (when possible) as well as surface/borehole variations in noise levels, are discussed for each site. Because the noise measurements were taken for a brief period and at different times of the day, averaged absolute noise levels may not exactly match the broadband results, but in all cases they are similar. In this section, "day" noise refers to data recorded any time during the working day, while "night" refers to data recorded between 10 p.m. and 6 a.m. local time. At KIV, all usable noise samples were taken at night, and at CHS (Chusal, the high-frequency location near GAR) only three noise samples were available with little noticeable dependence on time-of-day. Spectral estimates of power levels were calculated with the same section-averaging algorithm as previously mentioned, using 10 windows of 10 sec. The effect of a 6-pole, low-pass antialiasing filter with a corner frequency of 80 Hz has not been removed from the spectral estimates. A permanent deployment of high-frequency sensors is planned at the IRIS/IDA sites in a borehole environment. Thus, the borehole observations for basic comparisons of absolute noise levels between stations are emphasized.

Absolute High-Frequency Noise Levels

Nighttime borehole spectra are shown in Figure 5. The 95 per cent confidence levels of individual spectral estimates are within −1.8 dB and +2.3 dB of the calculated value at each frequency, and the one standard deviation limits from the averaging are given in Table 2 at selected frequencies. The NORESS noise estimate from Suteau-Henson and Bache (1988) is plotted for comparison on the vertical component between 1 and 20 Hz. CHS shows the lowest vertical noise levels between

TABLE 3

Number of Noise Samples per High-Frequency Average

Station	No. of Samples	Day Span of Samples
ARU day	4	2
ARU night	2	2
CHS	3	1
KIV night	6	2
OBN day	15	14
OBN night	19	14

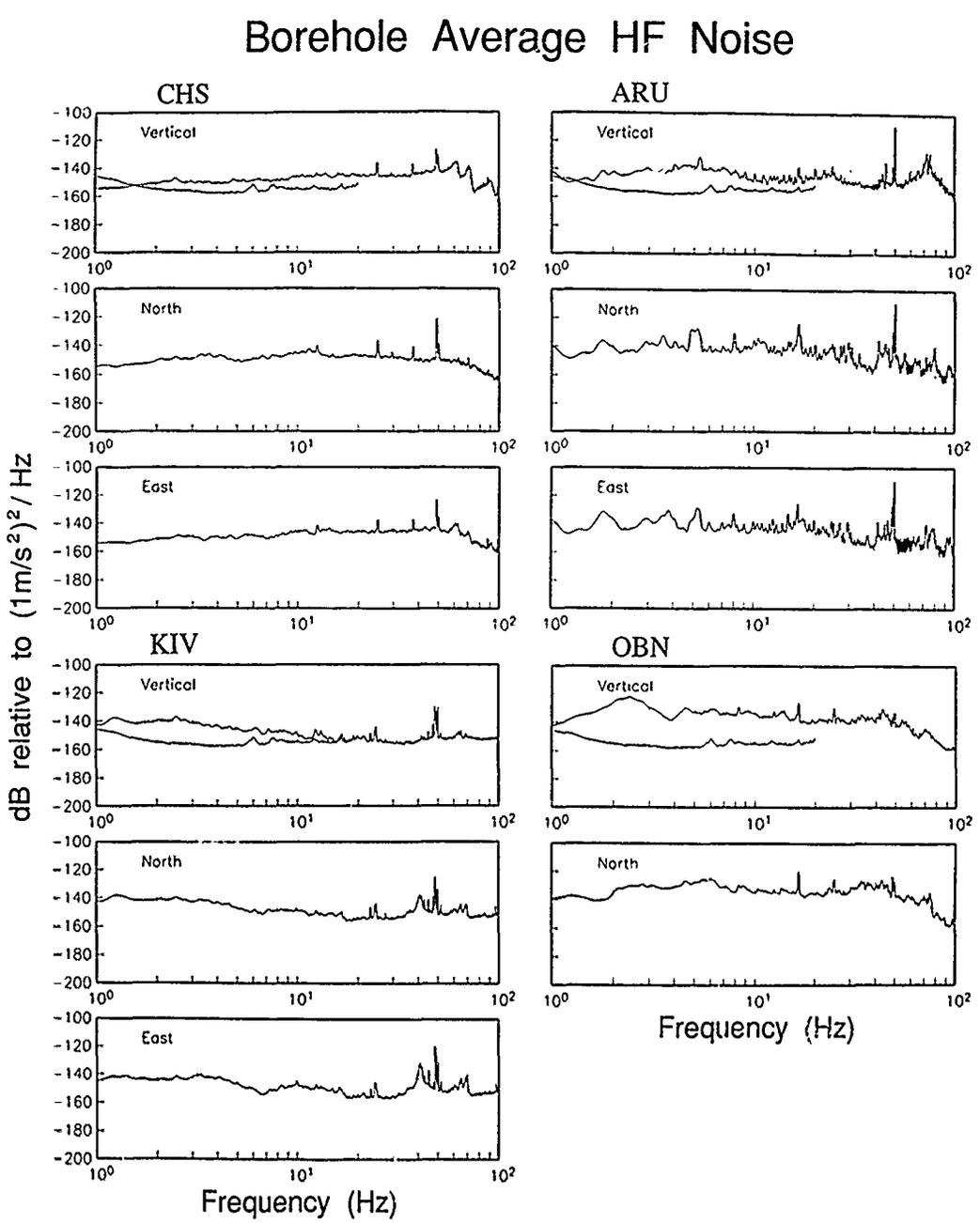

FIG. 5. Three-component ambient ground noise between 1 to 100 Hz recorded by high-frequency sensors deployed in boreholes between depths of 30 to 113 m during a 2-week experiment at the IRIS/IDA/USSR sites. Spectral estimates are averages between 2 (for ARU) and 19 (for OBN) individual noise samples, depending on the station. The lower line shown on the vertical component plots between 1 to 20 Hz is the average noise profile observed at NORESS (from Suteau-Henson and Bache, 1988). CHS denotes the location of the high-frequency system near GAR, approximately 100 km away. The effect of a low-pass, antialiasing filter with a corner frequency of 80 Hz was not removed, causing the apparent downturn in spectral amplitude.

1 to 10 Hz at −150 dB, with a very slight increase in noise beginning at about 10 Hz. Borehole noise at KIV between 1 to 5 Hz is similar to noise observed on the broadband instruments, except that the persistent spectral lines were not observed. KIV shows the lowest absolute noise between 10 to 20 Hz, where it matches the NORESS noise curve. ARU has similar noise performance to KIV from 1 to 10 Hz, with less of a noise decrease above 10 Hz. OBN borehole high-frequency noise is

persistently higher than at other stations in that it does not fall below −140 dB until above 50 Hz. OBN high-frequency noise is about 20 dB greater than NORESS noise between 4 to 20 Hz, similar to the levels that have been reported for the proposed regional array in the Bavarian Forest area of southeastern Germany (Harjes, 1990).

For all stations, horizontal noise levels observed in the borehole are similar to vertical noise except at isolated frequencies (i.e., 5 and 15 Hz at ARU; 40 Hz at KIV). At OBN, the east–west component sensor was not operating at the time of the experiment. All stations except OBN show large spectral lines at 50 Hz, the local AC line frequency.

Surface versus Borehole Noise Levels

The difference in vertical-component noise power spectra recorded on the surface and in the borehole versus frequency is shown for the four sites in Figure 6. ARU

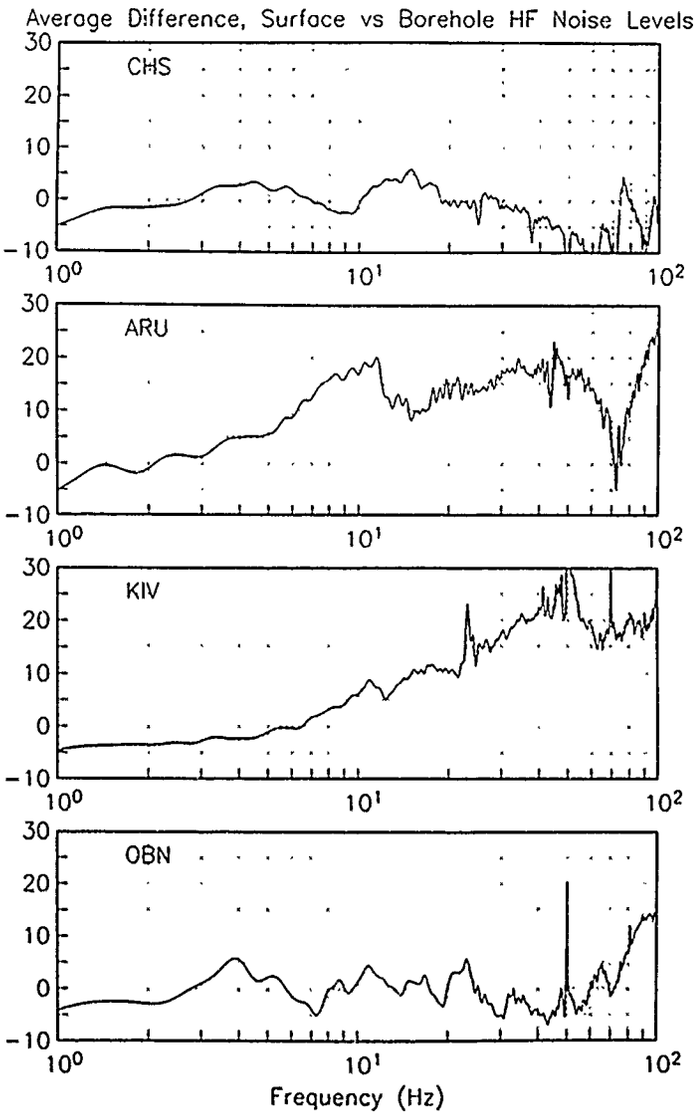

FIG. 6. Difference in decibels of averaged high-frequency noise spectra observed on the surface and in the borehole. Noise reduction of almost 20 dB is achieved above 20 Hz at ARU and KIV. A lesser degree of noise reduction is observed at CHS and OBN, where the surface seismometers are deployed in excavated tunnels in rock.

and KIV show a dramatic amount of noise reduction by deploying borehole instruments; noise levels are lower by 20 dB at high frequencies in the borehole. This is a similar noise reduction level to that observed at sites in the Western United States by Gurrola *et al.* (1990) using the same instrumentation. Borehole noise reduction is not significant at OBN, where the surface seismometers are already deployed 30 m below the surface; likewise, CHS, where the surface sensors are deployed at the rear of a long tunnel in rock, shows negligible difference between surface and borehole noise. At low frequencies, it appears that surface noise is slightly lower than borehole noise, which has been a consistent observation using this equipment in other deployments (Berger *et al.*, 1988; Gurrola *et al.*, 1990). The seismometer manufacturer estimates the system noise of the borehole sensors to be between −150 and −160 dB and between 1 to 2 Hz, which may cause some signal contamination, although observed IRIS/IDA borehole noise levels are in general above −150 dB at these frequencies. System noise performance for the high-frequency equipment is discussed in detail by Berger *et al.* (1988) and Gurrola *et al.* (1990).

Time-of-Day Variations in High-Frequency Noise

Figure 7 shows the time-of-day variation in vertical-component high-frequency noise observed in the borehole at OBN and ARU. OBN shows a factor of 2 noise power increase during the day from about 2 to 20 Hz. ARU has a larger increase in high-frequency noise during the day, about 15 dB from 3 to 80 Hz. These results are consistent with the levels of increase during the day on the broadband instruments above 1 Hz. Note that the OBN high-frequency average contained 34 samples taken over a 2-week period, whereas only six samples were available for the ARU average (Table 3).

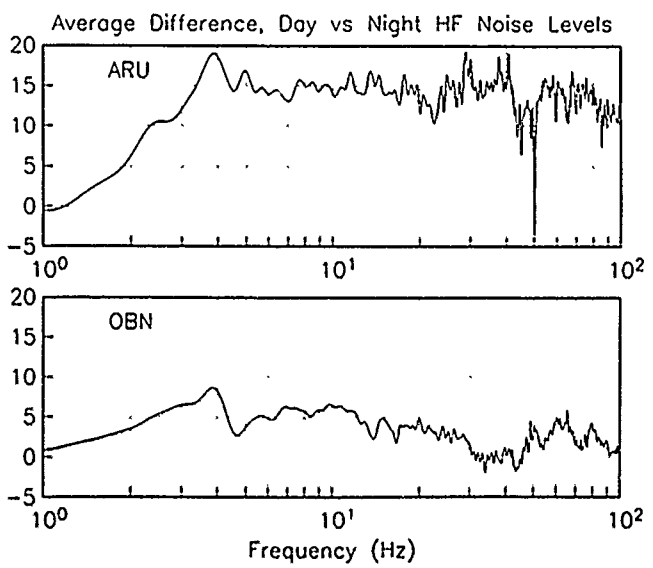

FIG. 7. Difference in decibels of averaged high-frequency noise spectra observed in the borehole during the day and at night at two stations. ARU shows an increase of 15 dB in high-frequency noise levels during the day, presumably due to its location on the outskirts of a small town. OBN shows a much smaller daytime increase, although it also is located near a town. The borehole depths at ARU and OBN are 30 and 87 m, respectively. At KIV and CHS, noise samples were not adequately distributed in time to allow a day-night comparison.

System Noise

Finally, a word should be said about system noise. Tests show that the dominant source of noise in the IRIS/IDA seismographic system deployed in the USSR is the electronics of the data acquisition system (DAS), specifically the analog-to-digital converter. Figure 8 illustrates noise from the IRIS/IDA/USSR data acquisition system at the time data were collected for this study, together with the lowest observed seismic noise level discussed, summer vertical night noise at station GAR. The system noise curve includes the effect of the analog-to-digital converter and the 5 Hz antialiasing filter. The DAS noise is at least 6 to 10 dB below the lowest noise observed during this study. STS1-VBB seismometers were not included in this test because their noise levels are in general lower than the DAS noise. Steim (1986) estimates the inherent noise of the STS1-VBB seismometer and its associated feedback circuit at between −195 and −205 dB at 0.01 Hz, which is below all known reports of observed minimum ground noise levels at 0.01 Hz. At higher frequencies, noise from the instrument is much lower (Wielandt and Streckeisen, 1982; Steim, 1986). Thus, noise from the STS1-VBB sensor itself is comparable to the IRIS/IDA/USSR data acquisition system noise near 0.01 Hz, but the DAS noise quickly dominates with increasing frequency. To summarize, all spectra recorded on the broadband system shown in this study reflect true seismic noise at all frequencies below 5 Hz, the corner of the antialiasing filter. Later versions of the data acquisition system will attempt to incorporate a quieter analog-to-digital conversion process.

Estimation of Minimum Detectable Magnitude

A rough estimate of the minimum detectable magnitude versus distance at the IRIS/IDA/USSR stations can be formed from the noise observations discussed previously if some assumptions are made. First, the average value of the observed power spectral density plus 2σ is used to quantify the range of noise levels possible at each station. (1σ ranges were given in Table 2.) The time domain amplitude of noise is then estimated from the observed power spectral density via Parseval's theorem. "Minimally detectable" is defined conservatively as six times the background noise amplitude. In general, four times background noise is a realistic level for detection and phase identification of a phase arriving amidst background noise;

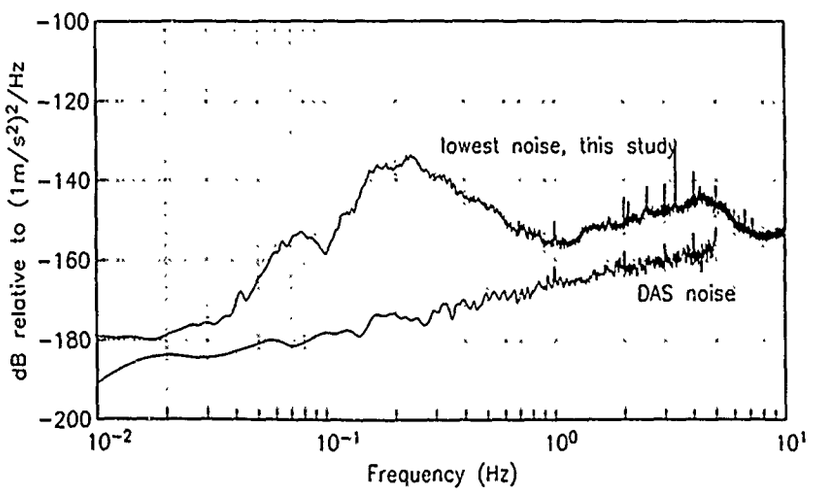

FIG. 8. Inherent noise of the electronics of the data acquisition system (DAS), which is the dominant source of system noise in the IRIS/IDA equipment. The lowest noise spectrum observed in this study, vertical-component winter night noise at GAR, is shown for comparison.

six times background was chosen as an estimate for a secondary phase arriving in coda (e.g., L_g). To relate this amplitude to event magnitude, it is assumed that the magnitude relation for M_L used at the NORSAR array (Båth *et al.*, 1976) holds for the continental USSR. Although this is a potential source of error, there are indications that crust and upper mantle attenuation in parts of the USSR do not differ radically from Scandinavia (Sereno, 1990). Because the correction term to the NORSAR magnitude is a function of both distance and signal frequency, two cases are considered, 1 Hz and 2 Hz, for day and night noise levels.

Results for a 1 Hz dominant signal are shown in Figure 9. Under night noise conditions, all stations should detect a magnitude 3 event within 1,000 km. GAR shows a significantly lower minimum magnitude due to a combination of its lower night noise profile at 1 Hz (Fig. 2) and a smaller standard deviation from the 5-day average. For day noise conditions, minimum detectable magnitudes increase by only 0.1 units at GAR and OBN, where 1 Hz day and night noise conditions are nearly equal (Fig. 3). KIV shows a large increase of 0.4 units for day noise. ARU shows a surprising decrease in the estimate of minimum detectable magnitude during the

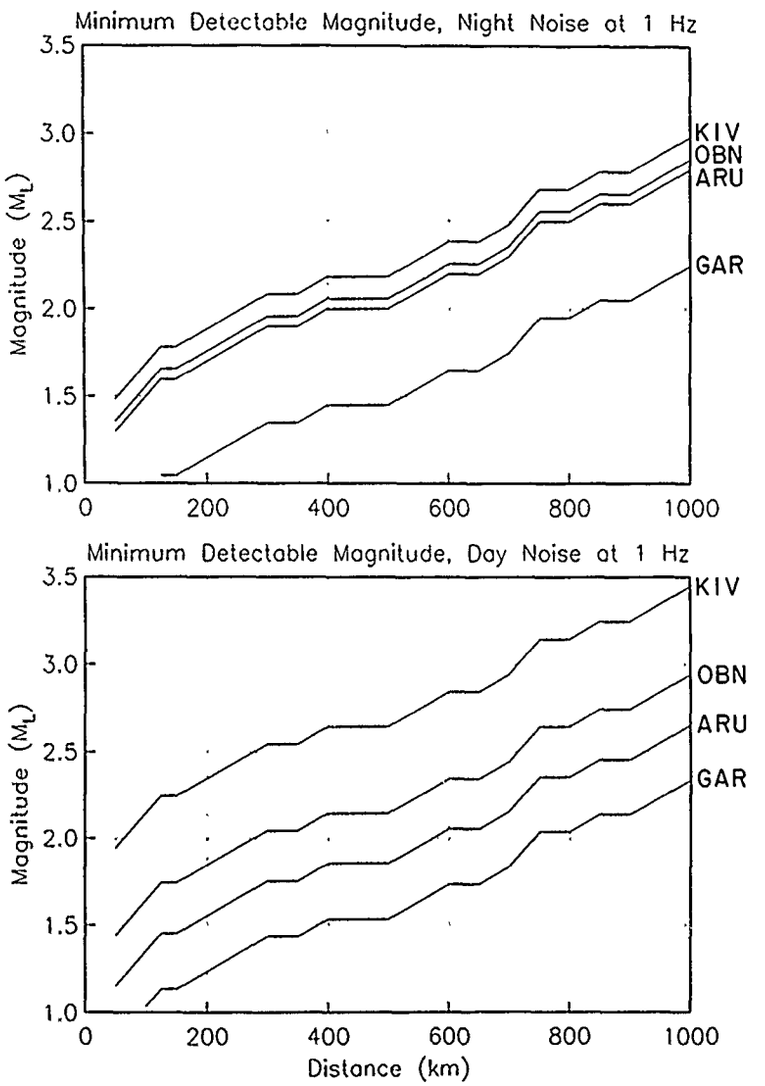

FIG. 9. Minimum detectable magnitudes for a signal with a dominant frequency of 1 Hz versus distance estimated from observed night and day IRIS/IDA/USSR noise levels, assuming the NORSAR magnitude relation.

day; this is because the standard deviation of the nighttime 5-day average is almost 2.5 times the daytime average.

For a dominant signal frequency of 2 Hz, minimum detectable magnitudes increase significantly (Fig. 10). Under night noise conditions, GAR is the only

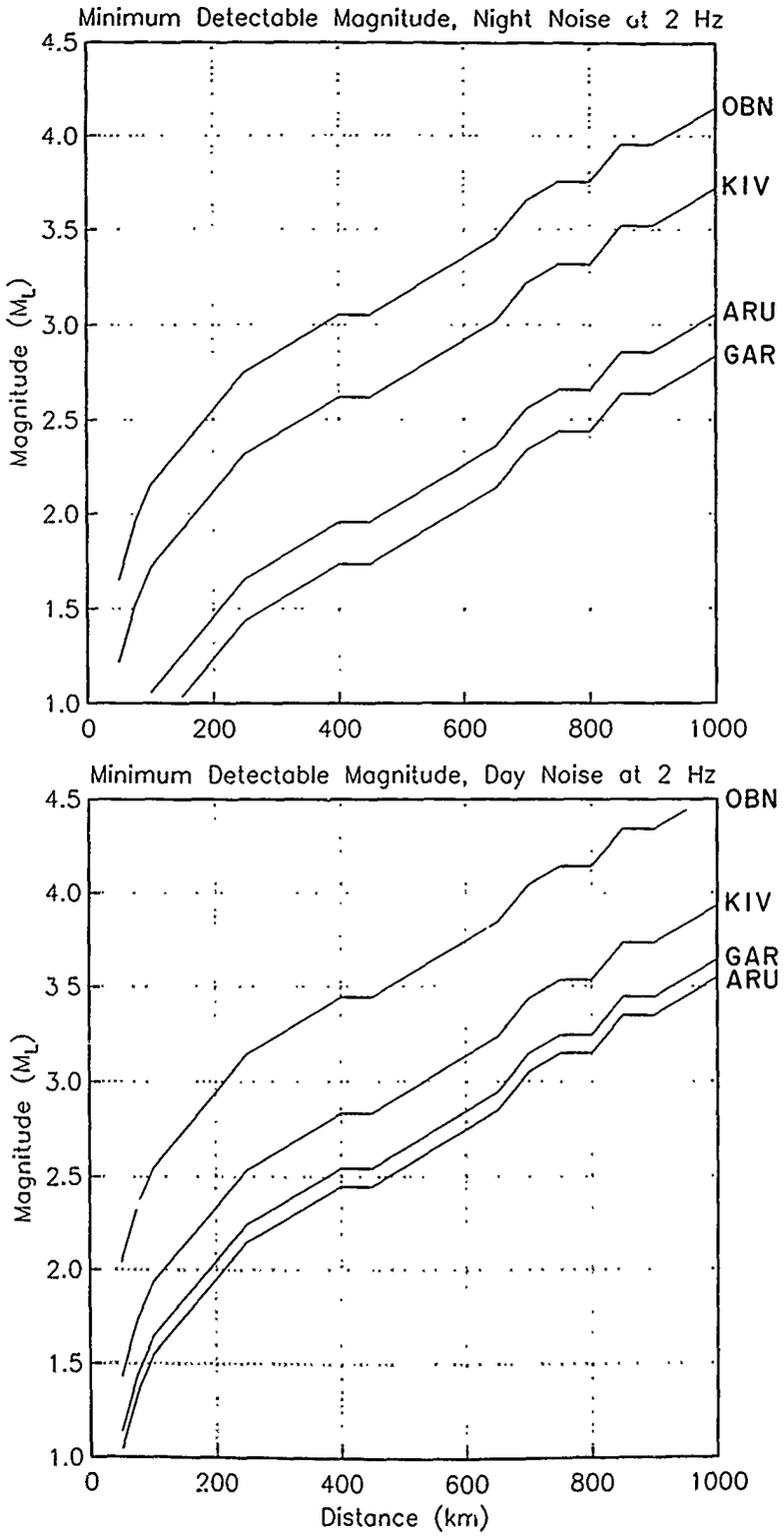

FIG. 10. Minimum detectable magnitudes estimated for a signal with a dominant frequency of 2 Hz.

station that can detect an event under magnitude 3 at 1,000 km. Under day noise conditions, minimum magnitudes at 1,000 km range from 3.5 to 4.5. OBN is particularly bad due to the high peak in its noise profile centered around 2.3 Hz. At other stations, the increase in detectable magnitude at 2 Hz is due mainly to signal attenuation, rather than an increase in noise levels. In reality, the dominant signal frequency decreases with distance, and thus a more appropriate estimate of minimum magnitude would use noise results and magnitude corrections for different frequencies with changing distance. Sereno and Bratt (1989) show estimates of 90 per cent M_L detection thresholds for noise levels and frequency-dependent attenuation models appropriate for the NORESS array. At 1,000 km, they estimate a detection threshold between magnitude 2.5 and 2.7, somewhat lower that the 1 Hz nighttime thresholds estimated for the IRIS/IDA/USSR stations.

Conclusions Regarding Noise at IRIS/IDA/USSR Sites

Above 1 Hz, average noise levels depend strongly on the station. In general, OBN has the highest noise levels, approaching −120 dB relative to $(1\ m/s^2)^2/Hz$ between 1 to 3 Hz, and GAR has the lowest noise levels, never exceeding −140 dB above 1 Hz. KIV and ARU show a large increase in noise levels during the day (over 10 dB), while OBN and GAR show smaller time-of-day noise dependence. At all stations, time-of-day noise differences are only significant above 1 Hz. OBN gives an example that a good vault cannot eliminate cultural noise, but becomes essential in reducing its impact.

Below 0.1 Hz, vertical noise levels at the IRIS/IDA/USSR sites are comparable. Average horizontal noise is about 15 dB lower at OBN than other stations, presumably due to the 30 m deep deployment at OBN. Horizontal noise below 0.1 Hz can vary by 15 to 20 dB at a given station, whereas vertical noise is quite stable in this band. At OBN and GAR, horizontal noise levels were observed that occasionally reached quiet vertical levels, but this was not seen at KIV or ARU. Absolute noise levels near the microseism frequency (0.1 to 0.2 Hz) were about equal at all stations at −135 dB during the summer sample. However, they have a very strong seasonal variation, with ARU and OBN showing a large increase in winter over summer noise levels. Seasonal variations in noise are significant only for frequencies less than 1 Hz.

Results from the high-frequency experiment are less representative in that data are limited to a 2-week (or less) period. Above 20 Hz, all stations were observed to have fairly flat noise spectra, with absolute levels between −140 and −155 dB under low noise conditions (recorded at night in the borehole). Between 1 to 20 Hz, OBN has the highest levels of high-frequency noise under low noise conditions. At OBN and CHS, the variation between surface noise and borehole noise, as well as between day versus night noise, is about a factor of 2. Thus, at these stations, deployment of high-frequency sensors in the tunnels would come close to representing the overall noise profile because of the isolation achieved by the tunnel conditions. At ARU and KIV, significant noise reduction is achieved at high frequencies by deploying borehole sensors. In addition, ARU shows an increase in borehole noise levels during the day of about 15 dB above 3 Hz, a consequence of the station location and perhaps the smaller borehole depth. Thus, during the day, ARU and OBN show comparatively high noise levels in the borehole.

In general, high-frequency noise levels are systematically higher than noise levels observed at NORESS from 1 to 20 Hz (Suteau-Henson and Bache, 1988) and in

eastern Kazakhstan from 1 to 80 Hz (Gurrola *et al.*, 1990); the maximum difference with NORESS under low noise conditions ranges from less than 10 dB to about 25 dB, depending on the site and the frequency band. The IRIS/IDA/USSR stations are situated in less remote locations than NORESS or the Kazakh stations, in part due to the requirement of access to communication lines for data telemetry.

A similar study of broadband noise levels at IRIS/IDA sites in the USSR has been carried out by V. D. Theofilaktov of the Obninsk Seismological Observatory in the USSR. He looked at noise levels six times per day from February through November to assess station noise levels averaged through time-of-day and seasonal variations. His results are identical to those presented in this study, once seasonal and daily variations are taken into account.

Beginning in summer 1990, the STS1-VBB sensors at KIV will operate in a new vault dug back into the face of the ridge, well below the ridge top, and isolated from barometric effects. Thus, the long-period horizontal noise should reduce substantially, and high-frequency spectral lines may be reduced as well.

Detectable magnitude versus distance was estimated for IRIS/IDA/USSR stations from observed noise levels with the assumption that the M_L magnitude relation used at NORSAR holds for the USSR. Results show that M_L 2.5 events should be seen within 600 km and M_L 3.0 events should be seen within 1,000 km for night noise conditions with a dominant signal frequency of 1 Hz. *Actual* minimum magnitudes detectable at the stations may be smaller than those estimated here due to conservativeness in the assumptions of signal-to-noise level and noise variance. Because of its low and constant noise level, station GAR shows the best performance for detection. For higher signal frequencies, minimum detectable magnitudes increase significantly. Development of frequency-dependent attenuation models from data observed at the IRIS/IDA/USSR sites should result in a more accurate measure of their detection capability.

ACKNOWLEDGMENTS

I would like to thank Jonathan Berger for discussions on instrumentation and global seismic noise. Jean-Francois Fels provided system noise measurements. Benjamin Powell assisted in data reduction. Vladimir Theofilaktov kindly shared his noise results with me. I thank Oleg Starovoit and his staff at the Obninsk Seismological Observatory, who provide operational support and maintenance for IRIS/IDA broadband operations in the Soviet Union. This research was supported by the National Science Foundation (Grant EAR-87-08478), IRIS, the Incorporated Research Institutions for Seismology (Grant IRIS0135), and the Air Force Geophysical Laboratory (Grant F19628-88-K-0026).

REFERENCES

Agnew, D. C. and J. Berger (1978). Vertical seismic noise at very low frequencies, *J. Geophys. Res.* **83**, 5420–5424.

Båth, M., O. Kulhánek, T. Van Eck, and R. Wahlström (1976). Engineering analysis of ground motion in Sweden: Fourier and response spectra, attenuation, regional magnitude, energy, acceleration, Report No. 5-76, Seismological Institute, Uppsala University, 48 pp.

Berger, J., H. K. Eissler, F. L. Vernon, I. L. Nersesov, M. B. Gokhberg, O. A. Stolyrov, and N. T. Tarasov (1988). Studies of high-frequency noise in eastern Kazakhstan, *Bull. Seism. Soc. Am.* **78**, 1744–1758.

Gurrola, H., J. B. Minster, F. L. Vernon, H. K. Given, J. Berger, and R. Aster (1990). Analysis of high-frequency seismic noise in the western United States and eastern Kazakhstan, *Bull. Seism. Soc. Am.* **80**, 951–970.

Harjes, H. P. (1990). Design and siting of a new regional array in central Europe, *Bull. Seism. Soc. Am.* **80**, Part B, 1801–1817.

Sereno, T. J. (1990). Frequency-dependent attenuation in eastern Kazakhstan and implications for seismic thresholds in the USSR, *Bull. Seism. Soc. Am.* **80**, Part B, 2089–2105.

Sereno, T. J. and S. R. Bratt (1989). Seismic detection capability at NORESS and implications for the detection threshold of a hypothetical network in the Soviet Union, *J. Geophys. Res.* **94**, 10397–10414.

Steim, J. M. (1986). The very-broad-band seismograph, *Ph.D. Thesis*, Harvard University, Cambridge, MA.

Suteau-Henson, A. and T. C. Bache (1988). Spectral characteristics of regional phases recorded at NORESS, *Bull. Seism. Soc. Am.* **78**, 708–725.

Wielandt, E. and G. Streckeisen (1982). The leaf-spring seismometer: Design and performance, *Bull. Seism. Soc. Am.* **72**, 2349–2367.

INSTITUTE OF GEOPHYSICS AND PLANETARY PHYSICS
SCRIPPS INSTITUTION OF OCEANOGRAPHY
UNIVERSITY OF CALIFORNIA–SAN DIEGO
LA JOLLA, CALIFORNIA 92093

Manuscript received 16 February 1990

Bulletin of the Seismological Society of America, Vol. 80, No. 6, pp. 2089–2105, December 1990

FREQUENCY-DEPENDENT ATTENUATION IN EASTERN KAZAKHSTAN AND IMPLICATIONS FOR SEISMIC DETECTION THRESHOLDS IN THE SOVIET UNION

BY THOMAS J. SERENO, JR.

ABSTRACT

The frequency-dependent attenuation of regional seismic phases recorded by three stations near the nuclear explosion test site in eastern Kazakhstan is estimated by inverting spectra from 21 events with magnitudes between 2.3 and 4.6 at distances between 200 and 1300 km. The *Pn* spectra are inverted between 1 and 10 Hz, and the *Lg* spectra are inverted between 0.5 and 2.5 Hz. The motivation for this study is that previous estimates of detection capability in the Soviet Union are based on data recorded in other regions (eastern North America and Scandinavia) and therefore have large uncertainty. The data recently recorded in eastern Kazakhstan provide an excellent opportunity to compare regional wave propagation and noise characteristics at these sites to conditions assumed in previous detection capability simulations. It is found that attenuation in eastern Kazakhstan is not much different from attenuation in Scandinavia, but it is greater than attenuation in eastern North America. This implies that estimates of detection thresholds that assume attenuation like that observed in eastern North America will be lower than estimates of detection thresholds that assume attenuation like that observed in eastern Kazakhstan or Scandinavia. However, it is not known how well data recorded in eastern Kazakhstan represent conditions in other areas of the Soviet Union.

INTRODUCTION

Simulations of detection and location capability are used to assess the ability of regional seismic networks to monitor existing and potential nuclear explosion test ban treaties. Four recent investigations have produced simulations of the detection capability of regional seismic networks including stations inside the Soviet Union (Evernden, 1976; Hannon, 1985; Evernden *et al.*, 1986; Sereno and Bratt, 1989). The accuracy of these esimates depends on the accuracy of the assumed frequency-dependent attenuation of regional seismic phases and ambient noisc levels. All of these studies extrapolate attenuation and noise characteristics estimated from data recorded in regions other than Soviet Union, and are therefore subject to much uncertainty. Evernden (1976) estimated the m_b detection threshold for a network including 15 stations external to the Soviet Union and 15 stations internal to the Soviet Union. He used regional *Pn* attenuation curves derived from 1 to 3 Hz amplitude data recorded in the eastern United States to normalize the simulations (Evernden, 1967). He estimated the 90 per cent m_b threshold for detection at four stations for this network to be between 3.2 and 3.6 for events within the Soviet Union. Hannon (1985) extended this calculation by replacing the 15 internal stations with regional arrays and by explicitly using multiple seismic phases. He estimated the 90% m_b detection threshold for this network to be between 2.4 and 3.1 for events in the Soviet Union. Hannon's (1985) simulations were normalized by the same *Pn* attenuation curves as used by Evernden (1976), but he assumed a 12 dB noise reduction for the array stations.

Evernden *et al.* (1986) and Sereno and Bratt (1989) used estimates of broadband propagation and noise characteristics to simulate detection capability. Evernden

et al. (1986) used a *Pn* attenuation model for the eastern United States characterized by r^{-2} geometric spreading and a constant Q of 9000. This model is approximately equal to the attenuation of a pure elastic head wave, and is used by Evernden *et al.* (1986) to extrapolate the 1 to 3 Hz attenuation model of Evernden (1967) to higher frequency. They express the detection capability of a network of 15 external and 25 internal broadband single stations at fixed frequency as the expected number of detections (at the 90% confidence level) for a given event size at epicenters internal to the Soviet Union. Their results imply a four-phase detection threshold of less than m_b 2 throughout the Soviet Union at 5 Hz, and a threshold of less than m_b 1 at 30 Hz. These results are remarkably different from those of Sereno and Bratt (1989). They simulated the detection capability of a network of 13 external and 20 internal broadband stations based on regional wave attenuation and noise estimates derived from data recorded by the NORESS array in Norway (Sereno *et al.*, 1988). For a network of single stations they estimate the 90% threshold for detecting three *P* phases to be M_L 2.7 to 3.3. If the single stations are replaced with arrays, the threshold is reduced to M_L 2.4 to 2.7. The large difference between the Evernden *et al.* (1986) and Sereno and Bratt (1989) capability estimates is a direct consequence of the different *Pn* attenuation models at frequencies greater than a few Hertz. Thus, it is clear that accurate estimates of *Pn* attenuation in the Soviet Union are vital for meaningful detection capability simulation.

The largest uncertainty in previous detection capability simulations is the result of an inadequate knowledge of regional wave attenuation and noise characteristics in the Soviet Union. This is particularly important for frequencies greater than a few Hertz, since high-frequency data recorded in the Soviet Union have only recently become available. One such data set includes regional seismograms recorded by three broadband stations near the nuclear explosion test site in eastern Kazakhstan. These data were recorded in 1987 as part of a joint experiment involving the National Resources Defense Council (NRDC) in the United States and the Academy of Sciences in the Soviet Union (e.g., Berger *et al.*, 1988; Given *et al.*, 1990). These data provide an excellent opportunity to compare regional wave propagation and noise models used to simulate detection capability to observed conditions at the three NRDC sites. In this article, I estimate the frequency-dependent attenuation of regional *Pn* and *Lg* phases recorded by the NRDC stations. The results are compared to previous attenuation estimates for the eastern United States and Scandinavia, and the implications for detection capability are discussed.

Three seismic stations were installed in 1987 within 200 km of the principal underground nuclear explosion test site in eastern Kazakhstan (Berger *et al.*, 1988). Each station is equipped with two three-component surface seismometers and a three-component borehole seismometer. The station locations and sensor depths of the borehole seismometers are listed in Table 1. The data recording mode was event-triggered, and the signals were digitized at 250 samples/sec. Berger *et al.* (1988) give a complete description of the NRDC sites and instrumentation.

The data used in this study consist of *Pn* and *Lg* phases recorded by one or more of the three NRDC stations from 21 regional events at distances between 200 and 1300 km. Event magnitudes are approximately 2.3 to 4.6. Table 2 lists the location, origin time, and magnitude of each event used in this study. The station locations and event epicenters are plotted on a map in Figure 1.

Events 1, 2, 3, 5, and 9 are earthquakes listed in the Preliminary Determination of Epicenters (PDE). Figure 2 displays waveforms for event 9 recorded by the borehole sensor at the three NRDC sites. The location of this event is from Thurber

TABLE 1
NRDC STATION LOCATIONS

Station Name	Latitude	Longtidue	Elevation (m)	Borehole Sensor Depth (m)
Karkaralinsk (KKL)	49.333	75.383	1000	66
Karasu (KSU)	49.950	81.083	420	101
Bayanaul (BAY)	50.817	75.550	600	99

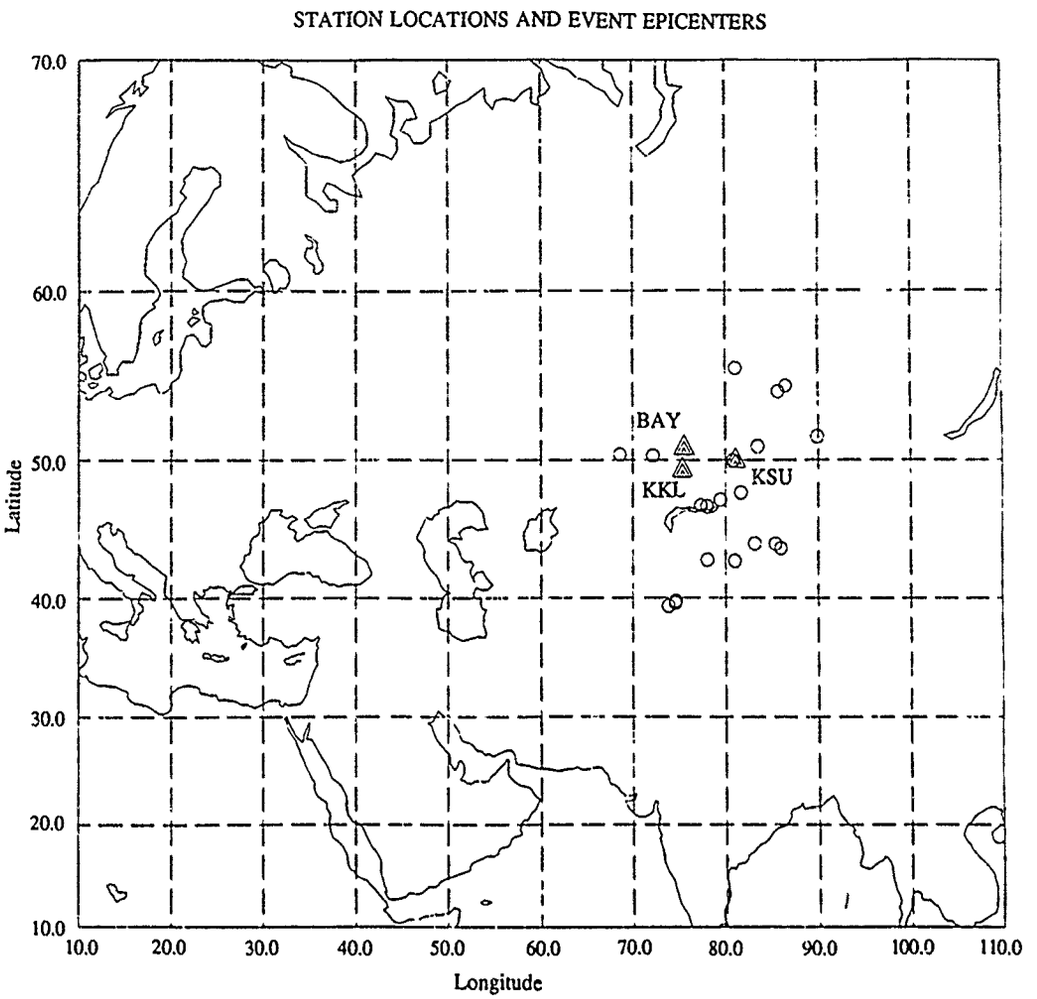

FIG. 1. Map showing the station locations (triangles) and event locations (circles) for the NRDC data set. The station parameters are listed in Table 1, and the event parameters are listed in Table 2.

et al. (1989), who used travel times and azimuths determined from data recorded at the three NRDC stations to obtain a location 40 km east of the PDE location. Event 17 is a smaller earthquake that occurred in the same region as event 9 (Tien Shan), but was not reported in the PDE (Thurber *et al.*, 1989). Event 13 is a mining explosion near Lake Balkash (Thurber *et al.*, 1989). Events 19 and 20 are 10-ton calibration shots detonated west of the city of Karaganda (Given *et al.*, 1990). The locations of the remaining events in Table 2 were determined by seismologists at the Center for Seismic Studies (CSS) based on travel time picks from the NRDC data. Event 21 is close to the mining explosion in the Lake Balkash area reported

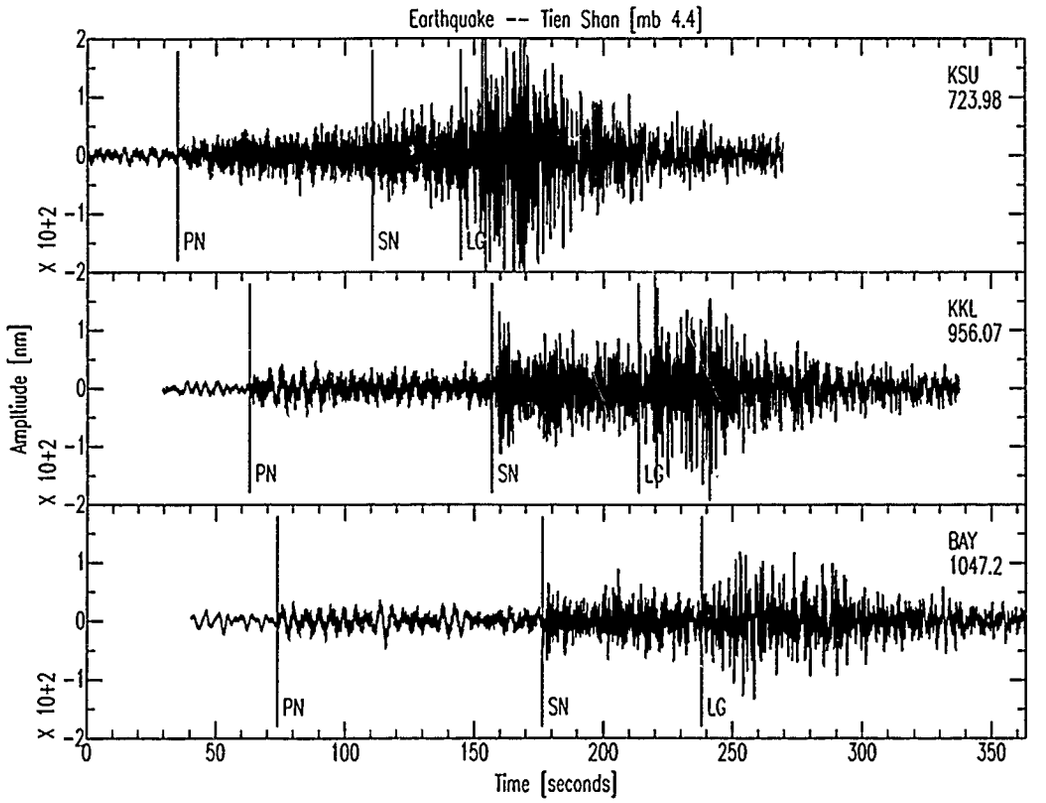

FIG. 2. Vertical-component seismic waveforms recorded by the borehole sensor at the three NRDC stations for an m_b 4.4 earthquake in Tien Shan (event 9, Table 2). The station name and epicentral distance are plotted in the upper right corner in each panel. *Pn*, *Sn*, and *Lg* arrival times are indicated. The amplitudes are plotted in nanometers at 1 Hz. These amplitudes are only approximate, since the instrument response (flat to velocity between 0.2 and 100 Hz) has not been deconvolved.

by Thurber *et al.* (1989) and occurred at a similar time of day. Also, the data recorded at Bayanaul display a strong *Rg* phase indicative of shallow depth. Thus, event 21 is probably a mining explosion in the Lake Balkash area. Events 7 and 10 are probably earthquakes. Their locations are between the PDE locations for events 5 and 9. The remainder of the events are of unknown origin, although it is likely that many are near-surface explosions.

All available short-period data were processed with the procedures described below, but the vertical-component borehole data are emphasized because the surface seismometers are typically characterized by higher noise levels (Berger *et al.*, 1988). Also, the vertical component data provide direct comparison to our previous results for NORESS. The vertical-component waveforms recorded by the borehole sensor for all of the events in Table 2 are displayed by Sereno (1989).

The waveforms are filtered over four frequency bands, 1 to 3, 3 to 5, 4 to 8, and 8 to 16 Hz. The broadband and filtered traces are displayed with theoretical arrival times (based on the locations in Table 2) for interactive picking of regional phases. Fourier spectra are computed for each phase. A symmetric 10% cosine taper is applied to a time window starting 0.3 sec before the picked arrival time. The duration of the analyzed segment depends on the phase identification. For *Pn* the duration was set to 10 sec and a fixed group velocity window of 3.6 to 3.0 km/sec was used to determine the duration for the *Lg* spectral estimate. Noise spectra for each phase are calculated for a 5-sec window starting 5.5 sec before the picked

TABLE 2
EVENT PARAMETERS

Event	Julian day	Origin time	Latitude	Longitude	Depth (km)	Magnitude*	Event type†
1	136	18:21:13.7	39.339	73.812	33.0	4.3 m_b	EQ
2	120	6:54:57.0	39.733	74.594	10.0	4.3 m_b	EQ
3	122	21:38:33.2	39.569	74.541	33.0	4.6 m_b	EQ
4	123	8:52:08.0	51.512	89.874			
5	146	13:44:19.9	42.923	78.063	20.0	4.6 m_b	EQ
6	164	2:19:13.2	47.300	79.473			
7	162	18:30:04.0	42.842	80.968			EQ
8	232	8:57:32.5	50.374	68.615			
9	234	0:21:50.7	44.129	85.363	58.0	4.4 m_b	EQ
10	239	7:52:21.5	44.148	83.133			EQ
11	239	8:05:26.2	49.982	80.832		2.6 M_L	EX
12	239	8:51:21.2	54.665	86.488			
13	239	9:38:34.8	46.900	77.389		2.5 M_L	EX
14	239	11:04:40.5	50.905	83.464		2.3 M_L	EX
15	242	4:57:11.3	47.808	81.658			
16	243	7:57:42.9	55.739	81.080		2.6 M_L	EX
17	244	3:44:38.8	43.808	85.948			EQ
18	244	11:58:21.6	54.316	85.648		2.5 M_L	EX
19	245	7:00:00.0	50.281	72.172	0.0	2.9 M_L	EX
20	246	7:00:00.0	50.281	72.172	0.0	2.9 M_L	EX
21	149	9:28:17.0	46.855	78.057		2.9 M_L	EX

* m_b: body wave magnitude (PDE); M_L: *Lg* magnitude based on a correction table for Scandinavia (Båth *et al.*, 1976).

† EQ: earthquake; EX: explosion.

arrival time and are normalized to the signal window length. The spectra are corrected for the instrument response and converted to units of displacement.

NOISE SPECTRA

Berger *et al.* (1988) and Gurrola *et al.* (1989) provide detailed descriptions of the noise at the NRDC stations, including plots of ambient moise spectra from 1 to 100 Hz for windy and calm conditions for the borehole and surface instruments at each of the three NRDC stations. This section compares the NORESS noise spectra used by Sereno and Bratt (1989) in their simulations of detection capability to the NRDC station noise spectra computed in exactly the same way between 1 and 20 Hz.

The NORESS single-channel noise spectrum is calculated from 43 samples with 5-sec windows (Suteau-Henson and Bache, 1988). Each of these "samples" is the average spectrum for all elements of the NORESS array. The NRDC station noise spectra are estimated from samples taken prior to *Pn* detections. They include 26 samples with 5-sec windows, and data from the three NRDC stations have been averaged together. Figure 3 plots the average NRDC ambient noise power spectral density (solid curve) bounded by one standard deviation (dashed curves). The dotted curve is the average ambient noise power spectral density at NORESS from Suteau-Henson and Bache (1988). The NORESS noise spectrum is within one standard deviation of the average noise spectrum for the NRDC stations.

GENERALIZED INVERSION

The method of Sereno *et al.* (1988) is used to estimate attenuation and source parameters from the *Pn* and *Lg* spectra recorded by the NRDC stations. The

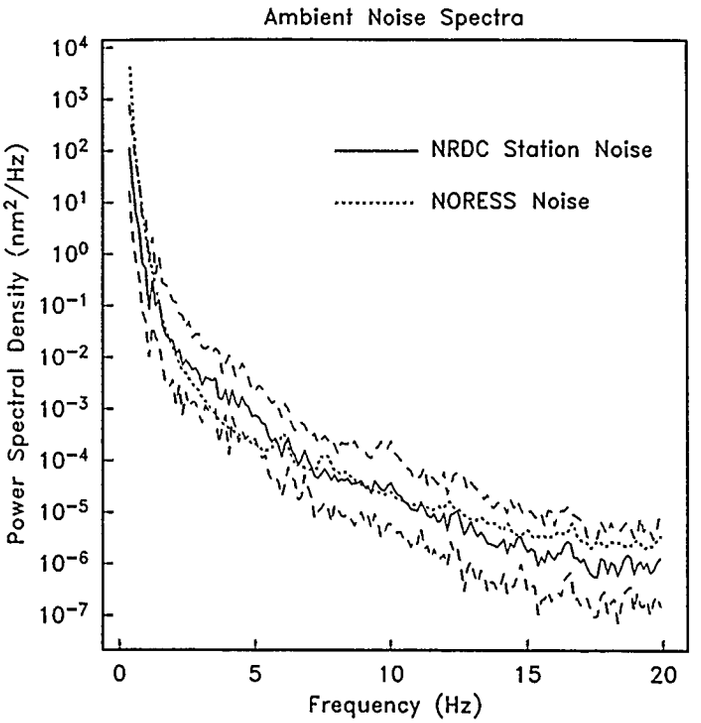

FIG. 3. Ambient noise power spectral density. The solid curve is the average noise spectrum at the three NRDC stations. The dashed curves indicate one standard deviation. The dotted curve is the average ambient noise spectrum at NORESS.

instrument-corrected amplitude spectra are parameterized as

$$A(f, r) = S(f)G(r, r_0) \exp\left[\frac{-\pi f t}{Q(f)}\right] \quad (1)$$

where $S(f)$ is the source spectrum, $G(r, r_0)$ is the geometric spreading function, and the last term is the apparent attenuation for travel time t. The spectra, $A(f, r)$ are corrected for an assumed geometric spreading function and inverted using damped least squares for two parameters describing the source spectrum and two parameters characterizing a power law frequency dependence of $Q(f)$.

The source spectrum is assumed to fall off as f^{-2} beyond a corner frequency that scales inversely with the cube root of the long-period level S_0. The source parameters estimated by the inversion are the long-period source level for each event (which is proportional to seismic moment) and a single parameter that relates corner frequency and long-period level for all events. The relationship between source moment and Lg S_0 for earthquakes is

$$S_0^{eq}(Lg) = \frac{M_0^{eq}}{4\pi\rho_c\beta_c^3} \quad (2)$$

where M_0^{eq} is the earthquake moment, ρ_c is the average crustal density, and β_c is the average shear-wave velocity of the crust. The relationship between Pn S_0 and earthquake moment depends on the source radiation pattern. Since the focal mechanisms for the events studied are unknown, it is not possible to obtain accurate estimates of source moment from the derived Pn source levels. However, explosion

moments can be estimated from Pn S_0 using

$$S_0^{\exp}(Pn) = \frac{M_0^{\exp}}{4\pi\rho_s\alpha_s^3} \tag{3}$$

where ρ_s and α_s are the near-surface density and compressional-wave velocity, respectively. The excitation of Lg by explosions is depth-dependent and complicated by near-surface wave conversions. Explosions generate Lg primarily through P–SV mode conversions and scattering, while earthquakes produce much more direct shear wave energy. Since the excitation function for Lg is unknown for near-surface explosions, it is not possible to estimate explosion moments from Lg S_0.

The geometric spreading function is assumed to be independent of frequency and is characterized by a power-law distance dependence

$$\begin{aligned} G(r, r_0) &= (1/r) \qquad \text{for } r \leqq r_0 \\ G(r, r_0) &= r_0^{-1}(r_0/r)^m \quad \text{for } r \geqq r_0 \end{aligned} \tag{4}$$

where r is epicentral distance and r_0 is a transition distance from spherical spreading to spreading rate m. The Lg phase consists of higher-mode surface waves which are accurately described at long ranges by cylindrical spreading ($m = \frac{1}{2}$), provided the window length is sufficient to encompass the entire dispersed wave train. By comparing the long-period amplitude spectrum of Lg to moments calculated from long-period surface waves, Street *et al.* (1975) empirically determined $r_0 \approx 100$ km, or roughly twice the crustal thickness. Measuring the decay rate of synthetic Lg phases computed for an elastic medium, Herrmann and Kijko (1983) verified that Lg frequency domain spreading was accurately described as cylindrical and substantiated the empirical result of Street *et al.* (1975) for r_0. Therefore Lg geometric spreading is approximated by (4) with $r_0 = 100$ km and $m = \frac{1}{2}$. Of course, this is only an approximation to the Lg spreading, and it is possible that the true spreading in eastern Kazakhstan is significantly more complicated and may include frequency dependence.

The geometric spreading of Pn is a complicated function of the velocity gradient in the upper mantle, and it is probably frequency-dependent. Therefore a simple parameterization such as (4) is not likely to be applicable to Pn over a broad frequency and distance range. Sereno and Given (1990) computed synthetic Pn phases for an elastic earth model consisting of a 40-km thick homogeneous crust over a mantle with a compressional-wave velocity gradient of 0.0013 sec^{-1}. This gradient approximately corresponds to the earth-flattening transformation of a homogeneous upper mantle. They found a strong frequency dependence in the Pn geometric spreading for this model. However, over limited distance ranges and at long periods a power-law range dependence may be adequate to approximate the spreading of Pn. For example, Figure 4 plots synthetic Pn attenuation at 1.25 Hz (Sereno and Given, 1990). The dashed curve is the best-fitting power law model determined by least squares. The spreading rate for this model is $r^{-1.25}$. This Pn spreading rate is consistent with the empirical results of Sereno *et al.* (1988) for data recorded at NORESS. Therefore, the Pn geometric spreading is approximated by (4) with $r_0 = 1$ km and $m = 1.3$. Note, however, that the Pn $Q(f)$ includes any frequency dependence occurring in the geometric spreading function, and so it probably does not represent upper mantle anelasticity.

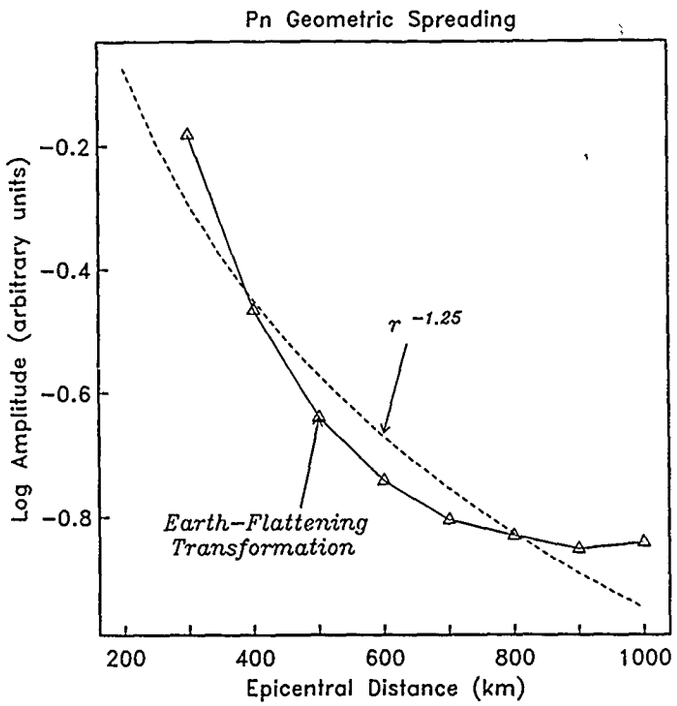

FIG. 4. *Pn* geometric spreading. The solid curve is *Pn* attenuation with distance at 1.25 Hz calculated for an elastic earth model with upper mantle velocity gradient equivalent to the earth-flattening transformation of a homogeneous medium (Sereno and Given, 1990). The dashed curve is $r^{-1.25}$. Note that the difference between these two curves is considerably less than 0.3, which is a typical standard deviation of log M_0 versus magnitude relations (e.g., Veith and Clawson, 1972; Dwyer *et al.*, 1983; Hasegawa, 1983; Sereno *et al.*, 1988).

Lg ATTENUATION

The *Lg* inversion includes 37 spectra from 21 events recorded by up to three stations. The spectra were inverted between 0.5 and 2.5 Hz. This frequency range is based on a comparison of the *Lg* spectra to the pre-*Lg* noise spectra normalized to the signal window length. The result of the inversion is a range of attenuation and source models corresponding to a broad minimum in the data residuals. For example, Figure 5 plots the value of *Lg* Q at 1 Hz (Q_0) against the exponent of a power-law frequency dependence (η) for models that produce data variances that differ by less than 1%. This range of models was determined by fixing η and inverting for S_0 for each event, Q_0, and the corner frequency scaling parameter. In general, models with low Q_0 are associated with higher source levels than models with high Q_0 since the combination these parameters is constrained to fit the same 1 Hz amplitude. Models with low Q_0 are also associated with high values of η since these parameters are constrained by spectral shape. Since most of the events have corner frequencies greater than the upper limit of the frequency band inverted, the attenuation results are insensitive to the source assumptions.

A simple constraint that can be applied to reduce the trade-off among model parameters is to require consistency in the source levels derived for each event from data recorded at different stations. For example, Figure 6 plots *Lg* S_0 for two of the $Q(f)$ models in Figure 5. The model with higher Q_0 produces more consistent source levels from data recorded at different stations than the model with lower Q_0. For example, the source levels for events 9 and 17 derived from three stations are nearly the same for *Lg* $Q(f) = 650$ but differ by over 50% for *Lg* $Q(f) = 345\ f^{0.4}$. The

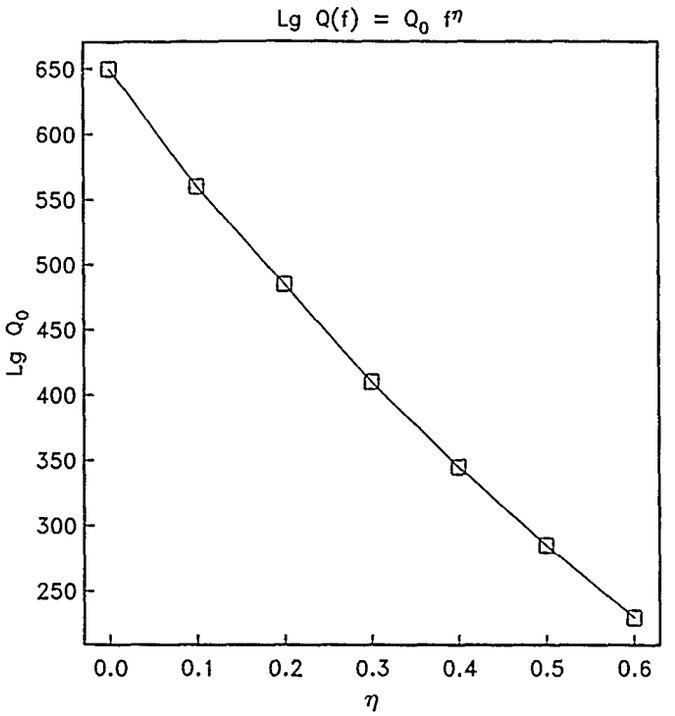

FIG. 5. *Lg* $Q(f)$ models consistent with the NRDC observations. The value of *Lg* Q at 1 Hz (Q_0) is plotted against the exponent of a power-law frequency dependence (η). These models combine with different source levels to produce data variances that differ by less than 1%.

difference in epicentral distance between the farthest and closest station for these events is over 300 km. Events 1, 5, 11, and 14 also have more consistent source levels for the higher Q_0 model. In general, there is a distance dependence in the derived source levels for events recorded at multiple stations for models with Q_0 less than about 500. This implies that *Lg* $Q(f)$ in eastern Kazakhstan is between 500 $f^{0.19}$ and a constant value of 650. Figure 7 is an example of the fit between theoretical and observed spectra at the three NRDC stations for event 9 in Table 2. The theoretical *Lg* spectra are based on a constant Q of 650. Note, however, that all other models in Figure 5 produce similar fits to the observed spectra. Comparisons of theoretical and observed spectra for all events used in the inversion are given by Sereno (1989).

The earthquake moments are estimated from *Lg* S_0 using (2) with ρ_c = 2.5 gm/cm^3 and β_c = 3.5 km/sec. The S_0 are approximately equal to the logarithmic mean of the source level below the corner frequency. Hermann and Kijko (1983) use synthetic *Lg* spectra to demonstrate that the logarithmic mean plus one standard deviation (close to the peak rather than the mean spectral amplitude) should be used for the S_0^{eq} in (2). Since the standard deviation of log S_0 is approximately 0.3, the S_0 are multiplied by two before estimating earthquake moment using (2). The earthquake moments for the five events in Table 2 which were assigned PDE magnitudes are generally consistent with moment versus magnitude relations determined for eastern North America and Scandinavia (e.g., Bungum *et al.*, 1982; Dwyer *et al.*, 1983; Hasegawa, 1983; Shin and Herrmann, 1987; Sereno *et al.*, 1988).

In a previous analysis of the NRDC data, Given *et al.* (1990) applied a spectral ratio method to estimate *Lg* attenuation in eastern Kazakhstan. They used data from one of the 10-ton calibration shots (event 20). They concluded that the average

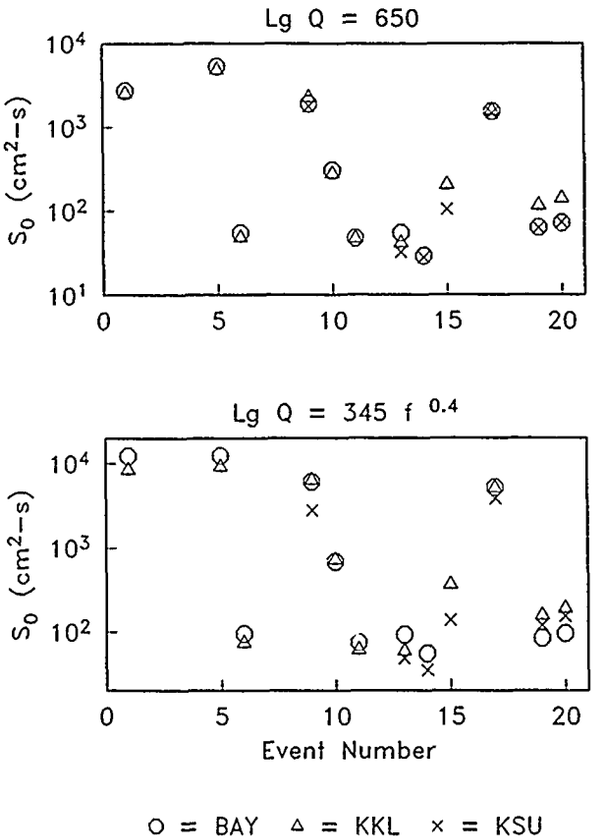

FIG. 6. Derived source levels (S_0) for (a) $Lg\ Q(f) = 650$ and (b) $Lg\ Q(f) = 345 f^{0.4}$. The event numbers are from Table 2. Only events recorded at multiple stations are plotted. Each station is plotted with a different symbol. Note that the higher Q_0 model reduces the variance in the derived source levels from multiple station observations.

value of *Lg Q* at 1 Hz is 500 and increases with frequency, although the frequency exponent is poorly constrained. They approximate the frequency dependence as $f^{0.4}$ to about 5 Hz with a possible increased dependency at higher frequency. Their *Lg Q* at 1 Hz is consistent with the value obtained here, but the frequency exponent is somewhat higher. For example, the model in Figure 5 with Q_0 equal to 500 has a frequency exponent close to 0.2. This model is constrained by data at frequencies less than 2.5 Hz. A comparison of the pre-*Lg* noise spectrum with the *Lg* signal spectrum for this event suggests that *Sn* coda may contaminate the *Lg* spectrum at KSU beyond 4 to 5 Hz. Thus, the higher frequency exponent for *Lg Q* determined by Given *et al.* (1990) may reflect an increased contribution of *Sn* coda at high frequencies.

It is interesting to compare *Lg* attenuation in eastern Kazakhstan to the attenuation in Scandinavia and eastern North America, since conditions in these regions have been used as a basis for normalizing simulations of detection capability in the Soviet Union (e.g., Evernden, 1976; Hannon, 1985; Evernden *et al.*, 1986; Sereno and Bratt, 1989). Sereno *et al.* (1988) estimated *Lg* attenuation for paths to NORESS. They found that the attenuation is consistent with cylindrical geometric spreading and $Lg\ Q(f) = 580 f^{0.18}$ between 1 and 3 Hz. This attenuation at 1 Hz is consistent with the range of models determined for eastern Kazakhstan (Figure 5), and the frequency exponent is only slightly higher. Thus, within the resolution of

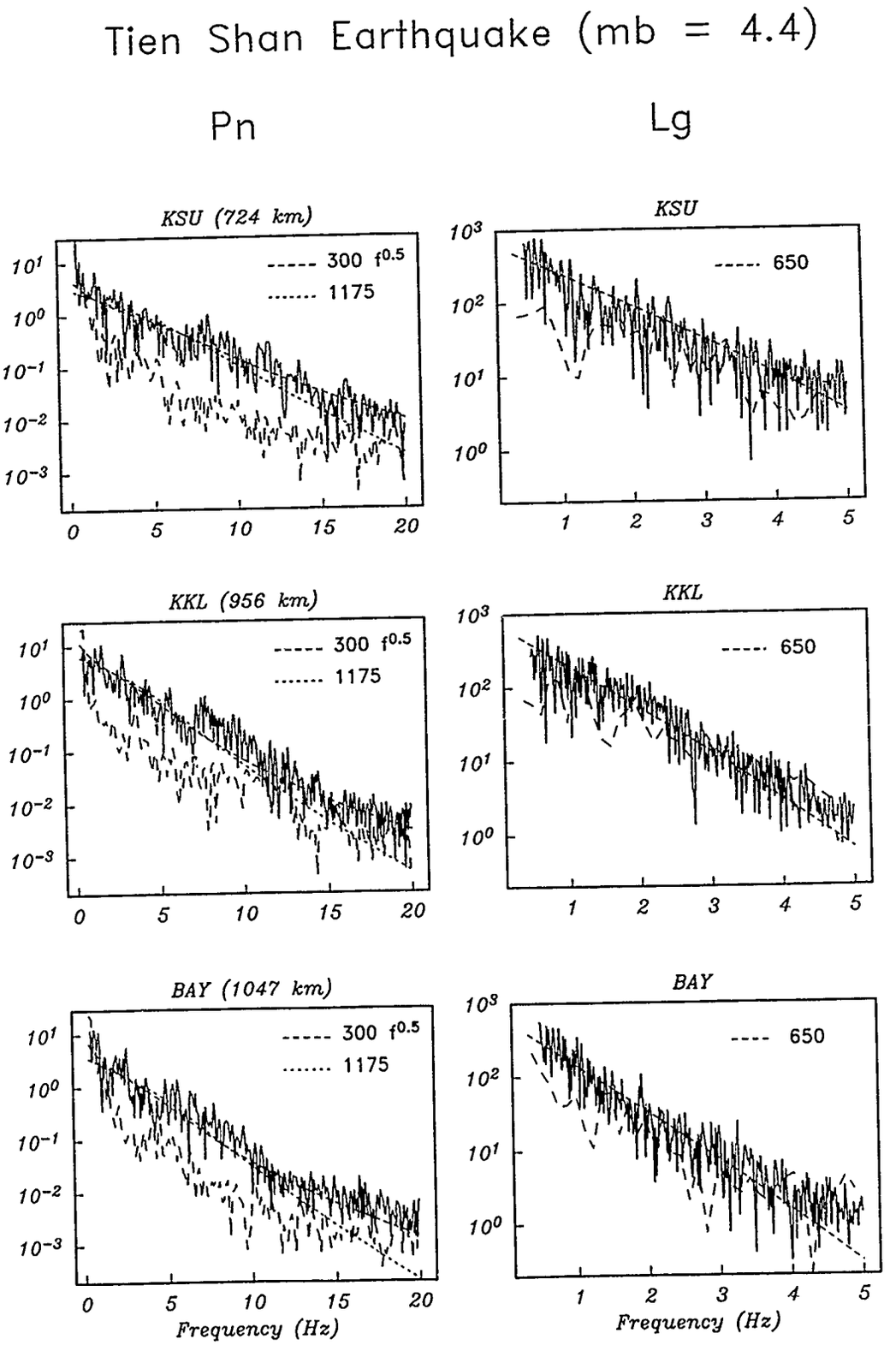

FIG. 7. Comparison of theoretical *Pn* (*left*) and *Lg* (*right*) spectra based on the inversion results to observed spectra for an m_b 4.4 earthquake in Tien Shan (event 9, Table 2). The Q models used to calculate the theoretical spectra are indicated in the upper right corner of each panel. The spectra are labeled by station name and epicentral distance. The lowest dashed curves in each panel are noise spectra calculated from a 5-sec window preceding the arrival. These noise spectra are scaled to the signal window length.

the data, *Lg* attenuation in Scandinavia is the same as *Lg* attenuation in eastern Kazakhstan. However, comparison to attenuation estimates for North America suggests that *Lg* propagation in that region is more efficient than it is in Scandinavia and eastern Kazakhstan. For example, typical *Lg* $Q(f)$ estimates for eastern North America vary between 800 $f^{0.3}$ and 1100 $f^{0.2}$ (e.g., Singh and Herrmann, 1983; Hasegawa, 1985; Goncz *et al.*, 1987; Chun *et al.*, 1987; Gupta and McLaughlin, 1987). Therefore, estimates of *Lg* detection thresholds that are based on attenuation in eastern North America are expected to be lower than the actual thresholds in eastern Kazakhstan. However, it is uncertain whether the conditions at the NRDC sites are representative of other areas within the Soviet Union.

Pn Attenuation

The *Pn* inversion includes 26 spectra from 21 events recorded by up to three stations. The spectra were inverted between 1 and 10 Hz based on signal-to-noise ratio. As was the case for *Lg*, a range of attenuation and source models produce similar data variances. Figure 8 plots *Pn* Q_0 against η for models that produce data variances that differ by less than 1%. However, unlike the *Lg* inversion, the range of *Pn* $Q(f)$ models cannot be resolved on the basis of the consistency of the source moment derived from data recorded at different stations. This is partly due to limitations of the data set (e.g., multiple station data are not available for many events, and nearly half of the events are earthquakes with unknown radiation patterns) and partly due to uncertainty in the *Pn* geometric spreading assumptions. Therefore, two attenuation models near the extremes of Figure 8 are used as a basis for comparison to *Pn* propagation in other regions, $Q(f) = 300\ f^{0.5}$ and $Q(f) = 1175$.

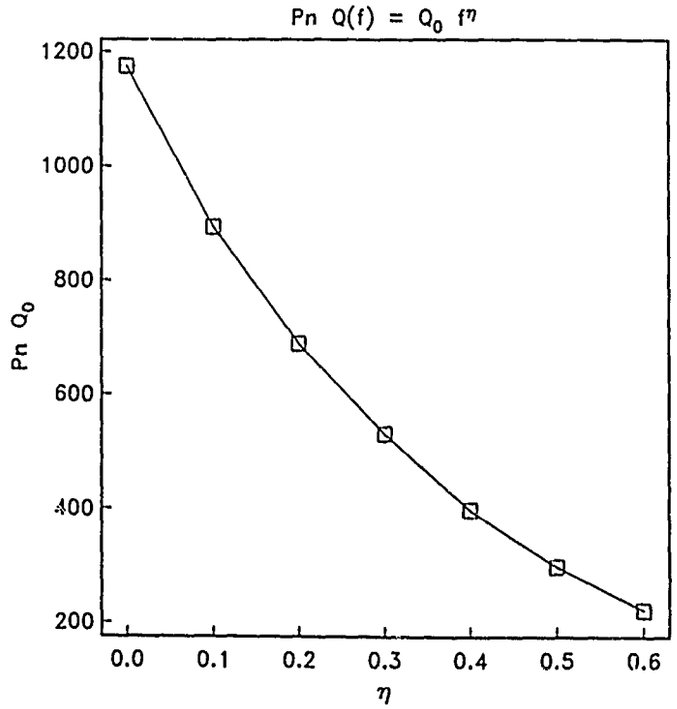

FIG. 8. *Pn* $Q(f)$ models consistent with the NRDC observations. The value of *Pn* Q at 1 Hz (Q_0) is plotted against the exponent of a power-law frequency dependence (η). These models combine with different source levels to produce data variances that differ by less than 1%.

The left side of Figure 7 compares theoretical *Pn* spectra for these two attenuation models to observed *Pn* spectra for event 9 in Table 2. Note that the two theoretical spectra are nearly identical between 1 and 10 Hz. The corner frequency for this event is approximately 4.0 Hz. In general, the corner frequency of an M_L 3.0 event is estimated from the inversion to be 5 to 6 Hz. This is consistent with the results of Given *et al.* (1990), who used a curve-fitting algorithm to determine the corner frequency of event 20 ($M_L = 2.9$) to be 5 to 6 Hz from *Lg* spectra and 7 Hz from *Pg* spectra. Corner frequency scales with event size such that the corner frequency of the largest event in the data set is between 3 and 4 Hz.

The explosion moments are calculated from *Pn* S_0 using (3) with $\rho_s = 2.5$ gm/cm^3 and $\alpha_s = 5.0$ km/sec. Events 13, 19, and 20 are known to be explosions (Thurber *et al.*, 1989). As discussed earlier, event 21 is probably an explosion in the Lake Balkash area. Other likely explosions are events 11, 14, 16, and 18, based on low *Lg/Pn* ratios, origin time (morning to mid-afternoon), location and general aseismicity of the region near the eastern Kazakhstan explosion test site, and the presence of *Rg* (Thurber *et al.*, 1989). The *Lg* magnitudes of these events are calculated using a correction table for paths in Scandinavia (Båth *et al.*, 1976). It was shown in the previous section that *Lg* attenuation in eastern Kazakhstan is similar to that observed at NORESS, so application of this correction table is reasonable. Figure 9 plots explosion moment versus *Lg* magnitude for the two *Pn* $Q(f)$ models. The moments are averaged for events recorded at multiple stations. The solid line is the log M_0 versus magnitude relation determined by Sereno *et al.* (1988) for mining explosions recorded at NORESS, $\log M_0^{exp} = 1.08\, M_L + 17.6$. The

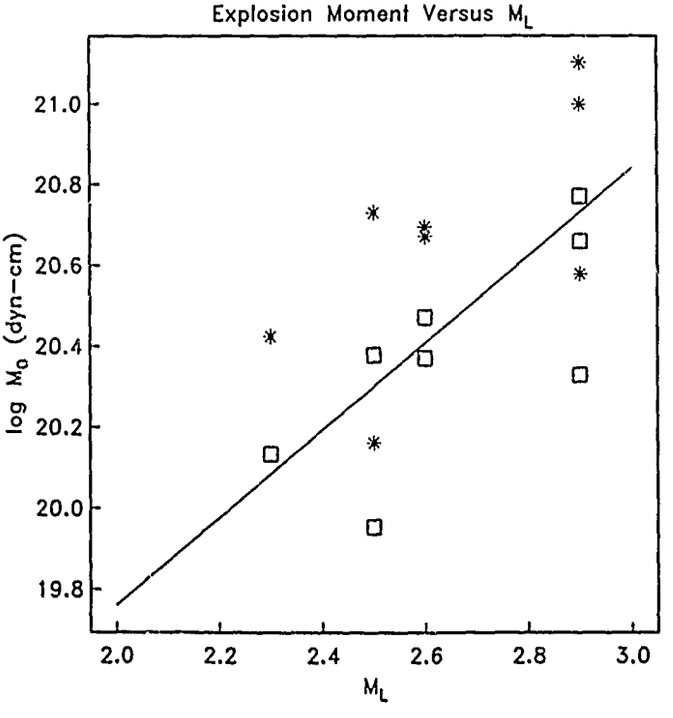

FIG. 9. Moment versus magnitude for presumed explosions (Table 2). The asterisks are moments for the model with *Pn* $Q(f) = 300f^{0.5}$ and the squares moments for the model with *Pn* $Q(f) = 1175$. The moments for the lower Q_0 model are about a factor of two higher than the moments associated the higher Q_0 model. The solid line is the explosion moment versus magnitude relation determined by Sereno *et al.* (1988) from NORESS observations.

model with Pn $Q(f) = 1175$ gives explosion moments consistent with this relation, while the moments for the model with $Q(f) = 300\ f^{0.5}$ fit the line about as well when the intercept is 0.3 higher.

Comparison of Pn attenuation in eastern Kazakhstan with attenuation in other regions is difficult because trade-offs among source and path parameters cannot be resolved with the limited NRDC data set. However, the range of $Q(f)$ models determined from the NRDC data includes the model determined by Sereno *et al.* (1988) from NORESS data, $325\ f^{0.48}$. This implies that the shape of the Pn spectrum as a function of distance in eastern Kazakhstan is similar to that observed at NORESS. However, the absolute amplitude of Pn is almost a factor of two larger for the NRDC stations than for NORESS for fixed Lg magnitude. This is because the intercept of the log M_0 versus M_L relation is 0.3 larger for events in eastern Kazakhstan than for events in Scandinavia if the same Pn attenuation model is assumed (Fig. 9). Since the ambient noise at NORESS is almost the same as the noise at the NRDC sites, this implies that estimates of Pn detection thresholds that assume attenuation like that observed in Scandinavia may be as much as 0.2 to 0.3 higher than estimates of thresholds that assume attenuation like that observed in eastern Kazakhstan (if event size is measured in terms of Lg magnitude).

Two recently published attenuation models for paths in eastern North America suggest very different conclusions about the propagation of Pn at high frequencies (>3 Hz). These are the models reported by Evernden *et al.* (1986) and Chun *et al.* (1989). Evernden *et al.* (1986) characterize frequency-dependent Pn attenuation by r^{-2} geometric spreading and a constant Q of 9000. These parameters are based primarily on 1 to 3 Hz amplitude data from paths in the eastern United States. They extrapolate this attenuation to frequencies as high as 40 Hz in their simulations of detection capability. Chun *et al.* (1989) show that the attenuation of regional Pn phases in eastern Canada between 3 and 15 Hz can be described by $r^{-n(f)}$, where $n(f) = 2.17 + 0.02f$. These two models predict similar attenuation at low frequency (1 to 3 Hz), but the model proposed by Evernden *et al.* (1986) predicts much lower attenuation at high frequency. Therefore, the very low detection thresholds estimated by Evernden *et al.* (1986) at high frequency are not supported by the more recent observations in eastern Canada.

The Pn attenuation models determined in this study for eastern Kazakhstan are very similar to the attenuation model proposed by Chun *et al.* (1989) for distances less than about 500 km. To illustrate this, Figure 10 displays theoretical Pn spectra at 300, 500, and 800 km for the attenuation model proposed by Chun *et al.* (1989) and for the two extreme models determined in this study for eastern Kazakhstan (note that the attenuation model determined by Sereno *et al.* (1988) for Scandinavia is nearly identical to the eastern Kazakhstan model with $Q(f) = 300\ f^{0.5}$). A flat source spectrum is assumed, and the spectra are scaled such that all models give the same 1 Hz amplitude at 300 km. The Pn spectra at 300 and 500 km calculated from the attenuation model proposed by Chun *et al.* (1989) for eastern Canada are very similar to the predicted spectra calculated from the attenuation estimated in this study for eastern Kazakhstan. However, the model proposed by Chun *et al.* (1989) predicts more efficient high-frequency propagation at 800 km than does either eastern Kazakhstan model. This suggests that estimates of Pn detection thresholds that assume attenuation like that observed in eastern North America will be lower than estimates of detection thresholds that assume attenuation like that observed in eastern Kazakhstan. However, nearly all of the Pn spectra used in this study at distances greater than 500 km are from earthquakes with $m_b > 4.0$,

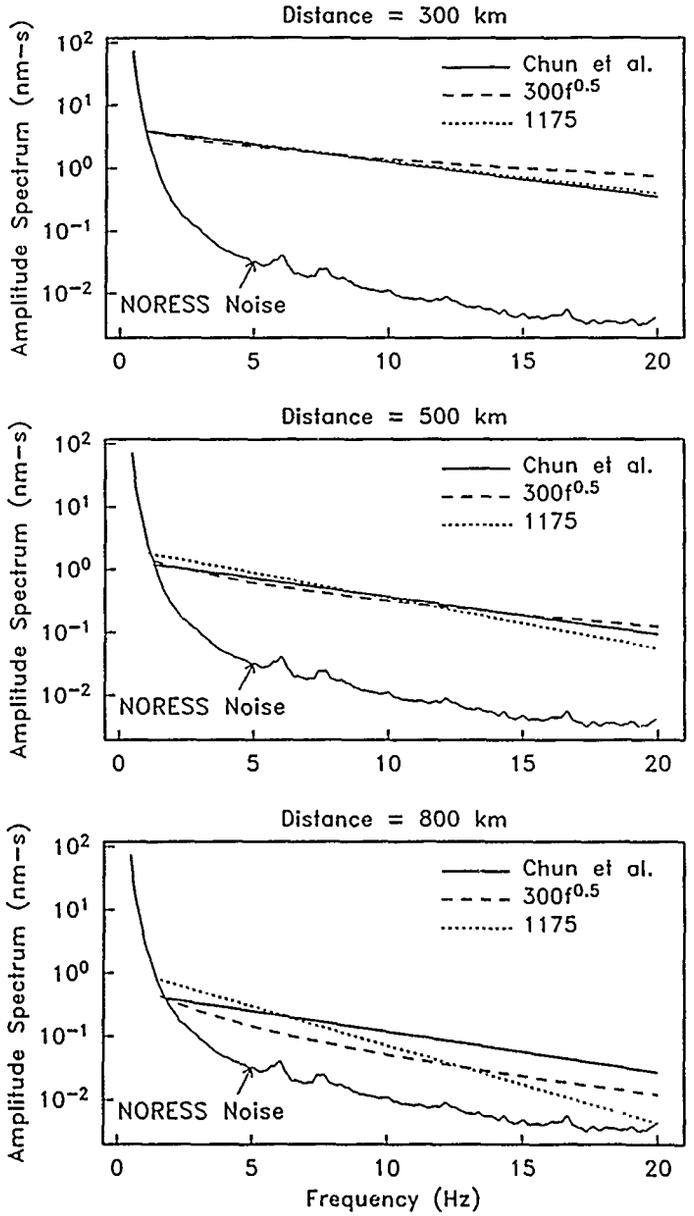

FIG. 10. Theoretical *Pn* spectra at 300, 500, and 800 km for two attenuation models for eastern Kazakhstan ($Q(f) = 300f^{0.5}$ and $Q(f) = 1175$) and for the attenuation model determined by Chun *et al.* (1989) for eastern North America. The lowest curve is the average ambient noise spectrum at NORESS (Suteau-Henson and Bache, 1988).

and the attenuation determined from these data is very sensitive to assumptions about the source spectrum. Also, nearly 80% of the data used by Chun *et al.* (1989) were recorded at distances less than 500 km. Thus, there is still much uncertainty in the efficiency *Pn* propagation at high frequency for distances greater than 500 km in these stable continential regions.

CONCLUSIONS

Accurate estimates of regional wave attenuation in the Soviet Union are required to produce meaningful estimates of the capability of regional seismic networks to monitor underground nuclear explosion testing. However, since data recorded in

the Soviet Union are scarce, simulations of the monitoring capability of seismic networks have been based on experience in other regions (eastern North America and Scandinavia), and therefore have large uncertainty. In this study, I estimated frequency-dependent regional wave attenuation in eastern Kazakhstan and compared the results to attenuation in Scandinavia and eastern North America. The main conclusions are: (1) *Lg* attenuation near the nuclear explosion test site in eastern Kazakhstan is consistent with cylindrical geometric spreading and $Q(f)$ between $500 f^{0.19}$ and 650. This is about the same as the attenuation in Scandinavia, and greater than the attenuation in eastern North America. (2) Trade-offs among source and attenuation parameters in eastern Kazakhstan cannot be resolved for *Pn* due primarily to limitations of the data set. However, it is found that the frequency dependence of *Pn* attenuation in eastern Kazakhstan is similar to that in Scandinavia (although the absolute amplitudes are about a factor of two larger in eastern Kazakhstan for fixed *Lg* magnitude), and that high frequencies (>5 Hz) attenuate more rapidly with distance in eastern Kazakhstan than is implied by previous attenuation models for eastern North America. However, predicted *Pn* spectra based on attenuation in eastern North America are nearly the same as those based on attenuation in eastern Kazakhstan for distances less than about 500 km.

These results imply that (1) estimates of the detection thresholds that assume attenuation like that observed in eastern North America will be lower than estimates of detection thresholds that assume attenuation like that observed in eastern Kazakhstan, and (2) estimates of the *Pn* detection thresholds that assume attenuation like that observed in Scandinavia will be higher than estimates of detection thresholds that assume attenuation like that observed in eastern Kazakhstan by as much as 0.2 to 0.3 (if event size is measured in terms of *Lg* magnitude). Estimates of *Lg* detection thresholds based on attenuation models for eastern Kazakhstan and Scandinavia are expected to be nearly the same. Note, however, that it is uncertain whether or not the attenuation and noise in eastern Kazakhstan are representative of conditions elsewhere in the Soviet Union.

The results for Scandinavia are based on data recorded at a single station, and the results for eastern Kazakhstan and eastern North America are based on limited data sets. Therefore, there still exists large uncertainty in the efficiency of regional *Pn* propagation at high frequencies in stable continental regions. It is likely that information gathered from more recent data recorded by the ARCESS and FINESA arrays in Scandinavia, the GERESS array in Germany, and the four IRIS/IDA stations in the Soviet Union will improve the accuracy with which the monitoring capability of seismic networks (including regional stations and arrays) can be estimated.

ACKNOWLEDGMENTS

I thank Jeff Given and Thomas Bache for many helpful discussions and for their careful review of the manuscript. I also thank Holly Given for her help in assembling the NRDC data set and for verifying the calibration data. Much of the data processing was done by Donna Williams at SAIC, and her contribution to the project is gratefully acknowledged.

REFERENCES

Båth, M., O. Kulhánek, T. Van Eck, and R. Wahlström (1976). Engineering analysis of ground motion in Sweden: Fourier and response spectra, attenuation, regional magnitude, energy, acceleration, Report no. 5-76, Seismological Institute, Uppsala University, 48 pp.

Berger, J., H. Eissler, F. Vernon, I. Nersesov, M. Gokhberg, O. Stolyrov, and N. Tarasov (1988). Studies of high-frequency seismic noise in eastern Kazakhstan, *Bull. Seism. Soc. Am.* **78**, 1744–1758.

Bungum, H., S. Vaage, and E. Husebye (1982). The Meløy earthquake sequence, northern Norway: source parameters and their moment scaling relations, *Bull. Seism. Soc. Am.* **72**, 197–206.

Chun, K., R. Kokoski, and G. West (1989). High-frequency *Pn* attenuation in the Canadian Shield, *Bull. Seism. Soc. Am* **79**, 1039–1053.

Chun, K., G. West, R. Kokoski, and C. Samson (1987). A novel technique for measuring *Lg* attenuation: results from eastern Canada between 1 to 10 Hz, *Bull. Seism. Soc. Am* **77**, 398–419.

Dwyer, J., R. Herrmann, and O. Nuttli (1983). Spatial attenuation of the *Lg* wave in the central United States, *Bull. Seism. Soc. Am.* **73**, 781–796.

Evernden, J. (1967). Magnitude determination at regional and near-regional distances in the United States, *Bull. Seism. Soc. Am.* **57**, 591–639.

Evernden, J. (1976). Study of seismic evasion. II. Evaluation of evasion possibilities using normal microseismic noise, *Bull. Seism. Soc. Am* **66**, 281–324.

Evernden, J., C. Archambeau, and E. Cranswick (1986). An evaluation of seismic decoupling and undergound nuclear monitoring using high-frequency seismic data, *Rev. Geophys.* **24**, 143–215.

Given, H., N. Tarasov, V. Zhuravlev, F. Vernon, J. Berger, and I. Nersesov (1990). High-frequency seismic observations in eastern Kazakhstan, USSR, with emphasis on chemical explosion experiments, *J. Geophys. Res.* **95**, 295–307.

Goncz, J., W. Dean, Z. Der, A. Lees, K. McLaughlin, T. McElfresh, and M. Marshall (1987). Propagation and excitation of *Lg*, *Sn*, and *P-Pn* waves from eastern United States earthquakes by regression analysis of RSTN data, Final Tech. Rept. TGAL-86-7, Teledyne Geotech Alexandria Lab., Alexandria, Virginia.

Gupta, I. and K. McLaughlin (1987). Attenuation of ground motion in the eastern United States, *Bull. Seism. Soc. Am.* **77**, 366–383.

Gurrola, H., J. Minster, F. Vernon, J. Berger, H. Given, and R. Aster (1989). A comparative study of high frequency seismic noise at selected sites in the USSR and USA, paper presented at Seismic Research Symp., Def. Adv. Res. Proj. Agency/Air Force Geophys. Lab., San Antonio, Texas, May 2–4.

Hannon, W. (1985). Seismic verification of a comprehensive test ban, *Science* **227**, 251–257.

Hasegawa, H. (1983). *Lg* spectra of local earthquakes recorded by the Eastern Canada Telemetered Network and spectral scaling, *Bull. Seism. Soc. Am.* **73**, 1041–1061.

Hasegawa, H. (1985). Attenuation of *Lg* waves in the Canadian Shield, *Bull. Seism. Soc. Am.* **75**, 1569–1582.

Herrmann, R., and A. Kijko (1983). Modeling some empirical vertical component *Lg* relations, *Bull. Seism. Soc. Am.* **73**, 157–171.

Sereno, T. (1989). Numerical modeling of *Pn* geometric spreading and empirically determined attenuation of *Pn* and *Lg* phases recorded in eastern Kazakhstan, *Semiannual Tech. Rept. SAIC 89/1555*, Sci. Appl. Int. Corp., San Diego, Calif.

Sereno, T., and S. Bratt (1989). Seismic detection capability at NORESS and implications for the detection threshold of a hypothetical network in the Soviet Union, *J. Geophys. Res.* **94**, 10397–10414.

Sereno, T., S. Bratt, and T. Bache (1988). Simultaneous inversion of regional wave spectra for attenuation and seismic moment in Scandinavia, *J. Geophys. Res.* **93**, 2019–2035.

Sereno, T. and J. Given (1990). *Pn* geometric spreading, *Geophys. Res. Lett.* **17**, 1141–1144.

Shin, T. and R. Herrmann (1987). *Lg* attenuation and source studies using 1982 Miramichi data, *Bull. Seism. Soc. Am.* **77**, 384–397.

Singh, S. and R. Herrmann (1983). Regionalization of crustal coda *Q* in the continental United States, *J. Geophys. Res.* **88**, 527–538.

Street, R., R. Herrmann, and O. Nuttli (1975). Spectral characteristics of the *Lg* wave generated by central United States earthquakes, *Geophys. J. R. Astrn. Soc.* **41**, 51–63.

Suteau-Henson, A. and T. Bache (1988). Spectral characteristics of regional phases recorded at NORESS, *Bull. Seism. Soc. Am.* **78**, 708–725.

Thurber, C., H. Given, and J. Berger (1989). Regional seismic event location with a sparse network: application to eastern Kazakhstan, USSR, *J. Geophys. Res.* **94**, 17767–17780.

Veith, K. and G. Clawson (1972). Magnitude form short-period *P*-wave data, *Bull. Seism. Soc. Am.* **62**, 435–452.

SCIENCE APPLICATIONS INTERNATIONAL CORPORATION
10260 CAMPUS POINT DRIVE
SAN DIEGO, CALIFORNIA 92121

Manuscript received 1 February 1990

Bulletin of the Seismological Society of America, Vol. 80, No. 6, pp. 2106-2126, December 1990

THE STABILITY OF RMS *Lg* MEASUREMENTS AND THEIR POTENTIAL FOR ACCURATE ESTIMATION OF THE YIELDS OF SOVIET UNDERGROUND NUCLEAR EXPLOSIONS

BY ROGER A. HANSEN, FRODE RINGDAL, AND PAUL G. RICHARDS

ABSTRACT

Data on underground nuclear explosions have recently become available from modern digital seismic stations installed within the Soviet Union and China. Observations of root mean square (rms) *Lg*-wave signals for Soviet underground nuclear explosions at the Shagan River Test Site in East Kazakhstan show that the relative amplitudes of the rms signals at stations in Norway, the USSR, and China are very similar for different explosions, the standard deviation of the differences being only about 0.03 in logarithmic units (i.e., magnitude units).

This is consistent with earlier observations comparing NORSAR and Graefenberg array data, and the observed scatter is significantly lower than has been reported for *Lg* data from Nevada Test Site explosions. In view of the excellent correspondence found by Nuttli (1986) and Patton (1988) for *Lg* versus yield at Nevada, this indicates that rms *Lg* has a potential for yield estimation with very high accuracy at Shagan River.

Our study has shown that: (a) selected stations in the USSR and China, situated at regional distances, provide a much improved signal-to-noise ratio of the *Lg* phase for events at Shagan River, as compared to NORSAR array data; (b) the scaling of rms *Lg* amplitudes between different-sized events recorded at the same single station site appears to be consistent with that of NORSAR, indicating a remarkable degree of precision in single station measurements of *Lg* signal; (c) rms *Lg* amplitude measurements for the best of these stations may be made at 1.5 to 2.0 magnitude units lower than at NORSAR or Graefenberg, allowing a much lower threshold for *Lg*-based yield determination; and (d) the *P*-wave detection capabilities of these single stations do not match those of the NORESS and ARCESS arrays; thus, teleseismic signals continue to be important for detection of small nuclear explosions.

Our conclusion is that *Lg* signals appear to provide an excellent basis for supplying estimates of the yields of nuclear explosions even down to below 1 kt when such signals are recorded at high-quality, digital in-country seismic stations, and when calibrated by access to independent (nonseismic) yield information for a few nuclear explosions at the test sites of interest. In the context of monitoring a low-yield threshold test ban treaty, it will, in addition, be important to take into consideration various environmental conditions in the testing area, such as the possible presence of cavities, and to devise appropriate procedures for on-site observations in this regard.

INTRODUCTION

We report our observations of root mean square (rms) *Lg*-wave signals for Soviet underground nuclear explosions at the Shagan River Test Site in East Kazakhstan. We show that the relative amplitudes of the rms signals, at stations in Norway, the USSR, and China, are very similar for different explosions. Thus, if we consider only well-recorded explosions (i.e., requiring that rms *Lg* be at least 1.5 times the rms level of noise preceding the *P* arrival), our basic observation is that rms *Lg* amplitudes at pairs of stations are in excellent agreement, the standard deviation of the differences being only about 0.03 in logarithmic units (i.e., magnitude units).

This observation indicates that a seismic measure of source size can be estimated with unprecedented precision from observations of *Lg* waves at a single station. (*P*-wave amplitudes, for example, as measured to obtain m_b, show significantly greater scatter.) We refer to such indications of precision of rms *Lg* as "stability."

Quantitative studies of *Lg* began much later in seismology than such studies of *P*, *S*, and teleseismic surface waves because *Lg* waveforms are in general more complex than those of other phases. *Lg* waveform modeling typically does not yet achieve the quality of fit between synthetics and data that has been attained with more conventional phases. It is, therefore, somewhat surprising to find that potentially the most precise estimator of seismic source size may be one based on a phase as complex as *Lg*.

In this paper, we are principally concerned with developing those properties of rms *Lg* that are pertinent to making accurate estimates of the yield of Soviet nuclear explosions, particularly at the Shagan River Test Site. For Shagan River explosions with $m_b > 5.5$, *Lg* signals at NORSAR alone were found to provide magnitude estimates that indicated stability comparable to and possibly better than those obtained from *P* waves recorded on a large worldwide network (Ringdal, 1983). Underlying this conclusion are the assumptions, articulated by Nuttli (1973), that the magnitude of seismic sources can usefully be assigned at "long-period" or "short-period," and that short-period magnitudes can be estimated either with *P* waves, or, in many circumstances, with *Lg* recorded at periods around 1 sec. We use m_b to denote short-period magnitude in general and m_b (*P*) or m_b (*Lg*) where it is necessary to indicate the wave type used for measurement.

We report the first analyses of rms *Lg* signals of Soviet nuclear explosions recorded within the USSR. We used data recorded at four in-country stations installed in the summer of 1988 by the Incorporated Research Institutions for Seismology (IRIS), under an agreement negotiated with the Soviet Academy of Sciences. What is important about these stations is that they have been allowed to run even during times when the Soviets were conducting underground nuclear explosions at weapons test sites, and for the first time this in-country data have routinely become available for analysis in the West. Using these four high-quality digital stations installed within the Soviet Union by IRIS and one installed by the British [GAM, The BSVRP Working Group, (1989)] located near the IRIS Garm station, we confirm that the stability of rms *Lg* is present at distances about 1,500 to 3,000 km from Shagan River, and can be used for explosions much smaller than those observed teleseismically. Specifically, we show an example for one of these IRIS stations, ARU (installed in 1988 at Arti in the Urals), indicating that the improvement in signal-to-noise ratio is such as to permit rms *Lg* to be used for yield estimation of explosions down to about m_b 4.0. A similar performance is found for the station GAM. We note that, according to the magnitude-yield relations presented by Vergino (1989a), m_b 4.0 would correspond to a yield well below 1 kt for nuclear explosions conducted under typical tamped conditions.

We further analyze rms *Lg* signals from Shagan River explosions recorded at two stations of the China Digital Seismograph Network (CDSN). These stations, which have sampling rates of 20 Hz and operate in a triggered mode, are at Urumqi (WMQ) and Hailar (HIA), at a distance of 950 and 2900 km, respectively, from Shagan River. Stability of rms *Lg* is again confirmed, and it appears that WMQ, if set to record continuously, could provide rms *Lg* for yield estimation down to m_b 3.5.

As part of this project to investigate *Lg*, we also address the excellent *P*-wave detection capability of the NORESS and ARCESS arrays (See Ringdal, 1990). We point out the advantages of combining the excellent *detection* capability of these teleseismic arrays with the potentially superior *yield-estimation* capability of in-country stations, for purposes of both detecting and estimating the yields of small nuclear explosions.

To place our new results in context, the next section reviews earlier studies describing the promise and problems of using *Lg* signals. This review is followed by a description of our analysis of the Soviet and Chinese data.

Review of Previous Studies of *Lg*

Lg waves are seismic waves that are observed to propagate across continental paths. They were first described by Press and Ewing (1952) from earthquakes in California that were observed at Palisades, New York, shortly after seismographs were installed at what then was called the Lamont Geological Observatory. The following characteristics were noted for what these authors called "surface shear waves":

1. initial period about 0.5 to 6 sec
2. sharp commencements
3. amplitudes larger than any conventional phase for continental paths at distances up to 6,000 km
4. observed for continental paths only, being gradually eliminated as the ocean path increases beyond 100 km
5. group velocity (near onset) around 3.5 km/sec, decreasing to below 2 km/sec for periods above 10 sec
6. inverse dispersion at distances greater than about 20° (i.e., frequency decreases for later times in the wave train).

Press and Ewing found that earthquakes as small as magnitude 4.7, at a distance of about 35°, consistently displayed the above properties. In remarking that amplitudes were "larger than any conventional phase," they were presumably comparing *Lg* to body waves that arrive more-or-less as isolated pulses, and/or to single-mode surface waves that could be identified with a particular dispersion curve.

Press and Ewing noted properties of the three components of ground motion that indicated another type of continental surface wave, which they called *Rg*, was also being observed with large amplitudes. It had group velocity about 3.05 km/sec and the characteristic retrograde elliptical particle motion of a Rayleigh wave.

The reason Press and Ewing labeled these waves *Lg* and *Rg* was that the speeds and some features of the commencement of the observed signals were similar to those predicted theoretically for Love and Rayleigh short-period surface waves in a granitic layer (i.e., for waves at periods shorter than periods seen in conventional teleseismic surface waves). They attempted quantitatively to show that *Lg* consists of *SH* waves multiply reflected within a superficial sialic layer. However, as noted by them and by Lehmann (1953), the idea of such a layer was quickly abandoned (although use of the names *Lg* and *Rg* has persisted) because:

1. The observed duration of the wave train was much longer than that indicated by Love-wave calculations in a superficial granitic layer.
2. *Lg* was recognized (even in these earliest papers) as having particle motion in vertical and radial directions, as well as in the transverse direction of conventional Love waves.

3. *Lg* was found to be strong in some earthquakes that originated below the proposed layer and thus at depths unfavorable for exciting *SH* multiples that propagate to great distances.

The basic observation that short-period *Lg* has considerable vertical and longitudinal motion was noted in these earliest studies, but not explained except to point out that a plate floating on a fluid substrate would retain *SV* multiples that arrived concurrently with *SH* out to great distances.

In retrospect, we may say that Press and Ewing identified what is still recognized as the defining properties of *Lg* waves. But, for many years after these properties were discovered, little progress was made in explaining them quantitatively in terms of synthetics. In contrast, the smaller amplitude "conventional phases" (body waves and teleseismic surface waves) have been synthesized more and more successfully. Quantitative fits to travel times and waveforms, including normal mode synthesis, have become standard methods for obtaining detailed information about Earth structure, and about earthquake and explosion sources.

However, the fact that *Lg* can be "larger than any conventional phase" carries its own imperative, whether or not it is a wave that can be fully explained with models of Earth structure and theories of seismic source and wave propagation. For decades, *Lg* (and *Rg*) have, therefore, of necessity been studied empirically by those scientists and engineers whose work inclines to a study of the largest seismic motions. Examples of such empirical work include the many uses of Richter local magnitude, M_L, comparative studies of areas of perceptibility of earthquakes in different continental regions, the related subject of how amplitudes of the largest seismic waves vary with epicentral distance, and studies of small magnitude events when only *Lg* may be apparent above noise levels.

Much pioneering work on *Lg* waves was done in the 1970s and 1980s by Otto Nuttli of St. Louis University. Thus, Nuttli (1973) proposed that, "since *Lg* represents a higher mode wave traveling with minimum group velocity," it would be appropriate to relate amplitude (A) and distance (Δ) via:

$$A = K[\Delta^{-1/3}](\sin\Delta)^{-1/2}e^{-\gamma\Delta} \tag{1}$$

where K is governed by the source strength, and γ is the spatial decay rate due to nongeometrical attenuation. This formula is the stationary phase approximation appropriate for frequencies, f, near a minimum in group velocity, U, and

$$\gamma = \pi f/(QU) \tag{2}$$

where $1/Q$ is a dimensionless measure of attenuation. For values of Δ small enough that $\sin\Delta$ is approximately proportion to Δ (i.e., when sphericity of the Earth can be ignored), the geometrical attenuation described by equation (1) is given by a factor of $\Delta^{-5/6}$. Nuttli (1973) claimed that the Richter local magnitude scale, M_L, developed for the Western United States, was based on waves that could be interpreted via equation (1), but with γ values about ten times higher than the γ values appropriate to the use of equation (1) in fitting observed amplitudes for *Lg* waves in Eastern North America.

With the goal of defining a magnitude scale for source strength at short periods, based on *Lg* observations that are corrected for path-dependent attenuation, he described in detail (Nuttli, 1973, 1986a) a three-step procedure to obtain what he called an m_b (*Lg*) value for an earthquake or an explosion of interest. The three

steps were as follows:

1. γ was estimated for a particular source-receiver path
2. equation (1) was used to predict an amplitude at one particular distance (he chose Δ corresponding to 10 km for reference)
3. magnitude was assigned via the formula

$$m_b(Lg) = 5.0 + \log[A(10 \text{ km})/110]$$

where $A(10 \text{ km})$ is the amplitude, in microns, resulting from step 2.

Nuttli's method is based on a mix of phenomenological properties of observed signals and theories of *Lg* propagation. Nuttli specified in detail his procedures for estimating γ. He used a method described by Herrmann (1980) in which the tendency of signal to move to lower frequencies in later portions of the *Lg* wave train is used to obtain Q values. Q itself is taken to have a power-law dependence upon frequency. A key assumption of Nuttli's method, namely that geometrical decay of *Lg* amplitudes is described essentially by a factor $\Delta^{-5/6}$, has subsequently been given some support by calculation of synthetics in layered crustal structures (e.g., Campillo *et al.*, 1984).

In order to improve the consistency of m_b (*Lg*) estimates resulting from different stations at different distances from the same event (this is the quality referred to as "stability" in the present paper), the measurement that Nuttli actually made from seismograms (short-period WWSSN vertical components) was based on the third largest amplitude in the time window corresponding to group velocities of 3.6 to 3.2 km/sec.

For 22 nuclear explosions below the water table at NTS, Nuttli (1986a) showed that his $m_b(Lg)$ values, using only three WWSSN stations in the Western United States, were remarkably well correlated with the logarithm of announced yield. He proposed a best-fitting line through this magnitude-yield data, from which magnitudes had a standard deviation of only about 0.05. Patton (1988) developed computer-automated measures of *Lg* amplitude aiming at reproducing Nuttli's NTS results. Patton measured *Lg* amplitudes from digital seismograms in two ways—by using the third-largest peak and by computing the rms amplitude in the *Lg* time window—and found very little difference (around 0.01 magnitude units) in the amount of scatter about regression lines using the two measures. However, he found that standard deviations from best-fitting $m_b(Lg)$ − log(yield) relations were low, 0.07 to 0.08 magnitude units, only if explosions were restricted to subregions of NTS (Pahute Mesa, northern Yucca Flat, southern Yucca Flat).

Based on the success in estimating yields for NTS explosions, Nuttli proceeded to apply the same magnitude-yield relation, together with *Lg* signals recorded at analog WWSSN stations in Eurasia, to estimate the yields of nuclear explosions at three Soviet test sites (Nuttli 1986b, 1987, 1988). For the period 1978 to 1984, after the 150 kt Threshold Test Ban Treaty had gone into effect, his yield estimates for Shagan River explosions included 20 that exceeded the threshold, including one (5 December 1982) estimated by Nuttli to be about 300 kt. While acknowledging the pioneering work involved in these studies, it is clear that the generally low signal-to-noise ratios and the problematic data quality of these analog recordings made very precise measurements impossible to attain, a fact also recognized by Nuttli himself. Also, at the teleseismic distances for which Nuttli had *Lg* data (1,900 to 4,400 km), yield estimates based on absolute measures of ground motion that have to be extrapolated back to 10 km are a severe test of the validity of equation (1)

[even if equation (1) is appropriate] and are very sensitive to errors in γ. Overestimating γ by 10 to 15 per cent would result in yield estimates about two times too high.

In the first of a number of *Lg* studies undertaken by the NORSAR staff during the 1980s, Ringdal (1983) analyzed digital NORSAR *Lg* data of selected Semipalatinsk underground nuclear explosions. He found that, when using NORSAR rms *Lg* instead of *P* waves recorded at NORSAR to estimate source size, it was possible to eliminate effectively the magnitude bias relative to worldwide m_b observed at NORSAR between Degelen and Shagan River explosions. The method consisted of averaging log (rms) values of individual NORSAR channels, filtered in a band of 0.6 to 3.0 Hz in order to enhance *Lg* signal-to-noise ratio. Ringdal and Hokland (1987) expanded the data base and introduced a noise compensation procedure to improve the reliability of measurement at low SNR values. They were able to identify a distinct *P–Lg* bias between the Northeast and Southwest portions of the Shagan River Test Site, a feature that was confirmed by Ringdal and Fyen (1988) using Graefenberg array data. Ringdal and Marshall (1989) combined *P*- and *Lg*-based source size estimators to estimate the yields of 96 Shagan River explosions from 1965 to 1988, using data on the cratering explosion of 15 January 1965 as a reference for the yield calculations.

Recent developments have permitted access to high-quality digital data from sites significantly closer to Shagan River and, in addition, some information on yields at this test site has become openly available. This obviates the need to make distance corrections to absolute measures of *Lg* ground motion amplitude for purposes of yield estimation at this site. Thus, the focus of this paper will be on using rms *Lg* measurements to investigate the stability of this measure for fixed station source combinations.

Data Analysis for Shagan River Nuclear Explosions

Recently, data have become available from seven stations located within the Soviet Union and China for explosions in the Semipalatinsk area (see Tables 1 and 2, and Fig. 1). These stations are comprised of the IRIS stations (Given and Berger, 1989), the CDSN stations, and the Garm station operated by the British as described previously. This new data allows the comparison of the stability of the rms *Lg* measurement technique for stations at various distances. In particular, we will compare *Lg* amplitudes of events recorded at the close-in stations with *Lg* recorded at NORSAR, and *P*-wave detectability at NORESS.

The seismograms from our data set were all processed in a manner similar to that used for the NORSAR recordings. The processing is illustrated in Figure 2. Figure 2a represents a well-recorded event of magnitude m_b (P) = 5.9, whereas

TABLE 1

Seismographic Station Locations

Station	Latitude	Longitude	Elevation (m)
WMQ	43.821°N	87.695°E	970
HIA	49.267°N	119.742°E	610
ARU	56.40°N	58.60°E	250
GAR	39.00°N	70.32°E	1300
KIV	43.95°N	42.68°E	1206
OBN	55.10°N	36.60°E	160
GAM	39.00°N	70.19°E	1300

TABLE 2

VERTICAL COMPONENT STATION VALUES

No.	Date	m_b	NAO *Lg*	WMQ *Lg*	HIA *Lg*	ARU *Lg*	GAR *Lg*	KIV *Lg*	OBN *Lg*	GAM *Lg*
1	87171	6.03	3.012	3.851	2.189	—	—	—	—	—
2	87214	5.83	2.911	3.693	2.072	—	—	—	—	—
3	87319	5.98	3.014	3.870	2.298	—	—	—	—	—
4	87347	6.06	3.133	3.907	2.352	—	—	—	—	—
5	87361	6.00	3.086	3.851	2.334	—	—	—	—	—
6	88044	5.97	3.082	3.911	—	—	—	—	—	—
7	88094	5.99	3.103	3.925	2.307	—	—	—	—	—
8	88125	6.09	3.084	3.958	—	—	—	—	—	—
9	88258	6.03	3.014	3.827	2.224	4.142	3.802	3.014	3.342	3.184
10	88270	3.8	—	—	—	2.215	—	—	—	1.196
11	88317	5.20	2.307	3.104	—	3.429	3.165	—	—	2.521
12	88352	5.80	2.846	3.636	1.947	3.935	—	—	3.191	3.034
13	89022	6.0	3.005	—	—	4.075	—	—	—	3.161
14	89043	5.90	2.836	3.619	1.921	3.891	—	—	3.228	2.923
15	89189	5.60	—	—	—	3.562	3.326	2.609	2.823	—
16	89292	5.9	2.834	—	—	3.942	—	—	3.208	—

Magnitudes (m_b) and log rms *Lg* values for vertical components at stations NORSAR, WMQ, HIA, ARU, GAR, KIV, OBN, and GAM for 16 explosions analyzed in this study. Note that the IRIS stations (ARU, GAR, KIV, and OBN) have been normalized to a constant gain level to adjust for response changes. The values for the three stations (WMQ, HIA, and GAM) reflect unadjusted count values of the raw seismograms.

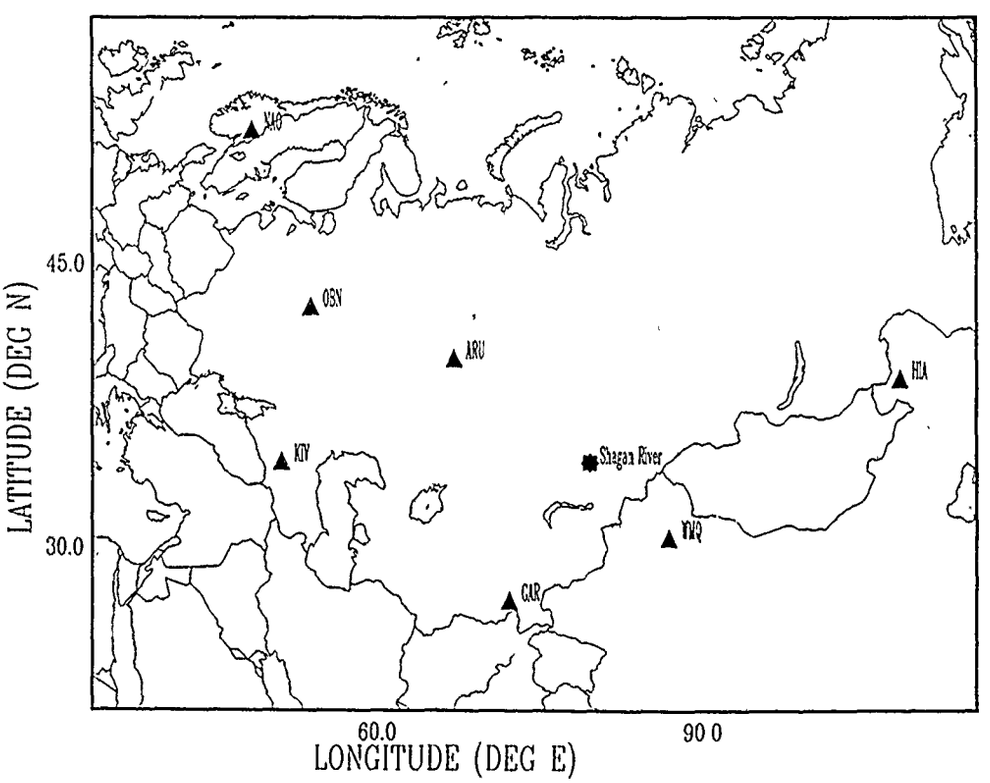

FIG. 1. Map indicating the locations of the Shagan River Test Site, the IRIS and British stations in the USSR, the NORSAR array in Norway, and the stations WMQ and HIA in China. The NORESS array is collocated near the NORSAR array, and station GAM is collocated near the GAR station.

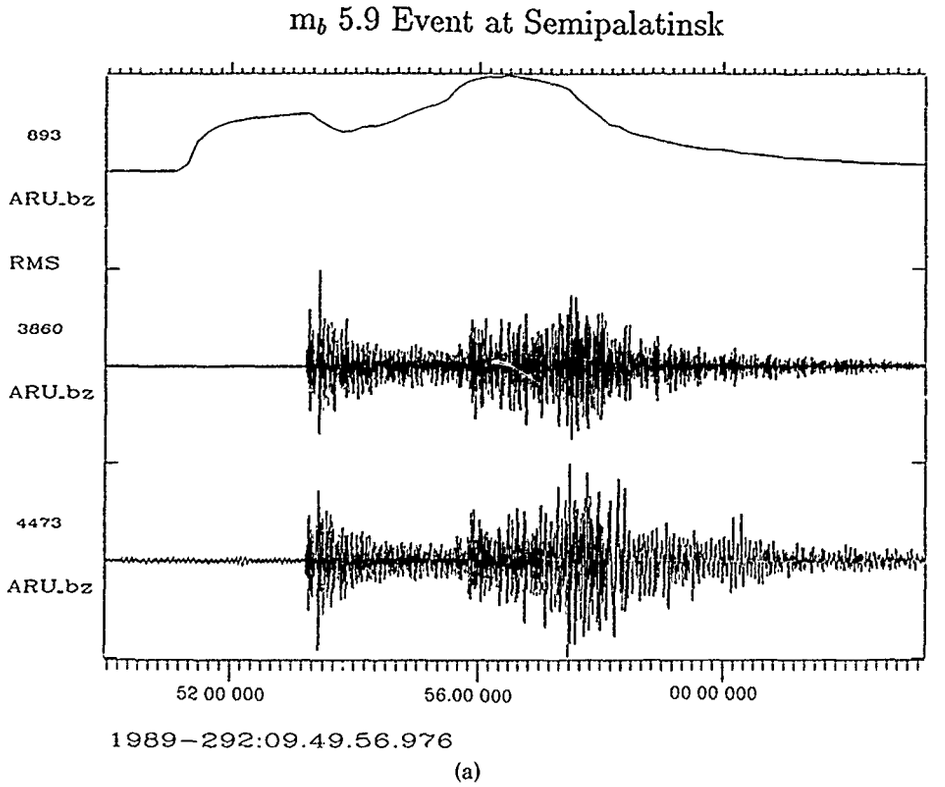

FIG. 2. Example of recordings from two Soviet nuclear explosions at the IRIS station ARU. (a) An m_b 5.9 event at Shagan River on 19 October 1989 illustrating a good SNR, and (b) an m_b 4.9 event at Degelen Mountains to illustrate the improvement in SNR by bandpass-filtering in the range 0.6 to 3.0 Hz. For each of the events, we show the unfiltered trace (bottom), the filtered trace (0.6 to 3.0 Hz) (middle), and the 120-sec window rms measure (top) as a function of time.

Figure 2b presents an event of magnitude $m_b(P) = 4.9$, each as recorded at station ARU. The bottom trace for each event in Figure 2 is the observed data. These seismograms illustrate the broadband character of the typical recordings from modern digital seismometers, where the response is flat from about 5 Hz to well below the frequencies of interest for *Lg* waves (to between 30 and 100 sec period for these stations). We first bandpass filter the seismograms shown in the bottom trace in the frequency band from 0.6 to 3 Hz to produce the bandpassed version in the center of each plot. This is clearly necessary to enhance the *Lg* waves relative to the long-period microseisms in Figure 2b and higher frequency *P* and *Sn* coda, as well as to allow comparison to analyses of short-period data.

An rms trace, shown on the top of each plot, is then computed where each point of the trace represents the rms amplitude measure for the subsequent time window. We then measure the rms amplitude for the window centered on the phase of interest. In this respect, we did not use a fixed-group velocity window for analysis, but rather for simplicity, the same length window of 120 sec was chosen for all distances and centered near the 3.5 km/sec group velocity arrival time. The rms measure of *Lg* was read for the particular 120 sec window for all recording stations (and individually for all components of recording). Again for simplicity, the largest value of the rms trace was chosen as the amplitude measurement as long as the window is still centered near the 3.5 km/sec group velocity. Likewise, an rms measurement of the noise preceding each event arrival was calculated and applied as a correction term for calculating the *Lg* amplitude measure as originally defined by Ringdal and Hokland (1987). In contrast to NORSAR, the Soviet and Chinese stations are single site stations, so no averaging of vertical component measures was possible. However, these stations do record three components that may be averaged. We thus computed both individual component rms data as well as average values, but our results were inconclusive as to whether reduced scatter could be achieved in this way. In this paper, we present results based on vertical components only.

Examples of the IRIS recordings are shown in Figure 3 for the JVE event of 14 September 1988. Again, in this figure, are the unfiltered three-component data along with bandpass-filtered versions in the frequency range from 0.6 to 3.0 Hz. Above each filtered trace, we show a 120 sec window rms measure of the amplitude. The first striking feature of the three-component seismograms is that the horizontal instruments consistently exhibit a larger amplitude for the *Lg* phase than the verticals. The closer stations, ARU and GAR, at a distance near 1,500 km, show this *Lg* phase as the largest amplitude, while stations OBN and KIV at a distance nearer to 2,900 and 2,800 km, respectively, have the *P* phase as the largest amplitude. Station KIV has no discernible *Lg* phase for this explosion, presumably because *Lg* does not propagate efficiently in the crustal structure associated with the Caspian Sea.

The CDSN stations at WMQ and HIA also show excellent *Lg* recordings of Semipalatinsk explosions, as illustrated by the examples in Figure 4. Note in particular the dominance of the *Lg* phase at HIA as the largest recorded phase even at the distance of 2,900 km for this azimuth.

Figure 5 compares the signal-to-noise ratios (SNRs) (defined as rms *Lg* signal to pre-*P* rms noise in the 0.6 to 3.0 Hz band) for stations at various distances, using five large explosions. The range in magnitude (m_b) is from 5.2 for the event on day 317 of 1988 to 6.1 for the JVE event on day 258 of 1988. The event on day 317 indicates the minimum for which rms *Lg* was measured at NORSAR at a

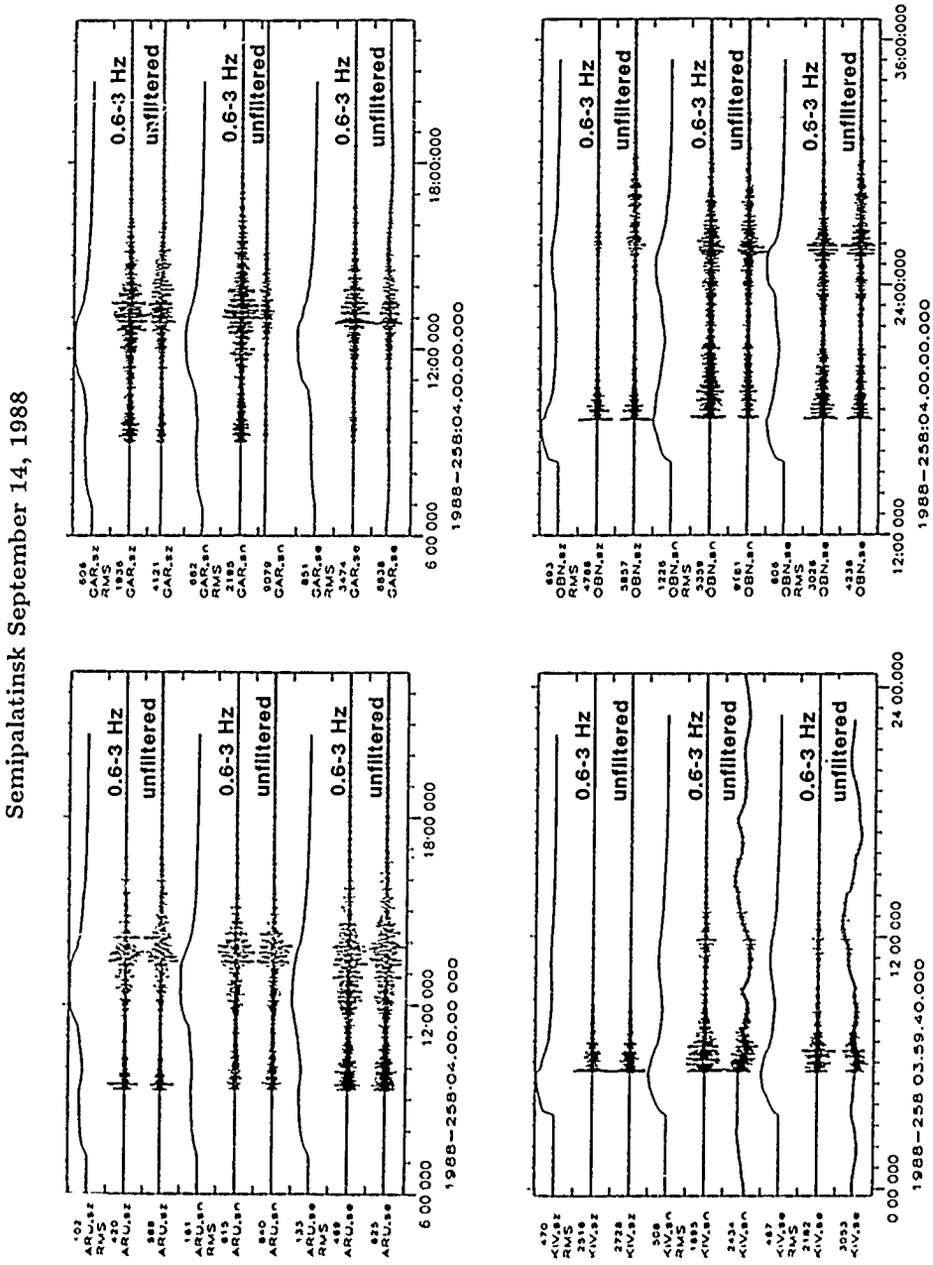

FIG. 3. Plots of the data recorded on the four IRIS stations located in the USSR for the Soviet JVE explosion of 14 September 1988. For each of three components at each site, we show the unfiltered trace (*bottom*), a filtered version in the band of 0.6 to 3.0 Hz (*middle*), and the 120-sec window rms amplitude measure (*top*) as a function of time.

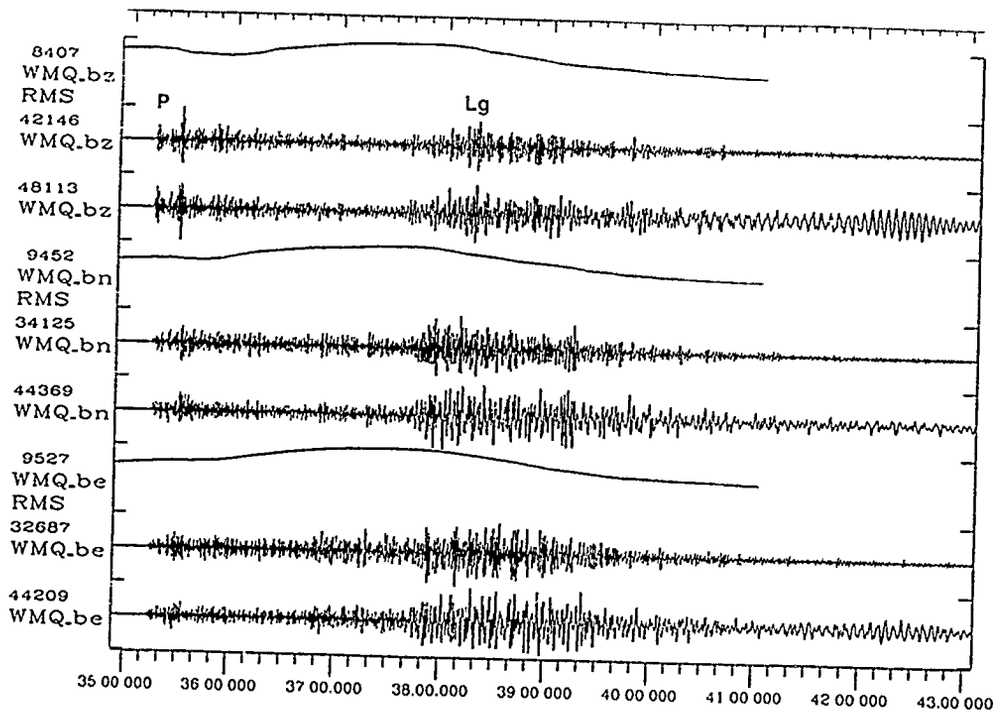

(a)

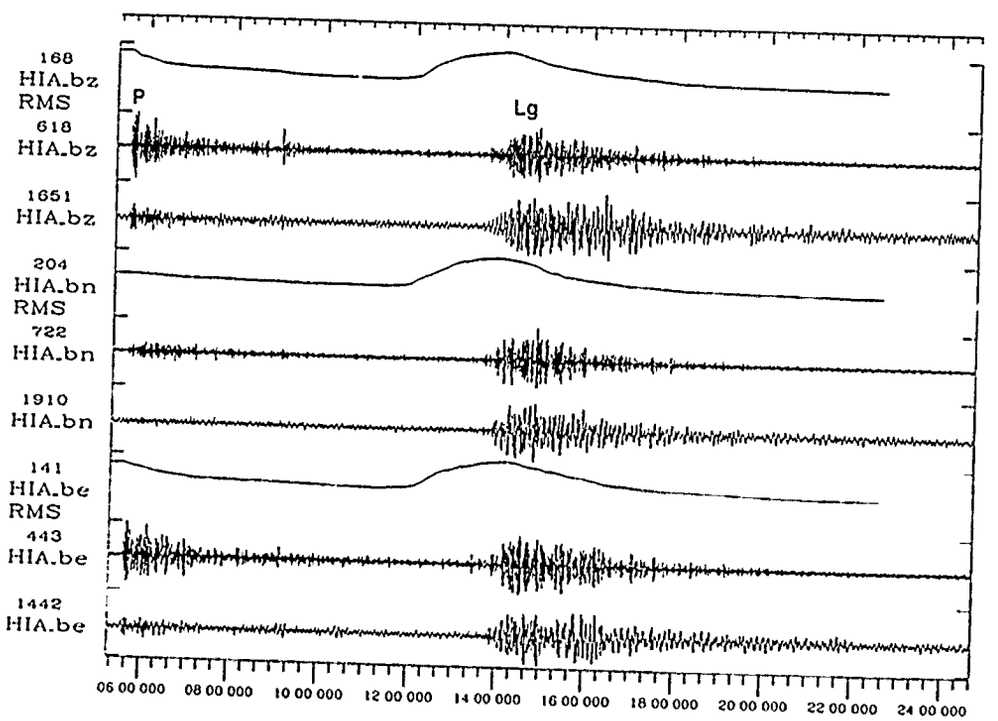

(b)

FIG. 4. Example of recordings from two Soviet nuclear explosions at the two CDSN stations. (a) 3 April 1988 at station WMQ and (b) 14 September 1988 at station HIA. For each of the three components, we show the unfiltered trace (*bottom*), the filtered trace (0.6 to 3.0 Hz) (*middle*), and the 120-sec window rms measure (*top*) as a function of time.

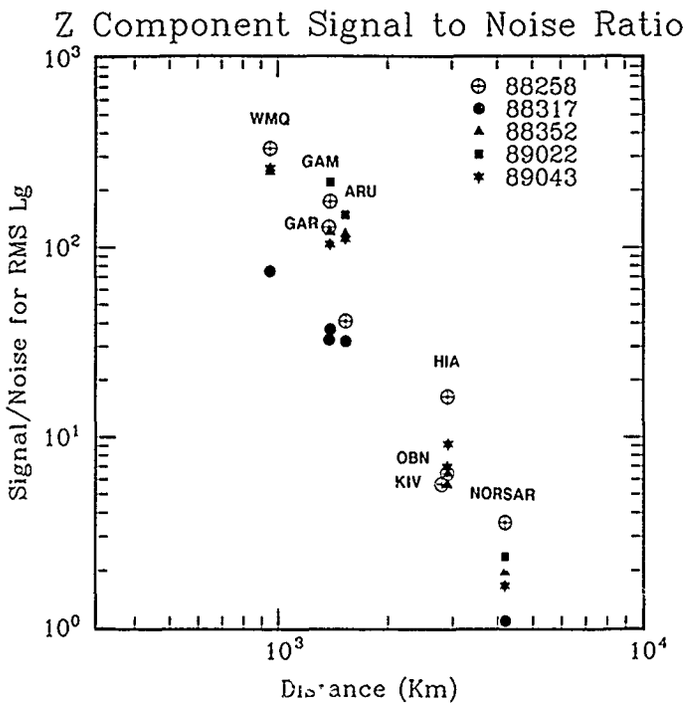

FIG. 5. Graph showing the variation of the SNRs (log rms *Lg* over log rms noise) among the four IRIS stations, the NORSAR array, the CDSN stations WMQ and HIA, and GAM. Epicentral distance to the Shagan River Test Site is plotted along the horizontal axis.

distance of about 4,200 km with an SNR of about 1.1. For this same event, an SNR of about 30 is observable at ARU and GAR at a distance of about 1,500 km and about 80 at WMQ at a distance of 950 km. Again, the event at day 258 of 1988 in Figure 5 (shown with the open circle around a plus sign) shows an SNR gain of nearly 100 between NORSAR with an SNR of 3.5 and WMQ with an SNR of 331. (It should be noted that the low SNR for this event at ARU is because this event was only recorded on the low-gain channel, which does not adequately resolve the background noise.) It is noteworthy that WMQ shows the best SNR for all the events. The figure suggests that WMQ, if set to record continuously, would be able to give *Lg* measurements for events close to two magnitude units smaller than the NORSAR threshold of approximately 5.5. Unfortunately, there were no low-magnitude events for WMQ in our data base, so we have not been able to confirm this hypothesis. We do, however, show an example of an $m_b(P)$ 3.8 explosion, whose *Lg* signal was recorded by ARU (see below).

In order to investigate the stability of the rms *Lg* amplitudes observed at the Soviet and Chinese stations, the amplitudes were compared with NORSAR amplitudes for common events. Since the instrument response of the different IRIS stations was changed several times, and was different at different stations (each being different from that of a NORSAR station), we decided to convert all measurements of IRIS stations to the equivalent gain of a typical short-period instrument in the 0.6 to 3 Hz range. The CDSN stations and station GAM had a constant gain throughout the recording period of this study, so no gain adjustment was required.

For comparison of actual measurements of rms *Lg* amplitudes between NORSAR and four of the new stations (ARU, GAM, WMQ, and HIA) for all common events, we plot in Figure 6 data for the vertical components of rms *Lg*. A straight line has been fit to the data for each of the four stations and a measure of the misfit is given

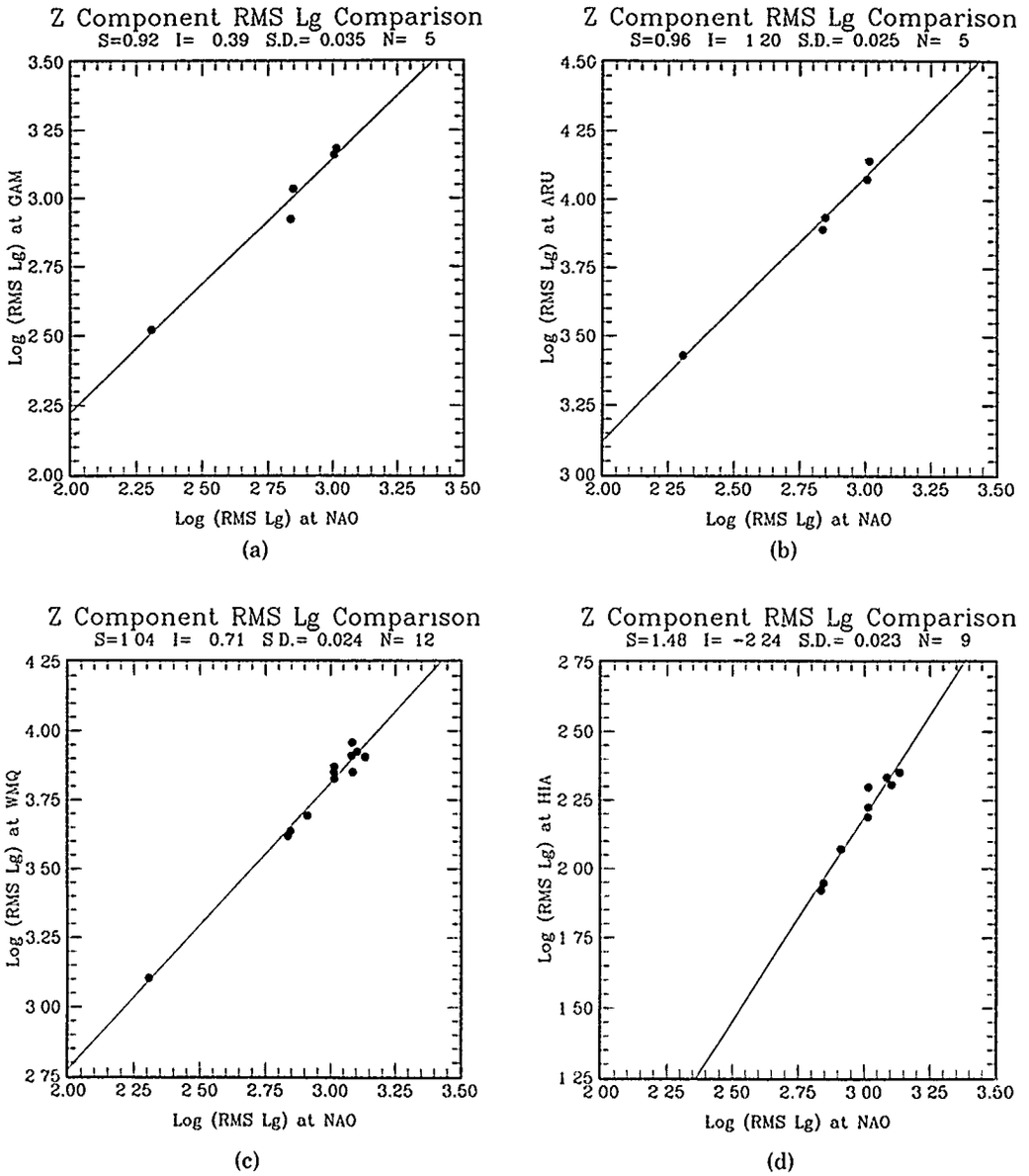

FIG. 6. Comparison of log rms *Lg* at NORSAR with rms *Lg* measurements obtained at four of the close-in stations. (a) GAM with a fitted slope of 0.92 and an orthogonal rms misfit of 0.035 magnitude units, (b) ARU with 0.96 and 0.022, (c) WMQ with 1.03 and 0.024, and (d) HIA with 1.48 and 0.023. The dotted lines correspond to ±2 S.D.

by an orthogonal standard deviation (dotted line in figure corresponds to two standard deviations).

Figure 6 (a to c) shows the comparison of GAM, ARU, and WMQ versus NORSAR log rms (*Lg*) estimates for all common events. The slopes of these plots are 0.92, 0.96, and 1.03, respectively, with orthogonal standard deviations of the misfits being only 0.035, 0.022, and 0.024 units.

Figure 6d shows a comparison of HIA and NORSAR log rms (*Lg*) estimates. In this case, the slope of the least-squares linear relationship (1.48) is significantly different from unity, and we note that a similar observation was also made by Ringdal and Marshall (1989) when comparing NORSAR and Graefenberg *Lg*. We will not go into any detail discussing possible underlying physical reasons for this

variability in slopes. For our purpose, the important point is to note that the scatter of the relationship is still very small; the orthogonal standard deviation relative to the straight line fit is 0.023, which compares very closely to the results found for the other station pairs. Although not shown on the figure, the fit between HIA versus WMQ log rms (*Lg*) values again gives a least-squares slope (1.36) that is significantly different from unity. Once more, however, the scatter is very small, with an orthogonal standard deviation of 0.028 units. We thus find essentially the same scatter for all data when comparing different station pairs, and this confirms the excellent stability of the rms *Lg* estimates when considering a suite of explosions within the limited source region of the Shagan River area.

In Figure 7a, we plot the rms *Lg* amplitude at WMQ against worldwide $m_b(P)$ magnitudes for all recorded events at Shagan River. The slope is 1.02 and the orthogonal standard deviation is 0.044. This scatter is also quite small, but it must be noted that only one event from the northeast part of Shagan is in the data base. Thus, we cannot assess whether the $m_b(Lg)$ versus $m_b(P)$ bias earlier found for this subregion (Ringdal and Marshall, 1989) is also present when measuring *Lg* at WMQ. For comparison, we have also plotted in Figure 7b the same $m_b(P)$ estimates against the logarithm of the largest *Pn* amplitude at WMQ measured within the first 5 sec of the first arrival. Here, we see a much larger scatter for the single station than for the rms *Lg* amplitudes. This is consistent with previous studies of teleseismic *P* at single stations. For example, Lilwall *et al.* (1988) found a typical standard deviation of 0.12 m_b units when comparing single station m_b to worldwide m_b for a set of Shagan River explosions.

Figure 8 illustrates the capabilities of the ARU station to record an $m_b(P)$ 3.8 event from the Shagan River Test Site on day 270 (September 26) of 1988. [This magnitude is based on the NORSAR $m_b(P)$ of 4.3 with an assumed regional correction of 0.5 units for comparison to worldwide m_b estimates, and therefore must be considered somewhat uncertain.] The unfiltered broadband trace at ARU essentially shows no signal for this event; however, the bandpass-filtered trace clearly shows energy arriving that can be identified as *Lg* with an SNR of about 2. (Similar SNR was obtained for the recording at GAM for this event.) This SNR is near the lower limit of about 1.5 for allowing reliable rms *Lg* estimates at a single site. In an attempt to enhance the detectability of other phases, the vertical component of ARU was filtered in several passbands. Even considering frequency bands up to the Nyquist frequency of 10 Hz, we found no additional enhancement of the *P* phase or other phases. (It may be noted that ARU is at a distance within a shadow zone for *P* waves from seismic sources in East Kazakhstan.) In comparison, the NORESS array is clearly capable of detecting the *P*-wave arrival with an SNR of nearly 30, as illustrated in Figure 9 and the ARCESS array also shows a clear *P* detection for this event. Thus, even though the ARU station may not be capable of detecting an event of this size in an automatic fashion, regional arrays such as NORESS and ARCESS can correctly detect the event while the analysis of the *Lg* phase at a much closer station can provide an estimate of the rms *Lg* magnitude suitable for giving independent information on explosion yield.

Figure 10 illustrates the stability of the rms *Lg* amplitudes by comparing GAM and ARU. These stations are chosen because they are the only pair for which we have *Lg* recordings of the $m_b(P)$ 3.8 event shown in Figure 8 and so illustrate the stability of measurement covering a span of two full magnitude units. Here, we again have a slope of very nearly one still with an orthogonal standard deviation of only 0.026 logarithmic units (i.e., magnitude units).

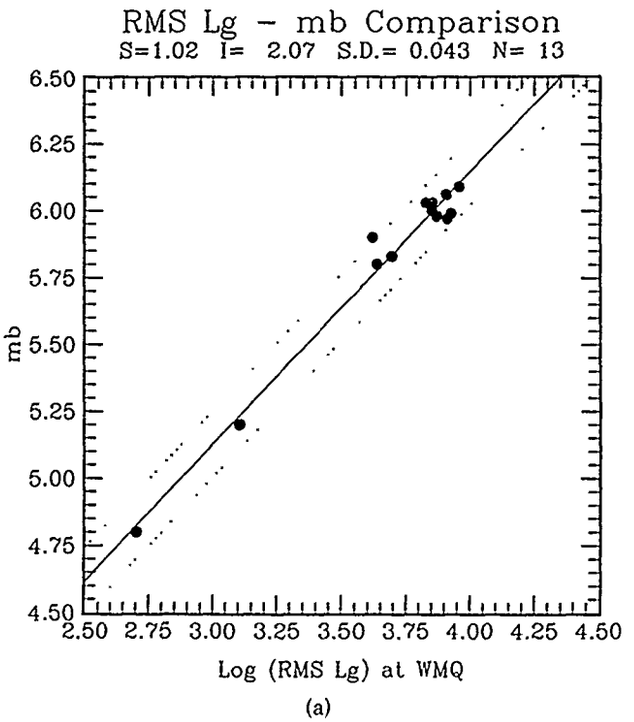

(a)

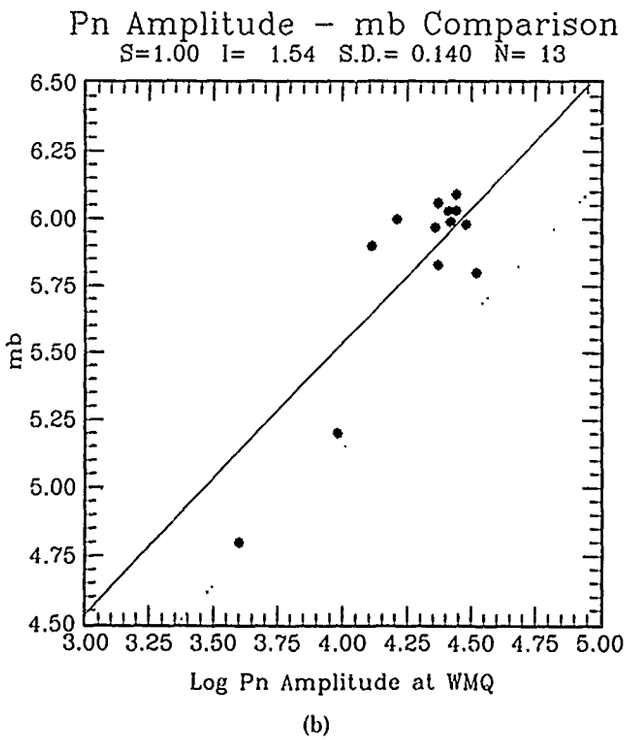

(b)

FIG. 7. (a) Comparison of log rms *Lg* at WMQ to worldwide m_b magnitude. Standard deviation is 0.044 orthogonal to the line. (b) Plot showing the WMQ log *Pn* amplitude measured within the first 5 sec of the *Pn* arrival against worldwide m_b. The slope of the straight line has been fixed to 1.0. The orthogonal standard deviation is 0.140. The dotted lines correspond to ±2 S.D.

Semipalatinsk September 26, 1988

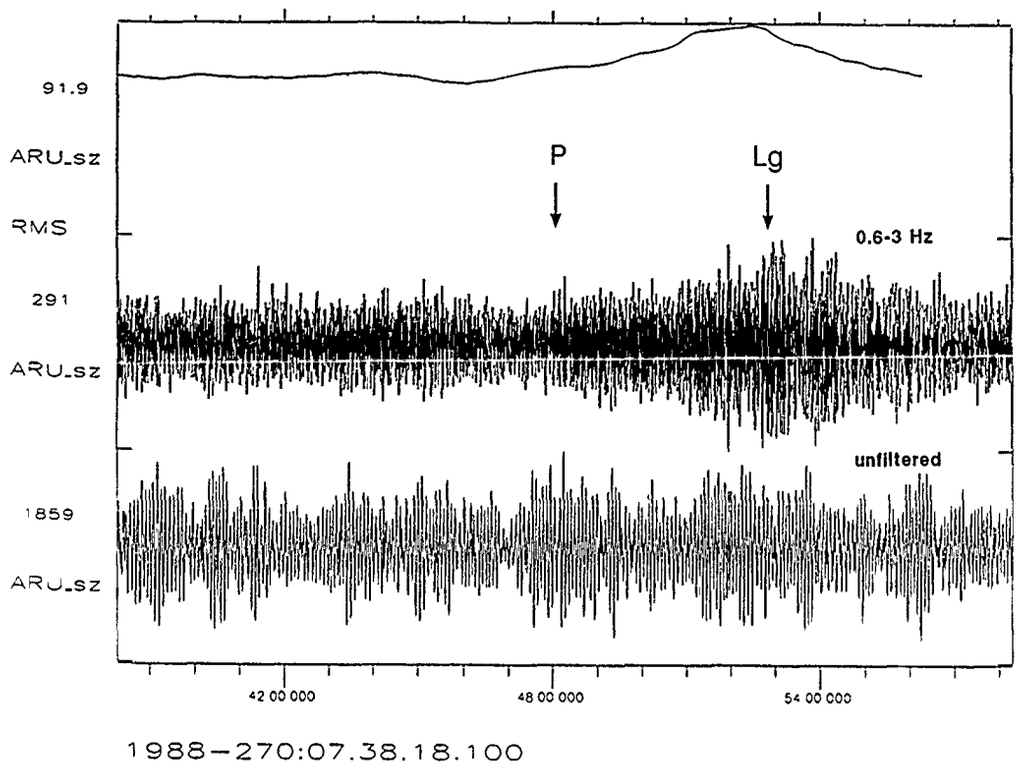

FIG. 8. The ARU vertical component seismogram for the m_b 3.8 explosion on 26 September 1988. The lower trace is the unfiltered seismogram, the middle trace is the bandpass-filtered seismogram between 0.6 and 3.0 Hz, and the upper trace is the rms amplitude as a function of time.

Semipalatinsk September 26, 1988

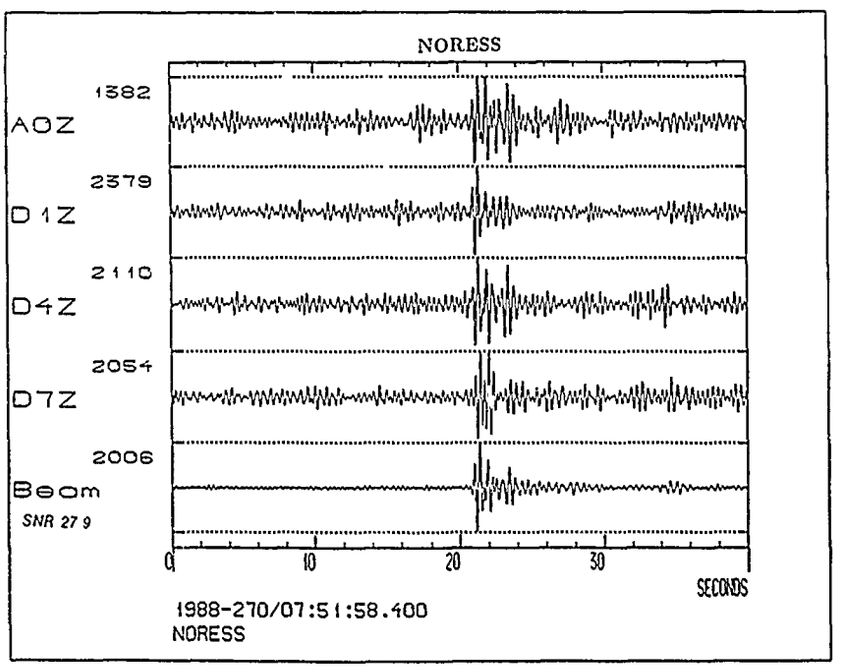

FIG. 9. Example of four vertical component seismograms from the NORESS array in Norway for the m_b 3.8 explosion on 26 September 1988. Shown on the bottom trace is the beam formed by steering toward the explosion site. Note the large improvement in SNR on the beam.

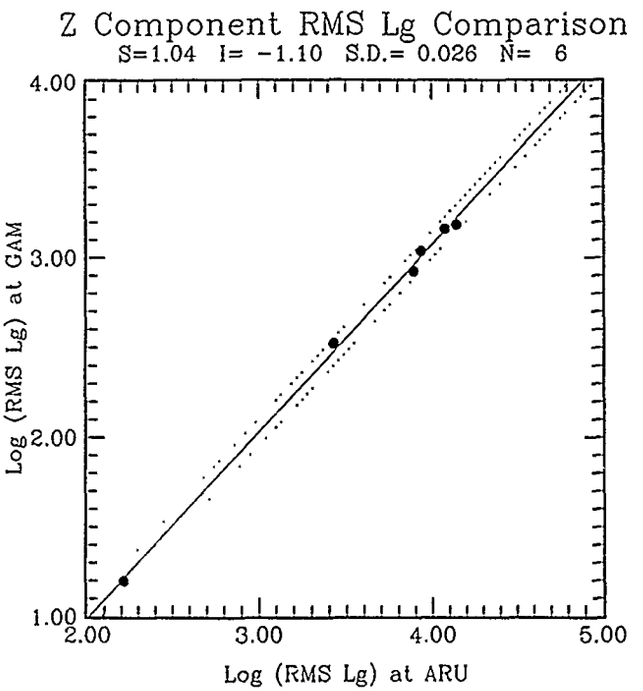

FIG. 10. Comparison of log rms *Lg* measurements at ARU and GAM. The slope of the line is 1.04, and the standard deviation of the misfit of the line to the data is 0.026 orthogonal to the line. The dotted lines correspond to ±2 S.D. Note the remarkable stability of measurement between the two stations over two full magnitude units.

DISCUSSION

A heuristic explanation for the superior stability of *Lg*, as compared to the stability of *P*, lies in the difference in the nature of the sampling of the seismic source for each of these phases. *P* waves for each source-station pair sample only a very limited portion of the focal sphere and are susceptible to focusing and defocusing. To get an improved average using *P* waves, it is necessary to use many stations around the globe and even when using a teleseismic network, only a relatively small part of the focal sphere will be sampled. But *Lg* waves are composed (for each source-station pair) of multiple rays that sample a larger portion of the focal sphere, and therefore, the Earth is doing the averaging for us.

In demonstrating that a single station can provide rms *Lg* measurements with a precision (one standard deviation) of about 0.03 magnitude units at Shagan River, we note that several issues are raised in considering how best to use such measurements for yield estimation.

For example, there are general questions concerning how to define $m_b(Lg)$: can we carefully define an $m_b(Lg)$ scale that is indeed a property of seismic sources, and then establish a procedure by which m_b on this scale can be estimated by measurements made with one or more stations in a seismograph network? One way to proceed would be to define $m_b(Lg)$ as the measurement made in a particular way with a particular seismographic network. The $m_b(Lg)$ for a particular seismic event could then be directly measured (to the extent that the full network supplied data) or, instead, estimated if only a subset of the data were available (e.g., from only a limited number of stations).

Fortunately, in many projects in which a suite of seismic events is under study, an accurate estimate of absolute $m_b(Lg)$ values is not needed. Rather, one may only

need estimates of the relative $m_b(Lg)$ values. The key quality needed is precision of measurement; absolute levels are unimportant or may be derived from separate information. This is the situation in making yield estimates based on seismic data for a suite of underground nuclear explosions at a particular test site, if independent (perhaps nonseismic) information on the yield of some of the events is made available. This information can be used to calibrate in absolute terms a seismic amplitude scale that may be defined uniquely for a particular source region and for a particular network of stations. In this context, in claiming that the stability of rms *Lg* is excellent, we mean that relative magnitudes of explosions in the same region can be estimated very accurately from one or two stations that record *Lg* if the SNR level is high enough.

However, for other purposes, we recognize that there is a need to work with absolute rather than relative $m_b(Lg)$ values. For sources and receivers at any location on the same continent (*Lg* does not propagate across oceans), the need eventually is to understand how to make path corrections to rms *Lg* measurements, for purposes of assigning $m_b(Lg)$ as a characteristic directly of source strength. It is clear that such corrections will depend on both source and receiver locations, and not merely on the scalar distance. (As noted, Nuttli did begin the process of making specific path corrections by making a correction for Q effects.) Obtaining accurate path corrections depending on four spatial coordinates (depth is a separate issue), whether determined empirically for each path or by predictions based on data from a coarse grid of sources and receviers, is certain to be a complex procedure. However, it is likely, too, to be associated with discovery of much new information about continental crustal structure. Our point here is that the precision of rms *Lg* measurements presents new challenges and new opportunities.

Assigning absolute levels of $m_b(Lg)$ for nuclear explosions at a fixed test site and for a fixed network is a far simpler task, one that we have addressed in this paper without special comment. While we have not discussed the problem of converting rms *Lg* to a magnitude value, this is a relatively straightforward task, implying calibration to a given magnitude scale. Presuming that magnitude in this sense, and yield, are related at the test site by a best-fitting line in the form

$$m_b(Lg) = a + b \cdot \log(\text{yield}),$$

it is clear that the scatter of points about this line is controlled by two factors. One is the precision with which $m_b(Lg)$ can be measured (e.g., 0.03 at a single station, as shown in this paper for the Shagan River area). The second is the additional uncertainty caused by variability of coupling from nuclear yield into *Lg* signal, a key issue that at present we are not in a position to resolve.

Assistance in addressing the second issue would come from open availability of yield information for some explosions at test sites of interest, preferably for the same explosions whose seismic signals were recorded at high-quality digital stations. We note that yields are not currently announced at the world's two main test sites (the Nevada Test Site and Shagan River), and yields announced at these sites for explosions in the past (Springer and Kinnaman, 1971, 1975; Bocharov *et al.*, 1989; Vergino, 1989a, b) were for the period prior to 1973 when few digital stations were in operation. However, preliminary indications, from a study of the four Semipalatinsk explosions for which there is both an announced yield from Bocharov *et al.* (1989) and an rms *Lg* signal measurement at NORSAR, are that rms *Lg* correlates well with log (announced yield) (Ringdal, 1989). This comparison can be used, for

example, to estimate the yield of the Joint Verification Experiment (JVE) explosion, conducted at Shagan River on 14 September 1988. From NORSAR *Lg* signals alone, the resulting estimate would be about 110 kt. As yet, the yield of this explosion, as determined from nonseismic measurements made on site, has not been announced, other than that it met the provisions of the JVE agreement between the United States and the USSR, and thus that it was indeed between 100 and 150 kt (Robinson, 1989).

An important advantage of the rms *Lg* method is its ease of use in combination with the robustness of the results. Thus, it makes essentially no difference where one uses a 2-min window or one based on a range of *Lg* group velocities (which would give a window about 40 sec at ARU for the range of group velocity used in NORSAR analyses). Also, the choice of filter band is not critical as long as the band enhances the main part of the *Lg* energy and is kept fixed in the analysis of different events. Our choice of a 0.6 to 3.0 Hz passband has been made in order to be consistent with previous NORSAR analyses.

Conclusions

This study has demonstrated that rms *Lg* amplitudes estimated from stations within the Soviet Union and China for Shagan River explosions show excellent consistency with NORSAR rms *Lg* estimates. This has several important implications:

1. rms *Lg* appears to be a stable source size estimator when computed at widely distributed stations and would therefore provide a reliable magnitude estimate once the proper correction term has been estimated for each station.
2. The stations studied (notably ARU, GAM, and WMQ) can be used to estimate *Lg* magnitudes for Shagan River explosions of much lower yield than is possible using the more distant NORSAR and Graefenberg arrays. Our analysis indicates that the SNR improvement allows rms *Lg* estimates to be made down to approximately m_b 3.5 at WMQ, compared to a threshold of about m_b 5.5 at NORSAR. An important precondition for WMQ is that it be set to provide continuous recording, rather than the triggered recording currently used.
3. Although single stations do not offer the increased stability obtained through array averaging, this is partly compensated by the higher SNR ratio, which means that modest noise fluctuations will be insignificant for the *Lg* measurements. Also, a possibility of decreasing scatter of magnitude estimates through averaging the three components of each station exists. Our initial analysis indicates that such an approach could be useful, but it may be necessary to determine correction terms for each component individually.
4. As more data (and possible additional stations) become available, a data base will be developed that will enable us to compute network averages, based on individual station data "calibrated" to NORSAR $m_b(Lg)$. This would facilitate both obtaining improved uncertainties of future explosions and maintaining a comparison to historic data. The calibration would best be done using direct, independent yield information, thus permitting reduced uncertainties in yield estimation (using seismic methods) for future explosions.
5. The *P*-wave detection capabilities of these single stations do not match those of the NORESS and ARCESS arrays; thus, teleseismic signals continue to be important for detection of small nuclear explosions.

It would be desirable to develop a theoretical basis to allow correction for attenuation of the *Lg* phase. Extension of the study to other nuclear explosion sites will also be an important topic. Of particular interest here is to study further the possible differences between the Shagan River and Degelen Mountains region.

Our studies confirm that *Lg* magnitude estimates of Semipalatinsk explosions are remarkably consistent between stations widely distributed in epicentral distance and azimuth. It thus appears that a single station with good SNR can provide $m_b(Lg)$ measurements with an accuracy (one standard deviation) of about 0.03 magnitude units. Therefore, *Lg* signals appear to provide an excellent basis for supplying estimates of the yields of nuclear explosions even down to below 1 kt, when such signals are recorded at high-quality digital, in-country seismic stations, and when calibrated by access to independent (nonseismic) yield information for a few nuclear explosions at the test sites of interest. In the context of monitoring a low-yield threshold test ban treaty, it will, in addition, be important to take into consideration various environmental conditions in the testing area, such as the possible presence of cavities, and to devise appropriate procedures for on-site observations in this regard.

ACKNOWLEDGMENTS

We appreciate the assistance of Dr. Holly Given of the University of California, San Diego, in providing prompt access to the data from IRIS stations in the USSR and details of instrument responses, Dr. Alan Ryall of the Center for Seismic Studies for access to the CDSN data, and Dr. Roger Clark of the University of Leeds for the BSVRP station GAM at Garm. P.G.R. thanks the Royal Norwegian Council for Scientific and Industrial Research for a fellowship that enabled his visiting NORSAR in the summer of 1989, and the Lawrence Livermore National Laboratory for support during the subsequent writing of this paper. His research on seismic monitoring is sponsored by Columbia University's Lamont-Doherty Geological Observatory by the Air Force Geophysics Laboratory under Contract F19628-89-K-0041. The NORSAR research reported here (R.A.H., and F.R.) was supported by the Advanced Research Project Agency of the Department of Defense and was monitored by the Air Force Office of Scientific Research under Contract F49620-89-C-0038.

REFERENCES

Bocharov, V. S., S. A. Zelentsoz, and V. N. Mikhailov (1989). Characteristics of 96 underground nuclear explosions at the Semipalatinsk test site (in Russian), *Soviet Atomic Energy (Atomnaya Energiya)* **67**, 210–214, September 1989.

The BSVRP Working Group (1989). The British Seismic Verification Research Project (BSVRP), *Q. J. R. Astr. Soc.* **30**, 311–324.

Campillo, M., M. Bouchon, and B. Massinon (1984). Theoretical study of the excitation, spectral characteristics, and geometrical attenuation of regional seismic phases, *Bull. Seism. Soc. Am.* **74**, 79–90.

Given, H. K. and J. Berger (1989). IRIS/IDA stations in the USSR: an update, Am. Geophys. Union Meeting, May 1989.

Herrmann, R. B. (1980). *Q* estimates using the coda of local earthquakes, *Bull. Seism. Soc. Am.* **70**, 447–468.

Lehmann, I. (1953). On the short period surface wave *Lg* and crustal structure, *Bulletin d'Information de L'Union Geodesique et Geophysique Internationale,* deuxième annee, 248–250, April 1953.

Lilwall, R. C., P. D. Marshall, and D. W. Rivers (1988). Body-wave magnitudes of some underground nuclear explosions at the Nevada (USA) and Shagan River (USSR) test sites, AWE Report No. 015/88, HMSO, London, England.

Nuttli, O. W. (1973). Seismic wave attenuation and magnitude relations for eastern North America, *J. Geophys. Res.* **78**, 876–885.

Nuttli, O. W. (1986a). Yield estimates of Nevada Test Site explosions obtained from seismic *Lg* waves, *J. Geophys. Res.* **91**, 2137–2151.

Nuttli, O. W. (1986b). *Lg* magnitudes of selected East Kazakhstan underground explosions, *Bull. Seism. Soc Am.* **76**, 1241–1251.

Nuttli, O. W. (1987). *Lg* magnitudes of Degelen, East Kazakhstan, underground explosions, *Bull. Seism. Soc. Am.* **77**, 679–681.

Nuttli, O. W. (1988). *Lg* magnitudes and yield estimates for underground Novaya Zemlya nuclear explosions, *Bull. Seism. Soc. Am.* **78**, 873–884.

Patton, H. P. (1988). Application of Nuttli's method to estimate yield of Nevada Test Site explosions recorded on Lawrence Livermore National Laboratory's digital seismic system, *Bull. Seism. Soc. Am.* **78**, 1759–1772.

Press, F. and M. Ewing (1952). Two slow surface waves across North America, *Bull. Seism. Soc. Am.* **42**, 219–228.

Ringdal, F. (1983), Magnitudes from *P* coda and *Lg* using NORSAR data, in *NORSAR Semiannual Technical Summary, 1 October 82–31 March 83*, NORSAR Sci. Rept. No. 2-82/83, NTNF/NORSAR, Kjeller, Norway.

Ringdal, F. and B. K. Hokland (1987). Magnitudes of large Semipalatinsk explosions using *P* coda and *Lg* measurements at NORSAR, in *Semiannual Technical Summary, 1 April–30 September 1987*, NORSAR Sci. Rept. 1-87/88, Kjeller, Norway.

Ringdal, F. and J. Fyen (1988). Comparative analysis of NORSAR and Graefenberg *Lg* magnitudes for Shagan River explosions, in *NORSAR Semiannual Technical Summary, 1 April–30 September 88*, NORSAR Sci. Rept. 1-88/89, NTNF/NORSAR, Kjeller, Norway.

Ringdal, F. and P. D. Marshall (1989). Yield determination of Soviet underground nuclear explosions at the Shagan River Test Site, in *NORSAR Semiannual Technical Summary, 1 October 1988–31 March 1989*, NORSAR Sci. Rept. 2-88/89, NTNF/NORSAR, Kjeller, Norway.

Ringdal, F. (1989). NORSAR *P*-wave detection and yield estimation of selected Semipalatinsk explosions, in *NORSAR Semiannual Technical Summary, 1 April–30 June 1989*, NORSAR Sci. Rept. 1-89/90, NTNF/NORSAR, Kjeller, Norway.

Ringdal, F. (1990). Teleseismic event detection using the NORESS array with special references to low-yield Semipalatinsk explosions, *Bull. Seism. Soc. Am.* **80**, Part B, 2127-2142.

Robinson, C. P. (1989). The Joint Verification Experiment: a unique approach to developing verification agreements, *Disarmament* **12**, 90–95.

Springer, D. L. and R. L. Kinnaman (1971). Seismic source summary for U.S. underground nuclear explosions, 1961–1971, *Bull. Seism. Soc. Am.* **61**, 1073–1098.

Springer, D. L. and R. L. Kinnaman (1975). Seismic source summary for U.S. underground nuclear explosions, 1971–1973, *Bull. Seism. Soc. Am.* **65**, 343–349.

Vergino, E. S. (1989a). Soviet Test Yields, *EOS, Trans. Am. Geophys. Union* 1511+, November 29, 1989.

Vergino, E. S. (1989b). Soviet test yields, corrections and additions, *EOS Trans. Am. Geophys. Union* 1569, December 26, 1989.

NTNF/NORSAR
P.O. Box 51
Kjeller, Norway
(R.A.H., F.R.)

Lamont-Doherty Geological Observatory
and Department of Geological Sciences
Columbia University
Pallisades, NY 10964
(P.G.R.)

Manuscript received 18 June 1990

Bulletin of the Seismological Society of America, Vol. 80, No. 6, pp. 2127–2142, December 1990

TELESEISMIC EVENT DETECTION USING THE NORESS ARRAY, WITH SPECIAL REFERENCE TO LOW-YIELD SEMIPALATINSK EXPLOSIONS

BY FRODE RINGDAL

ABSTRACT

The small-aperture NORESS array in Norway has been designed for improving signal-to-noise ratios at high frequencies (1 to 15 Hz). While the main motivation for this has been to enhance the capabilities for detecting and characterizing weak seismic events at regional distances, it has been found that the array is also very effective in the teleseismic distance range, in particular for Eurasia. This results from a combination of two factors: (1) due to high Q paths, Eurasian earthquake and explosion recordings generally show high dominant frequencies, typically in the range of 1.5 to 4.0 Hz, where the noise level at the site is low; and (2) the array provides a particularly high signal-to-noise ratio gain of 12 to 14 dB (0.6 to 0.7 m_b units) at these frequencies.

Analysis of NORESS on-line detection performance shows that there are large regional variations, even within small epicentral areas. This is interpreted as resulting mainly from signal focusing effects underneath the source areas, in analogy to the receiver focusing effects earlier observed across large arrays. A detailed study of NORESS recordings of underground nuclear explosions at the Semipalatinsk Test Site has shown that relative to worldwide m_b, NORESS has a significant positive m_b bias. It is highest (1.0 m_b units) for the eastern part (Shagan River) and somewhat lower (0.4 m_b units) for the western parts (Degelen/ Konystan), although there is a fair amount of scatter within each area.

Analyzing observed signal-to-noise ratios at the NORESS site for a set of low-yield nuclear explosions at Semipalatinsk, with published yields available in the Soviet literature, it is estimated that fully coupled explosions of yields as low as 0.1 kt would be detectable by NORESS under normal noise conditions. However, to give a precise threshold is difficult because of the low number of reference events available and the significant amount of extrapolation involved.

It is emphasized that this detection level will not be achieved in cases when the noise level is abnormally high (e.g., in the coda of a large earthquake) or if coupling conditions are not optimal (e.g., in the case of full or partial cavity decoupling). It must also be noted that the event identification threshold is necessarily higher than the signal detection threshold.

INTRODUCTION

The primary objectives of seismic arrays are to detect low-magnitude seismic events, to provide phase identification and approximate epicenter estimates, to suppress interfering signals, and (by beamforming) to reduce waveform distortion caused by local wave scattering effects.

The usefulness of small-aperture arrays for teleseismic detection was demonstrated as early as in the 1960s by the Vela arrays in the United States. These arrays (UBO, WMO, CPO, BMO, and TFO) remained in operation for about 10 yr and proved to be extremely efficient in detecting weak teleseismic signals, as documented by North (1977). From the results of Lilwall (1986), it can be inferred that the best of these stations (UBO, TFO, and BMO) had an effective 50 per cent detection threshold of 0.2 to 0.3 in terms of $\log(A/T)$ during the years 1964 to 1969. Here, the effective threshold is defined as the station's $\log(A/T)$ threshold

compensated for the average station bias relative to worldwide m_b. By adding a distance/depth correction term, it follows that these stations had a 50 per cent threshold of approximately $m_b = 4.0$ at typical teleseismic distances.

The NORESS and ARCESS arrays were designed primarily to process high-frequency signals recorded from events at local and regional distances, and their excellent performance in this regard has been documented by Sereno and Bratt (1989) and Mykkeltveit *et al.* (1990, this volume). However, the design was also aimed at obtaining improved detection and analysis possibilities for teleseismic phases, in particular at frequencies of about 2 Hz and higher. Significant energy at these frequencies is commonly observed even at teleseismic distances for high Q propagation paths.

The topic of this paper is teleseismic detection using the NORESS array. We discuss the NORESS detection algorithm and present statistics of a 1-yr period illustrating the main features of the real-time performance. As a case study, we analyze in detail the NORESS capabilities for detecting nuclear explosions in the Semipalatinsk area, with particular emphasis on low-yield explosions. We show that, for this region, NORESS has an outstanding detection capability, and we discuss some implications of these observations in the context of nuclear test ban monitoring. While this paper focuses upon *detection* capability using P waves, the results should be seen in conjunction with the potential for precise yield *estimation* using Lg waves, as discusses by Ringdal and Marshall (1989) and Hansen *et al.* (1990, this volume).

NORESS Detection Processing

Real-time detection of seismic events is performed at NORESS using the RONAPP algorithm described by Mykkeltveit and Bungum (1984). In terms of teleseismic P phase detection, the essential features are:

- application of multiple narrow-band filters
- beamforming using optimum (filter-dependent) subgeometries
- infinite-velocity as well as steered beams
- threshold detection on each individual beam (STA/LTA)
- F-K analysis of detected phases to provide phase velocity and azimuth information.

The NORESS geometry is shown in Figure 1, and Table 1 specifies the beam deployment used during 1985 to 1989. Later modifications (Mykkeltveit *et al.*, 1990, this volume) have mainly served to improve the detection of regional phases, whereas the NORESS capability in the teleseismic range is well illustrated by the performance of the original deployment as discussed in this paper.

In Figure 2, we show the distribution, by beam number, of NORESS detections for a typical 1-yr period (1987). Note that, whenever simultaneous detections occur on several beams, only the beam with the highest signal-to-noise ratio (SNR) is counted, and that detections are grouped together if they occur less than 4 sec apart. The total number of on-line detections during 1987 was 50,665. In Figure 2, only those detections with estimated phase velocity greater than 3.0 km/sec have been included, and the different types of hatching indicate the type of phase, based on the phase velocity estimated in the automatic frequency-wavenumber analysis procedure.

Figure 2 is instructive in several ways, and we note that the patterns are similar also for other years. Of the total number of 29,013 detections shown in Figure 2,

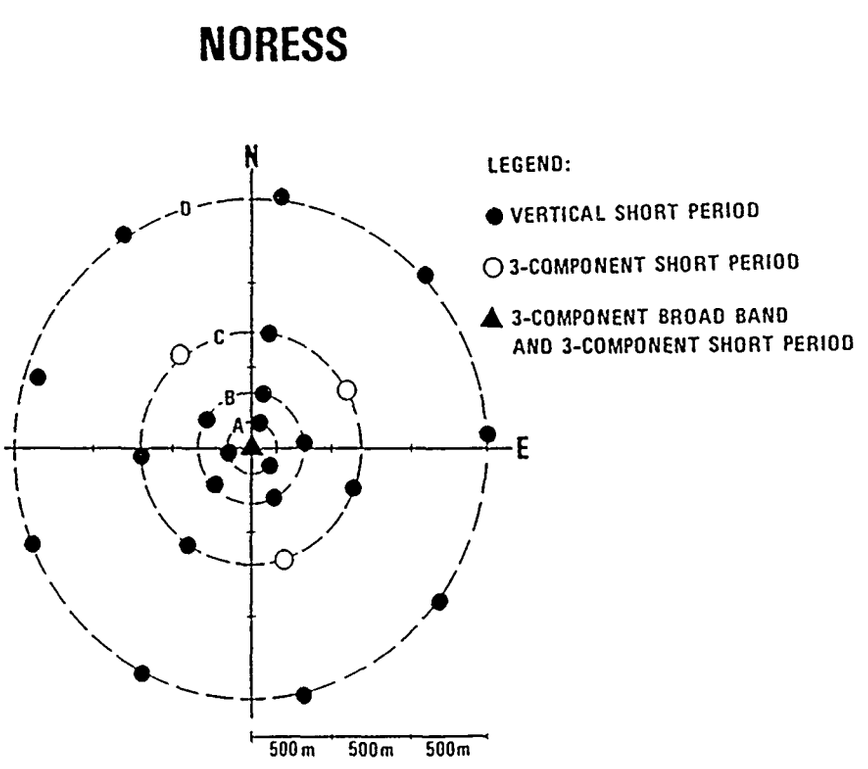

FIG. 1. NORESS array geometry. The seismometers are arranged in four concentric rings (denoted as A, B, C, and D) around a center site (denoted A0). NORESS is located within the geographical area of the large NORSAR array, and the coordinates of the center site are 60.73°N, 11.54°E.

TABLE 1

NORESS BEAM DEPLOYMENT (1985–1989)

Beam No.	Azimuth (°)	Slowness (sec/km)	Filter Band	Beam Type	*SP* Channels Used (1 = used, 0 = unused)	STA/LTA Threshold
1	0	.000	1.0–3.0	C	100000000111111111111111	4.0
2	0	.000	1.5–3.5	C	100000000111111111111111	4.0
3	0	.000	2.0–4.0	C	100011111111111111111111	4.0
4	0	.000	2.5–4.5	C	100011111111111100000000	4.0
5	0	.000	3.0–5.0	C	100011111111111000000000	4.0
6	0	.000	4.0–8.0	C	111111111000000000000000	5.0
7	0	.000	8.0–16.	C	111111111000000000000000	5.0
8	0	.070	2.0–4.0	C	100011111111111111111111	4.0
9	90	.070	2.0–4.0	C	100011111111111111111111	4.0
10	180	.070	2.0–4.0	C	100011111111111111111111	4.0
11	15	.070	2.5–4.5	C	100011111111111111111111	4.0
12	75	.070	2.5–4.5	C	100011111111111111111111	4.0
13	135	.070	2.5–4.5	C	100011111111111111111111	4.0
14	25	.070	3.0–5.0	C	100011111111111111111111	4.0
15	75	.070	3.0–5.0	C	100011111111111111111111	4.0
16	125	.070	3.0–5.0	C	1000[illegible]1111111111111111	4.0
17	0	.000	2.0–4.0	C	100011111111111000000000	4.0
18	0	.000	1.0–2.0	I	100000000111111000000000	2.5
19	0	.000	2.0–3.0	I	100000000111111000000000	2.5
20	0	.000	2.0–4.0	I	100000000000000111111111	2.1

Note. Beam Type "C" = coherent beam; "I" = incoherent (envelope) beam. The channel sequence is normal: A0Z, A1Z–A3Z, B1Z–B5Z, C1Z–C7Z, and D1Z–D9Z.

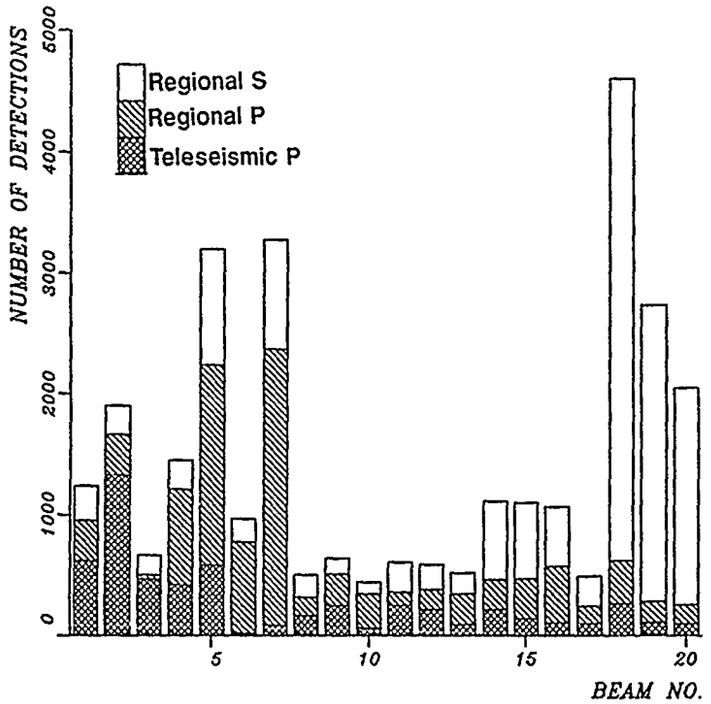

FIG. 2. NORESS on-line detections during the year 1987, distributed by beam number (see Table 1). For each detected phase, the beam with the largest SNR has been selected. Only detections with estimated phase velocity exceeding 3.0 km/sec have been included in the figure, and the distribution of phase velocities is indicted on the plot.

about 50 per cent have estimated phase velocities typical of *S* or *Lg* (<6 km/sec), about 30 percent are in the range from 6 to 12.5 km/sec (typical of local and regional *P* phases), and about 20 per cent have estimated phase velocity corresponding to teleseismic *P* or *PKP* (>12.5 km/sec). We note that detections with estimated phase velocity 3.0 km/sec or below (which are not included in Fig. 2) comprise about 43 per cent of the total number of detections during 1987. A detailed study of these "slow" phases has been conducted by Kværna (1990).

Most of the detections with teleseismic velocities occur on the infinite velocity beams 1 to 5, covering frequency bands from 1 to 3 Hz (beam 1) and from 3 to 5 Hz (beam 5). In contrast, high-frequency beams 6 (4 to 8 Hz) and beam 7 (8 to 16 Hz) are not very effective in the teleseismic range. The steered beams (nos. 8 to 16), directed toward Eurasia, do contribute to increase the number of teleseismic detections. Thus, even for a small aperture array, the deployment of steered beams is important in order to fully exploit its teleseismic detection potential. We note that the three incoherent beams (nos. 18 to 20) (see Ringdal *et al.*, 1975), mainly detect "slow" (secondary) phases, but they have also been found effective in detecting *P*-type phases arriving during the coda of large events.

CHARACTERISTICS OF DETECTED SIGNALS

Figure 3 shows the distribution of dominant signal period at NORESS for detected phases of teleseismic velocity. The large majority of observations are within 0.25 to 0.6 sec, or 1.5 to 4 Hz, which is the band in which NORESS has its optimum beamforming gain (Kværna, 1989). We have not been able to identify any consistent

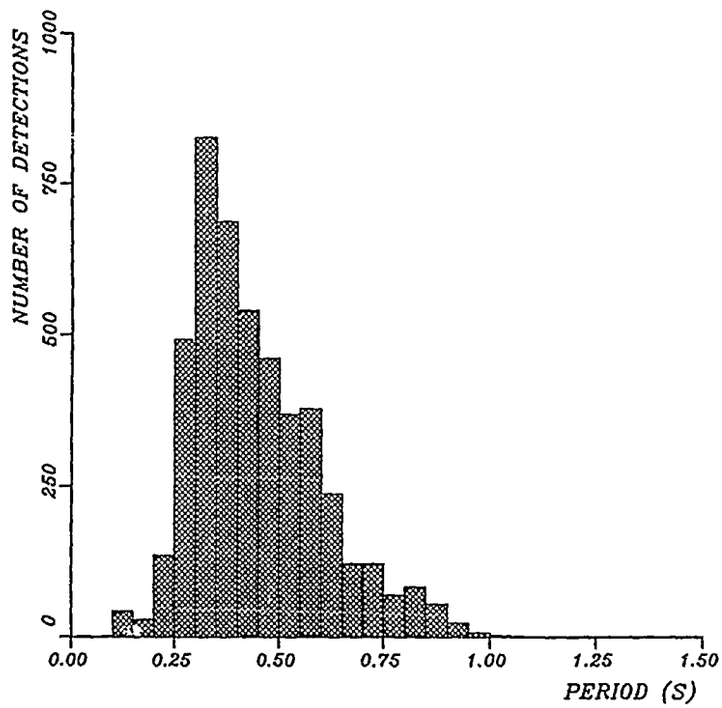

FIG. 3. Histogram showing the distribution of dominant signal period for teleseismic *P* and *PKP* phases detected by NORESS during 1987. Note that the majority of the observations are below 0.5 sec (i.e., with a dominant frequency exceeding 2 Hz).

difference in dominant frequency of earthquakes and explosions, and thus it appears that the effects of the propagation paths dominate the source effects in this regard.

The distribution of NORESS teleseismic detections by estimated azimuth during 1987 is shown in Figure 4. The predominance of high-frequency detections ($f > 2$ Hz) is seen at all azimuths, but the most striking feature is the large number of detections in directions toward north and (in particular) east. While this, of course, to a large extent reflects the distribution of seismicity, it has been verified by comparison to NEIC and ISC bulletins that the NORESS capability in detecting small teleseismic events is particularly good within Eurasia, as indicated by this azimuthal distribution.

A study comparing the teleseismic detection performance of NORESS and NORSAR was carried out by Ringdal (1985). The study showed that there were many similarities in the overall detection performance of the two arrays, even though NORESS is designed for high-frequency signal detection, whereas NORSAR has its optimum SNR gain at lower frequencies (around 1 Hz). On the average, NORESS detected 84.5 per cent of the events reported in the NORSAR bulletin, as well as many additional teleseismic phases. Not surprisingly, many of the detections missed by NORESS were small earthquakes of low dominant frequency, but also some high-frequency signals from certain regions in Eurasia were not detected at NORESS.

This latter observation requires some comments, and, in fact, touches upon one of the major reasons why large variations in regional detectability and *P*-wave amplitude patterns are commonly observed for teleseismic station networks (Ringdal, 1977). The key factor appears to be *P*-wave focusing effects in the upper

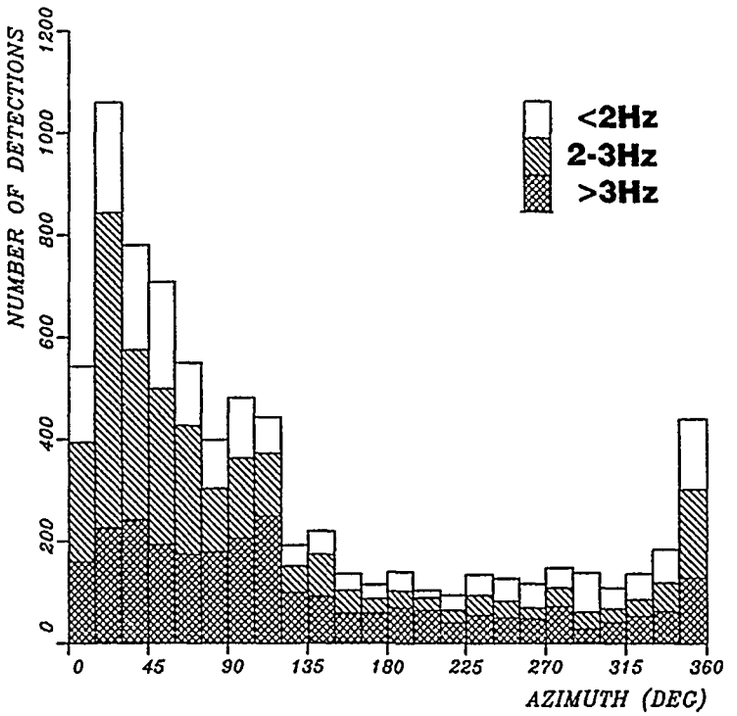

FIG. 4. NORESS on-line detections (teleseismic *P* and *PKP* phases) during 1987 distributed by azimuth. The number of phases with dominant frequency exceeding 3 Hz, between 2 and 3 Hz, and below 2 Hz are indicated for each azimuth interval.

mantle, both underneath the source and receiver. This can cause a strong, regionally dependent shift in amplitude patterns, even across the limited aperture of the NORSAR array (Berteussen, 1975). Thus, for regions like Hindu Kush and Kuriles Islands, the NORESS site has unfavorable focusing effects compared to some NORSAR subarrays, and consequently NORSAR has a better detection performance. For other epicentral regions, notably the Semipalatinsk area (to be discussed later), signal focusing at NORESS is very strong. In such cases, the added SNR gains at higher frequencies for the NORESS beam give this array a higher detection capability than NORSAR.

NORESS Detection of Semipalatinsk Explosions

As a particular case study, we will analyze in some detail the capability of the NORESS array to detect explosions conducted near Semipalatinsk, in Eastern Kazakhstan. This has for many years been the main Soviet nuclear weapons test site, and comprises three distinct subareas: Shagan River, Degelen Mountains, and Konystan (see Marshall *et al.*, 1985).

Figure 5 shows the *P*-wave amplitude pattern across the NORSAR array, which is typical for Semipalatinsk explosion recordings. The location of NORESS within the NORSAR array area is indicated, and the figure shows the very strong signal focusing effects at the NORESS site for this particular source area. It is noteworthy that the *P* coda amplitudes show less variability than the initial *P* phase (Ringdal, 1983). The use of *P* coda can thus increase the stability of m_b estimates, although for very low SNR its usefulness declines due to noise interference. Ringdal (1977) showed that the amount of variation in *P*-wave amplitudes across NORSAR

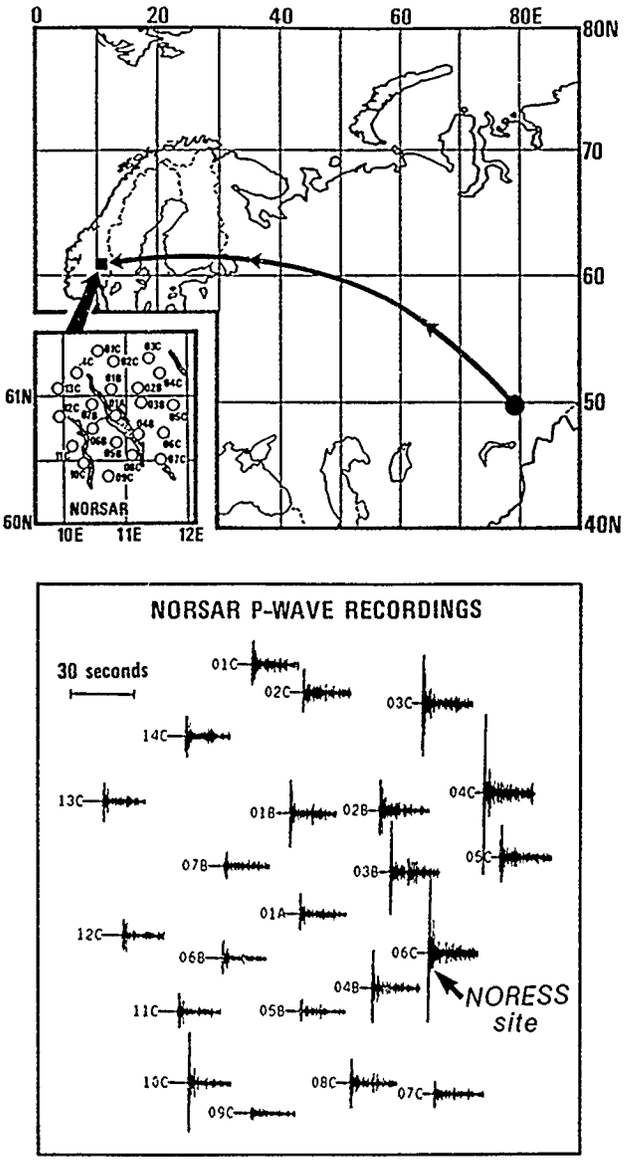

FIG. 5. The *top portion* shows the great circle path from Semipalatinsk to NORSAR (distance of 4200 km), with the NORSAR array configuration inserted. The *bottom portion* displays NORSAR *P*-wave recordings (one trace for each subarray) for an explosion at Semipalatinsk. The traces have been filtered in the band of 2 to 4 Hz. Note the large variations in signal amplitudes. The NORESS site (at subarray 06C) is seen to have very favorable receiver focusing effects for *P* waves from the Semipalatinsk area.

increases with increasing signal frequency. Thus, the receiver focusing effects are particularly important for seismic stations designed to detect high-frequency signals.

The NORESS beamforming SNR gain for Semipalatinsk is illustrated in Figure 6, which shows single sensor and beam recordings of a small nuclear explosion on 28 December 1988. The traces have been filtered in the 2 to 4 Hz band, which is near optimum for this epicentral region. The significant SNR improvement on the array beam is evident, and adds to the strong signal focusing effects in providing high detection capability.

NORESS *P*-wave recordings of the two underground nuclear explosions conducted during the Joint Verification Experiment (JVE) are shown in Figure 7.

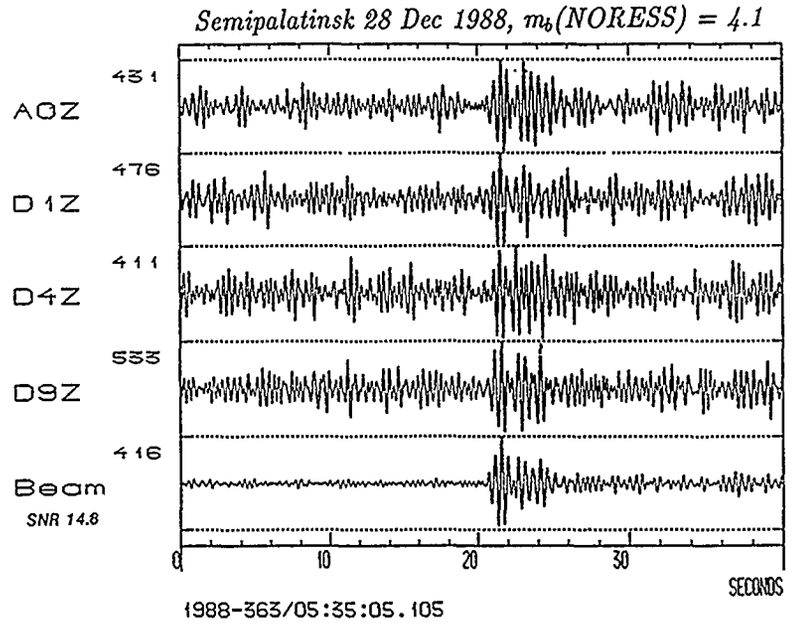

FIG. 6. NORESS recordings (four individual seismometers and the array beam) for a small underground nuclear explosion at Semipalatinsk 28 December 1988. The traces have been filtered in the band of 2 to 4 Hz. Note the significant improvement in signal-to-noise ratio on the array beam.

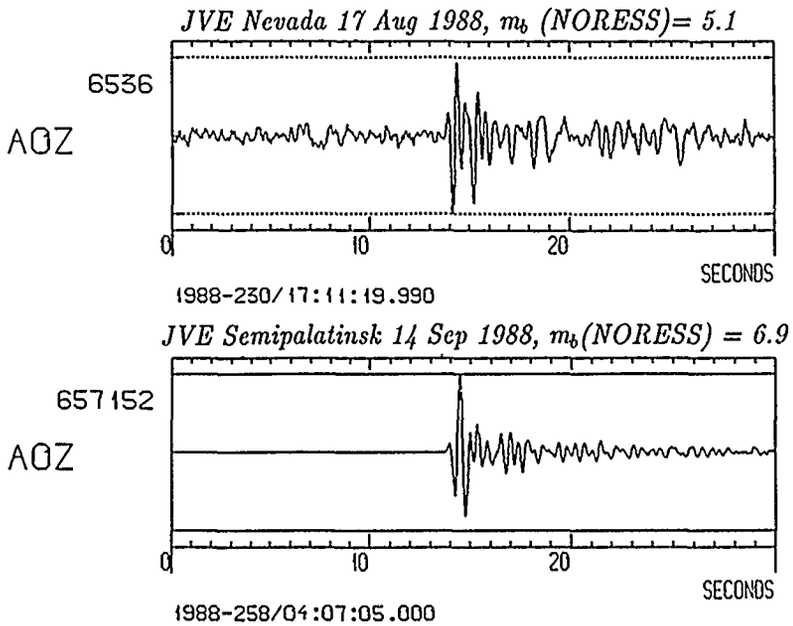

FIG. 7. NORESS center seismometer recordings of *P* waves from the two nuclear explosions (each in the range of 100 to 150 kt) conducted during the 1988 Joint Verification Experiment (JVE). The scaling (maximum count) is shown to the *left* of each trace. Note that the recorded amplitudes differ by two orders of magnitude, whereas the dominant frequency is similar, near 2 Hz.

These explosions, one at the Nevada Test Site, USA, and one at Semipalatinsk (Shagan River) USSR, were both in the yield range of 100 to 150 kt. The figure illustrates well the differences in signal strength as recorded at NORSAR, with m_b values of 5.1 and 6.9, respectively. It is noteworthy that both signals have dominant frequency at NORESS near 2 Hz, and the NORESS SNR is about two orders of

magnitude higher for the Semipalatinsk event. Relative to worldwide m_b, NORESS has a magnitude bias of about −0.4 and +0.8 m_b units for these two explosions.

A closer study of NORESS m_b bias relative to worldwide P-wave magnitudes shows that even within the limited area of the Semipalatinsk test site, there are significant variations (Figure 8). Explosions from the Shagan River area have an average bias of 1.0 m_b units, compared to 0.4 m_b units for Degelen Mountains. This can be interpreted as near-source P-wave focusing effects in the upper mantle, i.e., as a counterpart to the near-receiver focusing effects observed at NORSAR and illustrated in Figure 5.

The significant difference in station m_b corrections between Shagan and Degelen has previously been noted for NORSAR by Ringdal (1983) and for NORESS by Pulli (1987). Data published by Marshall *et al.* (1985) show that a similar bias also exists for many other stations in Fennoscandia. For the Konystan area, we have no NORESS recordings available, but we can infer from NORSAR data that the NORESS m_b bias would be similar to that observed for Degelen.

Detailed data on a number of nuclear explosions conducted at Semipalatinsk have recently been published in the Soviet literature by Bocharov *et al.* (1989) (see also Vergino, 1989a, b). The Soviet publication includes yields of a number of nuclear explosions at Semipalatinsk prior to 1973. We have analyzed available NORSAR data for these explosions for the purpose of assessing the detection threshold of the NORESS system in terms of explosion yields. Figure 9 shows NORSAR single instrument P-wave recordings of the three smallest explosions for

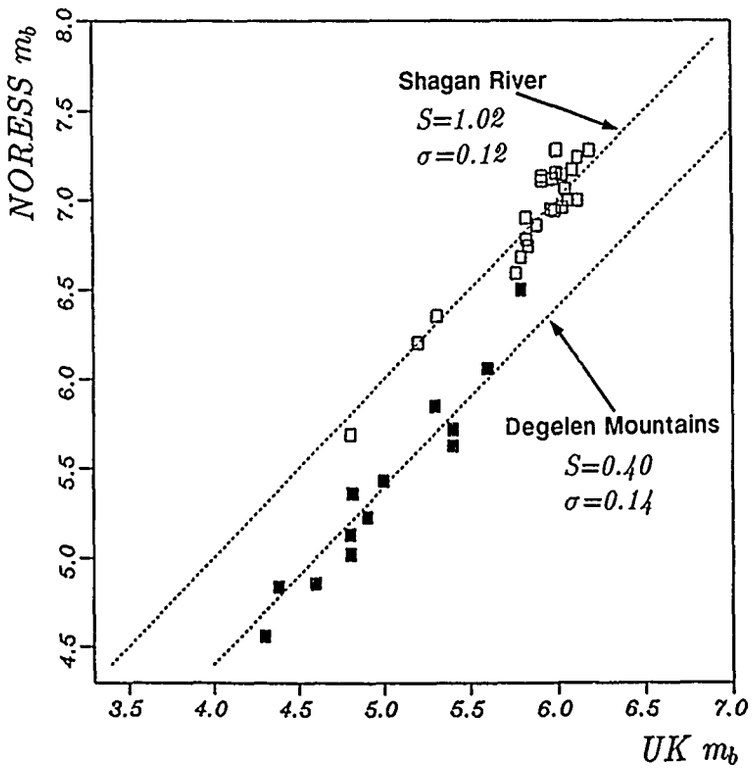

FIG. 8. Comparison of NORESS and worldwide m_b (as calculated at Blacknest, United Kingdom) for Semipalatinsk explosions. Note the difference in average m_b bias between events from Shagan River (1.0 m_b units) and Degelen Mountains (0.4 m_b units). The straight lines on the plot have a restricted slope of 1.00.

which we have data available: 2 September 1972 (2 kt), 28 March 1972 (6 kt), and 16 August 1972 (8 kt) (see also Table 2). We have chosen to display the instrument 06C02, which is co-located with the center seismometer of the NORESS array. (Note that NORESS data have only been available since 1984.) The traces have been filtered in the band 2.0 to 4.0 Hz, the signal-to-noise ratios (STA/LTA) are given for each trace.

It is clear from this figure that the NORESS detection threshold, even at the single seismometer level, is well below the yields of the three events shown. We will proceed to give a preliminary estimate of the NORESS capability using these single sensor data and taking into account the gain obtained through array beamforming.

Detection Capability in Terms of Yield

A simple model for estimating detection capability in terms of yield can be given as follows: let m denote even magnitude obtained from a global network. Assume

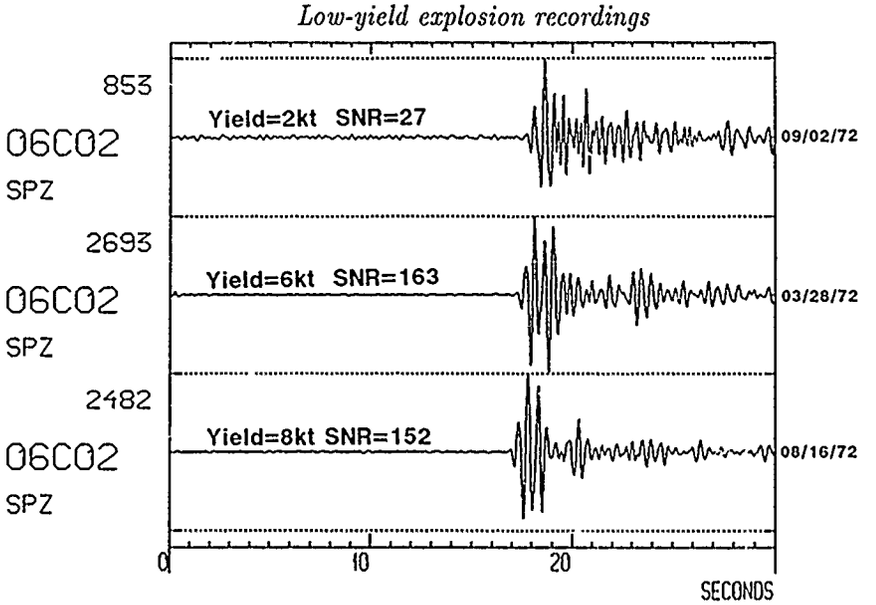

FIG. 9. NORESS single seismometer recordings (instrument 06C02) of three low-yield Semipalatinsk nuclear explosions in 1972. This recording site is co-located with the present NORESS center site. The traces have been filtered in the band of 2.0 to 4.0 Hz, and the SNR is shown for each trace. Note the very high SNR observed even at the single sensor level.

TABLE 2

Low-Yield Semipalatinsk Explosions

No.	Date	Origin Time	Latitude (°N)	Longitude (°E)	Region	Yield (kt)	m_b (UK)	NORSAR 06C02	
								m_b	SNR
1	06/06/71	04.02.59.7	49.975	77.660	Konystan	16	5.526	5.96	212
2	10/09/71	06.02.59.7	40.978	77.641	Konystan	12	5.371	5.80	141
3	10/21/71	06.02.59.7	49.974	77.597	Konystan	23	5.580	5.82	166
4	03/28/72	04.22.00.1	49.733	78.076	Degelen	6	5.177	5.74	163
5	08/16/72	03.16.59.8	49.765	78.059	Degelen	8	5.105	5.72	152
6	09/02/72	08.56.59.9	49.959	77.641	Konystan	2	4.788	5.19	27

Origin time, epicentral coordinates, and yields are those given by Bocharov *et al.* (1989). The m_b (UK) values are those listed in Vergino (1989a). The NORSAR measurements (m_b and signal-to-noise ratio) are based on seismometer 06C02, which is co-located with the present NORESS center site.

that, for an explosion of given yield Y (in kilotons), we have the following linear relation (setting $W = \log Y$):

$$m = a + b \cdot W + \varepsilon(\tau^2). \tag{1}$$

Here, $\epsilon(\tau^2)$ is a zero mean, normally distributed random term of variance τ^2, i.e., the conditional distribution of m, given W, is normal $(a + bW, \tau^2)$. The parameters a and b are unknown coefficients. We note, however, that in the literature, a value of b slightly below 1.0 is often used. Thus, Vergino (1989a) has estimated b to be in the range of 0.7 to 0.8 by comparing worldwide m_b with the yields published by Bocharov *et al.* (1989).

At a given seismic station, the observed magnitude m^* is assumed to be related to m by

$$m^* = m + S + \epsilon(\sigma^2) \tag{2}$$

where S is a station bias term for the region being considered, and σ^2 the associated variance. The magnitude-yield relation at the station thus becomes

$$m^* = a^* + b \cdot W + \epsilon(\sigma^2 + \tau^2) \tag{3}$$

where $a^* = a + S$.

Following Ringdal (1975), we will further assume that for a given false alarm rate an event is detected if $m^* > m_T$. Here, m_T is a normally distributed "threshold variable," i.e.,

$$m_T = G + \epsilon(\gamma^2) \tag{4}$$

where G is the 50 per cent detection threshold in terms of observed magnitudes at the station, and γ^2 is the associated variance.

From (2) and (4), we obtain

$$m^* - m_T = m + (S - G) + \epsilon(\sigma^2 + \gamma^2), \tag{5}$$

which leads to the following "detection curve," i.e., the probability of detection at the station, given the worldwide magnitude m:

$$\text{Prob(Detect}/m) = \text{Prob}(m^* - m_T > 0/m) = \Phi\left(\frac{m + (S - G)}{(\sigma^2 + \gamma^2)^{1/2}}\right) \tag{6}$$

where Φ denotes the standard (0, 1) cumulative Gaussian distribution function.

For a given yield, we can proceed in a similar way, combining (1) and (5) to obtain

$$m^* - m_T = a + b \cdot W + (S - G) + \epsilon(\sigma^2 + \gamma^2 + \tau^2). \tag{7}$$

This leads to a detection curve in terms of yield, i.e., the probability of detection at the station, given the yield, as follows:

$$\text{Prob(Detect}/W) = \text{Prob}(m^* - m_T > 0/W) = \Phi\left(\frac{a + bW + (S - G)}{(\sigma^2 + \gamma^2 + \tau^2)^{1/2}}\right). \tag{8}$$

In the preceding development, we have assumed that the error terms are statistically independent. We note that a, b, and τ, which characterize the magnitude-yield relationship (1), are estimated independently of the parameters G and γ in (4), which characterize the station detection threshold in terms of magnitude. Likewise, the parameters S and σ in (2), which characterize the station bias term, can be estimated separately.

In our particular case, we are considering a single station (NORESS) and a limited source region (Semipalatinsk). Thus, the distance correction term $B(\Delta)$ in the m_b calculations will be a constant. This means that we may obtain the threshold statistics directly from observations of $\log(A/T)$ during noise conditions. In order to obtain reliable thresholds, it is important that these statistics are tied to wave frequencies close to those where the signals are actually detected. In the case of NORESS detection of Semipalatinsk explosions, this means obtaining such statistics at frequencies near 2 Hz.

Using the 1-yr NORESS noise statistics published by Fyen (1990) and calibrating to $\log(A/T)$ values near 2 Hz, we have estimated the NORESS detection threshold for the Semipalatinsk region (with a beam deployment as discussed previously) to be $G = 3.7$, $\gamma = 0.1$. Taking the NORESS m_b bias into account ($S = 0.4$ for Degelen/Konystan, $S = 1.0$ for Shagan River), this implies by (6) a 50 per cent detection threshold estimate in terms of worldwide m_b of 3.3 and 2.7 for the two subregions, respectively.

In order to obtain a detectability estimate in terms of yield, a possible approach would be to substitute the above parameter values directly in (8), assuming the relationship (1) between yield and worldwide m_b to be known. However, as shown by Vergino (1989a), the slope of this relationship depends upon the method used in calculating m_b, and we note that even a small error in the slope would have significant effects on the estimated thresholds. For this reason, we choose instead to illustrate the NORESS detection capability by plotting observed station magnitudes against available published yields; thus, in effect estimating the relationship (3) directly. While we will still need to make assumptions about the slope, the graphical representation has the advantage of making it easy to visualize the effects on the threshold estimate resulting from changes in this parameter.

In Figure 10 we plot observed station m_b values for the six smallest explosions with available data at the NORESS site (Table 2). The limited number of data points precludes a reliable estimate of the slope b in (3) directly from the data, so we have used a fixed b value of 0.75. (A higher value of b would imply higher estimated yield thresholds.) The NORESS m_b threshold range (±2 S.D.) for the array beam is marked on the plot.

Figure 10 indicates that, given similar, coupling conditions and noise levels as in our data base of six explosions, Semipalatinsk explosions of yields at 0.1 kt would be expected to produce detectable signals at NORESS. We note that the six reference explosions are all from Degelen or Konystan. In view of the previous discussions, the detectability for Shagan River explosions would be expected to be even better. Supporting evidence in this regard comes from analysis of the 16 kt explosion at Shagan River on 10 February 1972, which was not included in Table 2 since its P-wave signals were so strong that they exceeded the dynamic range of the NORSAR digital recording system. It is evident that both the m_b and the SNR of this explosion would have exceeded the values for the explosions of similar size listed in Table 2.

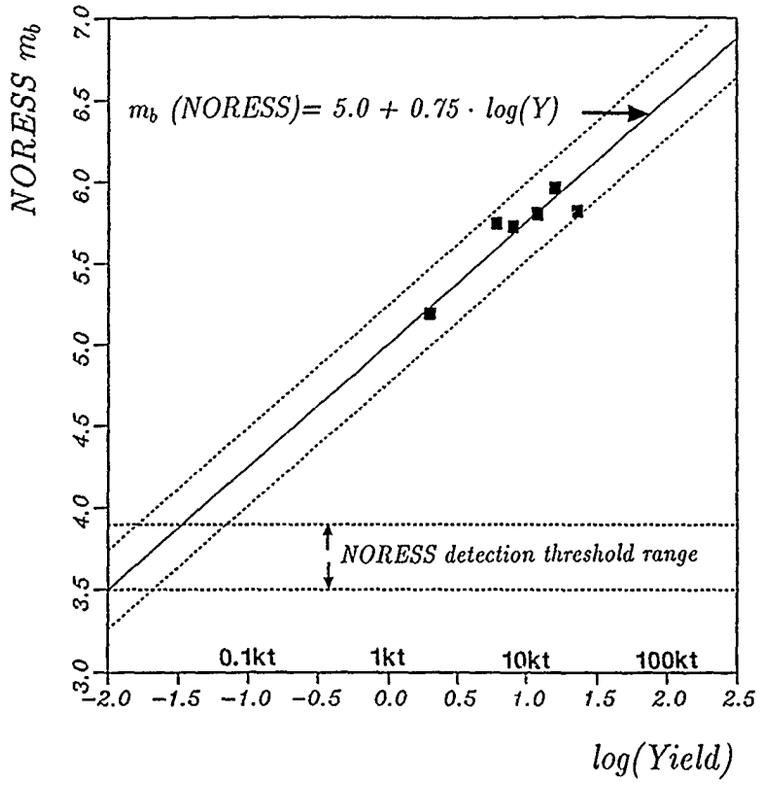

FIG. 10. Observed m_b versus yield (Bocharov *et al.*, 1989) for six Semipalatinsk nuclear explosions listed in Table 2. The straight line has been fitted using a restricted slope of 0.75. The m_b values are based on NORSAR seismometer 06C02, located at the present NORESS center site. The estimated range of the NORESS m_b detection threshold is indicated (see text for details).

CONCLUSIONS

Based on our studies of observed NORESS detection processing performance, the following conclusions can be made regarding teleseismic detection.

1. The NORESS experience shows that small arrays have a potential for providing excellent detection capability at teleseismic distances.
2. Array beamforming gain at NORESS is essentially determined by signal frequency contents and is highest (>10 dB) in the range of 1.5 to 4 Hz. Dominant signal frequencies in this range are commonly observed at teleseismic distances, in particular for earthquakes and explosions in Eurasia.
3. Application of multiple narrow-band filters, in conjunction with selection of an optimum subgeometry for each filter band in forming array beams is effective in detection processing.
4. Infinite-velocity beams are very effective for detecting teleseismic phases, but steered beams can provide additional gain in performance.
5. There is considerable regional variation in NORESS detection performance, and this is attributed to *P*-wave focusing effects in the upper mantle, both underneath the source and the receiver.
6. NORESS has particularly favorable signal focusing effects for *P* waves from events at the Semipalatinsk Test Site. The NORESS array detection threshold

in terms of explosion yield is estimated at about 0.1 kt for fully coupled Semipalatinsk explosions, assuming normal noise conditions.

While the excellent NORESS capability of Semipalatinsk explosions must be considered well documented, it is important to note that this does not imply a similar capability for other regions of Eurasia. Furthermore, the quoted threshold will not be achieved in cases where the noise level is abnormally high (e.g., in the coda of a large earthquake) or if coupling conditions are not optimal (e.g., in case of full or partial cavity decoupling). It must also be noted that the event identification threshold is necessarily higher than the signal detection threshold.

It is of interest in the connection to note that the processing of high frequency signals offered by regional arrays can be important in improving the possibilities to detect P waves from small underground explosions during the coda of large earthquakes. An illustration of this is given in Figure 11, which shows NORSAR single seismometer data for an actual case of a mixed earthquake-explosion recording in 1979. In this figure NORSAR signals (06C center instrument) from an m_b 5.8 earthquake near Kamchatka are followed 1 min later by signals from a small presumed explosion ($m_b \sim 4.0$) at Semipalatinsk. With the standard NORSAR bandpass filter of 1.2 to 3.2 Hz, the latter signal is completely masked by the earthquake coda, whereas a filter of 3.2 to 5.2 Hz shows the explosion signal dominating that of the earthquake. While this example points out an important benefit of high-frequency signal processing, it is emphasized that the frequency separation of the earthquake coda and the explosion P wave will decrease if the two sources are located more closely together.

Initial experience from the ARCESS array has shown capabilities for teleseismic detection similar to those of NORESS. While ARCESS does not have the same favorable receiver focusing effects as NORESS for Semipalatinsk explosions (and consequently has a threshold averaging about 0.5 m_b units higher for this region), initial analysis has shown that the ARCESS array surpasses NORESS in detecting small seismic events from some other parts of Eurasia. This is consistent with the assertion that regional variations in P-wave detectability can, to a large degree, be attributed to signal focusing effects, both underneath the source and receiver.

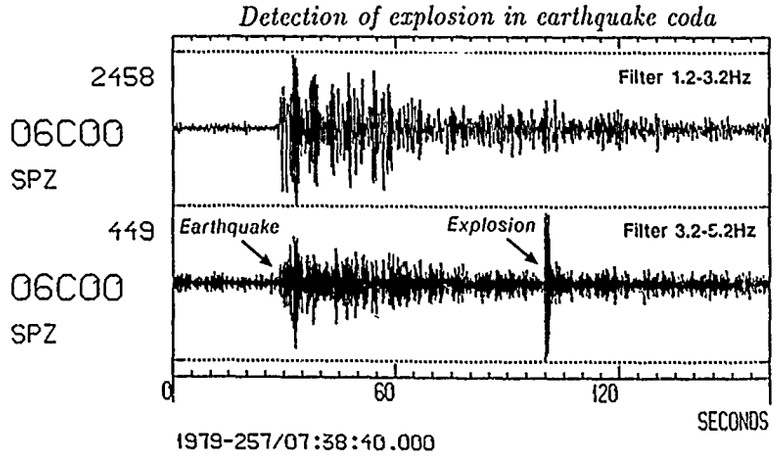

FIG. 11. Example of NORSAR recordings at the center seismometer of subarray 06C from a small Semipalatinsk presumed explosion with signal arrival 1 min later than that of a preceding large earthquake near Kamchatka. Note that the explosion signal is not visible on the *top trace* (1.2 to 3.2 Hz filter), but can be clearly seen on the *bottom trace* (3.2 to 5.2 Hz filter).

In a monitoring context, detection by by a single array will not be sufficient to provide precise location estimates or confident characterization of the nature of the seismic source. Furthermore, individual stations in monitoring networks will have capabilities that may vary significantly from one source region to another. For any given "target region" the most sensitive stations will therefore detect weak events that cannot be confirmed on a network basis. The continuous threshold monitoring approach introduced by Ringdal and Kværna (1989) will be useful to provide upper magnitude limits, at given levels of confidence, in such cases. In general, an assessment of seismic monitoring capabilities will need to take into account network detection models, where the individual station capabilities as well as minimum requirements with regard to the number of detecting stations and types of phases are explicitly formulated (Hannon, 1985).

It is nevertheless significant that a single regional array can achieve a teleseismic detection capability at the level estimated in this paper. It would appear that a network of such arrays, supplemented by high-quality, three-component stations at regional and teleseismic distances, would provide a much improved monitoring capability relative to existing global networks.

ACKNOWLEDGMENTS

This research was supported by the Advanced Research Projects Agency of the Department of Defense and was monitored by AFTAC, Patrick AFB, Florida, under Contract F08606-89-C-0005.

REFERENCES

Berteussen, K. A. (1975). *P*-wave amplitude variability at NORSAR, *J. Geophys.* **41**, 595–613.

Bocharov, V. S., S. A. Zelentsov, and V. I. Mikhailov (1989). Characteristics of 96 underground nuclear explosions at the Semipalatinsk test facility, *Atomic Energy*, **67**, 210–214 (in Russian).

Fyen, J. (1990). Diurnal and seasonal variations in the microseismic noise level observed at the NORESS array, *Phys. Earth Planet. Interiors* **63**, 252–268.

Hannon, W. J. (1985). Seismic verification of a comprehensive test ban, *Science* **227**, 251–257.

Hansen, R. A., F. Ringdal, and P. G. Richards (1990). The stability of RMS *Lg* measurements and their potential for accurate estimation of the yields of Soviet underground nuclear explosions, *Bull. Seism. Soc. Am.* **80**, Part B, 2106–2126.

Kværna, T. (1989). On exploitation of small-aperture NORESS type array for enhanced *P*-wave detectability, *Bull. Seism. Soc. Am.* **79**, 888–900.

Kværna, T. (1990). Sources of short-term fluctuations in the seismic noise level at NORESS, *Phys. Earth Planet. Interiors* **63**, 269–276.

Lilwall, R. C. (1986). Empirical amplitude-distance/depth curves for short-period *P*-waves in the distance range 20 to 180°, AWRE Report No. O 30-86, AWRE, MOD (PE), Aldermaston, Berkshire, United Kindgom.

Marshall, P. D., T. C. Bache, and R. C. Lilwall (1985). Body wave magnitudes and locations of Soviet underground explosions at the Semipalatinsk Test Site. AWRE Report No. O 16/84, AWRE, MOD(PE), Aldermaston, Berkshire, United Kindgom.

Mykkeltveit, S. and H. Bungum (1984). Processing of regional seismic events using data from small-aperture arrays, *Bull. Seism. Soc. Am.* **74**, 2313–2333.

Mykkeltveit, S., F. Ringdal, T. Kværna, and R. W. Alewine (1990). Application of regional arrays in seismic verification research, *Bull. Seism. Soc. Am.* **80**, Part B, 1777–1800.

North, R. G. (1977). Station magnitude bias—Its determination, causes and effects, Lincoln Laboratories Technical Report 1977-24, Lexington, Massachusetts.

Pulli, J. J. (1987). Body-wave magnitudes of Eastern Kazakh explosions calculated with NORESS data, in *Technical Report C87-02*, Center for Seismic Studies, Arlington, Virginia.

Ringdal, F. (1975). On the estimation of seismic detection thresholds, *Bull. Seism. Soc. Am.* **65**, 1631–1642.

Ringdal, F. (1977). *P*-wave amplitudes and sources of scattering in m_b observations, *J. Geophys.* **43**, 611–622.

Ringdal, F. (1983). Magnitudes from *P* coda and *Lg* using NORSAR data, in *NORSAR Semiannual Tech. Summary, 1 October 1982–31 March 1983*, NORSAR Sci. Rept. No. 2-82/83, Kjeller, Norway.

Ringdal, F. (1985). NORESS-NORSAR processing system comparison, in *NORSAR Semiannual Tech. Summary, 1 April–30 September 1985*, NORSAR, Sci. Rept. No. 1-85/86, Kjeller, Norway.

Ringdal, F., E. S. Husebye, and A. Dahle (1975). *P*-wave envelope representation in event detection using array data, in *Exploitation of Seismograph Networks*, K. G. Beauchamp, Editor, Nordhoff-Leiden.

Ringdal, F. and T. Kværna (1989). A multi-channel processing approach to real time network detection, phase association and threshold monitoring. *Bull. Seism. Soc. Am.* **79**, 1927–1940.

Ringdal, F. and P. D. Marshall (1989). Yield determination of Soviet underground nuclear explosions at the Shagan River Test Site, in *NORSAR Semiannual Tech. Summary, 1 October 1988–31 March 1989*, NORSAR Sci. Rept. No. 2-88/89, Kjeller, Norway.

Sereno, T. J. and S. R. Bratt (1989). Seismic detection capability at NORESS and implication for the detection threshold of a hypothetical network in the Soviet Union, *J. Geophys. Res.* **94**, 10,397–10,414.

Vergino, E. S. (1989a). Soviet test yields, *EOS, Trans. Am. Geophys. Union*, 1511+, November 28.

Vergino, E. S. (1989b). Soviet test yields, corrections and additions, *EOS, Trans. Am. Geophys. Union*, 1569, December 26.

NTNF/NORSAR
P.O. Box 51
N-2007 Kjeller, Norway

Manuscript received 25 April 1990

Bulletin of the Seismological Society of America, Vol. 80, No. 6, pp. 2143–2160, December 1990

AN AUTOMATIC MEANS TO DISCRIMINATE BETWEEN EARTHQUAKES AND QUARRY BLASTS

By Michael A. H. Hedlin, J. Bernard Minster, and John A. Orcutt

Abstract

In this article we discuss our efforts to use the NORESS array to discriminate between regional earthquakes and ripple-fired quarry blasts (events that involve a number of subexplosions closely grouped in space and time). The method we describe is an extension of the time versus frequency "pattern-based" discriminant proposed by Hedlin *et al.* (1989b). At the heart of the discriminant is the observation that ripple-fired events tend to give rise to coda dominated by prominent spectral features that are independent of time and periodic in frequency. This spectral character is generally absent from the coda produced by earthquakes and "single-event" explosions. The discriminant originally proposed by Hedlin *et al.* (1989b) used data collected at 250 sec^{-1} by single sensors in the 1987 NRDC network in Kazakhstan, U.S.S.R. We have found that despite the relatively low digitization rate provide by the NORESS array (40 sec^{-1}) we have had good success in our efforts to discriminate between earthquakes and quarry blasts by stacking all vertical array channels to improve signal-to-noise ratios.

We describe our efforts to automate the method, so that visual pattern recognition is not required, and to make it less susceptible to spurious time-independent spectral features not originating at the source. In essence, we compute a Fourier transform of the time-frequency matrix and examine the power levels representing energy that is periodic in frequency and independent of time. Since a double Fourier transform is involved, our method can be considered as an extension of "cepstral" analysis (Tribolet, 1979). We have found, however, that our approach is superior since it is cognizant of the time independence of the spectral features of interest. We use earthquakes to define what cepstral power is to be expected in the absence of ripple firing and search for events that violate this limit. The assessment of the likelihood that ripple firing occurred at the source is made automatically by the computer and is based on the extent to which the limit is violated.

Introduction

There is a peculiar breed of seismic event known as a ripple-fired explosion. Such an event differs markedly from a standard "single-event" explosion since it involves the detonation of numerous subexplosions closely, and generally regularly, grouped in space and time. Ripple-firing is a technique commonly used in quarry blasting (Langefors and Kihlström, 1978), where mine operators are striving to reduce ground motions in areas proximal to the mine, enhance rock-fracturing, and reduce the amount of material thrown into the air—"fly" or "throw" rock (Dowding, 1985). Ripple-firing is in widespread use, being employed both in the Americas and in Europe (Stump *et al.*, 1989).

There has been increased interest in recent years in discriminating mining events from earthquakes and nuclear explosions. A reduced Threshold Test Ban Treaty could potentially bring the magnitude of the largest nuclear explosions down to that of large "engineering" explosions, otherwise known as quarry blasts (Stump and Reamer, 1988). Aggravating the problem is the existence of numerous quarries in

the vicinity of the Semipalatinsk nuclear test site in the Soviet Union (Thurber *et al.*, 1989; Hedlin *et al.* 1989b). There have been a number of studies dealing directly and indirectly with this problem. Looking primarily at Scandinavian events recorded by the NORESS array, Baumgardt and Ziegler (1988) found prominent spectral modulation in events believed to involve ripple-firing but not in the spectra computed from earthquake seismograms. Hedlin *et al.* (1989b) observed similar spectral modulation in the coda produced by suspected quarry blasts in Kazakhstan, U.S.S.R. but not in the coda produced by single-event calibration explosions detonated at similar ranges. They found further that the modulation, when present, was independent of time from the onset, well into the *Lg* coda. This time-independent character has also been observed in the coda produced by quarry blasts and recorded in Scandinavia (Hedlin *et al.*, 1989a). Both Baumgardt and Ziegler (1988) and Hedlin *et al.* (1989b) found that the spectral modulation observed in the coda produced by mine explosions could be reproduced effectively by assuming that all subexplosions produce the same common waveform and that the motions superpose linearly. Stump and Reinke (1988) have investigated the validity of the assumption of linear superposition. They produced strong evidence supporting the assumption when wavefields from small closely spaced explosions are observed in the nearfield. Baumgardt and Ziegler (1988), Hedlin *et al.* (1989a, b), Stump and Reamer (1988) and Smith (1989), who also observed prominent peaks in the spectra of phases produced by some quarry blasts, all concluded that the unusual spectral color could be used to discriminate quarry blasts from other events with "whiter" spectra.

In this article we are extending the study described in Hedlin *et al.* (1989b)—hereafter referred to as paper 1—in a number of ways. We examine recordings of earthquakes, not single-event explosions, to determine if they can be discriminated from quarry blasts with a similar degree of success. We seek to determine the sensitivity of the method to the recording "environment." The recordings examined in the current study have been made at 40 sec^{-1} by the NORESS small aperture-array in Norway (Ringdal and Husebye, 1982; Mykkeltveit *et al.*, 1983). The data considered in paper 1 were recorded by single sensors and digitized at 250 sec^{-1}. We feel that any successful discriminant should not depend strongly on the local geologic setting and mining practice. In paper 1 we examined events that occurred in central Asia; in this article we consider Scandinavian events. We have automated the algorithm to the point where discrimination can be carried out solely by the computer. This type of problem has also been investigated by Baumgardt and Ziegler (1989). Their approach also relies heavily on the expected time-independence of spectral modulation in the coda produced by ripple-fired events. In both the present article and Baumgardt and Ziegler (1989) the underlying premise of this automation is that in the future, if lower thresholds are realized, and thus a significantly greater dataset must be examined, it will be beneficial and desirable to distance the human element from the discrimination process.

The Data Set

The bulk of the data used by this study were collected by sensors in the NORESS small-aperture array, located in south-eastern Norway, from 1985 to 1986 (see Fig. 1 and Table 1). The NORESS array is composed primarily of 25 vertical component sensors deployed roughly 2 meters deep in shallow vaults arranged in a set of concentric rings (Mykkeltveit *et al.*, 1983). The fourth and outermost ring is roughly 3 km across. The signal, collected by GS-13 seismometers which have a flat

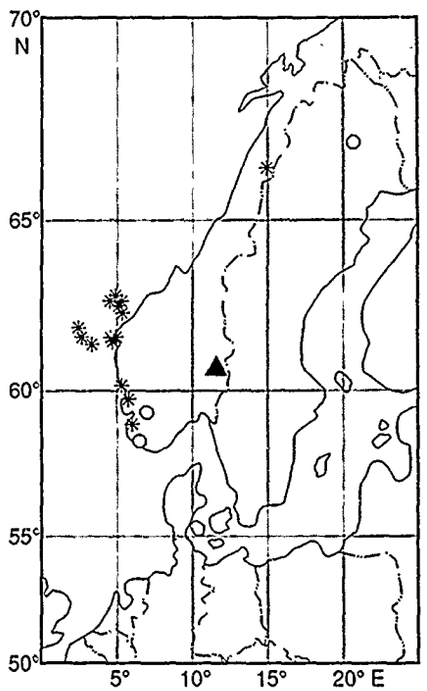

FIG. 1. Map showing the locations of the earthquake (stars), explosions (octagons) and the NORESS array (dark triangle).

response to ground velocity between 1 and 10 Hz, is digitized at 40 sec^{-1}. NORESS is actually part of a significantly larger array, known as NORSAR, and is situated within element 06C at this array, a site known to be particularly sensitive to signals propagating from Semipalatinsk (Richards, 1988). The seismometers are deployed in competent igneous rocks of granitic, rhyolitic, and gabbroic composition (Mykkeltveit, 1987) and Precambrian or Paleozoic age (Bungum *et al.*, 1985). The site is thus relatively immune to the near-surface resonance of seismic energy. A more complete description of the array can be found in Mykkeltveit *et al.* (1983).

In addition to the NORESS data, we shall use an event recorded by the NRDC high-frequency stations deployed in Kazakhstan, U.S.S.R. in 1987 (Given *et al.*, 1990). The recording we have chosen is of the calibration explosion, Chemex 2, and was made by the surface sensor at Bayanual.

The events recorded by the NORESS array consist of earthquakes and quarry blasts which, with the exception of one event, occurred within a range of 700 km from the array. Only regional events are considered here, since the analysis depends on the retention of high-frequency energy in the coda. All events fall within a local magnitude range of $1.6 \leqq M_L \leqq 3.0$. Event magnitudes, locations, origin times and identifications were obtained from Baumgardt and Ziegler (1988) and Sereno *et al.* (1987). All frequency-spectral estimates have been computed using a multi-taper algorithm. The rationale behind the choice of this algorithm is described in paper 1, and the theory describing this approach can be found in numerous papers, including Park *et al.* (1987) and Thompson (1982).

THE EFFECT OF RIPPLE-FIRING

At least at the macroscopic scale, the practice of ripple-firing appears to have little systematic effect on the seismic waveforms. It is well known, however, that

TABLE 1

EVENT LOCATIONS, ORIGIN TIMES, LOCAL MAGNITUDES, AND TYPES

Event	Latitude	Longitude	Origin Time	M_L	Event type
	°N	°E	y/d-h:m:s (UTC)		
030	59.31	06.95	1985/302-10:22:52.8	1.9	Blasjo ex
039	59.31	06.95	1985/310-14:50:51.4	2.4	Blasjo ex
501	58.34	06.43	1985/313-14:42:45.0		Titania ex
094	59.73	05.71	1985/331-04:53:32.1	3.0	earthquake
099	61.55	04.65	1985/334-19:05:13.4	3.0	earthquake
111	60.19	05.25	1985/341-14:15:43.2	2.2	earthquake
112	58.90	05.98	1985/341-14:39:09.9	1.9	earthquake
158	58.34	06.43	1985/365-13:36:49.6	2.1	Titania ex
196	58.34	06.43	1986/031-14:17:35.7	1.9	Titania ex
522	62.74	04.50	1986/036-23:35:41.0	2.6	earthquake
523	62.90	04.86	1986/037-06:19:52.0	2.3	earthquake
208	62.90	04.86	1986/037-06:20:05.4	1.9	earthquake
216	66.45	14.89	1986/038-21:03:21.1	2.2	earthquake
524	62.40	05.28	1986/044-13:39:00.0	2.5	earthquake
525	62.61	05.07	1986/044-19:03:48.0	2.6	earthquake
504	58.34	06.43	1986/045-14:13:25.0	2.7	Titania ex
505	67.10	20.60	1986/045-16:44:08.0	2.6	explosion
506	58.34	06.43	1986/045-17:54:11.0	2.3	Titania ex
526	61.69	04.90	1986/047-18:19:41.0	2.0	earthquake
239	62.76	05.29	1986/057-02:11:58.5	1.9	earthquake
247	61.67	02.58	1986/067-16:21:18.3	1.9	earthquake
266	61.66	04.53	1986/089-03:22:48.7	1.6	earthquake
270	58.34	06.43	1986/094-13:12:43.9	1.9	Titania ex
298	59.31	06.95	1986/120-10:18.48.2	2.2	Blasjo ex
507	59.31	06.95	1986/147-18:36:14.0	2.3	Blasjo ex
508	59.31	06.95	1986/148-17:51:57.0	2.4	Blasjo ex
509	58.34	06.43	1986/157-13:14:28.0	1.7	Titania ex
510	59.31	06.95	1986/170-03:55:08.0	2.5	Blasjo ex
511	58.34	06.43	1986/174-13:12:54.0	1.8	Titania ex
512	59.31	06.95	1986/191-20:10:42.0	2.3	Blasjo ex
513	59.31	06.95	1986/197-17:49:28.0	2.3	Blasjo ex
514	59.31	06.95	1986/204-20:47:10.0	2.2	Blasjo ex
515	59.31	06.95	1986/210-13:13:41.0	2.3	Blasjo ex
516	59.31	06.95	1986/211-17:59:39.0	2.4	Blasjo ex
517	58.34	06.43	1986/226-13:14:39.0	1.9	Titania ex
518	59.31	06.95	1986/226-14:39:57.0	2.4	Blasjo ex
519	59.31	06.95	1986/245-12:53:51.0	2.1	Blasjo ex
520	59.31	06.95	1986/252-17:55:58.0	2.4	Blasjo ex
503	58.34	06.43	1986/274-14:15:10.0	1.9	Titania ex
521	58.34	06.43	1986/282-14:13:52.0	2.0	Titania ex
407	61.97	02.33	1986/283-19:56:29.1	2.1	earthquake
422	61.46	03.29	1986/299-11:44:54.1	2.4	earthquake

ripple-fired events tend to give rise to seismic coda possessing highly colored spectra, that is, spectra enriched in power in certain preferred frequency bands and depleted in power in others (Bell, 1977; Baumgardt and Ziegler, 1988; Stump and Riemer, 1988; Smith, 1989). This spectral color is due to the interaction of the time-offset wavefields produced by each subexplosion. Briefly, the regular repetition and superposition of similar seismic motions in the time domain leads to regular amplification and suppression of power in the frequency domain. The manner in which the wavefields interact undoubtedly involves nonlinear processes; however, we feel that simple linear theory is sufficient to describe the most obvious result,

specifically the pronounced spectral modulation. As described in paper 1, and by numerous other authors (Baumgardt and Ziegler, 1988; Stump and Reinke, 1988; Smith, 1989; Stump *et al.*, 1989) this model makes the assumptions that the wavefields produced by each subexplosion $w(t)$ are identical and that they superpose linearly. Forcing all shots to occur at regular time intervals T we can construct the wavelet produced by the ensemble of subexplosions (lasting a total of D sec) by the equation:

$$x(t) = w(t) * \left[\frac{1}{T}\,\mathrm{III}\left(\frac{t}{T}\right) \cdot \mathrm{B}\left(\frac{t}{D}\right)\right], \tag{1}$$

where $\cdot$ represents multiplication and $*$ represents convolution. Here, III is the shah function (Bracewell, 1986) and B is the boxcar function. Hereafter, we refer to this representation as model 1. By Fourier transforming this expression we see that the spectrum of the entire seismogram equals that of an individual event multiplied by a set of equispaced sinc functions, collectively referred to as the modulation function:

$$\tilde{X}(f) = \tilde{W}(f) \cdot \left[\mathrm{III}(fT) * \frac{\sin(\pi f D)}{\pi f}\right]. \tag{2}$$

In Figure 2 we display the modulation function resulting when 39 subexplosions spaced at 25 msec are superposed in this manner. Primary reinforcement occurs at multiples of 40 Hz (the loci of the main lobes of the sinc functions). The side lobes have insignificant amplitudes relative to the main lobes. They can, however, in theory allow us to compute the duration of the entire quarry blast. The duration D is given by the inverse of the width of a single side lobe. In the event displayed in Figure 2, this value is 0.975 seconds, the known duration of the set of explosions.

As discussed in paper 1, using the model described above we predict that the modulation produced by ripple firing should be independent of time in the coda. In

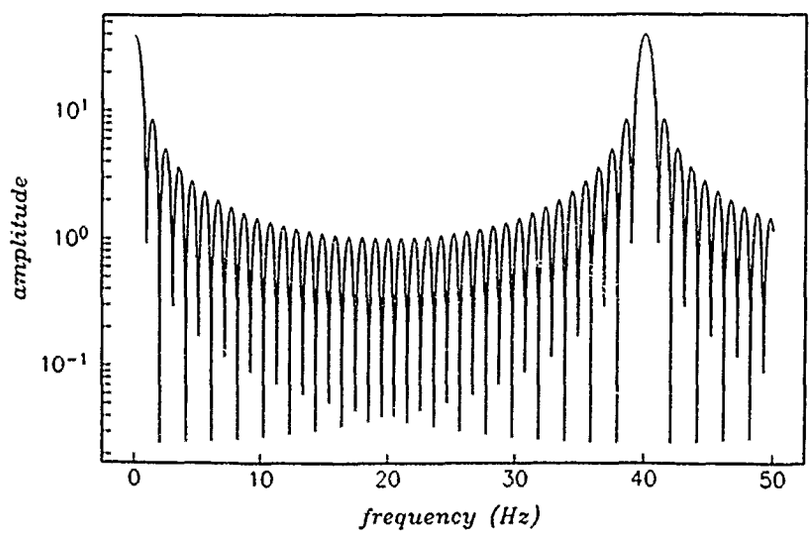

FIG. 2. Spectral modulation predicted for an event consisting of 39 subexplosions located at the same point in space and offset evenly in time at 25 msec.

paper 1 we found that this predicted character can be investigated efficiently by the computation of frequency-time displays known as sonograms (Markel and Gray, 1976; paper 1). In Figures 3 and 4 are displayed the sonograms computed from the coda generated by an earthquake and a quary blast, respectively. The quarry blast

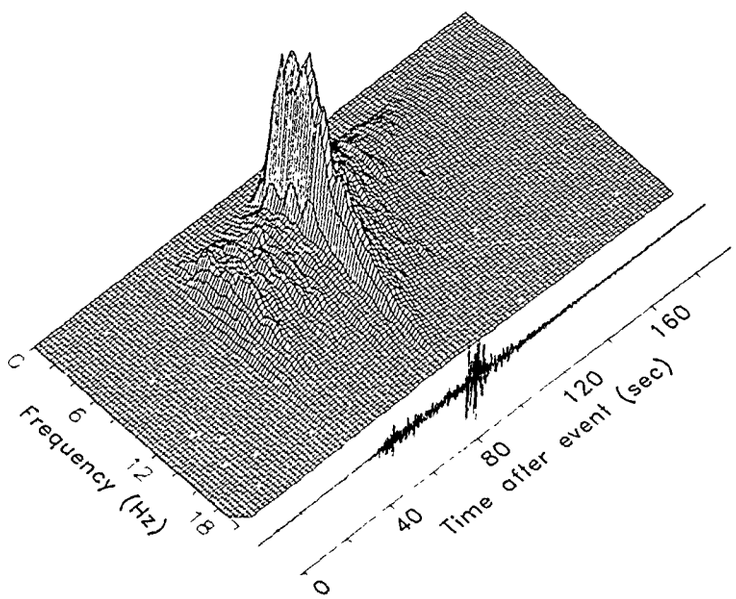

FIG. 3. Seismogram resulting from an earthquake located 342 km from NORESS (event 094) and corresponding sonogram. In Figures 3 through 6 the sonograms have been computed from a stack of 25 spectra, each computed from an individual vertical channel in the NORESS array. The stacks were computed after offsetting the seismograms to beamform for the *Pg* phase. In addition, all spectral estimates have been corrected for noise and the instrument response. The spectral amplitudes in Figures 3 and 4 are shown on a linear scale.

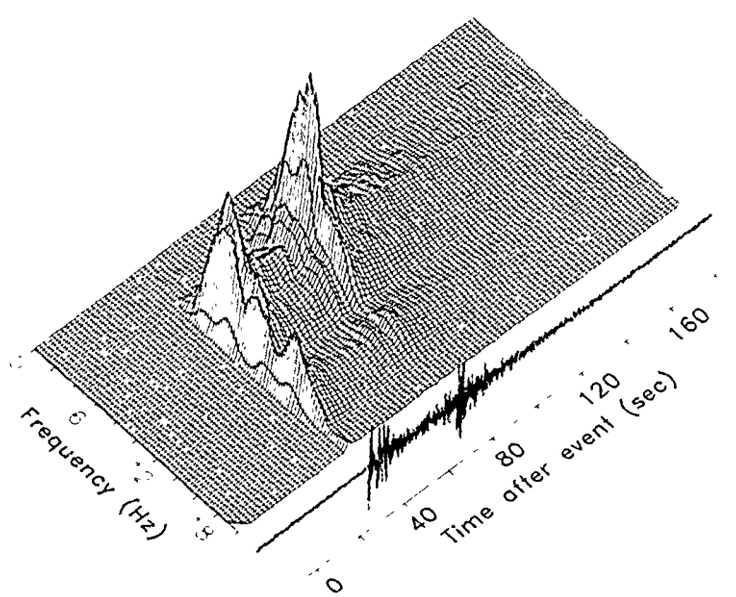

FIG. 4. Seismogram resulting from a quarry blast located 301 km from NORESS (event 030) and corresponding sonogram.

(Fig. 4) clearly shows a time-independent spectral modulation, whereas the earthquake (Fig. 3) does not. Often the two types of events do not contrast as well as these examples when presented in this format. For this reason, we have found it beneficial to convert the spectral estimates to binary form. The means by which we accomplish this conversion is discussed fully in paper 1 and involves comparing a relatively unsmoothed version of each spectrum with a more heavily smoothed one that resolves only the large scale structure, in order to extract the regular modulation. In practice, when analyzing the events considered in this article, we simply convolved the spectra with boxcar functions spanning 1.0 and 2.5 Hz, respectively. We then represent all sections of the spectra where the local power is high relative to the more regional average power by a value of +1 and where it is low by a value of −1. In this manner the bulk of the magnitude information is discarded and the spectra are "flattened" to very simple binary patterns. When analyzing array data, we generalize the procedure by computing such a binary pattern for each trace individually, and then stacking all the patterns. Because the procedure is quite nonlinear, this is very different from computing binary sonograms from beams as in Figures 3 and 4. As illustrated below, stacking *after* reduction to binary patterns is a more effective approach for our present purposes. In Figures 5 and 6 we display array stacks of the binary sonograms computed for the events displayed in Figures 3 and 4, respectively. Since typically 25 vertical sensors simultaneously record

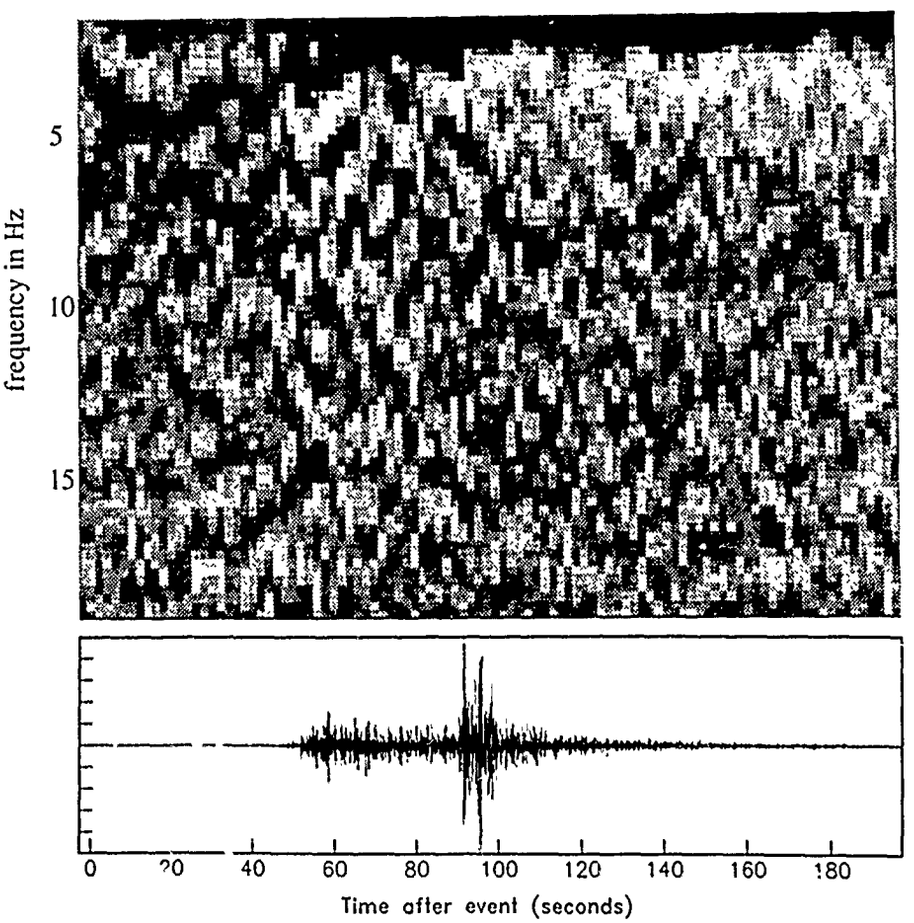

FIG. 5. Seismogram resulting from the earthquake presented in Figure 3 (094) and corresponding binary sonogram. The conversion to binary form was performed on each channel before stacking.

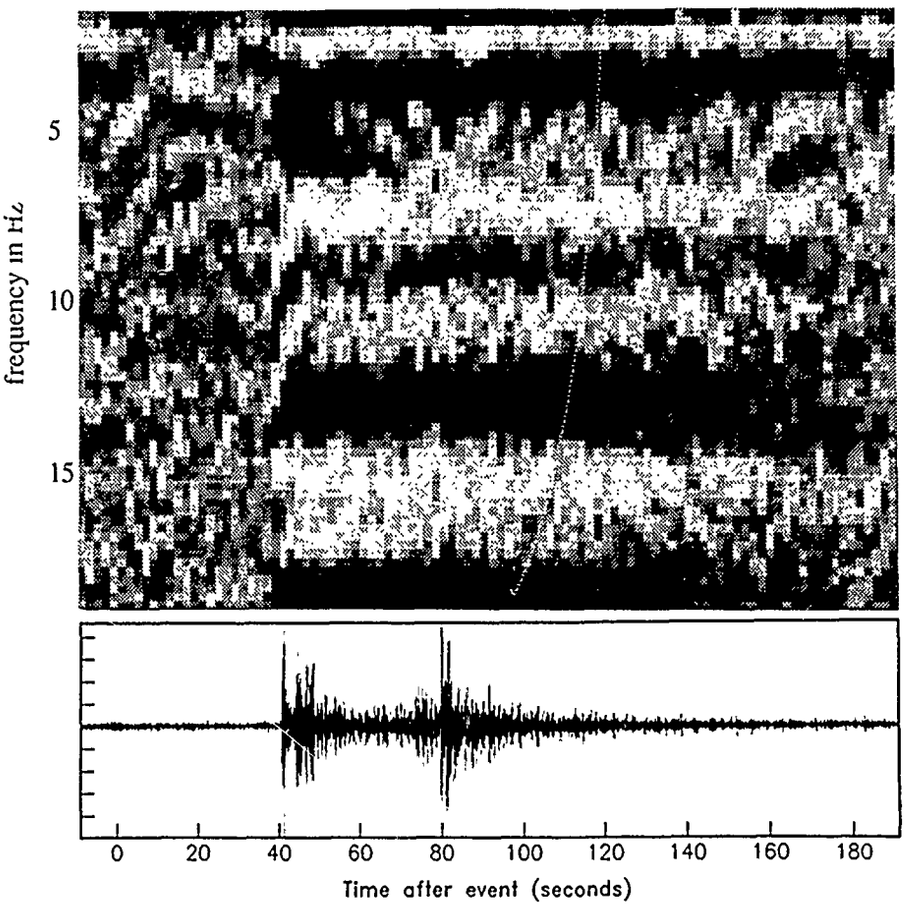

FIG. 6. Seismogram resulting from the quary blast presented in Figure 4 (030) and corresponding binary sonogram.

each event, the values in these binary stacks typically range from −25 to +25. The original spectral estimates have been corrected for noise by subtracting an average pre-event sample. Time-independent spectral modulation is present after the onset in the coda of the quarry blast only. This spectral character is not unique to this event but is shared by virtually all the events identified in Table 1 as explosions.

THE CAUSE OF THE OBSERVED SPECTRAL MODULATION

The simplest explanation of the observed spectral modulation is, as discussed in the previous section, that it is due to ripple firing. The main argument against this explanation is that the inferred delay times at the source are extremely long. Spectra computed from a typical event (030, pictured in Figs. 4 and 6) have power highs spaced at roughly 5 Hz leading to an inferred average shot spacing of 200 msec. In paper 1 we inferred delay times as high as 400 msec at quarries in Kazakhstan, U.S.S.R. As Baumgardt and Ziegler (1988) mention, "slow delays" (from 500 to 1000 msec) are used in subsurface mining where the intent is to use a shot to remove material prior to the next shot. We have reason to believe, however, that the explosions considered in paper 1 and the current data set did not occur in the subsurface. With the aid of satellite (SPOT) photos we know that a number of the

mines in Kazakhstan are at the free surface (Thurber *et al.*, 1989). The Blasjo explosions are known to be associated with the construction of a dam (Baumgardt and Ziegler, 1988). As discussed by several authors (including Langefors and Kihlström, 1978) the short delays employed at free-surface mining operations generally fall in the range from 1 to 100 msec and are typically on the order of 20 to 30 msec. Using the model described in the previous section, and 30 msec offsets, we predict spectral amplification at multiples of 33 Hz, well beyond the Nyquist frequency of the NORESS dataset. It is conceivable that the closely spaced modulations (shown in Figs. 4 and 6) could be an artifact of multiple-row blasting, where short delays are used between successive shots in each row, but adjacent rows are spaced by significantly greater delays. Synthetic experiments, in which modulation functions are computed for a variety of quarry blast configurations, suggest that this is a plausible argument; however, realistic examples taken from the literature do not. For example, Stump *et al.* (1989) describe multiple-row quarries which have inter-row time spacings of 42 msec. This argument does not rule out slow delays, either between successive shots or adjacent rows, but suggests that we should look for alternative explanations for the observed spectral modulation.

As discussed in paper 1 and Hedlin *et al.* (1988) it is possible for a wavefield to acquire a time-independent spectral modulation during propagation by reasonating in low-velocity layers. The most likely locations of layer resonance are in low-velocity sediments or weathered strata near the free surface close to the source and/or the array. Considering that many of the recorded events have given rise to unmodulated spectra, it is clear that no significant near-receiver resonance is taking place. Furthermore, since different modulation patterns are commonly produced by different events with the same location (such as successive mine explosions at the same mine), the modulations are clearly not due to near-source resonance. We conclude that the spectral modulation is most likely due to intrinsic source processes.

A third explanation relies again on source multiplicity. The modulation function produced by model 1 is dominated by the main lobes of the sinc functions. These are the only features that can realistically be expected to produce observable spectral peaks when the time delays are perfectly regular. Model 1, however, does not describe a very likely quarry blast. As discussed by many authors (including Langefors and Kihlström, 1978; Dowding, 1985; and Stump *et al.*, 1989) ripple-fired shots in quarries are spatially offset, usually in a regular pattern. At each shot location there are sometimes several vertically offset (decked) charges. The time-delays between the shots, especially in multiple-row blasting, are not necessarily going to be consistent. Actual shot times often deviate a considerable amount from the intended times (Stump and Reamer, 1988). Knowing the near-surface velocity and the slowness (p) of the energy under consideration we can replace actual time and space offsets (δT_i and δX_i, δY_i) with apparent time offsets δT_i^a by employing the formula of Smith (1989):

$$\delta T_i^a = p\sqrt{\delta X_i \cos^2\theta + \delta Y_i \sin^2\theta} + \delta T_i. \tag{3}$$

The azimuth from the quarry to the receiver is given by θ. All the aforementioned factors can cause a considerable deviation of the apparent times of the subexplosions from a common value. Using these apparent time-offsets, and assuming linear superposition and commonality of basis wavelet $w(t)$, we can construct the wavelet

due to a more general quarry blast.

$$x(t) = \sum_{i=1}^{n} w(t - \delta T_i^a). \tag{4}$$

In the frequency domain this expression is equivalent to:

$$\tilde{X}(f) = \tilde{W}(f) \cdot \left[\left(\sum_{i=1}^{n} \cos(2\pi f \delta T_i^a)\right)^2 + \left(\sum_{i=1}^{n} \sin(2\pi f \delta T_i^a)\right)^2\right]^{1/2}. \tag{5}$$

Scatter in the apparent times of the subexplosions reduces the dominance of the main lobes, or equivalently, lets the side lobes rise into prominence (paper 1). To illustrate this point, we have computed a theoretical modulation pattern for a quarry blast layout adapted from that of a real life quarry, the San Vel quarry, described and studied by Stump and Reimer (1988) and Stump *et al.* (1989). As displayed in Figure 7 the subexplosions are arranged in an en echelon pattern. The shots in each row are spaced at 25 msec proceeding from west to east. The row detonations are separated by 42 msec proceedings from south to north. The modulation functions, computed for energy traveling to observation points due north and east of the quarry with a slowness of $\frac{1}{7}$ sec/km are displayed in Figure 8. Although the dominant delay time is 25 msec, the 40-Hz peak does not dominate either modulation function. The function for the station to the north can be constructed by multiplying the modulation function due to 13 shots spaced at 25 msec (representing the intershot delays) with the function corresponding to three shots spaced at roughly 42 msec (representing the inter-row delays after taking into account the delay associated with the propagation of the energy between the rows). The two functions are in competition, and the result is that the broad main lobes of the latter accentuate the

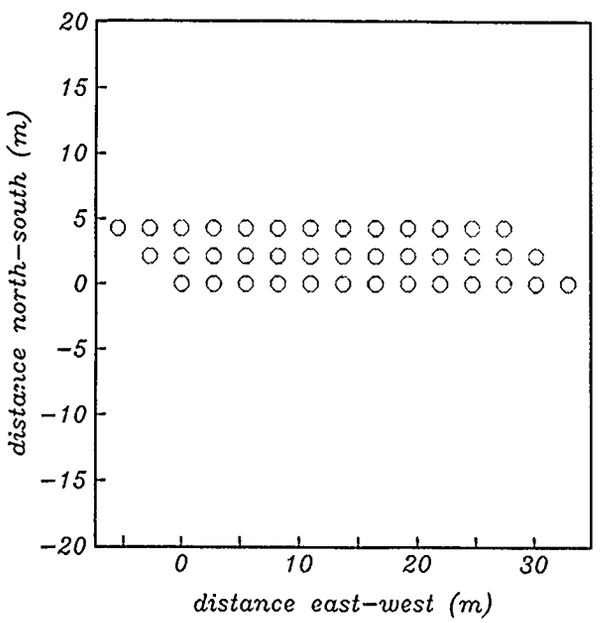

FIG. 7. The layout of subexplosions in an en echelon quarry blast. Shooting within the rows is spaced in time at 25 msec. Adajcent rows are separated by 42 msec in time. This pattern is adapted from Stump *et al.* (1989).

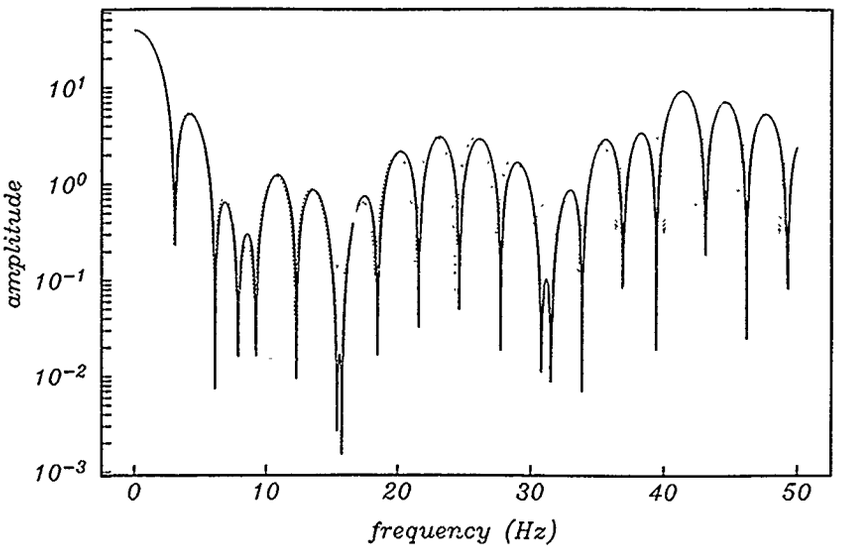

FIG. 8. The amplitude of modulation functions resulting from the shot introduced in Figure 7. The solid and dashed curves represent energy traveling at a slowness of 1/7 sec/km to stations due north and east of the quarry, respectively.

side lobes of the former to a point where they can be expected to have a significant impact on the spectrum of the quarry blast.

Using a technique employed in paper 1 we synthesize a quarry blast using the apparent subexplosion times occurring in the event described above. We assume a common waveform is generated by each subexplosion, and for that waveform we select the calibration explosion Chemex 2 detonated in Kazakhstan, U.S.S.R. and recorded at the station at Bayanaul. (We have resorted to this data set simply because the 40-Hz NORESS data do not have adequate resolution in time to permit the millisecond offsets required by this quarry.) The Chemex 2 recording was made at 250 sec^{-1}. This "Green's function" is linearly stacked upon itself 39 times after including the offsets appropriate for the observation point due north of the quarry. Although we have chosen to create the synthetic quarry blast by offsetting and stacking a Green's function in the time domain, the equivalent result could be achieved by multiplying the spectrum of the Green's function by the complex modulation function which underlies the solid curve pictured in Figure 8. Prior to computing the sonogram, the "synthetic" seismogram was low-pass filtered between 0 and 20 Hz and decimated to one point in 5 to mimic a NORESS recording. The sonogram (displayed in Fig. 9) is dominated by time-independent structure. Assuming this modulation pattern was due to main lobe activity, one would estimate a dominant delay time to be roughly 170 msec (the inverse of 6 Hz). We know, however, that this structure is due to side lobe activity and is controlled in this case by the total duration of the quarry blast. Because of the manner in which the sonogram is calculated, the frequency estimates are heavily smoothed. Longer time windows would allow a more accurate estimate of the frequency spacing of the modulation. In fact, we know that the average side lobe width is roughly 2.6 Hz (see Fig. 8) and that the duration of the quarry blast is 384 msec.

It seems that there is a fundamental ambiguity in the spectral modulation produced by ripple-fired, and hence noninstantaneous, events. Without *a priori* information about what occurred at the source we cannot be sure if the modulation spacing is controlled by the duration of the entire set or by the dominant intershot

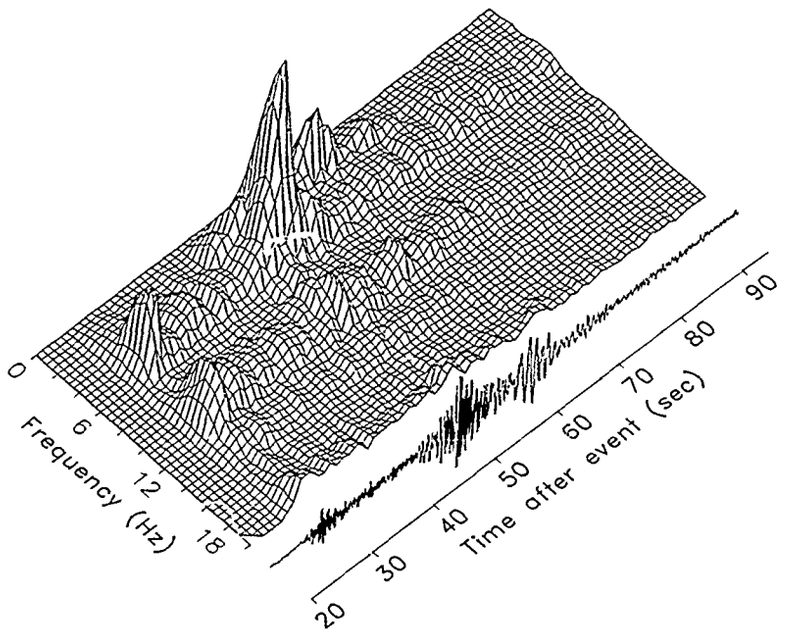

FIG. 9. Time series and sonogram representing a "synthetic" quarry blast. The synthetic was constructed by linearly stacking a seismogram produced by the Chemex 2 explosion in Kazakhstan U.S.S.R. upon itself after offsetting in time to mimic the quarry pictured in Figure 7 when observed from a point to the north (see Figure 8). The original seismogram was sampled at 250 sec^{-1}. The synthetic was low-pass filtered and decimated to simulate recording conditions similar to the NORESS array.

apparent time spacing. This experiment shows that our discriminant, perhaps, will not recognize quarry blasts because they are ripple fired per se but because they last an intermediate length of time. Instantaneous events give rise to unmodulated spectra. Extremely long events (for example, large earthquakes) should produce very finely modulated spectra, such that the modulation is masked by scattering and noise.

In paper 1 we considered two types of events, calibration explosions which were denoted by American and Soviet scientists (Given *et al.*, 1990) and did not involve ripple firing. Using *a priori* information we strongly suspected the rest of the events were quarry blasts. This information included satellite photos, provided by Prof. Clifford Thurber (at the University of Wisconsin), which showed surface mining activity in the vicinity of some of the events. In addition, it is known that the region has little natural seismicity (Leith, 1987). Time-independent spectral modulation was only observed in the latter set of events and was attributed to the source multiplicity. The present study and the previous one are consistent in suggesting that quarry blasts can be discriminated from non-ripple-fired events.

THE AUTOMATIC DISCRIMINANT

For our purposes it is irrelevant whether the time-independent spectral features observed in the coda produced by quarry blasts are due to main lobes or to side lobes in the modulation functions. Ripple-fired events tend to give rise to time-independent spectral modulation; the earthquakes examined in this study do not. To examine this modulation we have developed a means to "expand" a time series into a matrix of numbers depending on frequency and time. Typical patterns obtained from recordings of an earthquake and a quarry blast (Figs. 5 and 6) illustrate that it can be very easy to discriminate visually between these two types

of events given these time–frequency displays. In paper 1, using the same approach, we found a similar degree of success in discriminating between quarry blasts and single-event explosions. Given the current interest in the problem of discriminating quarry blasts from earthquakes and single-event explosions and the large numbers of events involved, we feel it is important to extend the algorithm so that human intervention is distanced from the discrimination process, to a point where the patterns can be recognized automatically by the computer. One method we have found to be very effective involves the computation of a two-dimensional Fourier transform of the sonogram matrices. This can be considered as an extension of *cepstral* analysis (Tribolet, 1979). In the standard cepstral analysis a Fourier transform of the log of the amplitude spectrum is computed to highlight any regular spectral modulation regardless of its longevity. The independent variable is known as the *quefrency* and has units of time. The form of cepstral analysis we are proposing is more demanding, however. A given point in the 2-D cepstral matrix represents spectral modulation at a certain quefrency that is also periodic along the time axis at a certain frequency. It is thus a simple matter to isolate energy periodic in frequency and independent of time.

To illustrate our point we display two 2-D cepstra in Figures 10 and 11. The first was computed from the first 100 sec of coda of event 030 (Figs. 4 and 6); the second was computed from the coda of the earthquake 094 (Fig. 3 and 5). The quarry blast has significantly more energy at zero frequency (along the time axis) than the earthquake. The quefrency at which the power is concentrated in the 2-D cepstrum computed from the coda produced by the quarry blast is roughly 0.2 sec (reflecting the spectral modulation with 5-Hz spacing. Slices at zero time-frequency through 2-D cepstra computed from the coda produced by a quarry blast (event 507) and all the earthquakes in the data set are shown in Figure 12. As expected, the quarry blast is a singular event. The most noticeable feature in the quarry blast cepstrum is, obviously, the significant peak at a quefrency of 0.2 sec. We expect that ripple-fired events should give rise to significantly larger extreme cepstral values than earthquakes. Supporting this thesis are the histograms in Figure 13 showing the observed distributions of cepstral extremes for the entire earthquake and quarry blast populations examined in this study.

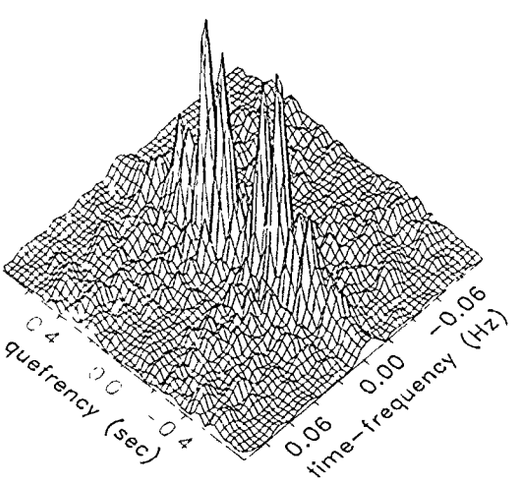

FIG. 10. Two-dimensional cepstrum computed from the coda produced by a quarry blast (event 030). The first 100 sec of the coda were considered.

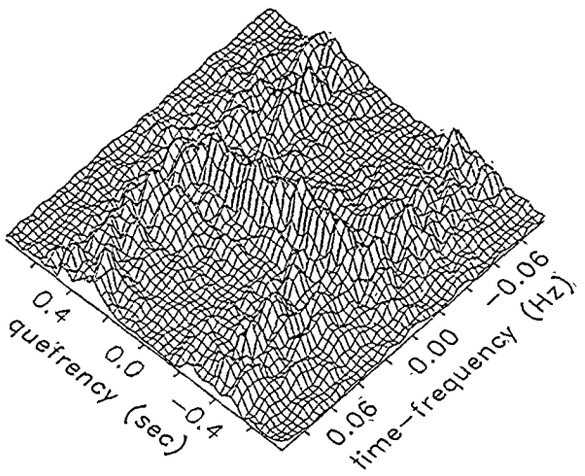

FIG. 11. Two-dimensional cepstrum computed from the coda produced by an earthquake (event 094). The first 100 sec of the coda were considered.

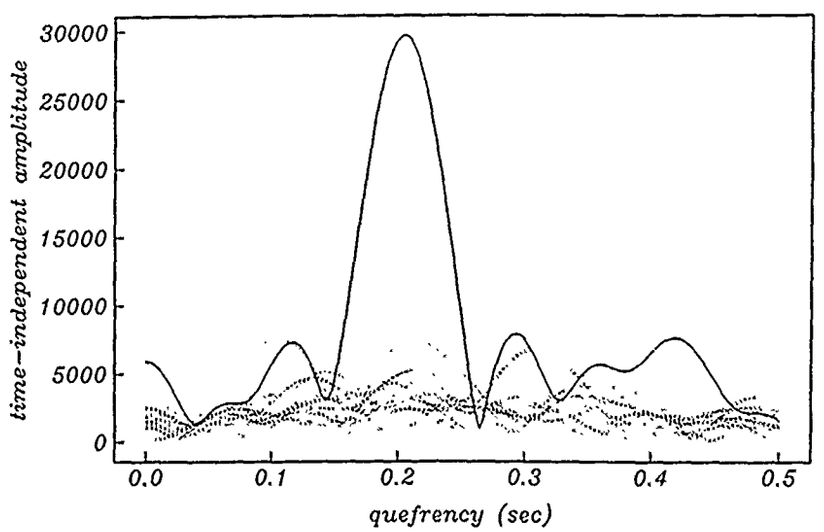

FIG. 12. Slices through the time-independent portions of two-dimensional cepstra computed from a quarry blast (event 507) and all the earthquakes considered in this study. The quarry blast is shown as the solid line.

Although we are most interested in the quarry blast cepstra, we can gain some important insight from the earthquake cepstra which illustrate the 2-D cepstral structure that can be expected in the absence of source multiplicity. These cepstra show what time-independent structure will be acquired by a propagating wavelet or, in other words, they are indicative of the region's natural level of resonance. We propose to identify events as quarry blasts by searching for anomalously high global extrema in the time-independent segments of the 2-D cepstra. To calibrate the algorithm, to account for the natural resonance in the region, we make the judgment of what is a large value on the basis of what extrema non-ripple-fired events produce. The consideration of global extrema in these 2-D cepstra is a problem that is well suited for analysis using the statistics of extremes (Gumbel,

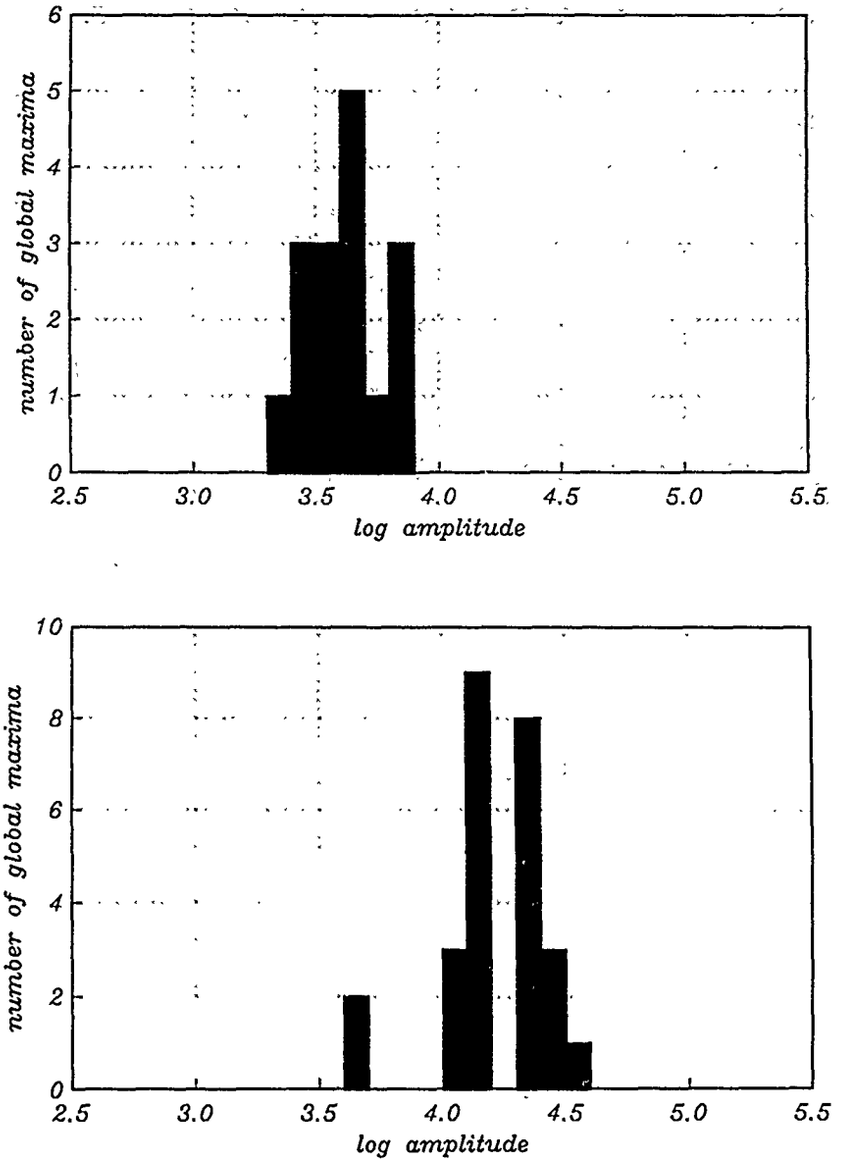

FIG. 13. Histograms showing the observed distributions of global extreme cepstral values computed from the coda produced by earthquakes (*top*) and quarry blasts (*bottom*).

1958). In Figure 13 it is clear that the logs of the extreme amplitudes are centrally distributed, and there are no significant outliers. The Kolmogorov-Smirnov test suggests that the earthquake cepstral extremes follow a log-normal distribution. However we would like to avoid the adoption of a specific underlying distribution since we have no fundamental reason for choosing one and since we only have 16 earthquakes. It is known (e.g., Gumbel, 1958 and Weissman, 1978) that when dealing with observations of extreme values the underlying distribution need not be assumed, but the behavior can be modeled using functions that are asymptotically valid as the number of samples examined and the number of points in each sample approaches infinity (Kennedy and Neville, 1974). Selecting the exponential asymptote, the cumulative probability (P) that an extremum belonging to the earthquake

population will be less than the one observed is given by:

$$P = e^{[-e^{(-y)}]} \tag{6}$$

where the expression for the reduced variate (y) is:

$$y = a(u - \hat{u}) \tag{7}$$

The terms a and $\hat{u}$ are the dispersion parameter and the mode of the distribution respectively, and are estimated directly from the population of earthquake extremes shown in Figure 13 (Kennedy and Neville, 1974). The log of the cepstral extremum of interest is represented by u. We find that for this distribution a and $\hat{u}$ equal 7.204 and 3.55, respectively.

Given this probability function we can pose the discrimination problem in terms of a standard hypothesis test: Let the null hypothesis (H_0) be that a newly recorded event belongs to the population of earthquakes used to calibrate the technique. If the cepstral extremum calculated for this event exceeds a certain threshold determined from the distribution (6), then we can reject the null hypothesis (H_0) at a preset confidence level and conclude that the event is probably a quarry blast. For example, in Figure 14 this threshold was selected such that for points that plot above the threshold line, the null hypothesis is rejected with only a 5 per cent risk of doing so erroneously. In other words, we state that events above the line do not belong to the earthquake population, at the 95 per cent confidence level. In spite of the apparent efficiency of the discriminant illustrated in Figure 14, we must remember that the calibration of the distribution (6) is based on our (small) sample of 16 identified earthquakes, so that the test is in fact "data fitted." Confirmation of our claim of success will have to be based on an independent sample. In this

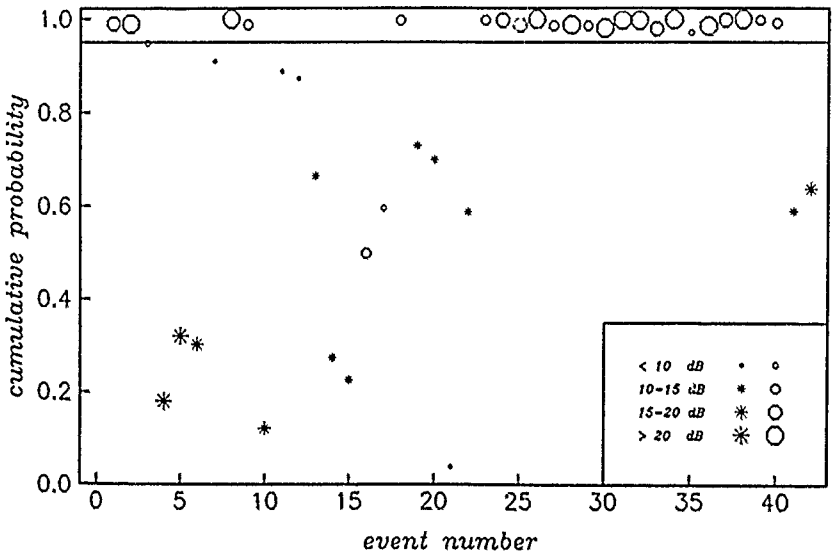

FIG. 14. The cumulative probabilities of extreme cepstral values derived from the coda produced by all events in the data set. The quarry blasts are denoted by octagons, the earthquakes are represented by stars. The likelihood that the assumption that the event is an earthquake is invalid increases with this probability. For points above the 0.95 thresholds, the hypothesis that the corresponding events belong to the earthquake population is rejected at the 5 per cent risk level. The event number (along the horizontal axis) indicates the location of the event in Table 1. The symbol size scales with the signal-to-noise ratio (see *insert*).

figure the symbol size is directly proportional to the signal-to-noise ratio (derived from average spectra encompassing the time from 50 sec before and after the compressional onset). Of the 26 quarry blasts considered, 23 lie above the 95 per cent confidence level. Of the two that fall well below this limit, one (event 505, located in northern Sweden) had extremely low signal-to-noise levels (less than 10 dB), and the other (event 504) produced only a very broad spectral modulation. The three earthquakes located above a probability of 0.8 (events 112, 523, and 208) all suffered from signal-to-noise ratios less than 10 dB.

Conclusions

In a previous paper (Hedlin *et al.*, 1989b) we advanced the preliminary observation that ripple-fired events tend to give rise to coda dominated by time-independent spectral features and that this quality should be exploited to discriminate these events from earthquakes and single-event explosions.

In this article we have demonstrated that this can be done with a high degree of success when considering earthquakes and quarry blasts. We have found that quarry blasts tend to produce modulated spectra, but the modulations may not result directly from the ripple firing; they may exist simply because the event is non-instantaneous. We have produced an empirical calibrated approach to the discrimination problem which allows for local seismic resonance. We have automated the approach to the point where discrimination can be carried out solely by the computer. We have examined a data set consisting of 26 quarry blasts and 16 earthquakes and have found that with few exceptions the two populations are well separated by our approach. The events which failed to be identified with a high degree of confidence generally suffered from low signal-to-noise ratios.

By comparing our current results with those in the earlier work we have illustrated the ability of the algorithm to accommodate changes in the recording environment, local geologic setting, and mining practice. Based on the results presented in paper 1, we expect that we would have a similar degree of success in discriminating between single-event explosions and quarry blasts.

Acknowledgments

We thank Dr. Thomas Carter at the Center for Seismic Studies for providing us with the bulk of the events used in this study. Dr. Thomas Sereno, at Science Applications International Corporation in San Diego, helped us obtain the rest of the NORESS events. We thank Graham Kent and an anonymous reviewer for helpful suggestions. The Kazakh event was recorded by a station installed and operated by the Institute of Physics of the Earth of the Soviet Academy of Sciences and the Natural Resources Defense Council. This research was sponsored by the Defense Advanced Research Projects Agency (DARPA)/Air Force Geophysics Laboratory (AFGL) under contracts No. F19628-89-K-0018 and F19628-88-K-0044.

References

Baumgardt, D. R. and K. A. Ziegler (1988). Spectral evidence for source multiplicity in explosions: Application to regional discrimination of earthquakes and explosions, *Bull. Seism. Soc. Am.* **78**, 1773–1795.

Baumgardt, D. R. and K. A. Ziegler (1989). Automatic recognition of economic and underwater blasts using regional array data, *Unpublished report to Science Applications Incorporated, 11-880085-51.*

Bell, A. G. R. (1977). A digital technique for detection of multiple seismic events, *EOS* **57**, 444.

Bracewell, R. N. (1986). *The Fourier Transform and Its Applications*, McGraw-Hill, New York.

Bungum, H., S. Mykkeltveit, and T. Kværna (1985). Seismic noise in Fennoscandia, with emphasis on high frequencies, *Bull. Seism. Soc. Am.* **75**, 1489–1513.

Dowding, C. H. (1985). *Blast Vibration Monitoring and Control*, Prentice-Hall, New York.

Given, H. K., N. T. Tarasov, V. Zhuravlev, F. L. Vernon, J. Berger, and I. L. Nersesov (1990). High-frequency seismic observations in eastern Kazakhstan, U.S.S.R., with emphasis on chemical explosion experiments, *J. Geophys. Res.* **95**, 295–307.

Gumbel, E. J. (1958). *Statistics of Extremes*, Columbia University Press, New York.

Hedlin, M. A. H., J. A. Orcutt and J. B. Minster (1988). A comparative study of high frequency signal and noise in oceanic and continental environments, *10th Annual AFGL/DARPA Seismic Res. Symp.*, Falbrook, California.

Hedlin, M. A. H., J. A. Orcutt, J. B. Minster, and H. Gurrola (1989a). The time-frequency characteristics of quarry blasts, earthquakes and calibration explosions recorded in Scandinavia and Kazakhstan, U.S.S.R., *11th Annual AFGL/DARPA Seismic Res. Symp.*, San Antonio, Texas.

Hedlin, M. A. H., J. B. Minster, and J. A. Orcutt (1989b). The time-frequency characteristics of quarry blasts and calibration explosions recorded in Kazakhstan, U.S.S.R., *Geophys. J.* **99**, 109–121.

Kennedy, J. B. and A. M. Neville (1974). *Basic Statistical Methods for Engineers and Scientists*, Harper and Row, New York.

Langefors, U. and B. Kihlström (1978). *The Modern Technique of Rock Blasting*, Halsted Press, Wiley, New York.

Leith, W. (1987). Geology of NRDC seismic stations in Eastern Kazakhstan, U.S.S.R., *U.S. Geol. Surv. Open-File Report 87-597.*

Markel, J. D. and A. H. Gray, Jr. (1976). *Linear Prediction of Speech*, Springer, New York.

Mykkeltveit, S. (1987). Local geology of the regional array sites in Norway. Norsar Semiannual Technical Summary, Scientific Report No. 1-87/88.

Mykkeltveit, S., K. Astebol, D. J. Doornbos, and E. S. Husebye (1983). Seismic array configuration optimization, *Bull. Seism. Soc. Am.* **73**, 173–186.

Park, J., C. R. Lindberg, and F. L. Vernon (1987) Multitaper spectral analysis of high-frequency seismograms, *J. Geophys. Res.* **92**, 12675–12684.

Richards, P. (1988). Nuclear test ban treaties and seismic monitoring of underground nuclear explosions: an overview of the historical, technical and political issues, *The Alan S. Attardo Symp. Science and Society.*

Ringdal, F. and E. S. Husebye (1982). Application of arrays in the detection, location, and identification of seismic events, *Bull. Seism. Soc. Am.* **72**, S201–S224.

Sereno, T. J. Jr., S. R. Bratt, and T. C. Bache (1987). Regional wave attenuation and seismic moment from the inversion of NORESS spectra, Unclassified semiannual report Air Force Geophysics Laboratory, AFGL-TR-87-0237.

Smith, A. T. (1989). High-frequency seismic observations and models of chemical explosions: implications for the discrimination of ripple-fired mining blasts, *Bull. Seism. Soc. Am.* **79**, 1089–1110.

Stump, B. W. and S. K. Reamer (1988). Temporal and Spatial Source Effects from Near-Surface Explosions, *10th Annual AFGL/DARPA Seismic Res. Symp*, Falbrook, California.

Stump, B. W. and R. E. Reinke (1988). Experimental confirmation of superposition from small-scale explosions, *Bull. Seism. Soc. Am.* **78**, 1059–1073.

Stump, B. W., S. K. Reamer, D. Anderson, K. Olsen, and R. Reinke (1989). Quantification of explosion source characteristics from near source, regional and teleseismic distances, Unclassified final report, Geophysics Laboratory, GL-TR-89-0194.

Thompson, D. J. (1982). Spectrum estimation and harmonic analysis, *IEEE Proc.* **70**, 1055–1096.

Tribolet, J. M. (1979), *Seismic Applications of Homomorphic Signal Processing*, Prentice-Hall, New York.

Thurber, C. H., H. Given, and J. Berger (1989). Regional seismic event location with a sparse network: Application to eastern Kazakhstan U.S.S.R., *J. Geophys. Res.* **94**, 17767–17780.

Weissman, I. (1978). Estimation of parameters and large quantiles based on the k largest observations, *J. Am. Statist. Assoc.* **73**, 812–815.

INSTITUTE OF GEOPHYSICS AND PLANETARY PHYSICS
SCRIPPS INSTITUTION OF OCEANOGRAPHY
LA JOLLA, CALIFORNIA 92093

Manuscript received 16 February 1990

Bulletin of the Seismological Society of America, Vol. 80, No. 6, pp. 2161–2176, December 1990

COHERENT PROCESSING OF REGIONAL SIGNALS AT SMALL SEISMIC ARRAYS

BY Z. A. DER, M. R. HIRANO, AND R. H. SHUMWAY

ABSTRACT

Regional arrivals, similarly to short-period teleseismic *P* waves, have a spectral structure that the Fourier transforms of individual sensors at arrays for events located in limited source regions can be decomposed into source and site spectral factors. This structure has been demonstrated to be valid for *Pn* and *Lg* arrivals at NORESS. This property of regional arrivals can be exploited for: (a) Grouping events with respect to relative location; (b) Identifying events with differing source mechanisms; and (c) Finding differences in the source time functions between closely spaced events.

Potentially useful techniques for accomplishing such analyses consist of computing site-averaged interevent coherences, interevent and intersite equalization methods combined with correlation techniques. The advantage of such approaches is that we need not know much about the propagation characteristics (Green's functions) along the paths to an array.

INTRODUCTION

Obtaining source information from regional recordings is very important in treaty monitoring because of the concern about small decoupled nonchemical explosions possibly hidden in conventional firing patterns of quarrying operations. Thus far, little progress has been made, and practically no work done, in extracting information from regional waveforms by coherent processing, although spectral expressions of multiple firing sequences hav been discovered (Willis, 1963; Baumgardt and Ziegler, 1988). The disadvantage of the spectral and cepstral methods is that the phase information in the signals is discarded and that the modulation patterns depend on the similarity in the waveforms from the various individual shots making up the firing sequence; the advantage of such methods is that they are robust and do not otherwise depend on the details of propagation. In this article we shall discuss the general problem of regional waveform analysis and show how investigating the spectral structure of the data may help in recovering source information in addition to that obtainable by other analysis methods.

A general conclusion that may be drawn from attempts of computing synthetic seismograms of regional arrivals such as *Pn*, *Pg*, *Sn*, and *Lg* and comparing them to real data is that it is quite impossible to compute Green's functions with sufficient precision to reproduce such high frequency waveforms in any detail. The reason is that we do not have detailed knowledge of the geological structures that determine the waveforms, and even if we had such knowledge we simply do not know how to compute synthetic seismograms for such complicated structures. While it is possible to obtain synthetic seismograms for long-period and some standard short-period seismograms that match observed waveforms in considerable detail, for regional seismograms the best we can hope for is to match the overall characteristics of wave envelopes and relative phase amplitudes. Details of individual waveforms for various events and recording sites vary so much, even for closely spaced sensors at small arrays, that it is hard to see any visual similarity between the raw waveforms.

The question arises whether it will ever be possible to derive source-related information from the detailed waveforms of regional seismograms if we accept the

fact that we shall never know the Green's functions. The answer to this question, based on the work presented below, is a qualified yes, although the possibilities seem to be limited due to the extreme variability of regional waveforms with source mechanism and the positions of the sources and receivers.

Theoretical Considerations

Before we review the results of our data analyses it is necessary to describe some expected spectral characteristics of regional seismic arrivals in the light of elementary seismological theory. Let us examine the general spectral structure of seismic arrivals in an arbitrary, heterogeneous anisotropic medium. The problem is completely frequency-separable in the frequency domain, as is seen by transcribing some known equations (Aki and Richard, 1980, p. 53)

$$F_j^i(\omega) = \left[\sum_{p,q} M_{pq}^i(\omega) \cdot G_{pqj}^i(\omega)\right] \tag{1}$$

into the frequency domain, where the M are the components of the moment tensor and the G are derivatives of Green's functions (they will be called Green's functions for simplicity in this article) associated with them. The index i is for the given source and j is for the sensor. In this expression the index for component in Aki and Richards (1980), which is always vertical in this article, was dropped and the summation over moment tensor components is explicitly indicated (rather than implied by repetition of indices) in order to avoid confusion, since some other indices will be repeated in some expressions. This structure is equivalent to a multichannel filtering problem in which we can consider a seismogram as a result of, alternatively, (a) filtering the source inputs for each component of a moment tensor with filters corresponding to the Green's functions; (b) filtering the Green's functions with the six independent components of the moment tensor.

It is sometimes advantageous to look at the problem using the second interpretation since, as we pointed out above, we shall probably never know the Green's functions, and any information we gain from the seismograms should depend only on the coherence relationships among the various seismograms. The relationship (1) is too general to be of much use, unless something is known about the spectral terms and factors in this expression. First of all, we know that the moment tensor components generally have a short time response relative to the length of the regional seismograms, since most seismic sources we consider are of short duration. Moreover, we have to exploit the spectral structures of seismograms discussed below and may also invoke the principles of reciprocity before we can derive any useful information from regional waveforms.

It has been shown that for short-period teleseismic P waveforms originating from sources in limited regions (such as known test sites) the spectra of individual short-period sensors can be adequately described in terms of the factorability condition (Filson and Frasier, 1972; Der *et al.*, 1987).

$$F_j^i(\omega) = S^i(\omega)R_j(\omega) \tag{2}$$

where R and S are the site and source factors and F is the Fourier transform of a P wave from the source i and observed at site j. The R are strongly dependent on the azimuths (slowness vectors) of the arrivals, thus equation (2) is valid only for

limited source regions. We have been successful in estimating the R and S and interpreting S for the teleseismic case based on the assumption that the site factors can be reduced by beaming over sites and that the Green's functions are otherwise simple and can be enhanced by the same process (Der *et al.*, 1987).

Fortunately, Green's functions for teleseismic short-period P waves can be described in terms of a few rays, such as P, pP, and sP and possibly a few multiple reflections in the crust near the source, all having the same slownesses, and thus the source waveforms can be interpreted in terms of a few phases. This is not generally the case for regional arrivals which contain a large number of rays, multiply reflecting in the various crustal layers and involving various values of slownesses, even though a single regional phase tends to be associated with a limited range of slownesses. Therefore, even if we could separate the source and site terms they could not be interpreted simply; for instance, pP would have different delays for the various rays. Alternatively, considering the regional arrivals as complex superpositions of high-frequency higher normal mode wavetrains, these are not easy to interpret in terms of source characteristics.

The factorability condition given above suggests a more useful form for the structures of regional seismograms as recorded at arrays

$$F_j^i(\omega) = \left[\sum_{p,q} M_{pq}^i(\omega) G_{pq}^i(\omega)\right] R_j(\omega) \tag{3}$$

in which we have factored the seismogram into spectral factors consisting of the moment tensor spectra, factors G appropriate to the source region location and source mechanism, and, finally, the site factors R that probably depend only on the type of wave we are analyzing, providing that the overall modal compositions do not change much, and the sensor location. The rest of this article is devoted to the examination of the properties of such factors and testing of the validities of relationships of this form for various types of regional data. The form of relationships given above includes the simple factorability equation (2) as a special case. We must point out that despite the fact that factoring matrices of seismograms works for array recordings of teleseismic signals (Filson and Frasier, 1972), there is no reason to believe *a priori* that such factorizations and associated methodologies will work for regional phases which are very complex superpositions of rays or modes, depending on the preferred way of interpreting them. Any such factorizations must be tested and verified observationally prior to any attempts to use them in data processing schemes.

We use the term "coherent processing" in this article for techniques that exploit the generalized factorability condition as defined above. This is somewhat different from the usual definition of coherent processing techniques, such as beaming and F-K analyses routinely applied to regional signals at seismic arrays (Mykkeltveit *et al.*, 1983; Ingate *et al.*, 1985; Kværna and Mykkeltveit, 1986) which basically depend on the assumption of complete signal similarity. These processes and the regional arrays layouts were optimized for signals coming from arbitrary directions using the concept of averaged signal coherences versus sensor distances and are applied only at intersensor distances and frequencies where the site effects can be neglected. However, if they satisfy equations of the forms (1) and (2), regional signals across a regional array are much more "coherent," in a more general sense, if we analyze regional arrivals from limited source regions. Let us consider now a few special cases of equation (2).

Events with Identical Green's Functions and Mechanisms

This is the most commonly studied case, and numerous simulations of spectral modulations due to various spatio-temporal patterns of ripple firing implicitly assume the similarity of single shots. At a given regional array far removed from the source region the seismograms at the individual sensors can be written as

$$F_j^i(\omega) = s^i(\omega)H_j(\omega) \tag{4}$$

where the $s(\omega)$ are the source functions for a given event and the $H(\omega)$ are common combinations for all events of the products of moment tensors and Green's functions. A commonly observed phenomenon for numerous shots is that the spectral modulation is the same for all regional arrivals (Baumgardt and Ziegler, 1988) even as seen at several regional arrays. This implies a purely temporal modulation, such as implied above, without any spatial structure for the source. Scenarios involving combined temporal-spatial shot configurations of shots can easily be simulated, and such are being actually applied for vibration control in quarrying operations (Anderson and Stump, 1989).

Equation (4) above implies that the waveforms of events complying with this model will be *coherent* at common sensors of an array; thus we can compute the interevent coherence

$$C = \frac{|P_{ij}|}{\sqrt{P_{ii}P_{jj}}} \tag{5}$$

between two events i and j, this should have a high value in the case of low background noise.

Central to this idea is the estimation procedure for the power spectral components P. These must be computed by some smoothing procedure such as smoothing the dot products of the signal Fourier transforms denoted as vectors f such that

$$P_{ij}(\omega) = \sum_s \overline{f_i(\omega)f_j^*(\omega)}, \tag{6}$$

where the overbar denotes spectral smoothing, the star denotes complex conjugation, and the summing of smoothed products is performed over sensors. Smoothing can be accomplished in various ways, by actually smoothing the spectra, by averaging over shorter time windows, or by some combination of the two. In our case, we use the combination of spectral smoothing and averaging over array sites. The equivalent time-bandwidth product (TBWP) of the result can be computed by multiplying together the spectral averaging bandwidth B, the total time length of the data for each array site T, and the number of array sites N. In any coherence measurement some decision must be made concerning the bandwidth to be used. High TBWP implies high stability of the coherence results; with a given amount of data this can be traded off against the resolution in spectral detail (Bendat and Piersol, 1966; Shumway, 1988). In the case discussed here we can assume that the waveform differences are associated with different effective source functions, i.e., firing sequences. Normally these have very short time durations. Generally, the amount of smoothing that can be applied in coherence calculations depends on the time length of the impulse response of the transfer function between the two time series. As a

rule of thumb one can smooth a bandwidth $1/T_i$, where T_i is the duration of such an impulse response. This implies that heavy spectral smoothing may be applied in the calculation of C above if the differences in waveforms are mostly due to different firing sequences. For further discussions of the particulars of coherence calculations we refer the reader to Shumway (1988, pp. 70 to 73).

Alternatively, this form of interrelationship implies the existence of a transfer function that can transform events one from the other with a filter of relatively short impulse response. This does not imply waveform similarity, however, although coherence and waveform similarity are often mistakenly used interchangeably.

Events with Identical Sets of Green's Functions and Different Mechanisms

In such cases, generally the waveforms of individual events will not be coherent in the sense of equation (5); the spectra of the superpositions of individual shots with different mechanisms will not be modulated in any easily predictable fashion. A possible scenario of such a situation in quarry blasting is a mix of shots, some of which may be applied to a vertical rock face (shear source) and some buried under a horizontal surface, but both kinds of shots being close the surface at roughly the same depth.

Nevertheless, as long as the six Green's functions are common to a set of events, any seven will be coherent if the multiple coherence is computed for them, where we may test the possibility of reconstructing the ith time series from the rest (Bendat and Piersol, 1966).

We believe that this is a worst case scenario, since not all six independent G will not contribute significantly to the waveforms, and some may correlate well, and thus only a few may be important. In such cases multiple coherences with lesser numbers of events may attain values significantly different from zero. Thus, no matter how complex the source mechanisms may be, it will be possible to "calibrate" parts of a quarry with a small number of events, and the high multiple coherences will identify all subsequent events in that quarry. In this study we shall not present any multiple coherence results.

Events with Different Green's Functions

This is analogous to testing outputs of several different systems with independent random inputs for coherence, and most of these should test as not being significantly different from zero. This case covers all events with different depths and at different locations. If all S's are different, then none of the single and multiple coherences between that event and the events at a "calibrated" quarry will be high. This may be a case for events at a quarry and a hidden decoupled larger explosion being at a significantly greater depth or an earthquake near a quarry. The lack of coherence could be used as a criterion for such events. Given the fact that decoupled, nonchemical explosions have to be buried deeper than conventional explosives in standard quarrying procedures, and that the effective mechanisms for the two types of events will no doubt be different, it does not seem to be very easy to mix the two types of explosions in order to hide testing that could not be revealed by some kind of coherence analysis.

Analyses of Data from Quarry Blasts

Our data come from NORESS recordings of events, listed in Tables 1 and 2, identified as quarry blasts at the Titania mine and two Estonian mines named

E1 and E4. We have also looked at one event at the Blasjo dam site. We do not know about the location accuracy of these events or the reasons, other than location, for their association with any particular mine. The locations of these events are shown in Figure 1.

In order to apply any of the ideas above, we must first verify the applicability of the factorability condition for any data set. We have applied the multichannel

TABLE 1
LIST OF "TITANIA" EVENTS

Event	Date	Origin Time	Latitude	Longitude	Magnitude
Titania1	14 Feb 86	14:13:24.9	58.3	6.4	2.7
Titania2	14 Feb 86*	17:54:10.6	58.3	6.4	2.3
Titania3	07 Jan 86	14:14:28.9	58.3	6.4	2.2
Titania4	17 Jan 86†	14:11:01.5	58.3	6.4	2.7

* Probably removed from or not as the same part of quarry.
† Reference event (unmodulated).

TABLE 2
LIST OF "ESTONIA" EVENTS

Event	Date	Origin Time	Latitude	Longitude	Magnitude
E4-1	19 Jan 88	11:55:35.0	59.3	27.2	2.5
E4-2	20 Jan 88	12:23:06.0	59.3	27.2	2.5
E4-3	21 Jan 88	11:25:30.0	59.3	27.2	2.4
E4-4	26 Jan 88	09:55:37.0	59.3	27.2	2.4
E1-1	19 Jan 88	11:50:50.0	59.3	24.4	2.5
E1-2	21 Jan 88	12:53:23.0	59.3	24.4	2.2

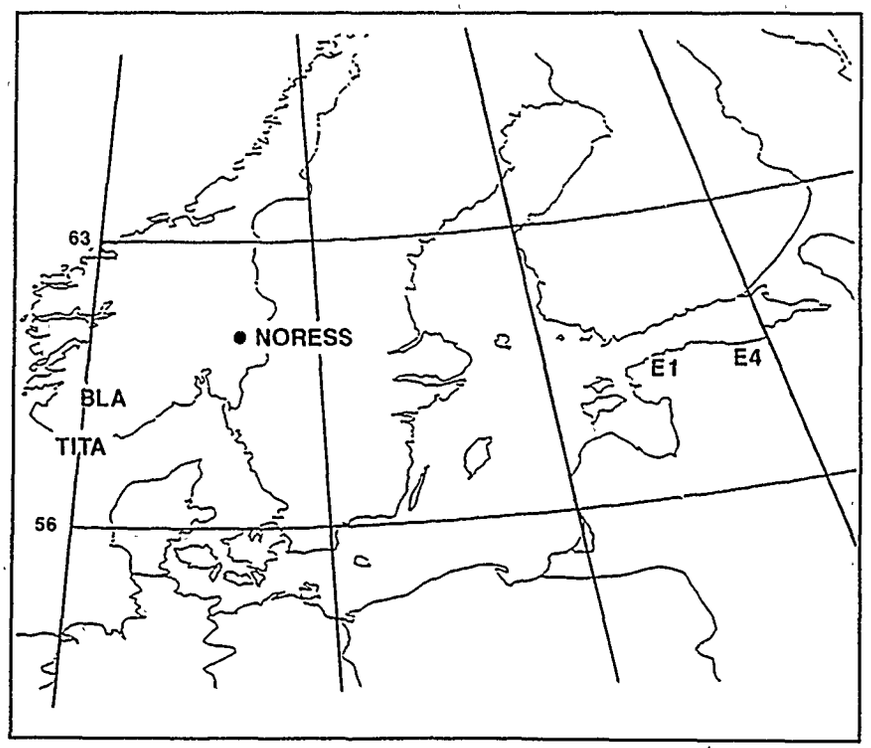

FIG. 1. Map of Scandinavia with the location of NORESS and the mines studied.

spectral factorization technique described by Shumway and Der (1985) and Der *et al.* (1987) to two data sets, the *Pn* arrivals from this group of Titania mine blasts and the *Lg* arrivals from a set of mine blasts in Estonia at mine E4. The decomposition of data into source and site factors is not totally unique (see Der *et al.*, 1987), but by successfully reconstructing the complete set of original waveforms from the much smaller set of estimated source and site spectral factors we verified that the data has the spectral structure described by equation (2). Figures 2 and 3 show some representative examples of these reconstructions for *Pn* and *Lg* phases, respectively; all of these have similar quality within each set. Typically, the correlation coefficients between the pairs of original and reconstructed traces were near or above 0.8, which is not as good as in the teleseimic case but still respectable considering the high signal frequencies we utilize here. Note that the waveforms are quite different at the various sensors for the same event and for the various events at the same sensors. Joint deconvolution of the Titania events and the Blasjo event did not result in acceptable reconstructions showing that an azimuth difference of 10° is too large for using the same site factors. In all the work we present in this paper, we have used 12 sensors of NORESS roughly evenly distributed over the area of the array.

Starting with the *Pn* data from the Titania mine, let us assume initially that all these events had the same source mechanism and/or location and test the idea that the differences in waveforms are totally attributable to differences in firing sequences, i.e., the factors H in equation (4) are common for all the events. Inspecting the spectra of mine blasts from the Titania mine in Norway at NORESS, it can be observed that some have strongly modulated spectra, while some others have quite smooth spectra (Fig. 4) for all phases *Pn*, *Pg*, *Sn*, and *Lg*. This points to a common, *temporal* modulation for each event, rather than to a pattern imposed by the spatial

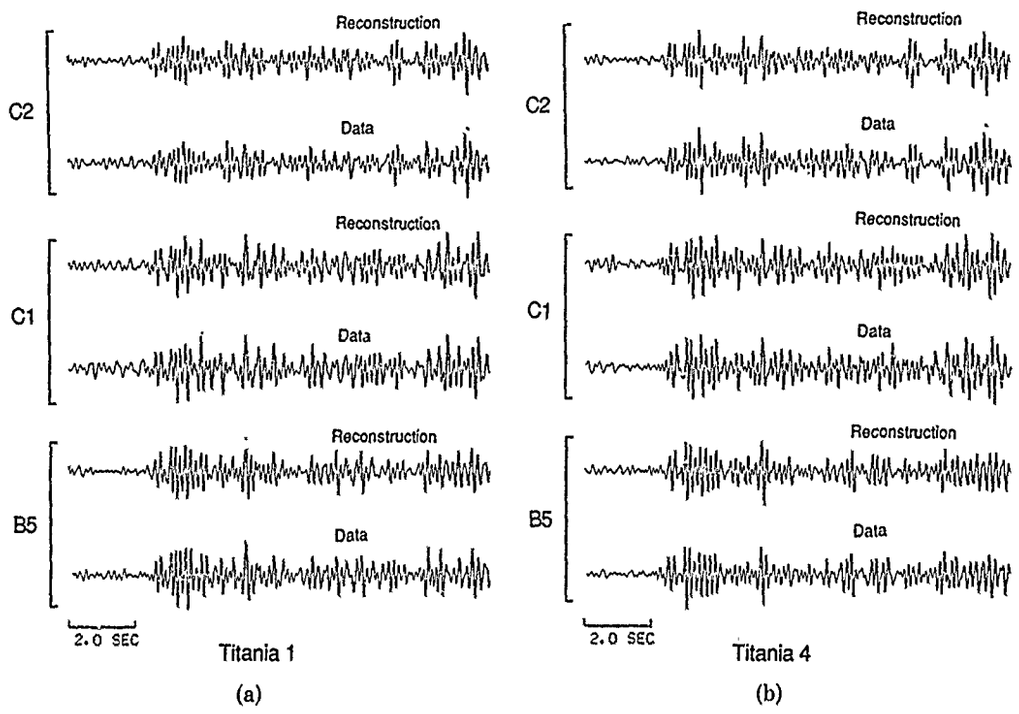

FIG. 2. (a) Selected reconstructed and data traces *Pn* arrivals from the Titania 1 event; (b) the same for the Titania 4 event. The designation C2 refers to the second sensor in the C ring of NORESS etc.

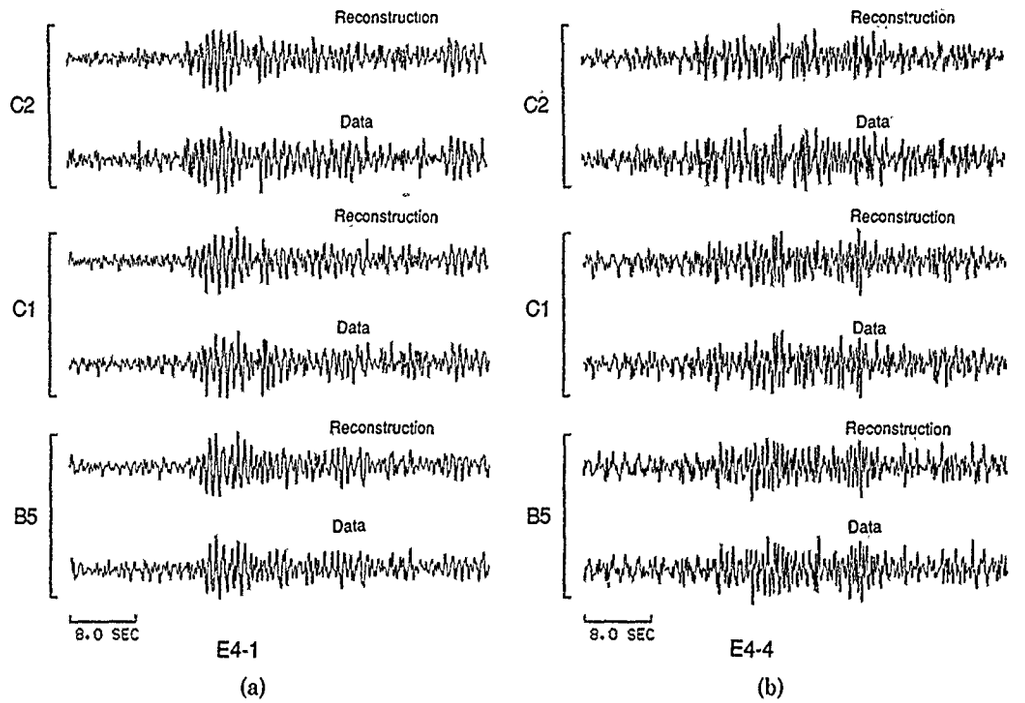

FIG. 3. (a) Selected reconstructed and data traces of *Lg* arrivals from the E4-1 event; (b) the same for the E4-4 event. The designation C2 refers to the second sensor in the C ring of NORESS, etc.

configuration of charges and also combined with a temporal sequence of explosions, since in the latter case we should see different modulation patterns for the various regional phases that possess notably different phase velocities. Although the lack of modulation does not rule out some very complex spatio-temporal modulation patterns of the source (although these must be quite unlikely) such that the spectral manifestations of it are suppressed, it is reasonable to assume that the spectrally unmodulated quarry blasts have simple impulsive source time functions or very small delays while the modulated ones have been ripple fired. The *Lg* phases of the Estonia mine blasts are somewhat noisy and the S/N ratio is only good below 4 Hz.

Let us compute now the interevent coherences according to formulas (5) and (6) above, for *Pn* phases from several pairs of these events including the relatively unmodulated one. The results show (Fig. 5) that the pairs Titania4-1 and Titania4-3 show relatively high average coherences indicating nearly identical source mechanism and/or location, while the pair Titania4-2 has low coherence indicating that event Titania3 has probably a different mechanism or location. Although the S/N ratio was the lowest for event 2, this coherence still seems to be too low for a coherent signal. The TBWP for these coherences was 120.

Let us hypothesize now that the unmodulated event Titania4 is a simple one, a single shot. Consequently, the time domain impulse response of the moving average (MA) filter that can transform the waveforms of this event to those of the Titania1 must be a band-limited representation of the firing sequence. Therefore, we decided to design a Wiener filter to transform *Pn* waveforms of event Titania4 into those of event Titania1 at all sensors of NORESS. Before applying this technique, we wanted to ensure that the traces processed were as free as possible from background noise and other distortions of the spectrum by applying a common, minimum phase

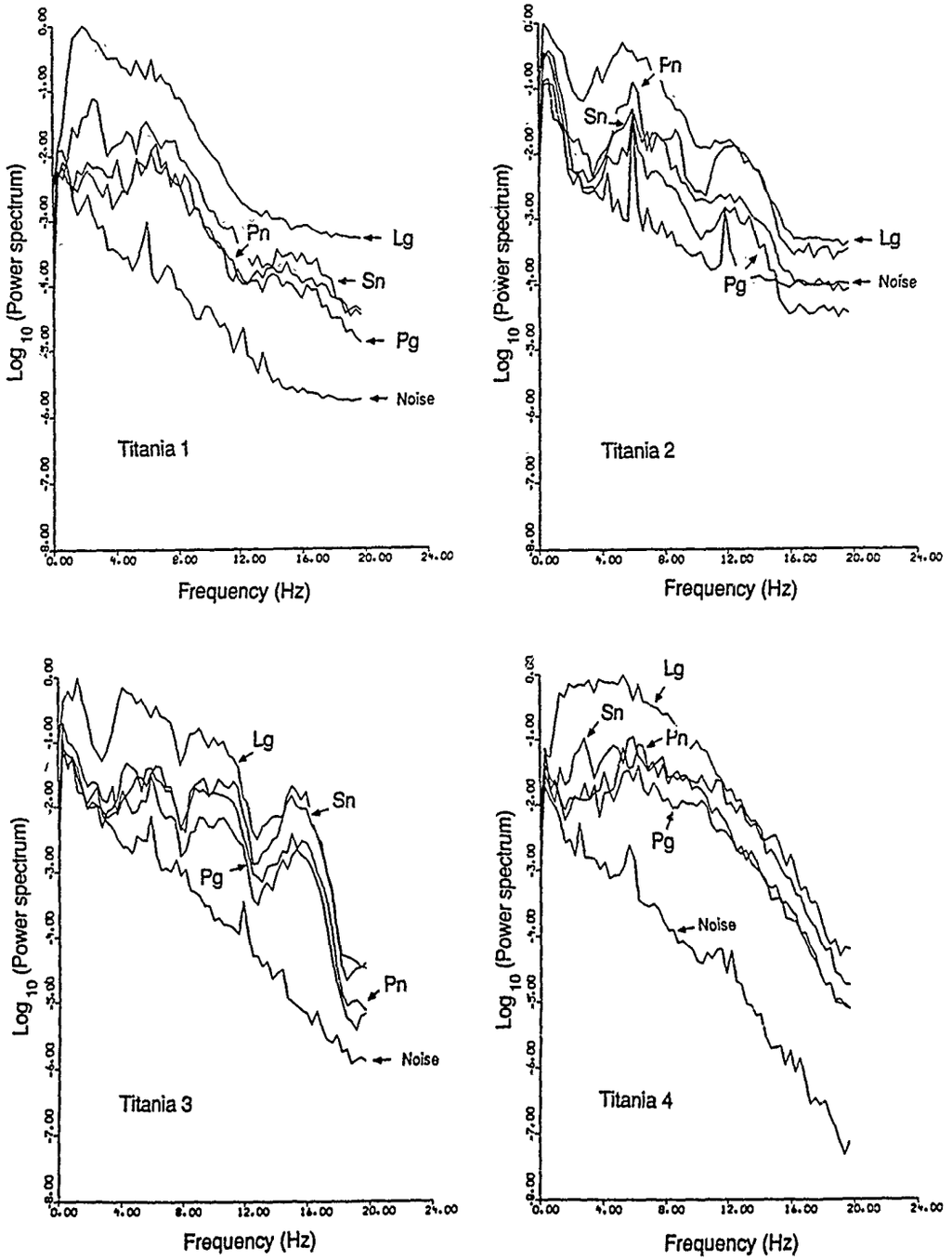

FIG. 4. Spectra for various regional arrivals from the Titania mine.

bandpass filter to all traces of both events that emphasized the energy and flattened the spectra in the 3 to 15 Hz frequency band where the S/N ratio was higher.

Computation of time-domain MA type filters can be easily accomplished by several well-known algorithms using computer codes widely available (Marple, 1987). Time domain design is convenient because we want to limit the length of the filter. The *Pn* arrivals were lined up for both events, windowed and tapered, and

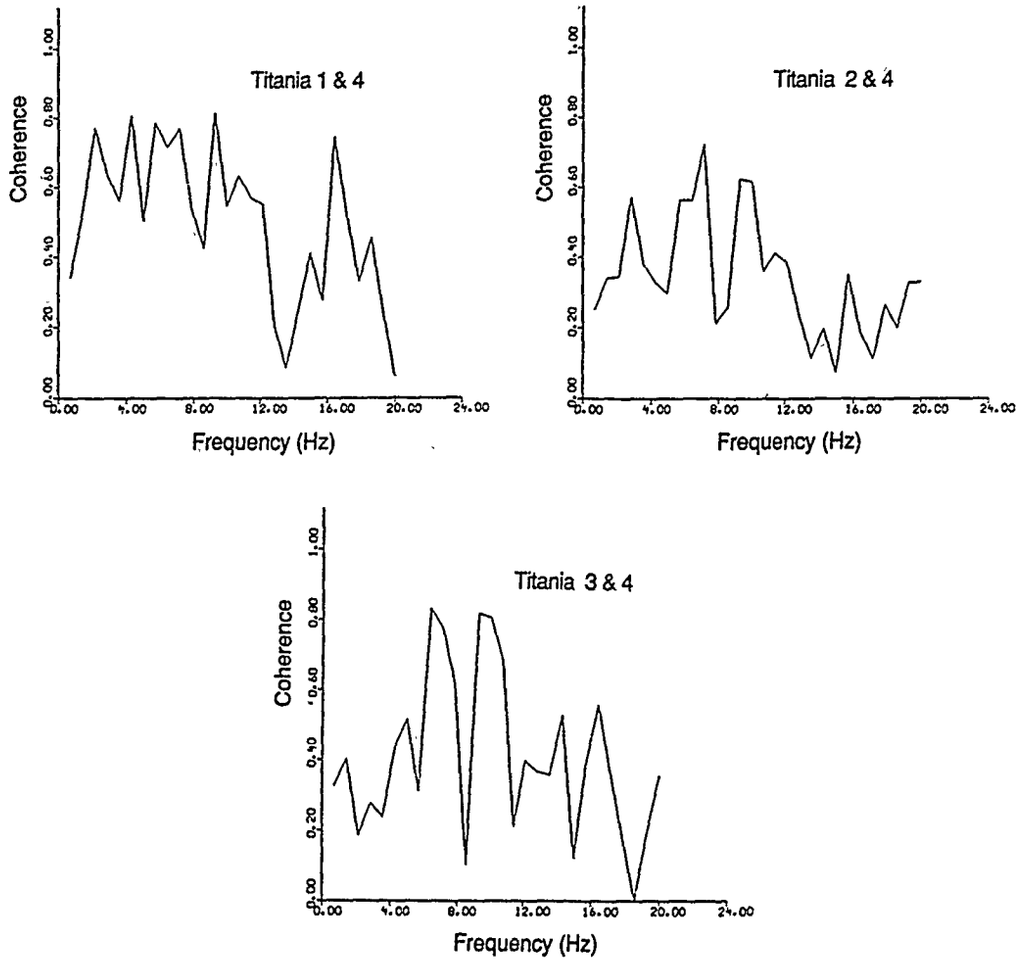

FIG. 5. Intervent coherences for *Pn* arrivals from the Titania mine.

the auto and cross-correlation functions needed by the filter design algorithms were computed by ensemble-averaging these correlation functions over sites. The ensemble averaging process of correlation functions over common sites suppresses the effects of the site functions and much reduces those of the ambient noise. The length of the portion of the cross-correlation function with highest amplitude gave a good indication of the maximum length of the ripple-firing sequence, since the time length of the large amplitudes in this function cannot exceed this length. For the cases discussed, this upper limit is roughly of the order of 0.5 sec. The compound correlation functions constitute the inputs to the Levinson algorithm used for the computation of the cross-equalizing Wiener filter consisting of 31 weights.

Subsequently, the filter was applied to the simple event to derive waveforms of the complex events at all sites. A set of traces showing the representative improvement between the two events at common sensors are shown in Figure 6. Note that the original waveforms are much more different for the two events and waveforms became more similar. Nevertheless, the increase in the time domain correlation coefficients was only modest, from 0.59 to 0.75 for the first pair, and 0.49 to 0.57 for the second. This indicates that either we need a longer filter or that the event pairs are too far from each other, and thus we cannot attribute the waveform

difference entirely to the source-time functions. The same method did not work at all for the pair Titania4-2.

We have also applied the cross-equalization for the whole wave trains, consisting of all the regional arrivals of events Titania4-1. The processing resulted in a spectacular increase of the correlation coefficients between the two events from 0.08 to 0.65 over the whole set of sensors, again confirming that the waveforms of these events are closely related.

Having established that such techniques may be suitable to identify groups of events with nearly identical mechanisms and/or locations, we shall examine now the nature of the relative intersite transfer functions for the same vent. We know that such transfer functions exist, and they are consistent from event to event. Otherwise we would not have been able to jointly deconvolve and reconstruct all these events. It would be desirable if these transfer functions would be simple, similar to the interevent transfer functions for the coherent event pair, because then relative displacement over distances of the order of the NORESS diameter would not destroy the interevent coherence (applying the principles of reciprocity). In that case, the lack of coherence among events in a limited source region observed at an array would be mostly due to differences in source mechanisms.

Unfortunately, this is not the case. We have tried to design short, 31-point, time domain filters for equalizing *Pn* waveforms at sensors D1 and D5 for the suite for four events, but they essentially failed to produce even remotely similar waveforms. Thus the intersite transfer functions are generally complex, with very long time domain impulse responses. Applying the reciprocity argument, this implies that a comparably small displacement in the location of a source would totally destroy the

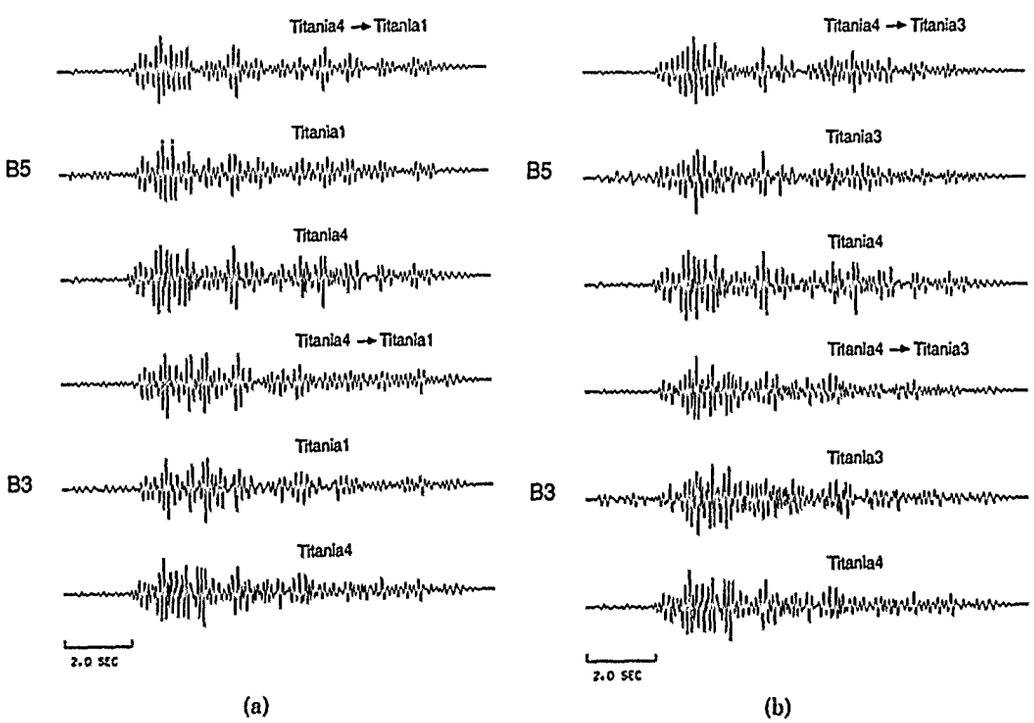

FIG. 6. (a) Wiener filtering results for transforming event Titania4 into event Titania1; (b) Wiener filtering results for transforming event Titania44 into event Titania3.

waveform similarity assuming that the source region and the NORESS site are similar in the degree of heterogeneity in structure.

Site Equalization Processing

A major problem in locating regional events is that the first arrivals are often small and buried in noise and that most phases are emergent, without clearly defined arrival times. Azimuths estimated from *F-K* analyses are often not very accurate, since the site effects tend to destroy the plane-wave character of the signals, thus broadening the main lobes of array response patterns. There are conflicting demands of keeping the array apertures small for ensuring signal similarity and increasing the directional resolution of the arrays. The fact that the site transfer functions are consistent, albeit not simple, still leaves open the possibility of utilizing this internal consistency for refining the estimation of *relative* azimuths among closely spaced events. If the forms of the intersite transfer functions do not change much with small azimuth changes except for some small time shifts, then such a property could be exploited. To test this idea, we have bandpass filtered the four Titania events to emphasize the band with the maximum S/N ratio, between 3 and 10 Hz. Subsequently, we have taken the frequency domain site factors derived from the multichannel deconvolution calculations and multiplied the Fourier transform of trace D1 with the site factor of D5 and vice versa. This is basically an intercorrelation technique applied to the broadband site (rather than event) equalization. The

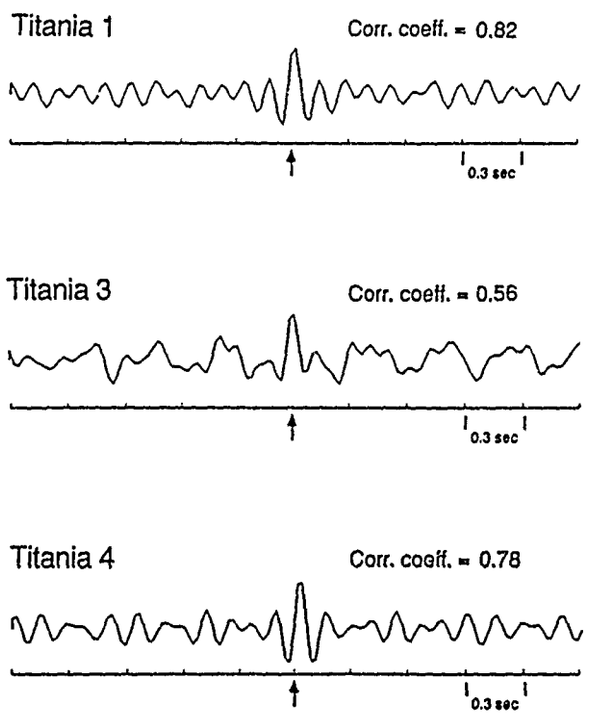

FIG. 7. Cross correlations of the site-equalized traces of *Pn* between the sensors D1 and D5 for selected Titania events.

resulting spectra were then correlated in the frequency domain and transformed back into the time domain

$$\Phi(t) = F^{-1} \mid d_1(\omega)R_5(\omega)(d_5(\omega)R_1(\omega))^* \mid \tag{9}$$

to view the cross-correlation function. In this expression, the d's are the Fourier transforms of the traces and the R's are the site transfer functions. The results for three of the events are shown in Figures 7 and 8, event 2 was too noisy. In inspecting these figures, we must point out that the results of cross-equalization do not have to look like normal seismograms, with clearly defined phases. In multiplying with the complex site factors, we essentially perform a circular convolution with considerable wraparound effect. It is interesting to note that the correlation peak for event Titania4 is not lined up with those of Titania3 and Titania1 (Fig. 7) indicating a small time shift. Figure 8 demonstrates that the site equalized trace waveforms indeed became quite similar. The shift in the peak does not seem to be associated with noise or mismatch since all cross-correlation functions for this set of events have a well-defined, single maximum with little ambiguity in value of the time shift.

The same process was repeated with the recordings of *Lg* phases from quarry blasts in Estonia as recorded at NORESS. Applying the process to four E4 mine events, we obtained good trace equalizations, with all correlation peaks lined up at zero lag. Using four events from E4 and two from E1 mines in a joint site-equalization process, we have found that the efficiency of the intersite

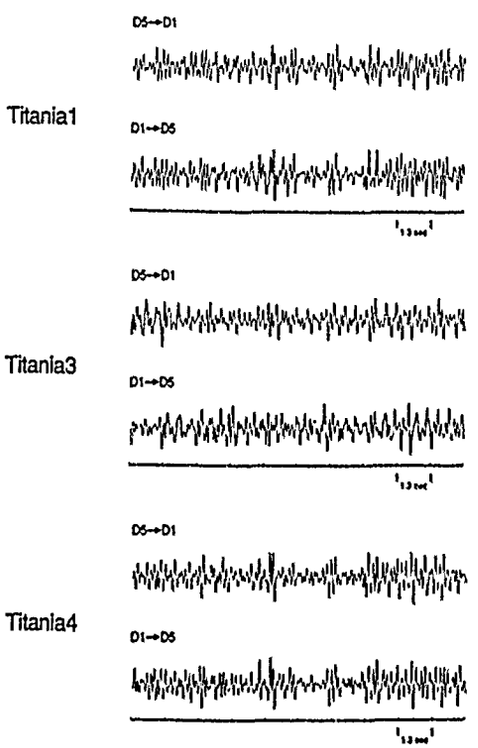

FIG. 8. Site-equalized *Pn* traces for selected Titania events between the sensors D1 and D5.

equalization drastically deteriorated as indicated by the decrease in the correlation coefficients between equalized traces (Fig. 9). The correlation peaks are still generally at the same times, but one of the peaks (for event E1-2) is shifted in time. The decrease in site equalization efficiency may be attributed to the fact that mines E4 and E1 are too far from each other to have identical site functions at NORESS. The waveform similarity is not even visible for this set (Fig. 10).

Given the fact that, after applying some cross-equalization treatment to the outputs of a pair of sensors located at the extremities of a small array for events in some limited source areas (not the two Estonia mines together), the waveforms become quite similar, it may be not justifiable to limit the sizes of regional arrays to a few kilometers. It appears that regional signals from limited source regions are actually "coherent," in the sense of a broader definition of this term, over much larger distances between sensors. Clearly the maximum array diameter dictated by the average waveform correlation properties (Mykkeltveit *et al.*, 1983; Der *et al.*, 1988) do not apply here. It could be fruitful to test and develop similar techniques using data from small arrays larger than NORESS.

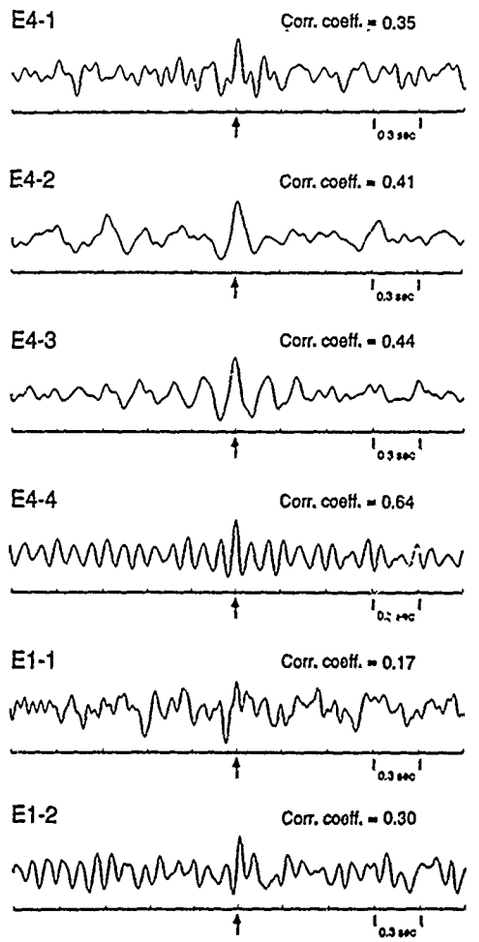

FIG. 9. Cross correlations of the site-equalized traces of *Lg* between sensors D1 and D5 for selected events at the Estonia mines E1 and E4.

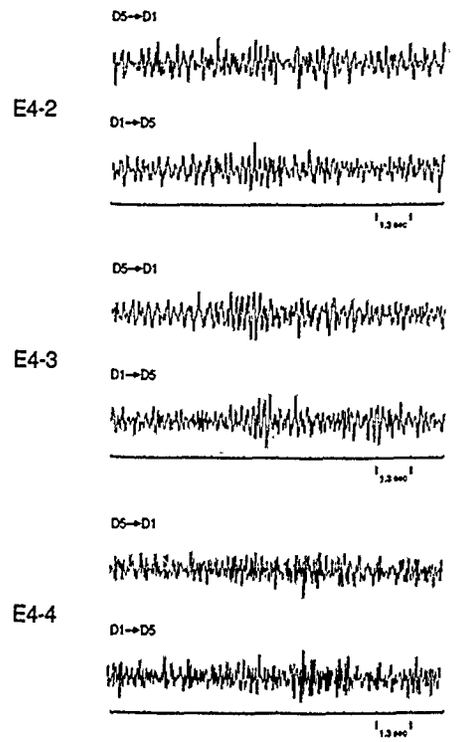

FIG. 10. Site-equalized *Lg* traces for selected events at the Estonia mine E4 between the sensors D1 and D5.

CONCLUSIONS

In this exploratory study of regional seismic waveforms, extending the concept of spectral factorability of teleseismic body-wave data (Filson and Frasier, 1972), we have demonstrated that spectra of regional phases can also be decomposed into source and recording site factors provided that the signals originated from a limited source region. Groups of events located close to each other can be identified by the fact that their waveforms can be reconstructed from their spectral source and site factors. This opens the way for relative source studies even though the Green's functions may not be known well enough to simulate waveforms.

In addition to the validation of the factorability concept, it was also found that events within such factorable groups could be further subdivided according to relative intervent coherence among them. The events which show high coherence probably are both close to each other and have very similar mechanisms although their source-time functions may be different enough to make their waveforms dissimilar. The opposite must be true for events that do not show high coherence. Cross-event equalization filtering between coherent events using short time domain filters resulted in increases in waveform similarity, and no such increase seemed possible between events pairs with low interevent coherence.

Site transfer functions between sensors located at the extreme ends of NORESS appear to be complex, describable only with transfer functions with impulse responses longer than a second. Assuming the same degree of crustal heterogeneity for a source region, this may imply changes in waveforms similar in nature over small displacements of source location. Further work needs to be done in exploring

the nature of such transfer functions. The work presented demonstrates that there is a considerable amount of relative source and path information that may be extracted from regional data applying fairly standard, simple coherent time series processing methods without requiring the knowledge or sophisticated modelling of propagation characteristics.

Acknowledgments

The authors acknowledge help and advice obtained from Dr. D. R. Baumgardt during this project. This work was performed under the DOD contract F19628-89-C-0030 and was monitored by the Air Force Geophysical Laboratory, Hanscom AFB, MA.

References

Aki, K. and P. G. Richards (1980). *Quantitative Seismology*, W. H. Freeman, San Francisco.

Anderson, D. A. and B. W. Stump (1989). Seismic wave generation by quarry blasts, in *Qualification of Explosion Source Characteristics from Near Source, Regional and Teleseismic Distances*, Southern Methodist University, GL-TR-89-0194.

Baumgardt, D. R. and K. A. Ziegler (1988). Spectral evidence for source multiplicity in explosions, application to regional discrimination of earthquakes and explosions, *Bull. Seism. Soc. Am.* **78**, 1773–1795.

Bendat, J. S. and A. G. Piersol (1966). *Measurement and Analysis of Random Data*, Wiley, New York.

Der, Z. A., R. H. Shumway, and A. C. Lees (1987). Multichannel deconvolution of *P* waves at seismic arrays, *Bull. Seism. Soc. Am.* **77**, 195–211.

Der, Z. A., R. H. Shumway, and A. C. Lees (1988). Frequency domain coherent processing of regional seismic signals at small arrays, *Bull. Seism. Soc. Am.* **78**, 326–338.

Filson, J. and C. W. Frasier (1972). Multisite estimation of explosive source parameters, *J. Geophys. Res.* **77**, 2045–2061.

Ingate, S. F., E. S. Husebye, and A. Christoffersson (1985). Regional arrays and optimum data processing schemes, *Bull. Seism. Soc. Am.* **75**, 1155–1177.

Kværna, R. and S. Mykkeltveit (1986). Optimum beam deployment for NORESS *P*-wave detection, in *NORSAR Semiannual Technical Summary*, L. B. Loughran (Editor), 1 April–30 September 1985, No. I-86/87, 61–76.

Marple, S. L. (1987). *Digital Spectral Analysis and Applications*, Prentice Hall, New York.

Mykkeltveit, S., K. Astebol, D. J. Doornbos, and E. S. Husebye (1983). Seismic array configuration optimization, *Bull. Seism. Soc. Am.* **73**, 173–186.

Shumway, R. H. (1988). *Applied Statistical Time Series Analysis*, Prentice Hall, New York.

Shumway, R. H. and Z. A. Der (1985). Deconvolution of multiple time series, *Technometrics* **27**, 385–393.

Willis, D. E. (1963). A note on the effect of ripple firing on the spectra of quarry shots, *Bull. Seism. Soc. Am.* **53**, 79–85.

ENSCO Incorporated
5400 Port Royal Road
Springfield, Virginia 22151-2388

Manuscript received 16 February 1990

Bulletin of the Seismological Society of America, Vol. 80, No. 6, pp. 2177–2193, December 1990

CORRELATION OF WAVEFORMS FROM CLOSELY SPACED REGIONAL EVENTS

By Hans Israelsson

Abstract

We studied the similarity of waveforms recorded at the high frequency element of the NORESS array from 137 events (M_L = 0.8 to 2.1) in or near the mining districts of Central Sweden. Waveform correlations based on the covariance matrices of three component recordings and on maximum amplitudes were calculated from traces filtered between 2.5 and 4.0 Hz, in which band the signal-to-noise ratio consistently peaked for the waveforms. A cutoff value for the correlations to separate waveforms with poor and good correlation values could be defined from the statistical uncertainty in back azimuth estimates of NORESS. More than 80 per cent of the events could be grouped with hierarchical clustering into one large group of 98 events and five smaller groups. The NORESS epicenters of the events in the large group were scattered over an area of 20 × 75 km. An exponential decay of the waveform correlation with event separation (d in km) could be fitted to the data of this group (exp(−d/8), taking NORESS epicenter uncertainties into account. A procedure for location of close events based on correlation values is defined. When applied to the large event group it limits the event epicenters to be within an area of about 4 km. For one small event group, high correlation values were obtained above 15 Hz. These frequencies are significantly higher than those reported in other studies, and the so called quarter wavelength argument constrains the event epicenters to within 0.1 km.

Introduction

In regional seismic monitoring one sometimes distinguishes between model-based and case-based approaches to identify seismic events (Dysart and Pulli, 1987). The model-based approach aims at defining some discriminant from the recorded waveforms that will in general identify events regardless of region. The discriminant should also relate to the physics of various seismic source types, like the ratio of radiated P- and S-wave energy. In spite of a number of studies, no single model-based method has so far been defined that performs successfully regardless of region. In contrast, the case-based approach attempts to take advantage of the repeatability of records from events in the same source area for location and identification. Similarities of waveforms recorded from closely spaced sources have been reported for several regions in the literature. For example, seismograms recorded at the NORESS array from several events at the Titania mine (400 km distance) showed remarkable similarity in time history (Jurkevics, 1987). Records may not only be consistent for a particular area but may also be distinct from those at nearby locations. Marked differences have, for example, been observed for records at NORESS from events in the Western U.S.S.R. at neighboring mines only 25 km apart (Suteau-Henson and Bache, 1988). From visual inspection of recordings of mining explosions, experienced analysts have even been able to pinpoint the particular mine of origin. The case-based approach is thus based on knowledge acquired from the recordings of many events from a particular area, and a new event is supposed to be identified by waveform comparisons with events previously recorded in the region.

Even if waveform repeatability has been observed in several studies, it seems that the case-based approach has not yet been fully explored. In particular, if one considers that the number of observations used to demonstrate repeatability is usually quite small (i.e., a handful compared to the total number of regional events detected and located). The NORESS array, for example, reports an average of about 30 events on a working day. The purpose of this article is to study repeatability and patterns of regional records from a fairly large number of events within a small area. An attempt is made to utilize automatic procedures to compare and group seismic waveforms.

Data

The seismic events used in this study were all located within a small region 50 by 200 km in central Sweden. In fact, this region has the highest number of events per unit area that are detected and located by NORESS. Most of the events are located in mining districts and are presumed to be ripple-fired quarry blasts. Because of the current interest in high frequency recordings and the short epicentral distances (around 200 km), data recorded at the high frequency element of NORESS were selected for the analysis. The analysis here is based on data recorded with Teledyne Geotech GS-13 seismometers installed in a surface vault at the central element (NRA0) of the array. These instruments with associated recording systems have responses that are essentially flat to ground velocity in the frequency band 2 to 50 Hz, and the data sampling rate was 125 events/sec.

About 1000 events were recorded with the GS-13 instruments between 1 January 1986 and 30 June 1988. Digital data were available in the NORESS high frequency waveform data base at the Center for Seismic Studies for about 700 of these events. Waveform data for 222 events were selected from the data base and reviewed with regard to data quality. In order to minimize tape handling this selection was based on the number of events available on each tape of the data base. In the review process 85 events were rejected for various reasons (e.g., insufficient signal-to-noise ratio, spikes in the data, uncertainties about horizontal components). This left 137 events to be used in the analysis. Epicenters and magnitudes, M_L, reported in the NORESS bulletin for these events have been compiled by Israelsson (manuscript in preparation). None of the events were reported in seismic bulletins based on local station networks in Fennoscandia, and the epicentral accuracy is therefore limited by the location accuracy of the array. The uncertainty of a NORESS location is in turn determined by the uncertainty in the backazimuth and in the distance determinations, as discussed in the following section. The magnitude, M_L, ranges between 0.8 and 2.1 and has a median value of 1.2.

Since most of the events are in the low magnitude range, attempts were made to define a frequency band with optimum signal-to-noise ratio, SNR, for the subsequent signal processing. For this purpose the SNR was calculated as a function of frequency for each event. Each record was filtered by a set of narrow bandpass filters that were obtained from low and high-pass Butterworth (three-pole) filters both at frequency f varying from 0.1 to 50 Hz in increments of 0.1 Hz. The SNR at frequency f was then defined by the ratio:

$$SNR(f) = \frac{\max_m |s(m; f)|}{\max_m |n(m; f)|}$$

Here $n(m;f)$ is noise prior to signal onset in a time interval of about 12 seconds as shown in Figure 1, and $s(m;f)$ denotes the signal segment. The maximum amplitude of the noise and signal segments was determined in the appropriate time intervals. Ratios were calculated as marked in Figure 1 for the four signal intervals P, P coda, S, and S coda. The $SNR(f)$ diagrams of these signal intervals for the two events in Figure 1 are typical of the data, and these functions usually show a pronounced peak at some frequency (peaking frequency). The peaking frequencies for P and S waves occurred for most of the data in a narrow band between 2.5 and 4.0 Hz, which we will subsequently use for prefiltering of the data (Israelsson, 1990). The fact that the maximum signal-to-noise ratio mostly occurs at such low frequencies could be due to increased daytime high-frequency noise levels when most of the events were recorded. Many of the events are also most likely ripple-fired, and delayed firing of shots may reduce the high frequency content (Willis, 1963).

Waveform Similarity

In order to compare the waveforms recorded from the 137 events, we use quantitative measures based on polarization and relative amplitude of the records. In polarization processing, various useful attributes like particle-motion ellipticity and orientation can be extracted from the polarization ellipse, which in turn is defined by the three polarization axes resolved from the covariance matrix of the three component recordings. Rather than use such polarization attributes we employ the approach of Jurkevics (1987) that simply forms particle-motion signatures from the covariance matrix. The band-filtered (2.5 to 4.0 Hz) seismogram of component i ($i = 1, 2, 3$) for event k is denoted $s_{ik}(m)$. For each event k the covariance matrix R_{ijk} of components i and j as a function of time t is defined as follows:

$$R_{ijk}(t) = \sum_{m=-T/2}^{m=T/2} \frac{(T - 2\,|\,m\,|)}{T} \cdot s_{ik}(t - m) \cdot s_{jk}(t - m) \qquad (1)$$

The matrix R_{ijk} is the 3 by 3 matrix of coefficients for a quadratic form, which is an ellipsoid and is symmetric with six unique terms. The three diagonal terms of R_{ijk} (i.e., $i = j$) are simply the envelopes of the three-component motions as a function of time. The three unique off-diagonal terms are the cross-products between components, and they provide important information about the phase and orientation of the particle motion. According to equation (1) the data are windowed into short overlapping time segments, T sec wide. The bandwidth of the filtered records and the window length determine the frequency and time resolution. The data window is also tapered, and its width is related to the center frequency of the passband in such a way that each frequency component is assumed to be purely polarized over several cycles of duration. The tapered sliding data window has a smoothing effect that will make the signatures less sensitive to minor variations in source and path properties. We use a window length of about $T = 1.5$ sec and move the center of the time window in steps (t) of about 0.5 sec. The signature correlations were calculated from a data window covering the entire wavetrain including both P and S phases. Cross correlations between events k and l are obtained by cross correlating the signature traces R_{ijk} and R_{ijl}. A summation of these cross correlations over the channels i and j (in all six unique) is then used to define a similarity

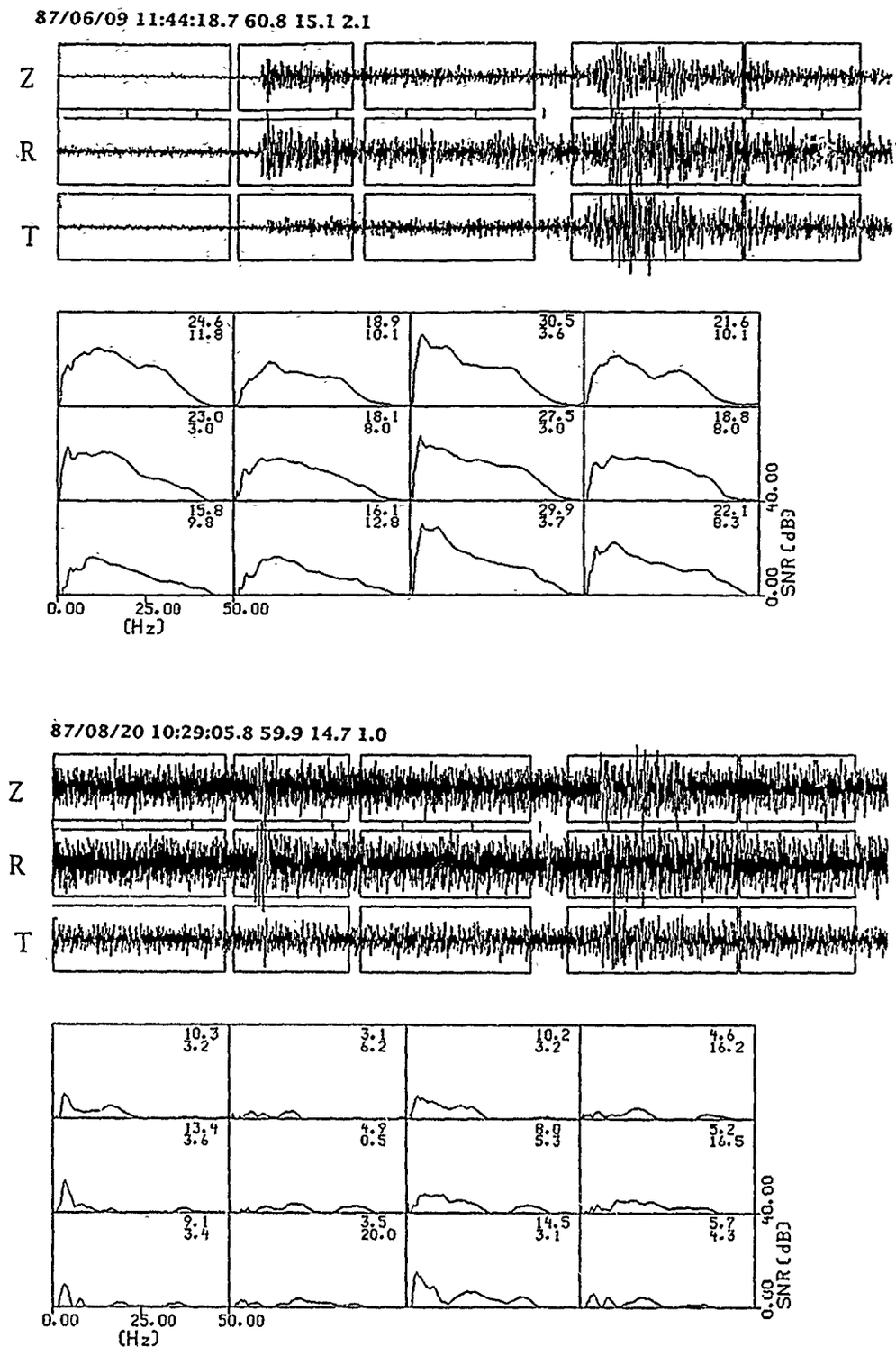

FIG. 1. Examples of waveforms for two of the events with dates, origin times, epicenters, and magnitudes, M_L, above the record sections. The horizontal east-west and north-south components have been rotated to the radial and transverse components. Time windows for noise, P, P coda, S, and S coda used to define the SNR are marked as boxes on each trace. The SNR is plotted as a function of frequency below the traces for the P, P coda, S, and S coda. In each SNR diagram, the upper number is the maximum SNR (dB) and the lower number the frequency (Hz) at which the maximum occurs.

measure, $\rho_{kl}(\tau)$:

$$\rho_{kl}(\tau) = \sum_{i \geq j} \left(\frac{\sum_t R_{ijk}(t) \cdot R_{ijl}(t - \tau)}{\sqrt{\sum_t R^2_{ijk}(t) \cdot \sum_t R^2_{ijl}(t - \tau)}} \right) \tag{2}$$

In order to account for different amplitudes in the comparison of waveforms we define the maximum amplitude of the three component recordings from the maximum amplitudes (positive or negative) of one of the components (vertical, $i = 1$):

$$A_k = \max\left(\max_m (s_{1k}(m)), \left| \min_m (s_{1k}(m)) \right| \right)$$

The maximum amplitudes defined in this manner can in turn be used to define the following measure of similarity between amplitudes of two recordings:

$$\rho_{kl}(A) = \sqrt{\min(A_k/A_l, A_l/A_k)} \tag{3}$$

This measure is normalized and is always in the interval (0, 1), and by taking the square root it is fairly insensitive to minor amplitude differences. The two correlation measures (equations 2 and 3) are finally combined to define the total correlation, ρ_{kl}, between waveforms of events k and l:

$$\rho_{kl} = \rho_{kl}(A) \cdot \max_\tau \rho_{kl}(\tau) \tag{4}$$

The total correlation defined in this manner is used in analysis of the events. Examples of particle signatures and correlations are given in Figure 2 for event pairs with high and low total correlation values, ρ_{kl}.

Correlation values ρ_{kl} were calculated for all possible event pairs (total of $137 \times 136/2 = 9{,}316$). In order to group similar waveforms we need to specify some cutoff value of ρ_{kl} above which waveforms are considered similar. The correlation ρ_{kl} depends on the signatures of all components and their relation to each other, and will therefore be sensitive to location of the event, in particular backazimuth, since the events are presumed to have similar epicentral distance. We use the uncertainty of the NORESS estimates of backazimuth to define this cutoff value. The standard deviation of the azimuth error is 6 to 7°, and we use here a minimum of 6.2° obtained by comparison with locations of regional station networks for regionalized sets of events. In other words, we assume that the error in backazimuth determined by NORESS for a group of events with identical sources and locations would have a standard deviation of 6.2°. The difference in backazimuths determined independently for pairs of such events would then have a standard deviation of $\sqrt{2} \times 6.2 = 8.8°$. If the events were gradually separated from each other the standard deviation of the difference in backazimuths would increase, and the correlation between waveforms would drop. It is reasonable to assume that for the data studied here event pairs with high correlations also have similar locations, and Figure 3 shows the standard deviation of the azimuth differences as a function of correlation values (grouped in bins 0.1 wide) for all event pairs. The *a priori* value of the standard deviation is indicated by the horizontal line in the diagram. For

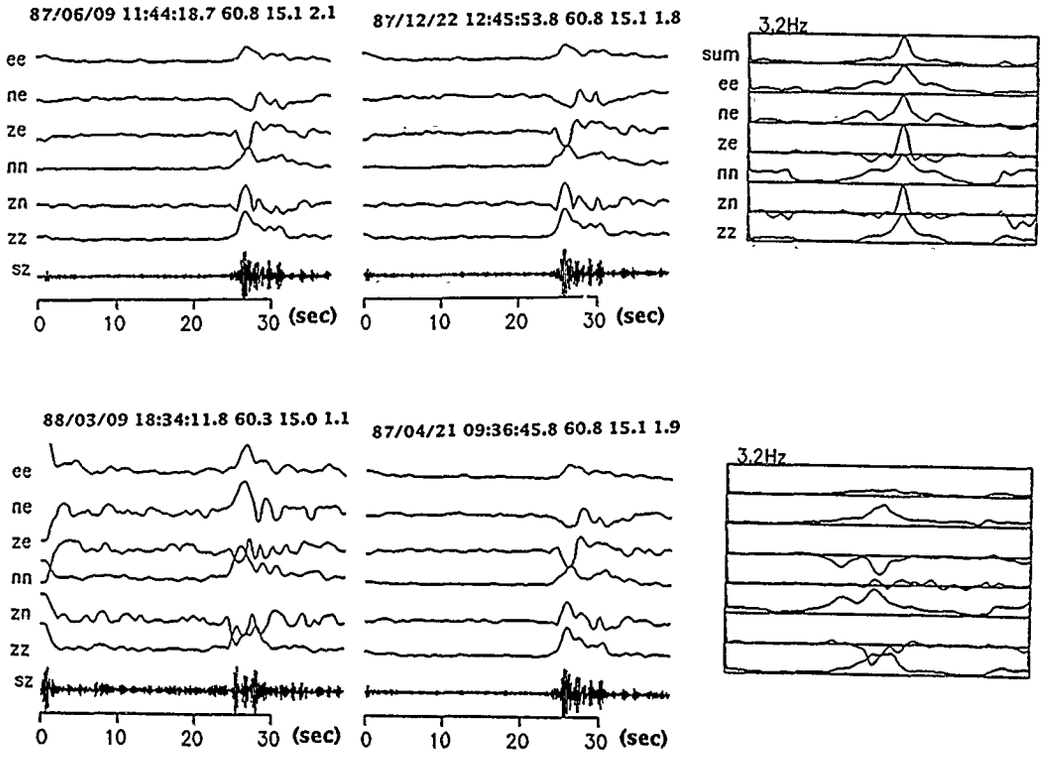

FIG. 2. Examples of cross correlations of three-component data for event pairs with high (*top*) and poor (*bottom*) correlation. Dates, origin times, epicenters, and magnitudes, M_L, for the events are given in the figure. The vertical component seismograms are plotted at the bottom of each diagram, and the six unique components of the covariance matrix as a function of time are shown above the vertical component seismograms. The cross correlation functions of the six covariance components and the sum of the cross correlations are displayed to the *right*, together with the sum of these six functions.

correlation values above about 0.7 the standard deviation is about the same as this expected value, and at lower correlations it becomes significantly larger. In the subsequent grouping we will therefore use this value as a cutoff for similarity between event pairs. A value of 0.6 for the cross correlation, based on one component only and defined in an entirely different way, was used by Pechmann and Kanamori (1982) and Thorbjarnardottir and Pechmann (1987) as a cutoff that separated well correlated from poorly correlated events. We can use $\max_{l \neq k} \rho_{kl}$ as an indicator of the similarity of event k with that of the rest of the events. If this value for a given event k is high there is at least one other event with a similar record, but if it is low the event would appear as "unique" in the data set. The distribution of these maximum values is shown by the histogram of Figure 4. There are 24 events (or about 17 per cent of all events) with $\max_{l \neq k} \rho_{kl} < 0.7$, that thus would be characterized as unique, and only 10 events (or 7 per cent) have a $\max_{l \neq k} \rho_{kl} < 0.65$.

EVENT GROUPING AND RELATIVE LOCATION

The locations and source properties for the events studied here are not precisely known, but from the correlation values and from a visual inspection of the records it is reasonable to assume that there are a number of events with close locations and similar source characteristics. We can therefore attempt to group the data so that events within groups are similar and unlike those from other groups without assuming anything about the number of such groups. This problem can be formally analyzed with clustering analysis techniques (Everitt, 1986). As a first attempt with

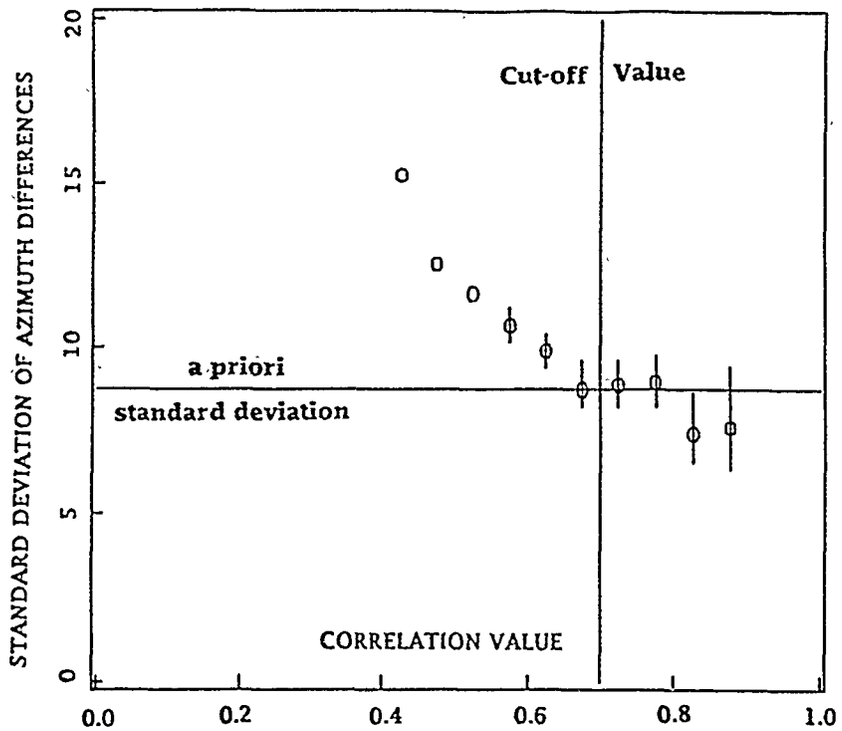

FIG. 3. The standard deviations of the difference in backazimuths for pairs of events located by NORESS are plotted against correlation (in bins 0.1 units wide). The error bars represent 95 per cent confidence intervals for the standard deviations. The horizontal line corresponds to an *a priori* standard deviation for differences in the back azimuth error of event pairs. The vertical line represents a correlation value 0.7 selected as cutoff value in the event grouping.

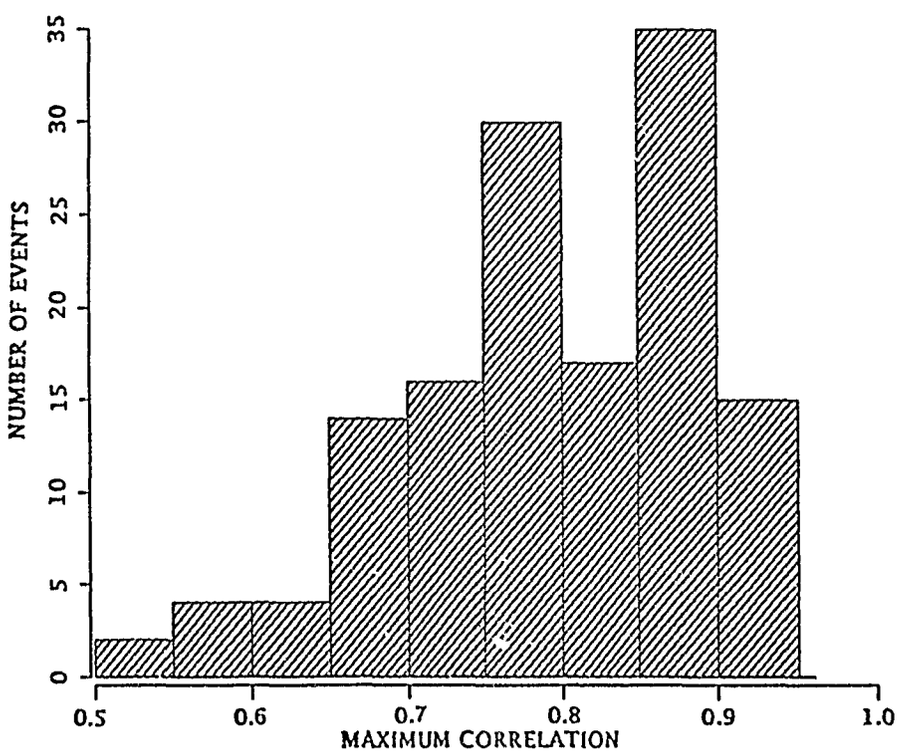

FIG. 4. The histogram shows the density of the maximum correlation between each of the 137 events and any other event, i.e., $\max_{l \neq k} \rho_{kl}$, for $k = 1, 2, \ldots 137$. The historgram shows, for example, that for 24 events the maximum correlation with any other event is less than the cutoff value of 0.7.

this technique we apply hierarchical clustering, which operates on the matrix of pairwise correlations between the event waveforms. The hierarchical clustering consists of a series of "fusions" of events into groups, and in each step in this process events or groups of events that are most similar are fused together. We use the single linkage method, in which each group initially consists of one event. As the clustering proceeds, groups are fused according to members with highest correlation. The correlation between groups is defined as the highest correlation between members. The results of this clustering are summarized by a dendrogram or cluster structure tree in Figure 5, which shows the successive fusions of events. If we use 0.7 as a cutoff value between groups, the events can be grouped into one large group with 98 members according to the dendrogram. In addition, there are two groups with four and three groups with two members. In the larger group there are also three subgroups with very high correlation (above 0.85) among the members. That is to say that more than 80 per cent of the events can be grouped in one way or another, with one large group containing about 70 per cent of the events. The hierarchical clustering gives a reordering of the events as described by the dendrogram. In general, this reordering can be used to place similar waveforms close to each other on a seismogram section (Israelsson, manuscript in preparation).

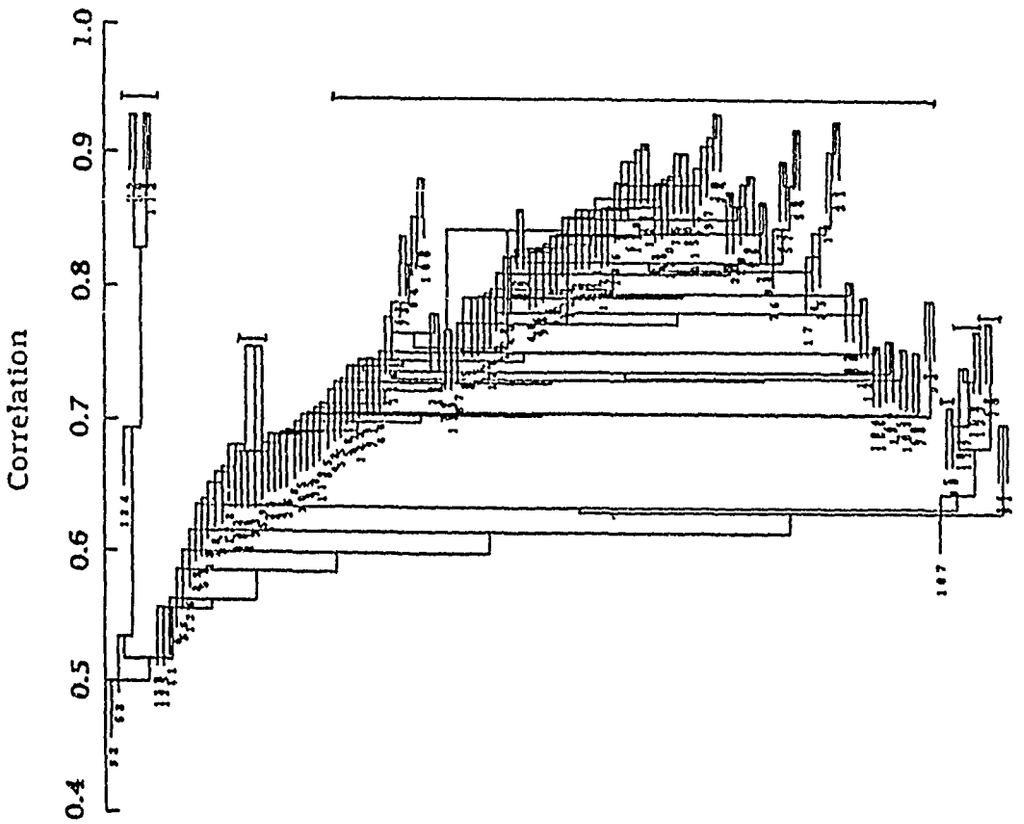

FIG. 5. Dendrogram or cluster tree structure as a result of hierarchical clustering with the single link method. The numbers in the tree refer to event numbering used by Israelsson (manuscript in preparation). Above the cutoff value of 0.7 the data cluster in one large and a few smaller event groups, which are marked with vertical lines above the dendrogram.

If we assume that events grouped together by the similarity measure also have the same location, an improved estimate of the epicenter can be obtained from the NORESS locations of these events and *a priori* assumptions about the uncertainties in determinations of backazimuth and distance. We assume that the azimuth and distance errors are both normally distributed, with zero mean (unbiased). For a group of n events with backzimuth ϕ_i and distance r_i, the confidence region of the epicenter (specified by uncertainties in distance and azimuth) becomes:

$$\bar{\phi} \pm t_{1-\sqrt{1-\alpha}} \cdot \frac{s_\phi}{\sqrt{n-1}}$$

$$\bar{r} \pm t_{1-\sqrt{1-\alpha}} \cdot \frac{s_r}{\sqrt{n-1}}$$

Here t is the standard t distribution, and s_ϕ and s_r are the standard errors of backazimuth (ϕ_i) and distance (r_i), respectively. If backazimuth and distance determinations are independent, then the confidence level is $1 - \alpha$. The point estimates $\bar{r}$ and $\bar{\phi}$ for all event groups and the 95 per cent confidence region for the large event group are shown in Figure 6 together with the NORESS epicenter determinations of the events. The extent of the confidence region, centered around 60.03°N and 14.84°E is about 10 km. The events in the large group are probably mining explosions in the Grangesberg district in Central Sweden, which has a diameter of about 2 km and has its center coordinates at 60.08°N and 15.00°E

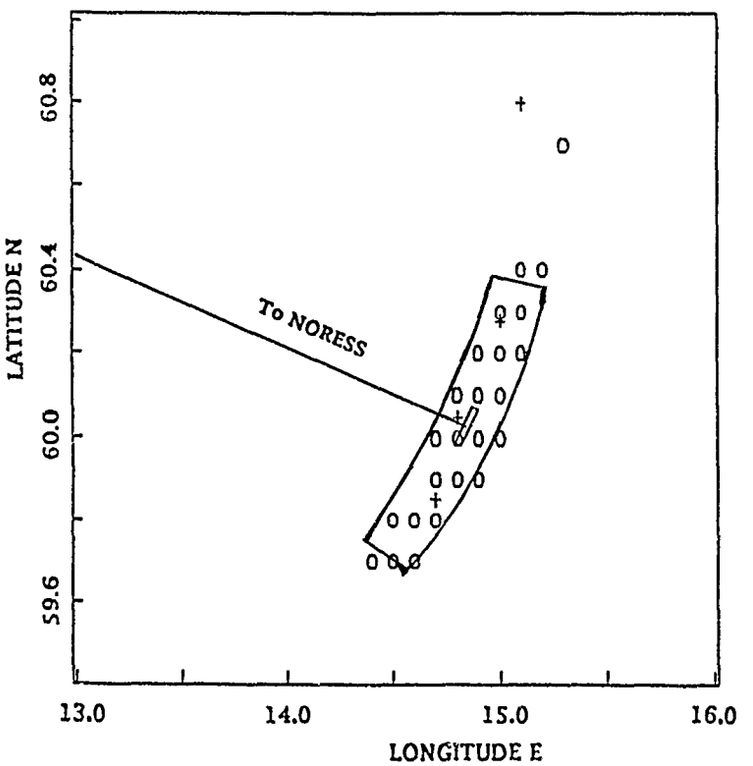

FIG. 6. NORESS locations of events in the large group (circles) and 95 per cent confidence region of their epicenter (small sector), assuming it is common to all events. The large sector represents the 95 per cent confidence region for one event at the estimated epicenter for large event group. Crosses mark point estimates of events in small groups. The direction to NORESS is also indicated.

(Mykkeltveit, personal communication). The standard deviation of the epicenter errors due to rounding errors in the NORESS bulletin (latitude and longitude given to 0.1°) is about 4 km. The shape of the confidence region is a circular sector since we approximate with plane geometry, and this approach of obtaining confidence regions for arrays operating at regional distances can be used for single events as well, if the t-distribution is replaced by a normal distribution (cf. confidence ellipses for spherical geometry by Bratt and Bache, 1988). The 95 per cent confidence area for one event with epicenter at 60.03°N and 14.84°E is drawn for comparison in Fig. 6 (standard deviations σ_ϕ (6.2°) and σ_r (3.7 km) are assumed). Confidence regions for the epicenters of the smaller event groups were not calculated since the number of events ranged only between 2 and 4. However, the northernmost group of four events, all with the same NORESS epicenters, 60.8°N and 15.1°E, seems to be at a location significantly different from that of the large event group.

Similarity as a Function of Source Separation

The degree of waveform similarity between two events recorded by the same instrument is a function of differences in path and source characteristics. For identical source pairs the correlation will be a function only of path differences, which sometimes are approximated with distance between sources. For example, MacLaughlin *et al.* (1983) approximated the correlation of waveforms recorded across an array as a function of array coordinates, with an exponential function of the moduli of the coordinates. If one simplifies further and assumes isotropic conditions, the correlation will have an exponential decay with source (or receiver) separation, d. We write this decay as $\exp(-d/a)$, with the constant a being a characteristic distance for the source (or receiver) region. A smoothed curve fit to the cross correlations obtained here as a function of source separation (from the NORESS locations) is shown in Figure 7. It should be noted that the calculated correlation values involve amplitude differences. This means that identical waveforms originating from the same location and differing in amplitude will have a correlation less than one. Since the distribution of the amplitude data for the events is sharply peaked (Israelsson, 1990), amplitude differences will, however, affect only a small number of correlation values in this manner. The curve in Figure 7 is almost flat to about 40 km, and at larger distances drops exponentially with different rates for different distance intervals. The flat part of the curve is caused by a bias in distance between event pairs computed from the NORESS locations. With assumptions about the distributions of the errors in backazimuth, ξ_ϕ, and epicentral distance, ξ_r, this bias can be estimated. Let r_i and ϕ_i be the true distance and backazimuth from NORESS for event i. The rounding errors of the latitude (ξ_{yi}) and longitude (ξ_{xi}) reported for event i in the NORESS bulletins can be assumed to be uniformly distributed over the intervals (−5.6, 5.6) and (−2.8, 2.8) km respectively. The esimated coordinates of the event in a Cartesian plane with NORESS at the center can then be written as:

$$x_i = (r_i + \xi_{ri}) \cdot \sin(\phi_i + \xi_{\phi i}) + \xi_{xi}$$

and

$$y_i = (r_i + \xi_{ri}) \cdot \cos(\phi_i + \xi_{\phi i}) + \xi_{yi}$$

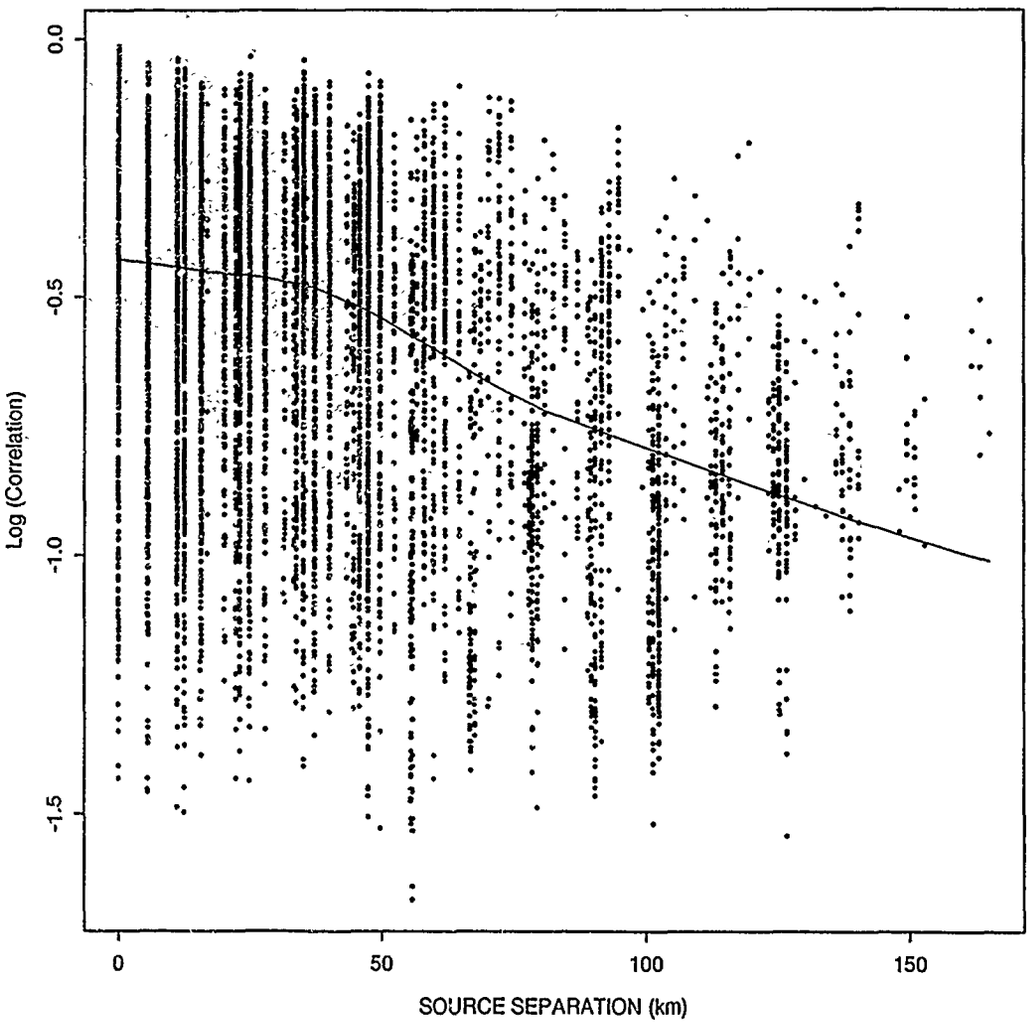

FIG. 7. The correlation curve was obtained from the correlation data in this study and represents a smoothed curve based on robust locally weighted regression (Becker and Chamber, 1984). Note that this curve is biased due to errors in the NORESS epicenter determinations.

The separation between two events obtained from the epicenters determined by NORESS is:

$$\delta_{ij} = \sqrt{(x_i - x_j)^2 + (y_i - y_j)^2}$$

whereas the true distance is:

$$d_{ij} = \sqrt{r_i^2 + r_j^2 - 2 \cdot r_i \cdot r_j \cdot \cos(\phi_i - \phi_j)}.$$

Even if the ξ variables have standard distributions the δ_{ij} variable does not. Therefore, we used random number generators for normal and uniform distributions to generate a sample of observations for this nonstandard distribution (9316 observations), with $r_i = r_j = 200$ km and $\phi_i = \phi_j = 111.0°$. This sample has a skewed distribution and $\delta_{ij}^{1/3}$ fits a normal distribution reasonably well. The median value, $E(\delta_{ij})$, for this sample was 21.36 km, which would represent the bias in the

correlation curve. By subtracting this bias, the characteristic distance, a, can now be estimated from:

$$\hat{a}_{ij} = \frac{E(\delta_{ij}) - \delta_{ij}}{\log(\rho_{ij})}.$$

The median value of $\hat{a}_{ij}$ was 8.0 km if the data were limited to $\rho_{ij} > 0.6$ (5024 event pairs). Although there is a very considerable scatter in the $\hat{a}_{ij}$ values, the 95 per cent confidence interval (Claerbout, 1976) for the median is limited to 7.0 to 9.5 km. Similar results were obtained for data with $\rho_{ij} > 0.8$ (1032 event pairs). This is in qualitative agreement with the characteristic distance obtained from correlations between station pairs of the NORESS array (Mykkeltveit *et al.* 1983; see also Figure 8). The correlation of P_g across NORESS in the frequency band 2.4 to 4.8 Hz, which is fairly close to the frequency band used here, is shown in Figure 8 with a linear regression fit to an exponential decay $e^{-d/a}$. The characteristic distance, a, estimated from this data is about 10 km.

Triangulation with the Cross Correlation

If cross correlation as a function of source separation, d, is known, together with the precise epicenters of at least three reference events at different locations, triangulation can be used to estimate epicenters of other events from cross correlations. This, of course, presumes that the events have the same source characteristics. Figure 9 shows the results of a computational example with this approach. This is included only for the sake of illustration; actual locations cannot be calculated without knowledge of the epicenters of the reference events. Three events that had high correlation among each other were selected as reference events. One of these events was then arbitrarily given the center coordinates, and one of the two remaining events was placed on the positive x-axis at distance, $-a \cdot \log \rho_{12}$ from the center. The coordinates of the third event were obtained from distances to the other two ($-a \cdot \log \rho_{13}$ and $-a \cdot \log \rho_{23}$). Of two possible locations, the one in the first quadrant was arbitrarily chosen as a reference. Relative location of the remaining events was obtained iteratively. In each step of this process a new event, having the largest number of correlation values with reference events above a certain minimum correlation threshold, $\rho_{\min}$, was added to the set of reference events. In the iteration this threshold was gradually reduced from 0.95 to 0.7. This means that, initially, events close to the reference events were added and as the iteration proceeded events further and further away were added. The relative coordinates x and y of a new event, $j = I + 1$, is obtained by minimizing the sum:

$$Q = \frac{1}{\sum \epsilon_{ij}} \cdot \sum_{i=1}^{I} \epsilon_{ij} \cdot (-\log(\rho_{ij}) \cdot a - \sqrt{(x_i - x)^2 + (y_i - y)^2})^2$$

The summation operator, ϵ_{ij}, is 1 if $\rho_{ij} > \rho_{\min}$. We also require that $\sum \epsilon_{ij} \geqq 3$. The circle about each event in Figure 9 is an indication of the spread in the estimated coordinates, i.e., $\sqrt{Q}/(\sum \epsilon_{ij} - 1)$.

The diameter (about 4 km) of the data points in Figure 9 is about as expected from a characteristic distance of 8 km and from correlations down to 0.7. It is also comparable to the diameter (about 2 km) of the Grangesberg mining district, from which these events probably originate.

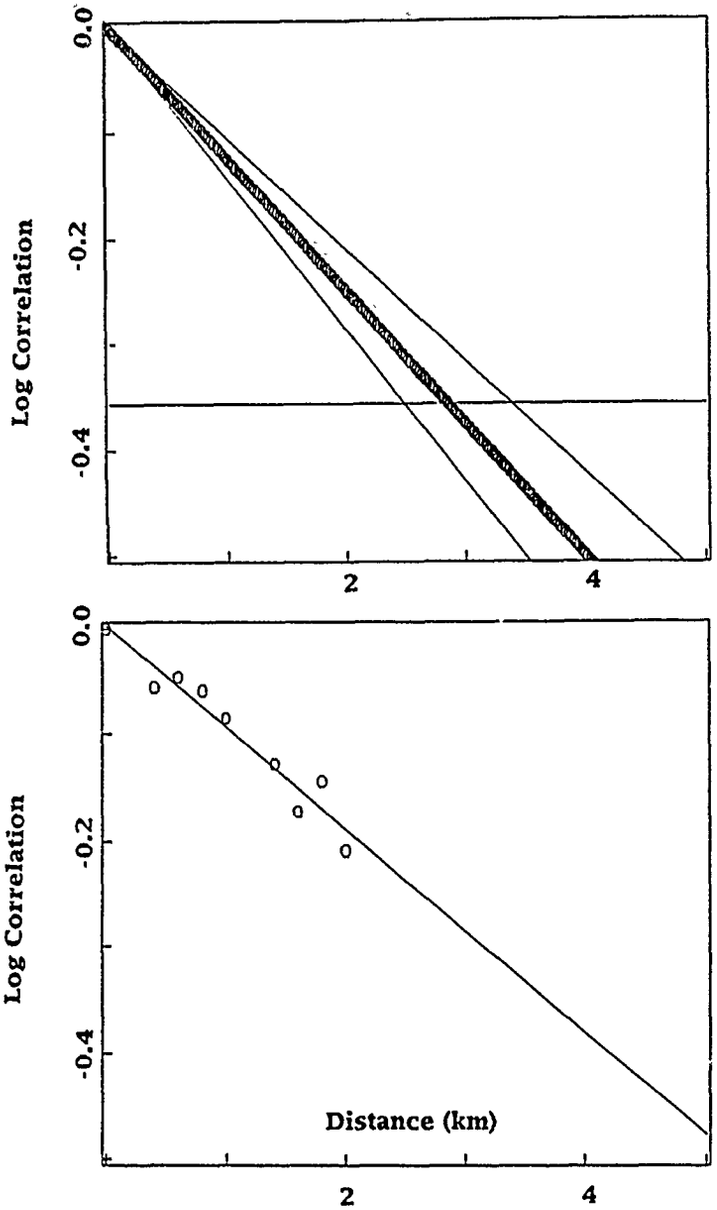

FIG. 8. The dark line in the top diagram represents an exponential decay of correlation as a function of source separation as obtained from a median estimate of the characteristic distance, $a = 8$ km. The thin lines in the same diagram represent 95% confidence levels of the characteristic distance, a (7, 9.5) km. The correlation in the lower diagram represents results obtained for P_g across the NORESS array in the band 2.4 to 4.2 Hz (Mykkeltveit, 1983), and the line corresponds to $a = 10$ km.

Similarity at High Frequencies

The results for waveform correlation presented above are limited to a band with rather low frequencies, 2.5 to 4.0 Hz, since the SNR is usually low at higher frequencies. There are, however, some events with high SNR at high frequencies, such as a suite of four events that all have NORESS epicenters at 60.8°N and 15.1°E (see Fig. 6). Correlation values based on particle signatures were calculated for these events, for portions of the records that were windowed for P and S waves (cf. Fig. 1). Calculated ρ_{kl} in these frequency bands, shown in Figure 10, indicate high correlations (0.90 or more) for data up to 20 Hz for P waves and 15 Hz for

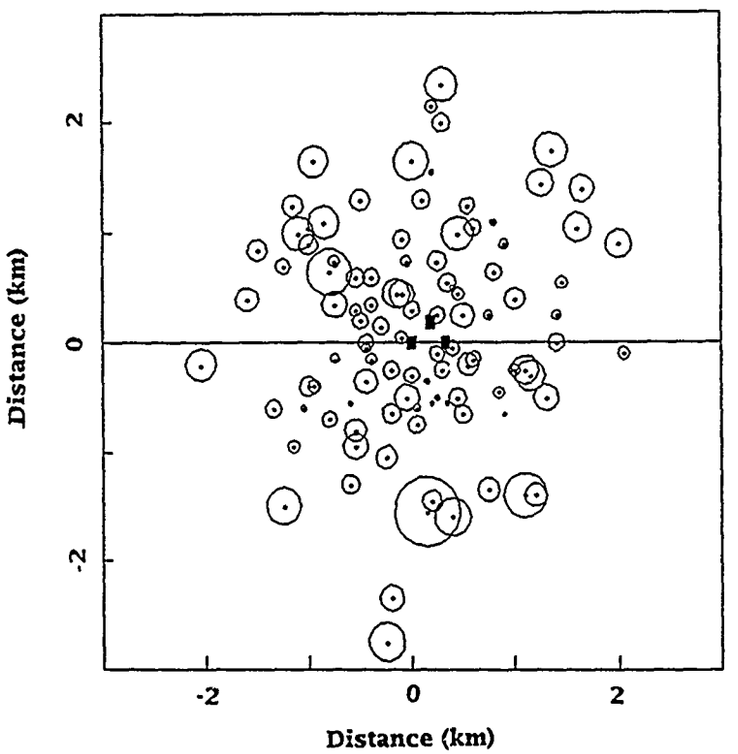

FIG. 9. Relative locations of events in large event group as obtained in a computational exercise with the triangulation method. The circles indicate the scatter in the locations. The location of the three reference events are marked with asterisks.

S waves. As a quantitative statement about the spatial clustering of earthquake aftershocks, it has been suggested that events with very similar waveforms at a particular wavelength can be assumed to have source locations within one-quarter of that wavelength (Geller and Mueller, 1980). Results for records of mine blasts by Thorbjarnardottir and Pechmann (1987) provide support for this hypothesis. If we use this argument for high-frequency correlations for the group of events near 60.8°N and 15.1°E, the quarter wavelengths are about 100 meters or less (assuming *P* velocity of 6.2 km/sec). The quarter wavelengths obtained for the *P*- and *S*-wave data in Figure 10, using a cutoff at 0.9 for the correlation, are fairly consistent with a $\sqrt{3}$ ratio of *P*- and *S*-wave velocities, except for one of the event pairs, for which the *S*-wave correlation drops already at about 4 Hz. Source separations derived from the quarter wavelength argument are of course only quantitative in nature. Frankel and Clayton (1986) demonstrate with synthetic examples that a decrease in waveform correlation may also depend on the medium characteristics, and not simply on a fixed fraction of the wavelength. Considering the 200-km epicentral distance for the four events in Figure 10, the frequencies at which their waveforms have strong correlations are high compared to results from other studies. Thorbjarnardottir and Pechmann (1987) study data recorded from mine blasts at about 100 km and get correlations (between two traces) around 0.6 or higher in the frequency band 2 to 4 Hz but little or no correlation in higher frequency bands. Geller and Mueller (1980) observed high correlations for regional earthquake data at less than 100 km for frequencies up to about 5 Hz. Lack of correlation at higher frequencies was attributed to small scale crustal heterogeneities and scattering.

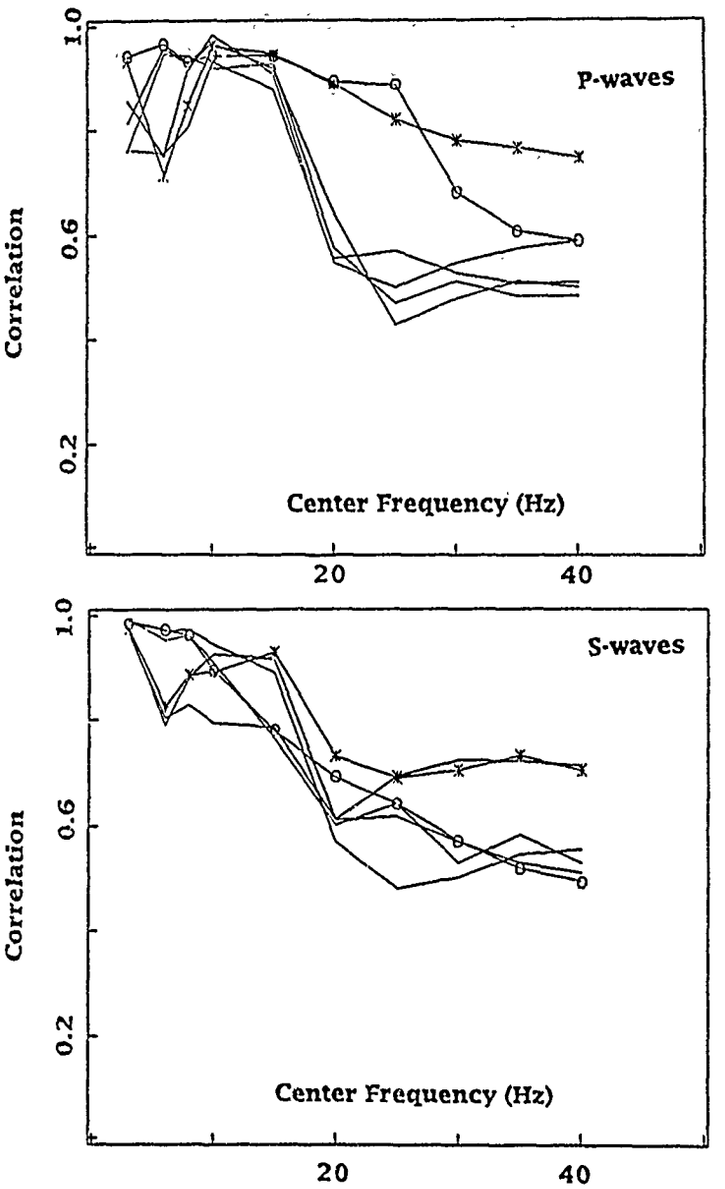

FIG. 10. Correlations in different passbands as a function of center frequency for *P*- and *S*-wave data windows. The curves represent data for a small suite of four events with the same NORESS location, 60.8°N and 15.1°E. The curves with the highest correlations for *P* waves (marked with circles and asterisks) correspond to two different pairs with no common events.

CONCLUDING REMARKS

In this article we have studied waveforms recorded at the high-frequency element of the NORESS array, from 137 events in or near the mining districts of central Sweden at epicentral distance of about 200 km from the array. The 137 events, recorded between 1 January 1986 and 30 June 1988, constitute about 10 per cent of all the events that were detected and located in this area by NORESS for this period. None of these events, which are in the magnitude range $M_L = 0.8 - 2.1$ has been reported in event bulletins based on local station networks in Norway and Finland; therefore the epicentral accuracy is limited by the location accuracy of the

NORESS array. Even if most events are believed to be ripple-fired, no explicit information on intrinsic source properties was available in this study. This situation, with uncertainties about both precise epicenters and source characteristics, is somewhat similar to test ban monitoring with stations that have to be deployed in areas with which the verifying party has little or no previous experience. The case-based approach for regional event detection and identification assumes that events can be identified on the basis of similarity with nearly identical waveforms of previously recorded events. Visual inspection of the records analyzed here indicated that there were comparatively few pairs or groups of nearly identical records, and that some variability seemed to be a significant characteristic of the data set. In order to quantify the comparisons, waveform correlations were calculated for all event pairs. Waveform correlations based on the covariance matrices of the three-component recordings as introduced by Jurkevics (1987), and the maximum amplitudes of the recordings were calculated from traces filtered between 2.5 and 4.0 Hz, the bandpass in which the SNR consistently peaked for the events. The correlation defined in this manner is fairly insensitive to minor variations in waveforms due to data smoothing but is quite sensitive to the location of the events, in particular, back-azimuth, because of the three-component nature of the waveforms. To separate waveforms with poor and good correlation, cutoff values of the cross correlations could be defined from the statistical uncertainty in backazimuth estimates of the NORESS array. The events could be grouped with hierarchical clustering analysis (single-link method) into one large group of 98 events and five smaller groups with 2 to 4 events each. Several subgroups of 2 to 5 events could also be identified in the large event group at higher cutoff values. The NORESS epicenters of the events in the large event group were scattered over an area of 20 by 75 km. If one assumes that these events had the same location, the 95 per cent confidence region of the epicenter has an extent of about 10 km. If the waveform correlation between nearby events drops monotonically in a known manner as a function of source separation, relative epicenters can be determined from waveform correlation values. An exponential decay of the waveform correlation with source separation (d in km) was estimated for the large event group ($\exp(-d/8)$). A least squares procedure for location of close events based on correlation values was defined, and when applied to the large event group it limits the epicenters of the individual events to an area within about 4 km. The estimate of the decay in correlation with *source* distance for the events in the large group is in quantitative agreement with estimates of the correlation decay with *receiver* distance across NORESS for regional waveforms in the frequency band 2.5 to 4.0 Hz. This suggests that, on the assumption of source receiver reciprocity, detailed studies of the characteristics of waveform correlations across a mini-array can provide valuable information to constrain the locations of closely spaced events in seismic source areas with little or no previous experience. Finally, high correlation values were obtained at frequencies above 15 Hz for one of the smaller event groups. These frequencies are significantly higher than those reported in other studies, and the so-called quarter wave length argument would constrain the epicenters of the events in this group to within 100 meters.

ACKNOWLEDGMENTS

I would like to thank Dr. Alan Ryall for his encouragement to prepare this report and for reviewing the original manuscript with thoughtful and valuable suggestions, Dr. Anne Henson for her editorial work with several suggestions, and the operational staff at the Center for Seismic Studies for its assistance in compiling the waveform data. I am also most grateful to an anonymous reviewer for very

constructive comments and suggestions. This study was supported by the Defense Advanced Research Projects Agency under contract F19628-88-C-0159 and was monitored by the Geophysics Laboratory.

REFERENCES

Becker, R. A. and J. M. Chambers (1984). *S: An Interactive Environment for Data Analysis and Graphics*, Wadworth, Belmont, California, 550 pp.

Bratt, S. R. and T. C. Bache (1988). Locating events with a sparse network of arrays. *Bull. Seism. Soc. Am.* **78**, 780–798.

Claerbout, J. F. (1976). *Fundamentals of Geophysical Data Processing*, McGraw Hill, New York, 274 pp.

Dysart, P. S. and J. J. Pulli (1987). Spectral study of regional earthquakes and chemical explosions recorded at the NORESS array, Center for Seismic Studies Tech. Rept. C87-03, 3.21–3.44.

Everitt, B. (1986). *Cluster Analysis*, 2nd ed., Wiley, New York, 136 pp.

Frankel, A. and R. W. Clayton (1986). Finite difference simulations of seismic scattering: implications for the propagation of short-period seismic waves in the crust and models of crustal heterogeneity. *J. Geophys. Res.* **91**, 6465–6489.

Geller, R. J. and C. S. Mueller (1980). Four similar earthquakes in central California. *Geophys. Res. Lett.* **7**, 821–824.

Jurkevics, Andy (1987). Particle motion signatures for source identification, Center for Seismic Studies Tech. Rept. C87-01, 3.1–3.11.

McLaughlin, K. L., L. R. Johnson, and T. V. McEvilly (1983). Two-dimensional array measurements of near source ground accelerations. *Bull. Seism. Soc. Am.* **73**, 349–375.

Mykkeltveit, S., Astebol, K., Doornbos, D. J., and E. S. Husebye (1983). Seismic array configuration optimization. *Bull. Seism. Soc. Am.* **73**, 173–186.

Pechmann, J. C. and H. Kanamori (1982). Waveforms and spectra of preshocks and aftershocks of the 1979 Imperial Valley, California, earthquake: evidence for fault heterogeneity? *J. Geophys. Res.* **87**, 10579–10597.

Suteau-Henson, A. and T. C. Bache (1988). Spectral characteristics of regional phases recorded at NORESS, *Bull. Seism. Soc. Am.* **78**, 708–725.

Thorbjanardottir, B. S. and J. C. Pechmann (1987). Constraints on relative locations from cross-correlation of waveforms, *Bull. Seism. Soc. Am.* **77**, 1626–1634.

Willis, D. E. (1963). A note on the effect of ripple firing on the spectra of quarry shots, *Bull. Seism. Soc. Am.* **53**, 79–85.

CENTER FOR SEISMIC STUDIES
1300 NORTH 17TH STREET
ARLINGTON, VIRGINIA 22209-3871

Manuscript received 1 February 1990

Bulletin of the Seismological Society of America, Vol. 80, No. 6, pp. 2194–2213, December 1990

UPPER MANTLE STRUCTURE ALONG A PROFILE FROM OSLO (NORESS) TO HELSINKI TO LENINGRAD, BASED ON EXPLOSION SEISMOLOGY

By Vladislav Ryaboy

Abstract

Waveforms from the NORESS array were analyzed for 147 industrial explosions during the 1985 to 1988 period, along a profile running east from Oslo (NORESS) to Helsinki to Leningrad (OHL profile). The events were 250 to 1300 km from NORESS and had local magnitude in the range 2.0 to 3.5. Event locations and origin times constrained by the University of Helsinki's regional seismic network provide a reliable basis for travel-time estimation at NORESS. We also used data recorded by NORSAR in 1979 for three shots on the FENNOLORA north–south, long-range seismic profile, which were near the OHL profile. Analysis of mantle *P*-wave signals from the explosions showed that first arrivals could be traced continuously to a distance of 750 to 800 km, where there is a cutoff and shift of approximately 2.0 to 2.5 sec in the travel-time curve and an increase in average apparent velocity. Interpretation of the observed travel times and waveforms for this profile suggests a low-velocity zone from approximately 105 to 135 km depth. Combined analysis of the seismic data with a Bouguer gravity map indicates the presence in the upper mantle of a high-velocity, high-density body of linear extent approximately from 200 to 300 to 500 to 600 km east of the NORESS array. It is postulated that this body may represent the root of an ancient volcanic system, in which lighter, silicic constituents were depleted from the upper mantle during the eruptive phase.

Introduction

Many problems of geology and geophysics require quantitative data on lateral and vertical inhomogeneities in the upper mantle. In monitoring a low-threshold test ban treaty, for example, accurate knowledge of upper-mantle structure would be critical for accurate location of events recorded at far-regional distances (1000 km or more) by a single station or array and for estimating magnitude or yield of seismic events from amplitudes of the recorded waves. In the same area, accurate knowledge of crust-upper mantle structure is also important in considerations related to the design of networks aimed at achieving specific monitoring capabilities.

The velocity structure of the upper mantle below the Baltic shield has been the subject of intensive investigations based on recorded body and surface waves from explosions and earthquakes. These studies indicate that, on average, the upper mantle in this region is characterized by relatively high velocity compared with neighboring areas (Herrin and Taggart, 1968; Masse and Alexander, 1974; King and Calcagnile, 1976; Given and Helmberger, 1980; Vinnik and Ryaboy, 1981; Husebye and Hovland, 1982; Calcagnile, 1982; Nolet *et al.*, 1986), although there is not total agreement between results of different investigations.

The most detailed *P*-wave velocity sections of the upper mantle are those for the Blue Road and FENNOLORA long-range profiles (Fig. 1; Lund, 1979a, b; Mueller and Ansorge, 1986; Stangl *et al.*, 1986; Fuchs *et al.*, 1987; Guggisberg and Berthelsen, 1987). These models were based on very detailed field observations along reversed and overlapping profiles. The main feature of the models is laminar structure

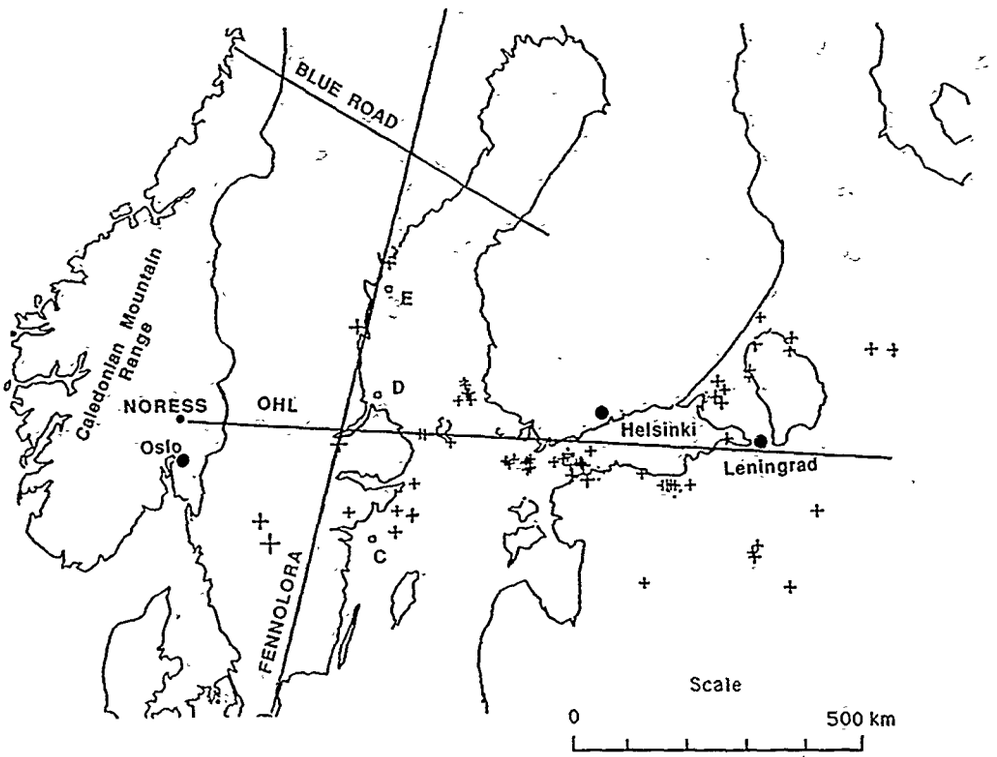

FIG. 1. Location map of NORESS array and shot points used in this study. Crosses, location of mine blasts (size of crosses proportional to event magnitude) for the Oslo–Helsinki–Leningrad (OHL) profile; squares, shot points C, D, and E for FENNOLORA profile; solid lines, FENNOLORA and Blue Road long-range seismic profiles and OHL profile.

beneath the Moho, with alternating high- and low-velocity layers in the upper mantle, determined from a number of breaks in the *Pn* travel-time curves, with the more distant branches successively shifted to later times (i.e., delayed).

To evaluate these results, we studied NORESS recordings of 147 mining and other industrial explosions, detonated during the period 1985 to 1988 along an east-west profile from Oslo (NORESS) to Helsinki to Leningrad (Fig. 1; OHL profile). We also used data recorded by the NORSAR array in 1979 for three shots on the FENNOLORA north-south profile, which were near the OHL profile.

PROFILE LOCATION AND EVENT ANALYSIS

The events used in this study are located on or near a 1300 km-long profile from the NORESS array to Helsinki to Leningrad. This profile crosses southeastern areas of the Precambrian Baltic shield. On the eastern part of the profile several events are located on the northwestern part of the Russian plate, where the sedimentary layer is rather thin (300 to 500 meters or less).

These events were listed and identified as possible explosions in the NORESS and Helsinki seismological bulletins. The events were in the range of epicentral distance from 250 to 1300 km and had local magnitude (M_L) 2.0 to 3.5. For distance less than 450 km, we reanalyzed NORSAR recordings for three of the 1979 FENNOLORA shots (C, D, and E), which were near the OHL profile. The FENNOLORA explosions had magnitude less than 2.0 based on the listings in the International Seismological Centre Bulletin (1982).

A comparison of locations and estimated origin times in the NORESS and Helsinki bulletins shows large discrepancies, up to several tens of kilometers in location and several seconds in origin time. According to the Helsinki bulletin, events identified as repeated explosions at the same mine occurred at several points of the profile. Travel times for such events typically agreed within 0.3 to 0.5 sec, and a value of ±0.5 sec can be used as a conservative estimate of the average origin-time error listed in the Helsinki bulletin. This conclusion can also be confirmed by the scatter in observed travel times of *Pn* waves from calculated travel-time curves averaging observed data (see Fig. 7 and accompanying discussion) which has an RMS deviation less than ±0.5 sec. A comparison of travel times for the same events listed in the NORESS bulletin gave markedly larger discrepancies. As a result, we used Helsinki bulletin locations and origin times as the basis for interpretation. As a final note, approximately half of the original 147 events were excluded from interpretation because of poor signal-to-noise ratio.

Crustal Thickness

Misunderstanding of deep velocity structure (e.g., in reference velocity models used in the bulletins) can be a major source of bias in locating events and estimating their origin times at far-regional distances. Therefore, a new contour map of Moho depth and schematic map of *Pn* velocity for the Baltic shield and neighboring geological units has been compiled from the most reliable data, namely from published deep seismic refraction and reflection profiles (Azbel *et al.*, 1989; Dahlman *et al.*, 1971; Galdin *et al.*, 1988; Guggisberg and Berthelsen, 1987; Korhonen and Porkka, 1981; Litvinenko and Platonenkova, 1978; Lund, 1979a, 1979b, 1980; Lund and Slunga, 1981; Luosto *et al.*, 1984, 1985, 1989; Mueller and Ansorge, 1986; Mykkeltveit, 1980; Prodehl, 1984; Prodehl and Kaminski, 1984; Sellevoll and Warrick, 1971; Weinrebe, 1981). We also used maps of Moho depth variations beneath Fennoscandia and adjacent regions published earlier (Bungum *et al.*, 1980; Calcagnile, 1982; Fluh and Berthelsen, 1986; Glaznev *et al.*, 1989; Meissner *et al.*, 1987; Sellevoll, 1973; Semov, 1987). A location map of seismic profiles used in compiling the crustal thickness map is shown on Figure 2. Velocity sections of the crust were constructed for these profiles based on various approaches to interpretation, but in general the discrepancy in Moho depth did not exceed 2 to 3 km at points where the seismic profiles crossed, which is not considered important for a map of crustal thickness with 5-km contour intervals.

Figure 2 shows that crustal thickness beneath Fennoscandia and adjacent geological provinces varies from about 30 to 55 km. The crust generally thickens from the coast to the Baltic shield interior. On average, the crust below the Caledonides (western areas of Norway) and Russian plate is thinner than that of the Baltic shield. Comparison of Figure 2 and geological data (Boyd *et al.*, 1985) indicates that there is no simple correlation between *Pn* velocity, crustal thickness, and surface geology or age. In southern areas of Sweden and Finland one can see relatively narrow zones of sharp crustal thickening up to 50 to 55 km and more. *Pn* velocities vary from 7.8 to 8.0 up to 8.3 to km/sec. The most frequently obtained values of *Pn* velocities for Fennoscandia are 8.1 to 8.2 km/sec.

For the OHL profile, crustal thickness beneath the NORESS array and at distances greater than 400 to 500 km from NORESS is about 40 km. In contrast, the Moho depth beneath FENNOLORA shots C, D, and E, and several other events is larger—up to 50 to 55 km (Figs. 1 and 2). As a result, *Pn* travel-time corrections were made to account for variations in crustal structure along the profile.

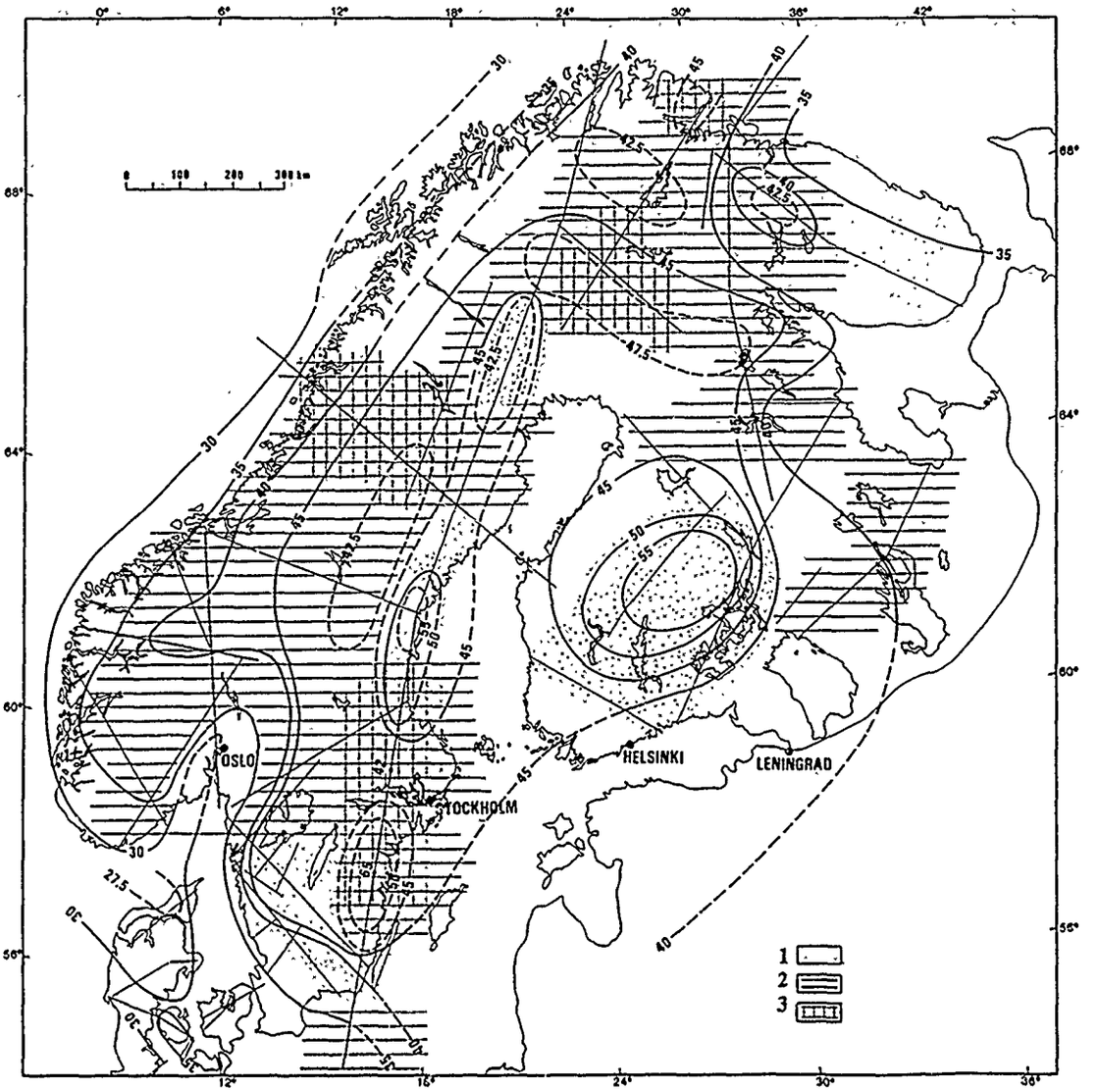

FIG. 2. Contour map of crustal thickness (km) and schematic map of *Pn* velocity for the Baltic Shield and adjacent areas, based on DSS data. Lines of equal Moho depth are represented by thick solid lines for reliable data and dashed lines for unreliable data. Values of *Pn* velocity (km/sec) are: 1, 7.8 to 8.0; 2, 8.1 to 8.2; 3, 8.3 to 8.5. Thin solid lines denote DSS profiles. The crustal thickness varies from as little as 30 to 35 km near the coast to 50 to 55 km within the interior areas. *Pn* wave velocity varies from 7.8 to 8.0 km/sec up to 8.3 to 8.5 km/sec (the most frequently observed values are 8.1 to 8.2 km/sec). There is no direct relation between variations of the crustal thickness and *Pn* velocity.

P-WAVES FROM THE UPPER MANTLE

Our study of NORESS and NORSAR recordings of explosions at far-regional distances confirmed an observation of previous authors, that the *Pn* wave of classical seismology has a very complicated structure and consists of several wave groups (Nersesov and Rautian, 1964; Ryaboy, 1966; 1979; 1989; Fuchs, 1986; Fuchs *et al.*, 1987; Lund, 1979a, b; Mueller and Ansorge, 1986). First arrivals of mantle *P*-waves on the OHL profile are typically characterized by small amplitudes and relatively high frequency (5 to 8 Hz), and these are followed by secondary arrivals with substantially larger (factor of 5 to 10 or more) amplitudes and lower frequency (2 to 4 Hz). In general, analysis of the weak first arrivals was possible only by

filtering and beamforming of signals. Figures 3 and 4 show examples of NORESS recordings of mantle *P*-waves, with phases designated by Pn_1, Pn_2 (first arrivals) and *P*1, *P*2 (later arrivals).

A number of shots detonated during the 1979 FENNOLORA project were recorded by the NORSAR array (Mereu *et al.*, 1983). These explosions usually had magnitudes less than 2.0 (International Seismological Centre, 1982). Three of the shots were located in the area where the FENNOLORA and OHL profiles crossed. Comparison of NORSAR *Pn* travel times for the FENNOLORA shots (C, D, and E in Fig. 1) (see Table 2 and Fig. 3 in Mereu *et al.*, 1983) showed that they were later than NORESS arrivals for the same distance range on the OHL profile.

To better understand this contradiction, we reanalyzed NORSAR recordings of shots C, D, and E. Mereu *et al.* showed that beams constructed for a group of NORSAR subarrays did not indicate a marked improvement in SNR over single-element traces because of lost coherency, and as result they analyzed filtered single-element signals. In contrast, we applied beamforming to each of seven NORSAR subarrays and constructed record sections consisting of filtered beams.

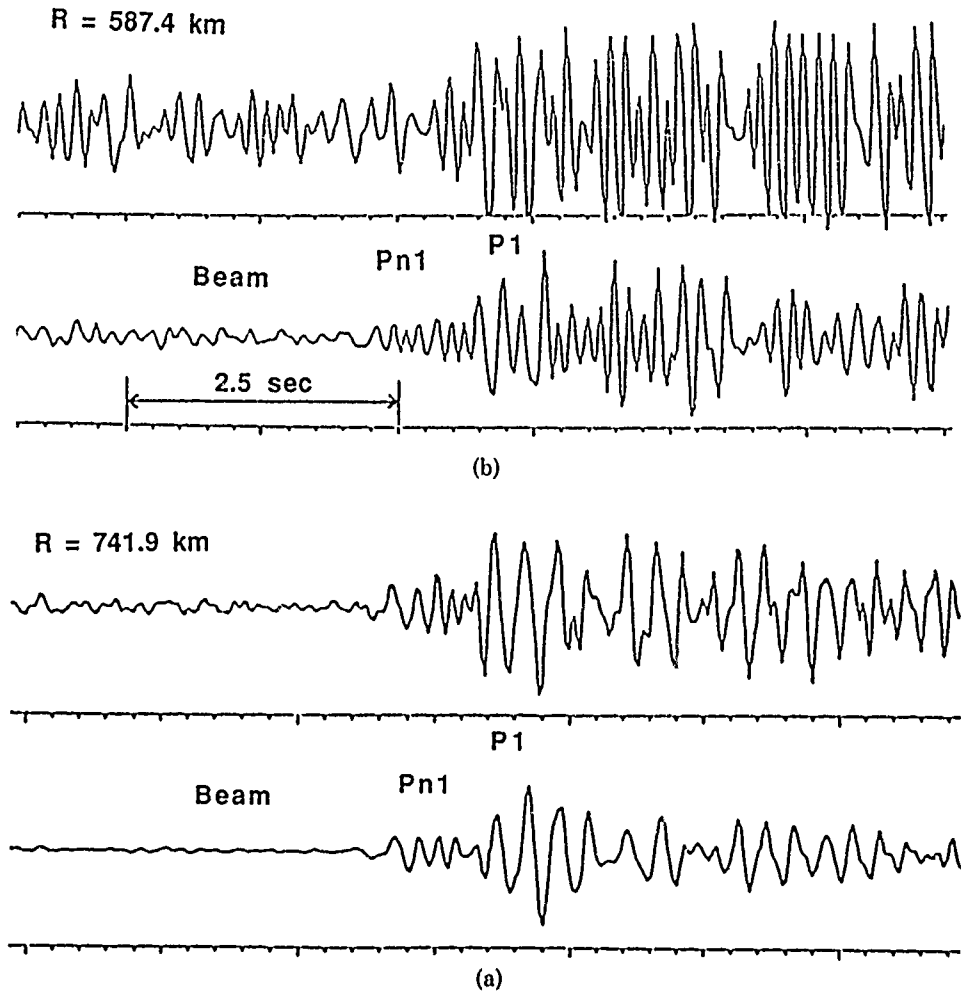

FIG. 3. NORESS recordings of mantle waves from two explosions (single sensor and array beam). (a) event 87274b, $M = 2.4$, filter: 3 to 12 Hz; (b) event 87147, $M = 2.9$, filter: 3 to 12 Hz. Two groups of mantle waves can be correlated in the first (Pn_1) and second (*P*1) arrivals. Pn_1 is usually characterized by smaller amplitudes and higher frequencies compared with later arrivals. The figure also illustrates signal-to-noise ratio improvement through beamforming.

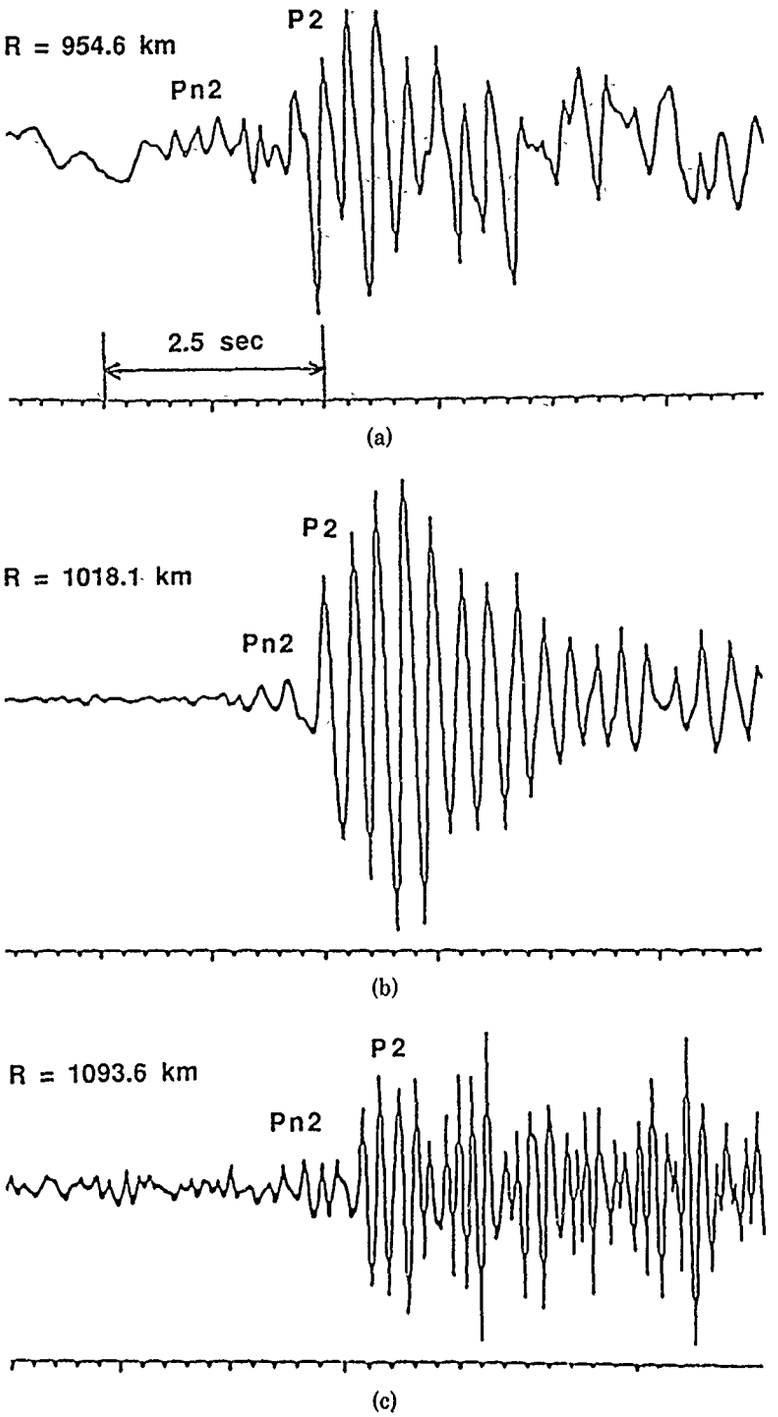

FIG. 4. NORESS recordings for: (a) event 86086 ($M = 3.5$, no filter); (b) event 86163 ($M = 3.7$, filter: 2 to 15 Hz); (c) event 87359 ($M = 3.0$, filter: 4 to 10 Hz). These records were obtained by applying beamforming. The distances are beyond the range where Pn_1 disappears and the first arrivals are delayed relative to an extension of the Pn_1 travel-time curve. Two groups of mantle waves can be correlated as first (Pn_2) and secondary (P2) arrivals.

Beaming even a small number of traces in this way improved SNR and made it possible to correlate weak first arrivals. Sometimes there was adequate SNR without beamforming, as illustrated by the single sensor (01B2) trace included in Figure 5 (406.3 km distance). The *Pn* first arrivals in Figure 5 are approximately 1.0 to 1.5

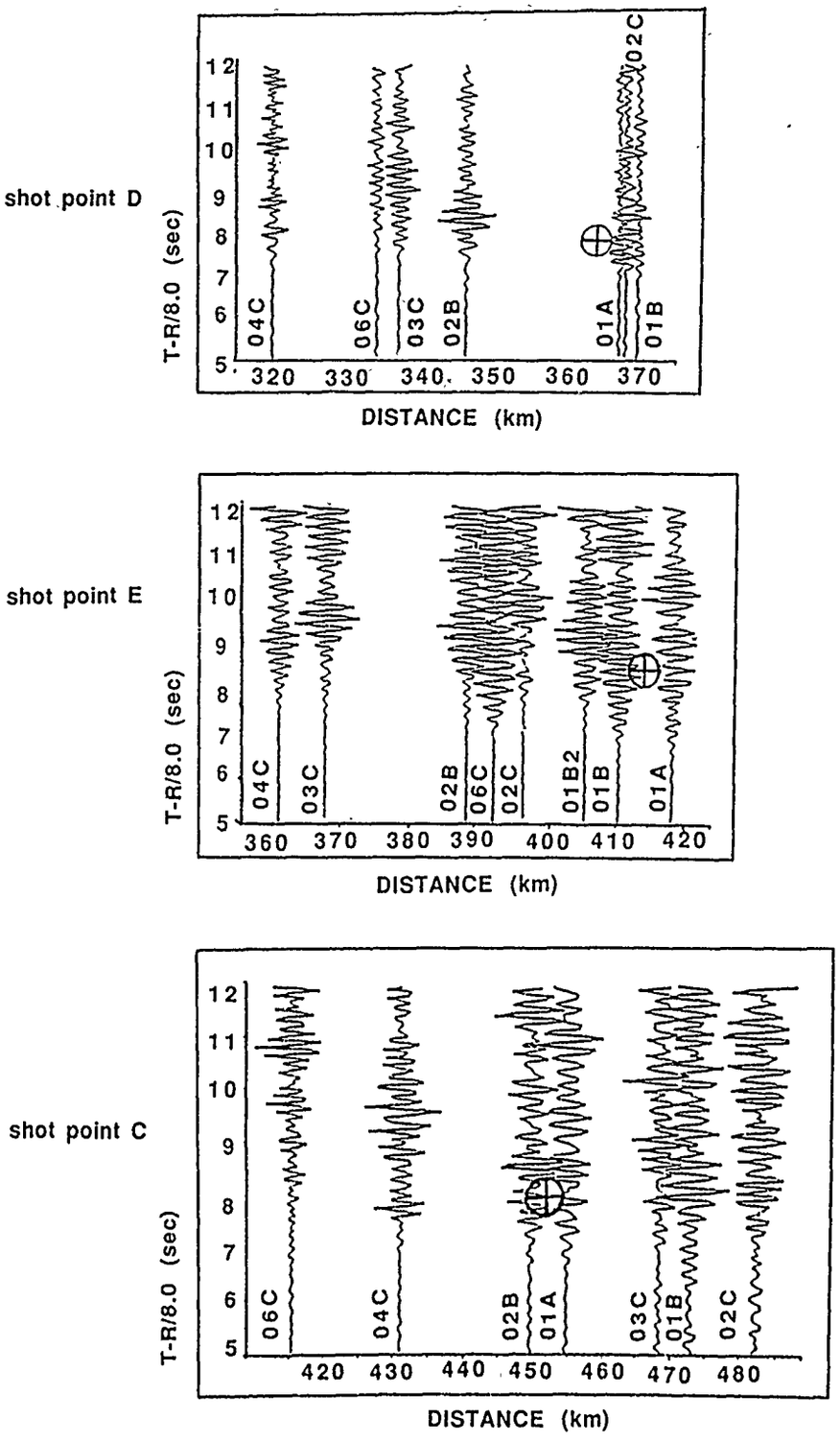

FIG. 5. Trace-normalized record sections from shot points D, E, and C (FENNOLORA experiment, 1979) recorded at the NORSAR array. The sections are arranged in order of increasing shot point distance and consist of filtered beams (filter: 2 to 10 Hz) constructed for each of seven subarrays of the NORSAR array. For shot point E we also included in the section the recording of the vertical sensor 01B2 (R = 406.3 km) because good signal-to-noise ratio was observed for this single sensor. Note the first *Pn* arrivals are approximately 1.0 to 1.5 sec earlier than data of Mereu *et al.* (1983) shown by circle with cross. Reduction velocity of the time axis is 8.0 km/sec.

sec earlier than those of the single-element records used by Mereu *et al.* We conclude that in analyzing single-element traces, one could mistakenly interpret larger secondary arrivals as primary arrivals, because the latter would be weak and buried in noise.

The same explanation may apply to a comparison of *Pn* travel times for the Swedish seismological network, for FENNOLORA explosions ($M_L < 2.0$) and regional earthquakes ($M_L \approx 3.0$ to 3.5) referred to zero focal depth. According to Bath (1981, Table 2) *Pn* travel times for earthquakes are consistently earlier (up to 1.0 to 1.4 sec for epicentral distance 1000 to 1400 km). This discrepancy can be explained by better SNR for the larger-magnitude earthquakes; the weak first arrivals from FENNOLORA explosions were probably buried in noise.

A record section was constructed for upper-mantle signals recorded by NORESS for the OHL profile, using short-period vertical traces (mainly beams) with good SNR, plotted at the appropriate epicentral distance (Fig. 6). The NORSAR subarray 06C beams for FENNOLORA shots C, D, and E were also plotted on the record section (NORESS is located within subarray 06C). All traces in Figure 6 were bandpass filtered.

Travel times for several of the explosions (including the FENNOLORA shots) were corrected to account for differences in crustal thickness (up to 50 to 55 km beneath shot points, compared with approximately 40 km beneath the NORESS array and most of the explosions on the OHL profile). For different shot points these corrections varied from −0.6 to −0.8 sec. Travel-time curves of *Pn* (Pn_1 and Pn_2) constructed for the OHL profile are shown in Figures 6 and 7. In both figures Pn_1 arrivals can be followed continuously to about 800 to 850 km, with average apparent velocity increasing with distance from 8.0 to 8.2, to 8.4 to 8.6 km/sec, approximately. Note that in the distance range 300 to 500 km the apparent velocity

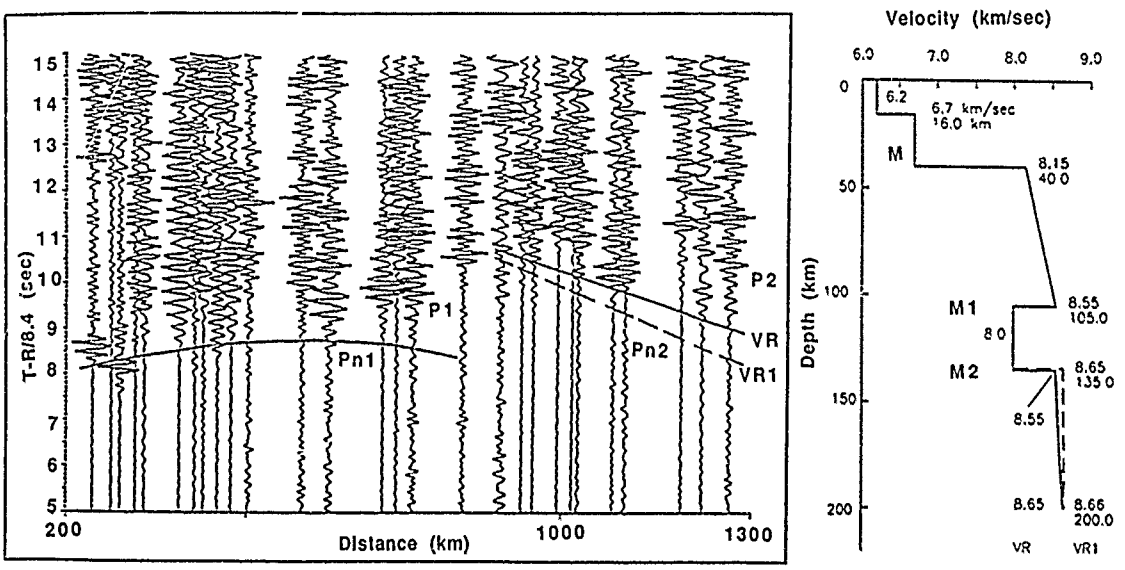

FIG. 6. Trace-normalized record section for the Oslo-Helsinki-Leningrad profile and theoretical travel-time curves of waves refracted in the upper mantle. Reduction velocity is 8.4 km/sec, and records are bandpass filtered between 3 and 10 Hz. Laterally homogeneous velocity models *VR* and *VR*1 used to calculate travel-time curves are shown to the right. Note the delayed travel time branch beyond 800 to 850 km for first arrivals. The intensive wave group *P*1 sharply attenuates at approximately the same distance range.

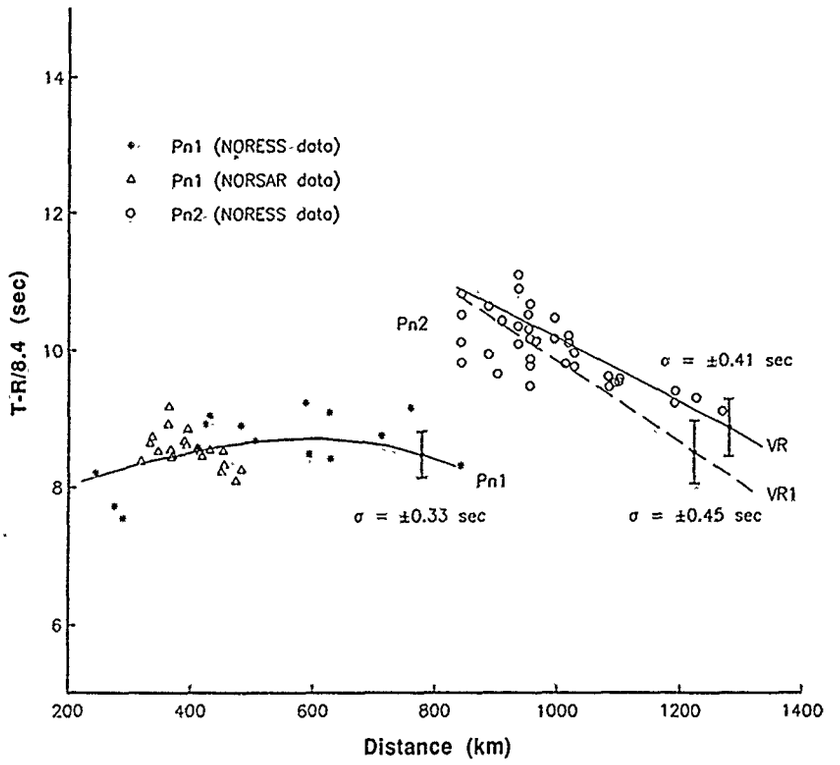

FIG. 7. Comparison of observed and theoretical travel times of *Pn* (Pn_1 and Pn_2) for the Oslo–Helsinki–Leningrad profile. Velocity models used in the calculations of the traveltime curves of waves refracted in the upper mantle are shown in Figure 6. Vertical bars are standard deviations of the observed travel times of Pn_1 and Pn_2 waves from the calculated travel times. Note the NORESS data shown by asterisks (Pn_1) and open circles (Pn_2), and NORSAR data (FENNOLORA explosions) shown by open triangles (Pn_1).

of Pn_1 is locally high, 8.5 to 8.6 km/sec. These observations are based mainly on NORSAR recordings of the FENNOLORA shots, for which the location and origin time of the events are accurately known. A second intensive arrival *P*1 is observed following Pn_1 over the same distance range (Fig. 6).

Beyond 800 to 850 km there is a shift of 2.0 to 2.5 sec in the travel-time curve, with Pn_1 and *P*1 dying out and a later phase Pn_2 appearing as the first arrival, followed by another intensive phase *P*2. The apparent velocity of Pn_2 is high, 8.6 to 8.8 km/sec. This break and shift of the *Pn* travel-time curve is similar to travel times observed for large industrial explosions recorded in adjoining areas of the East European platform (Vinnik and Ryaboy, 1981; Ryaboy *et al.*, 1987), but the 2-sec shift in that region was observed at smaller distance (550 to 650 km) in that study. On the FENNOLORA profile the *Pn* travel-time branch is delayed in the range 700 to 800 km, but the magnitude of this shift usually does not exceed 1.0 to 1.5 sec. If other *Pn* travel time shifts exist for the OHL profile at distances less than 700 to 800 km, they are not evident on the record section, and the magnitude of each shift has to be less than 0.5 to 1.0 sec.

Upper-Mantle Velocity Structure of the Southeastern Baltic Shield

Interpretation of the break and shift in the travel-time curve at 800 to 850 km is critical in interpreting *Pn* travel times for the OHL profile. Since we do not have

observations along reversed and overlapping profiles, we interpreted from the very beginning the travel-time curves and record section on the basis of a laterally homogeneous velocity model. In that case, the delayed travel-time branch could be explained by a low-velocity layer in the upper mantle.

Inversion of the travel-time curves to obtain a velocity section was accomplished by a ray tracing method. The theoretical travel-time curves and synthetic seismograms were calculated by the WKBJ method (Chapman *et al.*, 1988), using laterally homogeneous spherical earth models with the two-layered crustal velocity model used in processing data for the NORESS bulletin. In this modeling of first arrivals Pn_1 and Pn_2 are refracted waves traveling in two relatively high-velocity layers of

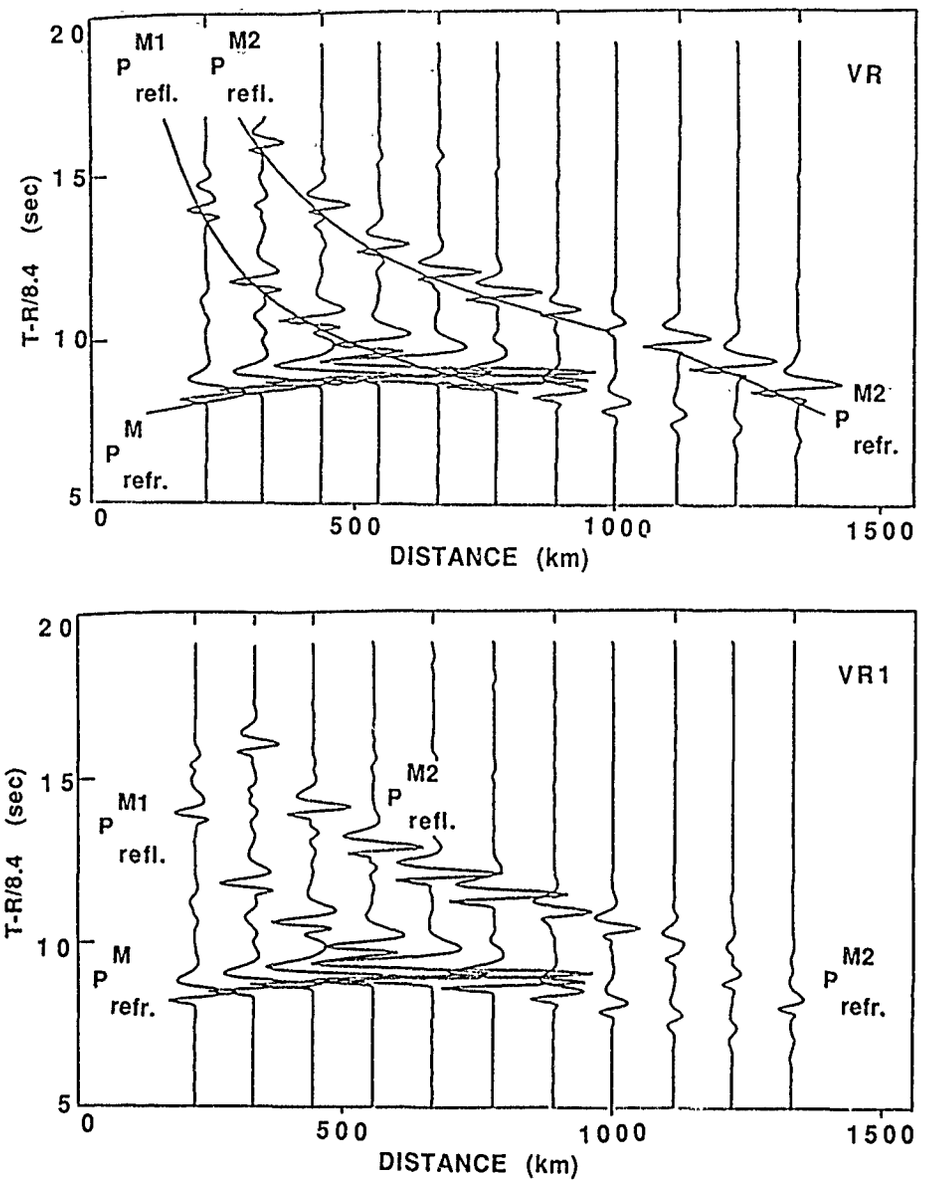

FIG. 8. Synthetic seismograms and travel-time curves of upper-mantle *P*-waves. Velocity models used in the calculations (*VR* and *VR*1) are shown in Figure 6. P^{M}_{refr} is a wave refracted in the upper layer of the mantle between boundaries M and M1, P^{M1}_{refl} is a wave reflected from boundary M1, P^{M2}_{refr} is a wave refracted in the upper mantle beneath boundary M2, P^{M2}_{refl} is a wave reflected from boundary M2. The amplitudes of the P^{M2}_{refr}-wave are significantly smaller for *VR*1 (*bottom*) than for *VR* (*top*), due to decreasing velocity gradient below boundary M2.

the upper mantle, separated by a low-velocity layer, which accounts for the travel-time delay beyond 800 to 850 km. The intensive waves $P1$ and $P2$ are probably reflected waves from the top of the low-velocity layer ($P1$) and boundaries below the base of this layer (P 2). Possible solutions of the problem were sought among the simplest velocity models, with the requirement that calculated and observed travel times agree to within ±0.5 sec. Figures 6 to 8 show the theoretical travel-

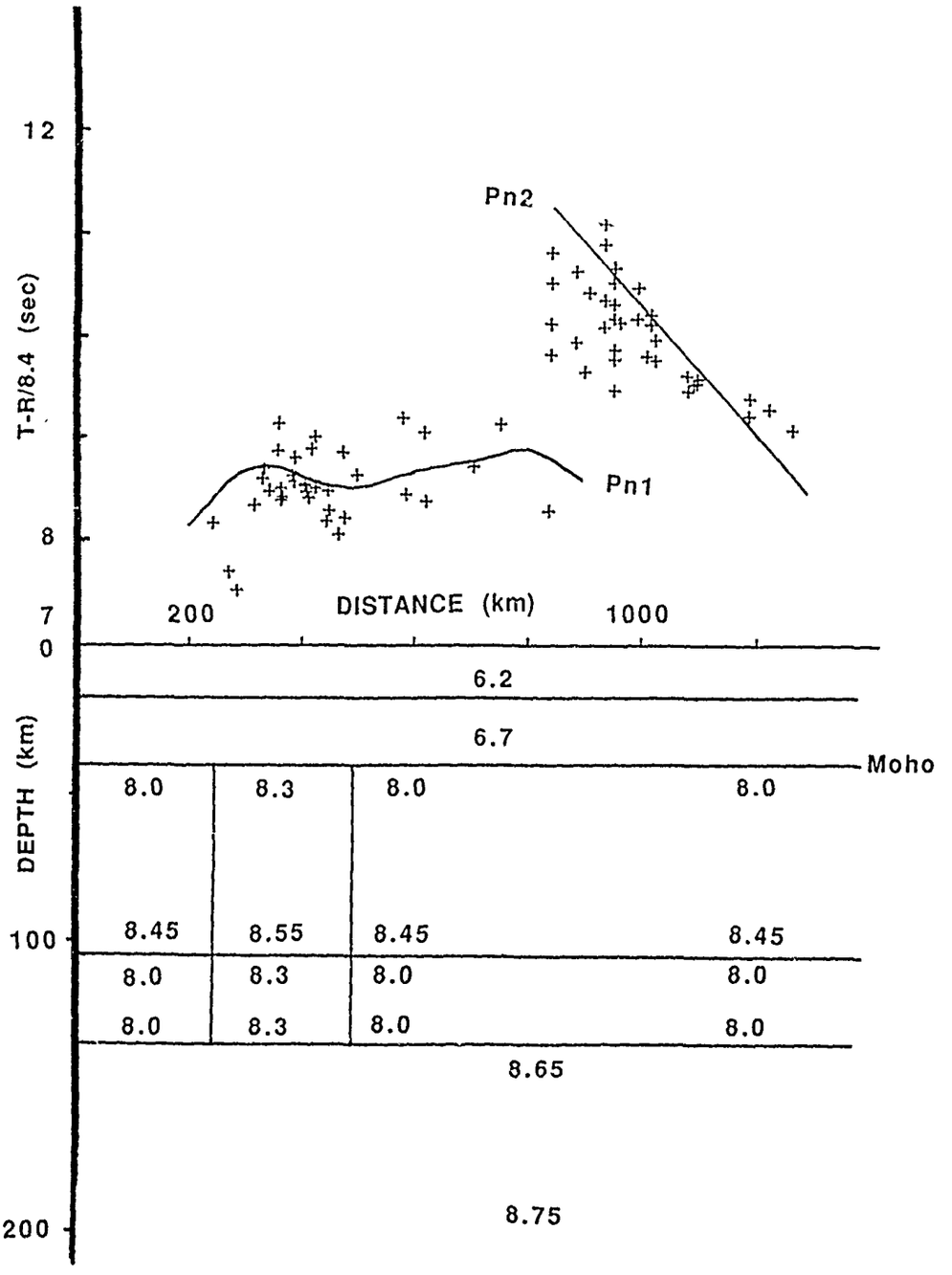

FIG. 9. (*Top*) comparison of observed and theoretical travel times of Pn (Pn_1 and Pn_2) for the Oslo-Helsinki-Leningrad profile. (*Bottom*) two-dimensional velocity model used in the calculations of the travel-time curves of waves refracted in the upper mantle.

time curves and synthetic seismograms calculated for velocity sections that best fit the data (*VR*, *VR*1).

The standard deviations of the observed Pn_1 and Pn_2 first arrivals from theoretical travel-time curves of waves refracted in the upper mantle layers are less than ±0.5 sec. Upper-mantle velocity models *VR* and *VR*1 are only representative of an aggregate of models consistent with the observed *P*-travel times. These velocity models give a comparable fit to travel times of Pn_1 and Pn_2, but model *VR*1 has a smaller velocity gradient below the bottom of the low-velocity layer and fits the small observed amplitudes of Pn_2 better than model *VR* (Fig. 8).

Note that on the basis of laterally homogeneous velocity models of the upper mantle we cannot explain locally increasing apparent velocity of Pn_1 in the distance range approximately 300 to 500 km (Fig. 7). One can assume that this anomaly of apparent velocity was generated by a high-velocity body in the upper mantle east of the NORESS and NORSAR arrays. We used a raytracing technique developed for laterally inhomogeneous media to estimate parameters of the high-velocity body and determine how our conclusion about a low-velocity layer at depths 105 to 135 km in the upper mantle, based on analysis of laterally homogeneous models, can be influenced by the high-velocity body.

The theoretical travel-time curves for two-dimensional velocity models were calculated on the basis of ray theory, using the program Ray84 of J. Leutgert (personal comm.) for a flat earth with spherical corrections. We analyzed the simplest laterally inhomogeneous models consisting of the velocity models *VR*, *VR*1 and a high velocity body in the upper mantle. Figure 9 compares observed and theoretical travel-time curves calculated for a two-dimensional model that fits the data. This velocity model belongs to an aggregate of similar velocity models, each of which fits the observed travel times. All these models include the high-velocity body and low-velocity layer in the upper mantle, but they are slightly distinguished by values of their parameters. We could not precisely estimate location of the high-velocity body in the upper mantle or its linear size and depth of penetration, for lack of observations along reversed and overlapping profiles. However, this interpretation can be checked by comparing the results of deep seismic studies with gravity data, and such a comparison is presented below.

Combined Seismic and Gravity Interpretation

The Baltic Shield is characterized by a relatively smooth gravity field, with variations of the Bouguer gravity anomalies from −(20 to 40) to +(20 to 40) mgal (Balling, 1984). A comparison of crustal thickness (Fig. 2) with Bouguer gravity map for Fennoscandia indicates that in western areas, beneath the Caledonian Mountains, a significant depression of the Moho up to depths of 40 to 45 km coincides with a very strong negative Bouguer anomaly (up to −80 to −100 mgal). At the same time, there are both small and extended zones of sharp crustal thickening up to 50 to 55 km beneath the Baltic Shield. One of these zones is crossed by the OHL profile in southern Sweden, and a second one is in an area adjacent to the profile in southern Finland. Such variations in crustal thickness *should* lead to strong negative gravity anomalies, −(100 to 150) mgal, but such anomalies are absent on the Bouguer gravity map. This suggests that the influence of crustal thickening on the gravity field is compensated by density variations in the crust and/or upper mantle.

To consider this problem further, we calculated the gravity influence of the crust along a profile from the North Sea to Leningrad, the central and eastern parts of

which coincide with the OHL profile, and the western part with the Flora–Asnes seismic profile (Sellevoll and Warrick, 1971). The North Sea–Leningrad line also crosses several deep seismic sounding profiles in southern Sweden (FENNOLORA), southern Norway, southern Finland, and northwestern U.S.S.R. (Dahlman *et al.*, 1971; Guggisberg *et al.*, 1984; Guggisberg and Berthelsen, 1987; Luosto *et al.*, 1984, 1985; Litvinenko and Platonenkova, 1978). Crustal thickness along the profile varies from about 30 to 40 km beneath the western part of profile to 45 to 55 km for the Baltic Shield, while the mean crustal velocity increases from approximately 6.4 to 6.5 to 6.65 to 6.70 km/sec. Thickening below the Baltic Shield is mainly in

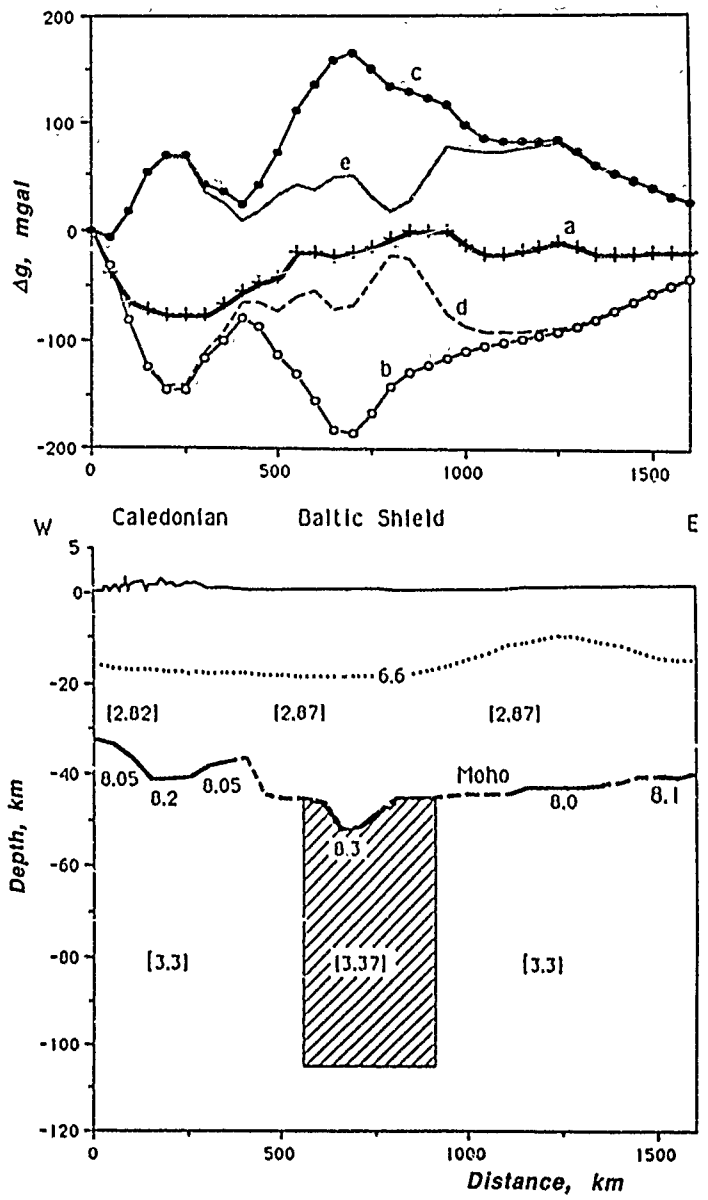

FIG. 10. Comparison of seismic and gravity data for the North Sea–Leningrad profile. (*Top*) gravity curves. (a) observed Bouguer gravity anomalies, (b) theoretical influence of the earth's crust, (c) difference between curves *a* and *b* (residual gravity anomalies); (d) theoretical influence of the crust and upper mantle; (e) difference between curves *a* and *d*. (*Bottom*) cross-section showing velocity and density. Dotted line, approximate location of 6.6 km/sec line in the earth's crust; numbers below Moho are *Pn* velocity (km/sec); numbers in brackets are average density (gm/cc); shaded area, high-velocity, high-density body in the upper mantle.

the lower crust (layers with velocities of 6.6 km/sec and more). One can see that increasing Moho depth in the central part of the profile up to 50 to 55 km accompanies an *increase* in the Bouguer gravity anomaly, from −(60 to 80) mgal to zero (Fig. 10). A similar correlation has also been observed for several other regions of Eurasia (Vol'vovskii *et al.*, 1962; Ryaboy, 1979; Bur'yanov *et al.*, 1983).

To calculate the gravity influence of the crust we estimated values of mean crustal density along the profile, based in turn on variations in mean crustal velocity from the seismic data and the velocity (V)-density (ρ) relationship, constructed as a result of statistical analysis of numerous laboratory measurements, $\rho = 0.60 + 0.34V$ (Krasovskii, 1979). Calculations show that the transition from the Caledonian Mountains to the Baltic Shield is accompanied by an increase in mean density of the earth's crust from 2.82 to 2.87 gm/cc. The average density of the upper mantle was assumed to be 3.3 gm/cc.

The gravity field constructed from the density model was calculated using a program of J. Leutgert (personal comm., 1989). The difference between observed Bouguer gravity and the theoretical anomaly due to the crust is more than 100 mgal in that part of the profile where Moho depths are 50 to 55 km (Fig. 10). Based on available seismic data, we cannot explain such large deviations by lateral variations in crustal structure. We conclude, therefore, that the discrepancy between observed and calculated gravity curves is caused mainly by lateral density variation in the upper mantle. A high-density body (density contrast of approximately +(0.05 to 0.07) gm/cc relative to the surrounding material) of linear extent 300 to 400 km is located within the mantle lid (or may penetrate deeper) east of the NORESS array. Such a two-dimensional density model fits the observed gravity within a precision of ±30 mgal. This amount of scatter can easily be explained by the influence of small-scale lateral density inhomogeneities in the crust and upper mantle along the profile.

Note that the high-density body was found in the upper mantle at approximately the same area of the OHL profile and at the same range of depth where the high-velocity body was located (Fig. 9). The interpretation of a high-velocity body in the upper mantle east of NORESS satisfies the observation of increased *Pn* velocity in southeastern Sweden, along both the OHL (NORSAR data in Fig. 7) and FENNOLORA (Guggisberg and Berthelsen, 1987) profiles, and it also agrees with observations of teleseismic data (Husebye *et al.*, 1986). Had we used some other velocity–density relationship in the interpretation, the parameters (linear dimension, thickness, density contrast) of the high-density body might have changed, but probably the main conclusion concerning the existence of such a body in the upper mantle would have remained unchanged.

Discussion and Conclusions

Analysis of record sections of mine blasts recorded by seismic arrays such as NORESS is an effective way to study upper mantle structure on long-range profiles, provided there is some local network control on the location and origin time of the explosions. This method is not a substitute for traditional detailed deep seismic profiling based on single-element recording of small chemical explosions, but the method is inexpensive and may be useful in mapping large-scale and pronounced velocity heterogeneities in the upper mantle. The main advantages of our method are that (1) beamforming of weak signals improves SNR, and (2) the mine explosions tend to be larger than chemical explosions usually used in seismic profiling. These

factors can be critical in identifying weak mantle waves recorded as first arrivals at far-regional distances.

A velocity section of the upper mantle was constructed for the OHL profile to depths of 200 km, based on interpretation of travel times and waveforms of the first arrivals. This section consists of two layers that have velocity increasing with depth, separated by a rather pronounced low-velocity layer in the depth range of approximately 105 to 135 km (Figs. 6 and 9). Other low-velocity layers (if they exist) must be thinner and cannot be reliably detected with the data on hand. Our combined interpretation of seismic and Bouguer gravity data for the OHL profile indicates that a high-velocity, high-density body probably exists below the Moho, in an area where the crust thickens to 50 to 55 km (Moho root) approximately 300 to 600 km east of NORESS. One might also hypothesize a high-density body in the upper mantle beneath southern Finland, where the crust thickens up to 50 to 55 km (Fig. 2).

Comparison of our results with other geophysical and geological data suggests that the low-velocity layer in the upper mantle approximately coincides with a frequency-dependent low-Q layer found by Der *et al.* (1986), with the top of a shear-wave low-velocity layer determined by Calcagnile (1982) and Nolet *et al.* (1986) on the basis of surface waves, and with a layer of reduced viscosity determined by Artyushkov (1979) from observations of post-glacial rebound. Deep geoelectrical studies carried out in various areas of the Baltic Shield (Jones, 1982; Kaikkonen *et al.*, 1983) and neighboring Russian plate (Vanyan *et al.*, 1977; Vanyan and Shilovskiy, 1983) generally show a gradual decrease in resistivity with depth. On the background of this decrease, a high-conductivity layer was detected in the upper mantle below Sweden and Finland at depths of about 100 to 200 km (Jones, 1982). The calculated thickness of this layer was about 40 km, and its depth varied beneath different geological units of the Baltic Shield. At the same time, the geothermal estimate of upper-mantle temperature under ancient platforms of Northern Eurasia is less than the solidus for upper-mantle material (Smirnov, 1970, 1980; Chermac, 1982; Milanovsky, 1984), and a petrological study of mantle xenoliths (Dobretsov, 1980; Luts, 1974) showed that beneath the Pre-Cambrian East European and Siberian platforms the upper mantle is crystalline.

The results discussed above can be qualitatively explained on the basis of a model of solid crystalline state of the lower lithosphere and asthenosphere beneath ancient platforms of Northern Eurasia (Ryaboy, 1985). Mantle rocks below the Baltic Shield from about 100 to 200 km depth probably have high subsolidus temperature (Milanovsky, 1984). According to theoretical results and data obtained in laboratories, the mantle rocks here are crystalline and have very specific physical and rheological properties. Namely, they can flow slowly, and are characterized by slightly decreased values (up to 3 to 5 per cent) of the velocity of P- and S-waves, electrical resistivity, and Q (Mizutani and Kanamori, 1964; Sato and Sacks, 1989; Sato *et al.*, 1989). These variations fit rather well with our results and those of previous geophysical studies of the upper mantle at 100 to 200 km depth below the Baltic Shield.

An interesting feature of the deep structure of the Baltic Shield in southeastern Sweden and southern Finland is the possible correlation of crustal thickening (to 50 to 55 km) with the presence of high-density, high-velocity bodies in the upper mantle. Comparison with surface geology indicates that this thickening occurs beneath Svecofennide units that were tectonically active over a long period during Proterozoic time, when numerous eruptions of felsic and mafic volcanic rocks

occurred in the area (Hain, 1977; Boyd *et al.*, 1985; Grigor'eva *et al.*, 1989). Major- and trace-element studies indicate that the batholiths observed in the upper crust consist of basic rocks that originated in the upper mantle as products of partial melting (Patchett *et al.*, 1981; Wilson *et al.*, 1985). Thus, the depressed Moho and deeper high-density bodies may represent residual roots of ancient Proterozoic volcanoes, with the deep high-velocity zones consisting of mantle rocks depleted of silicic constituents during the eruptive phase. This picture is similar to a high-velocity body postulated on the basis of teleseismic data in the upper mantle beneath the Silent Canyon caldera in southern Nevada, which Spence (1974) explained by extrusion of volatile magmatic components. Analogous structures have also been observed in the late Oligocene Questa caldera in north-central New Mexico (Lipman, 1983), and the late Proterozoic Salma caldera in the Arabian Shield (Kellogg, 1985).

We can hypothesize that similar high-density bodies should exist in the upper mantle of other ancient shields, particularly where crustal thickening has been observed in areas lacking pronounced negative gravity anomalies. Examples of such areas are the Ukrainian, Voronezh (Sollogub, 1986; Semov, 1987), and Canadian (Mooney and Braile, 1989) Shields. For example, thickening of the crust up to 50 km beneath Lake Superior (Canadian shield) is accompanied by a rather pronounced Bouguer gravity high (Gravity Anomaly Map Committee, 1987). A thin low-velocity layer was also found in the upper mantle of the Canadian Shield (Masse, 1973) at approximately the same depth range as under the OHL profile.

The lower-lithosphere/asthenosphere model presented here opens new possibilities for resolving geodynamic problems relative to the Baltic Shield. In the area of seismic verification of test ban treaties, the low-velocity zone together with high-velocity bodies in the upper mantle would significantly influence propagation of seismic signals recorded at far-regional and teleseismic distance ranges (McLaughlin *et al.*, 1989; Barker and Murphy, 1989). In particular, our velocity model of the upper mantle offers a possible explanation for observations by F. Ringdal and S. Mykkeltveit at the NORSAR and ARCESS seismic arrays, that the high-frequency content of regional seismic signals decreases abruptly at distances of 700 to 800 km (Loughran, 1986, 1988). An important goal of further investigations of deep structure of the Baltic shield will be to study lateral variations of the upper-mantle velocity model described in this article. With this aim the similar studies, as for OHL profile, will be reasonably to conduct for profiles connecting the NORESS, FINESA, ARCESS, and GERESS seismic arrays.

Acknowledgments

The author is grateful to Alan Ryall, Ken Olsen, Walter Mooney, and Jan Kutina for their constant helpfulness during this work and for their valuable criticism. Alan Ryall also made a very valuable contribution in editing the manuscript, and John Coyne helped with software and calculations used in this study. The manuscript was improved by critical comments from an anonymous reviewer. This research was supported by the Defense Advanced Research Projects Agency, under Contract MDA903-87-C-0037.

References

Artyushkov, Ye. V. (1979). Geodinamika (Geodynamics), Nauka, Moscow, 327 (in Russian).

Azbel, I. Ya., A. F. Buyanov, V. T. Ionkis, N. V. Sharov, and V. P. Sharova (1989). Crustal structure of the Kola peninsula from inversion of deep seismic sounding data, *Tectonophysics* **162**, 87–100.

Balling, N. (1984). Gravity and Isostacy in the Baltic Shield, in *First EGT Workshop: The Northern Segment*, European Science Foundation, Strasbourg, 53–68.

Barker, B. W. and J. R. Murphy (1989). A Lithospheric velocity anomaly beneath Shagan River test site. Part 1. Detection and location with network magnitude residuals, *Seism. Res. Lett.* **60**, 5.

Bath, M. (1981). Average crustal travel times in Sweden re-examined, *Pure Appl. Geophys.* **119**, 1116–1124.

Boyd, R., H. Papunen, A. Vorma, V. Zagorodny, and W. Robonen (1985). General Geological Map of the Baltic Shield (1:2 500 000 scale), *Geol. Surv. Finland, Bull.* **333**, 1.

Bungum, H., S. Pirhonen, and E. S. Husebye (1980). Crustal Thickness in Fennoscandia, *Geophys. J. R. Astr. Soc.* **63**, 759–774.

Bur'yanov, V. B., V. V. Gordienko, S. N. Kulik, and N. M. Loginov (1983). *Kompleksnoe Geofizicheskoye Izucheniye Tektonosfery Kontinentov* (*Complex Geophysical Study of the Tectonosphere of Continents*), Naukova Dumka, 76 (in Russian).

Calcagnile, G. (1982). The lithospher-astenospher system in Fennoscandia, *Tectonophysics* **90**, 19–35.

Chapman, C. H., Chu Jen-Yi, and D. G. Luness (1988). The WKBJ Seismogram Algorithm, in *Seismological Algorithms. Computational Methods and Computer Programs*, 47–74.

Chermac, V. (1982). Geothermal model of the lithosphere and chart of the thickness of the lithosphere in the territory of the USSR, *Izv. Akad. Nauk SSSR, Fizika Zemli* **1**, 25–38 (in Russian).

Dahlman, O., A. Vogel, C. E. Lund, R. Kanestrom, K. Haugland, and S. Gregersen (1971). The Trans-Scandinavian seismic profiles of 1969, in *Proc. Colloquium of Deep Seismic Sounding in Northern Europe*, Uppsala, December 1 and 2, 1969, 55–98.

Der, Z. A., A. C. Lees, and V. F. Cormier (1986). Frequency dependence of Q in the mantle underlying the shield areas of Eurasia. Part III. The Q Model, *Geophys. J. Astr. Soc.* **87**, 1103–1112.

Dobretsov, N. L. (1980). *Vvedenie v Global'nuyu Petrologiyu* (*Introduction to Globalpetrology*), Nauka, Moscow, 200 (in Russian).

Fluh, E. R. and A. Berthelsen (1986). Tectonic evaluation and crustal structure in Denmark, and southwest Sweden, in *Proc. Third Workshop on the European Geotraverse* (*EGT*) *Project*, 41–51.

Fuchs, K. (1986). Structure, physical properties and lateral heterogeneities of the subcrustal lithosphere from long-range deep seismic sounding observations on continents, *Tectonophysics* **56**, 1–15.

Fuchs, K., L. P. Vinnik, and C. Prodehl (1987). Exploring heterogeneities of the continental mantle by high resolution seismic experiments, in *Composition, Structure and Dynamics of the Lithosphere-Asthenosphere System. Geodynamics Series* **16**, 137–154.

Galdin, N. E., A. V. Egorkin, S. K. Zuganov, L. I. Kagalova, and N. M. Chernishov (1988). Deep Structure of the Earth's Crust Beneath the Kola Peninsula Along the MCWE-DSS Long-Range Profile Pechenga-Umbozero-Pulon'ga-Ruch'i, *Geotektonika* (*Geotectonics*) **4**, 30–44 (in Russian).

Given, J. W. and D. V. Helmberger (1980). Upper mantle structure of northwestern Eurasia, *J. Geophys. Res.* **85**, 7183–7196.

Glaznev, V. N., A. B. Raevsky, and N. V. Sharov (1989). A model of the deep structure of the northeastern part of the Baltic Shield based on joint interpretation of seismic, gravity, magnetic and heat flow data, *Tectonophysics* **162**, 151–164.

Gravity Anomaly Map Committee (1987). Gravity Anomaly Map of North America, Scale 1:5,000,000, The Geological Society of America.

Grigor'eva, L. V., V. V. Ivanikov, and N. F. Shinkarev (1989). Tectonic evolution of the Baltic Shield in Proterozoic, *Geotektonika* (*Geotectonics*) **1**, 37–47 (in Russian).

Guggisberg, B., J. Ansorge, and St. Mueller (1984). Structure of the upper mantle under southern Scandinavia from Fennolora data, in *Proc. First Workshop on the European Geotraverse* (*EGT*), The Northern Segment, 49–52.

Guggisberg, B. and A. Berthelsen (1987). A two-dimensional velocity model for the lithosphere beneath the Baltic Shield and its possible tectonic significance, *Terra Cognita* **7**, 631–638.

Hain, V. E. (1977). *Regional'naya Geotektonika* (*Regional Geotectonics*), Nedra, 359 (in Russian).

Herrin, E. and J. Taggart (1968). Regional variations in P travel times, *Bull. Seism. Soc. Am.* **58**, 1325–1337.

Huseby, E. S. and J. Hovland (1982). On upper mantle seismic heterogeneities beneath Fennoscandia, *Techonophysics* **90**, 1.

Huseby, E. S., J. Hovland, A. Christoffersson, K. Astrom, R. Slunga, and C. E. Lund (1986). Tomographical mapping of the lithosphere and asthenosphere beneath southern Scandinavia and adjacent areas, *Tectonophysics* **128i**, 229–250.

International Seismological Centre (1982). *Regional Catalogue of Earthquakes* (*July–December*, 1979), No. 16.

Jones, A. G. (1982). Observations of the electrical asthenosphere beneath Scandinavia, *Tectonophysics* **90**, 37–55.

Kaikkonen, P., L. L. Vanyan, S. E. Hjelt, A. P. Shilovsky, K. Pajunpää, and P. P. Shilovsky (1983). A preliminary geoelectrical model of the Karelian megablock of the Baltic Shield, *Phys. Earth Planet. Interiors* **32**, 301–305.

Kellogg, K. S. (1985). Root zone of the late Proterozoic Salma Caldera, northeastern Arabian Shield, Kingdom of Saudi Arabia, *J. Geophys. Res.* **90**, 11,253–11,262.

King, D. W. and G. Calcagnile (1976). *P*-wave velocities in the upper mantle beneath Fennoscandia and western Russia, *G. J. R. Astr. Soc.* **46**, 407–432.

Korhonen, H. and M. Porkka (1981). The structure of the Baltic Shield region on the basis of DSS and earthquake data, *Pure Appl. Geophys.* **119**, 1093–1099.

Krasovskii, S. S. (1979). On the relationship between seismic velocity and density of rocks of the earth crust and upper mantle, in *Gravitatsionnaia Model Zemnoi Kori i Verhnei Mantii* (*Gravity Pattern of the Earth Crust and Upper Mantle*), Naukova Dumka, 33–48 (in Russian).

Lipman, P. W. (1983). The Miocene Quest Caldera, northern New Mexico: relation to Batholith Emplacement and associated molybdenum mineralization, in *The Genesis of Rocky Mountain Ore Deposits: Changes with Time and Tectonics, Proc. Denver Region Exploration Geologists Society Symp.*, 133–148.

Litvinenko, I. V. and L. N. Platonenkova (1978). Structure of the earth crust and upper mantle in the eastern Baltic Shield, in *Stroenie Zemnoi Kori i Verhnei Mantii Tsentralnoi i Vostochnoi Evropi* (*Structure of the Earth Crust and Upper Mantle in the Central and Eastern Europe*), Naukova Dumka, 127–135 (in Russian).

Loughran, L. B. (Editor) (1986). NORSAR, Semiannual Technical Summary, 1 October 1985–31 March 1986, 93.

Loughran, L. B. (Editor) (1988). NORSAR, Semiannual Technical Summary, 1 October 1987–31 March 1988, 127.

Lund, C. E. (1979a). The fine structure of the lower lithosphere underneath the Blue Road profile in Northern Scandinavia, *Tectonophysics* **56**, 111–122.

Lund, C. E. (1979b). Crustal structure along the Blue Road profile in Northern Scandinavia, *Geol. Foren. Stockholm Forh.* **101**, 191–204.

Lund, C. E. (1980). Fennoscandian long-range project, 1979-Fennolora, in *Proc. 17th Assembly of the European Seismological Commission* **15**, 511–515.

Lund, C. E. and R. Slunga (1981). Crustal and upper-mantle structure of the Baltic Shield investigated by a combined interpretation of deep-seismic-sounding data and surface-wave analysis, *Pure Appl. Geophys.* **119**, 1100–1106.

Luosto, U., E. H. Flueh, C. E. Lund, and Working Group (1989). The crustal structure along the POLAR profile from seismic refraction investigations, *Tectonophysics* **162**, 51–86.

Luosto, U., H. Korhonen, I. P. Kosminskaya, S. M. Zverev, C. E. Lund, N. V. Sharov, E. Lanne, A. Tupperainen, V. M. Ilmola, and A. N. Foursov (1985). *First Results from the DSS Study on the Baltic Profile in SE Finland*, Institute of Seismology, University of Helsinki, 21.

Luosto, U., E. Lanne, H. Korhonen, A. Guterh, M. Grad, R. Materzok, and E. Perchuc (1984). Deep structure of the earth's crust on the SVEKA profile in central Finland, *Annales Geophysicae* **2**, 559–570.

Luts, B. G. (1974). *Petrologiya Glubinnyh zon Kontinental'noi kori i Verhnei Mantii* (*Petrology of Deep Continental Crust and Upper Mantle*), Nauka, Moscow, 304 (in Russian).

Masse, R. P. (1973). Compressional velocity distribution beneath central and eastern North America, *Bull. Seism. Soc. Am.* **63**, 911–935.

Masse, R. P. and S. S. Alexander (1974). Compressional velocity distribution beneath Scandinavia and western Russia, *Geophys. J. R. Astr. Soc.* **39**, 587–602.

McLaughlin, K. L., J. R. Murphy, and B. W. Barker (1989). A lithospheric velocity anomaly beneath Shagan River test site. Part 2. Imaging and inversion with amplitude transmission tomography, *Seism. Res. Lett.* **60**, 5.

Meissner, R., T. H. Wever, and E. R. Fluh (1987). The Moho in Europe: Implications for crustal development, *Annales Geophysicae* **5B**, 357–364.

Mereu, R. F., S. Mykkeltveit, and E. S. Husebye (1983). Fennolora recordings at NORSAR, *J. Geophys.* **52**, 119–130.

Milanovsky, S. Yu. (1984). Deep Geothermal Structure and Mantle heat Flow Along the Barents Sea–East Alps Geotraverse, *Tectonophysics* **103**, 175–192.

Mizutani, H. and H. Kanamori (1964). Variation of elastic wave velocity and attenuative property near the melting temperature, *J. Physics Earth* **12**, 43–49.

Mooney, W. D. and L. W. Braile (1989). The seismic structure of the continental crust and upper mantle

of North America, in *The Geology of North America* **A**, 39–52.

Mueller, St. and J. Ansorge (1986). Long-Range Seismic Refraction Profiles in Europe, in *Reflection Seismology: A Global Perspective. Geodynamics Series.* **13**, AGU, Washington, 167–182.

Mykkeltveit, S. (1980). A seismic profile in southern Norway, *Pure Appl. Geophysics, Pageoph3 118*, 1310–1325.

Nersesov, I. L. and T. G. Rautian (1964). Kinematics and dynamics of seismic waves to distances of 3,500 km from the epicenter, in *Eksperimental'naia Seismika* (*Experimental Seismology*), Nauka, 63–87 (in Russian).

Nolet, G., B. Dost, and H. Paulssen (1986). Preliminary results from the EGT's NARS project, in *Proc. Third Workshop on the European Geotraverse* (*EDT*) *Project*, European Science Foundation, 223–226.

Patchett, P. J., O. Kouvo, C. E. Hedge, and M. Tatsumoto (1981). Evolution of continental crust and mantle heterogeneity: evidence from Hf isotopes, *Contrib. Mineral. Petrol.* **78**, 279–297.

Prodehl, C. (1984). Structure of the earth's crust and upper mantle, *Landdt-Bornstein New Series* **V2**, 97–206.

Prodehl, C. and V. Kaminski (1984). Crustal Structure Under the Fennolora Profile, in *Proc. First Workshop on the European Geotraverse* (*EGT*), *The Northern Segment*, European Science Foundation, 43–68.

Ryaboy, V. Z. (1966). Kinematic and dynamic characteristics of deep waves associated with boundaries in the crust and upper mantle, *Izv. Acad. Sci. USSR, Geophys. Ser., AGU Transl.* **3**, 177–184.

Ryaboy, V. Z. (1979). *Struktura Verkhney Mantii Territorii SSR po Seismicheskim Dannym* (*The Upper Mantle Structure of the Territory of the USSR according to Seismic Data*), Nedra, 245 (in Russian).

Ryaboy, V. Z. (1985). Lower lithosphere and asthenosphere of central and eastern regions of northern Eurasia based on seismic data, *Izv. Acad. Sci. USSR, Physics of the Solid Earth* (*English edition*) **21**, 100–110.

Ryaboy, V. Z. (1989). *Upper Mantle Structure Studies by Explosion Seismology in the USSR*, DELPHIC Associates, 154.

Ryaboy, V. Z., Ju. A. Burmakov, L. N. Nikitini, and S. V. Poptap'ev (1987). The main features of the upper mantle velocity structure, in *Glubinnoe Stroenie Slaboseismichnih Regionov SSSR* (*Deep Structure of the Nonseismic Regions of the USSR Territory*), Nauka, Moscow, 86–116 (in Russian).

Sato, H. and I. S. Sacks (1989). Anelasticity and thermal structure of the oceanic upper mantle: Temperature calibration with heat flow data, *J. Geophys. Res.* **94**, 5705–5715.

Sato, H., I. S. Sacks, and T. Murase (1989). The use of laboratory velocity data for estimating temperature and partial melt fraction in the low-velocity zone: comparison with heat flow and electrical conductivity studies, *J. Geophys. Res.* **94**, 5689–5704.

Sellevoll, M. A. (1973). Mohorovicic discontinuity beneath Fennoscandia and adjacent parts, *Tectonophysics* **20**, 359–366.

Sellevoll, M. A. and R. E. Warrick (1971). A refraction study of the crustal structure in southern Norway, *Bull. Seism. Soc. Am.* **61**, 457–471.

Semov, V. N. (1987). Some regularities of structure and morfology of the Moho discontinuity, in *Glubinnoe Stroenie Slaboseismichnih Regionov SSR* (*Deep Structure of the Nonseismic Regions of the USSR Territory*), Nauka, Moscow, 71–80 (in Russian).

Smirnov, Ya. B. (1970). Values of Geothermal Research for Studying the Earth's Crust and Upper Mantle, in *Problemy Stroyeniya Zemnoy Kory i Verkhnei Mantii* (*Problems of the Structure of the Earth's Crust and Upper Mantle*), Nauka, Moscow, 250–265 (in Russian).

Smirnov, Ya. B. (1980). *Teplovoye Pole Territorii SSR* (*Heat Field in the Territory of the USSR*) GUGK, 150 (in Russian).

Sollogub, V. B. (1986). *Litosfera Ukrainy* (*Lithosphere of the Ukraine*), Naukova Dumka, 183 (in Russian).

Spence, W. (1974). *P*-wave residual differences and inferences on an upper mantle source for the Silent Canyon Volcanic Centre, southern Great Basin, Nevada, *Geophys. J. Astr. Soc.* **38**, 505–523.

Stangl, R., K. Fuchs, and C. Prodehl (1986). The structure of the upper mantle below Scandinavia: an interpretation of the travel time and amplitude data with the aid of the reflectivity method, *Teilproject* **B1**, 683–507.

Vanyan, L. L., M. N. Berdichevsky, E. B. Fainberg, and M. V. Fiskin (1977). The study of the asthenosphere of the East European Platform by electronmagnetic sounding, *Phys. Earth Planet. Interiors* **14**, P1–P2.

Vanyan, L. L. and P. P. Shilovsky (1983). *Glubinnaya Elektroprovodnost' Okeanov i Kontinentov* (*Depth Electroconductivity of the Oceans and Continents*), Nauka, Moscow, 86 (in Russian).

Vinnik, L. P. and V. Z. Ryaboy (1981). Deep structure of the East European Platform according to seismic data, *Phys. Earth Planet. Interiors* **25**, 27–37.

Vol'vovskii, I. S., V. Z. Ryaboy, and V. I. Shraibman (1962). On nature of regional gravity anomalies of Buhar-Hiva region and adjacent areas, *Izv. Acad. Sci. USSR, Geophysical Series* **5**, 644–651 (in Russian).

Weinrebe, W. (1981). Joint interpretation of earthquake travel-time residuals and seismic measurements along the 'Blue Norma' Profile in northern Scandinavia, *Pure Appl. Geophys.* **119**, 1107–1115.

Wilson, M. R., P. J. Hamilton, and A. E. Fallick (1985). Granites and early proterozoic crustal evolution in Sweden: evidence from Sm-Nd, U-Pb and O isotope systematics, *Earth Plan. Sci. Lett.* **72**, 376–388.

CENTER FOR SEISMIC STUDIES
1300 NORTH 17TH STREET
ARLINGTON, VIRGINIA 22209-3871

Manuscript received 1 February 1990

Bulletin of the Seismological Society of America, Vol. 80, No. 6, pp. 2214–2226, December 1990

SURFACE TOPOGRAPHIC EFFECTS AT ARRAYS AND THREE-COMPONENT STATIONS

BY E. ØDEGAARD, D. J. DOORNBOS, AND T. KVÆRNA

ABSTRACT

A unified method of slowness analysis has been applied to the NORESS and ARCESS arrays and to the three-component stations within these arrays, with the following results: (1) there is a relatively large scatter in the three-component solutions for events from the same source region, and (2) there are significant differences between the solutions at the different three-component stations. Evidence is presented that a uniform half-space model is inadequate to derive slowness solutions from three-component data: layering of the crust and upper mantle affect the surface response at long periods, and surface topography and near-surface structure perturb the surface particle motion and slowness solutions especially at short periods. Topographic effects are evaluated by means of numerical simulations based on a newly developed multiple scattering method. The theoretical results explain up to about half of the observed anomalies in the three-component solutions. On the other hand, the array solutions based on vertical-component phase delays are relatively stable, since the nongeometrical phase perturbations are negligible.

INTRODUCTION

In recent years, several new small-aperture (~3 km) arrays and three-component stations have been installed. The arrays are designed such that standard array processing, such as beamforming, provides a favorable signal-to-noise ratio enhancement in the frequency range up to a few Hertz and enhanced event detection (e.g., Mykkeltveit *et al.*, 1983; Kværna, 1989). Another purpose of routine array operation is to locate the events. Event locations can also be obtained from single site three-component records, and it is natural to compare the relative performance of arrays and three-component stations in this respect. It is particularly opportune to do such a comparison in Norway, where there are now in operation two small-aperture arrays of identical design, NORESS and ARCESS, each having within their structure 4 three-component stations. For a description of these two arrays, see Mykkeltveit *et al.* (1990).

Two other aspects should be considered in such an experiment: the data from the arrays and three-component stations should be subjected to a unified processing procedure, and the data base should consist of seismic phases from several events in the same source region so that the stability of the results can be evaluated. In this paper, we apply a unified method of slowness analysis to array and three-component data from a number of selected source regions. Evidence will be presented that local structure influences, in particular, the results from three-component data, and we investigate in some detail the effect of surface topography. Elastic wave scattering by surface topography has been discussed by several workers, mainly in connection with studies of seismic risk, but there are very few examples of a full three-dimensional treatment of the problem (e.g., Mosessian and Dravinski, 1989), presumably because the applicable (numerical) methods tend to be complicated and expensive. We introduce an approximation in the form of a perturbation series for surface particle displacement, and solve the terms in a recursive manner.

The method is used here to help understand the source of observed slowness anomalies especially from three-component data.

Slowness Analysis

A unified approach to slowness analysis with arrays and three-component stations is possible by expressing solutions in terms of a covariance matrix **C** (e.g., Esmersoy *et al.*, 1985). Here, we introduce **C** as a function of slowness **s** by phase shifting the signals:

$$C_{nm}(\mathbf{s}) = \int F_n(\omega, \mathbf{s}) F_m^*(\omega, \mathbf{s}) \frac{d\omega}{2\pi} \tag{1}$$

where

$$F_n(\omega, \mathbf{s}) = F_n(\omega) \exp(i\omega \mathbf{s} \cdot \mathbf{x}_n)$$

and $F_n(\omega)$ is the Fourier spectrum at channel n. Using **C** of equation (1), the generalization of conventional beamforming is given by the normalized response

$$P(\mathbf{s}) = \mathbf{g}^\dagger \mathbf{C} \mathbf{g} / \{ |\mathbf{g}|^2 \mathrm{tr}\ \mathbf{C} \} \tag{2}$$

where **g** is the predicted displacement vector for slowness **s**. The generalization (2) can be interpreted as a matched filter since the response P depends on our choice of matching the covariance matrix **C**:

$$\mathbf{g}^\dagger \mathbf{C} \mathbf{g} = \mathrm{tr}(\mathbf{C}\mathbf{G}) \quad \text{with} \quad \mathbf{G} = \mathbf{g}\mathbf{g}^\dagger. \tag{3}$$

Thus, for a single component array: $\mathbf{g}^\dagger = (1, \ldots, 1)$. For a three-component sensor: $\mathbf{g}^\dagger = (g_x, g_y, g_z)$ = displacement vector, and equation (2) reduces to the polarization state detector of Samson (1977). For a three-component array: $\mathbf{g}^T = (\mathbf{g}_1{}^T, \ldots, \mathbf{g}_N{}^T)$ with $\mathbf{g}_n{}^T = (g_{nx}, g_{ny}, g_{nz})$ = displacement vector at site n. The displacement vector is a function of slowness **s**, and the surface interaction must be taken into account. On this account, we may expect three-component slowness solutions to be relatively sensitive to the choice of near-surface model. The model commonly used for the conversion between slowness and surface displacement is that of a uniform half-space bounded by a plane surface.

A slowness solution is usually identified with a maximum of $P(\mathbf{s})$. A common alternative for three-component data is to identify the solution for displacement **g** with the major principal axis of **C** (e.g., Jurkevics, 1988). The relation with beamforming can be seen by rewriting equation (2) in the principal axes system of **C**. Writing $\mathbf{g}/|\mathbf{g}| = \mathbf{V}\mathbf{p}$ where **V** is the eigenvector matrix of **C**, equation (2) becomes

$$P = \sum_{i=1}^{3} \lambda_i p_i^2 \Big/ \sum_{i=1}^{3} \lambda_i \tag{4}$$

where p_i are the components of **p**, and λ_i are the eigenvalues of **C**. Clearly, the maximum of P occurs at $\mathbf{p}^T = (1, 0, 0)$, assuming λ_1 is the largest eigenvalue; hence, $\mathbf{g}/|\mathbf{g}|$ equals $\mathbf{v}_1$ which is the major principal axis of **C**.

It is possible to extend the procedure to a generalization of optimum beamforming. For example, the normalized response with the maximum-likelihood method is

$$P'(\mathbf{s}) = \{\mathbf{g}^{\dagger}\mathbf{C}^{-1}\mathbf{g}\}^{-1}|\,\mathbf{g}\,|^2/\mathrm{tr}\;\mathbf{C}, \tag{5}$$

which for an array reduces to the "high-resolution" method of frequency-wavenumber spectrum analysis of Capon (1969), and for a three-component sensor to the maximum-likelihood estimator of Christoffersson *et al.* (1988). Although equation (5) leads to solutions with apparently higher resolutions, the solutions are less stable, and for location purposes, stability is more important (Kværna and Doornbos, 1986). Hence, we will proceed with the analysis based on equation (2).

Analyses of *P* from Selected Source Regions

Regional P *from Events Near Leningrad*

Figure 1 shows a typical record at NORESS from a mining explosion near Leningrad. Four such events from the same location were recorded with good signal-to-noise ratio (Table 1), thus providing a suitable data base for comparing array and three-component slowness solutions. Our study here will be restricted to the *P* wave. Figure 2 summarizes both the array slowness solutions and the three-component solutions for four stations within NORESS, using the spectral bandwidth of 2 to 4 Hz. Standard error bars indicate the scatter of solutions for the four events. Error bars of three-component solutions are given for only one station, but the scatter for the other stations is similar. The theoretical results included in Figure 2 will be discussed later. The three-component slownesses show a relatively large scatter, both of solutions at different stations for the same event and of

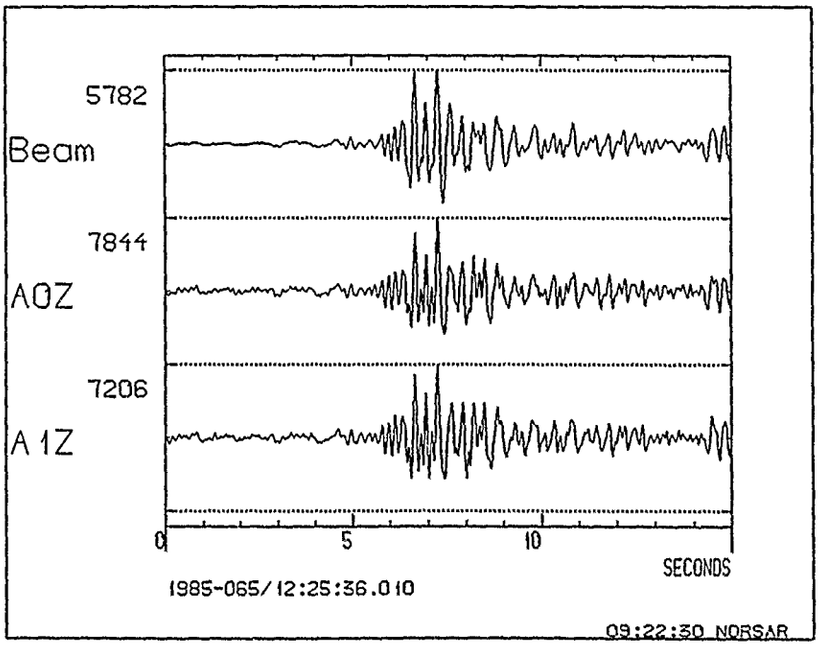

FIG. 1. Typical NORESS array beam and two single station vertical-component records from event in Leningrad region. Scaling factors of different traces are shown to the left.

TABLE 1

EVENTS NEAR LENINGRAD

Origin Time	Latitude (°E)	Longitude (°N)	*Mc*	SNR(*Z*)	SNR(*R*)
1985-031:12.30.53	59.3	28.1	2.9	12.3	5.6
1985-065:12.23.39	59.3	28.1	3.1	23.0	13.2
1985-066:12.04.14	59.3	28.1	2.9	16.0	8.8
1985-136:11.28.55	59.3	28.1	2.9	9.2	4.7

Origin times, epicenters, and duration magnitudes (M_C) are given by the *Seismic Bulletin of the University of Helskini*, signal-to-noise ratios for the vertical and radial components are computed in the 2 to 4 Hz band using the center element *A*0 of the NORESS array.

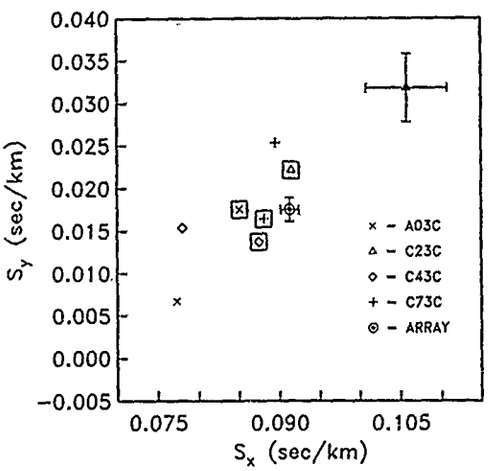

FIG. 2. Slowness solutions at NORESS. Average over *P* from four events near Leningrad. Array solution (ARRAY) with standard error bars. Three-component solutions at the indicated sites, with standard error bars for site C2. Theoretical solutions, including response to surface topograpy, are framed.

solutions for different events at the same station. To explain the differences between different stations, we hypothesize local site effects. To explain the scatter of solutions at a single station, we hypothesize that difference in slowness solutions for signals from events in the same source region are related to differences in the signal spectra.

Teleseismic P *from Events in Eastern Kazakh*

Teleseismic *P* waves from 19 nuclear explosions in Eastern Kazakh have been recorded, 14 of these at NORESS, and 9 of the more recent events have also been recorded at ARCESS (Table 2). The *P*-wave spectra from all events are similar at NORESS, but at ARCESS we can distinguish two groups, with 4 and 5 events. The spectra within a group are similar, but there is a systematic difference between the two groups. Representative spectra at NORESS and for the two groups at ARCESS are shown in Figure 3. The source of the spectral difference requires further investigation, but at this stage we analyze the two groups separately. Average slowness solutions for all events at NORESS are summarized in Figure 4, and for the two groups of events at ARCESS in Figure 5. The spectral bandwidth used was 0.9 to 4.0 Hz. There is a slight difference between the array slowness solutions for the two groups at ARCESS, but there is a large difference between the

TABLE 2

EVENTS IN EASTERN KAZAKH

Origin Time	Latitude (°E)	Longitude (°N)	M_b	Array*
1984-337:03.19.06.3	49.993	79.072	5.8	NRS
1984-351:03.55.02.7	49.957	78.862	6.1	NRS
1985-041:03.27.07.6	49.877	78.816	5.9	NRS
1985-181:02.39.02.7	49.861	78.696	6.0	NRS
1985-201:00.53.14.5	49.951	78.829	5.9	NRS
1987-071:01.57.17.3	49.932	78.785	5.4	NRS
1987-107:01:03.04.7	49.851	78.690	6.0	NRS
1987-214:00.58.06.7	49.841	78.886	5.9	NRS
1987-319:03.31.06.7	49.872	78.795	6.0	ARC-A
1987-347:03.21.04.7	49.955	78.852	6.1	NRS, ARC-B
1987-361:03.05.04.7	49.831	78.744	6.1	ARC-A
1988-044:03.05.05.9	49.922	78.904	6.0	NRS, ARC-B
1988-094:01.33.05.7	49.884	78.965	5.9	NRS, ARC-B
1988-125:00.57.06.8	49.916	78.725	6.2	ARC-B
1988-166:02.27.06.4	50.022	78.986	4.9	NRS
1988-258:03.59.57.4	49.821	78.796	6.1	NRS, ARC-A
1988-317:03.30.03.8	50.056	78.991	5.2	NRS
1989-022:03.57.06.1	49.924	78.831	6.1	ARC-B
1989-043:04.15.06.8	49.925	78.740	5.9	ARC-A

* Indicates recording at NORESS (NRS) and/or ARCESS (ARC). ARCESS recordings are divided in two groups: ARC-A and ARC-B.

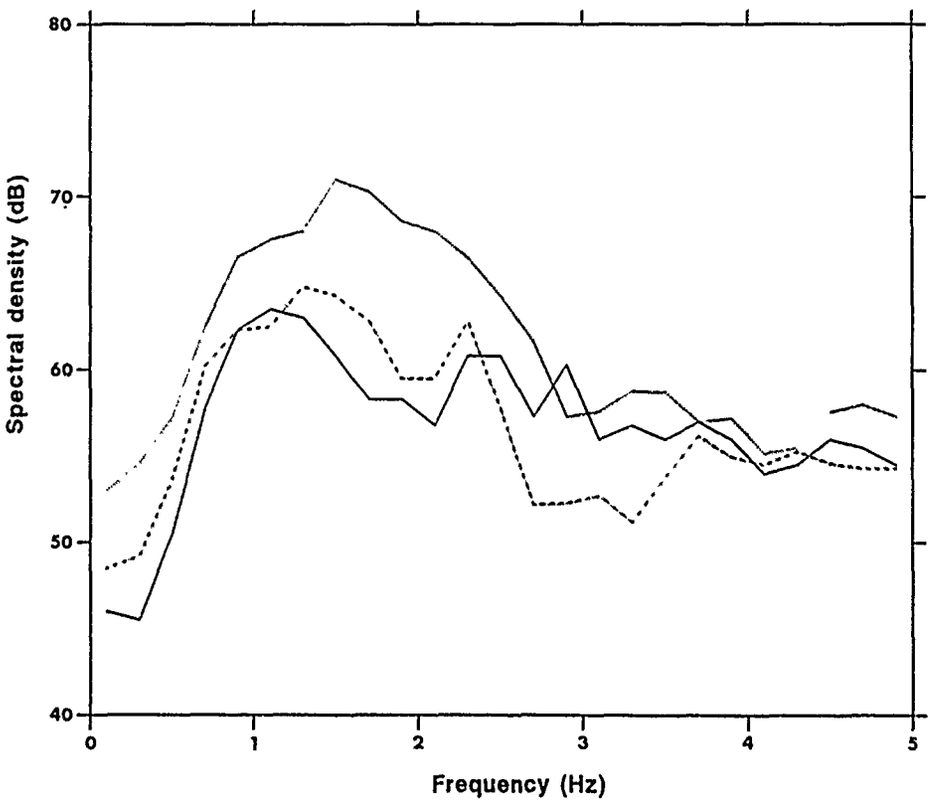

FIG. 3. Averaged *P*-wave signal spectra from nuclear explostions in Kazakh. Dotted line = at NORESS; dashed line = group A at ARCESS (high-frequency signals), and solid line = group B at ARCESS (low-frequency signals).

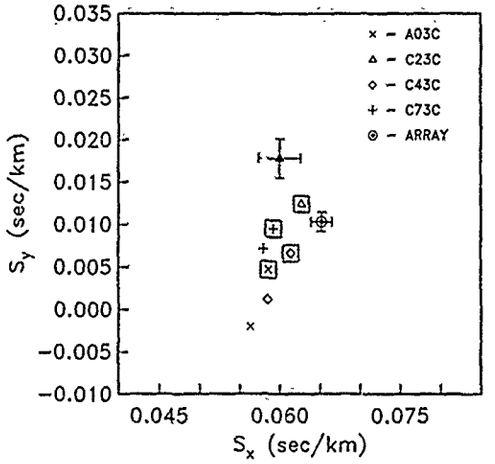

FIG. 4. Slowness solutions at NORESS. Average over P from 14 events in Kazakh. Details as in Figure 2.

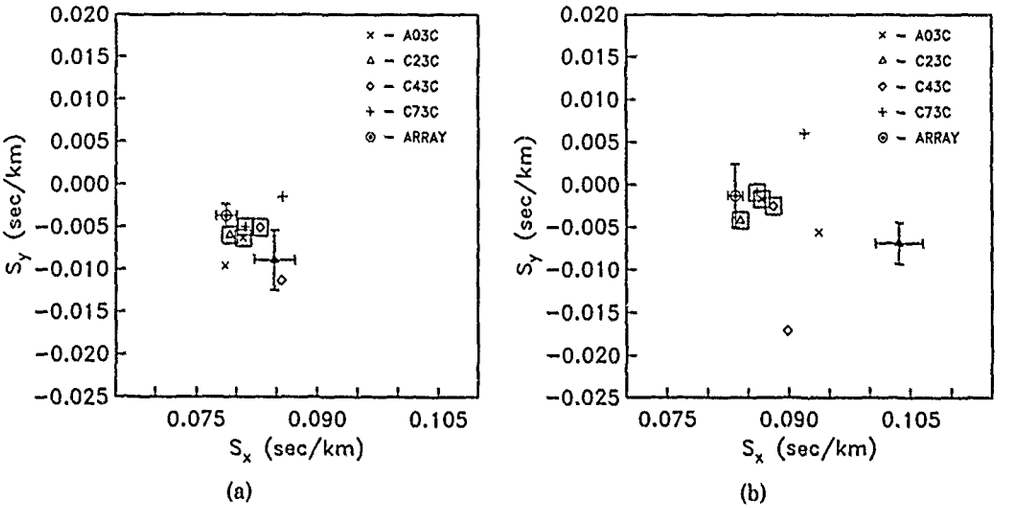

FIG. 5. Slowness solutions at ARCESS. Details as in Figure 2. (a) Average over four events (group A) in Kazakh. (b) Average over five events (group B) in Kazakh.

three-component solutions for the two groups. This result is consistent with the earlier hypothesis that three-component slowness solutions may be frequency-dependent.

Broadband P *from Event in Hindu Kush*

The predicted displacement vector, **g**, corresponding with a slowness, **s**, in equation (2), would be independent of frequency if the uniform half-space model used to convert **s** to **g** is valid. Observations show that this is usually not the case, not even for longer period P waves. Figure 6 shows the result of an analysis of three-component records from the broadband station in NORESS. The record (Fig. 6a) gives the three components of the P wave from an event in the Hindu Kush in three period ranges: long-period (LP), intermediate-period (IP), and short-period (SP). The slowness solutions, in the form of apparent velocity and azimuth as a function of frequency (Fig. 6b), show significant dispersion violating the

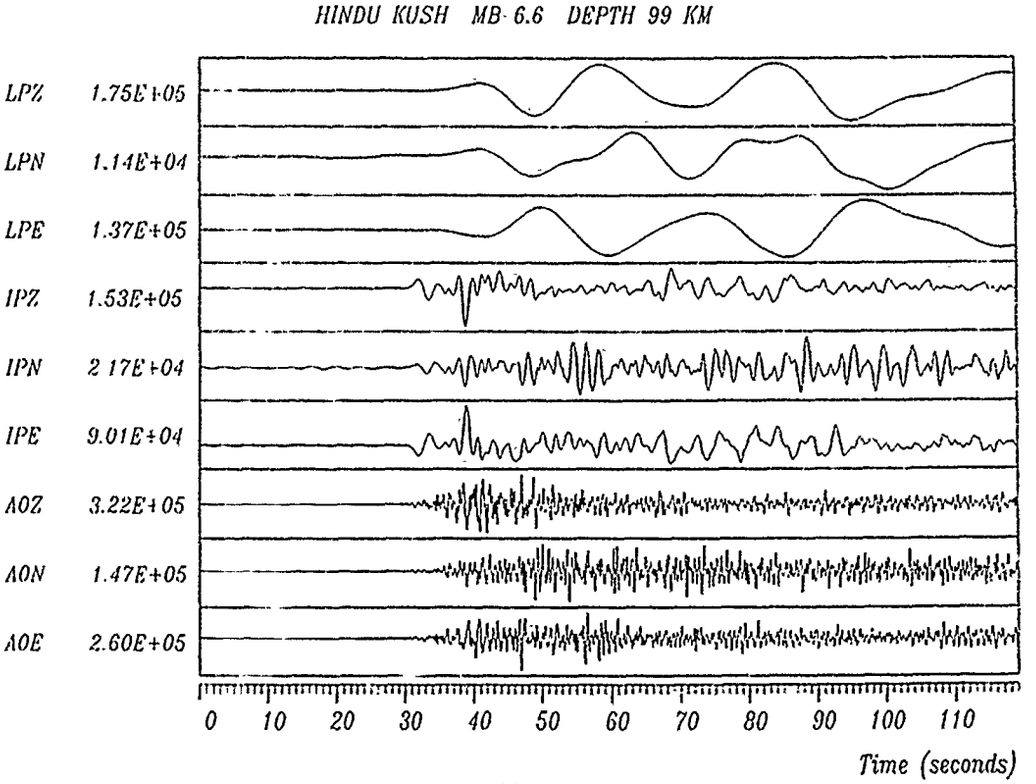

(a)

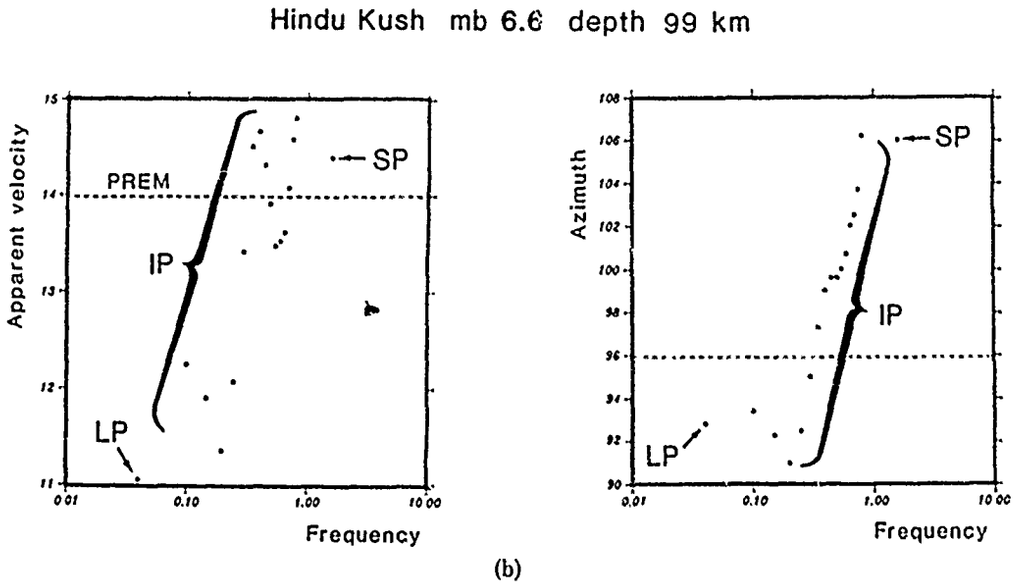

(b)

FIG. 6. (a) *P* wave from event in Hindu Kush recorded in three diffferent frequency bands of the broadband station in NORESS. Event date is 29.7.1985; origin time is 07.54, 44.5; and coordinates are 36.21°N, 70.90°E. (b) Slowness solutions as a function of frequency using uniform half-space model with v_P = 6.0 km/sec, v_S = 3.46 km/sec. Slowness vector decomposed in apparent velocity and azimuth.

assumption of frequency-independent g. The correct values are near the SP solution for apparent velocity, and near the LP solution for azimuth. This suggests that, in this particular example, relatively small-scale lateral structure is the dominant source of azimuth bias, whereas the apparent velocity for *P* is primarily affected by

large-scale vertical structure. Indeed, a simple modification of the uniform half-space model by introducing, in addition to the Moho, a discontinuity between the upper and lower crust at 15 km depth, does produce velocity dispersion of the observed order of magnitude (Fig. 7). The calculations for this model were based on

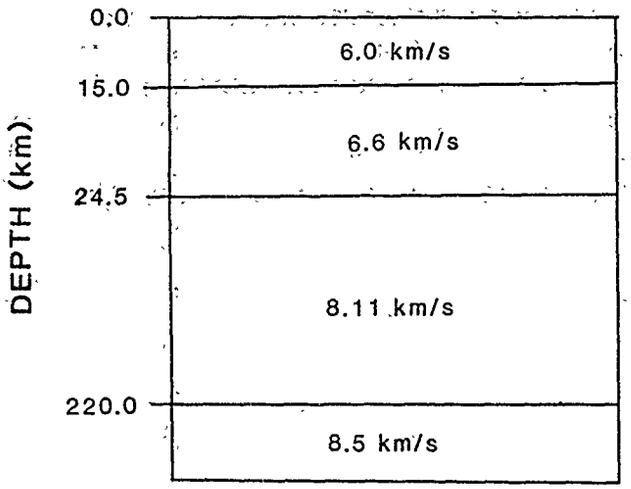

(a)

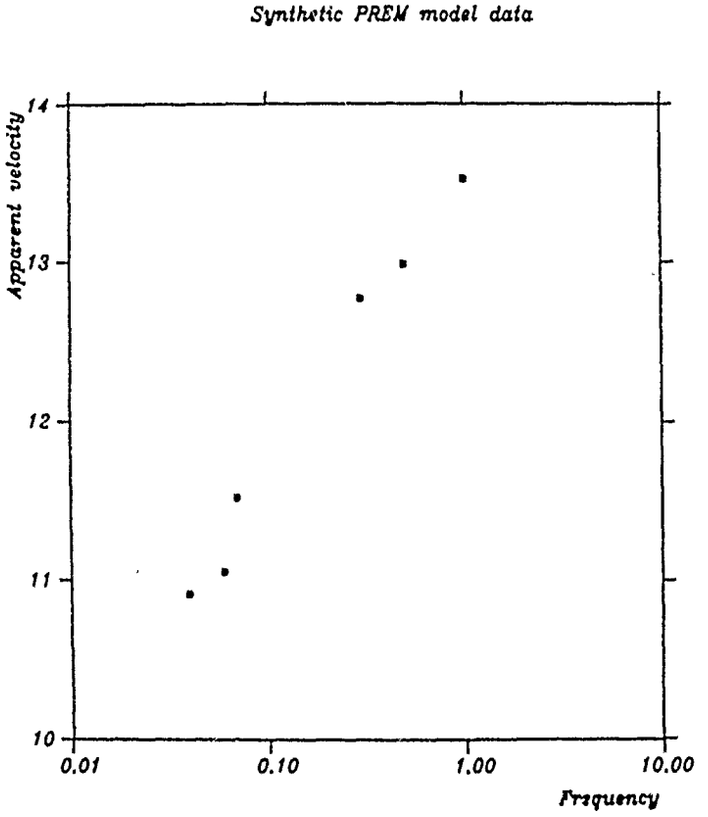

(b)

FIG. 7. (a) Crustal model used to generate synthetic broadband P. (b) Slowness solutions when applying the uniform half-space model ($v_P = 6.0$ km/sec, $v_S = 3.46$ km/sec) to the synthetic data generated in model of (a).

a stripped version of Kennett's (1988) reflectivity algorithm. Of course, the model introduced here is not meant to have any significance other than that it gives an indication of the required scale of inhomogeneity.

Scattering by Surface Topography

An obvious and realistic extension of the uniform half-space model is to include the effect of surface topography. The usual correction for surface topography implies a time correction for elevation and possibly a particle motion correction for elevation and possibly a particle motion correction for surface slope. These corrections are consistent with geometrical ray theory, which requires that topographic relief be smooth on the scale of a wavelength. However, topographic maps of the NORESS and ARCESS areas (Figs. 8 and 9) demonstrate that topographic relief is not smooth on the scale of the wavelengths involved (~2 km), and wave scattering effects may be important.

To evaluate the scattering, we have used a method that was originally developed for a comparatively simple problem of electromagnetic scattering by a perfectly conducting rough surface (e.g., Brown, 1985). The method is based on the so-called extinction theorem; it has also been called the extended boundary condition method (Waterman, 1971) or the null-field method. The appropriate boundary integral equations for an elastic medium were given by Doornbos (1988). For the present purpose, we need the surface displacement $\mathbf{u}(x, y)$. If the surface topography is described by a function, $f(x, y)$, the equations for $\mathbf{u}(x, y)$ are

$$\int\int \mathbf{v}^T \mathbf{R}_j \mathbf{u}(x, y) \exp[-i(K_j f + k_x x + k_y y)]\, dx\, dy = A_j(k_x, k_y) \qquad (6)$$

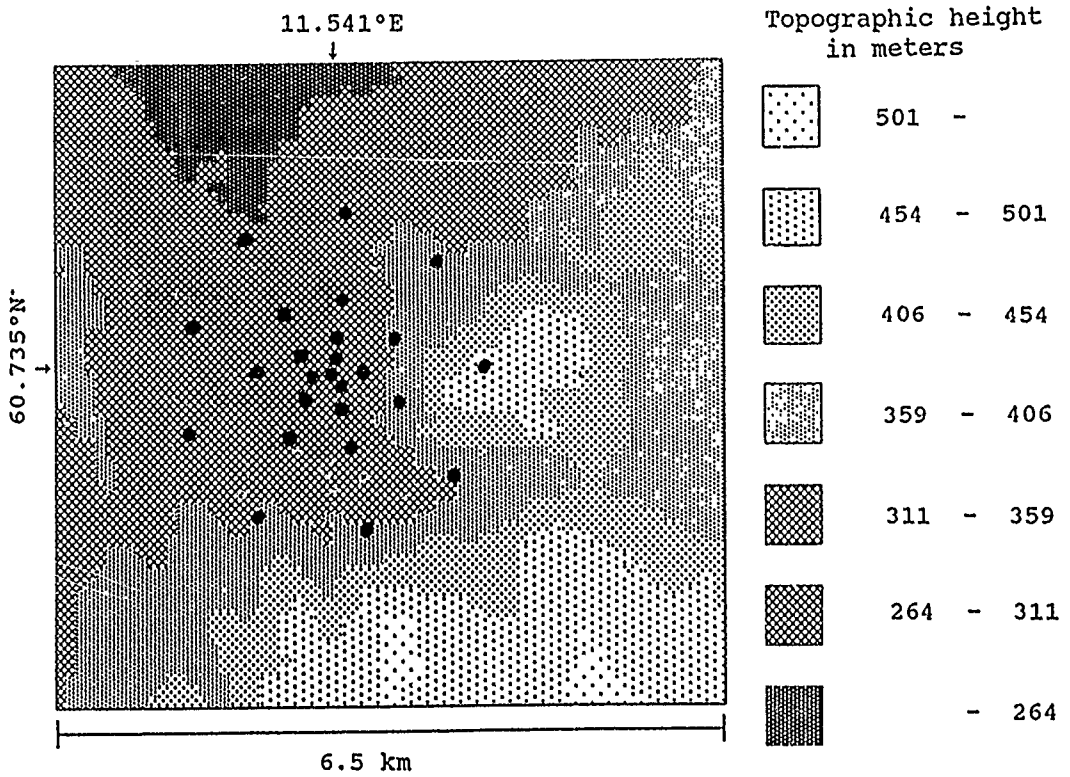

FIG. 8. Topographic map of the NORESS array area, centered at 60.735°N, 11.541°E.

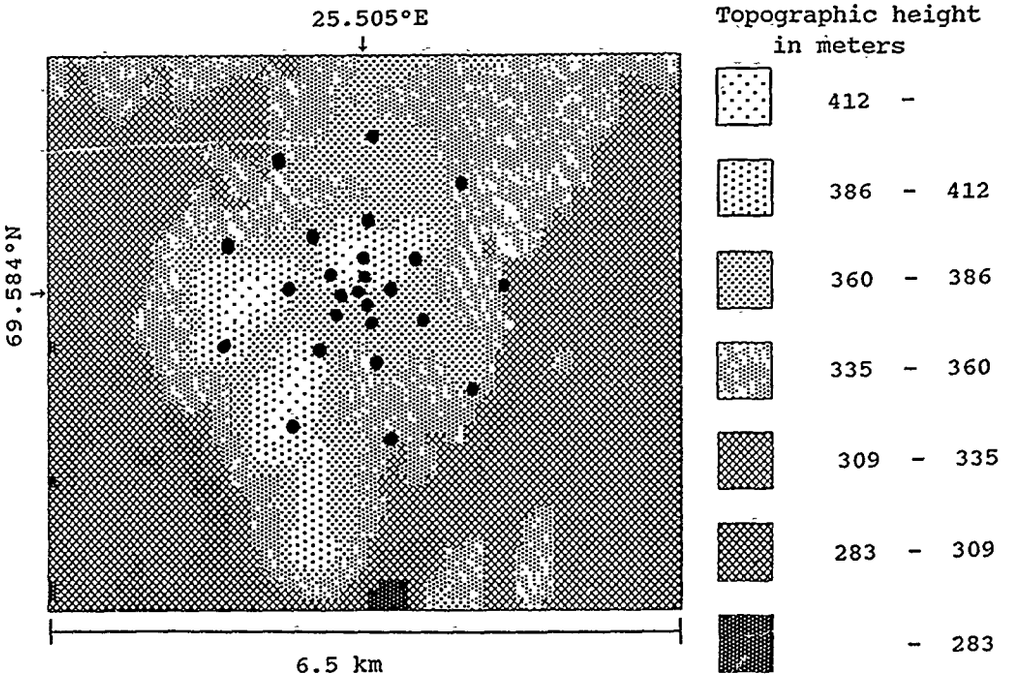

FIG. 9. Topographic map of the ARCESS array area, centered at 69.584°N, 25.505°E.

where k_x and k_y are wavenumbers corresponding to the x and y space coordinates, A_j is a wavenumber component of the incident wave with j indicating P, SV, or SH, $K_j = (\omega^2/v_j^2 - k_x^2 - k_y^2)^{1/2}$ with ω the angular frequency and v_j the P or S velocity, $\mathbf{v}^T = (-\partial f/\partial x, -\partial f/\partial y, 1)$, and $\mathbf{R}_j$ is a 3×3 matrix that depends on the wave velocities and on the directions of particle displacement and wave propagation. To obtain $\mathbf{u}(x, y)$ we substitute a perturbation series for the Fourier transform:

$$\mathbf{U}(k_x, k_y) = \sum_{n=0}^{\infty} \mathbf{U}^{(n)}(k_x, k_y). \tag{7}$$

Solutions for $\mathbf{U}^{(n)}$ can be obtained recursively. The nth order term $\mathbf{U}^{(n)}$ is a function of $\mathbf{U}^{(n-m)}$, $1 \leqq m \leqq n$, of the surface topography $f(x, y)$, and of the surface gradients $\partial f/\partial x, \partial f/\partial y$. The zeroth order term $\mathbf{U}^0$ gives the conventional free surface response for a plane, the first order term $\mathbf{U}^1$ includes the Born approximation, and the higher order terms account for multiple scattering.

A truncated series of the form (7) represents an approximation, but the method can be applied to any surface topography; the only restriction being implied by the condition of convergence of the series solution. In another test of the method, we have solved the system of equations (6) numerically by Gauss elimination. Since numerical solutions of this type are very expensive in a full three-dimensional treatment, we have restricted the comparison to two-dimensional problems. Figure 10 shows a cross section of the NORESS topography crossing the dominant peaks and troughs in the area. Figure 11 shows the resulting perturbations of amplitude and polarization angle for an incident P wave of 1.8 Hz. In this case, the results of the direct numerical solution method and the perturbation method are indistinguishable. It is nevertheless obvious that the perturbation series (7) will fail

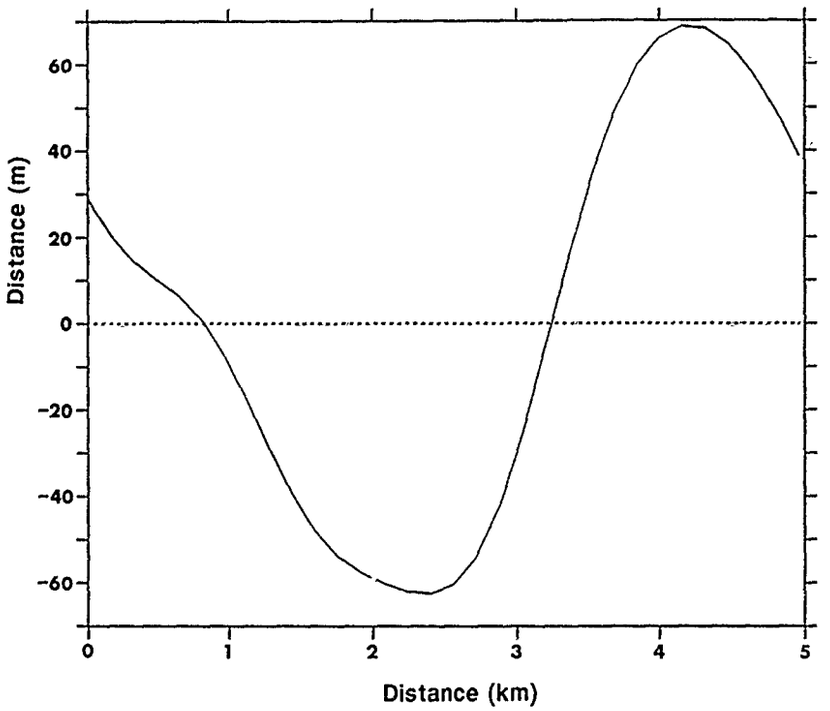

FIG. 10. Cross-section of topographic map at NORESS. Section through the array center from west to east. The reference plane (dashed line) is tilted with a dip of 1.8° and a strike of 229.6°. Elevation given as distance normal to reference plane.

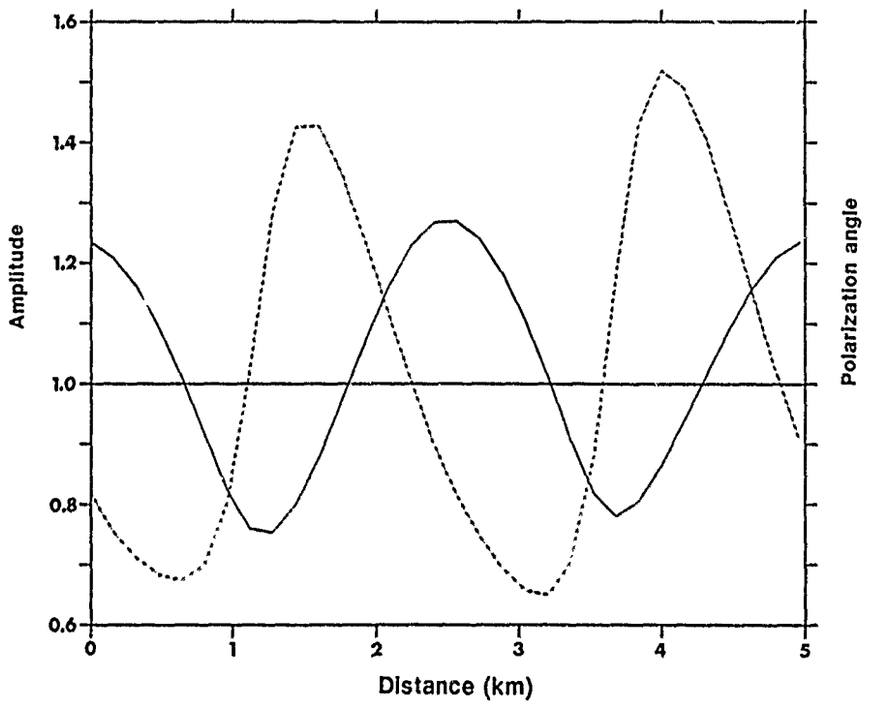

FIG. 11. Theoretical perturbation of amplitude (solid line) and polarization angle (dashed line) of incident *P* wave measured along the reference line of the model in Figure 10. The wave frequency is 1.8 Hz, and the angle of incidence is 33°. Perturbations are plotted as ratios in relation to reference values for a plane surface.

to converge if the topography exceeds a certain fraction of the wavelength. Such cases will not be considered in this paper.

Application to NORESS and ARCESS

Using the method of equations (6) and (7) and assuming an incident plane wave as specified by the array slowness solution, we have synthesized the free surface response over the observed signal bandwidth. We then applied the method of equation (2) to the three components of surface displacement to obtain theoretical slowness solutions for the three-component sites. We use a Cartesian coordinate system, but the reference x-y plane need not be horizontal. In the case of NORESS, we tilted the reference plane such that the extremum of the function $f(x, y)$ is minimal. This extends the range of convergence of the series solution. The results at NORESS for P from the events near Leningrad are included in Figure 2, and for P from the explosions in Eastern Kazakh in Figure 4 (NORESS) and Figure 5 (ARCESS). The theoretical results explain up to about half of the observed anomalies at NORESS. The surface topographic effect is less at ARCESS. We speculate that shallow subsurface structure may enhance the surface topographic effect, especially at ARCESS, which is situated on top of a gabbro intrusion. The results represent a weighted integral over the signal bandwidth, but single frequency solutions give a significant variation with frequency. This is also evident from the difference in the synthetic slowness solutions at ARCESS for P from the two groups of events in Eastern Kazakh. It is consistent with the notion of the response by a rough surface as an interference pattern.

Conclusions

For purposes of slowness determination and event location, there are, in principle, several differences between the use of a single-component array and a three-component sensor: across an array, phase differences are employed, the slowness solution represents an average over the array, the resolution increases with frequency provided signals are well correlated, and the solution is independent of the Earth model. Of course, a model must still be invoked to locate the event. With a three-component sensor, amplitude ratios are employed, the slowness solution represents one site, the resolution is constant with frequency, and the solution depends on the Earth model. Experience has shown that several of these principles are modified in practice. In particular, the implicit assumption of a uniform half-space is inadequate when using three-component data. Layering of the crust and upper mantle affect the surface response at long periods, and surface topography and near-surface structure perturb the surface particle motion and slowness solutions especially at short periods. The perturbation varies from site to site, and it also depends on details of the input signal spectrum. On the other hand, the array slowness solution based on vertical component phase delays is relatively stable since the additional phase perturbations are negligible.

Acknowledgments

This research was partly supported by the Advanced Research Projects Agency of the Department of Defense and was monitored by the Air Force Office of Scientific Research under Contract F49620-89-C-0038. This research was also partly supported by the Norwegian Council for Science and the Humanities (NAVF).

REFERENCES

Brown, G. S. (1985). A comparison of approximate theories for scattering from rough surfaces, *Wave Motion* **7**, 195–205.

Capon, J. (1969). High-resolution frequency-wavenumber spectrum analysis, *Proc. IEEE* **58**, 760–770.

Christoffersson, A., E. S. Husebye, and S. F. Ingate (1988). Wavefield decomposition using *ML*-probabilities in modelling single-site 3-component records, *Geophys. J.* **93**, 197–213.

Doornbos, D. J. (1988). Multiple scattering by topographic relief with application to the core-mantle boundary, *Geophys. J.* **92**, 465–478.

Esmersoy, L., V. F. Cormier, and M. N. Toksöz (1985). Three component array processing, in *The VELA Program*, A. U. Kerr (Editor), Defense Advanced Research Projects Agency, Executive Graphics Services.

Jurkevics, A. (1988). Polarization analysis of three-component array data, *Bull. Seism. Soc. Am.* **78**, 1725–1743.

Kennett, B. L. N. (1988). Systematic approximations to the seismic wavefield, in *Seismological Algorithms*, D. J. Doornbos (Editor), pp. 237–257, Academic Press, London.

Kværna, T. (1989). On exploitation of NORESS type arrays for enhanced *P*-wave detectability, *Bull. Seism. Soc. Am.* **79**, 888–900.

Kværna, T. and D. J. Doornbos (1986). An integrated approach to slowness analysis with arrays and three-component stations, in *NORSAR Semiannual Technical Summary Rept. No. 2-85/86*, Kjeller, Norway.

Mosessian, T. K. and M. Dravinski (1989). Scattering of elastic waves by three-dimensional surface topographics, *Wave Motion* **11**, 579–592.

Mykkeltveit, S., K. Åstebøl, D. J. Doornbos, and E. S. Husebye (1983). Seismic array configuration optimization, *Bull. Seism. Soc. Am.* **73**, 173–186.

Mykkeltveit, S., F. Ringdal, T. Kværna, and R. W. Alewine (1990). Application of regional arrays in seismic verification research, *Bull. Seism. Soc. Am.* **80**, Part B, 1777–1800.

Samson, J. C. (1977). Matrix and Stokes vector representations of detectors for polarized waveforms: theory with some applications to teleseismic waves, *Geophys. J. R. Astr. Soc.* **51**, 583–603.

Waterman, P. C. (1971). Symmetry, unitarity, and geometry in electromagnetic scattering, *Phys. Rev. D.* **3**, 925–939.

INSTITUTE OF GEOPHYSICS
UNIVERSITY OF OSLO
P.O. BOX 1022
BLINDERN 0315 OSLO 3, NORWAY
(E.O., D.J.D.)

NTNF/NORSAR
P.O. BOX 51
N-2007 KJELLER, NORWAY
(T.K.)

Manuscript received 28 February 1990

Bulletin of the Seismological Society of America, Vol. 80, No. 6, pp. 2227–2241, December 1990

F-K ANALYSIS OF NORESS ARRAY AND SINGLE STATION DATA TO IDENTIFY SOURCES OF NEAR-RECEIVER AND NEAR-SOURCE SCATTERING

BY I. N. GUPTA, C. S. LYNNES, T. W. MCELFRESH, AND R. A. WAGNER

ABSTRACT

***F-k* analyses of short-period recordings of both explosion and earthquake sources at the high-frequency NORESS array indicate secondary arrivals from a near-receiver source about 25 to 30 km southwest of the array. Use of residual seismograms, derived by subtracting the beamed record from each array channel, improved the identification of the same scatterer. *F-k* power difference plots, obtained by subtracting (after normalization) the *f-k* power versus slowness estimates for the initial *P* window from those for the latter windows, provided nearly identical results. The secondary seismic source appears to be short-period surface waves, *Rg*, generated by the scattering of incident *P* waves in the region of Lake Mjosa, 27 km southwest of NORESS, where there is about 1 km of relief from the bottom of the lake to the top of an adjacent hill. Polarization analysis of an explosion recorded on three-component elements of NORESS also suggested a secondary phase with polarization characteristic of *Rg* and arrival time and azimuth consistent with those derived from the *f-k* analysis. Near-source scattering is investigated by *f-k* analysis of data from reciprocal arrays formed by interchanging the roles of source and receiver. Application to closely spaced Yucca Flat (NTS) shots recorded at several stations provides evidence for *Rg* → *P* scattering near the northwestern and other basin boundaries of the Yucca Valley. It seems that deterministic locations of near-receiver *P* → *Rg* and near-source *Rg* → *P* scattering can be obtained by *f-k* techniques.**

INTRODUCTION

Few studies of teleseismic *P* waveforms have been successful in identifying and locating specific sources of scattering from observed seismograms. One of the most convincing analyses has been the identification of scattered arrivals from the region of Moffat Water, a narrow lake in Scotland about 8 miles long, which lies at the bottom of a 600 ft deep valley (Key, 1967, 1968). The valley lies in a NE-SW direction, and the apparent secondary source is at a point about one-third of its length from the northeastern end, where it cuts through a basalt and dolerite dyke. By beaming Eskdalemuir (EKA) array records from several earthquakes and nuclear explosions, Key identified a low-frequency Rayleigh-wave arrival with velocity of about 2.5 km/sec from the direction 315° and originating at a distance of about 13 km from the center seismometer. The direction and velocity of the local wave did not change in spite of variation in source azimuthal direction of over 50°, suggesting it to be due to a relatively small localized heterogeneity. Particle-motion analysis of three-component data confirmed the local wave, with an amplitude generally about 20 to 40 percent of that of the incident *P* wave, to have the character of a Rayleigh wave. Theoretical studies by Hudson (1967) and Hudson and Boore (1980) also indicated the source of the local wave to be due to scattering of incident *P* into Rayleigh wave. Broadband *f-k* analysis of EKA recordings of both United States and USSR nuclear explosions further confirmed the secondary seismic source to be from Moffat Water (Gupta *et al.*, 1990). Residual seismograms obtained by

subtracting the beamed record from each array channel significantly improved identification of the sources of locally scattered arrivals.

Our recent *f-k* analyses of data from the high-frequency seismic array NORESS (Norway) suggested the presence of a local scatterer about 25 to 30 km southwest of the array, in the region of Lake Mjosa (Gupta *et al.*, 1989, 1990). In this more detailed study, USSR and United States nuclear explosions and an earthquake are used as the seismic sources, providing significantly different source-receiver azimuthal directions. Two new *f-k* techniques based on the use of residual seismograms and *f-k* power difference plots help improve identification of the scatterer. Similar results are obtained by polarization analysis of three-component NORESS data.

In simple terms, the principle of reciprocity means that the source and receiver positions in a seismic experiment can be exchanged without affecting the observed seismograms. Consequently, single observation point records of closely spaced seismic sources can be used to form an array on which conventional array processing techniques can be applied (Spudich and Bostwick, 1987). Teleseismic *P* arrivals from Yucca Flat explosions are known to have complex waveforms that vary considerably from one shot to another. Finite-difference simulations have explained much of this complexity as being due to the scattering of explosion-generated Rayleigh waves into teleseismic body waves because of laterally varying structure (McLaughlin *et al.*, 1987; Stead and Helmberger, 1988). An attempt is made here to evaluate near-source scattering for Yucca Flat shots by *f-k* analysis of data from several stations by forming reciprocal arrays. The results are interpreted on the basis of the known geology of the Yucca Flat test site. Both near-receiver and near-source scattering play important roles in the monitoring of underground nuclear tests. For example, the *Lg* phase from explosions, known to be strongly influenced by scattering (e.g., Gupta and Blandford, 1983), is often used for the detection, source discrimination, and yield determination of underground nuclear explosions.

F-K Analysis and Polarization Analysis of USSR and United States Shots at NORESS

Array recordings of seismic events are useful for studying detailed characteristics of wave propagation across the array. Broadband *f-k* methods have been used to detect various seismic arrivals and determine their phase velocity and azimuth (Kværna and Doornbos, 1986; Kværna, 1989; Ringdal and Kværna, 1989). The *f-k* technique used here is described by Kværna and Doornbos (1986) and Kværna and Ringdal (1986).

We first applied the broadband *f-k* spectra method to the NORESS recordings of two underground nuclear explosions. The NORESS small-aperture array consists of sensors within a 3 km diameter, and the 24 short-period vertical-component sensors used in this study are located along four concentric rings (Kværna, 1989). The results are expressed in terms of frequency-slowness spectral estimates of the signal along various azimuthal directions. Starting a few seconds before the onset of *P*, Parzen-tapered 3.2 sec (128 point) windows, with incremental shift of 0.2 sec, were used to obtain the frequency-slowness plots. Results from the Kazakh shot of December 16, 1984 ($m_b = 6.1$, $\Delta \approx 38°$, backazimuth 75°) are shown in Figure 1. Here, the *P* window is centered on the onset of *P* so that it contains only 1.6 sec of signal. The window starting 1 sec after the *P* window (designated the *P* + 1 sec window) was generally found to have the highest power and may therefore be considered to represent the initial *P*. On each slowness plot, the highest amplitude value is indicated (with power in decibels) along with its direction of approach or

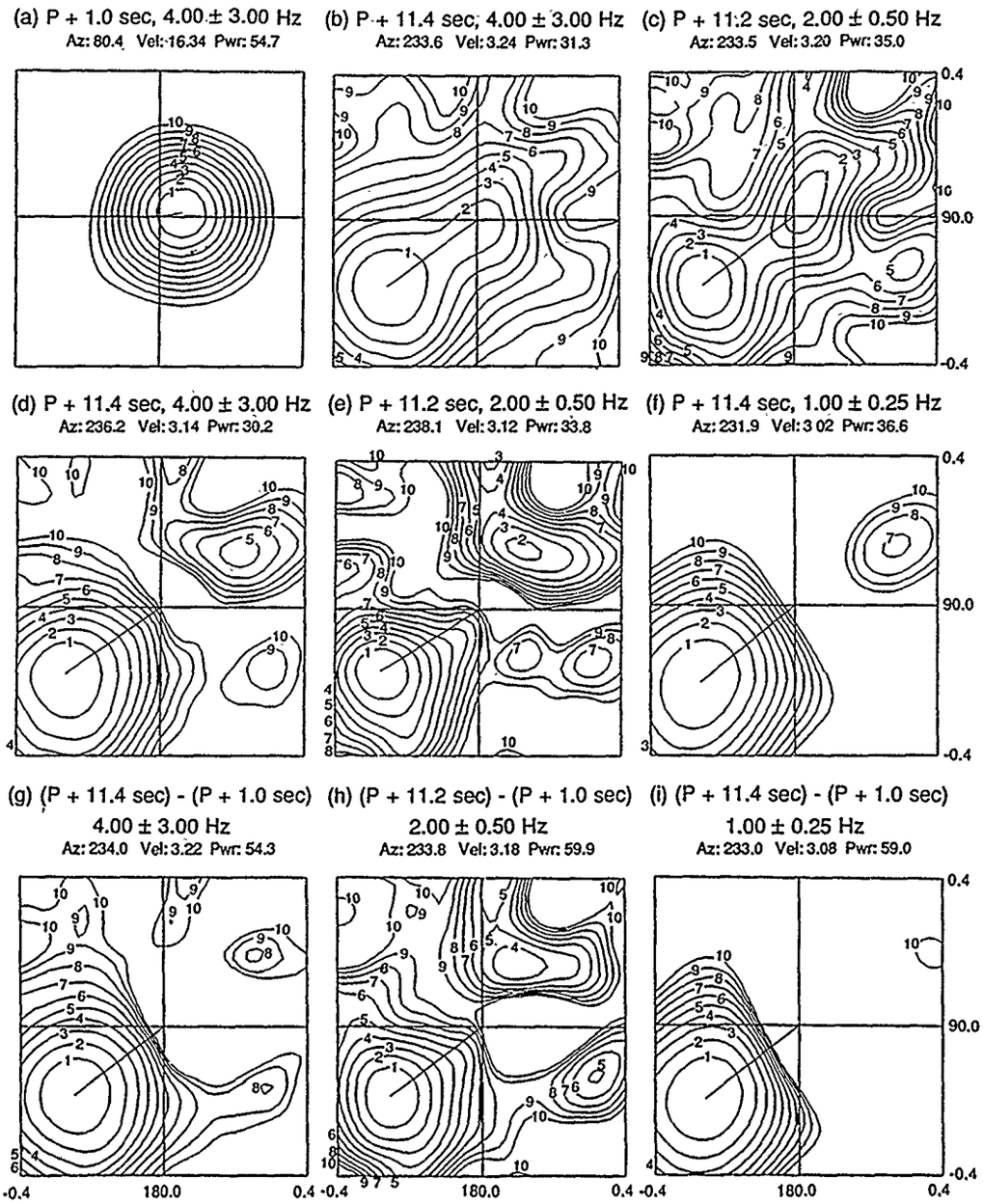

FIG. 1. Frequency-slowness spectral estimates derived from NORESS records of the Kazakh shot of December 16, 1984 based on the use of (a to c) normal (d to f) residual seismograms, and (g to i) *f-k* power difference plots. The numbers on top of each plot indicate backazimuth (in degrees), phase velocity (in kilometers/second), and signal power (in decibels), respectively of the highest amplitude arrival that is shown connected to the plot origin. The maximum slowness value is 0.4 sec/km. The signal windows and frequency passbands are indicated on each plot. Note the low-phase velocity arrival from the southwest direction appearing as the principal phase on all eight later arrival windows.

backazimuth (in degrees) and phase velocity (in kilometers/second). The contour interval is 1 dB, and a range of 10 dB is used. The signal/noise ratio for the NORESS recordings of this explosion is good over the frequency range of about 0.5 to 7.0 Hz. The broadband (1 to 7 Hz) results for the $P + 1$ sec and $P + 11.4$ sec windows are shown in Figures 1a and 1b, respectively. Figure 1c shows results from the narrow frequency passband of 2.0 ± 5.0 Hz. Dominant energy in the first window

shows a backazimuth of about 80° and phase velocity of about 16 km/sec; both are close to the expected values for initial *P*. In addition to main arrivals from the explosion source region, Figures 1b and 1c suggest low-phase velocity secondary sources of energy, especially from the southwest direction.

The local secondary arrivals were enhanced with respect to the primary arrival by subtracting the beamed waveform from the original *P* waveform for each array channel and using the resulting residual seismograms for *f-k* analysis (Gupta *et al.*, 1990). This simple but effective method constitutes a first step in iterative beamforming of two simultaneous signals and provides a first approximation to a maximum-likelihood estimate (Blandford *et al.*, 1976). Results for the same two windows and frequency passbands as in Figures 1b and 1c are shown in Figure 1d and 1e, respectively; a comparison clearly demonstrates the usefulness of residual seismograms in the identification and location of sources of near-receiver scattering. Figure 1f shows results, based on the use of residual seismograms, for the lower frequency passband of 1.00 ± 0.25 Hz. Figures 1d to 1f consistently indicate a prominent low-phase velocity arrival from nearly the same azimuthal direction.

An attempt was also made to investigate secondary sources of scattering with the help of *f-k* power difference plots obtained by subtracting the normalized two-dimensional matrix of *f-k* power versus slowness estimates of the initial *P* window from those for the later windows. Results for the same three frequency passbands as used in Figures 1d to 1f are shown in Figures 1g to 1i, respectively. The three figures indicate the same prominent low-phase velocity arrival from nearly the same azimuth. It appears, therefore, that *f-k* power difference plots provide another simple and effective method for studying the characteristics of secondary arrivals.

The maximum amplitude arrivals in all eight figures based on later time windows (Fig. 1b through 1i) indicate a phase velocity of about 3 km/sec and a backazimuth of about 235°. Combining this with the phase velocity and backazimuth in Figure 1a and assuming the scattering to take place near the surface, the scatterer should lie 25 to 30 km from the array. There is a large lake, Lake Mjosa, running along the northwest to southeast direction, about 24 km southwest of NORESS. The hills immediately to the west of the lake have an elevation of 600 m above the lake, which is approximately 400 m deep, meaning that there is a variation in elevation from the bottom of the lake to the top of the hill of 1000 m over a short horizontal distance (S. Mykkeltveit, personal comm., 1989). It seems likely that the scatterer is associated with this prominent geological feature, which has the largest topographical relief within at least 50 km of the array.

Frequency-slowness plots derived from NORESS records of the NTS shot LOCKNEY (September 24, 1987, $m_b = 5.7$, $\Delta \approx 74°$, backazimuth 319°) are shown in Figure 2, which includes results from normal *f-k* analysis (Figs. 2a to 2c), from residual seismograms (Figs. 2d to 2f), and from *f-k* power difference plots (Figs. 2g to 2i). Results are similar to those in Figure 1, indicating nearly the same azimuthal direction for the scatterer. The secondary arrival is most prominent in the *P* + 10.6 sec window. Its arrival time, somewhat earlier than that in Figure 1, is consistent with the somewhat shorter travel path of the scattered incident *P* wave relative to the direct *P*. The scattered arrivals in plots derived from residual seismograms (Figs. 2d to 2f) as well as those from difference *f-k* plots (Figs. 2g to 2i) are significantly more prominent than those from normal seismograms (Figs. 2b and 2c). Again, the results in Figure 2 suggest the source of scattering to be about 25 to 30 km from the array.

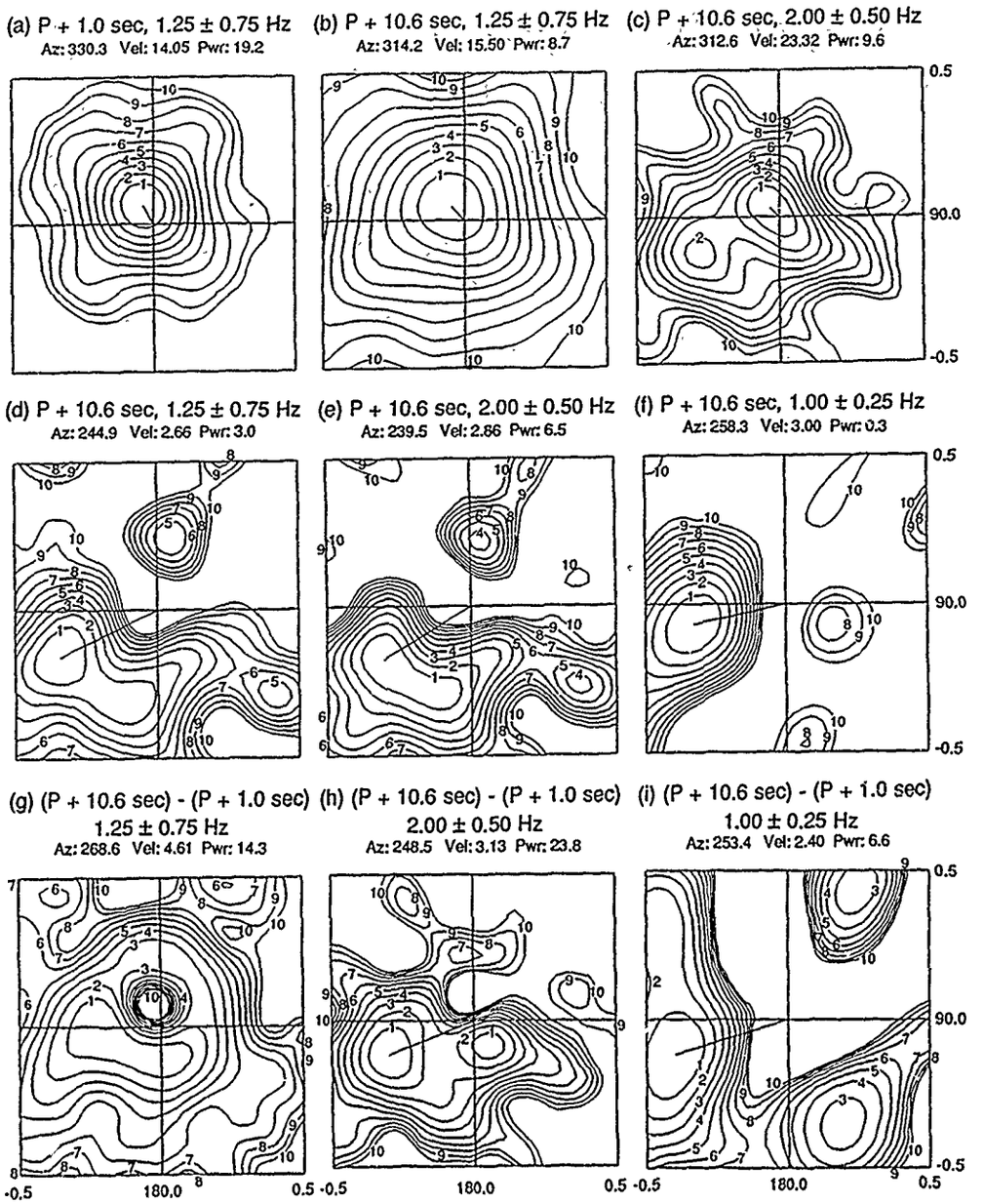

FIG. 2. Similar to Figure 1 but derived from NORESS records of LOCKNEY with a maximum slowness of 0.5 sec/km. The low-phase velocity arrival from the southwest direction is hardly seen in (b), appears as a secondary arrival in (c), but appears as the principal phase in nearly all other later arrival windows.

Polarization analysis of the 4 three-component short-period elements of NORESS for the USSR explosion described earlier was carried out using the method of Jurkevics (1988). A zero-phase Butterworth bandpass filter is applied to the data, and covariance matrices are averaged over the array for a sliding window. The polarization ellipsoid, representing the best fit to the data in a least-squares sense, is computed from the average covariance matrix. The characteristics of ground motion can be specified in terms of attributes derived from the principal axes of the polarization ellipsoid. Denoting the latter by λ_1, λ_2, and λ_3, where $\lambda_1 \geqq \lambda_2 \geqq \lambda_3$, the

degree of rectilinearity is given by $(1 - (\lambda_2 + \lambda_3)/2\lambda_1)$, which is 1.0 when there is only one nonzero eigenvalue, as for pure P waves. Pure Rayleigh-wave motion is elliptical and the particle motion is confined to a plane. Defining oblateness as $2(\lambda_2 - \lambda_3)(\lambda_1 - \lambda_3)/(\lambda_1^2 + \lambda_2^2 + \lambda_3^2)$, Rayleigh waves should be characterized by very oblate (i.e., flat elliptical) polarization (the maximum oblateness is 1, when $\lambda_1 = \lambda_2$ and $\lambda_3 = 0$). Results from the Kazakh shot, based on 3 sec long moving windows and 0.5 to 1.0 Hz zero-phase filtered band, shown in Figure 3, indicate a prominent phase with polarization characteristic of Rayleigh waves arriving about 11 sec after P. The backazimuth computed from the polarization is about 230° to 240°. The arrival time and azimuth are, therefore, consistent with those for the secondary seismic source in the *f-k* analyses (Fig. 1).

F-K Analysis of an Intermediate-Focus Earthquake at NORESS

We carried out *f-k* analysis on NORESS data from an earthquake in Romania (45.82°N, 26.65°E, 1 August 1986, $m_b = 4.7$, depth 122 km, $\Delta \approx 17°$, backazimuth 142°) in order to examine any possible influence of variations in source-type and source-receiver azimuth on the determination of near-receiver scattering. The results are shown in Figure 4. The $P + 1$ sec window (Fig. 4a) indicates the expected phase velocity and backazimuth, whereas the two $P + 11.6$ sec windows (Figs. 4b and 4c) contain some evidence of a low-phase velocity secondary arrival from the southwest direction. Comparing these with the results from explosions (Figs. 1b, 1c, 2b, and 2c), the earthquake P coda has considerably more energy coming from the source region, probably because of the significantly longer source duration. Nevertheless, *f-k* based on residual seismograms (Figs. 4d to 4f) and *f-k* power difference plots (Figs. 4g to 4i) produce results for the secondary source that are remarkably similar to those from the two explosions (Figs. 1 and 2). The *f-k* analyses for the lowest-frequency passbands (Figs. 4f and 4i) are especially distinct and stable.

F-K Analysis of Data from Reciprocal Arrays

We also used *f-k* analysis to investigate near-source scattering by forming reciprocal arrays in which the roles of source and receiver are interchanged. Short-period records at a single station of seismic sources that are fairly similar and closely spaced may be used for this purpose. In order to simulate a reciprocal array, arrival times of the first peak in the direct P wavetrain from each explosion are used as reference points, and the traces are shifted on the basis of their predicted travel times to the recording station. Yucca Flat (NTS) explosions recorded at several stations at teleseismic distances were used to construct four reciprocal arrays, and the sources of secondary arrivals were examined. The locations of 39 shots used in each of the four reciprocal arrays used in this study are shown in Figure 5. Two of these arrays were derived from groups of 10 shots each recorded at the ASRO station MAJO; these have been designated as MAJO-North and MAJO-South. The center element NA0 records of the NORSAR array for 15 shots provided another reciprocal array. Lastly, 18 records from a combination of the WWSSN stations, TOL, PTO, and MAL having nearly the same distance and backazimuth to Yucca Flat were combined to form the fourth reciprocal array. The long dimensions of these four arrays vary from about 3 to 5 km. The seismic velocities in the Yucca Flat region are known to be considerably smaller than those in the shield region of NORESS. For this reason, 6.4 sec windows were used for the *f-k* analysis, and the maximum slowness was increased to 1.0 sec/km on all slowness plots.

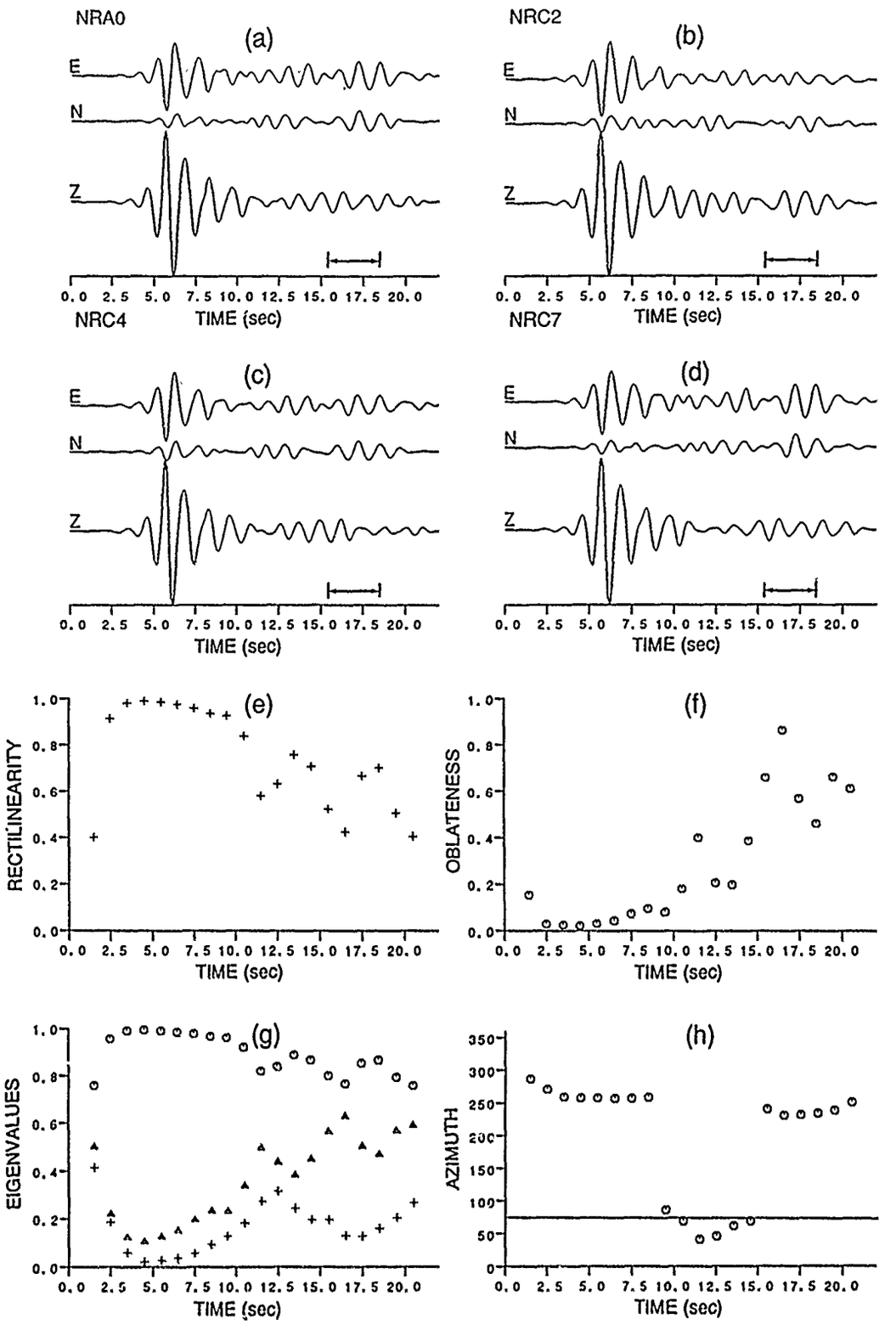

FIG. 3. Polarization analysis of 16 December 1984 Shagan River event. (a to d) Three-component NORESS seismograms, starting 4 sec before the onset of *P* and filtered 0.5 to 1.0 Hz; the arrows indicate the *P* + 11.4 sec window used in the *f–k* analysis in Figure 1. (e) Rectilinearity versus time. (f) Oblateness versus time. (g) Eigenvalue amplitudes (normalized to 1). (h) Backazimuth, assuming Rayleigh wave polarization; line shows backazimuth to Shagan River.

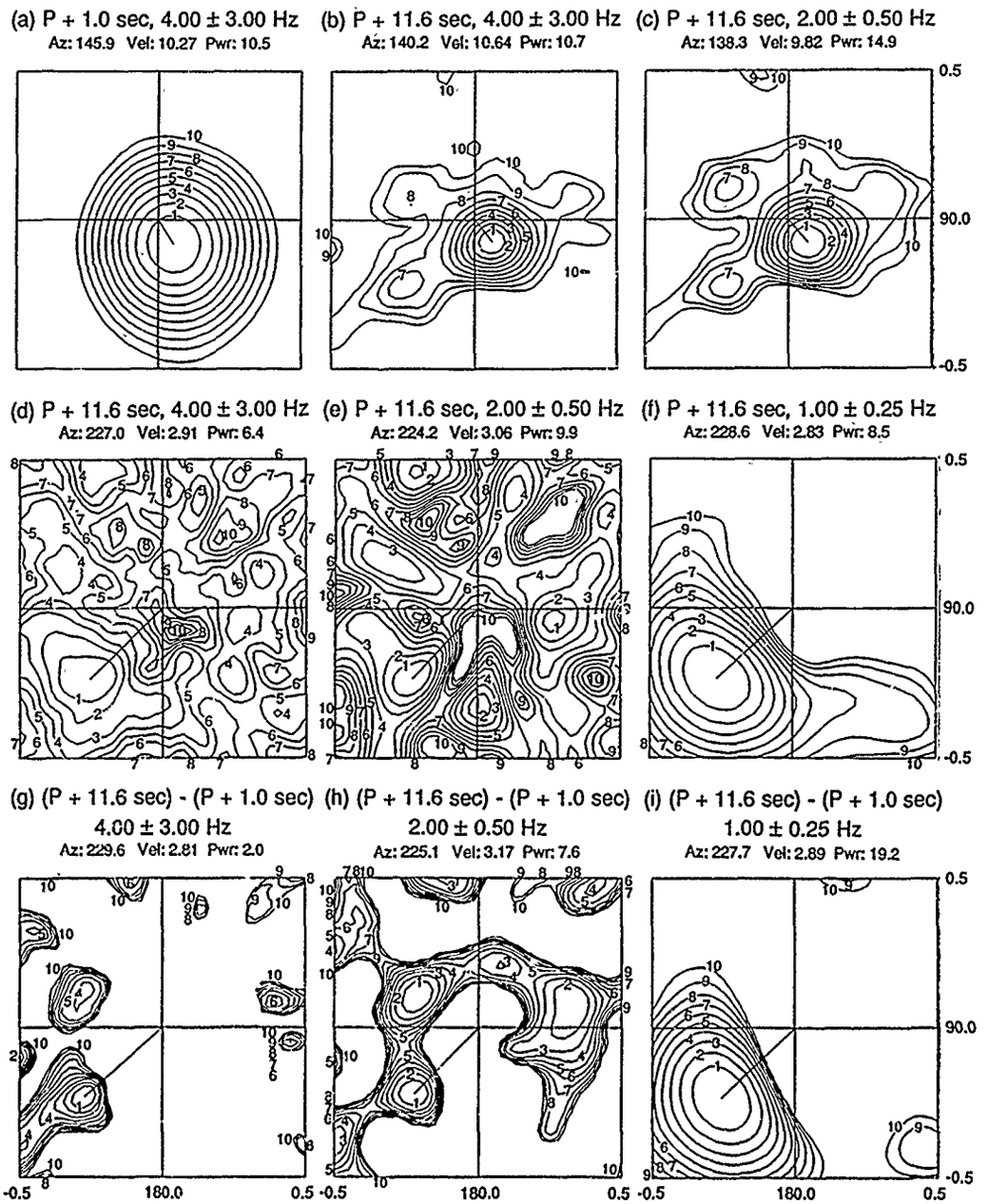

FIG. 4. Similar to Figure 1 but derived from NORESS records of the Romanian earthquake of 1 August 1985. The low-phase velocity arrival from the southwest direction appears as a secondary arrival in (b) and (c), but appears as the principal phase in all other later arrival windows.

Results from MAJO-North array are shown in Figure 6. Frequency-slowness plots, obtained with an incremental shift of 1 sec for three different frequency ranges, showed a prominent secondary arrival in the $P + 4$ sec window. Frequency-slowness plots of the initial P (i.e., the $P + 1$ sec) window indicate that the dominant energy arrives close to the expected azimuth and phase velocity. However, unlike the results from the initial P window from NORESS (Figs. 1a, 2a, and 4a), there are several other secondary sources of energy. This contamination is at least in

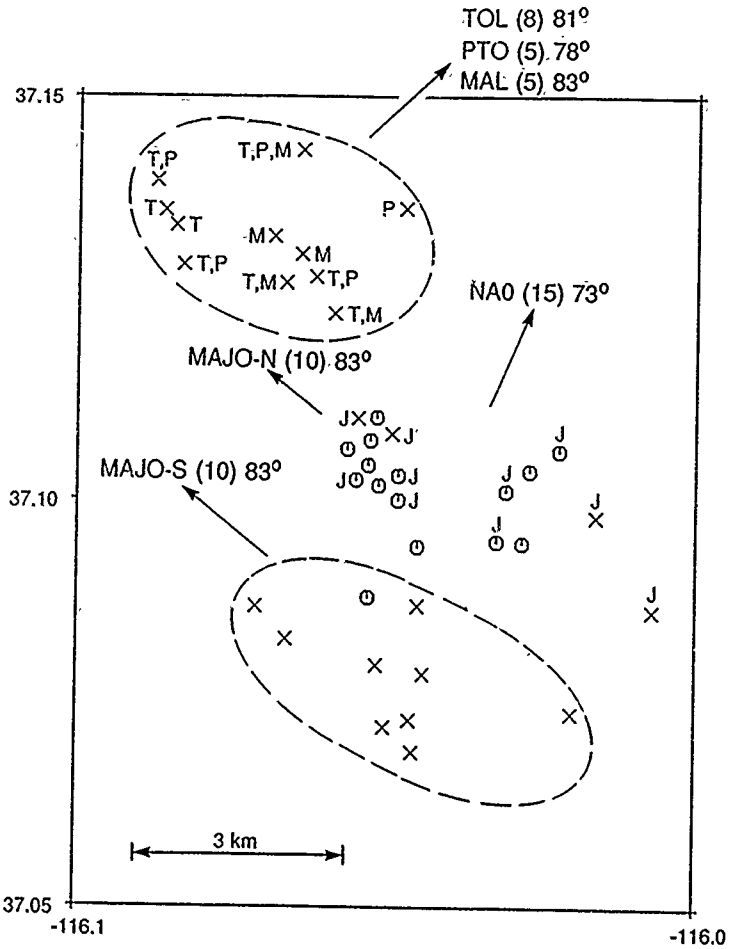

FIG. 5. Locatios of 39 Yucca Flat explosions used in forming four reciprocal arrays: (1) MAJO-North consists of 10 shots denoted by "J" (2) MAJO-South with 10 shots within the enclosed area, (3) NA0 consists of 15 shots denoted by "o," and (4) TOL-PTO-MAL array consisting of 18 records of 11 shots. Arrows indicate azimuthal direction to each station or mean azimuth to group of stations. The first number for each array (in parentheses) indicates the number of shots, and the second number indicates the distance in degrees.

part due to the irregular distribution of shot locations and variations in their source functions. The prominent secondary arrival has a phase velocity of about 1.6 km/sec and arrives with an azimuth of about 300°.

Figure 7 shows results from MAJO-South array for the same three frequency ranges as in Figure 6. A prominent secondary arrival appears in the $P + 6$ sec windows, with phase velocity of about 1.6 and azimuth of about 260°. Results from the NA0 array are shown in Figure 8. The secondary arrival appears best in the $P + 7$ sec window and has a phase velocity of about 1.8 km/sec and azimuth of about 270°. The array made by combining 18 records of 11 shots at 3 stations provided results shown in Figure 9. Here, the $P + 7$ sec window shows a low-phase velocity (about 2.3 km/sec) arrival as the primary phase, with azimuth of about 117°. This arrival in particular appears very similar in location and delay time to an arrival obtained by Lynnes and Lay (1989) from WWSSN and Canadian data using a semblance technique.

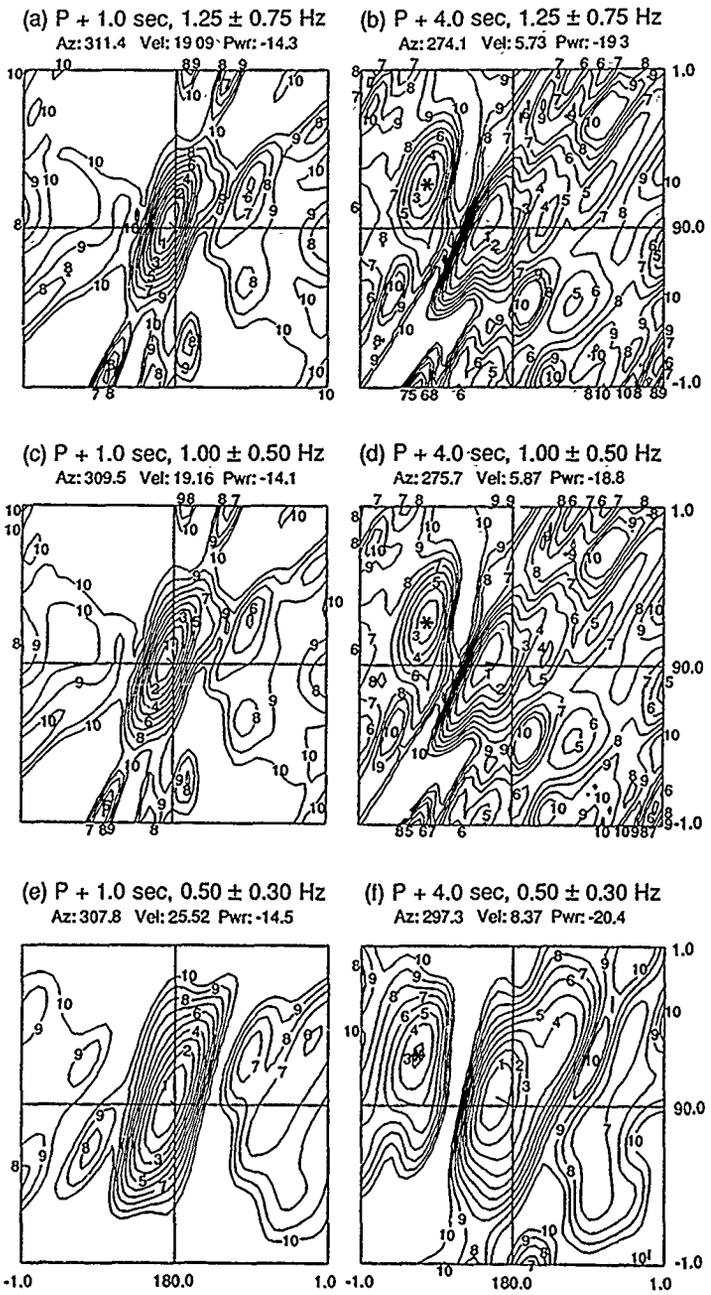

FIG. 6. Similar to Figure 1 but derived from the reciprocal array MAJO-North. The maximum slowness value is 1.0 sec/km, and results for three different frequency passbands are shown. The prominent secondary arrival in the P + 4 sec window (denoted by *) has a phase velocity of about 1.6 km/sec and azimuth of about 300°.

DISCUSSION

F-k analysis of NORESS data from three seismic sources provides remarkably consistent results regarding the azimuthal direction and phase velocity of a secondary source lying southwest of the array, in the region of Lake Mjosa. The source-receiver azimuthal directions were such that the secondary arrival represents backscattering for the Kazakh explosion and almost normal direction of scattering

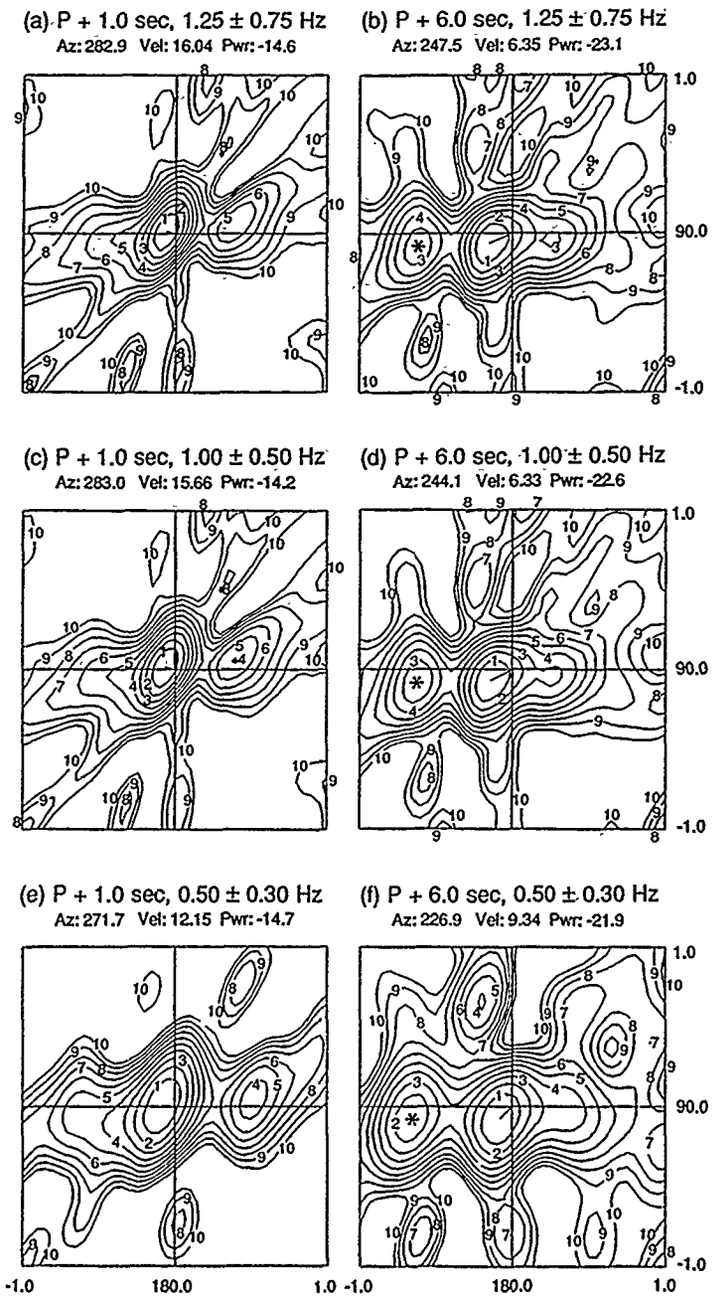

FIG. 7. Similar to Figure 6 but derived from the reciprocal array MAJO-South. The prominent secondary arrival in the P + 6 sec window (denoted by *) has a phase velocity of about 1.6 km/sec and azimuth of about 260°.

for the other two events. It seems, therefore, that the scattering observed in this study is not strongly dependent on the direction of the incident energy.

Considering the local structure of Yucca Flat as a basin containing low-velocity tuffs and alluvium, Stead and Helmberger (1988) obtained synthetics that matched well with the observed waveforms and also explained the variation of coda levels with shot location found by Lynnes and Lay (1988). Gradual basin terminations were found to cause the greatest conversion of surface wave energy into teleseismic

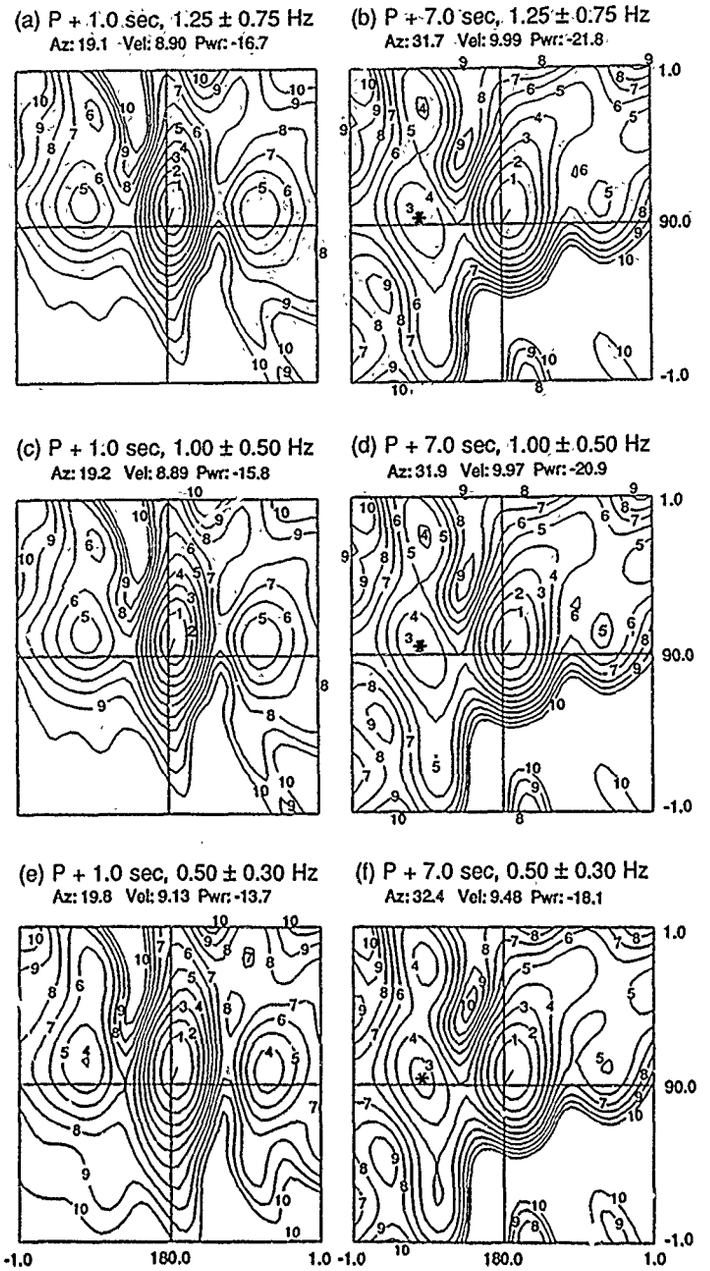

FIG. 8. Similar to Figure 6 but derived from the reciprocal array NAO. The prominent secondary arrival in the $P + 7$ sec window (denoted by •) has a phase velocity of about 1.8 km/sec and azimuth of about 270°.

P arrivals, appearing a few seconds after *P* and *pP*. Our results from the four reciprocal arrays based on the use of Yucca Flat explosions also indicate secondary sources of energy, arriving a few seconds after the direct *P*. Considering the seismic velocities in this region (Hays and Murphy, 1971), the observed low-phase velocity suggests these arrivals are due to Rayleigh waves. The azimuthal directions of the secondary sources in our study show large variations. Figure 10 shows Ferguson's (1981) model for Yucca Flat basin, derived from borehole data and gravity modeling,

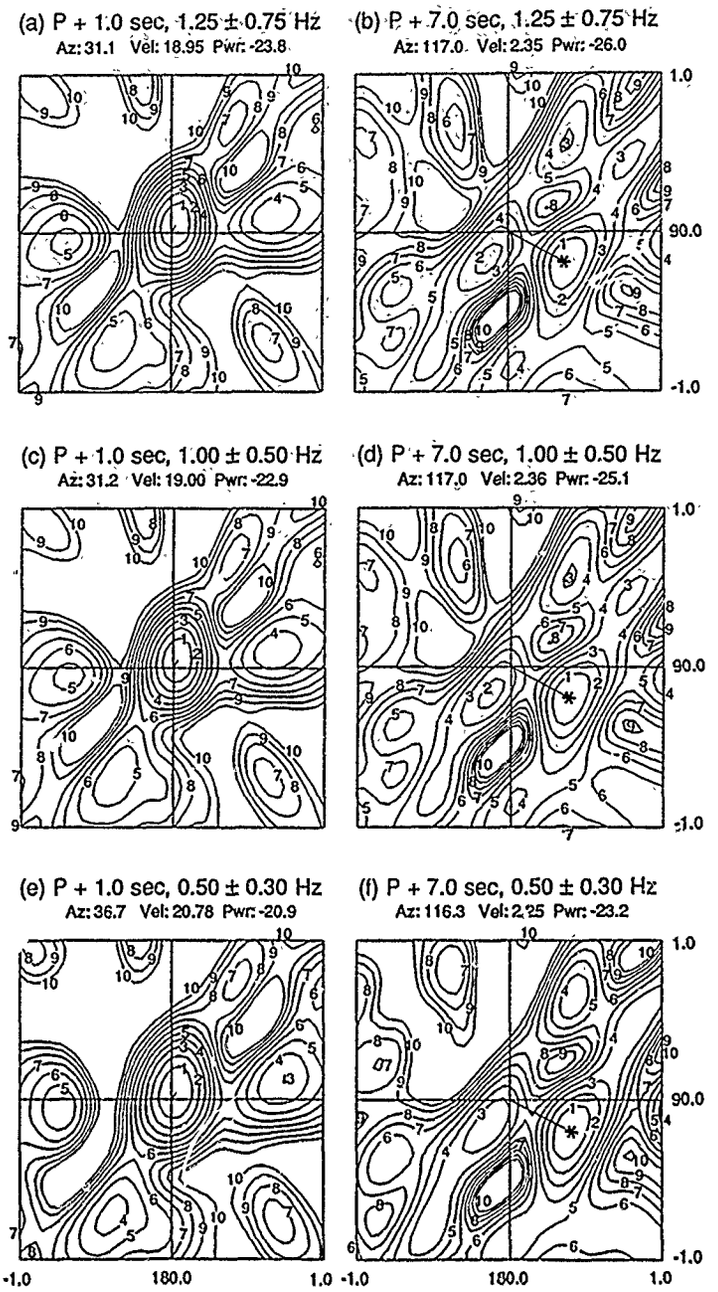

FIG. 9. Similar to Figure 6 but derived from the reciprocal array TOL-PTO-MAL. The prominent primary arrival in the $P + 7$ sec window (denoted by *) has a phase velocity of about 2.3 km/sec and azimuth of about 120°.

along with the Yucca fault. The contours indicate depth to the Tertiary–Paleozoic contact in meters. Locations of the 39 shots are superposed on this map. The secondary arrival observed from the MAJO-North reciprocal array (Fig. 6) is, therefore, likely to be due to Rayleigh → P scattering near the northwestern basin boundary of the Yucca Valley. Similarly, our results from the other three reciprocal arrays (Figs. 7 to 9) probably indicate arrivals due to Rayleigh → P scattering near other basin boundaries of the Yucca Valley (e.g., Lynnes and Lay, 1989).

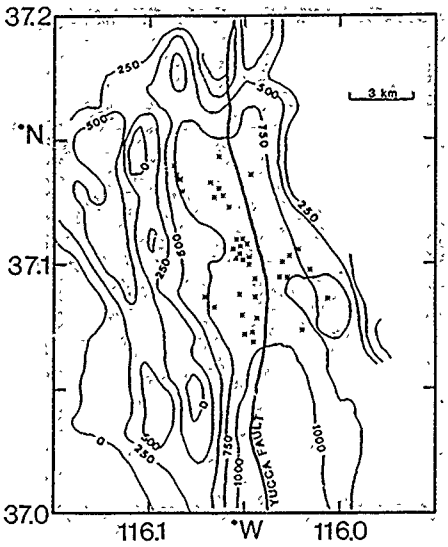

FIG. 10. Yucca Fault basin showing depth in meters to Tertiary-Paleozoic contact and the locations of 39 explosions used in the study.

CONCLUSIONS

Deterministic locations of both near-receiver and near-source scattering are investigated by using several *f-k* techniques and polarization analyses. *F-k* spectral analyses of NORESS array data from both explosion and earthquake sources are used to identify and locate sources of local scattering. Residual seismograms and *f-k* power difference plots have been found to be useful in isolating the secondary source from the effects of the primary source. The most prominent and consistent scattered arrivals have been identified as low-velocity *Rg* due to the scattering of incident *P* in the region of Lake Mjosa with large topographical relief. Four reciprocal arrays formed by using single station records of closely spaced Yucca Flat explosions are used to investigate near-source scattering. Considering the geological structure of Yucca Valley, the secondary sources of seismic energy appear to be due to $Rg \rightarrow P$ scattering near its basin boundaries.

ACKNOWLEDGMENTS

The authors thank Svein Mykkeltveit for providing valuable information regarding the Lake Mjosa region. This research was funded by the Defense Advanced Research Projects Agency and monitored by the Air Force Geophysics Laboratory under Contract F-19628-88-C-0051. The views and conclusions contained in this report are those of the authors and should not be interpreted as necessarily representing the official policies, either expressed or implied, of the Defense Advanced Research Projects Agency of the United States Government.

REFERENCES

Blandford, R., T. Cohen, and J. Woods (1976). An iterative approximation to the mixed-signal processor, *Geophys. J.* **45**, 677–687.

Ferguson, J. F. (1981). Geophysical Investigations of Yucca Flat, Nevada, *Ph.D. Thesis*, Southern Methodist University, Dallas, Texas

Gupta, I. N. and R. R. Blandford (1983). A mechanism for generation of short-period transverse motion from explosions, *Bull. Seism. Soc. Am.* **73**, 571–591.

Gupta, I. N., C. S. Lynnes, R. S. Jih, and R. A. Wagner (1989). A study of teleseismic *P* and *P* coda from U.S. and Soviet nuclear explosions, paper presented at the 11th Annual ARPA/AFGL Seismic Research Symposium, San Antonio, Texas.

Gupta, I. N., C. S. Lynnes, and R. A. Wagner (1990). Broadband *f-k* analysis of array data to identify sources of local scattering, *Geophys. Res. Letters* **17**, 183–186.

Hays, W. W. and J. R. Murphy (1971). The effect of Yucca Fault on seismic wave propagation, *Bull. Seism. Soc. Am.* **61**, 697–706.

Hudson, J. A. (1967). Scattered surface waves from a surface obstacle, *Geophys. J.* **13**, 441–458.

Hudson, J. A. and D. M. Boore (1980). Comments on "scattered surface waves from a surface obstacle" by J. A. Hudson, *Geophys. J.* **60**, 123–127.

Jurkevics, A. (1988). Polarization analysis of three-component array data, *Bull. Seism. Soc. Am.* **78**, 1725–1743.

Key, F. A. (1967). Signal-generated noise recorded at the Eskdalemuir seismometer array station, *Bull. Seism. Soc. Am.* **57**, 27–37.

Key, F. A. (1968). Some observations and analyses of signal generated noise, *Geophys. J.* **15**, 377–392.

Kværna, T. (1989) On exploitation of small-aperture NORESS type arrays for enhanced *P*-wave detectability, *Bull. Seism. Soc. Am.* **79**, 888–900.

Kværna, T. and D. J. Doornbos (1986). An integrated approach to slowness analysis with arrays and three-component stations, *NORSAR Sci. Rept. 2-85/86*, 60-69, Kjeller, Norway.

Kværna, T. and F. Ringdal (1986). Stability of various *f-k* estimation techniques, *NORSAR Sci. Rept. 1-86/87*, 29-40, Kjeller, Norway.

Lynnes, C. S. and Lay, T. (1988). Observations of teleseismic *P* wave coda for underground explosions, *Pageoph* **128, Nos. 1/2**, 231–249.

Lynnes, C. S. and Lay, T. (1989). Inversion of *P* coda for isotropic scatterers at the Yucca Flat Test Site, *Bull. Seism. Soc. Am.* **79**, 790–804.

McLaughlin, K. L., L. M. Anderson, and A. C. Lees (1987). Effects of local geologic structure on Yucca Flats, Nevada Test Site, explosion waveforms: two-dimensional linear finite-difference stimulations, *Bull. Seism. Soc. Am.* **77**, 1211–1222.

Ringdal, F. and T. Kværna (1989). A multi-channel processing approach to real time network detection, phase association, and threshold monitoring, *Bull. Seism. Soc. Am.* **79**, 1927–1940.

Spudich, P. and T. Bostwick (1987). Studies of seismic coda using an earthquake cluster as a deeply buried seismograph array, *J. Geophys. Res.* **92**, 10526–10546.

Stead, R. J. and D. V. Helmberger (1988). Numerical-analytical interfacing in two dimensions with applications to modeling NTS seismograms, *Pageoph* **128, Nos. 1/2**, 157–193.

TELEDYNE GEOTECH
ALEXANDRIA LABORATORIES
314 MONTGOMERY STREET
ALEXANDRIA, VIRGINIA 22314-1581

Manuscript received 6 March 1990

Bulletin of the Seismological Society of America, Vol. 80, No. 6, pp. 2242–2260, December 1990

ARRAY ANALYSIS OF SEISMIC SCATTERING

ANTON M. DAINTY AND M. NAFI TOKSÖZ

ABSTRACT

The use of high frequency arrays permits investigation of the spatial as well as the temporal character of the seismic wavefield in the frequency band 1–10 Hz. The authors have carried out investigations into seismic scattering at NORESS, FINESA, and ARCESS. Two principal methods have been used, frequency-wavenumber analysis of coda and coherency analysis of seismic phases. For regional seismograms, frequency-wavenumber analysis of *Lg* coda shows that *Lg*-to-*Lg* scattering dominates and that scattering is initially concentrated in the forward direction, changing to isotropic backscatter later in the coda. The *P* coda is more complex, although all cases studied show that energy is concentrated in the on-azimuth direction. However, different phase velocities are found for the three different cases studied, indicating that *P* coda is made up of several different contributions whose balance varies in different situations. In previous work, we have found that the decay of coherency with spatial separation scales as the wavelength for the *Lg* phase of regional events in the frequency band 1–10 Hz, declining to about 0.5 within one wavelength. Analysis of synthetic seismograms for realistic models of the area suggests that this loss of coherency is not due to dispersion, reaffirming a scattering interpretation. However, the decline in coherency is isotropic, seemingly contradicting the finding of forward scattering found in the frequency-wavenumber analysis. This may reflect a sensitivity of the coherency analysis to scattering within or very close to the array, while the frequency-wavenumber analysis favors scatterers at greater distance.

INTRODUCTION

The traditional method of gathering data in seismology is to record a detailed time history of motions from seismic events at sparsely distributed stations. Stations may be separated by tens or even hundreds of wavelengths or, where closer spacings are used, laid out as a linear profile to collect information in only one spatial dimension. The resulting data sets require strong simplification of the earth structure in the form of a model and the use of only those portions of the seismogram that can be interpreted as "phases," which usually only occupy a small portion in time of the data. These problems are particularly acute for regional data, where the frequencies are high (1–20 Hz), the wavelengths short (0.5–5 km), and the distances long (100–1000 km, of the order of 10–1000 wavelengths). With the advent of densely spaced, two-dimensional, high-frequency arrays, it is possible to examine the two-dimensional spatial structure of the wavefield under less restrictive models than conventional practice, and to examine portions of the seismogram such as coda that cannot be interpreted in terms of simple phases.

In this report we examine the effect of scattering on regional seismograms using data from three Fenoscandian arrays, ARCESS (Mykkeltveit *et al.*, 1987), FINESA (Korhonen *et al.*, 1987), and NORESS (Bungum *et al.*, 1985). The configurations and locations of these arrays are given in the cited references and also in Toksöz *et al.* (1990a, b). Two aspects of scattering will be examined. First, both *P* and *Lg* coda will be analyzed using frequency-wavenumber spectra. Second, the coherency of the *Lg* phase as a function of spatial separation between array seismometers

will be presented, with an emphasis on the topics of dispersion and isotropy. Since the primary purpose of this report is to illustrate the applicability of these types of analyses, we will concentrate on just three events, one from each array. All of the events are regional events at distances of 200–350 km; Table 1 gives details of the times, locations, and other relevant information. Details of theory, intepretation, and applications to teleseismic events are given in other articles (Harris and Dainty, 1988; Dainty and Harris, 1989; Dainty, 1990; Toksöz *et al.*, 1990a, b). The subjects chosen span the range of forward scattering (coherency of *Lg*) to back scattering (frequency-wavenumber spectral analysis of late *Lg* coda). Regional *P* coda may have a mixture of both forward and back scattering as well as crustal bounces and converted energy.

Frequency-Wavenumber Analysis of Regional Coda

Introduction

Seismic coda consists of the energy following a phase that cannot be readily explained by propagation in a layered model. The commonly accepted explanation for seismic coda is that it is due to scattered waves. There is considerable debate, however, as to what type of waves comprise coda, where they are scattered, and whether scattering is forward or back scattering and is single or multiple. For local events, the "standard model" of Aki and Chouet (1975) prescribes single back scattering, *S* to *S*, for coda following *S*. Sato (1977, 1984) points out that back scattering will only hold for times longer than about twice the *S* travel time and that forward scattering should be important between the *S* arrival and this time. For regional events, Herrmann (1980), Pulli (1984), and Nuttli (1986) suggested that coda following *Lg* ("*Lg* coda") consisted of *Lg* waves rather than *S* body waves; otherwise their theory is similar to that of Sato (1977), i.e., forward scattering is important between the *Lg* arrival and twice the *Lg* travel time, and a transition to back scattering occurs thereafter. All of the papers cited above assume single scattering, but increasingly multiple scattering is being considered on the basis of observation (Dainty *et al.*, 1987) or theory (Gao *et al.*, 1983; Wu, 1985; Frankel and Clayton, 1986; Frankel and Wennerberg, 1987), or both (Wu and Aki, 1988; Toksöz *et al.*, 1988).

Coda following *P* ("*P* coda") is more problematic. It is usually seen between the *P* arrivals and the first *S* arrival, typically *Sn* at regional distances. Sato (1984) models it as single scattering involving *P* to *P*, *P* to *S*, and *S* to *P*. The first two scattering types are "hindrunners" to *P*, but the third (*S* to *P*) is a "forerunner" to *S*. All three types are potentially important, and because the first *S* arrival time is

TABLE 1

Events Analyzed

(Azimuth is backazimuth from N)

Date	OT (UTC)	Latitude	Longitude	Location	Recorded	Distance (km)	Azimuth
2/27/85	12:58:31	59.3N	6.5E	Blåsjø*	NORESS	324	243°
11/15/85	13:53:37	61.1N	29.9E	Leningrad†	FINESA	209	99°
12/16/87	11:48:54	68.1N	33.2E	Kola‡	ARCESS	350	116°

* Blåsjø Quarry location from Dysart and Pulli (1987). OT from *S–P* time.

† OT and location from Ahjos *et al.* (1986).

‡ Quarry location from Mykkeltveit *et al.* (1987). OT from *S–P* time.

less than twice the P travel time for a normal P/S velocity ratio of 1.7, forward scattering should be important. In addition, Vogfjörd and Langston (1989) present evidence for multiple crustal bounces in the P coda time window for regional events recorded at NORESS. The examples they show have high stacking velocities, around 8 km/sec.

At least some aspects of the models presented above can be tested by frequency-wavenumber spectral analysis. In this analysis, the power spectrum in two spatial wavenumbers, east and north, for example, is estimated. This is equivalent to decomposing the seismic wavefield into plane waves. The backazimuth of a wave corresponding to a particular point in the spectrum is simply the angle measured from the north axis in a contour plot. If the signal is filtered with a narrow band pass filter around a center frequency f, the apparent velocity $V_a = f/k$, where k is the linear wavenumber measured from the origin of the contour plot. (The linear wavenumber is the reciprocal of the wavelength and bears the same relationship to the angular wavenumber as linear frequency to angular frequency.) For a guided or surface wave, V_a is the phase velocity, while for body waves, $V_a = V_t/\sin i = 1/p$, where V_t is the true velocity of the wave (P or S) in the surface rock beneath the array, i is the angle of incidence to the vertical, and p is the ray parameter for a flat layered medium. This relationship with the ray parameter or the phase velocity allows an identification of energy in the frequency-wavenumber spectrum with wavetype and raypath based on its apparent velocity and azimuth. While scattered energy may be off the backazimuth, it will still be identified with a phase if it has the apparent velocity characteristic of that phase. Furthermore, $V_a \geqq V_t$, further assisting in the identification of wavetype, although there is an ambiguity for near-vertically incident S.

In this paragraph we give a brief summary of the method of determining frequency-wavenumber spectrum by showing an application to teleseismic P coda (Harris and Dainty, 1988). Further details, together with some extensions to the method, will be presented in a future publication. Figure 1 shows a recording of a presumed nuclear test from the East Kazakh test site on the center seismometer of the NORESS array. A large coda analysis window for this seismogram and 21 similar seismograms from the B, C and D rings is indicated. The bottom half of Figure 1 shows the same seismogram filtered in a narrow pass-band with a center frequency of 2.4 Hz; analysis is carried out on this filtered signal. To calculate the frequency-wavenumber spectrum for such a long window, the window is broken up into subwindows of 1024 points (25.4 sec of data at NORESS), overlapped as necessary. The spatial covariance matrix (Capon, 1969) is computed for each window and averaged over the windows; this assumes that the coda is statistically stationary (Dainty, 1990). The frequency-wavenumber spectrum is then calculated by the Maximum Likelihood Method (MLM) (Capon, 1969). Figure 2 is a contour plot of the frequency-wavenumber spectrum for the data and window of Figure 1 out to a linear wavelength of 1.0. The prominent peak at low wavenumber has an apparent velocity of about 13 km/sec, typical of teleseismic P, and its azimuth is close to the source azimuth of 78°. Thus, we interpret this as energy that has traveled along a teleseismic P path but delayed relative to first P, i.e., scattered near the source. There is also a "ring" of energy with some embedded peaks at a linear wavenumber of about 0.6, corresponding to a velocity of 4 km/sec at this frequency, typical of Lg. We interpret this as energy scattered from teleseismic P within the crustal waveguide near the receiver, and coming into the receiver from a wide variety of azimuths. This example demonstrates the type of information that can be gained.

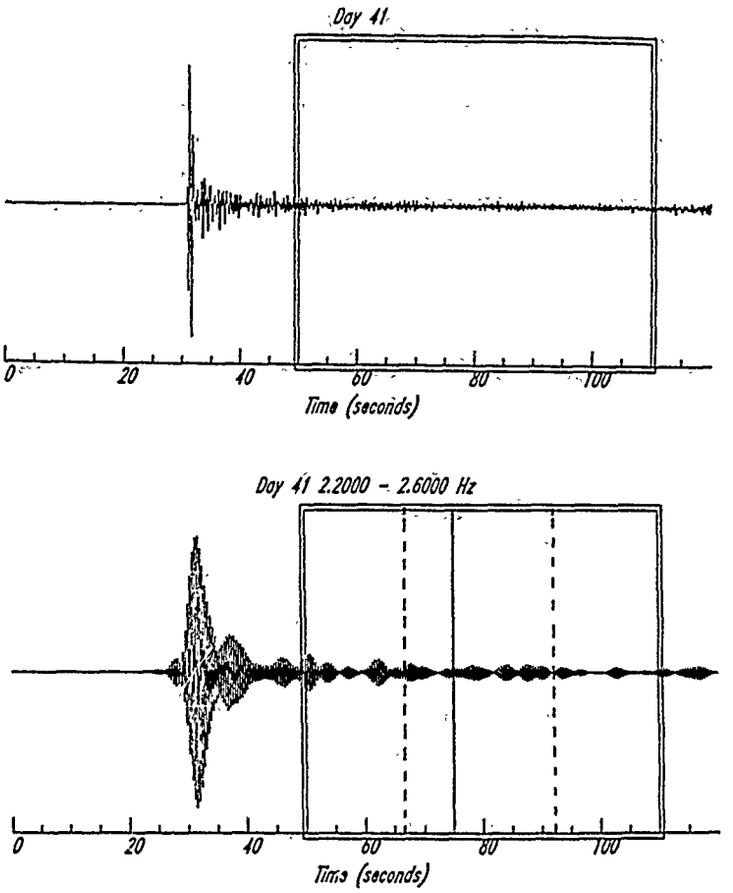

FIG. 1. Seismograms recorded at the center seismometer of NORESS 10 February 1985 from a suspected nuclear test at the East Kazakh test site (*top*). Original data with coda analysis window shown (*bottom*). Band-pass filtered data with two overlapping subwindows within the analysis windows. See text for discussion.

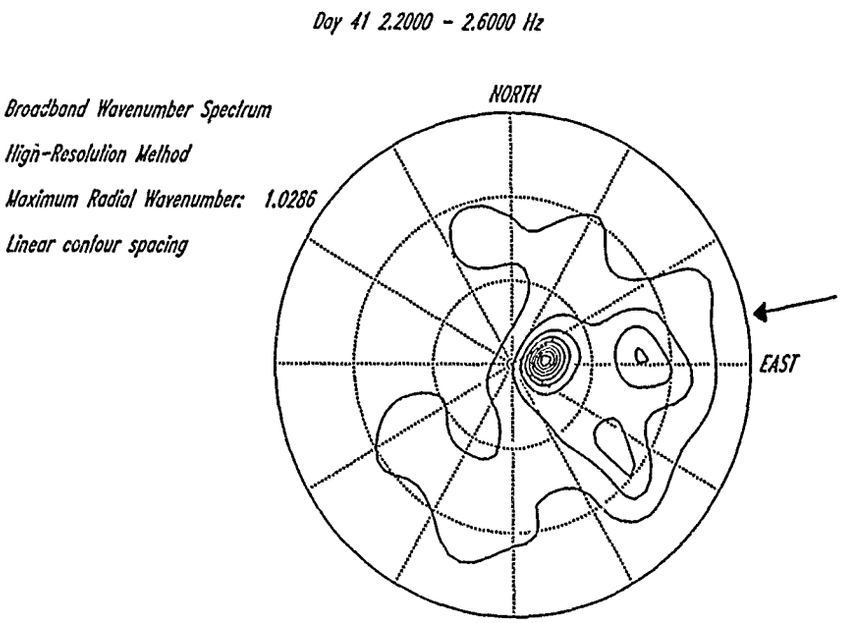

FIG. 2. Frequency-wavenumber spectrum for window in the bottom half of Figure 1. Wavenumber scale refers to linear wavenumber; arrow shows backazimuth to source.

Examples of Regional Coda

Three examples are shown, one each from NORESS, ARCESS, and FINESA. In these examples center frequencies in the range 2–4 Hz are used; we have found that results do not vary significantly in this frequency range. At lower frequencies the arrays do not have sufficient resolution to resolve different phases. At higher frequencies the spectra become more complicated, either because the wavefield contains more scattered wavetypes, or possibly because of spatial sampling problems.

Figure 3 is the seismogram of a quarry blast at Blåsjø recorded on the center seismometer at NORESS with three analysis windows indicated for *P*, early *Lg*, and late *Lg* coda. Frequency-wavenumber spectra are shown in Figures 4, 5, and 6, respectively. The *P* coda spectrum (Fig. 4) exhibits a peak at a velocity of 6 km/sec, typical of *Pg*, and an azimuth of 227°, close to the true azimuth of 243°. There is some indication of more widely scattered energy at this velocity and at velocities of 3–4 km/sec, typical of *Lg* and *Rg*, but the on-azimuth energy dominates. The early *Lg* coda (Fig. 5) shows overwhelmingly *Lg* phase velocities of about 4 km/sec, somewhat concentrated toward the on-azimuth direction. The late *Lg* coda (Fig. 6) again is dominated by *Lg* phase velocities, but the azimuth is widely scattered in a ring encompassing all directions. This is consistent with the back scattering model of late coda.

The seismogram from a quarry blast in the Kola Peninsula recorded at the center seismometer of ARCESS is shown in Figure 7 with similar analysis windows to the NORESS example. Figures 8, 9, and 10 are the corresponding frequency-wavenumber spectra. Energy in the *P* coda spectrum (Fig. 8) is again strong in the on-azimuth direction (114°), but the phase velocity of 8.5 km/sec is much faster than the NORESS example and is more typical of the multiple crustal reflections examined by Vogfjord and Langston (1989). The *Lg* coda spectra (Fig. 9, early coda; Fig. 10, late coda), on the other hand, confirms the NORESS observations. Velocities are close to an *Lg* phase velocity of 4 km/sec (although the dominant peaks may have a somewhat faster velocity, the "ring" has an average velocity near 4 km/sec). The azimuth distribution of energy changes from being grouped around the on-azimuth direction for the early coda to isotropic for the late coda.

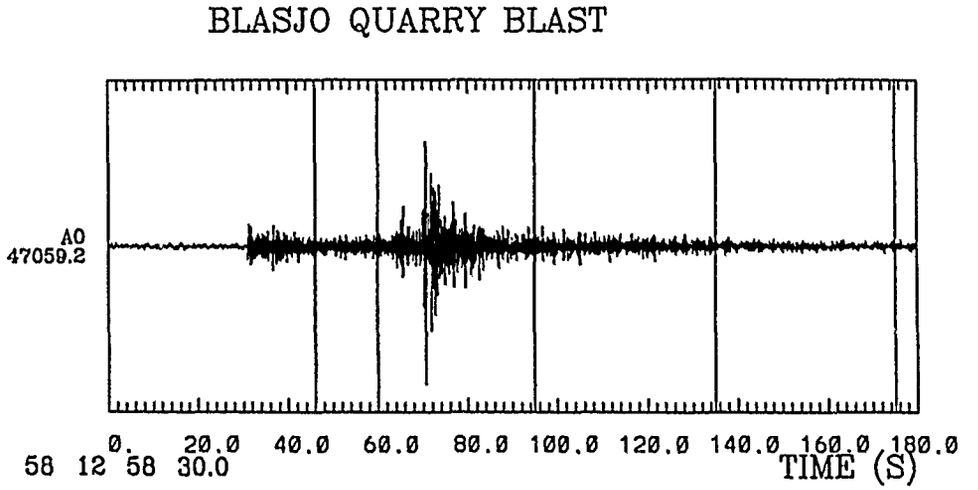

FIG. 3. Seismogram at center seismometer, NORESS, for a quarry blast on 27 February 1985 at Blåsjø quarry. Analysis windows shown for *P* coda (46 to 60 sec), early *Lg* coda (95 to 135 sec), and late *Lg* coda (135 to 175 sec).

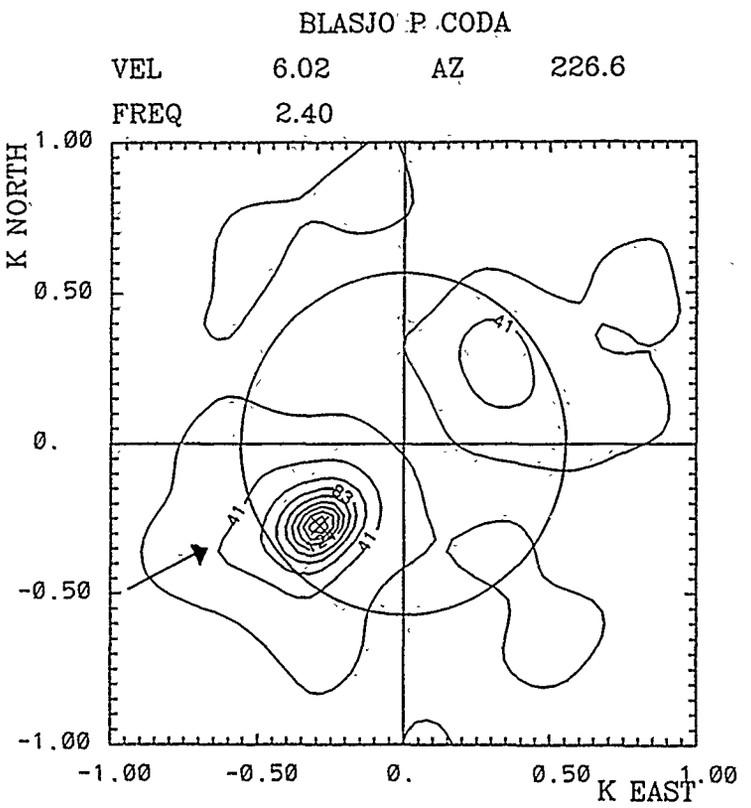

FIG. 4. Frequency-wavenumber spectrum for the *P* coda window, Figure 3. In this and all succeeding frequency-wavenumber spectra, wavenumber refers to linear wavenumber, the frequency (FREQ) is the analysis frequency, VEL and AZ are the phase velocity and azimuth, respectively, of the highest peak (marked by a cross), the arrow shows the backazimuth of the source, and the circle about the origin represents a phase velocity of 4 km/sec.

The final example is a quarry blast near Leningrad recorded at the FINESA array; one of the array seismograms is shown in Figure 11 with a window in the *P* coda and a window in the early *Lg* coda. Frequency-wavenumber spectra are given in Figures 12 and 13. The *P* coda (Fig. 12) shows on-azimuth (99°) energy, but with a phase velocity (4.1 km/sec) typical of *Lg*. The *Lg* coda window (Fig. 13) has the same ring of energy with an *Lg* phase velocity of 4 km/sec as seen for NORESS and ARCESS. There is a bias in the on-azimuth direction, presumably due to the window being in the early coda.

The results of this brief survey may be summarized as follows. The predictions of the "standard model" for *Lg* coda (Herrmann, 1980; Pulli, 1984; Nuttli, 1986) are confirmed: the coda consists of *Lg* waves, presumably scattered from *Lg*; at long times energy comes in from all directions, i.e., it is backscattered, but at shorter times forward scattering is important. The issue of multiple or single scattering, however, has not been addressed. These results indicate that coda *Q* from regional coda should be related to *Lg Q*, as suggested by Nuttli (1986) and used by him in assigning M_{Lg} to suspected nuclear tests. The situation for *P* coda is not so clear, however. In all three cases examined on-azimuth energy is dominant, but the phase velocity is different in each case. Only the ARCESS result (phase velocity 8.5 km/sec) is readily explainable by crustal bounces suggested by Vogfjord and Langston (1989). One important consideration for both types of coda, however, is that the frequency-wavenumber spectrum is an effective tool for separating components that have reasonably coherent wavefronts across the array. Scattering within the array,

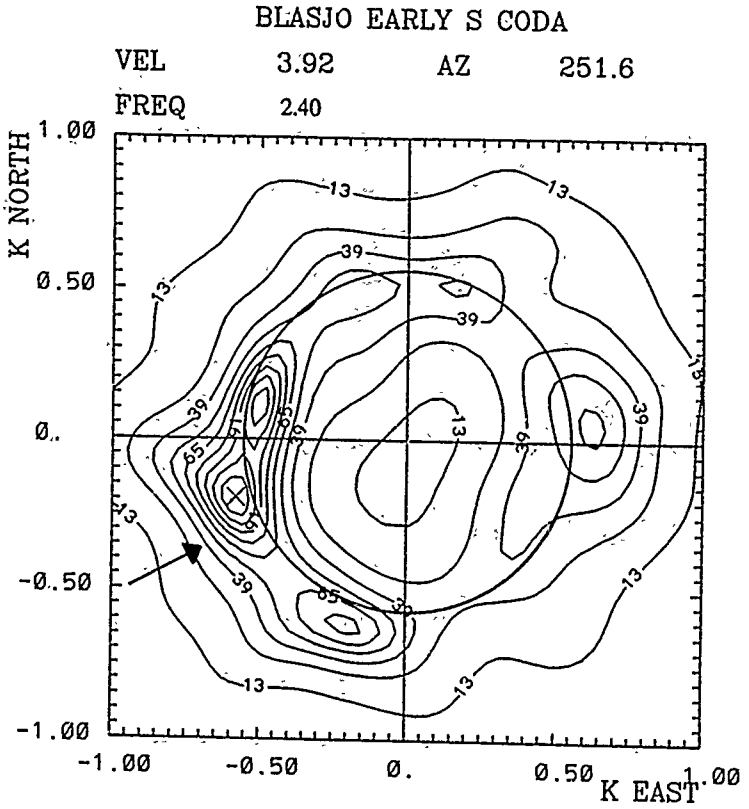

FIG. 5. Frequency-wavenumber spectrum for the early *Lg* coda window, Figure 3.

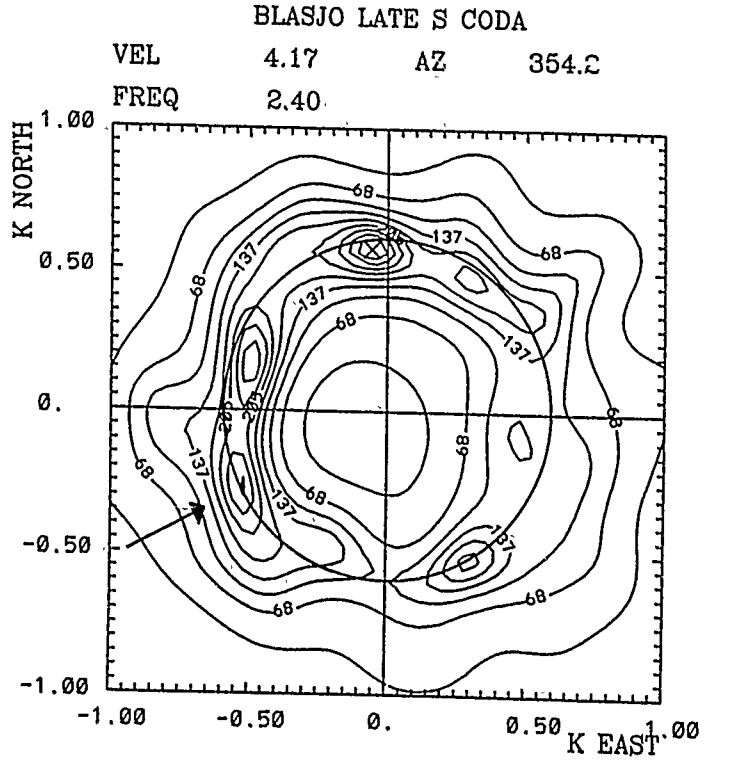

FIG. 6. Frequency-wavenumber spectrum for the late *Lg* coda window, Figure 3.

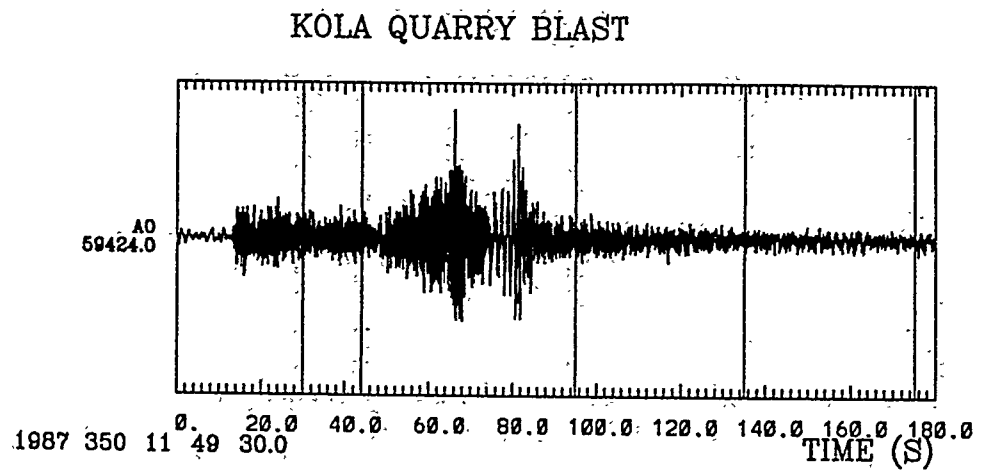

FIG. 7. Seismogram at center seismometer, ARCESS, for a quarry blast on 16 December 1987 in the Kola Peninsula. Analysis windows shown for *P* coda, early *Lg* coda, and late *Lg* coda.

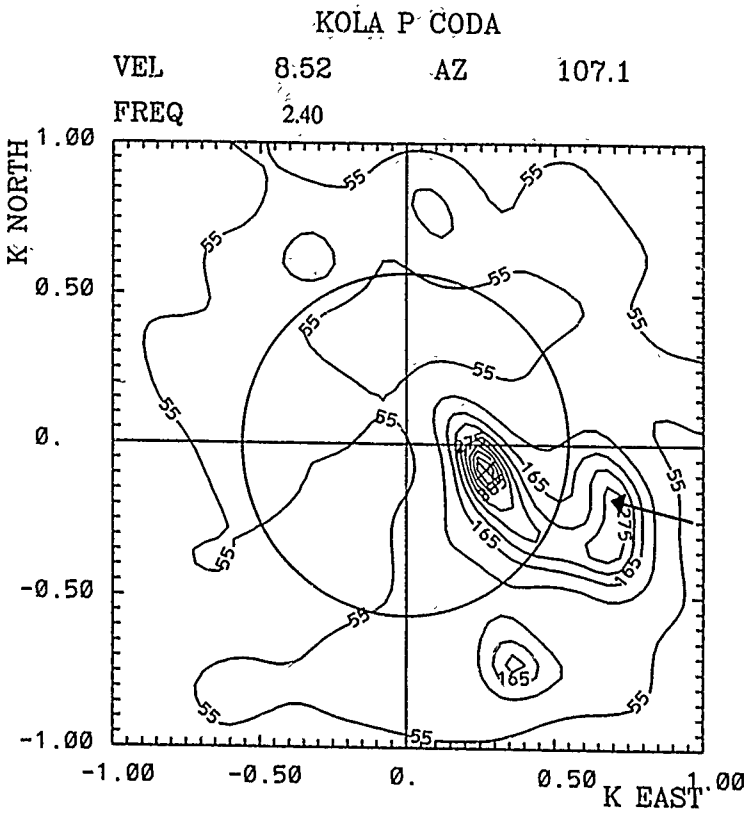

FIG. 8. Frequency-wavenumber spectrum for the *P* coda window, Figure 7.

for example, will not be readily detected because the resulting disturbance will not be a plane wave across the array. The next section will present a method sensitive to such an effect.

COHERENCY ANALYSIS OF *LG*

Introduction

An important effect of scattering at regional distances is the incoherence of seismic phases even at closely spaced stations, often called fluctuations. While some

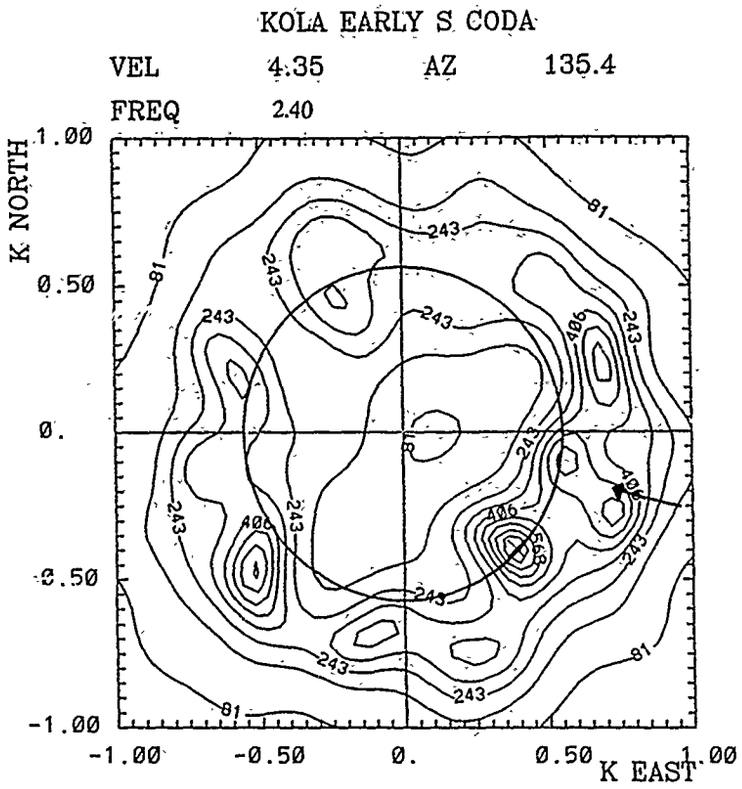

FIG. 9. Frequency-wavenumber spectrum for the early *Lg* coda window, Figure 7.

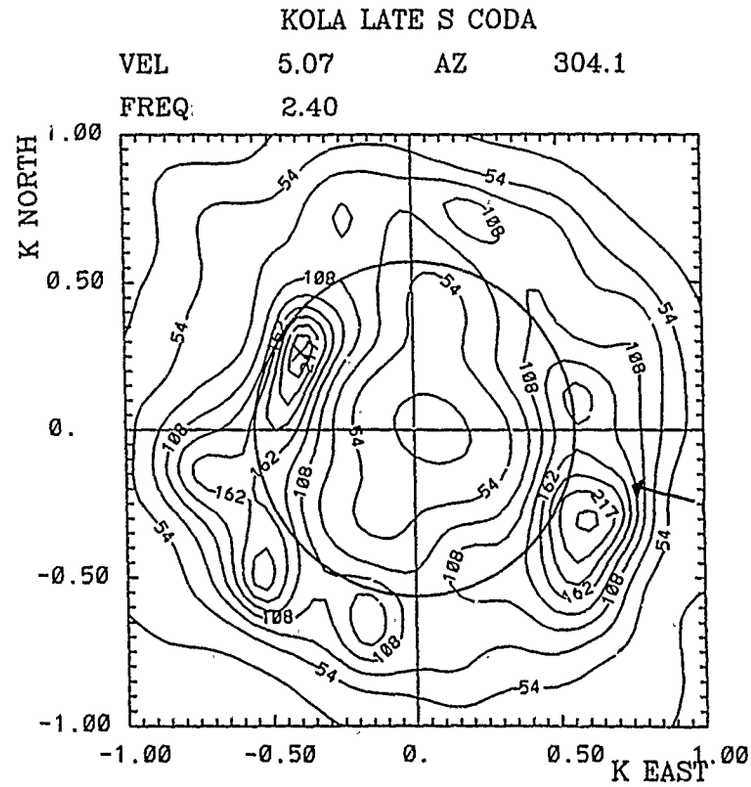

FIG. 10. Frequency-wavenumber spectrum for the late *Lg* coda window, Figure 7.

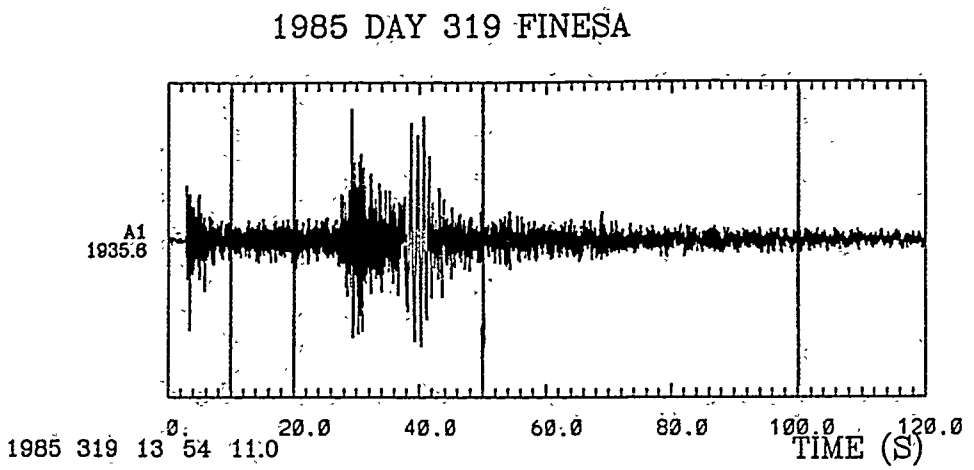

FIG. 11. Seismogram recorded at a seismometer of the FINESA array from a quarry blast on 15 November 1985 near Leningrad. Analysis windows indicated for *P* coda and *Lg* coda.

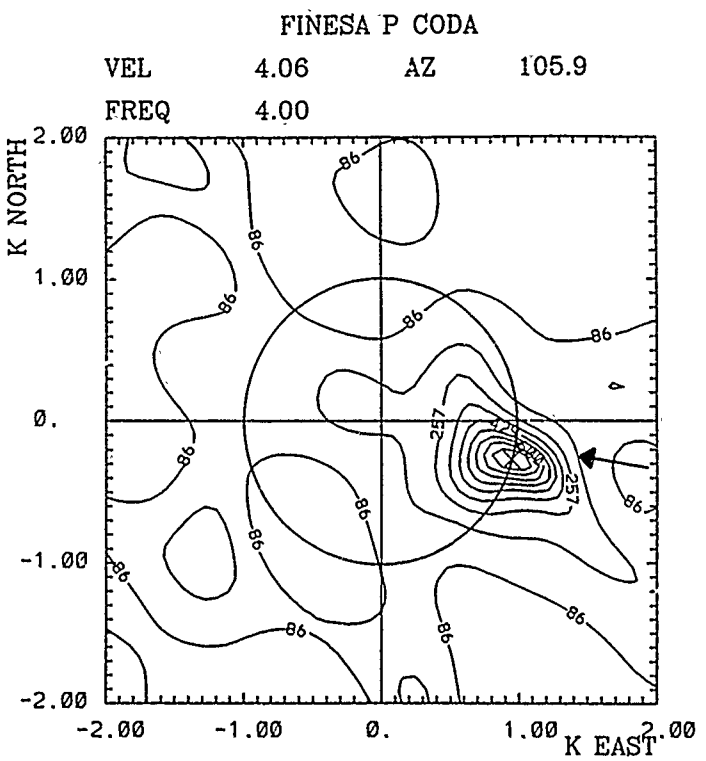

FIG. 12. Frequency-wavenumber spectrum for the *P* coda window, Figure 11.

work has been done on regional phases such as *Lg* (Der *et al.*, 1984; Ingate *et al.*, 1985), the effect has been studied more extensively for teleseismic arrivals (Aki, 1973; Capon, 1974; Flatté and Wu, 1988). In addition, some work has also been carried out in the field of strong-motion studies (Harichandran and Vanmarcke, 1986; Toksöz *et al.*, 1990a). Our goal in this section is to discuss measurements of the coherence of the regional phase *Lg* at NORESS, ARCESS, and FINESA. All of the areas studied have Precambrian or Paleozoic crystalline rock exposed at the surface, thus near-surface sedimentary layering or weathering is not a factor. Since these measurements and their interpretation in terms of a scattering model are the

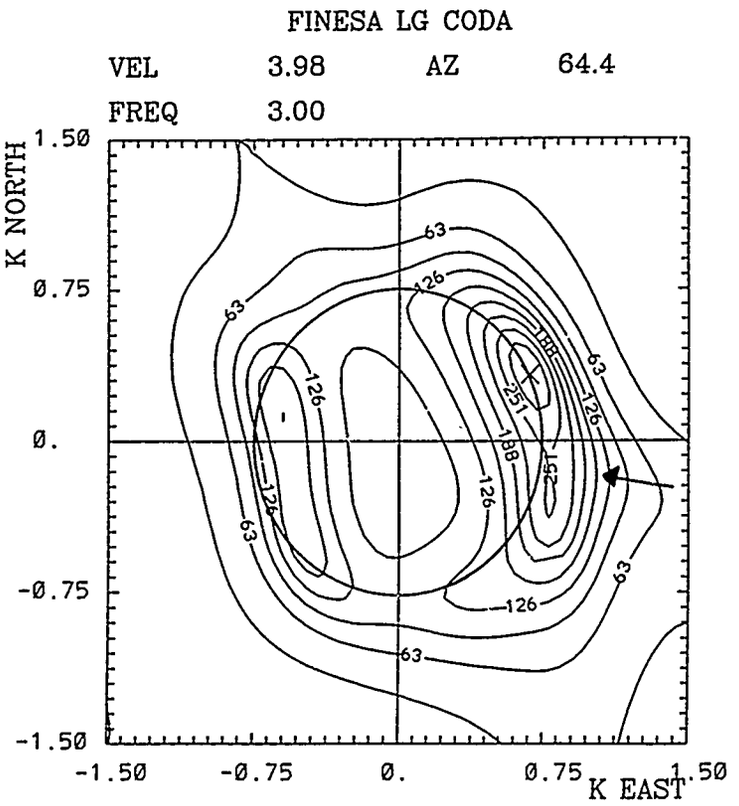

FIG. 13. Frequency-wavenumber spectrum for the *Lg* coda window, Figure 11.

subject of another communication (Toksöz *et al.*, 1990b), only a brief summary of the measurements will be presented here, and the interpretation in terms of a self-similar scattering model will not be presented, since it is a two-dimensional model at this stage (Toksöz *et al.*, 1990b). Instead, questions of the influence of dispersion on the coherence and of the isotropy of the coherence will be examined (Der *et al.*, 1984) and their implications for the location of scatterers discussed.

Previous work has used fluctuations in amplitude and phase (arrival time) of teleseismic *P* waves at the LASA (Aki, 1973; Capon, 1974) and NORSAR (Capon and Berteussen, 1974; Flatté and Wu, 1988) arrays to estimate statistical parameters of *P* velocity perturbations in the lithosphere. One result of some importance from this work is the short distance (~10 km) over which arrivals lose coherence. For regional phases at higher frequencies even more rapid loss of coherence is to be expected. To evaluate the effect of scattering on direct phases, the spatial coherency has been calculated using methods developed for analysis of strong-motion array records (Harichandran and Vanmarcke, 1986). The lagged coherency is

$$C(x,\omega) = \frac{S_{ij}(x,\omega)}{[S_{ii}(\omega)S_{jj}(\omega)]^{1/2}} \tag{1}$$

where S_{ij} is the cross spectrum of seismograms $s(x_i)$, $s(x_j)$, lagged to remove time shifts due to traveling wave propagation; the separation $x = x_i - x_j$. S_{ii} and S_{jj} are the autospectra of the two seismograms. To compute the coherency we used methods due to Jenkins and Watts (1969) and Harichandran and Vanmarcke (1986), further

described in Toksöz *et al.* (1990b). Lengths of data in the seismograms are 10–25 sec. The calculation is performed for every possible pair of seismograms in the array. These determinations are then averaged over an appropriate spatial interval and the standard deviations found; the Fisher Z-transform is used to normalize the distribution (Jenkins and Watts, 1969).

An important difference between teleseismic and regional propagation, however, is the direction of propagation of seismic energy relative to the plane of the array (the earth's surface). For teleseismic waves the energy travels nearly perpendicular to the earth's surface and is thus not dispersive. In addition, the coherence structure in the plane of the array will be spatially isotropic, since no direction is preferred. Regional phases, however, travel horizontally through a layered medium and thus *Lg* in particular should be dispersed; this could in principle cause a loss of coherency in the source-receiver direction. For this, and perhaps other reasons, the coherency of *Lg* could be different along the source-receiver direction and the direction perpendicular to it. Der *et al.* (1984) in fact found such a difference for frequencies less than 2 Hz, with coherence less in the perpendicular direction than the parallel direction at a separation of 5 km. They interpreted this as being due to the combined effects of dispersion and forward scattering ("multipathing") in a 30° wedge around the parallel direction. Our purpose in this section is to examine these questions for frequencies near 2 Hz, particularly the issue of forward scattering and scattering near the array.

Observations

First, a brief review of the observations of Toksöz *et al.* (1990b) will be given. Data from the three events in Table 1 recorded at ARCESS, FINESA, and NORESS were used. Time windows for analysis are selected to include not only *Lg* but also *Sn* and *Sg*, if they are present. Any *Rg* phase, however, was excluded. It was found that the coherency analysis was not sensitive to small shifts of the window. To illustrate the analysis, we choose the Blåsjø event recorded at the NORESS array. Figure 14 shows the center seismometer seismogram with the analysis window indicated. Figure 15 shows the coherency for 2 Hz. This Figure illustrates that coherency decays with increasing spatial separation; we attribute this decline in

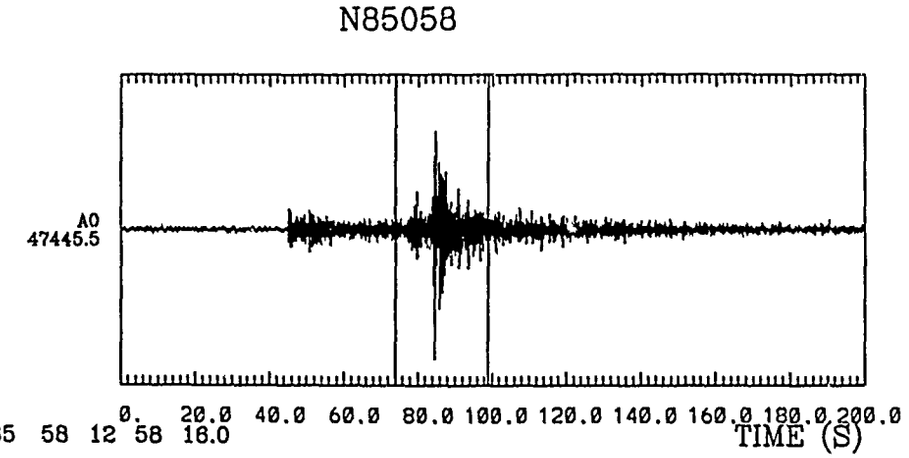

FIG. 14. Seismogram recorded at the center seismometer, NORESS, from a quarry blast on 27 February 1985 at Blåsjø quarry. Analysis window for spatial coherency of *Lg* indicated.

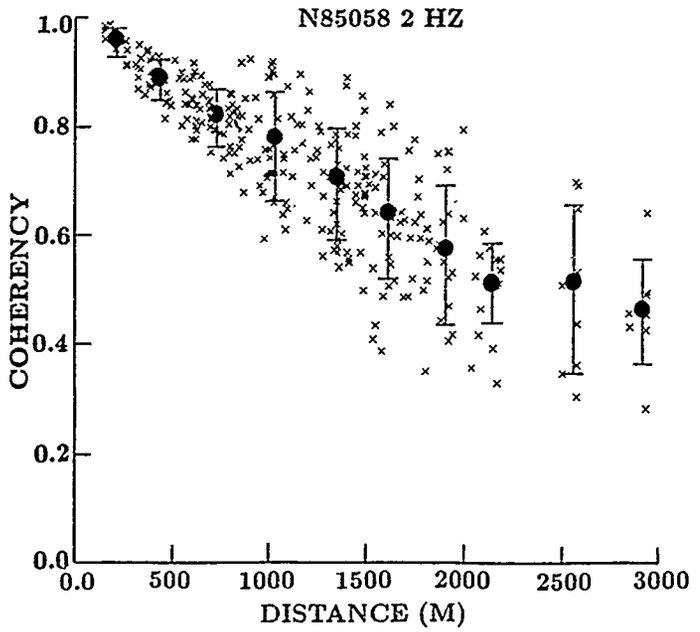

FIG. 15. Coherency as a function of spatial separation at 2 Hz for the *Lg* window, Figure 14. Each cross is a coherency estimate from a single pair of sensors without regard to the orientation of the separation vector. Filled circles with error bars are spatial averages.

coherency to scattering. By looking at different frequencies we may examine different wavelengths. In an attempt to gain an integrated look at the data, Figure 16 plots the spatially averaged coherencies for this event at all frequencies analyzed against distance in *wavelengths*. In Figures 15 and 16, spatial separation has been taken without regard to the orientation of the separation vector between individual stations. Intriguingly, within error limits it appears that the curves of decline of coherency with separation for the different frequencies are all very similar if the separation is scaled to the wavelength. The equivalent curves for the other events are similar; this may reflect the similarity of site/path heterogeneities for these crystalline rock sites within the Fenoscandian shield. Note that the coherency declines to ~0.5 within about one wavelength. These results were interpreted in terms of a self-similar model of scattering by Toksöz *et al.* (1990b).

We now wish to very briefly review some alternatives to the interpretation of Toksöz *et al.* While the results will be negative, this in itself will be enlightening. First, could the decline of coherency with increasing spatial separation be due to dispersion? To analyze this possibility, Figure 17 shows complete theoretical seismograms for a model of the Fenoscandian crust from Toksöz *et al.* (1990c) with an analysis window for *Lg* indicated. These seismograms were computed for a layered (one-dimensional) model using complete wavenumber integration (Mandal and Mitchell, 1986) at 100-meter intervals over a range of 249–251 km and include all effects of dispersion but no scattering. The source is a vertical point force at 40 meters depth, to simulate a quarry blast. Figure 18 presents the coherency at 4 Hz; it is high ($\geqq$0.9) over the full range of separations, approximately two wavelengths at this frequency. While a fuller investigation is needed, the preliminary results shown in Figure 18 suggest that dispersion is not the explanation of the observed coherencies.

The second alternative is the influence of forward scattering, which would make the coherency greater in the parallel direction than the perpendicular direction

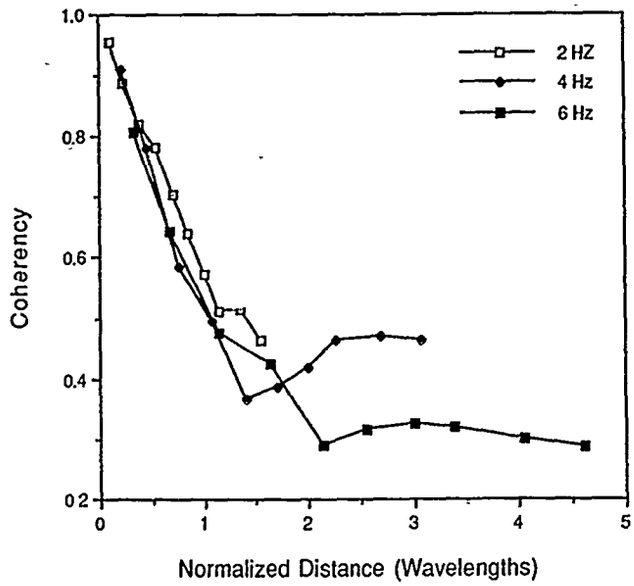

FIG. 16. Coherency versus distance normalized to wavelength for *Lg* window, Figure 14.

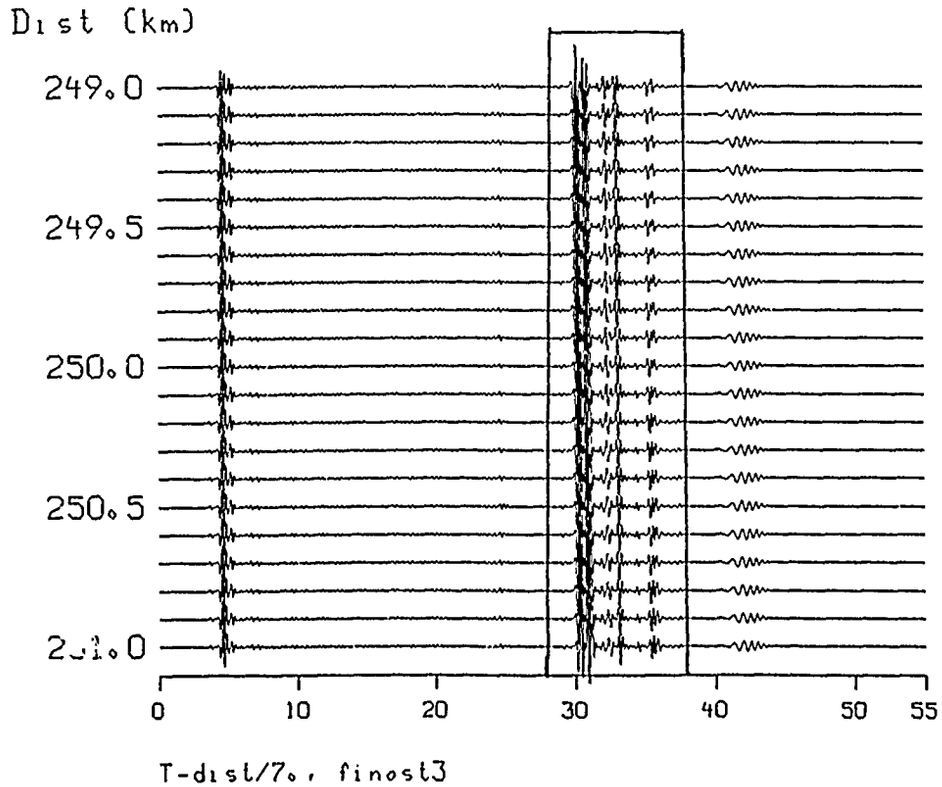

FIG. 17. Complete synthetic seismograms computed from model of Toksöz et al. (1990c) at intervals of 100 meters from 249–251 km range. Coherency analysis window for *Lg* shown.

relative to the source-receiver line, at the same separation. If dispersion is an important factor, it would have the opposite effect. Der *et al.* (1984) found coherency lower in the perpendicular direction for *Lg*, although at lower frequencies and larger separations than in this study, and ascribed it to the combined influence of forward

scattering and dispersion, with the effect of forward scattering presumably dominating. To test this idea, two subarrays were constructed from the NORESS array for the Blåsjø event of Figure 14, one parallel and one perpendicular to the source-receiver line (Figure 19). The coherency calculated for the two cases did not differ significantly; results are shown in Figure 20 for the 2 Hz case. This indicates that

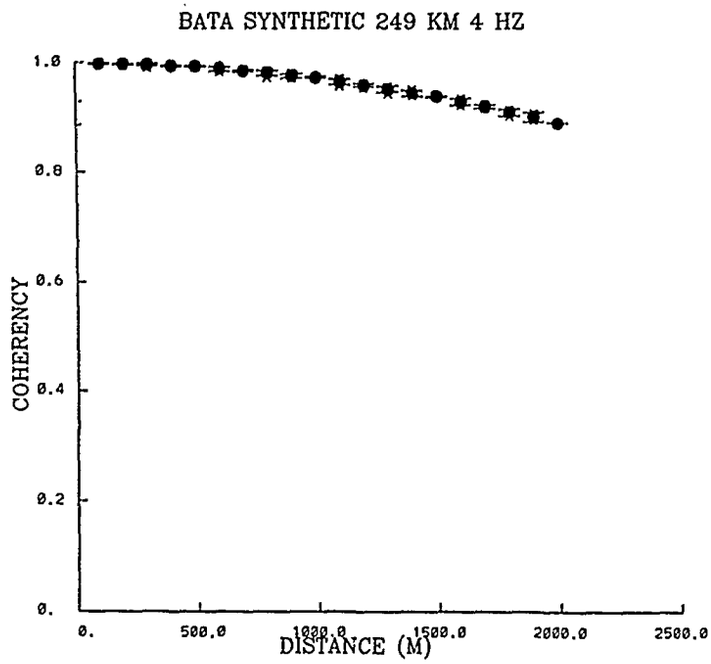

FIG. 18. Coherency against spatial separation at 4 Hz for the *Lg* window, Figure 17.

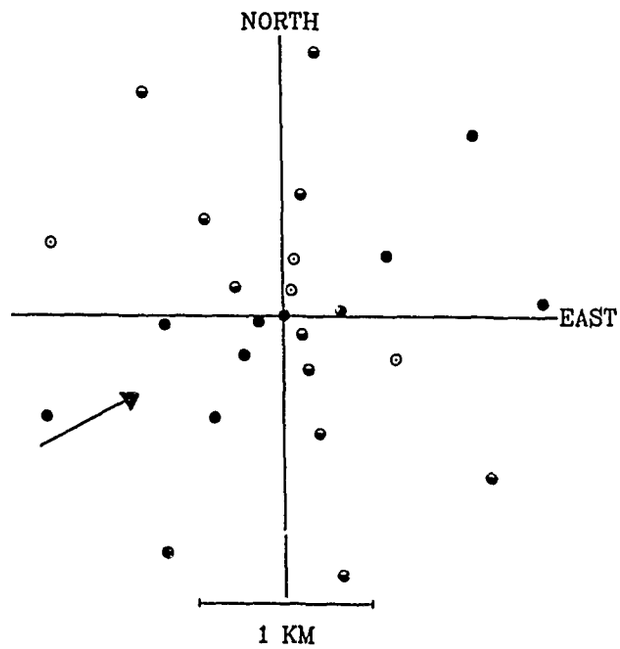

FIG. 19. Subarrays of NORESS for coherency analysis of the *Lg* window, Figure 14. Filled circles, parallel to propagation direction; half-filled, perpendicular (center station used for both); open circles, not used.

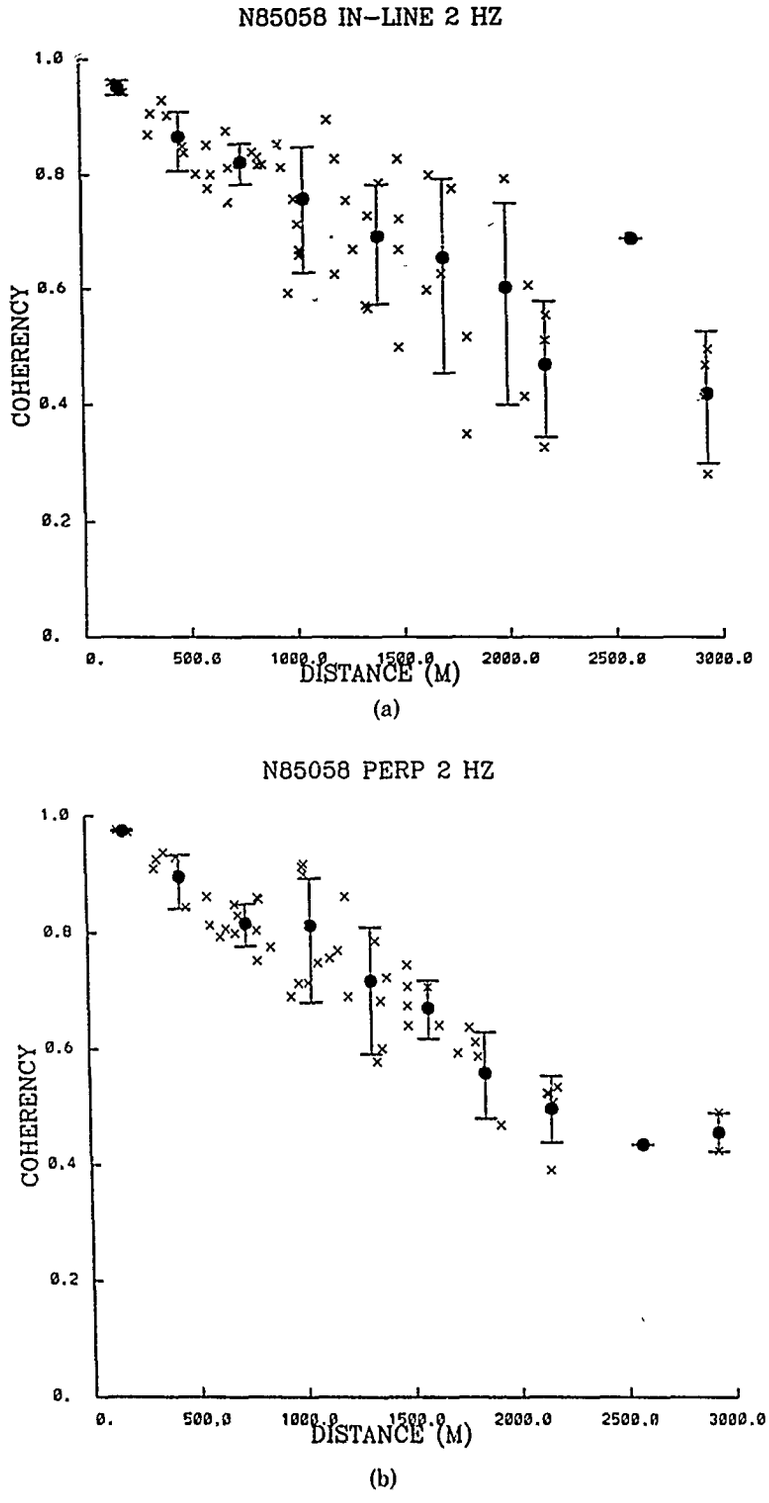

FIG. 20. Coherency against spatial separation at 2 Hz for the *Lg* window, Figure 14. (a) parallel; (b) perpendicular. See text for discussion.

the coherency is isotropic, presumably due to the effect of isotropic scattering. Such scattering must occur near the array, since there is not sufficient time for energy to propagate from further distances.

These alternatives, especially the second, are more subtle than might appear at

first sight because they deal with the issue of three-dimensional scattering. Interpretations in Toksöz *et al.* (1990b) were two-dimensional. However, the results shown here seem to support the conclusions of Toksöz *et al.* that scattering is the primary factor in controlling coherency for regional phases in the frequency range 2–10 Hz.

Discussion

In this article we have concentrated on analysis methods for arrays that may be used to examine scattering, rather than on interpretations. Nonetheless, the results obtained present a challenge of integration to theory. The first method presented, frequency-wavenumber spectra, is best suited for signals that consist of a number of plane wave components. It probably accentuates waves scattered at distances from the array greater than the array diameter, since such waves will have reasonably planar wavefronts by the time they cross the array. The second analysis method, spatial coherency, seems to be sensitive to scattering within or in the immediate vicinity of the array. The two methods, when applied to *Lg* and its coda, give seemingly contradictory results. Frequency-wavenumber spectra indicate that isotropic back scattering only becomes important late in the coda. Spatial coherency seems to indicate that scattering has an isotropic effect within the *Lg* phase itself. The frequency-wavenumber results are in agreement with the "standard model" of Aki and Chouet (1975), modified for the regional case by considering the scattering to be *Lg* to *Lg* (Herrmann, 1980; Pulli, 1984; Nuttli, 1986). The spatial coherency results do not agree with the standard model. The only possible explanation is that the two measurements are looking at different phenomena, even though the same phase and the same event are being examined. The different distances of the scatterers from the array apparently seen by the two methods may resolve this seeming paradox. The difference between results reported here and those of Der *et al.* (1984) are presumably due to different conditions of measurement: our measurements are at higher frequencies (2 Hz and greater instead of below 2 Hz) and shorter measurement baselines (up to 3 km instead of 5 km and greater). If this is so, it may imply a change in the nature of *Lg* scattering around 2 Hz.

The *P* wave coda, so far only investigated using frequency-wavenumber spectra, is more enigmatic. All three cases presented here show strongly on azimuth energy, but there is a different phase velocity in each case. This may indicate a greater complexity of the *P* coda due to a greater number of ways for energy to enter. Potentially, multiple crustal reflections, *P*-to-*P* scattering, *P*-to-*S* scattering, and *S*-to-*P* scattering could all contribute. The calculations of Sato (1984), who considers only the scattering components, show that differences can exist in the *P* coda because of different levels of each contribution. Vogfjord and Langston (1989) have demonstrated the presence of multiple crustal reflections. A composite model of *P* coda appears necessary.

Acknowledgments

D. Harris of Lawrence Livermore National Laboratory supplied programs for computing frequency-wavenumber spectra coherency and gave advice on their use. Data for the Fenoscandian events was collected during visits to the NORSAR Data Processing Center, Kjeller, Norway (by A.M.D.). The help of the director, F. Ringdal, and staff members S. Mykkeltveit and T. Kværna is gratefully acknowledged. B. Mandal made the calculations for Figure 17. Part of the work reported here was carried out while A.M.D. was a National Research Council Fellow at the Air Force Geophysics Laboratory. This work was supported by the Defense Advanced Research Projects Agency through contract F19628-89-K-0020 administered by the Air Force Geophysics Laboratory (AFGL).

REFERENCES

Ahjos, T., E. Pelkonen, M. Franssila, L. Mustila, and M. Komppa (1986). Seismic events in northern Europe November–December 1985, Institute of Seismology, University of Helsinki, Helsinki.

Aki, K. (1973). Scattering of *P* waves under the Montana Lasa, *J. Geophys. Res.* **78**, 1334–1346.

Aki, K. and B. Chouet (1975). Origin of coda waves: source, attenuation and scattering effects, *J. Geophys. Res.* **80**, 3322–3342.

Bungum, H., S. Mykkeltveit, and T. Kværna (1985). Seismic noise in Fenoscandia, with emphasis on high frequencies, *Bull. Seism. Soc. Am.* **75**, 1489–1513.

Capon, J. (1969). High-resolution frequency-wavenumber spectrum analysis, *Proc. IEEE* **57**, 1408–1418.

Capon, J. (1974). Characterization of crust and upper mantle structure under Lasa as a random medium, *Bull. Seism. Soc. Am.* **64**, 235–266.

Capon, J. and K. A. Berteussen (1974). A random medium analysis of crust and upper mantle structure under NORSAR, *Geophys. Res. Lett.* **1**, 327–328.

Dainty, A. M. (1990). Studies of coda using array and three-component processing, *Pageoph* **132**, 221–244.

Dainty, A. M. and D. B. Harris (1989). Phase velocity estimation of diffusely scattered waves, *Bull. Seism. Soc. Am.* **79**, 1231–1250.

Dainty, A. M., R. M. Duckworth, and A. Tie (1987). Attenuation and backscattering from local coda, *Bull. Seism. Soc. Am.* **77**, 1728–1747.

Der, Z., M. E. Marshall, A. O'Donnell, and T. W. McElfresh (1984). Spatial coherence structure and attenuation of the *Lg* phase, site effects, and interpretation of the *Lg* coda, *Bull. Seism. Soc. Am.* **74**, 1125–1147.

Dysart, P. S. and J. J. Pulli (1987). Spectral study of regional earthquakes and chemical explosions recorded at the NORESS array, in Tech. Rep. for the Period 1 April–30 June 1987, Tech. Rep. C87-03, Center for Seismic Studies, Arlington VA, pp. 3-21–3-44.

Flatté, S. M. and R.-S. Wu (1988). Small-scale structure in the lithosphere and asthenosphere deduced from arrival time and amplitude fluctuations at NORSAR, *J. Geophys. Res.* **93**, 6601–6614.

Frankel, A. and R. Clayton (1986). Finite difference simulations of seismic scattering: implications for the propagation of short-period seismic waves in the crust and models of crustal heterogeneity, *J. Geophys. Res.* **91**, 6465–6489.

Frankel, A. and L. Wennerberg (1987). Energy-flux model of seismic coda: separation of scattering and intrinsic attenuation, *Bull. Seism. Soc. Am.* **77**, 1223–1251.

Gao, L. S., L. C. Lee, N. N. Biswas, and K. Aki (1983). Comparison of the effects between single and multiple scattering on coda waves, *Bull. Seism. Soc. Am.* **73**, 377–389.

Harichandran, R. S. and E. H. Vanmarcke (1986). Stochastic variation of earthquake ground motion in space and time, *J. Eng. Mech. ASCE* **112**, 154–174.

Harris, D. B. and A. Dainty (1988). High-resolution investigation of teleseismic *P* coda at NORESS, *Seism. Res. Lett.* **59**, No. 1, 40.

Herrmann, R. B. (1980). Q estimates using the coda of local earthquakes, *Bull. Seism. Soc. Am.* **70**, 447–468.

Ingate, S. F., E. S. Husebye, and A. Christoffersson (1985). Regional arrays and processing schemes, *Bull. Seism. Soc. Am.* **75**, 1155–1177.

Jenkins, G. M. and D. G. Watts (1969). *Spectral Analysis and its Applications*, Holden-Day, Oakland, California.

Korhonen, H., S. Pirhonen, F. Ringdal, S. Mykkeltveit, T. Kværna, P. W. Larsen, and R. Paulsen (1987). The FINESA array and preliminary results of data analysis, Institute of Seismology, University of Helsinki, Rept. S-16.

Mandal, B. and B. J. Mitchell (1986). Complete seismogram synthesis in transversely isotropic medium, *J. Geophys.* **59**, 33-40.

Mykkeltveit, S., F. Ringdal, J. Fyen, and T. Kværna (1987). Initial results from analysis of data recorded at the new regional array in Finnmark, Norway, in Semiann. Tech. Sum., 1 April–30 Sept. 1987, L. B. Loughran (Editor), NORSAR Sci. Rept. 1-87/88.

Nuttli, O. W. (1986). *Lg* magnitudes of selected East Kazakhstan underground explosions, *Bull. Seism. Soc. Am.* **76**, 1241–1251.

Pulli, J. J. (1984). Attenuation of coda waves in New England, *Bull. Seism. Soc. Am.* **74**, 1149–1166.

Sato, H. (1977). Energy propagation including scattering effects, single isotropic scattering approximation, *J. Phys. Earth* **26**, 27–41.

Sato, H. (1984). Attenuation and envelope formation three component seismograms of small local earthquakes in randomly inhomogeneous lithosphere, *J. Geophys. Res.* **89**, 1221–1241.

Toksöz, M. N., A. M. Dainty, E. Reiter, and R.-S. Wu (1988). A model for attenuation and scattering in the earth's crust, *Pageoph* **128**, 81–100.

Toksöz, M. N., A. M. Dainty, and E. E. Charrette (1990a). Spatial variation of ground motion due to lateral heterogeneity, *Structural Safety* (in press).

Toksöz, M. N., A. M. Dainty, and E. E. Charrette (1990b). Coherency of ground motion at regional distances and scattering, *Phys. Earth Planet. Interiors* (in press).

Toksöz, M. N., B. Mandal, and A. M. Dainty (1990c). Frequency-dependent attenuation in the crust, *Geophys. Res. Lett.* **17**, 973–976.

Vogfjord, K. S. and C. A. Langston (1989). Multiple crustal phases from regional events recorded at NORESS, Papers Presented at the 11th Annual DARPA/AFGL Research Symposium, 466–473.

Wu, R.-S. (1985). Multiple scattering and energy transfer of seismic waves: separation of scattering effect from intrinsic attenuation. I. Theoretical modeling, *Geophys. J. R. Astr. Soc.* **82**, 57–80.

Wu, R.-S. and K. Aki (1988). Multiple scattering and energy transfer of seismic waves: separation of scattering effect from intrinsic attenuation. II. Application of the theory to the Hindu Kush region, *Pageoph* **128**, 49–80.

EARTH RESOURCES LABORATORY
DEPARTMENT OF EARTH, ATMOSPHERIC, AND PLANETARY SCIENCES
MASSACHUSETTS INSTITUTE OF TECHNOLOGY
CAMBRIDGE, MASSACHUSETTS 02139

Manuscript received 16 February 1990

Bulletin of the Seismological Society of America, Vol. 80, No. 6, pp. 2261–2281, December 1990

INVESTIGATION OF TELESEISMIC *Lg* BLOCKAGE AND SCATTERING USING REGIONAL ARRAYS

BY DOUGLAS R. BAUMGARDT

ABSTRACT

Incoherent beamforming and continuous frequency-wavenumber "polar-scan" analysis have been applied to study the characteristics of *P* coda and *Lg* waves recorded at the regional arrays NORESS and ARCESS from presumed explosions on the northwestern Russian platform and at test sites of Novaya Zemlya and eastern Kazakh. Also, recordings at the Graefenburg array, near the new GERESS regional array, of Novaya Zemlya events and an eastern European platform (White Sea) event have been compared with the Norwegian array recordings of the same events. The White Sea explosion, at distances of 14° and 22° from NORESS and Graefenburg, respectively, exhibits *Lg* rms amplitudes on incoherent beams that exceed those of *Sn*. However, for explosions at Novaya Zemlya at 20° from NORESS and eastern Kazakh at 30° from ARCESS, the *Lg* waves have much smaller amplitudes than *Sn*. In the case of Novaya Zemlya, the *Lg* wave is almost completely blocked at both NORESS and ARCESS, but is well recorded at Graefenburg. This reduction of the *Lg* amplitudes relative to those from events at longer distances cannot be accounted for by anelastic attenuation and spreading. Comparison of propagation paths suggests that the reduction in amplitudes may be due to blockage and scattering of *Lg* in the Barents Sea. Analysis of *Sn* coda waves on incoherent beams and continuous frequency-wavenumber analysis "polar scans" suggests that they can result from *Lg* to *Sn* scattering from the coastline between the Barents Sea and Scandinavia. Recent geologic studies have revealed significant variations in crustal structure in the Barents Sea basin, which may cause the blockage of *Lg* waves from Novaya Zemlya. In the case of eastern Kazakh explosions, ARCESS incoherent beams show much reduced *Lg* amplitudes relative to the *P* coda waves compared with NORESS, even though the distance to ARCESS (31°) is less than that to NORESS (38°). This reduction in *Lg* amplitude at both NORESS and ARCESS is accompanied by enhancement of *P* and *Sn* coda. The timing of the coda waves and the propagation paths suggest that *Lg* waves may be partially blocked and scattered by the Ural Mountains and that the *P* and *Sn* coda waves may result from *Lg*-to-*Pn*, *Pn*-to-*Sn*, *Sn*-to-*Lg*, and *Lg*-to-*Sn* conversions from lateral heterogeneities in the crust beneath the Urals. The blockage is greater for the Eastern Kazakh-to-ARCESS path because it crosses the middle part of the Urals whereas the Eastern Kazakh-to-NORESS path crosses the southern part of the Urals chain. These blockage effects seem to result from sudden lateral variations in shallow crustal structure, such as variations in sediment thicknesses in the sedimentary basins of the Russian platform and adjacent to the Urals. These blockage effects can be predicted from geologic studies and need to be accounted for when using *Lg* amplitudes to estimate absolute yields of explosions and for event identification.

INTRODUCTION

The regional arrays NORESS, ARCESS, FINESA, and GERESS were designed and installed as prototype regional array seismic systems for the monitoring of nuclear test ban treaties. As such, they have been optimized in their configuration and recording to detect and analyze regional seismic phases. The term regional in this context has usually designated phases that propagate primarily in the crust

and are most commonly observed at seismic stations at distances of 2,000 km or less from the seismic sources. The most important regional seismic phases include *Pn*, *Pg*, *Sn*, and *Lg*. Although these phases are the most important phases at regional distances, they have also been known to propagate in shield regions to distances much beyond 2,000 km (Baumgardt, 1985a).

One of the most important regional phases is *Lg*, which in some regions has been observed to propagate to distances of 5,000 km and beyond (e.g., Båth, 1954). Teleseismic *Lg* has been assessed as a method for estimating precise yields (Baumgardt, 1984; Ringdal and Hokland, 1987; Ringdal and Fyen, 1988; Ringdal and Marshall, 1989). In order to transport the *Lg* yield curve from one test site to another, propagation effects need to be taken into account.

The "*Lg* yield" method, developed to Otto Nuttli (Nuttli, 1986, 1988) presumes to provide transportability of 1 Hz. *Lg* magnitudes by estimating the *Lg* coda *Q*, assuming this to be the intrinsic *Q* of *Lg*, and correcting the *Lg* amplitudes for *Q*. This method assumes that anelastic attenuation causes all the amplitude variations in *Lg*. However, many studies have demonstrated that *Lg* can be partially or completely eliminated by heterogeneities in tectonic and geologic structure. The blockage of *Lg* to the stations in southern Eurasia has been observed by Ruzaikin *et al.* (1977), Kadinsky-Cade *et al.* (1981), and Ni and Barazangi (1983), and has been attributed to variations in crustal structure or low *Q* in the crust. Baumgardt (1985b, 1986), using NORSAR data, has observed partial and complete blockages of *Lg* along propagation paths in the northwestern Soviet Union that seem to relate to sudden variations of the sediment thicknesses in the upper crust that *Lg* encounters as it propagates in and out of sedimentary basins within the Russian Platform.

Scattering from tectonic heterogeneities may also affect *Lg* excitation. Baumgardt (1985a) has suggested that sudden bursts in the pre-*Sn* coda from Shagan River explosions recorded at NORSAR may be *P* waves produced by *Lg*-to-*P* scattering in the Ural Mountains. Baumgardt (1985b) has studied other *Lg* propagation paths from PNE explosions to NORSAR. *Lg* propagation paths that cross the Urals show elevated pre-*Sn* coda levels and reduction in the *Lg* level compared to those which do not.

Another possible scattering mechanism is *Lg*-to-*Sn* and *Sn*-to-*Lg* scattering. Studies by Isacks and Stephens (1975), Chinn *et al.* (1980), and Ni and Barazangi (1983) have revealed on regional seismograms so-called "early *Lg*" phases in the *Sn* coda, which arrive several seconds ahead of the 3.5 km/sec group velocity arrival time. In many of these cases, there was no apparent arrival at the expected *Lg* arrival time, which suggested that *Lg* may have been blocked. Thus, they have concluded that the "early *Lg*" phases may be *Sn*-to-*Lg* mode conversions at geologic discontinuities, such as coastlines.

The purpose of this study is to analyze *Lg* propagation at teleseismic distances, as recorded by the new regional arrays, with the goal of gaining a better understanding of the scattering and blockage effects along the extended paths. As will be shown later, regional phases are well recorded at teleseismic distances and much of the *P*-coda energy, not associated with known regional or teleseismic phases, appears to be caused by scattered energy that also propagates primarily in the continental crust. Thus, the regional arrays are well configured to study these phases, particularly the scattered *Sn* and *Lg* phases that appear to constitute much of the teleseismic coda.

DATA

The primary focus of this study has been the analysis of short-period regional array data for presumed nuclear explosions located at Novaya Zemlya, in eastern Kazakh near Seimipalatinsk, and on the northwestern part of the Russian Platform near the White Sea.

Most of the data included in this study was recorded at the regional arrays NORESS and ARCESS. The configuration of the NORESS array, located within the NORSAR array near Oslo, has been discussed by Mykkeltveit *et al.* (1983). The exact same configuration was used in the construction of the ARCESS array, located about 500 km north of NORESS in extreme northern Norway.

Because the GERESS array has only recently begun operating, there is little data available from this array for events in these regions. For this reason, we have used, for the purposes of this study, the larger Graefenburg array as a stand-in for GERESS. A description of the broadband Graefenburg array has been given by Harjes and Seidl (1978). Only Graefenburg data from the Novaya Zemlya and White Sea events were analyzed in this study. Comparative analyses of Graefenburg and NORSAR recordings of east Kazakh events have been reported by Baumgardt (1985a) and Ringdal and Fyen (1988).

Figure 1 shows the propagation paths from the different source regions to the arrays plotted on a geologic map of Eurasia. The paths cover a variety of tectonic and geologic regimes. Later, we shall relate the signal characteristics of these events to the geology of the propagation paths.

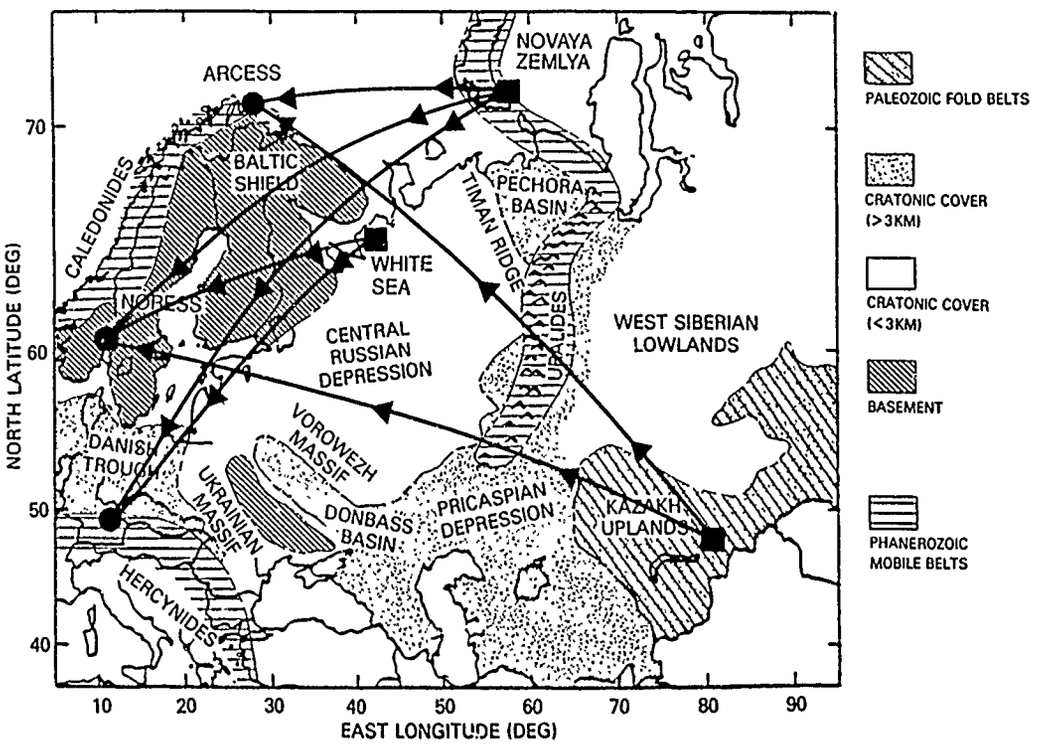

FIG. 1. Map showing the direct *Lg* propagation paths from the Novaya Zemlya, White Sea, and eastern Kazakh events (presumed nuclear explosions) to the ARCESS, NORESS, and Graefenburg arrays. The major geologic features that the paths cross are shown (after Watson, 1976).

Incoherent Beam Analysis

Incoherent beamforming template analysis provides a useful method for analyzing the coda shapes of regional and near-regional seismic signals recorded at arrays. The method has been described in detail in Baumgardt (1985a), where it was used to analyze the coda shapes of eastern Kazakh events recorded at the NORSAR and Graefenburg arrays. First, each of the array seismograms are prefiltered in a specified frequency band. Incoherent beams are then computed by first computing root-mean-square rms) time averages of the amplitudes on each array element trace within a set of adjacent time windows covering the signal coda. The logarithm of the average rms amplitude in each time window is then determined on each trace and the log-rms amplitudes are then averaged for each time window over all the array elements. The resulting log-rms averages plotted as a function of time provide a kind of coda envelope, as viewed in logarithmic or "seismic magnitude" space.

Novaya Zemlya and White Sea Events

Figure 2 shows two examples of incoherent beams for two different time window lengths, for a Novaya Zemlya event recored at the NORESS array. The NRA0 array

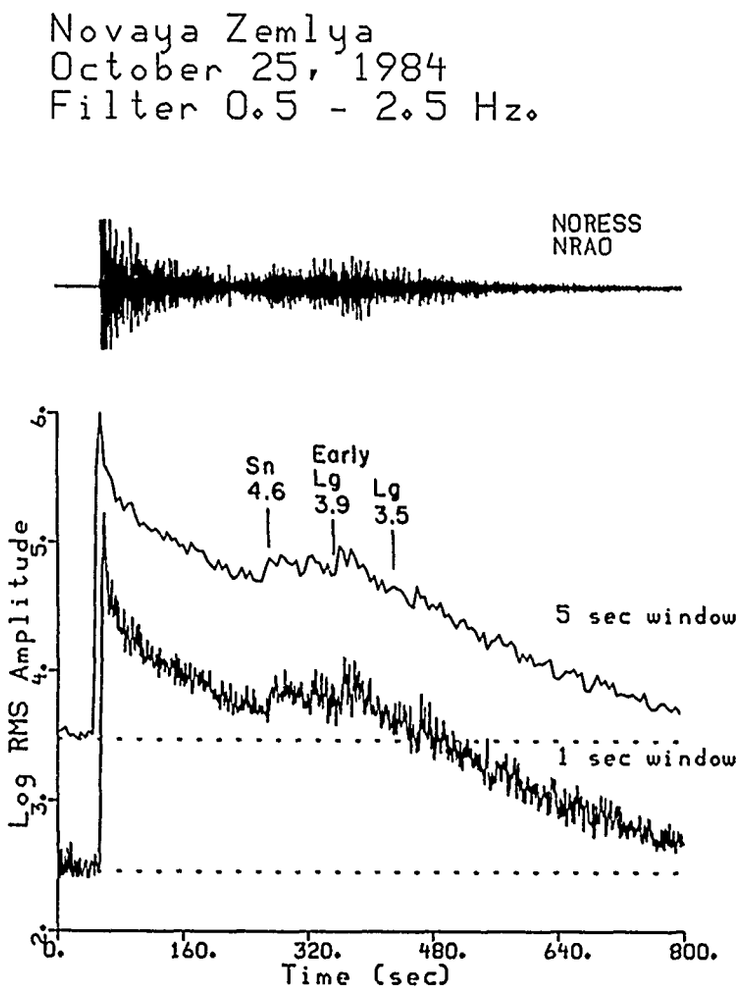

FIG. 2. (*Top*) NORESS NRA0 element trace of the 25 October 1984 Novaya Zemlya trace. (*Bottom*) NORESS incoherent beam traces for the same time period. The identified phases and their apparent group velocities are indicated.

element trace for the event is plotted at the top. The first arrival *P*-wave amplitude has been artificially clipped at 75 per cent its maximum amplitude in order to make the coda signals more visible. The two incoherent beams were computed in 5 and 1 sec windows, and are plotted at the bottom of the figure aligned in time with the signal trace. The dashed horizontal lines on incoherent beams refer to the average log-rms background noise computed in 2 min of noise ahead of the *P* wave. The 5 sec window incoherent beam has been shifted 1 log-rms unit up for visibility.

The log-rms incoherent beams provide an informative representation of the coda shape because the logarithm operation reduces the wide dynamic range between the large amplitude *P* wave and the rest of the coda without having to clip the *P*-wave amplitude. The incoherent beam computed with 5 sec windows provides a smoother representation of the coda shape than the 1 sec window beam. However, the 1 sec incoherent beam provides a more detailed description of the coda. In this study, we have analyzed incoherent beams with 1 sec windows.

The incoherent beams in Figure 2 reveal that Novaya Zemlya coda falls off gradually in amplitude until about 213 sec after *P*, when the first of three broad pulses are apparent. The three pulses are marked on the traces by their apparent velocities, assuming they all come directly from the Novaya Zemlya source at 21°. The first pulse at 4.6 km/sec appears to be the direct *Sn* phase. The second pulse has a velocity of 3.9 km/sec and will be called "early *Lg*" since it arrives significantly ahead of the expected *Lg* onset time at 3.5 km/sec. The third pulse comes in at about 3.3 km/sec, somewhat after the expected arrival time of *Lg*.

Figure 3 shows a record section of three incoherent beams for another Novaya Zemlya event recorded at ARCESS at 10°, NORESS at 21°, and Graefenburg at 30°. (*Note:* The ARCESS trace had a data dropout at about 100 sec after the *P* onset.) At ARCESS, the first *P*-coda pulse arrives at about 105 sec after *P*, which gives a group velocity of about 4.3 km sec. This pulse is interpreted to be *Sn*, although its group velocity is less than expected. Perhaps the actual onset occurs at the time of the data dropout. There are no other apparent arrivals after *Sn*, although there is a slight change in the slope of the *Sn* coda at about the 3.5 km/sec time. The Graefenburg incoherent beam is notable in that it has both a strong *Sn* at a velocity of 4.4 km/sec and a strong pulse at 3.3 km/sec, which appears to be a somewhat late *Lg*. Comparison of these three traces reveals that something has blocked the *Lg* phase coming into Norway but has not blocked the *Lg* arrival at Graefenburg. Clearly, anelastic attenuation cannot explain the elimination of *Lg*, since Graefenburg is at a greater distance from Novaya Zemlya than both ARCESS and NORESS.

Figure 4 compares the codas of the White Sea event recorded at NORESS at 14° and Graefenburg at 22°. Even though this event was smaller than the Novaya Zemlya event by about 0.6 magnitude units, is still produced excellent *P* and coda signals at the two arrays. The striking feature of the NORESS and Graefenburg recordings of this event is the strong *Lg* phase, whose amplitude at both arrays is almost as high as the first arrival *P*. The approximate group velocities of *Lg* at the two arrays are 3.6 km/sec for NORESS and 3.5 km/sec at Graefenburg. Apparently, whatever blocks the *Lg* waves into NORESS and ARCESS from Novaya Zemlya is not present in the case of the White Sea paths to the two arrays. Also, there appears to be less early coda before *Sn* for the White Sea event than for the Novaya Zemlya events at arrays of comparable distances. Perhaps this means that the part of the *Lg* energy lost in the blockage from Novaya Zemlya is scattered into early *P*-coda waves.

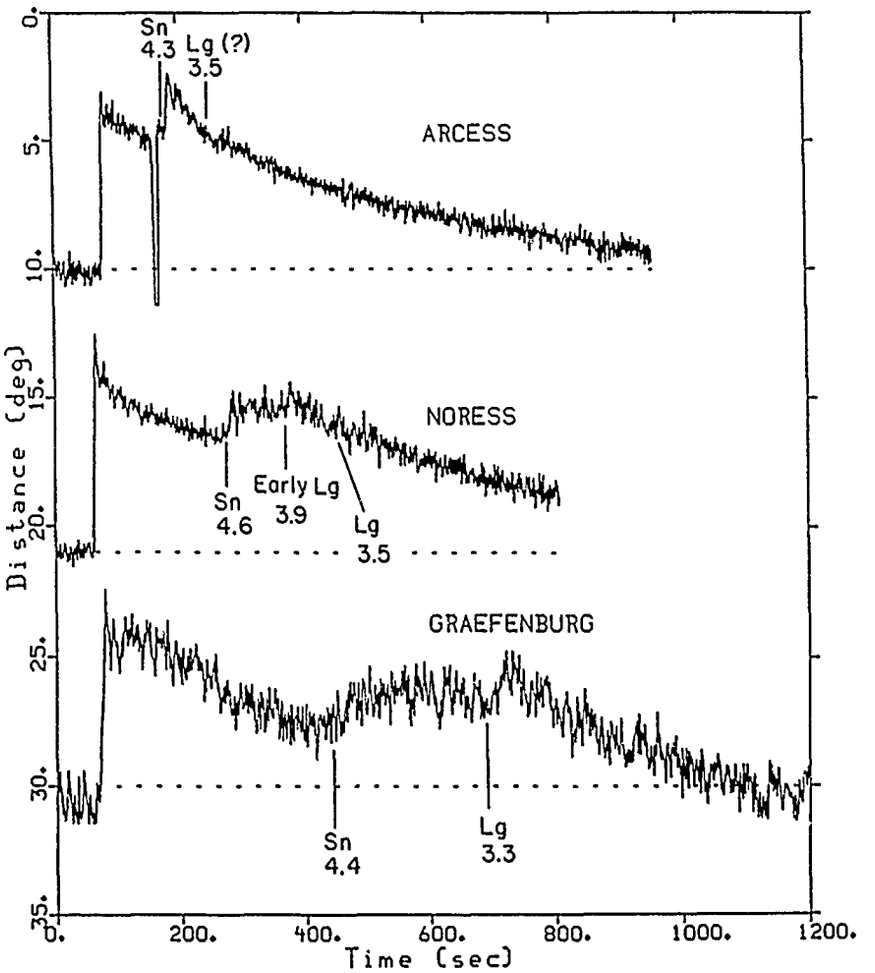

FIG. 3. Incoherent beam traces of the 24 October 1984 Novaya Zemlya event as recorded at ARCESS (*top*), NORESS (*middle*), and Graefenburg (*bottom*).

Comparing the various *Lg* propagation paths to the arrays, shown in Figure 1, reveals that the only difference in paths between the White Sea and Novaya Zemlya event is that the Novaya Zemlya paths must cross the central Barents Sea. Moreover, Figure 1 also shows that the path from Novaya Zemlya to Graefenburg does not cross the central Barents Sea. Apparently, the *Lg* blockage from Novaya Zemlya to the Norwegian arrays must be in the central Barents Sea. Later, a possible geologic explanation of this blockage will be presented.

Eastern Kazakh Events

This study will focus on the difference in coda shapes for eastern Kazakh events recorded at NORESS and ARCESS. A comparison of codas at NORSAR and Graefenburg was presented at Baumgardt (1985a).

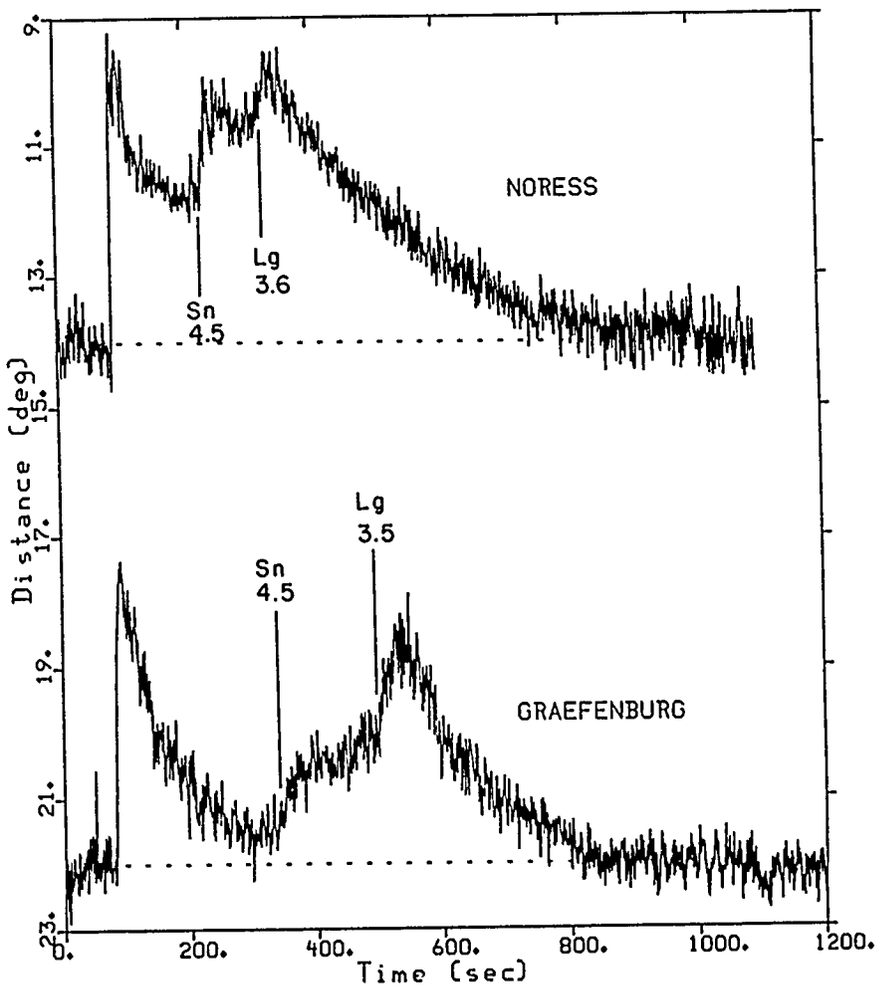

FIG. 4. Incoherent beam traces for the White Sea even as recorded at NORESS (*top*) and Graefenburg (*bottom*). The identified phases and their apparent group velocities are indicated.

Figure 5 shows a record section of incoherent beams recorded at ARCESS and NORESS from two different eastern Kazakh events. The ARCESS coda contains two early pulses, which we interpret as interfering *PP* and *Pn*, and *PcP*, respectively. This interpretation is based primarily on expected arrival times. However, it has also been confirmed by frequency-wavenumber (FK) analysis, discussed in the next section. After these pulses, the coda decays with only slight variations indicative of the onset of very weak *Sn* and *Lg* arrivals.

The NORESS coda is very similar in shape to the NORSAR codas of eastern Kazakh events discussed by Baumgardt (1985a). The early coda pulses are interpreted as, in order of time, interfering *PP* and *Pn*, teleseismic *S*, and *Lg*. Two changes in slope are apparent, the first at about 219 sec after *P* and the second at about 467 sec after *P*. The second slope change occurs at the time expected for the

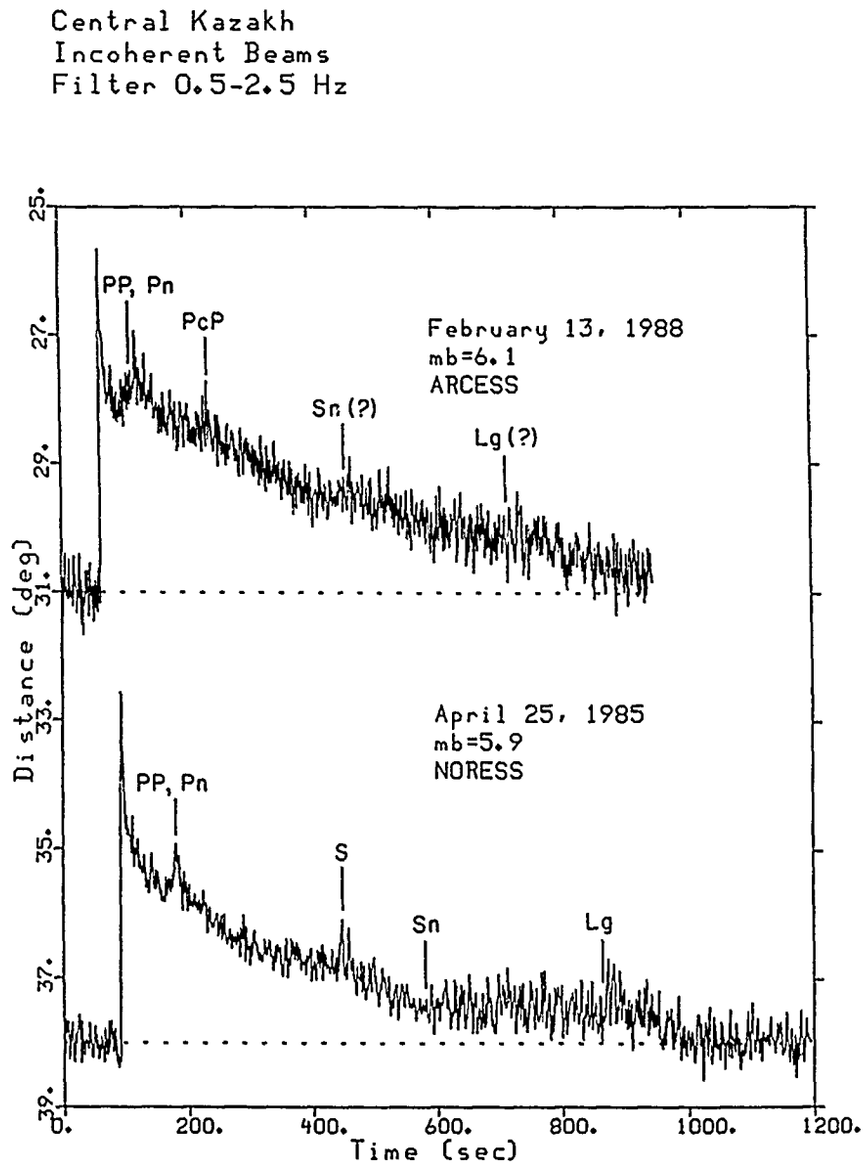

FIG. 5. Incoherent beam traces of two central Kazakh events recorded at ARCESS (*top*) and NORESS (*bottom*).

Sn onset. Baumgardt (1985a) has interpreted the first slope change as being caused by scattering of *Lg* to *P* in the Urals, based primarily on expected travel times. This interpretation will be reexamined in the following sections.

The major differences in the eastern Kazakh codas recorded at ARCESS and NORESS is the lack of a significant *Lg* at ARCESS. Examination of the propagation paths from the events to these two arrays reveals that the ARCESS path must cross the central Urals, whereas that to NORESS crosses the southern Urals. There appears to be a major blockage of *Lg* in the central Urals that is not as strong as the southern Urals. As in the case of the Novaya Zemlya blockages, the lack of *Lg* can be explained in terms of lateral variations in near-surface geology, as we shall discuss in the last section.

CONTINUOUS FK ANALYSIS

To gain a better understanding of the composition of the teleseismic *P* coda and the regional phases recorded at the regional arrays, continuous FK analysis has been applied to the data to determine the apparent velocity and arrival azimuths of the phases. The broadband FK analysis method, developed for NORESS by Kværna and Doornbos (1986), was used for this purpose because it provides more stable estimates of signal velocity and azimuth than single-frequency FK. Broadband FK power spectra were determined by first computing single-frequency FK power spectra over a band of frequencies for a windowed signal and then integrating each FK over the frequencies in the band. The frequency integration converts the wavenumber space (in units of cycles per kilometer), to slowness space (in seconds per kilometer). Location of the maximum power level peak in the slowness space gives the apparent slowness, or velocity, and azimuth of the signal. All the broadband FKs presented in this paper cover the band of 0.7 to 1.3 Hz.

In most FK analysis, even in incoherent noise, a single maximum power peak can always be found. In order to estimate the significance of the peak, an array parameter known as the *F* statistic is also computed (Shumway, 1971; Blandford, 1974). *F* statistic represents, in essence, the ratio of the coherent to the incoherent power of the signal. The name refers to the fact that the *F* statistic follows the *F* distribution, if the signal power is assumed to be normally distributed. In principle, a probability can be determined for the value of the *F* statistic, which is the likelihood that a coherent signal has been detected. In this study, the value of the *F* statistic has been used as an estimate of signal coherence. The *F* statistic value becomes very large for a coherent signal, sometimes in excess of 1,000 or more for teleseismic *P* waves recorded at the ARCESS and NORESS arrays. Generally, coherent regional phases produce *F* statistics of near 100 and coherent coda phases produce values of 20 or greater. Noise *F* statistics have wide variations, since much of the noise recorded at regional arrays consists of coherent, propagating modes. Generally, incoherent noise produces *F* statistics of less than 10.

Continuous FK templates were made by computing a suite of broadband FK power spectra for a set of overlapping time windows shifted down the trace. Each time window was 2 sec long and shifted by 1 sec, for a 1 sec overlap. In each window, the velocity. azimuth, and *F* statistic for the largest peak in the broadband FK spectrum was determined and stored. FK templates can then be displayed in the form of time traces (i.e., *F* statistic, velocity, and azimuth plotted as a function of time or as "FK polar scans").

Figure 6 shows an example of two FK polar scans for NORESS, plotted at the bottom of the figure, along with the incoherent beam for the October 25, 1984 Novaya Zemlya event recorded at NORESS. The early window in Figure 6, w1, covers a time period in the background noise. The polar scan on the left shows that much of the noise is coherent, with *F* statistics ranging from 10 to as high as 50. Most of the noise appears to propagate at *Lg* velocities from the southwest. (*Note:* It is also very possible that the background noise contains signals from local events, such as blasting activity or local microearthquakes to the southwest, which might explain the high coherence of these signals.) Window w2, positioned into the *P* coda, contains arrivals coming from a range of velocities and azimuths. The most coherent energy, represented by the larger triangular symbols, primarily comes from the expected azimuth of the Novaya Zemlya event. However, coherent signals can also arrive significantly off-azimuth. Note that most of the apparent velocities of

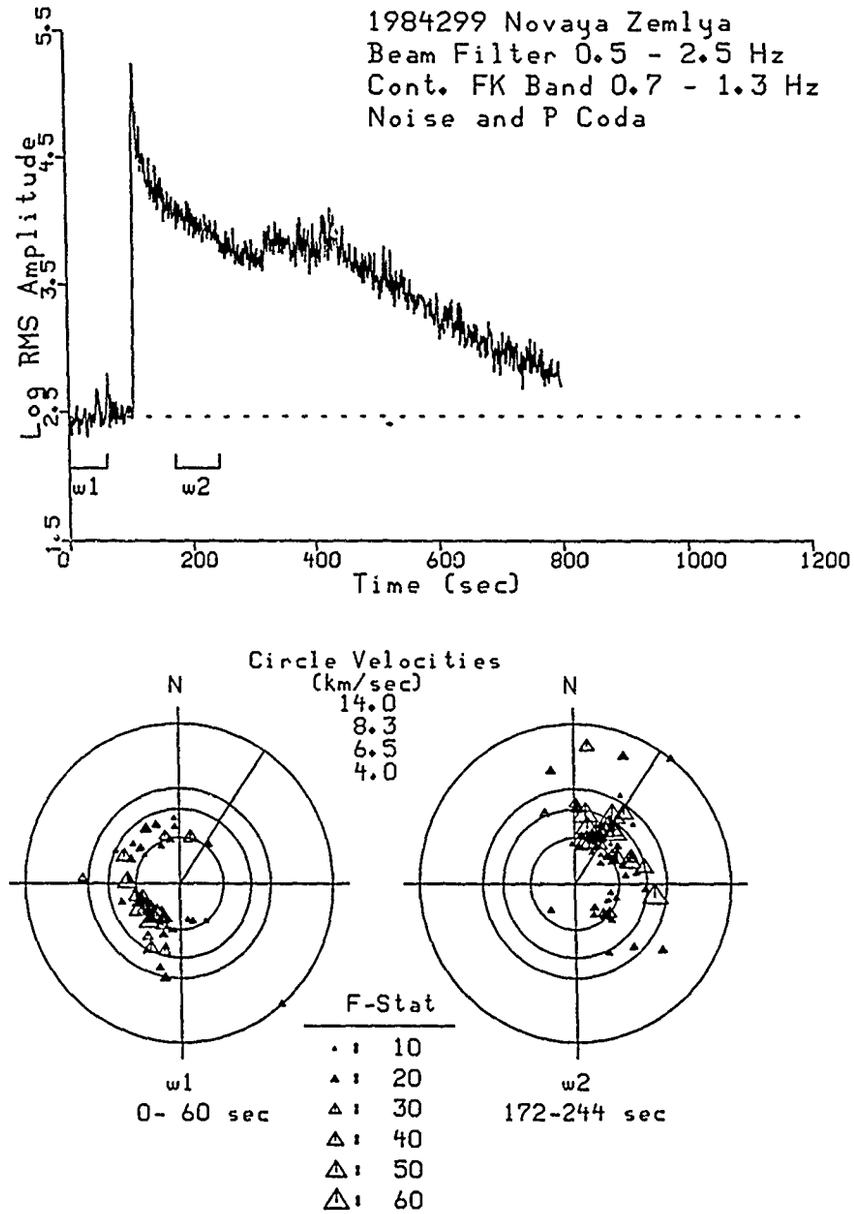

FIG. 6. Incoherent beam (*top*) and continuous FK polar scans (*bottom*) for windows on the background noise (window w1) and a part of the *P* coda (window w2) for a Novaya Zemlya event recorded at NORESS. The polar scans show the FK measurements in the windows plotted as triangle symbols in polar coordinates, with radius proportional to the apparent velocity in kilometers per second and at an angle equal to the FK-measured azimuth of the signal. The rings on the polar plots indicated velocities of 4.0 km/sec, an *Lg* velocity, 6.5 km/sec, a *Pg* velocity, 8.3 km/sec, a *Pn* velocity, and the outer circle is 14 km/sec for teleseismic *P*. The symbol size is proportional to the value of the *F* statistic, as shown in the legend. The line on each plot represents the azimuth of Novaya Zemlya relative to NORESS.

the coherent signals in the coda correspond to those expected for *Pg*, *Sn*, and *Lg* modes of propagation.

Figure 7 shows polar scans for a window at times corresponding to the 4.6 km/sec *Sn* phase discussed in the previous section. Comparing the "time-proportionate" and "*F* statistic proportionate" displays show that most of the coherent energy arrives on azimuth with velocities consistent with both *Sn* and *Lg* modes of propagation. Moreover, examination of the "time-proportionate" polar

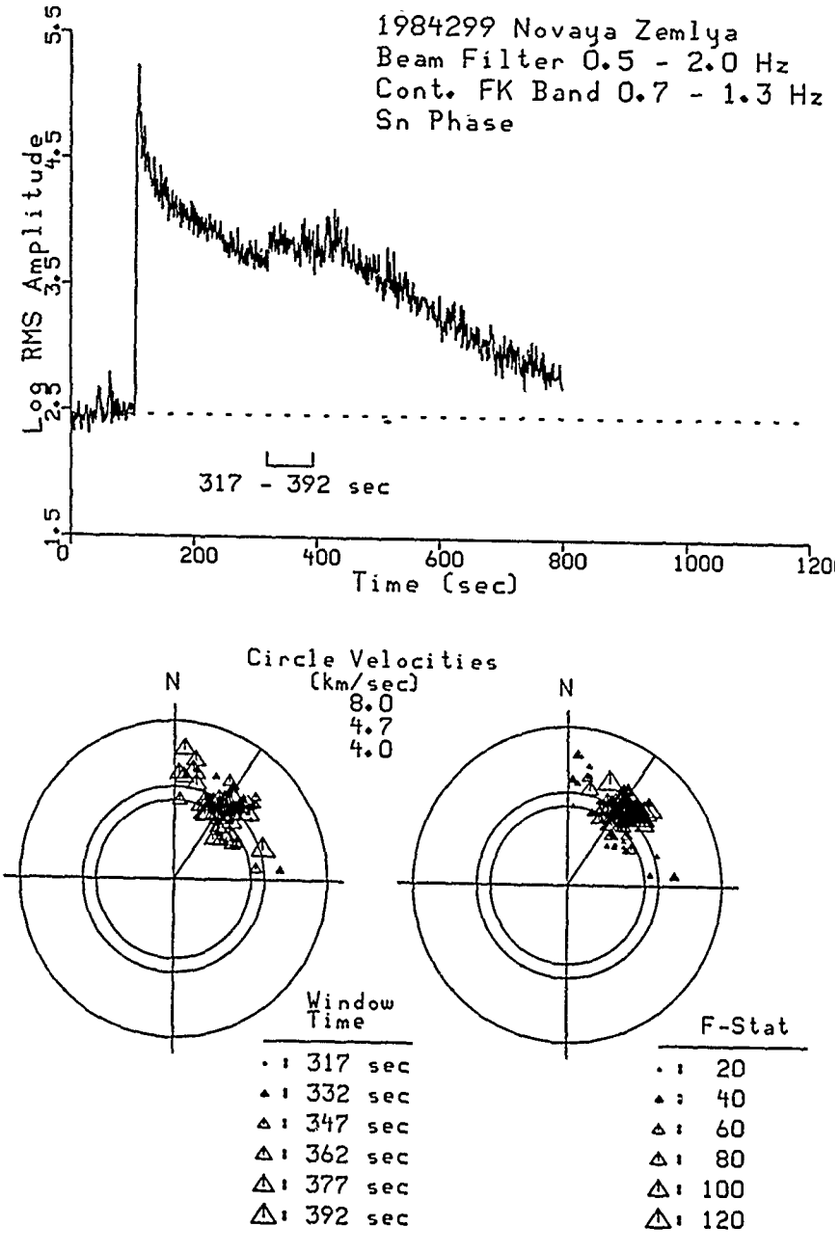

FIG. 7. Incoherent beam (*top*) and continuous FK polar scans (*bottom*) for a single window on the presumed *Sn* arrival from Novaya Zemlya recorded at NORESS. The polar scan on the *left* has triangle symbol sizes proportional to time into the window and on the *right* proportional to *F* statistic, as shown in the respective legends. The circles are plotted at velocities of 4.0 km/sec for *Lg* modes, 4.7 km/sec for *Sn* modes, and the outer circle is 8.0 km/sec for *Pn* modes.

scan shows that higher velocity signals arrive later in the window (at about 362 sec) with velocities consistent with *Pg* and *Pn* modes and from a northerly azimuth. These signals are not as coherent as the shear wave modes, although more coherent *Pg* modes do arrive more on the azimuth of the event.

Figure 8 compares "*F* statistic proportionate" polar scans for two windows in the late coda: w1, centered on the "early *Lg*," discussed in the previous section; and w2, centered approximately on the 3.5 km/sec group velocity *Lg* signal. This plot shows that the more coherent arrival in the "early *Lg*" part of the coda has apparent

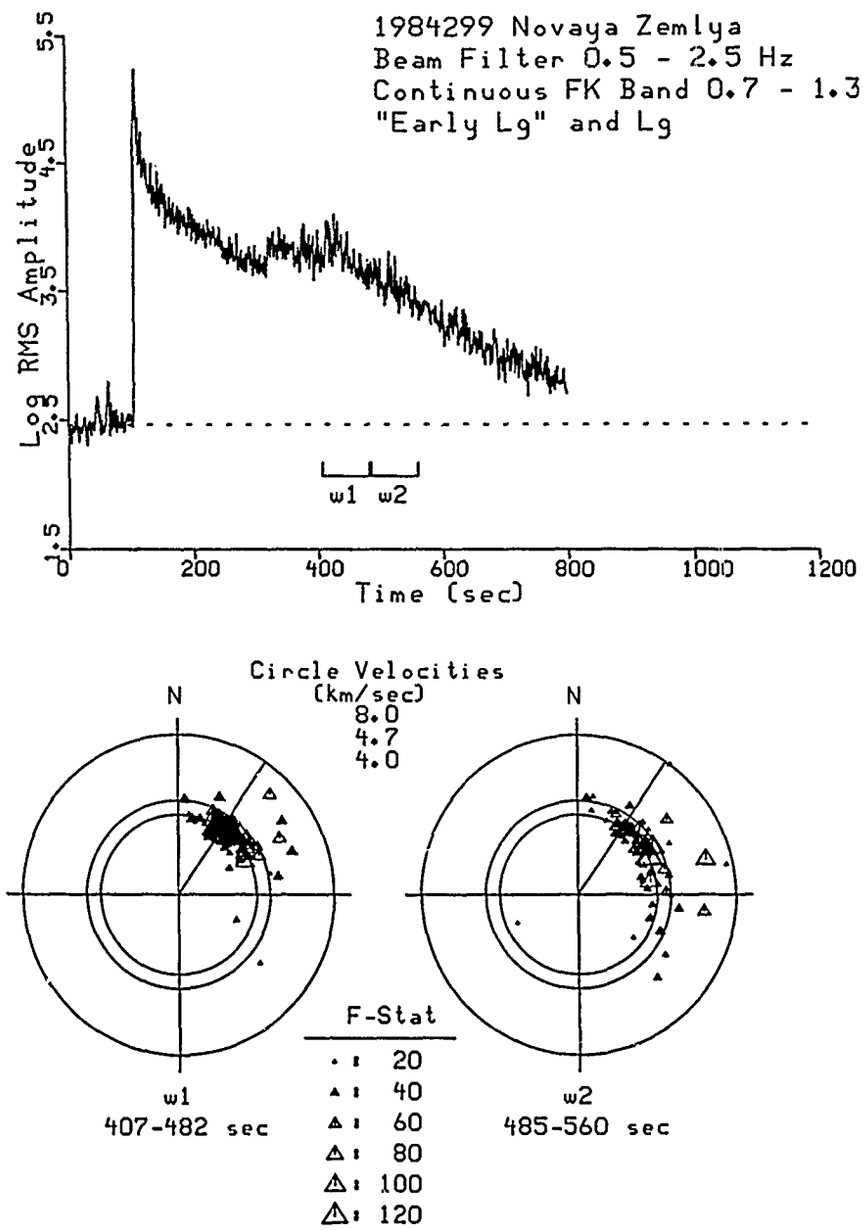

FIG. 8. Incoherent beam (*top*) and *F* statistic proportional polar scans (*bottom*) for windows on the "early *Lg*" and "on-time *Lg*" portions of the *Sn* coda from Novaya Zemlya recorded at NORESS.

velocities that cluster on the 4.0 km/sec ring. Although *Sn* modes and some off-azimuth modes with higher velocities are also apparent, it is striking that most of the symbols cluster inside the 4.7 km/sec ring, which confirms that most of this part of the coda consists of *Lg* waves. The second window on the right also shows that *Lg* modes arrive at the expected 3.5 km/sec time, with phase velocities on the 4.0 km/sec ring. However, many of these modes arrive significantly off-azimuth and tend to be spread out along the *Lg* phase velocity ring with azimuths to the south of the Novaya Zemlya azimuth.

Next, we examine the FK polar scans for one of the NORESS recordings of the eastern Kazakh events. Figure 9 shows the incoherent beam (top) and "time-proportionate" (left) and "*F* statistic proportionate" (right) polar scans for a window

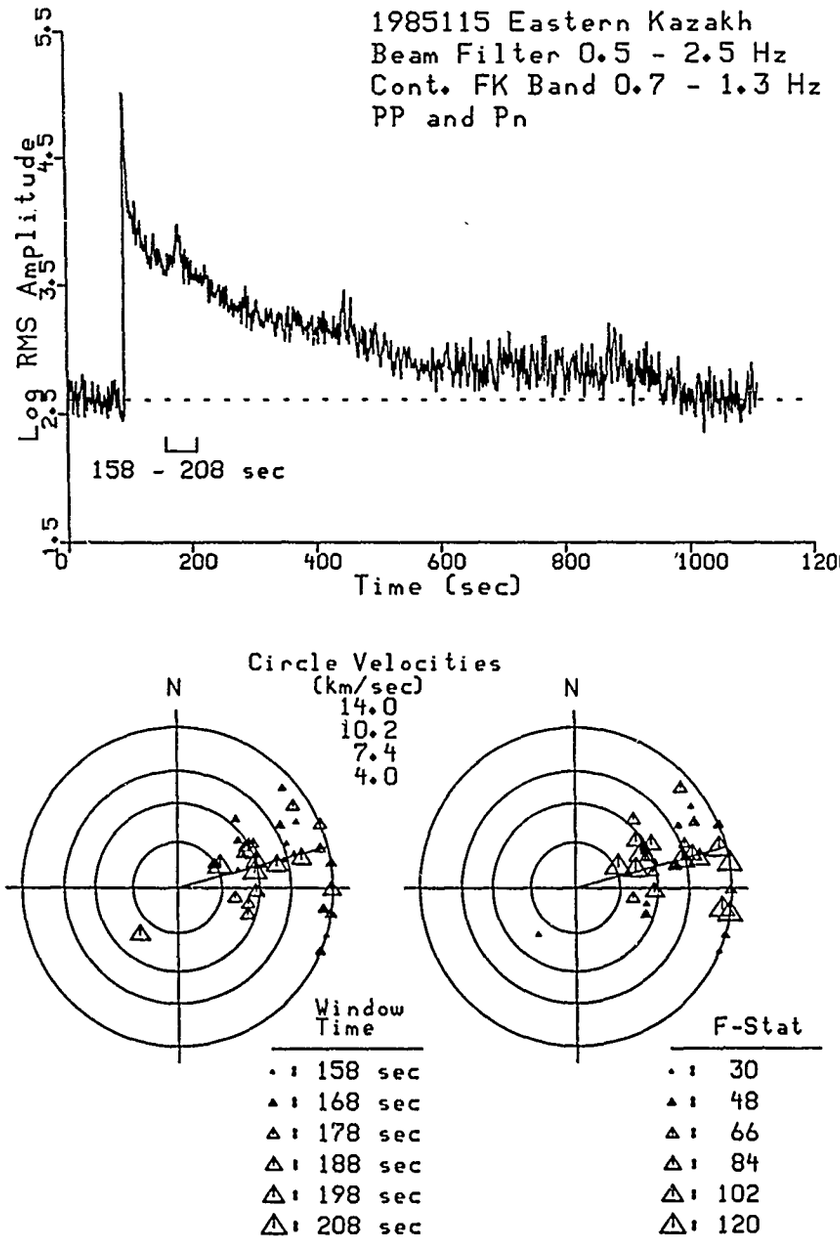

FIG. 9. Incoherent beam (*top*) and polar scans (*bottom*) on the interfering *PP* and *Pn* phases from an eastern Kazakh recorded at NORESS.

on the presumed *PP* phase arrival, discussed in the previous section. Both plots show that the signals in this part of the coda fall on two rings, the outer two rings between 10.2 km/sec (expected apparent velocity of *PP*) and 14 km/sec and on the ring at 7.4 km/sec. The lower velocities may be *Pn* signals, which are expected to arrive at NORESS at a time shortly after the *PP* arrival time. The time-proportionate plot shows that the higher velocity *PP*-type phases arrive in the early part of the window and that the lower velocity *Pn*-type phases arrive near the end of the window. Both sets of arrivals have high *F* statistics, generally in excess of 100, indicating high coherence.

Figure 10 shows polar scans for the flat part of the coda, which was interpreted by Baumgardt (1985a) as being caused by scattered arrivals in the Ural Mountains.

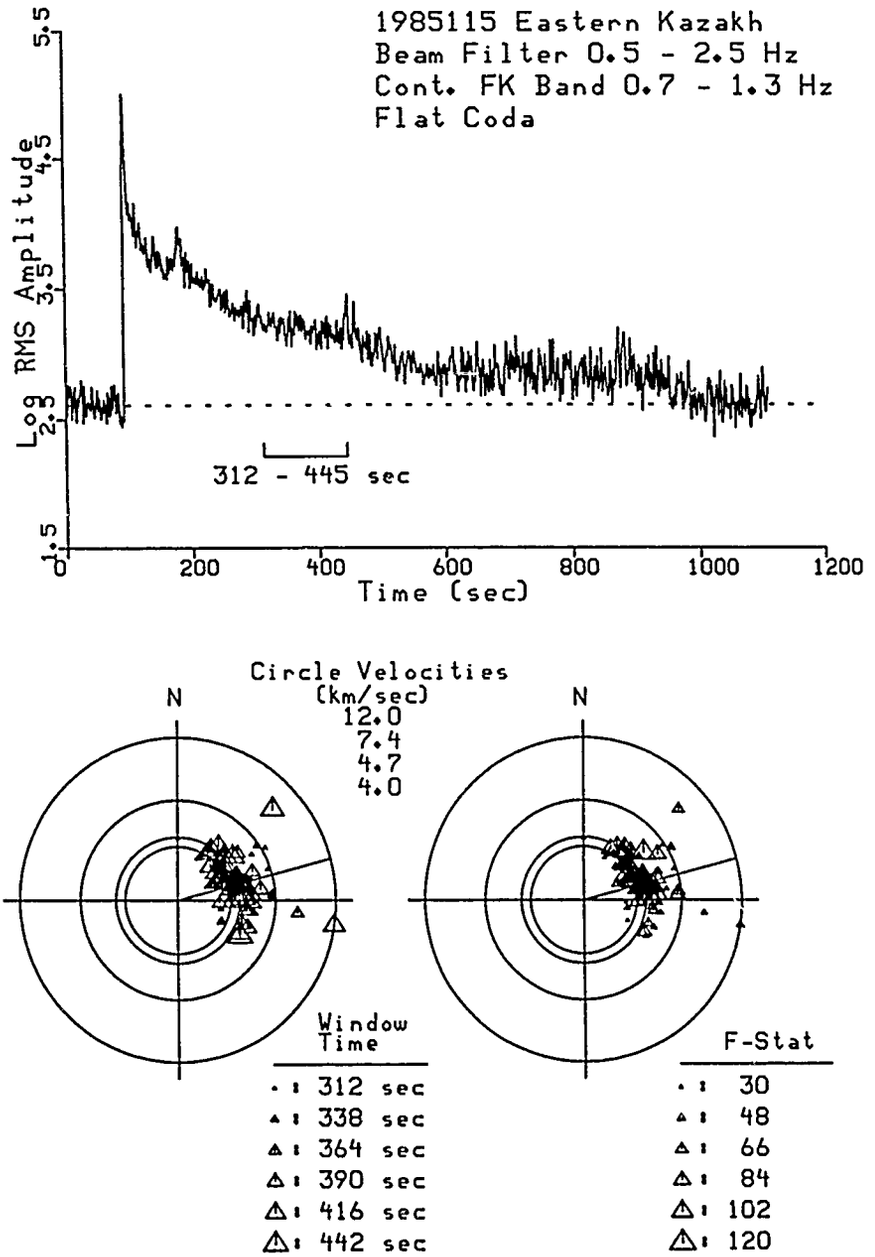

FIG. 10. Same as Figure 9 but for a window on the flat part of the pre-*Sn* coda.

Surprisingly, most of the arrivals in this part of the coda cluster around the 4.0 to 4.7 km/sec rings, which are *Lg* and *Sn* velocities, respectively. However, this part of the coda is well ahead of the *Sn* and *Lg* arrival times. There are also arrivals with velocities of 7.4 km/sec, which we interpreted above as being the phase velocity of *Pn*. These phases arrive primarily in the early part of the coda and have *F* statistics on the order of 60 and over. However, there is little evidence of any teleseismic *P* energy in this part of the coda. The flat coda seems to be composed primarily of *Sn* and *Lg* modes, with minor amounts of *Pn* modes.

Finally, Figure 11 compares "*F* statistic proportionate" FK polar scans for the *Sn* and *Lg* parts of the signal. The *Sn* coda window, w1, on the left contains many arrivals with *F* statistics above 10 coming from a wide range of velocity and azimuth.

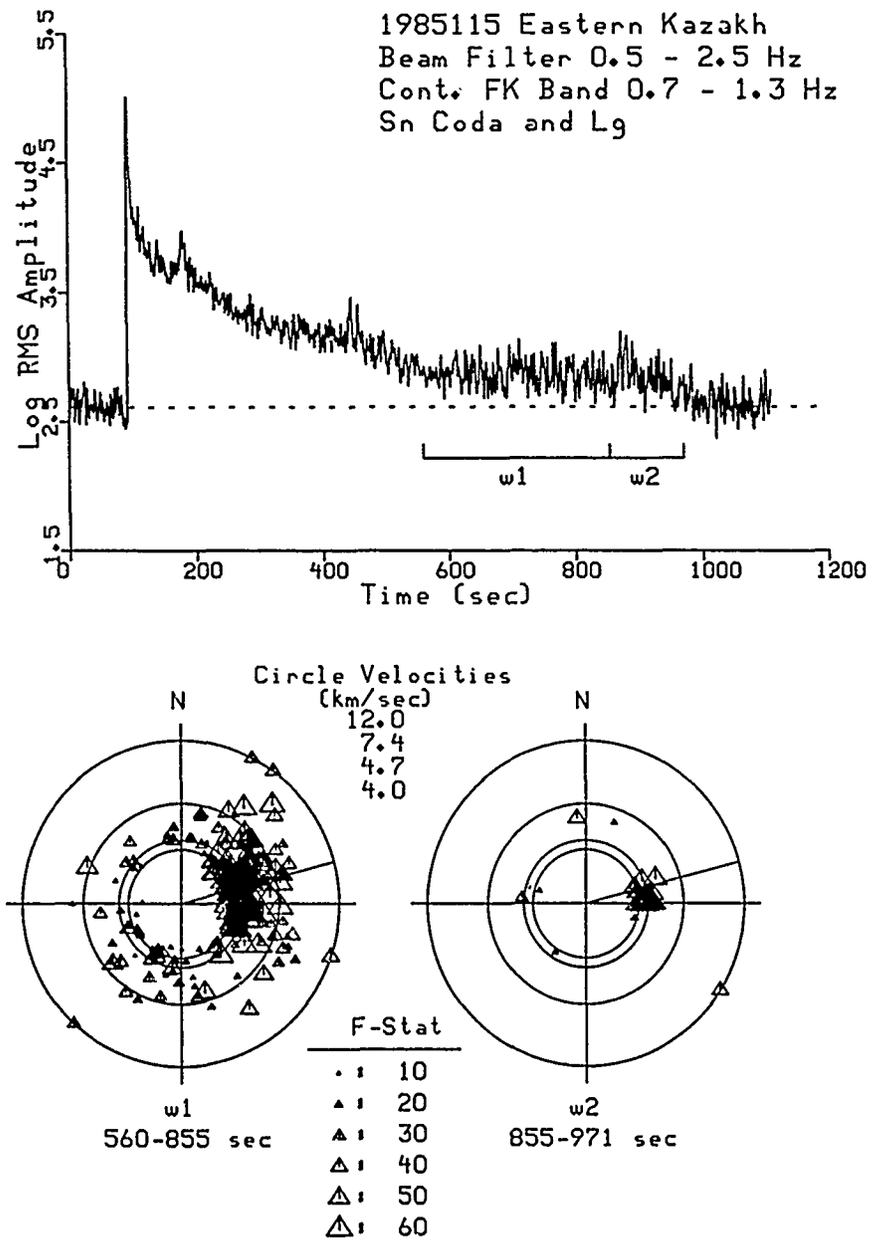

FIG. 11. Incoherent beam (*top*) and time-proportionate polar scans (*bottom*) for windows on the *Sn* and *Sn* coda (window w1) and *Lg* (window w2).

Apparently, most of the *Sn* coda is made up of scattered and multipathed modes whose velocities range from *Lg*- to *Pn*-type modes. The *Lg* arrival in the w2 window on the right are very coherent, with phase velocities of between 4.0 and 4.7 and on the expected azimuth.

DISCUSSION

The foregoing discussion of the characteristics of the high-frequency signals recorded at the regional arrays from presumed explosions at near regional and teleseismic distances reveals how useful regional arrays can be for understanding these signals. We have found that much of the *P* coda from these events consists of regional phases, in particular, *Sn*- and *Lg*-type modes. Many of these arrivals appear

in the coda much ahead of the times expected for *Sn* and *Lg*, indicating that they must result from scattering from *P* waves. *Lg* waves arriving ahead of the expected 3.5 km/sec velocity time in the *Sn* coda must come from *Sn*-to-*Lg* scattering. Moreover, *Lg*-to-*Pn*- and *Lg*-to-*Sn*-type scattering may also occur since *Pn*- and *Sn*-type modes appear in the codas at times different than those expected for direct arrivals. The polar scans indicate that coda signals arrive at the arrays from a wide range of azimuths but usually within about 45° of the expected azimuth. This shows that most of the codas result from forward-scattering at points along the path between the sources and the arrays, as opposed to back-scattering in the vicinity of the arrays.

Figure 12 shows our interpretation of the *Sn* coda waves from the Novaya Zemlya explosions, recorded at NORESS, as revealed by the FK polar scans. The early *Sn* coda waves appear to be a combination of *Sn*- and *Lg*-type modes, produced by direct *Sn* and *Sn*-to-*Lg* scattering. The latter part of the *Sn* coda, what we have called "early *Lg*," consists of mostly *Lg*-type modes. These arrivals may be the same as the early *Lg* arrivals observed by Isacks and Stephens (1975), Barazangi (1977), Chinn *et al.* (1980), and Ni and Barazangi (1983) on land from offshore events. Because they did not expect direct *Lg* phases from the offshore events, since their paths cover over 200 km of oceanic crust, they interpreted the observed *Lg* waves as resulting from mode conversion of *Sn* waves to *Lg* waves at the continent-ocean interface. For the Novaya Zemlya events, recorded at NORESS, the interface between the Barents Sea and the Kola Peninsula is about 13° from the source. As indicated in Figure 12, time delay between *Sn*-to-*Lg* conversions and direct *Sn*, which is the same as the delay time between *Lg*-to-*Sn* conversions and direct *Lg*, is 110 sec. These delay times are the ones indicated by the brackets in Figure 12. Energy bursts appear in the coda at the delay times for this type of scattering (consistent for several events) and the polar scan results support the conclusion that the early *Lg* arrivals come from *Sn*-to-*Lg* conversions at the Barents Sea-Kola interface.

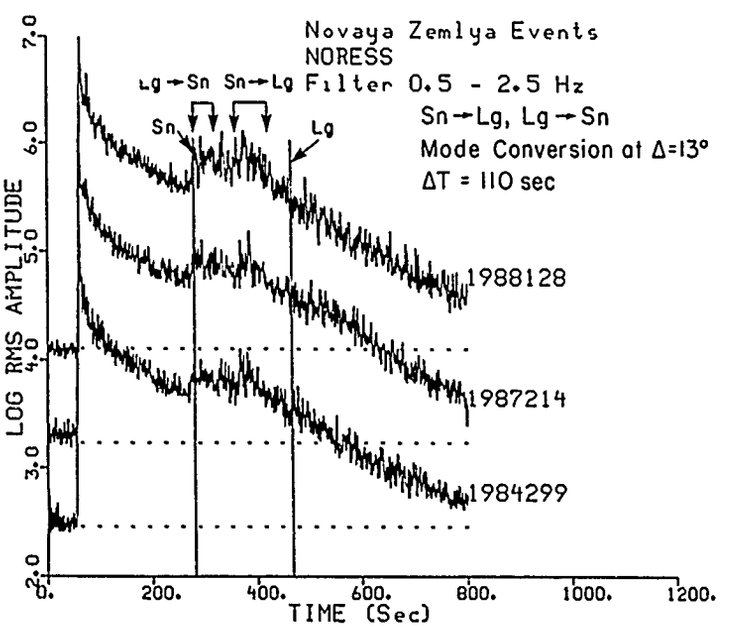

FIG. 12. Interpretation, in terms of scattering, of coda waves recorded at NORESS from three events at Novaya Zemlya.

As discussed earlier, direct *Lg* waves appear to be blocked in the Barents Sea basin, and therefore, the only *Lg* waves observed at NORESS and ARCESS come from the *Sn*-to-*Lg* mode conversion. Figure 13 shows a possible geologic explanation of the blockage taken from a recent study of the Barents Sea by Gramberg (1988). Figure 13a shows two maps of crustal thickness contours (left) and isolines of granitic/metamorphic layer thickness (right) on a map of the central Barents Sea. Gramberg (1988) indicates regions of the "missing granitic layer," indicated by the stippled and lined areas in the maps, which also coincide with a thinning of the crust by about 10 km. Figure 13b shows a cross-section through the central Barents

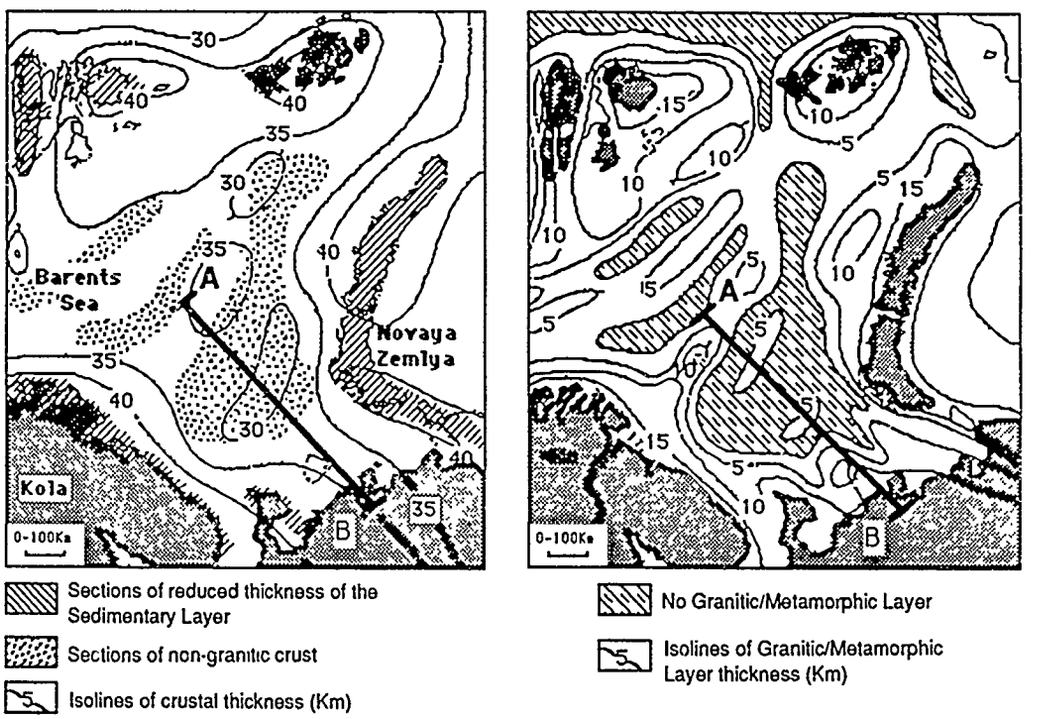

(a)

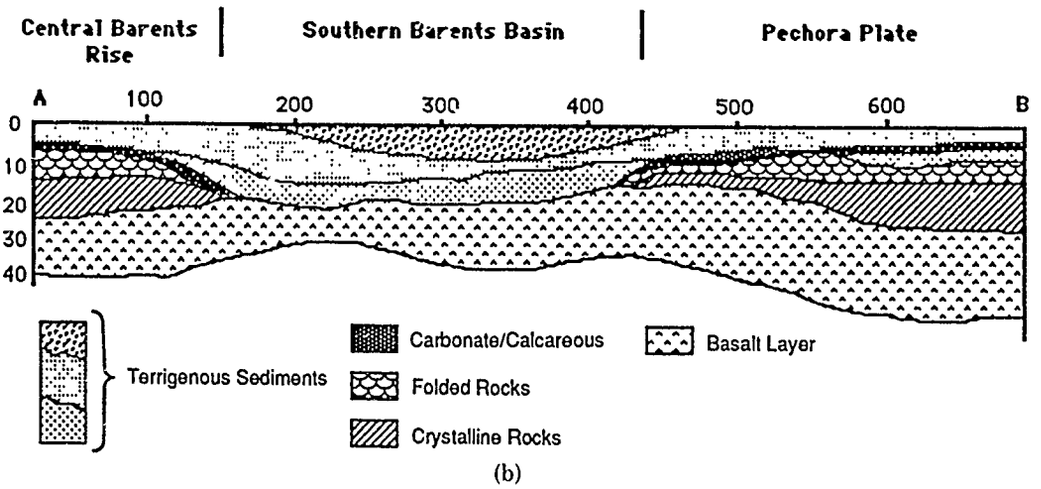

(b)

FIG. 13. (a) Geologic maps of the Barents Sea Basin (after Gramberg, 1988) showing contours of crustal thickness, granitic layer thickness, and regions of missing granitic layer. (b) NW–SE cross-section, labeled A–B in (a), across the southeastern part of the Barents Sea basin.

Sea Basin, which shows that the missing granitic/metamorphic layer is replaced by about 20 km of sediments. This region of thickened sediments occurs over an area of only about 300 km in lateral extent. The paths to NORESS and ARCESS must pass over these regions, whereas the path to Graefenberg passes to the southeast and misses this feature altogether. We argue that it is this feature that blocks the propagation of *Lg* across the Barents Sea.

Other authors have argued that crustal thickness variations can block the propagation of *Lg* (e.g., Kennett *et al.*, 1985). As shown in Figure 13, the crustal thickness in the Barents Sea can vary by as much as 10 km. However, we might expect that, if crustal thickness variations block *Lg*, *Sn* waves might also be affected. Kennett (1986), for example, has shown, using ray tracing, how the high-velocity modes (over 4.2 km/sec) that constitute both *Sn* and *Lg* would be diverted and scattered by crustal thickening. Even though *Sn* probably propagates primarily in the upper mantle, it would be expected to interact with a deformed crust-mantle interface, and thus, *Sn* should be partially affected by a strong change in crustal thickness. However, strong *Sn* waves have been observed at both NORESS and ARCESS crossing the Barents Sea. A near-surface heterogeneity, such as sediment thickness variations, would affect the lower-velocity modes in the *Lg* (3.5 to 4.0 km/sec) but not the higher velocity (over 4.2 km/sec) modes in *Sn*.

Another explanation for *Lg* blockage has been the "missing granitic layer" (e.g., Piwinskii, 1981), which might also explain why *Lg* does not propagate across oceanic basins. However, there is no apparent reason why a simple laterally homogeneous, two-layer continued crust, where the top granitic layer is replaced by a thick sedimentary layer, should not support the propagation of *Lg*.

Chan and Mitchell (1965) have suggested that *Lg* waves crossing the Barents Sea might be attenuated by the thick low-Q sediments. Nuttli (1988) has measured frequency-dependent Q for *Lg* waves from Novaya Zemlya to the WWSSN stations KEV and KBS. These *Lg* waves would have spent most of their time in the low Q sediments. Using the coda method, he estimates the *Lg* attenuation to be $Q = 252\ f^{0.6}$ for KEV and $Q = 315\ f^{0.5}$ for KBS. Although these values of Q are lower than others for continental propagation in Scandinavia, they are not low enough to explain the nearly complete elimination of *Lg* waves which cross the Barents Sea.

We argue that the blockage of *Lg* arises from the significant lateral variation of sediment thicknesses in the Barents Sea. This lateral heterogeneity causes the breakdown in the upper crustal wave guide and produces horizontal velocity contrasts that can cause scattering, such as *Lg*-to-*P* or *Lg*-to-*Sn*. Figure 13a shows that the region of "reduced sedimentary layer" on the Novaya Zemlya and Kola coasts could be the points where lateral velocity contrasts could cause the *Sn*-to-*Lg* scattering we have previously discussed. This mechanism would be very similar to one shown by Kennett (1986) for the elimination of *Lg* at a continent-ocean interface, except the breakdown would be due to the pinchout of the near-surface sedimentary layers at the Barents-Kola interface.

Finally, Figure 14 shows our interpretation of the coda shape variations observed in the Kazakh event codes. In this case, we believe that the scattering points occur in the vicinity of the Ural Mountains. The brackets in Figure 14 are the expected times for these conversions, and the fact that the *Sn* coda forms a kind of hump ahead of *Lg* may be produced by these scattered phases. The flat coda, which Baumgardt (1985a) argued was produced by *Lg*-to-*P* scattering in the Urals, appears to be devoid of any significant teleseismic *P* energy but rather appears to consist

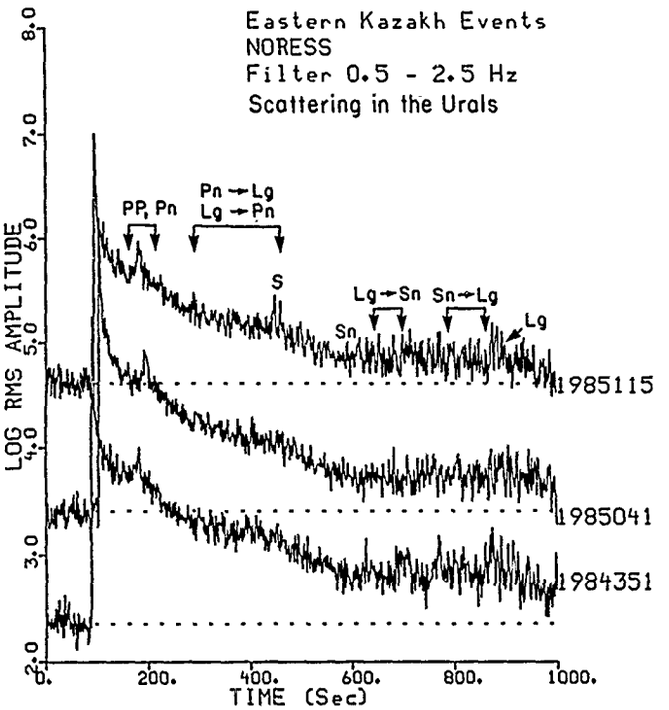

FIG. 14. Interpretation, in terms of scattering in the Ural Mountains, of coda waves recorded at NORESS from four events in eastern Kazakh.

mainly of *Pn* and *Lg* waves. Thus, as shown in Figure 14, we argue that this coda comes primarily from the reciprocal scattering of the *Pn*-to-*Lg* and *Lg*-to-*Pn* in the Urals. The FK scan analysis indicates that more of this energy arrives at the array as *Lg* energy than as *Pn* energy.

It should be noted that the polar-scan analysis only shows the apparent velocities of signals with the maximum FK power. Although the dominant energy in the flat coda comes from signals with *Pn* and *Lg* velocities, there could be coherent energy at higher velocities consistent with teleseismic *P* waves from the vicinity of the Urals. This energy could produce secondary peaks in FK space that were not picked in the polar scan analysis.

Comparison of the propagation paths to NORESS and ARCESS in Figure 1 suggests that the main blockage of *Lg* to ARCESS lies in the middle part of the Ural Mountains. A possible cause of this blockage may be the variation in the sediment thicknesses in the central part of the Uralides. The variations must be greater in the central part of the Urals than in the southern part, since *Lg* seems to propagate more efficiently across the southern Urals to NORESS than across the central Urals to ARCESS.

CONCLUSIONS

This regional array study of presumed explosions at far regional and teleseismic distances has shown the important effect that near-surface geologic structure has on the propagation of *Lg* waves to great distances. Since sediment-thickness variations seem to be an important factor that primarily or completely blocks *Lg* waves in shield regions, knowledge of near-surface geological structure can be very useful in understanding how efficiently *Lg* will propagate across a region. Such

effects must be taken into account when using the *Lg* wave for yield estimation or regional event identification.

One of the surprising observations in this study has been the fact that much of the early *P* coda, particularly the flat coda from the eastern Kazakh event, is composed of scattered *Lg* waves. This observation supports the earlier suggestion of Dainty (1985) that much of the coda is made up of *P*-to-*Lg* scattering in the vicinity of the receiver. However, our observations of *Lg* modes in the entire coda out to the arrival of direct *Lg* indicates that scattering of *Pn* and *Sn*-to-*Lg* occurs along the entire path. Moreover, we have also shown the importance of *Sn*-to-*Lg* scattering in the *Sn* coda. Finally, in the case of Novaya Zemlya and White Sea codas, we have observed enhanced pre-*Sn* codas whenever *Lg* appears to be blocked. This indicates that *Lg* energy may not be lost when it is blocked, but rather is simply converted to another form. Understanding this mechanism can be important in regional event identification and yield estimation.

ACKNOWLEDGMENTS

Jeanne Carney programmed most of the analysis programs and displays shown in this paper. I wish to thank Frode Ringdal and the Center for Seismic Studies for help in acquiring the NORESS and ARCESS data. I also thank Hans Peter Harjes for providing the Graefenburg data. Bill Leith of the USGS in Reston, Virginia, was very helpful in providing information from the Russian literature about the geologic structure in the Barents Sea and Ural Mountains regions, for which I am very grateful.

This research was sponsored by the Defense Advanced Research Projects Agency, Nuclear Monitoring Research Office, ARPA Order No. 5307, issued by the Air Force Geophysics Laboratory under Contract F-19628-89-C-0030.

REFERENCES

Barazangi, M. J. (1977). Relative excitation of the seismic shear waves *Sn* and *Lg* as a function of source depth and their propagation from Melanesia and Banda arcs to Australia, *Ann. di Geofis.* **30**, 385–407.

Båth, M. (1954). The elastic waves *Lg* and *Rg* along Euroasiatic paths, *Archiv. Geofysik* **2**, 295–342.

Baumgardt, D. R. (1984). Relative *Lg* and *P*-coda magnitude analysis of the largest Shagan River Explosions, Final Report to AFOSR, SAS-TR-84-03, ENSCO, Inc., Springfield, Virginia.

Baumgardt, D. R. (1985a). Comparative analysis of teleseismic *P* coda and *Lg* waves from underground nuclear explosions in Eurasia, *Bull. Seism. Soc. Am.* **75**, 1413–1433.

Baumgardt, D. R. (1985b). Attenuation, blockage, and scattering of teleseismic *Lg* from underground nuclear explosions in Eurasia, AFGL-TR-85-0332, ENSCO, Inc., Springfield, Virginia.

Baumgardt, D. R. (1986). Spectral determination of regional and teleseismic *Lg* attenuation, Final Report, AFGL-TR-87-0217, ENSCO, Inc., Springfield, Virginia.

Blandford, R. R. (1974). An automatic event detector at the Tonto Forest seismic observatory, Geophysics **39**, 633–643.

Chan, W. W. and B. J. Mitchell (1985). Surface wave dispersion, crustal structure, and sediment thickness variations across the Barents shelf, *Geophys. J. R. Astr. Soc.* **80**, 329–344.

Chinn, D. S., B. L. Isacks, and M. Barazangi (1980). High-frequency seismic wave propagation in western South America along the continental margin, in the Nazca plate and across the Altiplano, *Geophys. J. R. Astr. Soc.* **60**, 209–244.

Dainty, A. M. (1985). Coda observed at NORSAR and NORESS, Final Report, AFGL-TR-85-0199.

Gramberg, I. S. (1988). *The Barents Shelf Plate* (in Russian), vol. 196, Nedra, Leningrad, USSR.

Harjes, H. P. and D. Seidl (1978). Digital recording and analysis of broadband seismic data at the Graefenberg (GFR) array, *J. Geophys. Res.* **44**, 511–523.

Isacks, B. L. and C. Stephens (1975). Conversion of *Sn* to *Lg* at a continental margin, *Bull. Seism. Soc. Am.* **65**, 224–235.

Kadinsky-Cade, K., M. Barazangi, J. Oliver, and B. Isacks (1981). Lateral variations of high-frequency seismic wave propagation at regional distances across the Turkish and Iranian Plateaus, *J. Geophys. Res.* **86**, 9377–9396.

Kennett, B. L. N., S. Gregersen, S. Mykkeltveit, and R. Newmark (1985). Mapping of crustal heterogeneity in the North Sea basin via the propagation of *Lg* waves, *Geophys. J. R. Astr. Soc.* **83**, 299–306.

Kennett, B. L. N. (1986). *Lg* waves and structrual boundaries, *Bull. Seism. Soc. Am.* **76,** 1133–1142.

Kværna, T. and D. J. Doornbos (1986). An integrated approach to slowness analysis with arrays and three-component stations, in *NORSAR Scientific Rept. No. 1-85/86*, Kjeller, Norway.

Mykkeltveit, S. K., K. Astebol, D. J. Doornbos, and E. S. Husebye (1983). Seismic array configuration optimization, *Bull. Seism. Soc. Am.* **74,** 2313–2333.

Ni, J. and M. Barazangi (1983). High-frequency seismic wave propagation beneath the Indian Shield, Himalayan Arc, Tibetan Plateau and surounding regions: high uppermost mantle velocities and efficient *Sn* propagation beneath Tibet, *Geophys. J. R. Astr. Soc.* **72,** 665–689.

Nuttli, O. W. (1986). *Lg* magnitudes of selected East Kazakhstan underground explosions, Bull. Seism. Soc. Am. **76,** 1241–1251.

Nuttli, O. W. (1988). *Lg* magnitudes and yield estimates of Novaya Zemlya nuclear explosions, *Bull. Seism. Soc. Am.* **78,** 873–884.

Piwinskii, A. J. (1981). Deep structure of the earth's crust and upper mantle in the USSR according to geological, geophysical, and seismological data: Dneiper-Donetsk and Pri-Caspoan depressions, UCID-19203, Lawrence Livermore Laboratory, Livermore, California.

Ringdal, F. and B. K. Hokland (1987). Magnitudes of large Semipalatinsk explosions using *P* coda and *Lg* measurements at NORSAR, *NORSAR Sci. Rept. No. 1-87/88*, Kjeller, Norway.

Ringdal, F. and J. Fyen (1988). Comparative analysis of NORSAR and Graefenburg *Lg* magnitudes of Shagan River explosions, *NORSAR Scientific Rept. No. 1-88/89*, Kjeller, Norway.

Ringdal, F. and P. D. Marshall (1989). Yield determination of Soviet underground nuclear explosions at the Shagan River test site, *NORSAR Scientific Rept. No. 2-88/89*, Kjeller, Norway.

Ruzaikin, A., I. Nersesov, V. Khalturin, and P. Molnar (1977). Propagation of *Lg* and lateral variations in crustal structure in Asia, *J. Geophys. Res* **82,** 307–316.

Shumway, R. H. (1971). On detecting a signal in *N* stationarily correlated noise series, *Technometrics* **13,** 499–519.

Watson, J. (1976). Eo-Europa: the evolution of a craton, in *Europe from Crust to Core*, D. V. Ager and M. Brooks, Editors, Wiley, London.

ENSCO, INC.
5440 PORT ROYAL ROAD
SPRINGFIELD, VIRGINIA 22151

Manuscript received 16 February 1990

Bulletin of the Seismological Society of America, Vol. 80, No. 6, p. 2282, December 1990

MINUTES OF THE SPECIAL MEETING OF THE BOARD OF DIRECTORS

MAY 1, 1990

The Special Meeting of the Board of Directors of the Seismological Society of America was called to order by President John Filson at 12:45 PM on May 1, 1990 in the Santa Cruz Room at the Dream Inn, Santa Cruz, California. Present at roll call were: Directors Basham, Crosson, Langston, Slemmons and Wu; Secretary Litehiser; Treasurer Followill; *BSSA* Editor Boore; Eastern Section Chairman Talwani; and Headquarters Director Newman. Directors McGuire and Kanamori and Directors-Elect Johnston and Jones joined the meeting in progress during the afternoon. Treasurer Followill was called away by his duties as Annual Meeting convener during much of the meeting.

President Filson reviewed the actions taken by the Board at its special meeting in December. He presented a memorandum addressed to the Officers and Directors on "New Directions" for SSA growing out of the December meeting.

Following extended discussion, the Directors ask that the minutes record the following actions summarized from President Filson's memorandum:

"In order to fulfill the purposes and express the vigor of the Society and to better serve its members, the Board of Directors unanimously approved the following three resolutions:

1. From time to time the Society may conduct special meetings or forums for its members and other parties on special topics and issues within seismology or related fields. These meetings will consist of focused presentations and discussions that may include, in addition to research results, applications of these results to issues of public safety or other issues. The forums may be held in conjunction with the annual meeting or separately. The proceedings of these forums will be published by the Society and include reviewed papers presented at the meetings. The Society may submit proposals to government agencies or private institutions to raise funds for these meetings.
2. The Society will publish special volumes or extensions of the *Bulletin* on important earthquakes, proceedings of Society forums, and other topics. A special editor or editors will be named for each publication, and "outside" funding may be required to bear the cost of the publications.
3. An ad hoc Committee of the Board on Policy will be formed and charged with identifying and reviewing those issues and opportunities where a statement by the Society would be useful and appropriate. The members of the Policy Committee will participate in the drafting of such statements for the review and approval of the general Board. The Policy Committee shall consist of the President, Vice President, and Past President of the Society. The Board shall adopt such statements by consensus.

The Board agreed to define consensus as meaning that, after the Executive Committee of the Board had made a reasonable attempt to contact all Directors for comments on the draft statement, consensus would be obtained if no Director contacted strongly objected to the statement being issued publicly.

The Special Meeting of the Board adjourned at 3:55 PM.

JOE J. LITEHISER, JR.
Secretary

Bulletin of the Seismological Society of America, Vol. 80, No. 6, pp. 2283–2285, December 1990

MINUTES OF THE MEETING OF THE BOARD OF DIRECTORS OF THE SEISMOLOGICAL SOCIETY OF AMERICA

Coconut Grove Conference Center, Santa Cruz, California

MAY 1–2, 1990

The 1989–90 Board of Directors of the Seismological Society of America met at the Coconut Grove Conference Center, Santa Cruz, California, on May 1–2, 1990. President John Filson called the meeting to order at approximately 4:00 PM. The following Directors were present: Alexander, Basham, Crosson, Filson, Langston, McGuire, and Slemmons. Also present were: Secretary Litehiser, *BSSA* Editor Boore, Directors-Elect Johnston and Jones, and Eastern Section Chairman Talwani. Headquarters Director Newman was also in attendance. Director Kanamori joined the meeting in progress.

President Filson reviewed his efforts during the year to encourage the Board to consider new initiatives for SSA. A special meeting of the Board was held in December 1989 to discuss his white paper on the advantages and disadvantages of new initiatives. The meeting resulted in a consensus that some expansion of SSA's role would be appropriate. A second Special Meeting on May 1 resulted in specific proposals for new activities.

The Minutes of the Board of Directors Meeting of April 19, 1989 were approved as printed in the December 1989 *Bulletin of the Seismological Society of America* (pages 2020–2022). Minutes of the December 3, 1989 Board of Directors Meeting will appear in the August 1990 issue of the *Bulletin*.

Secretary Joe Litehiser's report was approved and ordered published in the *Bulletin*.

A written report from *BSSA* Editor Boore and the Board of Editors was accepted and placed on file. Discussion was begun on a special issue of *BSSA* on the Loma Prieta earthquake. Boore reported that the Editorial Committee had not met.

The 1989–90 Board was adjourned at 5:00 PM until 7:30 PM or May 2, 1990.

The 1989–90 Board was reconvened at 7:35 PM on May 2, 1990. In attendance were Directors Alexander, Basham, Filson, Heaton, Kanamori, Langston, McGuire, Slemmons and Wu; Directors-Elect Johnston and Jones; Secretary Litehiser; Treasurer Followill; Eastern Section Chairman Talwani; and Headquarters Staff Newman and Rowe.

The Board resumed discussion of a possible special issue of *BSSA* on the Loma Prieta earthquake. *BSSA* Editor Boore announced that Tom Hanks had agreed to serve as Special Editor. An engineer will be asked to serve as Co-Editor. Papers are to be submitted by October 19, 1990 and publication by October 17, 1991.

The Treasurer's report was accepted by the Board and ordered published in the *Bulletin*.

Director Newman's report was accepted by the Board. The staff is smaller than it was in the early 1970s, so much of the staff effort simply maintains basic operations. As time permits, the staff is addressing old problems and new initiatives. Recent and ongoing efforts include the new roster in SRL, abstract form revisions, marketing, and a thorough review of back issue inventories.

Annual Meeting Chairman Followill reported that persons submitting abstracts for the Annual Meeting had been asked to include their I.D. number on the abstract. This created a problem, because most people do not know their identification numbers. It was suggested that future rosters include the I.D. number. He also reported that the policy of giving a substantial discount to Corporate Members who exhibit at the meeting has been very well received and has resulted in at least one new corporate member.

Reproduction of the membership roster on floppy disk was considered by the Board and deferred.

McGuire stated that insurance policies need to be reviewed annually so that coverage does not get too out-of-date. Newman said this was being done and agreed to send further details to the Executive Committee.

The 1989–90 board adjourned at 8:42 PM. The 1990–91 board convened immediately thereafter.

John Filson served as Chairman until his successor was selected. Present at roll call were Directors Alexander, Filson, Heaton, Johnston, Jones, Langston, McGuire, Slemmons, and Wu. Also present were: Secretary Litehiser, Treasurer Followill, *BSSA* Editor Boore, Eastern Section Chairman Talwani, Headquarters Director Newman and Assistant Director Rowe. 1990 Annual Meeting Co-Convener Karen McNally, and 1991 Annual Meeting Chairman, Ivan Wong, joined the meeting for brief reports.

Alexander reported on behalf of Robert Crosson, Chair of the Board Nominating Committee. The following officers were elected by acclamation: President, Charles Langston; Vice-President, Robin McGuire; Secretary, Joe Litehiser; Treasurer, Fred Followill.

The meeting was turned over to President Langston who thanked President Filson for his leadership and also thanked the retiring board members.

Co-conveners Followill and McNally reported on the 1990 meeting. Two hundred and forty abstracts were submitted. There will be a poster session on Friday, which is a first for an SSA meeting. Followill stated that there were 302 people pre-registered; 53 attending as guests and approximately 60 people who had registered on site.

The Board of Directors appointed Robin McGuire to serve as the third member of the Executive Committee. The current Board of Editors, David M. Boore, C. B. Crouse, John Vidale, and Steven Wesnousky were reaffirmed. Lucile Jones was appointed to the Editorial Committee to replace Robin McGuire. Christopher Scholz and David Boore continue as the other members of the committee.

The Board reviewed the following changes to the membership rolls for the year ending January 31, 1990.

NEW REGULAR MEMBERS

Baxter H. Armstrong	Mark A. Hemphill-Haley	Robert L. Nigbor
Vishal Arora	Patrick J. Jenks	Edo Nyland
Richard E. Baldwin	Rong-Song Jih	William A. Peppin
William R. Berglof	Shigeo Kinoshita	C. V. Ramakrishna Rao
Firyal Bou-rabee	Edi Kissling	Frode Ringdal
Thomas M. Boyd	Michele Laharre	Peter M. Roberts
Yousef Bozorgnia	David B. Lapp	Robert K. Samuelson
Kenneth B. S. Burke	William R. Lettis	Rick J. Santa
Vlastislav Červeny	Conrad D. Lindholm	Laura Serpa
B. Chandra	Paul D. McCarthy	Joe W. Steelman
J. Peter Davis	Chris J. Marone	David M. Stone
Michael A. Ellis	Kevin Lee Mickus	J. Timothy Sullivan
Stanley M. Flatte	Kazuo Mino	Giuseppe Tranfaglia
Thomas A. Gaitley	Chin Man Mok	Andrew Vonk
Jean-Christophe Gariel	Pamela S. Morgan	Margaret D. Wiggins-Gradison
George Gazetas	Brian Moriarty	

New Members: 47

NEW STUDENT MEMBERS

Douglas B. Bausch	Tor Hilton	Arthur Rodgers
Benjamin J. Brantley	William E. Holt	Ann F. Sheehan
Claudia C. Carabajal	Prakash Chandra Jha	Michael P. Sleeman
Percy Chirinos-Arias	Grant Lindley	Tuncay Taymaz
Edward H. Field	Hanxing Liu	Lisa H. Tressler
James B. Gaherty	Hein Meidow	Yung-Tun Yang
Charles N. Herrick	Jorge Marino Protti-Quesada	Weiping Zhang
		Peter C. Zwick

New Student Members: 22

Total New Members: 69

Deaths of the following members were reported during the year: Henry J. Degenkolb, J. R. Goberna, Roy E. Hanson (Honorary), Sir Harold Jeffreys (Honorary), Robert Klotz, Guy C. Omer (Life), Harry B. Seed, and Roger Sumner.

Following a review of members whose dues were unpaid for 1989-90, and whose names had been removed from the *Bulletin* mailing list in January 1989, the Board instructed the Secretary to advise each delinquent member of his status and, if no response is received within 60 days of notification, to drop his name from the membership rolls. Directors were urged to contact those on the list whom they know to urge them to continue their membership.

The Board reviewed the Bar Graph prepared by Secretary Litehiser showing that membership has been essentially flat over the last ten years.

Ivan Wong reported on the progress of the 1991 annual meeting to be held in San Francisco in conjunction with the Cordilleran Section of GSA. The dates are March 25–27, 1991. Most sessions will be at the Cathedral Hill Hotel.

Pradeep Talwani reported on the activities of the Eastern Section of SSA. The 1990 meeting will be October 17–19 at the Virginia Polytechnic Institute in Blacksburg, Virginia. Gil Bollinger and Arthur Snoke are the Chairmen. There will be two special symposia.

The role of the eastern section and *Seismological Research Letters* (*SRL*) was discussed at the December Board Meeting. One suggestion was that *SRL* could become a newsletter for the whole society. Talwani reported that the Eastern Section leaders had discussed that suggestion and had some concerns. Talwani stated that *SRL* cannot become an *EOS*. *SRL* is a quarterly publication and cannot publish things with a short shelf life. He reminded the Board that *SRL* has an all-volunteer staff consisting of Arch Johnston, Robert Herrmann, and Margaret Hopper. In order for *SRL* to become more active in the affairs of the whole Society, it would need more support from the headquarters staff. Eastern Section members like the focus on Eastern issues, but it could take a larger role without competing with *BSSA*. *SRL* currently averages 6 papers per issue and would like to have about 10. A number of papers that are not appropriate for *BSSA* can be accommodated in *SRL*. He stated that the Eastern Section welcomes input from the SSA Board.

Alexander reported that the Board Nominating Committee had no recommendations for Honorary membership. The Committee suggested, and Alexander moved, that the Society consider an additional class of membership to be called Fellows. Election as a Fellow would recognize achievement without lifetime waiver of dues. After discussion the motion was defeated.

Litehiser presented a written report from William Lee on the IASPEI Software Library. SSA is distributing the software on a cost-sharing basis. It is seen as a benefit to members not as a money maker.

Litehiser reported that it cost the Society $10 K last year to supply reprints and recommended that the Board eliminate free reprints to those who pay page charges. He proposed that reprints be available at cost for those who pay page charges and with a 50% markup for those for whom page charges are waived. The proposition was discussed. Filson moved and Heaton seconded that the recommendation be accepted. Motion passed.

The Board discussed nominations for the Society Medal. The Executive Committee will make the final decision based on guidance from the Board. Any 1990 recipient will be announced with the Call for Papers for the 1991 meeting.

Newman, noting that some members and firms are already paying for members in soft-currency foreign countries, proposed that the Society encourage the expansion of this practice. The Board felt that it would be too difficult to keep ongoing sponsors beyond an initial year or two. The proposal was defeated. Newman was directed to pursue foundation funding and report to the Executive Committee.

The Board reviewed the dues and fees history and the budget for fiscal year ending January 31, 1991. Followill explained that the budget is actually a three-year budget. Some of the increases proposed will not take effect until fiscal 1992. McGuire moved and Heaton seconded that the proposed budget be accepted. Motion passed.

The Board accepted an invitation from James Ni of New Mexico State University on behalf of Los Alamos National Laboratory, New Mexico Technical Institute, and New Mexico State University to meet at Santa Fe, New Mexico, in 1992. Action was deferred on an invitation from Diane Doser and Randy Keller of the University of Texas at El Paso to meet in El Paso in 1993 or a future year.

A resolution expressing the Board's appreciation to Fred Followill and Karen McNally, co-conveners for the Meeting; Lawrence Livermore National Laboratory, University of California; Earth Science Board of The University of California at Santa Cruz and members of the organizing committee for the 1990 meeting was unanimously approved by the Board. The Board also expressed its thanks to David Schwartz of USGS and Roberta Smith-Evernden of UC-Santa Cruz for organizing the field trips.

The meeting adjourned at 12:00 PM.

JOE J. LITEHISER, JR.
Secretary

Bulletin of the Seismological Society of America, Vol. 80, No. 6, pp. 2286–2297, December 1990

MINUTES OF THE ANNUAL MEETING OF THE SEISMOLOGICAL SOCIETY OF AMERICA

MAY 3, 1990

The Eighty-Fifth Annual Meeting of the Seismological Society of America was held May 2–4, at the Coconut Grove Conference Center in Santa Cruz, California, sponsored by the Lawrence Livermore National Laboratory and the University of California, Santa Cruz.

The Annual Business Meeting was held at a luncheon on May 3. Approximately 230 people attended.

Retiring President John R. Filson welcomed members and guests to the meeting and introduced the officers and directors of SSA seated at the Head Table. He announced the newly elected SSA officers for 1990-91: President, Charles A. Langston; Vice-President, Robin K. McGuire; Secretary, Joe J. Litehiser, Jr.; and Treasurer, Fred E. Followill.

Incoming President Langston highlighted actions taken at the Board of Directors Meetings on May 1–2.

The 1991 Annual Meeting will be on March 25–27 in San Francisco with the Cordilleran Section of the GSA. Ivan Wong of Woodward-Clyde Consultants is the SSA Chairman. The 1992 Annual Meeting will be in Santa Fe, New Mexico, hosted by New Mexico State University, Los Alamos National Laboratory, and New Mexico Technical Institute. The 1990 Annual Meeting of the Eastern Section of the Society will be on October 17–19 at Virginia Polytechnical Institute in Blacksburg, Virginia.

Langston expressed the Board's thanks to the Eastern Section editorial committee, Arch Johnston, Robert Herrmann, and Margaret Hopper, for preparation of the abstract volume (*Seismological Research Letters*, Volume 61:1) that also contains the new SSA membership roster.

Plans for a special issue of *BSSA* on the Loma Prieta earthquake were announced. Tom Hanks will be Editor of the special issue.

President Langston expressed SSA's appreciation to Lawrence Livermore National Laboratory and the University of California, Santa Cruz, and especially to Dr. Fred E. Followill and Dr. Karen McNally for organizing an outstanding conference. Thanks were also expressed to David Schwartz of USGS and Roberta Smith-Evernden of UCSC for organizing the field trips.

The 1990 Society Medal was presented to Leon Knopoff.

Outgoing President Filson spoke on "The Status and Future of the Society."

PROGRAM OF TECHNICAL SESSIONS

WEDNESDAY, MAY 2, 1990

Nuclear Explosion Seismology
Presiders: S. Taylor and M. Denny
Wednesday AM

M. D. Denny: NTS Seismic Yield Experiment: An Overview

T. F. Hauk and S. P. Jarpe: NTS Seismic Yield Experiment: Comparison of Airgun and HE Seismic Sources

T. M. Daley and T. V. McEvilly: NTS Seismic Yield Experiment: VSP Site Characterization Study

L. R. Johnson: NTS Seismic Yield Experiment: Source Characterization

M. D. Denny, D. B. Harris, and D. M. Goodman: NTS Seismic Yield Experiment: Transfer Functions, Magnitudes and Corner Frequencies vs. Depth

D. E. Maxwell and M. D. Denny: NTS Seismic Yield Experiment: Computer Simulations of Freefield Ground Motion

Nuclear Explosion Seismology
Presiders: S. Taylor and M. Denny
Wednesday AM

G. Zandt, S. Jarpe, and H. Benz: NTS Seismic Yield Experiment: Rubble Zone Imaging

S. R. Taylor and M. D. Denny: An Analysis of Spectral Differences between NTS and Shagan River Nuclear Explosions

I. N. Gupta, W. W. Chan, and R. A. Wagner: Effect of Shot Depth on the Spectra of Regional Phases from NTS and East Kazakh Explosions

K. L. McLaughlin: Excitation of *Lg* and *P* Coda by Shallow Seismic Sources

C. A. Langston: High Frequency Tectonic Release from the Soviet JVE Explosion of September 14, 1988

K. G. Hinzen, S. K. Reamer, and B. W. Stump: Interaction of Coupling and Firing Time Variations in the Seismic Wavefields Radiated from Quarry Blasts

Earthquake Engineering
Presiders: S. D. Oaks and C. Stark
Wednesday AM

S. D. Oaks: The Damage Assessment Process After the October 17, 1989, Loma Prieta Earthquake: An Analysis of the Application of ATC 20

M. D. Trifunac: Dependence of Fourier Spectrum Amplitudes of Recorded Strong Earthquake Accelerations on Local Soil Conditions and Depth of Sediments

K. Sadigh and C.-Y. Chang: Response Spectra Relationships for Rock, Deep-Stiff Soil and Soft Soil Site Conditions

W. Silva, C. Stark, S. J. Chiou, R. Green, J. C. Stepp, J. Schneider, and D. Anderson: Nonlinear Soil Models Based upon Observations of Strong Ground Motions

K. W. King, R. A. Williams, D. L. Carver, E. Cranswick, and D. M. Worley: Site Response and Building Damage in Santa Cruz, California

M. I. Todorovska and M. D. Trifunac: Two Dimensional Building-Soil Interaction for Incident *P*-, *SV*-, and Rayleigh Waves

Strong Motions in Basin Settings
Presiders: G. T. Lindley and R. H. Clouser
Wednesday AM

M. Ordaz, S. K. Singh, R. Castro, E. Mena, and R. Quaas: Are the Seismic Waves Amplified Even in the Hill Zone of Mexico City?

G. T. Lindley and R. J. Archuleta: Topographic Effects on Ground Motion by Analysis of Loma Prieta Aftershocks

R. H. Clouser: Sedimentary Basin Structure and Attenuation from Modeling Aftershock Accelerograms of the 19 March 1984 Gazli Earthquake, Uzbekistan, USSR

H. Kawase and T. Sato: Study on Strong Ground Motion in a Soft Basin Considering Surface Waves Generated at the Edges

T. Sato and H. Kawase: The Effect of the Source Location on the Response Characteristics of a Sediment-Filled Basin

S. Yamamoto, Y. Hisada, and S. Tani: Simulation of Long-Period Seismic Motions on the Kanto Sedimentary Basin, Japan, during Shallow Earthquakes

Towards a Master Model for Southern California Earthquakes and Seismic Prediction
Presiders: K. Aki and K. McNally
Wednesday AM

K. Aki: Master Model for Seismogenic Structures and Earthquake Process (Invited)

R. J. Archuleta: Prediction of Strong Ground Motion: How Much Uncertainty? (Invited)

C. Nicholson and R. L. Wesson: An Updated Ten-Year Seismicity Forecast for California (1987–1996): How Are We Doing?

L. Knopoff: Are Unmapped Faults Important in Modeling Seismicity? (Invited)

D. C. Agnew and L. M. Jones: Prediction Probabilities from Foreshocks

K. C. McNally, M. Protti, J. Yellin, E. Malavassi, W. Schillinger, and Z. Zhang: The Occurrence of a Large ($Ms \geqq 7.0$) Earthquake Creates an Opportunity for Coordinated Research in a "Master Model" Context

Loma Prieta/Geology
Presiders: D. Schwartz and R. H. Sibson
Wednesday AM

L. Seeber and J. G. Armbruster: Evolution of Fault Kinematics in the Loma Prieta Rupture Area During 20 Years Before 1989

R. H. Sibson: Speculations on Structural Controls Affecting the Loma Prieta Earthquake of October 17, 1989 (Invited)

D. P. Schwartz and C. S. Prentice: Surface Fractures in the Loma Prieta Area, CA: 1906 and 1989

W. R. Cotton, W. L. Fowler, and J. E. van Velsor: Coseismic Bedding Plane Faulting Associated with the Loma Prieta Earthquake of October 17, 1989

D. J. Ponti and R. E. Wells: Origin of Surface Ruptures that Formed in the Santa Cruz Mountains, California, During the Loma Prieta Earthquake

M. Lisowski, W. H. Prescott, and J. C. Savage: Little Postseismic Deformation Detected After the Loma Prieta Earthquake

Nuclear Explosion Seismology
Presiders: D. Harris and T. Hauk
Wednesday PM

B. W. Stump and R. E. Reinke: Comparison Between Spectral Interpretation and Full-Wave Modeling Using Moment Tensor Inversion of Near-Source Explosion Waveforms

K. Koch and B. W. Stump: Observed and Synthetic Far-Regional Seismograms with Implications for Seismic Source Functions from Explosions with Spall

J. Schlittenhardt: The Effects of Spall on Teleseismic *P* Waves: An Investigation with Theoretical Seismograms

T. G. Barker, S. M. Day, and K. L. McLaughlin: A Simple Physical Model for Spall from Nuclear Explosions Based upon Numerical Simulations

W. W. Chan and R. R. Baumstark: Characteristics of Regional Phase Discrimination

S. S. Alexander: The Combined Use of Regional Phases to Distinguish Earthquakes from Explosions in Intraplate Settings

Nuclear Explosion Seismology
Presiders: D. Harris and T. Hauk
Wednesday PM

D. Harris and P. Goldstein: Slowness Precision and Resolution Capabilities of Dense Seismic Arrays

F. E. Followill: Configuration and Design of Sparse Broadband Seismic Arrays

P. W. Basham and R. G. North: The New Yellowknife Seismic Array—An Advanced Tool for Nuclear Test Monitoring and Seismological Research

J. R. Murphy: A New System for Seismic Yield Estimation of Underground Explosions

T. J. Bennett, A. K. Campanella, B. W. Barker, and J. R. Murphy: Analysis of Regional Seismic Signals from Soviet Explosions Recorded at CDSN and IRIS

R. J. Stead, S. R. Bratt, H. J. Swanger, and F. Ryall: Results from the Intelligent Monitoring System

Seismic Hazard Assessment
Presiders: R. K. Smith-Evernden and J. Marrone
Wednesday PM

N. Abrahamson, J. Marrone, and J. Litehiser: The Effect of Aftershocks on Seismic Hazard Analyses

B. A. Schell: Fault-rupture and Earthquake Potential along the Mojave Segment of the San Andreas Fault System

W. R. Lettis, K. L. Hanson, and N. T. Hall: Strain Partitioning: Implications for Seismic Hazards Assessment

A. S. Kiremidjian, H. Thrainsson, K. Ahrens, J. Schneider, and D. Schwartz: Probabilities of Occurrences of Events on the Northern San Andreas

D. Pantosti and G. Valensise: Coastal Uplift as a Tool for Assessing the Seismic Potential of Blind Faults, Two Case Histories: The 1908 Messina Straits and the 1989 Santa Cruz Earthquakes

R. K. Smith-Evernden and B. V. Vassil: Lessons about "Alquist-Priolo Zone" Earthquake Hazards Assessments from the October 17, 1989 Loma Prieta (Santa Cruz Mountains, California) Earthquake

Near-Field Source Inversion
Presiders: P. Goldstein and S. H. Seale
Wednesday PM

Y. H. Zeng, T. L. Teng, and K. Aki: A Recursive Stochastic Inversion Algorithm and Its Application to Seismological Inverse Problems

M. Cocco and P. Spudich: Iterative Frequency-Domain Inversion of Ground Motions to Determine Earthquake Rupture Behavior

R. Archuleta and P. Sangas: Earthquake Source Parameters Determined from the Gamer Valley Downhole Array of Accelerometers

P. Goldstein: Comments on Current Capabilities for Measuring Rupture Propagation During Earthquakes

S.-J. Chiou and B. A. Bolt: Resolution of Seismic Sources from Strong Motion Array Data

M. Iida: Preliminary Analysis of Resolving Power of Existing Strong-motion Arrays for Source Inversion

S. H. Seale and R. J. Archuleta: Strong Motion from a Simulated Earthquake on the Northern San Jacinto Fault

Tectonics
Presiders: S. N. Ward and R. A. Harris
Wednesday PM

W. Zhang: Aseismic Slip Rate Distribution in the Shumagin Seismic Gap, Alaska

P. Segall, Y. Du, and W. Thatcher: Were the 1934 and 1966 Parkfield Earthquakes Similar?

A. Sylvester, J. Helm, C. Hitchcock, and N. Howe: Minor Vertical, but No Horizontal Near-field Displacement Across the San Jacinto Fault at Anza and San Bernardino, California from 1988 to 1990

R. A. Harris and R. J. Archuleta: When Do Stepovers between En-Echelon Fault Segments Stop Propagating Shear Fractures?

P. L. Williams and S. P. Nishenko: Definition of the Loma Prieta Fault Segment: A Successful Geology-based Prediction

J. Adams: Speculations on the Mode of Failure of the Alpine Fault, New Zealand: A Consequence and Not the Cause of Great Earthquakes?

Tectonics
Presiders: S. N. Ward and R. A. Harris
Wednesday PM

D. L. Wells and W. R. Lettis: Empirical Assessment of Earthquakes on Reverse/Thrust Faults and Surface Deformation

R. Stein and G. Ekstrom: Anatomy of a 110-Km-Long Blind Thrust Fault in Central California, from Short- and Long-Period Seismology, Geodesy, and Seismic Reflection Profiles

S. Y. Schwartz, D. L. Orange, and R. S. Anderson: Complex Fault Interactions in a Restraining Bend on the San Andreas Fault, Southern Santa Cruz Mountains

K. P. Furlong and C. A. Langston: Geodynamic Aspects of the Loma Prieta Earthquake: Constraints from Rheological and Source Modeling

G. Valensise and S. N. Ward: Recurrence Interval of Loma Prieta-Type Earthquakes Based on Long-Term Uplift Patterns Along the Santa Cruz Coastline

THURSDAY, MAY 3, 1990

Site Response
Presiders: O. Bonamassa and P. Somerville
Thursday AM

M. Dravinski, H. Eshraghi, H. Deng, T. K. Mossessian, and H. Kagami: Observation of Long-Period Microtremors in the Los Angeles Sedimentary Basin

N. A. Abrahamson, J. F. Schneider, and J. C. Stepp: Spatial Variation of the Fourier Amplitudes of Strong Ground Motions

O. Bonamassa and J. E. Vidale: Investigation of Directional Site Resonances Using Aftershocks from the Loma Prieta Earthquake

J. E. Vidale, O. Bonamassa, and S. Y. Schwartz: Array Studies of Ground Motion Using Aftershocks of the Loma Prieta Earthquake

P. G. Somerville and J. Yoshimura: Influence of MOHO Reflections on Ground Motions Recorded in San Francisco and Oakland During the 1989 Loma Prieta Earthquake

V. Caillot and P. Y. Bard: Variability of Acceleration Response Spectra across SMART1 Array

General Strong Motion/Site Response Studies
Presiders: B. P. Cohee and B. Stump
Thursday AM

B. P. Cohee and P. G. Somerville: Simulated and Empirical Estimates of Strong Ground Motion from Wadati-Benloff Zone Earthquakes beneath Western Washington

J. H.-X. Liu: Scaling of Far-Field Displacement Amplitude Spectrum of Composite Model of Seismic Source based on Fractal Description of Fault Inhomogeneity

B. W. Stump, D. C. Pearson, and K. D. Thomason: Utilization of Complete Surface-Source, Experimental Green's Functions in Shallow Site Characterization

D. C. Pearson, B. W. Stump, and K. D. Thomason: Properties of Compressional and Shear Sources Utilized in Shallow Site Characterization

J. Yoshimura and N. Abrahamson: Quantitative Goodness-of-Fit of Strong Motion Simulations for Seismological Analyses

Earthquake Source Parameters
Presiders: J. Mori and L. Wennerberg
Thursday AM

R. E. Baldwin and G. C. Rogers: Source Parameters of Earthquakes Along the Eastern Margin of the Canadian Cordillera

R. Wahlstrom and G. C. Rogers: Source Parameters for Earthquakes in the Vancouver Island Region of the Cascadia Subduction Zone

R. P. Dziak and S. G. Wesnousky: Body-Waveforms and Source Parameters of some Moderate-Sized Earthquakes near North Island, New Zealand

T. C. Wallace: Determination of Source Parameters for Small Earthquakes from a Single Very Broad Band Seismic Station

K.-F. Ma and H. Kanamori: Broadband Study of the December 3, 1988 Pasadena Earthquake Sequence

L. Wennerberg: Observing Source Complexity in Locally Recorded Accelerograms from Coalinga, California

J. Mori: Rupture Directivity Observed for Two Magnitude 4 Earthquakes near the San Jacinto Fault

K. Satake, K.-F. Ma, and H. Kanamori: Tsunamis from the 1989 Loma Prieta and the 1906 San Francisco Earthquakes

Earthquake Source Parameters
Presiders: T. Wallace and J. S. Barker
Thursday AM

L. Ruff and B. Tichelaar: Is Seismic Moment the Best Measure of Earthquake Size?

Y.-B. Tsai: Relationships between Seismic Moment and Fault Rupture Length of Shallow Strike-Slip Earthquakes

H. Houston and S. Beck: A Broadband Waveform Analysis of the Rupture Process of the October 20, 1986 Kermadec Earthquake ($Mw = 7.7$)

G. C. Beroza and T. H. Jordan: Evidence for Slow Earthquake Rupture from 10 Years of Continuously-Monitored Normal-Mode Activity

A. J. Mendez and J. G. Anderson: Frequency Domain Inversion of Strong Motion Records from the September 19, 1985 Michoacán, Mexico Earthquake

S. K. Singh and F. Mortera: Source Time Functions of Large Mexican Subduction Zone Earthquakes Since 1928, Morphology of the Benloff Zone, and the Extent of the Guerrero Gap

J. S. Barker: Analysis of Teleseismic Long-Period and Broadband Body Waves from the October 18, 1989 Loma Prieta Earthquake

Probing Small-Scale Heterogeneities with Wave Propagation
Presiders: J. Vidale and S. M. Flatté
Thursday AM

S. M. Flatté: Probing Statistical Heterogeneities with Wave Propagation (Invited)

R. S. Wu: Seismic-Wave Propagation through Media with Power-Law Spectra (Invited)

B. L. N. Kennett, M. G. Bostock, G. Nolet, and J. K. Xie: The Interaction of the *S* Wavefield with Upper Mantle Heterogeneity (Invited)

Probing Small-Scale Heterogeneities with Wave Propagation
Presiders: J. Vidale and S. M. Flatté
Thursday AM

X. F. Chen and K. Aki: Seismic Mapping of Deep Discontinuity Topography by the *T*-Matrix Method. Part II. Toroidal Case

R. E. Reinke, K. R. Anderson, J. A. Leverette, and G. Y. Baladi: Imaging of Shallow Small-Scale Heterogeneities with Dense Receiver Arrays

D. C. Jepsen and B. L. N. Kennett: Three-Component Array Analysis of Regional Seismograms

J. Xie and B. J. Mitchell: Attenuation of *Lg* and Its Coda in the Basin and Range Province

D. N. Hagedorn and W. L. Nicholson: *Lg* Coda *Q* Estimation Using the Generalized Linear Model

M. S. Craig and L. T. Long: A Discrete-Scatterer Model of the *P* Coda

Peak Ground Motion and Hazard Assessment
Presiders: K. Campbell and M. Niazi
Thursday PM

M. Reichle, M. Huang, T. Cao, R. Darragh, U. Vetter, and A. Shakal: Peak Ground Motion and Spectra for the Loma Prieta Earthquake from CSMIP Strong Motion Records

M. Niazi and Y. Bozorgnia: Vertical to Horizontal PGA Ratios of October 17, 1989, Loma Prieta Earthquake as Compared to Distance Dependent Predictions of SMART1 Data

I. M. Idriss, P. Somerville, and J. Barneich: Influence of Blind Thrust Faults on Estimates of Earthquake Ground Motions in the Los Angeles Basin

K. L. McLaughlin: Maximum-Likelihood Estimation of Strong Motion Attenuation Relationships

R. R. Youngs, F. Makdisi, K. Sadigh, and N. A. Abrahamson: The Case for Magnitude Dependent Dispersion in Peak Ground Acceleration

K. W. Campbell: Preliminary Analysis of Strong Ground Motion from the October 18, 1989, Loma Prieta, California, Earthquake

Strong Motion Site Effects
Presiders: R. Nason and A. Kropp
Thursday PM

M. C. Chapman, G. A. Bollinger, M. S. Sibol, and D. E. Stephenson: Influence of the Coastal Plain Sedimentary Wedge on Strong Ground Motions from the 1886 Charleston, South Carolina, Earthquake

R. Nason: Seismic Shaking along Damage Profiles in the 1989 Loma Prieta Earthquake

A. Kropp, M. Thomas, and M. Scullin: Ground Failure in Downtown Santa Cruz Induced by the Loma Prieta Earthquake

R. Hansen: Comparison of 1906 and 1989 Earthquake Effects in San Francisco

Structure and Composition of the Mantle
Presiders: E. R. Engdahl and H. M. Benz
Thursday PM

J. Revenaugh: Reflection Seismology of the Mantle: Constraints on Composition Heterogeneity and Dynamics (Invited)

B. L. N. Kennett: The Velocity Structure of the Upper Mantle (Invited)

K. M. Toy and J. A. Orcutt: The *P*- and *S*-Wave Velocity Structure of the Lower Mantle (Invited)

E. R. Engdahl: Global Upper Mantle Structure from Well-Constrained Hypocenters of Explosions and Earthquakes

Structure and Composition of the Mantle
Presiders: E. R. Engdahl and H. M. Benz
Thursday PM

V. Z. Ryaboy: Crust-Upper Mantle Structure Beneath IRIS Stations in the USSR

R. P. Meyer, L. Powell, H. M. Meyer, A. Karaman, and X. R. Shih: Teleseismic Shear-Wave Characteristics Along the 2000-Km Traverse in Western North America

H. M. Benz, G. Zandt, and D. Oppenheimer: Seismic Imaging of the Subducting Plate and the Slabless Window beneath Northern California

J. C. VanDecar, R. S. Crosson, and K. C. Creager: Teleseismic Arrivals Recorded Over the Cascadia Subduction Zone: Amplitude Variation and Calibration of the Washington Regional Seismic Network

D. A. Wiens and M. P. Flanagan: Attenuation Structure of a Back Arc Spreading Center from Teleseismic S Phases

A. Rodgers and J. Wahr: Core-Mantle Boundary Topography from ISC Travel Times and Synthetic Tests of Data Noise and Distribution

Earthquake Rupture Process and Fault Zone Heterogeneity
Presiders: S. Beck and H. Houston
Thursday PM

S. Beck and D. H. Christensen: Asperity Distribution along the Aleutian-Alaska Subduction Zone

H. Houston: Rupture Processes of Four Large Subduction Zone Earthquakes: Implications for Heterogeneity of Fault Strength

E. Fukuyama. Source Process of the 1987 Earthquake Off East Chiba Based on Relocated Aftershock Distributions

L. Ruff: Asperities and Earthquake Triggering in Subduction Zones: Discrete Element Modeling

A. J. Michael and D. Eberhart-Phillips: Correlation of Heterogeneity in Seismic Behavior and Seismic Velocities

G. C. Beroza: Observations of Heterogeneous Rupture from Strong Motion Data: Examples from California Earthquakes

Earthquake Rupture Process and Fault Zone Heterogeneity
Presiders: S. Beck and H. Houston
Thursday PM

T. H. Heaton: Self-Healing Pulses of Slip in Earthquake Rupture

S. Hartzell and C. Mendoza: Simultaneous Inversion of Strong Motion Records and Teleseismic *P* Waveforms for Fault Slip and Rupture Times of the 1978 Tabas, Iran Earthquake

W. Thatcher: Fault Slip Heterogeneity and Patterns of Earthquake Recurrence

J. Braunmiller and J. L. Nábělek: The Macquarie Ridge Earthquake of May 23, 1989

K. Satake and H. Kanamori: Tsunami Excitation by a Large Strike-Slip Earthquake: The 1989 Macquarie Ridge Earthquake (*Mw* 8.1)

A. M. Pelayo and D. A. Wiens: Source Parameters of Tsunami Earthquakes: Slow Events within the Accretionary Prism

FRIDAY MORNING, MAY 4, 1990

Seismic Instrumentation and Systems
Presiders: C. R. Hutt and R. L. Nigbor
Friday AM

R. Butler: IRIS Global Seismographic Network

J. C. Fowler: Portable Seismic Acquisition Systems for the 1990s

T. K. Ahern: The Current Status of IRIS Data Management Systems

R. Buland. The U.S. National Seismograph Network—System Integration and Deployment (Invited)

C. E. Johnson: Regional Seismic Networks—Challenges for the Nineties (Invited)

A. Johnston, W. Arabasz, G. Bollinger, J. Filson, R. Herrmann, L. Jones, and W. Benson: The Future of Seismic Networks in the United States

Seismicity
Presiders: K. C. McNally and P. A. Reasenberg
Friday AM

K. C. McNally, Y. Zhou, G. Nelson, A. Velasco, and G. W. Simila: Comparisons of Intermediate Term Precursors for Two Recent California Earthquakes

G. W. Simila, K. C. McNally, E. Nava, M. Protti, J. Yellin, and X. Liu: Early Aftershocks of the October 18, 1989 Earthquake Along the Santa Cruz Mountains Segment of the San Andreas Fault

P. A. Reasenberg: Variations in the Omori Decay Parameter for "Composite Earthquake Clusters" in Central California

L. Knopoff and J. Lomnitz-Adler: Comparison of Percolation and Self-Organization Models of Seismicity (Invited)

J. Adams, R. G. North, R. J. Wetmiller, H. S. Hasegawa, and J. Drysdale: The December 25, 1989, $Ms = 6.2$ Ungava (Quebec) Earthquake: Yet Another M6 Event in the Canadian Craton

R. Du Berger and M. Lamontagne: The Saguenay Earthquake of November 25, 1988: A Strong Event Outside Seismic Source Zones in Eastern Canada

H. S. Hasegawa and J. Adams: Fault-Plane Solutions and Tectonic Implications of Recent Earthquakes Along the Northeastern Passive Margin of Canada

P. Talwani and K. Rajendran: Bad Creek Project: A Field Experiment in Reservoir-Induced Seismicity—Preimpoundment Phase

Seismicity
Presiders: S. M. Jackson and E. Hauksson
Friday AM

S. M. Jackson, G. S. Carpenter, and I. G. Wong: Microearthquake Investigations of the Eastern Snake River Plain, Idaho

P. Johnson, C. M. dePolo, and W. Peppin: The M 4.6 Fish Lake Valley, Nevada, Earthquake January 15, 1990 and the White Mountains Seismic Gap

S. J. Wang and G. W. Simila: Microseismicity of the San Andreas Fault in the Frazier Park, Ft. Tejon Region, California

E. Houksson: The 1933 Long Beach Earthquake and Its Aftershocks

R. L. Kovach: Recent Seismicity of the Northern Dead Sea Transform Fault

J. Shola-Taheri: Re-examination of Seismicity of the Iranian Plateau and Bordering Regions

Imaging and Inversion
Presiders: W. Foxall and D. M. Eberhart-Phillips
Friday AM

J. M. Lees and C. Nicholson: High-Resolution Travel-Time Tomography in the Northern Coachella Valley from Inversion of Aftershock Arrival Times of the 1986 M_L 5.9 North Palm Springs Earthquake

H. Magistrale and H. Kanamori: Inversion of Earthquake P-Wave Travel Times for Three-Dimensional Velocity Structure of Southern California

A. Michelini, W. Foxall, and T. V. McEvilly: Loma Prieta Sequence: Joint Inversion for Three-Dimensional Velocity Structure and Faulting Geometry

J. A. Olson: Seismicity in the Twenty Years Preceding the Loma Prieta Earthquake

D. M. Eberhart-Phillips, A. J. Michael, G. Fuis, and R. Luzitano: Three-Dimensional Crustal Velocity Structure in the Region of the Loma Prieta, California, Earthquake Sequence from Inversion of Local Earthquake and Shot Arrival Times

W. J. Arabasz and G. Atwood: Seismic Instrumentation—A Five-Element, $3M State Initiative for Utah's Earthquake Program

Seismic Instrumentation and Systems
Presiders: C. R. Hutt and R. L. Nigbor
Friday AM

C. R. Hutt and F. E. Followill: Standards for Seismometer Testing: A Progress Report (Invited)

R. L. Nigbor, W. J. Rihn, and E. L. Holbrook: Standardized Testing of Three Different Seismic Sensors (Invited)

P. W. Rodgers: Frequency Limits and Signal-to-Noise Ratios for Electromagnetic Seismometers

R. P. Kromer: Testing Medium and High-Resolution Digitizers for Seismic Applications (Invited)

V. W. Lee: Digitization and Processing of Strong Motion Accelerograms on a Personal Computer

Theory and Modeling
Presiders: M. S. Craig and D. W. Vasco
Friday AM

J. Regan: Hybrid FD-Propagator Matrix Method: Seismograms for Multiple Sources with one FD Calculation

Y. Hisada, S. Yamamoto, and S. Tani: Theoretical Modeling of Love Wave Propagation in Layered Media with a Vertical Discontinuity

D. W. Vasco: Seismic Source Representation in Orthogonal Functions with Applications to Static Displacements in Long Valley Caldera, California and Yellowstone Caldera, Wyoming

W. R. Walter and J. N. Brune: The Spectra of Seismic Radiation from a Tensile Crack

Y. Ben-Zion and K. Aki: The Response of Two Quarter Spaces with Vertical Layers in Between to *SH* Line Sources

M. Wu, C. Kuo, J. W. Rudnicki, and L. M. Keer: Modeling of Coseismic Surface Deformation Using Nonkinematic Approach

C. M. Laudon and F. R. Schult: Parametric Recompression Applied to Local Mine Blast Data

Reflection Seismology
Presiders: L. W. Wolf and C. J. Ammon
Friday AM

L. W. Wolf, J. Cipar, S. Mangino, and S. Dannolfo: Preliminary Interpretation of the 1989 PACE Seismic Refraction and Wide-Angle Reflection Data from the Colorado Plateau, Arizona

S. A. Katz and T. L. Henyey: Poststack Diffraction-Type Migration of the Signal Component of the Wave Field

J. N. Louie: Subsurface Trends of Some Active Southern California Faults

C. J. Ammon and J. Vidale: Seismic Travel-Time Tomography Using Combinatorial Optimization Techniques

P. C. Leary and Y.-G. Li: Amplitude Systematics of Basement Scatterers Observed in Surface Reflection Data from Cajon Pass, California

E. Nyland: Digital Observations of Microseismic Emissions from Thermal Floods of Heavy Oil Deposits

A. Michelini and T. V. McEvilly: Seismic Monitoring of Parkfield: Search for Temporal Variations Through Successive Joint Hypocenter and Velocity Inversion for Fault Zone Properties

W. Foxall, A. Michelini, and T. V. McEvilly: Effects of Three-Dimensional Velocity Structure on Focal Mechanism Solutions of Parkfield Earthquakes

J. M. Lees: Comparison of High-Resolution Tomographic *P*-Wave Inversions at Parkfield and Loma Prieta, California

E. D. Karageorgi, R. W. Clymer, and T. V. McEvilly: Seismic Monitoring at Parkfield: Variations in Controlled-Source Parameters

J. J. Zucca and J. R. Evans: Active High-Resolution Seismic Imaging for *P*-Wave Attenuation Structure at Newberry Volcano, Oregon Cascade Range

Seismic Gaps and Forecasting Large Earthquakes
Presiders: T. R. Toppozada and I. G. Wong
Friday PM

T. R. Toppozada, C. Hallstrom, and D. Ransom: $M \geqq 5.5$ Earthquakes within 100 Km of Parkfield, California

I. G. Wong, D. H. Wright, A. P. Ridley, and D. H. Oppenheimer: Seismicity in the Vicinity of the Rogers Creek, Bennett Valley and Tolay Faults, Northern California

J. C. Savage: Criticism of some Earthquake Forecasts

L. Ponce, L. Granados, D. Comte, and M. Pardo: Seismicity and *Q* Coda Temporal Variation in the Guerrero, Mexico, Seismic Gap: Evidences for a Soon-to-Break Gap?

J. Campos and E. Kausel: The Large 1939 Intraplate Earthquake of Southern Chile

S. Barrientos: Is the Pichllemu-Talcahuano (Chile) Region a Seismic Gap?

Seismotectonics
Presiders: J. C. Pechmann and K. B. Taylor
Friday PM

K. B. Taylor and R. B. Herrmann: Seismotectonics of the Illinois Basin and the Northern Extent of the New Madrid Seismic Zone—Preliminary Results

K. I. Kelson, F. H. Swan, and K. J. Coppersmith: Late Quatemary Faulting Along the Meers and Criner Faults, Southern Oklahoma: Implications for Assessments of Seismic Hazards in the Central and Eastern United States

J. C. Pechmann, S. J. Nava, and W. J. Arabasz: Left-Lateral Shear Beneath the NW Colorado Plateau: The 1988 San Rafael Swell and 1989 South Wasatch Plateau Earthquakes

T. E. Fumal, R. J. Weldon, and D. P. Schwartz: Recurrence of Large Earthquakes Along the San Andreas Fault at Wrightwood, California

Crustal Properties
Presiders: T.-L. Teng and L. K. Steck
Friday PM

P. S. Armand and G. W. Simila: Layered Crustal Velocity Model and Station Correction Analysis for the Northeastern Los Angeles Basin

R. C. Aster, P. M. Shearer, F. L. Vernon, and J. Berger: Seismic Polarizations Observed with Borehole Instruments in the Anza Seismic Gap

L. K. Steck and W. A. Prothero: Modeling Crustal Structure at Long Valley Caldera Using Three-Dimensional Ray Tracing of Teleseismic *P* Waves

J. M. Lee and S. S. Alexander: Combined Effects of Rock Fabric and Stress-Related Aligned Fractures on Observed In Situ Seismic Anisotropy

T.-L. Teng: Fault Zone Trapped Modes

Y.-G. Li and P. Leary: Fault Zone Trapped Waves Observed in a Near-Fault Borehole Seismometer at Parkfield, California

The Lithosphere and Crust
Presiders: S. Myers and S. K. Koyanagi
Friday PM

S. Myers and T. Wallace: Analysis of the Regional Distance Body Waves from the 1986 Chalfant Valley Earthquake Sequence

W. V. Green and R. P. Meyer: Data Report, 14-Site Two-Dimensional Portable Three-Component Array, Kenya

F. T. Wu and Z. M. Ke: Regionalization of Surface Wave Group Velocities Across China

N. N. Biswas, S. K. Koyanagi, V Ferranzzini, and K. Aki: Propagation of *T*-Phase Across the Island of Hawaii from Loma Prieta Earthquake

Bulletin of the Seismological Society of America, Vol. 80, No. 6, pp. 2298–2300, December 1990

REPORT OF THE SECRETARY AND ACTIONS OF THE EXECUTIVE COMMITTEE FOR THE PERIOD MARCH 11, 1989 TO APRIL 10, 1990

During the Society fiscal year ending January 31, 1990, the SSA published Volume 79 of the Bulletin comprising Numbers 1 through 6 and 2,060 pages.

The Eighty-fourth Annual Meeting was held April 19–21 in Victoria, British Columbia. The Minutes of the meeting have been printed as pages 2023-2032 of BSSA, Volume 79, Number 6.

An extraordinary meeting of the Board of Directors was held in San Francisco on December 3, 1989 to discuss the status of the Society. Minutes of that meeting will appear in the August 1990 issue of the Bulletin.

Susan Newman, Society Director, and Kathy Rowe, Assistant Director, assisted part time by Dorothy Goldman, continued to conduct the essential daily business of the Society from offices at 201 Plaza Professional Building, in El Cerrito, California.

Expansion of the use of the headquarters computer system continued with the purchase of a larger disc. Dues billing is now automatically posted to the general ledger, allowing better internal controls for auditing purposes. The larger disc also allowed the staff to prepare a membership roster during the peak dues renewal period.

The Executive Committee of the Society, consisting of President John Filson, Vice-President Charles Langston, and Secretary Joe Litehiser, made a number of decisions acting on behalf of the Board of Directors during the preceding year:

Approved a proposal to publish an updated roster of members in *Seismological Research Letters*, Volume 61, Number 1. This issue of *SRL* will be mailed to all SSA and Eastern Section SSA members.

Reviewed and approved format changes in the instructions for submitting abstracts for annual meetings, implementing the decision of the Board of Directors to replace the pre-printed forms with simple format instructions. Decided, in addition, to require SSA membership or SSA member sponsorship for submittal of an abstract.

Agreed to furnish the SSA membership roster to the American Geological Institute to aid AGI's preparation of a master list for all of their Member Societies.

Reviewed, as requested by the Board of Directors at the April 1989 meeting, the progress of discussions with the Cordilleran Section of the Geological Society of America concerning a joint SSA-GSA meeting in San Francisco in 1992, and, based on that review, accepted the GSA invitation and appointed Ivan G. Wong as the SSA Chairperson for the joint meeting.

Accepted an invitation from Shamsher Prakash and the University of Missouri, Rolla, to cosponsor the Second International Conference on Recent Advances in Geotechnical Earthquake Engineering and Soil Dynamics, March 11–15, 1991.

Accepted an invitation from Roger Borcherdt, Haresh Shah, and the Earthquake Engineering Research Institute to cosponsor the Fourth International Conference on Seismic Zonation to take place at Stanford University, August 26–29, 1991.

Accepted an invitation from the California Governor's Board of Inquiry on the Loma Prieta Earthquake to provide testimony on the implications of the earthquake and the expectations for future earthquakes, both in the San Francisco Bay Area and in Southern California. The text of this testimony is included.

Acting on the guidance of the Board, awarded the Society Medal to Leon Knopoff, who will receive it at the annual luncheon in Santa Cruz, California, on May 3, 1990.

The Nominating Committee for candidates for the 1990 Board of Directors Election consisted of: Robert B. Herrmann (Chairman), Hiroo Kanamori, Robin McGuire, Robert Sharp, and Francis Wu. The members of the Board of Election were: Robert A. Uhrhammer (Chairman), Shyh-Jeng Chiou, Richard W. Clymer, Eleni D. Karageorgi, and Don W. Vasco.

Abstracts for the 1990 Annual Meeting will appear in *Seismological Research Letters* to be mailed to members before the meeting.

Donations from members for the Minority Participation Program totaled $647.

The following computer counts of members and subscribers as of January 31, 1990 show:

Regular, Student, Life, Honorary, Emeritus	1,650
Corporate	15
Subscriptions (includes multiple copies sent to 908 subscribers)	965
Total	2,630

The total reported last year was 2,678.

JOE J. LITEHISER, JR.
Secretary

STATEMENT ON BEHALF OF THE SEISMOLOGICAL SOCIETY OF AMERICA BEFORE THE GOVERNOR'S BOARD OF INQUIRY ON THE LOMA PRIETA EARTHQUAKE

JANUARY 4, 1990

It is a pleasure and an honor to be here today to address this Board of Inquiry on the Loma Prieta earthquake. The Seismological Society of America, which I represent on behalf of its Executive Committee, was founded in 1906 shortly after the Great San Francisco earthquake of that year, "For the acquisition and diffusion of knowledge concerning earthquakes and allied phenomena, and to enlist the support of the people and government in the attainment of those ends." I need not say much to this Board about the Society because most of you are Society members of long standing and several have held Society office. Suffice to say that we are a small society and our primary activities are, by long tradition, publishing a journal and holding an annual meeting on important seismological research. We do not compete for government funding, we do not conduct or support independent research, and we do not carry out reviews or special studies. Thus, my comments today will be of a general nature and not the result of any independent or formal assessment or review.

The earthquake of October 17, 1989, was a sharp reminder that major cities in California lie on or near geological faults capable of releasing enormous energy. This energy can rupture the ground surface, trigger landslides, and cause other types of ground failures, and transmit potentially damaging levels of shaking to places far from the immediate region of the earthquakes focus. In his primitive state, before he took the trouble to build heavy structures over his head, Man was little endangered by the effects of earthquakes. In our modern society, however, with densely developed population centers consisting of buildings of many types and designs that are laced together with sophisticated and complex infrastructures of transportation, communication, and energy, these effects can be devastating.

The source of the energy periodically released in earthquakes is the latent heat of the Earth. In California, this latent heat drives large plates, of continental dimensions and extending from the Earth's surface to depths of over one hundred miles, past each other. The relative motion between these tectonic plates is slow, being measured in inches per year, but it is irresistible and persistent. At the plates boundaries, this relative motion is often seen not as a smooth continuous sliding but as intermittent sudden slip during damaging earthquakes of strain accumulated over decades or centuries. When the rocks break, the result is an earthquake. This, roughly, is the process that transfers the heat generated when the Earth formed to the ground shaking during an earthquake. The point in reviewing these very basic concepts is to emphasize the fact that these processes, the energy source in the heat of the Earth's interior, the motions and geometries of the plates, are, when measured in terms of centuries or millennia, unyielding and immutable. On any time scale for which we can reasonably plan, these processes have always been, are, and will always be, inevitable.

On the positive side, because these motions and geometries are unchanging and, to some degree, observable, earthquake occurrences and effects are somewhat repeatable and characteristic. The San Andreas fault system, which runs through California and which is the boundary between the Pacific and North American plates, is probably the most well-mapped and well-studied fault system in the world. The motion between the two plates is about 2 inches per year. It is now recognized that "how" and

"where" the strain accumulated due to this motion is relieved varies along the fault system. In some areas, such as west of the San Joaquin Valley, the system is relatively narrow with few major ancillary faults. In southern California and the San Francisco Bay Area, it forks into major segments that are each capable of producing major earthquakes. In some areas along the fault system, the relative motion is released by slow creep accompanied by numerous small earthquakes; in others, rupture is during very large earthquakes such as the Fort Tejon earthquake of 1857 and the 1906 San Francisco earthquake.

Given that the fundamental driving forces are not going to change and that we now have a rudimentary knowledge of where characteristic fault segments are and how they behave based on empirical field observation and the history of past earthquakes, it is possible to make forecasts on the size, location, and rough timing of large earthquakes on the various segments of the fault system. Several attempts of this kind now appear in the literature (for example, Sykes and Nishenko, 1984; Wesnousky, 1986). The most recent study of this problem was carried out by a Working Group of the National Earthquake Prediction Evaluation Council (NEPEC) and published in a U.S. Geological Report entitled, "Probabilities of Large Earthquakes Occurring in California on the San Andreas Fault." Probabilities of earthquakes of magnitude 7 or greater during the next thirty years on some seventeen segments of the San Andreas fault system were estimated along with a measure of the reliability of the estimate. On fourteen of the seventeen segments, the Working Group assigned a probability of 0.1 or greater for a large earthquake occurring during the next thirty years. More importantly, perhaps, is the probability of occurrence of a large earthquake on one of the several fault segments in a given area such as the San Francisco Bay area or along the southern San Andreas fault. The report concludes that during the thirty-year period, beginning in 1988, there is a 0.5 and 0.6 probability, respectively, of occurrence of a magnitude 7 or greater earthquake in these areas.

These precise fault characterizations and the probabilities derived from them are imperfect and contain uncertainty as is indicated by the variety of results in the several studies noted. Nevertheless, the general conclusion that can be drawn from any of these studies is clear. In our opinion, a catastrophic event in the next thirty years or less with a one-in-ten chance or greater of occurring is one that is significant to the public safety. We conclude, therefore, that there is a significant and increasing probability of a major damaging earthquake occurring near large population centers in central and southern California within the next thirty years or less.

The question arises concerning the implications of the Loma Prieta earthquake on future earthquakes in the Bay Area. The situation is not an easy one to assess, and we understand that it is under study by an extension of the same NEPEC Working Group that made the original study. Until the results of this new study are published, we can assume that the chances are very low during the next few decades of a magnitude 7 earthquake on the segment of the San Andreas fault that broke near Loma Prieta last October. However, the chances of a large earthquake on the segments of the fault just north of Loma Prieta or on segments in the East Bay are unchanged or may be increased. The original Working Group estimated the probability of a magnitude 7 earthquake on any of these segments to be 0.2 over the next thirty years. Under the assumptions of the Working Group study, the probability of a magnitude 7 earthquake on at least one of these faults in the same period is still about 0.5.

The problem of estimating seismic hazard over a specific time interval at a specific site is complex. It involves not only the probabilities of individual fault segments breaking, but also must consider the effect of smaller earthquakes not well-constrained to large, well-studied faults, the efficiency of transmission of seismic waves in the Earth's crust, and the geological conditions at the local site. Members of the Seismological Society of America have made significant contributions to the understanding of these phenomena and the solution of this problem over the past eighty-four years. Yet, we cannot give precise answers to the public about when the next "big one" will occur. In our view, policy cannot wait for such answers.

Hard-won experience tells us that some types of structures are more susceptible to damage than others and that some places are more susceptible to local shaking amplification and foundation failure than others, and that these structures and places will surely have problems in future earthquakes. Major population centers in the Bay Area and southern California lie astride or near segments of an active fault system, each of which is capable of producing a magnitude 7 earthquake at any time. In mitigating earthquake hazards in such an active area—through land use planning, strengthening of weak structures, and in designing and construction of important facilities and lifelines—it makes little difference whether the estimation of probability of earthquake occurrence is 0.1 or 0.2 over five or thirty years. The essential message in these statements is that serious earthquakes affecting these centers, as great as or greater than the Loma Prieta event, could occur any day.

Bulletin of the Seismological Society of America, Vol. 80, No. 6, pp. 2301–2307, December 1990

SEISMOLOGICAL SOCIETY OF AMERICA
FINANCIAL STATEMENTS
JANUARY 31, 1990 AND 1989

To the Board of Directors
The Seismological Society of America

We have audited the accompanying statement of assets, liabilities, and fund balances of the Seismological Society of America as of January 31, 1990 and 1989, and the related statements of revenues, expenses, and changes in fund balances and cash flows for the years then ended. These financial statements are the responsibility of the Society's management. Our responsibility is to express an opinion on these financial statements based on our audits.

We conducted our audits in accordance with generally accepted auditing standards. Those standards require that we plan and perform the audit to obtain reasonable assurance about whether the financial statements are free of material misstatement. An audit includes examining, on a test basis, evidence supporting the amounts and disclosures in the financial statements. An audit also includes assessing the accounting principles used and significant estimates made by management, as well as evaluating the overall financial statement presentation. We believe that our audits provide a reasonable basis for our opinion.

In our opinion, the financial statements referred to above present fairly, in all material respects, the financial position of the Seismological Society of America as of January 31, 1990 and 1989 and the results of its operations and its cash flows for the years then ended, in conformity with generally accepted accounting principles.

Our examinations were made for the purpose of forming an opinion on the basic financial statements taken as a whole. The schedules of revenues and expenses are presented for purposes of additional analysis and are not a required part of the basic financial statements. The information in these schedules has been subjected to the auditing procedures applied in the examination of the basic financial statements and, in our opinion, is fairly stated in all material respects in relation to the basic financial statements taken as a whole.

ADAMS, GRANT, WERNER & CO.
March 14, 1990

STATEMENT OF ASSETS, LIABILITIES, AND FUND BALANCES

Years Ended January 31, 1990 and 1989

	1990			
	General Funds	Restricted Funds	Total	1989 Total
ASSETS				
Cash-checking	$ 4,816		$ 4,816	$ 2,190
Savings and money market funds	219,098	$37,981	257,079	226,513
Accounts receivable:				
Page charges	44,651		44,651	40,319
Deposit-rent	910		910	910
Investments (Note 1)		11,592	11,592	10,381
Fixed assets, net of accumulated depreciation of $25,757 for 1990 and $16,853 for 1989	9,241		9,241	18,145
Total assets	$278,716	$49,573	$328,289	$298,458
LIABILITIES AND FUND BALANCES				
Accounts payable	$ 30,023		$ 30,023	$ 23,420
Deferred page charges	3,735		3,735	3,735
Deferred rent reimbursement (Note 1)	2,763		2,763	6,080
Funds held for others (Note 2)	30,135		30,135	12,843
Advance postage (Note 1)	2,191		2,191	1,524
Accrued vacation (Note 1)	4,027		4,027	11,684
Total liabilities	72,874		72,874	59,286
Fund balances	205,842	$49,573	255,415	239,172
Total liabilities and fund balances	$278,716	$49,573	$328,289	$298,458

STATEMENT OF REVENUES, EXPENSES, AND CHANGES IN FUND BALANCES

Years Ended January 31, 1990 and 1989

	1990			
	General Funds	Restricted Funds	Total	1989 Total
	REVENUES			
Dues	$101,834		$101,834	$ 94,150
Publications	270,938		270,938	259,288
Annual meetings	35,987		35,987	46,190
Interest and dividends	12,304	$ 4,157	16,461	10,858
Other	8,993		8,993	8,514
Total revenues	430,056	4,157	434,213	419,000
	EXPENSES			
Staff services	62,430		62,430	60,751
Publication, production, and distribution	244,226		244,226	209,448
Annual meetings	35,401		35,401	36,526
Other operating expenses	75,913		75,913	66,585
Total expenses	417,970		417,970	373,310
Excess of revenues over expenses	12,086	4,157	16,243	45,690
Fund balances, beginning of year	193,756	45,416	239,172	193,482
Fund balances, end of year	$205,842	$49,573	$255,415	$239,172

STATEMENT OF CASH FLOWS

Years Ended January 31, 1990 and 1989

	1990	1989
Cash flows from operating activities:		
Net income	$ 16,243	$ 45,690
Adjustments to reconcile net income to cash provided by operating activities:		
Depreciation expense which does not require an outlay of cash	8,904	8,904
Decrease (increase) in accounts receivable	(4,332)	22,658
Increase (decrease) in accounts payable	6,603	(17,554)
Increase (decrease) in deferred revenue	(3,317)	(3,316)
Increase in other liabilities	10,302	4,661
Total adjustments	18,160	15,353
Net cash provided from operating activities:	34,403	61,043
Cash flows from investing activities:		
Capital gains reinvested	1,211	2,030
Net cash used in investing activities	1,211	2,030
Net increase in cash	33,192	59,013
Beginning cash balance	228,703	169,690
Ending cash balance	$261,895	$228,703

NOTES TO FINANCIAL STATEMENTS

Years Ended January 31, 1990 and 1989

NOTE 1: SUMMARY OF SIGNIFICANT ACCOUNTING POLICIES

The Seismological Society of America (the Society) is a nonprofit organization dedicated to the advancement of the science and practice of seismology and related sciences. An organization, the Eastern Section of the Seismological Society of America, is a separate legal entity and is not included in these financial statements.

Basis of Accounting

The financial statements are presented on the accrual basis of accounting, under which revenues are recognized when services are performed and expenses are recognized when goods and services are received, except for dues and subscriptions income that is recorded on the cash basis. The effect of this departure from accrual accounting is not material to the financial statements, as membership is generally stable from year to year.

Fixed Assets

Fixed assets with a cost of $500 or more and expected life exceeding one year, are capitalized and depreciated over their estimated lives by the straight-line method. Estimated lives of fixed assets range from two to five years.

Short-Term Investments

The Society's short-term investments are carried at cost. The market value of these investments as of January 31, 1990 was $16,766.

Deferred Rent Reimbursement

Until January 1, 1988, the Society shared a joint headquarters with the Earthquake Engineering Research Institute (EERI). By mutual agreement, the two organizations decided to operate separately as of January 1, 1988.

Upon relocation of the Society from shared office space with EERI, EERI reimbursed the Society $9,672 for additional lease cost to be incurred by the Society. This reimbursement is being amortized over 35 months, the remaining life of the shared lease at January 1, 1988.

Advance Postage

This represents funds paid in advance by members who request that their issues be mailed other than by regular mail.

Accrued Vacation

The Society accrues a maximum vacation pay liability at 160 hours for each employee.

Income Taxes

The Society is exempt from Federal income taxes under Section 501(c)(3) of the Internal Revenue Code and is exempt from California franchise taxes under Section 23701d of the Revenue and Taxation Code. During the year under examination, none of the activities of the Society were considered unrelated to its exempt purpose.

NOTE 2: FUNDS HELD FOR OTHERS

For the convenience of its members and by agreement with each organization, the Society collects the dues, contributions, and other payments due to the Eastern Section of the Seismological Society of America, the American Geological Institute (AGI), the Minority Opportunity Program (MOP) of AGI, and the International Association of Seismology and Physics of the Earth's Interior (IASPEI).

NOTE 3: LEASING ARRANGEMENTS

The Society conducts its operations from facilities that are leased under a five-year operating lease expiring January 31, 1993. The future minimum rental payments required are $10,919 per year and $910 for the month ending January 31, 1993. The lease provides for increases on February 1, of each year of its term in accordance with changes in the consumer price index.

NOTE 4: EMPLOYEE BENEFITS

For the years ended January 31, 1990 and 1989, the Society contributed a maximum of 14% of each employee's salary to its employee benefit program consisting of health, dental reimbursement, and retirement plans. As a condition of employment, all employees are required, unless alternate coverage is held, to participate in the health insurance program, but each may direct the proportion of the balance, if any, of the employer's contribution of 14% of salary that will be contributed to the voluntary portions of the program. The retirement plan consists of tax-shelter annuities underwritten by the IDS Life Insurance Co., in accordance with Section 403(b) of the Internal Revenue Code.

NOTE 5: RESTRICTED FUNDS

Funds received or designated by the Board of Directors for specific purposes are accounted for separately from those available for the general operations of the Society. The Life Membership Fund, established prior to 1930, represents all moneys received for life memberships for permanent investment, the income from which may be expended at the discretion of the Board.

The Sayles Fund was established in 1911 upon receipt of a gift from Robert Wilcox Sayles (Harvard, A.B., 1901), a member of the Society. All, or any part of the original gift and its accumulated earnings from investment may be used at the discretion of the Board for publishing the *Bulletin of the Seismological Society of America.*

The current balances of these funds are as follows:

	Life Membership Fund		Sayles Fund	Total Restricted Funds
	Accumulated Income	Permanent Investment		
January 31, 1989	$7,841	$9,113	$28,462	$45,416
Capital gains reinvested			1,211	1,211
Interest	1,418		1,528	2,946
January 31, 1990	$9,259	$9,113	$31,201	$49,573

SCHEDULE OF REVENUES

Years Ended January 31, 1990 and 1989

	1990	1989
Dues Income:		
Regular and student members	$ 95,069	$ 85,400
Corporate members	6,500	8,500
Retired members	265	250
Total dues	101,834	94,150
Publications Income:		
Subscriptions	104,701	100,443
Sales of back issues	1,608	3,956
Sales of microforms	4,818	6,710
Page charges	153,108	136,277
Sales of authors' separates	6,703	11,902
Total publications	270,938	259,288
Annual Meetings Income:		
Registration and exhibit fees	30,882	36,780
Abstracts sales and fees	5,105	9,410
Total annual meetings	35,987	46,190
Other Income:		
Interest and dividends	16,461	10,858
Miscellaneous	8,993	8,514
Total other income	25,454	19,372
Total revenues	$434,213	$419,000

SCHEDULE OF EXPENSES

Years Ended January 31, 1990 and 1989

	1990	1989
Salaries and Wages	$ 62,430	$ 60,751
Publication, Production, and Distribution	244,226	209,448
Annual Meetings Expenses:		
Promotion and program costs	25,959	24,069
Printing of abstracts	3,513	5,582
Postage and mailing	3,967	5,891
Office costs	1,962	984
	35,401	36,526
Other Operating Expenses:		
Space costs	16,116	13,066
Equipment costs	18,704	17,611
Office postage and supplies	14,942	11,165
Accounting, mailing, and other services	17,809	15,784
Bad debt expense	3,868	4,086
Travel expenses	681	2,246
Miscellaneous	3,793	2,627
	75,913	66,585
Total expenses	$417,970	$373,310

Bulletin of the Seismological Society of America, Vo. 80, No. 6, pp. 2308–2325, December 1990

INDEX TO VOLUME 80

Compiled by David M. Boore

Earthquakes, Notes Concerning

CORPORATE MEMBERS, SEISMOLOGICAL SOCIETY OF AMERICA

Bechtel National, Inc.
Scientific Development
P.O. Box 3965
San Francisco, California 94119

Chevron Oil Field Research Co.
P.O. Box 446
La Habra, California 90631

Dames & Moore
Neville Donovan
221 Main Street
Suite 600
San Francisco, California 94105

Digital Technology Associates
Steve Pauly
1330-A Galaxy Way
Concord, California 94520

H. J. Degenkolb Associates
Consulting Structural Engineers
350 Sansome Street
San Francisco, California 94104

EQE, Incorporated
Peter I. Yanev, Chairman
595 Market Street
18th Floor
San Francisco, California 94105

Exxon Production Research Company
P. M. Shah
P.O. Box 2189
Houston, Texas 77001

Kinemetrics, Inc.
Robert J. Swain, President
222 Vista Avenue
Pasadena, California 91107

L.A. Department of Water and Power
S. Matsuda
P.O. Box 111, Terminal Annex
Los Angeles, California 90054

Pacific Gas and Electric Company
Lloyd S. Cluff
Geosciences Department
215 Market Street, Room 768
San Francisco, California 94106

Science Horizons, Inc.
710 Encinitas Blvd.
Suite 200
Encinitas, California 92024

Sprengnether Instruments, Inc.
4150 Laclede Avenue
Saint Louis, Missouri 63108

Teledyne Geotech Geosciences Group
P.O. Box 409007
Garland, Texas 75046

Western Geophysical Company
Damir Skerl, Senior Vice President, Technology
P.O. Box 2469
Houston, Texas 77001

Woodward Clyde Consultants
John Bisch ff
500 12th Street, Ste. 100
Oakland, California 94607